

# 中草藥研究中心

2018 年 9 月 1 日~2019 年 8 月 31 日

## 論文集(中)



CHANG GUNG UNIVERSITY OF SCIENCE AND TECHNOLOGY



長庚科技大學  
中草藥研究中心  
2018年9月1日~2019年8月31日  
論文集  
目 錄

(中冊)

序號	期刊論文	學校主要 負責教師	頁碼
41.	Lin, Y. H.; Wu, M. H.; Yeh, C. T.; Lin, K. H. Long Non-Coding RNAs as Mediators of Tumor Microenvironment and Liver Cancer Cell Communication. <i>Int J Mol Sci</i> 19, pii: E3742; 2018. DOI: 10.3390/ijms19123742.	林光輝	508
42.	Liu, C. H.; Liu, Y. X.; Wu, W. C. Facile development of medium optimization for antibody production: implementation in spinner flask and hollow fiber reactor. <i>Cytotechnology</i> 70:1631-1642; 2018. DOI: 10.1007/s10616-018-0255-z.	劉繼賢	529
43.	Huang, W. C.; Chen, Y. L.; Liu, H. C.; Wu, S. J.; Liou, C. J. Ginkgolide C reduced oleic acid-induced lipid accumulation in HepG2 cells. <i>Saudi Pharm J</i> 26:1178-1184; 2018. DOI: 10.1016/j.jsps.2018.07.006.	黃文忠、 吳淑如、 劉倩君	541
44.	Kumari, M.; Liu, C. H.; Wu, W. C. Protein moiety in oligochitosan modified vector regulates internalization mechanism and gene delivery: Polyplex characterization, intracellular trafficking and transfection. <i>Carbohydr Polym</i> 202:143-156; 2018. DOI: 10.1016/j.carbpol.2018.08.131.	劉繼賢	548
45.	Huang, P. C.; Lin, W. S.; Peng, B. R.; Chang, Y. C.; Fang, L. S.; Li, G. Q.; Hwang, T. L.; Wen, Z. H.; Sung, P. J. New Furanocembranoids from <i>Briareum violaceum</i> . <i>Mar Drugs</i> 17, pii: E214; 2019. DOI: 10.3390/md17040214.	張祐嘉、 黃聰龍	562
46.	Chen, C. Y.; Wu, S. M.; Lin, Y. H.; Chi, H. C.; Lin, S. L.; Yeh, C. T.; Chuang, W. Y.; Lin, K. H. Induction of nuclear protein-1 by thyroid hormone enhances platelet-derived growth factor A mediated angiogenesis in liver cancer. <i>Theranostics</i> 9:2361-2379; 2019. DOI: 10.7150/thno.29628.	林光輝	571
47.	Chang, C. C.; Sia, K. C.; Chang, J. F.; Lin, C. M.; Yang, C. M.; Huang, K. Y.; Lin, W. N. Lipopolysaccharide promoted proliferation and adipogenesis of preadipocytes through JAK/STAT and AMPK-regulated cPLA2 expression. <i>Int J Med Sci</i> 16:167-179; 2019. DOI: 10.7150/ijms.24068.	楊春茂	590
48.	Abdelaziz, H. M.; Elzoghby, A. O.; Helmy, M. W.; Samaha, M. W.; Fang, J. Y.; Freag, M. S. Liquid crystalline assembly for potential combinatorial chemo-herbal drug delivery to lung cancer cells. <i>Int J Nanomedicine</i> 14:499-517; 2019. DOI: 10.2147/IJN.S188335.	方嘉佑	603



49. Yang, S. C.; Tang, K. W.; Lin, C. H.; Alalaiwe, A.; Tseng, C. H.; Fang, J. Y. Discovery of Furanquinone Derivatives as a Novel Class of DNA Polymerase and Gyrase Inhibitors for MRSA Eradication in Cutaneous Infection. *Front Microbiol* 10:1197; 2019. DOI: 10.3389/fmicb.2019.01197. 方嘉佑 622
50. Huang, W. S.; Huang, C. Y.; Hsieh, M. C.; Kuo, Y. H.; Tung, S. Y.; Shen, C. H.; Hsieh, Y. Y.; Teng, C. C.; Lee, K. C.; Lee, K. F.; Kuo, H. C. Expression of PRDX6 Correlates with Migration and Invasiveness of Colorectal Cancer Cells. *Cell Physiol Biochem* 51:2616-2630; 2018. DOI: 10.1159/000495934. 郭星君 639
51. Lin, C. C.; Su, J. H.; Chen, W. F.; Wen, Z. H.; Peng, B. R.; Huang, L. C.; Hwang, T. L.; Sung, P. J. New 11,20-Epoxybriaranes from the Gorgonian Coral *Junceella fragilis* (Ellisellidae). *Molecules* 24, pii: E2487; 2019. DOI: 10.3390/molecules24132487. 黃聰龍 654
52. Lin, Y. C.; Chao, C. H.; Ahmed, A.F.; Chen, Y. Y.; Hwang, T. L.; Liu, H. Y.; Sheu, J. H. Withanolides and 26-hydroxylated derivatives with anti-inflammatory property from *solanum capsicoide*. *Bulletin of the Chemical Society of Japan*: 336-343; 2019. DOI: 10.1246/bcsj.20180225. 黃聰龍 662
53. Wang, P. W.; Cheng, Y. C.; Hung, Y. C.; Lee, C. H.; Fang, J. Y.; Li, W. T.; Wu, Y. R.; Pan, T. L. Red Raspberry Extract Protects the Skin against UVB-Induced Damage with Antioxidative and Anti-inflammatory Properties. *Oxid Med Cell Longev* 2019:9529676; 2019. DOI: 10.1155/2019/9529676. 方嘉佑、潘台龍 670
54. Liou, C. J.; Yang, C. M.; Lee, T. H.; Liu, P. S.; Hsieh, H. L. Neuroprotective Effects of Dehydroepiandrosterone Sulfate Through Inhibiting Expression of Matrix Metalloproteinase-9 from Bradykinin-Challenged Astroglia. *Mol Neurobiol* 56:736-747; 2019. DOI: 10.1007/s12035-018-1125-6. 劉倩君、楊春茂、謝喜龍 685
55. Hsu, C. Y.; Wang, P. W.; Alalaiwe, A.; Lin, Z. C.; Fang, J. Y. Use of Lipid Nanocarriers to Improve Oral Delivery of Vitamins. *Nutrients* 11, pii: E68; 2019. DOI: 10.3390/nu11010068. 許青雲、方嘉佑 697
56. Peng, K. T.; Chiang, Y. C.; Huang, T. Y.; Chen, P. C.; Chang, P. J.; Lee, C. W. Curcumin nanoparticles are a promising anti-bacterial and anti-inflammatory agent for treating periprosthetic joint infections. *Int J Nanomedicine* 14:469-481; 2019. DOI: 10.2147/IJN.S191504. 李江文 727
57. Huang, Y. H.; Kuo, H. C.; Yang, Y. L.; Wang, F. S. MicroRNA-29a is a key regulon that regulates BRD4 and mitigates liver fibrosis in mice by inhibiting hepatic stellate cell activation. *Int J Med Sci* 16:212-220; 2019. DOI: 10.7150/ijms.29930. 郭星君 740
58. Lee, I. T.; Lin, C. F.; Huang, Y. L.; Chong, K. Y.; Hsieh, M. F.; Huang, T. H.; Cheng, C. Y. Protective mechanisms of resveratrol derivatives against TNF-alpha-induced inflammatory responses in rat mesangial cells. *Cytokine* 113:380-392; 2019. DOI: 10.1016/j.cyto.2018.10.008. 林傳福、鄭靜宜 749
59. Tsai, Y. F.; Yang, S. C.; Chang, W. Y.; Chen, J. J.; Chen, C. Y.; Chang, S. H.; Hwang, T. L. *Garcinia Multiflora* Inhibits FPR1- 黃聰龍 762



- Mediated Neutrophil Activation and Protects Against Acute Lung Injury. *Cell Physiol Biochem* 51:2776-2793; 2018. DOI: 10.1159/000495970.
60. Wang, I. L.; Hsiao, C. Y.; Li, Y. H.; Meng, F. B.; Huang, C. C.; Chen, Y. M. Nanobubbles Water Curcumin Extract Reduces Injury Risks on Drop Jumps in Women: A Pilot Study. *Evid Based Complement Alternat Med* 2019:8647587; 2019. DOI: 10.1155/2019/8647587. 蕭千祐 780
  61. Chen, Y. M.; Huang, C. C.; Hsiao, C. Y.; Hu, S.; Wang, I. L.; Sung, H. C. *Ludwigia octovalvis* (Jacq.) raven extract supplementation enhances muscle glycogen content and endurance exercise performance in mice. *J Vet Med Sci* 81:667-674; 2019. DOI: 10.1292/jvms.18-0165. 蕭千祐 790
  62. Lam, S. H.; Li, Y. C.; Kuo, P. C.; Hwang, T. L.; Yang, M. L.; Wang, C. C.; Tzen, J. T. C. Chemical Constituents of *Vigna luteola* and Their Anti-inflammatory Bioactivity. *Molecules* 24, pii: E1371; 2019. DOI: 10.3390/molecules24071371. 黃聰龍 798
  63. Tsai, Y. L.; Lin, T. L.; Chang, C. J.; Wu, T. R.; Lai, W. F.; Lu, C. C.; Lai, H. C. Probiotics, prebiotics and amelioration of diseases. *J Biomed Sci* 26:3; 2019. DOI: 10.1186/s12929-018-0493-6. 賴信志 809
  64. Tang, W. F.; Huang, R. T.; Chien, K. Y.; Tang, P.; Horng, J. T. Large-Scale Proteomic Identification of Targets of Cellular miR-197 Downregulated by Enterovirus A71. *J Proteome Res* 18:449-460; 2019. DOI: 10.1021/acs.jproteome.8b00762. 洪錦堂 817
  65. Li, Y. C.; Kuo, P. C.; Yang, M. L.; Chen, T. Y.; Hwang, T. L.; Chiang, C. C.; Thang, T. D.; Tuan, N. N.; Tzen, J. T. C. Chemical Constituents of the Leaves of *Peltophorum pterocarpum* and Their Bioactivity. *Molecules* 24, pii: E240; 2019. DOI: 10.3390/molecules24020240. 黃聰龍 829
  66. Zayed, D. G.; Ebrahim, S. M.; Helmy, M. W.; Khattab, S. N.; Bahey-El-Din, M.; Fang, J. Y.; Elkhodairy, K. A.; Elzoghby, A. O. Combining hydrophilic chemotherapy and hydrophobic phytotherapy via tumor-targeted albumin-QDs nano-hybrids: covalent coupling and phospholipid complexation approaches. *J Nanobiotechnology* 17:7; 2019. DOI: 10.1186/s12951-019-0445-7. 方嘉佑 840
  67. Wu, T. R.; Lin, C. S.; Chang, C. J.; Lin, T. L.; Martel, J.; Ko, Y. F.; Ojcius, D. M.; Lu, C. C.; Young, J. D.; Lai, H. C. Gut commensal *Parabacteroides goldsteinii* plays a predominant role in the anti-obesity effects of polysaccharides isolated from *Hirsutiella sinensis*. *Gut* 68:248-262; 2019. DOI: 10.1136/gutjnl-2017-315458. 賴信志 859
  68. Woodman, A.; Lee, K. M.; Janissen, R.; Gong, Y. N.; Dekker, N. H.; Shih, S. R.; Cameron, C. E. Predicting Intraserotypic Recombination in Enterovirus 71. *J Virol* 93, pii: e02057-18; 2019. DOI: 10.1128/JVI.02057-18. 施信如 873
  69. Wei, H. T.; Pan, T. L.; Hsu, J. W.; Huang, K. L.; Bai, Y. M.; Ko, N. Y.; Su, T. P.; Li, C. T.; Tsai, S. J.; Lin, W. C.; Chen, T. J.; Chen, M. H. Risks of bipolar disorder, depressive disorder, and traumatic brain injury among siblings of patients with attention-



deficit hyperactivity disorder. *J Affect Disord* 245:335-339; 2019. DOI: 10.1016/j.jad.2018.11.057.


- |     |  |             |     |
|-----|--|-------------|-----|
| 70. | Lin, Y. H.; Chang, H. Y.; Wu, C. C.; Wu, C. W.; Chang, K. P.; Yu, J. S. BRAF protein immunoprecipitation, elution, and digestion from cell extract using a microfluidic mixer for mutant BRAF protein quantification by mass spectrometry. <i>Anal Bioanal Chem</i> 411:1085-1094; 2019. DOI: 10.1007/s00216-018-1536-2. | 余兆松         | 893 |
| 71. | Fang, J. Y.; Lin, C. H.; Huang, T. H.; Chuang, S. Y. In Vivo Rodent Models of Type 2 Diabetes and Their Usefulness for Evaluating Flavonoid Bioactivity. <i>Nutrients</i> 11, pii: E530; 2019. DOI: 10.3390/nu11030530.  | 方嘉佑、<br>林志鴻 | 903 |
| 72. | Anilkumar, T.S.; Lu, Y. J.; Chen, H. A.; Hsu, H. L.; Jose, G.; Chen, J. P. Dual targeted magnetic photosensitive liposomes for photothermal/photodynamic tumor therapy. <i>Journal of Magnetism and Magnetic Materials</i> 473:241-252; 2019. DOI: 10.1016/j.jmmm.2018.10.020.   | 陳志平         | 926 |
| 73. | Wang, T. H.; Chen, C. C.; Hsiao, Y. C.; Lin, Y. H.; Pi, W. C.; Huang, P. R.; Wang, T. V.; Chen, C. Y. Heterogeneous Nuclear Ribonucleoproteins A1 and A2 Function in Telomerase-Dependent Maintenance of Telomeres. <i>Cancers (Basel)</i> 11, pii: E334; 2019. DOI: 10.3390/cancers11030334.                            | 陳琦媛         | 938 |
| 74. | Chang, Y.; Hsieh, H. L.; Huang, S. K.; Wang, S. J. Neurosteroid allopregnanolone inhibits glutamate release from rat cerebrocortical nerve terminals. <i>Synapse</i> 73:e22076; 2019. DOI: 10.1002/syn.22076.  | 謝喜龍、<br>王素珍 | 954 |
| 75. | Yang, Y. L.; Kuo, H. C.; Wang, F. S.; Huang, Y. H. MicroRNA-29a Disrupts DNMT3b to Ameliorate Diet-Induced Non-Alcoholic Steatohepatitis in Mice. <i>Int J Mol Sci</i> 20, pii: E1499; 2019. DOI: 10.3390/ijms20061499.  | 郭星君         | 965 |





Review

# Long Non-Coding RNAs as Mediators of Tumor Microenvironment and Liver Cancer Cell Communication

Yang-Hsiang Lin <sup>1,2</sup>, Meng-Han Wu <sup>1</sup>, Chau-Ting Yeh <sup>2</sup> and Kwang-Huei Lin <sup>1,2,3,\*</sup> 

<sup>1</sup> Department of Biochemistry, College of Medicine, Chang Gung University, Taoyuan 333, Taiwan; yhlin0621@cgmh.org.tw (Y.-H.L.); snoopy740621@yahoo.com.tw (M.-H.W.)

<sup>2</sup> Liver Research Center, Chang Gung Memorial Hospital, Linkou, Taoyuan 333, Taiwan; chaoting@cgmh.org.tw

<sup>3</sup> Research Center for Chinese Herbal Medicine, College of Human Ecology, Chang Gung University of Science and Technology, Taoyuan 333, Taiwan

\* Correspondence: khlin@mail.cgu.edu.tw; Tel./Fax: +886-3-2118263

Received: 17 October 2018; Accepted: 21 November 2018; Published: 24 November 2018



**Abstract:** The tumor microenvironment is an important concept that defines cancer development not only through tumor cells themselves but also the surrounding cellular and non-cellular components, including stromal cells, blood vessels, infiltrating inflammatory cells, cancer stem cells (CSC), cytokines, and growth factors, which act in concert to promote tumor cell survival and metastasis. Hepatocellular carcinoma (HCC) is one of the most common and aggressive human malignancies worldwide. Poor prognosis is largely attributable to the high rate of tumor metastasis, highlighting the importance of identifying patients at risk in advance and developing novel therapeutic targets to facilitate effective intervention. Long non-coding RNAs (lncRNA) are a class of non-protein coding transcripts longer than 200 nucleotides frequently dysregulated in various cancer types, which have multiple functions in widespread biological processes, including proliferation, apoptosis, metastasis, and metabolism. lncRNAs are involved in regulation of the tumor microenvironment and reciprocal signaling between cancer cells. Targeting of components of the tumor microenvironment or cancer cells has become a considerable focus of therapeutic research and establishing the effects of different lncRNAs on this network should aid in the development of effective treatment strategies. The current review provides a summary of the essential properties and functional roles of known lncRNAs associated with the tumor microenvironment in HCC.

**Keywords:** tumor microenvironment; hepatocellular carcinoma; long non-coding RNA; therapeutic target

## 1. Introduction

The tumor microenvironment is an important concept that defines cancer development not by tumor cells alone but also the surrounding cellular and non-cellular components, including stromal cells, blood vessels, infiltrating inflammatory cells, cancer stem cells (CSC), cytokines, and growth factors, which act together to promote tumor cell survival and metastasis [1]. Stromal cells are recruited and activated in tumor progression, in turn, triggering downstream signals that promote invasion to distant organs. The surrounding environment appears to be a crucial partner for tumor cells and provides several of the hallmark functions necessary for angiogenesis, tumor formation, and metastasis [2]. Targeting of components of the tumor microenvironment or cancer cells is currently a considerable focus of research interest. In particular, angiogenesis and inflammatory pathways are well-characterized targets for inhibition in hepatocellular carcinoma HCC therapy. For instance,

sorafenib, a multiple kinase inhibitor, is one of the most effective suppressors of cell growth and angiogenesis in patients with late-stage HCC.

HCC is among the most common and aggressive human malignancies worldwide. A number of contributory mechanisms to accelerated tumor formation have been proposed to date, including telomere dysfunction and alterations in the microenvironment that induce cell proliferation [3,4]. Another important factor underlying poor prognosis of HCC is the high rate of tumor metastasis. The aggressive nature of the disease highlights the urgent need to identify patients at risk in advance and develop novel targeted agents for successful intervention [5]. Metastasis is a complex process regulated by multiple intrinsic and extrinsic cellular factors. Improved understanding of the associated molecular mechanisms should aid in the development of effective metastasis-targeted therapies and improvement of overall prognosis of patients with HCC [6].

The traditional concept of gene function in molecular biology is the central dogma explaining protein-coding genes (DNA→mRNA→protein). Notably, however, less than 2% of the mammalian genome encodes protein with >90% representing noncoding RNA (ncRNA) [7]. Accumulating evidence has demonstrated the significance of ncRNAs in the regulation of multiple major biological functions controlling development, differentiation, metabolism, cell growth and tumor progression [8]. In general, ncRNAs are classified into two groups based on length, designated small ncRNA and long ncRNA (lncRNA). Small ncRNAs include microRNA (miRNA), transfer RNA (tRNA) and some ribosomal RNA transcripts. MiRNAs are small (~22 nt) non-coding transcripts [9,10] that regulate gene expression at the post-transcriptional or translational level and thereby modulate physiological functions, such as cell growth, migration, invasion, sphere formation and metastasis [11]. Moreover, miRNAs have the ability to regulate hundreds of target genes simultaneously and thus control multiple signaling pathways [12]. Several lines of evidence have demonstrated differential expression of miRNAs, such as miR-155 [13], miR-34a [14] and miR-26 [15], in stromal cells of the tumor microenvironment and their contribution to liver cancer formation.

lncRNAs are a class of non-protein coding transcripts greater than 200 nucleotides in length [16] frequently dysregulated in various cancers, which also play multiple roles in biological processes, such as proliferation, apoptosis, metastasis and metabolism [8,17]. These transcripts regulate gene expression through effects on the production, splicing, decay or translation of target mRNAs. Interestingly, lncRNAs are transcribed from intergenic regions, antisense strands, introns, gene regulatory regions (promoters and enhancers), untranslated regions (UTR) and telomeres [18,19] and form RNA–RNA, RNA–DNA or RNA–protein interactions to perform their specific activities. lncRNAs are reported to function as guide, scaffold, signaling and decoy RNAs [20] (Figure 1). Guide lncRNAs, such as X inactive-specific transcript (Xist) and Hox transcript antisense RNA (HOTAIR), regulate gene expression *in cis* or *in trans* through recruiting chromatin-modifying enzymes to specific genomic regions [21,22]. As scaffold lncRNAs, HOTAIR or metastasis-associated lung adenocarcinoma transcript 1 (MALAT1) recruit multiple proteins to form ribonucleoprotein complexes and modulate gene expression [23]. Several signaling lncRNAs, including HOTAIR and regulator of reprogramming lincRNA (linc-ROR), act as molecular signals and integrate with specific signaling pathways [24] while the decoy lncRNAs, for instance, P21-associated ncRNA DNA damage activated (PANDA) and MALAT1, sequester transcription factors away from chromatin and regulate gene expression. Functional small peptides encoded by lncRNAs have been identified that are involved in cellular functions [25]. Increasing evidence suggests that the stability of lncRNAs is regulated by miRNAs. On the other hand, lncRNAs can act as competing endogenous (ce) RNAs and sequester specific miRNAs away from their target genes, consequently inhibiting miRNA-mediated functions [26]. Interplay patterns between lncRNAs and miRNAs appear to be crucial events in cancer progression. Emerging data support the involvement of lncRNAs in tumor-stroma communication, a potentially important event in cancer progression. Recently, Sang et al. [27] demonstrated that lncRNA for calcium-dependent kinase activation (CamK-A) is upregulated in several cancers and

involved in regulation of the tumor microenvironment through activation of calcium ( $\text{Ca}^{2+}$ )-mediated effects, consequently promoting macrophage recruitment, angiogenesis and cancer progression.

The main objective of this review is to summarize the basic properties and functional roles of the lncRNA-associated tumor microenvironment in HCC. In particular, we have encapsulated current knowledge on the contribution of hypoxia, cytokine- and exosome-modulated lncRNAs to tumor microenvironments that promote angiogenesis, metastasis and drug resistance, with the aim of providing indicators that may serve as future therapeutic markers for various areas of the tumor microenvironment/lncRNAs.

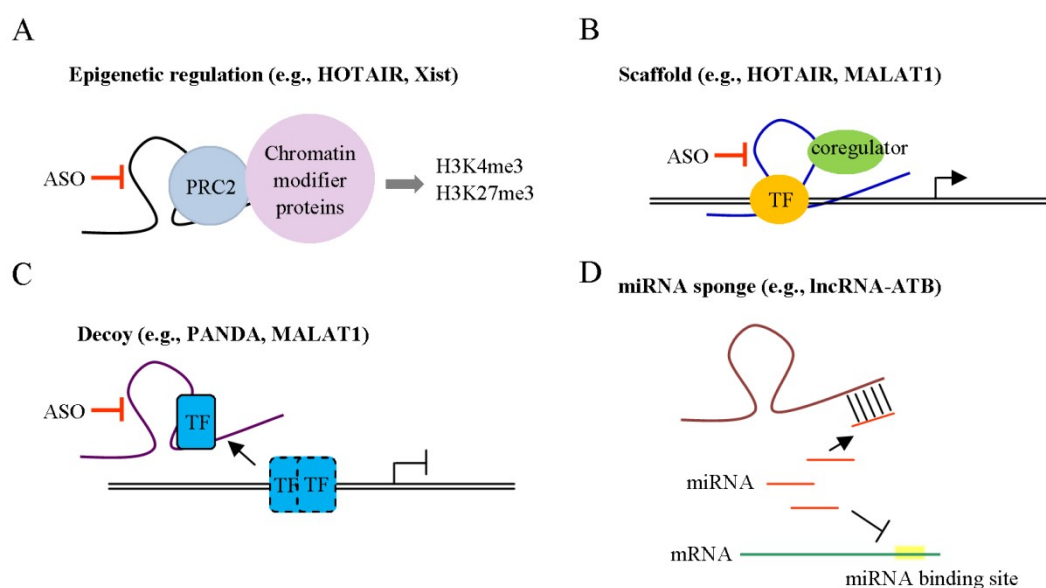


**Figure 1.** Different mechanisms of action of long non-coding RNAs (lncRNAs). lncRNAs mediate functions by regulating gene expression via diverse molecular mechanisms. **(A)** lncRNAs associate with chromatin-modifying complexes to modulate epigenetic modifications. **(B)** lncRNAs interact with transcriptional factors (TF) or coregulators to regulate gene expression. **(C)** lncRNAs sequester TFs away from chromatin to regulate gene expression. **(D)** lncRNAs serve as a sponge and interact with miRNAs to suppress miRNA-mediated effects. Antisense oligonucleotides (ASO) target lncRNAs, which associate with modulators that translocate to the nucleus, potentially providing a mechanism for targeting these pathways.

## 2. Cellular Components of the Tumor Microenvironment

Tumor progression is significantly attributable to surrounding non-tumor cells and non-cellular components secreted from the microenvironment. lncRNA-associated cellular and non-cellular components of the tumor microenvironment in HCC are summarized in Table 1. Cellular components of the tumor microenvironment include cancer-associated fibroblasts (CAF), hepatic stellate cells, tumor-associated macrophages (TAM), endothelial cells, cancer stem cells (CSC), and other immune factors that play crucial roles in inflammation and immunosuppression (Figure 2A) [28,29]. Secreted non-cellular components, including growth factors, cytokines, extracellular matrix proteins and metabolites [30,31], are also crucial in shaping tumor phenotypes and drug responses (Figure 2B). The cellular components are described below.



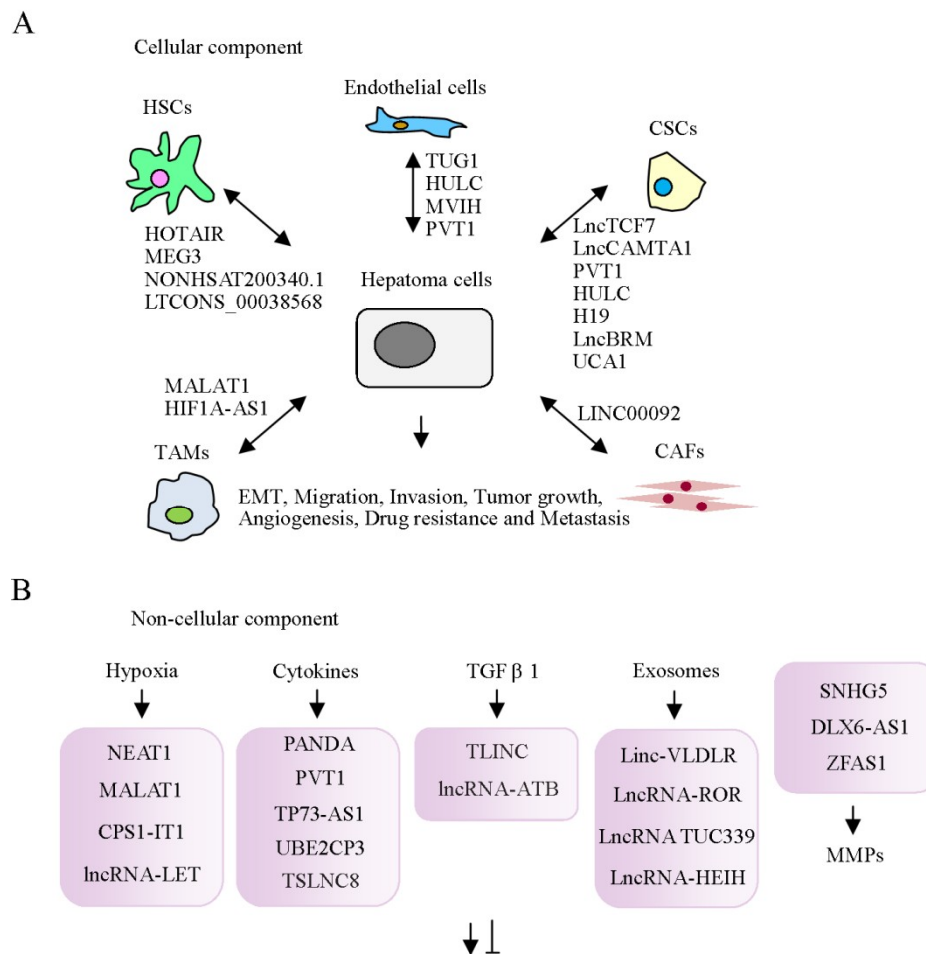


**Figure 2.** Schematic depiction of significant lncRNAs involved in interactions of hepatoma cells with tumor microenvironment components. (A) Cellular components: cancer-associated fibroblasts (CAF), hepatic stellate cells (HSC), tumor-associated macrophages (TAM), endothelial cells and cancer stem cells (CSC) cross-talk with hepatoma cells via multiple lncRNAs, as indicated. (B) Non-cellular components: reciprocal regulation of hypoxia, cytokines, TGF- $\beta$ 1, exosomes, matrix metalloproteinases (MMPs), and lncRNAs.

### 2.1. Cancer-Associated Fibroblasts

Several studies have highlighted the importance of cross-talk between cancer cells and CAFs. These molecules induce oncogenic phenotypes through production of various extracellular matrix proteins, growth factors and cytokines [32,33], such as hepatocyte growth factor (HGF), fibroblast growth factor (FGF), epidermal growth factor (EGF) and transforming growth factor  $\beta$  (TGF- $\beta$ ) [34–36]. In addition, HCC cells can be co-cultured with CAFs in vitro. CAFs induced by tissue inhibitor of metalloproteinase 1 (TIMP-1) suppress HCC apoptosis through increasing the Bcl-2/BAX ratio in association with SDF-1/CXCR4/PI3K/AKT signaling [37]. Moreover, CAFs recruit regulatory dendritic cells and facilitate their acquisition of a tolerogenic phenotype through interleukin (IL)-6-mediated signal transducer and activator of transcription 3 (STAT3) activation along with upregulation of Treg via secretion of TGF- $\beta$  in tumor microenvironments [38]. Signals triggered from cancer cells to CAFs promote tumor survival via these immunosuppressive phenotypes. The lncRNA, LINC00092, is upregulated in ovarian cancer and correlated with poor prognosis. LINC00092 is induced by CAF-secreted CXCL14 and enhances cell metastasis through modulation of phosphofructo-2-kinase/fructose-2 and 6-biphosphatase 2 (PFKFB2) expression [39]. These findings suggest that ovarian cancer cells and CAFs form a positive feedback loop driving glycolysis and tumor progression. The traditional anti-tumor approach involves targeting of epithelial cancer

cells. An alternative effective strategy to inhibit tumor formation would be to target CAFs and their communication networks, such as lncRNAs.

## 2.2. Hepatic Stellate Cells

During liver injury, HSCs undergo an important phenotypic change to become myofibroblasts that promote cell growth ability and induce alpha smooth muscle actin ( $\alpha$ -SMA) and  $\alpha$ -1 collagen expression [40]. Activated HSCs are responsible for production of cytokines, chemokines, growth factors and the extracellular matrix (ECM) [41]. Additionally, these cells penetrate the stromal environment of tumors and coexist with tumor sinusoids, fibrous septa and capsules. Cells treated with conditioned medium from HSC show enhanced growth and migration through modulation of NF- $\kappa$ B and extracellular-regulated kinase (ERK) pathways in vitro [42]. Bian et al. [43] reported a novel mechanism for epigenetic regulation in liver fibrogenesis involving lncRNA-lncRNA interactions. HOTAIR expression was shown to be significantly upregulated in CCl<sub>4</sub>-treated mouse models, human fibrotic liver and activated HSCs. HOTAIR, a component of the polycomb repressive complex 2 (PRC2) complex, controls H3K27me3 modification of chromatin at the promoter region of maternally expressed gene 3 (MEG3) and functions as a competing endogenous RNA (ceRNA) mediating repression of MEG3 via different pathways potentially attributable to localization in HSCs. This is an interesting finding, as it was thought up to now that this lncRNA is switched “on” or “off” in a manner dependent on another lncRNA. Mediation of this control through lncRNAs associated with epigenetic regulators provides an additional level of HSC activation and liver fibrogenesis. Li and co-workers analyzed the expression profiles of lncRNAs in HSC myofibroblasts to ascertain their potential regulatory roles in HSC activation and quiescence and hepatic fibrosis development. The key lncRNAs that could serve as therapeutic targets for suppression of liver fibrosis progression and their regulatory mechanisms were consequently determined. For example, the group reported that NONHSAT200340.1 targets FGF2 to regulate activation of hHSCs via c-Jun N-terminal kinases (JNK) signaling. Another lncRNA, LTCONS\_00038568, was shown to target netrin-4 (NTN4) and modulate liver fibrosis through inhibition of epithelial-mesenchymal transition (EMT) [44].

## 2.3. Tumor-Associated Macrophages

The anti-tumor response within the HCC microenvironment is impaired due to immune suppression through the activities of tumor-associated macrophages (TAM) [45]. Intercellular communications between tumor and stromal cells via TAMs play a crucial role in hepatoma [46]. TAMs, mainly comprising the infiltrating leukocyte population, are important for tumor progression. These cells are localized in the stromal component of the tumor mass and polarized to active status [46,47]. Specifically, M2-like TAMs act through the STAT3 signaling pathway and are involved in regulating angiogenesis and metastasis during HCC progression [48]. A number of cytokines, such as IL-4 and IL-10, expressed in the tumor microenvironment trigger TAM polarization to M2-type cells. M2-type TAM expresses a distinctive set of cytokines, including IL-10, and the chemokines CCL17, CCL22 and CCL24, inducing Treg association and inactivation of the Th2 polarized immune response. On the other hand, M2 macrophages are reported to induce vascular endothelial growth factor (VEGF) expression and promote tissue repair and angiogenesis. Kupffer cells are liver-specific TAMs capable of impairing the immune response mediated by T-cell CD8<sup>+</sup> through association with programmed death 1 (PD1) and programmed death ligand-1 (PD-L1) [49,50]. Huang et al. [51] demonstrated that knockdown of MALAT1 in TAM represses cell growth, migration and invasion of thyroid cancer cell line and reduces angiogenesis. Moreover, these effects were attenuated by overexpression of FGF2. In addition, HIF1A-AS1 was shown to be upregulated by TNF- $\alpha$  via promoting caspase 3 expression in Kupffer cells. Cell apoptosis was enhanced by TNF- $\alpha$  but suppressed upon knockdown of HIF1A-AS1 [52]. These findings support the utility of strategies aimed at modulating the expression of dysregulated lncRNAs in TAMs to facilitate repression of pro-tumorigenic properties.

## 2.4. Endothelial Cells

Endothelial cells are responsible for supporting blood vessel formation and tumor neovasculature. These cells have multiple functions and participate in various molecular signaling pathways in HCC and normal tissues. Several angiogenic receptors, such as C-X-C chemokine receptors (CXCR), epidermal growth factor receptor (EGFR), vascular endothelial growth factor receptor (VEGFR) and platelet-derived growth factor receptor (PDGFR), have been expressed *in vitro*. Interactions of ligands with these receptors activate signal transduction pathways that trigger survival, proliferation and invasion of endothelial cells [53]. Moreover, tumor-associated endothelial cells display high TGF- $\beta$ 1 and CD105 expression. TGF- $\beta$ 1 acts as a chemoattractant for CD105-expressing endothelial cells that promote angiogenesis [54]. Notably, CD105<sup>+</sup> endothelial cells from HCC display features of increased angiogenesis activity with higher resistance to chemotherapeutic agents and angiogenic inhibitors [55]. Previously, knockdown of taurine up-regulated gene 1 (TUG1) led to remarkable suppression of tumor-induced endothelial cell proliferation, migration and angiogenesis *in vitro* [56]. Similar results were obtained in xenograft mouse models. Highly upregulated in liver cancer (HULC), an oncogenic lncRNA, is significantly expressed in HCC [57]. Expression levels of these molecules are correlated with those of sphingosine kinase 1 (SPK1), VEGF and endothelial cell-specific molecule 1 (ESM1) in tumor tissues. Overexpression of HULC promotes tumor angiogenesis, which is blocked in SPK1-depleted cells. Conversely, its knockdown suppresses angiogenesis, tumor cell proliferation and invasion. Furthermore, HULC acts as a ceRNA to inhibit miR-107-mediated suppression of E2F1 and induces angiogenesis, both *in vitro* and *in vivo*. Inhibition of E2F1 promotes SPK1 transcription. lncRNA associated with microvascular invasion in hepatocellular carcinoma (MVIH) is encoded in the intron of ribosomal protein S24 (RPS24) gene. MVIH is highly expressed in HCC and positively correlated with tumor growth and intrahepatic metastasis [58] via activation of angiogenesis in mouse models. Phosphoglycerate kinase 1 (PGK1) has been shown to interact with MVIH using the RNA pulldown assay. Moreover, MVIH overexpression is associated with inhibition of PGK1 secretion. PGK1 secreted by tumor cells inhibits angiogenesis and exerts a negative impact on tumor growth and metastasis. A study by Zheng et al. [59] demonstrated that lncRNA-plasmacytoma variant translocation 1 (PVT1) promotes growth, migration and tube formation of endothelial cells. PVT1 inhibits miR-26b activity and induces connective tissue growth factor and angiopoietin 2 expression. Accordingly, the term “Angio-lncRs”, signifying regulation or association with angiogenesis, has been coined [60]. The finding that angiogenesis can be directly or indirectly regulated by lncRNAs further supports the targeting of these molecules to improve angiogenesis-mediated outcomes.

## 2.5. Association between lncRNAs and Cancer Stem Cells

Cancer exists as a heterogeneous population of cells. The different cell types within the population have distinct phenotypic and functional properties, thus limiting therapeutic efficacy. CSC or Tumor-Initiating Cell (TIC) concepts provide an alternative explanation for the failure of existing therapies. Accumulating evidence suggests that CSCs are the root of cancers and responsible for metastasis and resistance to traditional therapies [61,62]. CSCs can self-renew and have pluripotent capacity [63]. CSCs or TICs have been identified in multiple cancer types, including liver cancer. Based on their unique characteristics, CSCs are proposed as critical promoters of tumor initiation, development, metastasis and recurrence. CSC proliferation is regulated by various extrinsic factors derived from the cell microenvironment. For instance, HOTAIR is reported to enhance human liver CSC growth through inhibiting associations of P300, CREB and RNA pol II with the SETD2 promoter region, leading to suppression of SETD2 phosphorylation and expression [64]. lncTCF7 is another critical participant in the regulation of CSC maintenance and renewal in HCC [65] that contributes to cancer progression and development. This lncRNA promotes expression of its target gene, TCF7, through enhancing interactions between the SWI/SNF complex and the TCF7 promoter for transcription. Both lncTCF7 and TCF7 are involved in mediating sphere formation of liver cancer cells, highlighting their importance in CSCs. lncRNA-calmodulin binding transcription activator 1 (CAMTA1) is reported

to be upregulated in liver CSCs (CD13<sup>+</sup>/CD133<sup>+</sup> cells), compared with non-CSCs derived from parental Huh7 and HepG2 cells. Additionally, lncCAMTA1 is highly expressed in HCC tissues. Another study showed that functionally, lncCAMTA1 suppresses the promoter activity of CAMTA1 and induces a repressive chromatin structure, HCC cell proliferation and CSC-like properties [66]. Wang et al. [67] demonstrated that overexpression of PVT1 promotes cell proliferation through regulation of cell cycle-related genes and induces a stem cell-like phenotype of SMMC-7721 cells by stabilizing nucleolar protein 2 (NOP2) nucleolar protein. lncRNA-H19 has been identified in exosomes released by CSC-like CD90<sup>+</sup> cells. Interestingly, higher expression of lncRNA H19 was detected in exosomes derived from CD90<sup>+</sup> Huh7 relative to parental Huh7 cells. Moreover, lncRNA H19 was shown to induce pro-angiogenic factors, such as VEGF, in human umbilical vein endothelial cells (HUVECs) and promote adhesion of CD90<sup>+</sup> Huh7 cells to endothelial cells [68]. The lncRNA associating with Brahma (lncBRM) is additionally highly expressed in HCC tumors and CSC-like CD13<sup>+</sup>/CD133<sup>+</sup> cells. Mechanistically, lncBRM interacts with Brahma (BRM) to regulate the BRG1/BRM switch in the BRG1-associated factor (BAF) complex and induces YAP1 signaling, subsequently promoting sphere formation and self-renewal [69]. Yet another lncRNA, lncSox4, highly expressed in HCC tumors and CD133<sup>+</sup> TICs, has been shown to promote self-renewal and tumor-initiating ability through association with STAT3 and upregulation of Sox4 [70]. The lncRNA urothelial cancer associated 1 (UCA1) upregulated in HCC enhances proliferation and tumorigenesis of carcinoma cells [71]. Notably, UCA1 is also upregulated in liver CSCs and plays a critical role in governing their growth and differentiation through regulation of multiple pathways. For example, UCA1 facilitates the differentiation of human embryonic stem cells (ESC) into hepatocyte-like cells through modulation of histone modification. Moreover, UCA1 is reported to trigger hepatocyte-like cell transformation through inducing promoter methylation of HULC and chromatin loop formation of the  $\beta$ -catenin promoter-enhancer [72]. Pu et al. [73] further demonstrated that UCA1 enhances c-Myc expression, RB1 phosphorylation and activity of the retinoblastoma protein Su(var)3-9, Enhancer-of-zeste and Trithorax (SET) domain-containing 1A (pRB1-SET1A) complex, in turn, inducing tri-methylation of histone H3 (H3K4me3) involved in prolongation of telomere length. These findings highlight the critical roles of multiple lncRNAs in modulating CSC maintenance and self-renewal.

### 3. Networks of lncRNAs and Non-Cellular Components of the Tumor Microenvironment in HCC

#### 3.1. Association between lncRNAs and Hypoxia

Hypoxic conditions and high expression of the key regulator, hypoxia-inducible factor-1 (HIF-1), are common features in advanced cancers [74,75]. Hypoxic conditions in surrounding cells represent a critical step in the tumorigenic process. Indeed, hypoxia facilitates a number of events in the tumor microenvironment that promote metastasis of heterogeneous tumor cells and is significantly positively correlated with aggressive malignant phenotypes. HIF-1 is a heterodimeric complex composed of two transcription factors, HIF-1 $\alpha$  and HIF-2 $\alpha$  [76], which regulate genes with significant roles in oncogenic pathways, including apoptosis, proliferation, angiogenesis, tumor metabolism and metastasis. A previous study revealed that expression of the lncRNA TUG1 is enhanced under hypoxia and in human hepatoblastoma [56]. Zheng et al. [77] demonstrated high expression of nuclear paraspeckle assembly transcript 1 (NEAT1) in HCC specimens, which promotes epithelial-mesenchymal transition (EMT), migration and invasion capacities of tumor cells by stimulating HIF-2 $\alpha$  activity. Luo and co-workers showed a positive correlation between expression of MALAT1 expression and HIF-2 $\alpha$  in HCC tissues [78]. Moreover, arsenite promotes MALAT1 and HIF-2 $\alpha$  expression in hepatoma cells. MALAT1 is reported to enhance HIF-2 $\alpha$  activity through inhibition of von Hippel-Lindau (VHL) protein-mediated HIF-2 $\alpha$  ubiquitination and degradation. Conversely, MALAT1 is regulated by HIF-2 $\alpha$  via a feedback loop, supporting the co-involvement of MALAT1 and HIF-2 $\alpha$  in HCC. Wang and colleagues identified a novel tumor suppressor lncRNA, CPS1 intronic transcript 1 (CPS1-IT1), with low expression in HCC [79,80]. Overexpression of CPS1-IT1 reduced HIF-1 $\alpha$  activity and



consequently suppressed EMT progression and HCC metastasis, both in vitro and in vivo. Another lncRNA, Low expression in Tumor (termed lncRNA-LET), is additionally downregulated in HCC [81]. lncRNA-LET is suppressed by hypoxia-induced histone deacetylase 3 through reducing histone acetylation-mediated modulation of its promoter region. Knockdown of lncRNA-LET is a key step in stabilization of nuclear factor 90 protein, which leads to hypoxia-induced cancer cell invasion. HIF-1 and its downstream effectors have been identified as potential targets for cancer therapy. However, owing to the complexity of the hypoxia signaling pathway, inhibition of HIF-1 $\alpha$  activity presents a considerable challenge. Recent establishment of the involvement of lncRNAs in hypoxia response in cancers provides further evidence of their potential utility as therapeutic targets.

### 3.2. Association between lncRNAs and Cytokines

Cytokines are major target molecules in a number of inflammatory conditions, with targeted therapies for TNF- $\alpha$ , interferon (IFN), and IL-17 already in clinical use [82–84]. Accumulating studies support the involvement of cytokines in hepatocarcinogenesis. A number of investigations have focused on determining whether cytokine expression is correlated with disease progression in tumor-adjacent normal tissues and HCC. Cytokines secreted by tumors or stromal cells in the serum and plasma have been assessed for their predictive capacity in HCC [85,86]. The lncRNA, PANDA, is reported to be downregulated in HCC specimens. Unexpectedly, however, overexpression of PANDA appears to enhance HCC proliferation and tumor growth, both in vitro and in vivo. Mechanistically, PANDA suppresses transcriptional activity of the senescence-associated inflammatory factor, IL8, thereby inhibiting cellular senescence [87]. The lncRNA, PVT1, is induced by IFN- $\alpha$  in HCC cells [88]. Depletion of PVT1 leads to enhanced apoptosis and suppression of growth in IFN- $\alpha$  treated cells. Furthermore, PVT1 represses IFN- $\alpha$  induced phosphorylated signal transducer and activator of transcription 1 (STAT1) and interferon-stimulated gene (ISG) transcription through interactions with STAT1. Upregulation of another lncRNA, TP73-AS1, has been documented in HCC tissues and cell lines [89] in association with poorer prognosis and survival. Knockdown of TP73-AS1 leads to suppression of HMGB1, receptor for advanced glycation end products (RAGE) and NF- $\kappa$ B expression and consequent reduction of cell proliferation. miR-200a has been shown to directly bind TP73-AS1 and the 3'UTR of HMGB1 in the 3'UTR luciferase reporter assay. Moreover, miR-200a knockdown promotes HMGB1, RAGE, NF- $\kappa$ B as well as NF- $\kappa$ B-regulated cytokine (TNF $\alpha$ , IL6 and IL-1 $\beta$ ) levels. Expression of ubiquitin-conjugating enzyme E2C pseudogene 3 (UBE2CP3) is higher in HCC than adjacent non-tumor tissues and in tissues with high endothelial vessel density [90]. In studies using a co-culture system, UBE2CP3 promoted HUVEC tube formation, proliferation and migration through the ERK/HIF-1 $\alpha$ /p70S6K/VEGFA cascade and enhanced VEGFA expression in HCC cell supernatant fractions. Another novel lncRNA, tumor suppressor long noncoding RNA on chromosome 8p12 (termed TSLNC8), is frequently deleted or downregulated in HCC tissues [91]. Overexpression of TSLNC8 is associated with significant suppression of growth and metastasis, both in vitro and in vivo. TSLNC8 has been shown to modulate STAT3 phosphorylation levels (Tyr705 and Ser727) and transcriptional activity through competitive interactions with transketolase and STAT3, resulting in inactivation of the IL-6/STAT3 signaling pathway in HCC cells. Modulatory roles of lncRNAs in cytokine gene expression are well documented, generating significant research interest in the utility of lncRNAs in therapeutic targeting.

TGF- $\beta$  binds to type I and type II receptors (TGF- $\beta$  RI and TGF- $\beta$  RII) at the cell surface. Activated TGF- $\beta$  receptors induce phosphorylation of downstream signal transducer R-Smad (receptor-activated Smad: Smad2 and Smad3). Phosphorylated R-Smads, in turn, associate with Smad4 (Co-Smad) to form a trimeric Smad complex, which translocates into the nucleus and regulates target gene expression (Figure 3A). TGF- $\beta$  plays a complex role in tumor progression, in particular, liver fibrogenesis and hepatocarcinogenesis [92,93], and is upregulated in HCC tissues and peri-neoplastic stroma. Interestingly, TGF- $\beta$ 1 is known to exert dual effects during HCC progression [94]. In the early stages, the cytokine acts as a tumor suppressor with anti-proliferative effects and stimulation of

apoptosis signals. Notably, blockage of cell proliferation is mediated by cyclin-dependent kinase inhibitors and suppression of c-Myc-mediated functions. The tumor suppressor activity of TGF- $\beta$  is also exerted through suppression of tumor stroma mitogens and tumorigenic inflammation. Conversely, TGF- $\beta$  plays an oncogenic role, promoting tumorigenicity via several mechanisms, including stimulatory effects on cell migration, angiogenesis and metastasis. TGF- $\beta$  is proposed to contribute to EMT through downregulation of E-cadherin (epithelial marker) and upregulation of Snail (mesenchymal marker). Another previous report showed that TGF- $\beta$ 1 enhances miR-181b expression, promoting growth, survival, migration and invasion of HCC cells [95]. Similarly, miR-23a, miR-24 and miR-27a appear to enhance tumor cell survival in HCC [96]. A novel lncRNA, designated TGF- $\beta$ -induced long non-coding RNA (TLINC), was further identified as a target induced by TGF- $\beta$  in both hepatic and non-hepatic cells (Figure 3B) [97]. Interestingly, expression of two TLINC isoforms (long and short) was associated with the epithelial and mesenchymal phenotype, respectively. The long isoform of TLINC was positively correlated with metastatic phenotype and increased levels of proinflammatory cytokines (IL-8). TLINC was additionally detected in both epithelial and stromal cells and identified as a tumor marker. Another lncRNA (lncRNA-ATB) is reported to be induced by TGF- $\beta$ 1 [98]. Clinically, lncRNA-ATB was overexpressed in HCC specimens and enhanced EMT and metastasis through modulation of the ZEB1/ZEB2/miR-200 cascade. In addition, lncRNA-ATB increased colonization of migrating cells by triggering the IL-11/STAT3 signaling pathway. Mechanistically, IL-11 mRNA stability was enhanced via lncRNA-ATB interactions, which, in turn, facilitated IL-11 secretion, suggesting a role in phosphorylation of STAT3 (Figure 3B). This autocrine regulatory mechanism promotes cell survival and colonization to distant organ sites. The collective findings indicate that several lncRNAs are regulated by TGF- $\beta$  and play important roles in TGF- $\beta$ -mediated effects on EMT, migration and invasion.

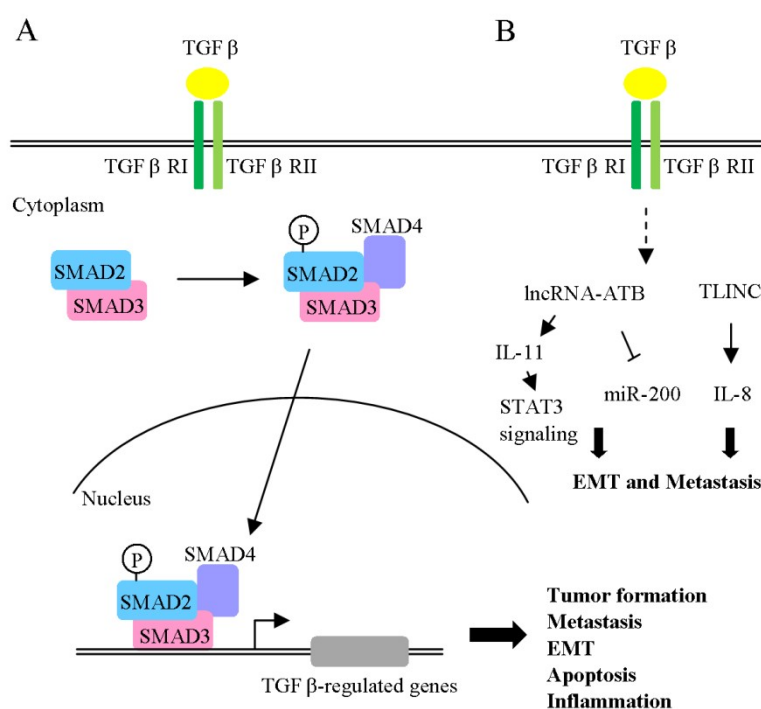


**Figure 3.** Schematic depiction of the TGF- $\beta$  signaling pathway. (A) TGF- $\beta$  binds to Type I (TGF- $\beta$  RI) and Type II receptor (TGF- $\beta$  RII), whereby TGF- $\beta$  RII phosphorylates and activates TGF- $\beta$  RI. Transcriptional factors Smad2 and 3 (Smad2/3) are phosphorylated by TGF- $\beta$  receptors and associated with Smad4. Activated Smad complexes translocate into the nucleus and regulate target gene transcription. (B) lncRNA-ATB and TLINC are induced by TGF- $\beta$ . The downstream molecules regulated by these lncRNAs are depicted. P: phosphorylation.



### 3.3. Regulation of the Tumor Microenvironment by lncRNAs in Exosomes

Exosomes have recently been identified as critical mediators of cell-to-cell communication in cancer progression through transfer of RNA and proteins to neighboring or distant cells [99]. The compositions of exosomes differ depending on cell type, physiological and pathological conditions. Previous studies have reported that exosomes are 40–150 nm in diameter and exist in both normal and tumor cells. Exosomes play an important role in crosstalk between tumor and stromal cells and deliver specific molecules to target cells through endocytosis and phagocytosis [100,101]. Moreover, exosomes fuse with membranes of target cells to deliver components into cells. According to their origin in the tumor microenvironment, exosomes can be classified as tumor cell or stromal cell secretions. Signal transduction between these cells in the tumor microenvironment is significantly involved in regulation of cell invasion, metastasis, drug resistance and cancer. The exoRBase database (<http://www.exoRBase.org>) contains information on circular RNAs (circRNA), lncRNAs and mRNAs derived from RNA-seq data analyses of human blood exosomes [102]. To date, few lncRNAs, such as lincRNA-VLDLR, ROR, and TUC339, have been detected in circulating HCC extracellular vesicles [103–105]. Takahashi et al. [88] demonstrated that anticancer drugs induce linc-VLDLR expression in cells as well as extracellular vesicles (EV) released from these cells. Notably, chemotherapy-induced HCC cell death was repressed upon incubation with EV. These effects were reduced upon knockdown of linc-VLDLR cell lines. Another lncRNA involved in HCC resistance against microenvironmental conditions is lncRNA-ROR, which promotes EMT, cancer stem cell maintenance and tumorigenesis. While overexpression of lncRNA-ROR has been established in normal hepatocytes, its selective enrichment within extracellular vesicles is correlated with TGF- $\beta$ -dependent HCC cell chemoresistance and knockdown shown to increase chemosensitivity. The lncRNA TUC339 is significantly expressed in extracellular vesicles derived from HCC cells and implicated in tumor growth, cell adhesion and cell cycle progression. Recently, Sun and co-workers reported the presence of higher levels of LINC00161 in serum exosome and urine samples from HCC patients, compared to controls [106]. Another group demonstrated increased lncRNA-HEIH expression in serum and exosomes of HCV-related HCC [107]. Clearly, lncRNAs are involved in exosome-mediated functions and may, therefore, serve as potential targets for therapeutic interventions.

### 3.4. Extracellular Matrix (ECM) and Matrix Metalloproteinases within the Microenvironment

Extracellular matrix (ECM) is produced by stromal cells in the microenvironment. The components of ECM, including laminin, collagens, fibronectin and proteoglycans, are associated with altering the phenotype and function of HCC cells. ECM production and reorganization can promote tumor cell proliferation and invasion and alter gene expression in different stromal cell and cancer cell types, leading to tumor progression [108]. Accumulating evidence supports the view that extracellular proteinases, such as matrix metalloproteinases (MMP), mediate many of the changes in the microenvironment during tumor progression. The complexity of the tumor microenvironment triggers regulatory cascades that determine the functions of the diverse MMPs expressed. Proteolytic cleavage of MMPs is regulated at different levels, including gene expression, conversion from the pro- to active form and specific inhibitors. Conversion of the pro-form (pro-MMP) into its active form is regulated by proteinases, such as furin and plasminogen, a critical step for MMP activity [109,110]. MMP activity is additionally modulated by lncRNAs. For example, functional knockdown of small nucleolar RNA host gene 5 (SNHG5) highly expressed in HCC is reported to induce apoptosis and suppress cell cycle progression, growth and metastasis in hepatoma cell lines whereas its overexpression has the opposite effects. Importantly, SNHG5 knockdown led to inhibition of MMP-2 and MMP-9 that are closely related to metastasis [111]. Zhang et al. [96] demonstrated upregulation of the lncRNA DLX6-AS1 in HCC samples, which was correlated with poor prognosis of HCC patients. Knockdown of DLX6-AS1 suppressed cell growth, migration and invasion, both in vitro and in vivo. MiR-203 targeting the 3'UTR region of DLX6-AS1 was negatively correlated with DLX6-AS1 expression. Data from the 3'UTR luciferase reporter assay

further revealed that miR-203a targets MMP-2 mRNA. These collective findings support an oncogenic role of DLX6-AS1 in clinical specimens and cellular experiments, indicative of the involvement of a potential DLX6-AS1/miR-203a/MMP-2 pathway in tumorigenesis [112]. lncRNA ZFAS1 gene amplification observed in HCC is positively correlated with hepatic invasion and metastasis through modulation of the miR-150/ZEB1/MMP14/MMP16 cascade [113]. These lines of evidence clearly support regulation of MMPs by lncRNAs. Direct inhibitors of MMP have been developed in previous studies. Another strategy to effectively achieve MMP inhibition is targeting specific lncRNAs to reduce MMP activity.

### 3.5. Metabolites and the Tumor Microenvironment

Interestingly, secreted metabolites function in decisions on the phenotypic diversity of cells in the tumor microenvironment. Accumulating evidence supports the theory that secreted metabolites act as tumor morphogens that shape unique tumor heterogeneity. CAFs residing in the tumor microenvironment promote cancer cell growth by producing metabolites, such as lactate, fatty acid and amino acids [114]. Earlier, liver-specific miR-122 expression was shown to be reduced in HCC. Moreover, overexpression of miR-122 led to inhibition of HCC formation in an animal model. Mechanistically, miR-122 reduces lactate production and promotes oxygen consumption through inhibition of pyruvate kinase M2 (PKM2) expression [115]. Consistent with this finding, another study demonstrated that miR-122 mediates inhibition of PKM2 protein expression by directly targeting its 3'UTR region in HCC [116]. Current knowledge, along with data obtained from high-throughput tools, such as RNA-seq and metabolomic analyses, indicate that interplay between metabolites and ncRNAs plays a crucial regulatory role in cancer progression.

## 4. lncRNAs as Novel Targets for HCC Therapy

Traditional cancer treatment is dependent on average patient response. However, treatments that can be successfully applied for some patients may not be effective for others. An emerging approach for disease treatment and prevention, known as precision medicine, has gained significant attention as a means to improve treatment outcomes. Precision medicine is based on knowledge of individual variabilities in the genes, epigenetic profiles and environments for each patient [117]. This theory assumes that a disease is caused by specific genes or molecular pathways. Individual diseases or cancers are therefore tightly associated with variations in genes and downstream signaling pathways. Identification of effective drug-specific targets for tumor cells that do not adversely affect normal cells is a considerable challenge in therapy. Therefore, effective treatments need to target specific molecules that act as drivers in development of cancer. Previously, miRNAs have been identified in biological fluids of patients, such as urine and blood [118], which act as potential biomarkers in diagnosis and prognosis of cancers. More recently, lncRNAs have been highlighted as potential candidates for biomarkers and precision medicine targets in cancer due to their specific expression patterns in tumor cells [119,120]. In addition, lncRNAs are detectable in biological fluids of patients and may, therefore, be applied as noninvasive markers for clinical analysis.

DNA methyltransferase (DNMT) and histone deacetylase (HDAC) inhibitor drugs [121] are commonly used to treat various cancer types. However, these agents that act via epigenetic regulation are nonspecific and should be delivered via venous injection. Notably, lncRNAs regulate similar genes or functions through epigenetic mechanisms and are considered drug targets with a lower incidence of side-effects and improved specificity. Drug resistance is an important issue that limits effective cancer treatment. lncRNAs involved in drug resistance through modulation of drug transporter expression, oncogenic survival signaling pathways, cell cycle, and apoptosis have been identified. As mentioned above, TGF- $\beta$ -dependent chemoresistance is regulated by lncRNA-ROR in HCC [105]. Another study by Li and co-workers demonstrated that lncRNA Activated in RCC with Sunitinib Resistance (lncARSR) is involved in doxorubicin resistance through regulation of the PTEN/PI3K/Akt pathway in HCC [122].

lncRNA-specific therapeutic approaches target lncRNA-mediated functions and pathways through gene silencing and structure disruption mechanisms. In fact, a single lncRNA can regulate several protein coding genes and pathways. In such situations, manipulating individual lncRNAs can modulate multiple genes and their functions. The currently available strategies are outlined below. For instance, expression of lncRNA could be suppressed with short interfering RNAs (siRNA), short hairpin RNAs (shRNA), antisense oligonucleotides (ASO), locked nucleic acid (LNA) gapmeRs and clustered regularly interspaced short palindromic repeat-associated nuclease 9 (CRISPR/Cas9) systems. However, the knockdown efficiency of these genes is dependent on their localization. Knockdown of nuclear lncRNAs is successfully achieved through ASOs whereas siRNAs work most effectively in the cytoplasm. Modulation of lncRNA expression with CRISPR interference through guide RNAs (gRNA) reduces the possibility of off-target effects and allows suppression independent of the subcellular location of the target. Although several lines of evidence provide convincing results regarding lncRNA-mediated functions and their utility as therapeutic targets, their use *in vivo* is extremely challenging owing to poor conservation of lncRNAs across species. The mechanisms of action of lncRNAs, such as recruiting/binding partners, in animal models, differ from *in vitro* experimental findings. Notably, lncRNAs differ from protein-coding genes in several ways that require consideration in analyzing their effects or therapeutic potential. The complex structures formed by lncRNA-lncRNA, lncRNA-protein and lncRNA-DNA molecules may provide new strategies to disrupt these interactions. Moreover, expression of lncRNAs is tissue- or cell-type specific. Finally, current knowledge of non-coding gene functions highlights the combinatorial nature of their actions, which involve complex interactions incorporating multiple associated effectors. Recently, Amodio et al. [123] demonstrated that inhibition of MALAT1 by LNA gapmeR ASO suppresses multiple myeloma cell growth and induces apoptosis *in vitro* and *in vivo*. In addition, a peptide nucleic acid (PNA)-targeting approach for lncRNA was established. This strategy was successful in blocking interactions of HOTAIR with EZH2, leading to suppression of HOTAIR-EZH2 activity and increased chemotherapy sensitivity [124]. Notably, the phenotypes of target lncRNAs could differ depending on the “tissue context”, which should be analyzed to achieve optimal therapeutic responses.

## 5. Conclusions

In the current article, lncRNAs in the tumor microenvironment involved in the regulation of tumor growth, angiogenesis and metastasis are comprehensively listed in Table 1. While several genetic, epigenetic, transcriptional and translational dysregulation processes collectively contribute to HCC, existing knowledge regarding the signaling pathways that influence HCC is incomplete. Recent extensive characterization of lncRNAs as initiators or diagnostic markers of HCC has highlighted their utility as important regulators in HCC progression. Due to their functional roles as either tumor suppressors or oncogenes involved in diverse cellular networks, lncRNAs may be developed as a molecular tool suitable for application in therapeutic and clinical strategies for HCC. The collective results support multiple interactions between the tumor microenvironment and lncRNA networks that drive cancer cell survival, resistance to therapy and metastasis. Increasing evidence of dysregulated lncRNAs in various malignant tumors that may serve as potential biomarkers has been documented. Liver cancer presents a complex model to investigate the relationship between the microenvironment and tumor development. Improved knowledge of these interactions is therefore essential to identify potential prognostic/predictive biomarkers and successfully develop novel targeted therapies.

**Table 1.** Tumor microenvironment-related lncRNAs and their potential mechanisms in hepatocellular carcinoma (HCC).

Gene Name	Principal Functions	Molecules and Signaling Pathways Involved <sup>a</sup>	Expression in HCC	Prognostic MARKERS in HCC <sup>b</sup>	Cellular/Non-Cellular Component <sup>c</sup>	Regulation Mechanism <sup>d</sup>	Reference
<i>TUG1</i>	Tumorigenesis Angiogenesis	MiR-34a-5p, VEGFA	Up	✓	Both	Hypoxia	[56]
<i>HULC</i>	Angiogenesis Cell growth Invasion	MiR-107, E2F1, SPK1, ESM-1 PI3k/ Akt/mTOR pathway	Up	✓	Cellular	-	[57]
<i>MVIH</i>	Tumor growth Metastasis Angiogenesis	PGK1	Up	-	Cellular	-	[58]
<i>HOTAIR</i>	Cell growth	P300, CREB, RNA pol II	Up	✓	Cellular	-	[64]
<i>lncTCF7</i>	Tumorigenicity Self-renewal EMT	Wnt signaling, SWI/SNF complex, TCF7	Up	-	Cellular	-	[65]
<i>lncCAMTA1</i>	Proliferation CSC-like properties	CAMTA1	Up	✓	Cellular	-	[66]
<i>H19</i>	Angiogenesis	Angiogenin, FGF18	Up	✓	Cellular	-	[68]
<i>lncBRM</i>	Sphere formation Tumor formation	BRG1/BRM switch, YAP1 signaling	Up	✓	Cellular	-	[69]
<i>lncSox4</i>	Self-renewal Tumor-initiating ability	STAT3, Sox4	Up	✓	Cellular	-	[70]
<i>UCA1</i>	Proliferation Tumorigenesis	MiR-216b, FGFR1/ERK signaling pathway	Up	-	Cellular	-	[71]
<i>NEAT1</i>	EMT Migration Invasion	HIF-2 $\alpha$ pathway	Up	✓	Non-cellular	HIF-2 $\alpha$	[77]
<i>MALAT1</i>	Transformation	VHL, HIF-2 $\alpha$	Up	✓	Non-cellular	MALAT1/HIF-2 $\alpha$ feedback loop	[78]
<i>CPS1-IT1</i>	EMT Metastasis	HIF-1 $\alpha$ activity	Down	✓	Non-cellular	-	[79,80]
<i>lncRNA-LET</i>	Invasion	NF90, HIF-1 $\alpha$ , CDC42	Down	-	Non-cellular	HDAC3	[81]
<i>PANDA</i>	Proliferation Tumor growth Cellular senescence	IL8	Down	✓	Non-cellular	-	[87]

Table 1. Cont.

Gene Name	Principal Functions	Molecules and Signaling Pathways Involved <sup>a</sup>	Expression in HCC	Prognostic MARKERS in HCC <sup>b</sup>	Cellular/Non-Cellular Component <sup>c</sup>	Regulation Mechanism <sup>d</sup>	Reference
<i>PVT1</i>	Proliferation Apoptosis Cell proliferation Stem cell-like phenotype	STAT1/ISG pathway, NOP2	Up	✓	Both	IFN- $\alpha$	[67,88]
<i>TP73-AS1</i>	Proliferation	HMGB1, RAGE, NF- $\kappa$ B, MiR-200a	Up	-	Non-cellular	-	[89]
<i>UBE2CP3</i>	Proliferation Migration Tube formation	ERK/HIF-1 $\alpha$ /p70S6K/VEGFA	Up	✓	Non-cellular	-	[90]
<i>TSLNC8</i>	Cell growth Metastasis	IL-6/STAT3 signaling pathway, Transketolase	Down	✓	Non-cellular	-	[91]
<i>TLINC</i>	EMT	IL8	Up	-	Non-cellular	TGF- $\beta$	[97]
<i>lncRNA-ATB</i>	Migration Invasion Metastasis	MiR-200, IL-11/STAT3 signaling pathway	Up	✓	Non-cellular	TGF- $\beta$ 1	[98]
<i>linc-VLDLR</i>	Chemotherapy	Exosome	Up	-	Non-cellular	-	[104]
<i>lincRNA-ROR</i>	EMT CSC maintenance Tumorigenesis	TGF- $\beta$ -dependent chemoresistance	Up	✓	Non-cellular	-	[105]
<i>lncRNA-TUC339</i>	Tumor growth Cell Adhesion Cell cycle	Exosome	Up	✓	Non-cellular	-	[103]
<i>LINC00161</i>	Migration Invasion	Serum exosome Urine sample	Up	✓	Non-cellular	-	[106]
<i>HEIH</i>	Cell cycle progression	EZH2	Up	✓	Non-cellular	-	[107]
<i>SNHG5</i>	Apoptosis Cell cycle Metastasis	MMP2, MMP9, miR-26a-5p, Wnt/ $\beta$ -catenin/GSK3 $\beta$ signal pathway	Up	✓	Non-cellular	-	[111]
<i>DLX6-AS1</i>	Cell growth Migration Invasion	MiR-203a/MMP2 pathway	Up	✓	Non-cellular	-	[112]
<i>ZFAS1</i>	Metastasis	MiR-150, ZEB1, MMP14, MMP16	Up	✓	Non-cellular	-	[113]

a: Downstream molecules and signaling pathways involved in lncRNA-mediated functions; b: ✓: lncRNAs acting as prognostic markers in HCC. -: Information is unavailable' c: lncRNAs related to the cellular or non-cellular component of the tumor microenvironment (Cellular: cellular component, Non-cellular: non-cellular; component, Both: cellular and non-cellular component); d: lncRNAs regulated by upstream transcriptional factor or cytokines, as indicated. -: Information is unavailable.

**Author Contributions:** Writing—Original Draft Preparation: Y.-H.L.; Writing—Review & Editing: Y.-H.L., M.-H.W., C.-T.Y. and K.-H.L.; Supervision: K.-H.L.

**Funding:** This research was funded by grants from Chang Gung Memorial Hospital, Taoyuan, Taiwan (CMRPD1D0383; CMRPD1G0421, CMRPD1G0422, CRRPD1F0011, CRRPD1F0012, CRRPD1F0013, NMRPD1G0951 to KHL; CMRPG3H0721, NZRPG3G0172 to YHL) and the Ministry of Science and Technology of the Republic of China (MOST 106-2320-B-182-032-MY3 to KHL; MOST 106-2321-B-182-003-MY3, MOST 106-2321-B-182A-004-MY3 to YHL).

**Conflicts of Interest:** The authors declare no conflicts of interest.

## References

1. Balkwill, F.R.; Capasso, M.; Hagemann, T. The tumor microenvironment at a glance. *J. Cell Sci.* **2012**, *125*, 5591–5596. [[CrossRef](#)] [[PubMed](#)]
2. Yuan, Y.; Jiang, Y.C.; Sun, C.K.; Chen, Q.M. Role of the tumor microenvironment in tumor progression and the clinical applications (Review). *Oncol. Rep.* **2016**, *35*, 2499–2515. [[CrossRef](#)] [[PubMed](#)]
3. El-Serag, H.B.; Rudolph, K.L. Hepatocellular carcinoma: Epidemiology and molecular carcinogenesis. *Gastroenterology* **2007**, *132*, 2557–2576. [[CrossRef](#)] [[PubMed](#)]
4. Artandi, S.E.; DePinho, R.A. Telomeres and telomerase in cancer. *Carcinogenesis* **2010**, *31*, 9–18. [[CrossRef](#)] [[PubMed](#)]
5. Uchino, K.; Tateishi, R.; Shiina, S.; Kanda, M.; Masuzaki, R.; Kondo, Y.; Goto, T.; Omata, M.; Yoshida, H.; Koike, K. Hepatocellular carcinoma with extrahepatic metastasis: Clinical features and prognostic factors. *Cancer* **2011**, *117*, 4475–4483. [[CrossRef](#)] [[PubMed](#)]
6. Mehlen, P.; Puisieux, A. Metastasis: A question of life or death. *Nat. Rev. Cancer* **2006**, *6*, 449–458. [[CrossRef](#)] [[PubMed](#)]
7. Wang, Z.; Li, X. The role of noncoding RNA in hepatocellular carcinoma. *Gland Surg.* **2013**, *2*, 25–29. [[PubMed](#)]
8. Li, X.; Wu, Z.; Fu, X.; Han, W. lncRNAs: Insights into their function and mechanics in underlying disorders. *Mutat. Res. Rev. Mutat. Res.* **2014**, *762*, 1–21. [[CrossRef](#)] [[PubMed](#)]
9. Tsai, W.C.; Hsu, S.D.; Hsu, C.S.; Lai, T.C.; Chen, S.J.; Shen, R.; Huang, Y.; Chen, H.C.; Lee, C.H.; Tsai, T.F.; et al. MicroRNA-122 plays a critical role in liver homeostasis and hepatocarcinogenesis. *J. Clin. Investing.* **2012**, *122*, 2884–2897. [[CrossRef](#)] [[PubMed](#)]
10. Xu, X.; Fan, Z.; Kang, L.; Han, J.; Jiang, C.; Zheng, X.; Zhu, Z.; Jiao, H.; Lin, J.; Jiang, K.; et al. Hepatitis B virus X protein represses miRNA-148a to enhance tumorigenesis. *J. Clin. Investing.* **2013**, *123*, 630–645. [[CrossRef](#)] [[PubMed](#)]
11. Melo, S.A.; Kalluri, R. Molecular pathways: MicroRNAs as cancer therapeutics. *Clin. Cancer Res.* **2012**, *18*, 4234–4239. [[CrossRef](#)] [[PubMed](#)]
12. Esquela-Kerscher, A.; Slack, F.J. Oncomirs-microRNAs with a role in cancer. *Nat. Rev. Cancer* **2006**, *6*, 259–269. [[CrossRef](#)] [[PubMed](#)]
13. He, M.; Xu, Z.; Ding, T.; Kuang, D.M.; Zheng, L. MicroRNA-155 regulates inflammatory cytokine production in tumor-associated macrophages via targeting C/EBPbeta. *Cell. Mol. Immunol.* **2009**, *6*, 343–352. [[CrossRef](#)] [[PubMed](#)]
14. Yang, P.; Li, Q.J.; Feng, Y.; Zhang, Y.; Markowitz, G.J.; Ning, S.; Deng, Y.; Zhao, J.; Jiang, S.; Yuan, Y.; et al. TGF-beta-miR-34a-CCL22 signaling-induced Treg cell recruitment promotes venous metastases of HBV-positive hepatocellular carcinoma. *Cancer Cell* **2012**, *22*, 291–303. [[CrossRef](#)] [[PubMed](#)]
15. Chai, Z.T.; Zhu, X.D.; Ao, J.Y.; Wang, W.Q.; Gao, D.M.; Kong, J.; Zhang, N.; Zhang, Y.Y.; Ye, B.G.; Ma, D.N.; et al. microRNA-26a suppresses recruitment of macrophages by down-regulating macrophage colony-stimulating factor expression through the PI3K/Akt pathway in hepatocellular carcinoma. *J. Hematol. Oncol.* **2015**, *8*, 56. [[CrossRef](#)] [[PubMed](#)]
16. Rinn, J.L.; Chang, H.Y. Genome regulation by long noncoding RNAs. *Annu. Rev. Biochem.* **2012**, *81*, 145–166. [[CrossRef](#)] [[PubMed](#)]
17. Di Gesualdo, F.; Capaccioli, S.; Lulli, M. A pathophysiological view of the long non-coding RNA world. *Oncotarget* **2014**, *5*, 10976–10996. [[CrossRef](#)] [[PubMed](#)]
18. Fitzgerald, K.A.; Caffrey, D.R. Long noncoding RNAs in innate and adaptive immunity. *Curr. Opin. Immunol.* **2014**, *26*, 140–146. [[CrossRef](#)] [[PubMed](#)]



19. Atianand, M.K.; Fitzgerald, K.A. Long non-coding RNAs and control of gene expression in the immune system. *Trends Mol. Med.* **2014**, *20*, 623–631. [[CrossRef](#)] [[PubMed](#)]
20. Wang, K.C.; Chang, H.Y. Molecular mechanisms of long noncoding RNAs. *Mol. Cell* **2011**, *43*, 904–914. [[CrossRef](#)] [[PubMed](#)]
21. Sado, T.; Hoki, Y.; Sasaki, H. Tsix silences Xist through modification of chromatin structure. *Dev. Cell* **2005**, *9*, 159–165. [[CrossRef](#)] [[PubMed](#)]
22. Tsai, M.C.; Manor, O.; Wan, Y.; Mosammamaparast, N.; Wang, J.K.; Lan, F.; Shi, Y.; Segal, E.; Chang, H.Y. Long noncoding RNA as modular scaffold of histone modification complexes. *Science* **2010**, *329*, 689–693. [[CrossRef](#)] [[PubMed](#)]
23. Tripathi, V.; Ellis, J.D.; Shen, Z.; Song, D.Y.; Pan, Q.; Watt, A.T.; Freier, S.M.; Bennett, C.F.; Sharma, A.; Bubulya, P.A.; et al. The nuclear-retained noncoding RNA MALAT1 regulates alternative splicing by modulating SR splicing factor phosphorylation. *Mol. Cell* **2010**, *39*, 925–938. [[CrossRef](#)] [[PubMed](#)]
24. Loewer, S.; Cabili, M.N.; Guttman, M.; Loh, Y.H.; Thomas, K.; Park, I.H.; Garber, M.; Curran, M.; Onder, T.; Agarwal, S.; et al. Large intergenic non-coding RNA-RoR modulates reprogramming of human induced pluripotent stem cells. *Nat. Genet.* **2010**, *42*, 1113–1117. [[CrossRef](#)] [[PubMed](#)]
25. Nelson, B.R.; Makarewich, C.A.; Anderson, D.M.; Winders, B.R.; Troupes, C.D.; Wu, F.; Reese, A.L.; McAnally, J.R.; Chen, X.; Kavalali, E.T.; et al. A peptide encoded by a transcript annotated as long noncoding RNA enhances SERCA activity in muscle. *Science* **2016**, *351*, 271–275. [[CrossRef](#)] [[PubMed](#)]
26. Kartha, R.V.; Subramanian, S. Competing endogenous RNAs (ceRNAs): New entrants to the intricacies of gene regulation. *Front. Genet.* **2014**, *5*, 8. [[CrossRef](#)] [[PubMed](#)]
27. Sang, L.J.; Ju, H.Q.; Liu, G.P.; Tian, T.; Ma, G.L.; Lu, Y.X.; Liu, Z.X.; Pan, R.L.; Li, R.H.; Piao, H.L.; et al. lncRNA CamK-A Regulates Ca(2+)-Signaling-Mediated Tumor Microenvironment Remodeling. *Mol. Cell* **2018**, *72*, 601. [[CrossRef](#)] [[PubMed](#)]
28. Petrova, V.; Annicchiarico-Petruzzelli, M.; Melino, G.; Amelio, I. The hypoxic tumour microenvironment. *Oncogenesis* **2018**, *7*, 10. [[CrossRef](#)] [[PubMed](#)]
29. Quail, D.F.; Joyce, J.A. Microenvironmental regulation of tumor progression and metastasis. *Nat. Med.* **2013**, *19*, 1423–1437. [[CrossRef](#)] [[PubMed](#)]
30. Martin, M.; Wei, H.; Lu, T. Targeting microenvironment in cancer therapeutics. *Oncotarget* **2016**, *7*, 52575–52583. [[CrossRef](#)] [[PubMed](#)]
31. Lyssiotis, C.A.; Kimmelman, A.C. Metabolic Interactions in the Tumor Microenvironment. *Trends Cell Biol.* **2017**, *27*, 863–875. [[CrossRef](#)] [[PubMed](#)]
32. Erdogan, B.; Webb, D.J. Cancer-associated fibroblasts modulate growth factor signaling and extracellular matrix remodeling to regulate tumor metastasis. *Biochem. Soc. Trans.* **2017**, *45*, 229–236. [[CrossRef](#)] [[PubMed](#)]
33. Xing, F.; Saidou, J.; Watabe, K. Cancer associated fibroblasts (CAFs) in tumor microenvironment. *Front. Biosci.* **2010**, *15*, 166–179. [[CrossRef](#)]
34. Tao, L.; Huang, G.; Song, H.; Chen, Y.; Chen, L. Cancer associated fibroblasts: An essential role in the tumor microenvironment. *Oncol. Lett.* **2017**, *14*, 2611–2620. [[CrossRef](#)] [[PubMed](#)]
35. Lau, E.Y.; Lo, J.; Cheng, B.Y.; Ma, M.K.; Lee, J.M.; Ng, J.K.; Chai, S.; Lin, C.H.; Tsang, S.Y.; Ma, S.; et al. Cancer-Associated Fibroblasts Regulate Tumor-Initiating Cell Plasticity in Hepatocellular Carcinoma through c-Met/FRA1/HEY1 Signaling. *Cell Rep.* **2016**, *15*, 1175–1189. [[CrossRef](#)] [[PubMed](#)]
36. Liu, J.; Chen, S.; Wang, W.; Ning, B.F.; Chen, F.; Shen, W.; Ding, J.; Chen, W.; Xie, W.F.; Zhang, X. Cancer-associated fibroblasts promote hepatocellular carcinoma metastasis through chemokine-activated hedgehog and TGF-beta pathways. *Cancer Lett.* **2016**, *379*, 49–59. [[CrossRef](#)] [[PubMed](#)]
37. Song, T.; Dou, C.; Jia, Y.; Tu, K.; Zheng, X. TIMP-1 activated carcinoma-associated fibroblasts inhibit tumor apoptosis by activating SDF1/CXCR4 signaling in hepatocellular carcinoma. *Oncotarget* **2015**, *6*, 12061–12079. [[CrossRef](#)] [[PubMed](#)]
38. Cheng, J.T.; Deng, Y.N.; Yi, H.M.; Wang, G.Y.; Fu, B.S.; Chen, W.J.; Liu, W.; Tai, Y.; Peng, Y.W.; Zhang, Q. Hepatic carcinoma-associated fibroblasts induce IDO-producing regulatory dendritic cells through IL-6-mediated STAT3 activation. *Oncogenesis* **2016**, *5*, e198. [[CrossRef](#)] [[PubMed](#)]
39. Zhao, L.; Ji, G.; Le, X.; Wang, C.; Xu, L.; Feng, M.; Zhang, Y.; Yang, H.; Xuan, Y.; Yang, Y.; et al. Long Noncoding RNA LINC00092 Acts in Cancer-Associated Fibroblasts to Drive Glycolysis and Progression of Ovarian Cancer. *Cancer Res.* **2017**, *77*, 1369–1382. [[CrossRef](#)] [[PubMed](#)]

40. Yin, C.; Evason, K.J.; Asahina, K.; Stainier, D.Y. Hepatic stellate cells in liver development, regeneration, and cancer. *J. Clin. Investing.* **2013**, *123*, 1902–1910. [[CrossRef](#)] [[PubMed](#)]
41. Seki, E.; Schwabe, R.F. Hepatic inflammation and fibrosis: Functional links and key pathways. *Hepatology* **2015**, *61*, 1066–1079. [[CrossRef](#)] [[PubMed](#)]
42. Amann, T.; Bataille, F.; Spruss, T.; Muhlbauer, M.; Gabele, E.; Scholmerich, J.; Kiefer, P.; Bosserhoff, A.K.; Hellerbrand, C. Activated hepatic stellate cells promote tumorigenicity of hepatocellular carcinoma. *Cancer Sci.* **2009**, *100*, 646–653. [[CrossRef](#)] [[PubMed](#)]
43. Bian, E.B.; Wang, Y.Y.; Yang, Y.; Wu, B.M.; Xu, T.; Meng, X.M.; Huang, C.; Zhang, L.; Lv, X.W.; Xiong, Z.G.; et al. Hotair facilitates hepatic stellate cells activation and fibrogenesis in the liver. *Biochim. Biophys. Acta Mol. Basis Dis.* **2017**, *1863*, 674–686. [[CrossRef](#)] [[PubMed](#)]
44. Li, X.Q.; Ren, Z.X.; Li, K.; Huang, J.J.; Huang, Z.T.; Zhou, T.R.; Cao, H.Y.; Zhang, F.X.; Tan, B. Key Anti-Fibrosis Associated Long Noncoding RNAs Identified in Human Hepatic Stellate Cell via Transcriptome Sequencing Analysis. *Int. J. Mol. Sci.* **2018**, *19*, 675. [[CrossRef](#)] [[PubMed](#)]
45. Smith, H.A.; Kang, Y. The metastasis-promoting roles of tumor-associated immune cells. *J. Mol. Med.* **2013**, *91*, 411–429. [[CrossRef](#)] [[PubMed](#)]
46. Capece, D.; Fischietti, M.; Verzella, D.; Gaggiano, A.; Ciciarelli, G.; Tessitore, A.; Zazzeroni, F.; Alesse, E. The inflammatory microenvironment in hepatocellular carcinoma: A pivotal role for tumor-associated macrophages. *Biomed. Res. Int.* **2013**, *2013*, 187204. [[CrossRef](#)] [[PubMed](#)]
47. Zheng, X.; Turkowski, K.; Mora, J.; Brune, B.; Seeger, W.; Weigert, A.; Savai, R. Redirecting tumor-associated macrophages to become tumoricidal effectors as a novel strategy for cancer therapy. *Oncotarget* **2017**, *8*, 48436–48452. [[CrossRef](#)] [[PubMed](#)]
48. Kubo, N.; Araki, K.; Kuwano, H.; Shirabe, K. Cancer-associated fibroblasts in hepatocellular carcinoma. *World J. Gastroenterol.* **2016**, *22*, 6841–6850. [[CrossRef](#)] [[PubMed](#)]
49. Makarova-Rusher, O.V.; Medina-Echeverez, J.; Duffy, A.G.; Greten, T.F. The yin and yang of evasion and immune activation in HCC. *J. Hepatol.* **2015**, *62*, 1420–1429. [[CrossRef](#)] [[PubMed](#)]
50. Ju, C.; Tacke, F. Hepatic macrophages in homeostasis and liver diseases: From pathogenesis to novel therapeutic strategies. *Cell. Mol. Immunol.* **2016**, *13*, 316–327. [[CrossRef](#)] [[PubMed](#)]
51. Huang, J.K.; Ma, L.; Song, W.H.; Lu, B.Y.; Huang, Y.B.; Dong, H.M.; Ma, X.K.; Zhu, Z.Z.; Zhou, R. lncRNA-MALAT1 Promotes Angiogenesis of Thyroid Cancer by Modulating Tumor-Associated Macrophage FGF2 Protein Secretion. *J. Cell. Biochem.* **2017**, *118*, 4821–4830. [[CrossRef](#)] [[PubMed](#)]
52. Wu, Y.; Ding, J.; Sun, Q.; Zhou, K.; Zhang, W.; Du, Q.; Xu, T.; Xu, W. Long noncoding RNA hypoxia-inducible factor 1 alpha-antisense RNA 1 promotes tumor necrosis factor-alpha-induced apoptosis through caspase 3 in Kupffer cells. *Medicine* **2018**, *97*, e9483. [[CrossRef](#)] [[PubMed](#)]
53. Hida, K.; Maishi, N.; Annan, D.A.; Hida, Y. Contribution of Tumor Endothelial Cells in Cancer Progression. *Int. J. Mol. Sci.* **2018**, *19*, 1272. [[CrossRef](#)] [[PubMed](#)]
54. Benetti, A.; Berenzi, A.; Gambarotti, M.; Garrafa, E.; Gelati, M.; Dessy, E.; Portolani, N.; Piardi, T.; Giulini, S.M.; Caruso, A.; et al. Transforming growth factor-beta1 and CD105 promote the migration of hepatocellular carcinoma-derived endothelium. *Cancer Res.* **2008**, *68*, 8626–8634. [[CrossRef](#)] [[PubMed](#)]
55. Xiong, Y.Q.; Sun, H.C.; Zhang, W.; Zhu, X.D.; Zhuang, P.Y.; Zhang, J.B.; Wang, L.; Wu, W.Z.; Qin, L.X.; Tang, Z.Y. Human hepatocellular carcinoma tumor-derived endothelial cells manifest increased angiogenesis capability and drug resistance compared with normal endothelial cells. *Clin. Cancer Res.* **2009**, *15*, 4838–4846. [[CrossRef](#)] [[PubMed](#)]
56. Dong, R.; Liu, G.B.; Liu, B.H.; Chen, G.; Li, K.; Zheng, S.; Dong, K.R. Targeting long non-coding RNA-TUG1 inhibits tumor growth and angiogenesis in hepatoblastoma. *Cell Death Dis.* **2016**, *7*, e2278. [[CrossRef](#)] [[PubMed](#)]
57. Lu, Z.; Xiao, Z.; Liu, F.; Cui, M.; Li, W.; Yang, Z.; Li, J.; Ye, L.; Zhang, X. Long non-coding RNA HULC promotes tumor angiogenesis in liver cancer by up-regulating sphingosine kinase 1 (SPHK1). *Oncotarget* **2016**, *7*, 241–254. [[CrossRef](#)] [[PubMed](#)]
58. Yuan, S.X.; Yang, F.; Yang, Y.; Tao, Q.F.; Zhang, J.; Huang, G.; Yang, Y.; Wang, R.Y.; Yang, S.; Huo, X.S.; et al. Long noncoding RNA associated with microvascular invasion in hepatocellular carcinoma promotes angiogenesis and serves as a predictor for hepatocellular carcinoma patients' poor recurrence-free survival after hepatectomy. *Hepatology* **2012**, *56*, 2231–2241. [[CrossRef](#)] [[PubMed](#)]

59. Zheng, J.; Hu, L.; Cheng, J.; Xu, J.; Zhong, Z.; Yang, Y.; Yuan, Z. lncRNA PVT1 promotes the angiogenesis of vascular endothelial cell by targeting miR26b to activate CTGF/ANGPT2. *Int. J. Mol. Med.* **2018**, *42*, 489–496. [[PubMed](#)]
60. Yu, B.; Wang, S. Angio-lncRs: lncRNAs that regulate angiogenesis and vascular disease. *Theranostics* **2018**, *8*, 3654–3675. [[CrossRef](#)] [[PubMed](#)]
61. Chiba, T.; Iwama, A.; Yokosuka, O. Cancer stem cells in hepatocellular carcinoma: Therapeutic implications based on stem cell biology. *Hepatol. Res.* **2016**, *46*, 50–57. [[CrossRef](#)] [[PubMed](#)]
62. Xiao, Y.; Lin, M.; Jiang, X.; Ye, J.; Guo, T.; Shi, Y.; Bian, X. The Recent Advances on Liver Cancer Stem Cells: Biomarkers, Separation, and Therapy. *Anal. Cell. Pathol.* **2017**, *2017*, 5108653. [[CrossRef](#)] [[PubMed](#)]
63. Ji, J.; Wang, X.W. Clinical implications of cancer stem cell biology in hepatocellular carcinoma. *Semin. Oncol.* **2012**, *39*, 461–472. [[CrossRef](#)] [[PubMed](#)]
64. Cai, B.; Song, X.Q.; Cai, J.P.; Zhang, S. HOTAIR: A cancer-related long non-coding RNA. *Neoplasma* **2014**, *61*, 379–391. [[CrossRef](#)] [[PubMed](#)]
65. Wang, Y.; He, L.; Du, Y.; Zhu, P.; Huang, G.; Luo, J.; Yan, X.; Ye, B.; Li, C.; Xia, P.; et al. The long noncoding RNA lncTCF7 promotes self-renewal of human liver cancer stem cells through activation of Wnt signaling. *Cell Stem Cell* **2015**, *16*, 413–425. [[CrossRef](#)] [[PubMed](#)]
66. Ding, L.J.; Li, Y.; Wang, S.D.; Wang, X.S.; Fang, F.; Wang, W.Y.; Lv, P.; Zhao, D.H.; Wei, F.; Qi, L. Long Noncoding RNA lncCAMTA1 Promotes Proliferation and Cancer Stem Cell-Like Properties of Liver Cancer by Inhibiting CAMTA1. *Int. J. Mol. Sci.* **2016**, *17*, 1617. [[CrossRef](#)] [[PubMed](#)]
67. Wang, F.; Yuan, J.H.; Wang, S.B.; Yang, F.; Yuan, S.X.; Ye, C.; Yang, N.; Zhou, W.P.; Li, W.L.; Li, W.; et al. Oncofetal long noncoding RNA PVT1 promotes proliferation and stem cell-like property of hepatocellular carcinoma cells by stabilizing NOP2. *Hepatology* **2014**, *60*, 1278–1290. [[CrossRef](#)] [[PubMed](#)]
68. Conigliaro, A.; Costa, V.; Lo Dico, A.; Saieva, L.; Buccheri, S.; Dieli, F.; Manno, M.; Raccosta, S.; Mancone, C.; Tripodi, M.; et al. CD90+ liver Cancer Cells modulate endothelial cell phenotype through the release of exosomes containing H19 lncRNA. *Mol. Cancer* **2015**, *14*, 155. [[CrossRef](#)] [[PubMed](#)]
69. Zhu, P.; Wang, Y.; Wu, J.; Huang, G.; Liu, B.; Ye, B.; Du, Y.; Gao, G.; Tian, Y.; He, L.; et al. lncBRM initiates YAP1 signalling activation to drive self-renewal of liver cancer stem cells. *Nat. Commun.* **2016**, *7*, 13608. [[CrossRef](#)] [[PubMed](#)]
70. Chen, Z.Z.; Huang, L.; Wu, Y.H.; Zhai, W.J.; Zhu, P.P.; Gao, Y.F. lncSox4 promotes the self-renewal of liver tumour-initiating cells through Stat3-mediated Sox4 expression. *Nat. Commun.* **2016**, *7*, 12598. [[CrossRef](#)] [[PubMed](#)]
71. Wang, F.; Ying, H.Q.; He, B.S.; Pan, Y.Q.; Deng, Q.W.; Sun, H.L.; Chen, J.; Liu, X.; Wang, S.K. Upregulated lncRNA-UCA1 contributes to progression of hepatocellular carcinoma through inhibition of miR-216b and activation of FGFR1/ERK signaling pathway. *Oncotarget* **2015**, *6*, 7899–7917. [[CrossRef](#)] [[PubMed](#)]
72. Gui, X.; Li, H.; Li, T.; Pu, H.; Lu, D. Long Noncoding RNA CUDR Regulates HULC and beta-Catenin to Govern Human Liver Stem Cell Malignant Differentiation. *Mol. Ther.* **2015**, *23*, 1843–1853. [[CrossRef](#)] [[PubMed](#)]
73. Pu, H.; Zheng, Q.; Li, H.; Wu, M.; An, J.; Gui, X.; Li, T.; Lu, D. CUDR promotes liver cancer stem cell growth through upregulating TERT and C-Myc. *Oncotarget* **2015**, *6*, 40775–40798. [[CrossRef](#)] [[PubMed](#)]
74. Masoud, G.N.; Li, W. HIF-1alpha pathway: Role, regulation and intervention for cancer therapy. *Acta Pharm. Sin. B* **2015**, *5*, 378–389. [[CrossRef](#)] [[PubMed](#)]
75. Luo, D.; Wang, Z.; Wu, J.; Jiang, C.; Wu, J. The role of hypoxia inducible factor-1 in hepatocellular carcinoma. *Biomed. Res. Int.* **2014**, *2014*, 409272. [[CrossRef](#)] [[PubMed](#)]
76. Palazon, A.; Goldrath, A.W.; Nizet, V.; Johnson, R.S. HIF transcription factors, inflammation, and immunity. *Immunity* **2014**, *41*, 518–528. [[CrossRef](#)] [[PubMed](#)]
77. Zheng, X.; Zhang, Y.; Liu, Y.; Fang, L.; Li, L.; Sun, J.; Pan, Z.; Xin, W.; Huang, P. HIF-2alpha activated lncRNA NEAT1 promotes hepatocellular carcinoma cell invasion and metastasis by affecting the epithelial-mesenchymal transition. *J. Cell. Biochem.* **2018**, *119*, 3247–3256. [[CrossRef](#)] [[PubMed](#)]
78. Luo, F.; Sun, B.; Li, H.; Xu, Y.; Liu, Y.; Liu, X.; Lu, L.; Li, J.; Wang, Q.; Wei, S.; et al. A MALAT1/HIF-2alpha feedback loop contributes to arsenite carcinogenesis. *Oncotarget* **2016**, *7*, 5769–5787. [[PubMed](#)]
79. Wang, T.H.; Yu, C.C.; Lin, Y.S.; Chen, T.C.; Yeh, C.T.; Liang, K.H.; Shieh, T.M.; Chen, C.Y.; Hsueh, C. Long noncoding RNA CPS1-IT1 suppresses the metastasis of hepatocellular carcinoma by regulating HIF-1alpha activity and inhibiting epithelial-mesenchymal transition. *Oncotarget* **2016**, *7*, 43588–43603. [[PubMed](#)]

80. Wang, T.H.; Wu, C.H.; Yeh, C.T.; Su, S.C.; Hsia, S.M.; Liang, K.H.; Chen, C.C.; Hsueh, C.; Chen, C.Y. Melatonin suppresses hepatocellular carcinoma progression via lncRNA-CPS1-IT-mediated HIF-1 $\alpha$  inactivation. *Oncotarget* **2017**, *8*, 82280–82293. [[PubMed](#)]
81. Yang, F.; Huo, X.S.; Yuan, S.X.; Zhang, L.; Zhou, W.P.; Wang, F.; Sun, S.H. Repression of the long noncoding RNA-LET by histone deacetylase 3 contributes to hypoxia-mediated metastasis. *Mol. Cell* **2013**, *49*, 1083–1096. [[CrossRef](#)] [[PubMed](#)]
82. Budhu, A.; Wang, X.W. The role of cytokines in hepatocellular carcinoma. *J. Leukoc. Biol.* **2006**, *80*, 1197–1213. [[CrossRef](#)] [[PubMed](#)]
83. Yu, L.X.; Ling, Y.; Wang, H.Y. Role of nonresolving inflammation in hepatocellular carcinoma development and progression. *NPJ Precis. Oncol.* **2018**, *2*, 6. [[CrossRef](#)] [[PubMed](#)]
84. Rider, P.; Carmi, Y.; Cohen, I. Biologics for Targeting Inflammatory Cytokines, Clinical Uses, and Limitations. *Int. J. Cell Biol.* **2016**, *2016*, 9259646. [[CrossRef](#)] [[PubMed](#)]
85. Hernandez-Gea, V.; Toffanin, S.; Friedman, S.L.; Llovet, J.M. Role of the microenvironment in the pathogenesis and treatment of hepatocellular carcinoma. *Gastroenterology* **2013**, *144*, 512–527. [[CrossRef](#)] [[PubMed](#)]
86. Capone, F.; Guerriero, E.; Sorice, A.; Colonna, G.; Ciliberto, G.; Costantini, S. Serum Cytokine Profile Evaluation: A Tool to Define New Diagnostic and Prognostic Markers of Cancer Using Multiplexed Bead-Based Immunoassays. *Med. Inflamm.* **2016**, *2016*, 3064643. [[CrossRef](#)] [[PubMed](#)]
87. Peng, C.; Hu, W.; Weng, X.; Tong, R.; Cheng, S.; Ding, C.; Xiao, H.; Lv, Z.; Xie, H.; Zhou, L.; et al. Over Expression of Long Non-Coding RNA PANDA Promotes Hepatocellular Carcinoma by Inhibiting Senescence Associated Inflammatory Factor IL8. *Sci. Rep.* **2017**, *7*, 4186. [[CrossRef](#)] [[PubMed](#)]
88. Ding, H.; Liu, J.; Liu, B.; Zeng, Y.; Chen, P.; Su, Y. Long noncoding RNA PVT1 inhibits interferon- $\alpha$  mediated therapy for hepatocellular carcinoma cells by interacting with signal transducer and activator of transcription 1. *Biochem. Biophys. Res. Commun.* **2018**, *500*, 973–980. [[CrossRef](#)] [[PubMed](#)]
89. Li, S.; Huang, Y.; Huang, Y.; Fu, Y.; Tang, D.; Kang, R.; Zhou, R.; Fan, X.G. The long non-coding RNA TP73-AS1 modulates HCC cell proliferation through miR-200a-dependent HMGB1/RAGE regulation. *J. Exp. Clin. Cancer Res.* **2017**, *36*, 51. [[CrossRef](#)] [[PubMed](#)]
90. Lin, J.; Cao, S.; Wang, Y.; Hu, Y.; Liu, H.; Li, J.; Chen, J.; Li, P.; Liu, J.; Wang, Q.; et al. Long non-coding RNA UBE2CP3 enhances HCC cell secretion of VEGFA and promotes angiogenesis by activating ERK1/2/HIF-1 $\alpha$ /VEGFA signalling in hepatocellular carcinoma. *J. Exp. Clin. Cancer Res.* **2018**, *37*, 113. [[CrossRef](#)] [[PubMed](#)]
91. Zhang, J.; Li, Z.; Liu, L.; Wang, Q.; Li, S.; Chen, D.; Hu, Z.; Yu, T.; Ding, J.; Li, J.; et al. Long noncoding RNA TSLNC8 is a tumor suppressor that inactivates the interleukin-6/STAT3 signaling pathway. *Hepatology* **2018**, *67*, 171–187. [[CrossRef](#)] [[PubMed](#)]
92. Marquardt, J.U. The Role of Transforming Growth Factor- $\beta$  in Human Hepatocarcinogenesis: Mechanistic and Therapeutic Implications From an Integrative Multiomics Approach. *Gastroenterology* **2018**, *154*, 17–20. [[CrossRef](#)] [[PubMed](#)]
93. Fabregat, I.; Caballero-Diaz, D. Transforming Growth Factor- $\beta$ -Induced Cell Plasticity in Liver Fibrosis and Hepatocarcinogenesis. *Front. Oncol.* **2018**, *8*, 357. [[CrossRef](#)] [[PubMed](#)]
94. Neuzillet, C.; Tijeras-Raballand, A.; Cohen, R.; Cros, J.; Faivre, S.; Raymond, E.; de Gramont, A. Targeting the TGF $\beta$  pathway for cancer therapy. *Pharmacol. Ther.* **2015**, *147*, 22–31. [[CrossRef](#)] [[PubMed](#)]
95. Wang, B.; Hsu, S.H.; Majumder, S.; Kutay, H.; Huang, W.; Jacob, S.T.; Ghoshal, K. TGF $\beta$ -mediated upregulation of hepatic miR-181b promotes hepatocarcinogenesis by targeting TIMP3. *Oncogene* **2010**, *29*, 1787–1797. [[CrossRef](#)] [[PubMed](#)]
96. Huang, S.; He, X.; Ding, J.; Liang, L.; Zhao, Y.; Zhang, Z.; Yao, X.; Pan, Z.; Zhang, P.; Li, J.; et al. Upregulation of miR-23a approximately 27a approximately 24 decreases transforming growth factor- $\beta$ -induced tumor-suppressive activities in human hepatocellular carcinoma cells. *Int. J. Cancer* **2008**, *123*, 972–978. [[CrossRef](#)] [[PubMed](#)]
97. Merdrignac, A.; Angenard, G.; Allain, C.; Petitjean, K.; Bergeat, D.; Bellaud, P.; Fautrel, A.; Turlin, B.; Clement, B.; Dooley, S.; et al. A novel transforming growth factor  $\beta$ -induced long noncoding RNA promotes an inflammatory microenvironment in human intrahepatic cholangiocarcinoma. *Hepatol. Commun.* **2018**, *2*, 254–269. [[CrossRef](#)] [[PubMed](#)]



98. Yuan, J.H.; Yang, F.; Wang, F.; Ma, J.Z.; Guo, Y.J.; Tao, Q.F.; Liu, F.; Pan, W.; Wang, T.T.; Zhou, C.C.; et al. A long noncoding RNA activated by TGF-beta promotes the invasion-metastasis cascade in hepatocellular carcinoma. *Cancer Cell* **2014**, *25*, 666–681. [[CrossRef](#)] [[PubMed](#)]
99. He, M.; Qin, H.; Poon, T.C.; Sze, S.C.; Ding, X.; Co, N.N.; Ngai, S.M.; Chan, T.F.; Wong, N. Hepatocellular carcinoma-derived exosomes promote motility of immortalized hepatocyte through transfer of oncogenic proteins and RNAs. *Carcinogenesis* **2015**, *36*, 1008–1018. [[CrossRef](#)] [[PubMed](#)]
100. Sun, Z.; Yang, S.; Zhou, Q.; Wang, G.; Song, J.; Li, Z.; Zhang, Z.; Xu, J.; Xia, K.; Chang, Y.; et al. Emerging role of exosome-derived long non-coding RNAs in tumor microenvironment. *Mol. Cancer* **2018**, *17*, 82. [[CrossRef](#)] [[PubMed](#)]
101. Hu, C.; Chen, M.; Jiang, R.; Guo, Y.; Wu, M.; Zhang, X. Exosome-related tumor microenvironment. *J. Cancer* **2018**, *9*, 3084–3092. [[CrossRef](#)] [[PubMed](#)]
102. Li, S.; Li, Y.; Chen, B.; Zhao, J.; Yu, S.; Tang, Y.; Zheng, Q.; Li, Y.; Wang, P.; He, X.; et al. exoRBase: A database of circRNA, lncRNA and mRNA in human blood exosomes. *Nucleic Acids Res.* **2018**, *46*, D106–D112. [[CrossRef](#)] [[PubMed](#)]
103. Kogure, T.; Yan, I.K.; Lin, W.L.; Patel, T. Extracellular Vesicle-Mediated Transfer of a Novel Long Noncoding RNA TUC339: A Mechanism of Intercellular Signaling in Human Hepatocellular Cancer. *Genes Cancer* **2013**, *4*, 261–272. [[CrossRef](#)] [[PubMed](#)]
104. Takahashi, K.; Yan, I.K.; Wood, J.; Haga, H.; Patel, T. Involvement of extracellular vesicle long noncoding RNA (linc-VLDLR) in tumor cell responses to chemotherapy. *Mol. Cancer Res.* **2014**, *12*, 1377–1387. [[CrossRef](#)] [[PubMed](#)]
105. Takahashi, K.; Yan, I.K.; Kogure, T.; Haga, H.; Patel, T. Extracellular vesicle-mediated transfer of long non-coding RNA ROR modulates chemosensitivity in human hepatocellular cancer. *FEBS Open Bio* **2014**, *4*, 458–467. [[CrossRef](#)] [[PubMed](#)]
106. Sun, L.; Su, Y.; Liu, X.; Xu, M.; Chen, X.; Zhu, Y.; Guo, Z.; Bai, T.; Dong, L.; Wei, C.; et al. Serum and exosome long non coding RNAs as potential biomarkers for hepatocellular carcinoma. *J. Cancer* **2018**, *9*, 2631–2639. [[CrossRef](#)] [[PubMed](#)]
107. Zhang, C.; Yang, X.; Qi, Q.; Gao, Y.; Wei, Q.; Han, S. lncRNA-HEIH in serum and exosomes as a potential biomarker in the HCV-related hepatocellular carcinoma. *Cancer Biomark.* **2018**, *21*, 651–659. [[CrossRef](#)] [[PubMed](#)]
108. Frantz, C.; Stewart, K.M.; Weaver, V.M. The extracellular matrix at a glance. *J. Cell Sci.* **2010**, *123*, 4195–4200. [[CrossRef](#)] [[PubMed](#)]
109. Noel, A.; Gutierrez-Fernandez, A.; Sounni, N.E.; Behrendt, N.; Maquoi, E.; Lund, I.K.; Cal, S.; Hoyer-Hansen, G.; Lopez-Otin, C. New and paradoxical roles of matrix metalloproteinases in the tumor microenvironment. *Front. Pharmacol.* **2012**, *3*, 140. [[CrossRef](#)] [[PubMed](#)]
110. Shuman Moss, L.A.; Jensen-Taubman, S.; Stetler-Stevenson, W.G. Matrix metalloproteinases: Changing roles in tumor progression and metastasis. *Am. J. Pathol.* **2012**, *181*, 1895–1899. [[CrossRef](#)] [[PubMed](#)]
111. Li, Y.; Guo, D.; Zhao, Y.; Ren, M.; Lu, G.; Wang, Y.; Zhang, J.; Mi, C.; He, S.; Lu, X. Long non-coding RNA SNHG5 promotes human hepatocellular carcinoma progression by regulating miR-26a-5p/GSK3beta signal pathway. *Cell Death Dis.* **2018**, *9*, 888. [[CrossRef](#)] [[PubMed](#)]
112. Zhang, L.; He, X.; Jin, T.; Gang, L.; Jin, Z. Long non-coding RNA DLX6-AS1 aggravates hepatocellular carcinoma carcinogenesis by modulating miR-203a/MMP-2 pathway. *Biomed. Pharmacother.* **2017**, *96*, 884–891. [[CrossRef](#)] [[PubMed](#)]
113. Li, T.; Xie, J.; Shen, C.; Cheng, D.; Shi, Y.; Wu, Z.; Deng, X.; Chen, H.; Shen, B.; Peng, C.; et al. Amplification of Long Noncoding RNA ZFAS1 Promotes Metastasis in Hepatocellular Carcinoma. *Cancer Res.* **2015**, *75*, 3181–3191. [[CrossRef](#)] [[PubMed](#)]
114. Gouirand, V.; Guillaumond, F.; Vasseur, S. Influence of the Tumor Microenvironment on Cancer Cells Metabolic Reprogramming. *Front. Oncol.* **2018**, *8*, 117. [[CrossRef](#)] [[PubMed](#)]
115. Bandiera, S.; Pfeiffer, S.; Baumert, T.F.; Zeisel, M.B. miR-122—a key factor and therapeutic target in liver disease. *J. Hepatol.* **2015**, *62*, 448–457. [[CrossRef](#)] [[PubMed](#)]
116. Liu, A.M.; Xu, Z.; Shek, F.H.; Wong, K.F.; Lee, N.P.; Poon, R.T.; Chen, J.; Luk, J.M. miR-122 targets pyruvate kinase M2 and affects metabolism of hepatocellular carcinoma. *PLoS ONE* **2014**, *9*, e86872. [[CrossRef](#)] [[PubMed](#)]

117. Shin, S.H.; Bode, A.M.; Dong, Z. Precision medicine: The foundation of future cancer therapeutics. *NPJ Precis. Oncol.* **2017**, *1*, 12. [[CrossRef](#)] [[PubMed](#)]
118. Weber, J.A.; Baxter, D.H.; Zhang, S.; Huang, D.Y.; Huang, K.H.; Lee, M.J.; Galas, D.J.; Wang, K. The microRNA spectrum in 12 body fluids. *Clin. Chem.* **2010**, *56*, 1733–1741. [[CrossRef](#)] [[PubMed](#)]
119. Wu, T.; Du, Y. lncRNAs: From Basic Research to Medical Application. *Int. J. Biol. Sci.* **2017**, *13*, 295–307. [[CrossRef](#)] [[PubMed](#)]
120. Nguyen, Q.; Carninci, P. Expression Specificity of Disease-Associated lncRNAs: Toward Personalized Medicine. *Curr. Top. Microbiol. Immunol.* **2016**, *394*, 237–258. [[PubMed](#)]
121. Prabhakar, B.; Zhong, X.B.; Rasmussen, T.P. Exploiting Long Noncoding RNAs as Pharmacological Targets to Modulate Epigenetic Diseases. *Yale J. Biol. Med.* **2017**, *90*, 73–86. [[PubMed](#)]
122. Li, Y.; Ye, Y.; Feng, B.; Qi, Y. Long Noncoding RNA lncARSR Promotes Doxorubicin Resistance in Hepatocellular Carcinoma via Modulating PTEN-PI3K/Akt Pathway. *J. Cell. Biochem.* **2017**, *118*, 4498–4507. [[CrossRef](#)] [[PubMed](#)]
123. Amodio, N.; Stamato, M.A.; Juli, G.; Morelli, E.; Fulciniti, M.; Manzoni, M.; Taiana, E.; Agnelli, L.; Cantafio, M.E.G.; Romeo, E.; et al. Drugging the lncRNA MALAT1 via LNA gapmeR ASO inhibits gene expression of proteasome subunits and triggers anti-multiple myeloma activity. *Leukemia* **2018**, *32*, 1948–1957. [[CrossRef](#)] [[PubMed](#)]
124. Ozes, A.R.; Wang, Y.; Zong, X.; Fang, F.; Pilrose, J.; Nephew, K.P. Therapeutic targeting using tumor specific peptides inhibits long non-coding RNA HOTAIR activity in ovarian and breast cancer. *Sci. Rep.* **2017**, *7*, 894. [[CrossRef](#)] [[PubMed](#)]



© 2018 by the authors. Licensee MDPI, Basel, Switzerland. This article is an open access article distributed under the terms and conditions of the Creative Commons Attribution (CC BY) license (<http://creativecommons.org/licenses/by/4.0/>).



# Facile development of medium optimization for antibody production: implementation in spinner flask and hollow fiber reactor

Chi-Hsien Liu  · Yi-Xin Liu · Wei-Chi Wu

Received: 29 May 2018 / Accepted: 8 September 2018  
© Springer Nature B.V. 2018

**Abstract** Most bio-industrial mammalian cells are cultured in serum-free media to achieve advantages, such as batch consistency, suspended growth, and simplified purification. The successful development of a serum-free medium could contribute to a reduction in the experimental variation, enhance cell productivity, and facilitate biopharmaceuticals production using the cell culture process. Commercial serum-free media are also becoming more and more popular. However, the cell line secretes its own recombinant product and

has special nutritional requirements. How can the composition of the proprietary medium be adjusted to support the specific cell's metabolism and recombinant protein? This article uses statistical strategies to modify the commercial medium. A design of experiments is adopted to optimize the medium composition for the hybridoma cell in a serum-free condition. The supplements of peptone, ferric citrate, and trace elements were chosen to study their impact on hybridoma growth and antibody production using the response surface methodology. The stimulatory effect of the developed formulation on hybridoma growth was confirmed by the steepest ascent path. The optimal medium stimulated the hybridoma growth

**Electronic supplementary material** The online version of this article (<https://doi.org/10.1007/s10616-018-0255-z>) contains supplementary material, which is available to authorized users.

C.-H. Liu (✉)  
Department of Chemical and Materials Engineering,  
Chang Gung University, 259, Wen-Hwa First Road,  
Kwei-Shan, Taoyuan 333, Taiwan  
e-mail: chl@mail.cgu.edu.tw

C.-H. Liu  
Research Center for Chinese Herbal Medicine and  
Research Center for Food and Cosmetic Safety, College  
of Human Ecology, Chang Gung University of Science  
and Technology, 261, Wen-Hwa First Road, Taoyuan,  
Taiwan

C.-H. Liu  
Department of Chemical Engineering, Ming Chi  
University of Technology, 84, Gung-Juan Road,  
New Taipei City, Taiwan

C.-H. Liu · W.-C. Wu  
Department of Ophthalmology, Chang Gung Memorial  
Hospital, 5, Fu-Hsing Street, Taoyuan, Taiwan

Y.-X. Liu  
Graduate Institute of Biochemical and Biomedical  
Engineering, Chang Gung University, 259, Wen-Hwa  
First Road, Kwei-Shan, Taoyuan 333, Taiwan

W.-C. Wu  
College of Medicine, Chang Gung University, 259, Wen-  
Hwa First Road, Taoyuan, Taiwan

and antibody production in three diverse systems: a static plate, an agitated spinner flask, and a hollow fiber reactor. The cells in the developed serum-free medium had a better antibody production as compared to that in the commercial medium in the hollow fiber reactor. Our results demonstrated that the facile optimization for medium and antibody production was successfully accomplished in the hybridoma cells.

**Keywords** Antibody · Hybridoma · Medium optimization

## Introduction

Scientists have gradually shifted from serum-containing media to serum-free media because serum ingredients have disadvantages, such as batch-to-batch variation, virus risk, and purification interference (Price 2017). Most of the mammalian cells used for the FDA-approved production of biopharmaceuticals are cultured in serum-free media since the presence of serum is a major obstacle for purification and product validation (McGillicuddy et al. 2018). However, serum-containing media are still in general use in the biological field of basic research. In addition, the question of how to develop the serum-free passage for attached cells and the weaning procedure shall be solved for the further application of serum-free media. Antibody production cells include Chinese hamster ovary cells, murine lymphoid NS0 and hybridoma cell lines, and human PER.C6. Hybridoma belongs to the hematopoietic cells, which are anchorage-independent and immortalized by the fusion of mortal splenocytes and immortal myelomas (Shukla and Thömmes 2010). Their secreted antibodies are important in the initial screening of protein drugs, future epitope determination, biomarker detection, and disease diagnosis (Corrêa et al. 2016). Concerns for animal welfare and quality assurance of the antibody drug hasten the development of serum-free media. Several commercially media are available for culturing hybridoma cells under a serum-free culture (Manna et al. 2015). One of the drawbacks of these commercial media is that their cost is several times higher than that of the basic medium. In addition, new cell lines have unique nutrient requirements for their culture environment. Specific ingredients shall be identified to optimize the

proliferation and antibody production of cells (Tan et al. 2015).

A culture medium is a complex mixture of nutrients, buffers, and trace elements that maintain the physical environment for cell growth. The early basal media like minimum essential medium (MEM) had limited amino acids and glucose. Dulbecco's modification of Eagle's MEM (DMEM) is fortified to have fourfold the concentrations of amino acids and vitamins present in Eagle's MEM. This medium also supplies the non-essential amino acids, glycine and serine, iron, and pyruvate (Price 2017). Blended media including DMEM/F-12 developed by Barnes and Sato and RPMI1640/DMEM/F-12 (RDF, mixing ratio 2:1:1) by Murakami have been applied to the serum-free culture of different mammalian cells (Yao and Asayama 2017). The reason for mixing two kinds of media can expand the number of nutritional constituents and the trace minerals. The modification of the medium composition is usually the first step of the cell culture process to increase antibody productivity. Finding a medium composition with the best cell growth is the main purpose of medium development. Optimization studies for medium can be carried out using multivariate methods, such as response surface methodology and the statistical design of experiments (DoEs) (Xing et al. 2011; Liu and Chang 2006). These methodologies organize statistical and mathematical tools established on the fit of a polynomial model to the data that can describe the experimental system and make statistical predictions (Yolmeh and Jafari 2017). These strategies can understand possible interactions of multiple medium compositions on the cell growth and antibody production that are not observed when changing one factor at a time (Knöspel et al. 2010). The sparsity-of-effects principle states that the effects of individual- and two-factor interactions significantly influence the experimental outcome when analyzing the results from the factorial experiments. Therefore, the statistical DoEs has been chosen by many researchers such as Dhanasekaran et al. (2013), Dong et al. (2008), and Sen and Roychoudhury (2013) to optimize the culture medium or procedure. These multivariate regression analyses significantly reduce the labor of parameter screening and process optimization.

Conventionally, the parental cells in a serum-contained medium are pre-weaned by using a commercial proprietary medium to facilitate the sequential adaption to the serum-free condition (van der Valk et al. 2010). However, these cells will be bound to this

commercial medium for further production. Modification of the proprietary medium will be beneficial for the development and reduces the uncertainty of biopharmaceuticals production. The purpose of this study is to develop a serum-free medium modified from the commercial serum-free medium for a hybridoma cell line. First, several mixing-ratio media were assayed to cultivate hybridoma cells. Second, five ingredients suggested by the papers were screened to choose the most important three supplements for optimization. Third, a DoE was applied to optimize the serum-free medium for antibody production using the hybridoma cells. Accordingly, the optimal concentrations for three supplements were added to the blended media. Finally, the effects of the optimal medium on the cell growth, antibody production, and scalability were evaluated in static plate, agitation, and perfusion systems.

## Materials and methods

### Materials

Ferric citrate, glutathione, glutamine, ascorbic acid were purchased from Sigma (St. Louis, MO, USA). SFM4MAB medium and DMEM were from Hyclone (Chicago, IL, USA). Meat peptone was from Conda (Torrejón de Ardoz, Madrid, Spain) and trace element solution (A, B) was from Corning (Tewksbury, MA, USA). Spinner flasks were from Bellco Glass (Vine-land, NJ, USA) and the hollow fiber reactor was from Fibercell System (C5011, MWCO: 20kd, fiber surface area: 2100 cm<sup>2</sup>, Frederick, MD, USA). Chemically defined supplement for high cell-density hybridoma culture (CDM-HD) was also purchased from Fibercell System. DMEM supplemented with 10% CDM-HD, termed CDMHD medium, was used to compare with the optimal medium in the hollow fiber reactor using three medium circulation rates.

### Cell line and cell culture

The hybridoma cell line (CRL-1754) used in this study was established by Reimer et al. (1984) and was obtained from American Type Culture Collection (Manassas, VA, USA). This cell line produces monoclonal antibody against human IgG (Fc). The cell line was weaned in the SFM4Mab medium

(GE HealthCare, Logan, UT, USA) according to the company's protocol. The cell line was maintained in T-25-flasks using a serum-free CD Hybridoma medium supplemented with 8 mM L-glutamine (Sigma) at 37 °C under a humidified atmosphere of 5% CO<sub>2</sub> and 95% air. The mixture of SFM4Mab with DMEM (Sigma) at 1:1, 1:2, and 1:3 ratios was compared for their influence on cell proliferation and antibody production. The SFM4Mab/DMEM medium (SDM 1:2) was used for medium optimization.

### Cell concentration and viability

The number of cells was determined using the Coulter Multisizer 3 (Beckman, Brea, CA, USA). For the analysis of viable cells, 1 mL of cells was harvested from the T-25-flasks (Nunc, Rochester, NY, USA) or 100 mL spinner flasks (Bellco). After mixing with Trypan blue (Sigma) for 5 min the cell viability was then determined using a hemocytometer. For DoE experiments,  $2 \times 10^5$  cells in 1 mL test medium were seeded in a 48-well plate. Antibody production and cell concentration were determined after 96 h of growth. Experiments were performed in triplicate in 48-well tissue culture plates.

### Experimental design and statistical analysis

Fractional factorial design and central composite design data were regressed and analyzed by running the GLM and RSREG procedures in SAS 9.4 software (Cary, NC, USA). The three-dimensional response surfaces were generated by Sigmaplot (Systat, San Jose, CA, USA) based on the second-order equation. For the factorial design, 0.5 mg/mL of ferric citrate, a trace element solution containing copper sulfate, zinc sulfate, manganese sulfate, and sodium orthosilicate, 5 mg/mL of ascorbic acid, 0.5 g/mL of peptone, and 5 mg/mL of glutathione were used as the serum supplements. According to the DoE (Table S1), the concentrated supplement (10 µL) and SDM medium was added into each well to reach a final volume of 1000 µL. (" + 1" presents the 10 µL addition, while " − 1" presents no addition.). After 96 h of culture, the influence of the ingredient was estimated utilizing glm regression analysis. The linear-regression coefficients of the fractional factorial design can be applied in the selection of important medium components. A

greater positive coefficient value indicates that the ingredient has a more stimulatory effect on cells, while a negative coefficient shows that the ingredient has an inhibitory effect on cells. Among the five ingredients, three important factors such as ferric citrate, peptone, and trace elements were chosen for further optimization based on the coefficients of the first-order linear equation. A Box–Behnken design for three levels ( $-1, 0, 1$ ) is a rotatable second-order response surface model that has been adopted for medium optimization (Souza et al. 2005; Ferreira et al. 2004). It consists of a central point and the middle points of the edges. A total of 15 experimental trials (Table S2) are needed for the three-level three-factor Box–Behnken experimental design.

#### Quantification of antibody using an enzyme-linked immunosorbent assay (ELISA)

The antibody secreted by hybridoma was measured using an ELISA assay. Ninety-six-well microplates coated with affinity purified antibody specific to mouse immunoglobulin G (IgG, KPL, Gaithersburg, MD, USA) and blocked with the blocking buffer (3 g of skim milk powder and 5 g of sucrose in 100 mL PBS) were used for the analysis of hybridoma antibody production. The conditioned medium after the appropriate dilution was added to each well, and the microplate was incubated for 2 h at room temperature. After washing step, 100  $\mu$ L of detecting antibody-HRP conjugate (KPL) was added to each well, and then the plates were incubated for 2 h at room temperature. After the plate was washed 3 times, 100  $\mu$ L of tetramethylbenzidine hydrogen peroxide solution was added to each well and was allowed to react for 20 min in the dark. The reaction was stopped by adding 2 N sulfuric acid (50  $\mu$ L/well), and the absorbance was measured at 450 nm with an ELISA reader (Molecular Device, Sunnyvale, CA, USA). A serially diluted mouse IgG (SCBT, Santa Cruz, CA, USA) was prepared for the standard curve. All experiments were performed in triplicate.

#### Cell culture in a spinner flask and hollow fiber reactor

The cells at a final concentration of  $2 \times 10^6$ /mL were seeded into 50 mL of the optimal SDM medium and cultured in a 100 mL spinner flask at a 60-rpm rate.

The operation of the hollow fiber reactor is based on the instruction in the Fibercell Manual. Prior to cell inoculation, the bioreactor was aseptically circulated with the phosphate-buffered saline (PBS) and DMEM. A total of  $10^8$  cells were seeded into the extra-capillary space to establish a hybridoma culture. The serum-free medium was circulated at a 50 mL/min rate between the intra-capillary space and the reservoir bottle. The cells and their antibody solution were sampled every day for analysis.

#### Statistical analysis

Data were reported as means  $\pm$  standard deviations. Two-tailed *T* test in MS Excel was used for evaluating the differences between the test group and the control group. The *p*-value less than 0.05 was considered statistically significant:  $^*(p < 0.05)$ ,  $^{**}(p < 0.01)$ , and  $^{***}(p < 0.001)$ .

## Results and discussion

#### Basal medium screening

The model cell line was firstly weaned to the commercial serum-free medium. To reduce the composition complexity and develop the production medium, we tested the mixing ratios of SFM4MAB and DMEM on cell growth and antibody production. Figure 1 shows the growth of hybridoma enhanced when the proportion of SFM4MAB medium increased. The viable cell concentrations were similar in the media of the 1:1 and 1:2 mixing ratios of SFM4MAB and DMEM. The cells in the 1:3 mixed medium only reached 70% of cells in the 1:2 mixed medium. The viability of cells in the 1:1 and 1:2 mixed media were maintained above 80% during the 96-h culture. The DMEM could only support 50% of hybridoma growth compared to the cells in the 1:2 mixture of SFM4MAB and DMEM. Previously, RDF medium composed by RPMI:DMEM:F12 (2:1:1) has been applied as the basal media for hybridoma to reduce the manufacturing cost of antibody (Lee et al. 2009). The cost of antibody production using RDF can be reduced 17–50% compared with other serum-containing media (Chua et al. 1994). After considering the subsequent optimization and medium cost, the mixed SFM4MAB and DMEM in 1:2 (referred to as

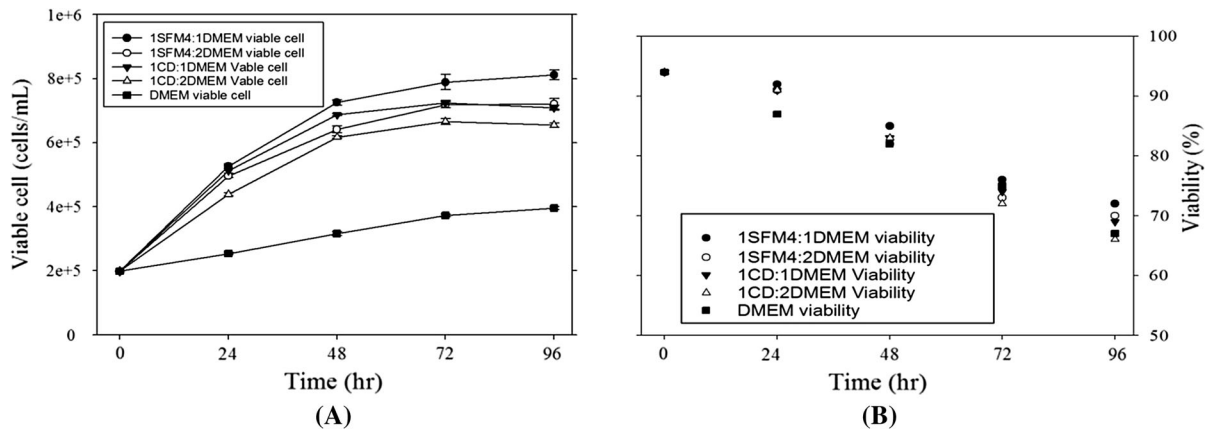


**Fig. 1** Effects of mixing ratio of medium on cell growth (a) and viability (b). The seeding concentration was  $2 \times 10^5$  cells/mL ( $N = 3$ )

SDM) was used as our basal medium for the following experiments.

#### Screening of medium supplements

We used the SDM medium as the basal medium for the evaluation of the five supplements using the two-level fractional factor experiments. The results of the cell concentration and antibody production after the 72-h culture are shown in Table S1. These data were used to fit two linear polynomials for cell growth and antibody production (Table 1). The magnitude and sign of the regression constants can be used to identify the significance of the ingredients on the key outcomes of hybridoma growth. When the coefficient is relatively large, it has more significant effects on the response than a small coefficient. Furthermore, a variable with a positive fitted coefficient increases the response, and one with a negative coefficient has an inhibitory effect on the response. The stimulatory and

inhibitory ingredients can be identified using the regression equations. For example, some supplements, such as ferric citrate, and trace elements, improve the cell growth at the 10% significant level (Table 1). Ferric citrate, peptone, and glutathione could enhance the antibody production significantly ( $p < 0.05$ ). Our results related to the promotion of ferric citrate on mammalian cell growth are similar to the study of Coombs et al. (2015). The trace elements have been reported to enhance cell growth (Liu et al. 1986). Peptone can improve hybridoma growth and enhance the production of antibodies (Zhang et al. 1994). Protein hydrolysates (peptone) can provide small peptides that have beneficial effects on animal cell proliferation and antibody production (van der Valk et al. 2010). The low-molecular peptides, derived from peptone, in the protein-free media allow an increase of the maximal cell density (Chabanon et al. 2008). The trace elements studied herein contain  $\text{CuSO}_4$ ,  $\text{ZnSO}_4$ , selenite,  $\text{MnSO}_4$ ,  $\text{Na}_2\text{SiO}_3$ , molybdic acid,  $\text{NH}_4\text{VO}_3$ ,

**Table 1** Regression coefficients of a fractional factorial design for cell growth and IgG production in SDM medium

	Cell concentration ( $10^5$ cells/mL)				Antibody production ( $\mu\text{g/mL}$ )			
	Coefficient	Standard error	t-value	p-value	Coefficient	Standard error	t-value	p-value
Constant	7.154	0.049	146.102	0.000	2.680	0.011	236.765	0.000
Ferric citrate	0.258	0.049	5.278	0.034*	0.238	0.011	20.982	0.002*
Trace elements	0.161	0.049	3.284	0.082*	0.010	0.011	0.883	0.470
Ascorbic acid	0.131	0.049	2.686	0.115	0.045	0.011	3.976	0.058*
Peptone	0.074	0.049	1.510	0.270	0.268	0.011	23.632	0.002*
Glutathione	0.147	0.049	3.003	0.095	0.088	0.011	7.730	0.016*

\* $p < 0.10$

NiSO<sub>4</sub>, and SnCl<sub>2</sub>. Selenium aids in the detoxification of free radicals as a cofactor for GSH synthetase, while iron, copper, and zinc may be bound by serum protein. The stimulatory effects of trace elements like selenium and manganese on hybridoma growth in a serum-free condition have been studied (Kovář 1988). The supplement of ferric citrate can improve the growth of NS0 cells, which constitutively produce a human IgG1 antibody (Spens and Häggström 2005). Nagira et al. (1995) evaluated various iron salts and chelating agents replacing transferrin to develop a protein-free medium for a human–human hybridoma and found that ferric citrate was favorable for the production of monoclonal antibodies. The iron may be important to the control of transmembrane electron transport and intracellular DNA synthesis in *in vitro* culture. Alcaín et al. have reported that addition of the impermeable iron chelator bathophenanthroline disulfonate (BPS) to cultured Chinese hamster lung fibroblast (CCL 39 cells) inhibits DNA synthesis in the *in vitro* culture. In contrast, BPS does not inhibit cell growth stimulated by fetal calf serum. BPS treatment also inhibits transplasma membrane electron which is restored by incubation of cells with 10 µM ferric ammonium citrate (Alcaín et al. 1995). The impacts of peptone supplementation for the mammalian cell culture are summarized as follows. The specific amino acid profile of peptone can enhance the glucose utilization and reduce lactate and ammonia production (Davami et al. 2015). Therefore, ferric citrate, trace elements, and peptone are chosen for the further optimization in the basal SDM medium in the next section.

#### Optimization of the supplements' concentrations for hybridoma cell growth

The effects of peptone, ferric citrate, and trace elements on cell growth and antibody production are shown in Supplementary Figs. S1–S3. Ferric citrate had a stimulatory effect on cell growth and antibody production around 3–6 µg/mL. This ferric salt would inhibit cell growth at the concentration of 12 µg/mL. The amount of antibody secreted by hybridoma is associated with its cell concentration. The effects of peptone and trace elements on hybridoma growth and antibody production were saturated at high concentrations (Figs. S1–S3). Peptone has been reported to enhance the antibody production in hybridoma cultures (Zhang et al. 1994).

This one-factor-at-a-time investigation can provide important information for cell growth under a simplified medium. However, the DoE has been adapted here to optimize the multiple ingredients in the medium simultaneously and understand the interaction between two supplements in an SDM medium. The rules and design for factorial experiments and response surface methodology have been recently reviewed (Yolmeh and Jafari 2017) and applied in this study. Fractional and full factorial design data were regressed by SAS 9.4 software to obtain the first-order and second-order polynomials. The regression models can be applied in screening of the important components in the medium and the construction of the steepest ascent path. In the screening tests, the magnitude and sign of the regression constants can be used to identify the significance of the components on responses such as cell growth and antibody production. When the coefficient is relatively large, it has more significant effects on the response than a small coefficient. Furthermore, a variable with a positive fitted constant increases the response and one with a negative coefficient has inhibitory effects on the response. We can identify the stimulatory and inhibitory ingredients by the regression models. The coefficients of model can be used to construct the steepest ascent path for cell growth. The direction of the maximal increase in cell concentration is generated by the gradient of the regressed polynomial. The first-order polynomial models for hybridoma growth obtained by the glm procedure of SAS software are shown in the following equation:

$$\begin{aligned} \text{Cell concentration } (\times 10^5 \text{ cells/mL}) &= 7.154 + 0.258 \\ &\times \text{ferric citrate} + 0.161 \times \text{trace elements} \\ &+ 0.131 \times \text{ascorbic acid} + 0.074 \\ &\times \text{peptone} + 0.147 \times \text{glutathione} \quad r^2 = 0.966 \\ \text{Antibody production } (\mu\text{g/mL}) &= 2.680 + 0.238 \\ &\times \text{ferric citrate} + 0.010 \times \text{trace elements} \\ &+ 0.045 \times \text{ascorbic acid} + 0.268 \times \text{peptone} \\ &+ 0.088 \times \text{glutathione} \quad r^2 = 0.999 \end{aligned}$$

The matrix of the Box-Behnken design and the comparison of data and predictions are shown in the Table S2. SAS software is applied to fit the growth data using the second-order response surface. The prediction error of the second-order polynomial



was < 3%, as indicated in Table S2. The coefficients of the second-order polynomial, the *p*-values, and the optimal concentrations are shown in Table 2. The response surface predicted that the addition of 7.7 µg/mL of ferric citrate, 0.625 mg/mL of peptone, and 0.125% of trace elements could support maximal growth. The impacts of ferric citrate, peptone, and trace elements on cell growth are visualized in Fig. 2a, b by using the second-order polynomial. The full second-order polynomial model for hybridoma growth obtained by the rsreg procedure of SAS software is shown in the following equation:

$$\begin{aligned} \text{Cell concentration (/mL)} = & 784,164 \\ & + 20,147 \times \text{ferric citrate} - 121,539 \times \text{peptone} \\ & + 3360.92 \times \text{trace elements} - 17,302 \\ & \times \text{ferric citrate}^2 + 1418.33 \times \text{ferric citrate} \\ & \times \text{peptone} - 82,153 \times \text{peptone}^2 - 2042.17 \\ & \times \text{ferric citrate} \times \text{trace elements} \\ & - 8881 \times \text{peptone} \times \text{trace elements} \\ & - 18,126 \times \text{trace elements}^2. \end{aligned}$$

The F-value and its probability for the full quadratic equation for cell growth was 50.32 and 0.001, respectively. The determination coefficient (R<sup>2</sup>) indicated that the second-order response surface could

explain 98.9% of the variability. Additionally, the optimal supplements for cell growth including 7.7 µg/mL of ferric citrate, 0.625 mg/mL of peptone, and 0.125% (v/v) of trace elements were obtained by canonical analysis in SAS software. The maximal peak of cell growth could be identified in the three-dimensional response surface plot. The steepest ascent path is used to validate the cell growth prediction in the SDM medium by the second-order polynomial. The medium composition along the ascent path and the cell growth are shown in Table S3 and Fig. 3, respectively. The maximal peak of cell growth ( $8.75 \times 10^5/\text{mL}$ ) could be observed at the fifth step, which was slightly higher than the model prediction ( $8.35 \times 10^5/\text{mL}$ ). Good agreement was shown to exist between the experimental points and the values predicted by the response model. The composition of the fifth step medium (the optimal SDM) was the same medium forecasted by the second-order polynomial, which had the maximal growth and antibody production (Figs. 3, 4).

We studied the growth kinetics of the hybridoma using a spinner flask and evaluated the impact of the developed medium on mechanically agitated cells. The optimal SDM medium containing three supplements could support cell proliferation in the agitation system, as shown in Fig. 5. The antibody yields of

**Table 2** Regression coefficient of the cell growth and the formulation of the optimal SDM medium predicted by DoEs

	Coefficient (cell/mL)	Standard error (cell/mL)	t-value	<i>p</i> -value
Constant	784,164	6885.41	113.89	< .0001
Ferric citrate	20,147	5443.39	3.7	0.0076
Peptone	− 121,539	5443.39	− 22.33	< .0001
Trace elements	3360.92	5443.39	0.62	0.5565
Ferric citrate <sup>2</sup>	− 17,302	7503.2	− 2.31	0.0545
Ferric citrate × Peptone	1418.33	7698.12	0.18	0.859
Peptone <sup>2</sup>	− 82,153	7503.2	− 10.95	< .0001
Ferric citrate × Trace elements	− 2042.17	7698.12	− 0.27	0.7984
Peptone × Trace elements	− 8881	7698.12	− 1.15	0.2865
Trace elements <sup>2</sup>	− 18,126	7503.2	− 2.42	0.0464
Factor	Code	Real concentration		
Ferric citrate	0.54	7.7 µg/mL		
Peptone	− 0.75	0.625 mg/mL		
Trace elements	0.25	0.125		
Maximal point prediction: 8.35 × 10 <sup>5</sup> /mL				

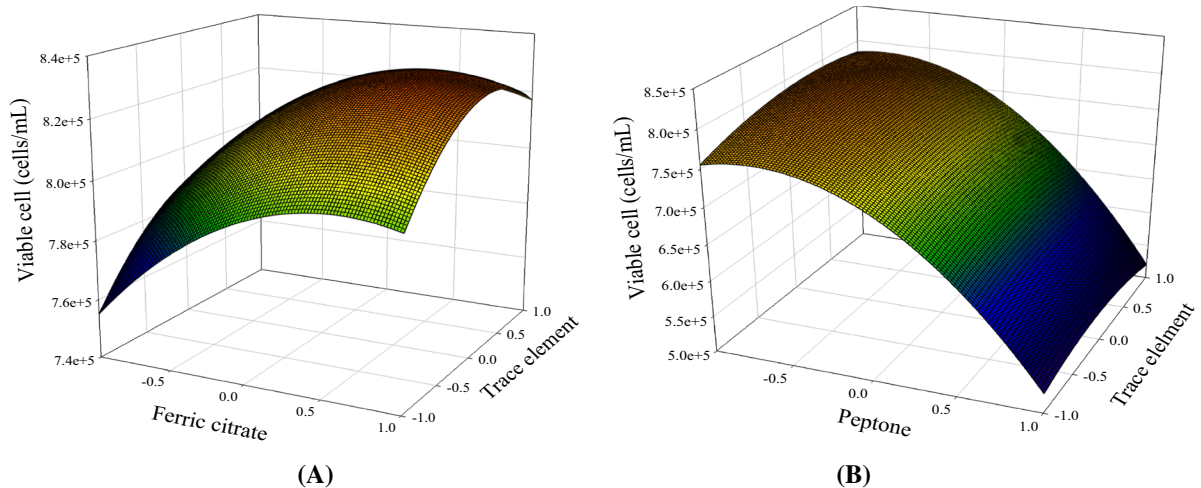
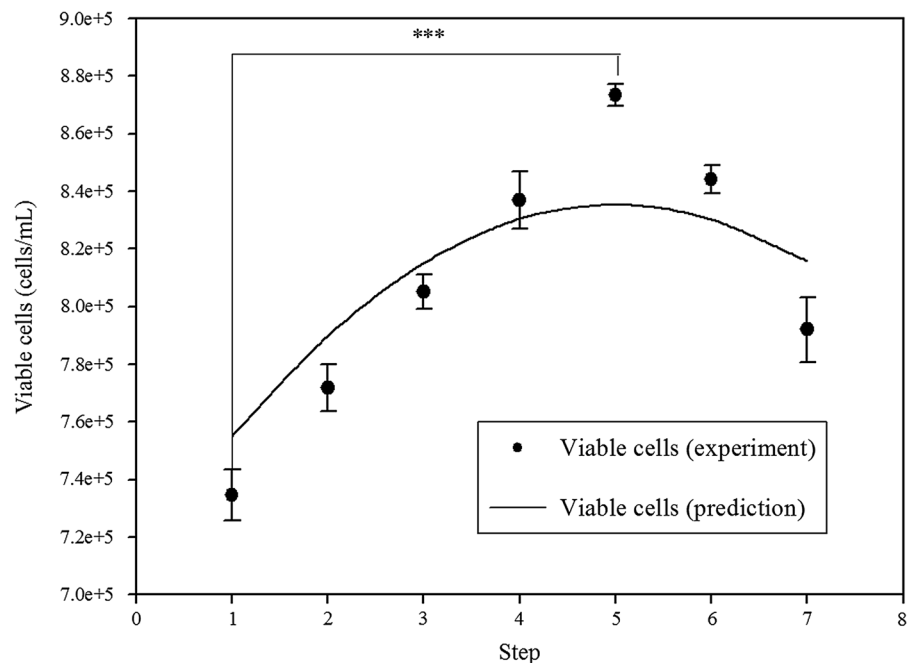


**Fig. 2** Response surfaces of ferric citrate and trace element (a) and peptone and trace elements (b) on cell growth in SDM medium

**Fig. 3** The steepest ascent path of viable cell concentration in SDM medium. (The composition of each step is shown in Table S3, seeding cell density was  $2 \times 10^5$  cells/mL, 72-h culture, 48 well; \*\*\*:  $p < 0.001$ )



cells in the static and agitation systems were similar when the optimal SDM medium was used (Fig. 6). However, the antibody production in the SDM medium only reached approximately 60% of that in the optimal SDM medium. This evidence suggested that the optimal SDM medium stimulated hybridoma growth and antibody production in static and agitation systems.

Additionally, the hollow fiber reactor can mimic a tissue-like condition with a high cell density of around

$10^7$ – $10^8$ /mL. The antibody production in a high-density bioreactor can maintain cell stability, enhance volumetric productivity, and reduce the production cost. However, the cell metabolic status and the medium are two critical factors for the successful development of the semi-continuous process. The optimal SDM medium was used to culture hybridoma in the hollow fiber reactor for semi-continuous IgG production. The antibody production in the high cell density culture device was similar at three culture

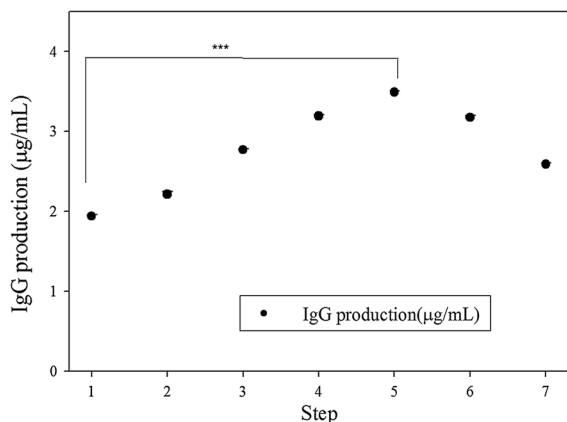


**Fig. 4** The steepest ascent path of IgG production by adding peptone, ferric citrate and trace elements. (The composition of each step is shown in Table S3, seeding cells density was  $2 \times 10^5$  cells/mL, 72-h culture, 48 well; \*\*\*:  $p < 0.001$ )

temperatures (35, 36, and 37 °C). Cell productivity in recombinant protein can be increased by cell cycle arrest through mild hypothermia (García Münzer et al. 2015). Hypothermia can simultaneously reduce cell growth, which is regulated by the cell cycle (Coronel et al. 2016). Herein the temperature shift did not enhance the antibody production of hybridoma in the hollow fiber reactor. The optimal SDM medium could support the antibody production using the high cell-density device at a temperature of  $36 \pm 1$  °C. These results suggested that the optimal SDM medium

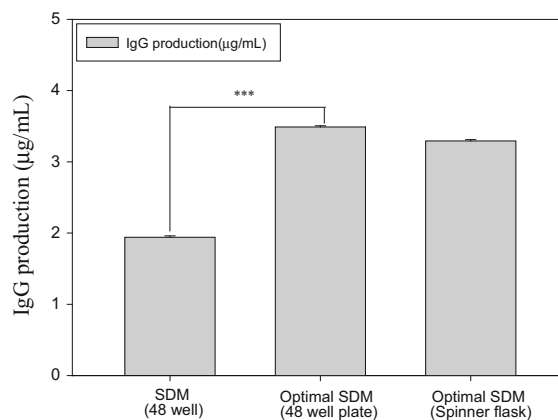


**Fig. 6** Comparison of antibody production in static and suspended systems (Seeding cells density was  $2 \times 10^5$  cells/mL, 72-h culture, spinner flask 100 mL; \*\*\*:  $p < 0.001$ )

stimulated hybridoma growth and antibody production in the static and hollow fiber systems as indicated in Fig. 7.

In order to prove the usefulness of our developed medium, a commercial serum-free medium, CDMHD, was used to compare with the optimal medium using three circulation rates at the temperature of 37 °C. CDM-HD is designed specifically for the culture of cells at high density by Fibercell Inc. The hybridoma cells cultivated in the optimal SDM had a 1.8-fold IgG production compared to that in the CDMHD medium at the rate of 182.5 mL/min (Fig. 8). In fact, the

**Fig. 5** Hybridoma cells growth in optimal SDM medium using the spinner flask (50 mL medium in 100 mL spinner flask)

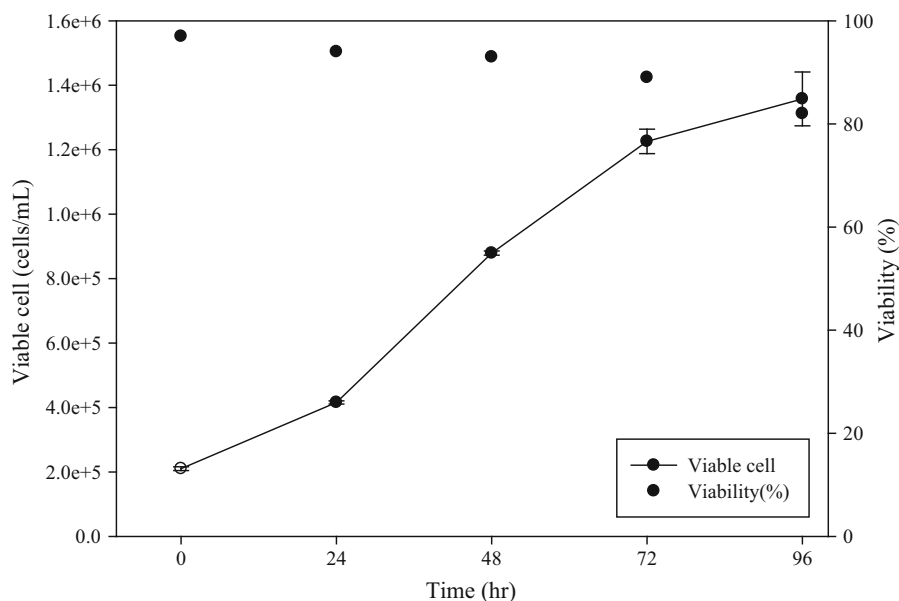


**Fig. 7** Effects of the optimal SDM medium on semi-continuous IgG production (solid line) using the hollow fiber reactor at 35, 36, and 37 °C (dash line)

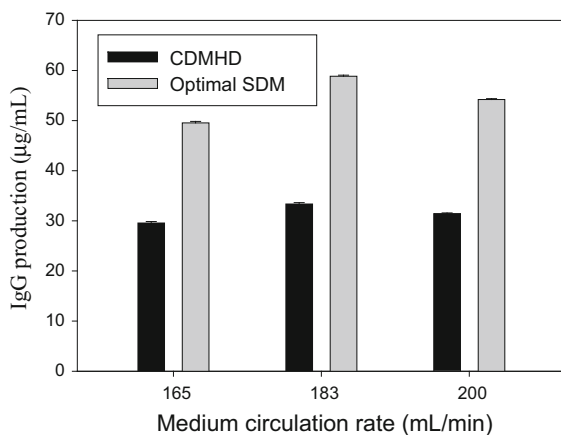
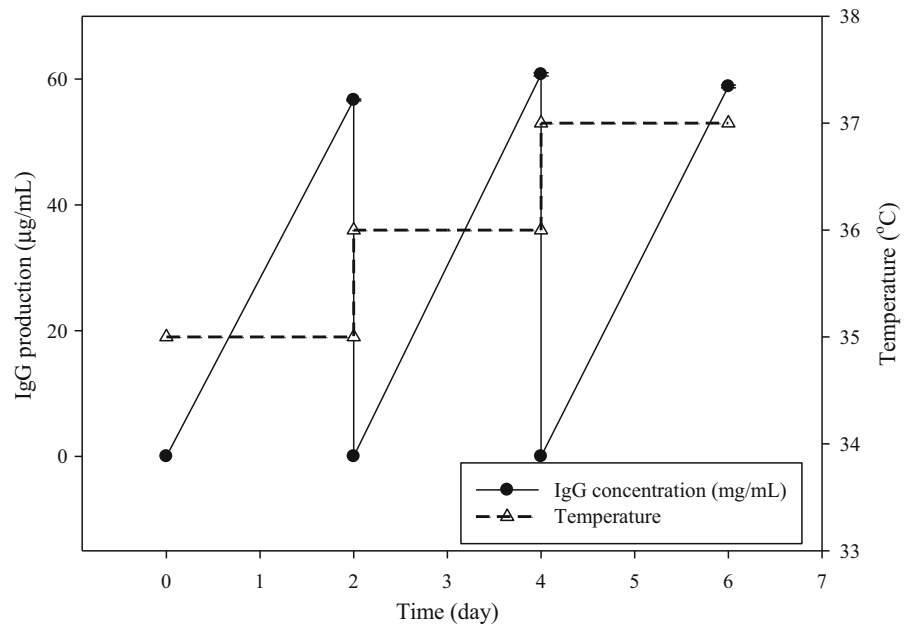


**Fig. 8** Comparison of IgG production by the hybridoma cell line (CRL-1754) in the optimal SDM medium with the commercial CDMHD medium in a hollow fiber reactor at 37 °C using three medium circulation rates

hybridoma cell line (CRL-1754) in the optimal SDM medium had better antibody production than those in CDMHD at all circulation rates. The medium composition dramatically affected the physiology, metabolism, growth and antibody production of the hybridoma cells. The proprietary composition of CDMHD makes it difficult to evaluate each ingredient's impact. The hybridoma cell line (CRL-1754) in this study is a type cell line from ATCC for the academical study, which has a low IgG titer. Our data

demonstrated that the facile optimization of the medium could be applied for the hybridoma cells and their antibody production by using the type cell as a model.

## Conclusion

The statistical development of serum-free media and their applications in different culture systems for hybridoma have been investigated in this study. First, the impacts of the 1:2 mixtures of SFM4MAB and DMEM on cell growth and antibody production were investigated to reduce the medium cost. To fortify the ingredients and optimize the new formulation, five supplements were evaluated to study their influences on cell growth in the SDM medium. Sequentially, the composition of three supplements (peptone, ferric citrate, and trace elements) was optimized using the response surface methodology. Taken together, the optimal SDM medium stimulated hybridoma growth and antibody production in the static culture, the agitated spinner flask, and the hollow fiber reactor. The facile medium optimization process was successfully accomplished for the model cell line. This platform has the potential to be a starting point for process improvements in animal cell cultures.

**Acknowledgements** We express gratitude to Ministry of Science and Technology (MOST 106-2221-E-182-050), Chang Gung University (BMRP 758) and Chang Gung Memorial Hospital (CMRPD2G0282, 2H0071) for funding and supporting this research. We would also like to thank the valuable suggestion of bioreactor operation from Frank R. H. Wang, United BioPharma Inc., Hsinchu, Taiwan.

#### Compliance with ethical standards

**Conflicts of interest** The authors would like to declare that no conflicting financial interests exist.

#### References

- Alcaín FJ, Löw H, Crane FL (1995) Iron at the cell surface controls both DNA synthesis and plasma membrane redox system. *Protoplasma* 184:233–237
- Chabanon G, Alves da Costa L, Farges B, Harscoat C, Chenu S, Goergen JL, Marc A, Marc I, Chevalot I (2008) Influence of the rapeseed protein hydrolysis process on CHO cell growth. *Biores Technol* 99:7143–7151
- Chua F, Oh SKW, Yap M, Teo WK (1994) Enhanced IgG production in eRDF media with and without serum, A comparative study. *J Immunol Methods* 167:109–119
- Coombs MRP, Grant T, Greenshields AL, Arsenault DJ, Holbein BE, Hoskin DW (2015) Inhibitory effect of iron withdrawal by chelation on the growth of human and murine mammary carcinoma and fibrosarcoma cells. *Exp Mol Pathol* 99:262–270
- Coronel J, Klausing S, Heinrich C, Noll T, Figueredo-Cardero A, Castilho LR (2016) Valeric acid supplementation combined to mild hypothermia increases productivity in CHO cell cultivations. *Biochem Eng J* 114:101–109
- Corrêa AL, Senna JPM, de Sousa ÁPB (2016) Effects of passage number on growth and productivity of hybridoma secreting MRSA anti-PBP2a monoclonal antibodies. *Cytotechnology* 68:419–427
- Davami F, Eghbalpour F, Nematollahi L, Barkhordari F, Mahboudi F (2015) Effects of peptone supplementation in different culture media on growth, metabolic pathway and productivity of CHO DG44 Cells; a new insight into amino acid profiles. *Iran Biomed J* 19:194–205
- Dhanasekaran M, Indumathi S, Lissa RP, Harikrishnan R, Rajkumar JS, Sudarsanam D (2013) A comprehensive study on optimization of proliferation and differentiation potency of bone marrow derived mesenchymal stem cells under prolonged culture condition. *Cytotechnology* 65:187–197
- Dong J, Mandenius CF, Lübberstedt M, Urbaniak T, Nüssler AKN, Knobloch D, Gerlach JC, Zeilinger K (2008) Evaluation and optimization of hepatocyte culture media factors by design of experiments (DoE) methodology. *Cytotechnology* 57:251–261
- Ferreira SL, Santos WND, Quintella CM, Neto BB, Bosques-Sendra JM (2004) Doehlert matrix: a chemometric tool for analytical chemistry—review. *Talanta* 63:1061–1067
- García Münzer DG, Ivarsson M, Usaku C, Habicher T, Soos M, Morbidelli M, Pistikopoulos EN, Mantalaris A (2015) An unstructured model of metabolic and temperature dependent cell cycle arrest in hybridoma batch and fed-batch cultures. *Biochem Eng J* 93:260–273
- Knöspel F, Schindler RK, Lübberstedt M, Petzolt S, Gerlach JC, Zeilinger K (2010) Optimization of a serum-free culture medium for mouse embryonic stem cells using design of experiments (DoE) methodology. *Cytotechnology* 62:557–571
- Kovář J (1988) Hybridoma cultivation in defined serum-free media: growth-supporting substances. V. Trace elements. *Folia Biol* 34:35–41
- Lee J, Tscheliessnig A, Chen A, Lee YY, Adduci G, Choo A, Jungbauer A (2009) Adaptation of hybridomas to protein-free media results in a simplified two-step immunoglobulin M purification process. *J Chromatogr A* 1216:2683–2688
- Liu CH, Chang TY (2006) Rational development of serum-free medium for Chinese hamster ovary cells. *Process Biochem* 41:2314–2319
- Liu YF, Tang RH, Zhang QX, Shi JY, Li XM, Liu ZQ, Zhao W (1986) Stimulation of cell growth of *Tetrahymena pyriformis* and *Chlamydomonas reinhardtii* by trace elements. *Biol Trace Elem Res* 9:89–99
- Manna L, Febo TD, Armillotta G, Luciani M, Ciarelli A, Salini R, Ventura MD (2015) Production of monoclonal antibodies in serum-free media. *Monoclon Antib Immunodiagn Immunother* 34:278–288
- McGillicuddy N, Floris P, Albrecht S, Bones J (2018) Examining the sources of variability in cell culture media used for biopharmaceutical production. *Biotechnol Lett* 40:5–21
- Nagira K, Hara T, Hayashida M, Osada K, Shiga M, Sasamoto K, Kina K, Murakami H (1995) Development of a protein-free medium with iron salts replacing transferrin for a human–human hybridoma. *Biosci Biotechnol Biochem* 59:743–745
- Price PJ (2017) Best practices for media selection for mammalian cells. *Vitro Cell Dev Biol Anim* 53:673–681
- Reimer CB, Phillips DJ, Aloisio CH, Moore DD, Galland GG, Wells TW, Black CM, McDougal JS (1984) Evaluation of thirty-one mouse monoclonal antibodies to human IgG epitopes. *Hybridoma* 3:263–275
- Sen S, Roychoudhury PK (2013) Development of optimal medium for production of commercially important monoclonal antibody 520C9 by hybridoma cell. *Cytotechnology* 65:233–252
- Shukla AA, Thömmes J (2010) Recent advances in large-scale production of monoclonal antibodies and related proteins. *Trends Biotechnol* 28:253–261
- Souza AS, Santos WNLD, Ferreira SLC (2005) Application of Box–Behnken design in the optimisation of an on-line pre-concentration system using knotted reactor for cadmium determination by flame atomic absorption spectrometry. *Spectrochim Acta Part B* 60:737–742
- Spens E, Häggström L (2005) Defined protein-free NS0 myeloma cell cultures: stimulation of proliferation by conditioned medium factors. *Biotechnol Prog* 21:87–95
- Tan KY, Teo KL, Lim JFY, Chen AKL, Reuveny S, Oh SKW (2015) Serum-free media formulations are cell line-specific and require optimization for microcarrier culture. *Cytotherapy* 17:1152–1165



- van der Valk J, Brunner D, De Smet K, Fex Svenningsen Å, Honegger P, Knudsen LE, Lindl T, Noraberg J, Price A, Scarino ML, Gstraunthaler G (2010) Optimization of chemically defined cell culture media—replacing fetal bovine serum in mammalian in vitro methods. *Toxicol In Vitro* 24:1053–1063
- Xing Z, Kenty B, Koyrakh I, Borys M, Pan SH, Li ZJ (2011) Optimizing amino acid composition of CHO cell culture media for a fusion protein production. *Process Biochem* 46:1423–1429
- Yao T, Asayama Y (2017) Animal-cell culture media: history, characteristics, and current issues. *Reprod Med Biol* 16:99–117
- Yolmeh M, Jafari SM (2017) Applications of response surface methodology in the food industry processes. *Food Bioprocess Technol* 10:413–433
- Zhang Y, Zhou Y, Yu J (1994) Effects of peptone on hybridoma growth and monoclonal antibody formation. *Cytotechnology* 16:147–150



## Original article

## Ginkgolide C reduced oleic acid-induced lipid accumulation in HepG2 cells

Wen-Chung Huang<sup>a,b,1</sup>, Ya-Ling Chen<sup>c,1</sup>, Hui-Chia Liu<sup>c</sup>, Shu-Ju Wu<sup>c,d,\*</sup>, Chian-Jiun Liou<sup>b,e,\*\*</sup><sup>a</sup> Graduate Institute of Health Industry Technology, Research Center for Food and Cosmetic Safety, Research Center for Chinese Herbal Medicine, College of Human Ecology, Chang Gung University of Science and Technology, No. 261, Wenhua 1st Rd., Guishan Dist., Taoyuan City 33303, Taiwan<sup>b</sup> Division of Allergy, Asthma, and Rheumatology, Department of Pediatrics, Chang Gung Memorial Hospital, Linkou, Guishan Dist., Taoyuan City 33303, Taiwan<sup>c</sup> Department of Nutrition and Health Sciences, Chang Gung University of Science and Technology, No. 261, Wenhua 1st Rd., Guishan Dist., Taoyuan City 33303, Taiwan<sup>d</sup> Aesthetic Medical Center, Department of Dermatology, Chang Gung Memorial Hospital, Linkou, Guishan Dist., Taoyuan City 33303, Taiwan<sup>e</sup> Department of Nursing, Research Center for Chinese Herbal Medicine, Chang Gung University of Science and Technology, No. 261, Wenhua 1st Rd., Guishan Dist., Taoyuan City 33303, Taiwan

## ARTICLE INFO

## Article history:

Received 15 February 2018

Accepted 19 July 2018

Available online xxxxx

## Keywords:

AMPK

Anti-obesity

Ginkgolide C

Lipogenesis

Lipolysis

## ABSTRACT

Ginkgolide C, isolated from *Ginkgo biloba*, is a diterpene lactone that has multiple biological functions and can improve Alzheimer disease and platelet aggregation. Ginkgolide C also inhibits adipogenesis in 3T3-L1 adipocytes. The present study evaluated whether ginkgolide C reduced lipid accumulation and regulated the molecular mechanism of lipogenesis in oleic acid-induced HepG2 hepatocytes. HepG2 cells were treated with 0.5 mM oleic acid for 48 h to induce a fatty liver cell model. Then, the cells were exposed to various concentrations of ginkgolide C for 24 h. Staining with Oil Red O and the fluorescent dye BODIPY 493/503 revealed that ginkgolide C significantly reduced excessive lipid accumulation in HepG2 cells. Ginkgolide C decreased peroxisome proliferator-activated receptor  $\gamma$  and sterol regulatory element-binding protein 1c to block the expression of fatty acid synthase. Ginkgolide C treatment also promoted the expression of adipose triglyceride lipase and the phosphorylation level of hormone-sensitive lipase to enhance the decomposition of triglycerides. In addition, ginkgolide C stimulated CPT-1 to activate fatty acid  $\beta$ -oxidation, significantly increased sirt1 and phosphorylation of AMP-activated protein kinase (AMPK), and decreased expression of acetyl-CoA carboxylase for suppressed fatty acid synthesis in hepatocytes. Taken together, our results suggest that ginkgolide C reduced lipid accumulation and increased lipolysis through the sirt1/AMPK pathway in oleic acid-induced fatty liver cells.

© 2018 The Authors. Production and hosting by Elsevier B.V. on behalf of King Saud University. This is an open access article under the CC BY-NC-ND license (<http://creativecommons.org/licenses/by-nc-nd/4.0/>).

## 1. Introduction

Obesity causes many chronic diseases, including diabetes mellitus, hyperlipidemia, and cancer (Forte et al., 2012). Many studies have also shown that excessive lipid accumulation in the liver of obese subjects induces nonalcoholic fatty liver disease (NAFLD) (Neuschwander-Tetri, 2017; Patil and Sood, 2017). NAFLD is defined as abnormal lipid accumulation in hepatocytes, and this interferes with the normal metabolism of carbohydrates and lipids for reduced glycogen synthesis and increased lipid synthesis, leading to lipid accumulation in the liver (Reccia et al., 2017). NAFLD can be divided into simple fat accumulation (hepatic steatosis) and deteriorated steatohepatitis. When the affected hepatocytes are not repaired, sustained inflammatory and oxidative damage occurs and nonalcoholic steatohepatitis (NAHS) develops (Benedict and Zhang, 2017). If NASH patients do not maintain a healthy lifestyle with moderate rest and regular exercise,

\* Corresponding author at: Department of Nutrition and Health Sciences, Chang Gung University of Science and Technology, No. 261, Wenhua 1st Rd., Guishan Dist., Taoyuan City 33303, Taiwan.

\*\* Corresponding author at: Department of Nursing, Research Center for Chinese Herbal Medicine, Chang Gung University of Science and Technology, No. 261, Wenhua 1st Rd., Guishan Dist., Taoyuan City 33303, Taiwan.

E-mail addresses: [sjwu@mail.cgu.edu.tw](mailto:sjwu@mail.cgu.edu.tw) (S.-J. Wu), [ccliu@mail.cgu.edu.tw](mailto:ccliu@mail.cgu.edu.tw) (C.-J. Liou).

<sup>1</sup> Wen-Chung Huang and Ya-Ling Chen contributed equally to the paper.

Peer review under responsibility of King Saud University.



Production and hosting by Elsevier

irreversible liver fibrosis, cirrhosis, and even liver failure and liver cancer may develop (Reccia et al., 2017). The development of NAFLD is closely associated with obesity and diabetes. Therefore, improving obesity and reducing liver lipid accumulation may attenuate its development.

The most promising treatments for NAFLD are regulated diet, moderate exercise, weight loss, and possibly bariatric surgery (Brouwers et al., 2016). Regulating food intake with excess triglycerides is especially important since free fatty acids in the digestive tract can be transported through the blood to the liver for metabolism and be converted to simple lipids or cholesterol (Romero-Gomez et al., 2017). Transcription factors regulating hepatic lipogenesis are important for liver lipid synthesis, and can activate fatty acid chain synthesis, causing excessive triglyceride synthesis and lipid accumulation in the liver (Guo et al., 2015). Thus, blocking the expression of lipogenesis transcription factors will attenuate the synthesis of triglycerides in the liver.

AMP-activated protein kinase (AMPK) is a source of energy, and some studies have found that AMPK activity can regulate lipogenesis transcription factors in hepatic steatosis (Smith et al., 2016). The excessive storage of energy in cells leads to AMPK phosphorylation, followed by phosphorylation of its substrate acetyl-CoA carboxylase (ACC) (Lim et al., 2010), which plays an essential role in regulating fatty acid synthesis (Smith et al., 2016). Interestingly, ACC phosphorylation reduces the synthesis of malonyl-CoA and the extension and synthesis of the fatty acid chain (Hou et al., 2008).

Recent studies have found that many plant extracts and flavonoids can improve liver steatosis and NAFLD (Feng et al., 2017; Tian et al., 2016). *Ginkgo biloba* is a herbal medicine that has long been used in Eastern and Western medicine to improve cardiovascular disease (Yin et al., 2014). Western medicine has used the *G. biloba* extract EGB-761 to treat cardiovascular disease and dementia, and the ginkgo fruit is used in Chinese medicine to improve asthma (Babayigit et al., 2009; Stein et al., 2015). In recent years, several diterpene lactones and flavonoids were isolated from *G. biloba* (Zeng et al., 2013). Ginkgolide A, B, and C are diterpene lactones that can improve atherosclerosis and attenuate platelet activating factor (Huang et al., 2014; Zeng et al., 2013). A previous study found that ginkgolide A can improve NAFLD in high fat diet-induced obese mice (Jeong et al., 2017). Another study found that ginkgolide C could reduce transcription factors of adipogenesis and increase lipolysis by enhancing Sirt1/AMPK activity in 3T3-L1 differentiated adipocytes (Liou et al., 2015). In this study, we investigated whether ginkgolide C reduced lipid accumulation and regulated the molecular mechanism of lipogenesis in oleic acid-induced HepG2 hepatocytes.

## 2. Materials and methods

### 2.1. Chemical reagent

Ginkgolide C (purity  $\geq 96\%$  by HPLC) was purchased from Sigma (St. Louis, MO, USA) and was dissolved in DMSO ( $\leq 0.1\%$  in all cell experiments).

### 2.2. Cell culture and induced fatty liver cells

The HepG2 cell line was obtained from the Bioresource Collection and Research Center (BCRC, Taiwan). HepG2 cells were grown in a humidified atmosphere of 5% CO<sub>2</sub> at 37 °C in DMEM medium containing 10% fetal bovine serum (FBS) and 100 mg/L penicillin and streptomycin. Hepatocytes were treated with 0.5 mM oleic

acid for 48 h and then 3–100  $\mu$ M ginkgolide C and were incubated in cell culture plates for 24 h.

### 2.3. Cell viability assay

HepG2 cells were seeded on culture plates and incubated with various concentrations of ginkgolide C for 24 h. The culture plates were treated with 5 mg/ml MTT solution (Sigma) as previously described (Huang et al., 2017), and purple formazan crystals were dissolved in isopropanol. Cell viability was determined via the absorbance at 570 nm using a spectrophotometer (Multiskan FC, Thermo, Waltham, MA, USA).

### 2.4. Oil Red O staining

HepG2 cells were seeded on culture plates and incubated with 0.5 mM oleic acid for 48 h. Then, cells were treated with ginkgolide C for 24 h. Next, cells were fixed with formalin, and Oil Red O staining was performed (Liou et al., 2015). Oil droplets were observed using microscopy (Olympus). Next, cells were treated with isopropanol and lipid accumulation was measured using a microplate reader (Multiskan FC, Thermo Fisher Scientific) and recording the absorbance at 490 nm.

### 2.5. Hepatic lipid accumulation

HepG2 cells were seeded on culture plates and incubated with oleic acid (0.5 mM) for 48 h. Then, cells were treated with ginkgolide C for 24 h. Cells were fixed with 10% formalin, and lipid accumulation was evaluated using BODIPY 493/503 (Invitrogen, Carlsbad, CA, USA) as previously described (Chang et al., 2018). Lipid accumulation was observed using fluorescence microscopy (Olympus, Tokyo, Japan) in cells with DAPI stained nuclei.

### 2.6. Western blot analysis

Equal amounts of protein were separated on 8–10% SDS–polyacrylamide gels, and transferred onto polyvinylidene fluoride (PVDF) membranes (Millipore, Billerica, MA, USA) using a previously described method (Liou and Huang, 2017). The PVDF membranes were blocked with TBST buffer (150 mM NaCl, 10 mM Tris-HCl pH 8.0, 0.1% Tween 20) containing 5% FBS for 1 h. Then, the membranes were incubated overnight at 4 °C with primary antibodies, including SREBP-1c, carnitine palmitoyltransferase 1 (CPT-1) and 2 (CPT-2) (Cell Signaling Technology, MA, USA); phosphorylated-AMPK $\alpha$  (pAMPK $\alpha$ ), AMPK $\alpha$ , fatty acid synthase (FAS) (Santa Cruz, CA, USA); sirtuin 1 (Sirt1) (Millipore); hormone-sensitive lipase (HSL), phosphorylated HSL (pHSL), adipose triglyceride lipase (ATGL), phosphorylated-acetyl CoA carboxylase-1 (pACC-1), ACC-1, peroxisome proliferator-activated receptor  $\alpha$  (PPAR- $\alpha$ ) and  $\gamma$  (PPAR- $\gamma$ ) (Epitomics, Burlingame, CA, USA), and  $\beta$ -actin (Sigma). The membranes were washed with TBST and incubated at room temperature with secondary antibodies for 1 h. All specific proteins were detected with an enhanced chemiluminescence reagent (Millipore), and protein signals were detected and quantified using the BioSpectrum 600 system (UVP, Upland, CA, USA).

### 2.7. Statistical analysis

Statistical analyses were performed using one-way ANOVA and Dunnett's post-hoc test. The results were expressed as the mean  $\pm$  standard deviation, and  $p < 0.05$  was considered statistically significant.

### 3. Results

#### 3.1. Cell viability of HepG2 cells treated with ginkgolide C

Cell viability was evaluated using the MTT method, and oleic acid did not have a significant effect on cell viability at concentrations  $\leq 0.5$  mM in HepG2 cells (Fig. 1A). Therefore, 0.5 mM oleic acid was used in all experiments. Moreover, ginkgolide C did not have a significant effect on cell viability at concentrations  $\leq 100$   $\mu$ M (Fig. 1B) in HepG2 cells. Therefore, 3–100  $\mu$ M ginkgolide C was used in all experiments.

#### 3.2. Effect of ginkgolide C on lipid accumulation in oleic acid-induced hepatic steatosis

Oleic acid was used to induce hepatic steatosis and cells were then treated with ginkgolide C for 24 h to evaluate lipid accumulation by Oil Red O staining. Oleic acid was able to induce lipid accumulation, which could be reduced by ginkgolide C (Fig. 1C). Hepatocytes were treated with isopropanol to release oil droplets, and we found that cells treated with ginkgolide C had significantly decreased lipid accumulation compared with cells treated only

with oleic acid (Fig. 1D). The fluorescent dye BODIPY 493/503 was also used to detect lipid accumulation, and fluorescence images demonstrated that ginkgolide C markedly attenuated lipid accumulation compared with the oleic acid-induced hepatic steatosis cells (Fig. 1E and F).

#### 3.3. The effect of ginkgolide C on transcription factors of lipogenesis

Ginkgolide C significantly suppressed transcription factors of lipogenesis, such as PPAR- $\gamma$  and SREBP-1c expression, compared with oleic acid-induced HepG2 cells. Ginkgolide C also reduced FAS expression for lipogenesis in fatty liver cells (Fig. 2).

#### 3.4. The effect of ginkgolide C on lipolysis in hepatocytes

Ginkgolide C significantly increased ATGL and pHSL expression in HepG2 cells compared with cells treated with only oleic acid (Fig. 3). Ginkgolide C also significantly promoted CPT-1, CD36, and PPAR- $\alpha$  expression for fatty acid  $\beta$ -oxidation, but CPT-2 was not increased compared with the oleic acid-induced HepG2 cells (Fig. 4).

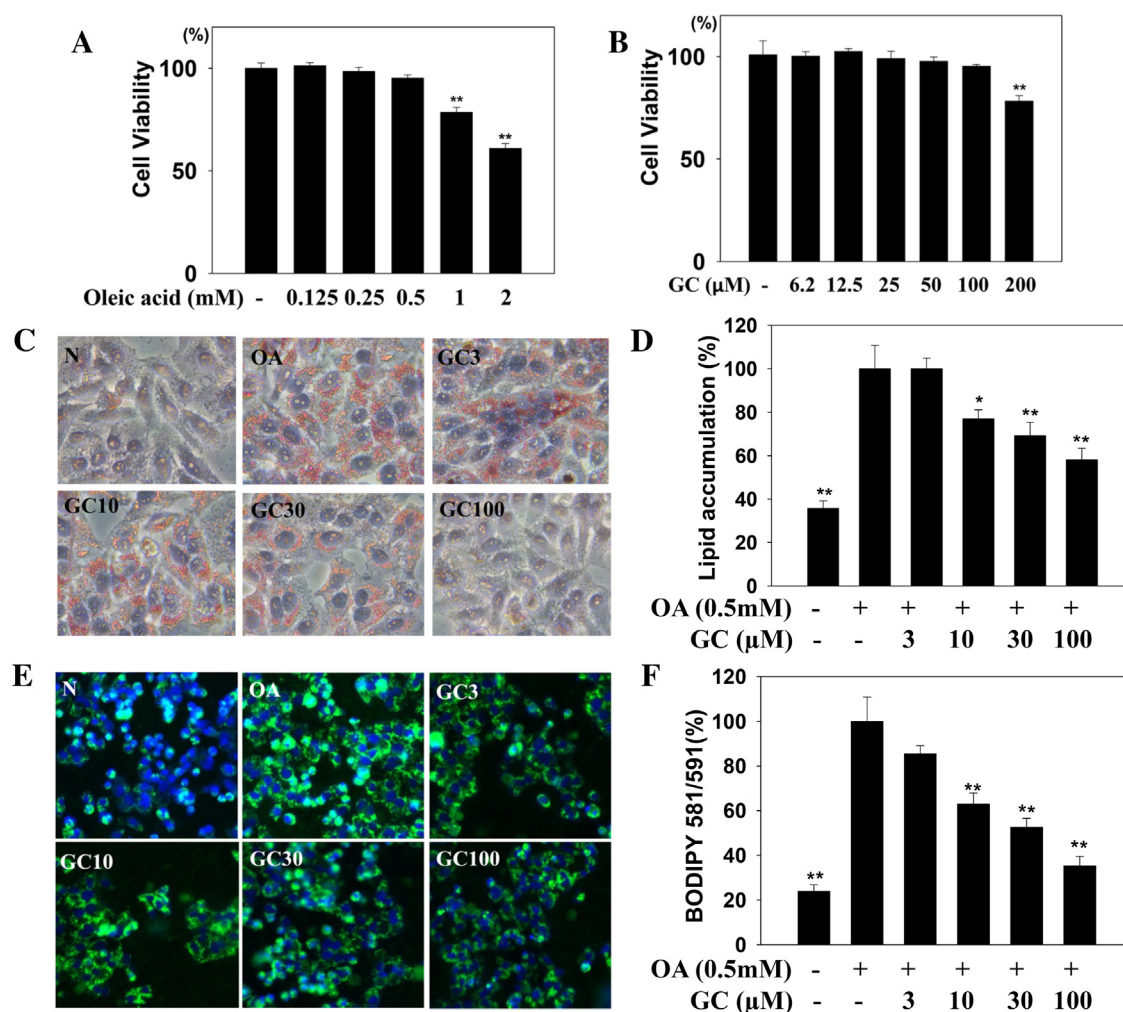


**Fig. 1.** Ginkgolide C reduced lipid accumulation in HepG2 cells. (A) Cell viability of oleic acid (OA) in HepG2 cells. (B) Cell viability of ginkgolide C (GC) in HepG2 cells. Data represent the mean  $\pm$  SD; \*\* $P$  < 0.01 compared with HepG2 cells not treated with OA or GC. Next, HepG2 cells were treated with 0.5 mM oleic acid (OA) at 37 °C for 48 h to induce lipid accumulation in hepatocytes, followed by ginkgolide C (3–100  $\mu$ M) for 24 h. (C) Oil Red O staining showed lipid accumulation that was observed with a microscope. (D) HepG2 cells were treated with isopropanol and lipid accumulation was measured using the absorbance at OD 490 nm. (E) Staining with the fluorescent dye BODIPY 493/503 (green) to detect hepatic lipid droplets. Nuclei were stained with DAPI (blue). (F) Fluorescent images were quantified, data represent the mean  $\pm$  SD; \* $P$  < 0.05, \*\* $P$  < 0.01 compared with OA group. Three independent experiments were analyzed.



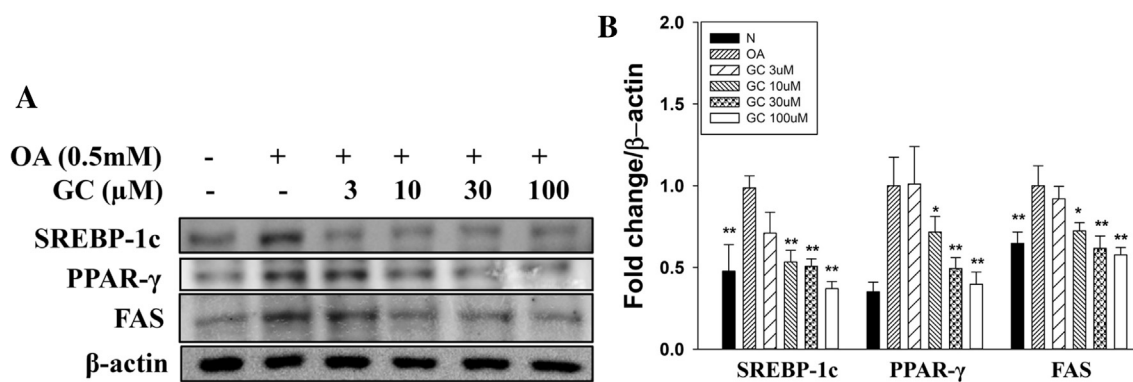


**Fig. 2.** Effects of ginkgolide C on lipid metabolism in HepG2 cells. HepG2 cells were treated with 0.5 mM oleic acid (OA) for 48 h to induce lipid accumulation, followed by ginkgolide C (3–100  $\mu$ M) for 24 h. (A) Transcription factors associated with lipogenesis and FAS were detected by Western blot. (B) Three independent experiments were analyzed, and the fold expression levels were measured relative to the expression of  $\beta$ -actin (internal control).

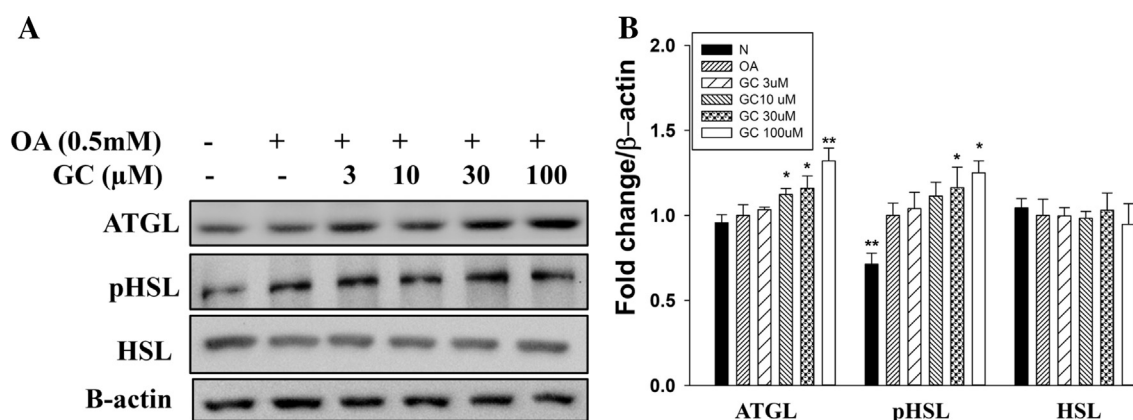


**Fig. 3.** Effects of ginkgolide C on lipid metabolism in HepG2 cells. HepG2 cells were treated with 0.5 mM oleic acid (OA) for 48 h to induce lipid accumulation in hepatocytes, followed by ginkgolide C (3–100  $\mu$ M) for 24 h. (A) Lipolysis proteins were detected by Western blot. (B) Three independent experiments were analyzed, and the fold expression levels were measured relative to the expression of  $\beta$ -actin (internal control).

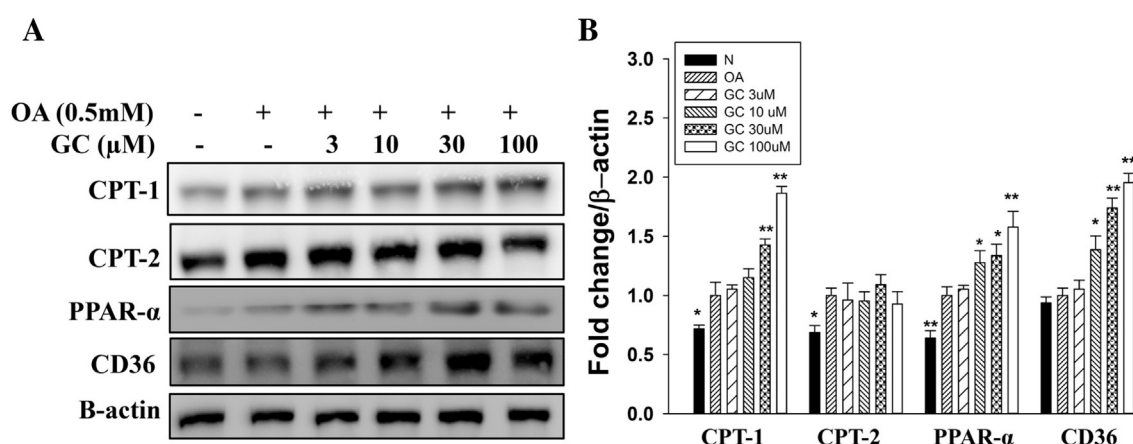


**Fig. 4.** Effects of ginkgolide C on  $\beta$ -oxidation in HepG2 cells. HepG2 cells were treated with 0.5 mM oleic acid (OA) for 48 h to induce lipid accumulation in hepatocytes, followed by ginkgolide C (3–100  $\mu$ M) for 24 h. (A)  $\beta$ -oxidation associated proteins were detected by Western blot. (B) Three independent experiments were analyzed, and the fold expression levels were measured relative to the expression of  $\beta$ -actin (internal control).

### 3.5. Ginkgolide C activated sirt1/AMPK in HepG2 cells

Western blotting was used to evaluate whether ginkgolide C regulated sirt1 and AMPK in oleic acid-induced

HepG2 cells. We found that ginkgolide C significantly promoted the expression of sirt1 and phosphorylation of ACC-1 and AMPK $\alpha$  compared with oleic acid-induced hepatocytes (Fig. 5).



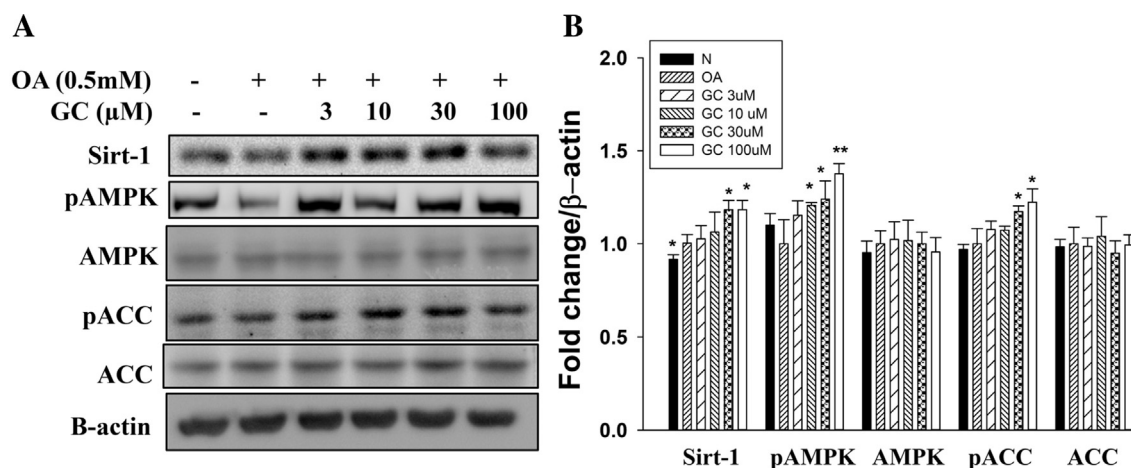


**Fig. 5.** Effects of ginkgolide C on the AMPK/Sirt-1 pathway in HepG2 cells. HepG2 cells were treated with 0.5 mM oleic acid (OA) for 48 h to induce lipid accumulation in hepatocytes, followed by ginkgolide C (3–100 μM) for 24 h. (A) The AMPK/Sirt-1 pathway proteins were detected by Western blot. (B) Three independent experiments were analyzed, and the fold expression levels were measured relative to the expression of β-actin (internal control).

#### 4. Discussion

This study demonstrated that the diterpene lactone ginkgolide C could stimulate AMPK, leading to suppressed ACC activity and the reduction of fatty acid chains, and CPT-1 for enhanced fatty acid β-oxidation. Ginkgolide C also decreased lipogenesis-related transcription factors for down-regulated FAS expression, and promoted expression of lipolysis-related enzymes to accelerate the decomposition of triglycerides. Hence, ginkgolide C significantly reduced lipid accumulation for improved hepatic steatosis in vitro.

Hepatocytes that take up excessive free fatty acids would activate enzymes associated with lipogenesis, leading to the synthesis of triglycerides and more energy accumulation in the liver (Cao et al., 2016). The expression of lipid synthesis enzymes requires lipid transcription factors to bind to the promoter of the FAS and switch on the lipid synthesis genes (Angeles and Hudkins, 2016). PPAR is the main transcription factor for lipid synthesis (Liss and Finck, 2017). Many studies confirmed that overexpression of PPARγ contributed to the differentiation of adipocytes and increased lipid accumulation in adipocytes and hepatocytes (Janani and Ranjitha Kumari, 2015). In the liver cells, oleic acid could activate PPARγ expression to accelerate lipid accumulation and cause hepatic steatosis (Kang et al., 2015). Our experiments showed that ginkgolide C had the ability to reduce PPARγ production and the accumulation of oil droplets; thus, it was confirmed that ginkgolide C could reduce excessive lipid accumulation by reducing PPARγ in liver cells. In addition, Srebp-1c could also bind to the promoter of FAS to switch on triglyceride synthesis (Wang et al., 2015). We found that oleic acid stimulated Srebp-1c expression and enhanced downstream FAS expression to initiate fat synthesis. Oil Red O and fluorescent staining demonstrated that oleic acid-stimulated hepatocytes had significantly increased oil droplet accumulation compared with normal hepatocytes. However, oleic acid-induced liver cells treated with ginkgolide C had reduced Srebp-1c expression, and ginkgolide C also significantly inhibited FAS expression to block lipid accumulation in hepatocytes. Thus, we believe that ginkgolide C can improve lipid accumulation in fatty liver cells by modulating the transcription of lipid synthesis and FAS.

Another strategy to improve the lipid accumulation in liver cells is to accelerate the decomposition of triglycerides (Romero-Gomez et al., 2017; Smith et al., 2016). The main enzymes that regulate this are ATGL and HSL. ATGL can break down triglycerides to produce diacylglycerol and a molecule of free fatty acid, and the active

HSL can also break down diacylglycerol to produce monoacylglycerol and a molecule of free fatty acid (Frühbeck et al., 2014). Many studies found that some flavonoids could enhance lipolysis and inhibit lipid accumulation in hepatocytes (Chang et al., 2013; Lasa et al., 2012). Quercetin could reduce lipid accumulation by enhancing ATGL expression in high glucose-induced fatty hepatocytes (Liu et al., 2015). Caffeic acid also promoted lipolysis via activated ATGL and HSL in oleic acid-induced hepatic steatosis (Liao et al., 2014). Our results demonstrated that ginkgolide C could significantly promote ATGL and phosphorylation of HSL for accelerated decomposition of triglycerides to glycerol and free fatty acids. Hence, ginkgolide C can accelerate lipolysis to improve lipid accumulation in fatty liver cells.

The excessive triglycerides broken down by the liver would release more free fatty acids to stimulate vascular epithelial cells and macrophages leading to an inflammatory response (Ducharme and Bickel, 2008; Young and Zechner, 2013). These macrophages will release pre-inflammatory cytokines to induce inflammation and interfere with the metabolism of carbohydrates and lipids, leading to insulin resistance in liver cells or adipocytes (Hazlehurst et al., 2016; Morrison and Kleemann, 2015). In recent years, it was determined that excessive fatty acids could be broken down by fatty acid β-oxidation to produce energy and reduce the damage to cells (Nguyen et al., 2007; Smith and Minson, 2012). Our findings suggest that ginkgolide C has the ability to enhance β-oxidation-associated enzyme expression, including CPT-1, CD36, and PPARα, while not significantly enhancing CPT-2 production. CD36 is a fatty acid translocase that can transfer free fatty acids or long chain fatty acids from the circulatory system into adipocytes, muscle cells, and liver cells (Pardina et al., 2017; Xie et al., 2017). Some studies showed that CD36 overexpression caused excessive free fatty acid uptake and hepatic steatosis, but reduced free fatty acid damage in hepatocytes, vascular epithelial cells, and adipocytes (Choi et al., 2017). Interestingly, CD36 can activate the β-oxidation break down of fatty acids in hepatocytes (Zingg et al., 2017). Previous studies found that a CD36 gene deletion blocked β-oxidation and increased lipid accumulation in hepatocytes; thus, CD36 contributed to β-oxidation expression and the decomposition of free fatty acids (Xie et al., 2017). The CPT enzyme is the most important for regulating β-oxidation, and can carry the free fatty acids from the cytoplasm into mitochondria (Pucci et al., 2016). CPT1 is located on the outer mitochondrial membrane and can convert the long-chain acyl-CoA to acylcarnitine, and assist carnitine translocase to carry acylcarnitine into the inner

membrane (Vishwanath, 2016). The CPT2 enzyme is located on the inner mitochondrial membrane and converts acylcarnitine to long-chain acyl-CoA that enters the fatty acid  $\beta$ -oxidation pathway and tricarboxylic acid cycle to produce ATP (Houten et al., 2016). Some studies confirmed that PPAR $\alpha$  was an important transcription factor to modulate mitochondrial fatty acid  $\beta$ -oxidation in liver tissue (Felicidade et al., 2015; Kim et al., 2017). Previous studies confirmed that the gene variants of PPAR $\alpha$  increased the development of cardiovascular disease and dyslipidemia as well as the fasting and postprandial blood sugar levels (Liss and Finck, 2017). Therefore, ginkgolide C could increase fatty acid  $\beta$ -oxidation leading to decreased free fatty acids, inflammation, and insulin resistance in hepatocytes.

Recent studies found that sirt1/AMPK activation could regulate the intracellular energy flow (Lim et al., 2010). When cells took up more energy, they increased AMPK activity to reduce lipid synthesis in liver cells or adipocytes (Forbes-Hernandez et al., 2017). AMPK phosphorylation also induced phosphorylation of ACC leading to decreased synthesis of the fatty acid chain (Smith et al., 2016). Resveratrol is a sirt1 inducer, and some studies showed that it could reduce lipid accumulation and improve NAFLD via the activated sirt1/AMPK pathway in HDF-induced obese mice (Elgebaly et al., 2017; Lasa et al., 2012). In a diabetic mouse model, resveratrol also regulated the oral glucose tolerance test and improved insulin resistance by promoting AMPK activity (Wu et al., 2016). Our result demonstrated that ginkgolide C significantly increased sirt1 expression and AMPK phosphorylation. Ginkgolide C also promoted ACC phosphorylation to block the synthesis of the fatty acid chain in oleic acid-induced hepatocytes.

In conclusion, ginkgolide C can inhibit hepatic accumulation by blocking transcription factors regulating lipid synthesis and FAS for lipogenesis. Ginkgolide C also promoted lipolysis and  $\beta$ -oxidation in hepatocytes, and increased sirt1/AMPK activity to suppress synthesis of the long fatty acid chain. Therefore, ginkgolide C has potential for improving hepatic steatosis.

## Acknowledgments

This study was supported in part by grants from the Chang Gung Memorial Hospital (CMRPF1G0081, CMRPF1F0083, and CMRPF1G0201) and by a grant from the Ministry of Science and Technology in Taiwan (106-2320-B-255-008-MY3).

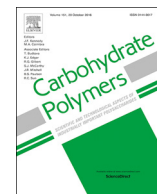
## Conflict of interest statement

The authors have declared no conflict of interest.

## References

- Angeles, T.S., Hudkins, R.L., 2016. Recent advances in targeting the fatty acid biosynthetic pathway using fatty acid synthase inhibitors. *Expert. Opin. Drug. Discov.* 11, 1187–1199.
- Babayigit, A., Olmez, D., Karaman, O., Ozogul, C., Yilmaz, O., Kivcak, B., Erbil, G., Uzuner, N., 2009. Effects of Ginkgo biloba on airway histology in a mouse model of chronic asthma. *Allergy Asthma Proc.* 30, 186–191.
- Benedict, M., Zhang, X., 2017. Non-alcoholic fatty liver disease: an expanded review. *World. J. Hepatol.* 9, 715–732.
- Brouwers, B., Hesselink, M.K., Schrauwen, P., Schrauwen-Hinderling, V.B., 2016. Effects of exercise training on intrahepatic lipid content in humans. *Diabetologia* 59, 2068–2079.
- Cao, P., Huang, G., Yang, Q., Guo, J., Su, Z., 2016. The effect of chitoooligosaccharides on oleic acid-induced lipid accumulation in HepG2 cells. *Saudi. Pharm. J.* 24, 292–298.
- Chang, J.J., Hsu, M.J., Huang, H.P., Chung, D.J., Chang, Y.C., Wang, C.J., 2013. Mulberry anthocyanins inhibit oleic acid induced lipid accumulation by reduction of lipogenesis and promotion of hepatic lipid clearance. *J. Agric. Food Chem.* 61, 6069–6076.
- Chang, Y.H., Chen, Y.L., Huang, W.C., Liou, C.J., 2018. Fucoxanthin attenuates fatty acid-induced lipid accumulation in FL83B hepatocytes through regulated Sirt1/AMPK signaling pathway. *Biochem. Biophys. Res. Commun.* 495, 197–203.
- Choi, Y.J., Lee, K.Y., Jung, S.H., Kim, H.S., Shim, G., Kim, M.G., Oh, Y.K., Oh, S.H., Jun, D.W., Lee, B.H., 2017. Activation of AMPK by berberine induces hepatic lipid accumulation by upregulation of fatty acid translocase CD36 in mice. *Toxicol. Appl. Pharmacol.* 316, 74–82.
- Ducharme, N.A., Bickel, P.E., 2008. Lipid droplets in lipogenesis and lipolysis. *Endocrinology* 149, 942–949.
- Elgebaly, A., Radwan, I.A., AboElnas, M.M., Ibrahim, H.H., Eltoomy, M.F., Atta, A.A., Mesalam, H.A., Sayed, A.A., Othman, A.A., 2017. Resveratrol supplementation in patients with non-alcoholic fatty liver disease: systematic review and meta-analysis. *J. Gastrointest. Liver Dis.* 26, 59–67.
- Felicidade, I., Marcarini, J.C., Carreira, C.M., Amarante, M.K., Afman, L.A., Mantovani, M.S., Ribeiro, L.R., 2015. Changes in gene expression in PBMCs profiles of PPARalpha target genes in obese and non-obese individuals during fasting. *Ann. Nutr. Metab.* 66, 19–25.
- Feng, X., Yu, W., Li, X., Zhou, F., Zhang, W., Shen, Q., Li, J., Zhang, C., Shen, P., 2017. Apigenin, a modulator of PPARgamma, attenuates HFD-induced NAFLD by regulating hepatocyte lipid metabolism and oxidative stress via Nrf2 activation. *Biochem. Pharmacol.* 136, 136–149.
- Forbes-Hernandez, T.Y., Giampieri, F., Gasparrini, M., Afrin, S., Mazzoni, L., Cordero, M.D., Mezzetti, B., Quiles, J.L., Battino, M., 2017. Lipid accumulation in HepG2 cells is attenuated by strawberry extract through AMPK activation. *Nutrients* 9, E621.
- Forte, V., Pandey, A., Abdelmessih, R., Forte, G., Whaley-Connell, A., Sowers, J.R., McFarlane, S.I., 2012. Obesity, diabetes, the cardiorenal syndrome, and risk for cancer. *Cardiorenal Med.* 2, 143–162.
- Frühbeck, G., Méndez-Giménez, L., Fernández-Formoso, J.A., Fernández, S., Rodríguez, A., 2014. Regulation of adipocyte lipolysis. *Nutr. Res. Rev.* 27, 63–93.
- Guo, L., Li, X., Tang, Q.Q., 2015. Transcriptional regulation of adipocyte differentiation: a central role for CCAAT/enhancer-binding protein (C/EBP) beta. *J. Biol. Chem.* 290, 755–761.
- Hazlehurst, J.M., Woods, C., Marjot, T., Cobbold, J.F., Tomlinson, J.W., 2016. Non-alcoholic fatty liver disease and diabetes. *Metabolism* 65, 1096–1108.
- Hou, X., Xu, S., Maitland-Toolan, K.A., Sato, K., Jiang, B., Ido, Y., Lan, F., Walsh, K., Wierzbicki, M., Verbeuren, T.J., Cohen, R.A., Zang, M., 2008. SIRT1 regulates hepatocyte lipid metabolism through activating AMP-activated protein kinase. *J. Biol. Chem.* 283, 20015–20026.
- Houten, S.M., Violante, S., Ventura, F.V., Wanders, R.J., 2016. The biochemistry and physiology of mitochondrial fatty acid beta-oxidation and its genetic disorders. *Annu. Rev. Physiol.* 78, 23–44.
- Huang, P., Zhang, L., Chai, C., Qian, X.C., Li, W., Li, J.S., Di, L.Q., Cai, B.C., 2014. Effects of food and gender on the pharmacokinetics of ginkgolides A, B, C and bilobalide in rats after oral dosing with ginkgo terpene lactones extract. *J. Pharm. Biomed. Anal.* 100, 138–144.
- Huang, W.C., Fang, L.W., Liou, C.J., 2017. Phloretin attenuates allergic airway inflammation and oxidative stress in asthmatic mice. *Front. Immunol.* 8, 134.
- Janani, C., Ranjitha Kumari, B.D., 2015. PPAR gamma gene—a review. *Diab. Metab. Syndr.* 9, 46–50.
- Jeong, H.S., Kim, K.H., Lee, I.S., Park, J.Y., Kim, Y., Kim, K.S., Jang, H.J., 2017. Ginkgolide A ameliorates non-alcoholic fatty liver diseases on high fat diet mice. *Biomed. Pharmacother.* 88, 625–634.
- Kang, O.H., Kim, S.B., Mun, S.H., Seo, Y.S., Hwang, H.C., Lee, Y.M., Lee, H.S., Kang, D.G., Kwon, D.Y., 2015. Puerarin ameliorates hepatic steatosis by activating the PPARalpha and AMPK signaling pathways in hepatocytes. *Int. J. Mol. Med.* 35, 803–809.
- Kim, S.M., Lee, B., An, H.J., Kim, D.H., Park, K.C., Noh, S.G., Chung, K.W., Lee, E.K., Kim, K.M., Kim, S.J., Chun, P., Lee, H.J., Moon, H.R., Chung, H.Y., 2017. Novel PPARalpha agonist MHY553 alleviates hepatic steatosis by increasing fatty acid oxidation and decreasing inflammation during aging. *Oncotarget* 8, 46273–46285.
- Lasa, A., Schweiger, M., Kotzbeck, P., Churruarín, I., Simon, E., Zechner, R., Portillo, M. P., 2012. Resveratrol regulates lipolysis via adipose triglyceride lipase. *J. Nutr. Biochem.* 23, 379–384.
- Liao, C.C., Ou, T.T., Huang, H.P., Wang, C.J., 2014. The inhibition of oleic acid induced hepatic lipogenesis and the promotion of lipolysis by caffeic acid via up-regulation of AMP-activated kinase. *J. Sci. Food Agric.* 94, 1154–1162.
- Lim, C.T., Kola, B., Korbonits, M., 2010. AMPK as a mediator of hormonal signalling. *J. Mol. Endocrinol.* 44, 87–97.
- Liou, C.J., Huang, W.C., 2017. Casticin inhibits interleukin-1 $\beta$ -induced ICAM-1 and MUC5AC expression by blocking NF- $\kappa$ B, PI3K-Akt, and MAPK signaling in human lung epithelial cells. *Oncotarget* 8, 101175–101188.
- Liou, C.J., Lai, X.Y., Chen, Y.L., Wang, C.L., Wei, C.H., Huang, W.C., 2015. Ginkgolide C suppresses adipogenesis in 3T3-L1 adipocytes via the AMPK signaling pathway. *Evid. Based Complement. Alternat. Med.* 2015, 298635.
- Liss, K.H., Finck, B.N., 2017. PPARs and nonalcoholic fatty liver disease. *Biochimie* 136, 65–74.
- Liu, L., Gao, C., Yao, P., Gong, Z., 2015. Quercetin alleviates high-fat diet-induced oxidized low-density lipoprotein accumulation in the liver: implication for autophagy regulation. *Biomed. Res. Int.* 2015, 607531.
- Morrison, M.C., Kleemann, R., 2015. Role of macrophage migration inhibitory factor in obesity, insulin resistance, type 2 diabetes, and associated hepatic comorbidities: a comprehensive review of human and rodent studies. *Front. Immunol.* 6, 308.
- Neuschwander-Tetri, B.A., 2017. Non-alcoholic fatty liver disease. *BMC Med.* 15, 45.

- Nguyen, M.T., Favelyukis, S., Nguyen, A.K., Reichart, D., Scott, P.A., Jenn, A., Liu-Bryan, R., Glass, C.K., Neels, J.G., Olefsky, J.M., 2007. A subpopulation of macrophages infiltrates hypertrophic adipose tissue and is activated by free fatty acids via Toll-like receptors 2 and 4 and JNK-dependent pathways. *J. Biol. Chem.* 282, 35279–35292.
- Pardina, E., Ferrer, R., Rossell, J., Ricart-Jane, D., Mendez-Lara, K.A., Baena-Fustegueras, J.A., Lecube, A., Julve, J., Peinado-Onsurbe, J., 2017. Hepatic CD36 downregulation parallels steatosis improvement in morbidly obese undergoing bariatric surgery. *Int. J. Obes.* 41, 1388–1393.
- Patil, R., Sood, G.K., 2017. Non-alcoholic fatty liver disease and cardiovascular risk. *World J. Gastrointest. Pathophysiol.* 8, 51–58.
- Pucci, S., Zonetti, M.J., Fisco, T., Polidoro, C., Bocchinfuso, G., Palleschi, A., Novelli, G., Spagnoli, L.G., Mazzearelli, P., 2016. Carnitine palmitoyl transferase-1A (CPT1A): a new tumor specific target in human breast cancer. *Oncotarget* 7, 19982–19996.
- Reccia, I., Kumar, J., Akladios, C., Virdis, F., Pai, M., Habib, N., Spalding, D., 2017. Non-alcoholic fatty liver disease: a sign of systemic disease. *Metabolism* 72, 94–108.
- Romero-Gomez, M., Zelber-Sagi, S., Trenell, M., 2017. Treatment of NAFLD with diet, physical activity and exercise. *J. Hepatol.* 67, 829–846.
- Smith, B.K., Marcinko, K., Desjardins, E.M., Lally, J.S., Ford, R.J., Steinberg, G.R., 2016. Treatment of nonalcoholic fatty liver disease: role of AMPK. *Am. J. Physiol. Endocrinol. Metab.* 311, E730–E740.
- Smith, M.M., Minson, C.T., 2012. Obesity and adipokines: effects on sympathetic overactivity. *J. Physiol.* 590, 1787–1801.
- Stein, C., Hopfeld, J., Lau, H., Klein, J., 2015. Effects of *Ginkgo biloba* extract EGb 761, donepezil and their combination on central cholinergic function in aged rats. *J. Pharm. Pharm. Sci.* 18, 634–646.
- Tian, Y., Ma, J., Wang, W., Zhang, L., Xu, J., Wang, K., Li, D., 2016. Resveratrol supplement inhibited the NF-kappaB inflammation pathway through activating AMPKalpha-SIRT1 pathway in mice with fatty liver. *Mol. Cell Biochem.* 422, 75–84.
- Vishwanath, V.A., 2016. Fatty acid beta-oxidation disorders: a brief review. *Ann. Neurosci.* 23, 51–55.
- Wang, Y., Viscarra, J., Kim, S.J., Sul, H.S., 2015. Transcriptional regulation of hepatic lipogenesis. *Nat. Rev. Mol. Cell Biol.* 16, 678–689.
- Wu, H., Sheng, Z.Q., Xie, J., Li, R., Chen, L., Li, G.N., Wang, L., Xu, B., 2016. Reduced HMGB 1-mediated pathway and oxidative stress in resveratrol-treated diabetic mice: a possible mechanism of cardioprotection of resveratrol in diabetes mellitus. *Oxid. Med. Cell Longev.* 2016, 9836860.
- Xie, Y., Cifarelli, V., Pietka, T., Newberry, E.P., Kennedy, S.M., Khalifeh-Soltani, A., Clugston, R., Atabai, K., Abumrad, N.A., Davidson, N.O., 2017. Cd36 knockout mice are protected against lithogenic diet-induced gallstones. *J. Lipid Res.* 58, 1692–1701.
- Yin, B., Xu, Y., Wei, R., Luo, B., 2014. Ginkgo biloba on focal cerebral ischemia: a systematic review and meta-analysis. *Am. J. Chin. Med.* 42, 769–783.
- Young, S.G., Zechner, R., 2013. Biochemistry and pathophysiology of intravascular and intracellular lipolysis. *Genes Dev.* 27, 459–484.
- Zeng, Z., Zhu, J., Chen, L., Wen, W., Yu, R., 2013. Biosynthesis pathways of ginkgolides. *Pharmacogn. Rev.* 7, 47–52.
- Zingg, J.M., Hasan, S.T., Nakagawa, K., Canepa, E., Ricciarelli, R., Villacorta, L., Azzi, A., Meydani, M., 2017. Modulation of cAMP levels by high-fat diet and curcumin and regulatory effects on CD36/FAT scavenger receptor/fatty acids transporter gene expression. *BioFactors* 43, 42–53.



# Protein moiety in oligochitosan modified vector regulates internalization mechanism and gene delivery: Polyplex characterization, intracellular trafficking and transfection

Monika Kumari<sup>a</sup>, Chi-Hsien Liu<sup>a,b,c,d,\*</sup>, Wei-Chi Wu<sup>d,e</sup>

<sup>a</sup> Department and Graduate Institute of Chemical and Materials Engineering, Chang Gung University, 259, Wen-Hwa First Road, Kwei-Shan, Tao-Yuan 333, Taiwan

<sup>b</sup> Research Center for Chinese Herbal Medicine and Research Center for Food and Cosmetic Safety, College of Human Ecology, Chang Gung University of Science and Technology, 261, Wen-Hwa First Road, Taoyuan, Taiwan

<sup>c</sup> Department of Chemical Engineering, Ming Chi University of Technology, 84, Gung-Juan Road, New Taipei City, Taiwan

<sup>d</sup> Department of Ophthalmology, Chang Gung Memorial Hospital, Linkou, 5, Fu-Hsing Street, Taoyuan, Taiwan

<sup>e</sup> College of Medicine, Chang Gung University, 259, Wen-Hwa First Road, Taoyuan, Taiwan

## ARTICLE INFO

### Keywords:

Oligochitosan-modified proteins  
Endocytosis  
Internalization  
Transfection  
Mechanism

## ABSTRACT

Oligochitosan-modified proteins have gained attention as efficient non-viral vectors for gene delivery. However, little information exists if protein moieties can serve as an important role for internalization and endosome escape ability of the genetic material. To explore this issue, we designed two cationic oligochitosan-modified vectors that consist of different proteins, namely a hydrophobic plant protein (zein) and a hydrophilic animal protein (ovalbumin (OVA)) to deliver pDNA to epithelial cell line CHO-K1 and HEK 293 T. These cationic vectors were systematically characterized by molecular weight, infrared (IR) structural analysis, transmission electron microscopy (TEM) morphology, and surface charge. A remarkable impact of protein moieties was observed on physicochemical properties of the developed vectors. Oligochitosan-modified zein containing hydrophobic protein exhibited high buffering capacity and excellent DNA binding ability compared to the oligochitosan-modified OVA. The data on transfection in the presence of endocytic inhibitors indicated that the caveolae-mediated pathway (CvME) played a key role in the internalization of the zein-based polyplex. However, the OVA-based polyplex was internalized in CHO-K1 cells via CvME and in HEK 293 T cells via the lipid-mediated pathway. Moreover, oligochitosan-modified zein exhibited lower cytotoxicity, greater lysosomal escape ability, better plasmid stability, and better transfection efficiency than the oligochitosan-modified OVA. This study offers a facile procedure for the synthesis of cationic vectors and elucidates the relationship that exists between protein moieties and transfection activity, thus providing an alternative, non-viral platform for the gene delivery.

## 1. Introduction

Chitin and its derivatives chitosan and oligochitosan (OC) are natural cationic polysaccharides that show excellent biological activity, such as low cytotoxicity coupled with good biodegradability. Moreover, positively charged OC can preferentially assist in electrostatic interaction with negatively charged DNA. Therefore, it is considered to be a good candidate for use in gene delivery systems (Shen et al., 2017). However, its marginal transfection efficiency limits its use as a non-viral system. This is because DNA binds tightly with OC, reducing the ability of the DNA to release from the complex into the target site (Peng et al., 2011). To address this limitation, several efforts have been made

to modify the chitin and its derivatives with proteins or other cationic polymers such as polyethylenimine (PEI), dendrimers to increase transfection efficiency; however, little of this research has obtained better transfection activity than OC alone (Ren et al., 2016). Syga et al. revealed that the addition of albumin enhances the transfection efficiency of the PEI-DNA complex. Thus, the presence of albumin increasing the interaction of the polyplex with cells (Syga, Nicoli, Kohler, & Shastri, 2016). Proteins such as bovine serum albumin (BSA) and human serum albumin (HSA) are water-soluble and stable over a wide pH range, from 4 to 9. Therefore, these proteins are used extensively for gene delivery systems. Moreover, the protein moieties provide a high number of reactive residues on their surface for the covalent attachment

\* Corresponding author at: Department and Graduate Institute of Chemical and Materials Engineering, Chang Gung University, 259, Wen-Hwa First Road, Kwei-Shan, Tao-Yuan 333, Taiwan.

E-mail address: [CHL@mail.cgu.edu.tw](mailto:CHL@mail.cgu.edu.tw) (C.-H. Liu).

<https://doi.org/10.1016/j.carbpol.2018.08.131>

Received 20 June 2018; Received in revised form 13 August 2018; Accepted 29 August 2018

Available online 31 August 2018

0144-8617/ © 2018 Elsevier Ltd. All rights reserved.



of other molecules. Ovalbumin (OVA) is also a hydrophilic protein, but few reports have been published on the surface modification of OVA through covalent cross-linking to enable its use as a gene delivery vector. Another protein is zein, which is a plant protein that is water-insoluble and hydrophobic in nature. It is isolated from the endosperm of the corn kernel and possesses ideal properties that make it an ideal candidate for use as a gene delivery vector, such as biocompatibility and biodegradability (Lohcharoenkal, Wang, Chen, & Rojanasakul, 2014). Regier et al. have demonstrated that the zein nanospheres interact with DNA and protect it from the endonuclease enzyme, which improves cellular uptake and transfection efficiency (Regier, Taylor, Borczyk, Yang, & Pannier, 2012). Hydrophilic animal proteins offer several advantages as gene delivery vectors but typically suffer from low stability because of their quick solubility. In addition, utilizing hydrophobic plant proteins (e.g., zein) surmount the shortcomings of hydrophilic animal proteins by providing advantages from their enzyme-degradable and pH-resistant properties. Zein has also been proven as a safe carrier for the pharmaceutical industry due to its insolubility, which allows for drug delivery via an oral route (Lee, Kim, & Park, 2016). A great deal of work has been undertaken with zein for drug delivery, but there has been scant research focused upon the use of zein as a gene delivery vector. Surveys of the literature have provided compelling proof that the use of proteins such as albumin or zein influence transfection efficiency. But the lack of understanding about internalization mechanism encourages researchers to synthesize new convincing polymers.

Currently, the molecular details behind the internalization and endosome escape abilities of protein-cationic polymer hybrid polyplexes are poorly understood. Hence, there is a crucial need for the study of their internalization mechanisms to improve their therapeutic acceptability. Typically, the entry method of polyplexes into cells is divided into two major groups: through an endocytic pathway (energy-dependent) and through a non-endocytic pathway (energy-independent). Some authors have suggested that most of the positively charged polyplexes can enter cells through endocytic pathways. These pathways are categorized into two different types: a clathrin-dependent pathway (CDE) and a clathrin-independent pathway (CIE) (Shi et al., 2017). Generally, the gene delivery pathway begins with the internalization of a polyplex through an endocytosis process, which is followed by escape from the endosomal-lysosomal compartment and then finally enter into the nucleus for the gene expression (Dean, Strong, & Zimmer, 2005). Some researchers have also demonstrated that the size of nanoparticles affects the uptake mechanism and transfection efficiency. Rejman et al. have proven that a particle of less than 200 nm is internalized via a CME pathway, whereas a particle in the 200–500 nm size range is internalized via a CvME pathway (Joanna Rejman, Bragonzi, & Conese, 2005). Keeping this in mind, we designed our DNA polyplexes with a size distribution around the range of 150 to 250 nm.

The cellular uptake mechanisms define the endosomal fates of particular gene carriers (Vercauteren et al., 2010). Therefore, we considered the possibility that the covalent conjugation of OC with two different proteins, hydrophilic animal protein (OVA) and hydrophobic plant protein (zein), might impact the delivery of DNA via different endocytic pathways and sequentially affect gene expression. To prove this hypothesis, we designed two cationic vectors: one consisting of a hydrophilic protein with OC (OVA-OC) and the other consisting of a hydrophobic protein with OC (zein-OC) to study their internalization mechanism and subsequent gene expressions. Our aim was to investigate intracellular trafficking mechanisms and their relationship to two different vectors in distinct mammalian cell lines. To do this, we chose two different cell lines: CHO-K1 (derived from Chinese hamster's ovary) and HEK 293 T (derived from human embryonic kidney), because these cells are often used to evaluate transfection efficiency as well as the production of recombinant protein. To understand the internalization mechanisms, we treated cells with different endocytic inhibitors specific for particular pathways in the presence of a polyplex

and determined transfection efficiency with IN Cell Investigator software. The cells were treated with fluorescein isothiocyanate (FITC)-labeled polyplexes and LysoTracker and imaged using confocal microscopy to determine whether the internalization mechanisms were related to the protein moiety in the synthesized vector.

## 2. Experimental section

### 2.1. Materials

The oligochitosan (MW = 662, degree of deacetylation > 90%) was obtained from Yaizu Suisan Kagaku Industry. Zein, OVA, Hoechst 33342, trypsin-EDTA, glutaraldehyde, chlorpromazine, sodium azide, genistein, monensin, FITC, ninhydrin, Heparin sodium salt from porcine, and potassium bromide (KBr) were purchased from Sigma-Aldrich (St. Louis, MO, USA). Methyl- $\beta$ -cyclodextrin was acquired from Wako Pure Chemical Industries, Ltd. (Osaka, Japan). LysoTracker Red was purchased from Molecular Probes/Invitrogen (Eugene, Oregon, USA). Plasmid EGFP-C3 (size 4.7 kb) was procured from Takara Bio (Shiga, Japan) and amplified in *Escherichia coli* strain DH-5 $\alpha$ . The plasmid was purified from the cell pellets using a purification kit (GeneMark, Taipei, Taiwan). Fetal bovine serum (FBS) was purchased from Biological Industries (Haemek, Israel). All reagents were used without further purification.

### 2.2. Synthesis and characterization of the OC-modified proteins

Protein (OVA or zein) was cross-linked with OC in the presence of glutaraldehyde via one-step process. The detail synthesis procedure was reported in our previous publication (Kumari, Liu, & Wu, 2018). For the oligochitosan modification on the protein moiety, OVA was dissolved in distilled water. Zein was dissolved in ethanol. The formation of isomer could be a major drawback in the case of covalent conjugation via glutaraldehyde cross-linker. Therefore, in order to restrict the formation of isomer, the molar concentration ratio of protein and OC molecules were controlled to maintain the degree of cross-linking. The molar concentration ratio of protein to OC molecules crosslinked in both vectors was 1:10 (mass ratio of protein/OC = 2 mg/0.2 mg), the amine group of OC molecules has higher crosslinking efficiency towards the amine group of OVA or zein molecules separately in the presence of 1.25% glutaraldehyde. The mixture of protein, OC, and glutaraldehyde was reacted for 2 h at room temperature. Finally, the free aldehyde group was quenched by addition of 0.1 mg/mL glycine and vortexed for 30 min. The unreacted reagents were removed by washing twice with deionized water using 50 kDa cutoff Vivaspin 6 tube through the centrifugation technique to obtain the purified vectors. The synthesized vectors were analyzed for their protein and OC content using bicinchoninic acid (BCA) and ninhydrin test. Additionally, the molecular weight of the developed vector was studied by using ZetaSizer<sup>®</sup> Nano ZS 90 (Malvern Instruments, Worcestershire, UK).

#### 2.2.1. Structural analysis of the OC-modified proteins

Structural analyses for zein, OVA, OC, zein-OC, and OVA-OC were performed by using Fourier Transform Infrared Spectroscopy (FTIR) (Alpha, Bruker Co., Germany). The IR spectra were recorded in the range of 500–4000  $\text{cm}^{-1}$  with a resolution of 2  $\text{cm}^{-1}$  at room temperature using KBr pellet. Background signals were corrected with pure KBr pellet. An average of 25 scans has been collected for each sample. The FTIR data was analyzed with Bruker Opus software. The amide I band of IR spectra between 1600–1700  $\text{cm}^{-1}$  were analyzed to determine the secondary structure of both vectors. The region of amide I band was evaluated by Fourier deconvolution and second derivative using Opus software (Bruker Co.). The second derivative spectra of amide I band was acquired after the base line correction followed by nine point smoothing function to enhance the spectral resolution. Further, Gaussian curve fitting profile was used for deconvoluted peaks



and the height, area, and position of each peak was automatically tuned to determine the contribution of each secondary structure component in the amide I band.

### 2.2.2. Physicochemical characterization of the OC-modified proteins

Transmission electron microscopy (TEM, JM-1011, JEOL, Tokyo, Japan) was used to assess the morphology of zein-OC and OVA-OC in the dry state, and the particle size was calculated by using ImageJ software (version 1.43). Briefly, 5  $\mu$ L of sample was dropped on the carbon coated copper grid (CF200-Cu, Electron Microscopy Science, Hatfield, PA, USA) and incubated for 5 min. The excess sample was carefully wiped by using a Kimwipe tissue. The same procedure was performed twice to ensure enough particles in each mesh of the copper grid. Finally, the grids were allowed to dry in a sealed desiccator before TEM analysis. To estimate the isoelectric point (pI) of zein, OVA, zein-OC, and OVA-OC, the samples were prepared at different pH (3–11) conditions. The zeta potential was measured by using ZetaSizer<sup>®</sup> Nano ZS 90. Zein and OVA samples were used as the controls.

### 2.3. Preparation and characterization of the polyplexes

Prior to polyplex preparation, the plasmid encoding for green fluorescent protein (GFP) was extracted from bacterial pellets using a plasmid extraction kit. The concentration of extracted plasmid was determined by NanoDrop spectrophotometer (Thermo, Wilmington, DE, USA) and the purity of the isolated plasmid DNA was analyzed by performing agarose gel electrophoresis. The isolated plasmid DNA was further used to prepare vector/pDNA polyplexes to assess their gene expression. Polyplexes were prepared at various weight ratios ranging from 10:1 to 60:1, by mixing 1  $\mu$ g of plasmid DNA with 10 to 60  $\mu$ g of zein-OC or OVA-OC in serum free DMEM media. The mixtures were mixed with the pipette and further incubated for 30 min in an incubator. The auto-assembly in the polyplex formation is based on the electrostatic charge attraction between the positive charge of synthesized vector and negative charge of pDNA. The particle size and zeta potential of polyplexes were analyzed using ZetaSizer<sup>®</sup> Nano ZS 90 at a backscattering angle of 173° and at a temperature of 25 °C.

#### 2.3.1. DNA condensation and stability test of polyplexes

The DNA condensation ability of zein-OC and OVA-OC was investigated using agarose gel electrophoresis assay. Briefly, 5  $\mu$ L of prepared polyplexes at the indicated weight ratio was mixed with 1  $\mu$ L of 6 $\times$  loading dye. The samples were electrophoresed on 1% agarose gel containing the SafeView DNA for 20 min at 100 V in 1X TAE buffer solution at room temperature. The gel images were acquired by Gel-Doc EZ Imager (Biorad, Hercules, CA). The pDNA protection ability of zein-OC and OVA-OC in nucleases microenvironment from enzymatic degradation was also assessed by agarose gel electrophoresis assay. Briefly, 10  $\mu$ L of prepared polyplexes at the indicated weight ratio were treated with 1U DNase I for 30 min at 37 °C. At the end of the reaction, DNase I was inactivated by using 8  $\mu$ L of EDTA (0.5 M, pH 8) solution and incubated for 10 min. The samples were electrophoresed as described above. The stability of zein-OC/pDNA polyplex and OVA-OC/pDNA polyplex against anionic heparin competition was investigated as follows. Briefly, 10  $\mu$ L of the prepared polyplexes were exposed to different concentration of heparin from 1  $\mu$ g/ $\mu$ L to 8  $\mu$ g/ $\mu$ L for 2 h at 37 °C. The disintegration of polyplexes was visualized by using the agarose electrophoresis.

### 2.4. Gene delivery

#### 2.4.1. Cell culture

HEK 293T and CHO-K1 were obtained from the Bioresource Collection and Research Center (Hsinchu, Taiwan). Both cells were cultured in Dulbecco's modified Eagle's medium-high glucose (DMEM-HG, HyClone; GE Healthcare Life Sciences, Logan, UT, USA)

supplemented with 10% FBS. The subculture was performed when cells had 80% of confluence using trypsin-EDTA. All cells were maintained in a humidified air atmosphere at 37 °C with 5% CO<sub>2</sub>. The cell morphology and growth were monitored daily using a light microscope. The cell density and viability were determined using a Beckman Coulter counter (MS3 model) and hemocytometer, respectively.

#### 2.4.2. Gene expression kinetics of the polyplexes

Prior to transfection, CHO-K1 and HEK 293 T cells were seeded onto sterile coverslips (10-mm) in 48-well culture plates at a density of 50,000 cells/well. After reaching 80–90% confluence, cells were transfected with 300  $\mu$ L of freshly prepared polyplexes in serum-free DMEM medium and incubated for 30–180 min at 37 °C. The transfection medium in each well was replaced with FBS-containing DMEM medium at the indicated time periods and cells were cultured for another 24 h. Finally, the cells were washed with 1X PBS and fixed with ethanol/acetic acid solution (0.5 mL 5% acetic acid in 9 mL 95% ethanol) for 5 min at room temperature. Then, the cell nuclei were stained by adding 300  $\mu$ L of Hoechst 33342 (10 ppm) for 20 min. After washing with 1X PBS solution, coverslips were mounted on glass slides with DAKO fluorescent mounting media (Dako, Carpinteria, CA) and the edges of the coverslip were sealed with nail polish. The cells were screened for GFP expression by using confocal microscopy at 20 $\times$  magnification. The excitation and emission wavelengths were 488 nm and 509 nm for GFP, 405 nm and 460 nm for Hoechst 33342. Further, the confocal images were analyzed using IN Cell Investigator software to determine the green fluorescence intensity and blue fluorescence intensity.

#### 2.4.3. Cytotoxicity of endocytic inhibitors

WST-1 (Roche, Mannheim, Germany) assay was used to evaluate the cytotoxicity of endocytic inhibiting drugs. Cell viability test was performed on 96-well plates, according to the company's instructions. Briefly, 4000 cells were seeded in each well of 96-well plates and cultured for 24 h. After reaching 80–90% confluence, the cultured medium was replaced with 100  $\mu$ L of serum-free medium containing different endocytic inhibitor and incubated for 3 h at 37 °C. After 3 h, the medium containing endocytic inhibitor was aspirated and replaced with complete DMEM medium and the cells were cultured for another 24 h. Subsequently, 10  $\mu$ L of WST-1 solution was added in each well and incubated for an additional 4 h. Prior to measurement, the plate was shaken for 10 min and the absorbance of the sample was recorded at 440 nm using 660 nm as a reference wavelength. Untreated cells were considered as 100% cell viability.

The cell viability was calculated as follows:

$$\text{Viability (\%)} = \frac{\text{OD of treated cells}}{\text{OD of control cells}} \times 100$$

#### 2.4.4. Analysis of transfection efficiency in the presence of an endocytic inhibitor

CHO-K1 and HEK 293 T cells were seeded onto 48 well plates at a density of 50,000 cells/well. To clarify the mechanism of intracellular delivery of the polyplexes, the cells were treated with different endocytic inhibitor and incubated for 1 h prior to transfection. Then, the medium containing inhibitor replaced with freshly prepared polyplex and co-incubated with polyplex and endocytic inhibitor for another 3 h at 37 °C. After 3 h, the medium was replaced with 300  $\mu$ L per well of complete DMEM medium and further cultured for another 24 h. By the end of the incubation, the cells were fixed and labeled with Hoechst 33342 as mentioned above. Thereafter, the GFP positive cells with  $\lambda_{\text{ex}}/\lambda_{\text{em}} = 480/525$  nm and nuclei of cells with  $\lambda_{\text{ex}}/\lambda_{\text{em}} = 350/455$  nm were monitored by using IN Cell Analyzer 1000 microscope (GE Healthcare, Piscataway, NJ) at 10 $\times$  magnification. Ten images per well were captured and analyzed by the IN Cell Investigator software following the manufacturer's protocol. Finally, each image of one well was

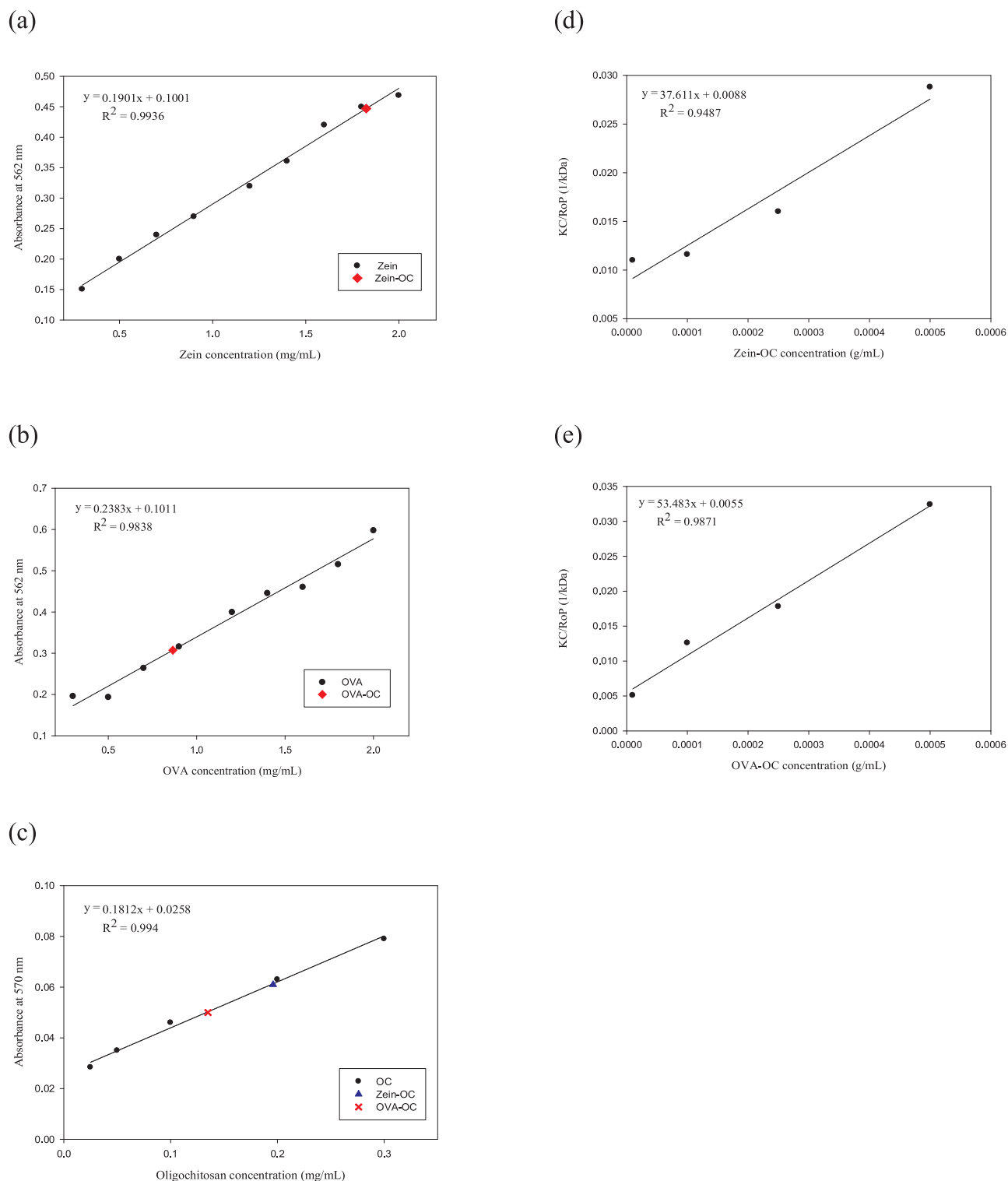


**Fig. 1.** Characterization of protein content and molecular weight of the OC-modified proteins. BCA assays are used to determine protein content in (a) Zein-OC and (b) OVA-OC. Ninhydrin tests are used to determine the OC content in (c) Zein-OC and OVA-OC. Debye plots are used to determine the molecular weight for (d) Zein-OC and (e) OVA-OC.

averaged as one measurement and the percentage of GFP positive cells is defined as follows:

Transfection efficiency (%)

$$= \frac{\text{The number of cells exhibiting both blue and green fluorescence}}{\text{The number of cells exhibiting blue fluorescence}} \times$$

100

The cells treated with polyplex, in absence of inhibitor were used as a control and their efficiency was considered as 100%. Meanwhile, the cells grown on a separate plate were incubated with polyplex at low temperature (4 °C) to study the uptake metabolism.

#### 2.4.5. Intracellular trafficking of the polyplexes

The cells were seeded onto 48-well culture plate containing glass

coverslip as described above. For the tracking of intracellular distribution of vector, the polyplex was prepared by using FITC labeled OC-modified proteins/DNA at a weight ratio of 60:1 and incubated for 3 h. After incubation, the cells were treated with diluted LysoTracker Red DND (50 nM) in DMEM medium for 30 min. Following LysoTracker incubation, the cells were treated as stated previously for confocal imaging. The image was captured at excitation and emission wavelength of 488 nm and 560 nm for LysoTracker Red and further, the percentage of lysosome escape ability was calculated by using IN Cell Investigator software. Complex colocalization with LysoTracker Red is defined as:

Complex colocalization (%)

$$= \frac{\text{Area containing green and red fluorescence}}{\text{Area containing green fluorescence}} * 100$$

## 2.5. Statistical analysis

Data are presented as mean  $\pm$  standard deviation. All experiments were performed at least twice at the same condition and in duplicate to assure reproducibility. Statistical analysis was carried out by using general linear models (GLM) procedure (SAS, version 9.4, SAS Institute Inc.) to determine the differences between two groups. The difference was statistically significant when  $p$ -value  $< 0.05$ .

## 3. Results and discussion

Leggat et al. indicate that a strong binding of chitosan with DNA results in a poor release of DNA within cells, and it thus provides lower transfection efficiency than commercially available transfection reagents (Kedjarune-Leggat, Supapruksakul, & Chotigeat, 2014). To overcome this problem, we have established a BSA-OC hybrid biopolymer, which significantly increases transfection efficiency by up to 90% (Kumari et al., 2018). Additionally, Du et al. have shown that the conjugation of BSA with a cationic polymer provides good transfection efficiency with low cytotoxic activity (Du, Li, Zhang, & Wang, 2016). However, their detailed mechanisms for transfection still require investigation. We have continued our efforts to design an efficient non-viral gene delivery vector by incorporating two different types of proteins (zein and OVA) with OC and to investigate the effect of protein moiety on the transfection pathway. To avoid self-conjugation and isomer formation, the protein and OC were reacted at a 1:10 M ratio. We explore the OC conjugation and the secondary structure of the synthesized vectors in the following sections.

### 3.1. Protein and OC contents in the OC-modified proteins

To assess the degree of conjugation efficiency, the protein and OC contents in the developed vectors were measured separately by performing a BCA assay and a ninhydrin test, respectively. Furthermore, we also determined the molecular weight of both vectors with the static light scattering (SLS) method. The ninhydrin test was performed following the protocol developed by Prochazkova, Vårum, and Ostgaard (1999). The linear calibration curve was obtained by using absorbance at 570 nm against the different concentrations of pure OC. The reaction of a glucosamine unit of chitosan with ninhydrin results in the formation of a Ruhemann's purple colored product. As shown in Fig. 1(c), the plotting of absorbance against concentration was used to determine the relative concentration of OC in zein-OC and OVA-OC. Moreover, a quantitative analysis of the protein was performed by a BCA test using a custom-developed protocol. BCA reacts with copper ions in the presence of peptide bonds, resulting in the formation of a reduced copper ion complex, which leads to the formation of a purple-colored product. The intensity of the produced colour is directly related to the amount of protein in the sample (Olson & Markwell, 2007). Thus, linear standard

curves were obtained with a known concentration of each protein (zein and OVA) by measuring absorbance at 562 nm. As shown in Fig. 1(a) and (b), the protein concentrations in zein-OC and OVA-OC were estimated by comparing the absorbance value with a standard curve. The initial reaction was carried out in the presence of 2 mg/mL of the protein and 0.2 mg/mL of OC. The estimated amounts of protein and OC in the OVA-OC were 0.86 mg/mL and 0.13 mg/mL, respectively, and, in the zein-OC, the amount was 1.82 mg/mL and 0.196 mg/mL, respectively. The data showed that the loading capacity of OC in zein was greater than that in OVA. The amount of protein and OC present in zein-OC and OVA-OC was used to calculate the weight ratio for the gene delivery system.

To investigate the average molecular weight of the zein-OC and OVA-OC, the SLS technique was followed for determining the weight of the suspended particles. The SLS technique follows the Rayleigh theory, which states that the intensity of scattered light produced by macromolecules is proportional to the molecular weight of these molecules. Furthermore, the Rayleigh equation helps to create a Debye plot for calculating the molecular weight of a protein by generating a linear equation plot of  $KC/R_{90}$  as a function of the different concentrations of protein. Molecular weight is defined as the inverse of the intercept value (Murphy, 1997). As shown in Fig. 1(d) and (e), the graph was plotted by using the values for scattered light intensity against different sample concentrations to measure the molecular weight of both vectors from the intercept. On the graph,  $K$  is an optical constant dependent upon the sample  $dn/dc$ ,  $dn/dc$  is a refractive index increment,  $C$  is the concentration of the particle, and  $R_{90}$  is the Rayleigh ratio. From the inverse of the intercept of Y-axis ( $KC/R_{90}$ ), the calculated molecular weight for zein-OC and OVA-OC are 119 kDa and 182 kDa, respectively. Furthermore, the second virial coefficient ( $A_2$ ) values were obtained from the slope for the zein-OC and OVA-OC, which were about 0.0185 and 0.0268, respectively. A positive  $A_2$  value indicates that a maximum quantity of molecules is dissolved in a solvent to develop a stable solution. In a recent report, Quigley and Williams utilize the second virial coefficient to understand the aggregation tendency of a protein sample in differing formulation conditions (Quigley & Williams, 2015). Likewise, we calculated the molecular weight of zein and OVA as 60 kDa and 97 kDa, respectively. The increased molecular weight of zein-OC and OVA-OC showed an effective conjugation of OC molecules with proteins. Layman et al. have shown that the molecular weight of polydimethylaminoethyl methacrylate (PDMAEMA) influences the luciferase expression and the cytotoxicity. When their molecular weight increases above 215 kDa, the cell viability treated by the PDMAEMA decreases greatly (Layman, Ramirez, Green, & Long, 2009). Similarly, our data also indicated that the molecular weight of OC-modified proteins below 215 kDa did not damage the cell viability.

### 3.2. Structural analysis of the OC-modified proteins

FTIR is a technique used to determine the molecular conformations of conjugates or components by analyzing for the presence or absence of specific interactions among them. The representative infrared spectra for zein, OVA, OC, zein-OC, and OVA-OC are shown in Figure S1. The spectra for zein and OVA show their characteristic peaks. Amide I and amide II are two major well-defined peaks observed in IR spectra of proteins. The amide I band represents the C=O stretching vibrations (between 1700–1600  $\text{cm}^{-1}$ ) while the amide II band is associated with the N–H bending vibrations coupled with C–N stretching vibrations (between 1500–1400  $\text{cm}^{-1}$ ) (Barth, 2007). The amide I and amide II bands were located at 1647  $\text{cm}^{-1}$  and 1548  $\text{cm}^{-1}$  for zein, respectively, and at 1657  $\text{cm}^{-1}$  and 1555  $\text{cm}^{-1}$  for OVA, respectively. The spectra of OC contain a broad band at 1585  $\text{cm}^{-1}$  from C–O stretching of the amide bond. The peaks present at 1738  $\text{cm}^{-1}$  represent the carbonyl bond of the acetamide group and at 1072  $\text{cm}^{-1}$  represent the glycosidic bond in OC. The IR spectra for the OC and proteins show good agreement with a previous study (Silva et al., 2012). In the OVA-OC and zein-

OC, there is an increase in the intensity of the broad peak in the range between 3600–3400  $\text{cm}^{-1}$ , and this may be due to the increased number in the amino group after conjugation. Meanwhile, the decreased intensity of amide I and amide II indicate structural changes in the intramolecular bonding of the protein conformation. The increased wavenumber of the amide II band from 1531  $\text{cm}^{-1}$  to 1548  $\text{cm}^{-1}$  for zein-OC (Fig. S1(a)) and 1527  $\text{cm}^{-1}$  to 1555  $\text{cm}^{-1}$  for OVA-OC (Fig. S1(b)) may be attributed to the cross-linking of protein with OC through the glutaraldehyde cross-linker. Also, it has been previously reported that an increased wave number in the amide II bands reflects that an amine group has reacted with the carbonyl group of glutaraldehyde to form a new covalent bond (C=N) (Farris, Song, & Huang, 2010). The peak at 1463  $\text{cm}^{-1}$  for both vectors represented the Schiff base formation, which resulted from the reaction between the carbonyl group of glutaraldehyde and the amino group of the proteins or OC. Furthermore, the formation of OC-modified protein was also confirmed by the emergence of new peaks in the range between 1800–1700  $\text{cm}^{-1}$  and 1100–1000  $\text{cm}^{-1}$ , which was attributed to the acetyl group and glycosidic bond from OC, which confirms the effective conjugation of OC with protein.

To study the secondary structure of the proteins, the area of the amide I band (1700–1600  $\text{cm}^{-1}$ ) has been widely used due to its great sensitivity for protein structural analysis. This band originates from the C=O stretching vibrations of a peptide backbone and is constituted by distinct overlapping bands representing different secondary structures (Barth, 2007). Employing the Fourier self-deconvolution and curve-fitting techniques for amide I bands helps to identify the different secondary structures of a protein. A curve fitting procedure can be employed to evaluate the area of an individual band representing a particular protein's secondary structure, for example an  $\alpha$  helix (1660–1650  $\text{cm}^{-1}$ ),  $\beta$  sheet (1640–1610  $\text{cm}^{-1}$ ),  $\beta$  turn (1690–1660  $\text{cm}^{-1}$ ), or random coil (1640–1648  $\text{cm}^{-1}$ ) (Yang, Yang, Kong, Dong, & Yu, 2015). Baldassarre et al. used the deconvoluted spectra of the amide I band followed by a curve fitting procedure with the Gaussian-Lorentzian line shapes to de-convolute the secondary structures of a protein (Baldassarre, Li, Eremina, Goormaghtigh, & Barth, 2015). In another study, the author quantitatively estimated the secondary structures by performing a second derivatization of spectra followed by a curve fitting procedure (Dong, Malecki, Lee, Carpenter, & Lee, 2002). We used the second derivative spectra of the amide I band for zein, OVA, zein-OC, and OVA-OC followed by a curve fitting procedure using OPUS software. The peaks of the individual bands were fitted with Gaussian band shapes. The spectra showed the characteristic peaks of the secondary structures. Then, the relative width and intensity of each position was used for the quantitative estimation of each secondary structure as shown in Table 1. Zein and OVA both had random coil and  $\beta$  turn as the most populated secondary structures followed by  $\alpha$  helix and  $\beta$  sheet. After the modification of OC, an increased amount of  $\alpha$  helix and a decreased amount of  $\beta$  sheet were observed. A plausible

interpretation for the gain in  $\alpha$  helix and loss in  $\beta$  sheet may be due to the partially folded state of the proteins or due to the structure replacement after OC conjugation. Additionally,  $\beta$  turns were determined by the presence of more than one band and the total amounts of  $\beta$  turns were 68.4% and 68.6% for zein-OC and OVA-OC, respectively. An increased number of  $\beta$  turns represented the formation of an intermolecular  $\beta$  component structure. Previously, Wang et al. have stated that a decrease in  $\alpha$  helix and an increase in  $\beta$ -sheet and random coil indicates the considerable loosening of the protein structure (Wang et al., 2011). Our data also suggested that the covalent conjugation of protein with OC influenced the  $\alpha$ -helical structure which helps to retain the protein in its folded conformations.

### 3.3. Physicochemical characterization of the OC-modified proteins

To investigate physicochemical properties of the developed vectors, their morphology, particle size distribution, and pI were assessed using TEM and the ZetaSizer. TEM provides essential information about the morphology, particle size distribution, and dispersibility of nanoparticles. It entails a counting method that directly allows for particle size analysis based upon number-weighted size distributions (Fissan, Ristig, Kaminski, Asbach, & Eppele, 2014). The TEM micrographs are shown in Fig. 2(a) and (b) revealed that the particles were nearly spherical in shape for both vectors and are well-dispersed without agglomeration. Particle size was analyzed manually for diameter by using ImageJ software, and the size distribution data was plotted in a histogram form (Fig. 2(c) and (d)). A histogram graph depicts the frequency distribution against the size range (Akbari, Pirhadi, & Zandrahimi, 2011). The histogram analysis of over 25 particles give the estimated size values for zein-OC and OVA-OC as 382 nm  $\pm$  82 and 110 nm  $\pm$  31, respectively.

To evaluate the buffering capacity and pI value of the developed vectors, zeta potential was measured in solutions of differing pH. As shown in Fig. 2(e), the zeta potential of zein-OC and OVA-OC decreased when pH values increased from 3 to 11. The probable reason for this increase in surface charge at a low pH is the protonation of the carboxyl group (Xu et al., 2017). The pI values were calculated from a zeta potential curve. The pI values of zein and OVA are 5.8 and 5.0, respectively. After conjugation, the zeta potential curve shifted to the right side of the graph and the obtained pI values were 9.8 and 7.7 for zein-OC and OVA-OC, respectively. This indicates that the increase in the surface charge of the protein may be due to an increase in the number of the amine group. Discussing the pI value related to the amino group of a protein, Zhang et al. have mentioned that increasing the number of an amino group in modified BSA leads to an increase in pI value (Zhang et al., 2015). Furthermore, a zeta potential value range from 7 to 5 was used to examine the buffering capacity of the vectors. The large increase in surface charge at pH 5 indicates the high buffering capacity of the vectors. When the pH value was changed from 7 to 5, the surface charge of zein-OC and OVA-OC increased from +21 mV to +27 mV and +4 mV to +6 mV, respectively. The surface charge of zein-OC had an increase greater than that of OVA-OC, suggesting that zein-OC has a higher buffering capacity. The nanoparticle with high buffering capacity can presumably provide a greater ability to escape an endosomal-lysosomal compartment. However, a major rate-limiting step for the delivery of a gene is the endosomal escape potency of the internalized nanoparticles. The buffering capacity of chitosan is dependent upon molecular weight and the degree of deacetylation (Alameh et al., 2018). Therefore, the buffering capacity of chitosan or a chitosan-modified product is important to evaluate their DNA binding ability and its effect on polyplex release from a lysosomal compartment to achieve good transfection efficiency. Ishii et al. showed that the chitosan complex more effectively increased surface charge than DEAE-Dextran complex by changing the pH value from 7 to 6, indicating that the chitosan complex has a higher buffering capacity and a better ability to escape the endosomal-lysosomal compartment as compared to DEAE-Dextran

**Table 1**

The secondary structure contents for the characterization of zein-OC and OVA-OC.

Secondary structure	Gaussian center $\text{cm}^{-1}$ (% of secondary structure) of zein	Gaussian center $\text{cm}^{-1}$ (% of secondary structure) of zein-OC	Gaussian center $\text{cm}^{-1}$ (% of secondary structure) of OVA	Gaussian center $\text{cm}^{-1}$ (% of secondary structure) of OVA-OC
$\beta$ -Sheet	1615 (11.7 %)	1629 (8.4 %)	1637 (27 %)	1636 (6 %)
$\beta$ -turn	1686 (36.1 %)	1666 (12.9 %) 1670 (42.4 %) 1678 (3.10 %)	1683 (27.6 %)	1667 (0.97 %) 1680 (67.7 %)
$\alpha$ -helix	1652 (10.4 %)	1650 (17.3 %)	1658 (11.2 %)	1657 (25 %)
Random coil	1649 (52 %)	1647 (15.8 %)	1641 (33.4 %)	Not determined

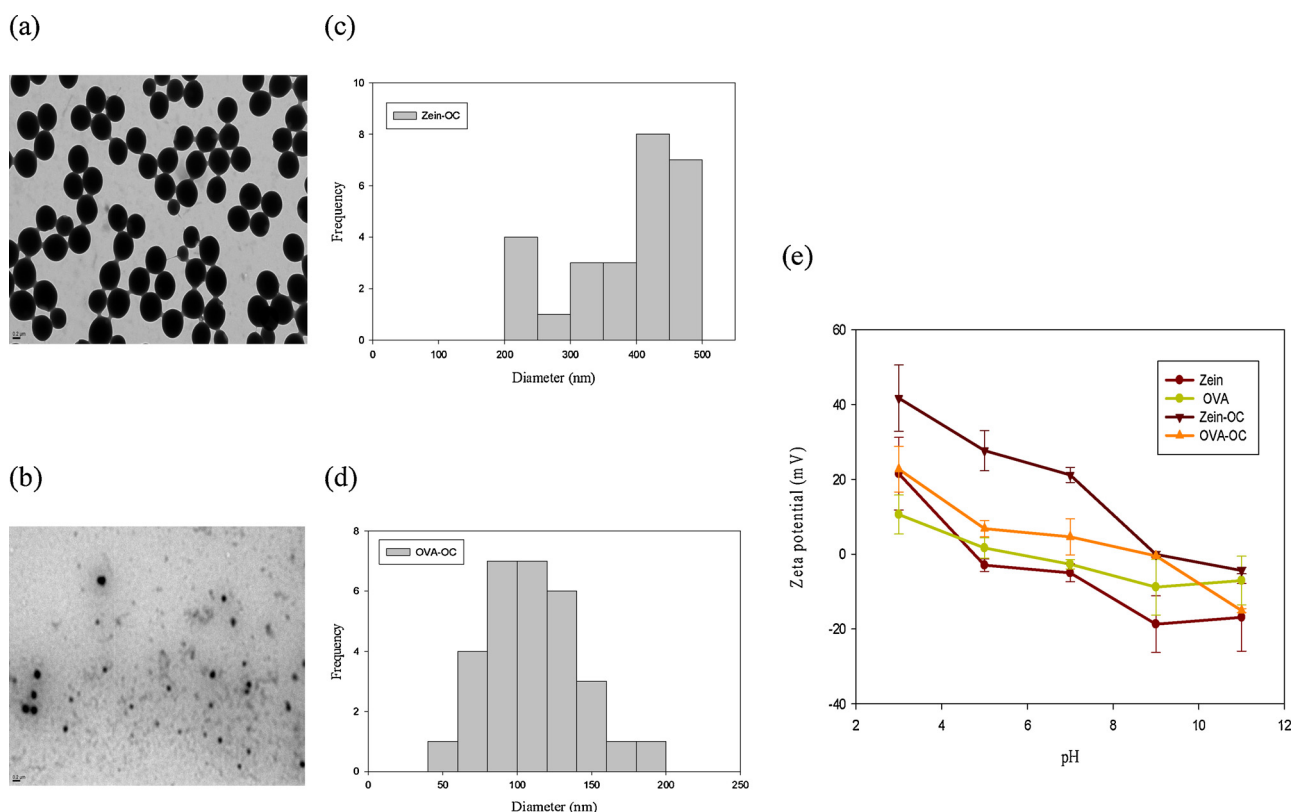


**Fig. 2.** Physicochemical characterization of OC-modified proteins. TEM images of (a) Zein-OC and (b) OVA-OC. The size distribution analysis is obtained from TEM image for (c) Zein-OC and (d) OVA-OC; (e) The zeta potentials of both vectors measured at different pH values are used to determine the isoelectric point as well as buffering capacity. Measurements are performed in triplicate with error bars representing the standard deviation.

(Ishii, Okahata, & Sato, 2001). The data are shown in Fig. 2(e) indicating that the conjugation of different types of protein with OC influenced their buffering capacity.

### 3.4. Analysis of the surface charge and particle size of the polyplexes

Polyplex properties, such as particle size and surface charge at different weight ratios, should be considered as important factors that influence the internalization of nanoparticles and can also affect transfection efficiency (Rejman, Oberle, Zuhorn, & Hoekstra, 2004). The particle size, polydispersity index (PDI), and surface charge of the zein-OC and OVA-OC polyplexes were analyzed at different weight ratios. The results in Fig. 3(a) and (b) show that the particle sizes and zeta potential of polyplexes were dependent upon weight ratio, whereas increasing the weight ratio of a polyplex resulted in an increase in surface charge and a decrease in particle size. The reason for the higher zeta potential and a smaller particle size were mainly ascribed to the surplus amount of the vector's positive charge. Previously, a high zeta potential is due to an excess of cationic polymer and a reduction in particle size is due to the compact of DNA by a cationic polymer (Lv, Zhou, Zhao, Liao, & Yang, 2017). It has also been reported that zeta potential values represent nanoparticle stability. Zhang et al. have stated that a higher zeta potential decreases the stability of a nanoparticle suspension and increases the toxicity against mammalian cell lines (Zhang et al., 2016). Zeng et al. have also shown that the surface charge of dendrimers plays a major role in determining the extent of cytotoxicity as when their surface charge increases above +30 mV, the cytotoxicity of the dendrimers increases greatly (Zeng et al., 2016). As shown in Fig. 3, particle size was found to be maintained below 300 nm, and zeta potential exhibited between +6 mV to +30 mV for both polyplexes. Previous studies have inferred that nanoparticles ranging in size from 50 to 500 nm are suitable for endocytosis and cell transfection

(Rejman et al., 2004). The physicochemical properties of nanoparticles, such as their surface charge and particle size, affect the mechanism related to the internalization of a polyplex. Interestingly, in our study, the polyplexes showed an intermediate positive surface charge, which can interact with the negative charge of cell membranes for internalization of polyplexes without affecting the cytotoxicity of cells. It has been previously reported that a positive charge in a complex can adhere to negatively charged cell membranes, which influences transfection efficiency (O'Keeffe Ahern et al., 2018). In contrast, PDI values also play an important role in determining the monodispersibility of vectors along with colloidal stability. The PDI values of zein-OC and OVA-OC were 0.31 and 0.26. The size of zein-OC and OVA-OC were found to be 221 nm and 169 nm by using ZetaSizer. Additionally, an agarose gel retardation assay was performed to investigate the DNA condensation ability of both vectors. Subsequently, the stability of polyplex in nuclease containing environment and DNA releasing ability from the polyplex was investigated by using endonuclease enzymes (DNase I) and large polyanionic molecules (heparin). Fig. S5 (a) and (b) shows the DNA condensation of zein-OC and OVA-OC at various weight ratio from 10:1 to 60:1. The condensation ability of pDNA increased with an increasing amount of vector. Moreover, no degradation of pDNA was observed for both polyplexes by DNase I exposure, but naked DNA was completely degraded. Following the addition of heparin, the pDNA was released from the vector without any degradation (Fig. S5 (a) and (b)). These results clearly indicate that the charge of the prepared polyplexes was stabilized through electrostatic interaction. Hence, these synthesized vectors were suitable for an endocytosis process.

### 3.5. Transfection efficiency of the polyplexes

Optimal transfection efficiency was elucidated by using various weight ratios of vector/pDNA. The weight ratios were defined by fixing



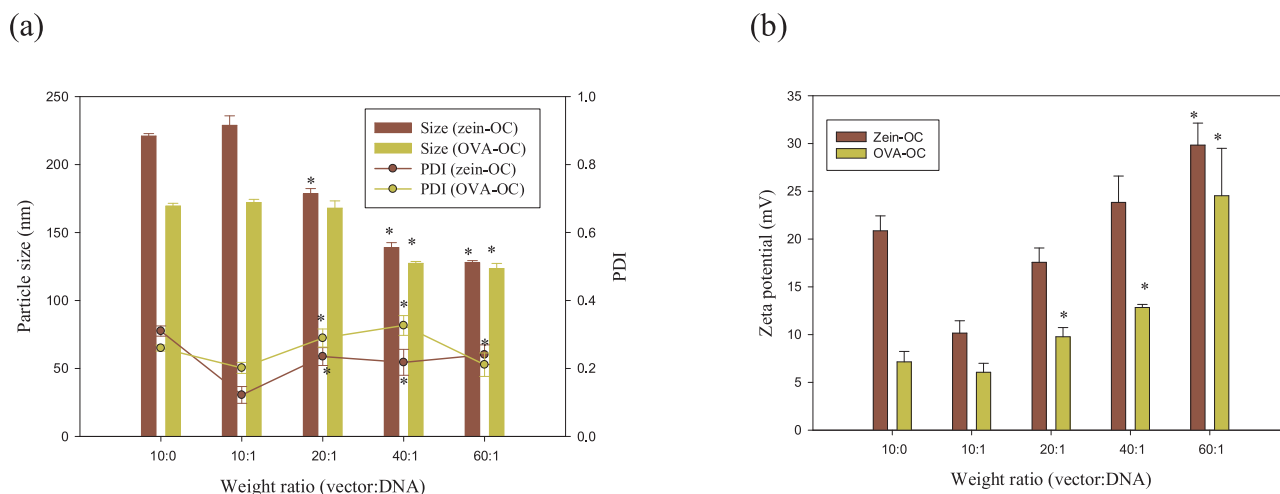


**Fig. 3.** Effect of vector/pDNA polyplexes weight ratios on (a) particle size, polydispersity index (PDI) and (b) zeta potential, obtained by dynamic light scattering. Measurements were performed in triplicate with error bars representing the standard deviation. Stars (\*) indicate the significant difference as compared with the weight ratio of 10:1.

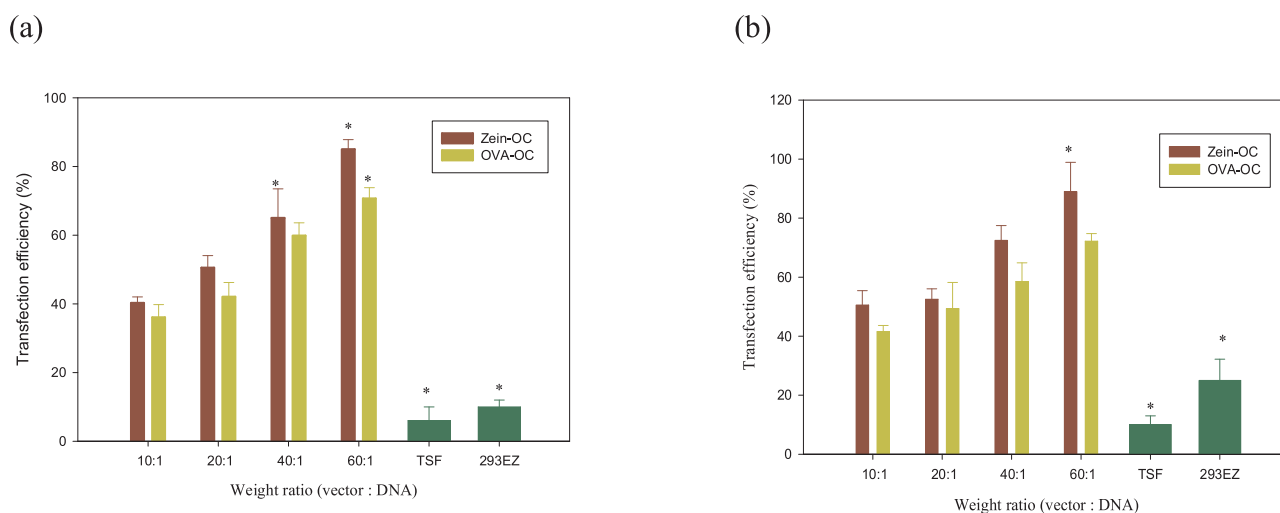


**Fig. 4.** Transfection results of zein-OC and OVA-OC polyplexes at various weight ratios in (a) CHO-K1 cells and (b) HEK 293 T cells. Measurements were performed in duplicate with error bars representing the standard deviation. Stars (\*) indicate the significant difference as compared with the weight ratio of 10:1.

the concentration of plasmid DNA at 1  $\mu$ g and varying the vector concentration from 10  $\mu$ g to 60  $\mu$ g. Plasmid DNA encoding green fluorescent protein (GFP) was used to evaluate transfection efficiency. Fig. 4(a) and (b) compare the transfection efficiency of zein-OC and OVA-OC polyplexes in the two different cell lines (CHO-K1 and HEK 293 T) at vector/pDNA weight ratios ranging from 10:1 to 60:1. We found that a higher weight ratio could significantly increase cell transfection efficiency for both polyplexes. Fig. 4 indicates that the zein-OC polyplex had greater transfection efficiency than that of OVA-OC polyplex. Moreover, the HEK 293 T cells ensured better transfection efficiency than the CHO-K1 cells at each weight ratio. The results also indicated that both types of polyplexes exhibited greater gene transfection levels than that of the positive controls, such as TOOLSsmooth-Fect (TSF) and 293EZ-FECT transfection reagents. This may be due to the strong electrostatic interaction of the vectors with plasmid DNA, which prevented its enzymatic degradation, and thus led to high transfection efficiency. Even the lower weight ratios (10:1) of both polyplexes exhibited superior transfection efficiency, ranging from 40% to 50%, than the commercially available transfection agents.

To investigate the kinetics of gene expression, the cells were treated with polyplexes at a weight ratio of 60:1 at 37  $^{\circ}$ C for various time periods. This time-course study was performed to determine the

minimal time required for maximum GFP expression. Plasmid DNA encoding GFP expression was monitored using confocal microscopy. A quantitative analysis of the image captured from confocal microscopy was performed by IN Cell Investigator software, which allows for a direct comparison of the GFP expression level and blue fluorescence intensity under different conditions. The intensities of the green and blue fluorescence were calculated by determining the average intensity of the fluorescence of each cell. It has previously been reported that the incubation time of a polyplex with a cell plays a key role in transfection efficiency due to the over-delivery of the polyplex from cell membrane disruption. Likewise, a shorter incubation time did not provide a sufficient period for the interaction of a polyplex with the cell membrane, limiting transfection efficiency (Guo et al., 2017). Therefore, maintaining an adequate incubation period was essential to obtain the good transfection efficiency. Figs. S2(a) and S3(a) show an image of gene expression in the CHO-K1 and HEK 293 T cell lines. In both cell lines, the minimum level of gene expression was detected after 30 min into the incubation period and reached a maximum after 120 min. The incubation longer than 120 min did not enhance gene expression, and the fluorescence intensity reached a plateau value except for the OVA-OC polyplex in the HEK 293 T cells. The HEK 293 T cells showed greater

transfection efficiency and gene expression than the CHO-K1 cells, suggesting cell surface receptors play an important role in the internalization of a polyplex. Some authors indicate that the presence of mannose receptors on cell surfaces increase the efficiency of OC binding. This phenomenon that enhances the transfection activity of OC is due to the precise binding mediated by the mannose receptors on the cell surface (Douglas, Piccirillo, & Tabrizian, 2008). The results of the current study revealed that the high level of gene expression in the HEK 293 T cell line may be due to the presence of mannose receptors on the cell surface. However, a lack of these receptors on the CHO-K1 cell membrane slightly decreased the gene expression level. This suggests that membrane physiology is an important factor for the internalization of the polyplexes. Further, for both cell lines, the zein-OC polyplex showed a higher level of gene expression than the OVA-OC polyplex. This higher level of GFP expression may be related to the particle size of the polyplex. The zein-OC polyplexes had a somewhat larger particle size than the OVA-OC polyplexes. Large particle supporting a large payload of DNA can rapidly sediment onto cells, which results in higher levels of gene expression. Van der Aa et al. demonstrate that the PEI polyplex showed a more rapid internalization than that of the PDMAEMA. The quicker uptake of the PEI polyplex may be due to the bigger payload of DNA delivered through the larger particle size (van der Aa et al., 2007). In addition, the larger sized particles quickly settled onto cell surfaces and increased internalization (Wu et al., 2018).

A quantitative analysis of toxicity at different incubation times could be obtained by studying the intensity of the blue fluorescence in the nuclei stained with the Hoechst, and the measurement was performed with the IN Cell Investigator software. Hoechst 33342 is a nucleic acid stain that binds to dsDNA, and the intensity of the fluorescence is directly proportionate to the chromatin state in cells. The fluorescent signal of the Hoechst provides an understanding of cellular conditions and the physiological characteristics of cells that reflect cellular viability (Gilbert et al., 2011). As shown in Fig. S2(c), there was no significant difference in the blue intensity observed for both polyplexes in the CHO-K1 cells, suggesting a non-toxic effect of the polyplexes. However, in the HEK 293 T cells, the OVA-OC polyplex showed a higher cytotoxicity at 180 min as compared to that at 30 min (Fig. S3(c)). The cytotoxicity of the developed polyplexes depended on both polyplex composition and cell type.

### 3.6. Endocytosis mechanism and pathways of the polyplexes

#### 3.6.1. Effect of ATP-dependent endocytic pathways on the transfection efficiency of the polyplexes

The pathways involved in the internalization of polyplexes into living cells are the energy-independent direct translocation and the energy-dependent endocytic pathways. To distinguish between these internalization pathways, the cells were treated with the polyplex at a low temperature. Upon reduction of the temperature to 4 °C, transfection efficiency was assumed to decrease, which can be rationalized by the fact that the cooling of the cells leads to a change in the lipid membrane from a fluid phase to a gel phase, which blocks adenosine triphosphate (ATP)-dependent endocytic pathways (Leroueil et al., 2007). Therefore, the transfection experiment was performed at a low temperature to study the major pathway leading to the uptake of the polyplex. Fig. 5(a) and (b) shows the effect of low temperature on the transfection efficiency of the polyplexes in the CHO-K1 and HEK 293 T cell lines. The cells treated with polyplexes at 4 °C had significantly reduced transfection efficiency in both cell lines as compared to the treatment at 37 °C. As mentioned previously, endocytosis is an energy-dependent process, consuming energy for the active transportation of the polyplex (Gautam et al., 2015). In particular, the treatment of cells at a low temperature blocks the uptake of the polyplexes through endocytic pathways, whereas the direct pathways experienced no effect and thus allowed the entry of the polyplex. Fig. 5 indicates that endocytic pathways were primarily responsible for polyplex

internalization. However, recent studies have reported that reduced transfection efficiency at a low temperature may be due to the physiological malfunctioning of cells (Gu, Hao, Fang, & Sha, 2016).

To further assess if the lower transfection efficiency of polyplexes at 4 °C was not due to membrane rigidity, the following procedure was performed: both cell lines were treated with sodium azide to decrease intracellular levels of energy by inhibiting ATP production followed by treatment with the polyplexes at 37 °C. As anticipated, the cells treated with sodium azide showed lower transfection efficiency for both polyplexes in the tested cell lines as compared to the control cells (Fig. 6, Table 2). These results indicate that an efficient transfection of polyplexes depends upon an ATP-dependent endocytic process.

#### 3.6.2. Effect of endocytic inhibitor on the transfection efficiency of the polyplexes

To probe the specific endocytic pathways responsible for the internalization of the polyplexes, we measured the cell transfection efficiency of the polyplexes following treatment with different endocytic inhibitors and compared their activity with untreated cells. Therefore, the cells treated with polyplexes in the absence of the inhibitors were considered as control. Generally, different endocytic pathways, such as clathrin-mediated endocytosis (CME), caveolae-mediated endocytosis (CvME), or macropinocytosis are involved in the entry of a polyplex. However, treatments with endocytic inhibitors can block specific pathways and assist in the study of which pathway is responsible for the cellular internalization of a polyplex (Salatin & Yari Khosroushahi, 2017). Some authors have stated that chitosan and albumin prepared polyplexes are internalized via CvME pathways in some types of cells (Pérez-Martínez, Guerra, Posadas, & Ceña, 2011; Xu, Liu, Wang, & Shao, 2014). We chose five different endocytosis inhibitors to investigate which endocytic routes were essential for efficient cell transfection. Table 2 summarizes the concentrations of endocytic inhibitors and their possible mechanisms. It has been reported that endocytic inhibitors are toxic towards mammalian cell lines. Therefore, it is imperative to assess their *in vitro* cytotoxicity profile, before studying their effect on the transfection efficiency of a polyplex (Shah, Bournier, Ali, Al-Enazy, & Rytting, 2017). Cell viability of the CHO-K1 and HEK 293 T cell lines after exposure to the endocytic inhibitors were tested to avoid the toxicity effect of the inhibitors. Fig. S4 indicated that the concentration of each inhibitor used in this study did not reduce cell viability significantly as compared to the control.

**3.6.2.1. Role of the clathrin-mediated endocytosis (CME) pathway.** To evaluate the participation of the CME pathway, we used chlorpromazine (CPZ) to investigate the mechanism. Chlorpromazine is a cationic amphipathic molecule that prevents the formation of clathrin-coated pits on the plasma membrane. Thus, the loss of the cellular protein clathrin and AP2 adaptor complex inhibit the formation of large intracellular vesicles (Salatin & Yari Khosroushahi, 2017). The chlorpromazine treatment enhanced the transfection efficiency of the polyplexes in both cell lines as compared to the control. In previous studies, other authors have also demonstrated that transfection efficiency increased after treatment with endocytic inhibitors. One of the reasons for this increased transfection efficiency may be due to the up-regulation of the pathways that are usually involved in the internalization of a polyplex (Peng et al., 2011). The data in Fig. 6 and Table 2 implies that the CME pathway was not involved in the internalization of the polyplexes in the tested cell lines.

**3.6.2.2. Role of caveolae-mediated endocytosis (CvME) and lipid-mediated pathways.** The inhibition of CvME and lipid-mediated pathways was performed using an isoflavone glycoside (genistein) and cyclic oligomer of glucopyranoside (Methyl- $\beta$ -cyclodextrin) (Danciu et al., 2012). CvME creates flask-shaped structures on the plasma membrane called caveolae, which are made of protein, cholesterol, and sphingolipids. The internalization via caveolae-mediated endocytosis (CvME) provides

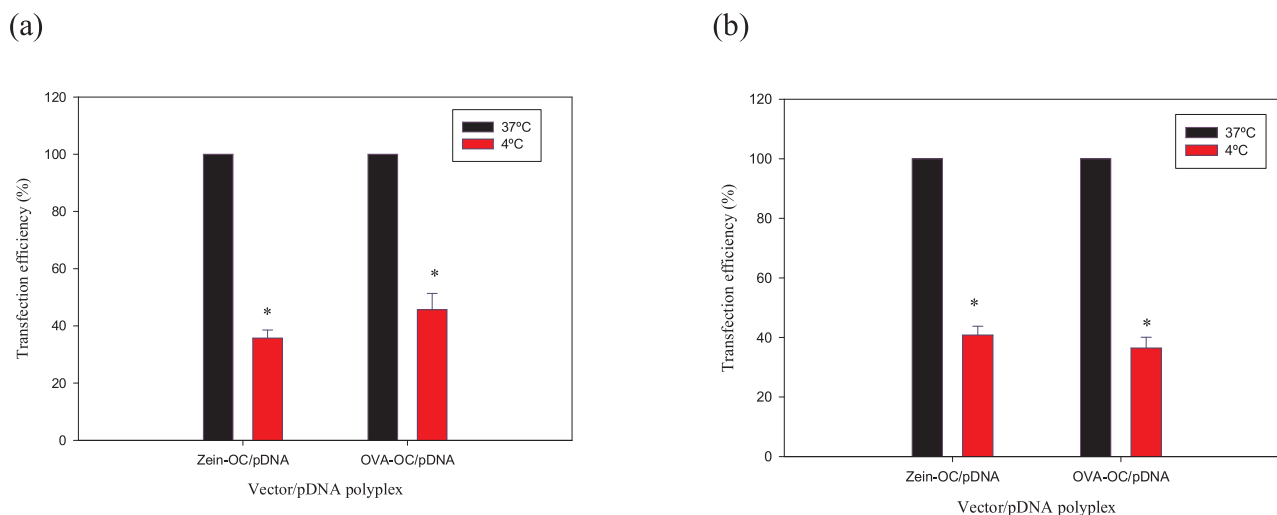


**Fig. 5.** Effect of low temperature (4 °C) on the transfection efficiency of polyplexes. (a) CHO-K1 and (b) HEK 293 T cell lines. Measurements were performed in duplicate with error bars representing the standard deviation. Stars (\*) indicate the significant difference as compared with 37 °C.

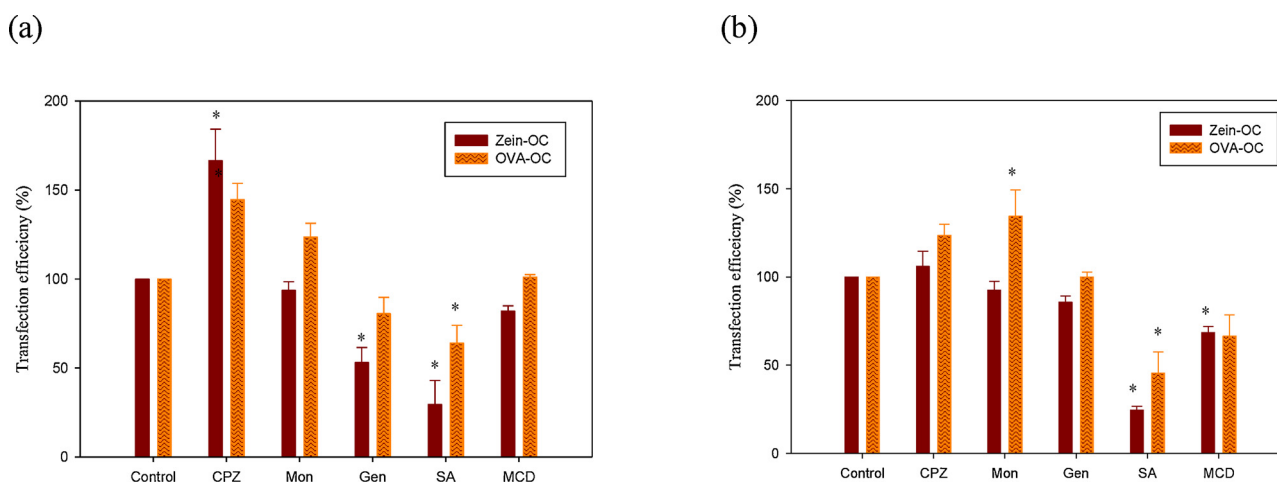


**Fig. 6.** Effect of endocytic inhibitors on the transfection efficiency of both polyplexes in (a) CHO-K1 and (b) HEK 293 T cells. The cells without inhibitor treatment were considered as control and the percentage of transfection efficiency was calculated by considering the transfection efficiency of control as 100%. Measurements were performed in duplicate with error bars representing the standard deviation. Stars (\*) indicate the significant difference as compared with control.

**Table 2**

Summary of endocytic inhibitor and their mechanisms.

Inhibitor	Function	Concentration	Zein-OC polyplex		OVA-OC polyplex	
			CHO-K1	HEK 293T	CHO-K1	HEK 293T
Chlorpromazine	Clathrin-mediated endocytosis inhibitor	30 $\mu$ M	+	+	+	+
Monensin	Block transport from Golgi complex to plasma membrane.	3 $\mu$ M	–	–	+	+
Genistein	Caveolae-mediated endocytosis inhibitor	200 $\mu$ M	–	–	–	No effect
Sodium azide	Active transport inhibitor	1%	–	–	–	–
Methyl- $\beta$ -cyclodextrin	Cholesterol dependence endocytosis inhibitor	10 mM	–	–	No effect	–

Plus (+) sign indicates the transfection efficiency increased after treatment with a particular endocytic inhibitor as compared with control. Minus (–) sign indicates the transfection efficiency decreased after treatment with a particular endocytic inhibitor as compared with control.

greater transfection efficiency than clathrin-mediated endocytosis (CME). This is predominantly attributed to the fact that if the polyplex is internalized via CME and is unable to escape the acidic compartment without degradation, then this further reduces transfection efficiency. In other words, successful transfection via a CME pathway is dependent upon the proton-sponge ability of the polyplex (Ross, Munsell, Sabanayagam, & Sullivan, 2015). In contrast, CvME takes place under neutral pH conditions by delivering the polyplex to neutral, stable organelles called caveosomes, and so later

the polyplex can reach the cytoplasm with less of a chance for degradation (Dalal, Saha, & Jana, 2016). Genistein is a specific inhibitor for CvME as it prevents tyrosine phosphorylation, which inhibits the action of Src kinase for caveolin. In addition, it also interferes with the actin network and blocks the appearance of dynamin II at the site of endocytosis (Wang, Wang, Aylor, & Barrett, 2015). The treatment with genistein markedly reduced the transfection efficiency in the CHO-K1 cell line for both polyplexes (Fig. 6(a)). In contrast, the HEK 293 T cell line slightly reduced transfection efficiency

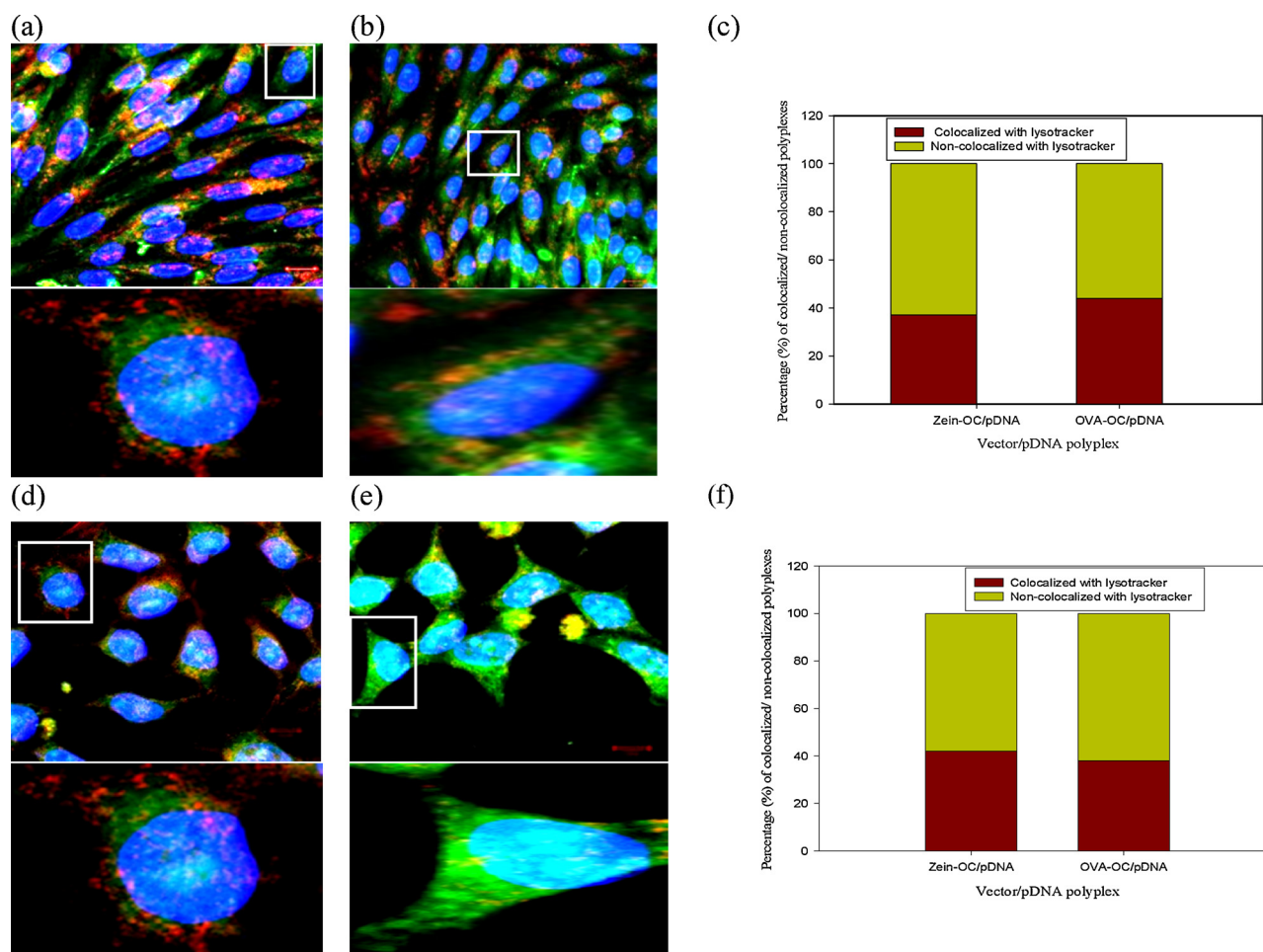


**Fig. 7.** Confocal microscopy image of the intracellular distribution of both polyplexes with LysoTracker in (a–c) CHO-K1 and (d–f) HEK 293 T cells. The results include (a and d) Zein-OC polyplex, (b and e) OVA-OC polyplex, and (c and f) summary. Confocal images were quantified by IN Cell Investigator software. The white box indicated the zoomed region of the cells showing colocalization. Blue fluorescence indicated the nuclei stained with Hoechst 33342. Green fluorescence indicated the FITC-labeled OC-modified proteins, and red fluorescence indicated the lysosome stained with LysoTracker Red. (For interpretation of the references to colour in this figure legend, the reader is referred to the web version of this article).

for the zein-OC polyplex (9%) and created no significant change for the OVA-OC polyplex as compared to the control (Fig. 6(b)). This data suggests that both polyplexes were internalized via the CvME pathway except for the OVA-OC polyplex in the HEK 293 T cell line.

Methyl- $\beta$ -cyclodextrin blocks lipid-raft mediated endocytosis by sequestering membrane cholesterol and damaging the lipid-rich domain on the cell membrane (Wang, Yuan, Peng, & Zhao, 2010). Transfection efficiency was reduced as compared to the control by treatment with Methyl- $\beta$ -cyclodextrin for all tested samples except for the OVA-OC polyplex in the CHO-K1 cell line. These results indicate that lipid-mediated pathways were involved in the internalization of both polyplexes in the HEK 293 T cell line (Fig. 6(b)). In CHO-K1 cells, the internalization of the zein-OC polyplex depended upon the lipid-mediated pathway, but the OVA-OC polyplex showed no effect from the treatment with Methyl- $\beta$ -cyclodextrin (Fig. 6(a)).

The data of transfection in the presence of genistein and methyl- $\beta$ -cyclodextrin indicated that the CvME and lipid-mediated pathways played a key role in the internalization of the zein-OC polyplex for the two cell lines. On the other hand, the transfection efficiency of the OVA-OC polyplex was reduced by treatment with genistein in CHO-K1 cells, whereas incubation of HEK 293 T cells with methyl- $\beta$ -cyclodextrin marginally reduced the transfection efficiency of polyplex. It is therefore plausible that OVA-OC polyplex was internalized in CHO-K1 cells via CvME and in HEK 293 T cells via the lipid-mediated pathway.

**3.6.2.3. Role of the endosomal-lysosomal system.** Monensin is a lysosomotropic agent that blocks the endocytosis pathway by dissipating a proton gradient and interfering with the transport of a polyplex at the level of the Golgi complex toward the plasma membrane (Chen et al., 2009; Harada et al., 1996). Treatment with monensin increased transfection efficiency in the CHO-K1 and HEK 293 T cell lines for the OVA-OC polyplex. However, it slightly reduced the transfection efficiency of zein-OC polyplex by 7% and 8% in the CHO-K1 and HEK 293 T cells, respectively, as compared to the control (Fig. 6(a) and (b)). The acidification of the lysosome compartment slightly reduced transfection efficiency, which means that low endosomal pH requires the transportation of the zein-OC polyplex towards the cytoplasm. Conversely, the OVA-OC polyplex showed high transfection efficiency after the blocking of the Golgi-plasma membrane (G/PM) pathway. Polyplexes may directly translocate within vesicles present in the plasma membrane and later enter the nucleus. Furthermore, prior studies have illustrated that treatment with monensin increased the transcytosis of solid lipid nanoparticles (SLNs), which means the inhibition of G/PM pathway enhanced the activity of the direct pathway for the transportation of SLNs (Chai et al., 2014). Gu et al. have stated that treatment with an endosomal-lysosomal acidification inhibitor can increase the transfection efficiency of lipopolyplexes by protecting the plasmid DNA in the lysosome from degradation (Gu et al., 2016). Interestingly, the zein-OC polyplex showed higher transfection efficiency than the OVA-



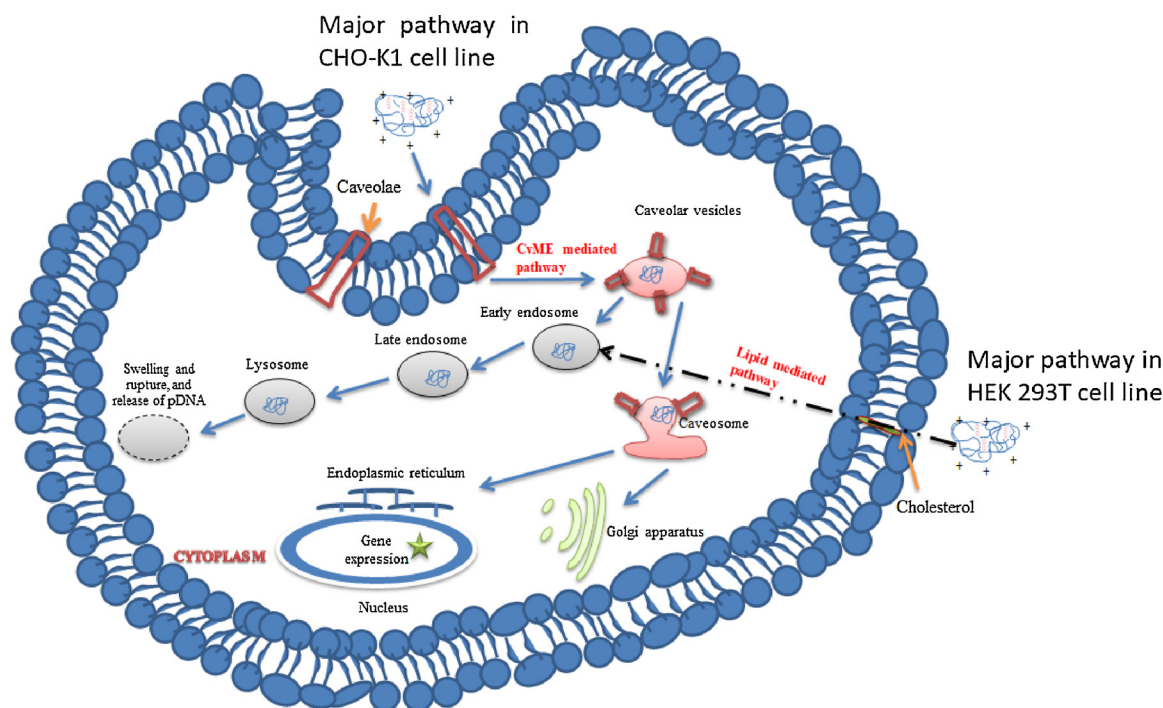


Fig. 8. Schematic illustration of the endocytic pathways involved in internalization of zein-OC polyplexes in CHO-K1 and HEK 293 T cell lines.

OC polyplex. The result may be due to the high buffering capacity of the zein-OC, facilitating endosomal escape and subsequently enhancing transfection efficiency. The zein-OC polyplex efficiently escaped from the endosomal-lysosomal system and enhanced the gene expression. In contrast, the OVA-OC polyplexes were not internalized via the endosomal-lysosomal system; they may enter directly into the endoplasmic reticulum or Golgi body from a caveosome.

### 3.6.3. Intracellular trafficking of the polyplexes

To investigate the intracellular distribution of the polyplexes, the cells were treated with polyplexes prepared with FITC-labeled OC-modified proteins and subsequently labeled with LysoTracker Red, a pH-sensitive dye used to stain the acidic environment of a lysosome for the observation of polyplex colocalization in an endosomal-lysosomal system (Zhang, Allen, & Grinstaff, 2011). Before examining the intracellular trafficking of the polyplex by using confocal microscopy, the nuclei of the cells were stained with Hoechst 33342 (nucleus-selective dye). Further, the quantification of the captured images was performed by IN Cell Investigator software. Fig. 7 shows that the colocalization of red and green signals produces a yellow signal.

In the CHO-K1 cells (Fig. 7(a) and (b)), green fluorescence was observed in the peri-nuclear region and in the nucleus, suggesting that both polyplexes could escape from the lysosome and reach the nucleus. Furthermore, Fig. 7(c) indicates that zein-OC polyplex showed lower entrapment efficiency (37%) in the lysosome as compared to OVA-OC polyplex (44%). Indeed, the zein-OC polyplex showed better transfection efficiency via endosome escape due to its proton-sponge effect. Another reason may also be the size of the polyplex as particle sizes above 200 nm are efficiently taken up through CvME pathways. Rejman et al. have reported that nanoparticles ranging in size from 200 to 500 nm are internalized via CvME and follow neutral pH conditions for the delivery of the nanoparticle (Rejman et al., 2005). This CvME pathway protects the degradation of polyplex from an acidic compartment, which helps to enhance the GFP expression level.

In the HEK 293 T cells (Fig. 7(d), (e) and (f)), the OVA-OC polyplexes showed little aggregation and were entrapped within the lysosomal vesicles. Moreover, diffused fluorescence was also observed for both polyplexes in the peri-nuclear region and in the nucleus,

suggesting that most of the polyplex can escape from the lysosome and enter the nucleus (Fig. 7(d) and (e)). The percentages of zein-OC polyplex and OVA-OC polyplex that colocalized with a lysosome were 42% and 38%, respectively (Fig. 7(f)). Cells treated with zein-OC polyplexes affected by endosomal-lysosomal system acidification because of treatment with monensin had their transfection efficiency reduced by 8% as compared to the control. Moreover, they showed high-level gene expression after 3 h of incubation, suggesting that most of these polyplexes escaped the lysosome without degradation due to the high buffering capacity of the OC-modified proteins. Furthermore, the OVA-OC polyplex also demonstrated internalization via the lipid-mediated pathway.

The endosome escape ability of a polyplex is one of the important factors that influence transfection efficiency. However, after endocytosis, lysosomal degradation also plays a major role as a barrier for gene delivery via non-viral vectors. Internalization of the polyplex through a CvME pathway has a high ability to escape the lysosome and deliver the gene into the nucleus (Pérez-Martínez et al., 2011). Colocalizations of blue and green fluorescence were observed for both polyplexes in the tested cell lines. Therefore, a substantial number of polyplexes successfully escaped from the lysosome and entered the nucleus.

The fact that sodium azide (an ATPase inhibitor) and low temperature (4 °C) treatments significantly reduced transfection efficiency suggests that endocytosis was the dominant pathway for the internalization of both polyplexes. Indeed, both polyplexes were internalized via the CvME and lipid-mediated pathways, depending on the cell line. In the CHO-K1 cell line, zein-OC polyplexes mainly transferred to the caveosome from caveolar vesicles in neutral pH conditions. Furthermore, the polyplex was trafficked towards perinuclear membrane organelles, such as the endoplasmic reticulum or Golgi complex. Later, the polyplexes in organelles might be delivered to the nucleus via nuclear pores or by fusing the reticulum membrane directly with the nuclear membrane. However, the data of monensin treatment demonstrated that a small portion of zein-OC polyplex was internalized through the endosomal-lysosomal system. In contrast, most of the zein-OC polyplexes were internalized via the lipid-mediated pathway and were trafficked to the endosomal-lysosomal system, in the HEK 293 T

cell line (Fig. 8). Additionally, the colocalization results suggested that the polyplexes successfully escaped from the endosomal-lysosomal pathways, which may be due to the high proton-sponge capacity of the OC-modified proteins. Previously, Fernandez et al. have reported that chitosan complexes can successfully escape the endosomal-lysosomal pathway due to the large number of amino groups on its D-glucosamine residue (Fernandez Fernandez, Santos-Carballal, Weber, & Goycoolea, 2016). Overall, these reports suggest that internalization via the CvME pathway has played a significant role in successful gene expression.

#### 4. Conclusion

Two OC-modified proteins (zein-OC and OVA-OC) were designed to improve transfection efficiency. The data confirms that greater transfection efficiency (up to 84%) was obtained by the zein-OC polyplex as compared to the OVA-OC polyplex (up to 70%). This greater transfection efficiency could be attributed to the larger buffering capacity of the zein-OC in the lysosome. Moreover, the particle sizes of the polyplexes were maintained in a range of 150 to 250 nm, which indicated that the polyplexes were suitable for endocytosis processes. In addition, the data confirm the hypothesis that the nature of a protein regulates the internalization mechanism of a polyplex, which in turn is influenced by transfection efficiency. Consequently, the synthesized vectors efficiently escaped from an acidic compartment without pDNA degradation and produced a high gene expression in both cell lines. In conclusion, we successfully synthesized a non-viral vector for a gene delivery system and demonstrated that the protein moiety in OC-modified proteins can influence the transfection efficiency of a polyplex and modulate its internalization pathways.

#### Acknowledgements

We express gratitude to Ministry of Science and Technology (MOST 106-2221-E-182-050), Chang Gung University (BMRP 758) and Chang Gung Memorial Hospital (CMRPD2G0282, 2H0071) for funding and supporting this research.

#### Appendix A. Supplementary data

Supplementary material related to this article can be found, in the online version, at doi:<https://doi.org/10.1016/j.carbpol.2018.08.131>.

#### References


- Akbari, B., Pirhadi, T. M., & Zandrahimi, M. (2011). Particle size characterization of nanoparticles—A practical approach. *Iranian Journal of Materials Science and Engineering*, 8(2), 48–56.
- Alameh, M., Lavertu, M., Tran-Khanh, N., Chang, C.-Y., Lesage, F., Bail, M., ... Buschmann, M. D. (2018). siRNA delivery with chitosan: Influence of chitosan molecular weight, degree of deacetylation, and amine to phosphate ratio on in vitro silencing efficiency, hemocompatibility, biodistribution, and in vivo efficacy. *Biomacromolecules*, 19(1), 112–131.
- Baldassarre, M., Li, C., Eremina, N., Goormaghtigh, E., & Barth, A. (2015). Simultaneous fitting of absorption spectra and their second derivatives for an improved analysis of protein infrared spectra. *Molecules*, 20(7), 12599–12622.
- Barth, A. (2007). Infrared spectroscopy of proteins. *Biochimica et Biophysica Acta*, 1767(9), 1073–1101.
- Chai, G.-H., Hu, F.-Q., Sun, J., Du, Y.-Z., You, J., & Yuan, H. (2014). Transport pathways of solid lipid nanoparticles across Madin-Darby canine kidney epithelial cell monolayer. *Molecular Pharmaceutics*, 11(10), 3716–3726.
- Chen, C.-L., Hou, W.-H., Liu, I.-H., Hsiao, G., Huang, S. S., & Huang, J. S. (2009). Inhibitors of clathrin-dependent endocytosis enhance TGF $\beta$  signaling and responses. *Journal of Cell Science*, 122(11), 1863–1871.
- Dalal, C., Saha, A., & Jana, N. R. (2016). Nanoparticle multivalency directed shifting of cellular uptake mechanism. *The Journal of Physical Chemistry C*, 120(12), 6778–6786.
- Danciu, C., Soica, C., Csanyi, E., Ambrus, R., Feflea, S., Peev, C., ... Dehelean, C. (2012). Changes in the anti-inflammatory activity of soy isoflavonoid genistein versus genistein incorporated in two types of cyclodextrin derivatives. *Chemistry Central Journal*, 6(1), 58.
- Dean, D. A., Strong, D. D., & Zimmer, W. E. (2005). Nuclear entry of nonviral vectors. *Gene Therapy*, 12, 881.
- Dong, A., Malecki, J. M., Lee, L., Carpenter, J. F., & Lee, J. C. (2002). Ligand-induced conformational and structural dynamics changes in Escherichia coli cyclic AMP receptor protein. *Biochemistry*, 41(21), 6660–6667.
- Douglas, K. L., Piccirillo, C. A., & Tabrizian, M. (2008). Cell line-dependent internalization pathways and intracellular trafficking determine transfection efficiency of nanoparticle vectors. *European Journal of Pharmaceutics and Biopharmaceutics*, 68(3), 676–687.
- Du, J., Li, B., Zhang, P., & Wang, Y. (2016). Cationized bovine serum albumin as gene carrier: Influence of specific secondary structure on DNA complexibility and gene transfection. *Colloids and Surfaces B: Biointerfaces*, 143, 37–46.
- Farris, S., Song, J., & Huang, Q. (2010). Alternative reaction mechanism for the cross-linking of gelatin with glutaraldehyde. *Journal of Agricultural and Food Chemistry*, 58(2), 998–1003.
- Fernandez Fernandez, E., Santos-Carballal, B., Weber, W. M., & Goycoolea, F. M. (2016). Chitosan as a non-viral co-transfection system in a cystic fibrosis cell line. *International Journal of Pharmaceutics*, 502(1–2), 1–9.
- Fissan, H., Ristig, S., Kaminski, H., Asbach, C., & Eppe, M. (2014). Comparison of different characterization methods for nanoparticle dispersions before and after aerosolization. *Analytical Methods: Advancing Methods and Applications*, 6(18), 7324–7334.
- Gautam, A., Sharma, M., Vir, P., Chaudhary, K., Kapoor, P., Kumar, R., ... Raghava, G. P. S. (2015). Identification and characterization of novel protein-derived arginine-rich cell-penetrating peptides. *European Journal of Pharmaceutics and Biopharmaceutics*, 89, 93–106.
- Gilbert, D. F., Erdmann, G., Zhang, X., Fritzsche, A., Demir, K., Jaedicke, A., ... Boutros, M. (2011). A novel multiplex cell viability assay for high-throughput RNAi screening. *PLoS One*, 6(12) e28338.
- Gu, J., Hao, J., Fang, X., & Sha, X. (2016). Factors influencing the transfection efficiency and cellular uptake mechanisms of Pluronic P123-modified polypropyleneimine/pDNA polyplexes in multidrug resistant breast cancer cells. *Colloids and Surfaces B: Biointerfaces*, 140, 83–93.
- Guo, L., Wang, L., Yang, R., Feng, R., Li, Z., Zhou, X., ... Xu, X. (2017). Optimizing conditions for calcium phosphate mediated transient transfection. *Saudi Journal of Biological Sciences*, 24(3), 622–629.
- Harada, M., Sakisaka, S., Yoshitake, M., Kin, M., Ohishi, M., Shakado, S., ... Tanikawa, K. (1996). Bafilomycin A1, a specific inhibitor of vacuolar-type H<sup>+</sup>-ATPases, inhibits the receptor-mediated endocytosis of asialoglycoproteins in isolated rat hepatocytes. *Journal of Hepatology*, 24(5), 594–603.
- Ishii, T., Okahata, Y., & Sato, T. (2001). Mechanism of cell transfection with plasmid/chitosan complexes. *Biochimica et Biophysica Acta*, 1514(1), 51–64.
- Kedjarune-Leggat, U., Supapratsakul, C., & Chotigeat, W. (2014). Ultrasound treatment increases transfection efficiency of low molecular weight chitosan in fibroblasts but not in KB cells. *PLoS One*, 9(3) e92076.
- Kumari, M., Liu, C.-H., & Wu, W.-C. (2018). Efficient gene delivery by oligochitosan conjugated serum albumin: Facile synthesis, polyplex stability, and transfection. *Carbohydrate Polymers*, 183, 37–49.
- Layman, J. M., Ramirez, S. M., Green, M. D., & Long, T. E. (2009). Influence of polycation molecular weight on poly(2-dimethylaminoethyl methacrylate)-mediated DNA delivery in vitro. *Biomacromolecules*, 10(5), 1244–1252.
- Lee, S., Kim, Y.-C., & Park, J.-H. (2016). Zein-alginate based oral drug delivery systems: Protection and release of therapeutic proteins. *International Journal of Pharmaceutics*, 515(1), 300–306.
- Leroueil, P. R., Hong, S., Mecke, A., Baker, J. R., Orr, B. G., & Banaszak Holl, M. M. (2007). Nanoparticle interaction with biological membranes: Does nanotechnology present a Janus face? *Accounts of Chemical Research*, 40(5), 335–342.
- Lohcharoenkal, W., Wang, L., Chen, Y. C., & Rojanasakul, Y. (2014). Protein nanoparticles as drug delivery carriers for cancer therapy. *BioMed Research International*, 2014, 12.
- Lv, P., Zhou, C., Zhao, Y., Liao, X., & Yang, B. (2017). Modified-epsilon-polyllysine-grafted-PEI- $\beta$ -cyclodextrin supramolecular carrier for gene delivery. *Carbohydrate Polymers*, 168, 103–111.
- Murphy, R. M. (1997). Static and dynamic light scattering of biological macromolecules: What can we learn? *Current Opinion in Biotechnology*, 8(1), 25–30.
- O'Keeffe Ahern, J. A. S., Zhou, D., Gao, Y., Lyu, J., Meng, Z., & Wang, W. (2018). Brushlike cationic polymers with low charge density for gene delivery. *Biomacromolecules*, 19(5), 1410–1415.
- Olson, B. J., & Markwell, J. (2007). Assays for determination of protein concentration. *Current Protocols in Protein Science* Chapter 3, Unit 3.4.
- Peng, S. F., Tseng, M. T., Ho, Y. C., Wei, M. C., Liao, Z. X., & Sung, H. W. (2011). Mechanisms of cellular uptake and intracellular trafficking with chitosan/DNA/poly (gamma-glutamic acid) complexes as a gene delivery vector. *Biomaterials*, 32(1), 239–248.
- Pérez-Martínez, F. C., Guerra, J., Posadas, I., & Ceña, V. (2011). Barriers to non-viral vector-mediated gene delivery in the nervous system. *Pharmaceutical Research*, 28(8), 1843–1858.
- Prochazkova, S., Vårum, K. M., & Ostgaard, K. (1999). Quantitative determination of chitosans by ninhydrin. *Carbohydrate Polymers*, 38(2), 115–122.
- Quigley, A., & Williams, D. R. (2015). The second virial coefficient as a predictor of protein aggregation propensity: A self-interaction chromatography study. *European Journal of Pharmaceutics and Biopharmaceutics*, 96, 282–290.
- Regier, M. C., Taylor, J. D., Borczyk, T., Yang, Y., & Pannier, A. K. (2012). Fabrication and characterization of DNA-loaded zein nanospheres. *Journal of Nanobiotechnology*, 10(1), 44.
- Rejman, J., Bragonzi, A., & Conese, M. (2005). Role of clathrin- and caveolae-mediated endocytosis in gene transfer mediated by lipo- and polyplexes. *Molecular Therapy: The Journal of the American Society of Gene Therapy*, 12(3), 468–474.
- Rejman, J., Oberle, V., Zuhorn, I. S., & Hoekstra, D. (2004). Size-dependent internalization of particles via the pathways of clathrin- and caveolae-mediated endocytosis. *The Biochemical Journal*, 377(Pt 1), 159–169.



- Ren, H., Liu, S., Yang, J., Zhang, X., Zhou, H., Chen, J., ... Guo, T. (2016). N,N,N-Trimethylchitosan modified with well defined multifunctional polymer modules used as pDNA delivery vector. *Carbohydrate Polymers*, 137, 222–230.
- Ross, N. L., Munsell, E. V., Sabanayagam, C., & Sullivan, M. O. (2015). Histone-targeted polyplexes avoid endosomal escape and enter the nucleus during postmitotic redistribution of ER membranes. *Molecular Therapy Nucleic Acids*, 4(2), e226.
- Salatin, S., & Yari Khosroushahi, A. (2017). Overviews on the cellular uptake mechanism of polysaccharide colloidal nanoparticles. *Journal of Cellular and Molecular Medicine*, 21(9), 1668–1686.
- Shah, M., Bourner, L., Ali, S., Al-Enazy, S., & Rytting, E. (2017). Cytotoxicity of Endocytosis and efflux inhibitors in the BeWo cell line. *Journal of Pharmaceutical Research International*, 17(5) JPRI.34606.
- Shen, J.-W., Li, J., Zhao, Z., Zhang, L., Peng, G., & Liang, L. (2017). Molecular dynamics study on the mechanism of polynucleotide encapsulation by chitosan. *Scientific Reports*, 7(1), 5050.
- Shi, B., Zheng, M., Tao, W., Chung, R., Jin, D., Ghaffari, D., ... Farokhzad, O. C. (2017). Challenges in DNA delivery and recent advances in multifunctional polymeric DNA delivery systems. *Biomacromolecules*, 18(8), 2231–2246.
- Silva, S. M. L., Braga, C. R. C., Fook, M. V. L., Raposos, C. M. O., Carvalho, L. H., & Canedo, E. L. (2012). *Application of infrared spectroscopy to analysis of chitosan clay nanocomposites infrared spectroscopy. Materials science, engineering and technology. Europe: In Tech*43–63.
- Syga, M.-I., Nicoli, E., Kohler, E., & Shastri, V. P. (2016). Albumin incorporation in polyethylenimine–DNA polyplexes influences transfection efficiency. *Biomacromolecules*, 17(1), 200–207.
- van der Aa, M. A. E. M., Huth, U. S., Häfele, S. Y., Schubert, R., Oosting, R. S., Mastrobattista, E., ... Crommelin, D. J. A. (2007). Cellular uptake of cationic Polymer–DNA complexes via caveolae plays a pivotal role in gene transfection in COS-7 cells. *Pharmaceutical Research*, 24(8), 1590–1598.
- Vercauteren, D., Vandenbroucke, R. E., Jones, A. T., Rejman, J., Demeester, J., De Smedt, S. C., ... Braeckmans, K. (2010). The use of inhibitors to study endocytic pathways of gene carriers: Optimization and pitfalls. *Molecular Therapy: the Journal of the American Society of Gene Therapy*, 18(3), 561–569.
- Wang, C., Jiang, L., Wei, D., Li, Y., Sui, X., Wang, Z., ... Li, D. (2011). Effect of secondary structure determined by FTIR spectra on surface hydrophobicity of soybean protein isolate. *Procedia Engineering*, 15, 4819–4827.
- Wang, H., Wang, A. X., Aylor, K., & Barrett, E. J. (2015). Caveolin-1 phosphorylation regulates vascular endothelial insulin uptake and is impaired by insulin resistance in rats. *Diabetologia*, 58(6), 1344–1353.
- Wang, S. H., Yuan, S. G., Peng, D. Q., & Zhao, S. P. (2010). High-density lipoprotein affects antigen presentation by interfering with lipid raft: A promising anti-atherogenic strategy. *Clinical and Experimental Immunology*, 160(2), 137–142.
- Wu, D., Zhang, Y., Xu, X., Guo, T., Xie, D., Zhu, R., ... He, L. (2018). RGD/TAT-functionalized chitosan-graft-PEI-PEG gene nanovector for sustained delivery of NT-3 for potential application in neural regeneration. *Acta Biomaterialia*, 72, 266–277.
- Xu, L., Huo, M., Sun, C., Cui, X., Zhou, D., Crittenden, J. C., ... Yang, W. (2017). Bioresources inner-recycling between bioflocculation of *Microcystis aeruginosa* and its reutilization as a substrate for bioflocculant production. *Scientific Reports*, 7, 43784.
- Xu, T., Liu, W., Wang, S., & Shao, Z. (2014). Elucidating the role of free polycationic chains in polycation gene carriers by free chains of polyethylenimine or N,N,N-trimethyl chitosan plus a certain polyplex. *International Journal of Nanomedicine and Nanosurgery*, 9, 3231–3245.
- Yang, H., Yang, S., Kong, J., Dong, A., & Yu, S. (2015). Obtaining information about protein secondary structures in aqueous solution using Fourier transform IR spectroscopy. *Nature Protocols*, 10(3), 382–396.
- Zeng, Y., Kurokawa, Y., Win-Shwe, T. T., Zeng, Q., Hirano, S., Zhang, Z., ... Sone, H. (2016). Effects of PAMAM dendrimers with various surface functional groups and multiple generations on cytotoxicity and neuronal differentiation using human neural progenitor cells. *The Journal of Toxicological Sciences*, 41(3), 351–370.
- Zhang, H., Li, Q., Zhang, Y., Xia, Y., Yun, L., Zhang, Q., ... Li, W. (2016). A nanogel with passive targeting function and adjustable polyplex surface properties for efficient anti-tumor gene therapy. *RSC Advances*, 6(87), 84445–84456.
- Zhang, T., Song, X., Kang, D., Zhang, L., Zhang, C., Jin, S., ... Liang, X.-J. (2015). Modified bovine serum albumin as an effective charge-reversal platform for simultaneously improving the transfection efficiency and biocompatibility of polyplexes. *Journal of Materials Chemistry B, Materials for Biology and Medicine*, 3(23), 4698–4706.
- Zhang, X.-X., Allen, P. G., & Grinstaff, M. (2011). Macropinocytosis is the major pathway responsible for DNA transfection in CHO cells by a charge-reversal amphiphile. *Molecular Pharmaceutics*, 8(3), 758–766.

Article

# New Furanocembranoids from *Briareum violaceum*

Pin-Chang Huang <sup>1,2,†</sup>, Wen-Sou Lin <sup>3,4,†</sup>, Bo-Rong Peng <sup>2</sup>, Yu-Chia Chang <sup>5</sup>, Lee-Shing Fang <sup>6,7</sup>, Guo-Qiang Li <sup>8,9</sup> , Tsong-Long Hwang <sup>5,10,11,12</sup> , Zhi-Hong Wen <sup>4,\*</sup> and Ping-Jyun Sung <sup>1,2,4,13,14,15,\*</sup> 

- <sup>1</sup> Graduate Institute of Marine Biology, National Dong Hwa University, Pingtung 94450, Taiwan; foter25632@gmail.com
- <sup>2</sup> Department of Planning and Research, National Museum of Marine Biology and Aquarium, Pingtung 94450, Taiwan; pengpojung@gmail.com
- <sup>3</sup> Department of Neurology, Kaohsiung Armed Forces General Hospital, Kaohsiung 80284, Taiwan; linvincent1009@gmail.com
- <sup>4</sup> Department of Marine Biotechnology and Resources, National Sun Yat-sen University, Kaohsiung 80424, Taiwan
- <sup>5</sup> Research Center for Chinese Herbal Medicine, Research Center for Food and Cosmetic Safety, Graduate Institute of Healthy Industry Technology, College of Human Ecology, Chang Gung University of Science and Technology, Taoyuan 33303, Taiwan; jay0404@gmail.com (Y.-C.C.); htl@mail.cgu.edu.tw (T.-L.H.)
- <sup>6</sup> Center for Environmental Toxin and Emerging-Contaminant Research, Cheng Shiu University, Kaohsiung 83347, Taiwan; lsfang@csu.edu.tw
- <sup>7</sup> Super Micro Mass Research and Technology Center, Cheng Shiu University, Kaohsiung 83347, Taiwan
- <sup>8</sup> Key Laboratory of Marine Drugs, Chinese Ministry of Education, School of Medicine and Pharmacy, Ocean University of China, Qingdao 266033, China; liguoqiang@ouc.edu.cn.
- <sup>9</sup> Laboratory of Marine Drugs and Biological Products, National Laboratory for Marine Science and Technology, Qingdao 266235, China
- <sup>10</sup> Graduate Institute of Natural Products, College of Medicine, Chang Gung University, Taoyuan 33302, Taiwan
- <sup>11</sup> Chinese Herbal Medicine Research Team, Healthy Aging Research Center, Chang Gung University, Taoyuan 33302, Taiwan
- <sup>12</sup> Department of Anaesthesiology, Chang Gung Memorial Hospital, Taoyuan 33305, Taiwan
- <sup>13</sup> Graduate Institute of Natural Products, Kaohsiung Medical University, Kaohsiung 80708, Taiwan
- <sup>14</sup> Research Center for Natural Products and Drug Development, Kaohsiung Medical University, Kaohsiung 80708, Taiwan
- <sup>15</sup> Chinese Medicine Research and Development Center, China Medical University Hospital, Taichung 40447, Taiwan
- \* Correspondence: wzh@mail.nsysu.edu.tw (Z.-H.W.); pjsung@nmmmba.gov.tw (P.-J.S.); Tel.: +886-7-525-2000 (ext. 5038) (Z.-H.W.); +886-8-882-5037 (P.-J.S.); Fax: +886-7-525-5021 (Z.-H.W.); +886-8-882-5087 (P.-J.S.)
- † These authors contributed equally to this work.

Received: 17 February 2019; Accepted: 3 April 2019; Published: 5 April 2019



**Abstract:** Three new furanocembranoids—briaviodiol F (1) and briaviotriols A (2) and B (3)—along with a known analogue, briaviodiol A (4), were obtained from a cultured-type octocoral *Briareum violaceum*. The structures of cembranoids 1–3 were elucidated by using spectroscopic methods. In vitro study demonstrated that compounds 2 and 4 exerted inhibition effects on inducible nitric oxide synthase (iNOS) release from RAW 264.7, a macrophage cell line that originated from a mouse monocyte macrophage, stimulated with lipopolysaccharides.

**Keywords:** *Briareum violaceum*; briaviodiol; briaviotriol; anti-inflammatory; iNOS

## 1. Introduction

*Briareum violaceum* (Quoy and Gaimard, 1883) is a soft coral of the family Briareidae [1,2], which has been found to contain cembrane-type diterpenoids in abundance [3–10]. Diterpenoids of this type have been reported to have complicated structures and possess a variety of bioactivities [3–10]. Recently, in our research into the chemical constituents and properties of a cultured octocoral *B. violaceum*, we have isolated three previously unreported furanocembranoids—briaviodiol F (1), and briaviotriols A (2) and B (3)—along with a known analogue, briaviodiol A (4) [9] (Figure 1). A pro-inflammatory suppression assay was employed to assess the activities of these isolated compounds against the release of inducible nitric oxide synthase (iNOS) from macrophage cells.

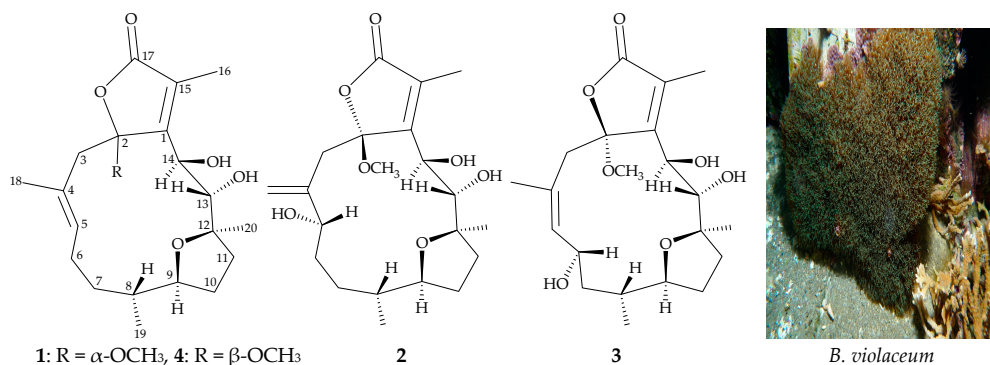


**Figure 1.** Structures of briaviodiol F (1), briaviotriols A (2) and B (3), and briaviodiol A (4), and a picture of the octocoral *B. violaceum*.

## 2. Results and Discussion

Briaviodiol F (1) was isolated as a colorless oil. Compound 1 displayed a pseudomolecular ion at  $m/z$  403.20886 in the (+)-HRESIMS, which indicated its molecular formula was C<sub>21</sub>H<sub>32</sub>O<sub>6</sub> (calcd. for C<sub>21</sub>H<sub>32</sub>O<sub>6</sub> + Na, 403.20911), suggesting six degrees of unsaturation. Additionally, IR absorptions at 3497 and 1754 cm<sup>−1</sup> indicated that 1 contained hydroxy and ester groups. As shown in Table 1, DEPT and <sup>13</sup>C NMR spectra indicated that a suite of <sup>13</sup>C resonances at  $\delta_C$  172.1 (C-17), 154.3 (C-1), 127.2 (C-15), 109.5 (C-2), and 9.2 (CH<sub>3</sub>-16) were due to an  $\alpha$ -methyl- $\gamma$ -butenolide moiety by comparison with the data of known cembranoids briaviodiol A (4) [9] and pachyclavariolide F [6]. Moreover, resonances at  $\delta_C$  127.1 (C-4) and 135.1 (CH-5), and the olefinic proton at  $\delta_H$  5.30 (1H, dd,  $J$  = 8.0, 5.6 Hz, H-5) (Table 1), indicated an additional unsaturated functionality, suggesting the presence of a trisubstituted olefin. In the HSQC spectrum, an sp<sup>2</sup> carbon ( $\delta_C$  135.1) correlated with the methine proton ( $\delta_H$  5.30). This proton had <sup>3</sup> $J$ -correlations with H<sub>2</sub>-6 ( $\delta_H$  1.93–1.99, 2H, m) in the <sup>1</sup>H–<sup>1</sup>H COSY spectrum, and had <sup>3</sup> $J$ -correlations with C-3 and C-18 in the HMBC spectrum (Table 1), further confirming the existence of a trisubstituted olefin. In light of the <sup>1</sup>H and <sup>13</sup>C NMR data, together with the degrees of unsaturation, 1 was determined as a tricyclic cembrane diterpene.

The <sup>1</sup>H NMR coupling information in the COSY spectrum of 1 enabled the determination of the proton sequences between H-5/H<sub>2</sub>-6/H<sub>2</sub>-7/H-8/H-9/H<sub>2</sub>-10/H<sub>2</sub>-11 and H-8/H<sub>3</sub>-19 (Table 1). The carbon skeleton of 1 was elucidated based on the key HMBC from H-3 $\beta$ , H-13, H-14, H<sub>3</sub>-16 to C-1; H<sub>2</sub>-3, H-14 to C-2; H<sub>2</sub>-3, H<sub>3</sub>-18 to C-4; H-10 $\beta$ , H-11 $\alpha$ , H-13, H-14, H<sub>3</sub>-20 to C-12; H-14, H<sub>3</sub>-16 to C-15; and H<sub>3</sub>-16 to C-17. The presence of a vinyl methyl group on C-4 was supported by HMBC from H<sub>3</sub>-18 to C-3, C-4, C-5; H-3 $\alpha$  ( $\delta_H$  2.78) to C-18 and H-5 to C-18. Furthermore, HMBC from OH-13 to C-13, C-14 and OH-14 to C-1, C-13, C-14 suggested the existence of hydroxy groups at C-13 and C-14, respectively. Therefore, the methoxy group was on C-2, since the HMBC spectrum exhibited a correlation between the singlet at  $\delta_H$  3.39 (OMe) and C-2 ( $\delta_C$  109.5). Taking into account the molecular formula, the remaining oxygen atom must be part of the tetrahydrofuran ring located between C-9 and C-12.

Based on NOESY correlations and further information provided by MM2 forcefield calculations [11], the relative stereochemistry of **1** with the stable conformation is shown in Figure 2 (Supplementary Figures S1–10). When H-9 was  $\alpha$ -oriented in **1**, a correlation between H-9 and H<sub>3</sub>-19 was observed, suggesting that these protons were on the  $\alpha$ -face, and H-8 was  $\beta$ -oriented. H-8 correlated with H-13, and the hydroxy proton OH-13 correlated with H<sub>3</sub>-20, suggesting that the hydroxy group at C-13 and the Me-20 at C-12 were  $\alpha$ -oriented. H-14 exhibited a NOESY correlation with H-13, and no coupling constant was detected between H-13 and H-14 in the <sup>1</sup>H NMR spectrum, implying that the dihedral angle located between H-13 and H-14 was about 90°, and the 14-hydroxy group was  $\beta$ -oriented. Correlations between H-5 and H-3, and H-14 and H-3 ( $\delta_{\text{H}}$  2.78) suggested that this proton is  $\alpha$ , and the proton at  $\delta_{\text{H}}$  3.04 is 3 $\beta$ . Additionally, the proton signal of a methoxy group displayed NOESY correlations with both H-3 $\alpha$ / $\beta$ , which indicated that the methoxy group at C-2 was  $\alpha$ -oriented. H<sub>3</sub>-18 was found to show a NOESY correlation with H-3 $\beta$ , but not with H-5, and H-5 was shown to be correlated with H-3 $\alpha$  and H-14, which suggested an *E*-configuration of the C-4/5 double bond. The aforementioned results enabled establishment of the relative configuration of **1**, and therefore its stereogenic carbons were assigned as 2*R*\*,8*R*\*,9*S*\*,12*R*\*,13*S*\*, 14*R*\*.

**Table 1.** <sup>1</sup>H (400 MHz, CDCl<sub>3</sub>) and <sup>13</sup>C (100 MHz, CDCl<sub>3</sub>) NMR, COSY, HMBC data for **1**.

Position	$\delta_{\text{H}}$ (J in Hz)	$\delta_{\text{C}}$ , type	COSY	HMBC
1		154.3, C		
2		109.5, C		
3 $\alpha$ / $\beta$	2.78 d (14.0); 3.04 d (14.0)	44.8, CH <sub>2</sub>		C-1, C-2, C-4, C-5, C-18
4		127.1, C		
5	5.30 dd (8.0, 5.6)	135.1, CH	H <sub>2</sub> -6	C-3, C-18
6	1.93–1.99 m	26.3, CH <sub>2</sub>	H-5, H <sub>2</sub> -7	C-4, C-5, C-7, C-8
7 $\alpha$ / $\beta$	1.80 m; 1.26 m	34.9, CH <sub>2</sub>	H <sub>2</sub> -6, H-8	C-5, C-6, C-8, C-9, C-19
8	0.68 m	41.4, CH	H <sub>2</sub> -7, H-9, H <sub>3</sub> -19	C-9
9	3.68 ddd (9.6, 9.6, 6.0)	85.2, CH	H-8, H <sub>2</sub> -10	C-7
10 $\alpha$ / $\beta$	1.51 m; 1.98 m	30.3, CH <sub>2</sub>	H-9, H <sub>2</sub> -11	C-11, C-12
11 $\alpha$ / $\beta$	1.56 m; 2.38 dd (12.0, 6.4)	36.9, CH <sub>2</sub>	H <sub>2</sub> -10	C-9, C-10, C-12, C-13, C-20
12		84.1, C		
13	3.60 d (10.0)	70.7, CH	OH-13	C-1, C-11, C-12, C-20
14	5.06 s	63.9, CH	-	C-1, C-2, C-12, C-15
15		127.2, C		
16	2.11 s	9.2, CH <sub>3</sub>		C-1, C-15, C-17
17		172.1, C		
18	1.44 s	15.3, CH <sub>3</sub>		C-3, C-4, C-5
19	0.78 d (6.4)	17.3, CH <sub>3</sub>	H-8	C-7, C-8, C-9
20	1.30 s	20.9, CH <sub>3</sub>		C-11, C-12, C-13
OMe-2	3.39 s	51.0, CH <sub>3</sub>		C-2
OH-13	3.14 d (10.0)		H-13	C-13, C-14
OH-14	3.34 s		-	C-1, C-13, C-14

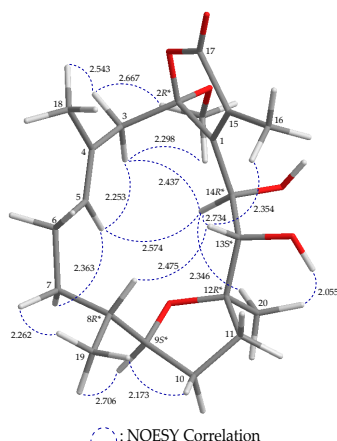


**Figure 2.** Computer-depicted model drawing of **1** and calculated distances (unit = Å) between protons with main NOESY correlations.

Briaviotriol A (**2**) was found to have the molecular formula  $C_{21}H_{32}O_7$ , as established by (+)-HRESIMS at  $m/z$  419.20377 (calcd. for  $C_{21}H_{32}O_7 + Na$ , 419.20402). The  $^1H$  and  $^{13}C$  NMR spectra of **2** were very similar to those of **1**. Comparison between the  $^1H$  and  $^{13}C$  NMR data of **2** (Table 2) and those of **1** suggested that the double bond is located between C-4 and C-18 in **2** instead of C-4 and C-15 in **1**. HMBC from  $H_2$ -18 to C-3, C-4, C-5; and from  $H_2$ -3 and H-5 to C-18, corroborated the existence of an exocyclic double bond at C-4. In the HSQC spectrum, an oxymethine carbon ( $\delta_C$  69.1) correlated with the methine proton ( $\delta_H$  4.57), and this proton had  $^3J$ -correlations with  $H_2$ -6 ( $\delta_H$  1.81, 1H, m and 1.93, 1H, m) in the  $^1H$ - $^1H$  COSY spectrum, demonstrating that a hydroxy group was attached to C-5.

**Table 2.**  $^1H$  (400 MHz,  $CDCl_3$ ) and  $^{13}C$  (100 MHz,  $CDCl_3$ ) NMR, COSY, HMBC data for **2**.

Position	$\delta_H$ (J in Hz)	$\delta_C$ , type	COSY	HMBC
1		157.9, C		
2		107.8, C		
3 $\alpha$ / $\beta$	2.67 d (14.4); 3.15 d (14.4)	42.2, $CH_2$		C-1, C-2, C-4, C-5, C-18
4		146.4, C		
5	4.57 dd (7.2, 6.0)	69.1, CH	$H_2$ -6	C-4, C-6, C-18
6/6'	1.81m; 1.93 m	32.2, $CH_2$	H-5, $H_2$ -7	-
7/7'	1.33 m; 1.89 ddd (14.4, 4.8, 4.4)	30.6, $CH_2$	$H_2$ -6, H-8	C-5
8	1.53 m	37.4, CH	$H_2$ -7, H-9, $H_3$ -19	-
9	3.65 ddd (8.4, 8.4, 6.0)	85.4, CH	H-8, $H_2$ -10	-
10/10'	1.52 m; 2.10 m	31.5, $CH_2$	H-9, $H_2$ -11	-
11/11'	1.65 m; 2.16 m	37.2, $CH_2$	$H_2$ -10	C-9, C-10, C-12, C-13, C-20
12		84.4, C		
13	3.50 d (5.6)	75.2, CH	OH-13	-
14	5.18 br s	67.7, CH	OH-14	-
15		130.0, C		
16	2.11 s	10.1, $CH_3$		C-1, C-15, C-17
17		171.1, C		
18a/b	5.13 s; 5.30 s	115.6, $CH_2$		C-3, C-4, C-5
19	0.85 d (6.4)	16.7, $CH_3$	H-8	C-7, C-8, C-9
20	1.29 s	21.8, $CH_3$		C-11, C-12, C-13
OMe-2	3.26 s	50.7, $CH_3$		C-2
OH-13	2.42 br d (5.6)		H-13	-
OH-14	2.29 br d (4.4)		H-14	-

The stereochemistry of **2** was established from the correlations observed in the NOESY spectrum (Figure 3 and Supplementary Figures S2–10). In addition, in the NOESY spectrum H-9 was correlated with  $H_3$ -19, which suggested that these protons were positioned on the same face and were assigned as  $\alpha$  protons, as H-8 was  $\beta$ -oriented. H-13 correlated with H-8 and H-14, but no coupling between H-13 and H-14 was observed, demonstrating that the hydroxy groups at C-13 and C-14 were  $\alpha$ - and  $\beta$ -oriented, respectively. Correlations between an oxygen-bearing methyl ( $\delta_H$  3.26) and H-13 suggested that the C-2 methoxy group was situated on the  $\beta$  face. Additionally, correlation between H-5 and H-8 supported a  $\beta$ -orientation of H-5. Based on the aforementioned results, the relative configurations of the stereogenic carbons of **2** were determined as  $2S^*, 5S^*, 8R^*, 9S^*, 12R^*, 13S^*, 14R^*$ .



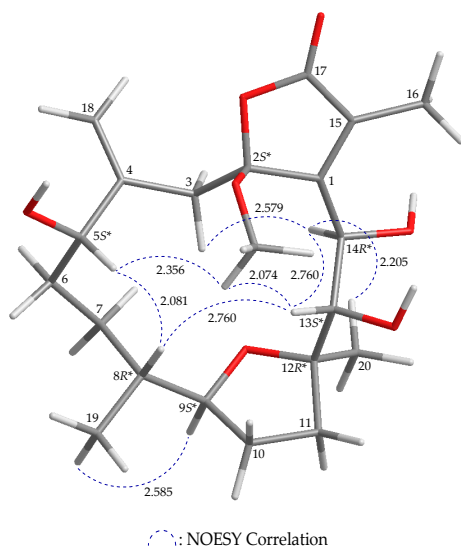


**Figure 3.** Computer-depicted model drawing of **2** and calculated distances (unit = Å) between protons with main NOESY correlations.

Compound **3** has a molecular formula  $C_{21}H_{32}O_7$  according to its (+)-HRESIMS  $m/z$  419.20399 (calcd. for  $C_{21}H_{32}O_8 + Na$ , 419.20402). The  $^1H$  and  $^{13}C$  NMR features of **3** resemble those of **1**; comparison of the  $^1H$  and  $^{13}C$  NMR chemical shifts of the  $sp^2$  methine proton and its respective carbon ( $\delta_H$  5.29, 1H, d,  $J = 8.4$  Hz;  $\delta_C$  133.5, CH-5), and the  $sp^2$  quaternary carbon ( $\delta_C$  131.0, C-4) of **3** (Table 3) with those of **1** ( $\delta_H$  5.30, 1H, dd,  $J = 8.0, 5.6$  Hz;  $\delta_C$  135.1, CH-5;  $\delta_C$  127.1, C-4) (Table 1), as well as a NOESY correlation between H-5 and H<sub>3</sub>-18, indicated the Z-configuration of the C-4/5 double bond (Figure 4 and Supplementary Figure S3–10). Furthermore, the HSQC spectrum showed that an oxymethine carbon ( $\delta_C$  68.7) was correlated with a methine proton ( $\delta_H$  4.86; H-6), and this proton exhibited  $^3J$ -correlations with the olefinic proton H-5 ( $\delta_H$  5.29) and H<sub>2</sub>-7 ( $\delta_H$  1.34, 1H, m; 1.80, 1H, m) in the COSY spectrum, which confirmed a hydroxy group at C-6. As H-6 showed a NOESY correlation with H-3 $\beta$ , this suggested that the C-6 hydroxy group was  $\alpha$ -oriented. Based on a NOESY experiment (Figure 4 and Supplementary Figures S3–10), **3** was identified to have the stereogenic centers 2R\*,6S\*,8R\*,9S\*,12R\*,13S\*,14R\*. Since **3** has never been previously reported, it was named briaviotriol B.

**Table 3.**  $^1H$  (400 MHz,  $CDCl_3$ ) and  $^{13}C$  (100 MHz,  $CDCl_3$ ) NMR, and COSY, HMBC data for **3**.

Position	$\delta_H$ (J in Hz)	$\delta_C$ , type	COSY	HMBC
1		159.8, C		
2		107.7, C		
3 $\alpha/\beta$	1.76 d (14.4); 3.56 d (14.4)	39.6, CH <sub>2</sub>		C-1, C-2, C-4, C-5, C-18
4		131.0, C		
5	5.29 d (8.4)	133.5, CH	H-6	C-3, C-18
6	4.86 ddd (12.0, 8.4, 3.2)	68.7, CH	H-5, H <sub>2</sub> -7	-
7/7'	1.34 m; 1.80 m	44.9, CH <sub>2</sub>	H-6, H-8	C-5, C-6, C-8, C-9, C-19
8	1.21 m	35.3, CH	H <sub>2</sub> -7, H-9, H <sub>3</sub> -19	-
9	3.65 ddd (10.0, 10.0, 4.4)	87.3, CH	H-8, H <sub>2</sub> -10	-
10/10'	1.38 m; 2.05 m	32.8, CH <sub>2</sub>	H-9, H <sub>2</sub> -11	C-9, C-11, C-12
11/11'	1.61 m; 2.22 dd (13.2, 8.0)	35.5, CH <sub>2</sub>	H <sub>2</sub> -10	C-9, C-12, C-13, C-20
12		85.1, C		
13	3.40 d (8.4)	76.7, CH	OH-13	C-1, C-12, C-20
14	4.75 d (5.2)	63.5, CH	OH-14	C-1, C-2, C-12, C-13, C-15
15		128.5, C		
16	2.08 s	9.6, CH <sub>3</sub>		C-1, C-15, C-17
17		171.9, C		
18	1.83 s	24.0, CH <sub>3</sub>		C-3, C-4, C-5
19	0.84 d (6.8)	20.1, CH <sub>3</sub>	H-8	C-7, C-8, C-9
20	1.28 s	21.1, CH <sub>3</sub>		C-11, C-12, C-13
OMe-2	3.20 s	51.1, CH <sub>3</sub>		C-2
OH-13	3.05 d (8.4)		H-13	C-13, C-14
OH-14	2.70 d (5.2)		H-14	C-13, C-14

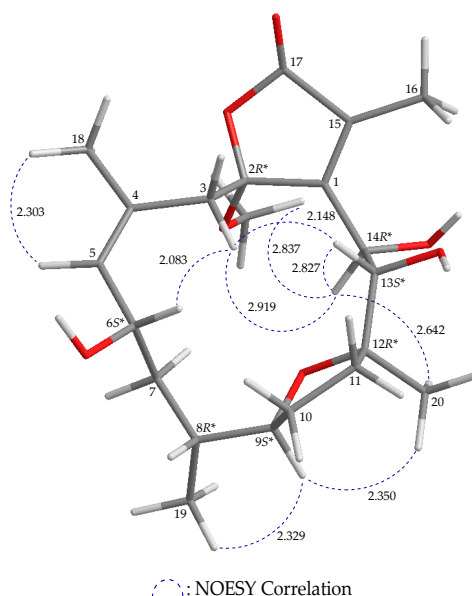


**Figure 4.** Computer-depicted model drawing of **3** and calculated distances (unit = Å) between protons with main NOESY correlations.

Compound **4** was identified as briaviiodiol A (Figure 1), by comparison of its  $^1\text{H}$  and  $^{13}\text{C}$  NMR data with those in the literature [9].

Using an in vitro pro-inflammatory suppression assay, the effects of **1–4** on the release of iNOS protein from lipopolysaccharide (LPS)-stimulated RAW 264.7 macrophage cells were assessed. First, alamar blue cell viability assessment revealed that **1–4** did not have significant cytotoxic effects in RAW 264.7 cells. The results of the in vitro pro-inflammatory suppression assay showed that **2** and **4** at 10  $\mu\text{M}$  suppressed the release of iNOS to 67.7 and 61.9%, respectively, when compared with results of the cells stimulated with only LPS (Table 4). Compound **1** showed no suppression effect on iNOS release.

**Table 4.** Effects of **1–4** on LPS-induced pro-inflammatory iNOS release in RAW 264.7 cells at a concentration of 10  $\mu\text{M}$ . The data presented are the relative intensity normalized to the LPS-stimulated group. Compounds **2** and **4** were found to have the higher inhibition effects on LPS-induced iNOS expression in macrophages expression.

	iNOS
	Expression (% of LPS)
LPS	100.0 $\pm$ 7.0
<b>1</b>	109.0 $\pm$ 19.2
<b>2</b>	67.7 $\pm$ 2.4
<b>3</b>	79.5 $\pm$ 9.4
<b>4</b>	61.9 $\pm$ 7.3

### 3. Experimental Section

#### 3.1. General Experimental Procedures

The JEOL NMR spectrometer (model ECZ400S, Tokyo, Japan) was used to record the spectra with the solvent peak of  $\text{CHCl}_3$  ( $\delta_{\text{H}}$  7.26 ppm) and  $\text{CDCl}_3$  ( $\delta_{\text{C}}$  77.1 ppm) as internal references for  $^1\text{H}$  NMR and  $^{13}\text{C}$  NMR, respectively. ESIMS and HRESIMS were obtained from the Bruker mass spectrometer with 7 Tesla magnets (model: Solarix FTMS system) (Bremen, Germany). Column chromatography, IR spectra and optical rotation were performed according to our earlier research [10].

### 3.2. Animal Material

Specimens of *B. violaceum* used for this study were collected in December 2016 from the cultivation tank (capacity = 270 tons) at the National Museum of Marine Biology and Aquarium (NMMBA) in Southern Taiwan. For its identification, this coral species was compared to reliable sources published earlier [1,2]. A voucher specimen was deposited in the NMMBA (voucher no.: NMMBA-CSC-005).

### 3.3. Extraction and Isolation

Sliced bodies (wet/dry weight = 358.7/144.5 g) of the coral specimen were prepared and extracted with a 1:1 mixture of MeOH and CH<sub>2</sub>Cl<sub>2</sub> to give 17.2 g of crude extract which was partitioned between EtOAc and H<sub>2</sub>O to obtain 6.3 g of the EtOAc extract. The EtOAc extract was then applied onto a silica gel column and eluted with gradients of *n*-hexane/EtOAc (100% *n*-hexane–100% EtOAc, stepwise), to furnish 14 fractions (fractions: A–N). Fraction G was further chromatographed on a silica gel column and eluted with gradients of *n*-hexane/Me<sub>2</sub>CO (20:1–100% Me<sub>2</sub>CO, stepwise) to afford 11 subfractions (fractions: G1–G11). Fraction G4 was applied onto a silica gel column and eluted with gradients of *n*-hexane and Me<sub>2</sub>CO (20:1–100% Me<sub>2</sub>CO, stepwise) to give 12 subfractions (fractions: G4A–G4L). Afterwards, fraction G4E was then separated by normal-phase HPLC (NP-HPLC) using a mixture of *n*-hexane and Me<sub>2</sub>CO (5:1) as solvent to obtain 5 subfractions (fractions: G4E1–G4E5). Then, fraction G4E1 was separated by NP-HPLC using a mixture of CH<sub>2</sub>Cl<sub>2</sub> and Me<sub>2</sub>CO (with volume: volume = 80:1; at a flow rate = 3.0 mL/min) to afford **1** (62.7 mg). Fraction G4H was separated by NP-HPLC using a mixture of *n*-hexane and Me<sub>2</sub>CO (with volume: volume = 4:1; at a flow rate = 2.0 mL/min) to afford **4** (17.0 mg). Fraction G4J was repurified by NP-HPLC using a mixture of *n*-hexane and Me<sub>2</sub>CO (with volume: volume = 3:1; at a flow rate = 2.0 mL/min) to afford **3** (0.9 mg). Fraction G8 was separated by NP-HPLC using a mixture of *n*-hexane and Me<sub>2</sub>CO (3:1) to obtain 6 subfractions G8A–G8F. Fraction G8F was repurified by reverse-phase HPLC (RP-HPLC) using a mixture of MeCN and H<sub>2</sub>O (with volume: volume = 1:1; at a flow rate = 1.0 mL/min) to yield **2** (1.2 mg).

Briaviodiol F (**1**): Colorless oil;  $[\alpha]_D^{21} +223$  (c 1.48, CHCl<sub>3</sub>); IR (neat)  $\nu_{\max}$  3497, 1754 cm<sup>−1</sup>; <sup>1</sup>H and <sup>13</sup>C NMR data (see Table 1); ESIMS: *m/z* 403 [M + Na]<sup>+</sup>; HRESIMS: *m/z* 403.20886 (calcd. for C<sub>21</sub>H<sub>32</sub>O<sub>6</sub> + Na, 403.20911).

Briaviotriol A (**2**): Colorless oil;  $[\alpha]_D^{22} -68$  (c 0.06, CHCl<sub>3</sub>); IR (neat)  $\nu_{\max}$  3424, 1749 cm<sup>−1</sup>; <sup>1</sup>H and <sup>13</sup>C NMR data (see Table 2); ESIMS: *m/z* 419 [M + Na]<sup>+</sup>; HRESIMS: *m/z* 419.20377 (calcd. for C<sub>21</sub>H<sub>32</sub>O<sub>7</sub> + Na, 419.20402).

Briaviotriol B (**3**): Colorless oil;  $[\alpha]_D^{23} -39$  (c 0.04, CHCl<sub>3</sub>); IR (neat)  $\nu_{\max}$  3424, 1749 cm<sup>−1</sup>; <sup>1</sup>H and <sup>13</sup>C NMR data (see Table 3); ESIMS: *m/z* 419 [M + Na]<sup>+</sup>; HRESIMS: *m/z* 419.20399 (calcd. for C<sub>21</sub>H<sub>32</sub>O<sub>7</sub> + Na, 419.20402).

Briaviodiol A (**4**): Colorless crystal;  $[\alpha]_D^{21} -52$  (c 0.85, CHCl<sub>3</sub>) (Reference [9]  $[\alpha]_D^{23} -31$  (c 0.14, CHCl<sub>3</sub>)); IR (neat)  $\nu_{\max}$  3467, 1747 cm<sup>−1</sup>; <sup>1</sup>H and <sup>13</sup>C NMR data were found to be in absolute agreement with previous study [9]; ESIMS: *m/z* 403 [M + Na]<sup>+</sup>.

### 3.4. Molecular Mechanics Calculations

The molecular models were generated by implementing the MM2 force field [11] in ChemBio 3D Ultra software (ver. 12.0) which was created by CambridgeSoft (PerkinElmer, Cambridge, MA, USA).

### 3.5. In Vitro Anti-Inflammatory Assay

The pro-inflammatory suppression assay was performed using a murine macrophage cell line, RAW 264.7, which was purchased from the American Type Culture Collection (ATCC cell line no. TIB-71; Manassas, VA, USA). Untreated or LPS-induced RAW 264.7 cells were used to determine the anti-inflammatory activities of cembranoids **1–4** by assessing the inhibition of pro-inflammatory iNOS release from macrophage cells. The iNOS protein levels were measured by using western blotting

analysis [12–14]. Briefly, in the control group, macrophages were incubated in compound-free medium with LPS (10  $\mu$ M) alone for 16 h; and in the cembranoid-treated groups, the cells were pre-treated with cembranoids 1–4 (10  $\mu$ M) for 10 min followed by an LPS challenge for 16 h. After the incubation, cell lysates were collected, and equal amounts of the total protein samples were subjected to western blot analysis. The immunoreactivities were calculated based on the optical densities of the corresponding iNOS bands of each group on the membrane, and the cells with LPS treatment alone were set to be 100%. Viability of macrophage cells of different groups was determined after treatment with alamar blue (Invitrogen, Carlsbad, CA, USA), a chemical of tetrazolium dye that is reduced by living cells to a fluorescent substance. The assay has been shown to have accurate measurement in determining the survival of RAW 264.7 cells [15,16], which is based on a mechanism similar to that of an assay using 3-(4,5-dimethylthiazol-2-yl)-2,5-diphenyltetrazolium bromide. Data analyses were firstly performed using one-way analysis of variance (ANOVA), and further analyzed by the Student-Newman-Keuls post hoc test for multiple comparison. All the data with a *p*-value of < 0.05 were considered as a significant difference.

#### 4. Conclusions

*B. violaceum* has been demonstrated to have a wide structural diversity of interesting diterpenoids that possess various pharmacological properties [17]. This specimen was encrusted on different species of scleractinian hard corals in the Indo-Pacific coral reef system [18]. In our continued study of *B. violaceum*, three previously unreported furanocembranoids 1–3 were isolated, together with the previously described briaviodiol A (4). In the present study, the anti-inflammatory activities of 1–4 were assessed using inhibition of pro-inflammatory iNOS release from macrophages. The results indicated that briaviotriol A (2) and briaviodiol A (4) showed the most potent suppressive effects on iNOS release.

**Supplementary Materials:** The Supplementary Materials are available online at <http://www.mdpi.com/1660-3397/17/4/214/s1>. ESIMS, HRESIMS, IR, 1D ( $^1$ H NMR,  $^{13}$ C NMR, and DEPT spectra), and 2D (COSY, HSQC, HMBC, and NOESY) spectra of new compounds 1–3 and  $^1$ H and  $^{13}$ C NMR spectra of 4.

**Author Contributions:** P.-C.H., W.-S.L., Z.-H.W., and P.-J.S. designed the whole experiment and contributed to manuscript preparation. B.-R.P., Y.-C.C., L.-S.F., G.-Q.L., and T.-L.H. analyzed the data and performed data acquisition.

**Funding:** This research was supported by grants from the National Museum of Marine Biology and Aquarium; the National Dong Hwa University; and the Ministry of Science and Technology, Taiwan (Grant Nos: MOST 104-2320-B-291-001-MY3 and 107-2320-B-291-001-MY3) awarded to Ping-Jyun Sung.

**Conflicts of Interest:** The authors declare no conflicts of interest.

#### References

- Samimi-Namin, K.; van Ofwegen, L.P. Overview of the genus *Briareum* (Cnidaria, Octocorallia, Briareidae) in the Indo-Pacific, with the description of a new species. *ZooKeys* **2016**, *557*, 1–44. [CrossRef] [PubMed]
- Bayer, F.M. Key to the genera of octocorallia exclusive of Pennatulacea (Coelenterata: Anthozoa), with diagnoses of new taxa. *Proc. Biol. Soc. Wash.* **1981**, *94*, 902–947.
- Bowden, B.F.; Coll, J.C.; Mitchell, S.J.; Raston, C.L.; Stokie, G.J.; White, A.H. Studies of Australian soft corals XV. The structure of pachyclavulariadiol, a novel furano-diterpene from *Pachyclavularia violacea*. *Aust. J. Chem.* **1979**, *32*, 2265–2274. [CrossRef]
- Inman, W.; Crews, P. The structure and conformational properties of a cembranolide diterpene from *Clavularia violacea*. *J. Org. Chem.* **1989**, *54*, 2526–2529. [CrossRef]
- Sheu, J.-H.; Wang, G.-H.; Sung, P.-J.; Duh, C.-Y.; Chiang, M.Y. Pachyclavulariolides G–L and seco-pachyclavulariaenone A, seven novel diterpenoids from the soft coral *Pachyclavularia violacea*. *Tetrahedron* **2001**, *57*, 7639–7648. [CrossRef]
- Xu, L.; Patrick, B.O.; Roberge, M.; Allen, T.; van Ofwegen, L.; Andersen, R.J. New diterpenoids from the octocoral *Pachyclavularia violacea* collected in Papua New Guinea. *Tetrahedron* **2000**, *56*, 9031–9037. [CrossRef]

7. Sheu, J.-H.; Wang, G.-H.; Duh, C.-Y.; Soong, K. Pachyclavariolides M–R, six novel diterpenoids from a Taiwanese soft coral *Pachyclavularia violacea*. *J. Nat. Prod.* **2003**, *66*, 662–666. [[CrossRef](#)] [[PubMed](#)]
8. Duh, C.-Y.; El-Gamal, A.A.H.; Chu, C.-J.; Wang, S.-K.; Dai, C.-F. New cytotoxic constituents from the Formosan soft corals *Clavularia viridis* and *Clavularia violacea*. *J. Nat. Prod.* **2002**, *65*, 1535–1539. [[CrossRef](#)] [[PubMed](#)]
9. Chang, Y.-C.; Huang, I.-C.; Chiang, M.Y.-N.; Hwang, T.-L.; Kung, T.-H.; Lin, C.-S.; Sheu, J.-H.; Sung, P.-J. Briaviodiols A, a new cembranoid from a soft coral *Briareum violacea*. *Chem. Pharm. Bull.* **2010**, *58*, 1666–1668. [[CrossRef](#)] [[PubMed](#)]
10. Huang, P.-C.; Tseng, C.-C.; Peng, B.-R.; Hu, C.-C.; Lin, N.-C.; Chen, N.-F.; Chen, J.-J.; Wen, Z.-H.; Wu, Y.-C.; Sung, P.-J. Briaviodiols B–E, new anti-inflammatory hydroperoxyfuranembranoids from *Briareum violaceum*. *Tetrahedron* **2019**, *75*, 921–927. [[CrossRef](#)]
11. Allinger, N.L. Conformational analysis. 130. MM2. A hydrocarbon force field utilizing  $V_1$  and  $V_2$  torsional terms. *J. Am. Chem. Soc.* **1977**, *99*, 8127–8134. [[CrossRef](#)]
12. Huang, S.-Y.; Chen, N.-F.; Chen, W.-F.; Hung, H.-C.; Lee, H.-P.; Lin, Y.-Y.; Wang, H.-M.; Sung, P.-J.; Sheu, J.-H.; Wen, Z.-H. Sinularin from indigenous soft coral attenuates nociceptive responses and spinal neuroinflammation in carrageenan-induced inflammatory rat model. *Mar. Drugs* **2012**, *10*, 1899–1919. [[CrossRef](#)] [[PubMed](#)]
13. Jean, Y.-H.; Chen, W.-F.; Sung, C.-S.; Duh, C.-Y.; Huang, S.-Y.; Lin, C.-S.; Tai, M.-H.; Tzeng, S.-F.; Wen, Z.-H. Capnellene, a natural marine compound derived from soft coral, attenuates chronic constriction injury-induced neuropathic in rats. *Br. J. Pharmacol.* **2009**, *158*, 713–725. [[CrossRef](#)] [[PubMed](#)]
14. Jean, Y.-H.; Chen, W.-F.; Duh, C.-Y.; Huang, S.-Y.; Hsu, C.-H.; Lin, C.-S.; Sung, C.-S.; Chen, I.-M.; Wen, Z.-H. Inducible nitric oxide synthase and cyclooxygenase-2 participate in anti-inflammatory and analgesic effects of the natural marine compound lemnalol from Formosan soft coral *Lemnalia cervicorni*. *Eur. J. Pharmacol.* **2008**, *578*, 323–331. [[CrossRef](#)] [[PubMed](#)]
15. Chen, L.-C.; Lin, Y.-Y.; Jean, Y.-H.; Lu, Y.; Chen, W.-F.; Yang, S.-N.; Wang, H.-M.D.; Jang, I.-Y.; Chen, I.-M.; Su, J.-H.; et al. Anti-inflammatory and analgesic effects of the marine-derived compound comaparvin isolated from the crinoid *Comanthus bennetti*. *Molecules* **2014**, *19*, 14667–14686. [[CrossRef](#)] [[PubMed](#)]
16. Oliveira, T.; Figueiredo, C.A.; Brito, C.; Stavroullakis, A.; Prakki, A.; da Silva Velozo, E.; Nogueira-Filho, G. Effect of *Allium cepa* L. on lipopolysaccharide-stimulated osteoclast precursor cell viability, count, and morphology using 4',6-diamidino-2-phenylindole-staining. *Int. J. Cell Biol.* **2014**, *2014*, 535789. [[CrossRef](#)] [[PubMed](#)]
17. Chang, Y.-C.; Sheu, J.-H.; Wu, Y.-C.; Sung, P.-J. Terpenoids from octocorals of the genus *Pachyclavularia*. *Mar. Drugs* **2017**, *15*, 382. [[CrossRef](#)] [[PubMed](#)]
18. Geetha, S.; Kumar, J.S.Y.; Raghunathan, C.; Sornaraj, R. Space competition studies between *Briareum violaceum* (Octocorallia; Alcyonacea) and scleractinian corals in Shark Island, North Andaman, India. *Indian J. Geo-Mar. Sci.* **2018**, *47*, 2390–2394.



© 2019 by the authors. Licensee MDPI, Basel, Switzerland. This article is an open access article distributed under the terms and conditions of the Creative Commons Attribution (CC BY) license (<http://creativecommons.org/licenses/by/4.0/>).



## Research Paper

# Induction of nuclear protein-1 by thyroid hormone enhances platelet-derived growth factor A mediated angiogenesis in liver cancer

Ching-Ying Chen<sup>1,2</sup>, Sheng-Ming Wu<sup>3,4</sup>, Yang-Hsiang Lin<sup>5</sup>, Hsiang-Cheng Chi<sup>6</sup>, Syuan-Ling Lin<sup>1</sup>, Chau-Ting Yeh<sup>5</sup>, Wen-Yu Chuang<sup>7</sup> and Kwang-Huei Lin<sup>1,5,8</sup>✉

1. Department of Biochemistry, College of Medicine, Chang-Gung University, Taoyuan, Taiwan
2. Department of Biomedical Sciences, College of Medicine, Chang-Gung University, Taoyuan, Taiwan
3. Division of Pulmonary Medicine, Department of Internal Medicine, Shuang Ho Hospital, Taipei Medical University, New Taipei City, Taiwan
4. Division of Pulmonary Medicine, Department of Internal Medicine, School of Medicine, College of Medicine, Taipei Medical University, Taipei, Taiwan
5. Liver Research Center, Chang Gung Memorial Hospital, Linkou, Taoyuan, Taiwan
6. Radiation Biology Research Center, Institute for Radiological Research, Chang Gung University / Chang Gung Memorial Hospital, Linkou, Taoyuan, Taiwan
7. Department of Pathology, Chang Gung Memorial Hospital and Chang Gung University, Taoyuan, Taiwan
8. Research Center for Chinese Herbal Medicine, College of Human Ecology, Chang Gung University of Science and Technology, Taoyuan, Taiwan

✉ Corresponding author: Kwang-Huei Lin, PhD., Department of Biochemistry, College of Medicine, Chang-Gung University, 259 Wen-Hwa 1 Road, Taoyuan, Taiwan, Republic of China. Tel./Fax: +886-3-2118263. E-mail: khlin@mail.cgu.edu.tw

© Ivyspring International Publisher. This is an open access article distributed under the terms of the Creative Commons Attribution (CC BY-NC) license (<https://creativecommons.org/licenses/by-nc/4.0/>). See <http://ivyspring.com/terms> for full terms and conditions.

Received: 2018.08.31; Accepted: 2019.02.24; Published: 2019.04.13

## Abstract

**Background & Aims:** Hepatocellular carcinoma (HCC) is among the leading causes of cancer deaths worldwide. Many studies indicate that disruption of cellular thyroid hormone signaling promotes HCC progression. However, the mechanisms underlying the regulation of genes downstream of thyroid hormone actions in HCC have remained elusive. In the current study, we identified NUPR1 (nuclear protein-1), a stress-induced protein that overexpresses in various neoplasia, is upregulated by triiodothyronine/thyroid hormone receptor (T<sub>3</sub>/TR) signaling and aimed to elucidate its role in angiogenesis in cancer progression.

**Methods:** Quantitative reverse transcription-PCR, luciferase promoter and chromatin immunoprecipitation assays were performed to identify the NUPR1 regulatory mechanism by T<sub>3</sub>/TR. *In vitro* and *In vivo* vascular formations were performed to detect the angiogenic function of NUPR1. Human angiogenesis arrays were performed to identify the downstream angiogenic pathway. The sorafenib resistant ability of TR/NUPR1 was further examined *in vitro* and *in vivo*. Clinical relevance of TR, NUPR1 and platelet-derived growth factor A (PDGFA) were investigate in HCC samples using qRT-PCR and western blot.

**Results:** Our experiments disclosed positive regulation of NUPR1 expression by T<sub>3</sub>/TR through direct binding to the -2066 to -1910 region of the NUPR1 promoter. Elevated NUPR1 and TR expression link to poor survival in clinical HCC specimens. An analysis of clinicopathological parameters showed that expression of NUPR1 is associated with vascular invasion and pathology stage. Functional studies revealed that NUPR1 induced endothelial cell angiogenesis *in vitro* and *in vivo*. Using a human angiogenesis array, we identified PDGFA as a target of NUPR1 in the downstream angiogenic pathway. NUPR1 induced transcription of PDGFA through direct binding to the corresponding promoter region, and inhibition of the PDGFA signaling pathway impaired angiogenesis in human umbilical vein endothelial cells (HUVECs). Notably, the angiogenic effects of NUPR1/PDGFA were mediated by the MEK/ERK signaling pathway. TR/NUPR1 expression increased cell viability and resistance to sorafenib treatment. Moreover NUPR1 expression was positively correlated with TR $\alpha$ , TR $\beta$ , and PDGFA expression.

**Conclusions:** We propose that the T<sub>3</sub>/TR/NUPR1/PDGFA/MEK/ERK axis has a vital role in hepatocarcinogenesis and suggest NUPR1 as a potential therapeutic target in HCC.

Key words: Thyroid hormone receptor, NUPR1, Hepatocellular carcinoma, PDGFA, sorafenib

## Introduction

Hepatocellular carcinoma (HCC) accounts for 80%–90% of primary liver cancers and is among the leading causes of cancer deaths worldwide [1]. The major risk factors for HCC include hepatitis B and hepatitis C virus infection, alcohol consumption, diabetes, and aflatoxins [2, 3]. HCC is usually diagnosed at an advanced stage, with patients typically presenting with upper-abdominal pain and weight loss. Treatment of HCC, which is stage-guided and varies according to the cause of the disease, includes surgery, liver transplantation, and targeted therapy [4]. Although diagnostic and treatment methods have improved, the 5-year survival rate has remained below 12%. Thus, a new therapeutic strategy is essential for improving the prognosis and treatment of HCC.

Thyroid hormone (3,3',5-triiodo-L-thyronine; T<sub>3</sub>) is a potent mediator of a variety of physiological processes, including embryonic development, cellular differentiation, metabolism, and regulation of cell proliferation [5]. T<sub>3</sub> binds to specific high-affinity thyroid hormone receptors (TRs), which are ligand-dependent transcription factors belonging to the nuclear receptor superfamily [6]. TRs regulate gene expression by binding to thyroid hormone response elements (TREs) in the promoter region of target genes. Human TRs are encoded by the TR $\alpha$  (*THRA*) and TR $\beta$  (*THRB*) genes, located on human chromosomes 17 and 3, respectively, and yield several additional isoforms through alternative splicing and differential promoter usage. These receptors are comprised of functional domains, including a ligand-binding domain, DNA-binding domain, and dimerization and transactivation domains [7]. Considerable evidence has accumulated to show that aberrant expression of TRs is associated with human cancers [8–10]. In one study, Cristofanilli *et al.* reported that hypothyroid patients have a reduced incidence of primary breast carcinoma and a reduced risk of developing the invasive disease [11]. Treatment with the antithyroid drug, propylthiouracil, in combination with tamoxifen increases survival in patients with glioblastoma multiforme [12]. Moreover, epidemiological studies have demonstrated that hyperthyroidism associates with an increased risk of ovarian cancer [13]. In our previous studies, genes and microRNA regulated by T<sub>3</sub>/TR signaling were shown to be involved in tumor cell invasion and migration in HCC [14–17]. However, these studies did not adequately elucidate the detailed molecular mechanism by which T<sub>3</sub>/TR signaling leads to hepatocarcinogenesis.

In the current study, we used oligonucleotide microarrays to screen for genes regulated by T<sub>3</sub> in HepG2 cells stably expressing TR $\alpha$  (HepG2-TR $\alpha$ ). Among the T<sub>3</sub>-regulated genes identified, nuclear protein-1 (NUPR1) was the most notably upregulated by T<sub>3</sub> treatment. NUPR1, which shares biochemical homology with high mobility group (HMG)-like proteins [18], was first identified in the rat pancreas during acute pancreatitis [19, 20]. NUPR1 has been implicated in diverse functions, and its expression is crucial for tumor development. Previous studies have reported NUPR1 overexpression in primary human HCC samples, and shown that it influences cell proliferation, migration, invasion and sorafenib resistance through induction of the downstream genes, RELB, IER3, and RUNX2 [21]. NUPR1 was also shown to be involved in mitochondrial defect-derived glycolytic activation in liver cancer [22]. Here, we report that T<sub>3</sub>/TR induced NUPR1 expression through direct binding to thyroid hormone response element (TRE) in the NUPR1 promoter region. Functional studies revealed that NUPR1 induced endothelial cell angiogenesis *in vitro* and *in vivo*. Using a human angiogenesis array, we identified the gene encoding platelet-derived growth factor A (PDGFA) as a target of NUPR1 in the activation of the downstream angiogenic pathway. We further found that the angiogenic effects of NUPR1/PDGFA are mediated by the MEK/ERK signaling pathway. Also, NUPR1 mediated transcriptional induction of PDGFA through direct binding to the corresponding promoter region. The viability of tumor cell following the addition of sorafenib was significantly increased in TR/NUPR1 expression cell. Clinicopathological analyses revealed that elevated expression of NUPR1 and TRs in clinical HCC specimens were linked to poor survival; moreover, NUPR1 expression was positively correlated with TR $\alpha$ , TR $\beta$ , and PDGFA expression. Thus, this study demonstrates a mechanism that implicates the T<sub>3</sub>/TR/NUPR1/PDGFA axis in HCC, providing novel therapeutic targets for tumorigenesis.

## Materials and Methods

### Cell cultures

The human hepatoma cell lines, HepG2, Huh7, Mahlavu and J7 were routinely grown in Dulbecco Modified Eagle medium (DMEM) supplemented with 10% (v/v) fetal bovine serum (FBS). The human umbilical vein endothelial cells (HUVECs) line was grown in endothelial cell basal medium-2 (EBM-2; Lonza, CC-3156) supplemented with EBM-2

SingleQuots (Lonza, CC-4176). Stably transfected HepG2-TR $\alpha$ , HepG2-TR $\beta$ , and HepG2-neo cells were cultured in DMEM containing 10% (v/v) FBS with G418 [23]. NUPR1-overexpressing (ovNUPR1) and luciferase control Mahlavu cells were cultured in DMEM containing 10% (v/v) FBS with blasticidin. NUPR1-knockdown (shNUPR1) and luciferase control (shLuc) Huh7 cells were cultured in DMEM containing 10% (v/v) FBS with puromycin. T<sub>3</sub> was purchased from Sigma-Aldrich (T2752). Serum was depleted of T<sub>3</sub> (0 nM T<sub>3</sub>) using an AG 1-X8 resin (Bio-Rad, 40-1451). Cells were cultured at 37 °C in a humidified atmosphere of 95% air and 5% CO<sub>2</sub>.

### Quantitative reverse transcription-polymerase chain reaction (qRT-PCR) analyses

Total RNA was extracted from cells using TRIzol reagent (Invitrogen). cDNA was synthesized from total RNA using a Superscript II kit (Invitrogen, 18064-014) according to the manufacturer's protocols. qRT-PCR was conducted in a 15- $\mu$ l reaction mixture containing 25 nM forward and reverse primers, 1 $\times$ SYBR Green reaction mix (Applied Biosystems), and varying quantities of the template. SYBR Green fluorescence was measured with an ABI PRISM 7500 sequence detection system (Applied Biosystems). Primers used to amplify NUPR1 were 5'-AAG CTG AGG GAG TGG AGA GG-3' (forward) and 5'-TAT TGT TGC TGC CAC CCT GG-3' (reverse).

### Immunoblot analysis

Total cell lysates, nuclear extracts, and conditioned medium (CM) were isolated and fractionated by sodium dodecyl sulfate-polyacrylamide gel electrophoresis (SDS-PAGE) on 8–12% gels. Separated proteins were transferred to a PVDF (polyvinylidene difluoride) membrane and blocked by incubating in 5% (w/v) nonfat milk. PVDF membranes were incubated with appropriate primary and horseradish peroxidase (HRP)-conjugated secondary antibodies, and immunoreactive proteins were subsequently detected by chemiluminescence using an ECL detection kit (Amersham Inc., RPN2232) and visualized with X-ray film. The intensities of immunoreactive bands were quantified using Image Gauge software (Fuji Film, Tokyo, Japan). The indicated antibodies against the following proteins were used: NUPR1 (made in-house), lamin A/C (Santa Cruz, sc-20681), GAPDH (Millipore, MAB374),  $\beta$ -actin (Chemicon, MAB1501R), PDGFA (Abcam, ab135881), fascin (Santa Cruz, sc-21743), phospho-PDGFR $\alpha$  (Santa Cruz, sc-12911), PDGFR $\alpha$  (R&D Systems, AF-307-NA), phospho-MEK1/2 (Cell Signaling, #9154), MEK1/2 (Cell Signaling, #4694), phospho-ERK1/2 (Cell Signaling, #4370), ERK1/2

(Cell Signaling, #9211), and TR (Santa Cruz, sc-739).

### Luciferase reporter assay

Serial deletion mutants of the NUPR1 promoter (-2944/+96) were prepared by PCR amplification and inserted into a pGL2 plasmid and extracted using plasmid extraction kit (Tools#DPT-BA17). The effects of T<sub>3</sub> on the transcriptional activity of the resulting NUPR1 promoter fragments were determined by co-transfecting HepG2-TR $\alpha$  cells with the corresponding NUPR1 promoter-reporter plasmids and LacZ/ $\beta$ -galactosidase expression vector (included to normalize transfection efficiency) and then treating with 0–100 nM T<sub>3</sub> for 24 h. Cells were lysed and luciferase activity was measured. A mutant form of the NUPR1 promoter construct was created by changing the TRE sequence, aggtcaCCTGaggtca to ggggggCCTGgggggg, using site-direct mutagenesis.

The PDGFA promoter region (-3090/+16) and two additional deletion constructs, -2128/+16 and -1242/+16, were prepared and inserted upstream of a minimal thymidine kinase promoter (pA3-TK). PDGFA 5'-flanking DNA reporter construct and a pcDNA3-NUPR1 expression plasmid were co-transfected into 293TN cells for 24 h. Mutant forms of PDGFA promoters were created by changing the mutant 1 sequence tattttaata to tctgttactg and mutant 2 sequence ccaataca to ccgccgca using site-direct mutagenesis.

### Chromatin immunoprecipitation (ChIP) assay

HepG2-TR $\alpha$  cells were treated with or without 100 nM T<sub>3</sub> for 48 h. After harvesting cells, DNA and proteins were crosslinked by incubating with 1% formaldehyde for 10 min, and complexes were sonicated to obtain DNA fragments in the 200–500-bp range. DNA fragments were immunoprecipitated with nonspecific mouse immunoglobulin G or specific antibodies against TR. Immunoprecipitated DNA fragments were amplified using specific primers targeting the binding region. FURIN and GAPDH promoter regions were used as positive and negative controls, respectively. For PDGFA promoter ChIP assays, NUPR1-overexpressing Mahlavu cells were harvested and crosslinked. Lysates were sonicated and immunoprecipitated with nonspecific rabbit immunoglobulin G or specific antibodies against NUPR1, and amplified using specific primers targeting the binding region.

### HUVECs in vitro tube formation assay

For tube formation assays, 48-well culture plates were coated with 70% matrigel (BD Matrigel Basement Membrane Matrix) in EBM-2 media. After 24 h, 3  $\times$  10<sup>5</sup> HUVECs were mixed with 30  $\mu$ g CM and

seeded onto matrigel-coated culture plates. After 16 h, HUVECs tube formation was observed under a microscope.

### Chick chorioallantoic membrane assay

Day-0 fertilized chicken eggs were incubated for 7 days at 37 °C. After that, a 3 × 3 cm hole was opened in eggs, and a 1:1 mix of CM and matrigel mixture was implanted in the embryo; the hole was then sealed with tape. After a 4-day incubation, 6 mL of 20% cream, used to visualize vessels, was injected into chick chorioallantoic membrane.

### In vivo matrigel plug angiogenesis assay and immunohistochemical staining

NUPR1-overexpressing, -knockdown, or control cells ( $2 \times 10^6$ ) in 100  $\mu$ l PBS were mixed with 150  $\mu$ l matrigel and injected subcutaneously into the flanks of nude mice (BALB/cAnN.Cg-Foxn1nu/CrlNarl) ( $n > 3$ ). Mice were sacrificed 2 weeks later, and tumor weight and size were measured, and hemoglobin content was determined using Drabkin's reagent (Sigma-Aldrich). Histological sections from xenografts were immunostained for the angiogenesis marker CD31 (Abcam, ab28364). All experimental protocol was approved by Chang-Gung Institutional Animal Care and Use Committee (IACUC Approval No. CGU16-112).

### Human angiogenesis array

Human angiogenesis array analyses were performed according to the manufacturer's protocol (B&D System). Briefly, 250  $\mu$ l of CM from NUPR1-overexpressing or control Mahlavu cells was diluted and mixed with a cocktail of biotinylated detection antibodies. The resulting sample/antibody complexes were bound on membranes by their conjugate immobilized capture antibody. After washing to remove unbound material, streptavidin-HRP and chemiluminescence detection reagents were added sequentially. The light was produced at each spot in proportion to the amount of analyte bound. Mean pixel densities were quantified using Image J.

### Measurement of PDGF-AA by enzyme-linked immunosorbent assay (ELISA)

The levels of PDGF-AA proteins in NUPR1-overexpressing or -knockdown cells were quantified using commercially available ELISA kits (R&D Systems) according to the manufacturer's instructions.

### Cell viability assay

Cells were seeded at  $6-12 \times 10^3$  cells/well in 96-well plates with or without 100 nM  $T_3$  and

incubated overnight at 37 °C. Cells were treated with 0–10  $\mu$ M sorafenib (Santa Cruze, sc-20125A) for 24 h. The medium was replaced by 100  $\mu$ l of fresh medium containing 0.5 mg/ml MTT (Sigma, M5655) per well. After incubation at 37 °C for 4 h, the medium was removed, then 100  $\mu$ l of isopropanol was added to each well. Pipette up and down several times to make sure the converted dye dissolved completely. The absorbance of each well was measured at 570 nm/650 nm.

### Sorafenib treatment for Xenograft models of tumor progression

To investigate the antitumor effects of sorafenib on thyroid hormone receptor overexpressing tumors, J7-neo and J7-TR $\alpha$  cells ( $1 \times 10^6$ ) were injected subcutaneously into the flanks of nude mice (BALB/cAnN.Cg-Foxn1nu/CrlNarl) ( $n > 6$ ). After the tumors reached the size of approximately 100 mm<sup>3</sup>, mice were orally administered 30 mg/kg sorafenib twice a week for 20 days. Control mice received the only vehicle. Tumor growth was measured twice a week. Animals were sacrificed at the end of experiment. All experimental protocol followed the United States National Institutes of Health guidelines and the Guide for the Care and Use of Laboratory Animals issued by the Chang-Gung Institutional Animal Care and Use Committee.

### Human HCC specimens

Paired human HCC specimens ( $n = 158$ ) were obtained from the Taiwan Liver Cancer Network (TLCN). Total RNA was reverse transcript to cDNA, and mRNA expression level was analyzed using qRT-PCR. Expression of NUPR1 and TR protein was determined by western blot analysis. The protocol was approved by the Medical Ethics and Human Clinical Trial Committee at Chang-Gung Memorial Hospital (IRB:103-4866B).

### Statistical analysis

Data are presented as means  $\pm$  SD of at least three independent experiments. Statistical analyses were performed using Student t-test and one-way analysis of variance (ANOVA). *P*-values  $< 0.05$  were considered significant.

## Results

### NUPR1 is upregulated by $T_3$ /TR

To identify genes regulated by  $T_3$  in hepatoma cells, we performed oligonucleotide microarrays in HepG2-TR $\alpha$  cells [24]. Among the  $T_3$ -regulated genes identified, NUPR1 was the most notably upregulated by  $T_3$  treatment (8-fold with 100 nM  $T_3$  for 48 h), and the result was verified by qRT-PCR (Figure 1A).



Incubation of HepG2-TR $\alpha$  cells with 100 nM T<sub>3</sub> for 48 h increased NUPR1 mRNA levels by 40–53-fold. Similar results were also observed in HepG2-TR $\beta$  cells, where treatment with 100 nM T<sub>3</sub> for 48 h increased NUPR1 expression levels by 35–48-fold. NUPR1 mRNA levels trended higher in T<sub>3</sub>-treated HepG2-neo control cells, but this difference did not reach statistical significance.

The effect of T<sub>3</sub>/TR signaling on NUPR1 protein expression in HepG2 isogenic cell lines was assessed at different time points and different concentrations of T<sub>3</sub> (Figure 1B). T<sub>3</sub> induced a time- and concentration-dependent increase in NUPR1 protein levels in HepG2-TR $\alpha$  cells. Similar results were obtained in HepG2-TR $\beta$  cells. In contrast, exposure of control HepG2-neo cells to 100 nM T<sub>3</sub> for 72 h did not significantly affect NUPR1 protein expression. The same phenomena were also observed in other hepatoma cell lines. J7-overexpression TR $\alpha$  and TR $\beta$  cells have shown increased NUPR1 expression with T<sub>3</sub> treatment (Figure 1C). Notably, activated NUPR1 were also obtained in Huh7 cells, another HCC cell line that expresses detectable endogenous TR proteins (Figure S1) [25]. These results indicate that the effect of T<sub>3</sub> on NUPR1 expression in TR-overexpressing cells depends on the level of TR proteins in these cells.

### T<sub>3</sub> induces expression of NUPR1 at the transcriptional level

To determine whether the regulation of NUPR1 expression by T<sub>3</sub> occurred at the transcriptional level, we conducted promoter activity assays. To this end, the -2344 to +96-bp (-2344/+96) upstream region of the NUPR1 gene (transcription start site, +1), was inserted into the pGL2 plasmid to create the luciferase-based reporter plasmid, NUPR1-pGL2-luc. A bioinformatics search revealed putative TREs in the NUPR1 promoter, including a palindromic (Pal) TRE, a direct repeat 4 (DR4) TRE, and an inverted palindrome (F2) TRE. A series of pGL2-luc reporter constructs were transfected in HepG2-TR $\alpha$  cells, followed by treatment with 0–100 nM T<sub>3</sub> for 24 h (Figure 1D). T<sub>3</sub> at a concentration of 100 nM stimulated approximately a 3-fold increase in the activity of the full-length -2344/+96 NUPR1 promoter but had no effect on deletion mutant constructs lacking the most distal -2344/-1373 region, suggesting that this region contains a potential positive TRE. To confirm this and further refine the location of the TRE,

we transfected HepG2-TR $\alpha$  cells with a luciferase-based reporter construct containing a -2201/-1798 fragment inserted upstream of a minimal thymidine kinase promoter. Subsequent transcription analyses showed that T<sub>3</sub> increased the reporter activity, demonstrating that a possible TRE in the -2201/-1798 upstream region of NUPR1 is responsible for T<sub>3</sub>-induced transcription of the human NUPR1 gene. Notably, T<sub>3</sub>/TR-stimulated NUPR1 promoter activity was lost following mutation of the TRE sequence in the NUPR1 promoter. Collectively, these findings identify the -2201/-1798 region as the location of the TRE site in the NUPR1 promoter.

To further determine whether TR proteins directly target the TRE region of the NUPR1 promoter, we performed ChIP assays (Figure 1E). Immunoprecipitation with specific anti-TR antibodies followed by PCR amplification of precipitated DNA fragments clearly demonstrated that TR was recruited to the TRE binding site at -2066/-1910, whereas immunoprecipitation with control IgG yielded only background signals. The TRE-containing human FURIN gene was used as a positive control, whereas human GAPDH gene was used as the negative control. Collectively, these ChIP assay results reveal that the TR binds to the endogenous NUPR1 promoter in intact cells.

### NUPR1 overexpression is linked to poor survival in clinical HCC specimens

To gain insight into the clinicopathological significance of NUPR1, NUPR1 expression in HCC was investigated. Expression of NUPR1 in 158 paired samples of human HCC tumor and their adjacent normal tissue were determined using qRT-PCR. NUPR1 was significantly overexpressed in HCC specimens compared with adjacent normal tissue (Figure 2A, left panel). An analysis of clinicopathological parameters showed that expression of NUPR1 was associated with vascular invasion and pathology stage (Figure 2A, right panel). Moreover, elevated TR $\alpha$  and TR $\beta$  levels were expressed in human HCC tumor specimens and were all correlated with vascular invasion (Figure S2A–B). Immunohistochemical study for angiogenesis marker CD31 and NUPR1 expression in clinical specimens showed that NUPR1 was highly expressed in tumors with vascular invasion (Figure S2C).



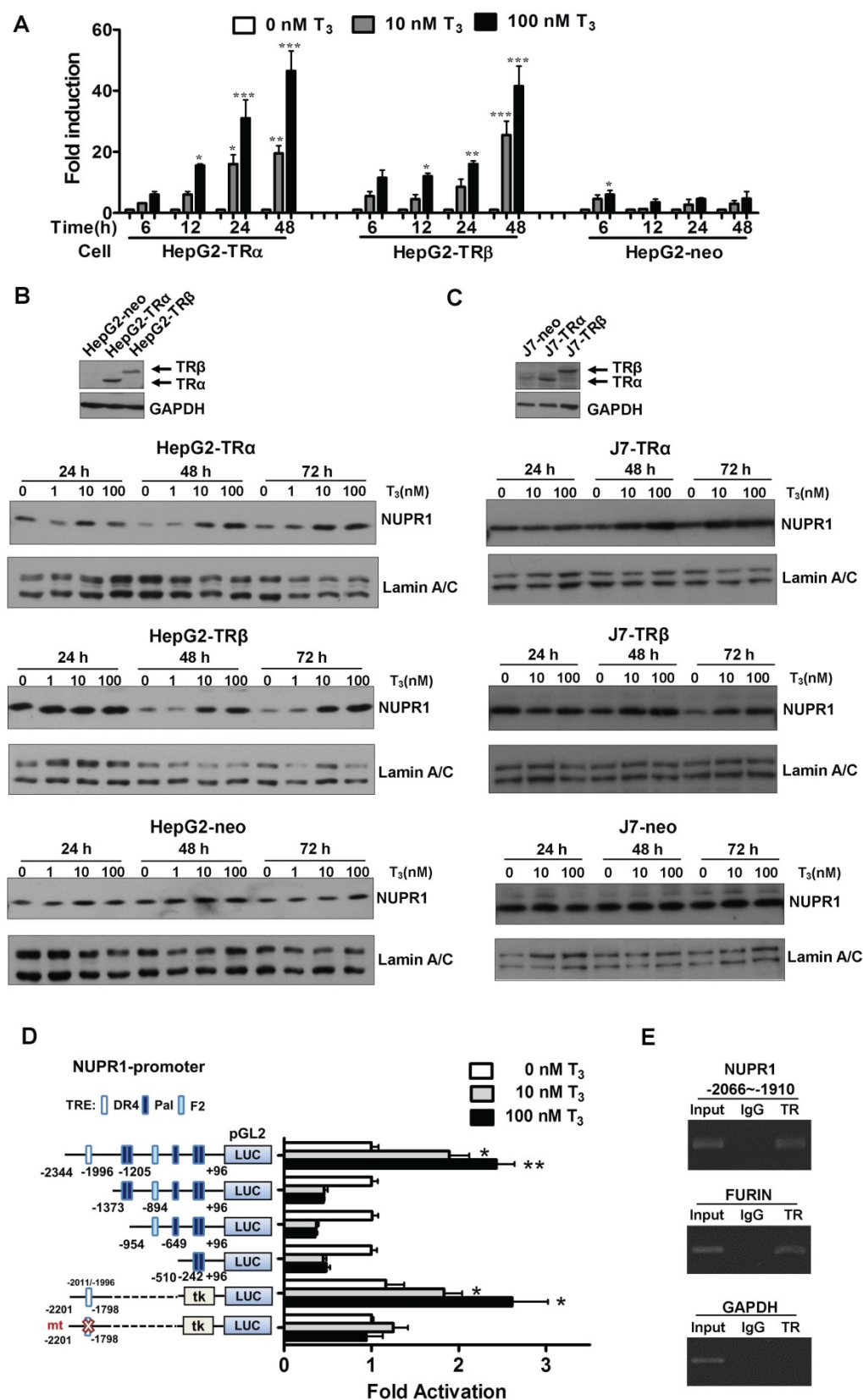


**Figure 1: T<sub>3</sub>/TR signaling induces an increase in NUPR1 mRNA and protein expression.** (A) HepG2-TR $\alpha$ , HepG2-TR $\beta$ , and HepG2-neo cells were treated with T<sub>3</sub> (0–100 nM) for 6–48 h, and NUPR1 expression levels were measured using qRT-PCR. Expression of NUPR1 mRNA was normalized to that of 18s rRNA. (B–C) NUPR1 protein expression levels were determined in TR overexpression and control HepG2 and J7 cell lines treated for different times with different concentrations of T<sub>3</sub>. Lamin A/C was used as an internal control. (D) Schematic representation of the NUPR1 promoter, indicating potential TREs (squares). HepG2-TR $\alpha$  cells were transfected with serially deleted NUPR1 5'-flanking DNA pGL2-luc reporter constructs, and treated with 0–100 nM T<sub>3</sub>. After 24 h, cells were lysed and promoter activity was determined. (E) HepG2-TR $\alpha$  cell lysates were immunoprecipitated with nonspecific mouse IgG or antibodies against TR. FURIN and GAPDH promoter regions were used as positive and negative controls, respectively. Differences were analyzed using a one-way ANOVA (\*p < 0.05, \*\*p < 0.01, \*\*\*p < 0.001).

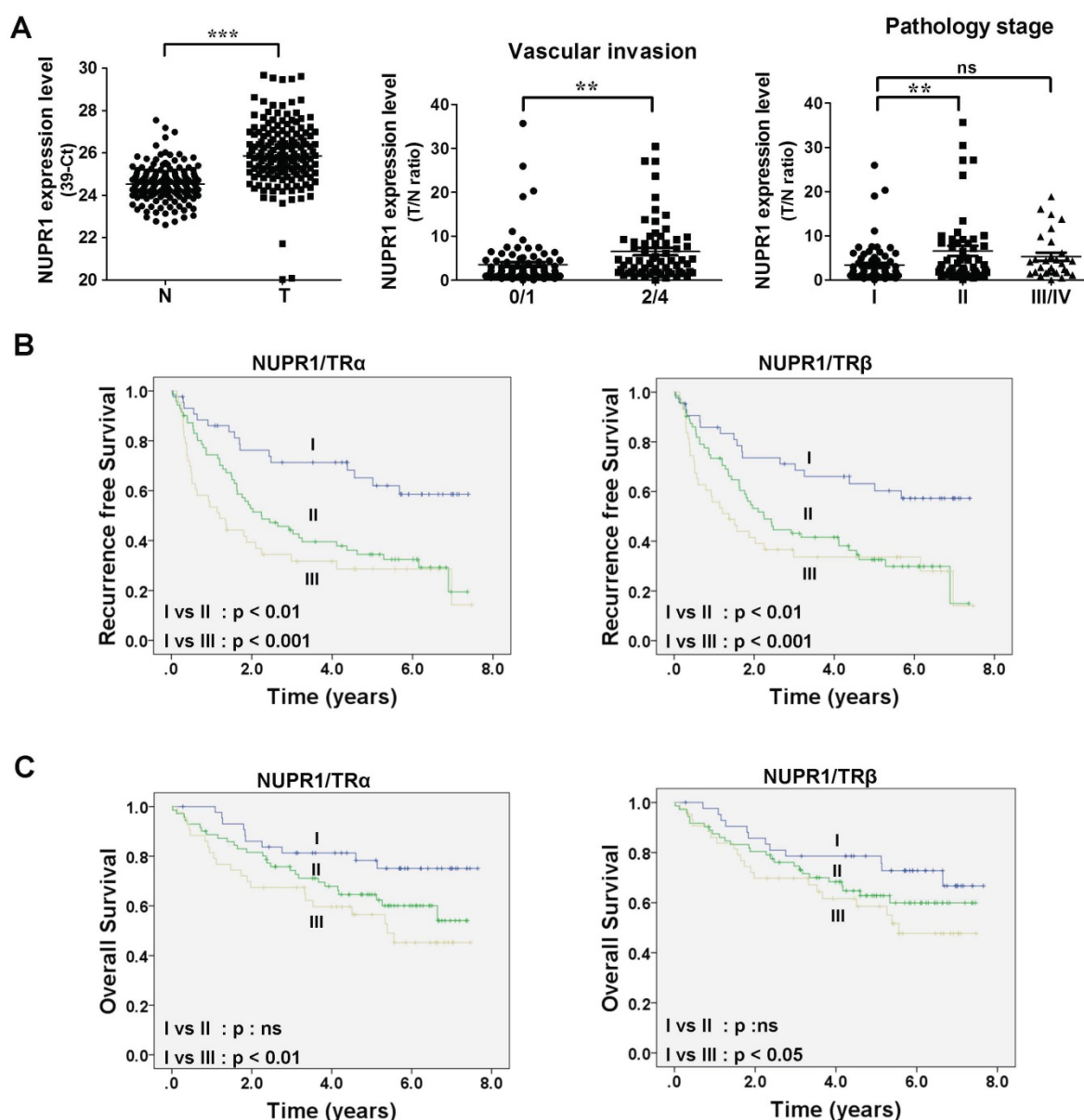


**Figure 2: High NUPR1 expression is linked to poor prognosis.** (A) Expression of NUPR1 in 158 paired human HCC (T) and adjacent normal (N) tissues were determined by qRT-PCR; expression of NUPR1 mRNA was normalized to that of 18s rRNA (left panel). NUPR1 expression levels were presented as 39-Ct values. Statistical significance was calculated using paired Student's t test. NUPR1 mRNA expression level were presented as the T/N ratio (right two panels). NUPR1 expression levels were highly correlated with vascular invasion (0/1 grade,  $n = 93$ ; 2/4 grade,  $n = 65$ ) and pathology stage (stage I,  $n = 76$ ; stage II,  $n = 52$ ; stage III/IV,  $n = 30$ ). Differences were analyzed using one-way ANOVA (\* $p < 0.05$ , \*\* $p < 0.01$ , \*\*\* $p < 0.001$ ). (B-C) Recurrence-free survival and overall survival were analyzed using the Kaplan-Meier method. Median expression levels of NUPR1 and TRs were used as a cutoff. NUPR1 and TR expression levels were separated to three groups: group I, low levels of NUPR1 and TRs (TR $\alpha$ ,  $n = 44$ ; TR $\beta$ ,  $n = 43$ ); group II, high levels of NUPR1 and low levels of TRs, or low levels of NUPR1 and high levels of TRs (TR $\alpha$ ,  $n = 71$ ; TR $\beta$ ,  $n = 72$ ); group III, high levels of NUPR1 and TRs (TR $\alpha$ ,  $n = 43$ ; TR $\beta$ ,  $n = 43$ ).

Tumor samples were then dichotomized into NUPR1 low- and high-expression groups, using the median T/N ratio of HCC specimens as a cutoff. Patients in the high NUPR1 expression group displayed worse recurrence-free survival ( $p = 0.009$ ), but the overall survival was not significantly different. We then separated NUPR1 and TR expression levels into three groups: group I, low expression of NUPR1 and TRs; group II, high expression of NUPR1 and low expression of TRs, or low expression of NUPR1 and high expression of TRs; and group III, high expression of NUPR1 and TRs.

Patients with high expression of NUPR1 and TRs showed significantly poorer recurrence-free survival (Figure 2B) and overall survival (Figure 2C) than those with low expression of NUPR1 and TRs. However, NUPR1, TR $\alpha$ , and TR $\beta$  were not an independent prognostic factor associated with survival (Table S1).

### NUPR1 promotes angiogenesis *in vitro*

Clinical data showed an association of high expression of NUPR1 with vascular invasion. Previous reports have indicated that thyroid hormone

sustains angiogenesis [26-28]. Accordingly, we analyzed the effect of conditioned medium (CM) derived from NUPR1-knockdown or control HepG2-TR $\alpha$  cells, incubated in the presence of 100 nM T<sub>3</sub> or T<sub>3</sub>-depleted serum (0 nM T<sub>3</sub>), on tube formation

by HUVECs. As shown in Figure 3A, CM from T<sub>3</sub>-stimulated HepG2-TR $\alpha$  cells promoted a prominent and significant increase in tube formation compared with T<sub>3</sub>-depleted cells.

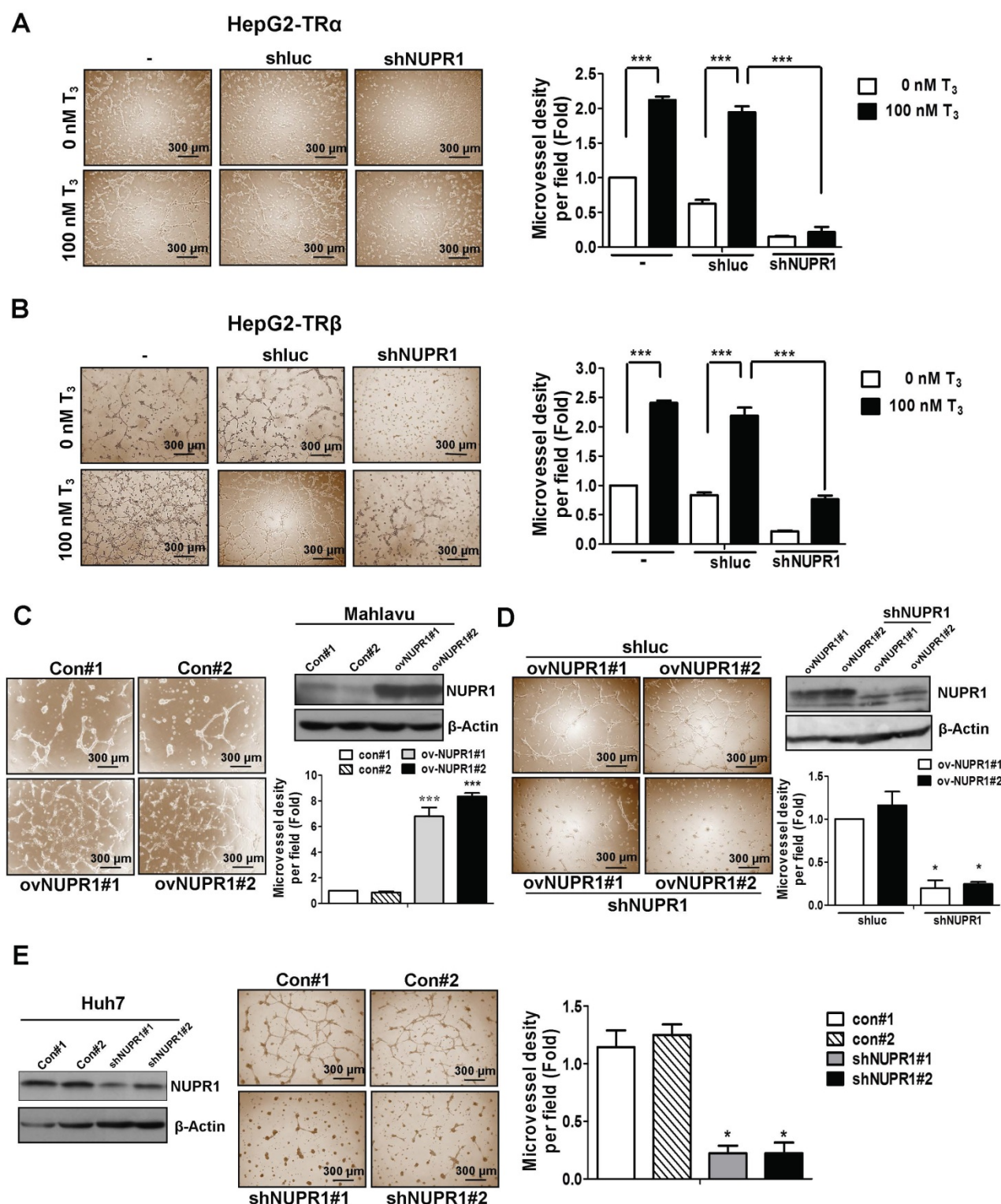


**Figure 3: NUPR1 promotes cells angiogenesis in vitro.** (A, B) CM was harvested from HepG2-TR $\alpha$  and HepG2-TR $\beta$  cells, transfected with or without luciferase or shNUPR1 plasmids, and treated with 0 nM or 100 nM T<sub>3</sub> for 24 h. HUVECs were seeded onto matrigel-coated dishes and incubated with CM for 16 h. Representative images are shown. (C) HUVECs were mixed with CM from NUPR1-overexpressing or control Mahlavu cells for 16 h. Representative images are shown. (D) HUVECs were treated with CM from NUPR1-knockdown or control Mahlavu-NUPR1 cells for 16 h. The number of branching points were quantified. (E) HUVECs were seeded on matrigel and treated with CM from NUPR1-knockdown or control Huh7 cells for 16 h. Representative images are shown. Bar plot represents means  $\pm$  SD (\*p < 0.05, \*\*p < 0.01, \*\*\*p < 0.001).



Notably, HUVECs tube formation was significantly decreased in T<sub>3</sub>-treated NUPR1-knockdown HepG2-TR $\alpha$  cells compared that induced by control cells. Similar results were observed in HepG2-TR $\beta$  cells (Figure 3B), J7-TR $\alpha$  cells and J7-TR $\beta$  cells (Figure S3A). To determine the angiogenesis function of NUPR1 in HCC cell lines, we stably expressed NUPR1 in the Mahlavu HCC cell line, which expresses relatively low endogenous levels of NUPR1 (Figure S3B). We then treated HUVECs with CM from NUPR1-overexpressing or control Mahlavu cells. These experiments showed that NUPR1-overexpressing cells significantly induced HUVECs tube formation compared with that induced by control cells (Figure 3C). Conversely, NUPR1-knockdown Mahlavu-NUPR1 cells inhibited HUVECs tube formation compared with control Mahlavu-NUPR1 cells (Figure 3D). To determine the consequences of NUPR1 depletion in hepatoma cells, we established NUPR1-knockdown and control Huh7 cells, and assessed the effect of CM from these cells on angiogenesis. In contrast to the angiogenic effect of NUPR1-overexpressing cells, NUPR1-knockdown Huh7 cells significantly decreased HUVECs tube formation (Figure 3E). These results indicate that T<sub>3</sub>/TR-upregulated NUPR1 promotes angiogenesis *in vitro*.

### Expressed NUPR1 in hepatoma cells promotes angiogenesis *in vivo*

We next assessed whether NUPR1 promotes angiogenesis *in vivo*, we performed chick chorioallantoic membrane (CAM) assays. Vessel growth on chick chorioallantoic membranes of eggs treated with NUPR1-overexpressing CM was higher than control cells (Figure 4A). Conversely, CM derived from NUPR1-knockdown Huh7 cells significantly suppressed vessels formation on membranes of eggs (Figure 4B). To further validate the role of NUPR1 *in vivo*, matrigel plug angiogenesis assay was performed. Weights and volumes of tumors formed from NUPR1-overexpressing cells were not significantly different from those of tumors formed from control cells. However, the hemoglobin content in xenograft tumors from NUPR1-overexpressing cells was 8–11-fold higher than that in control xenograft tumors (Figure 4C). Histological analysis of sections from NUPR1 overexpressing xenograft tumors immunostained for the angiogenesis marker CD31 revealed that CD31-positive microvessel density areas were higher in NUPR1-overexpressing xenograft tumors than control tumors (Figure 4D). We further examine the effect of NUPR1-knockdown on matrigel plug

angiogenesis assay. As expected, Huh7-shNUPR1-derived tumors displayed a significant decrease in blood vessels and hemoglobin content compared with control groups (Figure 4E-F). These data demonstrate that NUPR1 play an essential role in angiogenesis in hepatocellular carcinoma.

### NUPR1-dependent angiogenesis is mediated by induction of PDGFA expression and secretion

To investigate the mechanism underlying NUPR1-induced angiogenesis, we profiled the expression of 55 angiogenesis related proteins in CM from NUPR1-overexpressing or control Mahlavu cells. These screens showed that expression levels of the angiogenesis-related proteins, PDGF-AA (platelet-derived growth factor AA), TGF- $\beta$ 1 (tumor-derived growth factor- $\beta$ 1), CCL3 (C-C motif chemokine ligand 3) and VEGF-C (vascular endothelial growth factor-C) were higher in NUPR1-overexpressing cells compared with control cells (Figure 5A). Of these, the gene encoding PDGFA, which is known to be critical for HCC progression [29, 30], was most notably upregulated with NUPR1 overexpression. Thus, we selected PDGF-AA for further study. To validate the PDGF-AA expression level in NUPR1-overexpressing and knockdown cells, we performed ELISA and western blotting. ELISAs showed that secreted PDGFA levels were increased in CM from NUPR1-overexpressing cells and decreased in CM from NUPR1-knockdown cells compared with that from control cells (Figure 5B). A similar phenomenon was observed in western blot data (Figure 5C), confirming that NUPR1 enhances PDGFA expression/secretion.

To validate the involvement of PDGFA in promoting angiogenesis, we knocked down PDGFA expression in NUPR1-overexpressing Mahlavu cells and assessed HUVECs tube formation following treatment with Mahlavu cell-derived CM. HUVECs tube formation induced by CM from PDGFA-knockdown NUPR1-overexpressing cells was reduced compared with control cells (Figure 5D). Furthermore, pretreatment of HUVECs with a neutralizing antibody against human PDGFR $\alpha$  significantly decreased tube formation by CM from NUPR1-overexpressing cells (Figure 5E). Conversely, we found that treatment of HUVECs with recombinant human PDGFA protein in the presence of NUPR1-knockdown CM significantly increased tube formation (Figure 5F). Collectively, these results demonstrate that the pro-angiogenic activity of NUPR1 is mediated by PDGFA.

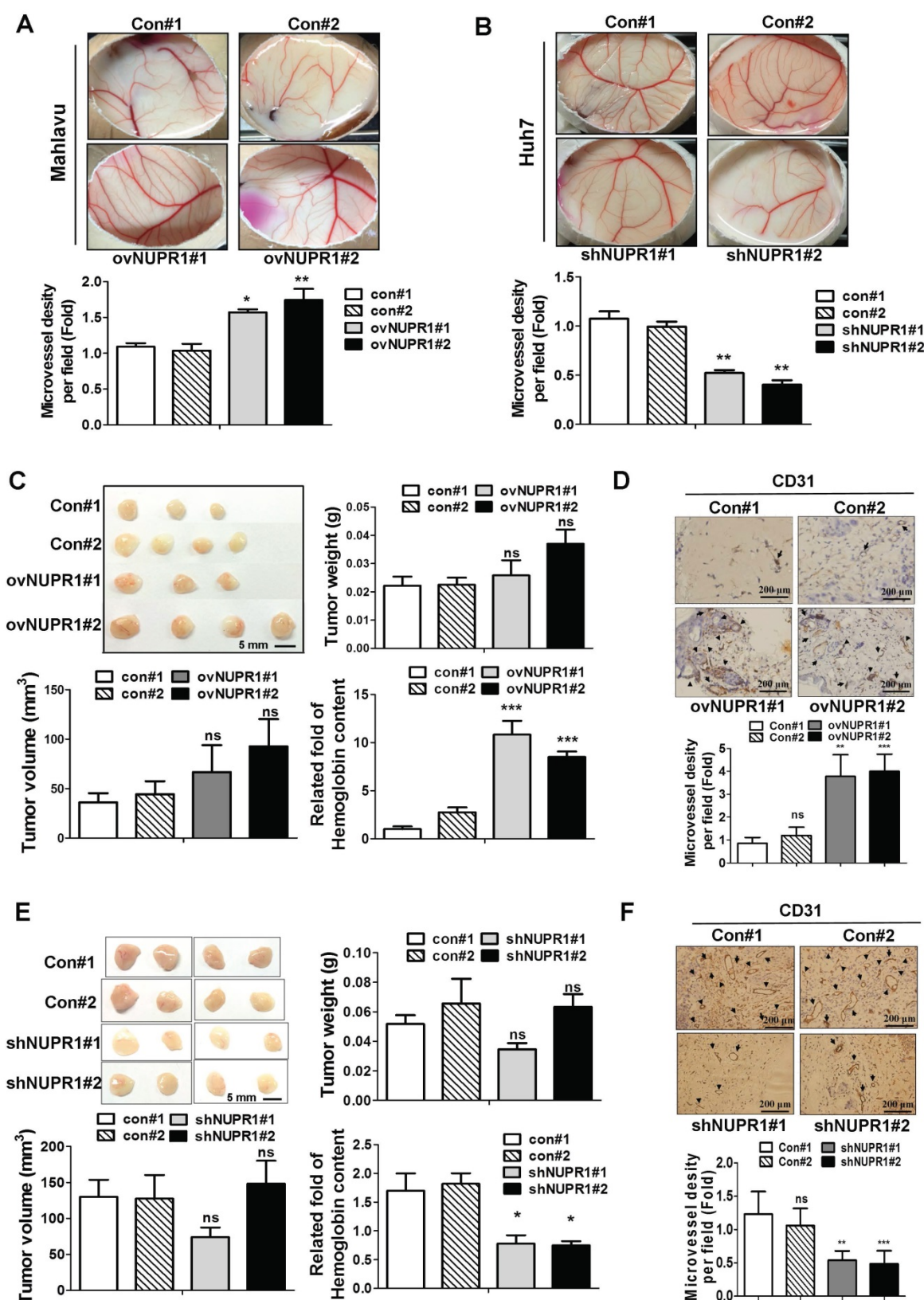


**Figure 4: NUPRI promotes angiogenesis in vivo.** (A, B) A 1:1 mixture of matrigel and CM from NUPRI-overexpressing Mahlavu cells, or NUPRI-knockdown Huh7 cells, or their respective controls, were implanted into the embryo. After a 4-day incubation, vessels on the chick chorioallantoic membrane were counted. (C, E) NUPRI-overexpressing Mahlavu cells, or NUPRI-knockdown Huh7 cells, or their respective controls, were mixed with matrigel and injected subcutaneously into the flanks of nude mice ( $n > 3/\text{group}$ ). Two weeks later, mice were sacrificed and tumor weight, tumor size, and hemoglobin content were measured. (D, F) Histological sections from C, E xenografts were immunostained for the angiogenesis marker CD31. CD31-positive blood vessels are indicated by arrows. Bar plot represents means  $\pm$  SD (\* $p < 0.05$ , \*\* $p < 0.01$ , \*\*\* $p < 0.001$ ).



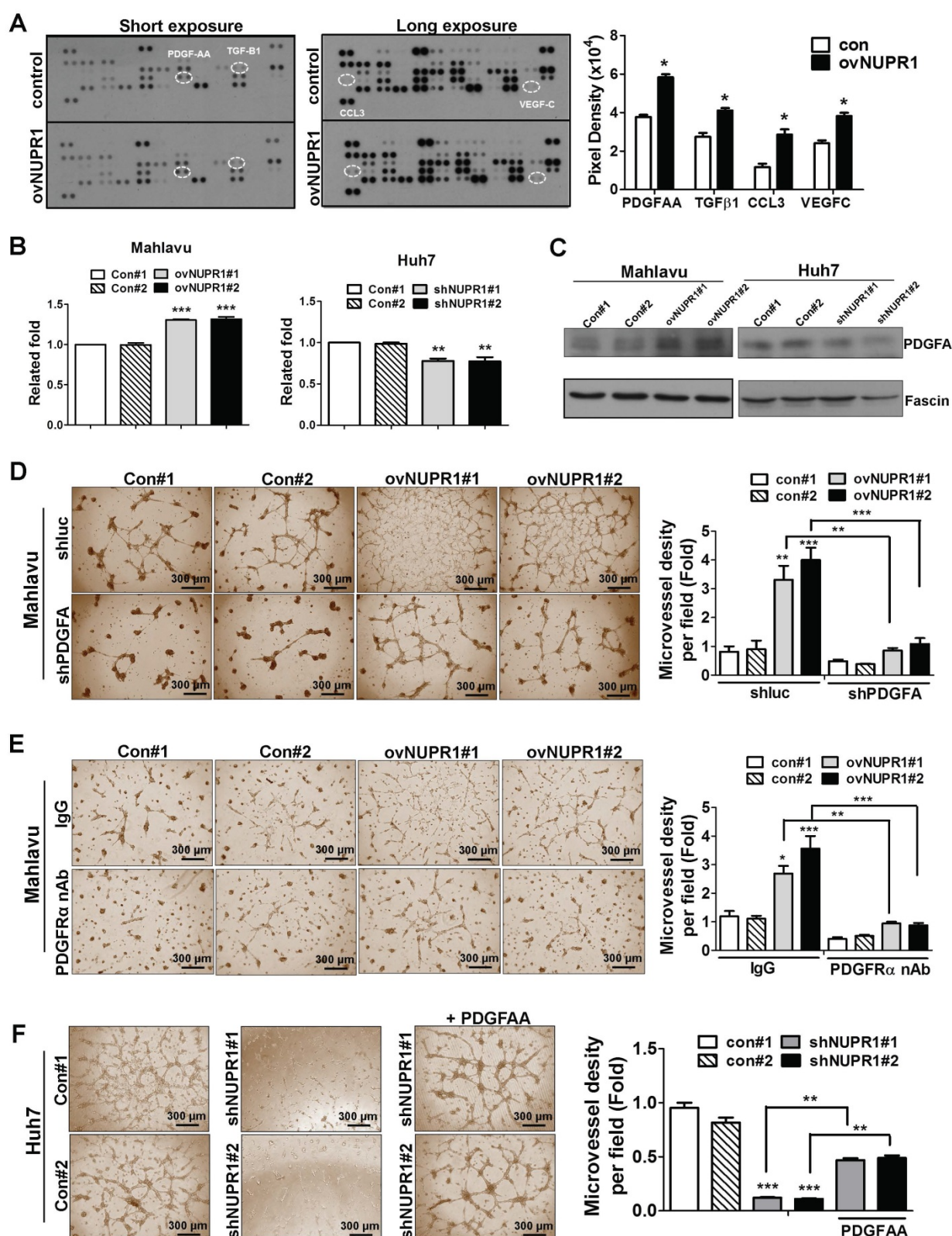


**Figure 5: NUPRI acts through induction of PDGFA expression to promote angiogenesis.** (A) Human-specific angiogenesis antibody array membranes were incubated with CM from NUPRI-overexpressing or control Mahlavu cells. Quantification of mean pixel densities were shown. (B, C) Relative levels of PDGF-AA secreted by NUPRI-overexpressing Mahlavu cells, or NUPRI-knockdown Huh7 cells, or their respective controls, were analyzed by ELISA and western blotting. Results were shown as the fold-change in PDGF-AA secretion compared with control cell lines. Fascin was used as a loading control. (D) HUVECs were seeded on matrigel and treated with CM from NUPRI-overexpressing or control Mahlavu cells transfected with control shLuc or shPDGFA plasmid for 16 h. (E) HUVECs were pretreated with 10  $\mu$ g/ml nonspecific rabbit IgG or PDGFR $\alpha$  neutralizing antibodies for 1 h, then seeded onto matrigel together with CM from NUPRI-overexpressing or control Mahlavu cells for 16 h. (F) HUVECs were seeded onto matrigel and treated with CM from NUPRI-knockdown or control Huh7 cells. The third panel shows HUVECs treated with CM from NUPRI-knockdown Huh7 cells together with 20 ng/ml PDGFA ligand. Bar plot represents means  $\pm$  SD (\* $p$  < 0.05, \*\* $p$  < 0.01, \*\*\* $p$  < 0.001; one-way ANOVA).

### **NUPR1 promotes angiogenesis through a PDGFA/MEK/ERK signaling cascade**

To investigate the signaling pathway downstream of NUPR1/PDGFA that is involved in inducing angiogenesis, we treated HUVECs with CM from NUPR1-overexpressing Mahlavu cells or NUPR1-knockdown Huh7 cells, or their respective controls, and performed western blotting. These analyses showed that expression levels of the phosphorylated forms of PDGFR $\alpha$ , MEK1/2, and ERK1/2 proteins were increased in HUVECs cultured with CM from NUPR1-overexpressing cells compared with control cells (Figure 6A). Conversely, the phosphorylated forms of these proteins in HUVECs were decreased after treatment with CM from NUPR1-knockdown cells (Figure 6B). To further clarify the signaling pathway involved in angiogenesis *in vitro*, we treated HUVECs with CM from NUPR1-overexpressing or control cells containing the ERK inhibitor U0126 or dimethylsulfoxide (DMSO). As shown in Figure 6C, treatment with ERK inhibitor-containing CM significantly disrupted NUPR1-mediated tube formation. Furthermore, the blood vessels in chick embryo chorioallantoic membranes were decreased in the presence of the ERK inhibitor (Figure 6D). These results suggest that NUPR1 acts through induction of PDGFA expression to promote endothelial tube formation, an effect that requires activation of the MEK/ERK signaling pathway.

### **NUPR1 drives transcriptional activation of PDGFA through direct binding to the promoter region**

To further explore the mechanisms by which NUPR1 regulates PDGFA transcription, we conducted promoter activity assays. Although the consensus sequence of the NUPR1 binding site has not been demonstrated, NUPR1 has been reported to share biochemical homology with HMG-like proteins [18], which bind to an A/T-rich sequence. To confirm this, we created a luciferase-based reporter plasmid by inserting an upstream promoter region (-3090/+16) of the PDGFA gene into a minimal thymidine kinase promoter. In addition to the full-length promoter region, two deletion constructs, -2128/+16 and -1242/+16, were prepared. Predicated potential NUPR1 binding sites are indicated by squares. The -3090/+16 region of PDGFA promoter increased luciferase transcriptional activity by approximately 2-fold, whereas other PDGFA deletion reporter constructs had no effect (Figure 6E, left panel). These data indicate that the potential NUPR1

binding site in the PDGFA promoter is located within the -3090/-2128 region. To confirm this and further refine the NUPR1 binding site, we generated PDGFA promoter -3090/+16 with first binding site mutant (mutant 1) or two binding sites mutant (mutant 2) and the results showed that promoter activity was significantly decreased in PDGFA promoter mutant 2 compared with wild type promoter, demonstrating that a possible NUPR1 binding site in the -2231/-2027 upstream region of PDGFA (Figure 6E, right panel). To further determine whether NUPR1 proteins directly target the PDGFA promoter, we performed ChIP assays (Figure 6F). The results clearly demonstrated that NUPR1 was recruited to the PDGFA promoter at -2231/-2027 region, whereas control IgG yielded only background signals. Collectively, these ChIP assay results reveal that the NUPR1 binds to the endogenous PDGFA promoter in intact cells.

### **TR-NUPR1 increase hepatoma cells chemoresistance**

Chemotherapy resistance is a major cause of treatment failure in a malignant tumor. Up to now, sorafenib is the only approved drug for treatment of advanced HCC to inhibit angiogenesis and growth of tumor cell. However, it is increasingly reported that drug resistance often develops and the mechanism remains unclear [31, 32]. Our previous studies indicated that T<sub>3</sub>/TR signaling promoted chemoresistance in hepatoma cells [14, 33]. Elevated thyroid hormone was associated with poor outcomes in advanced HCC patients receiving sorafenib treatment [34]. NUPR1 has also been reported that it participated in sorafenib resistance [21]. To investigate whether TR-NUPR1 is involved in sorafenib resistance, TR overexpression HepG2 and J7 cells were treated with sorafenib and cell viability was evaluated. Cell viability following the addition of sorafenib was significantly increased in T<sub>3</sub>-treated HepG2-TR $\alpha$  and HepG2-TR $\beta$  cells. In contrast, exposure of control HepG2-neo cells to T<sub>3</sub> did not significantly affect cell viability (Figure 7A). Similar results were obtained in J7-TR $\alpha$  and J7-TR $\beta$  cells (Figure 7B). Moreover, rescue experiments have been performed by depletion of NUPR1 expression after T<sub>3</sub> treatment. Knockdown of NUPR1 suppressed cell viability in T<sub>3</sub>-treated TR overexpressing HepG2 and J7 cell lines following the addition of sorafenib (Figure 7C-D). These results suggest that TR increases hepatoma cells chemoresistance through upregulating NUPR1.



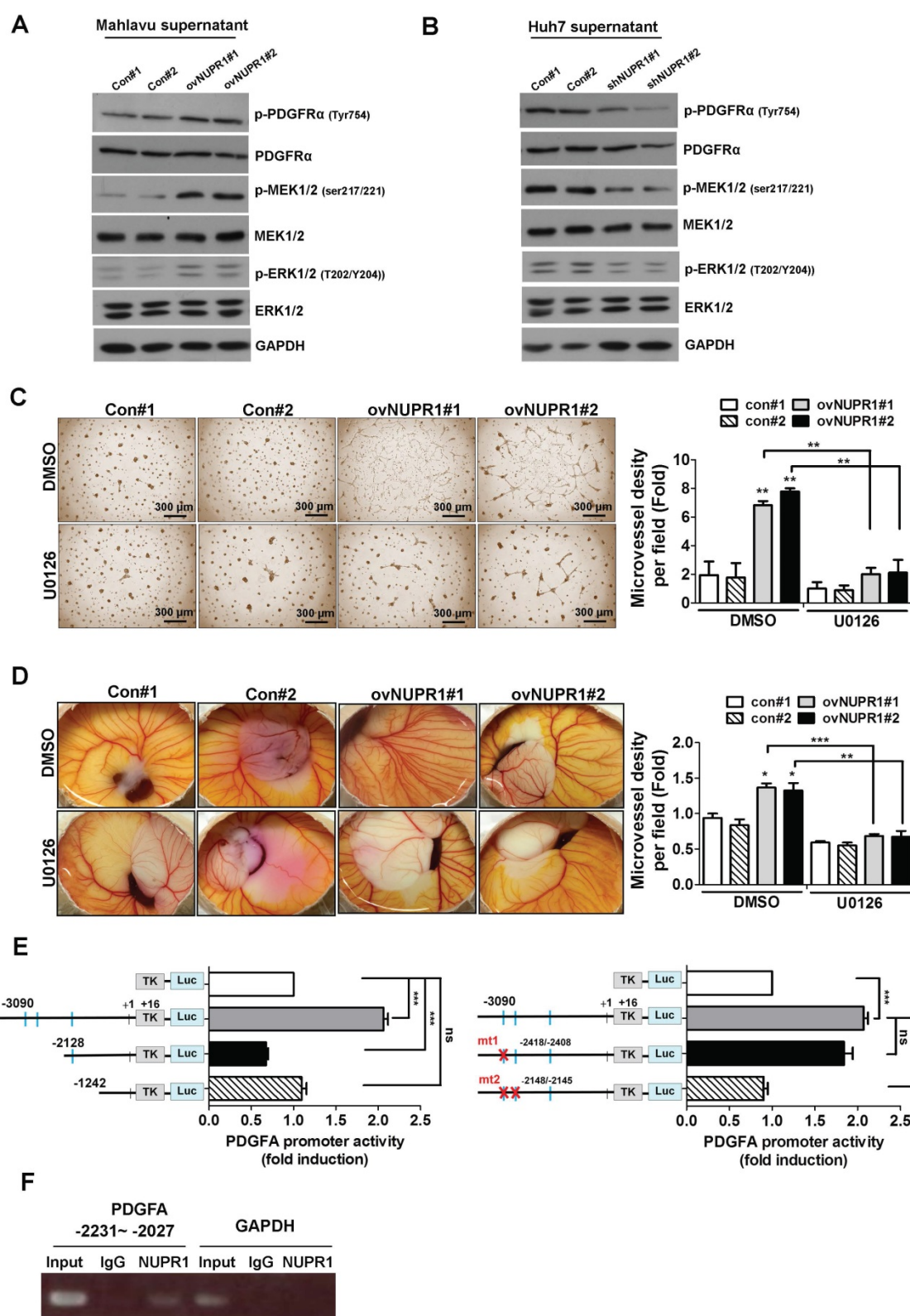


**Figure 6: NUPR1 promotes angiogenesis through a PDGFA/MEK/ERK signaling cascade.** (A, B) The expression levels of total and phosphorylated forms of PDGFRα, MEK1/2, and ERK1/2 proteins in HUVECs cultured with CM from NUPR1-overexpressing, -knockdown, or control Mahlavu and Huh7 cells for 48 h were analyzed by western blotting. GAPDH was used as a loading control. (C) HUVECs were pretreated with DMSO (vehicle control) or the ERK inhibitor U0126 (10 μM) for 1 h, then seeded on matrigel together with CM from NUPR1-overexpressing and control Mahlavu cells for 16 h. (D) Chick embryo were treated with DMSO or U0126 for 1 h, after which a mixture of matrigel and CM from NUPR1-overexpressing or control Mahlavu cells was implanted on the chick embryo. After a 4-day incubation, the number of vessel branching points were quantified by image analysis. (E) Serially deleted pA3TK-PDGFA promoter-report constructs and pcDNA3-NUPR1 expression plasmid were co-transfected in 293TN cells, after 24 h, cells were lysed and promoter activity was determined (left panel). Wild type and mutant forms of PDGFA promoter constructs were co-transfected with pcDNA3-NUPR1 plasmid in 293TN cells, after 24 h, cells were lysed and promoter activity was determined (right panel). (F) NUPR1-overexpression Mahlavu cell lysates were immunoprecipitated with nonspecific rabbit IgG or antibodies against NUPR1. GAPDH promoter region was used as negative control, respectively. Bar plot represents means ± SD (\*p < 0.05, \*\*p < 0.01, \*\*\*p < 0.001; one-way ANOVA).

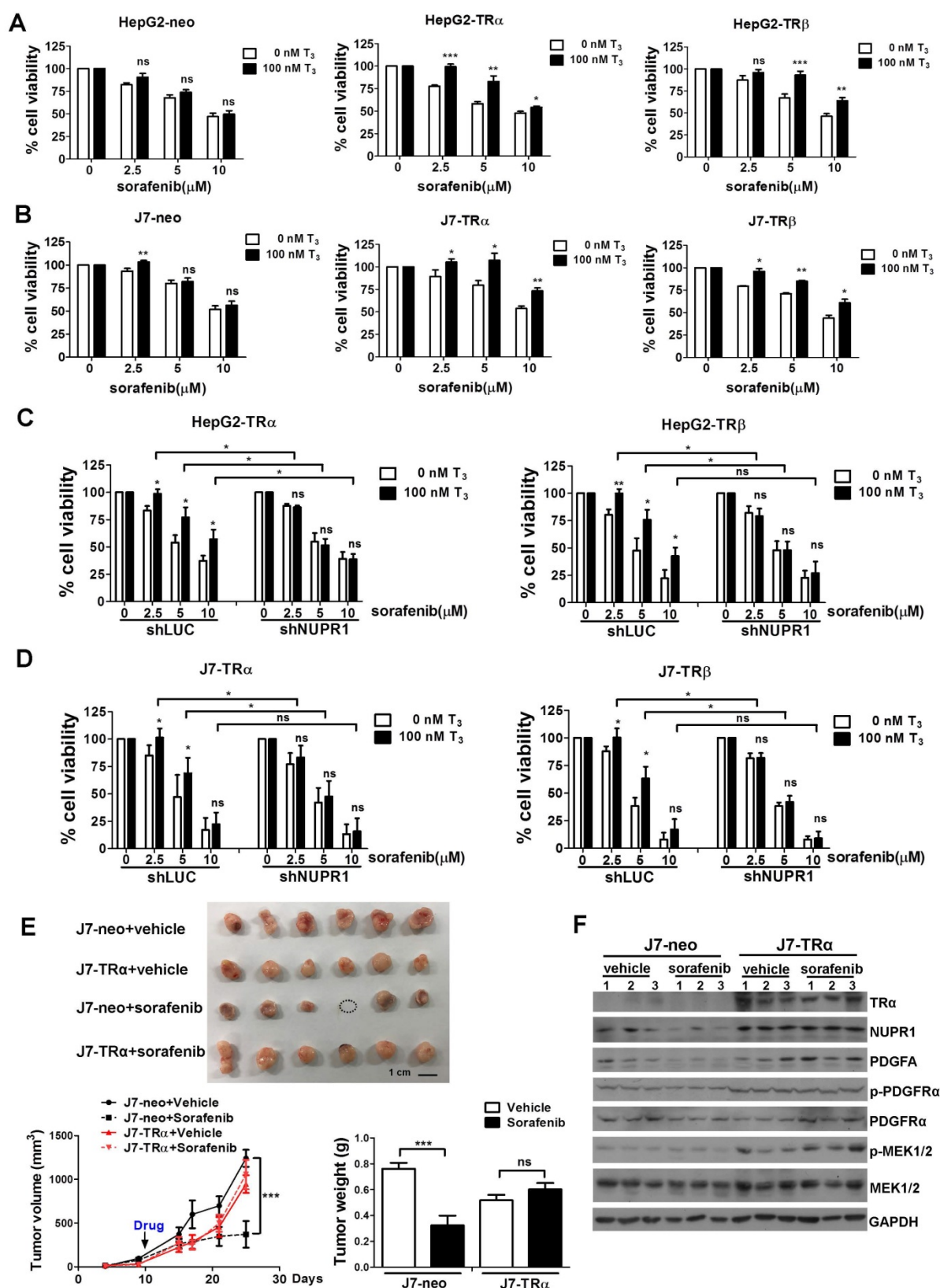


**Figure 7: TR-NUPR1 induces sorafenib resistance in hepatoma cells *in vitro* and *in vivo*.** (A–B) Cells were seeded at  $6\text{--}12 \times 10^3$  cells/well in 96-well plates with or without 100 nM T<sub>3</sub> and incubated overnight at 37 °C. After that, cells were treated with 0–10  $\mu\text{M}$  sorafenib for 24 h. The MTT assay absorbance of each well was measured at 570 nm/650 nm. (C–D) NUPR1 was knocked down in TR overexpression HepG2 and J7 cell lines and cells were treated with T<sub>3</sub> and sorafenib. The MTT assay absorbance of each well was measured at 570 nm/650 nm. (E)  $1 \times 10^6$  of J7-neo and J7-TR $\alpha$  cells were injected subcutaneously into the flanks of nude mice ( $n > 6$ ). After the tumors reached the size of approximately 100 mm<sup>3</sup>, mice were administered 30 mg/kg sorafenib by oral gavage twice a week for 20 days. Control mice received only the vehicle (DMSO). Tumor growth was measured twice a week. Mice were sacrificed and the tumors were removed, weighed, and processed for western blot analysis. (F) TR $\alpha$ , NUPR1, PDGFA, PDGFR $\alpha$  and MEK1/2 expression level were determined by western blot from J7-neo or J7-TR $\alpha$  xenografts. GAPDH was used as a loading control. Data represents means  $\pm$  SD (\* $p < 0.05$ , \*\* $p < 0.01$ , \*\*\* $p < 0.001$ ).

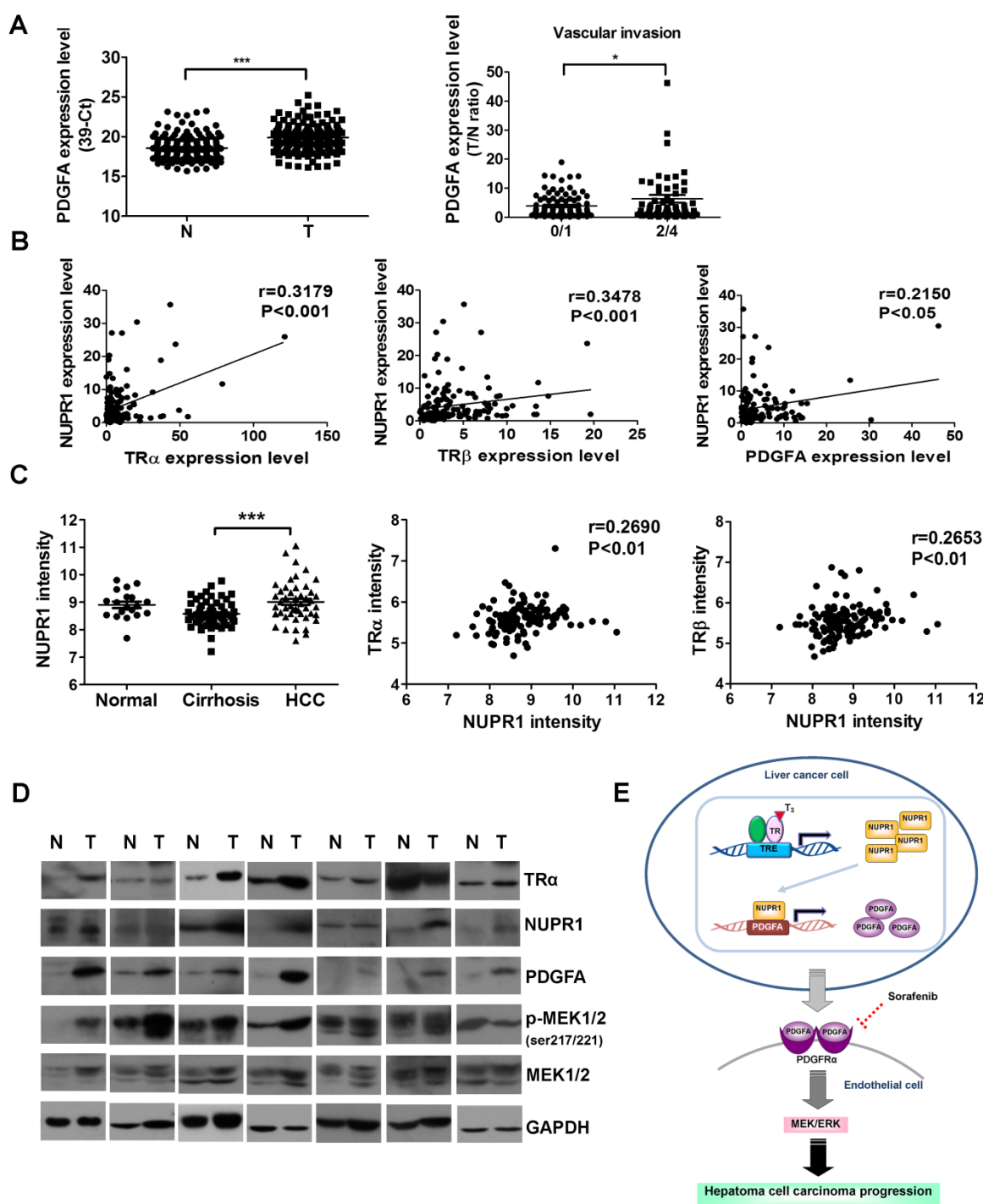


**Figure 8: NUPR1 expression is positively correlated with TR and PDGFA expression in hepatoma specimens.** (A) Expression of PDGFA in 158 paired human HCC (T) and adjacent normal (N) tissues were determined by qRT-PCR; expression of PDGFA mRNA was normalized to that of 18s rRNA (left panel). PDGFA expression levels were highly correlated with vascular invasion. Differences were analyzed using one-way ANOVA (\* $p < 0.05$ , \*\* $p < 0.01$ , \*\*\* $p < 0.001$ ). (B) Spearman correlations of TR $\alpha$ , TR $\beta$ , and PDGFA with NUPR1 in 158 paired human specimens were analyzed and shown. (C) NUPR1 expression levels in HCC tissues were higher than those in cirrhotic tissue (normal,  $n = 19$ ; cirrhosis,  $n = 58$ ; HCC,  $n = 47$ ). Spearman analyses showed that TR $\alpha$  and TR $\beta$  expression were positively correlated with NUPR1 expression. Expression levels of these genes are presented as microarray intensities. (D) Expression of angiogenic related proteins, PDGFA, p-MEK1/2, NUPR1 and TR $\alpha$  protein expression levels in paired HCC tissues were determined by western blotting. GAPDH was used as a loading control. (E) Schematic model of the regulation of angiogenesis in hepatoma cell carcinoma progression by the T<sub>3</sub>/TR/NUPR1/PDGFA/MEK/ERK pathway.

To explore the effect of sorafenib resistance mediated by T<sub>3</sub>/TR-induced NUPR1 expression *in vivo*, J7-neo and J7-TR $\alpha$  cells were injected subcutaneously into the flanks of nude mice. After the tumors reached the size of approximately 100 mm<sup>3</sup>,

mice were administered sorafenib by oral gavage. Concordant with *in vitro* results, TR overexpression conferred sorafenib resistance. In contrast, exposure of control J7-neo xenografts to sorafenib significantly affect tumor growth and tumor weight (Figure 7E). In



addition, western blot analyses showed that NUPR1, PDGFA, p-PDGFR $\alpha$  and p-MEK1/2 expression levels were higher in J7-TR $\alpha$  xenografts compared with J7-neo xenografts (Figure 7F). Moreover, these genes were suppressed in sorafenib-treated groups compared with vehicle-treated groups in J7-neo xenografts, but its expression was not affected or only slightly decreased in sorafenib-treated groups in J7-TR $\alpha$  xenografts. Collectively, these findings confirm that T<sub>3</sub>/TR mediated sorafenib resistance via NUPR1 and its downstream targets.

### **NUPR1 is positively correlated with TR $\alpha$ , TR $\beta$ , and PDGFA expression in clinical HCC specimens**

The clinicopathological significance of PDGFA expression in HCC was also investigated. PDGFA was significantly overexpressed in 158 paired HCC specimens compared with adjacent normal tissue (Figure 8A, left panel). An analysis of clinicopathological parameters showed that expression of PDGFA was associated with vascular invasion (Figure 8A, right panel). A linear regression analysis further revealed a significant positive correlation between NUPR1 and TR $\alpha$ , TR $\beta$ , PDGFA levels, based on the T/N ratio (Figure 8B). Furthermore, an analysis of the public Oncomine database containing 124 human hepatoma samples (Mas liver) revealed that NUPR1 expression levels were higher in HCC samples than in cirrhosis samples (Figure 8C, left panel). A Spearman analysis showed that TR $\alpha$  and TR $\beta$  expression were positively correlated with NUPR1 expression (Figure 8C, right panel). In addition, western blot analyses showed that angiogenic-related genes- PDGFA, p-MEK1/2, NUPR1 and TR $\alpha$  expression levels were increased in HCC tissues in 7 representatives paired specimens (Figure 8D). Clinical investigations reveal associations among TR, NUPR1, and PDGFA, supporting an important role of NUPR1 in HCC progression.

### **Discussion**

Liver cancer is one of the leading causes of cancer deaths worldwide [1-3], at least in part because of the high angiogenic and metastatic potential of liver tumor cells. High levels of angiogenesis-related factors are significantly associated with rapid recurrence and poor survival [35], but the underlying mechanisms are not fully understood. Hence, identification of novel therapeutic targets is crucial for the prognosis of HCC. Here, our findings support an oncogenic role of NUPR1 in HCC, suggesting that the PDGFA/MEK/ERK signaling pathway is involved in TR/NUPR1-induced angiogenesis and sorafenib chemoresistance in HCC (Figure 8E).

Accumulating evidence has implicated aberrant expression of TRs in human cancers [5, 8, 9, 36]. Cristofanilli *et al.* reported that hypothyroid patients have a reduced incidence of primary breast carcinoma in association with a lower risk of developing the invasive disease [11]. Moreover, treatment with the antithyroid drug, propylthiouracil, in combination with tamoxifen increased survival in patients with glioblastoma [12]. Consistent with this, epidemiological studies have demonstrated that hyperthyroidism is associated with an increased risk of ovarian cancer [13]. Interestingly, treatment of hypothyroidism with levothyroxine (T<sub>4</sub>) was shown to be associated with a significantly reduced risk of colorectal cancer [37], and a previous case-control study revealed that hypothyroidism was associated with a significantly elevated risk of HCC in women [38]. Our previous studies also indicated that numerous oncogenes and suppressor genes regulated by T<sub>3</sub>/TR could promote or suppress HCC progression [14-17, 25, 39, 40]. Collectively, these observations demonstrated that T<sub>3</sub>/TR signaling could play dual roles in carcinogenesis, possibly reflecting the various TR isoforms, functions of T<sub>3</sub>/TR in different tissues, and different stages of tumor development. Thus, how T<sub>3</sub>/TR switches between an oncogenic role and tumor suppressor role will require further investigation.

Several reports have demonstrated that NUPR1 is involved in the progression of various cancers. Elevated NUPR1 level has been found in pancreatic cancer patients [20], and NUPR1 expression has been shown to promote pancreatic cancer cell metastasis and invasion. Jung *et al.* reported that expression of NUPR1 in early-stage breast cancers is associated with poorer prognosis [41]. Moreover, knockdown of NUPR1 was shown to inhibit tumor growth and deregulate autophagic flux and impairs autolysosomal clearance in human non-small-cell lung cancer [42, 43], and inhibit anti-apoptotic and tumor cell promoter activity in colorectal cancer [44]. In the current study, we provide the first demonstration that T<sub>3</sub>/TR-induced increases in NUPR1 upregulate expression of PDGFA, which promotes angiogenic effects in HCC through activation of the MEK/ERK signaling pathway. A clinicopathological analysis revealed that patients with high expression of NUPR1 and TRs displayed significantly poorer overall survival than those with low expression of NUPR1 and TRs. Consistent with our data, Emma *et al.* found that NUPR1 expression was significantly higher in primary human HCC tissues, and further showed that NUPR1 increased cell growth, migration, and invasion [21]. Lee *et al.* also identified NUPR1 as a key modulator of a

mitochondrial respiratory defect during liver cancer progression [22]. In addition, Bak *et al.* reported that NUPR1 is activated by hepatitis B virus X protein, the primary risk factor in HCC, through a Smad4 pathway, and modulates cell growth and survival in liver cancer [45]. These reports support the conclusion that NUPR1 plays an important role in hepatocarcinogenesis.

Angiogenesis, a hallmark of cancer, is induced early during the multistage development of invasive cancers [46]. Here, we provide the first evidence that NUPR1 acts through transactivation of PDGFA to promote endothelial tube formation in HCC. PDGFA is a member of the PDGF family, which consists of five isoforms that regulate angiogenesis and participate in cancer progression [47]. Each isoform binds to a dimeric form of one of two different receptors—PDGFR $\alpha$  or PDGFR $\beta$ —to activate downstream signal pathways, with PDGFA binding to PDGFR $\alpha$  [48]. Several studies have reported that PDGFA is involved in tumor development. PDGFA expression is elevated in oral cancer, pancreatic cancer, and mantle cell lymphoma, and its expression was shown to promote tumor cell migration, invasion, and angiogenesis [49–51]. In addition, it has been reported that higher expression of PDGFA is associated with hepatic fibrogenesis in chronic hepatitis C [30]. PDGFA also contributes to HCC progression by enhancing NRF2 expression [29]. In the current study, we found that the angiogenic effects of NUPR1 were disrupted by a PDGFR $\alpha$  neutralizing antibody and an ERK inhibitor, demonstrating that these actions of NUPR1 are mediated by activation of PDGFA/MEK/ERK signaling pathway.

Sorafenib, a multikinase inhibitor with activity against Raf kinase, VEGF receptors, PDGFRs and other tyrosine kinases, has been approved for the treatment of advanced HCC [52]. Sorafenib improves survival in HCC patients, reduces tumor cell proliferation and angiogenesis, and increases apoptosis [31]. However, the benefits of sorafenib are modest [32], and its mechanism of action is incompletely understood. Recently, Emma *et al.* reported that NUPR1 is involved in sorafenib resistance in HCC, showing that NUPR1 knockdown decreased cell growth and increased tumor cell sensitivity to sorafenib treatment [21]. Several studies have also demonstrated that sorafenib impairs tumor cell proliferation and viability through the MEK/ERK pathway. Our previous studies revealed that T<sub>3</sub>/TR upregulated TRAIL and Bcl-xL, suppressed FoxO1 and Bim to promote hepatoma cells metastasis and chemotherapies resistance [14, 33]. Higher value of thyroid-stimulating hormone (TSH) and free T<sub>4</sub> (FT<sub>4</sub>)

were associated with unfavorable tumor progression and overall survival in advanced HCC patients received sorafenib treatment. An index of thyroid function can significantly predicted opposite clinical outcomes in advanced HCC patients receiving sorafenib or chemotherapy treatment [34]. Consistent to our results, we confirmed the sorafenib resistance effect of T<sub>3</sub>/TR and this ability was mediated through NUPR1 by directly regulating the levels of PDGFA expression and secretion. PDGFA expression may account for the increased angiogenesis of tumor cells that inhibited by sorafenib. Our findings thus suggest potential molecular mechanisms for sorafenib chemoresistance in HCC tumorigenesis.

In conclusion, we have identified NUPR1-mediated regulation of angiogenesis via the PDGFA/MEK/ERK cascade as a novel pathway of thyroid hormone receptor-dependent HCC progression. Modulation of this angiogenesis pathway may provide potential therapeutic targets for HCC.

## Abbreviations

HCC: hepatocellular carcinoma; NUPR1: nuclear protein-1; T<sub>3</sub>: 3,3'-5-triiodo-L-thyronine; TR: thyroid hormone receptor; PDGFA: platelet-derived growth factor A; HUVECs: human umbilical vein endothelial cells; TREs: thyroid hormone response elements; HMG: high mobility group; qRT-PCR: quantitative reverse transcription-polymerase chain reaction; ChIP: chromatin immunoprecipitation; CM: conditioned medium; CAM: chick chorioallantoic membrane; TGF- $\beta$ 1: tumor-derived growth factor- $\beta$ 1; CCL3: C-C motif chemokine ligand 3; VEGF-C: vascular endothelial growth factor-C; ELISA: enzyme-linked immunosorbent assay; PDGFR $\alpha$ : platelet-derived growth factor receptor  $\alpha$ .

## Supplementary Material

Supplementary figures and table.

<http://www.thno.org/v09p2361s1.pdf>

## Acknowledgments

This work was supported by grants from Chang Gung Memorial Hospital, Taoyuan, Taiwan (CMRPD1G0421, CMRPD1G0422, CRRPD1F0011, CRRPD1F0012, CRRPD1F0013, BMRP130, NMRPD1D1021, NMRPD1D1022 and NMRPD1D1023 to K. H. Lin) and from the Ministry of Science and Technology of the Republic of China (MOST 103-2320-B-182-018-MY3 to KHLin). We would like to thank the Taiwan Liver Cancer Network (TLCN) for providing the hepatoma tissue samples and related clinical data (all anonymous).

## Author contributions

CYC performed most experiments and wrote the manuscript. SMW performed promoter assay and ChIP assay experiments. YHL, HCC, SLL, CTY, WYC contributed experience on methods. KHL supervised and reviewed the manuscripts.

## Competing Interests

The authors have declared that no competing interest exists.

## References

- McGlynn KA, London WT. The global epidemiology of hepatocellular carcinoma: present and future. *Clin Liver Dis*. 2011; 15: 223-43, vii-x.
- Porru S, Placidi D, Carta A, Gelatti U, Ribero ML, Tagger A, et al. Primary liver cancer and occupation in men: a case-control study in a high-incidence area in Northern Italy. *Int J Cancer*. 2001; 94: 878-83.
- El-Serag HB. CURRENT CONCEPTS Hepatocellular Carcinoma. *New Engl J Med*. 2011; 365: 1118-27.
- Galun D, Srdic-Rajic T, Bogdanovic A, Loncar Z, Zuvela M. Targeted therapy and personalized medicine in hepatocellular carcinoma: drug resistance, mechanisms, and treatment strategies. *J Hepatocell Carcinoma*. 2017; 4: 93-103.
- Wu SM, Cheng WL, Lin CD, Lin KH. Thyroid hormone actions in liver cancer. *Cell Mol Life Sci*. 2013; 70: 1915-36.
- Cheng SY. Multiple mechanisms for regulation of the transcriptional activity of thyroid hormone receptors. *Rev Endocr Metab Disord*. 2000; 1: 9-18.
- Cheng SY, Leonard JL, Davis PJ. Molecular aspects of thyroid hormone actions. *Endocr Rev*. 2010; 31: 139-70.
- Chi HC, Chen CY, Tsai MM, Tsai CY, Lin KH. Molecular functions of thyroid hormones and their clinical significance in liver-related diseases. *Biomed Res Int*. 2013; 2013: 601361.
- Aranda A, Martinez-Iglesias O, Ruiz-Llorente L, Garcia-Carpizo V, Zambrano A. Thyroid receptor: roles in cancer. *Trends Endocrinol Metab*. 2009; 20: 318-24.
- Gonzalez-Sancho JM, Garcia V, Bonilla F, Munoz A. Thyroid hormone receptors/THR genes in human cancer. *Cancer Lett*. 2003; 192: 121-32.
- Cristofanilli M, Yamamura Y, Kau SW, Bevers T, Strom S, Patangan M, et al. Thyroid hormone and breast carcinoma. Primary hypothyroidism is associated with a reduced incidence of primary breast carcinoma. *Cancer*. 2005; 103: 1122-8.
- Hercbergs AA, Goyal LK, Suh JH, Lee S, Reddy CA, Cohen BH, et al. Propylthiouracil-induced chemical hypothyroidism with high-dose tamoxifen prolongs survival in recurrent high grade glioma: a phase I/II study. *Anticancer Res*. 2003; 23: 617-26.
- Ness RB, Grisso JA, Cottreau C, Klapper J, Vergona R, Wheeler JE, et al. Factors related to inflammation of the ovarian epithelium and risk of ovarian cancer. *Epidemiology*. 2000; 11: 111-7.
- Chi HC, Chen SL, Liao CJ, Liao CH, Tsai MM, Lin YH, et al. Thyroid hormone receptors promote metastasis of human hepatoma cells via regulation of TRAIL. *Cell Death Differ*. 2012; 19: 1802-14.
- Chung IH, Chen CY, Lin YH, Chi HC, Huang YH, Tai PJ, et al. Thyroid hormone-mediated regulation of lipocalin 2 through the Met/FAK pathway in liver cancer. *Oncotarget*. 2015; 6: 15050-64.
- Lin YH, Liao CJ, Huang YH, Wu MH, Chi HC, Wu SM, et al. Thyroid hormone receptor represses miR-17 expression to enhance tumor metastasis in human hepatoma cells. *Oncogene*. 2013; 32: 4509-18.
- Wu SM, Huang YH, Yeh CT, Tsai MM, Liao CH, Cheng WL, et al. Cathepsin H regulated by the thyroid hormone receptors associate with tumor invasion in human hepatoma cells. *Oncogene*. 2011; 30: 2057-69.
- Encinar JA, Mallo GV, Mizyrycki C, Giono L, Gonzalez-Ros JM, Rico M, et al. Human p8 is a HMG-I/Y-like protein with DNA binding activity enhanced by phosphorylation. *J Biol Chem*. 2001; 276: 2742-51.
- Mallo GV, Fiedler F, Calvo EL, Ortiz EM, Vasseur S, Keim V, et al. Cloning and expression of the rat p8 cDNA, a new gene activated in pancreas during the acute phase of pancreatitis, pancreatic development, and regeneration, and which promotes cellular growth. *J Biol Chem*. 1997; 272: 32360-9.
- Sandi MJ, Hamidi T, Malicet C, Cano C, Loncle C, Pierres A, et al. p8 expression controls pancreatic cancer cell migration, invasion, adhesion, and tumorigenesis. *J Cell Physiol*. 2011; 226: 3442-51.
- Emma MR, Iovanna JL, Bachvarov D, Puleio R, Loria GR, Augello G, et al. NUPR1, a new target in liver cancer: implication in controlling cell growth, migration, invasion and sorafenib resistance. *Cell Death Dis*. 2016; 7: e2269.
- Lee YK, Jee BA, Kwon SM, Yoon YS, Xu WG, Wang HJ, et al. Identification of a mitochondrial defect gene signature reveals NUPR1 as a key regulator of liver cancer progression. *Hepatology*. 2015; 62: 1174-89.
- Lin KH, Shieh HY, Hsu HC. Negative regulation of the antimetastatic gene Nm23-H1 by thyroid hormone receptors. *Endocrinology*. 2000; 141: 2540-7.
- Shih CH, Chen SL, Yen CC, Huang YH, Chen CD, Lee YS, et al. Thyroid hormone receptor-dependent transcriptional regulation of fibrinogen and coagulation proteins. *Endocrinology*. 2004; 145: 2804-14.
- Lin YH, Wu MH, Liao CJ, Huang YH, Chi HC, Wu SM, et al. Repression of microRNA-130b by thyroid hormone enhances cell motility. *J Hepatol*. 2015; 62: 1328-40.
- Liu X, Zheng N, Shi YN, Yuan J, Li L. Thyroid hormone induced angiogenesis through the integrin alphavbeta3/protein kinase D/histone deacetylase 5 signaling pathway. *J Mol Endocrinol*. 2014; 52: 245-54.
- Mousa SA, Lin HY, Tang HY, Hercbergs A, Luidens MK, Davis PJ. Modulation of angiogenesis by thyroid hormone and hormone analogues: implications for cancer management. *Angiogenesis*. 2014; 17: 463-9.
- Pinto M, Soares P, Ribatti D. Thyroid hormone as a regulator of tumor induced angiogenesis. *Cancer Lett*. 2011; 301: 119-26.
- Liu D, Zhang Y, Wei Y, Liu G, Liu Y, Gao Q, et al. Activation of AKT pathway by Nrf2/PDGFA feedback loop contributes to HCC progression. *Oncotarget*. 2016; 7: 65389-402.
- Tanikawa AA, Grotto RM, Silva GF, Ferrasi AC, Sarnighausen VC, Pardini MI. Platelet-derived growth factor A mRNA in platelets is associated with the degree of hepatic fibrosis in chronic hepatitis C. *Rev Soc Bras Med Trop*. 2017; 50: 113-6.
- Ziogas IA, Tsoulfas G. Evolving role of Sorafenib in the management of hepatocellular carcinoma. *World J Clin Oncol*. 2017; 8: 203-13.
- Zhu YJ, Zheng B, Wang HY, Chen L. New knowledge of the mechanisms of sorafenib resistance in liver cancer. *Acta Pharmacol Sin*. 2017; 38: 614-22.
- Chi HC, Chen SL, Cheng YH, Lin TK, Tsai CY, Tsai MM, et al. Chemotherapy resistance and metastasis-promoting effects of thyroid hormone in hepatocarcinoma cells are mediated by suppression of FoxO1 and Bim pathway. *Cell Death Dis*. 2016; 7: e2324.
- Chu YD, Lin KH, Huang YH, Lin CC, Hung CF, Yeh TS, et al. A novel thyroid function index associated with opposite therapeutic outcomes in advanced hepatocellular carcinoma patients receiving chemotherapy or sorafenib. *Asia Pac J Clin Oncol*. 2018.
- Fernandez M, Semela D, Bruix J, Colle I, Pinzani M, Bosch J. Angiogenesis in liver disease. *J Hepatol*. 2009; 50: 604-20.
- Kim WG, Cheng SY. Thyroid hormone receptors and cancer. *Biochim Biophys Acta*. 2013; 1830: 3928-36.
- Rennert G, Rennert HS, Pinchev M, Gruber SB. A case-control study of levotyroxine and the risk of colorectal cancer. *J Natl Cancer Inst*. 2010; 102: 568-72.
- Hassan MM, Kaseb A, Li D, Patt YZ, Vauthey JN, Thomas MB, et al. Association between hypothyroidism and hepatocellular carcinoma: a case-control study in the United States. *Hepatology*. 2009; 49: 1563-70.
- Chen RN, Huang YH, Yeh CT, Liao CH, Lin KH. Thyroid hormone receptors suppress pituitary tumor transforming gene 1 activity in hepatoma. *Cancer Res*. 2008; 68: 1697-706.
- Liao CH, Yeh CT, Huang YH, Wu SM, Chi HC, Tsai MM, et al. Dickkopf 4 positively regulated by the thyroid hormone receptor suppresses cell invasion in human hepatoma cells. *Hepatology*. 2012; 55: 910-20.
- Jung SH, Lee A, Yim SH, Hu HJ, Choe C, Chung YJ. Simultaneous copy number gains of NUPR1 and ERBB2 predicting poor prognosis in early-stage breast cancer. *Bmc Cancer*. 2012; 12: 382.
- Guo X, Wang W, Hu J, Feng K, Pan Y, Zhang L, et al. Lentivirus-mediated RNAi knockdown of NUPR1 inhibits human nonsmall cell lung cancer growth in vitro and in vivo. *Anat Rec (Hoboken)*. 2012; 295: 2114-21.
- Mu Y, Yan X, Li D, Zhao D, Wang L, Wang X, et al. NUPR1 maintains autolysosomal efflux by activating SNAP25 transcription in cancer cells. *Autophagy*. 2018; 14: 654-70.
- Li X, Martin TA, Jiang WG. COM-1/p8 acts as a tumour growth enhancer in colorectal cancer cell lines. *Anticancer Res*. 2012; 32: 1229-37.
- Bak Y, Shin HJ, Bak I, Yoon DY, Yu DY. Hepatitis B virus X promotes hepatocellular carcinoma development via nuclear protein 1 pathway. *Biochem Biophys Res Commun*. 2015; 466: 676-81.

46. Hanahan D, Weinberg RA. Hallmarks of cancer: the next generation. *Cell*. 2011; 144: 646-74.
47. Andrae J, Gallini R, Betsholtz C. Role of platelet-derived growth factors in physiology and medicine. *Genes Dev*. 2008; 22: 1276-312.
48. Chen PH, Chen X, He X. Platelet-derived growth factors and their receptors: structural and functional perspectives. *Biochim Biophys Acta*. 2013; 1834: 2176-86.
49. Ong HS, Gokavarapu S, Tian Z, Li J, Xu Q, Cao W, et al. PDGFRA mRNA is overexpressed in oral cancer patients as compared to normal subjects with a significant trend of overexpression among tobacco users. *J Oral Pathol Med*. 2017; 46: 591-7.
50. Sahraei M, Roy LD, Curry JM, Teresa TL, Nath S, Besmer D, et al. MUC1 regulates PDGFA expression during pancreatic cancer progression. *Oncogene*. 2012; 31: 4935-45.
51. Palomero J, Vegliante MC, Rodriguez ML, Eguileor A, Castellano G, Planas-Rigol E, et al. SOX11 promotes tumor angiogenesis through transcriptional regulation of PDGFA in mantle cell lymphoma. *Blood*. 2014; 124: 2235-47.
52. Keating GM, Santoro A. Sorafenib: a review of its use in advanced hepatocellular carcinoma. *Drugs*. 2009; 69: 223-40.



## Research Paper

# Lipopolysaccharide promoted proliferation and adipogenesis of preadipocytes through JAK/STAT and AMPK-regulated cPLA2 expression

Chao-Chien Chang<sup>1,2,3,4</sup>, Kee-Chin Sia<sup>5</sup>, Jia-Feng Chang<sup>5,6,7</sup>, Chia-Mo Lin<sup>5,8,9</sup>, Chuen-Mao Yang<sup>10,11,12</sup>, Kuo-Yang Huang<sup>13</sup>, Wei-Ning Lin<sup>5✉</sup>

1. Division of Cardiology, Department of Internal Medicine, Cathay General Hospital, Taipei, Taiwan;
2. Graduate Institute of Medical Sciences, College of Medicine, Taipei Medical University, Taipei, Taiwan;
3. Department of Pharmacology, School of medicine, College of Medicine, Taipei Medical University, Taipei, Taiwan;
4. School of Medicine, College of Medicine, Fu Jen Catholic University, New Taipei City, Taiwan;
5. Graduate Institute of Biomedical and Pharmaceutical Science, College of Medicine, Fu Jen Catholic University, New Taipei City, Taiwan;
6. PhD Program in Nutrition and Food Science, Fu Jen Catholic University, New Taipei City, Taiwan;
7. Department of Internal Medicine, En-Chu-Kong Hospital, New Taipei City, Taiwan;
8. Department of Chemistry, Fu-Jen Catholic University, New Taipei, Taiwan;
9. Division of Chest Medicine, Shin Kong Hospital, Taipei, Taiwan;
10. Department of Physiology and Pharmacology and Health Ageing Research Center, College of Medicine, Chang Gung University, Kwei-San, Tao-Yuan, Taiwan;
11. Department of Anesthetics, Chang Gung Memorial Hospital at Linkou and Chang Gung University, Kwei-San, Tao-Yuan, Taiwan;
12. Research Center for Chinese Herbal Medicine and Research Center for Food and Cosmetic Safety, College of Human Ecology, Chang Gung University of Science and Technology, Tao-Yuan, Taiwan;
13. Graduate Institute of Pathology and Parasitology, National Defense Medical Center, Taipei, Taiwan

✉ Corresponding author: Wei-Ning Lin, Ph.D. Graduate Institute of Biomedical and Pharmaceutical Science, College of Medicine, Fu Jen Catholic University, No. 510 Zhongzheng Road, Xinzhuang District, New Taipei City 242, Taiwan. TEL (02) 29053398 FAX (02) 29053412 E-Mail: 081551@mail.fju.edu.tw

© Ivyspring International Publisher. This is an open access article distributed under the terms of the Creative Commons Attribution (CC BY-NC) license (<https://creativecommons.org/licenses/by-nc/4.0/>). See <http://ivyspring.com/terms> for full terms and conditions.

Received: 2017.11.28; Accepted: 2018.12.04; Published: 2019.01.01

## Abstract

The proliferation and adipogenesis of preadipocytes played important roles in the development of adipose tissue and contributed much to the processes of obesity. On the other hand, lipopolysaccharide (LPS), also known as endotoxin, is a key outer membrane component of gram-negative bacteria in the gut microbiota, and has a dominant role in linking inflammation to high-fat diet-induced metabolic syndrome. Studies suggested the potential roles of LPS in hepatic steatosis and in obese mice models. However, the molecular mechanisms underlying LPS-regulated obesity remained largely unknown. Here we reported that LPS stimulated expression of cytosolic phospholipase A2 (cPLA2), one of inflammation regulators of obesity, in the preadipocytes. Pretreatment the inhibitors of JAK2, STAT3, STAT5 or AMPK significantly reduced LPS-increased mRNA and protein expression of cPLA2 together with phosphorylation of JAK2, STAT3, STAT5 and AMPK, separately. Similarly, transfection of siRNA against JAK2 or AMPK abolished expression of cPLA2 and phosphorylation of JAK2 or AMPK together with downregulated expression of JAK2 and AMPK protein. LPS enhanced activation of STAT3 and STAT5 via JAK2-dependent manner in the preadipocytes. Transfection of JAK2 or AMPK siRNA further proofed the independence of JAK2 and AMPK in LPS-treated preadipocytes. In addition, LPS-increased DNA synthesis, cell numbers and cell viability of preadipocytes were attenuated by AACOCF3, AG490, BML-275, cPLA2 siRNA, JAK2 siRNA or AMPK siRNA. Attenuation JAK2/STAT or AMPK-dependent cPLA2 expression reduced LPS-mediated adipogenesis of preadipocytes. Stimulation of arachidonic acid or AMPK activator, A-769662, increased cell numbers and cell viability and promoted differentiation of preadipocytes. Collectively, these results indicated that LPS increased preadipocytes proliferation and adipogenesis via JAK/STAT and AMPK-dependent cPLA2 expression. The mechanisms of LPS-stimulated cPLA2 expression may be a link between bacteria and obesity and provides the molecular basis for preventing metabolic syndrome or hyperplastic obesity.

Key words: cPLA2, Lipopolysaccharide, Adipocyte, Proliferation, Adipogenesis



## Introduction

Obesity, defined as “abnormal or excessive fat accumulation, is a chronic disease and a worldwide epidemic problem. Obesity contributes to the development of a group of potentially life-threatening conditions including, insulin resistance, Type 2 Diabetes Mellitus, dyslipidemia, cardiovascular disease, metabolic syndrome, nonalcoholic fatty liver disease, osteoarthritis, stillbirth, and some cancer [1-3]. Adipose tissue consists of approximately one-third of mature adipocytes and two-thirds of stromal cells including macrophages, fibroblasts, endothelial cells and preadipocytes [4]. Preadipocytes originate from a multi-potent stem cell of mesodermal origin and function as source of new fat cells persists during the entire human life. The cellular changes of adipose tissue in obesity include fat depot hypertrophy (increase in adipocyte volumes) and hyperplasia (increase in adipocyte numbers) [5, 6]. Excess triglyceride accumulation in existing adipocytes due to a positive energy balance (energy intake in excess of energy expenditure) results in hypertrophy. On the other way, hyperplasia, regarded as ‘adipogenesis’, results from the recruitment of new adipocytes from precursor cells in adipose tissue and involves the proliferation and differentiation of preadipocytes [5]. Because increase in adipocyte number from preadipocyte proliferation and differentiation may result in more units to storage lipid. Hyperplastic fat expansion with poorest prognosis for treatment is addressed as more important than hypertrophic expansion [5].

The proliferation of preadipocytes was tightly regulated. In addition to the action of various hormone, several cytokines such as transforming growth factor- $\beta$  (TGF $\beta$ ), tumor necrosis factor- $\alpha$  (TNF- $\alpha$ ), macrophage colony-stimulating factor (MCSF), angiotensin II, basic fibroblast growth factor (bFGF) and bone morphogenetic protein (BMP) are reported to positively or negatively regulating adipocyte proliferation [7-16]. Lipopolysaccharide (LPS), also known as endotoxin, is a key component of the outer membranes of gram-negative bacteria and has a dominant role in the host responding to gram-negative bacterial infection. It is proposed that LPS derived from gram-negative bacteria residing in the gut microbiota acts as a triggering factor linking inflammation to high-fat diet-induced metabolic syndrome [17]. Studies found that a high-fat diet in mice increases endotoxemia and affect intestinal bacterial populations by favoring an increase in the gram-negative to gram-positive ratio. And chronic metabolic endotoxemia induces obesity, insulin resistance, and diabetes [17]. Similarly, treatment of

rats with polymyxin B, an antibiotic that specifically targets gram-negative organisms, is shown to reduce LPS concentration and hepatic steatosis [18]. In culture system, LPS stimulates the expression and secretion of serum amyloid A, LPS binding protein, soluble CD4 and RANTES (a chemokine) in adipocytes [19]. Similar results also show in ob/ob mice or high-fat-diet mice model that intravenous injection of LPS increase the level of serum amyloid A, LPS binding protein, soluble CD4 and RANTES in plasma [19]. Although several reports implied the participation of LPS on obesity, the cellular mechanisms are still largely unknown. Moreover, the role of AMP-activated protein kinase (AMPK) in preadipocytes proliferation and adipogenesis is controversial. It is found that AMPK inhibitor cannot prevent the inhibition effects of EGCG on insulin growth factor-stimulated preadipocyte proliferation [20]. However, AMPK siRNA reversed ursolic acid-inhibited adipogenesis [21]. Thus, AMPK differently contributed to the preadipocytes proliferation and adipogenesis. Whether AMPK involved in LPS-regulated preadipocytes proliferation and adipogenesis was less evaluated.

Cytosolic phospholipase A2 (cPLA2), one of inflammation regulators, contributes to inflammation via upregulating the production of arachidonic acid (AA) and the following eicosanoid. It is found that expression of cPLA2 facilitates the infiltration of neutrophils into adipose tissue [22]. cPLA2 contributes to the process of adipogenesis by promoting the proliferation of preadipocytes and cell cycle progress [23]. Expression of cPLA2 is regulated by Janus tyrosine kinase (JAK)2 that inhibition of JAK2 activation by AG490 abolishes TNF- $\alpha$  and IL-5-regulated cPLA2 expression in human pulmonary alveolar epithelial cells and eosinophils, separately [24, 25]. Also, AG490 suppresses the phosphorylation of signal transducer and activator of transcription (STAT)-3, and both AG490 and dominant-negative mutant of STAT-3 attenuated expression of cPLA2, AA release, and DNA synthesis in PDGF-BB-stimulated vascular smooth muscle cells [26]. In addition, STAT-5 is also reported to be one of JAK2 downstream molecules that may opsonize the effects of LPS [27]. It is found that NVP-BSK805, a specific JAK2 inhibitor, suppressed STAT5 phosphorylation and microglia survival in response to LPS [28]. Whether activation of JAK/STAT pathway involved in LPS-regulated preadipocytes proliferation and adipogenesis was less studied.

In this study, we determined the effects of LPS on preadipocytes proliferation and adipogenesis together with the related molecular mechanisms. Here we reported that LPS increased expression of cPLA2

gene via activation of AMPK and JAK/STAT pathway. Suppression the phosphorylation of AMPK and JAK2 or inhibition of cPLA2 attenuated LPS-stimulated preadipocytes proliferation and adipogenesis. Collectively, LPS contributed to hyperplastic obesity via AMPK and JAK/STAT-dependent activation of cPLA2 gene.

## Materials and methods

### Materials

Fetal bovine serum (FBS), DMEM medium, and TRIZOL were purchased from Invitrogen (Carlsbad, CA, USA). Antibodies against cPLA2 (SC-454), p-JAK2 (SC-21870), p-STAT3 (SC-8059), p-STAT5 (SC-101806) and GAPDH (SC-32233) were obtained from Santa Cruz Biotechnology (Santa Cruz, CA, USA). PhosphoPlus AMPK antibody (#43705) kits were obtained from New England Biolabs (Beverly, MA, USA). AG490, WP1066, STAT5-I, BML-275 and AACOCF3 were obtained from Biomol (Plymouth Meeting, PA, USA). Hybond C membrane and Hyperfilms were obtained from GE Healthcare Biosciences (Buckinghamshire, UK). siRNA of scrambled, AMPK, JAK2, and cPLA2 were purchased from MDBio, Inc. (Taipei, Taiwan). An enhanced chemiluminescence (ECL) Western blotting detection system was obtained from Visual Protein Biotechnology Co. (Taipei, Taiwan). XTT assay kit was purchased from Biological Industries (Beth-Haemek, Israel). LPS, enzymes and other chemicals were obtained from Sigma (St. Louis, MO, USA).

### Cell culture and adipogenesis

3T3-L1 preadipocytes were purchased from Food Industry Research and Development Institute (Hsinchu, Taiwan) and cultured in 37 °C, 5% CO<sub>2</sub> with DMEM medium containing 10% FBS. Differentiation of preadipocytes to adipocytes was induced by incubating cells in differentiation medium (DM)-I (DMEM medium containing 0.5 mM of methylisobutylxanthine, 1 µg/ml of insulin, 0.25 µM of dexamethasone) for 48 h. And then cells were changed to DM-II medium (DMEM medium containing 1 µg/ml of insulin) for another 2 to 6 days. Mature adipocytes was confirmed by Oil Red O (from sigma)-stained fat droplets in the cytoplasm.

### Oil Red O stain

At the end of differentiation, adipocytes were washed with PBS and fixed with 10% formalin by incubating 1 h at RT. At the end of incubation, formalin was removed and washed with 60% isopropanol once. Then Oil Red O working solution (from invitrogen) was added into cells for 10 min then

washed out by H<sub>2</sub>O four times. Lipids appeared in red and cells were viewed on a phase contrast microscope (DMI 3000 B; Leica, Wetzlar, Germany). For quantification the amount of lipid in adipocytes, Oil Red O was eluted by adding 100% isopropanol for 10 min. After pipet up and down to sure that all Oil Red O was in the solution, the isopropanol with Oil Red O was transfer to 96-well plate and measure OD at 490 nm by Epoch™ Multi-Volume Spectrophotometer System (BioTek, Vermont, USA). 100% isopropanol was used as blank control.

### Transfection with small interference RNA (siRNA)

3T3-L1 cells were plated in 3 X 10<sup>5</sup> cells/mL (1 mL/well) in 12-well culture plates for 24 h, reaching approximately 80% confluence [29]. The cells were replaced with 0.4 mL of DMEM containing 10% FBS. The DNA Metafectene reagent complex was prepared according to manufacturer instructions (Biontex, Martinsried, Planegg, Germany). The amount of transfected DNA was maintained constant with 100 nM scrambled, AMPK, JAK2, or cPLA2 siRNA for each well. The sense sequences of siRNA used are as follows: JAK2: CGGGUCGGCGCAACCUAAGAU UAAU; AMPKα: AUGAUGUCAGAUGGUGAA UUU; cPLA2: CGAGACACUCAAUAAUGAUU; and scramble: UUCUCCGAACGUGUCACGU. The DNA METAFECTENE complex (0.1 mL) was added to each well and then incubated at 37 °C for 24 h. After 24 h of transfection, the cells were washed with PBS and maintained in DMEM medium for 72 h (before treatment with LPS for the indicated time intervals).

### Cell lysate extraction and Western blot

After treatment, the cells were then rapidly washed with ice-cold PBS, scraped, and collected by centrifugation at 1,000 g for 10 min. The collected cells were lysed with ice-cold lysis buffer. The lysates were centrifuged at 4,500 g for 1 h at 4 °C to yield the whole cell extract. Samples from these supernatant fractions (30 µg protein) were subjected to SDS-PAGE using a 10% running gel. Proteins were transferred to nitrocellulose membrane, and the membrane was incubated successively at room temperature with 5% BSA in Tris-buffered saline with 0.1% Tween 20 (TTBS) for 1 h. Membranes were incubated overnight at 4°C with an anti-cPLA2, anti-COX-2, anti-phospho-AMPK, anti-phospho-JAK2, anti-phospho-STAT3, anti-phospho-STAT5, or anti-GAPDH according to the recommendation of the manufacturer. Membranes were incubated with a 1:2,000 dilution of anti-mouse or anti-rabbit horseradish peroxidase antibody for 1 h. The immunoreactive bands detected by ECL reagents were developed by Hyperfilm-ECL.

### RNA extraction and semi-quantified PCR

Total RNA was extracted from 3T3-L1 cells using Trizol, as previously described [30]. The cDNA containing 2 µg of RNA was used as a template to analyze cPLA2 mRNA level. Oligonucleotide primers for β-actin and cPLA2 were as follows: for β-actin: 5'-GGCAT TGTTA CCAAC TGGGA CGAC-3' (sense), 5'-GGCAT TGTTA CCAAC TGGGA CGAC-3' (antisense); for cPLA2: 5'-GTGAG GGGCT TTATT CCACA-3' (sense), 5'-GGTGA GAGTA CAAGG TTGAC A-3' (antisense). The amplification profile included one cycle of initial denaturation at 94 °C for 5 min, 30 cycles of denaturation at 94 °C for 1 min, primer annealing at 55 °C (cPLA2) and 60 °C (β-actin) for 1 min, extension at 72 °C for 1 min, and then one cycle of final extension at 72 °C for 5 min. The expression of β-actin was used as an internal control for the assay of a constitutively expressed gene.

### Cell viability assay and cell number counts

The working solution of XTT assay kit was prepared as manufacturer's direction. The Cultured cells (5000 cells/well) were treated with or without various inhibitors and then incubated with LPS for 48 h. At the end of incubation, 50 µL of XTT kit reaction solution was added into each well and incubated in an incubator for 2 h. The absorbance of each well was detected at OD450 and OD630 (reference absorbance) by Epoch™ Multi-Volume Spectrophotometer System (BioTek, Vermont, USA). Or cells were cultured in 6-cm dishes, and incubated with various treatments. At the end of stimulation, cell numbers were counted by HoloMonitor M4 (Phase Holographic Imaging PHI AB, Lund, Sweden).

### Bromodeoxyuridine (BrdU) incorporation assay

10 µM BrdU labeled cells were pretreated with various inhibitors and then incubated with 20 µg/mL of LPS for 48 h. At the end of treatment, cells were washed 3 times with PBS followed by methanol fixation and permeabilization for 20 minutes at -20°C. After washing cells, anti-BrdU antibody (1:100) was added for 1 h at 37°C. After washes, the FITC-conjugated secondary antibody were added at 1:200 at 37°C for 1 h. Cells were visualized under a fluorescence microscope (DMI 3000 B; Leica, Wetzlar, Germany).

### Statistical Analysis of Data

All data are expressed as the mean ± standard error of the mean by using the GraphPad Prism Program (GraphPad, San Diego, CA, USA) [30]. Quantitative data were analyzed using one-way

ANOVA followed by Tukey's post hoc test at a  $p < 0.05$  level of significance. All of the experiments were performed at least 5 times.

## Results

### LPS stimulated expression of cPLA2 in preadipocytes

It is reported that endotoxemia occurs in high-fat diet-fed mice and chronic metabolic endotoxemia induces obesity, insulin resistance, and diabetes [17]. LPS, also known as endotoxin, is the key component of the outer membranes of gram-negative bacteria and plays important roles in inducing host responses against infection. On the other hand, cPLA2 shows a proadipogenic function in regulating the process of adipogenesis [23]. The ability whether LPS promoted cPLA2 expression in preadipocytes were determined. Low serum-growth arrested cells were stimulated by 20 or 10 µg/mL of LPS for 0, 2, 4, 6, 16 or 24 h. At the end of incubation, cells were washed and cell lysates were extracted. Protein lysates were subjected into 10% SDS-PAGE and Western blot was performed with the usage of anti-cPLA2 antibody. We found that LPS stimulated expression of cPLA2 protein in a time-dependent manner with maximum response occurred after 16 h of stimulation (Fig. 1A). In addition, to detect whether LPS mediated cPLA2 mRNA expression in preadipocytes, cells were treated with 20 µg/mL of LPS for 0, 0.5, 1, 2, 4 or 6 h. RT-PCR was performed to detect the mRNA expression of cPLA2. As showed in Fig. 1B, LPS induced increased expression of cPLA2 mRNA in preadipocytes with maximum responses at the end of studied time point. Thus, LPS increased cPLA2 gene expression in preadipocytes.

### LPS mediated cPLA2 expression via activation of JAK2 kinase

It is reported that expression of cPLA2 gene is mediated by TNF-α or IL-5-increased JAK2 activity [24, 25]. To elucidate whether LPS increased phosphorylation of JAK2 in 3T3-L1 cells, serum-starved cells were treated with 20 µg/mL of LPS for 0, 1, 2, 4, 6 or 8 h. Phosphorylation of JAK2 was detected by Western blot with anti-phospho-JAK2 antibody. Phosphorylation of JAK2 began as early as 2 h after LPS stimulation, and sustained to 8 h. Pretreatment of AG490, inhibitor of JAK2, significantly attenuated LPS-regulated JAK2 phosphorylation in 3T3-L1 cells (Fig. 2A). Similarly, transfection of JAK2 siRNA down-regulated JAK2 protein expression together with abolished JAK2 phosphorylation in LPS-stimulated preadipocytes (Fig. 2B). To evaluate whether JAK2 involve in



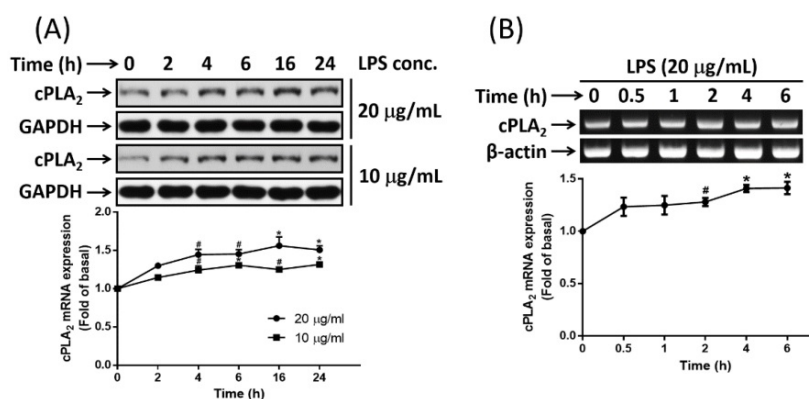


**Figure 1. LPS enhanced cPLA<sub>2</sub> gene expression in 3T3-L1 cells.** Serum-starved 3T3-L1 cells were stimulated with different concentrations of LPS for the indicated time points. At the end of incubation, cells were harvested and cell lysates or mRNA were extracted. (A) Western blot was used to evaluate the expression of cPLA<sub>2</sub> protein. (B) RT-PCR was used to analyze the expression of cPLA<sub>2</sub> mRNA. Data are expressed as means ± SEM of at least 3 independent experiments (n≥3). #P < 0.01, \*P < 0.05, as compared with the basal group.

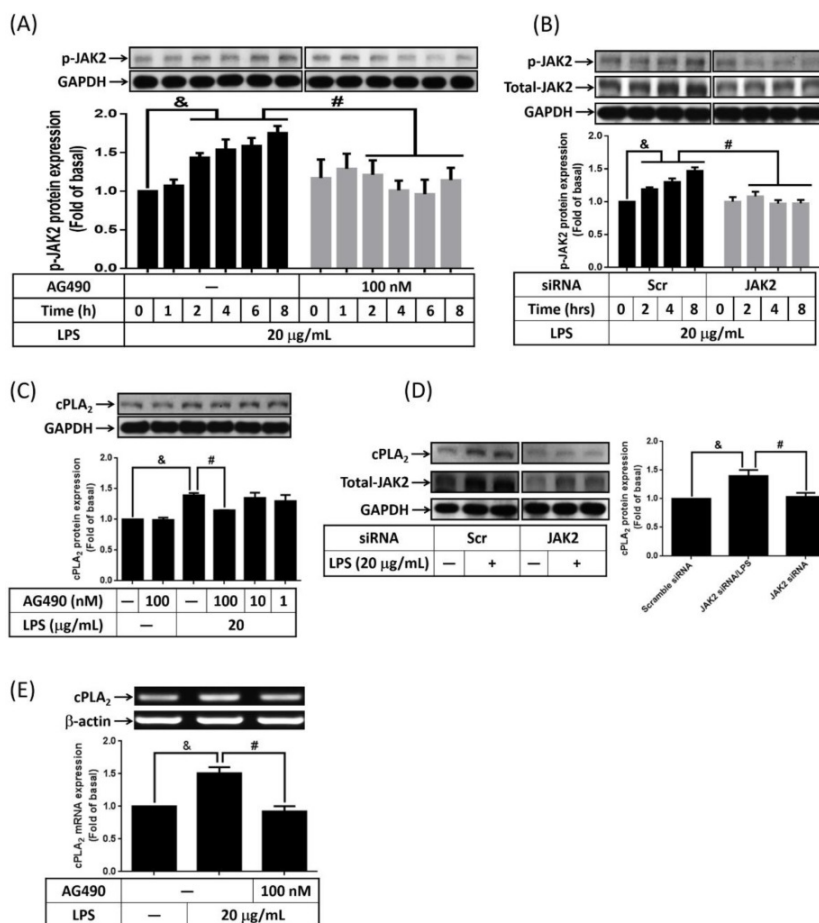


**Figure 2. LPS modulated cPLA<sub>2</sub> gene expression via activation of JAK2.** Serum-starved 3T3-L1 cells were pretreated with 100 nM or different concentrations of AG490 for 1 h. Or cells were transfected with 100 nM of scramble (Scr) or JAK2 siRNA for 24 h. Inhibitor or siRNA-treated cells were then incubated 20 µg/mL of LPS for the indicated time points (A, B), 16 h (C, D) or 6 h (E). At the end of incubation, cells were harvested and cell lysates or mRNA were extracted. (A, B, C, D) Western blot was used to evaluate the expression of phosphorylated JAK2, total JAK2, cPLA<sub>2</sub> or GAPDH protein. (E) RT-PCR was used to analyze the expression of cPLA<sub>2</sub> mRNA. Data are expressed as means ± SEM of at least 3 independent experiments (n≥3). &P < 0.05, as compared with the 0 point or indicated group. #P < 0.05, as compared with the same time points or LPS treated alone.

LPS-stimulated cPLA<sub>2</sub> expression, cells were pretreated with AG490 for 1 h. After treated with 20 µg/mL of LPS for another 16 h, cell lysates were collected and subjected into 10% SDS-PAGE. As showed in Fig. 2C, AG490 significantly attenuated LPS-induced cPLA<sub>2</sub> expression. Transfection of JAK2

siRNA also reduced LPS-regulated cPLA<sub>2</sub> expression (Fig. 2D). Similarly, blockage JAK2 by AG490 obviously reduced LPS-regulated cPLA<sub>2</sub> mRNA expression (Fig. 2E). These data suggested that LPS enhanced cPLA<sub>2</sub> gene expression via activation of JAK2 in preadipocytes.

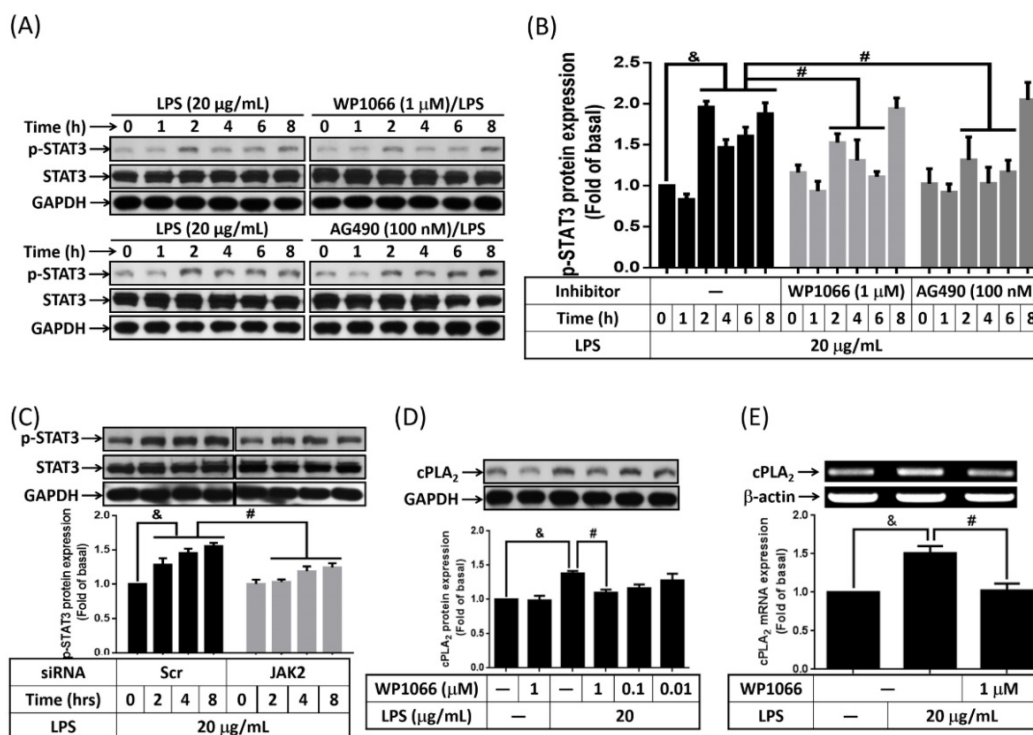


**Figure 3. Activation of STAT3 contributed to LPS-regulated cPLA<sub>2</sub> gene expression.** Serum-starved 3T3-L1 cells were pretreated with AG490 (100 nM) or WP1066 (1 µM or different concentration) for 1 h. Or cells were transfected with 100 nM of scramble (Scr) or siRNA for 24 h. At the end of inhibitor or siRNA treatment, cells were incubated 20 µg/mL of LPS for the indicated time points (A, B, C), 16 h (D) or 6 h (E). Cells were harvested and cell lysates or mRNA were extracted. (A, C, D) Western blot was used to evaluate the phosphorylation of STAT3, total STAT3 or cPLA<sub>2</sub> protein. (B) The phosphorylated STAT3 was quantified and showed as bar graph. (E) RT-PCR was used to analyze the expression of cPLA<sub>2</sub> mRNA. Data are expressed as means ± SEM of at least 3 independent experiments (n ≥ 3). &P < 0.05, as compared with the 0 point group or the indicated group. #P < 0.05, as compared with the same time points or LPS treated alone.

### Involvement of STAT3 in LPS-stimulated cPLA<sub>2</sub> expression

STAT3 is one of JAK2 downstream signaling molecular that regulating PDGF-BB-stimulated cPLA<sub>2</sub> expression in vascular smooth muscle cells [26]. Whether LPS increased cPLA<sub>2</sub> expression via JAK2-dependent activation of STAT3 was investigated in preadipocytes. Serum-starved 3T3-L1 cells were stimulated by 20 µg/mL of LPS for 0, 1, 2, 4, 6, or 8 h. The phosphorylation of STAT3 was detected by Western blot with anti-phospho-STAT3 antibody. LPS increased STAT phosphorylation was detected as early as 2 h after stimulation. Pretreatment of WP1066 (inhibitor of STAT3) or AG490 significantly decreased STAT3 phosphorylation in LPS-stimulated cells (Fig. 3A and B). Moreover, JAK2 siRNA transfection decreased STAT3 phosphorylation level in LPS-treated preadipocytes (Fig. 3C). To ensure the role of STAT3 in regulating LPS-induced cPLA<sub>2</sub> gene expression, cells were pretreated with different concentrations or 1 µM of WP1066 for 1 h, then incubated with LPS for 16 h or 6 h. We found that LPS-stimulated cPLA<sub>2</sub> protein expression was significantly reduced by WP1066 (Fig. 3D). Similarly, inhibition of STAT3 by WP1066 significantly attenuated cPLA<sub>2</sub> mRNA expression in LPS-treated

cells (Fig. 3E). Briefly, these data suggested that the participation of STAT3 in LPS-stimulated cPLA<sub>2</sub> expression.

### Activation of STAT5 in LPS-increased cPLA<sub>2</sub> expression

Activation inhibition of STAT5 by peroxiredoxin V-dependent suppression of JAK2 attenuated LPS-induced immune response [27]. Whether LPS activated STAT5 in preadipocytes was studied. Cells were treated with or without AG490 or STAT5-I (inhibitor of STAT5) for 1 h, and then stimulated by 20 µg/mL of LPS for the indicated time intervals. Phosphorylation of STAT5 was detected by Western blot. As showed in Fig. 4A and B, LPS increased phosphorylation of STAT5 as early as 2 h after treatment, and sustained to 8 h. Pretreatment of STAT5-I and AG490 significantly attenuate LPS-induced phosphorylation of STAT5 in preadipocytes (Fig. 4A and B). LPS-increased phosphorylation of STAT5 also be reduced by transfection of JAK2 siRNA (Fig. 4C). To know whether activated STAT5 contributed to LPS-increased expression of cPLA<sub>2</sub> gene, cells were pretreated with various concentrations or 10 µM of STAT5-I for 1 h, and incubated with LPS for 16 or 6 h. Protein lysates or mRNA were extracted and analyzed



by Western blot and RT-PCR, separately. LPS-enhanced expression of cPLA2 protein and mRNA was significantly reversed by STAT5-I (Fig. 4D and E). Collectively, these data revealed that LPS regulated cPLA2 gene expression via activation of JAK/STAT5 pathway.

### Participation of AMPK in LPS-enhanced cPLA2 expression

The role of AMPK in LPS-promoted hyperplasia obesity is controversial. It is reported that inhibition of AMPK reversed ursolic acid but not EGCG effects of adipogenesis [20, 21]. The effects of LPS on AMPK activity was examined on preadipocytes, cells were pretreated with AMPK inhibitor, BML-275, for 1 h, and then incubated with LPS for the indicated time points. Or AMPK siRNA transfected cells were incubated with 20  $\mu\text{g}/\text{mL}$  of LPS for the indicated time points. After harvested, cells lysates were subjected into 10% SDS-PAGE. Western blot was performed with the usage of anti-phospho-AMPK. LPS increased phosphorylation of AMPK in preadipocytes, which was significantly attenuated by BML-275 (Fig. 5A). Similarly, LPS-increased AMPK phosphorylation was abolished by knockdown AMPK (Fig. 5B). To delink the relationship between

AMPK and cPLA2 expression in LPS-regulated preadipocytes, cells were pretreated with different concentrations or 100 nM of BML-275 for 1 h or cells were transfected with 100 nM scramble or AMPK siRNA. After treated with 20  $\mu\text{g}/\text{mL}$  of LPS, cell lysates or mRNA were collected and analyzed. LPS-increased expression of cPLA2 was significantly attenuated by BML-275 (Fig. 5C) or AMPK siRNA (Fig. 5D). Similarly, pretreatment of BML-275 reversed cPLA2 mRNA expression in LPS-stimulated preadipocytes (Fig. 5E). These data suggested that LPS induced cPLA2 gene expression via activation of AMPK in preadipocytes. To distinguish the relationship between AMPK and JAK2 activation in LPS-treated cells. Preadipocytes were transfected with scramble, AMPK or JAK2 siRNA and then incubated with LPS for the indicated time points. Knockdown AMPK protein did not attenuated LPS-increased JAK2 phosphorylation (Fig. 5F). In addition, LPS-stimulated AMPK phosphorylation did not affected by knock down JAK2 protein (Fig. 5B), suggested the independence of AMPK and JAK2 in LPS-treated preadipocytes. Collectively, LPS enhanced cPLA2 gene expression via two manners, JAK2 and AMPK.

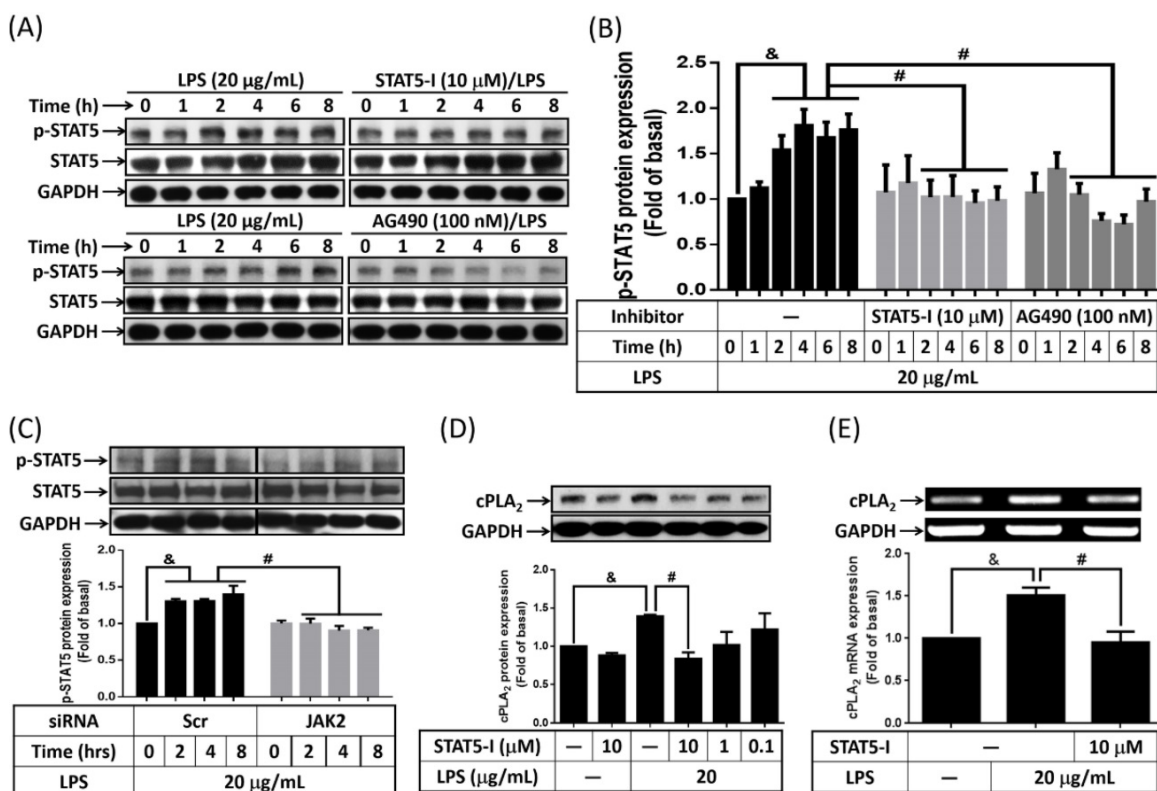


**Figure 4. Participation of STAT5 in LPS-mediated cPLA<sub>2</sub> gene expression.** Serum-starved 3T3-L1 cells were pretreated with AG490 (100 nM) or STAT5-I (10  $\mu\text{M}$  or different concentration) for 1 h. Or cells were transfected with 100 nM of scramble (Scr) or JAK2 siRNA for 24 h. After inhibitor or siRNA treatment, cells were incubated with 20  $\mu\text{g}/\text{mL}$  of LPS for the indicated time points (A, B, C), 16 h (D) or 6 h (E). Protein lysates or mRNA were extracted. (A, C, D) Western blot was used to evaluate the phosphorylation of STAT5, total STAT5 or cPLA<sub>2</sub> protein. (B) The phosphorylated STAT5 was quantified and showed as bar graph. (E) RT-PCR was used to analyze the expression of cPLA<sub>2</sub> mRNA. Data are expressed as means  $\pm$  SEM of at least 3 independent experiments ( $n \geq 3$ ). &P < 0.05, as compared with the 0 point group or the indicated group. #P < 0.05, as compared with the same time points or LPS treated alone.

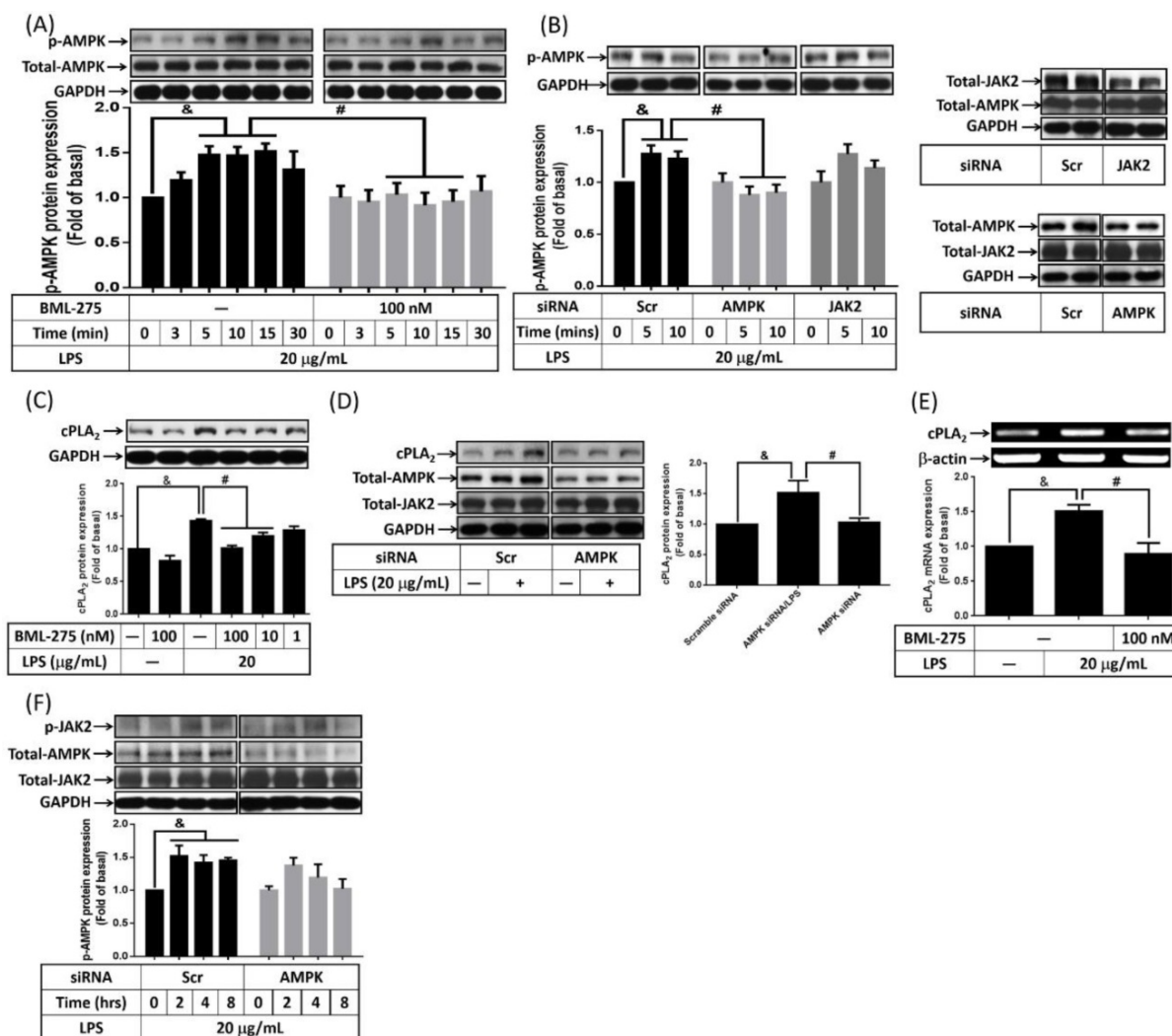


**Figure 5. LPS increased cPLA<sub>2</sub> gene expression through activation of AMPK.** Serum-starved 3T3-L1 cells were pretreated with BML-275 (100 nM or different concentration) for 1 h or transfected with 100 nM of scramble (Scr) or AMPK siRNA for 24 h, then incubated 20 µg/mL of LPS for the indicated time points (A, B, F), 16 h (C, D) or 6 h (E). At the end of incubation, cells were harvested and cell lysates or mRNA were extracted. (A, B, C, D, F) Western blot was used to evaluate the expression of p-AMPK, total-AMPK, p-JAK2, total-JAK2, cPLA<sub>2</sub> or GAPDH. (E) RT-PCR was used to analyze the expression of cPLA<sub>2</sub> mRNA. Data are expressed as means ± SEM of at least 3 independent experiments (n≥3). &P < 0.05, as compared with the 0 point group or control group. #P < 0.05, as compared with the same time points or LPS treated alone.

### Attenuation of LPS-increased cell proliferation by blockage JAK2/AMPK-dependent cPLA<sub>2</sub> expression

To study whether LPS-increased cPLA<sub>2</sub> gene expression contributed to proliferation of preadipocytes, 10 µM BrdU-labeled cells were pretreated with AACOCF<sub>3</sub>, inhibitor of cPLA<sub>2</sub> for 1 h, and then stimulated by LPS for 48 h. The BrdU incorporation was observed by fluorescence microscope. LPS increased the DNA synthesis or preadipocytes, which was reversed by AACOCF<sub>3</sub> (Fig. 6A). This suggested that LPS facilitated preadipocyte proliferation via cPLA<sub>2</sub> protein. Similarly, pretreatment of AG490 and BML-275 both attenuated LPS-stimulated DNA synthesis in preadipocytes (Fig. 6A). In the aspect of cell counts, pretreatment of AACOCF<sub>2</sub>, AG490 or BML-275 significantly reduced LPS-increased cell numbers of

preadipocytes (Fig. 6B and C). Cell viability assay also revealed that LPS increased the viability of preadipocytes, which was significantly reduced by pretreatment of AACOCF<sub>3</sub>, AG490 or BML-275 (Fig. 6D). To ascertain whether LPS promoted cell proliferation via JAK2 and AMPK-regulated cPLA<sub>2</sub> gene, cells were transfected with siRNA of scramble, cPLA<sub>2</sub>, JAK2 or AMPK, and then incubated with LPS. Transfection of cPLA<sub>2</sub> siRNA significantly reduced cPLA<sub>2</sub> expression in LPS-treated cells (Fig. 6E). We found that LPS-increased cell numbers and viability were significantly reversed by knockdown expression of cPLA<sub>2</sub>, JAK2 or AMPK protein (Fig. 6F, G and H). Furthermore, Application of arachidonic acid increased cell numbers and viability of preadipocytes (Fig. 6I, J and K). These data revealed that LPS enhanced proliferation of preadipocytes via JAK2 and AMPK-regulated cPLA<sub>2</sub> protein.

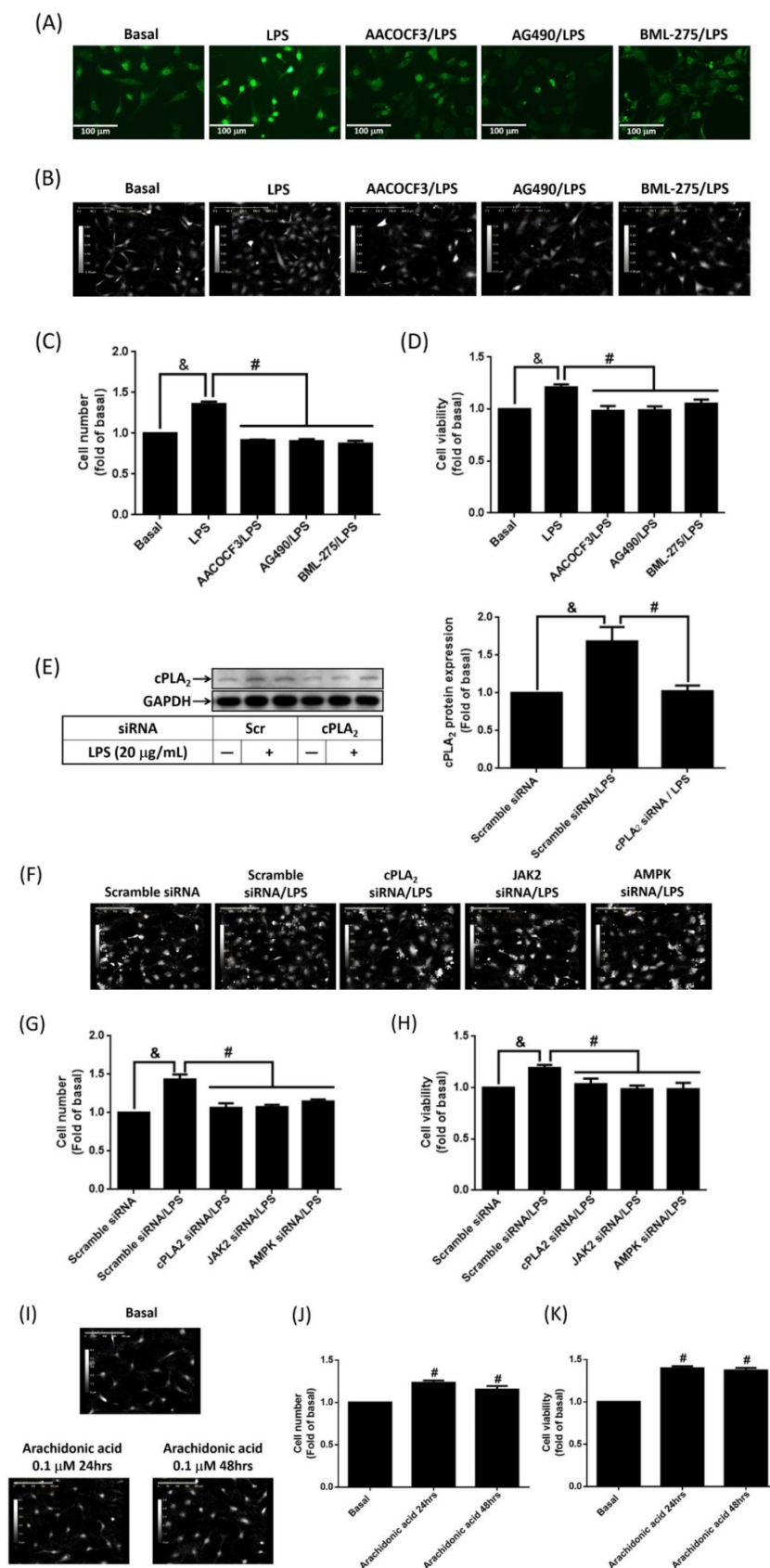


**Figure 6. LPS enhanced proliferation of preadipocytes via JAK2 and AMPK-regulated cPLA<sub>2</sub> protein.** Serum-starved 3T3-L1 cells were pretreated with AACOCF3 (1  $\mu$ M), AG490 (100 nM) or BML-275 (0.1  $\mu$ M) for 1 h. Or cells were transfected with siRNA against scramble, JAK2, AMPK or cPLA<sub>2</sub> for 24 h. Then cells were incubated 20  $\mu$ g/mL of LPS 48 h. Or, cells were incubated with 0.1  $\mu$ M of arachidonic acid for 0, 24 or 48 h. At the end of incubation, (A) BrdU incorporation assay, (B, F, I) HoloM4 system detection, (C, G, J) cell number counts, and (D, H, K) XTT assay were performed. (E) Western blot was used to detect the expression of cPLA<sub>2</sub>. Data are expressed as means  $\pm$  SEM of at least 3 independent experiments ( $n \geq 3$ ).  $P < 0.05$ , as compared with the control group or scramble siRNA transfected alone group.  $\#P < 0.05$ , as compared with the LPS treated alone or the basal group.



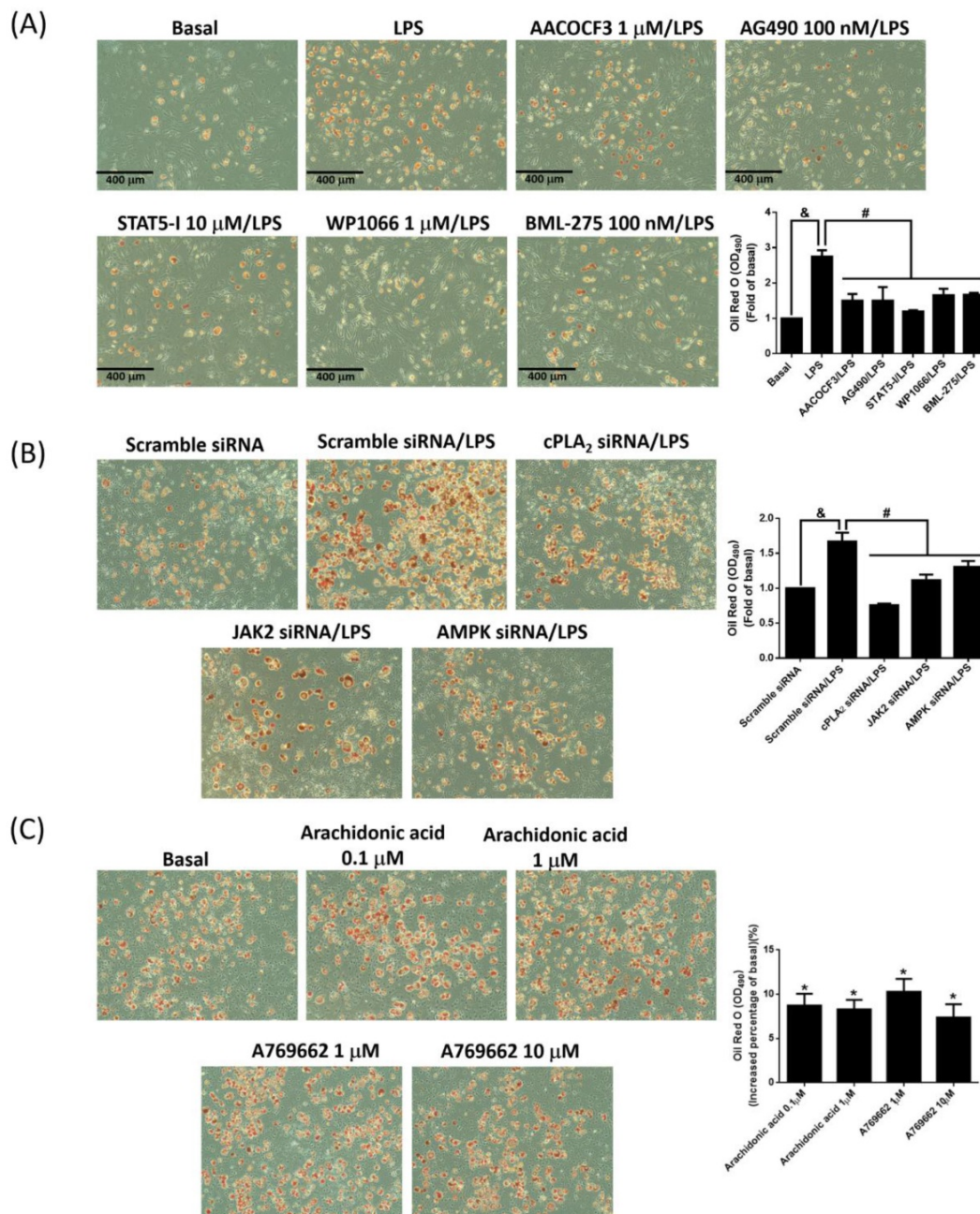


**Figure 7. LPS promoted adipogenesis via JAK/STAT and AMPK-dependent cPLA<sub>2</sub> expression.** (A) Serum-starved 3T3-L1 cells were pretreated with AACOCF3 (1 μM), AG490 (100 nM), STAT5-I (10 μM), WP1066 (1 μM) or BML-275 (0.1 μM) for 1 h. (B) Or cells were transfected with siRNA of scramble, cPLA<sub>2</sub>, JAK2 or AMPK for 24 h. Then, cells were incubated with 20 μg/mL of LPS 48 h. Or (C) cells were stimulated without or with arachidonic acid (0.1 or 1 μM) or A769662 (1 or 10 μM) for 24 h. At the end of incubation, the adipogenesis was performed with DM-I and DM-II medium. After the process of adipogenesis, the images were captured by microscope. Data are expressed as means ± SEM of at least 3 independent experiments (n≥3). &P < 0.05 or \*P < 0.05, as compared with the control group or scramble siRNA alone group. #P < 0.05, as compared with the LPS treated alone.

To evaluate whether LPS accelerated adipogenesis via JAK2/STAT and AMPK-dependent cPLA<sub>2</sub> expression, adipogenesis assay were performed with the addition of LPS alone or coexistence of various inhibitors or siRNAs. LPS increased the rates of adipogenesis, and attenuation of cPLA<sub>2</sub> activity reduced adipogenesis in LPS-stimulated preadipocytes (Fig. 7A). Consistently, inhibition cPLA<sub>2</sub> expression by blockage JAK2/STAT or AMPK pathway also reversed LPS-increased

adipogenesis (Fig. 7A). On the aspect of knockdown experiments, LPS-promoted adipogenesis were significantly blockage by protein knockdown of cPLA<sub>2</sub>, JAK2 or AMPK (Fig. 7B). Moreover, application of arachidonic acid or AMPK activator alone slightly increased the adipogenesis of preadipocytes (Fig. 7C). In summary, these data indicated that LPS increased proliferation and adipogenesis of preadipocytes via JAK2/STAT and AMPK-regulated cPLA<sub>2</sub> expression.

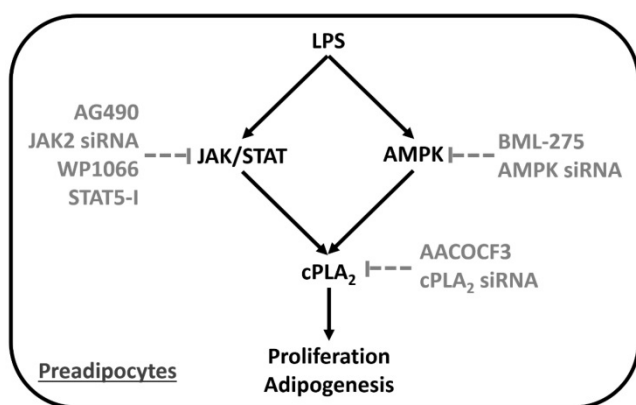


**Figure 8. Proposed model underlying LPS regulated preadipocyte proliferation and adipogenesis.** LPS increased preadipocyte proliferation and adipogenesis via induction of inflammatory gene, cPLA2, expression. Series studies revealed that LPS stimulated cPLA2 expression via activation JAK/STAT and AMPK in preadipocytes.

## Discussion

The obese problem of the world was getting worse, but the drug against weight gain was lack. The proliferation and adipogenesis of preadipocytes were the cellular changes of hypertrophic obesity. It is found that inflammation mediator, cPLA2, contributes to obesity by inducing the infiltration of neutrophil and adipogenesis [17, 23]. On the other hand, LPS from gut microbiota was reported as linker between inflammation and high-fat diet-induced metabolic syndrome [17]. However, whether LPS directly regulated proliferation and adipogenesis of preadipocytes via promoting cPLA2 gene expression and the related molecular mechanisms were less studied. Here we reported that LPS increased mRNA and protein expression of cPLA2 in preadipocytes. Blockage the activation of JAK2, STAT3, STAT5 or AMPK significantly attenuated LPS-induced cPLA2 expression together with phosphorylation of JAK2, STAT3, STAT5 and AMPK, separately. Inhibition of JAK2 also reduced phosphorylation level of STAT3 and STAT5 in LPS-treated preadipocytes, suggesting the upstream role of JAK2 on mediating STAT3 and STAT5 activation. Moreover, LPS-stimulated DNA synthesis, increased cell numbers and cell viability were attenuated by AACOCF3, AG490 or BML-275. Attenuation JAK2/STAT or AMPK-dependent cPLA2 expression reduced LPS-mediated adipogenesis of preadipocytes. These results indicated that LPS increased preadipocytes proliferation and adipogenesis via JAK/STAT and AMPK-dependent cPLA2 expression (Fig. 7).

Several studies reported the correlation of gut microbial composition and metabolic syndromes including obesity [31]. Microbiota-related LPS played roles in linking and regulating the inflammation and metabolic outcomes [17]. The serum levels of LPS

binding protein, LPB, were high in obese children than in nonobese controls [32]. LPS induced mRNA expression of cytokines and chemokines in stromal vascular (SV) cells including preadipocytes [33]. It is also been proved that LPS promoted the activation of immune cells in adipose tissue [34, 35]. However, the action of LPS directly on preadipocytes was less addressed. Here we reported that LPS directly increased proliferation and differentiation of preadipocytes. Moreover, LPS promoted cPLA2 expression in preadipocytes, and attenuation of cPLA2 abolished LPS-mediated proliferation and differentiation of preadipocytes, indicating that LPS accelerated increase of adipocytes numbers via up-regulating cPLA2 gene. These results were supported by the finding that increased adipogenesis in LPS-injected adipose tissue [36], and similar to the finding that LPS increased the expression of cytokine mRNA in preadipocytes [33]. And resembled to the finding that increased activation of inflammasome pathway in obesity of children and adolescents [37].

Activation of JAK/STAT participated in various physiological processes such as development and inflammation. It is reposted that knock down the expression of JAK2 and STAT3 attenuated adipogenesis [38, 39]. Dominant negative of STAT5 reduced adipogenesis of 3T3-L1 cells [40]. Here we found that inhibition of JAK2 reduced LPS-increased proliferation and adipogenesis of preadipocytes. LPS enhanced phosphorylation of STAT3 and STAT5 in a JAK2-dependent manner in 3T3-L1 cells. Reduced activation of JAK2/STAT pathway abolished LPS-regulated cPLA2 expression. These data revealed that LPS involved in pathologies of obesity via upregulated proliferation and adipogenesis of preadipocytes in a JAK2/STAT-dependent cPLA2 expression manner. It is found that knock out adipocyte JAK2 expression increased adiposity in both male and female mice via reducing lipolysis [39]. Constitutive activated STAT3 is found to reverse the development of brown adipose tissue in Tyk2(-/-) mice [41]. Specific deletion of STAT5 in adipocytes impaired lipid mobilization via transcription inactivation of adipose triglyceride lipase expression [42]. After affecting proliferation and differentiation of preadipocytes, whether LPS regulated lipolysis and development of brown adipose tissue will be studied in the future.

The roles of activated AMPK in obesity were controversial. It is reported that AMPK activators cannot increase the expression of p21 together with compound C-upregulated preadipocytes expansion [43]. Activation of AMPK contributed to germacrone-reduced adipogenesis [44]. It seems that the activation of AMPK in obesity was differentially



regulated in response to different treatments. Here we found that pretreatment of AMPK inhibitor attenuated LPS-increased cPLA2 expression together with proliferation and adipogenesis of preadipocytes. Activation of AMPK contributed to increased numbers of preadipocyte and adipocyte in response to LPS stimulation. This is different to what found on EGCG-stimulated preadipocytes that inhibitor of AMPK cannot reverse the proliferative effects of insulin growth factor [20]. However, ursolic acid-inhibited adipogenesis was reversed by AMPK siRNA [21]. High glucose promoted lipid accumulation of 3T3-L1 cells via substance P-activated AMPK [45]. Activation of AMPK may differently contribute to proliferation and adipogenesis of preadipocytes.

AMPK is reported as an energy sensor and regulator of metabolism, with the suppression of immune and inflammatory processes [46]. The inhibition effects of AMPK on cytokine-activated JAK/STAT had been proved in human fibrosarcoma cells and adipocytes [47, 48]. Thus, we further demonstrated the relationship of AMPK and JAK2 in LPS-stimulated preadipocytes. The usage of AMPK siRNA reduced LPS-regulated AMPK phosphorylation but did not attenuate JAK2 activation. On the other hand, knockdown protein expression of JAK2 did not reduce LPS-regulated AMPK phosphorylation. These results suggested the independence of activated AMPK and JAK2/STAT pathway in LPS-treated preadipocytes. This is resemble to the effects of LPS on the triple-negative breast cancer cell lines, MDA-MB-231 that both AMPK and JAK2 are activated [49]. Moreover, adipocyte-derived hormone leptin is also reported to activate both AMPK and JAK2 in hepatic cells and hypothalamus [50, 51]. Whether LPS facilitated the differentiation of preadipocytes via regulating leptin expression will be elucidated further.

Collectively, based on the literature and our findings, Fig. 7 showed a model that LPS facilitated proliferation and adipogenesis of preadipocytes via up-regulated cPLA2 expression. Activation of JAK/STAT or AMPK pathway were necessary for the expression of cPLA2. Inhibition of cPLA2 reduced LPS-mediated proliferation and adipogenesis of preadipocytes. Similarly, decreased activation of JAK/STAT or AMPK pathway attenuated LPS-stimulated cPLA2 expression together with proliferation and adipogenesis of preadipocytes. The mechanisms of LPS-stimulated cPLA2 expression may be a link between bacteria and obesity, suggesting novel strategies for treatment.

## Acknowledgements

This work was supported by grants 102-CGH-FJU-02 from Cathay General Hospital, Taiwan; 9991A01 from Fu Jen Catholic University Research Foundation, Taiwan; and NSC 102-2320-B-030-001 from Ministry of Science and Technology, Taiwan.

## Author Contributions

Chao-Chien Chang, Kee-Chin Sia, and Jia-Feng Chang performed the experiments; Chao-Chien Chang, Jia-Feng Chang, Chia-Mo Lin, and Wei-Ning Lin carried out the study design; Kee-Chin Sia, Chuen-Mao Yang and Kuo-Yang Huang help the set up of transfection assay. Wei-Ning Lin and Chao-Chien Chang wrote the manuscript. All authors approved the final version of the paper.

## Competing Interests

The authors have declared that no competing interest exists.

## References

- Ogden CL, Yanovski SZ, Carroll MD, Flegal KM. The epidemiology of obesity. *Gastroenterology*. 2007; 132: 2087-102.
- Bonomini F, Rodella LF, Rezzani R. Metabolic syndrome, aging and involvement of oxidative stress. *Aging Dis*. 2015; 6: 109-20.
- Wang K, Cao P, Wang H, Tang Z, Wang N, Wang J, et al. Chronic administration of Angelica sinensis polysaccharide effectively improves fatty liver and glucose homeostasis in high-fat diet-fed mice. *Scientific reports*. 2016; 6: 26229.
- Otto TC, Lane MD. Adipose development: from stem cell to adipocyte. *Critical reviews in biochemistry and molecular biology*. 2005; 40: 229-42.
- Hausman DB, DiGirolamo M, Bartness TJ, Hausman GJ, Martin RJ. The biology of white adipocyte proliferation. *Obes Rev*. 2001; 2: 239-54.
- Muir LA, Neeley CK, Meyer KA, Baker NA, Brosius AM, Washabaugh AR, et al. Adipose tissue fibrosis, hypertrophy, and hyperplasia: Correlations with diabetes in human obesity. *Obesity (Silver Spring, Md)*. 2016; 24: 597-605.
- Stewart A, Guan H, Yang K. BMP-3 promotes mesenchymal stem cell proliferation through the TGF-beta/activin signaling pathway. *Journal of cellular physiology*. 2010; 223: 658-66.
- Yan A, Avraham T, Zampell JC, Haviv YS, Weitman E, Mehrara BJ. Adipose-derived stem cells promote lymphangiogenesis in response to VEGF-C stimulation or TGF-beta1 inhibition. *Future oncology (London, England)*. 2011; 7: 1457-73.
- Xing H, Northrop JP, Grove JR, Kilpatrick KE, Su JL, Ringold GM. TNF alpha-mediated inhibition and reversal of adipocyte differentiation is accompanied by suppressed expression of PPARgamma without effects on Pref-1 expression. *Endocrinology*. 1997; 138: 2776-83.
- Wang X, Huang M, Wang Y. The effect of insulin, TNFalpha and DHA on the proliferation, differentiation and lipolysis of preadipocytes isolated from large yellow croaker (*Pseudosciaena crocea* R.). *PLoS One*. 2012; 7: e48069.
- Levine JA, Jensen MD, Eberhardt NL, O'Brien T. Adipocyte macrophage colony-stimulating factor is a mediator of adipose tissue growth. *The Journal of clinical investigation*. 1998; 101: 1557-64.
- Saint-Marc P, Kozak LP, Ailhaud G, Darimont C, Negrel R. Angiotensin II as a trophic factor of white adipose tissue: stimulation of adipose cell formation. *Endocrinology*. 2001; 142: 487-92.
- Janke J, Engeli S, Gorzelniak K, Luft FC, Sharma AM. Mature adipocytes inhibit in vitro differentiation of human preadipocytes via angiotensin type 1 receptors. *Diabetes*. 2002; 51: 1699-707.
- Hebert TL, Wu X, Yu G, Goh BC, Halvorsen YD, Wang Z, et al. Culture effects of epidermal growth factor (EGF) and basic fibroblast growth factor (bFGF) on cryopreserved human adipose-derived stromal/stem cell proliferation and adipogenesis. *Journal of tissue engineering and regenerative medicine*. 2009; 3: 553-61.
- Yamashiro H, Inamoto T, Yagi M, Ueno M, Kato H, Takeuchi M, et al. Efficient proliferation and adipose differentiation of human adipose tissue-derived vascular stromal cells transfected with basic fibroblast growth factor gene. *Tissue engineering*. 2003; 9: 881-92.
- Sethi JK. Activatin' human adipose progenitors in obesity. *Diabetes*. 2010; 59: 2354-7.

17. Cani PD, Amar J, Iglesias MA, Poggi M, Knauf C, Bastelica D, et al. Metabolic endotoxemia initiates obesity and insulin resistance. *Diabetes*. 2007; 56: 1761-72.
18. Pappo I, Becovier H, Berry EM, Freund HR. Polymyxin B reduces cecal flora, TNF production and hepatic steatosis during total parenteral nutrition in the rat. *The Journal of surgical research*. 1991; 51: 106-12.
19. Nakarai H, Yamashita A, Nagayasu S, Iwashita M, Kumamoto S, Ohyama H, et al. Adipocyte-macrophage interaction may mediate LPS-induced low-grade inflammation: potential link with metabolic complications. *Innate immunity*. 2012; 18: 164-70.
20. Ku HC, Liu HS, Hung PF, Chen CL, Liu HC, Chang HH, et al. Green tea (-)-epigallocatechin gallate inhibits IGF-I and IGF-II stimulation of 3T3-L1 preadipocyte mitogenesis via the 67-kDa laminin receptor, but not AMP-activated protein kinase pathway. *Molecular nutrition & food research*. 2012; 56: 580-92.
21. He Y, Li Y, Zhao T, Wang Y, Sun C. Ursolic acid inhibits adipogenesis in 3T3-L1 adipocytes through LKB1/AMPK pathway. *PLoS One*. 2013; 8: e70135.
22. Hadad N, Burgazliev O, Elgazar-Carmon V, Solomonov Y, Wueest S, Item F, et al. Induction of cytosolic phospholipase A2alpha is required for adipose neutrophil infiltration and hepatic insulin resistance early in the course of high-fat feeding. *Diabetes*. 2013; 62: 3053-63.
23. Pena L, Meana C, Astudillo AM, Lorden G, Valdearcos M, Sato H, et al. Critical role for cytosolic group IVA phospholipase A2 in early adipocyte differentiation and obesity. *Biochim Biophys Acta*. 2016; 1861: 1083-95.
24. Yang CM, Lee IT, Chi PL, Cheng SE, Hsiao LD, Hsu CK. TNF-alpha induces cytosolic phospholipase A2 expression via Jak2/PDGFR-dependent Elk-1/p300 activation in human lung epithelial cells. *Am J Physiol Lung Cell Mol Physiol*. 2014; 306: L543-51.
25. Zhu X, Jacobs B, Boetticher E, Myou S, Meliton A, Sano H, et al. IL-5-induced integrin adhesion of human eosinophils caused by ERK1/2-mediated activation of cPLA2. *J Leukoc Biol*. 2002; 72: 1046-53.
26. Yellaturu CR, Rao GN. Cytosolic phospholipase A2 is an effector of Jak/STAT signaling and is involved in platelet-derived growth factor BB-induced growth in vascular smooth muscle cells. *J Biol Chem*. 2003; 278: 9986-92.
27. Choi HI, Chung KJ, Yang HY, Ren L, Sohn S, Kim PR, et al. Peroxiredoxin V selectively regulates IL-6 production by modulating the Jak2-Stat5 pathway. *Free radical biology & medicine*. 2013; 65: 270-9.
28. Kamigaki M, Hide I, Yanase Y, Shiraki H, Harada K, Tanaka Y, et al. The Toll-like receptor 4-activated neuroprotective microglia subpopulation survives via granulocyte macrophage colony-stimulating factor and JAK2/STAT5 signaling. *Neurochem Int*. 2016; 93: 82-94.
29. Hsu PS, Wu CS, Chang JF, Lin WN. Leptin Promotes cPLA(2) Gene Expression through Activation of the MAPK/NF-kappaB/p300 Cascade. *International journal of molecular sciences*. 2015; 16: 27640-58.
30. Chen HM, Yang CM, Chang JF, Wu CS, Sia KC, Lin WN. AdipoR-increased intracellular ROS promotes cPLA2 and COX-2 expressions via activation of PKC and p300 in adiponectin-stimulated human alveolar type II cells. *Am J Physiol Lung Cell Mol Physiol*. 2016; 311: L255-69.
31. Boulange CL, Neves AL, Chilloux J, Nicholson JK, Dumas ME. Impact of the gut microbiota on inflammation, obesity, and metabolic disease. *Genome medicine*. 2016; 8: 42.
32. Kheirandish-Gozal L, Peris E, Wang Y, Tamae Kakazu M, Khalyfa A, Carreras A, et al. Lipopolysaccharide-binding protein plasma levels in children: effects of obstructive sleep apnea and obesity. *J Clin Endocrinol Metab*. 2014; 99: 656-63.
33. Chung S, Lapoint K, Martinez K, Kennedy A, Boysen Sandberg M, McIntosh MK. Preadipocytes mediate lipopolysaccharide-induced inflammation and insulin resistance in primary cultures of newly differentiated human adipocytes. *Endocrinology*. 2006; 147: 5340-51.
34. Castoldi A, Naffah de Souza C, Camara NO, Moraes-Vieira PM. The Macrophage Switch in Obesity Development. *Frontiers in immunology*. 2015; 6: 637.
35. Huh JY, Park YJ, Ham M, Kim JB. Crosstalk between adipocytes and immune cells in adipose tissue inflammation and metabolic dysregulation in obesity. *Molecules and cells*. 2014; 37: 365-71.
36. Wernstedt Asterholm I, Tao C, Morley TS, Wang QA, Delgado-Lopez F, Wang ZV, et al. Adipocyte inflammation is essential for healthy adipose tissue expansion and remodeling. *Cell Metab*. 2014; 20: 103-18.
37. Rainone V, Schneider L, Saule I, Ricci C, Biasin M, Al-Daghri NM, et al. Upregulation of inflammasome activity and increased gut permeability are associated with obesity in children and adolescents. *International journal of obesity (2005)*. 2016; 40: 1026-33.
38. Deng J, Hua K, Caveney EJ, Takahashi N, Harp JB. Protein inhibitor of activated STAT3 inhibits adipogenic gene expression. *Biochemical and biophysical research communications*. 2006; 339: 923-31.
39. Richard AJ, Stephens JM. The role of JAK-STAT signaling in adipose tissue function. *Biochim Biophys Acta*. 2014; 1842: 431-9.
40. Nanbu-Wakao R, Morikawa Y, Matsumura I, Masuho Y, Muramatsu MA, Senba E, et al. Stimulation of 3T3-L1 adipogenesis by signal transducer and activator of transcription 5. *Molecular endocrinology (Baltimore, Md)*. 2002; 16: 1565-76.
41. Derecka M, Gornicka A, Koralov SB, Szczepanek K, Morgan M, Raj V, et al. Tyk2 and Stat3 regulate brown adipose tissue differentiation and obesity. *Cell Metab*. 2012; 16: 814-24.
42. Kaltenecker D, Mueller KM, Benedikt P, Feiler U, Themanns M, Schleder M, et al. Adipocyte STAT5 deficiency promotes adiposity and impairs lipid mobilisation in mice. *Diabetologia*. 2017; 60: 296-305.
43. Nam M, Lee WH, Bae EJ, Kim SG. Compound C inhibits clonal expansion of preadipocytes by increasing p21 level irrespectively of AMPK inhibition. *Archives of biochemistry and biophysics*. 2008; 479: 74-81.
44. Guo YR, Choung SY. Germacrone inhibits adipogenesis and stimulates lipolysis via the AMP-activated protein kinase signalling pathway in 3T3-L1 preadipocytes. *The Journal of pharmacy and pharmacology*. 2017; 69: 202-12.
45. Dubon MJ, Byeon Y, Park KS. Substance P enhances the activation of AMPK and cellular lipid accumulation in 3T3L1 cells in response to high levels of glucose. *Mol Med Rep*. 2015; 12: 8048-54.
46. Weng JR, Dokla EME, Bai LY, Chen CS, Chiu SJ, Shieh TM. A 5' AMP-Activated Protein Kinase Enzyme Activator, Compound 59, Induces Autophagy and Apoptosis in Human Oral Squamous Cell Carcinoma. *Basic Clin Pharmacol Toxicol*. 2018.
47. Mancini SJ, White AD, Bijland S, Rutherford C, Graham D, Richter EA, et al. Activation of AMP-activated protein kinase rapidly suppresses multiple pro-inflammatory pathways in adipocytes including IL-1 receptor-associated kinase-4 phosphorylation. *Molecular and cellular endocrinology*. 2017; 440: 44-56.
48. Rutherford C, Speirs C, Williams JJ, Ewart MA, Mancini SJ, Hawley SA, et al. Phosphorylation of Janus kinase 1 (JAK1) by AMP-activated protein kinase (AMPK) links energy sensing to anti-inflammatory signaling. *Science signaling*. 2016; 9: ra109.
49. Lee KH, Hsu EC, Guh JH, Yang HC, Wang D, Kulp SK, et al. Targeting energy metabolic and oncogenic signaling pathways in triple-negative breast cancer by a novel adenosine monophosphate-activated protein kinase (AMPK) activator. *J Biol Chem*. 2011; 286: 39247-58.
50. Uotani S, Abe T, Yamaguchi Y. Leptin activates AMP-activated protein kinase in hepatic cells via a JAK2-dependent pathway. *Biochemical and biophysical research communications*. 2006; 351: 171-5.
51. Su H, Jiang L, Carter-Su C, Rui L. Glucose enhances leptin signaling through modulation of AMPK activity. *PLoS One*. 2012; 7: e31636.

# Liquid crystalline assembly for potential combinatorial chemo–herbal drug delivery to lung cancer cells

This article was published in the following Dove Medical Press journal:  
*International Journal of Nanomedicine*

Hadeer M Abdelaziz,<sup>1,2</sup> Ahmed O Elzoghby,<sup>1,3–5</sup> Maged W Helmy,<sup>1,6</sup> Magda W Samaha,<sup>1,3</sup> Jia-You Fang,<sup>7–9</sup> May S Freag<sup>1,4,5,10</sup>

<sup>1</sup>Cancer Nanotechnology Research Laboratory (CNRL), Faculty of Pharmacy, Alexandria University, Alexandria 21521, Egypt; <sup>2</sup>Department of Pharmaceutics, Faculty of Pharmacy, Damanhur University, Damanhur, Egypt; <sup>3</sup>Department of Industrial Pharmacy, Faculty of Pharmacy, Alexandria University, Alexandria 21521, Egypt; <sup>4</sup>Division of Engineering in Medicine, Department of Medicine, Brigham and Women's Hospital, Harvard Medical School, Boston, MA 02115, USA; <sup>5</sup>Harvard-MIT Division of Health Sciences and Technology (HST), Cambridge, MA 02139, USA; <sup>6</sup>Department of Pharmacology and Toxicology, Faculty of Pharmacy, Damanhur University, Damanhur, Egypt; <sup>7</sup>Pharmaceutics Laboratory, Graduate Institute of Natural Products, Chang Gung University, Taoyuan 333, Taiwan; <sup>8</sup>Research Center for Industry of Human Ecology and Research Center for Chinese Herbal Medicine, Chang Gung University of Science and Technology, Kweishan, Taoyuan 333, Taiwan; <sup>9</sup>Department of Anesthesiology, Chang Gung Memorial Hospital, Kweishan, Taoyuan 333, Taiwan; <sup>10</sup>Department of Pharmaceutics, Faculty of Pharmacy, Alexandria University, Alexandria 21521, Egypt

Correspondence: May S Freag  
Department of Pharmaceutics, Faculty of Pharmacy, Alexandria University, 1-azarita square, Alexandria 21521, Egypt  
Tel +20 10 6503 4721  
Fax +20 3 487 3273  
Email may.s.freag@alexu.edu.eg

Jia-You Fang  
Pharmaceutics Laboratory, Graduate Institute of Natural Products, Chang Gung University, Taoyuan 333, Taiwan  
Email fajy@mail.cgu.edu.tw

**Background:** Lung cancer is the most common cancer and the leading cause of total deaths worldwide. Its classified into two major types including non-small cell lung carcinoma (NSCLC) and small cell lung carcinoma (SCLC) based on the origin of abnormal lung cells as well as the smoking status of the patient. NSCLC is the most common and aggressive type of lung cancer representing 80%–85% of all cases.

**Purpose:** The aim of the study was to present lyotropic liquid crystalline nanoparticles (LCNPs) as promising carriers for co-delivery of the chemotherapeutic agent, pemetrexed (PMX) and the herbal drug, resveratrol (RSV) for effective lung cancer management.

**Methods:** The proposed PMX-RSV-LCNPs were prepared by hydrotrope method. Hydrophobic ion pairing with cetyl trimethyl ammonium bromide (CTAB) was implemented to increase the encapsulation efficiency of the hydrophilic PMX up to 95%±3.01%.

**Results:** The tailored PMX-RSV-LCNPs exhibited a particle size of 173±0.26 nm and biphasic release pattern with a relatively initial burst release within first 3–4 hour followed by sustained release up to 24 hours. Moreover, PMX-RSV-LCNPs manifested superior concentration and time dependent cytotoxicity profile against A549 lung cancer cells with IC<sub>50</sub> 4.0628 µg/mL. Besides, the enhanced cellular uptake profile based on bioadhesive properties of glyceryl monoolein (GMO) as well as energy independent (cholesterol dependent) pattern. In-vivo evaluations against urethane induced lung cancer bearing mice demonstrated the potentiality of PMX-RSV-LCNPs in tumor growth inhibition via inhibition of angiogenesis and induction of apoptosis. The results were supported by histopathological analysis and immunohistochemical Ki67 staining. Moreover, PMX-RSV-LCNPs displayed a promising safety profile via attenuating nephro- and hepatotoxicity.

**Conclusion:** PMX-RSV-LCNPs elaborated in the current study hold a great promise for lung cancer treatment.

**Keywords:** hydrophobic ion pairing, liquid crystalline nanoparticles, lung cancer, glyceryl monoolein, pemetrexed, resveratrol

## Introduction

Lung cancer is one of the most dreadful cancers for both men and women.<sup>1</sup> American Cancer Society estimated that in 2018 lung and bronchus cancers would be responsible for 234,030 new cases which represent 14% of all new cancer cases and 154,050 deaths.<sup>2</sup> Lung cancer is mainly classified into non-small-cell lung cancer (NSCLC; major and common form responsible for 85% cases) and small-cell lung carcinoma.<sup>3,4</sup> Despite the researcher's attempts to improve outcomes among lung cancer patients, results are still unsatisfactory.<sup>5</sup> For advanced stages of lung cancer, chemotherapy is considered the first line of treatment which is usually administered intravenously via systemic circulation.<sup>4,6</sup> However, conventional chemotherapy either used alone or in combination with others

faces many obstacles that limit its use. Most of the chemotherapeutic agents have poor aqueous solubility, lack of selectivity, and extensive metabolism via first-pass effect which in turn require higher doses to achieve the therapeutic level that subsequently affect tumor cells as well as normal healthy cells.<sup>7-9</sup>

Alimta® (pemetrexed, PMX, Eli Lilly and Company, Indianapolis, Indiana, USA), a promising Food and Drug Administration (FDA)-approved chemotherapeutic agent as monotherapy for the maintenance treatment of NSCLC, is also considered as the first-line treatment in combination with cisplatin.<sup>10</sup> PMX disodium ( $C_{20}H_{19}N_5Na_2O_6$ ) is a white freely water-soluble crystalline powder with a molecular weight of 471.37 g/mol.<sup>11</sup> PMX is a potent multi-targeted antifolate agent that exerts its action by disrupting de novo biosynthesis of thymidine and purine nucleotides essential for cell replication. The use of PMX, either as monotherapy or in combination, is accompanied with many undesirable adverse effects including bone marrow suppression manifested as anemia, neutropenia, leukopenia, and thrombocytopenia as well as nephro- and hepatotoxicities.<sup>12-16</sup> Moreover, PMX is rapidly eliminated and unchanged by renal tubular secretion and to a lesser extent by glomerular filtration. In addition, it undergoes limited hepatic metabolism with terminal half-life between 2 and 5 hours.<sup>12</sup> Therefore, encapsulating PMX in a suitable drug delivery system seems to be a promising approach to surmount PMX pharmaceutical obstacles and improve its clinical utility.

Recently, the use of herbal drugs has magnetized the researchers' attention based on their great tendency in sensitizing tumor cells and imparting synergistic activity to chemotherapeutic agents.<sup>17-19</sup> Among promising herbal drugs, resveratrol (RSV) proved its great capability in protecting against cancer.<sup>20</sup> RSV (3,5,4'-trihydroxystilbene) is a polyphenolic phytoalexin produced in various plants in response to stress.<sup>21,22</sup> RSV has several activities including antioxidant, anti-inflammatory, proapoptotic, antiproliferative, antiangiogenesis, and chemopreventive properties.<sup>21-24</sup> In addition, it plays a vital role in overcoming multidrug resistance (MDR) associated with most of the chemotherapeutic agents. This was attributed to its ability to prohibit P-glycoprotein (P-gp) activity, thus potentiating intracellular accumulation of coadministered chemotherapeutic payloads.<sup>25,26</sup> A promising synergistic combination of RSV and PMX was previously reported by Chen et al,<sup>27</sup> where PMX significantly decreased the expression of ERCC1, phospho-p38 MAPK protein levels, and the DNA repair capacity, thus enhancing the RSV-induced cytotoxic effect on NSCLC cells and proposing the potential outcomes of coadministering PMX and RSV for the treatment of lung carcinoma. However, RSV has many limitations

including instability, poor water solubility, low bioavailability, and short biological half-time. In addition, rapid and extensive metabolism hindered the anticancer activity of RSV even in high doses.<sup>28</sup> Therefore, optimizing a nanoscale drug delivery system encapsulating both drugs could be of prime importance for enhanced lung cancer treatment.

Recently, researchers pay great attention to lyotropic liquid crystalline nanoparticles (LCNPs) as new lipid-based drug delivery systems for cancer therapy. They are self-assembled structures formed when several polar lipids including Glyceryl monooleate (GMO), phytantriol, glycolipids, and glycerates were dispersed in water in the presence of stabilizers. LCNPs possess bicontinuous lipid bilayer enclosing water channels. Their unique multi-compartmental structure enables them to efficiently deliver hydrophilic, hydrophobic, or amphiphilic molecules.<sup>29-31</sup> The biocompatibility, biodegradability, bioadhesion, and prolonged drug release characteristics make LCNPs suitable carriers for cancer therapy. Their inherent small particle size (PS) facilitates passive targeting via enhanced permeation and retention effect.<sup>32-35</sup> Recently, Freag et al<sup>30</sup> successfully formulated surface-modified PEGylated aloe-emodin-loaded LCNPs (AE-polyethylene glycol [PEG]-LCNPs) for breast cancer treatment. The LCNPs investigated in their study demonstrated improved hemocompatibility, increased serum stability, and enhanced cytotoxicity and cellular uptake in breast cancer cells compared to free drug.

In view of the abovementioned information, the current study focused, for the first time, on the fabrication of LCNPs for the combined delivery of both PMX and RSV. The proposed formulation was evaluated *in vitro* and *in vivo* for their efficacy in lung cancer treatment. *In vitro* cytotoxicity and cellular uptake studies were performed using A549 lung carcinoma cells. In addition, *in vivo* antitumor activity of PMX-RSV-LCNPs was evaluated in urethane-induced lung cancer-bearing mice.

## Materials and methods

### Materials

PMX (purity 98%) and RSV were purchased from Baoji Guokang Bio-Technology Co., Ltd (Baoji, People's Republic of China). Peceol® (GMO) was kindly provided by Gattefosse (Saint-Priest, France). Human A549 lung cancer cell line was purchased from Egyptian Organization for Biological Products and Vaccines (VACSERA Holding Company, Giza Governorate, Egypt). Poloxamer-407 (P407), cetyltrimethylammonium bromide (CTAB), DMEM, FBS, and MTT were purchased from Sigma-Aldrich Co. (St Louis, MO, USA). Caspase 3 (CASP-3) ELISA Kit was purchased from WKEA Med



Supplies Corp. (Chaoyang District, Changchun, Jilin, People's Republic of China). Vascular endothelial growth factor (VEGF) ELISA kit, RayBio® (catalog number: ELR-VEGF-001) was purchased from RayBio Tech Inc. (Norcross, GA, USA). All other reagents and chemicals were of analytical grade.

## Methodology

### Preparation of PMX-RSV-loaded LCNPs

PMX-RSV-LCNPs were fabricated via the hydrotrope method.<sup>36</sup> Briefly, RSV (10 mg) was dissolved in an isotropic mixture of 200 mg GMO and 0.18 mL absolute ethanol. The resulting isotropic solution was added dropwise onto 2 mL of P407 solution (0.5% w/v) containing 10 mg PMX under magnetic stirring. The mixture was equilibrated at room temperature for 24 hours and then dispersed into another 6 mL of P407 solution (0.5% w/v) followed by homogenization at 13,000 rpm for 3 minutes to finally obtain the LCNP dispersion.

Different formulation variables including the type of hydrotrope (ethanol, PEG 400, propylene glycol), concentration of ethanol, P407 concentration, and percentage loading of PMX and RSV were investigated. The influence of different variables on PS, size distribution, zeta potential, and encapsulation efficiency of the prepared LCNPs was investigated.

For cellular uptake studies, fluorescent-labeled LCNPs were prepared, where 0.08% w/w coumarin-6 (with respect to lipid) was added to the isotropic mixture of GMO and absolute ethanol and then processed as mentioned earlier.

### Preparation of ion-paired PMX-RSV-loaded LCNPs

To increase the hydrophobicity of PMX and improve its lipid solubility, in situ hydrophobic ion pairing (HIP) of PMX with the cationic surfactant CTAB was performed following the previously reported protocol.<sup>37,38</sup> Briefly, 34 mg of CTAB was added with 10 mg PMX into P407 solution prior to the addition of the isotropic (GMO and ethanol) mixture and then processed as mentioned earlier. Optimization of the in situ ion-pairing process involved the investigation of different PMX:CTAB molar ratios of 1:2 and 1:4 on the % entrapment efficiency (% EE) of PMX.

### Development of novel HPLC method for simultaneous determination of PMX and RSV

A novel, accurate, precise, and sensitive HPLC method was developed and validated for simultaneous determination of both RSV and PMX using Agilent 1260 Infinity HPLC system. Details of the test are provided in Supplementary materials.

## Characterization of LCNPs

### EE of PMX and RSV

The %EE of different LCNP formulations was determined using the dialysis bag method following a protocol previously reported by Swarnakar et al.<sup>39</sup> Briefly, 1 mL of LCNP dispersion was transferred to dialysis bag. The bags were then placed in 50 mL PBS and subjected to centrifugation (Model 3 K-30; Sigma Laboratory Refrigerated Centrifuge, Osterode am Harz, Germany) at 500 rpm for 30 minutes to separate free PMX and RSV. The procedure was optimized and validated in-house for complete separation of free drugs from the formulation. The actual concentrations of PMX and RSV entrapped within LCNPs represent the difference between the initial amounts added during LCNP fabrication and free untrapped drug separated after centrifugation (Equation 1). The concentrations of PMX and RSV were quantified using HPLC at  $\lambda_{\text{max}}$ =225 and 306 nm, respectively.

$$\% \text{ EE} = \frac{\text{Amount of drug entrapped in LCNPs}}{\text{Initial amount of drug}} \times 100 \quad (1)$$

### PS and zeta potential

The mean PS, polydispersity index (PDI), and zeta potential ( $\delta$ -potential) of LCNP formulations were measured via dynamic light scattering (DLS) and electrophoretic mobility technique using Zetasizer (Nano ZS/ZEN3600 Zetasizer; Malvern Instruments, Malvern, UK). The samples were diluted with distilled water (1:50) to obtain final experimental values in triplicate at room temperature. Results were shown as mean size  $\pm$  SD.<sup>40</sup>

### Study of the phase behavior of LCNPs

Investigation of the phase behavior of both placebo and dual drug-loaded formulations was performed using a polarizing microscope. Micron-sized liquid crystalline particles were fabricated as described earlier but without the size reduction homogenization step. After that, a drop of the dispersion was placed onto a slide and imaged under polarizing light microscope (Zeiss Axiovert 40 MAT microscope fitted with camera) at magnification power of 100 $\times$  to evaluate the occurrence of birefringence.<sup>41</sup>

### Transmission electron microscopy (TEM)

The morphology of ion-paired PMX-RSV-LCNPs was examined via TEM (Jeol JEM-2100; JEOL, Tokyo, Japan) at an accelerating voltage of 80 kV.<sup>42</sup> After sample dilution with distilled water (1:20), a drop of the sample was placed onto

a carbon-coated copper grid and left for air-drying. Then, the films were visualized under TEM and photographed.

## In vitro release study

In vitro drug release profile from different LCNP formulations was performed using the dialysis bag method.<sup>43</sup> Samples investigated encompassed free aqueous solution of PMX, free ethanolic solution of RSV, PMX-RSV-LCNPs (F8), and ion-paired PXM-RSV-LCNPs (F10). Samples were added into a sealed dialysis bag (molecular weight cutoff [MWCO]: 12–14 kDa). The dialysis bags were placed in 100 mL phosphate buffer, pH 7.4, and incubated at 37°C with a shaking speed of 100 rpm in shaking water bath. Aliquots (2 mL) were withdrawn at different time intervals (0.25, 0.5, 1, 2, 4, 6, 8, and 24 hours) followed by compensation with the same volume of fresh release medium. The samples were filtered using 0.45 µm Millipore filter (Millipore®; Thermo Fisher Scientific, Waltham, MA, USA) and then quantified for their PMX and RSV content using validated HPLC method as mentioned earlier.

## In vitro anticancer study

### Cell culture

A lung carcinoma cell line A549 was used for examining in vitro cytotoxicity of the proposed formulations. For the propagation of A549 cells, American Type Culture Collection (ATCC) complete growth medium (Ham's F12K medium with 2 mM L-glutamine adjusted to contain 1.5 g/L sodium bicarbonate, 90%; FBS, 10%) was utilized. The cells were grown in 75 mL flasks in an atmosphere of 5% CO<sub>2</sub> and 100% relative humidity and subcultured two to three times per week.

### In vitro cytotoxicity

In vitro cytotoxicity of free PMX, free RSV, free combined PMX/RSV solution, blank LCNPs, and ion-paired PMX-RSV-LCNPs (F10) was evaluated in A549 lung cancer cells using MTT assay.<sup>44</sup> Details of the test are provided in Supplementary materials.

### In vitro cellular uptake

A549 lung cancer cells were seeded on CELL view™ slide at a density of 3,000 cells/well and left overnight to allow enough time for cell attachment. Cells were incubated with fresh medium containing free coumarin-6 dye and coumarin-6-loaded LCNPs at the concentration of 0.08% w/w coumarin-6 (with respect to lipid). Details of the test are provided in Supplementary materials.

## In vivo study

### Animals

The guidelines developed by the Animal Care and Use Committee, Faculty of Pharmacy, Alexandria University, Alexandria, Egypt, and in accordance with regulations of the National Research Council's guide for the care and use of laboratory animals were adopted for in vivo study. Twenty-eight Balb/c male mice (15±5 g, 3–4 weeks) were housed in stainless steel cages in four groups (seven mice per group). The animals were kept under standard environmental conditions (23°C±1°C, 55%±5% humidity and 12 hours/12 hours light/dark cycle) and maintained with free access to standard laboratory diet (balanced nutrient of chow and water). Lung cancer was induced within mice via intraperitoneal injection of chemical carcinogen and urethane (ethyl carbamate, 1 g/kg) followed by post-dose of urethane (0.5 g/kg) after 15 days. The mice were left for 12–16 weeks to ensure complete induction of lung cancer. After that, experimental model of mice was sacrificed to evaluate tumor incidence and precancerous lesions prior to exposing rest of mice to treatment. The excised lungs were stained with H&E and undergone histopathological and immunohistochemical investigations.

## Evaluation of antitumor efficacy

After tumor induction, 28 mice were classified randomly into four groups, 7 mice each. The groups encompassed as follows: positive control group (untreated tumor-bearing mice), negative control group (healthy mice treated with saline), free PMX/RSV-treated group, and ion-paired PMX/RSV-LCNP (F10)-treated group. All animals were administered their formulation via intravenous (IV) route into the tail vein. Animals of the last two groups were injected with equivalent concentration of PMX and RSV (0.94 mg/kg) twice per week for 21 days. Free PMX/RSV mixture was dissolved in cosolvent (dimethyl sulfoxide/PEG 400/saline 0.5/4.5/5 v/v/v). At 25th day, the mice were sacrificed and the excised lungs were weighted and divided for tumor growth biomarker measurement as well as histopathological and immunohistochemical examinations.

## Evaluation of tumor growth biomarkers

The excised parts of lung tumors were carefully weighed and homogenized in cold PBS using tissue homogenizer to make a final 40% tissue homogenate. This homogenate was centrifuged at 1,700 rpm at 4°C for 10 minutes, and the supernatants were divided into separate small aliquots and stored at –80°C for further quantitative determination of

tumor growth biomarkers. The degree of angiogenesis was determined via detecting the level of the angiogenic VEGF using “VEGF ELISA Kit” (RayBio Tech Inc.), while the induction of apoptosis was confirmed by determining the level of tissue CASP-3 using “caspase-3 (CASP-3) ELISA Kit” (WKEA Med Supplies Co.). All the markers were quantified according to the manufacturer’s protocol.

## Histopathological studies

A part of excised lung tumors was preserved and fixed with 10% neutral formalin for 24 hours, then stained with hematoxylin for 5 minutes and eosin for 2 minutes (H&E), dehydrated in alcohol, and mounted in Canada balsam before microscopical examination. The tumors obtained from different groups were examined in ten random sections ( $\times 40$ ) for histopathological neoplastic changes. Moreover, the average number of microscopic metastatic lung foci and their diameter were determined.

## Immunohistochemical analysis

The previously conserved excised lungs in formalin and embedded in paraffin as blocks were cut and rinsed using xylene and then rehydrated before staining steps. Methanolic solution of hydrogen peroxide (7%) was added for 20 minutes, then left for 5 minutes in heated citrate phosphate buffer (pH 6.0) using microwave then immersed in milk/distilled water (5%) for 45 minutes. Individual treatment of sections was performed using Ki-67 antibody at 4°C overnight. After that, the sections were washed and retreated with a secondary anti-mouse biotinylated antibody in a dark room for 1 hour. Nuclear staining was carried out to localize cellular Ki-67 immunoreactivity. Each tumor sample was examined for Ki-67 expressions in ten random sections ( $\times 40$ ) in which the number of positive cells/total was calculated. Moderate-to-strong brownish cellular cytoplasmic staining was accounted for positive, whereas unstained or faint stained cellular cytoplasm was accounted for negative.

## Statistical analyses

Statistical analysis of in vitro results was carried out using Student’s *t*-test ( $P \leq 0.05$ ; GraphPad Prism version 3.02; GraphPad Software, Inc., La Jolla, CA, USA). However, the results of the in vivo antitumor activity were analyzed using IBM SPSS Software package (version 20; IBM Corporation, Armonk, NY, USA). Statistical significance between the groups was analyzed using ANOVA and Tukey’s multiple comparison tests. Statistical significance was judged at the 5% level.

## Results and discussion

### Preparation of ion-paired PMX-RSV-LCNPs

The aim of the current study was to develop lyotropic LCNPs for the co-delivery of PMX and RSV. Thanks to the unique structure of LCNPs which facilitate incorporation of different types of drugs, both hydrophilic (PMX) and lipophilic (RSV) drugs were successfully loaded in the LCNPs. Herein, the hydrotrope method, previously developed by Spicer et al,<sup>36</sup> was adopted for the fabrication of LCNPs in which a hydro-trope was used to increase the aqueous solubility of poorly soluble GMO lipid. The dropwise addition of this hydro-tropic mixture to water containing P407 resulted in gradual decrease in the solubility of GMO resulting in instantaneous formation of stable liquid crystalline particles in a nanometric range. In addition, the hydrotrope method guaranteed the stability of the thermosensitive drug RSV bypassing the drastic conditions accompanied by conventional method including elevated temperature and pressure. The composition of the prepared LCNP formulations (F1–F10) is summarized in Table 1. As given in the table, PMX (F8) demonstrated relatively low %EE due to its anionic nature and high aqueous solubility ( $\log P$  1.54) that could result in its poor entrapment into lipid-based systems and subsequent partitioning into the continuous aqueous phase. Generally, sustained release of water-soluble drugs from nanocarrier delivery systems remains a challenging task. Many attempts have been exploited to overcome this challenge including chemical cross-linking and HIP.<sup>45,46</sup> Therefore, in the current study, the HIP technique was applied to enhance the hydrophobicity of PMX and enhance its EE.<sup>38</sup> HIP technique is simply performed by the interaction between ionic drug and the opposite ionic head group of a fatty acid, surface-active agents, or other amphiphilic molecules at suitable pH without the modification of their chemical structures. In the current study, CTAB was selected as a counter-cationic surface-active agent for in situ formation of HIP with PMX. CTAB was added to the aqueous phase containing PMX, and the influence of different PMX:CTAB molar ratios on the %EE was investigated. As summarized in Table 1, 1:4 PMX:CTAB molar ratio (F10) showed the highest %EE of PMX (95%), so it was selected as an optimum ratio for further studies.

### Physicochemical characterization of LCNPs

#### PS

#### Effect of different hydrotropes

The effect of different hydrotropes including propylene glycol, PEG 400, and absolute ethanol on the quality attributes

**Table 1** Composition and physicochemical characterization of placebo and PMX-RSV-loaded LCNPs

Formula	Hydrotrope (% w/v)	P407 <sup>a</sup> (% w/v)	PMX (mg)	RSV (mg)	Size (nm)	PDI	Zeta potential (mV)	RSV %EE	PMX %EE
F1 <sup>a</sup>	1.72	0.5	–	–	190±0.83	0.35±0.01	–30.42±2.91		
F2 <sup>a</sup>	1.76	0.5	–	–	220±0.91	0.42±0.04	–32.01±3.21		
F3	1.75	0.5	–	–	167±0.25	0.22±0.01	–34.85±2.03		
F4	1.25	0.5	–	–	190±1.50	0.26±0.01	–32.45±2.94		
F5	2.5	0.5	–	–	155±0.93	0.18±0.05	–31.69±1.57		
F6	1.75	0.25	–	–	218±1.02	0.35±0.01	–31.44±2.03		
F7	1.75	1	–	–	150±1.22	0.14±0.01	–33.91±3.12		
F8	1.75	0.5	10	10	168±0.51	0.22±0.01	–39.34±1.15	90%±2.03%	50%±1.65%
F9 <sup>b</sup>	1.75	0.5	10	10	176±0.16	0.20±0.01	+48.05±3.12	98%±2.01%	80%±1.01%
F10 <sup>b</sup>	1.75	0.5	10	10	173±0.26	0.19±0.01	+58.03±1.12	98%±2.01%	95%±3.01%

**Notes:** All formulations were prepared using GMO 2.5% (w/v) with respect to total dispersion volume. <sup>a</sup>F1 and F2 contain propylene glycol and PEG 400, respectively. <sup>b</sup>F9 and F10 contain ion-paired PMX at molar ratio of PMX:CTAB (1:2 and 1:4, respectively).

**Abbreviations:** CTAB, cetyltrimethylammonium bromide; %EE, % entrapment efficiency; GMO, glyceryl monooleate; LCNPs, liquid crystalline nanoparticles; PDI, polydispersity index; PMX, pemetrexed; P407, poloxamer-407; RSV, resveratrol.

of the prepared formulations was investigated (F1–F3). The concentration of hydrotropes represented 70% w/w of the amount of GMO.<sup>47</sup> As summarized in Table 1, ethanol (F3) possessed a great tendency in reducing the viscosity of GMO which in turn facilitates prompt diffusion of the hydrotropic mixture into aqueous phase. This was evidenced by significant ( $P<0.05$ ) decrease in both PS and PDI compared to (F1, propylene glycol; F2, PEG 400). Therefore, ethanol was selected as the suitable hydrotrope for further investigations.

### Effect of ethanol concentration

The influence of other ethanol concentrations (F4, 50; F5, 100% w/w relative to total lipid) on PS and PDI was investigated. As summarized in Table 1, it was obvious that increasing solvent concentration was associated with significant reduction in PS and PDI ( $P<0.05$ ). Increasing ethanol concentration beyond 70% w/w revealed insignificant decrease ( $P>0.05$ ) in the PS. Therefore, ethanol at the concentration of 70% w/w was chosen as an optimum hydrotrope concentration which resulted in promising PS of 167 nm and PDI of 0.2 (F3).

### Effect of stabilizer concentration

P407 is a triblock copolymer widely used in stabilizing LCNPs. This hydrophilic nonionic surfactant has a unique capability in adsorbing to the surface of LCNPs, thus inhibiting their aggregation. In addition to its great tendency in stabilizing internal structure of LCNPs through preventing transition to other mesophase structures, herein, the influence of three different concentrations of P407 (0.25%, 0.5%, and 1% w/v) was screened (F3, F6–F7). As summarized in Table 1, increasing P407 concentration from 0.25% to 0.5% w/v relative to total dispersion volume was associated

with obvious reduction in PS and PDI. Increasing P407 concentration beyond 0.5% w/v resulted in insignificant reduction in PS (F3, 167 nm; F7, 150 nm). Therefore, 0.5% w/v P407 concentration was selected as the optimum concentration for additional investigations. Our results were in good agreement with Freag et al<sup>47</sup> who reported that 0.5% w/v P407 concentration relative to total dispersion volume was quite sufficient to stabilize LCNPs and maintain their internal structure.

### Effect of percentage drug loading

In an attempt to minimize the dose of cytotoxic PMX and reduce its associated adverse effects, PMX and RSV were successfully loaded within LCNPs at the weight ratio of 1:1. The characteristic absorption bands of PMX and RSV (Figure S2) on the validated HPLC analysis (Table S1) with good linearity ranging from 0.4 to 2 mg% PMX and RSV concentration (Figure S1) proved that both PMX and RSV were successfully loaded into LCNPs and the drug carrier was effective for the co-delivery of the two drugs. It was obviously observed that CTAB modification significantly increased %EE of PMX (Table 1). The average %EE of PMX and RSV in the optimized ion-paired nanoformulation was 95% and 98%, respectively. Physicochemical characterization results indicated that loading RSV and PMX did not affect the physicochemical properties of LCNPs; it was found that PMX-RSV-loaded LCNPs possess almost similar PS and PDI to blank LCNPs.

### Zeta potential

All LCNPs that were formulated without CTAB (F1–F8) showed a negatively charged zeta potential around –34 mV although GMO is a neutral lipid, which could be explained by adsorption of free hydroxyl groups on the surface of



LCNPs in addition to free oleic acid found in commercially available GMO.<sup>48</sup> A significant alteration in zeta potential upon the addition of CTAB was detected. As summarized in Table 1, ion-paired PMX-RSV-LCNPs (F9–F10) displayed a positively charged zeta potential which is sufficient for the colloidal stability and preventing aggregation.

## Phase behavior

Polarized light microscope is commonly utilized to study the liquid crystalline phases depending on their textures. The hexagonal phases exhibit a fan-like texture, whereas the cubic phases show a dark diffraction pattern when viewed under a polarizing light microscope. Herein, both blank and PMX-RSV-loaded LCNPs demonstrated a dark diffraction patterns when examined under polarizing microscope reflecting the isotropic nature of the formulations.<sup>41</sup>

## Transmission electron microscopy

The surface morphology of optimized ion-paired PMX-RSV-LCNPs was visualized via TEM. As depicted in Figure 1A,

LCNPs displayed spherical particles with an average PS of 180 nm which was in agreement with the measurements obtained by DLS.

## In vitro release study

In vitro release behavior of each free RSV, free PMX, PMX-RSV-LCNPs (F8), and ion-paired PMX-RSV-LCNPs (F9–F10) was examined in commonly utilized release media PBS (pH = 7.4). As shown in Figure 1B, both free RSV and PMX exhibited burst release profile, a relatively rapid and entire release was observed after 2 and 4 hours for PMX and RSV, respectively. However, after incorporation of drugs into LCNPs, a sustained release behavior of both drugs was observed. The release behavior of RSV was characterized by a biphasic release pattern where a relatively initial burst release within first 3–4 hours was observed followed by sustained release up to 24 hours. The initial burst release could be explained via relatively large surface area-to-volume ratio provided by LCNPs, while the continuous sustained release of drugs from PMX-RSV-LCNPs could be referred to the

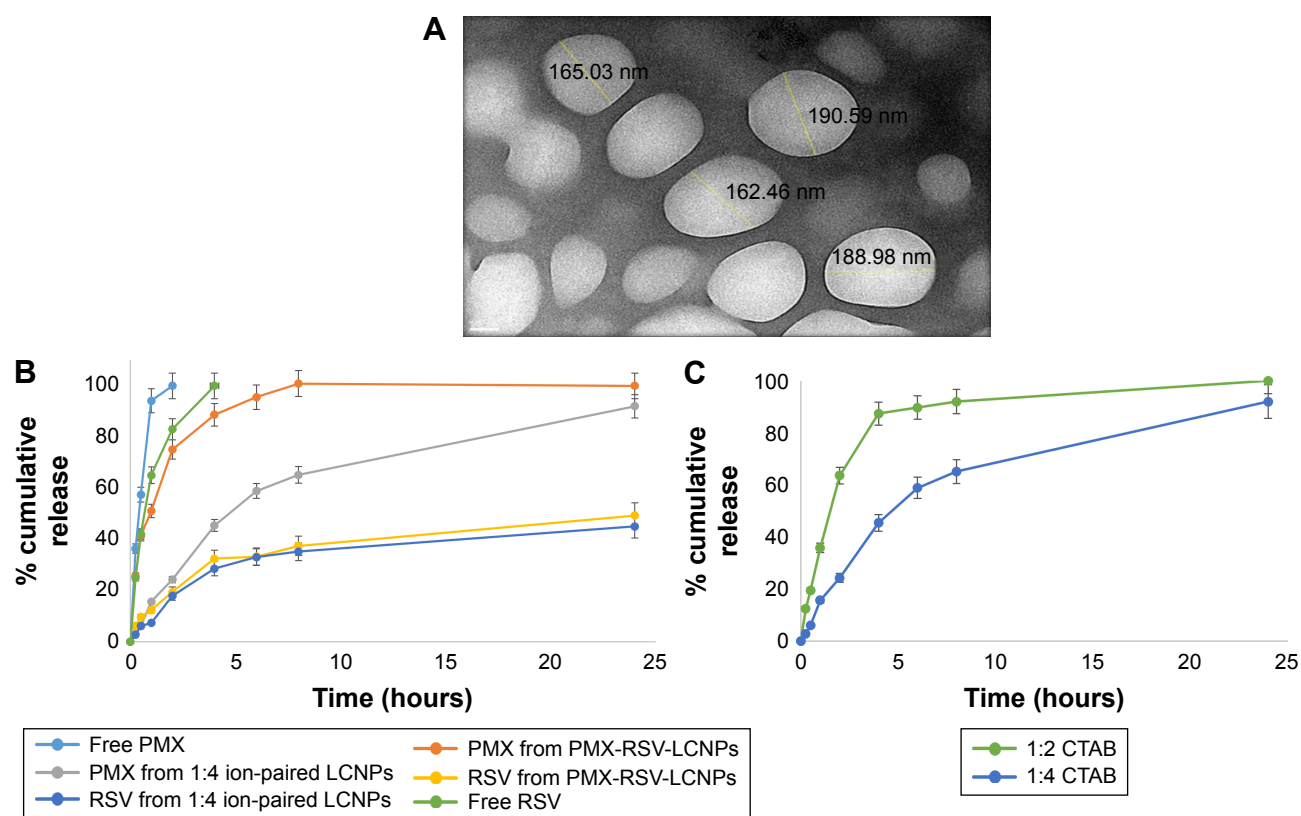


**Figure 1** Physicochemical characterization of optimized LCNPs.

**Notes:** (A) Transmission electron micrograph displaying morphology of ion-paired PMX-RSV-LCNPs (F10). (B) In vitro release of PMX and RSV from PMX-RSV-LCNPs (F8) and ion-paired PMX-RSV-LCNPs (F10) in comparison to free PMX and RSV solution in PBS (pH 7.4) at 100 rpm and 37°C using the dialysis bag diffusion method. (C) The influence of different CTAB:PMX molar ratios on the release of PMX from ion-paired LCNPs in PBS (pH 7.4) at 100 rpm and 37°C using the dialysis bag diffusion method.

**Abbreviations:** CTAB, cetyltrimethylammonium bromide; LCNPs, liquid crystalline nanoparticles; PMX, pemetrexed; RSV, resveratrol.

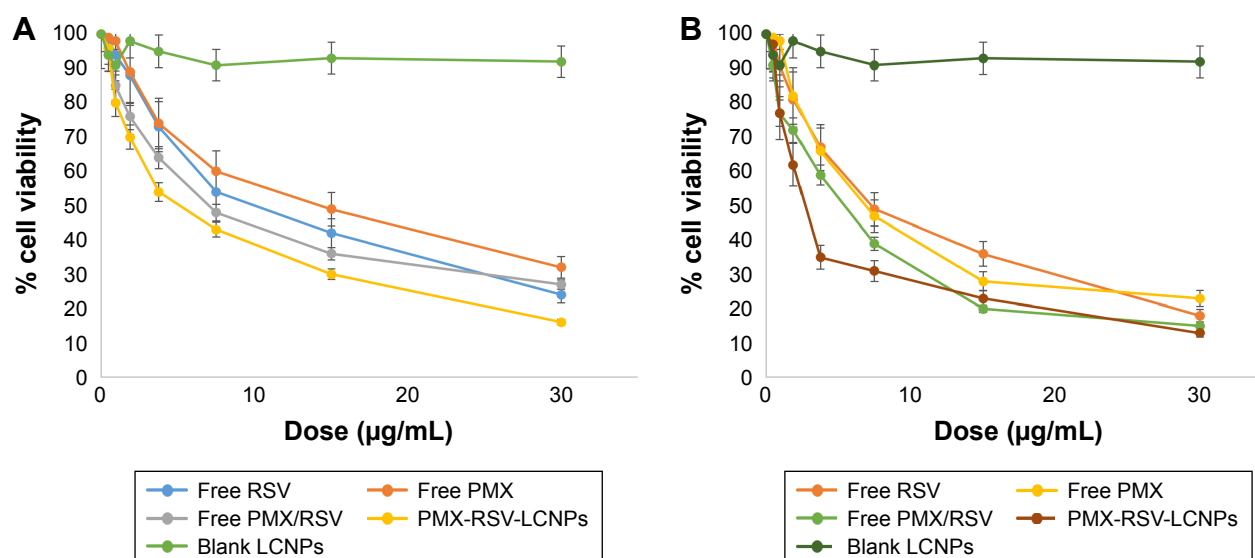


**Figure 2** In vitro cytotoxicity of ion-paired PMX-RSV-LCNPs (F10) compared to blank LCNPs, free PMX, free RSV, and free PMX/RSV cosolvent on A549 NSCLC cell line at the concentration of 0.468–30 µg/mL expressed as % cell viability after (A) 24 hours and (B) 48 hours.

**Abbreviations:** LCNPs, liquid crystalline nanoparticles; NSCLC, non-small-cell lung cancer; PMX, pemetrexed; RSV, resveratrol.

diffusion of both drugs from the lipid core of bicontinuous bilayer of the liquid crystalline structure.<sup>49</sup> To check the effect the HIP process on the release behavior of PMX (Figure 1C), two formulations of modified PMX-RSV-LCNPs with two different concentrations of CTAB (F9–F10) were compared to unmodified PMX-RSV-LCNPs (F8). Compared to unmodified LCNPs, CTAB-modified LCNPs possess an additional controlled release of PMX and upon increasing the concentration of CTAB (F10), more sustained release behavior from regular lipid channels was observed. This may be attributed to the extra hydrophobic nature imparted to LCNPs by CTAB. Obviously, the proposed ion-paired PMX-RSV-LCNPs provided an acceptable sustained release pattern of PMX up to 24 hours. This sustained drug release behavior is an essential prerequisite to guarantee constant and controlled release of anticancer drugs within tumor cells which in turn reduce their systemic cytotoxicity.

## In vitro cytotoxicity studies

The cytotoxic influence of free RSV, free PMX, free RSV/PMX mixture, blank LCNPs, and ion-paired PMX-RSV-LCNPs (F10) on A549 lung cancer cell line was determined using MTT assay (Figure 2A and B). Better therapeutic outcomes for resistant tumor cells were mainly achieved via combinational therapy based on two or more anticancer agents. Co-administering of herbal drugs with potent anticancer drugs hold great promise, particularly, PMX and RSV have been reported for their in vitro cytotoxic activity on lung cancer cells.<sup>27</sup> Furthermore, the combined doses of PMX and RSV

loaded into PMX-RSV-LCNPs were precisely determined by their dose dependency and relative amount of PMX vs RSV to A549 cells, to maximize the synergistic antitumor efficacy. Blank LCNPs demonstrated good cytocompatibility with insignificant cytotoxicity on A549 cancer cells after 24 hours (Figure 2A) and 48 hours (Figure 2B; % cell viability >85%). RSV and PMX were evaluated at concentration ranged from 0.468 to 30 µg/mL. Free PMX and RSV exhibited a dose-dependent cytotoxic efficacy on the lung cancer cells. To check the synergistic activity between both drugs, the combined  $IC_{50}$  was calculated and is summarized in Table 2. As summarized in the table, free RSV/PMX mixture exhibited a lower  $IC_{50}$  value (4.5 µg/mL) compared to each free PMX and free RSV ( $IC_{50}$ : 7.9 and 8.4 µg/mL, respectively). It was clearly observed that PMX-RSV-LCNPs had a significant superior cytotoxic activity on lung cancer cells compared to free RSV/PMX mixture. This superiority in the cytotoxicity of LCNP formulations could be attributed to the enhanced internalization of LCNPs facilitated by both bioadhesive property of GMO and energy-independent (cholesterol-dependent)

**Table 2**  $IC_{50}$  of free drugs and optimized LCNPs after 24 and 48 hours using Compusyn® software

$IC_{50}$ (µg/mL)	Free PMX	Free RSV	Free RSV/PMX	Ion-paired PMX-RSV-LCNPs
After 24 hours	10.10	12.66	7.96	5.50
After 48 hours	7.94	8.43	4.51	4.0628

**Abbreviations:** LCNPs, liquid crystalline nanoparticles; PMX, pemetrexed; RSV, resveratrol.

uptake mechanism associated with LCNPs resulting into higher intracellular concentration of both RSV and PMX.<sup>50</sup> It is worth to mention that the cytotoxicity of PMX-RSV-LCNPs was more evident following 48-hour incubation than 24 hours which could be ascribed to the sustained release behavior of RSV and PMX imparted by LCNPs.

## Cellular uptake of optimized LCNPs

The qualitative cellular uptake study of the proposed LCNPs was carried out on A549 cell line using confocal microscopy. Coumarin-6 was used as a model hydrophobic fluorescent dye which could be easily entrapped within lipid bilayer of LCNPs. To assess the entrapment and retention of dye in LCNPs, the coumarin-6-loaded LCNPs were placed in

centrifugal ultrafilter (Vivaspin® 6, molecular weight cutoff [MWCO]100 kDa; Vivaproducts, Inc, Littleton, MA). The ultrafilters were then centrifuged at 4,000 rpm for 30 minutes. The fraction of dye released (unentrapped) during 24 hours with all formulations was within 1%–2%, suggesting a good entrapment. Untreated A549 cells were used to exclude cellular autofluorescence. A549 cells were incubated with free coumarin-6 and coumarin-6-loaded LCNPs for 4 (Figure 3A) and 24 hours (Figure 3B). As shown in the figure, LCNPs demonstrated superior cellular uptake compared to free dye. The increased intracellular concentration after 24 hours confirmed the time-dependent cellular uptake of LCNPs. To guarantee that ion-paired LCNPs were taken up and internalized into A547 and not only adsorbed onto the

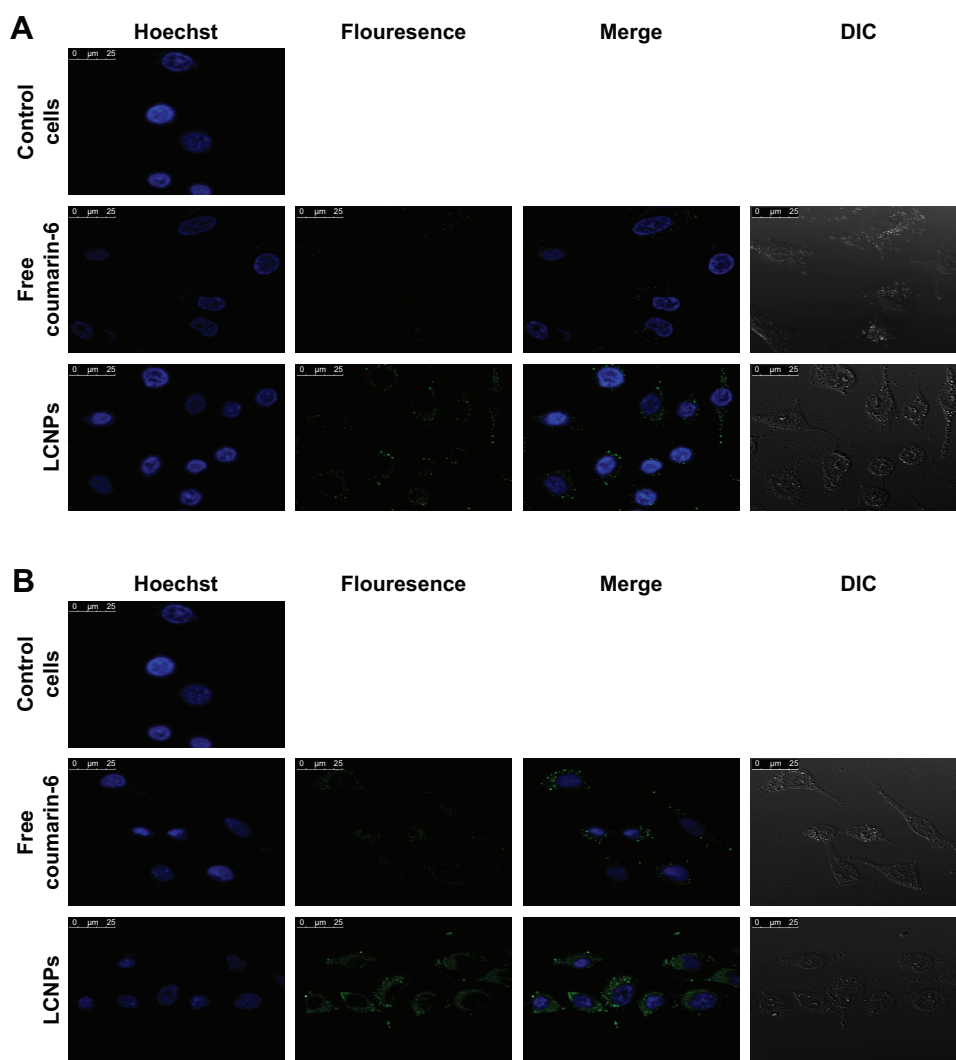


**Figure 3** Confocal microscopy images demonstrating cellular uptake of coumarin-6-loaded LCNPs relative to free coumarin-6 and control cells after incubation with A549 lung cancer cell line for (A) 4 hours and (B) 24 hours in which the first channel of nuclei is represented by blue stain of Hoechst, the second channel of free coumarin-6 or coumarin-6-loaded LCNPs is represented by green fluorescence, third channel of merge is represented by overlay between two channels, and finally the fourth channel of DIC is represented by the light microscopic image of A549 cells.

**Abbreviations:** LCNPs, liquid crystalline nanoparticles; DIC, differential interference contrast.

surface of cellular membrane, their uptake was evaluated using z-stack images. The z-direction image (Figure S3) displayed the cross-sectional uptake of coumarin-6-loaded LCNPs in which they were traveled from the apical surface of cellular membrane toward the basolateral membrane represented from z-0 to z-29. Image of z-29 represents maximum intensity projections of whole A549 cells. The fluorescence images manifested that LCNPs with a size of 173 nm move rapidly across the cellular membrane, distribute within the cytosol, successively move across different cellular planes, and localize in the perinuclear region. The video displaying z-stacks confirmed particle localization within the cells mainly within the cytoplasm and seldom dispersed in the nuclei was included as provided in Supplementary materials. The enhanced cellular uptake of coumarin-6-loaded LCNPs could be attributed to GMO bioadhesive and membrane-fusing features in addition to the unique structure of LCNPs in which water channels surrounded by bicontinuous lipid bilayer offer hydrophilic–hydrophobic pattern which facilitates interaction with hydrophobic cholesterol on cell surface.<sup>50</sup> In addition, it is worth mentioning that nanoparticle size, shape, and surface charge could possibly affect their interaction with the cellular membrane. It was previously reported that NPs with an average size between 200 and 350 nm could successfully distribute to different tissues, whereas NPs <70 nm were instantly excreted by the kidneys. Moreover, the positively charged surface imparted by CTAB could further facilitate cellular uptake by binding to the anionic surface proteoglycans via adsorptive-mediated endocytosis.<sup>51</sup> On the other hand, free coumarin-6 entered the cell via simple diffusion resulted in rapid saturation of intracellular region prohibiting further entry of free dye by time unlike LCNPs which entered via endocytosis resulted in gradual release of free dye thus evading intracellular saturation. These findings were in accordance with MTT assay in which optimized PMX/RSV-loaded LCNPs displayed higher cytotoxic effect than free PMX/RSV mixture.

### In vivo antitumor activity

The purpose of this study was to investigate the antitumor efficacy and systemic toxicity of the synergistic combination (PMX and RSV) administered intravenously either in free form or loaded within the optimized LCNPs. This study was carried out over 25 days on Balb/c male urethane-induced lung cancer-bearing mice. The antitumor efficacy of PMX-RSV-LCNPs (F10) was evaluated via both macroscopic and microscopic examination after lung cancer induction and/or PMX-RSV-LCNP treatment. The average lung weight of tumor-bearing mice treated with free PMX/RSV mixture

(380 mg±10) was significantly lower than the positive control group (605±25) ( $P<0.05$ ). However, the mice treated with PMX-RSV-LCNPs showed the best reduction in average lung weight (260±15 mg) with insignificant difference to that of the negative control group (195±10 mg), confirming the great potentiality of optimized ion-paired PMX-RSV-LCNPs (F10) in improving the therapeutic outcomes (Figure 4A). Figure 4B shows the representative images of excised lungs from different mice groups where excised lungs of positive control group showed malignant surface lesions characterized by a massive number of lung adenomatous foci, while lungs obtained from PMX-RSV-LCNP (F10)-treated group significantly possess normal physiological features with significantly reduced malignant surface lesions.

### Tumor biomarkers

To determine the therapeutic efficacy of intravenously administered free PMX/RSV mixture and optimized ion-paired PMX-RSV-LCNPs (F10), tumor biomarkers were assessed. As depicted in Figure 4C, the level of VEGF in lungs treated with ion-paired PMX-RSV-LCNPs (F10; 3.5 pg/g) was significantly ( $P<0.05$ ) lower than those treated with free PMX/RSV mixture (5.21 pg/g). The FDA-approved multi-targeted antifolate PMX plays a major role in decreasing growth rate of tumor cells which subsequently minimizes the need for vascularization and angiogenesis and decreases the tumor burden.<sup>52</sup> Moreover, the chemopreventive polyphenolic RSV was reported as antiangiogenic factor which reduces VEGF secretion from cocultured A549.<sup>53</sup> Thanks to the synergistic effect of our chemo–herbal combination (PMX-RSV), the developed nanocarriers succeeded to develop additional control for tumor growth.<sup>27</sup>

These results were in agreement with CASP-3 level (Figure 4D) that is activated in the apoptotic cells in which lungs treated with ion-paired PMX-RSV-LCNPs (F10) showed significantly higher active CASP-3 (2.8 ng/g tissue) than those treated with free PMX/RSV (1.9 ng/g tissue) ( $P<0.05$ ).

### Histopathological and immunohistochemical analysis

As depicted in Figure 5A, the H&E-stained lung sections revealed normal physiological features of negative control mice in which normal alveoli were lined with single epithelial tissues, whereas the positive urethane-treated control group exhibited various preneoplastic to neoplastic lesions extending from epithelial hyperplasia to adenoma (blue arrow). In addition to hemorrhage and inflammatory cells, infiltration



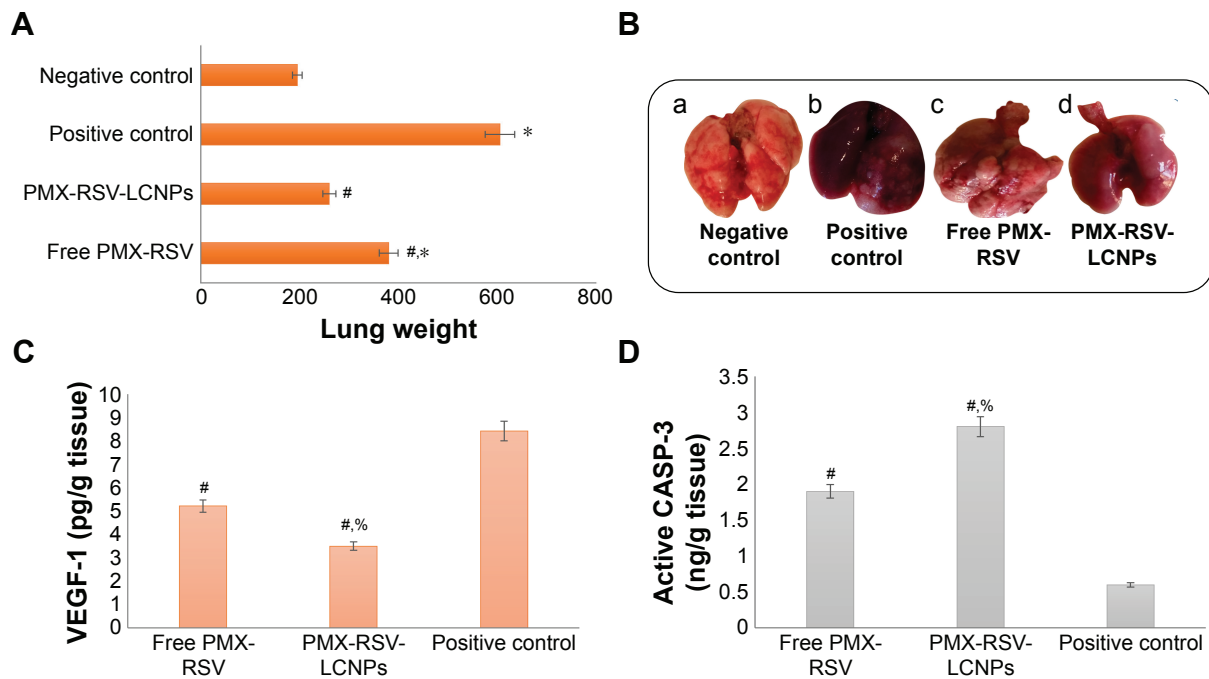


**Figure 4** In vivo antitumor activity.

**Notes:** (A) Average weight of excised lungs of mice measured at the end of treatment course. (B) Representative images of excised lung tumors displaying differences among mice groups after 3 weeks of exposing to different treatments; (a) negative control, (b) positive control, (c) free PMX-RSV mixture, and (d) ion-paired PMX-RSV-LCNPs (F10). The level of the tumor biomarkers measured using ELISA in tumor homogenate including (C) VEGF and (D) CASP-3 in urethane-induced lung cancer-bearing mice treated with free PMX-RSV and ion-paired PMX-RSV-LCNPs (F10) compared to untreated positive control. \* $P < 0.05$  vs negative control, # $P < 0.05$  vs positive control, % $P < 0.05$  vs free PMX/RSV mixture.

**Abbreviations:** CASP-3, caspase 3; LCNPs, liquid crystalline nanoparticles; PMX, pemetrexed; RSV, resveratrol; VEGF, vascular endothelial growth factor.

represented by white and black, respectively. Free PMX/RSV mixture-treated mice were associated with reduction in histopathological profile of neoplastic transformation, while the ion-paired PMX-RSV-LCNP (F10)-treated group displayed

an outstanding amelioration in the carcinogenic histopathological profile. It was observed that, compared to the positive control groups, lungs harvested from lung cancer-bearing mice treated with IV injection of free PMX/RSV mixture

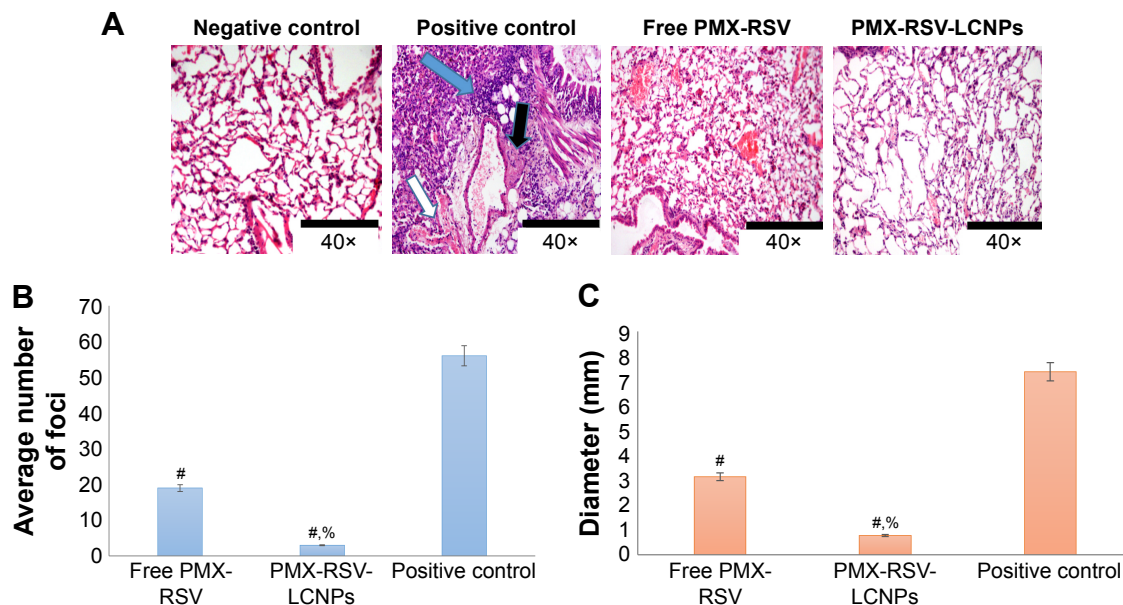


**Figure 5** (A) Histopathological analysis of H&E-stained excised lung sections of mice treated with free PMX-RSV and ion-paired PMX-RSV-LCNPs (F10) in comparison to positive control and negative control groups. (B) Average number of foci in the excised lungs, (C) The diameter of lung foci (mm).

**Notes:** # $P < 0.05$  vs positive control, % $P < 0.05$  vs Free PMX/RSV mixture.

**Abbreviations:** LCNPs, liquid crystalline nanoparticles; PMX, pemetrexed; RSV, resveratrol.

resulted in the reduced number of adenomatous foci while those harvested from mice treated systemically with optimized ion-paired PMX-RSV-LCNPs (F10) displayed the best reduction in both number and diameter of lung adenomatous foci (Figure 5B and C). Furthermore, the immunohistochemical analysis revealed the reduced expression of the proliferation marker Ki-67 protein indicating the superiority of ion-paired PMX-RSV-LCNPs (F10) in attenuating proliferation of urethane-induced adenomas (Figure 6A and B).

## Safety index

It was observed that positive control mice suffered from gradual loss in body weight of along the whole experimental duration which could be attributed to lung tumor invasion and malfunction. Compared to the free combined PMX/RSV group, the PMX-RSV-LCNP (F10) group showed less changes in total body weight which suggested lower adverse effects of PMX-RSV-LCNPs (Figure 7A). Strikingly, PMX-RSV-LCNP (F10)-treated mice maintained the well-organized alveolar structure of lung tissues which significantly improved their survival rates up to 60% during the experimental period compared to only 30% survival rate of mice treated with free PMX/RSV mixture (Figure 7B).

The death of mice was based on remarkable disruption of alveolar structure resulted from lung damage of urethane-treated mice.<sup>54,55</sup>

PMX is well known for its hepato- and nephrotoxicity. However, RSV plays an important role in attenuating toxicity associated with PMX as it exerts hepato- and nephroprotective effect.<sup>56–59</sup> Our proposed LCNPs enabled the delivery of the synergistic combination of RSV and PMX which played an important role in improving treatment outcomes based on their capability in killing cancerous cells in addition to remarkable reduction in the dosages of PMX which alleviates the toxicity concerns of the proposed PMX-RSV-LCNP formulation at the systemic level. Compared to untreated positive control or mice treated with free PMX/RSV mixture, optimized nanoformulation induced the least damage to the kidney and liver as demonstrated in Figure 7C and D, respectively. Conclusively, the improved therapeutic outcomes of urethane-induced lung cancer-bearing mice receiving PMX-RSV-LCNPs could be attributed to the great tendency of LCNPs in protecting these payloads from premature release in blood stream and reaching other organs which in turn maximize accumulation of synergistic combination (PMX/RSV) in cancer tissue. In addition, the leaky vasculature within

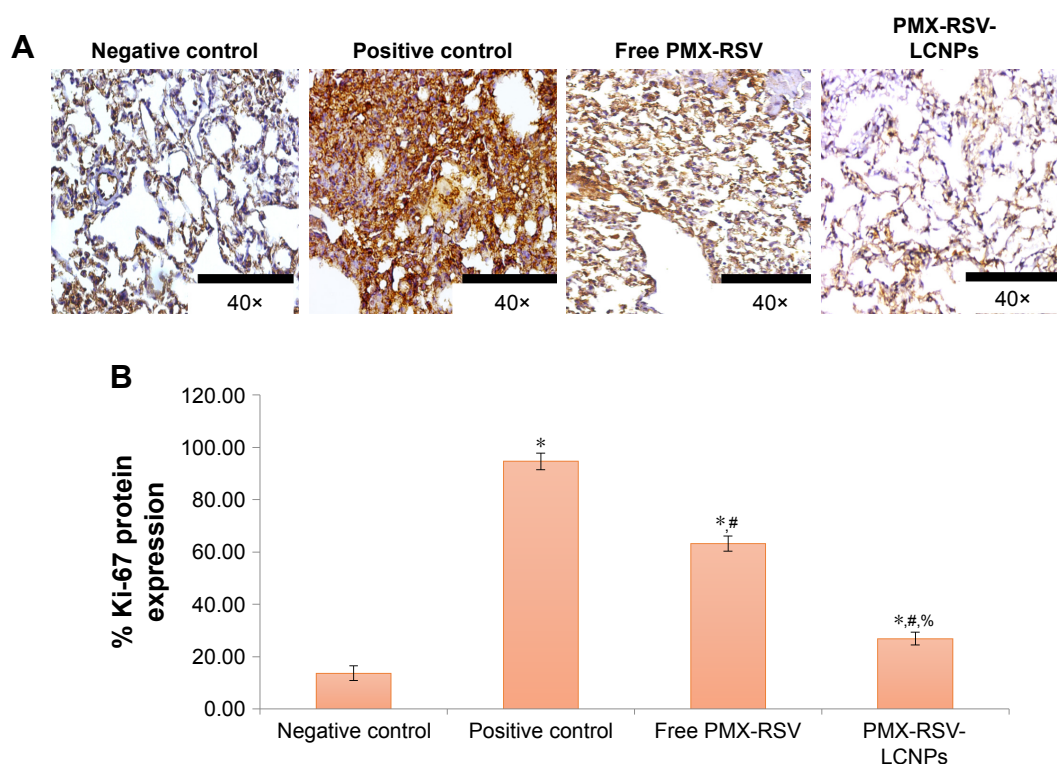


**Figure 6** Immunohistochemical analysis: (A) Ki-67 staining. (B) % expression of Ki-67 of excised lung sections of urethane-induced lung cancer-bearing mice received free PMX-RSV and ion-paired PMX-RSV-LCNPs (F10) in comparison to untreated positive control.

**Note:** \* $P < 0.05$  vs negative control, # $P < 0.05$  vs positive control, % $P < 0.05$  vs free PMX-RSV mixture.

**Abbreviations:** LCNPs, liquid crystalline nanoparticles; PMX, pemetrexed; RSV, resveratrol.

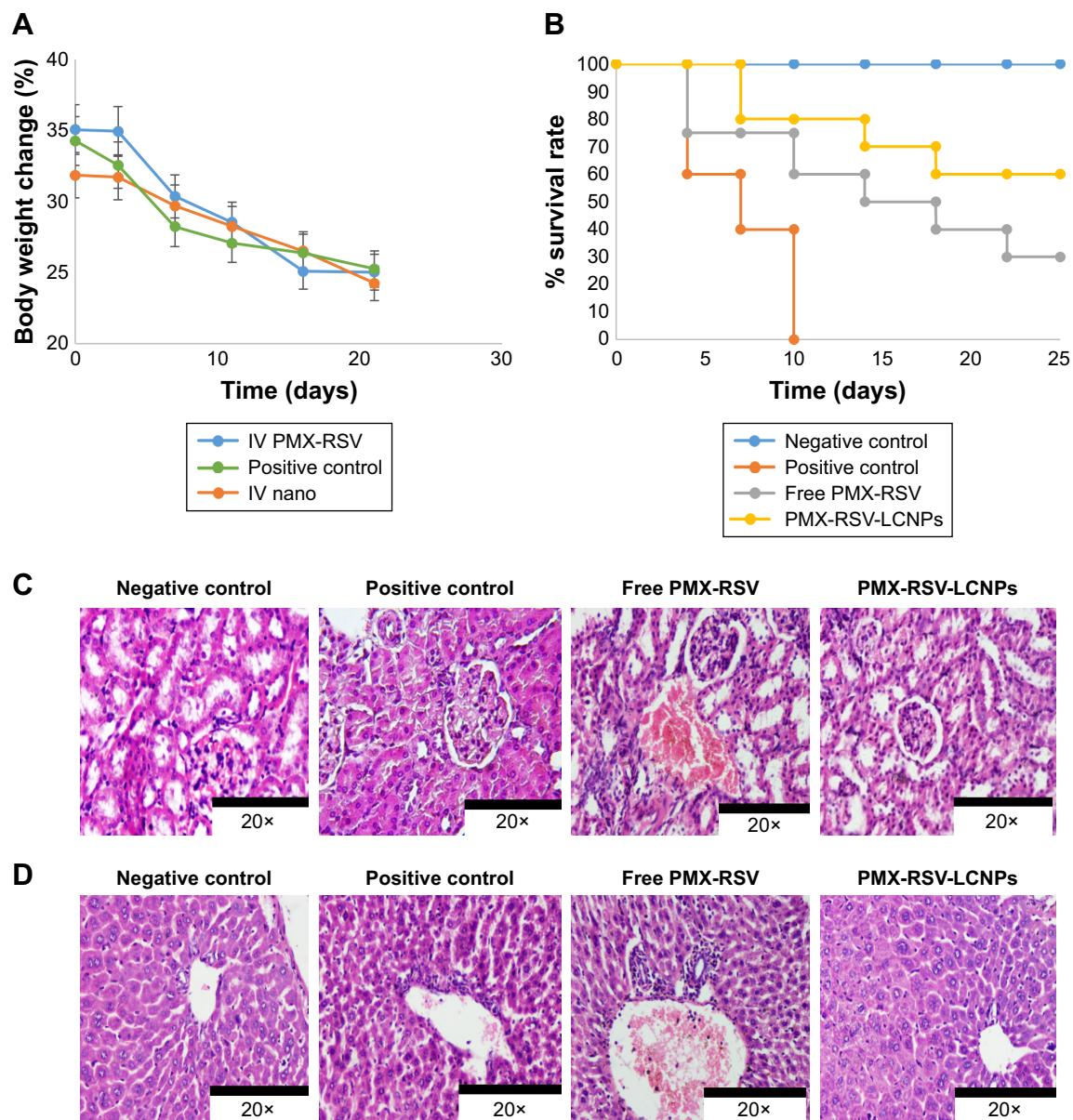


**Figure 7** Assessment of safety index of optimized LCNPs.

**Notes:** (A) Average body weights of urethane-induced lung cancer-bearing mice treated with free PMX-RSV and ion-paired PMX-RSV-LCNPs (F10) for 3 weeks compared to untreated positive control. (B) Survival rate curve among treated groups in comparison to positive and negative control groups. H&E-stained kidney (C) and liver (D) of different treatment groups.

**Abbreviations:** IV, intravenous; LCNPs, liquid crystalline nanoparticles; PMX, pemetrexed; RSV, resveratrol.

tumor site and impaired lymphatic drainage facilitate penetration and retention of the proposed LCNPs with nanometric PS of 173 nm. Obviously, PMX-RSV-LCNPs could efficiently target and suppress lung cancers which in turn enhanced survival rates and remarkably minimized systemic side effects as compared to free PMX/RSV.

## Conclusion

In this study, we shed light on the potential of LCNPs for the co-delivery of promising synergistic combination of

FDA-approved PMX and herbal RSV for lung cancer treatment. PMX-RSV-LCNPs were prepared via simple hydro-trope method. In situ HIP was carried out using CTAB to improve encapsulation efficiency and to guarantee extended release behavior of hydrophilic PMX up to 24 hours. This can interestingly minimize the dose of chemotherapeutic PMX and overcome MDR. The proposed dual drug-loaded LCNPs manifested promising cytotoxic effects as well as enhanced cellular uptake against A549 lung cancer cells. The superior in vivo antitumor efficacy of ion-paired PMX-RSV-LCNPs



was demonstrated in terms of reduced lung weights, reduced number of lung adenomatous foci and their corresponding diameter, lower angiogenic biomarker (VEGF), and higher apoptotic biomarker (CASP-3). Furthermore, they are associated with an improved histopathological and immunohistochemical profile. Strikingly, the proposed system reduced hepato- and nephrotoxicity commonly associated with PMX. Collectively, the ion-paired PMX-RSV-LCNPs offer a promising avenue for lung cancer treatment via combining the merits of chemotherapeutic and herbal drugs.

## Summary points

- This work has been directed to the preparation of LCNPs for the co-delivery of chemo-herbal drug combination of RSV and PMX for effective lung cancer treatment.
- In situ ion-pairing approach was utilized to alter the solubility characteristics of PMX and enhance its EE into the lipidic matrix. LCNPs co-loaded with RSV and ion-paired PMX were successfully tailored with PS around 173 nm and high %EE for both drugs.
- Sustained and continuous drug release behavior up to 24 hours was successfully achieved. Such sustained release pattern is preferred to decrease the systemic cytotoxicity associated with PMX.
- PMX-RSV-LCNPs demonstrated enhanced cytotoxicity on A549 lung cancer cell line as determined by MTT assay as well as superior cellular uptake attributed to the bioadhesive and membrane-fusing features of GMO.
- The in vivo antitumor efficacy of PMX-RSV-LCNPs was evaluated on lung cancer-bearing mice. PMX-RSV-LCNPs showed a superior antitumor efficacy evidenced by reduced lung weights, diminished number of lung adenomatous foci as well as their diameter, lower level of the angiogenic biomarker (VEGF), and higher apoptotic biomarker (CASP-3) level.
- PMX-RSV-LCNPs demonstrated an improved histopathological and immunohistochemical profile compared to free drugs.
- In vivo toxicity study revealed that the proposed PMX-RSV-LCNP system reduced hepato- and nephrotoxicity associated with free PMX.
- In summary, LCNPs gathered the privileges of both chemotherapeutic and herbal drugs which could offer a new potential avenue for lung cancer treatment.

## Acknowledgment

This work was supported by the research grant (No 5731) from Science and Technology Development Fund (STDF), Ministry of Scientific Research, Egypt.

## Disclosure

The authors report no conflicts of interest in this work.

## References

1. Abdelaziz HM, Gaber M, Abd-Elwakil MM, et al. Inhalable particulate drug delivery systems for lung cancer therapy: nanoparticles, microparticles, nanocomposites and nanoaggregates. *J Control Release*. 2018; 269:374–392.
2. Smith RA, Andrews KS, Brooks D, et al. Cancer screening in the United States, 2017: a review of current American Cancer Society guidelines and current issues in cancer screening. *CA Cancer J Clin*. 2017;67(2): 100–121.
3. American Cancer Society. *What Is Non-Small Cell Lung Cancer?* Atlanta, GA: American Cancer Society; 2016.
4. Zappa C, Mousa SA. Non-small cell lung cancer: current treatment and future advances. *Transl Lung Cancer Res*. 2016;5(3):288–300.
5. Midhun DE. Early detection of lung cancer. *F1000Res*. 2016;5:739.
6. American Cancer Society. *Treatment Choices for Non-Small Cell Lung Cancer, by Stage*. Atlanta, GA: American Cancer Society; 2017.
7. Chidambaram M, Manavalan R, Kathiresan K. Nanotherapeutics to overcome conventional cancer chemotherapy limitations. *J Pharm Pharm Sci*. 2011;14(1):67–77.
8. Chemotherapy And Selective Toxicity [webpage on the Internet]. All Answers Ltd.; 2013. Available from: <https://www.ukessays.com/essays/biology/chemotherapy-and-selective-toxicity-biology-essay.php?vref=1>. Accessed December 28, 2018.
9. Elzoghby AO, Elgohary MM, Kamel NM. Implications of protein- and Peptide-based nanoparticles as potential vehicles for anticancer drugs. *Adv Protein Chem Struct Biol*. 2015;98:169–221.
10. Cohen MH, Johnson JR, Wang YC, Sridhara R, Pazdur R. FDA drug approval summary: pemetrexed for injection (Alimta) for the treatment of non-small cell lung cancer. *Oncologist*. 2005;10(6):363–368.
11. PubChem [homepage on the Internet]. Compound Database; CID=446556. Available from: <https://pubchem.ncbi.nlm.nih.gov/compound/446556>. Accessed December 3, 2017.
12. Adjei AA. Pharmacology and mechanism of action of pemetrexed. *Clin Lung Cancer*. 2004;5(Suppl 2):S51–S55.
13. Chattopadhyay S, Moran RG, Goldman ID. Pemetrexed: biochemical and cellular pharmacology, mechanisms, and clinical applications. *Mol Cancer Ther*. 2007;6(2):404–417.
14. Fuld AD, Dargatzis KH, Rigas JR. Pemetrexed in advanced non-small-cell lung cancer. *Expert Opin Pharmacother*. 2010;11(8):1387–1402.
15. Ho C, Davies AM, Sangha RS, et al. Phase I/II trial of pemetrexed plus nab-paclitaxel in advanced solid tumor patients with emphasis on non-small cell lung cancer. *Invest New Drugs*. 2013;31(6):1587–1591.
16. Mahmud F, Jeon OC, Alam F, et al. Oral pemetrexed facilitates low-dose metronomic therapy and enhances antitumor efficacy in lung cancer. *J Control Release*. 2018;284:160–170.
17. El-Far SW, Helmy MW, Khattab SN, Bekhit AA, Hussein AA, Elzoghby AO. Phytosomal bilayer-enveloped casein micelles for code-livery of monascus yellow pigments and resveratrol to breast cancer. *Nanomedicine*. 2018;13(5):481–499.
18. Kabary DM, Helmy MW, Elkhodairy KA, Fang JY, Elzoghby AO. Hyaluronate/lactoferrin layer-by-layer-coated lipid nanocarriers for targeted co-delivery of rapamycin and berberine to lung carcinoma. *Colloids Surf B Biointerfaces*. 2018;169:183–194.
19. Sabra SA, Elzoghby AO, Sheweita SA, et al. Self-assembled amphiphilic zein-lactoferrin micelles for tumor targeted co-delivery of rapamycin and wogonin to breast cancer. *Eur J Pharm Biopharm*. 2018;128:156–169.
20. Elzoghby AO, El-Lakany SA, Helmy MW, Abu-Serie MM, Elgindy NA. Shell-crosslinked zein nanocapsules for oral codelivery of exemestane and resveratrol in breast cancer therapy. *Nanomedicine (Lond)*. 2017;12(24): 2785–2805.
21. Donnelly LE, Newton R, Kennedy GE, et al. Anti-inflammatory effects of resveratrol in lung epithelial cells: molecular mechanisms. *Am J Physiol Lung Cell Mol Physiol*. 2004;287(4):L774–L783.



22. Bishayee A. Cancer prevention and treatment with resveratrol: from rodent studies to clinical trials. *Cancer Prev Res (Phila)*. 2009;2(5):409–418.
23. Varoni EM, Lo Faro AF, Sharifi-Rad J, Iriti M. Anticancer molecular mechanisms of resveratrol. *Front Nutr*. 2016;3:8.
24. Hamza RZ, El-Shenawy NS. Anti-inflammatory and antioxidant role of resveratrol on nicotine-induced lung changes in male rats. *Toxicol Rep*. 2017;4:399–407.
25. Elzoghby A. Editorial (Thematic issue: nanocarriers based on natural polymers as platforms for drug and gene delivery applications). *Curr Pharm Des*. 2016;22(22):3303–3304.
26. Elzoghby A, Freag M, Mamdouh H, Elkhodairy K. Zein-based nanocarriers as potential natural alternatives for drug and gene delivery: Focus on cancer therapy. *Curr Pharm Des*. 2017;23(35):5261–5271.
27. Chen RS, Ko JC, Chiu HC, et al. Pemetrexed downregulates ERCC1 expression and enhances cytotoxicity effected by resveratrol in human nonsmall cell lung cancer cells. *Naunyn Schmiedebergs Arch Pharmacol*. 2013;386(12):1047–1059.
28. Summerlin N, Soo E, Thakur S, Qu Z, Jambhrunkar S, Popat A. Resveratrol nanoformulations: challenges and opportunities. *Int J Pharm*. 2015;479(2):282–290.
29. Angelova A, Angelov B, Mutafchieva R, Lesieur S, Couvreur P. Self-assembled multicompartiment liquid crystalline lipid carriers for protein, peptide, and nucleic acid drug delivery. *Acc Chem Res*. 2011;44(2):147–156.
30. Freag MS, Elnaggar YS, Abdelmonsif DA, Abdallah OY. Stealth, biocompatible monoolein-based lyotropic liquid crystalline nanoparticles for enhanced aloe-emodin delivery to breast cancer cells: in vitro and in vivo studies. *Int J Nanomedicine*. 2016;11(11):4799–4818.
31. Liu R, Wang S, Fang S, et al. Liquid crystalline nanoparticles as an ophthalmic delivery system for tetrandrine: development, characterization, and in vitro and in vivo evaluation. *Nanoscale Res Lett*. 2016;11(1):254.
32. Elzoghby AO, Abd-Elwakil MM, Abd-El salam K, Elsayed MT, Hashem Y, Mohamed O. Natural polymeric nanoparticles for brain-targeting: implications on drug and gene delivery. *Curr Pharm Des*. 2016;22(22):3305–3323.
33. Elzoghby AO, Hemasa AL, Freag MS. Hybrid protein-inorganic nanoparticles: from tumor-targeted drug delivery to cancer imaging. *J Control Release*. 2016;243:303–322.
34. Gaber M, Medhat W, Hany M, Saher N, Fang JY, Elzoghby A. Protein-lipid nanohybrids as emerging platforms for drug and gene delivery: challenges and outcomes. *J Control Release*. 2017;254:75–91.
35. Sabra S, Abdelmoneem M, Abdelwakil M, et al. Self-assembled nanocarriers based on amphiphilic natural polymers for anti-cancer drug delivery applications. *Curr Pharm Des*. 2017;23(35):5213–5229.
36. Spicer PT, Hayden KL, Lynch ML, Ofori-Boateng A, Burns JL. Novel process for producing cubic liquid crystalline nanoparticles (Cubosomes). *Langmuir*. 2001;17(19):5748–5756.
37. Devrim B, Bozkir A. Design and evaluation of hydrophobic ion-pairing complexation of lysozyme with sodium dodecyl sulfate for improved encapsulation of hydrophilic peptides/proteins by lipid-polymer hybrid nanoparticles. *J Nanomed Nanotechnol*. 2015;6(1):259.
38. Meyer JD, Manning MC. Hydrophobic ion pairing: altering the solubility properties of biomolecules. *Pharm Res*. 1998;15(2):188–193.
39. Swarnakar NK, Thanki K, Jain S. Bicontinuous cubic liquid crystalline nanoparticles for oral delivery of doxorubicin: implications on bioavailability, therapeutic efficacy, and cardiotoxicity. *Pharm Res*. 2014;31(5):1219–1238.
40. Elzoghby AO, Mostafa SK, Helmy MW, ElDemellawy MA, Sheweita SA. Superiority of aromatase inhibitor and cyclooxygenase-2 inhibitor combined delivery: hyaluronate-targeted versus PEGylated protamine nanocapsules for breast cancer therapy. *Int J Pharm*. 2017;529(1–2):178–192.
41. Swarnakar NK, Thanki K, Jain S. Bicontinuous cubic liquid crystalline nanoparticles for oral delivery of doxorubicin: implications on bioavailability, therapeutic efficacy, and cardiotoxicity. *Pharm Res*. 2014;31(5):1219–1238.
42. Elgindy N, Elkhodairy K, Molokhia A, Elzoghby A. Biopolymeric nanoparticles for oral protein delivery: design and in vitro evaluation. *J Nanomed Nanotechnol*. 2011;02(03):110.
43. Elzoghby AO, Mostafa SK, Helmy MW, ElDemellawy MA, Sheweita SA. Multi-reservoir phospholipid shell encapsulating protamine nanocapsules for co-delivery of letrozole and celecoxib in breast cancer therapy. *Pharm Res*. 2017;34(9):1956–1969.
44. Khattab SN, Abdel Naim SE, El-Sayed M, et al. Design and synthesis of new s-triazine polymers and their application as nanoparticulate drug delivery systems. *New J Chem*. 2016;40(11):9565–9578.
45. Elzoghby AO, Vranic BZ, Samy WM, Elgindy NA. Swellable floating tablet based on spray-dried casein nanoparticles: near-infrared spectral characterization and floating matrix evaluation. *Int J Pharm*. 2015;491(1–2):113–122.
46. Freag MS. Hyaluronate-lipid nanohybrids: fruitful harmony in cancer targeting. *Curr Pharm Des*. 2017;23(35):5283–5291.
47. Freag MS, Elnaggar YS, Abdelmonsif DA, Abdallah OY. Layer-by-layer-coated lyotropic liquid crystalline nanoparticles for active tumor targeting of rapamycin. *Nanomedicine (Lond)*. 2016;11(22):2975–2996.
48. Deshpande S, Venugopal E, Ramagiri S, Bellare JR, Kumaraswamy G, Singh N. Enhancing cubosome functionality by coating with a single layer of poly-ε-lysine. *ACS Appl Mater Interfaces*. 2014;6(19):17126–17133.
49. Jain V, Swarnakar NK, Mishra PR, et al. Paclitaxel loaded PEGylated glyceryl monooleate based nanoparticulate carriers in chemotherapy. *Biomaterials*. 2012;33(29):7206–7220.
50. Deshpande S, Singh N. Influence of cubosome surface architecture on its cellular uptake mechanism. *Langmuir*. 2017;33(14):3509–3516.
51. Harush-Frenkel O, Debotton N, Benita S, Altschuler Y. Targeting of nanoparticles to the clathrin-mediated endocytic pathway. *Biochem Biophys Res Commun*. 2007;353(1):26–32.
52. Li Q, Yano S, Ogino H, et al. The therapeutic efficacy of anti vascular endothelial growth factor antibody, bevacizumab, and pemetrexed against orthotopically implanted human pleural mesothelioma cells in severe combined immunodeficient mice. *Clin Cancer Res*. 2007;13(19):5918–5925.
53. Sahin E, Baycu C, Koparal AT, Burukoglu Donmez D, Bektur E. Resveratrol reduces IL-6 and VEGF secretion from co-cultured A549 lung cancer cells and adipose-derived mesenchymal stem cells. *Tumour Biol*. 2016;37(6):7573–7582.
54. Luo T, Loira-Pastoriza C, Patil HP, et al. PEGylation of paclitaxel largely improves its safety and anti-tumor efficacy following pulmonary delivery in a mouse model of lung carcinoma. *J Control Release*. 2016;239:62–71.
55. Wu J, Deng C, Meng F, Zhang J, Sun H, Zhong Z. Hyaluronic acid coated PLGA nanoparticulate docetaxel effectively targets and suppresses orthotopic human lung cancer. *J Control Release*. 2017;259:76–82.
56. Kitada M, Koya D. Renal protective effects of resveratrol. *Oxid Med Cell Longev*. 2013;2013(1):1–7.
57. Wang Y, Jiang Y, Fan X, et al. Hepato-protective effect of resveratrol against acetaminophen-induced liver injury is associated with inhibition of CYP-mediated bioactivation and regulation of SIRT1-p53 signaling pathways. *Toxicol Lett*. 2015;236(2):82–89.
58. Chen WM, Shaw LH, Chang PJ, et al. Hepatoprotective effect of resveratrol against ethanol-induced oxidative stress through induction of superoxide dismutase in vivo and in vitro. *Exp Ther Med*. 2016;11(4):1231–1238.
59. Osman AM, Telity SA, Damanhoury ZA, et al. Chemosensitizing and nephroprotective effect of resveratrol in cisplatin-treated animals. *Cancer Cell Int*. 2015;15(1):6.

## Supplementary materials

### Methodology

#### HPLC method for the assay of pemetrexed (PMX) and resveratrol (RSV)

A novel, accurate, precise, and sensitive HPLC method was developed and validated for simultaneous determination of both RSV and PMX using Agilent 1260 Infinity HPLC system equipped with a quaternary pump, an autosampler, vacuum degasser, diode array detector, and Agilent Chemstation data-processing system. The HPLC analysis was carried out with an Inertsil® ODS-3 reversed-phase column (250 × 4.6 mm, 5 µm; GL Sciences Inc, Torrance, CA, USA). The column was maintained at room temperature. For chromatographic elution, the injection volume was 20 µL. A step gradient was utilized for elution in which the mobile phase consisted of acetonitrile: dibasic phosphate buffer (pH adjusted to 4.9 using orthophosphoric acid) with the following ratio 15:85 to 6 minutes then converted into 50:50 gradually over 0.5 minutes, and the flow rate was 1.5 mL/min. Total run time was 10 minutes; PMX was eluted at 4.8 minutes and RSV at 9.8 minutes. PMX was detected at 225 nm, while RSV was detected at 306 nm.

#### Evaluation of in vitro cytotoxicity

In vitro cytotoxicity of free PMX, free RSV, free combined PMX/RSV solution, blank liquid crystalline nanoparticles (LCNPs), and ion-paired PMX-RSV-LCNPs was evaluated in A549 lung cancer cells using MTT assay.<sup>1</sup> Briefly, 1,000–5,000 cells/well were seeded in 96-well culture plates containing 100 µL of cell line-specific medium and incubated at 37°C in a 5% CO<sub>2</sub> atmosphere. The cells were then treated with each formulation at concentrations ranged from 0.468 to 30 µg/mL of each PMX and/or RSV and incubated at 37°C for 24 and 48 hours. Then, cells were subjected to the MTT analysis for cell viability determination. The optic density was measured at 490 nm on a microplate reader with control wells containing only cell culture medium. The viability data were analyzed in GraphPad Prism, and the IC<sub>50</sub> value for each system was calculated. Each IC<sub>50</sub> value was calculated from n=6 viability measurements per concentration. IC<sub>50</sub> was calculated after 24 and 48 hours.

#### In vitro cellular uptake

A549 lung cells were seeded on CELL view™ slide at a density of 3,000 cells/well and left overnight to allow enough time for cell attachment. Cells were incubated with fresh medium containing free coumarin-6 dye and coumarin-6-loaded LCNPs at the concentration of 0.08% w/w coumarin-6 (with

respect to lipid). After incubation for 4 and 24 hours, the medium was removed and cells were rinsed twice using PBS to eliminate any extracellular residues. Then, cells were fixed using 4% paraformaldehyde solution in dark. The nuclei were stained using 2-(4-ethoxyphenyl)-6-[6-(4-methylpiperazin-1-yl)-1H-benzimidazol-2-yl]-1H-benzimidazole (Hoechst AG, Frankfurt, Germany) containing DPX (DePeX [Distrene 80: A commercial polystyrene, a plasticizer, e.g., dibutyl phthalate and xylene]) as mounting medium. Finally, the intracellular uptake of optimized LCNPs into A549 cell line was visualized via confocal laser scanning microscopy (DMi8; Leica Microsystems, Wetzlar, Germany) using the following filter set: excitation wavelength, 450 nm; emission wavelength, 505 nm. All obtained confocal images were analyzed using Leica AF software. Moreover, the internalization of particles within each section of the cells at various cell depths was visualized using three-dimensional cellular images per time (z-stacks), where serial sections were taken across 30 fields and stacked with cross-sectional slices (25 µm) perpendicular to the plane of the cell monolayer midpoint (z-axis).<sup>2,3</sup>

## Results and discussions

### HPLC method for the assay of PMX and RSV

Several attempts were carried out for simultaneous quantitation of PMX and RSV in mixture. Isocratic elution using different proportions of mobile phases including methanol, acetonitrile, acidified water, and buffer at different ratios was not enough to provide satisfactory separation for the mixture's components. Therefore, gradient elution was applied to separate peaks of both drugs.<sup>4</sup> In the literature, various methods were reported for individual quantitation of PMX and RSV in formulations and biological fluids.<sup>4–8</sup> The optimized mobile phase composed of HPLC grade acetonitrile: dibasic phosphate buffer (pH adjusted to 4.9 using orthophosphoric acid) with the following ratio 15:85 to 6 minutes and then converted into 50:50 gradually over 0.5 minutes; flow rate was 1.5 mL/min. A rapid, sensitive, simple, and efficient method was developed for simultaneous determination of RSV and PMX in stock solution and nano-formulations. The principal peak obtained with the standard solution was at 225 nm which was selected as the  $\lambda_{\max}$  of the PMX, whereas the major peak of RSV was detected at  $\lambda_{\max}$  306 nm. A good linearity was shown by the calibration curve obtained from 0.4 to 2 mg% PMX and RSV concentration (Figure S1). The coefficient of determination (R<sup>2</sup>) of 0.9997 was obtained from the linear regression analysis of the data (peak area vs concentration). Selected chromatograms were displayed (Figure S2), in which retention time of PMX was

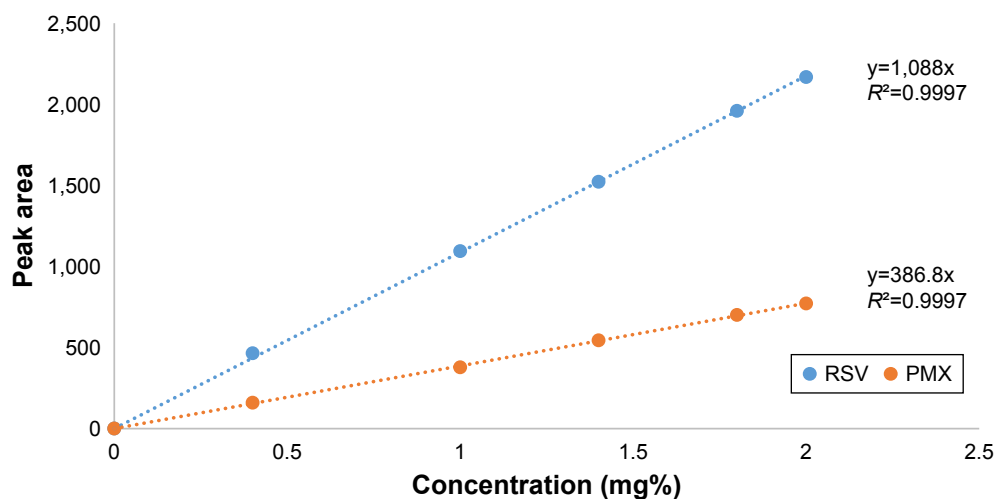


**Figure S1** HPLC calibration curve of PMX and RSV in methanol at  $\lambda_{\text{max}}$  225 and 306 nm, respectively.

**Abbreviations:** PMX, pemetrexed; RSV, resveratrol.

4.427 minutes and of RSV was 11.87 minutes so that the total run time was 12 minutes.

As summarized in Table S1, the HPLC method was validated according to International Conference on Harmonization (ICH) guidelines for intra- and inter-day precision and accuracy. The low values of relative standard deviation

(RSD) as well as % error of mean <2 confirmed the precision and accuracy of the developed HPLC method. Limit of detection was 0.2 mg%, while the limit of quantitation was 0.4 mg%. The proposed assays were also successfully applied to evaluate the entrapment efficiency (EE) of the novel LCNPs for the co-delivery of PMX and RSV for lung cancer.

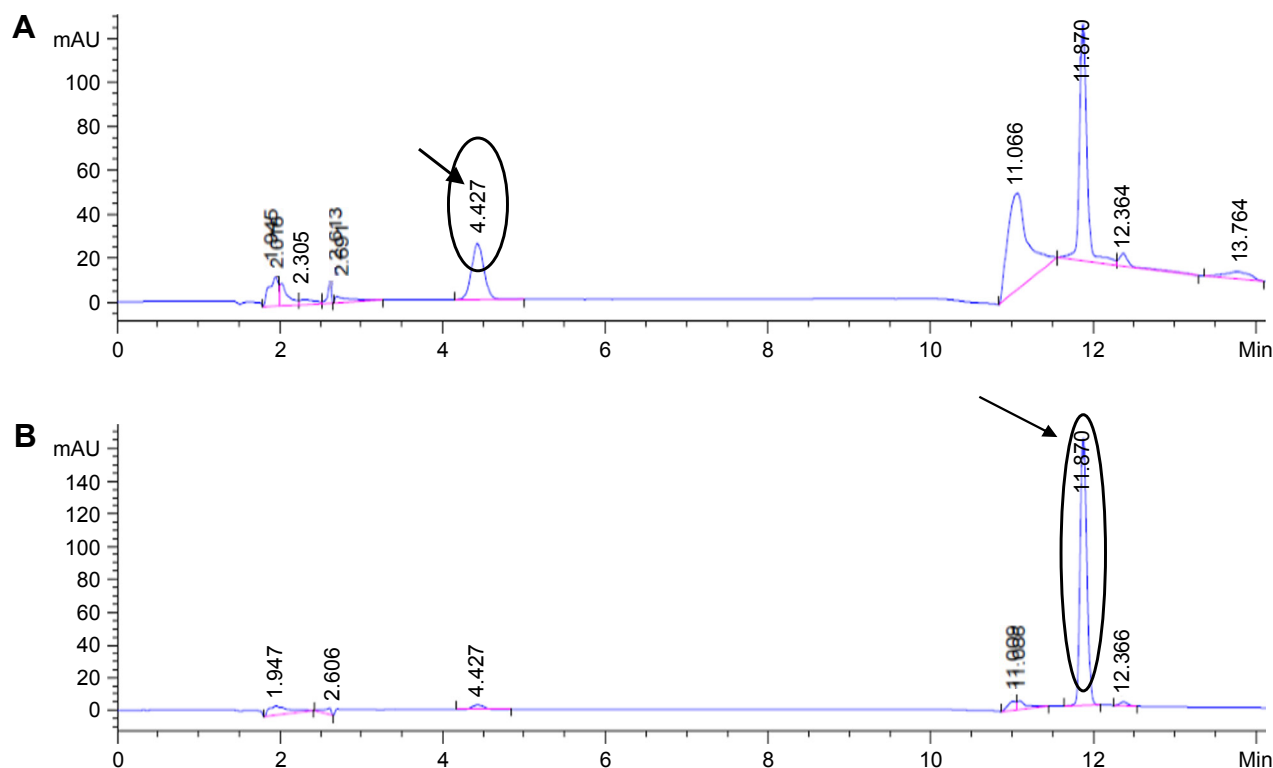


**Figure S2** Selected chromatogram of (A) PMX and (B) RSV displaying retention time at their corresponding  $\lambda_{\text{max}}$ .

**Abbreviations:** PMX, pemetrexed; RSV, resveratrol.

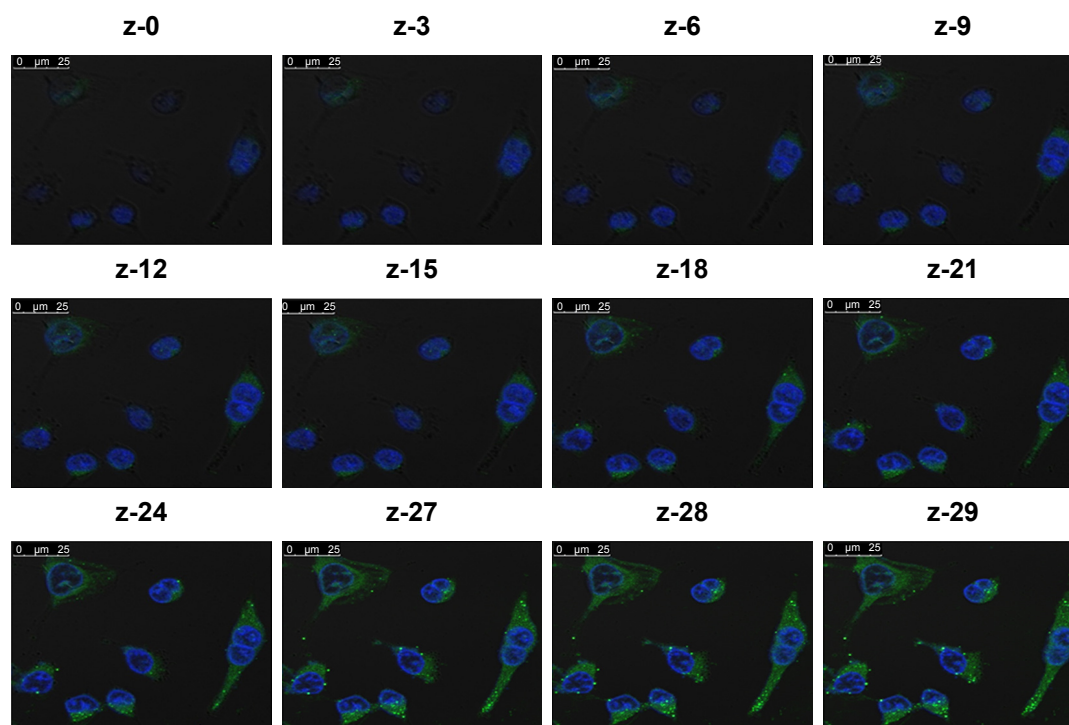


**Figure S3** Live uptake of ion-paired LCNPs in A549 cells in which three-dimensional time laps images distinguishing between cystolic and perinuclear accumulation of 178 nm LCNPs of 30 z-stacks inside the cells in the z-direction along the total depth measured (z-stack = 30 slices at 25  $\mu\text{m}$  per slices).

**Note:** The individual stacks were assembled as video displaying the oscillation of green fluorescence along the cross-sectional internalization of LCNPs from the apical to basolateral cellular membrane represented from z-0 to z-29.

**Abbreviation:** LCNPs, liquid crystalline nanoparticles.

**Table S1** Intra- and inter-day precision and accuracy of PMX and RSV (n=5 for each concentration)

Concentration (mg%)	Drug	Intra-day (n=5)			Inter-day (n=5)		
		Mean $\pm$ SD	RSD	% error	Mean $\pm$ SD	RSD	% error
0.6	PMX	0.611 $\pm$ 0.001	0.262	1.940	0.604 $\pm$ 0.011	1.903	0.733
	RSV	0.611 $\pm$ 0.011	1.864	1.916	0.588 $\pm$ 0.003	0.619	-1.933
0.8	PMX	0.801 $\pm$ 0.001	0.127	0.140	0.805 $\pm$ 0.012	1.600	0.625
	RSV	0.787 $\pm$ 0.016	2.084	-1.507	0.790 $\pm$ 0.012	1.553	-1.201
1	PMX	0.999 $\pm$ 0.001	0.154	-0.043	0.998 $\pm$ 0.004	0.459	-0.201
	RSV	0.996 $\pm$ 0.018	1.823	-0.401	0.990 $\pm$ 0.015	1.613	-0.980
1.8	PMX	1.797 $\pm$ 0.001	0.080	-0.133	1.814 $\pm$ 0.017	0.989	0.777
	RSV	1.806 $\pm$ 0.020	1.107	0.350	1.799 $\pm$ 0.017	0.957	-0.055
2	PMX	1.999 $\pm$ 0.001	0.052	-0.007	1.974 $\pm$ 0.035	1.776	-1.301
	RSV	1.994 $\pm$ 0.019	0.994	-0.270	1.999 $\pm$ 0.009	0.463	-0.050

**Abbreviations:** PMX, pemetrexed; RSV, resveratrol.

## References

1. Khattab SN, Naim SEA, El-Sayed M, et al. Design and synthesis of new s-triazine polymers and their application as nanoparticulate drug delivery systems. *New J Chem*. 2016;40(11):9565–9578.
2. Yadav KS, Jacob S, Sachdeva G, Sawant KK. Intracellular delivery of etoposide loaded biodegradable nanoparticles: cytotoxicity and cellular uptake studies. *J Nanosci Nanotechnol*. 2011;11(8):6657–6667.
3. Teskač K, Kristl J. The evidence for solid lipid nanoparticles mediated cell uptake of resveratrol. *Int J Pharm*. 2010;390(1):61–69.
4. El-Lakany SA, Elzoghby AO, Elgindy NA, Hamdy DA. HPLC methods for quantitation of exemestane-luteolin and exemestane-resveratrol mixtures in nanoformulations. *J Chromatogr Sci*. 2016;54(8):1282–1289.
5. Rivory LP, Clarke SJ, Boyer M, Bishop JF. Highly sensitive analysis of the antifolate pemetrexed sodium, a new cancer agent, in human plasma and urine by high-performance liquid chromatography. *J Chromatogr B Biomed Sci Appl*. 2001;765(2):135–140.
6. Singh G, Pai RS, Pandit V. Development and validation of a HPLC method for the determination of trans-resveratrol in spiked human plasma. *J Adv Pharm Technol Res*. 2012;3(2):130–135.
7. Warner A, Piraner I, Weimer H, White K. Development of a purity control strategy for pemetrexed disodium and validation of associated analytical methodology. *J Pharm Biomed Anal*. 2015;105:46–54.
8. Katsagonis A, Atta-Politou J, Koupparis MA. HPLC method with UV detection for the determination of trans-resveratrol in plasma. *J Liquid Chromatogr Relat Technol*. 2005;28(9):1393–1405.



## International Journal of Nanomedicine

Dovepress

### Publish your work in this journal

The International Journal of Nanomedicine is an international, peer-reviewed journal focusing on the application of nanotechnology in diagnostics, therapeutics, and drug delivery systems throughout the biomedical field. This journal is indexed on PubMed Central, MedLine, CAS, SciSearch®, Current Contents®/Clinical Medicine,

Journal Citation Reports/Science Edition, EMBase, Scopus and the Elsevier Bibliographic databases. The manuscript management system is completely online and includes a very quick and fair peer-review system, which is all easy to use. Visit <http://www.dovepress.com/testimonials.php> to read real quotes from published authors.

Submit your manuscript here: <http://www.dovepress.com/international-journal-of-nanomedicine-journal>



# Discovery of Furanoquinone Derivatives as a Novel Class of DNA Polymerase and Gyrase Inhibitors for MRSA Eradication in Cutaneous Infection

Shih-Chun Yang<sup>1</sup>, Kai-Wei Tang<sup>2</sup>, Chih-Hung Lin<sup>3</sup>, Ahmed Alalaiwe<sup>4</sup>,  
Chih-Hua Tseng<sup>2,5,6,7\*</sup> and Jia-You Fang<sup>8,9,10,11\*</sup>

## OPEN ACCESS

### Edited by:

Santi M. Mandal,  
Indian Institute of Technology  
Kharagpur, India

### Reviewed by:

Rajendra H. Patil,  
Savitribai Phule Pune University, India  
Nagendran Tharmalingam,  
Alpert Medical School, United States

### \*Correspondence:

Chih-Hua Tseng  
chihhua@kmu.edu.tw  
Jia-You Fang  
fajy@mail.cgu.edu.tw

### Specialty section:

This article was submitted to  
Antimicrobials, Resistance  
and Chemotherapy,  
a section of the journal  
Frontiers in Microbiology

**Received:** 22 February 2019

**Accepted:** 13 May 2019

**Published:** 29 May 2019

### Citation:

Yang S-C, Tang K-W, Lin C-H,  
Alalaiwe A, Tseng C-H and Fang J-Y  
(2019) Discovery of Furanoquinone  
Derivatives as a Novel Class of DNA  
Polymerase and Gyrase Inhibitors  
for MRSA Eradication in Cutaneous  
Infection. *Front. Microbiol.* 10:1197.  
doi: 10.3389/fmicb.2019.01197

<sup>1</sup> Department of Cosmetic Science, Providence University, Taichung, Taiwan, <sup>2</sup> School of Pharmacy, College of Pharmacy, Kaohsiung Medical University, Kaohsiung, Taiwan, <sup>3</sup> Center for General Education, Chang Gung University of Science and Technology, Taoyuan, Taiwan, <sup>4</sup> Department of Pharmaceutics, College of Pharmacy, Prince Sattam Bin Abdulaziz University, Al Kharj, Saudi Arabia, <sup>5</sup> Department of Fragrance and Cosmetic Science, College of Pharmacy, Kaohsiung Medical University, Kaohsiung, Taiwan, <sup>6</sup> Department of Medical Research, Kaohsiung Medical University Hospital, Kaohsiung, Taiwan, <sup>7</sup> Department of Pharmacy, Kaohsiung Municipal Ta-Tung Hospital, Kaohsiung, Taiwan, <sup>8</sup> Pharmaceutics Laboratory, Graduate Institute of Natural Products, Chang Gung University, Taoyuan, Taiwan, <sup>9</sup> Chinese Herbal Medicine Research Team, Healthy Aging Research Center, Chang Gung University, Taoyuan, Taiwan, <sup>10</sup> Research Center for Food and Cosmetic Safety and Research Center for Chinese Herbal Medicine, Chang Gung University of Science and Technology, Taoyuan, Taiwan, <sup>11</sup> Department of Anesthesiology, Chang Gung Memorial Hospital, Taoyuan, Taiwan

Methicillin-resistant *Staphylococcus aureus* (MRSA) is the primary microbe responsible for skin infections that are particularly difficult to eradicate. This study sought to inhibit planktonic and biofilm MRSA using furanoquinone-derived compounds containing imine moiety. A total of 19 furanoquinone analogs were designed, synthesized, and assessed for anti-MRSA potency. Among 19 compounds, (Z)-4-(hydroxyimino)naphtho[1,2-b]furan-5(4H)-one (HNF) and (Z)-4-(acetoxylimino)naphtho[1,2-b]furan-5(4H)-one (ANF) showed antibacterial activity superior to the others based on an agar diffusion assay. HNF and ANF exerted a bactericidal effect with a minimum inhibitory concentration (MIC) of 9.7 ~ 19.5 and 2.4 ~ 9.7  $\mu\text{g/ml}$ , respectively. Both compounds were able to reduce the MRSA count by 1,000-fold in biofilm as compared to the control. *In vivo* efficacy was evaluated using a mouse model of skin infection. Topical application of lead compounds significantly suppressed abscess occurrence and the MRSA burden, and also ameliorated the skin-barrier function. The biochemical assay indicated the compounds' inhibition of DNA polymerase and gyrase. *In silico* docking revealed a favorable interaction of the compounds with DNA polymerase and gyrase although the binding was not very strong. The total DNA analysis and proteomic data suggested a greater impairment

of some proteins by HNF than ANF. In general, HNF and ANF were similarly potent in MRSA inhibition *in vitro* and *in vivo*. The findings demonstrated that there was room for structural modification of furanoquinone compounds that could be used to identify anti-MRSA agent candidates.

**Keywords:** MRSA, furanoquinone, skin, DNA polymerase, gyrase

## INTRODUCTION

*Staphylococcus aureus* is largely involved in hospital- and community-acquired infections. *S. aureus* has become resistant to conventional antibiotics due to its resilient ability to develop several approaches to fight against the antibiotics. More than 2 million people are infected by superbug pathogens, which cause >700,000 deaths each year (Fair and Tor, 2014). The most remarkable strain among the antibiotic-resistant bacteria is methicillin-resistant *S. aureus* (MRSA). More than 50% of clinical isolates from *S. aureus* show methicillin resistance (Hiramatsu et al., 2014). About 75% of MRSA causes infection in the skin and soft tissues (Kurosu et al., 2013). MRSA facilely locates in the lesions of atopic dermatitis and chronic wounds, playing a critical role in disease progression (Shi et al., 2018). As a resident microbe in skin appendages, MRSA is also responsible for causing folliculitis and hidradenitis suppurativa. The development of new agents for eradicating cutaneous drug-resistant *S. aureus* is urgently needed.

Previously, some compounds belonging to the quinine family were reported to show inhibitory activity against MRSA (Nagata et al., 1998; Rejiniemon et al., 2014; May Zin et al., 2017). We recently demonstrated the anti-MRSA capability of two furanoquinones, naphtho[1,2-*b*]furan-4,5-dione and naphtho[2,3-*b*]furan-4,9-dione (Yang et al., 2017). In this study, we designed alternatives for imine in the 4-position of both compounds in the search for derivatives with improved MRSA inhibition. The aim of the present work was to assess furanoquinone analogs for their *in vitro* killing of drug-resistant *S. aureus* and their *in vivo* efficacy in fighting skin infection. Bacteria generate extracellular polymeric substances to form biofilm, which is innately resistant to conventional antibiotics. MRSA is recognized as the frequent cause of biofilm (Vergara et al., 2017). The morbidity and mortality of patients with cutaneous wounds increase once the MRSA biofilm colonizes in the open lesion (Song et al., 2016). In addition to the planktonic form of MRSA, we also examined the anti-biofilm activity of the furanoquinone derivatives.

The antibacterial effect of new drugs or lead compounds is associated with a variety of targets such as ribosomes, polymerases, and topoisomerases (Brown and Wright, 2016). The anti-MRSA mechanisms of the furanoquinone derivatives with potential activity were investigated by using the experimental platforms of wrapping assay and proteomics. The biocidal action was further validated by docking simulation using the crystallographic structure of the target proteins in complex with the lead compounds to elucidate the binding modes at enzymes' active sites.

## MATERIALS AND METHODS

### Synthetic Procedures

Commercial reagents were used as received without additional purification. Melting points were determined with the Electrothermal IA9100 micro-melting point apparatus and were uncorrected. NMR spectra were recorded with a Varian Unity-400 MHz spectrometer using DMSO-*d*<sub>6</sub> and CDCl<sub>3</sub> as solvent and tetramethylsilane as the internal standard. Chemical shifts were expressed as  $\delta$  (ppm). Splitting patterns had been described as follows: s = singlet; brs = broad singlet; d = doublet; t = triplet; dt = double triplet; m = multiplet. The raw data of NMR for all compounds are shown in **Supplementary Materials**. Analytical TLC was performed on Art. 5554 Kieselgel 60 GF254 produced by Merck, and the compound spots were detected with a UV light indicator irradiated at 254 and 366 nm. Art. 7734 Kieselgel 60 GF254 (70–400 mesh) made by Merck was used for column chromatography. The purity of the compounds was determined with elemental analysis (EA). EA was recorded on an Heraeus CHN-O Rapid apparatus and the results were within  $\pm 0.4\%$  of the theoretical value.

### General Procedure for the Synthesis of Compounds 3a–3c

The protocol for synthesizing compounds 3a, 3b, and 3c was described in our previous study (Tseng et al., 2010).

### General Procedure for the Synthesis of Compounds 4a–4c

To a suspension of 2 (0.20 g, 1.0 mmol) in ethanol (30 ml) was added appropriate hydroxylamines hydrochloride (3.0 mmol), and the mixture was refluxed for 1 h. The solvent was removed in vacuum and the residue suspended in H<sub>2</sub>O (20 ml). The resulting precipitate was purified by methanol:CH<sub>2</sub>Cl<sub>2</sub> (1:50) and recrystallized from ethanol to give the title products.

### (Z)-4-(Hydroxyimino)Naphtho[1,2-*b*]Furan-5(4*H*)-One (4a)

Yield 67%. Mp.: 233–234°C. <sup>1</sup>H NMR (400 MHz, DMSO-*d*<sub>6</sub>): 8.69 (brs, 1H, -OH), 8.06–8.04 (m, 1H, 9-H), 7.96 (d, *J* = 2.0 Hz, 1H, 2-H), 7.80–7.75 (m, 2H, 6-H, 8-H), 7.53–7.49 (m, 1H, 7-H), 7.26 (d, *J* = 2.0 Hz, 1H, 3-H). <sup>13</sup>C NMR (100 MHz, DMSO-*d*<sub>6</sub>): 181.15, 148.98, 144.85, 143.28, 134.90, 128.84, 128.68, 128.48, 128.20, 120.75, 113.35, 112.71. Anal. calcd for C<sub>12</sub>H<sub>7</sub>NO<sub>3</sub> : C 67.61, H 3.31, N 6.57; found: C 67.47, H 3.36, N 6.53.

### **(Z)-4-(Methoxyimino)Naphtho[1,2-b]Furan-5(4H)-One (4b)**

Yield 71%. Mp.: 143–144°C.  $^1\text{H}$  NMR (400 MHz,  $\text{CDCl}_3$ ): 8.19–8.17 (m, 1H, 9-H), 7.72–7.70 (m, 1H, 6-H), 7.62 (dt,  $J = 1.2$ , 7.6 Hz, 1H, 8-H), 7.50 (d,  $J = 2.0$  Hz, 1H, 2-H), 7.42–7.37 (m, 1H, 7-H), 7.11 (d,  $J = 2.0$  Hz, 1H, 3-H), 4.31 (s, 3H,  $\text{CH}_3$ ).  $^{13}\text{C}$  NMR (100 MHz,  $\text{CDCl}_3$ ): 181.86, 150.86, 143.55, 143.08, 134.55, 129.22, 129.11, 129.05, 128.42, 120.02, 113.47, 112.87, 64.50. Anal. calcd for  $\text{C}_{13}\text{H}_9\text{NO}_3$ : C 68.72, H 3.99, N 6.16; found: C 68.65, H 4.02, N 6.12.

### **(Z)-4-[(Benzyloxy)Imino]Naphtho[1,2-b]Furan-5(4H)-One (4c)**

Yield 59%. Mp.: 146–147°C.  $^1\text{H}$  NMR (400 MHz,  $\text{CDCl}_3$ ): 8.19–8.17 (m, 1H, 9-H), 7.71–7.69 (m, 1H, 6-H), 7.62 (dt,  $J = 1.2$ , 7.6 Hz, 1H, 8-H), 7.47–7.34 (m, 7H, 2-H, 7-H, Ar-H), 7.04 (d,  $J = 1.6$  Hz, 1H, 3-H), 5.55 (s, 2H,  $\text{CH}_2$ ).  $^{13}\text{C}$  NMR (100 MHz,  $\text{CDCl}_3$ ): 181.92, 150.88, 143.48, 143.38, 136.13, 134.57, 129.20, 129.10, 129.05, 128.60 (2C), 128.48, 128.45 (2C), 124.03, 120.03, 113.53, 113.07, 79.18. Anal. calcd for  $\text{C}_{19}\text{H}_{13}\text{NO}_3$ : C 75.24, H 4.32, N 4.62; found: C 75.03, H 4.37, N 4.43.

### **General Procedure for the Synthesis of Compounds 5e–5h**

To a suspension of 1 (0.20 g, 1.0 mmol) in ethanol (30 ml) was added appropriate hydrazines (3.0 mmol), and the mixture was refluxed for 4 h. The solvent was removed in vacuum and the residue suspended in  $\text{H}_2\text{O}$  (20 ml). The resulting precipitate was purified by methanol: $\text{CH}_2\text{Cl}_2$  (1:50) and recrystallized from ethanol to give the title products.

### **(Z)-4-(2-Phenylhydrazono)Naphtho[2,3-b]Furan-9(4H)-One (5e)**

Yield 43%. Mp.: 237–238°C.  $^1\text{H}$  NMR (400 MHz,  $\text{DMSO}-d_6$ ): 10.58 (s, 1H, NH), 8.60–8.58 (m, 1H, 8-H), 8.42 (d,  $J = 2.0$  Hz, 1H, 2-H), 8.20–8.18 (m, 1H, 5-H), 7.94 (d,  $J = 2.0$  Hz, 1H, 3-H), 7.78–7.74 (m, 1H, 6-H), 7.64–7.57 (m, 3H, 7-H, Ar-H), 7.43–7.40 (m, 2H, Ar-H), 7.08–7.05 (m, 1H, Ar-H).  $^{13}\text{C}$  NMR (100 MHz,  $\text{DMSO}-d_6$ ): 171.35, 149.38, 147.25, 144.41, 136.13, 132.12, 129.99, 129.18 (2C), 127.74, 127.61, 125.43, 123.98, 122.76, 122.46, 115.13 (2C), 110.44. Anal. calcd for  $\text{C}_{18}\text{H}_{12}\text{N}_2\text{O}_2 \cdot 0.1\text{H}_2\text{O}$ : C 74.51, H 4.25, N 9.66; found: C 74.27, H 4.23, N 9.57.

### **(Z)-4-(2-(4-Fluorophenyl)Hydrazono)Naphtho[2,3-b]Furan-9(4H)-One (5f)**

Yield 47%. Mp.: 222–223°C.  $^1\text{H}$  NMR (400 MHz,  $\text{DMSO}-d_6$ ): 10.57 (s, 1H, NH), 8.58–8.56 (m, 1H, 8-H), 8.43 (d,  $J = 2.0$  Hz, 1H, 2-H), 8.20–8.18 (m, 1H, 5-H), 7.93 (d,  $J = 2.0$  Hz, 1H, 3-H), 7.77–7.73 (m, 1H, 6-H), 7.65–7.57 (m, 3H, 7-H, Ar-H), 7.28–7.24 (m, 2H, Ar-H).  $^{13}\text{C}$  NMR (100 MHz,  $\text{DMSO}-d_6$ ): 171.35, 158.07 ( $^1J_{\text{CF}} = 237.3$  Hz), 149.39, 147.23, 141.05 ( $^4J_{\text{CF}} = 1.5$  Hz), 136.07, 132.08, 130.00, 127.83, 127.68, 125.43, 123.98, 122.73, 116.59 (2C,  $^3J_{\text{CF}} = 8.3$  Hz), 115.79 (2C,  $^2J_{\text{CF}} = 22.0$  Hz), 110.42. Anal. calcd for  $\text{C}_{18}\text{H}_{11}\text{FN}_2\text{O}_2$ : C 70.58, H 3.62, N 9.15; found: C 70.29, H 3.50, N 9.15.

### **(Z)-4-(2-(4-Methoxyphenyl)Hydrazono)Naphtho[2,3-b]Furan-9(4H)-One (5g)**

Yield 51%. Mp.: 178–179°C.  $^1\text{H}$  NMR (400 MHz,  $\text{DMSO}-d_6$ ): 10.54 (s, 1H, NH), 8.58–8.56 (m, 1H, 8-H), 8.46 (d,  $J = 2.0$  Hz, 1H, 2-H), 8.21–8.18 (m, 1H, 5-H), 7.94 (d,  $J = 2.0$  Hz, 1H, 3-H), 7.76–7.72 (m, 1H, 6-H), 7.61–7.55 (m, 3H, 7-H, Ar-H), 7.03–7.00 (m, 2H, Ar-H), 3.78 (s, 3H,  $\text{OCH}_3$ ).  $^{13}\text{C}$  NMR (100 MHz,  $\text{DMSO}-d_6$ ): 171.13, 155.32, 149.37, 147.02, 138.06, 136.24, 131.91, 129.86, 127.35, 126.24, 125.38, 123.81, 122.71, 116.47 (2C), 114.54 (2C), 110.21, 55.33. Anal. calcd for  $\text{C}_{19}\text{H}_{14}\text{N}_2\text{O}_3$ : C 71.69, H 4.43, N 8.80; found: C 71.29, H 4.39, N 8.76.

### **(Z)-4-(2-(p-Tolyl)Hydrazono)Naphtho[2,3-b]Furan-9(4H)-One (5h)**

Yield 49%. Mp.: 212–213°C.  $^1\text{H}$  NMR (400 MHz,  $\text{DMSO}-d_6$ ): 10.54 (s, 1H, NH), 8.59–8.57 (m, 1H, 8-H), 8.42 (d,  $J = 2.0$  Hz, 1H, 2-H), 8.20–8.18 (m, 1H, 5-H), 7.93 (d,  $J = 2.0$  Hz, 1H, 3-H), 7.77–7.73 (m, 1H, 6-H), 7.60–7.56 (m, 1H, 7-H), 7.54–7.52 (m, 2H, Ar-H), 7.23–7.21 (m, 2H, Ar-H), 2.31 (s, 3H,  $\text{CH}_3$ ).  $^{13}\text{C}$  NMR (100 MHz,  $\text{DMSO}-d_6$ ): 171.25, 149.36, 147.15, 142.10, 136.20, 132.01, 131.53, 129.93 (2C), 129.62, 127.55, 126.86, 125.40, 123.90, 122.73, 115.15 (2C), 110.32, 20.44. Anal. calcd for  $\text{C}_{19}\text{H}_{14}\text{N}_2\text{O}_2 \cdot 0.15\text{H}_2\text{O}$ : C 75.02, H 4.72, N 9.21; found: C 74.83, H 4.50, N 9.15.

### **General Procedure for the Synthesis of Compounds 6d–6h**

To a suspension of 2 (0.20 g, 1.0 mmol) in ethanol (30 ml) was added appropriate hydrazines (3.0 mmol), and the mixture was refluxed for 2 h. The solvent was removed in vacuum and the residue suspended in  $\text{H}_2\text{O}$  (20 ml). The resulting precipitate was purified by methanol: $\text{CH}_2\text{Cl}_2$  (1:50) and recrystallized from ethanol to give the title products.

### **(Z)-N'-(5-Oxonaphtho[1,2-b]Furan-4(5H)-Ylidene)Acetohydrazide (6d)**

Yield 65%. Mp.: 188–189°C.  $^1\text{H}$  NMR (400 MHz,  $\text{DMSO}-d_6$ ): 13.66 (brs, 1H, NH), 8.08–8.06 (m, 1H, 9-H), 7.93–7.92 (m, 1H, 2-H), 7.80–7.76 (m, 1H, 8-H), 7.72–7.70 (m, 1H, 6-H), 7.49–7.45 (m, 1H, 7-H), 6.90–6.89 (m, 1H, 3-H), 2.36 (s, 3H,  $\text{CH}_3$ ).  $^{13}\text{C}$  NMR (100 MHz,  $\text{DMSO}-d_6$ ): 181.72, 148.18, 145.96, 135.56, 129.03, 128.45, 128.20, 127.69, 120.38, 120.00, 107.36, 19.56. Anal. calcd for  $\text{C}_{14}\text{H}_{10}\text{N}_2\text{O}_3$ : C 66.14, H 3.96, N 11.02; found: C 66.22, H 4.02, N 10.91.

### **(Z)-2-(5-Oxonaphtho[1,2-b]Furan-4(5H)-Ylidene)Hydrazine-1-Carboxamide (6e)**

Yield 55%. Mp.: 221–222°C.  $^1\text{H}$  NMR (400 MHz,  $\text{DMSO}-d_6$ ): 13.23 (brs, 1H, NH), 8.17–8.15 (m, 1H, 9-H), 7.94 (d,  $J = 2.0$  Hz, 1H, 2-H), 7.84–7.76 (m, 2H, 6-H, 8-H), 7.52–7.47 (m, 1H, 7-H), 7.36 (brs, 2H,  $\text{NH}_2$ ), 7.28 (d,  $J = 2.0$  Hz, 1H, 3-H).  $^{13}\text{C}$  NMR (100 MHz,  $\text{DMSO}-d_6$ ): 181.20, 155.15, 146.96, 145.53, 135.09, 128.72, 128.48, 128.19, 127.20, 120.54, 120.17, 107.87. Anal. calcd for  $\text{C}_{13}\text{H}_9\text{N}_3\text{O}_3 \cdot 0.1\text{H}_2\text{O}$ : C 60.73, H 3.61, N 16.35; found: C 60.71, H 3.53, N 16.18.



### (Z)-2-(5-Oxonaphtho[1,2-b]Furan-4(5H)-Ylidene)Hydrazine-1-Carbothioamide (6f)

Yield 53%. Mp.: 219–220°C. <sup>1</sup>H NMR (400 MHz, DMSO-*d*<sub>6</sub>): 13.84 (brs, 1H, NH), 9.33 (brs, 1H, NH<sub>2</sub>), 9.00 (brs, 1H, NH<sub>2</sub>), 8.17–8.15 (m, 1H, 9-H), 7.94 (d, *J* = 2.0 Hz, 1H, 2-H), 7.83–7.76 (m, 2H, 6-H, 8-H), 7.53–7.49 (m, 1H, 7-H), 7.35 (d, *J* = 2.0 Hz, 1H, 3-H). <sup>13</sup>C NMR (100 MHz, DMSO-*d*<sub>6</sub>): 181.57, 179.26, 148.24, 145.60, 135.34, 128.93, 128.44, 128.26, 127.52, 120.33, 120.29, 108.12. Anal. calcd for C<sub>13</sub>H<sub>9</sub>N<sub>3</sub>O<sub>2</sub>S : C 57.55, H 3.34, N 15.49; found: C 57.72, H 3.45, N 15.15.

### (Z)-N-Methyl-2-(5-Oxonaphtho[1,2-b]Furan-4(5H)-Ylidene)Hydrazine-1-Carbothioamide (6g)

Yield 58%. Mp.: 218–219°C. <sup>1</sup>H NMR (400 MHz, DMSO-*d*<sub>6</sub>): 14.00 (brs, 1H, NH), 9.51–9.48 (m, 1H, NHCH<sub>3</sub>), 8.17–8.15 (m, 1H, 9-H), 7.95 (d, *J* = 2.0 Hz, 1H, 2-H), 7.83–7.76 (m, 2H, 6-H, 8-H), 7.53–7.48 (m, 1H, 7-H), 7.28 (d, *J* = 2.0 Hz, 1H, 3-H), 3.14 (d, *J* = 4.8 Hz, 3H, NHCH<sub>3</sub>). <sup>13</sup>C NMR (100 MHz, DMSO-*d*<sub>6</sub>): 181.35, 177.91, 148.08, 145.62, 135.28, 128.87, 128.37, 128.23, 128.10, 127.48, 120.29, 120.20, 107.91, 31.56. Anal. calcd for C<sub>14</sub>H<sub>11</sub>N<sub>3</sub>O<sub>2</sub>S · 0.5H<sub>2</sub>O : C 57.12, H 4.11, N 14.27; found: C 57.43, H 3.95, N 13.94.

### (Z)-4-(2-Phenylhydrazono)Naphtho[1,2-b]Furan-5(4H)-One (6h)

Yield 65%. Mp.: 159–160°C. <sup>1</sup>H NMR (400 MHz, CDCl<sub>3</sub>): 15.70 (brs, 1H, NH), 8.37–8.35 (m, 1H, 9-H), 7.87–7.85 (m, 1H, 6-H), 7.68–7.64 (m, 1H, 8-H), 7.58 (d, *J* = 2.0 Hz, 1H, 2-H), 7.56–7.54 (m, 2H, Ar-H), 7.44–7.39 (m, 3H, Ar-H), 7.19–7.15 (m, 1H, 7-H), 6.99 (d, *J* = 2.0 Hz, 1H, 3-H). <sup>13</sup>C NMR (100 MHz, CDCl<sub>3</sub>): 178.82, 145.87, 144.17, 142.39, 133.25, 129.55, 128.90, 128.58, 128.22 (2C), 127.78, 126.00 (2C), 125.20, 121.22, 120.22, 116.24, 106.70. Anal. calcd for C<sub>18</sub>H<sub>12</sub>N<sub>2</sub>O<sub>2</sub> · 0.1H<sub>2</sub>O : C 74.51, H 4.25, N 9.66; found: C 74.28, H 4.23, N 9.53.

### General Procedure for the Synthesis of Compounds 7a, 7b, 8a, and 8b

The synthetic protocol of compound 7a was described in the previous study (Tseng et al., 2010). To a suspension of 3a or 4a (0.21 g, 1.0 mmol) in acetic anhydride (3 ml) or methanesulfonyl chloride (3 ml) was added pyridine (1.0 ml). The reaction mixture was stirred at room temperature for 1 h. The solvent was removed in vacuum, and the residue was triturated with H<sub>2</sub>O (20 ml), filtered, and washed with H<sub>2</sub>O. The crude product was recrystallized from ethanol to give the title product.

### (Z)-4-[[[(Methylsulfonyl)Oxy]Imino}Naphtho[2,3-b]Furan-9(4H)-One (7b)

Yield 78%. Mp.: 226–227°C. <sup>1</sup>H NMR (400 MHz, CDCl<sub>3</sub>): 8.40–8.37 (m, 1H, 8-H), 8.34–8.30 (m, 1H, 5-H), 7.84 (d, *J* = 2.0 Hz, 1H, 2-H), 7.73–7.68 (m, 2H, 6-H, 7-H), 7.42 (d, *J* = 2.0 Hz, 1H, 3-H), 3.37 (s, 3H, CH<sub>3</sub>). <sup>13</sup>C NMR (100 MHz, CDCl<sub>3</sub>) δ 172.50, 149.76, 148.67, 148.59, 148.24,

133.29, 131.90, 131.42, 130.83, 127.35, 124.97, 113.59, 36.87. Anal. calcd for C<sub>13</sub>H<sub>9</sub>NO<sub>5</sub>S : C 53.60, H 3.11, N 4.81; found: C 53.49, H 3.11, N 4.88.

### (Z)-4-(Acetoxymino)Naphtho[1,2-b]Furan-5(4H)-One (8a)

Yield 82%. Mp.: 170–171°C. <sup>1</sup>H NMR (400 MHz, DMSO-*d*<sub>6</sub>): 8.03 (d, *J* = 2.0 Hz, 1H, 2-H), 8.02–8.00 (m, 1H, 9-H), 7.81–7.74 (m, 2H, 6-H, 8-H), 7.56–7.52 (m, 1H, 7-H), 7.26 (d, *J* = 2.0 Hz, 1H, 3-H), 2.40 (s, 3H, CH<sub>3</sub>). <sup>13</sup>C NMR (100 MHz, DMSO-*d*<sub>6</sub>): 180.99, 167.73, 152.31, 146.35, 145.52, 135.48, 129.55, 128.49, 128.34, 128.05, 121.33, 113.08, 112.72, 19.46. Anal. calcd for C<sub>14</sub>H<sub>9</sub>NO<sub>4</sub> : C 65.88, H 3.55, N 5.49; found: C 65.45, H 3.64, N 5.44.

### (Z)-4-[[[(Methylsulfonyl)Oxy]Imino}Naphtho[1,2-b]Furan-5(4H)-One (8b)

Yield 84%. Mp.: 196–197°C. <sup>1</sup>H NMR (400 MHz, DMSO-*d*<sub>6</sub>): 8.05 (d, *J* = 2.0 Hz, 1H, 2-H), 8.02–8.00 (m, 1H, 9-H), 7.83–7.75 (m, 2H, 6-H, 8-H), 7.58–7.54 (m, 1H, 7-H), 7.07 (d, *J* = 2.0 Hz, 1H, 3-H), 3.50 (s, 3H, CH<sub>3</sub>). <sup>13</sup>C NMR (100 MHz, DMSO-*d*<sub>6</sub>): 180.01, 153.24, 147.52, 145.79, 135.64, 129.88, 128.59, 128.31, 127.81, 121.54, 112.64, 112.02, 36.77. Anal. calcd for C<sub>13</sub>H<sub>9</sub>NO<sub>5</sub>S : C 53.60, H 3.11, N 4.81; found: C 53.21, H 3.29, N 4.86.

### Bacterial Strains

MRSA (ATCC 33591) and *Escherichia coli* (ATCC 8739) were supplied by American Type Culture Collection. The clinical isolates of MRSA (KM-1 and KM-5) were isolated from Kaohsiung Medical University Hospital. KV-1 and KV-5 were vancomycin-intermediate *S. aureus* (VISA) strains found in Kaohsiung Medical University Hospital provided by Dr. Po-Liang Lu. The clinical isolates were taken from infected patients using a protocol approved by the institutional review board at Kaohsiung Medical University Hospital. The patients provided written informed consent to participate. These strains were cultured in tryptic soy broth (TSB) at 37°C with 150 rpm.

### Agar Diffusion Test

We began the antibacterial study with an agar diffusion assay. MRSA (OD<sub>600</sub> = 0.7) was inoculated in TSB agar (0.75%). The MRSA-agar mixture (5 ml) was distributed in the dish for 15 min, followed by the dropping of lead compounds (10 μl) onto the agar. DMSO was used as the vehicle of the compounds. The inhibition-zone diameter was measured after a 16-h treatment. The control group was the MRSA-agar mixture added with DMSO alone.

### Minimum Inhibitory Concentration (MIC) and Minimum Bactericidal Concentration (MBC)

A twofold serial dilution method was employed to detect MIC. An overnight bacteria culture was diluted in TSB to achieve OD<sub>600</sub> = 0.01 (about 2 × 10<sup>6</sup> CFU/ml). The

detailed procedure for examining MIC and MBC was described previously (Yang et al., 2017).

### Live/Dead MRSA Assay

The viability and death of MRSA by treatment of compounds (10, 50, and 100  $\mu\text{g/ml}$ ) for 4 h were stained with a Live/Dead BacLight® (Molecular Probes). The kit was incubated with bacteria for 15 min. The death rate was then determined by flow cytometry (Accuri C6, BD Biosciences). The image of live/dead MRSA distribution was visualized using Leica DMi8 fluorescence microscopy.

### Biofilm Detection

A Cellview® dish was used by inoculating the microbes ( $\text{OD}_{600} = 0.1$ ) in TSB with 1% glucose at 37°C for 24 h to form biofilm. The biofilm was treated by furanoquinone derivatives at 25, 50, or 100  $\mu\text{g/ml}$  or cetylpyridinium chloride (CPC) at 100  $\mu\text{g/ml}$  for 24 h. PBS was utilized to rinse the biofilm for removing the loosely adherent planktonic bacteria and suspended in PBS. The biofilm structure in PBS was broken by strong vortex for recovering MRSA inside the biofilm. The recovered MRSA outside and inside the biofilm were serially diluted and plated in an agar plate for 24 h in order to count CFU. The biofilm, which was treated with 100  $\mu\text{g/ml}$  compounds, was stained by BacLight® for 15 min for confocal microscopic observation. The 3D structure and thickness of the biofilm were evaluated by Leica confocal microscopy (TSC SP2).

### Cutaneous MRSA Infection

A female BALB/c mouse (8 weeks old) was purchased from the National Laboratory Animal Center (Taipei, Taiwan). This study was carried out in accordance with the principles of the Basel Declaration and recommendations of Guidelines for the Care and Use of Laboratory Animals of Chang Gung University. The protocol was approved by the Chang Gung University. After shaving the mouse's back hair, MRSA ( $1 \times 10^6$  CFU) in PBS (150  $\mu\text{l}$ ) was subcutaneously injected into the dorsal region. The topical lead compounds (100  $\mu\text{g/ml}$ ) with a volume of 0.1 ml were applied onto the injection site every 24 h for 6 days. The appearance of the skin surface was monitored using a Mini Scope-V digital magnifier (M&T Optics). Transepidermal water loss (TEWL) was assessed using Tewameter (TM300, Courage and Khazaka) from 0 to 6 days after MRSA injection. The yellow-brown color ( $b^*$ ) of the skin was quantified by CD100 colorimeter (Yokogawa). The skin was excised for homogenization by MagNA Lyser (Roche) at the end of the experiment. CFU of bacteria within the skin was detected by serially diluted skin homogenates on TSB.

### Cutaneous Tolerance

The 10% DMSO/PBS containing 100  $\mu\text{g/ml}$  lead compounds was topically applied daily (0.1 ml) on the mouse's back for 5 consecutive days. The compound-containing solution was replaced with a new one each day. After removal, the treated skin area was determined by TEWL, erythema ( $a^*$ ), and cutaneous surface pH value.

### Morphology of MRSA

MRSA morphology was observed by scanning electron microscopy (SEM). The bacteria at  $\text{OD}_{600} = 0.1$  were treated with furanoquinone compounds or CPC at 100  $\mu\text{g/ml}$  for 24 h. MRSA was then fixed with 3% glutaraldehyde and 2% paraformaldehyde in cacodylate buffer several times. After dehydration in an ascending series of ethanol, the samples were coated with gold and visualized under Hitachi SU8220 SEM.

### Total DNA in MRSA

The bacteria were grown in TSB to  $\text{OD}_{600} = 3$  and then treated with furanoquinone compounds (200  $\mu\text{g/ml}$ ) at 37°C for 4 h. The centrifuged pellet was resuspended in water. The analysis of total DNA was carried out using a Presto Mini Bacteria Kit based on the manufacturer's instructions (Yang et al., 2017).

### Total RNA in MRSA

The MRSA culture and compound treatment protocol for total RNA quantification was the same with total DNA measurement. The RNA in MRSA was extracted using a Direct-zol RNA Miniprep kit (Zymo) based upon the manufacturer's instructions. The total RNA concentration was analyzed using a UV/visible spectrophotometer at 260 nm.

### Total Protein in MRSA

The MRSA culture and subsequent treatment for the protein concentration measurement was the same with the total DNA measurement. The total protein content was analyzed using a Bio-Rad protein assay kit in an ELISA reader at 595 nm.

### Anti-Taq DNA Polymerase Activity

The polymerase chain reaction (PCR) was performed with a 50- $\mu\text{l}$  volume at the following concentrations: 100 ng MRSA genomic DNA as the template, 0.4  $\mu\text{M}$  primer 1 (isaB-F: 5'-atgaataaaaccagtaaagtgtg-3'), 0.4  $\mu\text{M}$  primer 2 (isaB-R: 5'-ttattactgtgtttgatgg-3'), 1x YEA Taq PCR reaction buffer, 2.5 mM dNTP, 2.5 U YEA Taq DNA polymerase, and lead compounds (0.1 ~ 2  $\mu\text{g}/\mu\text{l}$ ). The PCR reaction was done with the instrument at 95°C for 1 min to complete 30 cycles of 10 s at 95°C and 30 s at 56°C to generate 528 bp amplicons and analyzed by agar electrophoresis.

### Wrapping Assay

The relaxed form of Pbr322 DNA was prepared by incubating supercoiled pBR322 DNA with topoisomerase I according to the manufacturer's instructions. The relaxed DNA was extracted with a Gel/PCR DNA Fragments Extraction kit and resuspended in buffer. For the gyrase supercoiling reaction, the reaction mixture (20  $\mu\text{l}$ ) of 100 ng relaxed from DNA, gyrase reaction buffer, 2 U gyrase, and lead compounds (0.1 ~ 2  $\mu\text{g}/\mu\text{l}$ ) was incubated at 37°C for 1 h. The reaction was terminated by increasing the temperature to 65°C for 20 min. The DNA products were analyzed by electrophoresis on the agarose gel.

## Proteomic Characterization

The treatment procedure of the lead compounds was the same as for the total DNA quantification. The SDS-PAGE was carried out followed by Coomassie blue staining. The bands were taken and digested with trypsin for 12 h. Trichloroacetic acid (0.5%) was employed to acidify the digested proteins. The MALDI-mass analysis was carried out on a Bruker Ultraflex MALDI-TOF mass spectrometer. The spectra were collected from 400 shots per spectrum over an  $m/z$  range of 600 ~ 3000, and calibrated by 4-point internal calibration. The fold change of the protein expression after lead compound treatment was estimated by band quantification of Prodigy Samespots analysis software. The protein masses were assigned and used for a database search with the MASCOT search engine<sup>1</sup>. The detailed information of mass/mass analysis was the same as previous study (Pan et al., 2012).

## In silico Docking

The crystal structures of the proteins were downloaded from the RCSB Protein Data Bank. The 3D conformation of the compounds was generated by ChemBio 3D Ultra 14.0. The molecular docking was conducted using an Achilles Blind Docking Server<sup>2</sup>. The “blind docking” approach was the setup for docking of the small molecule to the targets (Sánchez-Linares et al., 2012). Visual representation of molecules was created with 3Dmol described by Rego and Koes (2015).

<sup>1</sup> www.matrixscience.com

<sup>2</sup> http://bio-hpc.ucam.edu/achilles/

**TABLE 1** | The physicochemical properties of furanoquinone derivatives and diameter of inhibition zone of MRSA after treatment with furanoquinone derivatives.

Code	Formula	AlogP	HBD	HBA	MW (Da)	Inhibition zone (mm)
3a	C <sub>12</sub> H <sub>7</sub> NO <sub>3</sub>	2.27	1	3	213.19	0
3b	C <sub>13</sub> H <sub>9</sub> NO <sub>3</sub>	2.31	0	3	227.22	0
3c	C <sub>19</sub> H <sub>13</sub> NO <sub>3</sub>	3.89	0	3	303.31	0
4a (HNF)	C <sub>12</sub> H <sub>7</sub> NO <sub>3</sub>	2.27	1	3	213.19	23.49 ± 1.24
4b	C <sub>13</sub> H <sub>9</sub> NO <sub>3</sub>	2.31	0	3	227.22	23.10 ± 0.76
4c	C <sub>19</sub> H <sub>13</sub> NO <sub>3</sub>	3.89	0	3	303.31	0
5e	C <sub>18</sub> H <sub>12</sub> N <sub>2</sub> O <sub>2</sub>	4.06	1	3	288.30	0
5f	C <sub>18</sub> H <sub>11</sub> FN <sub>2</sub> O <sub>2</sub>	4.27	1	3	306.29	0
5g	C <sub>19</sub> H <sub>14</sub> N <sub>2</sub> O <sub>3</sub>	4.05	1	4	318.33	0
5h	C <sub>19</sub> H <sub>14</sub> N <sub>2</sub> O <sub>2</sub>	4.55	1	3	302.33	0
6d	C <sub>14</sub> H <sub>10</sub> N <sub>2</sub> O <sub>3</sub>	1.63	1	3	254.24	0
6e	C <sub>18</sub> H <sub>12</sub> N <sub>2</sub> O <sub>2</sub>	4.06	1	3	288.30	0
6f	C <sub>18</sub> H <sub>11</sub> FN <sub>2</sub> O <sub>2</sub>	4.27	1	3	306.29	0
6g	C <sub>19</sub> H <sub>14</sub> N <sub>2</sub> O <sub>3</sub>	4.05	1	4	318.33	15.34 ± 0.73
6h (TNF)	C <sub>19</sub> H <sub>14</sub> N <sub>2</sub> O <sub>2</sub>	4.55	1	3	302.33	9.12 ± 0.16
7a	C <sub>14</sub> H <sub>9</sub> NO <sub>4</sub>	2.09	0	4	255.23	0
7b	C <sub>13</sub> H <sub>9</sub> NO <sub>5</sub> S	2.04	0	5	291.28	0
8a (ANF)	C <sub>14</sub> H <sub>9</sub> NO <sub>4</sub>	2.09	0	4	255.23	24.35 ± 2.84
8b	C <sub>13</sub> H <sub>9</sub> NO <sub>5</sub> S	2.04	0	5	291.28	14.98 ± 15.47

Each value represents the mean and SD (n = 3).

## Statistical Analysis

The data presented as mean and standard deviation (SD). The difference in the data of the experimental groups was analyzed using the Kruskal–Wallis test. The *post hoc* test for checking the individual difference was Dunn’s test. The significance was demonstrated as \* for  $p < 0.05$ , \*\* for  $p < 0.01$ , and \*\*\* for  $p < 0.001$  in the figures.

## RESULTS

### Inhibitory Activity Screening Against Drug-Resistant Bacteria

We herein synthesized imine-containing furanoquinone derivatives from their alkoxime and hydrazino precursors in the regiospecific and stereospecific modes. **Schemes 1, 2** describe the synthetic routes to the furanoquinone derivatives. Both schemes are illustrated in **Supplementary Materials**. The physicochemical properties including Alog P, hydrogen-bonding donor number (HBD), hydrogen-bonding acceptor number (HBA), and molecular weight (MW) are estimated by molecular modeling (Discovery Studio 3.1, Accelrys) as shown in **Table 1**. We first tested the anti-MRSA activity of compounds 3a through 8b by agar diffusion assay. The initial antibacterial screening showed no inhibition zone against MRSA by all linear furanoquinones (3, 5, and 7 series) as demonstrated in **Table 1**. Some angular furanoquinones (4, 6, and 8 series) were found to effectively inhibit MRSA growth. The angular compounds with an alkoxime linker (4 series) displayed stronger inhibition than those with a hydrazino linker (6 series). Compounds 4a ((Z)-4-(hydroxyimino)naphtho[1,2-*b*]furan-5(4*H*)-one, HNF) and 8a ((Z)-4-(acetoxymino)naphtho[1,2-*b*]furan-5(4*H*)-one, ANF) provided the largest inhibition zone with a diameter of 23.5 and 24.4 mm, respectively. Most of the compounds with a hydrazino linker were inactive, except for compounds 6g and 6h (TNF), which had the moderate inhibition zone of 15.3 and 9.1 mm. HNF, ANF, and TNF were selected for further evaluation of MIC and MBC against MRSA isolates. As shown in **Table 2**, HNF and ANF were more active than TNF against ATCC 33591 in terms of MIC and MBC. ANF was found to be twofold more active than HNF according to MIC. The presence of many MRSA isolates in clinics highlights the need for improved potency of new compounds. The lead compounds revealed comparable MIC and MBC between ATCC 33591 and clinical MRSA isolates (KM-1 and KM-2). Again, TNF exhibited poorer activity than HNF and ANF against clinical isolates. Vancomycin is approved as the first choice for MRSA infection treatment. However, vancomycin resistance has emerged in *S. aureus*. The clinical isolates of vancomycin-intermediate *S. aureus* (VISA) were also employed to test the inhibitory potency of the lead compounds. A high anti-VISA effect for HNF and ANF with MIC between 9.7 and 19.5 µg/ml was detected. The compounds were also evaluated for activity against *E. coli*, which is a Gram-negative species. The selected agents were less effective against *E. coli* than against Gram-positive bacteria.



**TABLE 2 |** The MIC and MBC of MRSA, VISA, and *E. coli* after treatment with furanoquinone derivatives.

Strain	MIC ( $\mu\text{g/ml}$ )			MBC ( $\mu\text{g/ml}$ )		
	HNF	ANF	TNF	HNF	ANF	TNF
MRSA	9.7 ~ 19.5	2.4 ~ 9.7	625 ~ 1250	19.5	19.5	625 ~ 1250
KM-1	9.7 ~ 19.5	19.5	>312.5	19.5 ~ 39	19.5 ~ 39	>312.5
KM-5	2.4 ~ 19.5	2.4 ~ 19.5	>312.5	19.5 ~ 156	19.5 ~ 39	>312.5
KV-1	9.7 ~ 19.5	19.5	>312.5	3.9 ~ 19.5	19.5 ~ 39	>312.5
KV-5	9.7 ~ 19.5	9.7 ~ 19.5	>312.5	9.7 ~ 39	39	>312.5
<i>E. coli</i>	39	19 ~ 39	>312.5	312.5	312.5	>312.5

Each value represents the mean and SD ( $n = 3$ ).

## Inhibitory Activity of HNF and ANF Against Planktonic MRSA

The selected compounds at various concentrations were assessed using an agar diffusion test as shown in **Figure 1A**. HNF and ANF displayed a clear inhibition zone on the agar media against planktonic MRSA. Both compounds showed a dose-dependent inhibition zone at 39 ~ 1,250  $\mu\text{g/ml}$ . HNF and ANF had a similar effect on the inhibition zone. TNF displayed an inhibition zone at all concentrations tested, but the zone was smaller than with HNF and ANF. None of the zone diameters exhibited statistical significance. Flow cytometry was employed to measure the MRSA death rate. As shown in **Figure 1B**, the representative profiles of flow cytometry evidenced a high survival of MRSA without any treatment (97% in the red circle). HNF and ANF killed >98% of MRSA. TNF was less potent than HNF and ANF against the majority of MRSA. **Figure 1C** illustrates the viable bacteria percentage calculated from flow cytometry. ANF revealed greater reduction in viability compared to HNF, as ANF diminished the MRSA burden by more than 99%. HNF and ANF were chosen as the most promising of the derivatives based on an agar diffusion assay and flow cytometry. For this reason, both compounds were further evaluated by live/dead staining observed under a fluorescence microscope. Live MRSA with an intact membrane would be stained green by SYTO9-DNA interaction. Propidium iodide with red fluorescence is a molecule that diffuses to bacteria with a compromised membrane, implying cell death. As shown in **Figure 1D**, the non-treatment control exhibited a diffuse distribution of live MRSA with green staining. The green signal decreased following the increase of compound concentration from 10 to 100  $\mu\text{g/ml}$ . Although the live bacteria were significantly reduced by lead compound treatment, the propidium iodide signal was very low. This indicates that HNF and ANF killed MRSA with limited cell-membrane damage.

## Inhibitory Activity of HNF and ANF Against Biofilm MRSA

The bacteria in biofilm virulently resist antibiotics. Therefore, we examined whether HNF and ANF were also useful for eradicating biofilm MRSA. **Figure 2A** presents the effect of furanoquinone compounds on the MRSA CFU outside and inside the biofilm. Cetylpyridinium chloride (CPC) as an effective biofilm inhibitor was used as a reference. We found that HNF and ANF inhibited MRSA production outside the biofilm at

concentrations of >25  $\mu\text{g/ml}$ . A complete MRSA inhibition occurred at 100  $\mu\text{g/ml}$ . The comparator agent CPC showed a preferential inhibition on MRSA outside the biofilm, which was comparable to 50  $\mu\text{g/ml}$  HNF or ANF. An ideal antibacterial agent should disrupt and transport into the biofilm matrix to eradicate pathogens. The anti-MRSA activity of lead compounds toward bacteria inside the biofilm was dose-dependent. HNF prevented MRSA growth inside the biofilm more effectively than ANF. HNF at 100  $\mu\text{g/ml}$  achieved a 4-log CFU reduction compared to the non-treatment control.

**Figure 2B** shows the antibiofilm effect seen by live/dead staining. The viable MRSA in the intact biofilm (control) revealed a massive, thick architecture. The green fluorescence was weakened by treatment of lead compounds and CPC, suggesting the restriction of bacterial colonization. **Figure 2C** illustrates the average thickness of biofilm calculated from confocal microscopy. The biofilm thickness could be reduced from 30.1 to 17.2, 14.0, and 15.1  $\mu\text{m}$  by HNF, ANF, and CPC, respectively.

## Inhibitory Activity of HNF and ANF Against Cutaneous MRSA Infection

The mouse was subcutaneously infected with the bacteria to determine the *in vivo* antimicrobial effect of HNF and ANF. **Figure 3A** depicts the appearance of the skin surface with and without infection 0, 2, 4, and 6 days post-injection. We observed the abscess after injection, finding that it resembled localized skin infection. The diameter of the abscess was about 3 mm. The topical application of HNF and ANF significantly reduced the lesional area after a 2-day treatment. The phyma nearly disappeared after a 6-day application of ANF. The MRSA CFU was detected 6 days post-infection as shown in **Figure 3B**. A 3-log increase of bacterial CFU in the skin could be seen by MRSA invasion. HNF and ANF suppressed the bacterial load in the skin relative to the vehicle control by about 2 logs. ANF and HNF were similarly efficient in the reduction of the MRSA burden in the skin.  $\Delta\text{TEWL}$  (TEWL at the lesional site minus TEWL at the non-treatment control site) was detected daily to estimate the skin-barrier characteristic disrupted by MRSA-associated inflammation. As shown in **Figure 3C**, the MRSA-infected lesion displayed an increase of  $\Delta\text{TEWL}$  from Day 1. This indicates MRSA's deficient barrier property. Topical administration of both compounds



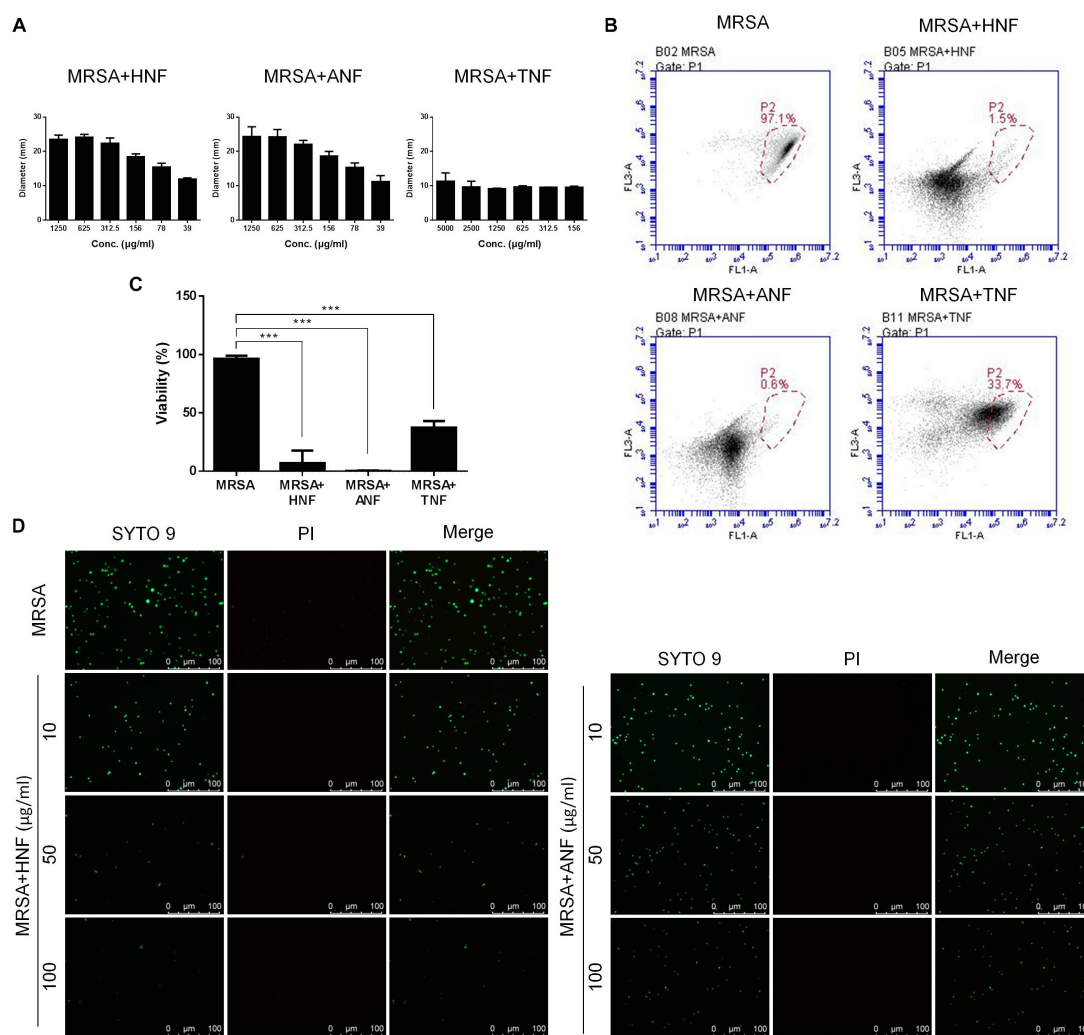


**FIGURE 1 |** Determination of the anti-MRSA activity of furanoquinone derivatives. **(A)** Zone of inhibition measured from disk diffusion assay. Panel **(B)** represented flow cytometry diagram of live/dead MRSA. **(C)** MRSA viability measured from flow cytometry. **(D)** The planktonic live/dead MRSA strain viewed under fluorescence microscopy. All data are presented as the mean of three experiments ± SD. \*\*\* $p < 0.001$ .

significantly ameliorated the barrier function, approximating the TEWL baseline. The abscess generally exhibited a yellow–brown color. This appearance is analyzed by  $b^*$  axis of colorimetry as depicted in **Figure 3D**. MRSA infection was significantly elevated to  $b^*$  level in the injection region. The furanoquinone compounds had no potential effect on the improvement of  $b^*$  although the compounds reduced the abscess size. This could be because we measured  $b^*$  right on the lesional surface although the lesional size of the compound-treated skin was smaller than that of the vehicle-treated skin.

## Cutaneous Tolerance of HNF and ANF

A prerequisite of the development of new candidates for antibiotics is the assurance of the safety use. HNF and ANF were administered on intact mouse skin to examine the possibility of irritation. As shown in **Figure 4A**, no redness or scaling was observed on cutaneous surface of the vehicle control. In contrast,

mice treated with HNF and ANF revealed a slight redness.  $\Delta$ TEWL was increased following the increase of the treatment duration for all groups tested (**Figure 4B**). This could be due to the ability of the aqueous vehicle to hydrate the stratum corneum and disturb the barrier function. Although the skin's appearance showed a slight erythema after compound treatment, this trend was not detected by erythema quantification ( $a^*$ ) since no groups demonstrated a significant difference (**Figure 4C**). A similar tendency was observed in the skin-surface pH (**Figure 4D**). The cutaneous tolerance study suggested that HNF and ANF showed only marginal irritation.

## Anti-MRSA Mechanisms of HNF and ANF

Further experiments aimed to explore the antibacterial mechanisms of furanoquinone compounds against MRSA. SEM allowed us to directly visualize MRSA integrity and morphology. As shown in **Figure 5A**, the untreated bacteria

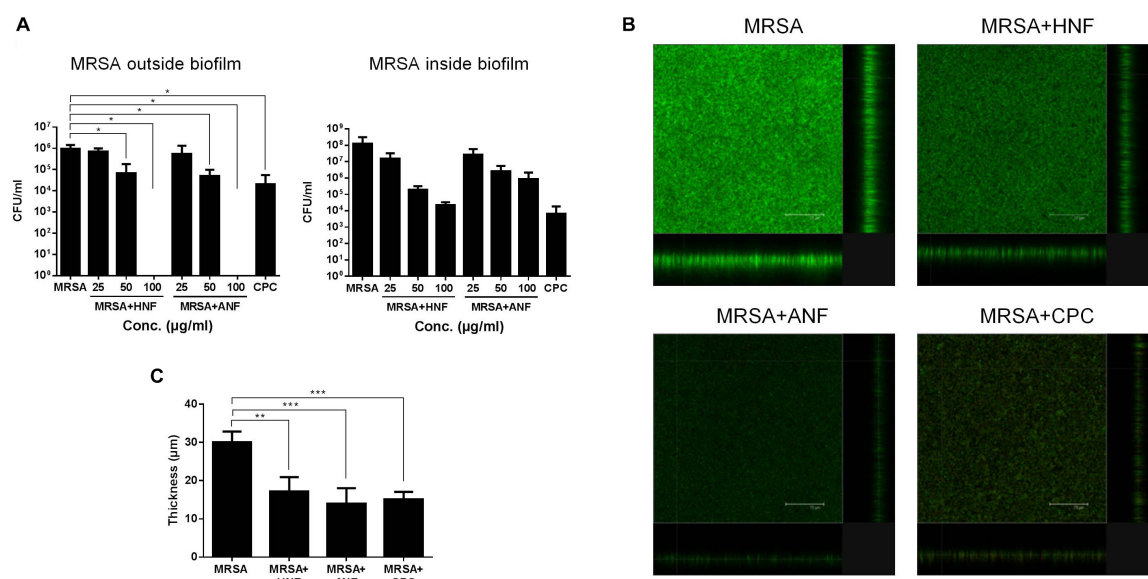


**FIGURE 2 |** Determination of the antibacterial activity of HNF and ANF against biofilm MRSA. **(A)** MRSA CFU outside and inside the biofilm. **(B)** The three-dimensional images of biofilm visualized by confocal microscopy. **(C)** The corresponding biofilm thickness measured by confocal microscopy. All data are presented as the mean of three experiments  $\pm$  S.D. \*\*\* $p < 0.001$ , \*\* $p < 0.01$ , \* $p < 0.05$ .

exhibited a smooth surface without debris. CPC as a comparator agent altered the cell structure. The enlarged image (30 K magnification) showed membrane destruction and the leakage of cytoplasm materials, resulting in the bacterial shrinkage. Most of the bacteria remained intact after the HNF and ANF treatment. Some cells revealed an irregular shape without obvious membrane disintegration and cell lysis. The total DNA, RNA, and protein of furanoquinone-treated MRSA are quantified as shown in **Figures 5B–D**, respectively. The genomic DNA analysis indicated that the content of DNA decreased significantly in furanoquinone-treated bacteria. HNF or ANF exerted about a threefold reduction of DNA concentration compared to the untreated control. Total RNA was also decreased by HNF and ANF although the reduction level was minor as compared to the DNA decrease. ANF caused a 63% inhibition of the total protein content than the control. A significant degradation was shown with HNF-treated MRSA, leading to an 84% decrease.

Enzymes such as DNA polymerases and topoisomerases are potential targets of antibacterial mechanisms. We hypothesized that HNF and ANF could affect these enzymes, thus disrupting the transcription from DNA to RNA and the translation from RNA to proteins. The gene products of DNA polymerase, topoisomerase I, and gyrase were chosen for the enzyme-inhibition study. As illustrated in **Figure 5E**, furanoquinone compounds significantly inhibited PCR products of DNA polymerase. This inhibition activated by HNF and ANF was concentration-dependent, with stronger activity with ANF than with HNF. Mitomycin C (MMC), an anticancer agent known to induce DNA damage via interstrand DNA crosslink with no effect on DNA polymerase activity, was used as the comparator. **Figure 5E** demonstrates a momentous presence of PCR products by MMC application. The compounds

were also utilized for targeted enzyme inhibition using a wrapping assay to analyze the suppression of supercoiling by topoisomerase I and gyrase. As shown in **Figure 5F**, HNF and ANF at concentrations from 0.1 to 2  $\mu\text{g}/\mu\text{l}$  did not inhibit DNA relaxation activity of topoisomerase I. On the other hand, furanoquinone treatment markedly reduced gyrase activity (**Figure 5G**). Based on these results, we can suggest that HNF and ANF deactivated both DNA polymerase and gyrase consistent with a dual-targeting mechanism.

MRSA was analyzed by SDS-PAGE for the soluble proteins as shown in **Figure 5H**. Protein bands of MRSA treated by vehicle, HNF, and ANF were somewhat different. There were 13 proteins differentially expressed after the treatment of compounds. The mass spectra and the related data of these proteins are summarized in the **Supplementary Materials**. Most of these bands were apparently shallow after compound intervention as summarized in **Table 3**. The alteration in the proteins caused by HNF and ANF was detected by mass spectrometry. HNF produced a distinct reduction in DNA-directed RNA polymerase (band Nos. 1 and 2), acetyltransferases (band Nos. 5 and 7), and elongation factors Tu and Ts (band Nos. 9 and 12). However, the change in these proteins was minor for ANF. Both compounds significantly downregulated elongation factor G (band No. 4).

### In silico Docking

Induced fit docking is a tool to anticipate the binding affinity between the screened proteins and the active agents. To determine the possible binding modes of HNF and ANF, we docked the compound structures against DNA polymerase and gyrase. TNF with the lower anti-MRSA activity was also used in the docking experiment for comparison. **Figure 6A** shows the 3D molecular interaction of furanoquinones against

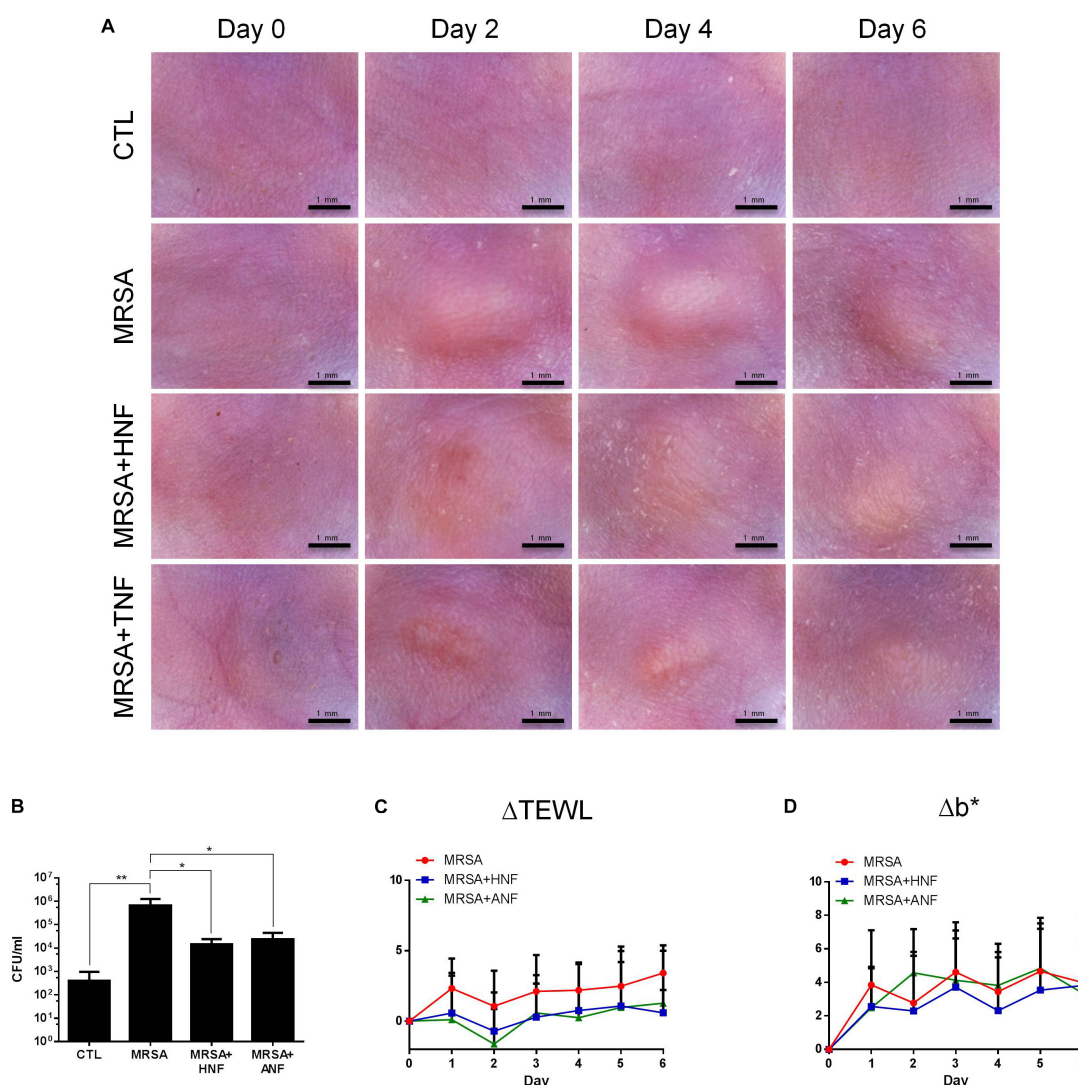
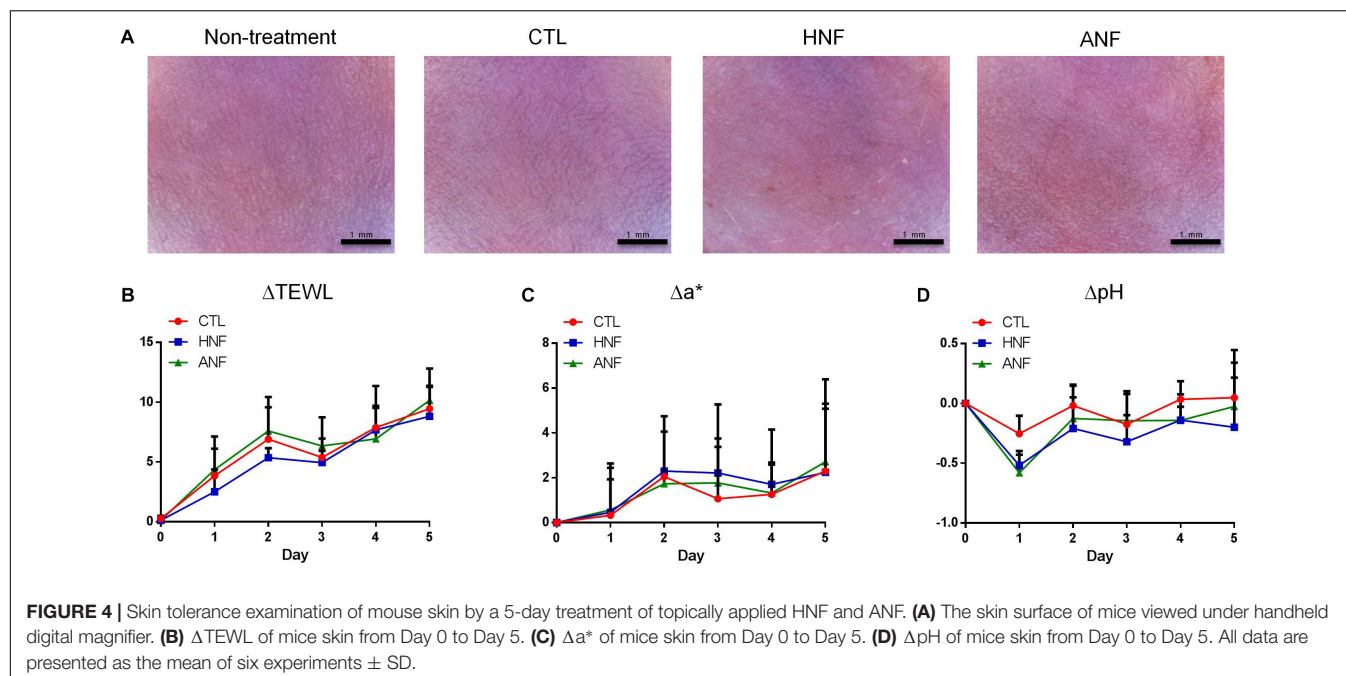


**FIGURE 3 |** *In vivo* topical application of HNF and ANF against MRSA. **(A)** The skin surface of mice after treatment of MRSA at Days 0, 2, 4, and 6 viewed under handheld digital magnifier. **(B)** Survival of MRSA in mice skin treated with MRSA. **(C)**  $\Delta$ TEWL of mice skin after treatment of MRSA from Day 0 to Day 6. **(D)**  $\Delta b^*$  of mice skin after treatment of MRSA from Day 0 to Day 6. All data are presented as the mean of six experiments  $\pm$  S.D. **\*\*** $p < 0.01$ , **\*** $p < 0.05$ .

DNA polymerase. All three compounds were located in the same binding pocket. HNF caused van der Waals interaction and hydrogen binding at the active sites with Val319, Val320, Val322, Phe371, and Asp372 residues. The binding between ANF and DNA polymerase was stabilized through van der Waal interaction, hydrogen binding, salt bridge, and  $\pi$ -cation interaction. The amino acids involved included Phe371, Tyr429, Glu321, Asp372, and Lys450. Val319, Phe371, Asp372, Asp425, Arg375, and Lys450 located in the binding pocket played vital roles in the conformation of TNF. The calculated binding energy between the compounds and DNA polymerase (PDB code 4B9T) was identified as shown in **Figure 6A**. HNF and ANF had a comparable binding energy of  $-7.9$  and  $-7.6$  kcal/mol, respectively. TNF revealed a lower energy ( $-9.0$  kcal/mol) as compared to the others.

**Figure 6B** shows the docking poses of the compounds with gyrase. The three compounds were docked in the same binding pocket with similar conformations. Hydrophobic interaction, hydrogen bonds, and  $\pi$ - $\pi$  stacking could be observed between HNF and the pocket. The most involved amino acids of gyrase in the binding of HNF were Met1113, Phe1266, Gln1267, and Gly1115. ANF imparted hydrophobic interaction with Phe1097, Met1113, Phe1266, and Gln1267, and a hydrogen binding with Gln1095, Ser1112, and Gly1115. TNF projected into Phe1097, Met1113, Phe1266, and Gln1267 to form hydrophobic interaction. Hydrogen binding was built between TNF and Ser1112, Met1113, and Gly1115. TNF and gyrase Phe1097 formed stable  $\pi$ - $\pi$  stacking. The binding energy between the compounds and gyrase was of comparable strength (**Figure 6B**).





## DISCUSSION

The continued development of antibiotic resistance in superbug microbes has limited the spectra of clinically approved drugs. The introduction of a new class of antibacterial agents is required to improve the management of drug-resistant pathogens. To address this need, we designed furanoquinone derivatives of a novel class of polymerase and gyrase inhibitors. HNF and ANF had the strongest anti-MRSA activity as assessed in both forms of planktonic and biofilm bacteria. We found some correlations between the compound structure and anti-MRSA activity. The furanoquinone derivatives with linear structure were totally devoid of MRSA inhibition. The angular structure was required to exhibit the growth inhibition. The presence of alkoxime linker in the angular furanoquinones was of utmost importance to showing the MRSA inhibition. The alkoxime-containing compounds conjugated with  $-H$  (HNF) and  $-COMe$  (ANF) were particularly promising. An increase in the bulkiness of the substituent at the alkoxime part (4c and 8b) was associated with less activity against MRSA. This may have been due to the smaller size of HNF and ANF compared to 4c and 8b for facile binding to the pocket of the target enzymes. Most of the compounds containing hydrazino linker showed no inhibition. The introduction of methoxyphenyl (6g) or the methylphenyl (6h, TNF) group in the hydrazino part led to a moderate potency. However, the replacement of methyl moiety in the methoxyphenyl group of 6g with fluorine (6f) ended the activity.

The data of MIC and MBC also confirmed the superior anti-MRSA activity of HNF and ANF. An agent is considered bactericidal but not bacteriostatic as its MBC is no more than 4x MIC (French, 2006). Our data indicated that both compounds were bactericidal against MRSA. HNF and ANF showed broad activity against drug-resistant *S. aureus*, including clinical isolates

of MRSA and VISA. There are 3% of MRSA strains classified as VISA (Zhang et al., 2015). Many MRSA-infected patients do not respond favorably to vancomycin. The potential of the furanoquinones was also tested against *E. coli*. The MBC for *E. coli* killing was greater than 300  $\mu$ g/ml. The lower activity on Gram-negative bacteria could be due to the complex cell-wall composition. There are two cell-envelope membranes in *E. coli*, leading to the limitation of interaction and penetration of antibacterial agents. This result suggested a potential specificity of HNF and ANF for Gram-positive microbes.

The resistance of bacteria in biofilm is attributed to the penetration barrier and the persistence of slow-growing bacteria with a low metabolic rate (Nair et al., 2016). MRSA is known to create the biofilm by producing exopolysaccharides, DNA, and proteins (McCarthy et al., 2015). Biofilm acts as a barrier restricting antibiotic delivery, resulting in the increased survival rate against antibiotics and host defense. HNF and ANF could reduce MRSA CFU in biofilm and biofilm height. This suggests that the furanoquinone-derived compounds could facilitate entry into the biofilm for MRSA killing. The decrease in biofilm formation could be related to the decreased MRSA survival rate. CPC is a quaternary ammonium surfactant revealing strong antibiofilm activity by destabilizing the bacterial membrane (Latimer et al., 2015). The antibiofilm effect of HNF and ANF achieved a comparable level to CPC. Some of the MRSA can be dispersed from the biofilm to the perimeter in the final stage of development (Chung and Toh, 2014). HNF and ANF showed a greater MRSA inhibition outside the biofilm as compared to CPC. Biofilm represents different gene expression profiles and physiologies compared with the planktonic form (Abouelhassan et al., 2018). Our results indicated the efficient eradication of both forms by HNF and ANF. HNF and ANF were profiled in the murine efficacy experiment. The result demonstrated the



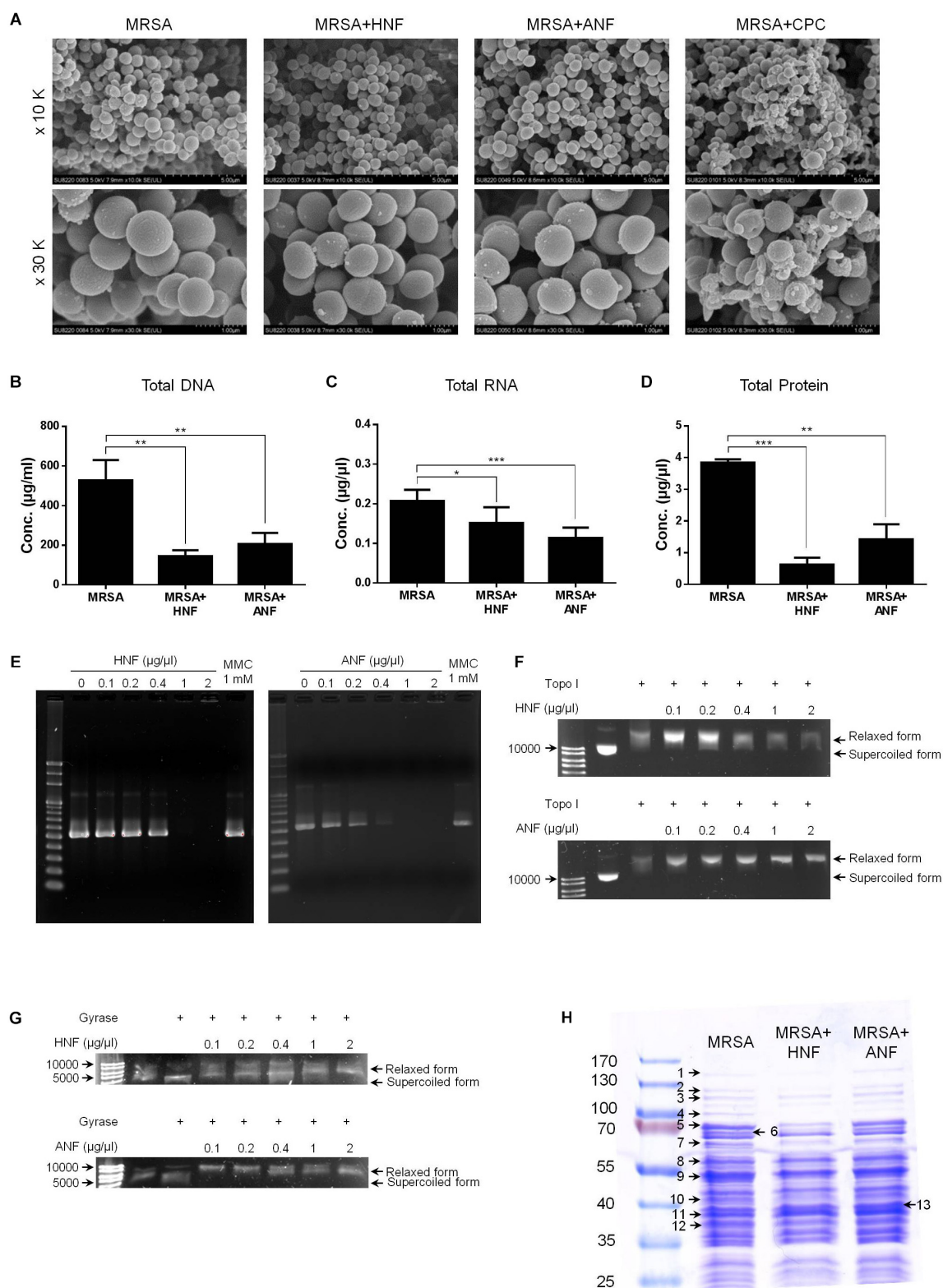


**FIGURE 5 |** Anti-MRSA mechanisms of HNF and ANF. **(A)** Morphological changes of MRSA viewed under SEM at the magnification of 10 K or 30 K. **(B)** Total DNA amount in MRSA. **(C)** Total RNA amount in MRSA. **(D)** Total protein amount in MRSA. **(E)** Taq DNA polymerase in PCR. **(F)** Topoisomerase I in wrapping assay. **(G)** DNA gyrase in wrapping assay. **(H)** The protein change of MRSA analyzed by SDS-PAGE and MALDI-TOF/TOF mass. All data are presented as the mean of three experiments  $\pm$  SD. \*\*\* $p < 0.001$ , \*\* $p < 0.01$ , \* $p < 0.05$ .

translation from *in vitro* to *in vivo* anti-MRSA activity. Both compounds were effective in reducing MRSA-infected abscess and bacterial burden with the recovery of the skin barrier.

The inhibition of MRSA colonization by furanoquinones was expected to impede the cutaneous inflammation for improving barrier function. The topical application of the lead compounds

**TABLE 3 |** Differentially expressed proteins of MRSA after treatment of lead compounds HNF and ANF.

Band no	Protein	Accession no.	MW (Da)	Matched-peptides	Sequence Coverage % (SCORE)	Ratios to MRSA <sup>a,b</sup>		Biological function
						HNF	ANF	
1	DNA-directed RNA polymerase subunit beta	P60279	133.418	20	112(18%)	0.345	1.323	DNA-dependent RNA polymerase catalyzes the transcription of DNA into RNA using the four ribonucleoside triphosphates as substrates
2	DNA-directed RNA polymerase subunit beta'	P60286	134.748	25	125(25%)	0.152	1.084	DNA-dependent RNA polymerase catalyzes the transcription of DNA into RNA using the four ribonucleoside triphosphates as substrates.
3	Aconitate hydratase A	P63434	99.135	22	120(34%)	0.698	1.245	Involved in the catabolism of short chain fatty acids (SCFA) via the tricarboxylic acid (TCA) (acetyl degradation route) and probably the 2-methylcitrate cycle 1 (propionate degradation route).
4	Isoleucyl-tRNA synthetase	Q8NX29	97.364	20	94(30%)			Catalyzes the attachment of isoleucine to tRNA(Ile).
	Elongation factor G	P68791	76.877	25	186(49%)	0.025	0.262	Catalyzes the GTP-dependent ribosomal translocation step during translation elongation.
5	Formate acetyltransferase	Q7A1W9	85.250	40	226(70%)	0.240	0.883	Activated by pfl-activating enzyme under anaerobic conditions via generation of an organic free radical.
6	Formate acetyltransferase	Q7A1W9	85.278	36	226(49%)	0.382	0.771	Activated by pfl-activating enzyme under anaerobic conditions via generation of an organic free radical.
7	Dihydrolipoyllysine-residue acetyltransferase component of pyruvate dehydrogenase complex	Q8NX76	46.452	17	88(44%)	0.330	0.710	The pyruvate dehydrogenase complex catalyzes the overall conversion of pyruvate to acetyl-CoA and CO <sub>2</sub> . It contains multiple copies of three enzymatic components: pyruvate dehydrogenase (E1), dihydrolipoamide acetyltransferase (E2) and lipoamide dehydrogenase (E3).
8	Phosphoenolpyruvate carboxykinase (ATP)	Q8NVZ8	59.599	26	168(56%)	0.860	1.010	Involved in the gluconeogenesis.
9	Elongation factor Tu	P64029	43.148	16	95(49%)	0.496	0.944	This protein promotes the GTP-dependent binding of aminoacyl-tRNA to the A-site of ribosomes during protein biosynthesis.
10	2-phosphoglycerate dehydratase	P64079	46.036	14	90(47%)			Catalyzes the reversible conversion of 2-phosphoglycerate into phosphoenolpyruvate.
	Phosphoglycerate kinase	P6S82I	28.722	12	87(61%)	0.428	0.841	
11	Ornithine carbamoyltransferase	QKNX44	37.781	15	128(61%)	0.943	1.713	Reversibly catalyzes the transfer of the carbamoyl group from carbamoyl phosphate (CP) to the N(epsilon) atom of ornithine (ORN) to produce L-citrulline.
12	Elongation factor Ts	Q8NWZ6	32.618	13	77(40%)	0.484	0.986	Associates with the EF-Tu.GDP complex and induces the exchange of GDP to GTP. It remains bound to the aminoacyl-tRNA.

(Continued)

TABLE 3 | Continued

Band no	Protein	Accession no.	MW (Da)	Matched-peptides	Sequence Coverage % (SCORE)	Ratios to MRSA <sup>a,b</sup>		Biological function
						HNF	ANF	
13	Ornithine carbamoyltransferase	Q8NX44	37.739	17	137(71%)	0.884	1.673	Reversibly catalyzes the transfer of the carbamoyl group from carbamoyl phosphate (CP) to the N(epsilon) atom of ornithine (ORN) to produce L-citrulline.

<sup>a</sup>Ratios to MRSA indicated the fold changes in protein amount between HNF- and ANF-treated samples vs. MRSA control samples, respectively. The higher ratios (>1.0) mean that the protein expression levels were increased upon treatments of compounds, while lower ratios (<1.0) indicate that the proteins were downregulated under the exposure to compounds. <sup>b</sup>Analyzing the gel images using Gene Tools software. MW, molecular weight.

did not induce remarkable skin irritation although a slight erythema was visualized.

The genes involved in transcription and translation, as well as the metabolic process related to DNA, RNA, or protein synthesis, strongly affect bacterial viability. The data pertaining to the total amount of DNA, RNA, and protein in furanoquinone-treated MRSA showed an obvious reduction compared with the control. The loss of these components could be due to the cell-membrane damage's causing leakage of cytoplasm materials or the inhibition of enzyme systems related to DNA replication (Yang et al., 2018). The SEM images displayed very slight cell-membrane damage of the MRSA treated by the lead compounds. Fluorescence microscopy of the live/dead bacteria showed very few bacteria with a damaged membrane; these damaged bacteria were stained red. These results implied that DNA replication suppression but not membrane disintegration governed the anti-MRSA activity of HNF and ANF. The physicochemical nature of both compounds could make feasible their permeation into MRSA for enzyme inhibition. We hypothesized that the targets of HNF and ANF were synthetic enzymes to selectively interfere with DNA and the subsequent RNA or protein synthesis. DNA polymerases and topoisomerases are major virulence determinants to impact MRSA infection persistence via their effect on viability (Lakhundi and Zhang, 2018). Our data validated the role of DNA polymerase inhibitors for both HNF and ANF. DNA topoisomerase enzymes function to regulate DNA topology for maintaining essential bacterial performance during replication and transcription (Savage et al., 2016). Topoisomerases such as topoisomerase I and gyrase are potential targets for antibacterial agents (Ranjan et al., 2017). The wrapping assay indicated the important role of gyrase but not topoisomerase I for MRSA eradication by the lead compounds. Gyrase belongs to the type IIA topoisomerase family. It relieves torsional tension by introducing negative supercoils to DNA during replication, which is vital for bacterial survival (Franco-Ulloa et al., 2018). Gyrase is the target for fluoroquinolone antibiotics. Thus, it can be a potential target for new anti-MRSA agents. Furanoquinone compounds might inhibit gyrase and further block DNA replication, resulting in the total DNA lessening and cell death. Inhibition of gyrase in *S. aureus* can affect membrane morphology, creating a rough surface and blebs (Franci et al., 2018). Our SEM images verified a slight alteration of the normal shape and some blebs on the MRSA surface after HNF or ANF treatment.

We also used proteomics to elucidate the possible anti-MRSA mechanisms of furanoquinones. Besides DNA polymerase, RNA polymerase might be the possible target for HNF because of a significant reduction in both subunits  $\beta$  and  $\beta'$ . The transcriptional process should be controlled for *S. aureus* to adjust the environment for survival (Elgaher et al., 2016). Rifamycins are a group of conventional antibiotics used to bind with the RNA polymerase subunit  $\beta$  to kill bacteria. RNA polymerase can also be the target of HNF. Since the enzyme is required through the development of *S. aureus* biofilm (Weiss et al., 2017), the inhibition of RNA polymerase might be the reason of biofilm disruption by HNF treatment. HNF but not ANF also apparently downregulated formate acetyltransferase. Acetyltransferase can act as a detoxifying enzyme to acetylate non-metabolizing carbohydrates to retard the reentry into MRSA (Stogios et al., 2014). The acetyltransferase superfamily is demonstrated to be reduced in MRSA in the presence of fusidic acid (Luo et al., 2013). Fusidic acid also works by blocking elongation factor G on the ribosomes, thus interfering with protein synthesis (Koripella et al., 2012). A similar mechanism was observed for furanoquinone compounds. The drug-resistant bacteria can upregulate the elongation factor superfamily to defend against antibiotics in order to survive. Furanoquinones may have been inhibiting elongation factor G, Tu, and Ts to eradicate MRSA.

DNA polymerase and gyrase were possible targets for furanoquinone compounds. We applied docking calculation and measured the free energy of the binding of the compounds using crystalline structures of DNA polymerase and gyrase. Induced fit docking indicated that HNF and ANF identically bound to both enzymes. The formation of van der Waal interaction, hydrogen binding, and  $\pi$ - $\pi$  stacking contributed to good stability and strong affinity to these proteins. The binding energy for the lead compounds on both proteins was  $-8 \sim -7$  kcal/mol. It can be recognized that the binding energy score of  $<-9$  kcal/mol is meaningful to produce a direct dock for deactivating the proteins. The binding energy of HNF and ANF may be insufficient to directly interact with DNA polymerase and gyrase to induce protein inhibition. Modification of the 4-position of furanoquinones was related to the antibacterial potency. TNF showed weaker anti-MRSA activity than HNF and ANF, but their binding energy was comparable. The result suggests that, besides the direct targeting to the enzymes, HNF and ANF might function with the other

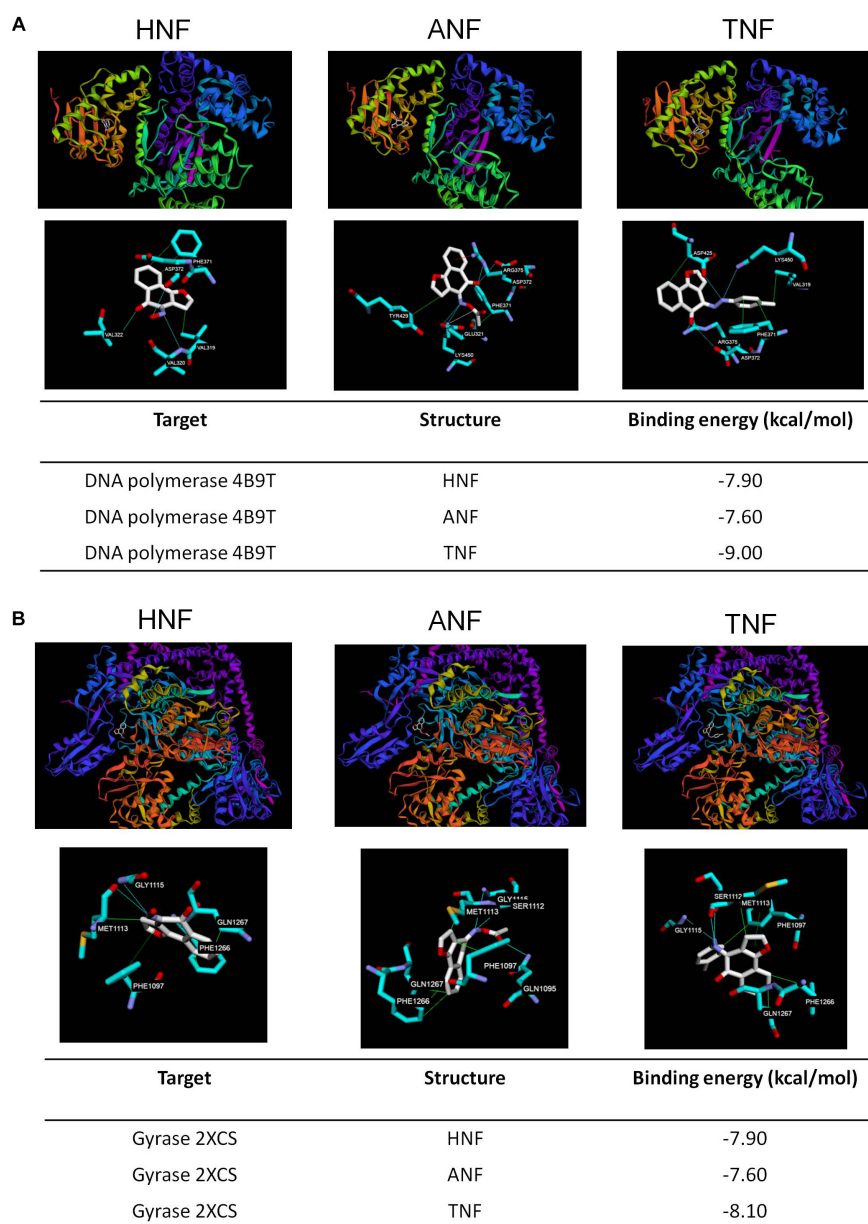


**FIGURE 6 |** Docking poses and binding energy (kcal/mol) of HNF, ANF, and TNF at the enzymes. **(A)** The docking pose between the compounds and DNA polymerase (PDB code 4B9T). **(B)** The docking pose between the compounds and gyrase (PDB code 2XCS).

DNA or proteins in suppressing the activity of DNA polymerase and gyrase. The mechanisms of furanoquinones can be more complex than our study's investigation showed. The precise mechanisms of HNF and ANF interference with enzymatic activity were not determined in detail in this work. Additional mechanistic study is needed to clarify the actual target of the lead compounds. Although molecular docking can assist the elucidation of the enzymatic target, it cannot promise the correlation with antibacterial activity. The other factors such as bacterial membrane permeation and the influence of the microenvironment in cytoplasm also largely impact the outcome of antibacterial efficiency (Werner et al., 2014).

The MRSA-related growth inhibition by HNF and ANF was related to DNA polymerase and gyrase. Both proteins in prokaryotic cells show considerable difference as compared to eukaryotes (Sissi and Palumbo, 2010). DNA gyrase is even absent in eukaryotes (Chiriac et al., 2015). Furanquinones exhibit a specific toxicity against MRSA with limited impact on humans. The dual inhibition of both enzymes further delays the occurrence of bacterial resistance because the simultaneous mutation on two targets is very low (Durcik et al., 2018). Topical administration of anti-MRSA agents for treating cutaneous infection have the advantages over oral or systemic counterparts of avoiding side effects, lowering cost, and decreasing drug



resistance (Mohammad et al., 2015). However, most of the antibiotics currently used to treat MRSA such as vancomycin, tigecycline, and rifampicin manifest a large molecular size (Kurosu et al., 2013). The large size may impede the penetration into the biofilm and skin. The small MW of HNF and ANF is beneficial for cutaneous delivery.

## CONCLUSION

Furanoquinone derivatives with imine moiety were successfully synthesized via regiospecific and stereospecific modes. The resulting compounds were examined for their capability to eradicate MRSA infection *in vitro* and *in vivo*. The attempt had been made to discover potent and safe anti-MRSA agents for cutaneous infection treatment. Among 19 compounds tested, HNF and ANF had powerful anti-MRSA potency, which was proved by agar diffusion assay, MIC, MBC, and live/dead staining. Both compounds also showed great potential to inhibit biofilm formation with bacterial viability reduction. The lead compounds demonstrated antibacterial activity against skin MRSA infection with very slight irritation. The inhibition of DNA polymerase and gyrase could be the mechanism for bactericidal activity on MRSA. The docking assay indicated that the compounds interacted with DNA polymerase and gyrase although the binding was only mild. HNF and ANF might also suppress the upstream proteins to indirectly inhibit the enzymes. HNF and ANF generally revealed a comparable MRSA lethality. A small increase in antibacterial activity could be observed with ANF as compared to HNF according to MIC, cell death determined by flow cytometry, the gross appearance of skin abscess, and DNA polymerase inhibition. On the other hand, the total protein analysis and proteomic profiles demonstrated a greater loss of proteins by HNF than ANF. Our results suggested that the lead furanoquinone compounds possessed potential anti-MRSA activity for further antibiotic development.

## ETHICS STATEMENT

### Humans

The clinical isolates of MRSA (KM-1 and KM-5) were isolated from Kaohsiung Medical University Hospital. KV-1 and KV-5 were vancomycin-intermediate *S. aureus* (VISA)

strains found in Kaohsiung Medical University Hospital provided by Dr. Po-Liang Lu. The clinical isolates were taken from infected patients using a protocol approved by the institutional review board at Kaohsiung Medical University Hospital. The patients provided written informed consent to participate.

## Animals

A female BALB/c mouse (8 weeks old) was purchased from the National Laboratory Animal Center (Taipei, Taiwan). This study was carried out in accordance with the principles of the Basel Declaration and recommendations of Guidelines for the Care and Use of Laboratory Animals of Chang Gung University. The protocol was approved by the Chang Gung University.

## AUTHOR CONTRIBUTIONS

S-CY initiated the study and drafted the manuscript. J-YF involved in the design of all experiments. S-CY and K-WT carried out the experiments. C-HL and AA analyzed data and wrote the manuscript. J-YF supervised the entire project. C-HT reviewed critically and approved the final manuscript. All authors read and approved the final manuscript.

## FUNDING

We are grateful to the financial support by Ministry of Science and Technology of Taiwan (MOST-105-2320-B-182-010-MY3 and MOST-107-2320-B-037-015). We also thank Center for Research Resources and Development at Kaohsiung Medical University for the instrumentation and equipment support.

## SUPPLEMENTARY MATERIAL

The Supplementary Material for this article can be found online at: <https://www.frontiersin.org/articles/10.3389/fmicb.2019.01197/full#supplementary-material>

**SCHEMES 1, 2 |** The synthetic routes to the furanoquinone derivatives.

## REFERENCES

- Abouelhassan, Y., Zhang, Y., Jin, S., and Huigens, R. W. III (2018). Transcript profiling of MRSA biofilms treated with a halogenated phenazine eradicating agent: a platform for defining cellular targets and pathways critical to biofilm survival. *Angew. Chem. Int. Ed. Engl.* 57, 15523–15528. doi: 10.1002/anie.201809785
- Brown, E. D., and Wright, G. D. (2016). Antibacterial drug discovery in the resistance era. *Nature* 529, 336–343. doi: 10.1038/nature17042
- Chiriac, A. I., Kloss, F., Krämer, J., Vuong, C., Hertweck, C., and Sahl, H. G. (2015). Mode of action of closthioamide: the first member of the polythioamide class of bacterial DNA gyrase inhibitors. *J. Antimicrob. Chemother.* 70, 2576–2588. doi: 10.1093/jac/dkx161
- Chung, P. Y., and Toh, Y. S. (2014). Anti-biofilm agents: recent breakthrough against multi-drug resistant *Staphylococcus aureus*. *Pathog. Dis.* 70, 231–239. doi: 10.1111/2049-632X.12141
- Durcik, M., Lovison, D., Skok, Ž., Cruz, C. D., Tammela, P., Tomašič, T., et al. (2018). New N-phenylpyrrolamide DNA gyrase B inhibitors: optimization of efficacy and antibacterial activity. *Eur. J. Med. Chem.* 154, 117–132. doi: 10.1016/j.ejmech.2018.05.011
- Elgaher, W. A. M., Sharma, K. K., Haupenthal, J., Saladini, F., Pires, M., Real, E., et al. (2016). Discovery and structure-based optimization of 2-uredothiophene-3-carboxylic acids as dual bacterial RNA polymerase and viral reverse transcriptase inhibitors. *J. Med. Chem.* 59, 7212–7222. doi: 10.1021/acs.jmedchem.6b00730
- Fair, R. J., and Tor, Y. (2014). Antibiotics and bacterial resistance in 21st century. *Perspect. Med. Chem.* 6, 25–64.

- Franci, G., Folliero, V., Cammarota, M., Zannella, C., Sarno, F., Schiraldi, C., et al. (2018). Epigenetic modulator UV15008 inhibits MRSA by interfering with bacterial gyrase. *Sci. Rep.* 8:13117. doi: 10.1038/s41598-018-31135-9
- Franco-Ulloa, S., La Sala, G., Miscione, G. P., and De Vivo, M. (2018). Novel bacterial topoisomerase inhibitors exploit Asp83 and the intrinsic flexibility of the DNA gyrase binding site. *Int. J. Mol. Sci.* 19:453. doi: 10.3390/ijms19020453
- French, G. L. (2006). Bactericidal agents in the treatment of MRSA infections: the potential role of daptomycin. *J. Antimicrob. Chemother.* 58, 1107–1117. doi: 10.1093/jac/dkl393
- Hiramatsu, K., Katayama, Y., Matsuo, M., Sasaki, T., Morimoto, Y., Sekiguchi, A., et al. (2014). Multi-drug-resistant *Staphylococcus aureus* and future chemotherapy. *J. Infect. Chemother.* 20, 593–601. doi: 10.1016/j.jiac.2014.08.001
- Koripella, R. K., Chen, Y., Peisker, K., Koh, C. S., Selmer, M., and Sanyal, S. (2012). Mechanism of elongation factor G-mediated fusidic acid resistance and fitness compensation in *Staphylococcus aureus*. *J. Biol. Chem.* 287, 30257–30267. doi: 10.1074/jbc.M112.378521
- Kurosu, M., Siricilla, S., and Mitachi, K. (2013). Advances in MRSA drug discovery: where are we and where do we need to be? *Expert. Opin. Drug Discov.* 8, 1095–1116. doi: 10.1517/17460441.2013.807246
- Lakhundi, S., and Zhang, K. (2018). Methicillin-resistant *Staphylococcus aureus*: molecular characterization, evolution, and epidemiology. *Clin. Microbiol. Rev.* 31:e00020-18.
- Latimer, J., Munday, J. L., Buzza, K. M., Forbes, S., Sreenivasan, P. K., and McBain, A. J. (2015). Antimicrobial and anti-biofilm activity of mouthrinses containing cetylpyridinium chloride and sodium fluoride. *BMC Microbiol.* 15:169. doi: 10.1186/s12866-015-0501-x
- Luo, H. B., Knapik, A. A., Petkowski, J. J., Demas, M., Shumilin, I. A., Zheng, H., et al. (2013). Biophysical analysis of the putative acetyltransferase SACOL2570 from methicillin-resistant *Staphylococcus aureus*. *J. Struct. Funct. Genomics* 14, 97–108. doi: 10.1007/s10969-013-9158-6
- May Zin, W. W., Buttachon, S., Dethoup, T., Pereira, J. A., Gales, L., Inácio, A., et al. (2017). Antibacterial and antibiofilm activities of the metabolites isolated from the culture of the mangrove-derived endophytic fungus *Eurotium chevalieri* KUFA 0006. *Phytochemistry* 114, 86–97. doi: 10.1016/j.phytochem.2017.05.015
- McCarthy, H., Rudkin, J. K., Black, N. S., Gallagher, L., O'Neill, E., and O'Gara, J. P. (2015). Methicillin resistance and the biofilm phenotype in *Staphylococcus aureus*. *Front. Cell. Infect. Microbiol.* 5:1. doi: 10.3389/fcimb.2015.00001
- Mohammad, H., Cushman, M., and Seleem, M. N. (2015). Antibacterial evaluation of synthetic thiazole compounds in vitro and in vivo in a methicillin-resistant *Staphylococcus aureus* (MRSA) skin infection mouse model. *PLoS One* 10:e0142321. doi: 10.1371/journal.pone.0142321
- Nagata, K., Hirai, K. I., Koyama, J., Wada, Y., and Tamura, T. (1998). Antimicrobial activity of novel furanonaphthoquinone analogs. *Antimicrob. Agents Chemother.* 42, 700–702. doi: 10.1128/aac.42.3.700
- Nair, S., Desai, S., Poonacha, N., Vipra, A., and Sharma, U. (2016). Antibiofilm activity and synergistic inhibition of *Staphylococcus aureus* biofilms by bactericidal protein P128 in combination with antibiotics. *Antimicrob. Agents Chemother.* 60, 7280–7289.
- Pan, T. L., Wang, P. W., Huang, C. C., Yeh, C. T., Hu, T. H., and Yu, J. S. (2012). Network analysis and proteomic identification of vimentin as a key regulator associated with invasion and metastasis in human hepatocellular carcinoma cells. *J. Proteomics* 75, 4676–4692. doi: 10.1016/j.jpro.2012.02.017
- Ranjan, N., Story, S., Fulcrand, G., Leng, F., Ahmad, M., King, A., et al. (2017). Selective inhibition of *Escherichia coli* RNA and DNA topoisomerase I by Hoechst 33258 derived mono- and bisbenzimidazoles. *J. Med. Chem.* 60, 4904–4922. doi: 10.1021/acs.jmedchem.7b00191
- Rego, N., and Koes, D. (2015). 3Dmol.js: molecular visualization with WebGL. *Bioinformatics* 31, 1322–1324. doi: 10.1093/bioinformatics/btu829
- Rejiniemon, T. S., Arasu, M. V., Duraipandian, V., Ponmurugan, K., Al-Dhabi, N. A., Arokiyaraj, S., et al. (2014). In-vitro antimicrobial, antibiofilm, cytotoxic, antifeedant and larvicidal properties of novel quinine isolated from *Aegle marmelos* (Linn.) Correa. *Ann. Clin. Microbiol. Antimicrob.* 13:48. doi: 10.1186/s12941-014-0048-y
- Sánchez-Linares, I., Pérez-Sánchez, H., Cecilia, J. M., and García, J. M. (2012). High-throughput parallel blind virtual screening using BINDSURF. *BMC Bioinformatics* 13(Suppl. 14):S13. doi: 10.1186/1471-2105-13-S14-S13
- Savage, V. J., Charrier, C., Salisbury, A. M., Moyo, E., Forward, H., Chaffer-Malam, N., et al. (2016). Stokes, Biological profiling of novel tricyclic inhibitors of bacterial DNA gyrase and topoisomerase IV. *J. Antimicrob. Chemother.* 71, 1905–1913. doi: 10.1093/jac/dkw061
- Shi, B., Leung, D. Y. M., Taylor, P. A., and Li, H. (2018). MRSA colonization is associated with decreased skin commensal bacteria in atopic dermatitis. *J. Invest. Dermatol.* 138, 1668–1671. doi: 10.1016/j.jid.2018.01.022
- Sissi, C., and Palumbo, M. (2010). In front of and behind the replication fork: bacterial type IIA topoisomerases. *Cell. Mol. Life Sci.* 67, 2001–2024. doi: 10.1007/s00018-010-0299-5
- Song, Z., Sun, H., Yang, Y., Jing, H., Yang, L., Tong, Y., et al. (2016). Enhanced efficacy and anti-biofilm activity of novel nanoemulsions against skin burn wound multi-drug resistant MRSA infections. *Nanomedicine* 12, 1543–1555. doi: 10.1016/j.nano.2016.01.015
- Stogios, P. J., Kuhn, M. L., Evdokimova, E., Courvalin, P., Anderson, W. F., and Savchenko, A. (2014). Potential for reduction of streptogramin A resistance revealed by structural analysis of acetyltransferase VtaA. *Antimicrob. Agents Chemother.* 58, 7083–7092. doi: 10.1128/AAC.03743-14
- Tseng, C. H., Chen, Y. L., Yang, S. H., Peng, S. I., Cheng, C. M., Han, C. H., et al. (2010). Synthesis and antiproliferative evaluation of certain iminonaphtho[2,3-b]furan derivatives. *Bioorg. Med. Chem.* 18, 5172–5182. doi: 10.1016/j.bmc.2010.05.062
- Vergara, A., Normanno, G., Di Ciccio, P., Pedonese, F., Nuvoloni, R., Parisi, A., et al. (2017). Ianiro, biofilm formation and its relationship with the molecular characteristics of food-related methicillin-resistant *Staphylococcus aureus* (MRSA). *J. Food Sci.* 82, 2364–2370. doi: 10.1111/1750-3841.13846
- Weiss, A., Moore, B. D., Tremblay, M. H. J., Chaput, D., Kremer, A., and Shaw, L. N. (2017). The  $\omega$  subunit governs RNA polymerase stability and transcriptional specificity in *Staphylococcus aureus*. *J. Bacteriol.* 199:e00459-16. doi: 10.1128/JB.00459-16
- Werner, M. M., Li, Z., and Zauhar, R. J. (2014). Computer-aided identification of novel 3,5-substituted rhodamine derivatives with activity against *Staphylococcus aureus* DNA gyrase. *Bioorg. Med. Chem.* 22, 2176–2187. doi: 10.1016/j.bmc.2014.02.020
- Yang, S. C., Huang, T. H., Chiu, C. H., Chou, W. L., Alalaiwe, A., Yeh, Y. C., et al. (2018). The atopic dermatitis-like lesion and the associated MRSA infection and barrier dysfunction can be alleviated by 2,4-dimethoxy-6-methylbenzene-1,3-diol from *Antrodia camphorate*. *J. Dermatol. Sci.* 92, 188–196. doi: 10.1016/j.jdermsci.2018.09.002
- Yang, S. C., Yen, F. L., Wang, P. W., Aljuffali, I. A., Weng, Y. H., Tseng, C. H., et al. (2017). Naphtho[1,2-b]furan-4,5-dione is a potent anti-MRSA agent against planktonic, biofilm, and intracellular bacteria. *Future Microbiol.* 12, 1059–1073. doi: 10.2217/fmb-2017-0044
- Zhang, S., Sun, X., Cheng, W., Dai, Y., and Ma, X. (2015). Systemic review and meta-analysis of the epidemiology of vancomycin-intermediate and heterogeneous vancomycin-intermediate *Staphylococcus aureus* isolates. *PLoS One* 10:e0136082. doi: 10.1371/journal.pone.0136082

**Conflict of Interest Statement:** The authors declare that the research was conducted in the absence of any commercial or financial relationships that could be construed as a potential conflict of interest.

Copyright © 2019 Yang, Tang, Lin, Alalaiwe, Tseng and Fang. This is an open-access article distributed under the terms of the Creative Commons Attribution License (CC BY). The use, distribution or reproduction in other forums is permitted, provided the original author(s) and the copyright owner(s) are credited and that the original publication in this journal is cited, in accordance with accepted academic practice. No use, distribution or reproduction is permitted which does not comply with these terms.

Original Paper

# Expression of PRDX6 Correlates with Migration and Invasiveness of Colorectal Cancer Cells

Wen-Shih Huang<sup>a,b</sup> Cheng-Yi Huang<sup>a</sup> Meng-Chiao Hsieh<sup>a,c</sup> Yi-Hung Kuo<sup>a,c</sup>  
Shui-Yi Tung<sup>b,d</sup> Chien-Heng Shen<sup>c,d</sup> Yung-Yu Hsieh<sup>d</sup> Chih-Chuan Teng<sup>e,f</sup>  
Ko-Chao Lee<sup>g</sup> Kam-Fai Lee<sup>h</sup> Hsing-Chun Kuo<sup>e,f,i,j</sup>

<sup>a</sup>Division of Colon and Rectal Surgery, Department of Surgery, Chang Gung Memorial Hospital, Chiayi,  
<sup>b</sup>Chang Gung University College of Medicine, Taoyuan, <sup>c</sup>Graduate Institute of Clinical Medical Sciences,  
College of Medicine, Chang Gung University, Taoyuan, <sup>d</sup>Department of Hepato-Gastroenterology,  
Chang Gung Memorial Hospital, Chiayi, <sup>e</sup>Institute of Nursing and Department of Nursing, Chang Gung  
Institute of Technology Chiayi Campus, Chiayi, <sup>f</sup>Research Fellow, Chang Gung Memorial Hospital,  
Chiayi, <sup>g</sup>Department of Colorectal Surgery, Department of Surgery, Chang Gung Memorial Hospital  
- Kaohsiung Medical Center, Kaohsiung, <sup>h</sup>Department of Pathology, Chang Gung Memorial Hospital  
at Chiayi, Chiayi, <sup>i</sup>Chronic Diseases and Health Promotion Research Center, CGUST, Chiayi, <sup>j</sup>Research  
Center for Industry of Human Ecology and Research Center for Chinese Herbal Medicine, College of  
Human Ecology, Chang Gung University of Science and Technology, Taoyuan, Taiwan

## Key Words

Colorectal cancer (CRC) • PRDX6 • Tumorigenicity • PI3K/AKT/p38/p50

## Abstract

**Background/Aims:** Colorectal cancer (CRC) is the third most common type of cancer and the second leading cause of cancer-related deaths worldwide. PRDXs are antioxidant enzymes that play an important role in cell differentiation, proliferation and apoptosis and have diverse functions in malignancy development. However, the mechanism of aberrant overexpression of PRDX6 in CRC remains unclear. **Methods:** Boyden chamber assay, flow cytometry and a lentiviral shRNA targeting PRDX6 and transient transfection with pCMV-6-PRDX6 plasmid were used to examine the role of PRDX6 in the proliferation capacity and invasiveness of CRC cells. Immunohistochemistry (IHC) with tissue array containing 40 paraffin- embedded CRC tissue specimens and Western blot assays were used to detect target proteins. **Results:** PRDX6 was significantly up-expressed in different comparisons of metastasis of colorectal adenomas in node-positive CRC ( $P = 0.03$ ). In *in vitro* HCT-116, PRDX6 silencing markedly suppressed CRC cell migration and invasiveness while also inducing cell cycle arrest as well as the generation of reactive oxygen species (ROS); specific overexpression of PRDX6 had the opposite effect. Mechanistically, the PRDX6 inactivation displayed decreased levels of PRDX6,

W.-S. Huang and C.-Y. Huang contributed equally to this work.

Kam-Fai Lee  
and Hsing-Chun Kuo, Ph.D.

Department of Pathology, Chang Gung Memorial Hospital;  
Chang Gung University of Science and Technology, Chia-Yi Campus, Chiayi (Taiwan)  
Tel. +886-5-3628800, Fax 886-5-3628866, E-Mail guscsi@gmail.com

N-cadherin,  $\beta$ -catenin, Vimentin, Slug, Snail and Twist-1 through the activation of the PI3K/AKT/p38/p50 pathways, but they were also significantly inhibited by PRDX6 transfectants. There was also increased transcriptional activation of dimethylation of histone H3 lysine 4 (H3K4me3) of PRDX6 promoter via the activation of the PI3K/Akt/NFkB pathways. **Conclusion:** Our findings demonstrated that PRDX6 expression plays a characteristic growth-promoting role in CRC metastasis. This study suggests that PRDX6 may serve as a biomarker of node-positive status and may have a role as an important endogenous regulator of cancer cell tumorigenicity in CRC. PRDX6 may also be an effective therapeutic target.

© 2018 The Author(s)  
Published by S. Karger AG, Basel

## Introduction

Colorectal cancer, one of the most common cancers worldwide, is frequently categorized as a leading cause of cancer-related deaths. Death due to colorectal cancer, which arises from epithelial cells, usually results from uncontrolled metastatic disease [1]. Only a minority of CRC cases are detected at a stage early enough for potential treatment with medicinal therapies such as surgery, chemotherapy, and radiotherapy. Rapid tumor growth has the features of rapid progression and poor outcome [2], which is the major problem affecting CRC therapy; however, patients with vascular and lymph node metastases are not eligible for surgical therapy. The presence of positive lymph nodes, which distinguishes stage I/II from stage III CRC, is a particularly key factor in patient management [3]. During this period, the progression of CRC appears to follow a precise series of molecular events, requiring the accumulation in proto-oncogenes and aberrant tumor suppressor genes in these initially benign lesions [4]. Access to specimens of CRC at different stages of the malignancy has allowed the analysis of the molecular alterations most frequently associated with each step of the CRC [5]. Several clinical and experimental studies have shown that a loss of E-cadherin at the cell membrane surface is a key hallmark of epithelial-mesenchymal transition (EMT), and these studies have described a reverse relationship between E-cadherin and tumorigenicity [6]. In addition, EMT occurs widely in tumor cell invasion and metastasis, and the Phosphatidylinositol-3-kinase (PI3K)/Akt pathway has been shown to be critical in promoting cell survival, inhibiting apoptosis, and creating tumorigenicity (You et al., 2009; Shin et al., 2010; Chen et al., 2012) [7]. These observations have led to studies on the potential mechanism for the association between EMT induction and the development of CRC metastasis, and to discussions concerning new biomarkers of node-positive status that underlie the signaling pathways that are altered in CRC and that are responsible for the initiation and progression [8].

Peroxiredoxins (PRDXs), a ubiquitously expressed family of small (22-27 kDa) non-seleno peroxidases that catalyze the peroxide reduction of H<sub>2</sub>O<sub>2</sub>, organic hydroperoxides and peroxynitrite, have emerged as having important physiological functions, including growth, survival, migration, and differentiation [9]. Several studies have indicated that PRDXs overexpression in cancer tissues strongly correlates with a more aggressive cancer behavior, tumor metastasis and the tumor-node-metastasis (TNM) stage, indicating a possible role in tumorigenesis progression [10]. PRDXs contain protein composed of 6 mammalian PRDXs, namely PRDX I to VI [11]. PRDX6 is expressed in almost all mammalian tissues and is highly expressed in solid organs. In some cancers, which might be attractive for solid organ tumorigenesis, PRDX6 created an altered redox environment between oxidant balance and cancer [12]. These data suggest that the mechanism by which PRDX6 exerts its oncogenic action in CRC is still poorly understood, and further studies are required.

Previous studies have indicated that CRC metastasis is a multistage process [12]. A previous report demonstrated that EMT is a transcriptional program that occurs normally during embryonic development and is characterized by changes in the expression levels for E-cadherin, a mediator of cell-cell adhesion, and other markers characteristic of mesenchymal and epithelial cells. In addition, another process that is frequently associated with metastasis is the epithelial-to-mesenchymal transition (EMT) [13]. A downstream effector of MAPK in



response to EMT is phosphorylated on PI3K/AKT/p38 pathways and regulates cell cycle progression by controlling the transcriptional output of several key genes, including CDK2 with Cyclin E and CDK4 with Cyclin D1 [14]. However, no studies have documented a role for the PRDX6 signaling axis in the regulation of CRC cell growth. In the present study, we investigated whether experimental manipulation of PRDX6 expression in established CRC cell lines influenced invasion, survival, and EMT. We showed that the expression of PRDX6 was upregulated in response to the activation of the PI3K/AKT/p38 pathways' intracellular signaling cascades through histone H3 lysine 4 (H3K4me3) of the PRDX6 promoter, a well-known marker of transcriptional activation [15]. Our findings provide evidence of the molecular mechanism by which PRDX6 mediates an invasiveness pathway in colorectal cancer cells, suggesting associations of PRDX6 with lymph node metastasis.

## Materials and Methods

### Materials

All culture materials were purchased from Gibco (Grand Island, NY, USA). 3-(4, 5-dimethylthiazol-2-yl)-2, 5-diphenyltetrazolium bromide (MTT), ROS scavenger (N-acetyl cysteine [NAC]), 2, 7-dichlorodihydrofluorescein diacetate (H2DCFDA), dihydroethidium (DHE), phosphoinositide 3-kinase inhibitor (wortmannin) and p38 MAPK inhibitor (SB203580) were purchased from Sigma (St. Louis, MO, USA). Mouse monoclonal antibodies against PRDX6, N-cadherin, b-catenin, Vimentin, Slug, Snail, Twist-1 and acetylation of H3 (Ac-Histone H3) at Lys 9 and Lys 14, and  $\beta$ -actin were purchased from Santa Cruz Biotechnology (Santa Cruz, CA, USA). Rabbit polyclonal antibodies against ERK1/2<sup>Thr<sup>202</sup>Tyr<sup>204</sup></sup>, p38<sup>Thr<sup>180</sup>Tyr<sup>182</sup></sup>, and phosphoinositide 3-kinase<sup>Tyr<sup>458</sup></sup> mouse/rabbit monoclonal antibody were purchased from Cell Signaling Technology (Beverly, MA, USA). The TdT-mediated dUTP Nick End Labeling (TUNEL) kits were from Roche (Germany). SDS, NP-40, sodium deoxycholate, protease inhibitor cocktails were purchased from Sigma (St. Louis, MO, USA). SDS, NP-40, sodium deoxycholate, protease inhibitor cocktails were purchased from Sigma.

### Tissue samples and assessment of CRC tissue microarrays (TMAs)

Tissues from 40 cases of primary colorectal cancer from the Chang Gung Memorial Hospital, Chiayi, Taiwan, were surgically resected. Forty patients with CRC (18 node-negative, 22 node-positive), who underwent surgery without presurgical chemotherapy or radiation therapy from 2003 to 2006, were included (Table 1). The institutional review boards of the Chang Gung Memorial Hospital approved the study (IRB103-2992C/CGMH), and informed consent was obtained from all patients and the tissue bank, department of medical research. Written informed consent was obtained from each patient before surgery. The Ethics Committee of Chang Gung Memorial Hospital and our institute approved the protocol. The excised samples were obtained from polyp and cancer tissues within one hour of surgery. All excised tissues were immediately placed in liquid nitrogen and stored at -80°C for further analyses. The pathologist confirmed diagnosis of all samples used in the study. TMA used in the confirmatory studies represented 94 cases of eligible CRC specimens (14 node-negative, 22 node-positive) and was used for immunohistochemistry with anti-PRDX6 antibody. This TMA contained carcinoma samples in duplicate, with normal control colonic mucosa [16]. Immunostaining was assessed independently by a pathologist in a blinded manner. The staining of PRDX6 was scored as the product of the staining intensity (on a scale of 0–2: negative = 0, low = 1, high = 2) and the percentage of cells stained (on a scale of 0–3: 0 = zero, 1 = 1%–25%, 2 = 26%–50%, 3 = 51%–100%), resulting in scores on a scale of 0–5 [17].

**Table 1.** Baseline characteristics of patients with colorectal cancer

Parameter	Cases
Gender	
Male	21
Female	19
Baseline characteristics	64.8 (27–89)
Tumor location	
Colon	28
Rectum	12
Average tumor diameter (cm)	4.2
Differentiation degree	
Moderately or poorly differentiated	29
Highly differentiated	11
TNM staging	
I + II stage	18
III + IV stage	22

## Cell culture

Human colon cancer cell line DLD-1 (CCL-221) and human colorectal carcinoma cell line HCT-116 (CCL-247) were purchased from American Type Culture Collection (ATCC). DLD-1 cells were cultured in RPMI 1640 medium composed of 10% fetal calf serum (FCS) (S0113; Biochrom KG, Berlin, Germany) and 1% antibiotics (100 units/mL of penicillin and 100 µg/mL of streptomycin) (Sigma Chemicals, St. Louis, MO, USA) and incubated at 37°C with 5% CO<sub>2</sub>. Adhered cells were washed twice with PBS. HCT-116 was cultured in DMEM supplemented with 10% heat-inactivated newborn calf serum at 37°C in a humidified 5% CO<sub>2</sub> incubator [18].

## Generation of stably and transiently expressing PRDX6 colorectal cancer cell clone

HCT-116 cells were transfected with PRDX6 short hairpin RNA (shRNA) (sc-40835-v) or scrambled shRNA (sc-108084; purchased from Santa Cruz Biotechnology) lentiviral particles in 0.5 mL of serum-free media, then selected in 10 µg/mL puromycin for an additional 10 days (sc-108071; Santa Cruz Biotechnology). Surviving cell colonies were picked and cultured before testing for PRDX6 expression. In addition, for transient transfection, the cells ( $5 \times 10^5$ ) were plated in 6-well plates and transfection was performed with pCMV-6-PRDX6 tag plasmids, purchased from Origene, in serum-free medium that contained Lipofectamine Plus (Invitrogen, Carlsbad, CA, USA). Transfection efficiency was assessed by Western blot analysis [19, 20].

## Cell cycle distribution analysis and reactive oxygen species

Changes in cell morphological characteristics during apoptosis were examined using fluorescence microscopy of 4',6-diamidino-2-phenylindole (DAPI)-stained cells. The monolayer of cells was fixed with 4% paraformaldehyde for 30 min at room temperature. The fixed cells were permeabilized with 3 treatments in 0.2% Triton X-100 in phosphate-buffered saline, followed by incubation with 1 µg/mL of DAPI for 30 min. The apoptotic nuclei were detected under 200× magnification using a fluorescent microscope with a 340/380 nm excitation filter and were scored according to the percentage of apoptotic nuclei found in samples containing 200 to 300 cells. Cell-cycle distribution was analyzed using flow cytometry. Cells stained with propidium iodide were analyzed with a FACScalibur™ (Becton Dickinson), and the data were analyzed using a mod-fit cell cycle analysis program [21].

The intracellular accumulation of ROS was determined by using the fluorescent probes of 10 µM 2', 7'-dichlorofluorescein diacetate (H2DCFDA, Molecular Probes) for the measurement of hydrogen peroxide (H2O2), and the cells were washed prior to FACS analysis. Cell Quest software (Becton Dickinson) was described earlier. The results were presented as a percentage of the fluorescent intensity compared with the control sample [22].

## Preparation of total cell extracts and immunoblot analyses

Cells were lysed with a buffer containing 1% NP-40, 0.5% sodium deoxycholate, 0.1% sodium dodecyl sulfate (SDS), and a protease inhibitor mixture (phenylmethylsulfonyl fluoride, aprotinin, and sodium orthovanadate). The total cell lysate (50 µg of protein) was separated by SDS-polyacrylamide gel electrophoresis (PAGE) (12% running, 4% stacking) and analyzed by using the designated antibodies and the Western-Light chemiluminescent detection system (Bio-Rad, Hercules, CA, USA). The area of the photo images in immunoblot was determined by measuring the numbers of pixels using ImageGauge 3.46 software (Fujifilm, Inc.) as previously described [23]. Through quantitative analysis of fluorescence assays using ImageJ, images were captured on the hard drive of the workstation computer [22].

## Matrigel invasion assay and scratch assays

A straight wound line, a scratch (4 mm), was made in the monolayer of the cells by plating cells in a 6-well culture dish. The cells were transfected with lentiviral shRNA targeting PRDX6 (siPRDX6) or PRDX6 plasmid, and the wound line was monitored for 24 h. Pictures of cells along the wound line were taken by phase-contrast microscope, and Openlab v3.0.2 image analysis software (Improvision, Coventry, UK) was used to quantify the area progressively filled with cells over the period of the experiment [23].

The Boyden chamber assay used for the analysis of tumor cell invasion is based on a chamber with two medium-filled compartments as described before.<sup>19</sup> Cells ( $1 \times 10^5$ /ml) in serum-free medium were added to an inner cup of the 48-well Transwell chamber (Corning Life Sciences, Corning, NY, USA) that had been coated with 50 µl of Matrigel (BD Biosciences, Franklin Lakes, NJ, USA; in serum-free medium). Medium

supplemented with 10% serum or indicated agent was added to the outer cup. Cells were allowed to migrate for 24 h, and then the membrane was fixed and stained with modified Giemsa stain (Sigma-Aldrich). The human HCT-116 cells and DLD-1 cells on the lower side of the membrane were counted using a light microscope at 200× magnification. The number of cells that migrated to the lower side of the membrane was determined.<sup>13</sup> Five random fields that migrated to the lower side of the membrane in each well were counted, and the average number/field from triplicated wells was plotted [24].

#### Chromatin immunoprecipitation (ChIP) analysis

HCT-116 cells were cross-linked with 1% formaldehyde in the medium at room temperature for 10 min, followed by the addition 125 mM glycine at room temperature for 5 min, and then scraped into sodium dodecyl sulfate (SDS) lysis buffer (50 mM Tris-HCl [pH 8.1], 1% SDS, and 10 mM EDTA) with antibodies against H3K4me3 and IgG. Soluble lysate was rotated with 2 µl antibody overnight at 4°C with protease inhibitors (1 µg/ml leupeptin, aprotinin and pepstatin A, 1 mM phenylmethylsulfonyl fluoride [PMSF]). Immunoprecipitated complexes were eluted with elution buffer (50 mM Tris-Cl [pH 7.5], 1 mM EDTA, 1% SDS), and cross-links were reversed by incubation for at least 2 h at 65°C. DNA was purified by ChIP DNA Clean & Concentrator Kit (Zymo) and DNA enrichment was measured by quantitative PCR analysis. To analyze the Prdx 6 promoter region, primer sets consisting of the promoter region (position-530 to -328 from the translation start site, forward: 5'-AGCACTGACATTGGTACGGG-3', reverse: 5'-AGCTCCCTACAGAGGAGTGG-3') were used. The amplification reaction was performed under the following conditions: 40 cycles of denaturation at 94°C, annealing at 60°C, and extension at 72°C. Disassociation curves were generated after each PCR was run to ensure that a single product of appropriate length was amplified. The mean CT ± SE was calculated from individual CT values obtained from triplicate determinations per stage. The normalized mean CT was estimated as ΔCT by subtracting the mean CT of input from that of the individual region [25].

#### Statistical analysis

The experiments were performed in triplicate independent experiments, and data were presented as three repeats from one independent experiment. Data were reported as the mean ± standard deviation and evaluated by one-way ANOVA. Significant differences were established at  $P < 0.05$  [25]. Differences in the distribution of the staining score between the groups were assessed using the Mann-Whitney U test. Probability values ( $p$ ) less than 0.05 ( $P < 0.05$ ) were considered as statistically significant. Analysis was performed with SPSS software (version 10.0; SPSS, Chicago, IL, USA) [26].

## Results

#### PRDX6 expression patterns on TMAs

To identify the potential role of PRDX6 in CRC, we evaluated 40 CRC samples of CRCs stratified by node status tumor tissues. We collected CRC samples from 18 node-negative and 22 node-positive patients (Table 1). Each CRC sample was paired with a duplicate from the same patient at the time of resection. Significance analysis of microarrays was used to evaluate each intergroup. We further investigated the correlation between PRDX6 expression and node status in a larger, independent patient cohort by immunohistochemical staining of TMAs. TMAs from two sources, representing 40 eligible cases from different geographic regions in a limitation, were analyzed. Fig. 1 shows the representative patterns of PRDX6 staining in the cytoplasm. Using a 0–5 scale representing a combination of staining intensity and fraction of cells stained, an increased frequency of high-level PRDX6 expression in node-positive CRC was seen in this intergroup. The distribution of scores for the node-negative and node-positive groups was significantly different statistically, based on a Mann-Whitney U test ( $P = 0.03$ ; Table 2) [26]. These findings indicate that PRDX6 expression might contribute to CRC progression and be a potential therapeutic target of this disease.

### Effects of PRDX6 on cell invasion and survival

To establish stable colon cancer cell lines continuously to determine the potential mechanisms by which PRDX6 might promote metastasis in CRC, HCT-116 cells were transfected with PRDX6 short hairpin RNA (shRNA) or scrambled shRNA lentiviral particles. We next studied the effect of an altered PRDX6 expression level on biologic processes that are relevant to metastasis in human HCT-116 stably expressing PRDX6. We determined a number of CRC cell lines for the PRDX6 level and selected HCT116 or DLD-1 for studies based on their moderate levels of endogenous PRDX6 expression that could be operated genetically. From our study, using the scratch-wound assay, with a lasting rapid movement, down-regulation of PRDX6 by specific shRNAs (siPRDX6) resulted in a marked reduction of the HCT-116 cell migration front compared with the control siRNA-transfected (siControl) or untreated group (Control) at 24 h ( $^{*}p < 0.05$ , Fig. 2A). The Boyden chamber assay was used to evaluate the *in vitro* migration and invasion effect of siPRDX6 associated with the aggressive status of siControl HCT-116 cells. Knockdown of PRDX6 reduced the invasion by more than 30% in the siControl-transfected cells and by 25% in the control cells ( $^{*}p < 0.05$ , Fig. 2B). The EMT is the cell intermediate filament system of switches that connects to adherens junctions and to focal adhesions [27]. Typical elements of the EMT include loss of expression of proteins associated with adhesive junctions (such as E-cadherin). Down-regulation of PRDX6 significantly increased the expression of E-cadherin compared with the siControl-transfected cells or the untreated group (Control) (Fig. 2C). However, while transient transfection with PRDX6 recovered plasmid in the PRDX6+siPRDX6 group, it significantly restored the capability of CRC invasion, survival and E-cadherin expression to HCT-116 siPRDX6 knockdown cells (Fig. 2).

### Effects of PRDX6 expression on cell cycle checkpoint and epithelial mesenchymal markers

The eukaryotic cell cycle control system incorporates a complex process that monitors and dictates the progression by which these checkpoints are frequently dysregulated in cancer [28]. Cell cycle analysis to assess whether PRDX6 is involved in the cell cycle distribution of HCT-116 cells revealed that siPRDX6-transfected cells induce G1/S arrest in HCT-116 cells. These data suggest that PRDX6 inactivation induces G1 and S arrest by 75% and 12%, respectively. Similarly, as expected, transient transfection with PRDX6 reversed to HCT-116 siPRDX6 knockdown cells by approximately 58% and 21% in the PRDX6+siPRDX6 group (Fig. 3A). PRDX6, is highly expressed in cancer cells and transcriptionally regulated by various oxidative stresses and signaling regulators [29]. PRDX6 plays an important role in the oxidative stress response, as an anti-apoptotic function, and then loss of Prdx6 increases susceptibility to oxidative stress [30]. Previous studies found that peroxiredoxin (PRDX6)

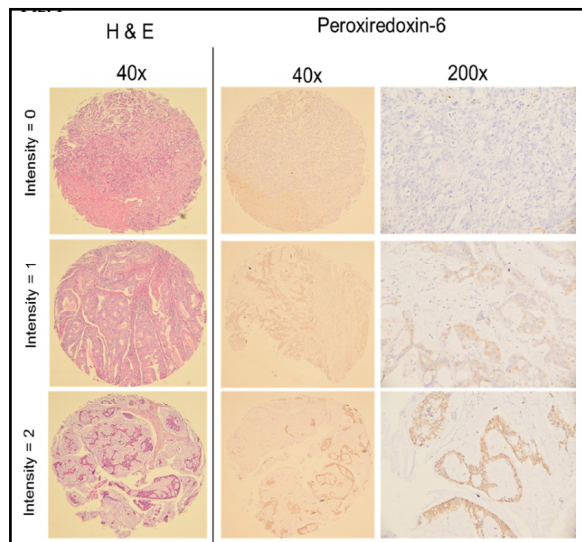


**Fig. 1.** Illustrations of hematoxylin and eosin staining and immunohistochemistry of PRDX6 on CRC tissue microarrays.

**Table 2.** Summary of PRDX6 expression on tissue microarrays

Staining(Score)	Node-Negative CRC (n)	Node-Positive CRC (n)	Total (n)
None (0)	8 (57 %)	7 (32 %)	15
Low (1-3)	6 (43 %)	9 (41 %)	15
Height (4-6)	0 (0 %)	6 (27 %)	6
Total (n)	14	22	36
P	0.025		



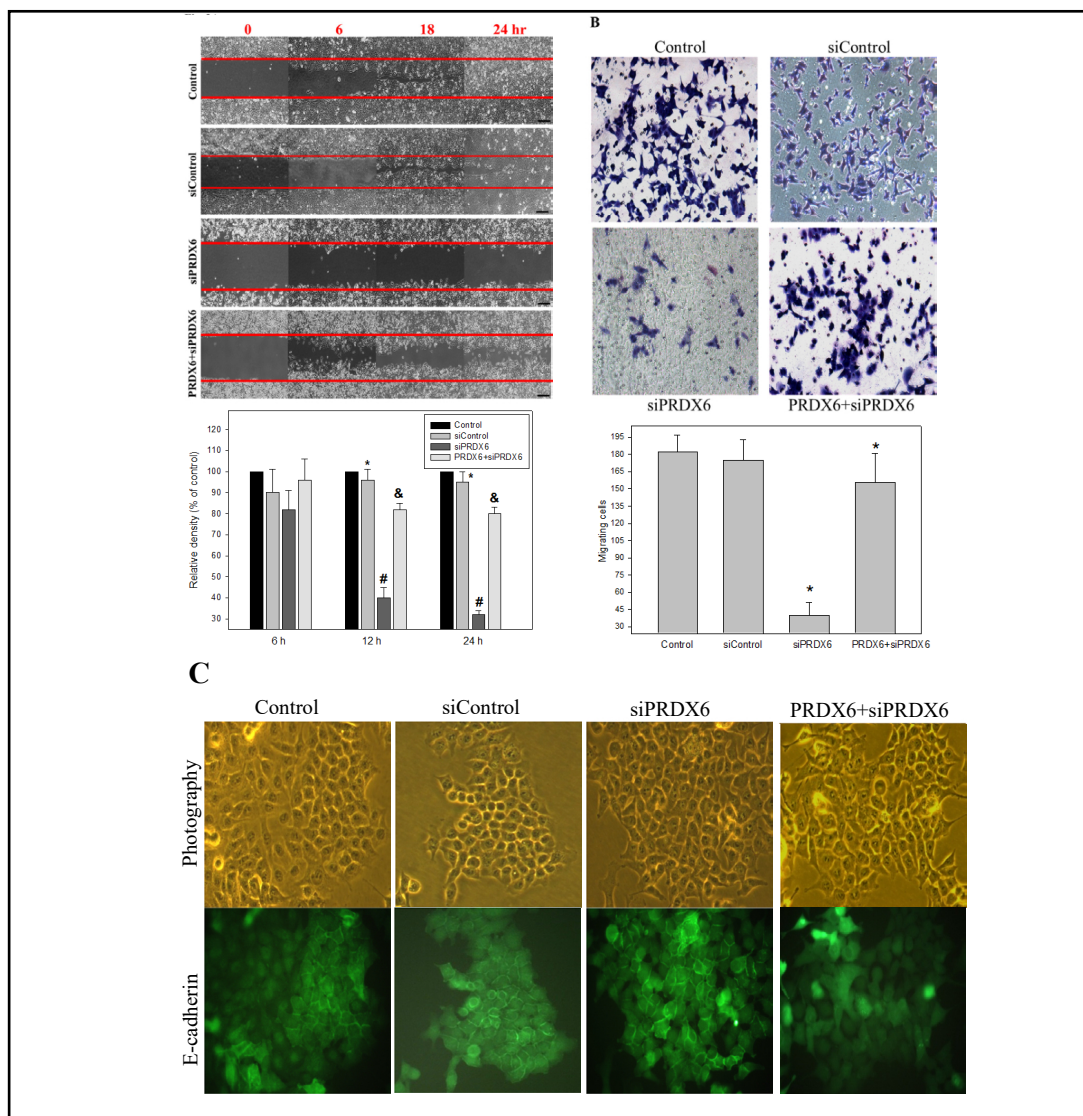


**Fig. 2.** Effects of PRDX6 inactivation on in vitro cell migration and invasiveness of human colorectal cancer cells. (A) HCT-116 cells were transfected with lentiviral shRNA targeting PRDX6 (siPRDX6) or nontargeting control (siControl); meanwhile, the cells were transfected with PRDX6 plasmid followed by 24 h (PRDX6+siPRDX6) and the migration for 6, 12 and 24 h using the scratch-wound assay was visualized as described in “Methods.” The percentage of surface area filled by the HCT-116 cells was subsequently quantified by densitometric analyses relative to the control, which was set at 100% in the photograph. Data are presented as means  $\pm$  SD based on three independent experiments. The experiments were performed in triplicate, and data are presented as means  $\pm$  SD. \* $P$ <0.05, compared with the control group for 6 h. # $P$ <0.05, compared with the control group for 12 h. & $P$ <0.05, compared with the control group for 24 h. (B) PRDX6 knockdown on invasiveness of HCT-116 cells. Cells were transfected with various shRNA. Invasion for 24 h through a layer of matrigel was determined by the Boyden Chamber method as described in “Methods.” The lower and upper chemotaxis cells were separated by a polycarbonate membrane. Microscopy images detected cells that migrated into the inner membrane. Magnification:  $\times$  200. The cell migration was quantified by counting the number of cells that migrated into the inner membrane. The control cells remained untreated. The experiments were performed in triplicate, and data are presented as means  $\pm$  SD. The symbol \* indicates means that are significantly different when compared to the control group with  $P$ <0.05, respectively. (C) HCT-116 cells were transfected with various shRNA for the indicated times, and immunofluorescence analysis showed expression of markers E-cadherin in the parental cell line of HCT-116 as described in “Materials and Methods”.

**Fig. 3.** Effect of PRDX6 inactivation on cell cycle distribution in HCT-116 cells. (A) After treatment with shRNA for 24 h, the cells were fixed and stained with propidium iodide, and the DNA content was analyzed by flow cytometry (FACS). The cell number percentage in each phase (G1, S, and G2/M) of the cell cycle was calculated and (B) intracellular ROS were determined by FACS analysis as described in “Materials and Methods.” Representative histograms were typical for H2DCFDA profiles. The production of ROS was expressed as the fold of the control group. (C) Lysates from control, siPRDX6 and PRDX6+siPRDX6 clones of HCT-116 cells were used for western blot analysis. Data presented in the western blot are derived from a representative study for the indicated time 24 h. The association of PRDX6 with Nox1 was determined by immunoprecipitation followed by western blot with antibody.

6 participates in activation of NADPH oxidase (Nox) enzymes in human endothelial cells. Nox1 complex is most abundant in colon epithelial cells [31, 32] and participates in mucosal cell migration, wound healing, and epithelial homeostasis, which binds to PRDX6 and activate NADPH oxidase Nox1. We also investigated the association of PRDX6 with the Nox1 complex, whether Prdx6 may have increasing effects on superoxide generation by Nox1. Extracellular

superoxide release was detected by using the fluorescent probes of H2DCFDA. The results of down-regulation of PRDX6 (siPRDX6) reduced the generation of ROS compared to the invasiveness of the untreated group (Control) HCT-116 cells, indicating the involvement of PRDX6 in cell sensitivity by free radicals. Transient transfection with PRDX6 rescue plasmid restored free radical susceptibility of the PRDX6+siPRDX6 group cells (Fig. 3B). In addition, the results of down-regulation of PRDX6 reduced the Prdx6 and Nox1 protein

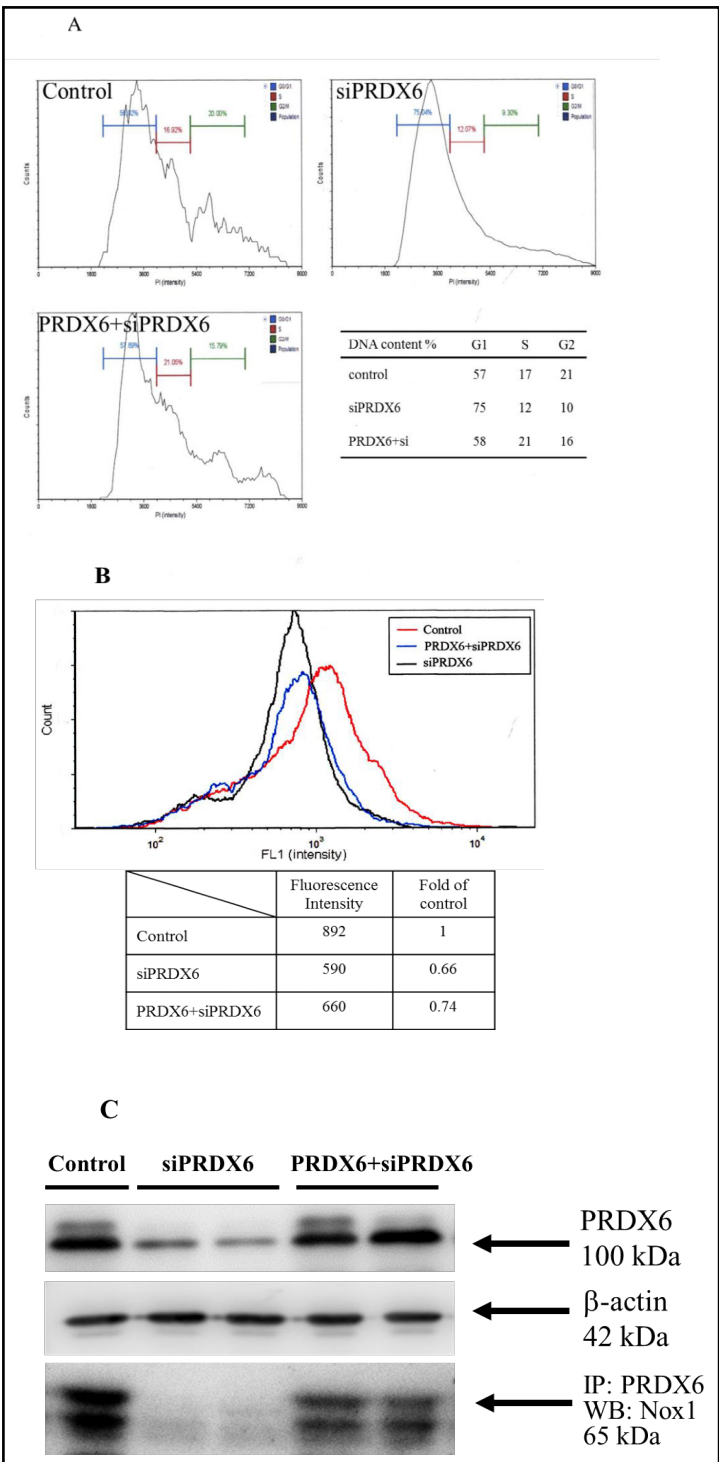


**Fig. 4.** PRDX6 inactivation inhibited tumorigenicity and metastasis *in vitro* and modulation of cell cycle-related proteins in HCT-116 cells. Lysates from control, siControl, siPRDX6 and PRDX6+siPRDX6 clones of HCT-116 cells were used for Western blot analysis. Data presented in the Western blot are derived from a representative study, and comparisons of protein expression are calculated from three replicate experiments for the indicated time of 18 h. The effect of PRDX6 knockdown on the protein levels of PRDX6, N-cadherin,  $\beta$ -catenin, Vimentin, Slug, Snail, Twist-1 and  $\beta$ -actin were detected with the indicated antibodies. The association of CDK2 with Cyclin E and the association of CDK4 with Cyclin D1 were determined by immunoprecipitation followed by Western blot with antibody.

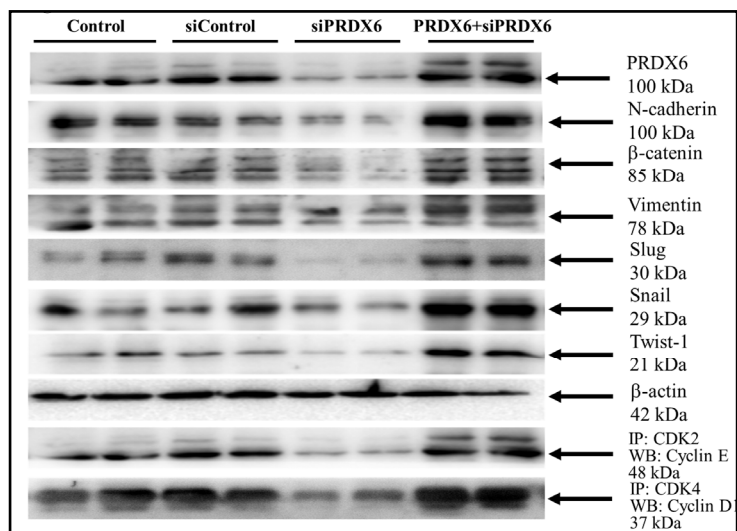
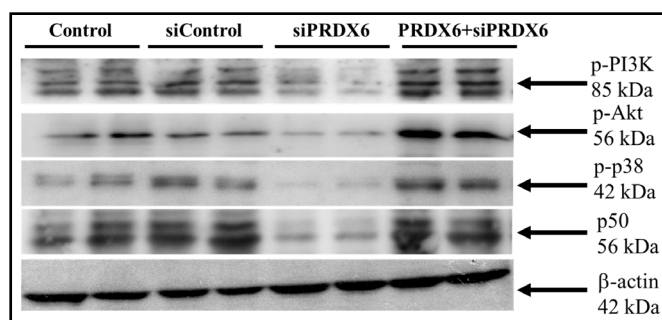
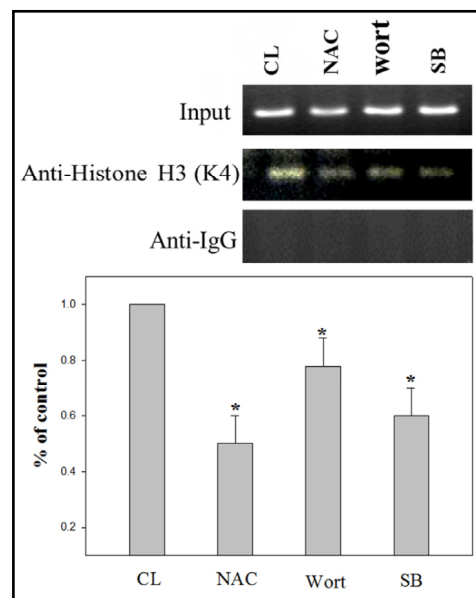


**Fig. 5.** Effect of PRDX6 inactivation on the activation of PI3K/AKT/p38 pathway and expression of p50 NF $\kappa$ B. HCT-116 cells were transfected with lentiviral shRNA PRDX6 (siPRDX6) or nontargeting control (siControl); meanwhile, the cells were transfected with PRDX6 plasmid, PRDX6+siPRDX6. Whole cell lysate proteins for the indicated time of 18 h were prepared and analyzed by Western blot, with  $\beta$ -actin serving as the loading control. Cell lysates were analyzed by 10% SDS-PAGE and subsequently treated with antibodies against phosphorylation of PI3K, AKT, p38, p50 and NF $\kappa$ B.



levels in these cells when compared with HCT-116 cells (CL). In this case, transient transfection with PRDX6 rescue plasmid restored PRDX6 and Nox1 components and superoxide generation when compared with siPRDX6 transfectant (Fig. 3C), indicating the activation of PRDX6 led to higher levels of these Nox1 components and higher superoxide generation. However, further findings may determine that PRDX6 promotes cell motility, migration, and invasion and ROS production in HCT-116 cells and then aberrant ROS, such as the superoxide radical contribution to cancer progression and metastases is mostly due to ability to affecting EMT via phosphoinositide 3-kinase, and Akt signaling [33]; therefore, PRDX6 was the most abundant and widely distributed member of the mammalian Prxs [29, 30, 34]. The pathophysiological role of CRC in its appearance in tumor cells of epithelial origin is consistent with the engagement of the EMT, but the process by which tumor cells acquire a more aggressive phenotype remains unclear. The Western blotting assay was used to evaluate the EMT-related proteins in *in vitro* migration and the invasion effect of PRDX6 with the aggressive status of HCT-116, siControl, siPRDX6 as well as PRDX6+siPRDX6 cells. Epithelial-mesenchymal transition (EMT) is a key developmental process often activated during cancer invasion and metastasis [35]. As shown in Fig. 4, these results demonstrated that the PRDX6 shRNA can effectively knock down PRDX6 expression at the protein level and be used to study PRDX6-mediated effects. PRDX6 inactivation significantly decreased the

**Fig. 6.** Effect of the kinase inhibitors in blocking histone modification of PRDX6 promoter. HCT-116 cells were incubated with various concentrations of the specific inhibitors NAC, wortmannin and SB203580 for 24 h. Next, the chromatin immunoprecipitation (ChIP) assays were performed by using antibodies against Histone H3 (H3K4me3) to pull down associated DNA. The precipitated DNA was amplified by PCR using primer sets specific to the target sites (-530/-375) of PRDX6 promoter. Input DNA was amplified as a loading control. DNA pulled down by the anti-IgG antibody was served to identify background amplification. The quantitative data were presented as the mean of three repeats from one independent experiment. The data were presented as mean  $\pm$  SD of three independent experiments. \* $P < 0.05$ , compared to the control group.



expression of EMT-related proteins, including N-cadherin, b-catenin, Vimentin, Slug, Snail, and Twist-1, rather than in the PRDX6-transfected siPRDX6 cells, PRDX6+siPRDX6 group. The results from these experiments confirmed that PRDX6 expression has a pivotal role in tumor metastasis, showing that it is actively implicated in the phenotype and function of EMT during cell proliferation and metastasis initiation in CRC cancer progression.

#### *PI3K/Akt/p38 signaling pathways mediated histone modification of PRDX6 promoter*

Previous studies have shown that EMT activation involves more pleiotropic signals, as in the case of reactive oxygen species produced in response to signal transducers [36]. EMT can be regulated by several signaling pathways including SMADs, signal transducers and activators of phosphoinositide 3-kinase (PI3K)/Akt, and mitogen-activated [37, 38]. Therefore, in this study, we aimed to examine whether the cross talk between the p38 and PI3K/Akt pathways could mediate the EMT process by regulating PRDX6 expression in HCT-116 cells. To evaluate the effect of an altered PRDX6 expression level on biologic processes relevant to the molecular mechanism involved in the PI3K/Akt/p38 signaling pathways of CRC, we checked the protein levels p-PI3K, p-Akt, p-p38 and NFkB p50 in HCT-116 cells by Western blot analysis. We observed that PRDX6 shRNA significantly increased the expression of p-PI3K, p-Akt, p-p38, NFkB p50 in human HCT-116 and siControl, which are widely used as a model for studies of cell signaling and invasion (Fig. 5). To elucidate the exogenous PRDX6 transfected cell lines, we transfected with the PRDX6 expression vector in siPRDX6 HCT-116 cells (RDX6+siPRDX6). We found that these cells exhibited markedly increased protein levels p-PI3K, p-Akt, p-p38 and NFkB p50 (Fig. 5). Previous study has shown that methylation modifiers also modulate methylation at histone H3 lysine 4 (H3K4me3), including key effectors and components in cellular PI3K/Akt/p38 signaling pathways that regulate cell proliferation, growth, and survival [39]. To investigate the role of the PI3K/Akt/p38 signaling pathways or endogenous ROS in regulating histone modification of PRDX6 promoter, we performed ChIP to analyze the change in histone methylation (H3K4me3) following treatment with HCT-116 cells [40]. As shown in Fig. 6, HCT-116 cell lines were incubated with inhibitors, including ROS scavenging NAC (1 mM), PI3K/AKT inhibitor wortmannin (10  $\mu$ M), and p38 MAPK inhibitor SB203580 (30  $\mu$ M). This resulted in a decreased trimethylation of histone H3 lysine 4 (H3K4me3), a well-known marker of transcriptional activation. Taken together, the results showed that PRDX6 expression in HCT-116 cells is essential to involvement in the PI3K/Akt/p38 signaling pathways or endogenous ROS signaling mediated cell survival and metastasis.



## Discussion

CRC is one of the most commonly occurring malignant tumors in the digestive tract. CRC has posed a substantial threat to the health of numerous patients worldwide. Although important advances have been made in the area of CRC treatment methods, the promising molecular biomarkers involved in the diagnosis, prognosis and prediction in early- or late-stage CRC remain rather poor [41, 42]. Peroxiredoxins (PRDXs) are a ubiquitously expressed family of small (22-27 kDa) non-seleno peroxidases that catalyze the peroxide reduction, currently known to possess six isozymes, namely, PRDX1-6 in mammalian systems. PRDXs are also a novel sensitive and highly specific marker for metastatic tumors in *in vitro* or *in vivo* models [30]. Previous studies have reported findings in regard to the high expressions of PRDX6 in certain cells, indicating that PRDX6 may be involved in the cancer's development [29]. Based on these reports, this study aimed to survey the effects of PRDX6 expression in tissues on the diagnosis and prognosis in human CRC specimens of positive lymph nodes, which distinguish stage I/II from stage III/VI CRC. We used IHC of TMAs as a high throughput method, containing 40 tissue specimens to evaluate the correlation between PRDX6 and node status (Table 1, Fig. 1). Our study's results indicated PRDX6 as showing significant promise as a novel marker for the diagnosis and prognosis of CRC patients (Table 2, Fig. 1). It has been previously reported that epithelial-mesenchymal transition (EMT), which modulates cancer progression and metastasis, has been involved in aberrant ROS levels driving signaling pathways due to a loss of proper redox control [43]. Their contribution to cancer progression and metastases is mainly due to their association with cell proliferation, EMT and apoptosis through PI3K/AKT/p38/p50 [38]. Furthermore, previous studies also demonstrated that abnormal expression of PRDX6, an indication of its tumor-promoting effects, was found in breast cancer, bladder cancer, ovarian cancer, pancreatic cancer and other tumors [44, 45, 46, 47]. PRDX6 is an important regulator of the invasiveness state and survival, not only in several types of normal cells, but also in cancer cells, and it possibly indicates a worse prognosis of clinical prostate cancer with radical prostatectomy [46]. In this study, we established a knockdown of the PRDX6 cell line, siPRDX6, and evaluated the biological characters' cell invasion, survival and EMT-associated markers. Interestingly, we determined that inactivated PRDX6 cells significantly showed more features associated with decreasing migratory and invasive potential compared to parental cells *in vitro* (Fig. 2). The alteration of PRDX6 in siPRDX6 cells was found to be associated with the downregulation of the expression of N-cadherin,  $\beta$ -catenin, Vimentin, Slug, Snail and Twist-1, and inactivation of the PI3K/AKT/p38/p50 pathways (Fig. 4, Fig. 5). PRDX6, a promoter-selective regulator of transcription, is distributed in all organs and essentially in all cell types [40]. Having an ability to regulate the transcription of other genes and the tumor microenvironment, the TGF- $\beta$ /SMAD signaling pathway and the epigenetic pathway provide a mechanism by which PRDX6 might broadly influence the processes relevant to metastasis. Further study will be needed to determine whether PRDX6 is mediated [7].

TGF- $\beta$ /SMAD signaling has a complex role in CRC progression and diagnosis. It has a role in the activation of the p38-MAPK and PI3K/Akt, and changes in the expression of these cell-cycle regulatory proteins might decrease the phosphorylation of Rb that results in G1-S transition and cell proliferation [14, 28]. Studies in a variety of experimental systems have demonstrated ROS induction and activation of TGF- $\beta$ /PI3K/AKT/p38 and their involvement in the modulation of gene transcription [7]. ROS levels and thereby abnormal expression and activation of NF $\kappa$ B p50 may be a major underlying mechanism for pathologic and abnormal physiologic changes in cells with induced levels of cytoprotective protein PRDX6. Additionally, the PI3K/AKT/p38/p50/NF $\kappa$ B pathway might be directly induced to leading to CRC cell cycle proliferation and invasion [38, 39]. Previous findings suggested that the deregulation of cyclin D1 and cyclin E complexes' expression and activation directly lead to some cancer hallmarks by inducing cell cycle distribution [14, 28]. More-recent studies that we have conducted have also defined PRDX6 inactivation induced cell cycle G1 arrest with a decrease in the association of the CDK2/cyclin E and CDK4/cyclin D1 complexes directly

implicated in cell survival, which is consistent with previous reports. Consistently, our present work demonstrated that PRDX6 re-expression accelerated the cell cycle transition, which is similar to the effects shown in numerous other studies with respect to PRDX6 control of tumorigenesis (Fig. 3). Numerous histone post-translational modifications contribute to chromatin and gene regulation, the tri-methylation of histone 3 lysine 4 (H3K4me3) is a well-established marker of active transcription [48] and associated enzymes in the pathogenesis of CRC have been implicated in oncogenesis and cancer-related functions [49]. Histone methylation not only regulates many biological functions, including gene transcription, nucleosomal positioning, DNA replication and repair, but also influences the carcinogenesis of cancers by affecting various cancer pathways. Moreover, we have shown the role of PRDX6 in mediating CRC development via ROS and PI3K/Akt signaling pathways involved in methylation at histone H3 lysine 4 (H3K4) of PRDX6 promoter transcriptional activation in HCT-116 cells (Fig. 6) [40, 44]. Several studies have reported increases in ROS levels leading to a number of human diseases, such as cancer, because of over-ROS-mediated PRDX6 expression and activation of such factors as TGF- $\beta$  and PI3K/AKT/p38/p50 pathways; it has also been shown that PRDX6 promoter has various putative regulatory elements [7, 13, 37]. Further work is needed to explore the role of transcriptional factors, particularly in PRDX6 regulation. A cohort study with a greater number of human CRC tissues and an examination to investigate the association with invasiveness are also needed.

Recently, peroxiredoxins have an important function in carcinogenesis, suggesting a possible role in cancer cell maintenance. Park et al. [29] have demonstrated that the dual action of PRDX6 in tumorigenesis, depending on increased level of PRDX6. We determined that an attempt to identify PRDX6 and validated that the phenotype in CRC is offered by the modulation of PRDX6. We hypothesized that CRC cells would exhibit up-expression of PRDX6 in otherwise normal cells may be tumorigenic in CRC tissues compared with metastasis of colorectal adenomas in node-positive CRC, as observed in immunohistochemical staining of tissue microarrays while loss of PRDX6 suppressed PI3K/AKT/p38/p50 signaling pathways that resulted in down-regulation of epithelial-mesenchymal transition (EMT) proteins N-cadherin,  $\beta$ -catenin, Vimentin, Slug, Snail and Twist-1. PRDX6 suppression in CRC cells alter cell-cycle regulatory proteins CDK2/cyclin E and CDK4/cyclin D1 complex leads to inhibition of tumorigenicity, migration, invasion, and metastasis. In this study, we determined by immunohistochemical staining of CRC TMAs that in the case of HCT-116 cells, a loss of PRDX6 expression in CRC promotes cancer cell progression and metastasis. The present investigation provides a molecular mechanism demonstrating the role of PRDX6 in mediating CRC cancer cell proliferation and migration/invasion. PRDX6 overexpression in many human cancers, serving a potential prognostic marker, regulated cell-cycle regulatory proteins and its transcriptional induction by oxidative stress via increased activity of redox-sensitive transcription factors and activation of PI3K/AKT/p38/p50 signaling pathways, which are able to interact with the PRDX6 gene promoter region and/or increased oncogenic activity present in cancer cells leading to cancer progression [29, 34, 44, 34]. These data suggest that the levels of PRDX6 and Nox1 components are closely linked positively regulates NADPH oxidase Noxa1 activity involved in superoxide generation (Fig. 3B, Fig. 3C). PRDX6 expression serve as a biomarker of node-positive status and may have a role as an important endogenous regulator of cancer cell tumorigenicity in CRC through the activation of endogenous ROS and the PI3K/AKT/p38/p50 pathways. Recently, the NADPH oxidase (Nox1 enzyme complex) was shown to direct colon epithelial cell migration and wound healing through the VEGF receptor type2 (VEGR2, KDR/Flk1) and Akt, p38 MAP kinase and PAK (p21-activated kinase) mediated pathways previously, plays a critical role in the correlation with CRC cancer migration, invasion and epithelial-mesenchymal transition [48]. Nox1 is most abundant in colon epithelial cells and participates in epithelial cell migration, while inappropriate or excessive ROS production can damage surrounding tissues and promote inflammation, the activity of NADPH oxidases is subject to tight regulation [50]. Here, we show PRDX6 as a novel regulator of Nox1-based superoxide generation and activated cells survival and aggressive pathways in colorectal cancer cells, which appears to involve the ROS

and PI3K/Akt/NFκB signalling pathways and that PRDX6 was involved in methylation at histone H3 lysine 4 (H3K4) of PRDX6 promoter in HCT-116 cells. In addition, Prdx6 deficiency results in destabilization of Nox1 components, whereas PRDX6 rescue plasmid restored increasing levels of oxidase activity. These results highlight a novel pathway in which PRDX6 supports the oxidant-generating activity of Nox1 to promote cell migration which PRDX6 recruitment into the Nox1 complex. PRDX6 modulates Nox1-dependent activation and migration of HCT-116 cells and then future work determine whether proposes that PRDX6 has a role in the expression of NOX1 protein, which may suggest novel strategies for therapeutic intervention.

## Conclusion

Our results imply that PRDX6 mediated cell survival and aggressive pathways in colorectal cancer cells via ROS and PI3K/Akt/NFκB signaling pathways and that PRDX6 was involved in methylation at histone H3 lysine 4 (H3K4) of PRDX6 promoter in HCT-116 cells (Fig. 7). This study provides evidence that PRDX6 expression in established CRC cell lines influenced invasion, survival, and EMT, and it also shows that PRDX6 may participate in the regulation of the tumorigenicity.

## Acknowledgements

Funding for this study was provided in part by research grants BMRPD42, CLRP8G0591, CMRPG6E0191, CMRPG6E0192, CMRPG6H0031, CMRPG6H0032, CMRPF6G0011, CMRPF6G0012, CMRPF6G0013 from Chang Gung Memorial Hospital, Chiayi, Taiwan, and Chang Gung University of Science and Technology, Chia-Yi Campus, Taiwan, and by the Ministry of Science and Technology, Taiwan (MOST 107-2320-B-255 -001 -MY3).

## Disclosure Statement

There is no financial/commercial conflict of interests.

## References

- 1 Brenner H, Kloor M, Pox CP: Colorectal cancer. *Lancet* 2014;383:1490-1502.
- 2 Jonker DJ, O'Callaghan CJ, Karapetis CS, Zalberg JR, Tu D, Au HJ, Berry SR, Krahn M, Price T, Simes RJ, Tebbutt NC, van Hazel G, Wierzbiński R, Langer C, Moore MJ: Cetuximab for the treatment of colorectal cancer. *N Engl J Med* 2007;357:2040-2048.
- 3 Siegel R, Naishadham D, Jemal A: Cancer statistics, 2012. *CA Cancer J Clin.* 2012;62:10-29.
- 4 Hagggar FA, Boushey RP: Colorectal cancer epidemiology: incidence, mortality, survival, and risk factors. *Clin Colon Rectal Surg* 2009;22:191-197.
- 5 Compton CC: Optimal pathologic staging: defining stage II disease. *Clin Cancer Res.* 2007;13:6862s-6870s.
- 6 Chiang AC, Massagué J: Molecular basis of metastasis. *N Engl J Med* 2008;359:2814-2823.
- 7 Tse JC, Kalluri R: Mechanisms of metastasis: epithelial-to-mesenchymal transition and contribution of tumor microenvironment. *J Cell Biochem* 2007;101:816-829.

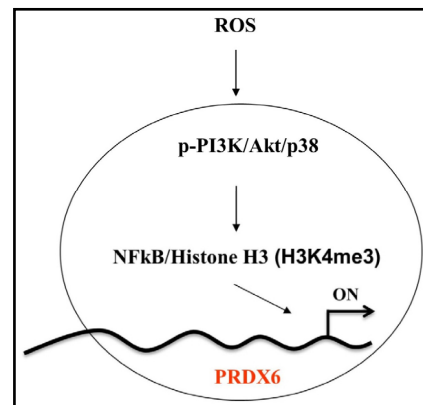


**Fig. 7.** Schematic presentation of the histone modification (H3K4me3) of PRDX6 promoter by endogenous ROS and PI3K/Akt/NFκB signaling pathways in HCT-116 cells.




- 8 Sillars-Hardebol AH, Carvalho B, de Wit M, Postma C, Delis-van Diemen PM, Mongera S, Ylstra B, van de Wiel MA, Meijer GA, Fijneman RJ: Identification of key genes for carcinogenic pathways associated with colorectal adenoma-to-carcinoma progression. *Tumour Biol* 2010;31:89-96.
- 9 Hall A, Nelson K, Poole LB, Karplus PA: Structure-based insights into the catalytic power and conformational dexterity of peroxiredoxins. *Antioxid Redox Signal* 2011;15:795-815.
- 10 Lu W, Fu Z, Wang H, Feng J, Wei J, Guo J: Peroxiredoxin 2 is upregulated in colorectal cancer and contributes to colorectal cancer cells' survival by protecting cells from oxidative stress. *Mol Cell Biochem* 2014;387:261-270.
- 11 Dammeyer P, Arnér ES: Human Protein Atlas of redox systems - what can be learnt? *Biochim Biophys Acta* 2011;1810:111-138.
- 12 Raatikainen S, Aaltonmaa S, Kärjä V, Soini Y: Increased Peroxiredoxin 6 Expression Predicts Biochemical Recurrence in Prostate Cancer Patients After Radical Prostatectomy. *Anticancer Res* 2015;35:6465-6470.
- 13 Xu J, Lamouille S, Derynck R: TGF-beta-induced epithelial to mesenchymal transition. *Cell Res* 2009;19:156-172.
- 14 Duronio RJ, Xiong Y: Signaling pathways that control cell proliferation. *Cold Spring Harb Perspect Biol* 2013;5:a008904.
- 15 Garcia BA, Hake SB, Diaz RL, Kauer M, Morris SA, Recht J, Shabanowitz J, Mishra N, Strahl BD, Allis CD, Hunt DF: Organismal differences in post-translational modifications in histones H3 and H4. *J Biol Chem* 2007;282:7641-7655.
- 16 Lin Y, Buckhaults PJ, Lee JR, Xiong H, Farrell C, Podolsky RH, Schade RR, Dynan WS: Association of the actin-binding protein transgelin with lymph node metastasis in human colorectal cancer. *Neoplasia* 2009;11:864-873.
- 17 Wang Z, Jiang L, Huang C, Li Z, Chen L, Gou L, Chen P, Tong A, Tang M, Gao F, Shen J, Zhang Y, Bai J, Zhou M, Miao D, Chen Q: Comparative proteomics approach to screening of potential diagnostic and therapeutic targets for oral squamous cell carcinoma. *Mol Cell Proteomics* 2008;7:1639-1650.
- 18 Lee KC, Kuo HC, Shen CH, Lu CC, Huang WS, Hsieh MC, Huang CY, Kuo YH, Hsieh YY, Teng CC, Lee LY, Tung SY: A proteomics approach to identifying novel protein targets involved in erinacine A-mediated inhibition of colorectal cancer cells' aggressiveness. *J Cell Mol Med* 2017;21:588-599.
- 19 Kuo HC, Kuo YR, Lee KF, Hsieh MC, Huang CY, Hsieh YY, Lee KC, Kuo HL, Lee LY, Chen WP, Chen CC, Tung SY: A Comparative Proteomic Analysis of Erinacine A's Inhibition of Gastric Cancer Cell Viability and Invasiveness. *Cell Physiol Biochem* 2017;43:195-208.
- 20 Tao RR, Wang H, Hong LJ, Huang JY, Lu YM, Liao MH, Ye WF, Lu NN, Zhu DY, Huang Q, Fukunaga K, Lou YJ, Shoji I, Wilcox CS, Lai EY, Han F: Nitrosative stress induces peroxiredoxin 1 ubiquitination during ischemic insult via E6AP activation in endothelial cells both *in vitro* and *in vivo*. *Antioxid Redox Signal* 2014;21:1-16.
- 21 Gao W, Xua J, Wang F, Zhang L, Peng R, Zhu Y, Tang Q, Wu J: Mitochondrial Proteomics Approach Reveals Voltage-Dependent Anion Channel 1 (VDAC1) as a Potential Biomarker of Gastric Cancer. *Cell Physiol Biochem* 2015;37:2339-2354.
- 22 Lu CC, Huang WS, Lee KF, Lee KC, Hsieh MC, Huang CY, Lee LY, Lee BO, Teng CC, Shen CH, Tung SY, Kuo HC: Inhibitory effect of Erinacines A on the growth of DLD-1 colorectal cancer cells is induced by generation of reactive oxygen species and activation of p70S6K and p21. *J Funct Foods* 2016;21:474-484.
- 23 Huang WS, Kuo YH, Kuo HC, Hsieh MC, Huang CY, Lee KC, Lee KF, Shen CH, Tung SY, Teng CC: CIL-102-induced cell cycle arrest and apoptosis in colorectal cancer cells via upregulation of p21 and GADD45. *PLoS One* 2017;12:e0168989.
- 24 Huang WS, Hsieh MC, Huang CY, Kuo YH, Tung SY, Shen CH, Hsieh YY, Teng CC, Lee KF, Chen TC, Lee KC, Kuo HC: The Association of CXC Receptor 4 mediated signaling pathway with oxaliplatin-resistant human colorectal cancer cells. *PLOS One* 2016;11:e0159927.
- 25 Huang WS, Chin CC, Chen CN, Kuo YH, Chen TC, Yu HR, Tung SY, Shen CH, Hsieh YY, Guo SE, Shi CS, Liu TJ, Kuo HC: Stromal cell-derived factor-1/CXC receptor 4 and  $\beta$ 1 integrin interaction regulates urokinase-type plasminogen activator expression in human colorectal cancer cells. *J Cell Physiol* 2012; 227:1114-1122.
- 26 Lu CC, Kuo HC, Wang FS, Jou MH, Lee KC, Chuang JH: Upregulation of TLRs and IL-6 as a marker in human colorectal cancer. *Int J Mol Sci* 2014;16:159-177.
- 27 Chaffer CL, Weinberg RA: A perspective on cancer cell metastasis. *Science*. 2011;331:1559-1564.
- 28 Malumbres M, Barbacid M: Cell cycle, CDKs and cancer: a changing paradigm. *Nat Rev Cancer* 2009;9:153-166.



- 29 Park MH, Jo M, Kim YR, Lee CK, Hong JT: Roles of peroxiredoxins in cancer, neurodegenerative diseases and inflammatory diseases. *Pharmacol Ther* 2016;163:1-23.
- 30 Neumann CA, Fang Q: Are peroxiredoxins tumor suppressors? *Curr Opin Pharmacol* 2007;7:375-380.
- 31 Kwon J, Wang A, Burke DJ, Boudreau HE, Lekstrom KJ, Korzeniowska A, Sugamata R, Kim YS, Yi L, Ersoy I, Jaeger S, Palaniappan K, Ambruso DR, Jackson SH, Leto TL: Peroxiredoxin 6 (Prdx6) supports NADPH oxidase1 (Nox1)-based superoxide generation and cell migration. *Free Radic Biol Med* 2016;96:99-115.
- 32 Suh YA, Arnold RS, Lassegue B, Shi J, Xu X, Sorescu D, Chung AB, Griendling KK, Lambeth JD: Cell transformation by the superoxide-generating oxidase Mox1. *Nature* 1999;401:79-82.
- 33 Clerkin JS, Naughton R, Quiney C, Cotter TG: Mechanisms of ROS modulated cell survival during carcinogenesis. *Cancer Lett* 2008;266:30-36.
- 34 Seo MS, Kang SW, Kim K, Baines IC, Lee TH, Rhee SG: Identification of a new type of mammalian peroxiredoxin that forms an intramolecular disulfide as a reaction intermediate. *J Biol Chem* 2000;275:20346-20354.
- 35 Thiery JP: Epithelial-mesenchymal transitions in development and pathologies. *Curr Opin Cell Biol* 2003;15:740-746.
- 36 Chaffer CL, Weinberg RA: A perspective on cancer cell metastasis. *Science*. 2011;331:1559-1564.
- 37 Stec R, Bodnar L, Smoter M, Mączewski M, Szczylik C: Metastatic colorectal cancer in the elderly: An overview of the systemic treatment modalities (Review). *Oncol Lett* 2011;2:3-11.
- 38 Kucuksayan H, Akca H: The crosstalk between p38 and Akt signaling pathways orchestrates EMT by regulating SATB2 expression in NSCLC cells. *Tumour Biol* 2017;39:1010428317706212.
- 39 Testa JR, Tschlis PN: AKT signaling in normal and malignant cells. *Oncogene* 2005;24:7391-7393.
- 40 Valekunja UK, Edgar RS, Oklejewicz M, van der Horst GT, O'Neill JS, Tamanini F, Turner DJ, Reddy AB: Histone methyltransferase MLL3 contributes to genome-scale circadian transcription. *Proc Natl Acad Sci U S A* 2013;110:1554-1559.
- 41 Jemal A, Siegel R, Ward E, Hao Y, Xu J, Murray T, Thun MJ: Cancer statistics, 2008. *CA Cancer J Clin* 2008;58:71-96.
- 42 Christofori G: New signals from the invasive front. *Nature* 2006;441:444-450.
- 43 Fiaschi T, Chiarugi P: Oxidative stress, tumor microenvironment, and metabolic reprogramming: a diabolic liaison. *Int J Cell Biol* 2012;2012:762825.
- 44 Alam H, Gu B, Lee MG: Histone methylation modifiers in cellular signaling pathways. *Cell Mol Life Sci* 2015;72:4577-4592.
- 45 Zhang J, Wang K, Zhang J, Liu SS, Dai L, Zhang JY: Using proteomic approach to identify tumor-associated proteins as biomarkers in human esophageal squamous cell carcinoma. *J Proteome Res* 2011;10:2863-2872.
- 46 Raatikainen S, Aaltomaa S, Kärjä V, Soini Y: Increased Peroxiredoxin 6 Expression Predicts Biochemical Recurrence in Prostate Cancer Patients After Radical Prostatectomy. *Anticancer Res* 2015;35:6465-6470.
- 47 Thongwatchara P, Promwikorn W, Srisomsap C, Chokchaichamnankit D, Boonyaphiphat P, Thongsuksai P: Differential protein expression in primary breast cancer and matched axillary node metastasis. *Oncol Rep* 2011;26:185-191.
- 48 Huang T, Lin C, Zhong LL, Zhao L, Zhang G, Lu A, Wu J, Bian Z: Targeting histone methylation for colorectal cancer. *Therap Adv Gastroenterol* 2017;10:114-131.
- 49 Bannister AJ, Kouzarides T: Regulation of chromatin by histone modifications. *Cell Res* 2011;21:381-395.
- 50 Sadok A, Bourgarel-Rey V, Gattacceca F, Penel C, Lehmann M, Kovacic H: Nox1-dependent superoxide production controls colon adenocarcinoma cell migration. *Biochim Biophys Acta* 2008;1783:23-33.

Communication

# New 11,20-Epoxybriaranes from the Gorgonian Coral *Junceella fragilis* (Ellisellidae)

Chia-Cheng Lin <sup>1</sup>, Jui-Hsin Su <sup>2,3</sup>, Wu-Fu Chen <sup>1,4</sup>, Zhi-Hong Wen <sup>4</sup> , Bo-Rong Peng <sup>2</sup>,  
Lin-Cyuan Huang <sup>2,3,\*</sup>, Tsong-Long Hwang <sup>5,6,7,8,9,10,\*</sup>  and Ping-Jyun Sung <sup>2,3,4,11,12,\*</sup> 

<sup>1</sup> Department of Neurosurgery, Kaohsiung Chang Gung Memorial Hospital and Chang Gung University College of Medicine, Kaohsiung 833, Taiwan

<sup>2</sup> National Museum of Marine Biology and Aquarium, Pingtung 944, Taiwan

<sup>3</sup> Graduate Institute of Marine Biology, National Dong Hwa University, Pingtung 944, Taiwan

<sup>4</sup> Department of Marine Biotechnology and Resources, National Sun Yat-sen University, Kaohsiung 804, Taiwan

<sup>5</sup> Research Center for Chinese Herbal Medicine, College of Human Ecology, Chang Gung University of Science and Technology, Taoyuan 333, Taiwan

<sup>6</sup> Research Center for Food and Cosmetic Safety, College of Human Ecology, Chang Gung University of Science and Technology, Taoyuan 333, Taiwan

<sup>7</sup> Graduate Institute of Healthy Industry Technology, College of Human Ecology, Chang Gung University of Science and Technology, Taoyuan 333, Taiwan

<sup>8</sup> Graduate Institute of Natural Products, College of Medicine, Chang Gung University, Taoyuan 333, Taiwan

<sup>9</sup> Chinese Herbal Medicine Research Team, Healthy Aging Research Center, Chang Gung University, Taoyuan 333, Taiwan

<sup>10</sup> Department of Anaesthesiology, Chang Gung Memorial Hospital, Taoyuan 333, Taiwan

<sup>11</sup> Graduate Institute of Natural Products, Kaohsiung Medical University, Kaohsiung 807, Taiwan

<sup>12</sup> Chinese Medicine Research and Development Center, China Medical University Hospital, Taichung 404, Taiwan

\* Correspondence: bigpa830123@gmail.com (L.-C.H.); htl@mail.cgu.edu.tw (T.-L.H.); pjsung@nmmba.gov.tw (P.-J.S.); Tel.: +886-8-882-5001 (ext. 1384) (L.-C.H.); +886-3-211-8800 (ext. 5523) (T.-L.H.); +886-8-882-5037 (P.-J.S.); Fax: +886-8-882-5087 (L.-C.H. & P.-J.S.); +886-3-211-8506 (T.-L.H.)

Academic Editors: Pavel B. Drasar and Vladimir A. Khripach

Received: 14 June 2019; Accepted: 5 July 2019; Published: 7 July 2019



**Abstract:** Two new 11,20-epoxybriaranes, fragilides P (1) and Q (2), as well as two known analogues, robustolide F (3) and juncin Z (4), were obtained from the gorgonian coral *Junceella fragilis*. The structures, including the absolute configurations of briaranes 1 and 2, were elucidated by using spectroscopic methods and comparing the spectroscopic and rotation data with those of known related analogues. Briarane 4 decreased the generation of superoxide anions by human neutrophils. The propionate group in 1 is rarely found.

**Keywords:** *Junceella fragilis*; fragilide; briarane; superoxide anion

## 1. Introduction

Since the first structure elucidation of a briarane-type natural product, briarein A, in 1977 by single-crystal X-ray diffraction analysis [1], over 700 marine origin briaranes have been isolated and reported from various octocorals, especially from genera *Briareum* (family Briareidae) [2] and *Junceella* (family Ellisellidae) [3–5]. Among these compounds, 11,20-epoxybriaranes were proven to be a chemical marker for the gorgonian corals belonging to family Ellisellidae [6]. During the course of our research on new natural substances from the marine invertebrates distributed in the waters of Taiwan, a series of briarane-type diterpenoids were isolated from various octocorals belonging to the

genera *Junceella* [7] and *Briareum* [8], and the compounds of this type were proven to possess various interesting bioactivities. Recently, we focused our ongoing studies on a gorgonian coral identified as *Junceella fragilis*. From the results of our studies on this species, we report herein the isolation, structural determination, and bioactivity of two new briaranes, fragilides P (1) and Q (2), along with two known metabolites, robustolide F (3) [9,10] and juncin Z (4) [11] (Figure 1).

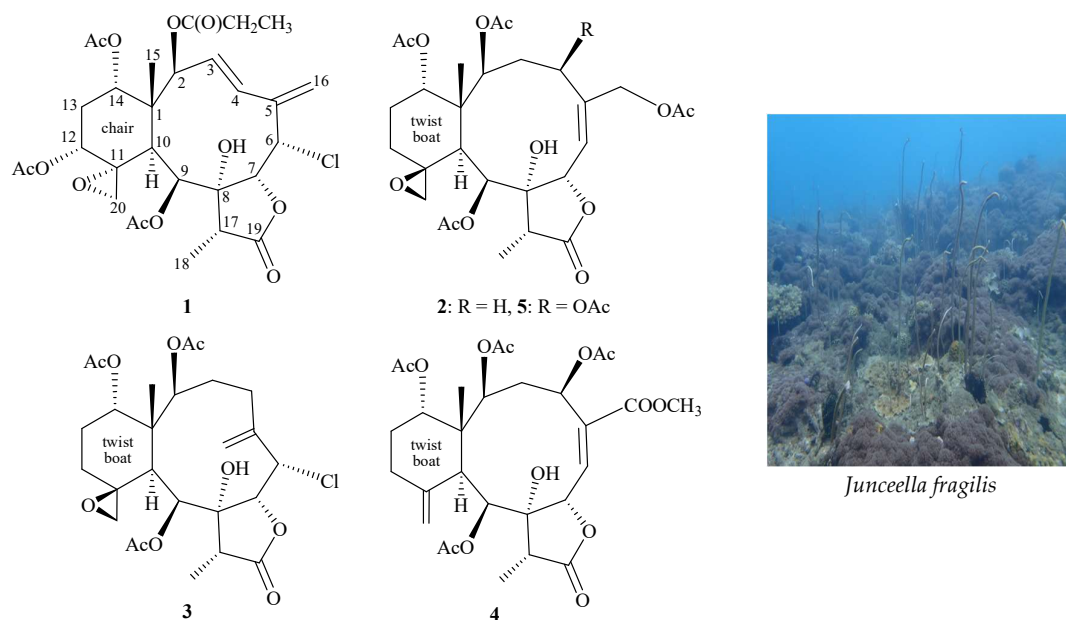


**Figure 1.** Structures of fragilides P (1), Q (2), juncins Z (4), X (5), and robustolide F (3) and a picture of *Junceella fragilis*.

## 2. Results and Discussion

Fragilide P (1) has the molecular formula  $C_{29}H_{37}ClO_{12}$  as deduced by (+)-ESIMS—which showed a pair of peaks at  $m/z$  635/637 (3:1)  $[M + H]^+$ , suggesting a chlorine atom in 1—and further confirmed by (+)-HRESIMS at  $m/z$  635.18683 (calcd. for  $C_{29}H_{37}^{35}ClO_{12} + Na$ , 635.18658). The IR spectrum of 1 indicated the presence of hydroxy ( $3466\text{ cm}^{-1}$ ),  $\gamma$ -lactone ( $1783\text{ cm}^{-1}$ ), and ester carbonyl ( $1735\text{ cm}^{-1}$ ) groups. The  $^{13}\text{C}$ -NMR spectral data (Table 1) showed the presence of a disubstituted olefin ( $\delta_C$  132.7, CH-4; 130.4, CH-3) and an exomethylene ( $\delta_C$  142.0, C-5; 115.1,  $\text{CH}_2$ -16). Moreover, five carbonyl resonances at  $\delta_C$  174.6, 173.3, 170.3, 169.9, and 169.6 in the  $^{13}\text{C}$  spectrum confirmed the presence of a  $\gamma$ -lactone and four other ester groups. In the  $^1\text{H}$  NMR spectrum, three acetate methyls ( $\delta_H$  2.11, 2.09, 2.06, each 3H, s) and a propionate ( $\delta_H$  2.31, 2H, q,  $J = 7.6\text{ Hz}$ ; 1.11, 3H, t,  $J = 7.6\text{ Hz}$ ) were observed. An exocyclic epoxy group was elucidated from the signals of two oxygenated carbons at  $\delta_C$  57.3 (C-11) and 49.2 ( $\text{CH}_2$ -20). The proton chemical shifts at  $\delta_H$  2.77 (1H, dd,  $J = 3.2, 1.2\text{ Hz}$ , H-20a) and 2.64 (1H, d,  $J = 3.2\text{ Hz}$ , H-20b) confirmed the presence of this group. Moreover, a methyl singlet, a methyl doublet, two aliphatic protons, a pair of aliphatic methylene protons, five oxymethine protons, a chlorinated methine proton, and a hydroxy proton were observed in the  $^1\text{H}$ -NMR spectrum of 1 (Table 1).

**Table 1.**  $^1\text{H}$  and  $^{13}\text{C}$ -NMR data for **1** and **2**.

C/H	1		2	
	$\delta_{\text{H}}^{\text{a}}$ (J in Hz)	$\delta_{\text{C}},^{\text{b}}$ Mult.	$\delta_{\text{H}}^{\text{c}}$ (J in Hz)	$\delta_{\text{C}},^{\text{d}}$ Mult.
1		49.2, C		46.9, C
2	5.73 d (9.6)	75.6, CH	4.80 d (5.0)	74.8, CH
3	6.00 dd (15.6, 9.6)	130.4, CH	2.44 m; 1.68 m	32.3, CH <sub>2</sub>
4	6.89 d (15.6)	132.7, CH	2.47 m; 2.01 m	24.9, CH <sub>2</sub>
5		142.0, C		139.8, C
6	5.07 d (4.0)	65.0, CH	5.53 d (10.5)	119.2, CH
7	4.16 d (4.0)	80.6, CH	5.20 d (10.5)	77.0, CH
8		82.8, C		80.4, C
9	5.19 d (2.0)	72.2, CH	5.61 d (6.0)	67.6, CH
10	3.84 br s	33.8, CH	2.29 d (6.0)	39.6, CH
11		57.3, C		62.4, C
12	4.52 dd (2.4, 2.4)	73.7, CH	2.28 m; 1.16 m	23.6, CH <sub>2</sub>
13 $\alpha$ / $\beta$	2.32 m; 2.06 m	29.0, CH <sub>2</sub>	1.77 ddd (15.5, 10.0, 10.0); 2.16 m	24.5, CH <sub>2</sub>
14	4.96 dd (2.4, 2.4)	73.1, CH	4.90 d (5.0)	72.9, CH
15	1.18 s	14.4, CH <sub>3</sub>	1.01 s	14.9, CH <sub>3</sub>
16a/b	5.34 s; 5.26 s	115.1, CH <sub>2</sub>	5.26 dd (16.0, 2.0); 4.23 d (16.0)	67.1, CH <sub>2</sub>
17	2.84 q (7.2)	50.1, CH	2.34 q (7.0)	42.3, CH
18	1.25 d (7.2)	6.9, CH <sub>3</sub>	1.16 d (7.0)	6.7, CH <sub>3</sub>
19		174.6, C		176.4, C
20a/b	2.77 dd (3.2, 1.2); 2.64 d (3.2)	49.2, CH <sub>2</sub>	2.82 d (4.5); 3.23 br d (4.5)	59.0, CH <sub>2</sub>
2-OCOEt	2.31 q (7.6) 1.11 t (7.6)	173.3, C 27.7, CH <sub>2</sub> 8.8, CH <sub>3</sub>		
Acetate methyls	2.11 s	21.4, CH <sub>3</sub>	2.22 s	21.0, CH <sub>3</sub>
	2.09 s	21.1, CH <sub>3</sub>	2.14 s	20.9, CH <sub>3</sub>
	2.06 s	21.0, CH <sub>3</sub>	2.04 s	20.9, CH <sub>3</sub>
			2.01 s	20.9, CH <sub>3</sub>
Acetate carbonyls		170.3, C		170.8, C
		169.9, C		170.8, C
		169.6, C		170.2, C
				169.5, C
8-OH	3.07 s		5.19 s	

<sup>a</sup> Spectra recorded at 400 MHz in CDCl<sub>3</sub> at 25 °C. <sup>b</sup> Spectra recorded at 100 MHz in CDCl<sub>3</sub> at 25 °C. <sup>c</sup> Spectra recorded at 500 MHz in CDCl<sub>3</sub> at 25 °C. <sup>d</sup> Spectra recorded at 125 MHz in CDCl<sub>3</sub> at 25 °C.

Analyses of 2D-NMR (COSY and Heteronuclear Multiple Bond Correlation (HMBC)) data established a tetracyclic nucleus. This assignment was evident from the spin systems from H-2 to H-3, H-3 to H-4, H-6 to H-7, H-9 to H-10, H-12 to H<sub>2</sub>-13, H<sub>2</sub>-13 to H-14, and H-17 to H<sub>3</sub>-18 (Figure 2), while the HMBC between protons and quaternary carbons, such as H-2, H-10, H<sub>3</sub>-15/C-1; H-3, H-6, H-16b/C-5; H-6, H-9, H-10, H-17, H<sub>3</sub>-18, OH-8/C-8; H-9, H-10, H-20b/C-11; and H-17, H<sub>3</sub>-18/C-19 revealed the carbon skeleton (Figure 2). The epoxy group positioned at C-11/20 was further confirmed by the HMBC between H-20b to C-11 and C-12. The C-15 methyl group was positioned at C-1 from the HMBC between H<sub>3</sub>-15 to C-1 and C-14. The HMBC spectrum also revealed that the carbon signal at  $\delta_{\text{C}}$  173.3 (C) was correlated with the signals of the methylene and methyl protons of propionate at  $\delta_{\text{H}}$  2.31 and 1.11, and it was assigned to the carbon atom of the propionate carbonyl group. The propionate at C-2 was confirmed from the connectivity between H-2 and the carbonyl carbon of the propionate group. The HMBC revealed that an acetoxy group is attached to C-9. The hydroxy group at C-8 was deduced from the HMBC of a hydroxy proton ( $\delta_{\text{C}}$  3.07) to C-7, C-8, and C-9. Thus, the remaining acetoxy groups were positioned at C-12 and C-14 by analysis of the characteristic NMR signals ( $\delta_{\text{H}}$  4.52,



1H, dd,  $J = 2.4, 2.4$  Hz;  $\delta_C$  73.7, CH-12;  $\delta_H$  4.96, 1H, dd,  $J = 2.4, 2.4$  Hz;  $\delta_C$  73.1, CH-14), although no HMBC was observed between H-12 and H-14 and the acetate carbonyl carbons.

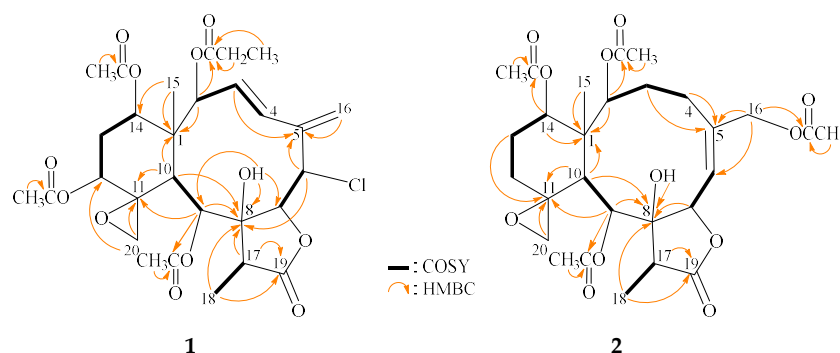


**Figure 2.** The COSY correlations and selective HMBC of **1** and **2**.

According to a summary of the chemical shifts of 11,20-epoxy groups in briarane derivatives, with  $^{13}\text{C}$ -NMR data for C-11 and C-20 at  $\delta_C$  55–61 and 47–52 ppm, respectively, the epoxy group was  $\alpha$ -oriented and the cyclohexane ring existed in a chair conformation [12]; hence, the configuration of the 11,20-epoxy group in **1** ( $\delta_C$  57.3, C-11; 49.2, CH<sub>2</sub>-20) should be  $\alpha$ -oriented, and the cyclohexane ring should be in a chair conformation. The *E* configuration of the C-3/4 double bond was determined from the large proton coupling constant ( $J = 15.6$  Hz) between H-3 and H-4. The stereochemistry of the 11 stereogenic centers of **1** was established by analysis of NOE correlations observed in a NOESY experiment and further supported by molecular mechanics 2 (MM2) force field analysis [13], as shown in Figure 3. In the NOESY spectrum, NOE correlations were observed between H-10 and H-2/H-9/OH-8, while no NOE correlation was seen with Me-15, suggesting that H-2, H-9, H-10, and OH-8 were all  $\alpha$ -oriented; meanwhile, a NOE correlation of Me-15 with H-14 indicated that H-14 was  $\beta$ -oriented. In addition, H-12 was found to correlate with H-13 $\alpha/\beta$  and one proton of C-20 methylene ( $\delta_H$  2.77, H-20a), indicating that the C-12 acetoxymethyl group was  $\alpha$ -oriented. H<sub>3</sub>-18 showed a NOE correlation with OH-8, indicating that Me-18 was  $\alpha$ -oriented at C-17. H-7 exhibited NOE correlations with H-6 and H-17, suggesting that H-6 and H-7 were positioned on the  $\beta$  face. Furthermore, H-3 showed a NOE correlation with H<sub>3</sub>-15; and H-4 showed NOE correlations with H-2 and OH-8, demonstrating the *E*-configuration of  $\Delta^3$  and establishing the *s-cis* diene moiety. As briaranes **1** and **2** were isolated along with a known metabolite **3** (robustolide F) from the same organism, and the absolute configuration of **3** was determined by single-crystal X-ray diffraction analysis [10], it is reasonable on biogenetic grounds and supported by the equal sign of optical rotation of **1**, **2**, and **3** to assume that **1** and **2** have the same absolute configurations as **3**. Therefore, based on the above findings, the configurations of the stereogenic carbons of **1** were determined as 1*R*, 2*S*, 6*S*, 7*R*, 8*R*, 9*S*, 10*S*, 11*R*, 12*R*, 14*S*, and 17*R* (see Figures S1–S10). It is interesting to note that the propionate group is rarely found in briarane-type natural products [12,14–18].

Fragilide Q (**2**) was found to have the molecular formula C<sub>28</sub>H<sub>38</sub>O<sub>12</sub> as determined from its (+)-HRESIMS at  $m/z$  589.22562 (calcd. for C<sub>28</sub>H<sub>38</sub>O<sub>12</sub> + Na, 589.22555) ( $\Omega = 10$ ). Its absorption peaks in the IR spectrum showed ester carbonyl,  $\gamma$ -lactone, and broad OH stretching at 1740, 1778, and 3273 cm<sup>−1</sup>, respectively. It was found that the  $^1\text{H}$  and  $^{13}\text{C}$ -NMR spectra of **2** resembled those of a known analogue, juncin X (**5**) (Figure 1), isolated from gorgonian coral *Junceella juncea* collected off the South China Sea [11], except that the signals corresponding to the acetoxymethyl group at C-4 in **5** were replaced by a proton in **2**. The locations of the functional groups were further confirmed by HMBC and COSY correlations (Figure 2); hence, fragilide Q was assigned the structure of **2**, with the same stereochemistry as that of **1**, and the configurations of the stereogenic carbons were elucidated as 1*S*, 2*S*, 7*S*, 8*R*, 9*S*, 10*S*, 11*S*, 14*S*, and 17*R* (Figure 3) (see Figures S11–S20). Due to the chemical shifts for

C-11 and C-20 which appeared at  $\delta_C$  62.4 and 59.0 ppm, respectively, the epoxy group was  $\beta$ -oriented and the cyclohexane ring should exist in a twisted boat conformation [12].

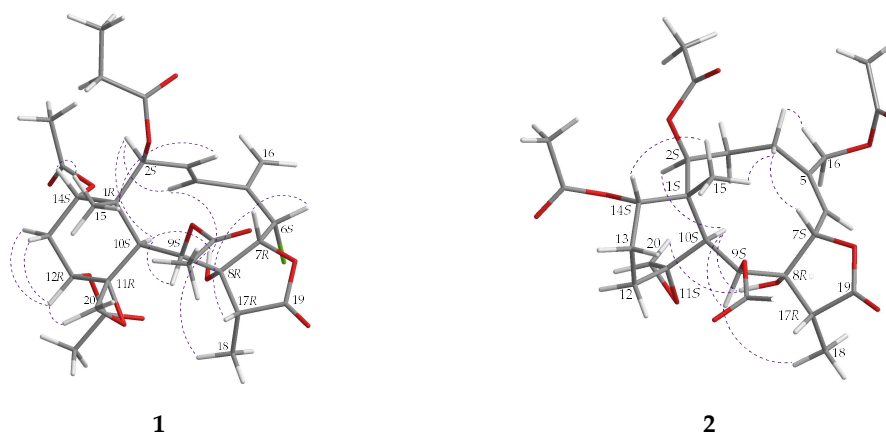


Figure 3. Selected protons with key NOESY (---) correlations of **1** and **2**.

Two known briaranes were isolated and identified as robustolide F (**3**) [9,10] and juncin Z (**4**) [11] by way of comparison with the spectroscopic and physical data reported in the literature.

In an *in vitro* anti-inflammatory activity assay, it was found that briarane **4** (juncin Z) showed a 25.56% inhibitory effect on the generation of superoxide anions by human neutrophils at a concentration of 10  $\mu$ M, and briaranes **1–3** were inactive.

### 3. Materials and Methods

#### 3.1. General Experimental Procedures

The optical rotations were recorded using a Jasco P-1010 digital polarimeter (Japan Spectroscopic, Tokyo, Japan). IR spectra were measured on a Thermo Scientific Nicolet iS5 FT-IR spectrophotometer (Waltham, MA, USA). NMR spectra were taken on a Jeol Resonance ECZ 400S (Tokyo, Japan) or on a Varian Inova (Palo, Alto, CA, USA) 500 NMR spectrometer using the residual  $\text{CHCl}_3$  signal ( $\delta_H$  7.26 ppm) and  $\text{CDCl}_3$  ( $\delta_C$  77.1 ppm) as the internal standard for  $^1\text{H}$  and  $^{13}\text{C}$ -NMR, respectively; coupling constants ( $J$ ) are presented in Hz. Multiplicities of  $^{13}\text{C}$ -NMR data were determined by Distortionless Enhancement by Polarization Transfer (DEPT) experiments. ESIMS and HRESIMS mass spectra were measured on a Bruker mass spectrometer with 7 tesla magnets (model: SolariX FTMS system; Bruker, Bremen, Germany). HPLC separations were carried out on a Hitachi L-2130 pump (Tokyo, Japan) equipped with a Hitachi L-2455 photodiode array detector. The column used for HPLC was reversed-phase silica (250 mm  $\times$  21.2 mm, 5  $\mu\text{M}$ , Luna RP-18e; Phenomenex Inc., Torrance, CA, USA). Column chromatography was carried out with Kieselgel 60 (230–400 mesh, Merck, Darmstadt, Germany). TLC was performed on precoated Kieselgel 60 F<sub>254</sub> (0.25 mm thick, Merck), then sprayed with 10%  $\text{H}_2\text{SO}_4$  solution, followed by heating to visualize the spots.

#### 3.2. Animal Material

The sea whip gorgonian coral *Junceella fragilis* was collected by hand in April 2017 using self-contained underwater breathing apparatus (SCUBA) gear at depths of 10–15 m off the coast of South Bay, Kenting, Taiwan. The samples were then stored in a  $-20^\circ\text{C}$  freezer until extraction. A voucher specimen was deposited in the National Museum of Marine Biology and Aquarium, Taiwan (NMMBA-TW-GC-2017-022). Identification of the species of this organism was performed by comparison as described in previous publications [3–5].

### 3.3. Extraction and Isolation

The freeze-dried and sliced bodies (wet/dry weight = 795/313 g) of the coral specimen were prepared and extracted with a 1:1 mixture of MeOH and CH<sub>2</sub>Cl<sub>2</sub> to give 19.0 g of crude extract which was partitioned between EtOAc and H<sub>2</sub>O. The EtOAc extract (8.0 g) was applied on silica gel column chromatography (C.C.) and eluted with gradients of n-hexane/acetone (50:1 to 1:2, stepwise) to furnish eight fractions (fractions A–H). Fraction G was chromatographed on silica gel C.C. and eluted with gradients of n-hexane/EtOAc (4:1 to 1:1, stepwise) to afford 16 subfractions (fractions G1–G16). Afterward, fraction G9 was separated by RP-HPLC using a mixture of MeOH and H<sub>2</sub>O (with volume/volume = 60:40; at a flow rate of 4.0 mL/min) to afford fragilide P (**1**, 2.7 mg), fragilide Q (**2**, 1.8 mg), robustolide F (**3**, 1.4 mg), and juncin Z (**4**, 1.2 mg).

Fragilide P (**1**): amorphous powder;  $[\alpha]_D^{27} -14$  (c 0.9, CHCl<sub>3</sub>); IR (ATR)  $\nu_{\max}$  3466, 1783, 1735 cm<sup>-1</sup>; <sup>1</sup>H and <sup>13</sup>C-NMR data (see Table 1); ESIMS: *m/z* 635 [M + Na]<sup>+</sup>; HRESIMS: *m/z* 635.18683 (calcd. for C<sub>29</sub>H<sub>37</sub><sup>35</sup>ClO<sub>12</sub> + Na, 635.18658).

Fragilide Q (**2**): amorphous powder;  $[\alpha]_D^{28} -59$  (c 0.6, CHCl<sub>3</sub>); IR (ATR)  $\nu_{\max}$  3273, 1778, 1740 cm<sup>-1</sup>; <sup>1</sup>H and <sup>13</sup>C-NMR data (see Table 1); ESIMS: *m/z* 589 [M + Na]<sup>+</sup>; HRESIMS: *m/z* 589.22562 (calcd. for C<sub>28</sub>H<sub>38</sub>O<sub>12</sub> + Na, 589.22555).

Robustolide F (**3**): amorphous powder;  $[\alpha]_D^{23} -37$  (c 0.07, CHCl<sub>3</sub>) (ref. [9]  $[\alpha]_D^{26} -26.8$  (c 1.038, CHCl<sub>3</sub>)); ref. [10]  $[\alpha]_D^{25} -28$  (c 0.24, CHCl<sub>3</sub>)); IR (ATR)  $\nu_{\max}$  3288, 1780, 1735 cm<sup>-1</sup>; <sup>1</sup>H and <sup>13</sup>C-NMR data were found to be in absolute agreement with previous studies [9]; ESIMS: *m/z* 565 [M + Na]<sup>+</sup>.

Juncin Z (**4**): amorphous powder;  $[\alpha]_D^{23} +28$  (c 0.06, CHCl<sub>3</sub>) (ref. [11]  $[\alpha]_D +31.57$  (c 0.95, CHCl<sub>3</sub>)); IR (ATR)  $\nu_{\max}$  3433, 1782, 1738 cm<sup>-1</sup>; <sup>1</sup>H and <sup>13</sup>C-NMR data were found to be in absolute agreement with previous studies [11]; ESIMS: *m/z* 617 [M + Na]<sup>+</sup>.

### 3.4. Molecular Mechanics Calculations

The molecular models were generated by implementing the MM2 force field [13] in ChemBio 3D Ultra software (version 12.0) which was created by CambridgeSoft (PerkinElmer, Cambridge, MA, USA).

### 3.5. Superoxide Anion Generation by Human Neutrophils

Human neutrophils were obtained by means of dextran sedimentation and Ficoll centrifugation. Measurements of elastase release and superoxide anion generation were carried out according to previously described procedures [19]. Briefly, superoxide anion production was assayed by monitoring the superoxide-dismutase-inhibitable reduction of ferricytochrome c. Elastase release experiments were performed using MeO-Suc-Ala-Ala-Pro-Valp-nitroanilide as the elastase substrate.

## 4. Conclusions

The sea whip gorgonian coral *Junceella fragilis*, a zooxanthella-containing species [20], has been demonstrated to have a wide structural diversity of interesting marine-origin briarane-type diterpenoids [7], and the compounds of this type were suggested originally to be produced by the host corals and not by its zooxanthellae [21]. In our continued study of *Junceella fragilis* collected in the waters of Taiwan, two previously unreported briaranes, fragilides P (**1**) and Q (**2**), were isolated along with two previously described analogues, robustolide F (**3**) and juncin Z (**4**). The structures, including the absolute configurations of **1** and **2**, were determined by using spectroscopic methods and comparing the spectroscopic and rotation values with those of a known related analogue, robustolide F (**3**) [9,10]. Juncin Z (**4**) was found to display an inhibitory effect on the generation of superoxide anions by human neutrophils.

**Supplementary Materials:** The Supplementary Materials are available online. ESIMS, HRESIMS, IR, 1D (<sup>1</sup>H, <sup>13</sup>C-NMR, and DEPT spectra) and 2D (HSQC, COSY, HMBC, and NOESY) spectra of new compounds **1** and **2** and ESIMS, <sup>1</sup>H, <sup>13</sup>C-NMR, and DEPT spectra of **3** and **4**.

**Author Contributions:** C.-C.L., L.-C.H., T.-L.H. and P.-J.S. designed the whole experiment and contributed to manuscript preparation. J.-H.S., W.-F.C., Z.-H.W. and B.-R.P. analyzed the data.

**Funding:** This research was supported by grants from the National Museum of Marine Biology and Aquarium; the National Dong Hwa University; and the Ministry of Science and Technology, Taiwan (Grant Nos: MOST 104-2320-B-291-001-MY3 and 107-2320-B-291-001-MY3) awarded to Ping-Jyun Sung.

**Conflicts of Interest:** The authors declare no conflicts of interest.

## References

- Burks, J.E.; van der Helm, D.; Chang, C.Y.; Ciereszko, L.S. The crystal and molecular structure of briarein A, a diterpenoid from the gorgonian *Briareum asbestinum*. *Acta Cryst.* **1977**, *33*, 704–709. [\[CrossRef\]](#)
- Samimi-Namin, K.; van Ofwegen, L.P. Overview of the genus *Briareum* (Cnidaria, Octocorallia, Briareidae) in the Indo-Pacific, with the description of a new species. *ZooKeys* **2016**, *557*, 1–44. [\[CrossRef\]](#) [\[PubMed\]](#)
- Bayer, F.M. Key to the genera of octocorallia of Pennatulacea (Coelenterata: Anthozoa), with diagnoses of new taxa. *Proc. Biol. Soc. Wash.* **1981**, *94*, 902–947.
- Bayer, F.M.; Grasshoff, M. The genus group taxa of the family Ellisellidae, with clarification of the genera established by J.E. Gary (Cnidaria: Octocorallia). *Senckenberg. Biol.* **1994**, *74*, 21–45.
- Chen, C.-C.; Chang, K.-H. Gorgonacea (Coelenterata: Octocorallia) of Southern Taiwan. *Bull. Inst. Zool. Acad. Sin.* **1991**, *30*, 149–181.
- Su, Y.-M.; Fan, T.-Y.; Sung, P.-J. 11,20-Epoxybriaranes from the gorgonian coral *Ellisella robusta* (Ellisellidae). *Nat. Prod. Res.* **2007**, *21*, 1085–1090. [\[CrossRef\]](#)
- Chung, H.-M.; Wang, Y.-C.; Tseng, C.-C.; Chen, N.-F.; Wen, Z.-H.; Fang, L.-S.; Hwang, T.-L.; Wu, Y.-C.; Sung, P.-J. Natural product chemistry of gorgonian corals of genus *Junceella*—Part III. *Mar. Drugs* **2018**, *16*, 339. [\[CrossRef\]](#)
- Su, Y.-D.; Su, J.-H.; Hwang, T.-L.; Wen, Z.-H.; Sheu, J.-H.; Wu, Y.-C.; Sung, P.-J. Briarane diterpenoids isolated from octocorals between 2014 and 2016. *Mar. Drugs* **2017**, *15*, 44. [\[CrossRef\]](#)
- Tanaka, C.; Yamamoto, Y.; Otsuka, M.; Tanaka, J.; Ichiba, T.; Marriott, G.; Rachmat, R.; Higa, T. Briarane diterpenes from two species of octocorals, *Ellisella* sp. and *Pteroeides* sp. *J. Nat. Prod.* **2004**, *67*, 1368–1373. [\[CrossRef\]](#)
- Sung, P.-J.; Chiang, M.Y.; Tsai, W.-T.; Su, J.-H.; Su, Y.-M.; Wu, Y.-C. Chlorinated briarane-type diterpenoids from the gorgonian coral *Ellisella robusta* (Ellisellidae). *Tetrahedron* **2007**, *63*, 12860–12865. [\[CrossRef\]](#)
- Qi, S.-H.; Zhang, S.; Qian, P.-Y.; Xiao, Z.-H.; Li, M.-Y. Ten new antifouling briarane diterpenoids from the South China Sea gorgonian *Junceella juncea*. *Tetrahedron* **2006**, *62*, 9123–9130. [\[CrossRef\]](#)
- Sheu, J.-H.; Chen, Y.-P.; Hwang, T.-L.; Chiang, M.Y.; Fang, L.-S.; Sung, P.-J. Junceallolides J–L, 11,20-epoxybriaranes from the gorgonian coral *Junceella fragilis*. *J. Nat. Prod.* **2006**, *69*, 269–273. [\[CrossRef\]](#) [\[PubMed\]](#)
- Allinger, N.L. Conformational analysis. 130. MM2. A hydrocarbon force field utilizing  $V_1$  and  $V_2$  torsional terms. *J. Am. Chem. Soc.* **1977**, *99*, 8127–8134. [\[CrossRef\]](#)
- Guerriero, A.; D’Ambrosio, M.; Pietra, F. Bis-allylic reactivity of the funicolides, 5,8(17)-diunsaturated briarane diterpenes of the sea pen *Funiculina quadrangularis* from the Tuscan archipelago, leading to 16-nortaxane derivatives. *Helv. Chim. Acta* **1995**, *78*, 1465–1478. [\[CrossRef\]](#)
- Chiasera, G.; Guerriero, A.; D’Ambrosio, M.; Pietra, F. On the funicolides, briaranes of the Pennatulacean coral *Funiculina quadrangularis* from the Tuscan archipelago: Conformational preferences in this class of diterpenes. *Helv. Chim. Acta* **1995**, *78*, 1479–1489. [\[CrossRef\]](#)
- Sheu, J.-H.; Sung, P.-J.; Su, J.-H.; Wang, G.-H.; Duh, C.-Y.; Shen, Y.-C.; Chiang, M.Y.; Chen, I.-T. Excavatolides U–Z, new briarane diterpenes from the gorgonian *Briareum excavatum*. *J. Nat. Prod.* **1999**, *62*, 1415–1420. [\[CrossRef\]](#)
- Sung, P.-J.; Chen, Y.-P.; Su, Y.-M.; Hwang, T.-L.; Hu, W.-P.; Fan, T.-Y.; Wang, W.-H. Fragilide B: A novel briarane-type diterpenoid with a *s-cis* diene moiety. *Bull. Chem. Soc. Jpn.* **2007**, *80*, 1205–1207. [\[CrossRef\]](#)
- Cheng, W.; Ji, M.; Li, X.; Ren, J.; Yin, F.; van Ofwegen, L.; Yu, S.; Chen, X.; Lin, W. Fragilolides A–Q, norditerpenoid and briarane diterpenoids from the gorgonian coral *Junceella fragilis*. *Tetrahedron* **2017**, *73*, 2518–2528. [\[CrossRef\]](#)



19. Yu, H.-P.; Hsieh, P.-W.; Chang, Y.-J.; Chung, P.-J.; Kuo, L.-M.; Hwang, T.-L. 2-(2-Fluorobenzamido) benzoate ethyl ester (EFB-1) inhibits superoxide production by human neutrophils and attenuates hemorrhagic shock-induced organ dysfunction in rats. *Free Radic. Biol. Med.* **2011**, *50*, 1737–1748. [[CrossRef](#)]
20. Walker, T.A.; Bull, G.D. A newly discovered method of reproduction in gorgonian coral. *Mar. Ecol. Prog. Ser.* **1983**, *12*, 137–143. [[CrossRef](#)]
21. Kokke, W.C.M.C.; Epstein, S.; Look, S.A.; Rau, G.H.; Fenical, W.; Djerassi, C. On the origin of terpenes in symbiotic associations between marine invertebrates and algae (zooxanthellae). *J. Biol. Chem.* **1984**, *259*, 8168–8173. [[PubMed](#)]

**Sample Availability:** Samples of the compounds 1–4 are not available from the authors.



© 2019 by the authors. Licensee MDPI, Basel, Switzerland. This article is an open access article distributed under the terms and conditions of the Creative Commons Attribution (CC BY) license (<http://creativecommons.org/licenses/by/4.0/>).

**Withanolides and 26-Hydroxylated Derivatives with Anti-inflammatory Property from  
*Solanum capsicoide***

You-Cheng Lin, Chih-Hua Chao, Atallah F. Ahmed, Yang-Yih Chen,  
Tsong-Long Hwang, Ho-Yih Liu, and Jyh-Horng Sheu\*

Advance Publication on the web November 17, 2018

doi:10.1246/bcsj.20180225

# Withanolides and 26-Hydroxylated Derivatives with Anti-inflammatory Property from *Solanum capsicoide*

You-Cheng Lin,<sup>†1</sup> Chih-Hua Chao,<sup>†2,3</sup> Atallah F. Ahmed,<sup>4</sup> Yang-Yih Chen,<sup>5</sup> Tsong-Long Hwang,<sup>6,7,8</sup> Ho-Yih Liu,<sup>9</sup> and Jyh-Horng Sheu<sup>\*1,10,11,12,13</sup>

<sup>1</sup>Doctoral Degree Program in Marine Biotechnology, National Sun Yat-sen University, Kaohsiung 804, Taiwan

<sup>2</sup>School of Pharmacy, China Medical University, Taichung 404, Taiwan

<sup>3</sup>Chinese Medicine Research and Development Center, China Medical University Hospital, Taichung 404, Taiwan

<sup>4</sup>Department of Pharmacognosy, College of Pharmacy, King Saud University, Riyadh 11451, Saudi Arabia

<sup>5</sup>Department of Marine Environment and Engineering, National Sun Yat-sen University, Kaohsiung 804, Taiwan

<sup>6</sup>Graduate Institute of Natural Products, College of Medicine and Chinese Herbal Medicine Research Team, Healthy Aging Research Center, Chang Gung University, Taoyuan 333, Taiwan

<sup>7</sup>Research Center for Chinese Herbal Medicine, Research Center for Food and Cosmetic Safety, and Graduate Institute of Health Industry Technology, College of Human Ecology, Chang Gung University of Science and Technology, Taoyuan 333, Taiwan

<sup>8</sup>Department of Anesthesiology, Chang Gung Memorial Hospital, Taoyuan 333, Taiwan

<sup>9</sup>Department of Biological Sciences, National Sun Yat-sen University, Kaohsiung 804, Taiwan

<sup>10</sup>Department of Marine Biotechnology and Resources, National Sun Yat-sen University, Kaohsiung 804, Taiwan

<sup>11</sup>Graduate Institute of Natural Products, Kaohsiung Medical University, Kaohsiung 807, Taiwan

<sup>12</sup>Department of Medical Research, China Medical University Hospital, China Medical University, Taichung 404, Taiwan

<sup>13</sup>Frontier Center for Ocean Science and Technology, National Sun Yat-sen University, Kaohsiung 804, Taiwan

<sup>†</sup>These authors contributed equally to this work

\* E-mail: sheu@mail.nsysu.edu.tw (J.H.S.)



**Jyh-Horng Sheu**

Jyh-Horng Sheu received his Ph.D. degree from University of California, San Diego in 1985. He has been working at Department of Marine Biotechnology and Resources, National Sun Yat-sen University after the completion of Ph.D. study, and appointed to Director (Frontier Center for Ocean Science and Technology) at 2012 and to Distinguished Professor since 2016. His research interests are focused on the chemistry of marine natural products, organic synthesis, and drug discovery.

## Abstract

A phytochemical investigation of the leaves of *Solanum capsicoide* resulted in the isolation and characterization of five new withanolide-type steroids, capsisteroids G–K (**1–5**), along with three known analogues (**6–8**). Their structures were identified by interpretation of the NMR and HRESIMS data as well as by spectral data comparison with known analogues. The isolated steroids were found to be not cytotoxic against a limited panel of cancer cell lines. The ability of the isolated steroids to suppress superoxide anion generation and elastase release in *N*-formyl-methionyl-leucyl-phenylalanine/cytochalasin B (fMLF/CB)-induced human neutrophils was also evaluated and displayed variable activities.

## Keywords:

*Solanum capsicoide*, capsisteroid, 26-hydroxylated

## 1. Introduction

Withanolides are belonging to a group of C<sub>28</sub>-ergostane type steroids with a lactone ring in their side chain. These

compounds were mainly discovered in plants of the genus *Solanum* (Solanaceae)<sup>1–19</sup> and in few marine organisms.<sup>20,21–23</sup> Previous studies on withanolides have proven their wide spectrum of biological activities, including phytotoxic activities,<sup>1</sup> cytotoxic,<sup>12,18,21, 22, 24, 25</sup> anti-inflammatory,<sup>7,11,14,23</sup> anti-microbial,<sup>26</sup> chemopreventive,<sup>27</sup> and antiviral activities.<sup>19</sup> Although the genus *Solanum* has been unveiled to produce bioactive withanolides, there are few reports about the chemical constituents of *S. capsicoide* (syn. *Solanum aculeatissimum*).<sup>28</sup> Our prior investigation on this plant has led to the isolation of a series of C-26 hydroxylated withanolide derivatives, capsisteroids A–F.<sup>29</sup> In this paper, we report our further investigation on the same plant which led to the discovery of five withanolide-type steroids, capsisteroids G–K (**1–5**), three known withanolides, jaborosalactone D (**6**),<sup>30</sup> cistol J (**7**),<sup>5</sup> and cistol P (**8**),<sup>4</sup> (Figure 1) and other known compounds, 24 $\alpha$ -hydroperoxy-24-vinylcholesterol,<sup>31</sup> ergosta-5,24(28)-dien-3 $\beta$ -ol,<sup>32</sup> stigmasterol,<sup>33</sup> (6S, 9S)-roseoside,<sup>34</sup> blumenol C glucoside,<sup>35</sup> *N*-cis-coumaroyltyramine,<sup>36</sup> *N*-trans-coumaroyltyramine,<sup>36</sup> *N*-trans-feruloyltyramine,<sup>37</sup> *N*-cis-feruloyltyramine,<sup>37</sup> *N*-acetyltyramine,<sup>38</sup> and vomifoliol.<sup>39</sup> The isolated withanolides

**1–4** and **6** were not cytotoxic against the growth of a limited panel of cancer cell lines, but exhibited anti-inflammatory effects through the suppression of superoxide anion generation and elastase release in *N*-formyl-methionyl-leucyl-phenylalanine/cytochalasin B (fMLF/CB)-induced human neutrophils with variable potencies.

## 2. Results and Discussion

The powdered leaves of *S. capsicoides* were exhaustively extracted with EtOAc and the solvent-free extract was then separated and purified by reversed-phase HPLC to afford new compounds **1–5**. (Figure 1)

Capsisteroid G (**1**) was isolated as a colorless gum and its molecular formula was established as  $C_{28}H_{44}O_7$  using HRESIMS ( $m/z$  calcd 515.2979, found 515.2979  $[M+Na]^+$ ), implying seven degrees of unsaturation. The IR spectrum of **1** revealed the presence of hydroxyl ( $\nu_{\max}$  3420  $cm^{-1}$ ) and carbonyl ( $\nu_{\max}$  1690  $cm^{-1}$ ) groups. All protons and carbons were assigned with  $^1H$  and  $^{13}C$  NMR spectra (Tables 1 and 2), in conjunction with HSQC spectra, which led to the assignment of one ketone ( $\delta_C$  214.7), one trisubstituted double bond ( $\delta_C$  138.8 and  $\delta_H$  5.55, 1H, d,  $J = 5.6$  Hz;  $\delta_C$  126.8), two hydroxyl-bearing methines ( $\delta_H$  4.25, 1H, m,  $w_{1/2} = 11.2$  Hz,  $\delta_C$  69.1;  $\delta_H$  4.61, 1H, s,  $\delta_C$  97.7), and three  $sp^3$  oxygenated quaternary carbons ( $\delta_C$  86.6, 77.4, and 75.2). A comparison of NMR data of **1** with those of known withanolides revealed analogy with capsisteroid A.<sup>29</sup> However, the differences were found in ring A,

in which the 2,3-double bond of capsisteroid A was converted to a single bond with a hydroxy group at C-3. The COSY and HMBC spectra were further analyzed to confirm the above findings for **1**. The HMBC correlations from  $H_{2-2}$  to C-3 and from  $H_{2-4}$  to C-3 and C-10, along with the COSY correlations of  $H_{2-2}/H_3$  and  $H_3/H_{2-4}$ , indicated that the hydroxy group should be positions at C-3 (Figure 2). Additionally, a  $\Delta^{5,6}$  double bond and an 1-oxo group were confirmed from the HMBC correlations observed from  $H_{3-19}$  to C-1, C-5, C-9, and C-10 and from  $H_6$  to C-4, C-8, and C-10.

The relative configurations of **1** were determined by analysis of the NOESY correlations. The correlations of  $H_{3-19}$  with  $H_8$  ( $\delta_H$  1.47), one proton of  $H_{2-2}$  ( $\delta_H$  2.98), and one of  $H_{2-4}$  ( $\delta_H$  2.89) suggested that the above protons are  $\beta$ -oriented, as  $H_{3-19}$  is  $\beta$ -oriented in natural steroids (Figure 3). Moreover, NOESY correlations of  $H_3$  with both  $H_{2\beta}$  and  $H_{4\beta}$  implied the  $\alpha$ -orientation of 3-OH. This was also confirmed by the small  $J$  value (3.2 Hz) between both protons at C-2 and  $H_3$ . The configurations of the D ring and side chain of **1** were found to be the same as those of capsisteroid A, due to their superimposability of carbon resonances at the respective carbons. Similar to our previous findings,<sup>29</sup> compound **1** was found to be an epimeric mixture which exhibited a 3:1 ratio of 26*S*/*R* diastereomers by integration of the respective  $^1H$  NMR signals. Thus, the structure of compound **1** was elucidated as (3*S*, 17*S*, 22*R*, 24*R*, 25*S*, 26*S*)-22,26-epoxy-3 $\alpha$ ,17 $\alpha$ ,24,25,26-pentahydroxyergost-5-en-1-one, with a 26*R* diastereoisomer as the minor component.

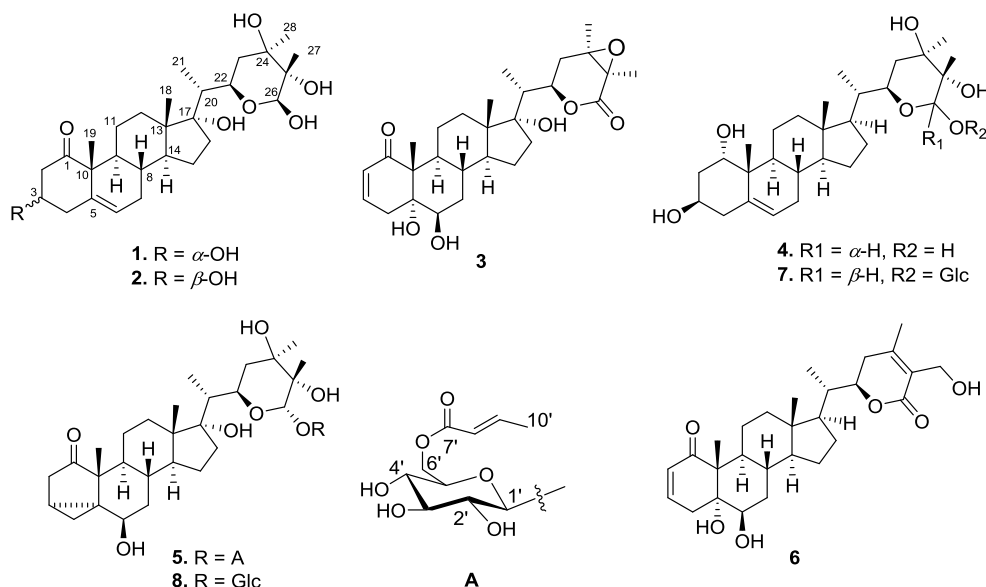


**Figure 1.** Structures of compounds **1–8**.

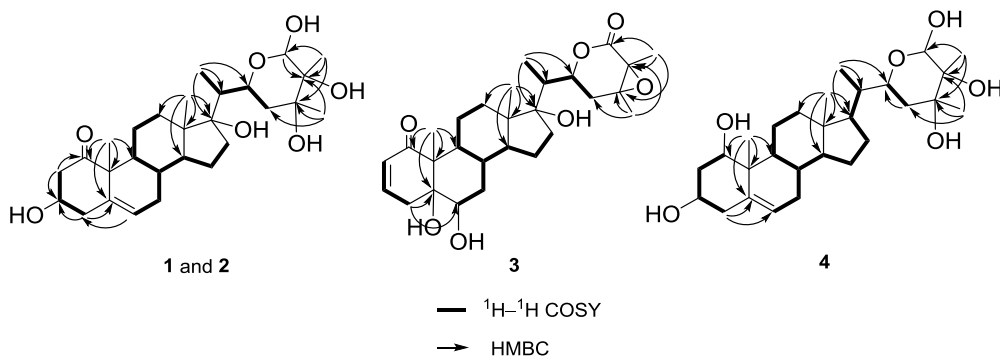


**Figure 2.** Selected  $^1H$ - $^1H$  COSY and HMBC correlations of **1–4**.



The HRESIMS data of capsisteroid H (**2**) established a molecular formula of  $C_{28}H_{44}O_7$ , the same as that of **1**. The  $^1H$  and  $^{13}C$  data (Tables 2 and 1, respectively) of **2** are very similar to those of **1**, except for the NMR signals at ring A (Tables 1 and 2). Also, the analysis of HMBC and COSY correlations elucidated the same planar structure as that of **1** (Figure 2), implying **2** to be an epimer of **1**. The relative configuration of **2** was evidenced by the analysis of NOESY spectrum. Assuming the  $\beta$ -orientation of H<sub>3</sub>-19 ( $\delta_H$  1.30), NOESY correlations of H<sub>3</sub>-19 with both H-8 ( $\delta_H$  1.52) and H-2 $\beta$  ( $\delta_H$  2.68) as well as H-3 with H-2 $\alpha$  ( $\delta_H$  2.55) suggested the  $\alpha$ -orientation of H-3 (Figure 3), which was confirmed by a large coupling constant (12.0 Hz) between H-3 and H-2 $\beta$  (Table 2). Thus, **2** was determined as a C-3 epimer of **1** and the structure was assigned as (3*R*,17*S*,22*R*,24*R*,25*S*,26*S*)-22,26-epoxy-3 $\beta$ ,17 $\alpha$ ,24,25,26-pentahydroxyergost-5-en-1-one.

**Table 1.**  $^{13}C$  NMR spectroscopic data of compounds **1–4**.

No.	<b>1</b> <sup>a)</sup>	<b>2</b> <sup>b)</sup>	<b>3</b> <sup>b)</sup>	<b>4</b> <sup>a)</sup>
1	214.7 (C) <sup>c)</sup>	206.2 (C)	207.7 (C)	73.8 (CH)
2	46.9 (CH <sub>2</sub> )	48.9 (CH <sub>2</sub> )	129.2 (CH)	39.2 (CH <sub>2</sub> )
3	69.1 (CH)	70.1 (CH)	144.0 (CH)	67.0 (CH)
4	39.9 (CH <sub>2</sub> )	42.1 (CH <sub>2</sub> )	36.8 (CH <sub>2</sub> )	42.6 (CH <sub>2</sub> )
5	138.8 (C)	137.1 (C)	78.5 (C)	139.4 (C)
6	126.8 (CH)	126.8 (CH)	75.4 (CH)	125.2 (CH)
7	32.3 (CH <sub>2</sub> )	32.6 (CH <sub>2</sub> )	34.4 (CH <sub>2</sub> )	32.9 (CH <sub>2</sub> )
8	33.6 (CH)	33.7 (CH)	31.8 (CH)	42.5 (CH)
9	43.5 (CH)	44.0 (CH)	42.5 (CH)	42.5 (CH)
10	54.9 (C)	53.9 (C)	53.2 (C)	42.6 (C)
11	23.6 (CH <sub>2</sub> )	23.6 (CH <sub>2</sub> )	24.7 (CH <sub>2</sub> )	21.3 (CH <sub>2</sub> )
12	33.4 (CH <sub>2</sub> )	33.5 (CH <sub>2</sub> )	34.0 (CH <sub>2</sub> )	40.9 (CH <sub>2</sub> )
13	49.5 (C)	49.5 (C)	49.7 (C)	43.8 (C)
14	51.7 (CH)	51.8 (CH)	51.1 (CH)	57.7 (CH)
15	24.7 (CH <sub>2</sub> )	24.8 (CH <sub>2</sub> )	24.4 (CH <sub>2</sub> )	25.4 (CH <sub>2</sub> )
16	37.8 (CH <sub>2</sub> )	40.9 (CH <sub>2</sub> )	37.8 (CH <sub>2</sub> )	28.4 (CH <sub>2</sub> )
17	86.6 (C)	86.7 (C)	86.0 (C)	54.3 (CH)
18	15.4 (CH <sub>3</sub> )	15.5 (CH <sub>3</sub> )	15.9 (CH <sub>3</sub> )	12.2 (CH <sub>3</sub> )
19	19.8 (CH <sub>3</sub> )	19.7 (CH <sub>3</sub> )	16.4 (CH <sub>3</sub> )	20.5 (CH <sub>3</sub> )
20	44.8 (CH)	44.9 (CH)	44.7 (CH)	40.5 (CH)
21	10.3 (CH <sub>3</sub> )	10.2 (CH <sub>3</sub> )	9.7 (CH <sub>3</sub> )	13.7 (CH <sub>3</sub> )
22	74.9 (CH)	75.0 (CH)	79.1 (CH)	74.3 (CH)
23	40.8 (CH <sub>2</sub> )	40.9 (CH <sub>2</sub> )	32.6 (CH <sub>2</sub> )	37.2 (CH <sub>2</sub> )
24	77.4 (C)	77.6 (C)	60.5 (C)	76.9 (C)
25	75.2 (C)	75.3 (C)	64.9 (C)	74.9 (C)
26	97.7 (CH)	97.9 (CH)	172.2 (C)	97.9 (CH)
27	14.9 (CH <sub>3</sub> )	15.0 (CH <sub>3</sub> )	13.9 (CH <sub>3</sub> )	14.8 (CH <sub>3</sub> )
28	22.7 (CH <sub>3</sub> )	22.8 (CH <sub>3</sub> )	18.1 (CH <sub>3</sub> )	22.7 (CH <sub>3</sub> )

a) Spectrum recorded 100 MHz in methanol-*d*<sub>4</sub>.

b) Spectrum recorded 125 MHz in methanol-*d*<sub>4</sub>.

c) Multiplicities deduced by DEPT.

HRESIMS analysis of capsisteroid I (**3**) supported the evidence for a molecular formula of  $C_{28}H_{40}O_7$  from the sodiated molecular ion peak at  $m/z$  511.2665  $[M+Na]^+$ . The  $^1H$  and  $^{13}C$  data (Tables 1 and 2, respectively) of **3** were found to be similar to those of capsisteroid D<sup>29</sup> except that the hydroxyl bearing carbons C-24 ( $\delta_C$  77.4), C-25 ( $\delta_C$  75.2), and C-26 ( $\delta_C$  97.7) in the side chain of capsisteroid D was found to be replaced by epoxy carbons ( $\delta_C$  60.5 and  $\delta_C$  64.9) and a carbonyl carbon ( $\delta_C$  172.2) in **3**, respectively. In the HMBC spectrum of **3** (Figure 2), correlations from H<sub>3</sub>-27 ( $\delta_H$  1.49) to C-24 ( $\delta_C$  60.5), C-25 ( $\delta_C$  64.9), and C-26 ( $\delta_C$  172.2) and from

H<sub>3</sub>-28 ( $\delta_H$  1.47) to C-23 ( $\delta_C$  32.6), C-24, and C-25 assigned the carbonyl group and the epoxy group to be located at C-26, C-24, and C-25 of the steroidal side chain, respectively. In the NOESY spectrum of **3**, the correlations of one proton of H<sub>2</sub>-23 ( $\delta_H$  2.54) with both of H<sub>3</sub>-28 ( $\delta_H$  1.47) and the  $\alpha$ -oriented H-22 ( $\delta_H$  4.78) as well as H-22 with both of H<sub>2</sub>-16 were observed, suggesting the  $\alpha$  orientation of H<sub>3</sub>-28 (Figure 3). The latter protons in turn showed a correlation with H<sub>3</sub>-27 ( $\delta_H$  1.49), indicating that H<sub>3</sub>-27 was also positioned on the  $\alpha$  face. Accordingly, **3** was assigned to be (17*S*,22*R*,24*R*,25*R*)-22,26:24,25-diepoxy-5 $\alpha$ ,6 $\beta$ ,17 $\alpha$ -trihydroxy-1-oxoergost-2-en-2,6,22-olide.

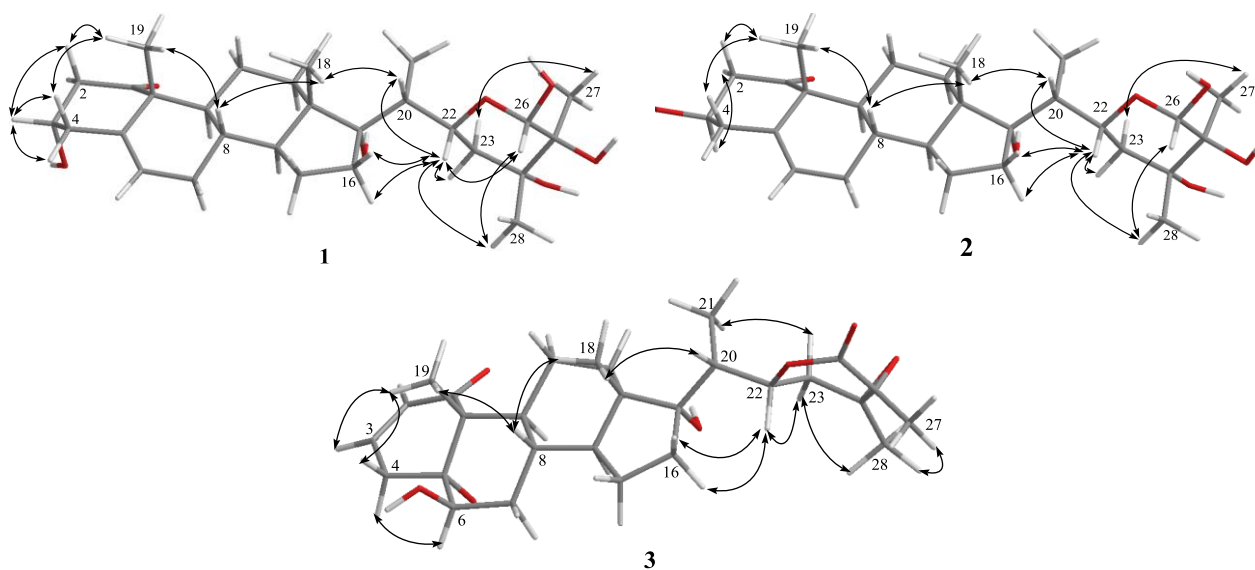
Compound **4** was obtained as white powder and its molecular formula was established as  $C_{28}H_{46}O_6$  based on HRESIMS data ( $m/z$  501.3189  $[M+Na]^+$ ), appropriating for six degrees of unsaturation. Comparison of the NMR data of **4** with those of cistol J (**7**) (Tables S1 and S2, supplementary materials) indicated that, except for the sugar moiety, the NMR data of the two compounds were highly similar. This suggested **4** to be a deglycosyl derivative of **7** or its 26-diastereomer. In the  $^1H$  NMR data of **4**, the coupling patterns of **4** were also found to be identical to those of the aglycone moiety of **7**. In addition, the 26*S*-configuration was determined for **4** according to the carbon resonance of the adjacent methyl group (C-27) at  $\delta_C$  14.8, as compared to the respective resonances of **1** ( $\delta_C$  14.9 for 26*S*;  $\delta_C$  22.0 for 26*R*). Therefore, the structure of **4** was assigned to be (22*R*,24*R*,25*S*,26*S*)-22,26-epoxy-1 $\alpha$ ,3 $\beta$ ,24,25,26-pentahydroxyergost-5-ene.

The HRESIMS analysis established a molecular formula of  $C_{38}H_{58}O_{13}$  for compound **5**. The NMR spectroscopic data of **5** showed signals due to four methyl groups ( $\delta_H$  0.85, 1.10, 1.26, and 1.47; each 3H, s), one secondary methyl group ( $\delta_H$  0.99, 3H, d,  $J=7.2$  Hz), a *trans*-but-2-enoate moiety ( $\delta_C$  165.1;  $\delta_H$  5.89, 1H, dd,  $J=15.6, 1.8$  Hz;  $\delta_H$  7.02, 1H, ddd,  $J=15.6, 6.6, 1.8$  Hz;  $\delta_H$  1.89, 3H, dd,  $J=6.6, 1.8$  Hz), two hemiacetal ( $\delta_H$  4.85, 1H, br s /  $\delta_C$  102.0;  $\delta_H$  4.52, 1H, d,  $J=7.8$  Hz /  $\delta_C$  98.5), four hydroxy methines ( $\delta_H$  3.26, 1H, br s;  $\delta_H$  3.30, 1H, m;  $\delta_H$  3.39, 1H, m;  $\delta_H$  3.35, 1H, m), and one  $sp^3$  oxygenated quaternary carbon ( $\delta_C$  86.6) (Table 3). Except for the *trans*-but-2-enoate moiety, the NMR data were quite similar to a structurally-related co-isolate, cistol P (**8**),<sup>4</sup> revealing that **5** is a *trans*-but-2-enoate derivative of **8**. Due to the inadequate amount of **5** (0.5 mg), a satisfactory HMBC spectra could not be acquired. However, the presence of COSY correlations confirmed the spin systems from H-8' ( $\delta_H$  5.89) to H<sub>3</sub>-10' ( $\delta_H$  1.89) of *trans*-but-2-enoate moiety. Furthermore, the mass fragments at  $m/z$  677  $[M+Na-68]^+$ , 515  $[M+Na-68-162]$ , and 493  $[M+H-68-162]$  were ascribable to the loss of a but-2-enoyl and a glucosyl moieties. The but-2-enoyl group was assigned to be located at C-6' position of the glucosyl residue according to the downfield  $^1H$  proton chemical shift observed at  $\delta_H$  4.28, 1H, dd,  $J=12.0, 6.0$  Hz; and 4.41, 1H, dd,  $J=12.0, 1.8$  Hz (H<sub>2</sub>-6'). Consequently, we determined the structure of **5** to be (17*S*,22*R*,24*R*,25*R*,26*S*)-22,26-epoxy-1-oxo-3 $\alpha$ ,5 $\alpha$ -cycloergostan-6 $\beta$ ,17 $\alpha$ ,24,25,26-pentaol-26-*O*-(6'-*O*-but-2-enoyl)- $\beta$ -D-glucopyranoside.

The cytotoxic activity of compounds **1–3**, **6**, and **7** against four human cancer cell lines, including human erythroleukemia (K562), human promyelocytic leukemia (HL-60), acute lymphoblastic leukemia (Molt-4), and human liver bile duct carcinoma (HuCCT1), was assayed. However, none of the compounds explicated any appreciable cytotoxicity at 20  $\mu$ M. On the other hand, the *in vitro* pro-inflammatory effect of the above compounds was also tested by evaluating the suppression of *N*-formyl-methionyl-leucylphenylalanine/cytoc-

**Table 2.**  $^1\text{H}$  NMR spectroscopic data of compounds **1–4**.

No.	<b>1</b> <sup>a)</sup>	<b>2</b> <sup>b)</sup>	<b>3</b> <sup>b)</sup>	<b>4</b> <sup>a)</sup>
1				3.80 brs
2	2.31 dd (13.6, 3.2) <sup>c)</sup>	2.55 dd (12.0, 5.5)	5.77 dd (10.5, 2.5)	1.71 m
	2.98 dd (13.6, 3.2)	2.68 dd (12.0, 12.0)		2.00 m
3	4.25 m ( $w_{1/2}$ = 11.2)	3.70 m ( $w_{1/2}$ = 21.4)	6.64 ddd (10.0, 5.0, 2.5)	3.89 m
4	2.23 br d (14.8)	2.50 br d (7.5)	2.04 dd (20.0, 5.0)	1.72 m
	2.89 br d (14.8)		3.26 td (20.0, 2.5)	2.28 m
6	5.55 d (5.6)	5.64 d (5.0)	3.52 br s	5.49 d (4.4)
7	1.65 m	1.57 m	1.57 m	1.38 m
	1.99 m	2.02 m	1.74 m	1.98 m
8	1.47 m	1.52 m	1.79 m	2.25 m
9	1.70 m	1.70 m	1.78 m	2.25 m
11	1.41 m	1.43 m	1.21 m	1.49 m
	1.79 m	1.73 m	1.72 m	1.52 m
12	1.62 m	1.64 m	1.56 m	1.23 m
	1.75 m	1.70 m	1.73 m	2.03 m
14	1.75 m	1.71 m	1.81 m	1.12 m
15	1.17 m	1.18 m	1.33 m	1.12 m
	1.70 m	1.71 m	2.24 m	1.67 m
16	1.68 m	1.69 m	1.66 m	1.38 m
	2.04 m	2.03 m	1.97 m	1.75 m
17				1.13 m
18	0.81 s	0.81 s	0.85 s	0.74 s
19	1.31 s	1.30 s	1.30 s	1.02 s
20	2.08 m	2.09 m	2.14 m	1.80 m
21	1.01 d (7.2)	1.00 d (7.5)	0.98 d (7.0)	0.99 d (6.8)
22	3.82 br d (12.0)	3.82 dt (12.0, 3.0)	4.78 dt (12.0, 3.0)	3.59 br d (12.0)
23	1.70 m	1.69 m	2.12 m	1.33 m
	1.80 m	1.82 m	2.54 dd (15.5, 3.0)	1.62 m
26	4.61 br s	4.60 br s		4.61 s
27	1.21 s	1.21 s	1.49 s	1.21 s
28	1.33 s	1.32 s	1.47 s	1.31 s

a) Spectrum recorded at 400 MHz in methanol- $d_4$ .b) Spectrum recorded at 500 MHz in methanol- $d_4$ .c)  $J$  values in Hz in parentheses.**Figure 3.** Selected NOESY correlations of compounds **1–3**.

**Table 3.**  $^1\text{H}$  and  $^{13}\text{C}$  NMR spectroscopic data of compounds **5** and **8**.

No.	<b>5</b> <sup>a)</sup>	<b>8</b> <sup>b)</sup>	<b>5</b> <sup>d)</sup>	<b>8</b> <sup>e)</sup>
1			— <sup>f)</sup>	220.4 (C)
2	2.03 br d (18.6) <sup>c)</sup> 2.87 dd (18.6, 4.2)	2.03 br d (18.4) 2.88 ddd (18.4, 4.0, 1.2)	40.3 (CH <sub>2</sub> ) <sup>g)</sup>	40.4 (CH <sub>2</sub> )
3	1.37 m	1.36 m	16.3 (CH)	16.3 (CH)
4	-0.01 dd (5.0, 2.5) 0.84 dd (5.0, 2.5)	-0.01 dd (4.8, 2.0) 0.84 dd (4.8, 2.0)	18.2 (CH <sub>2</sub> )	18.2 (CH <sub>2</sub> )
5			—	53.8 (C)
6	3.26 br s	3.25 br s	—	73.6 (CH)
7	1.36 m 1.92 m	1.35 m 1.91 m	38.7 (CH <sub>2</sub> )	38.7 (CH <sub>2</sub> )
8	1.89 m	1.87 m	30.7 (CH)	30.7 (CH)
9	1.00 m	1.00 m	48.4 (CH)	48.4 (CH)
10			—	35.9 (C)
11	1.30 m 1.48 m	1.30 m 1.50 m	23.0 (CH <sub>2</sub> )	23.0 (CH <sub>2</sub> )
12	1.60 m	1.60 m	—	33.4 (CH <sub>2</sub> )
13			49.6 (C)	49.5 (C)
14	1.71 m	1.71 m	51.0 (CH)	51.0 (CH)
15	1.20 m 1.70 m	1.20 m 1.70 m	24.7 (CH <sub>2</sub> )	24.7 (CH <sub>2</sub> )
16	1.66 m 2.12 m	1.67 m 2.14 m	—	37.8 (CH <sub>2</sub> )
17			86.6 (C)	86.6 (C)
18	0.85 s	0.85 s	15.5 (CH <sub>3</sub> )	15.5 (CH <sub>3</sub> )
19	1.10 s	1.09 s	14.9 (CH <sub>3</sub> )	14.9 (CH <sub>3</sub> )
20	2.04 m	2.05 m	44.1 (CH)	44.0 (CH)
21	0.99 d (7.2)	0.99 d (7.2)	9.7 (CH <sub>3</sub> )	9.7 (CH <sub>3</sub> )
22	4.35 dt (12.0, 3.0)	4.36 br d (12.4)	71.6 (CH)	71.5 (CH)
23	1.70 m 1.93 m	1.70 m 1.92 m	40.3 (CH <sub>2</sub> )	40.4 (CH <sub>2</sub> )
24			—	75.1 (C)
25			—	73.9 (C)
26	4.85 br s	4.90 br s	102.0 (CH)	102.4 (CH)
27	1.26 s	1.28 s	22.0 (CH <sub>3</sub> )	22.1 (CH <sub>3</sub> )
28	1.47 s	1.48 s	24.4 (CH <sub>3</sub> )	24.4 (CH <sub>3</sub> )
1'	4.52 d (7.8)	4.50 d (8.0)	98.5 (CH)	99.9 (CH)
2'	3.30 m	3.27 m	74.6 (CH)	74.7 (CH)
3'	3.39 m	3.37 dd (18.4, 8.8)	78.4 (CH)	78.5 (CH)
4'	3.35 m	3.29 m	74.6 (CH)	71.4 (CH)
5'	3.49 ddd (12.0, 6.0, 1.8)	3.27 m	—	78.0 (CH)
6'	4.28 dd (12.0, 6.0) 4.41 dd (12.0, 1.8)	3.67 dd (12.0, 5.2) 3.85 dd (12.0, 2.4)	—	62.5 (CH <sub>2</sub> )
7'			165.1 (C)	
8'	5.89 dd (15.6, 1.8)		123.3 (CH)	
9'	7.02 ddd (15.6, 6.6, 1.8)		146.8 (CH)	
10'	1.89 dd (6.6, 1.8)		18.0 (CH <sub>3</sub> )	

a) Spectrum recorded at 600 MHz in methanol-*d*<sub>4</sub>.b) Spectrum recorded at 400 MHz in methanol-*d*<sub>4</sub>.c) *J* values in Hz in parentheses.d) Spectrum recorded 150 MHz in methanol-*d*<sub>4</sub>.e) Spectrum recorded 100 MHz in methanol-*d*<sub>4</sub>.

f) Designate signal not detected.

g) Multiplicities deduced by DEPT.

halasin B (fMLF/CB)-induced superoxide anion ( $O_2^{\cdot -}$ ) generation and elastase release in human neutrophils (Table 4). At a concentration of 30  $\mu$ M, compounds **2**, **3**, and **6** were found to inhibit superoxide anion generation (14.8%, 20.9% and 14.8%, respectively). Also, compounds **3** and **6** displayed 42.9% and 25.6% inhibition toward elastase release, respectively.

### 3. Conclusion

In present study, we characterized five new withanolide-type steroids (**1–5**). Among them, compounds **1**, **2**, **4**, and **5** are 26-hydroxylated analogues, belonging to a rare group of withanolides from natural sources. This work also provided further exploration of bioactive natural products from *S. capsicoides* and found that this plant elaborated a lot of withanolides and 26-hydroxylated derivatives, which could be a source of anti-inflammatory agents.

**Table 4.** Inhibitory effects of compounds **1–3** and **6** on superoxide anion generation and elastase release in fMLF/CB-induced human neutrophils.

Compound	Superoxide anion		Elastase release	
	Inh % <sup>a)</sup>		Inh %	
<b>1</b>	5.4 $\pm$ 5.3		14.4 $\pm$ 2.3	**
<b>2</b>	14.8 $\pm$ 7.0		3.1 $\pm$ 5.4	
<b>3</b>	20.9 $\pm$ 2.1	***	42.9 $\pm$ 3.4	***
<b>6</b>	14.8 $\pm$ 2.3	**	25.6 $\pm$ 6.7	**
Genistein <sup>b)</sup>	100.3 $\pm$ 1.5	***	72.3 $\pm$ 5.0	***

a) Percentage of inhibition (Inh %) at a concentration of 30  $\mu$ M. Results are presented as mean  $\pm$  S.E.M. (n=3–4). \*  $P < 0.05$ , \*\*  $P < 0.01$ , \*\*\*  $P < 0.001$  compared with the control (DMSO).

b) Positive control.

### 4. Experimental

**General Experimental Procedures.** The following instruments were used for acquiring the physical data: a JASCO P-1020 digital polarimeter (JASCO Corporation, Tokyo, Japan) for optical rotation values; a JASCO J-815 infrared spectrophotometer (JASCO Corporation, Tokyo, Japan) for IR spectra; a Varian 400 NMR, 500 NMR and 600 NMR (Varian Inc., Palo Alto, CA, USA) instruments for the  $^1H$  NMR and  $^{13}C$  NMR spectra; a Bruker APEX II mass spectrometer (Bruker, Bremen, Germany) for ESI mass. Separation and purification by HPLC was performed on a C18 column (250  $\times$  21.2 mm, 5  $\mu$ m, Sciences Inc., Tokyo, Japan) equipped by a HiTachi L-7100 HPLC (Hitachi Ltd., Tokyo, Japan) system.

**Plant Material.** The fresh leaves of *S. capsicoides* were collected in July 2013 from Pingtung County, southern Taiwan. This plant material was identified by H.-Y. Liu, Department of Biological Sciences, National Sun Yat-sen University, Kaohsiung, Taiwan. The deposition of voucher specimen (SC-20130701) was also performed in the Department of Marine Biotechnology and Resources.

**Extraction and Isolation.** The air-dried leaves (132.1 g) were powdered and extracted with EtOAc overnight. The EtOAc extract (22.0 g) was chromatographed over silica gel column and eluted with a gradient of a hexane in acetone (0–100%, stepwise), which afforded 20 fractions. Fraction 13, eluted with hexane–acetone (1:2), was purified over a RP-18 column using acetonitrile ( $CH_3CN$ )– $H_2O$  (1:1) to afford nine

subfractions (A1–A9). Subfractions A5 and A7 were further purified by RP-HPLC ( $CH_3CN$ – $H_2O$ , 1:2.5) to afford compounds **6** (1.7 mg) and **3** (1.0 mg), respectively. Fraction 15 eluted with hexane–acetone (1:3) was separated over a RP-18 column using  $MeOH$ – $H_2O$  (1:2) to afford 10 subfractions (B1–B10). Subfractions B6 was further separated by RP-HPLC using  $MeOH$ – $H_2O$  (1.2:1) to afford compounds **1** (3.8 mg) and **2** (1.1 mg). Subfraction B9 was purified over a RP-HPLC using  $MeOH$ – $H_2O$  (2:1) to afford compound **4** (0.7 mg). Fraction 17, eluted with hexane–acetone (1:5), was rechromatographed over an RP-18 column using  $CH_3CN$ – $H_2O$  (1:1) to afford four subfractions (C1–C4). Subfractions C3 was further chromatographed by RP-HPLC using  $CH_3CN$ – $H_2O$  (1:3) containing 0.1% trifluoroacetic acid (TFA) to afford compounds **5** (0.5 mg) and **8** (1.2 mg). Fraction 20 eluted with 100% acetone was further purified over a RP-18 column using  $MeOH$ – $H_2O$  (1:2) to yield seven subfractions (D1–D7). Subfraction D5 was purified by RP-HPLC ( $MeOH$ – $H_2O$ , 1:1.2) to afford compound **7** (4.4 mg).

Capsisteroid G (**1**): colorless oil;  $[\alpha]_D^{25}$  –5 ( $c$  1.1,  $MeOH$ ); IR (neat)  $\nu_{max}$  3420, 2941, 1690, 1372, 1115, 1057, and 753  $cm^{-1}$ ;  $^1H$  and  $^{13}C$  NMR data, see Tables 1 and 2; ESIMS  $m/z$  515  $[M + Na]^+$ ; HRESIMS  $m/z$  515.2979  $[M + Na]^+$  (calcd for  $C_{28}H_{44}O_7Na$ , 515.2979). The selective  $^1H$  NMR ( $CD_3OD$ ) data of 26*R* isomer:  $\delta$  1.00 (3H, d,  $J = 6.8$  Hz,  $H_{3-21}$ ), 1.25 (3H, s,  $H_{3-27}$ ), 1.48 (3H, s,  $H_{3-28}$ ), 4.31 (1H, br d,  $J = 12.0$  Hz,  $H_{-22}$ ), 4.82 (1H, br s,  $H_{-26}$ ). The selective  $^{13}C$  NMR ( $CD_3OD$ ) data of 26*R* isomer:  $\delta$  10.1 ( $CH_3$ , C-21), 22.0 ( $CH_3$ , C-27), 24.4 ( $CH_3$ , C-28), 44.4 ( $CH_2$ , C-23), 70.5 ( $CH$ , C-22), 99.3 ( $CH$ , C-26).

Capsisteroid H (**2**): colorless oil;  $[\alpha]_D^{25}$  –25 ( $c$  0.3,  $MeOH$ ); IR (neat)  $\nu_{max}$  3395, 2939, 1702, 1375, 1114, 1051, and 752  $cm^{-1}$ ;  $^1H$  and  $^{13}C$  NMR data, see Tables 1 and 2; ESIMS  $m/z$  515  $[M + Na]^+$ ; HRESIMS  $m/z$  515.2980  $[M + Na]^+$  (calcd for  $C_{28}H_{44}O_7Na$ , 515.2979).

Capsisteroid I (**3**): colorless oil;  $[\alpha]_D^{25}$  –7 ( $c$  0.3,  $MeOH$ ); IR (neat)  $\nu_{max}$  3336, 2926, 2851, 1722, 1456, 1307, 1132, and 974  $cm^{-1}$ ;  $^1H$  and  $^{13}C$  NMR data, see Tables 1 and 2; ESIMS  $m/z$  511  $[M + Na]^+$ ; HRESIMS  $m/z$  511.2665  $[M + Na]^+$  (calcd for  $C_{28}H_{40}O_7Na$ , 511.2666).

Capsisteroid J (**4**): white powder;  $[\alpha]_D^{25}$  –24 ( $c$  0.2,  $MeOH$ ); IR (neat)  $\nu_{max}$  3396, 2929, 2871, 1372, 1262, 1033, and 669  $cm^{-1}$ ;  $^1H$  and  $^{13}C$  NMR data, see Tables 1 and 2; ESIMS  $m/z$  501  $[M + Na]^+$ ; HRESIMS  $m/z$  501.3189  $[M + Na]^+$  (calcd for  $C_{28}H_{46}O_6Na$ , 501.3187).

Capsisteroid K (**5**): Colorless oil;  $[\alpha]_D^{25}$  –15 ( $c$  0.1,  $MeOH$ ); IR (neat)  $\nu_{max}$  3384, 2925, 2870, 1724, 1670, 1375, 1040, and 756  $cm^{-1}$ ;  $^1H$  and  $^{13}C$  NMR data, see Table 3; ESIMS  $m/z$  745  $[M + Na]^+$ ; HRESIMS  $m/z$  745.3772  $[M + Na]^+$  (calcd for  $C_{38}H_{58}O_{13}Na$ , 745.3770).

**Cytotoxicity Assay.** Cancer cell lines were purchased from the American Type Culture Collection (ATCC; Manassas, VA, USA). Compounds **1–3**, **5**, and **6** were subjected for cytotoxicity testing by using the Alamar Blue assay as previous reported.<sup>40,41</sup>

**Preparation of Human Neutrophils.** The experiment was approved by the Institutional Review Board at Chang Gung Memorial Hospital. According the prior method,<sup>42,43</sup> neutrophils were isolated from the blood samples obtained from healthy human donors aged 20–30 years old. The purified neutrophils were pelleted and then resuspended in a calcium ( $Ca^{2+}$ )-free Hank's balanced salt solution buffer at pH 7.4 and were maintained at 4  $^{\circ}C$ .



**Measurement of Superoxide Anion Generation and Elastase Release.** The experiment for measuring superoxide anion generation and elastase release were manipulated according to previously reported method.<sup>42,43</sup> Genistein was included as a positive control for inhibition of superoxide anion generation (IC<sub>50</sub> 1.5 ± 0.5 μM) and elastase release (IC<sub>50</sub> 37.5 ± 4.3 μM).

#### Acknowledgement

We gratefully appreciate the financial support awarded to J.-H. S., including grants from the National Science Council of Taiwan (NSC-100-2320-B-110-001-MY2), and NSYSU-KMU JOINT RESEARCH PROJECT (NSYSUKMU 02C030117) from National Sun Yat-sen University and Kaohsiung Medical University.

#### Supporting Information

<sup>1</sup>H, <sup>13</sup>C, and 2D NMR spectra of compounds 1–5. <sup>1</sup>H and <sup>13</sup>C NMR spectroscopic data of compounds 4 and 7. This material is available on the web at <http://dx.doi.org/10.1246/bcsjxxxx>.

#### References

- V. E. Nicotra, N. S. Ramacciotti, R. R. Gil, J. C. Oberti, G. E. Feresin, C. A. Guerrero, R. F. Baggio, M. T. Garland, G. Burton, *J. Nat. Prod.* **2006**, 69, 783.
- E. J. Kennelly, C. Gerhauser, L. L. Song, J. G. Graham, C. W. W. Beecher, J. M. Pezzuto, A. D. Kinghorn, *J. Agric. Food Chem.* **1997**, 45, 3771.
- X.-H. Zhu, M. Takagi, T. Ikeda, K. Midzuki, T. Nohara, *Phytochemistry* **2001**, 56, 741.
- X.-H. Zhu, J. Ando, M. Takagi, T. Ikeda, A. Yoshimitsu, T. Nohara, *Chem. Pharm. Bull.* **2001**, 49, 1440.
- X.-H. Zhu, J. Ando, M. Takagi, T. Ikeda, T. Nohara, *Chem. Pharm. Bull.* **2001**, 49, 161.
- R. Niero, I. T. Da Silva, G. C. Tonial, B. D. Santos Camacho, E. Gacs-Baitz, G. Delle Monache, F. Delle Monache, *Nat. Prod. Res.* **2006**, 20, 1164.
- B.-Y. Yang, R. Guo, T. Li, J.-J. Wu, J. Zhang, Y. Liu, Q.-H. Wang, H.-X. Kuang, *Steroids* **2014**, 87, 26.
- S.-T. Fang, J.-K. Liu, B. Li, *Steroids* **2012**, 77, 36.
- H. Zhang, C.-M. Cao, R. J. Gallagher, V. W. Day, G. Montenegro, B. N. Timmermann, *Phytochemist* **2014**, 98, 232.
- B.-N. Su, R. Misico, E. J. Park, B. D. Santarsiero, A. D. Mesecar, H. H. S. Fong, J. M. Pezzuto, A. D. Kinghorn, *Tetrahedron* **2002**, 58, 3453.
- B. Jayaprakasam, M. G. Nair, *Tetrahedron* **2003**, 59, 841.
- L. Ma, M. Ali, M. Arfan, L.-G. Lou, L.-H. Hu, *Tetrahedron Lett.* **2007**, 48, 449.
- A. M. Cirigliano, A. S. Veleiro, R. I. Misico, M. C. Tettamanzi, J. C. Oberti, G. Burton, *J. Nat. Prod.* **2007**, 70, 1644.
- I.-ul Haq, U. J. Youn, X. Chai, E.-J. Park, T. P. Kondratyuk, C. J. Simmons, R. P. Borris, B. Mirza, J. M. Pezzuto, L.-C. Chang, *J. Nat. Prod.* **2013**, 76, 22.
- M. Kuroyanagi, M. Murata, T. Nakane, O. Shiota, S. Sekita, H. Fuchino, Z. K. Shinwari, *Chem. Pharm. Bull.* **2012**, 60, 892.
- H. Zhang, H. Motiwala, A. Samadi, V. Day, J. Aubé, M. Cohen, K. Kindscher, R. Gollapudi, B. Timmermann, *Chem. Pharm. Bull.* **2012**, 60, 1234.
- C.-M. Cao, H. Zhang, R. J. Gallagher, V. W. Day, K. Kindscher, P. Grogan, M. S. Cohen, B. N. Timmermann, *J. Nat. Prod.* **2014**, 77, 631.
- H. Zhang, J. Bazzill, R. J. Gallagher, C. Subramanian, P. T. Grogan, V. W. Day, K. Kindscher, M. S. Cohen, B. N. Timmermann, *J. Nat. Prod.* **2013**, 76, 445.
- T. Ikeda, J. Ando, A. Miyazono, X.-H. Zhu, H. Tsumagari, T. Nohara, K. Yokomizo, M. Uyeda, *Biol. Pharm. Bull.* **2000**, 23, 363.
- M. B. Ksebati, F. J. Schmitz, *J. Org. Chem.* **1988**, 53, 3926.
- C.-Y. Hung, C.-C. Liaw, B.-W. Chen, P.-C. Chen, J.-H. Su, P.-J. Sung, C.-F. Dai, M. Y. Chiang, J.-H. Sheu, *J. Nat. Prod.* **2013**, 76, 1902.
- C.-Y. Hung, A. F. Ahmed, J.-H. Su, P.-J. Sung, T.-L. Hwang, P.-L. Chiang, C.-F. Dai, C.-C. Liaw, J.-H. Sheu, *Bioorg. Med. Chem. Lett.* **2017**, 27, 3267.
- C.-H. Chao, K.-J. Chou, Z.-H. Wen, G.-H. Wang, Y.-C. Wu, C.-F. Dai, J.-H. Sheu, *J. Nat. Prod.* **2011**, 74, 1132.
- Y.-H. Pan, X.-C. Wang, X.-M. Hu, *J. Nat. Prod.* **2007**, 70, 1127.
- L. Ma, X.-W. Gan, Q.-P. He, H.-Y. Bai, M. Arfan, F.-C. Lou, L.-H. Hu, *Helv. Chim. Acta.* **2007**, 90, 1406.
- J. A. Bravo B., M. Sauvain, A. Gimenez T., E. Balanza, L. Serani, O. Laprevote, G. Massiot, C. Lavaud, *J. Nat. Prod.* **2001**, 64, 720.
- B.-N. Su, E. J. Park, D. Nikolic, B. D. Santarsiero, A. D. Mesecar, J. S. Vigo, J. G. Graham, F. Cabieses, R. B. van Breemen, H. H. S. Fong, N. R. Farnsworth, J. M. Pezzuto, A. D. Kinghorn, *J. Org. Chem.* **2003**, 68, 2350.
- R. Saijo, C. Fuke, K. Murakami, T. Nohara, T. Tomimatsu, *Phytochemistry* **1983**, 22, 733.
- B.-W. Chen, Y.-Y. Chen, Y.-C. Lin, C.-Y. Hung, T.-L. Hwang, J.-H. Sheu, *RSC Adv.* **2015**, 5, 88841.
- A. S. Veleiro, G. B. Burton, E. G. Gros, *Phytochemistry* **1985**, 24, 1799.
- J.-H. Sheu, P.-J. Sung, *J. Chin. Chem. Soc.*, **1991**, 38, 501.
- V. U. Ahmad, A. H. Memon, M. S. Ali, S. P. Perveen, M. Shameel, *Phytochemistry* **1996**, 42, 1141.
- T. Shen, L. Zhang, Y.-Y. Wang, P.-H. Fan, X.-N. Wang, Z.-M. Lin, H.-X. Lou, *Bio. & Med. Chem. Lett.* **2012**, 22, 4801.
- Y. Yamano, M. Ito, *Chem. Pharm. Bull.* **2005**, 53 (5), 541.
- K. Matsunami, H. Otsuka, Y. Takeda, *Chem. Pharm. Bull.* **2010**, 58, 438.
- J. Sun, H.-X. Huo, J. Zhang, Z. Huang, J. Zeng, Q. Zeng, Y.-F. Zhao, J. Li, P.-F. Tu, *Biochem. Syst. Ecol.* **2015**, 58, 265.
- R. R. King, L. A. Calhoun, *Phytochemistry* **2005**, 66, 2468.
- W. S. Garcez, D. Martins, F. R. Garcez, M. R. Marques, A. A. Pereira, L. A. Oliveira, J. N. Rondon, A. D. Peruca, *J. Agric. Food Chem.* **2000**, 48, 3662.
- B. S. Siddiqui, M. N. Kardar, S. T. Ali, S. Khan, *Helvetica Chimica Acta* **2003**, 86, 2164.
- G. R. Nakayama, M. C. Caton, M. P. Nova, Z. Parandoosh, *J. Immunol. Methods* **1997**, 204, 205.
- J. O'Brien, I. Wilson, T. Orton, F. Pognan, *Eur. J. Biochem.* **2000**, 267, 5421.
- S.-C. Yang, P.-J. Chung, C.-M. Ho, C.-Y. Kuo, M.-F. Hung, Y.-T. Huang, W.-Y. Chang, Y.-W. Chang, K.-H. Chan, T.-L. Hwang, *J. Immunol.* **2013**, 190, 6511.
- H.-P. Yu, P.-W. Hsieh, Y.-J. Chang, P.-J. Chung, L.-M. Kuo, T.-L. Hwang, *Free Radic. Biol. Med.* **2011**, 50, 1737.

## Research Article

# Red Raspberry Extract Protects the Skin against UVB-Induced Damage with Antioxidative and Anti-inflammatory Properties

Pei-Wen Wang,<sup>1</sup> Yu-Chen Cheng,<sup>2</sup> Yu-Chiang Hung<sup>ID</sup>,<sup>2</sup> Chih-Hung Lee<sup>ID</sup>,<sup>3</sup> Jia-You Fang,<sup>4</sup> Wen-Tai Li,<sup>5</sup> Yun-Ru Wu,<sup>6</sup> and Tai-Long Pan<sup>ID</sup><sup>6,7,8,9</sup>

<sup>1</sup>Department of Medical Research, China Medical University Hospital, China Medical University, Taichung, Taiwan

<sup>2</sup>Department of Chinese Medicine, College of Medicine, Kaohsiung Chang Gung Memorial Hospital and Chang Gung University, Kaohsiung, Taiwan

<sup>3</sup>Department of Dermatology, College of Medicine, Kaohsiung Chang Gung Memorial Hospital and Chang Gung University, Kaohsiung, Taiwan

<sup>4</sup>Pharmaceutics Laboratory, Graduate Institute of Natural Products, Chang Gung University, Taoyuan, Taiwan

<sup>5</sup>National Research Institute of Chinese Medicine, Ministry of Health and Welfare, Taipei, Taiwan

<sup>6</sup>School of Traditional Chinese Medicine, Chang Gung University, Taoyuan, Taiwan

<sup>7</sup>Liver Research Center, Chang Gung Memorial Hospital, Taoyuan, Taiwan

<sup>8</sup>Chinese Herbal Medicine Research Team, Healthy Aging Research Center, Chang Gung University, Taoyuan, Taiwan

<sup>9</sup>Research Center for Chinese Herbal Medicine and Research Center for Food and Cosmetic Safety, College of Human Ecology, Chang Gung University of Science and Technology, Taoyuan, Taiwan

Correspondence should be addressed to Tai-Long Pan; [pan@mail.cgu.edu.tw](mailto:pan@mail.cgu.edu.tw)

Received 21 July 2018; Revised 29 September 2018; Accepted 21 October 2018; Published 6 January 2019

Academic Editor: Francisco J. Romero

Copyright © 2019 Pei-Wen Wang et al. This is an open access article distributed under the Creative Commons Attribution License, which permits unrestricted use, distribution, and reproduction in any medium, provided the original work is properly cited.

Extensive exposure to UVB (280–320 nm) is the major risk responsible for various skin injuries. Numerous reports have shown that natural products could demonstrate photochemopreventive efficacy against UVB damage. We investigated the preventive effects and associated molecular mechanisms of red raspberry extract upon UVB-caused damage in human epidermal keratinocytes and a nude mouse model. The protein profiles and immunohistological study on a nude mouse skin indicated that red raspberry extract could prevent UVB-caused cell death and protect the skin against UVB-exposed injury manifested by wrinkling, scaling, tanning, and water loss as well as epidermal thickening. In addition, red raspberry extract application effectively abolished oxidative damage in DNA and attenuated the carbonylation level of proteins, which attributed to the activation of SOD, Nrf2 and its target genes, and HO-1. Red raspberry extract also altered the cells' apoptotic signaling pathways including caspase-3 as well as the inflammatory cascade such as c-jun and attenuated UVB-induced activation of NF- $\kappa$ B and COX-2. Red raspberry extract could alleviate direct photodamage to the skin caused by UVB exposure through the ROS scavenger and protection against inflammatory responses, which may allow the development of novel strategies in protecting the skin subjected to UVB radiation.

## 1. Introduction

Photon energy, especially ultraviolet B (UVB) radiation, induces many deleterious effects including deoxyribonucleic acid (DNA) and protein damage, oxidative stress, inflammation, and carcinogenesis. Previous studies have suggested that these events are mainly caused by reactive oxygen species (ROS), which would eventually result in various skin diseases

[1–3]. Application of antioxidants should therefore be the effective strategy for photoprotection of the skin [4–6].

Compelling evidence showed that berry fruits possess antioxidative, anti-inflammatory, and anticarcinogenic properties because berries contain large amounts of phytochemicals, including flavonoids, tannins, stilbenoids, phenolic acids, lignans, triterpenes, and sterols [7]. The dietary consumption of whole fruits could reduce ROS, which have

been implicated in UVB-caused problems [8–10]. The traditional Chinese medicine book “Essential of Materia Medica” has described that raspberry could exhibit the effect of moistening the skin and reducing the redness as well as swelling of the skin. As expected, several bioactive constituents, including polyphenolic compounds, antioxidants, vitamins, and minerals, have been extracted from red raspberries (*Rubus idaeus*) [11–13], while the effects and molecular mechanisms of red raspberry on skin photodamage have not been reported. Herein, UVB-exposed hairless mice and keratinocyte models were applied to investigate the protective effect of ethanol extract of red raspberry (RBE) on a photodamaged skin.

ROS generation due to UVB radiation would disturb the normal redox balance and lead to highly oxidative stress, which subsequently promotes the carbonylation of specific groups of proteins and results in physiological dysfunction [14–16]. When carbonyl groups form, they can react with 2,4-dinitrophenylhydrazine (DNP) and are detected by two-dimensional electrophoresis (2-DE) oxyblotting; therefore, we utilized redox proteomics to prove our hypothesis concerning the anti-UVB effect of red raspberry.

UVB could also elicit acute inflammatory skin problems such as erythema and cell apoptosis. UVB-caused promotion of proinflammatory enzymes and the subsequent activation of an associated signaling pathway such as cyclooxygenase-2 (COX-2) would in turn trigger the production of specific inflammatory mediators including prostaglandins (PGs) and various cytokines. COX-2 cascades mediate the inflammatory process and cause pain, edema, cell growth, and tumor progression [17, 18]. It has been implied that inflammation plays a pivotal role in the pathogenesis of skin diseases under UVB exposure [19].

We performed an immunohistological investigation and established the redox proteome profiles on a nude mouse skin to verify the hypothesis that RBE could attenuate the oxidative stress caused by UVB and protect the skin from photoinjury. In addition, the associated molecular mechanisms would provide the clinical and commercial utility of herbal intervention in UVB prevention on the skin.

## 2. Materials and Methods

**2.1. Preparation of Red Raspberry Ethanolic Extract.** Commercial dry powder of raspberry was purchased and authenticated by a traditional Chinese medicine dispensary (local pharmaceutical company, Taiwan). The ethanol-extracted solution was then concentrated to give brown syrup. The filtered and sterile extract was stored at  $-80^{\circ}\text{C}$  for use in all subsequent experiments. The concentration used in each experiment was calculated based upon the dry weight of the extract which was resuspended in normal saline.

**2.2. Cell Viability.** HaCaT cells ( $5 \times 10^4$ ) were seeded in 24-well plates for 24 hours (h). UVB radiation (0 or  $100 \text{ mJ}/\text{cm}^2$ ) was exposed to the cells after treating with various concentrations (0, 62.5, 125, 250, 500, and  $1000 \mu\text{g}/\text{mL}$ ) of RBE and incubated for 48 h. Isopropanol solution mixed with tetrazolium salt was then added to the wells and

incubated for additional 4 h at  $37^{\circ}\text{C}$  [20]. The optical density of the dissolved material was measured spectrophotometrically at 570 nm, and assays were performed in triplicate.

**2.3. Western Blot Analysis.** HaCaT cells were pretreated with  $200 \mu\text{g}/\text{mL}$  RBE and exposed to  $100 \text{ mJ}/\text{cm}^2$  UVB radiation. The protein derived from the treatment was isolated using 1x cell lysis buffer (Cell Signaling), and the concentration was measured using the Bradford Protein Assay Kit (AMRESCO). Protein lysates were evaluated with Western blot analyses as previously described [20, 21]. Western blot analysis was performed using the specific antibodies: PARP, caspase-3 (DAKO), catalase (Bioss), Cu/ZnSOD (ABBIO-TEC), GAPDH, MnSOD, Nrf2, HO-1,  $\beta$ -actin, phos-p38, p38, c-Jun, NF $\kappa$ Bp65, and NF $\kappa$ Bp50 (Santa Cruz). The levels of GAPDH or  $\beta$ -actin were used as the internal loading control. Densitometric analyses of scanned images were performed using GeneTools software (Syngene, UK).

**2.4. siRNA and p-38 Kinase Inhibitor Administration.** HaCaT cells were plated onto 24-well plates ( $2 \times 10^4$  cells/well), maintained in antibiotic-free medium for 6 h, and transfected with a mixture containing Opti-MEM,  $8 \mu\text{L}/\text{well}$  Lipofectamine 2000 (Invitrogen, San Diego, CA) and  $0.5 \mu\text{g}/\text{well}$  a mixture of three Nrf2 siRNAs. At 24 h post transfection, cells were exposed to UVB and treated with  $200 \mu\text{g}/\text{mL}$  RBE dissolved in medium for another 24 h. Then, the cells were harvested for Western blot analyses [22]. HaCaT cells were preincubated with or without SB203580 for 1 h, irradiated with UVB, and then treated with or without RBE for 6 h. The cells were harvested for Western blot analyses [20].

**2.5. Assessment for Generation of Intracellular ROS.** HaCaT cells were seeded in a slide chamber, grown to 60% confluence, and cultured in DMEM medium overnight. Cells were then incubated with or without RBE for 6 h and irradiated by  $100 \text{ mJ}/\text{cm}^2$  UVB [23]. Carboxy-H2DCFDA ( $2 \mu\text{M}$ , dissolved in PBS) was added to the wells and incubated for 30 min at  $37^{\circ}\text{C}$ . To terminate the reaction, the cells were washed with PBS twice. Next,  $500 \mu\text{L}$  culture medium was added to each well and incubated for 20 min at  $37^{\circ}\text{C}$ . The cells were observed and photographed using a fluorescent microscope (Olympus BX51) with a DP72 PhotoImage system [21].

**2.6. Constituents Analysis with HPLC.** A high-performance liquid chromatographic (Shimadzu SCL-10A VP) coupled with an SPD-M10A VP diode array detector was performed for the qualitative determination of compounds in the RBE [24].

**2.7. Animals.** Female nude mice (ICR-Foxn/nu strain) were purchased from Taiwan's National Laboratory Animal Center (Taipei). The laboratory diet and water were given ad libitum before experiments. The mice were treated according to the Ethical Guidelines of the Animal Center, and the experimental protocol was reviewed and approved by the Institutional Animal Care and Use Committee of Kaohsiung Chang Gung Memorial Hospital (2017081401). The mice were randomly divided into three groups (CTL,

–/UVB, and RBE/UVB) of five mice each. 750  $\mu\text{g/mL}$  RBE was applied on the dorsal region of the nude mice in the RBE/UVB group. The daily standard erythema dose of UVB for the human skin is more than 25  $\text{mJ/cm}^2$ . A Bio-Sun system illuminator (Vilber Lourmat, Marne-la-Vallée, France) was applied to generate UVB radiation which was utilized to irradiate the peak wavelengths of 312 nm. The distance between the nude mice and the lamps was 10 cm, and the spectral irradiance was 30  $\text{mJ/cm}^2$  for UVB in the dorsal region of the mouse once a day for five days. Hence, the total UVB dose received by each mouse during the irradiation course was 150  $\text{mJ/cm}^2$ . TEWL was calculated by a Tewameter® (TM300, Courage and Khazaka, Köln, Germany) to determine the water evaporation rate ( $\text{g/m}^2/\text{h}$ ) [16]. A spectrophotometer (CD100, Yokogawa, Tokyo, Japan) was used to quantify skin erythema [25, 26].

**2.8. Histologic Examination of the Skin.** The skin specimens were then fixed in buffered formaldehyde solution and sliced into 5  $\mu\text{m}$  sections which were stained with H&E for a histological assessment. Immunohistochemistry staining with 8-hydroxydeoxyguanosine (8-OHdG) and COX-2 (1:100 dilution by PBS; Santa Cruz) was treated as described in a previous study [16, 27]. The histological changes were evaluated by using optical microscopy (Olympus BX51, Tokyo, Japan) in nonconsecutive, randomly chosen histological fields. The digital photomicrographs were then processed with DP-72. Image-Pro® plus 4.5 (Media Cybernetics, Bethesda, MD) image analysis software was used to quantify image signals according to a modified version of a protocol described by McGinley and Thompson [28].

**2.9. Two-Dimensional Electrophoresis (2-DE).** The smashed skin powder was immersed with extraction buffer (7 M urea, 2 M thiourea, 4% CHAPS, 65 mM DTT, and 1 mM PMSF) to homogenize and centrifuge the sample at 10,000  $g$  for 20 min at 4°C (KUBOTA 3500, Japan). The concentration of the supernatant was measured by using the Bradford Protein Assay Kit. Protein (200  $\mu\text{g}$ ) was solubilized in IPG buffer containing 7 M urea, 2 M thiourea, 4% CHAPS, 65 mM DTT, and 1% IPG buffer to a volume of 350  $\mu\text{L}$ . The samples were then separated by the Immobiline Drystrip (pH 4–7, 18 cm IPG strip, GE Healthcare) on the IPGphor III System for the first dimension. The 2-DE was carried out on 10% acrylamide gels (PROTEAN II XL, Bio-Rad, Hercules, CA, USA) at 30 mA/gel. All gels were visualized by silver staining and then scanned using an Imagescanner (GE Healthcare) [22, 29]. All experiments were repeated three times to confirm the reproducibility.

**2.10. 2D-Oxyblot.** Following IEF, IPG strips were placed in 15 mL test tubes and incubated in 2 N HCl with DNPH (10 mM) at 25°C for 20 min. After the incubation, samples were washed with 2 M Tris-Base/30% glycerol for 15 min. The protein was separated according to molecular weight as described above. 2-DE gels were transferred to a PVDF membrane which was incubated overnight at 4°C with the primary antibody solution consisting of a 1:16,000 dilution of the primary antibody (Molecular Probes) in TBST buffer containing

5% milk. The blots were washed and incubated with goat anti-rabbit IgG-conjugated HRP for 2 h. Enhanced chemiluminescence (Immobilon Western Chemiluminescent AP substrate, Millipore) was used for detection [29].

**2.11. In-Gel Digestion of Proteins and Mass Spectrometric (MS) Analysis.** Spots of interest were excised and in-gel digested with trypsin according to previously described procedures [22]. Monoisotopic peptide masses were assigned and used for database searches with the MASCOT search engine (<http://www.matrixscience.com>) (Matrix Science, London). Search parameters were set as follows: a maximum allowed peptide mass error of 50 ppm and consideration of one incomplete cleavage per peptide.

**2.12. Statistical Analysis.** All values are presented as the mean  $\pm$  standard deviation (SD). The statistical analysis of the mean values was carried out with the ANOVA using SPSS software [SPSS Inc., Chicago, IL, USA].

### 3. Results

**3.1. Cell Viability after UVB Exposure under Pretreatment of Different Concentrations of RBE.** To evaluate the pharmaceutical effects of red raspberry extract *in vitro*, cell viability was determined by MTT assays. Different concentrations of RBE were applied to the HaCaT cells that were then exposed to 0 or 100  $\text{mJ/cm}^2$  UVB radiation. As illustrated in Figure 1(a), the results showed that RBE application could effectively attenuate the cell death caused by the UVB exposure in a dose-dependent manner. The  $\text{EC}_{50}$  of the RBE was 150  $\mu\text{g/mL}$ . Next, we determined the signaling marker proteins, caspase-3, and PARP, with Western blot analysis to further validate the effect of RBE on cell apoptosis. As indicated in Figure 1(b), active forms of caspase-3 (17 kDa) and cleaved PARP (89 kDa) were significantly increased under exposure to 100  $\text{mJ/cm}^2$  UVB compared to the control whereas administration of RBE could effectively attenuate UVB-induced cell apoptosis, which was accompanied by more moderate cleavage of caspase-3 as well as PARP. Accordingly, UVB irradiation might induce oxidative stress that results in skin cell apoptosis. Dichlorofluorescein (DCF) fluorescent intensity showed that UVB treatment obviously promoted intracellular ROS production compared with the control group within 6 h whereas RBE application alleviated the DCF signal (Figure 1(c)).

**3.2. Identification of Pure Compounds from RBE.** The ethanol-extracted solution was then concentrated to generate brown syrup. The filtered, sterile extract was applied in the subsequent experiments. A high-performance liquid chromatographic method coupled with ultraviolet (UV) was conducted for qualitative determination of the compounds in the RBE. The main compounds contained in RBE were identified by comparing the retention time with the reference standard as follows: cyanidin, ellagic acid, pelargonidin-3-sophoroside, methylquercetin-pentose conjugate, and cyanidin-3-rutinoside (Figure 2).



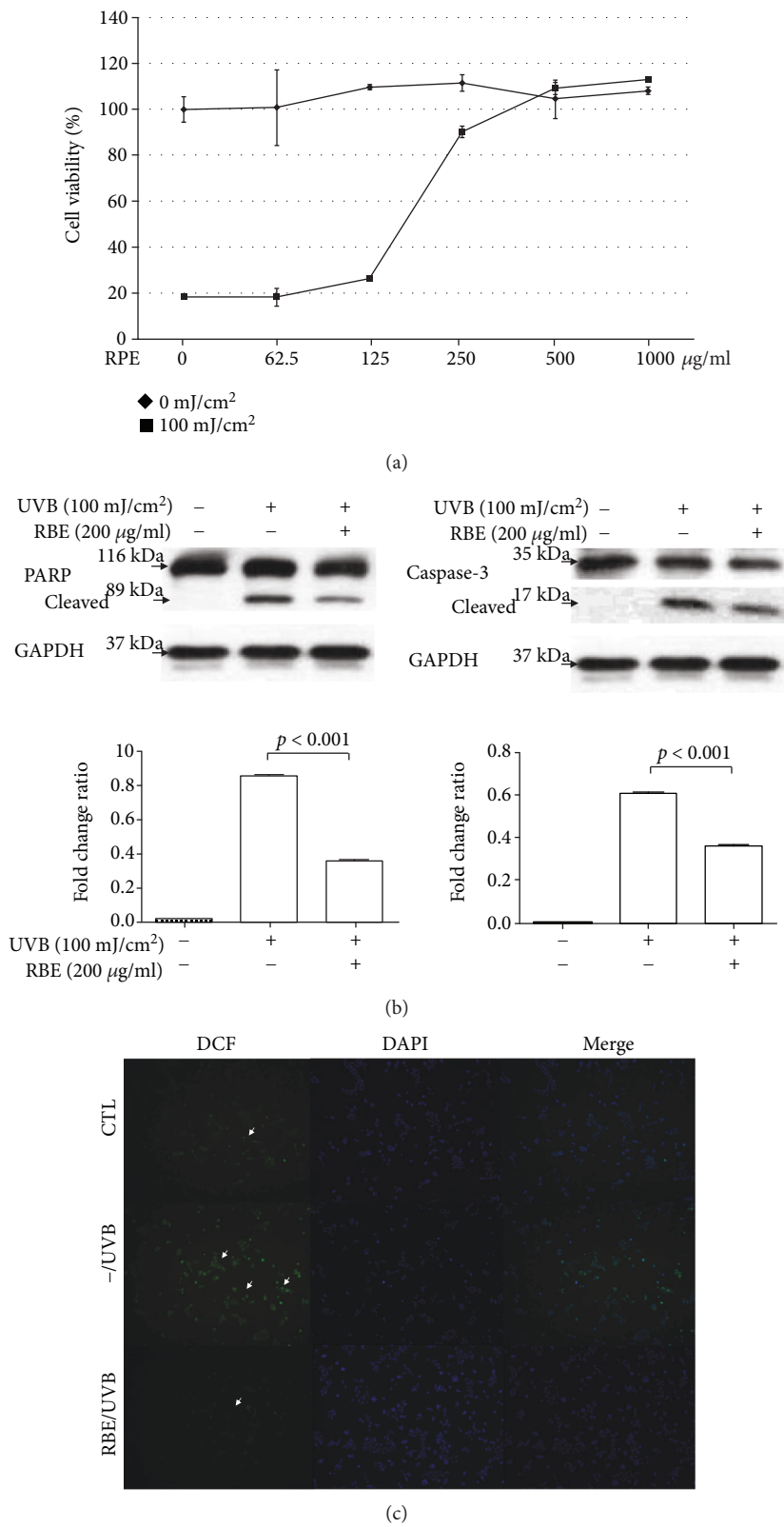


FIGURE 1: (a) Effects of red raspberry extract on keratinocyte viability with (square) or without (diamond) 100 mJ/cm<sup>2</sup> UVB exposure as measured by the MTT assays. The cells were applied with different concentrations of red raspberry extract ( $x$ -axis). Data were the mean  $\pm$  SD of three independent experiments. (b) PARP and caspase-3 and their cleaved forms were detected by Western blot analysis. GAPDH was used as an internal control. The quantified results were presented by the bar chart. The caspase-3 images were cropped from different parts and exposures of the same gel. (c) Cells were incubated with or without RBE and irradiated by 100 mJ/cm<sup>2</sup> UVB. The DCF fluorescence was observed under a fluorescence microscope and indicated by arrows.

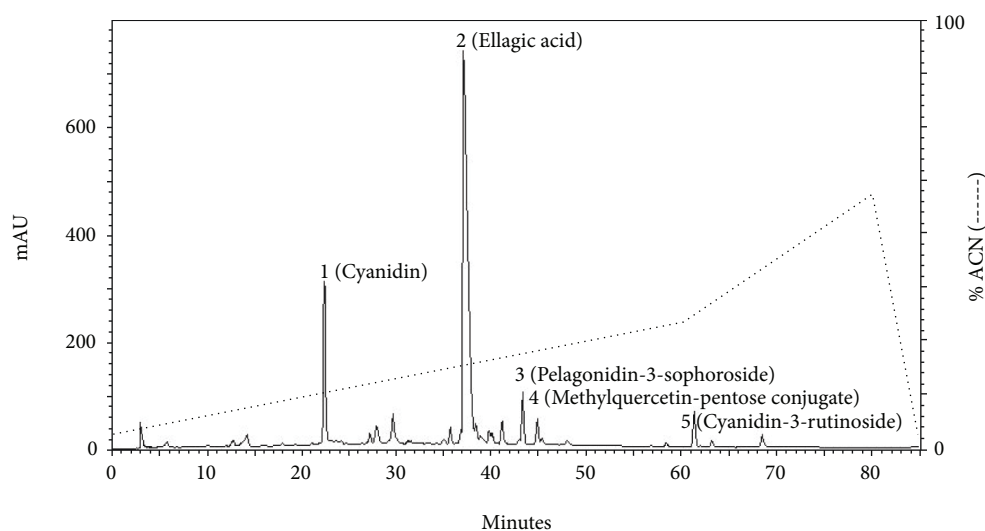


FIGURE 2: HPLC – UV $_{\lambda=365\text{ nm}}$  chromatograms of ethanol extract produced from red raspberry. The quantification of samples was preformed using a HP1100 series HPLC system comprising a gradient pump, and the column used the Agilent Hypersil BDS-C<sub>18</sub>, maintained at ambient room temperatures. 1: cyanidin; 2: ellagic acid; 3: pelargonidin-3-sophorose; 4: methylquercetin-pentose conjugate; 5: cyanidin-3-rutinoside.

**3.3. Effects of RBE upon UVB-Induced Skin Damage.** UVB radiation (150 mJ/cm<sup>2</sup>) was applied to the back of the mice once a day for 5 days. Prior to UVB exposure, the experimental animals were pretreated with or without 750  $\mu$ g/mL RBE (Figure 3(a)). After a 5-day irradiation course, the control skin exhibited a flat surface and showed no remarkable wrinkle formation whereas significant wrinkling and scaling were observed in the mouse directly exposed to UVB (Figure 3(b)). As expected, administration of RBE before UVB exposure could effectively prevent the skin injury from the UVB irradiation, which was characterized as mild wrinkling and a low level of scaling as well as dryness on the skin surface (Figure 3(b)). Transepidermal water loss (TEWL) was measured to determine the skin barrier function and the baseline TEWL value of the nude mouse skin, which was about 6–8 g/m<sup>2</sup>/h [30]. As indicated in Figure 3(c), UVB application on day 5 resulted in a 150% enhancement of TEWL compared to the control baseline. Pretreatment of RBE caused a much milder TEWL increment ( $p = 0.0276$ ). UVB irradiation also led to a significant promotion in skin erythema and edema compared to the control. Again, RBE application could significantly alleviate UVB-caused erythema in the skin ( $p = 0.0024$ ; Figure 3(d)). On the other hand, UVB irradiation significantly stimulated cell proliferation of epidermal keratinocytes and the epidermal thickness of the control by 2.25-fold. Utilization of RBE could protect the skin from the abnormal phenomenon (Figure 3(e)). As expected, global protein profile also showed the UVB-induced overexpression of keratins K14 and K17, which may enhance hyperproliferation of keratinocytes (Supplement Figure 1). These findings imply that pretreatment of RBE could minimize various forms of skin damage caused by UVB irradiation.

**3.4. Antioxidant Ability of RBE in UVB-Irradiated Skin.** As far as we know, UVB exposure induces the production of

oxidative stress, which further attacks DNA and results in 8-OHdG modification. As shown in Figure 4(a), DNA oxidation manifested by the level of 8-OHdG was elicited in the UVB-irradiated skin with respect to that in the control while RBE treatment markedly attenuated the formation of 8-OHdG in the presence of UVB irradiation. Moreover, protein carbonylation is also a critical parameter of oxidative stress. Figure 4(b) shows that, in the case of the control, protein carbonylation was significantly induced in a UVB-exposed skin. Pretreatment of RBE could effectively prevent the protein oxidation under UVB exposure. The view of oxyblots obtained from the UVB group demonstrates that the extent of oxidation in albumin was dramatically upregulated and there was an obviously decreasing tendency with respect to the protein oxidation in the RBE/UVB group. These results suggest that UVB irradiation directly causes DNA damage and protein oxidation in the skin without the protection of RBE. The equal amount of  $\beta$ -actin protein demonstrates that the loading protein volume for all groups is the same. MS analysis was used to unambiguously identify albumin as presented in Figure 4(c).

**3.5. Signal Transduction Pathways Associated with the Anti-UVB Property of RBE.** Since UVB stimulates the generation of an excessive level of ROS, we then surveyed the content of oxidative stress markers, including catalase and superoxide dismutase (SOD) in different treatments. Decreased catalase and SOD levels were observed in the UVB-applied subjects compared with the control group, while treatments with RBE could enhance the liver catalase and SOD content, protecting the cell against UVB injury. To further reveal the molecular mechanism related to modulation of the antioxidant enzymes, we assessed the critical transcription factor Nrf-2 as a critical contributor to the activation of the antioxidant system. Again, UVB exposure remarkably inhibited Nrf-2 expression with respect to the

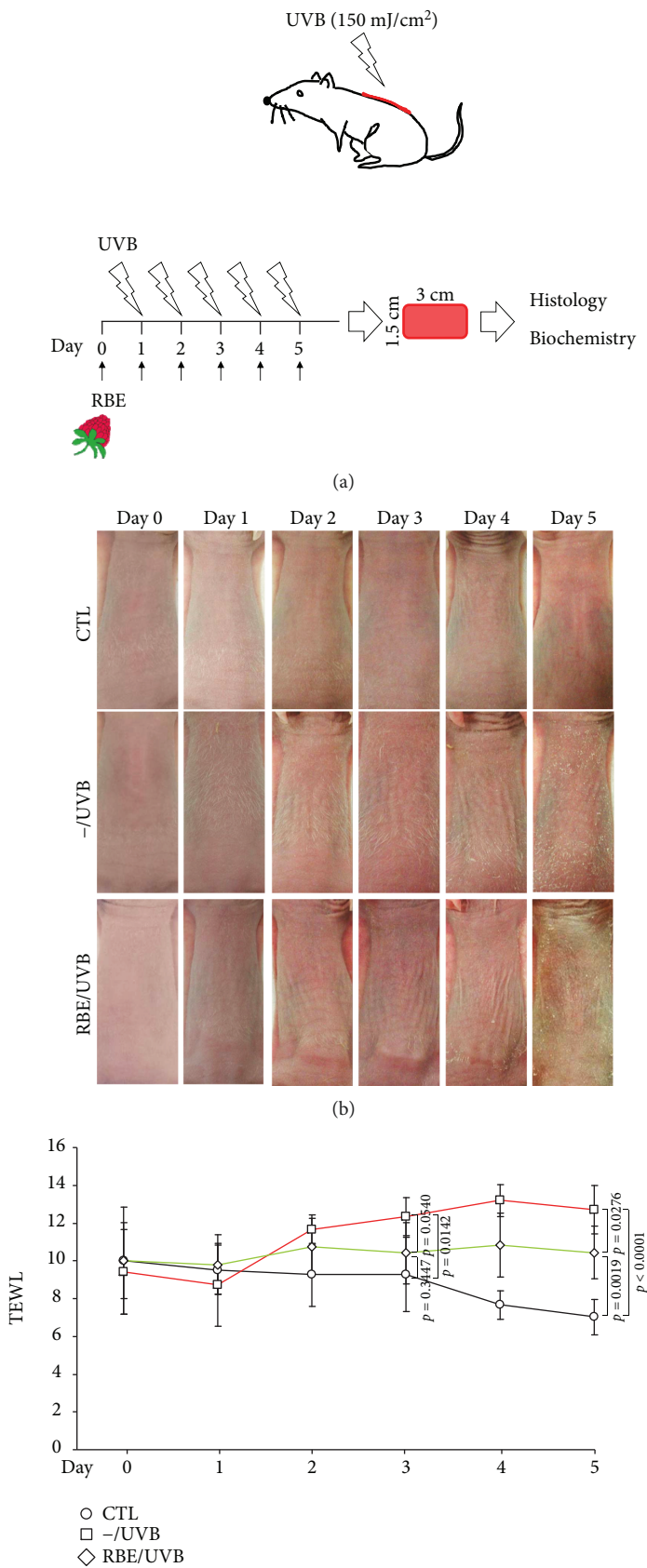


FIGURE 3: Continued.

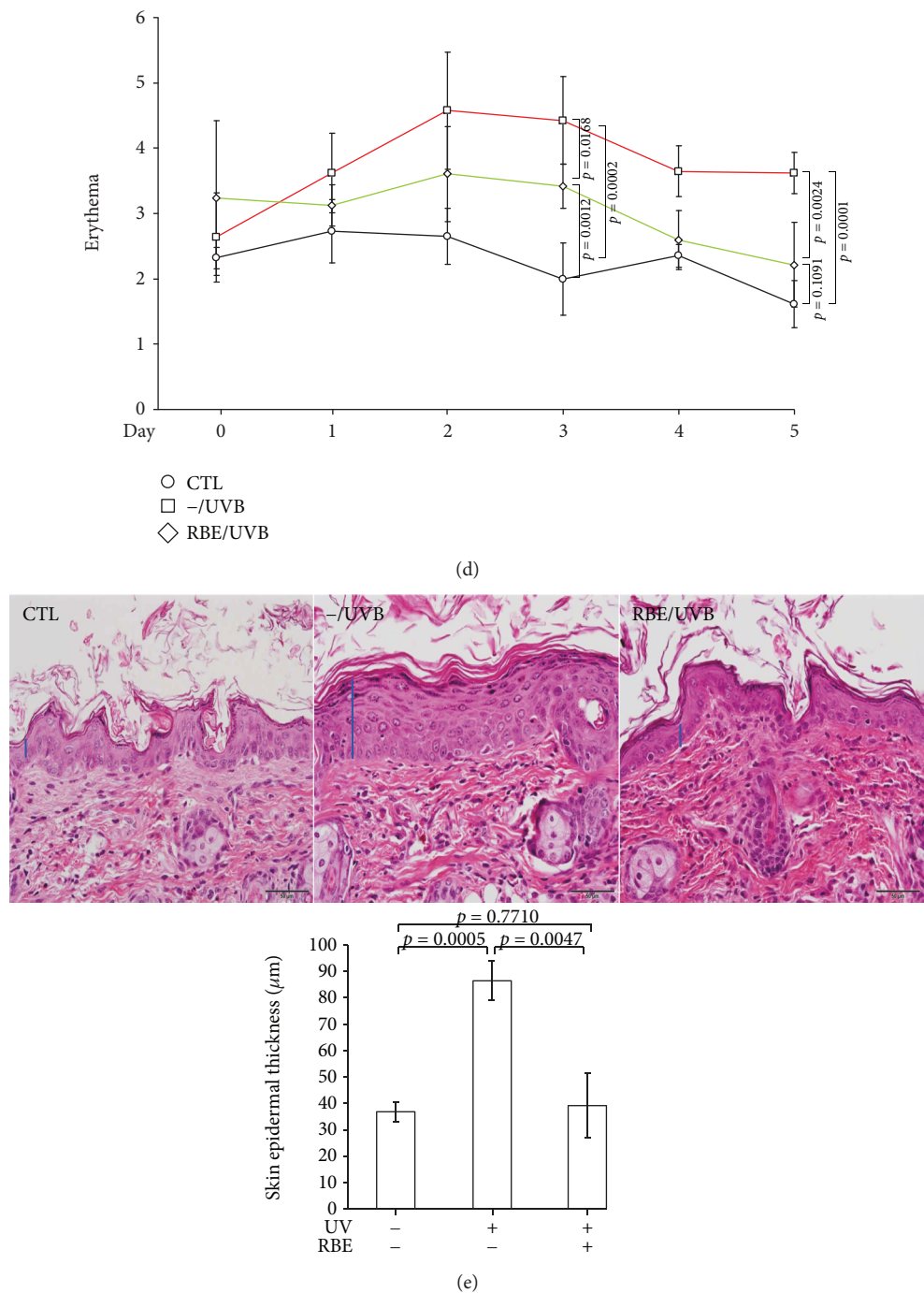


FIGURE 3: (a) The red raspberry extract was pipetted on a sheet made of nonwoven polyethylene ( $1.5 \times 1.5$  cm), and this sheet was applied to the dorsal region of nude mice. Then, the mice were irradiated with UVB ( $150 \text{ mJ}/\text{cm}^2$ ) for continuous 5 days and sacrificed. (b) The changes of nude mouse skin quality under different treatments including control (-/-), UVB exposure only (UVB/-), and red raspberry extract application followed by UVB exposure (UVB/R). (c) The effect of red raspberry extract against water loss represented by TEWL. Error bars: mean  $\pm$  SD. (d) The effect of red raspberry extract against erythema and edema. Error bars: mean  $\pm$  SD. (e) Histological analysis and assessment of nude mouse skin epidermal thickness from control (CTL), UVB exposure only (-/UVB), and red raspberry extract application followed by UVB exposure (RBE/UVB). Upper panels: H&E staining. Original magnification: 100x. Lower panels: the quantified intensity was indicated by the bar chart. Results represent the mean  $\pm$  SD of three independent experiments.

control, while RBE administration promoted the level of Nrf-2. In line with this finding, a marked decrease in HO-1 expression under UVB exposure was observed. The HO-1

level was significantly restored in response to RBE pretreatment (Figure 5(a)). Moreover, we have utilized Nrf2 RNA interference (siNrf2) to verify RBE-mediated antioxidant



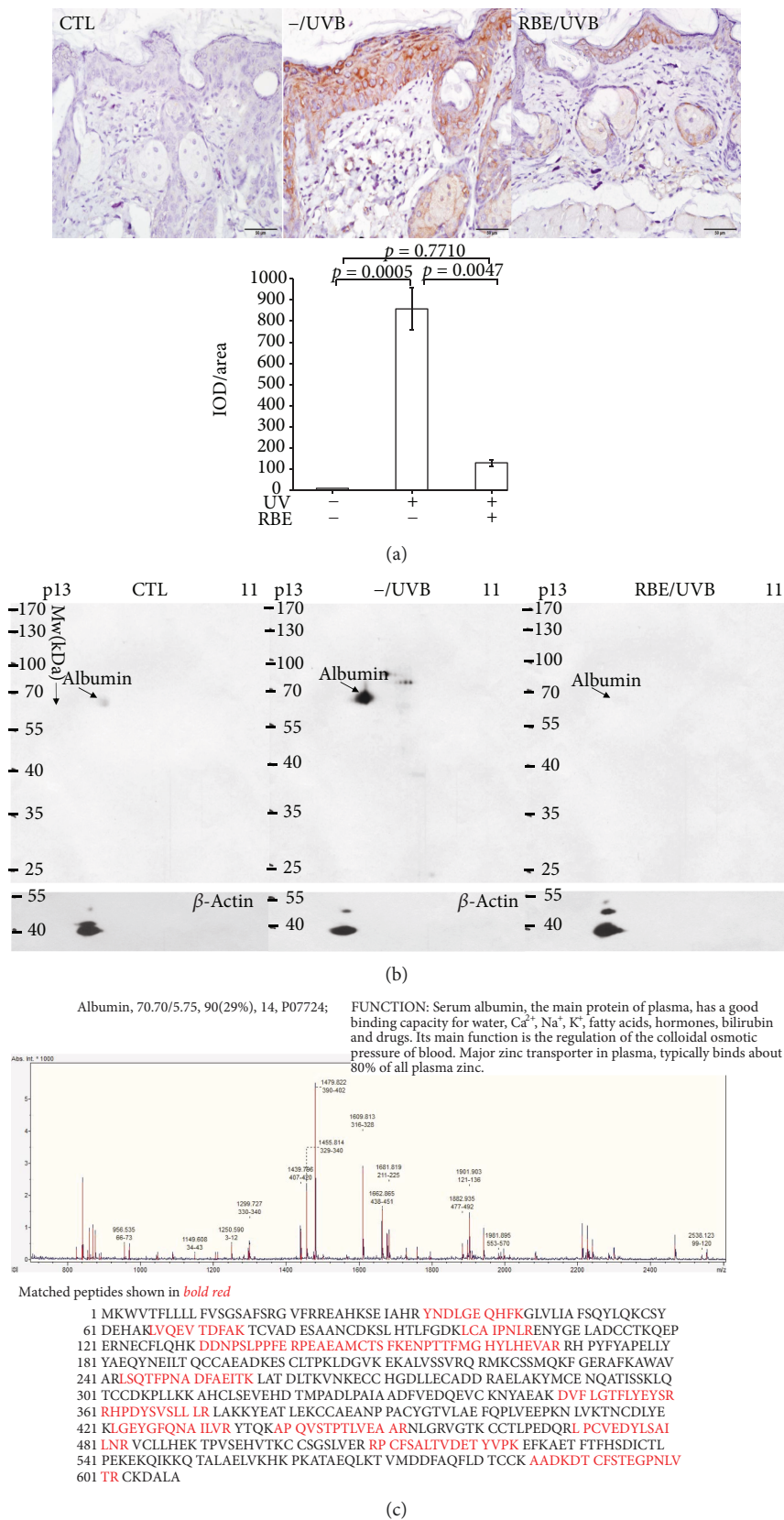
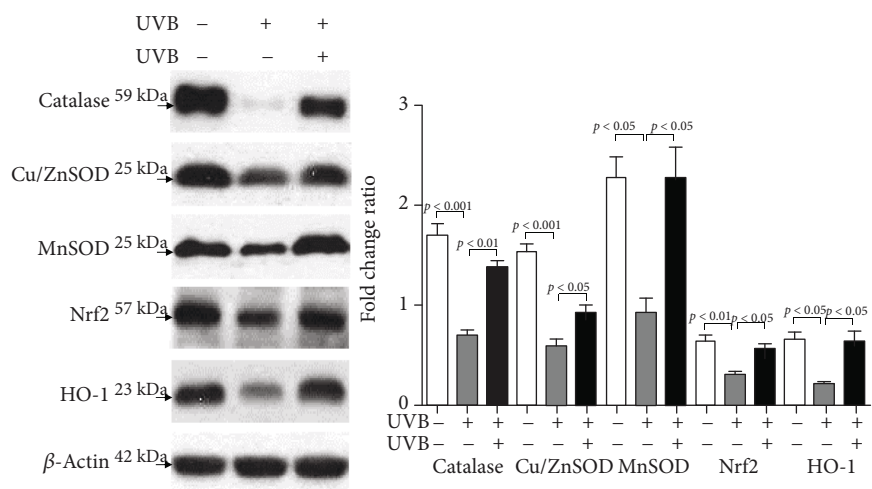
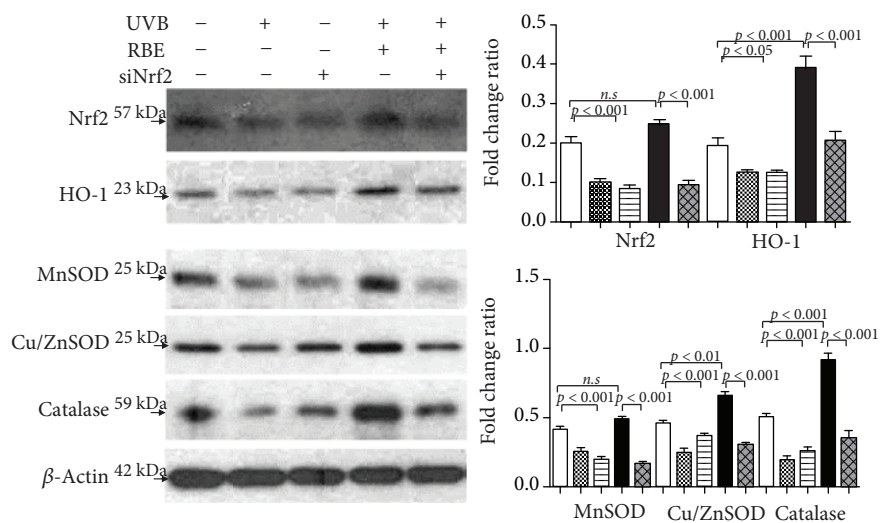


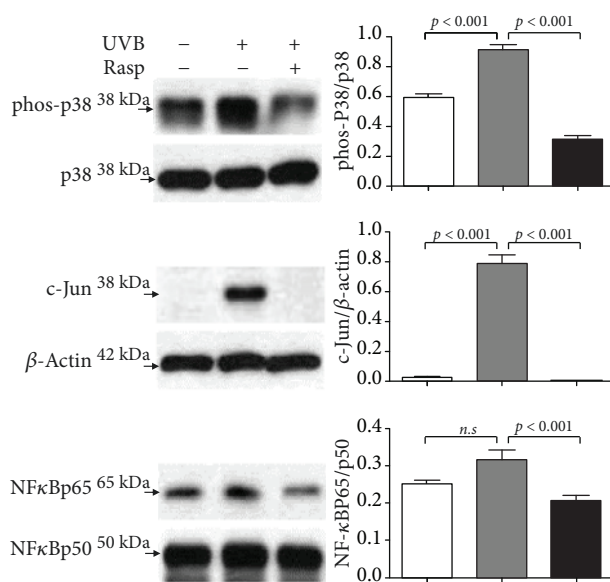
FIGURE 4: (a) 8-OHdG levels were measured by immunocytochemistry, and the positive cells are demonstrated by brown color staining. The quantified results were indicated by the bar chart. (b) Levels of protein carbonylation. Significantly increased expression of carbonylated proteins were observed in the UVB-exposed group compared to the control, while red raspberry extract could obviously reduce the levels of carbonylated proteins.  $\beta$ -Actin was utilized as the loading control. (c) The MALDI-TOF spectrum of tryptic digested albumin.



(a)



(b)



(c)

FIGURE 5: Continued.

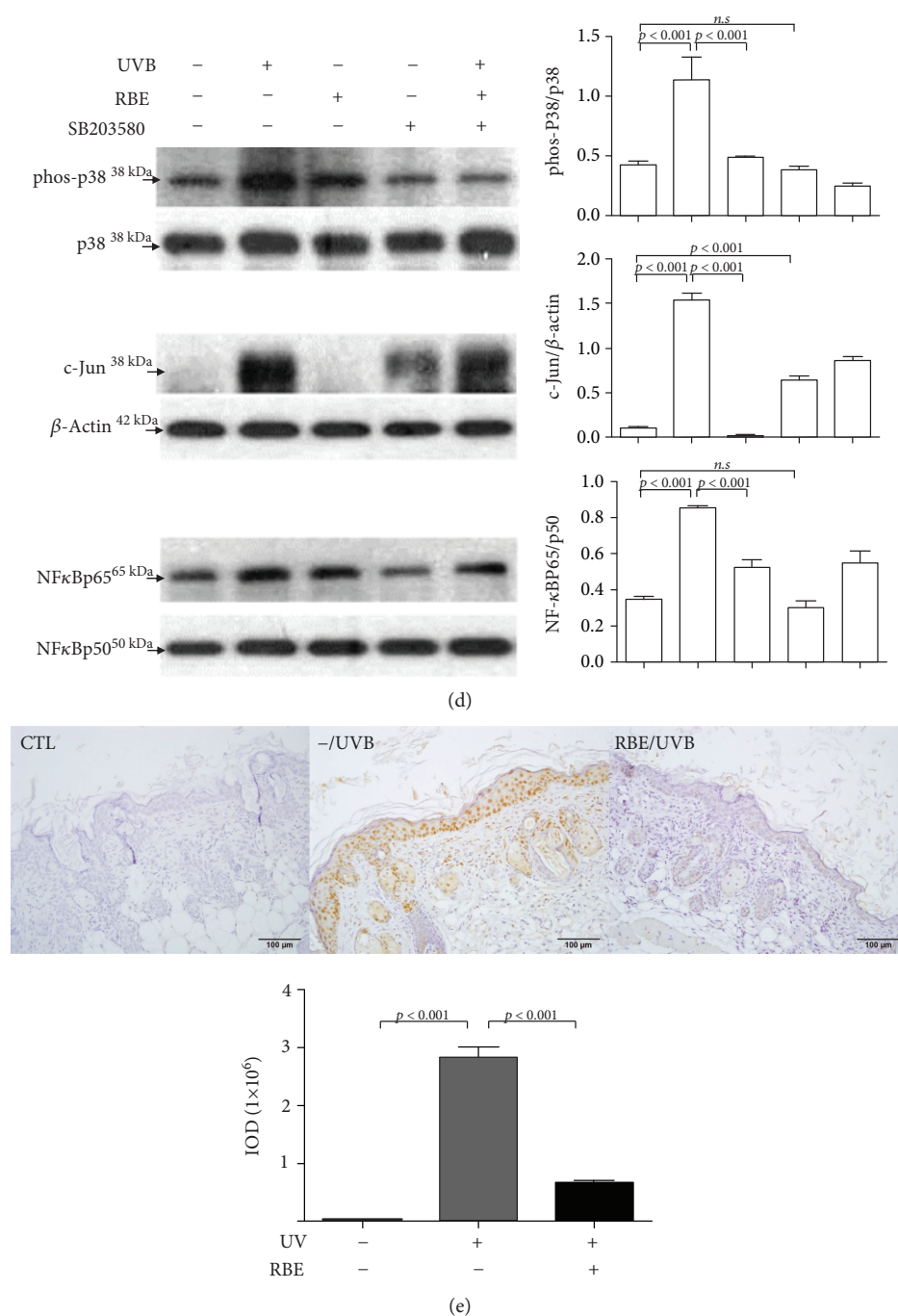


FIGURE 5: (a) Validation of changes in protein expression after different treatments. Protein levels of catalase, Cu/ZnSOD, MnSOD, Nrf2, and HO-1 were determined by a Western blot analysis.  $\beta$ -Actin was used as an internal control. The quantified results were indicated by the bar chart and represent the mean  $\pm$  SD of three independent experiments. The images were cropped from different gels. (b) HaCaT cells transfected with Nrf2 siRNA were treated with RBE and then exposed to UVB irradiation. Protein levels were measured by Western blot analysis.  $\beta$ -Actin was used as an internal control. The quantified results were indicated by the bar chart. (c) Western blot analysis for phosphorylation and total protein levels with different treatments. The phosphorylation levels were normalized by total protein levels.  $\beta$ -Actin was applied as the internal control. The images were cropped from different gels. (d) HaCaT cells were preincubated with or without SB203580 for 1 h, irradiated with UVB, and then treated with or without RBE for 6 h. The phosphorylation of p-38 as well as the protein levels of c-Jun and NF- $\kappa$ B subunits (p65 and p50) was determined by specific antibodies.  $\beta$ -Actin was applied as the loading control. Quantification of the result was presented as the bar diagram, and the results represent the mean  $\pm$  SD of three independent experiments. (e) Immunohistochemical staining for the control group (CTL), UVB only group (UVB/-), and RBE/UVB-treated group. The signal with differently expressed cox-2 was shown with brown color. Original magnification: 200x.

ability in a cell model. UVB and siNrf2 significantly reduced the levels of Nrf2, HO-1, and antioxidant enzyme proteins including SOD and catalase while RBE administration could obviously recover the expression of Nrf2, HO-1, and antioxidant systems under UVB exposure (Figure 5(b)). Treatment of the keratinocytes with RBE remarkably attenuated UVB-caused lower expression of Nrf2.

UVB radiation could activate proinflammatory genes that subsequently trigger ROS. In this regard, we next explored the contribution of MAPK family protein p38 and c-Jun signaling to RBE-mediated protection against UVB-induced cell death and inflammatory responses. Our results indicated that the phosphorylation of p38 (p-p38) was significantly upregulated after UVB exposure and pretreatment of RBE obviously suppressed the expression of p-p38 while the total protein level of p38 showed no significant changes under various treatments. Meanwhile, a high level of c-Jun was induced under UVB administration, but exposure to RBE could almost completely inhibit the expression of c-Jun. Moreover, the NF- $\kappa$ B pathway plays a pivotal role in the modulation of gene expression involved in inflammatory responses. The level of NF- $\kappa$ B increased under UVB stimulation while administration with RBE could suppress translocation, activation, and the expression of NF- $\kappa$ B in the mouse skin (Figure 5(c)). Next, we used an upstream signaling p-p38 inhibitor (SB203580) to confirm the molecular mechanism by which RBE inhibits inflammatory cascades induced by UVB. Our results showed that UVB strongly induced the protein expression of p-p38 as well as the inflammatory molecules such as NF- $\kappa$ B and c-Jun. RBE treatment and p-p38 inhibitor could effectively suppress the levels of p-p38, c-Jun, and activated NF- $\kappa$ B in the presence of UVB (Figure 5(d)). These findings implied that RBE could ameliorate p-p38-mediated NF- $\kappa$ B activation and nuclear translocation which will lead to skin inflammatory responses.

Consistently, COX-2 protein expression was evaluated by immunohistochemical analysis to clarify the anti-inflammatory effect of RBE in the skin. As shown in Figure 5(e), COX-2 protein was rarely expressed in the control group. However, the protein expression of COX-2 was markedly augmented upon UVB treatment, and pretreatment of RBE abrogated UVB-induced COX-2 protein expression. These results implied that RBE performs anti-UVB efficacy through modulating the antioxidant and anti-inflammatory signaling pathways.

#### 4. Discussion

Exposure to UV radiation, particularly UVB (290–320 nm), elicited harmful biological effects on the skin that could eventually result in histologic and clinical injuries such as skin aging and cancers [31, 32]. Prolonged exposure to UVB radiation would lead to apoptosis of keratinocytes and consequently destroy the skin's natural barrier, thus predisposing the skin to inflammation, infection, and carcinogenesis [33, 34]. Numerous reports have shown that natural product-derived agents would exhibit photoprotective efficacy on a UVB-damaged skin due to their diverse bioactive compounds [35–37]. Moreover, the

extract from berries has been added to various skin products such as creams and lotions because the extract is believed to have an efficacy on skin care with a low rate of side effects [38, 39]. In this regard, we investigated the anti-photodamaging activity of RBE both *in vitro* and *in vivo* because the protective potentials of RBE on the skin have remained unresolved.

In our study, the administration of RBE was able to prevent UVB injuries as manifested by the attenuation of cell death of keratinocytes. Meanwhile, animal experiment showed that pretreatment of RBE could attenuate the skin photoaging characterized by skin thickening, erythema, wrinkles, dryness, tanning, and histologic changes, including damage to collagen fibers and abnormal growth of keratinocytes. Particularly, a previous study has indicated that the apoptotic dose of UVB is very similar to the minimal erythema dose (MED) of UVB, implying that UV-induced erythema might be an inflammatory response to the appearance of “sunburn cells” such as apoptotic cells in native human epidermis [40]. It clearly suggests that the epidermis displays abnormal proliferation and differentiation after the UVB-caused sunburn, which appears to be crucially correlated with the impact on skin barrier function leading to photoaging or photocarcinogenesis.

The primary compounds of RBE applied here contain various types of antioxidants including cyanidin, ellagic acid, pelargonidin-3-sophorose, and their derivatives. These bioactive compounds scavenge free radicals, particularly superoxide anions, and therefore may prevent skin injury since the increased oxygen-derived free radical has been suggested as a pivotal factor in UVB-caused skin problems [41–43]. Our findings showed that UVB exposure induced the ROS production that initiates apoptosis of skin cells and stimulates several genes implicated in the apoptotic process such as the caspase-3 signaling pathway. RBE provided protection against UVB-induced death of skin cells by removal of oxidative stress. Again, ROS production will induce damage to cellular macromolecules such as DNA and protein. In the current study, 8-OHdG and protein carbonylation were surveyed as important hallmarks of oxidative stress. Our results indicated that DNA and protein were highly oxidized in the UVB-administrated subjects compared to the control samples while oxidation of protein and DNA characterized by protein carbonylation and 8-OHdG modification was ameliorated by RBE pretreatment, which attenuated skin injury caused by UVB radiation. Oxidative stress caused by the UVB would result in increased ROS generation and reduced antioxidant capacity, leading to a visible deterioration in skin condition. Albumin, with a good binding capacity for water, was destroyed by carbonylated modification, leading to the decrease of TEWL in the UVB-treated mice [44].

In addition, antioxidant enzymes such as catalase and SOD are consumed during oxidative stress. Therefore, the levels of these enzymes could be used as a hallmark of oxidative stress [45, 46]. Our results also showed that the application of RBE significantly inhibits UVB-induced oxidative stress by upregulating the catalase and SOD levels in the



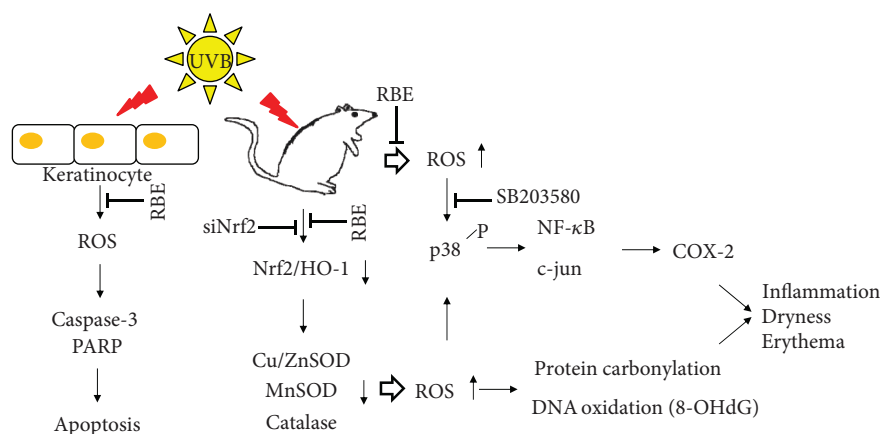


FIGURE 6: Schematic diagram of UVB-mediated skin injury through suppression of antioxidant enzymes and inducing oxidative modification of biological molecules such as protein and DNA. RBE application could protect the skin against UVB damage via enhancement of antioxidant system as well as inhibition of inflammatory or apoptotic cascades.

photodamaged skin. The aforementioned findings implied that the protective effects of RBE at least partially contribute to its capability in the ROS-scavenging and antioxidant activity after UVB irradiation.

The transcription factor, Nrf2, may serve as a critical regulator responsible for oxidative stress. It is released and translocated to the nucleus where it stimulates the expression of detoxification enzymes and antioxidant proteins [47, 48]. Of the antioxidant enzymes, HO-1 is considered beneficial for removing ROS in different types of cells. Herein, the levels of Nrf2 and HO-1 were significantly diminished by UVB stimulation accompanied by ROS production whereas RBE remarkably inhibited the Nrf2/HO-1 signaling and inflammatory responses indicated by the suppression of c-Jun as well as NF- $\kappa$ B. UVB-mediated COX-2 expression is associated with erythema, and therefore, COX-2 could be a feasible target for preventing photo-inflammation [18, 49, 50]. RBE remarkably suppressed UVB-promoted protein levels of COX-2 *in vivo*. These results provide evidence that RBE inhibits UVB-induced inflammation and injury in the skin and is mediated by Nrf2/HO-1 activation as well as suppression of the NF- $\kappa$ B pathway, thereby promoting its clinical use in skin therapy. Furthermore, RBE seems to play a functional role against UVB-induced damage via suppressing the activation of p38 MAPK kinases induced by UVB irradiation. Previous research indicated that the blockade of the p38 MAPK pathway inhibited the expression of the proinflammatory cytokines and COX-2, which is in line with our findings [51–53]. In addition, we have measured the absorption spectrum of RBE, which shows that RBE could moderately absorb the UV and the ABS is approximately equal to 0.5 (Supplement Figure 2). In this regard, RBE should partially exhibit the anti-UVB effects via the absorption function, which might explain some of the skin protection effects.

In summary, RBE administration protects against UVB-induced photodamage via activating Nrf2 signaling cascade which is referred to as the master regulator of the antioxidant response, modulating various antioxidant enzymes. RBE also inhibits MAPK P38 kinase, c-Jun, and

NF- $\kappa$ B to diminish UVB-induced skin inflammation. The RBE may be a promising reagent used in the prevention of photodamage in acute UVB-exposed and chronic inflammatory skin diseases (Figure 6).

## Data Availability

The supplementary data are freely available and can be found in this manuscript.

## Conflicts of Interest

The authors have declared no conflict of interest.

## Authors' Contributions

T.-L. P. and P.-W. W. designed the protocol and prepared the manuscript, P.-W. W., Y.-C. C., Y.-C. H., C.-H. L., J.-Y. F., W.-T. L., and Y.-R. W. helped to conduct the experiments as well as acquisition of data, and T.-L. P. was in charge of the whole experiment conduction and proofreading of the manuscript.

## Acknowledgments

This work was supported by a grant from the Ministry of Science and Technology (MOST105-2320-B-182-007-MY3), Chang Gung Memorial Hospital (CRRPD1F0061~3, CMRPG8G0801, and BMRP445), and Healthy Aging Research Center, Chang Gung University, from The Featured Areas Research Center Program within the framework of the Higher Education Sprout Project by the Ministry of Education, Taiwan (MOE) (EMRPD1H0381).

## Supplementary Materials

Supplementary data include typical 2-DE protein profiles of nude mouse skin samples. Close-up pictures indicate the changes in the levels of protein expression among various groups (Supplement Figure 1). Each spot volume was

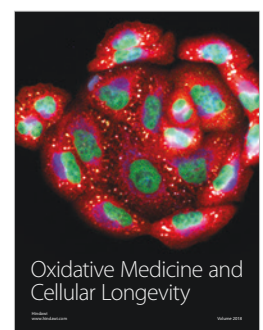
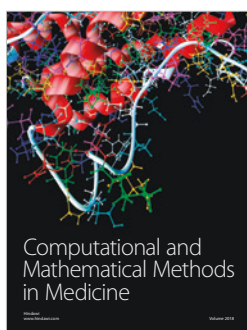
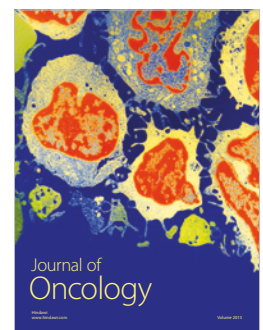
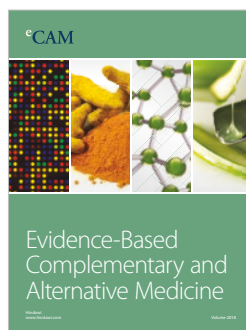
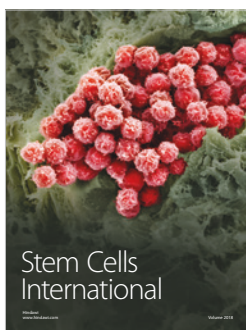
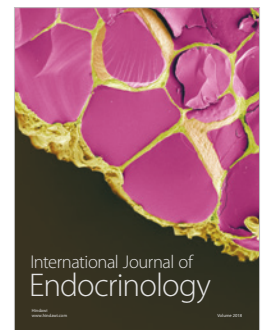
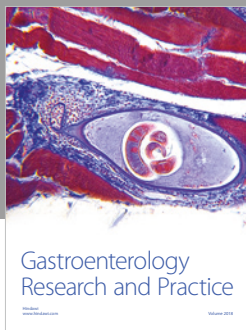
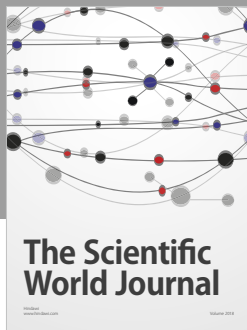
quantified by Prodigy SameSpots software and characterized by MALDI-TOF. Differential expression proteins were listed in the supplement table. Absorption spectrum of RBE in methanol had been shown in Supplement Figure 2. (Supplementary Materials)

## References

- [1] P. Karran and R. Brem, "Protein oxidation, UVA and human DNA repair," *DNA Repair*, vol. 44, pp. 178–185, 2016.
- [2] J. Cadet, T. Douki, and J. L. Ravanat, "Oxidatively generated damage to cellular DNA by UVB and UVA radiation," *Photochemistry and Photobiology*, vol. 91, no. 1, pp. 140–155, 2015.
- [3] T. G. Polefka, T. A. Meyer, P. P. Agin, and R. J. Bianchini, "Effects of solar radiation on the skin," *Journal of Cosmetic Dermatology*, vol. 11, no. 2, pp. 134–143, 2012.
- [4] L. Zastrow, M. C. Meinke, S. Albrecht, A. Patzelt, and J. Lademann, "From UV protection to protection in the whole spectral range of the solar radiation: new aspects of sunscreen development," *Advances in Experimental Medicine and Biology*, vol. 996, pp. 311–318, 2017.
- [5] S. D. Varma, S. Kovtun, and K. R. Hegde, "Role of ultraviolet irradiation and oxidative stress in cataract formation-medical prevention by nutritional antioxidants and metabolic agonists," *Eye & Contact Lens*, vol. 37, no. 4, pp. 233–245, 2011.
- [6] R. Bosch, N. Philips, J. A. Suárez-Pérez et al., "Mechanisms of photoaging and cutaneous photocarcinogenesis, and photoprotective strategies with phytochemicals," *Antioxidants*, vol. 4, no. 2, pp. 248–268, 2015.
- [7] N. P. Seeram, "Berry fruits for cancer prevention: current status and future prospects," *Journal of Agricultural and Food Chemistry*, vol. 56, no. 3, pp. 630–635, 2008.
- [8] G. A. Manganaris, V. Goulas, A. R. Vicente, and L. A. Terry, "Berry antioxidants: small fruits providing large benefits," *Journal of the Science of Food and Agriculture*, vol. 94, no. 5, pp. 825–833, 2014.
- [9] L. Calvo-Castro, D. N. Syed, J. C. Chamcheu et al., "Protective effect of tropical highland blackberry juice (*Rubus adenotrichos* Schltdl.) against UVB-mediated damage in human epidermal keratinocytes and in a reconstituted skin equivalent model," *Photochemistry and Photobiology*, vol. 89, no. 5, pp. 1199–1207, 2013.
- [10] S. D. Sharma, S. M. Meeran, and S. K. Katiyar, "Dietary grape seed proanthocyanidins inhibit UVB-induced oxidative stress and activation of mitogen-activated protein kinases and nuclear factor- $\kappa$ B signaling in *in vivo* SKH-1 hairless mice," *Molecular Cancer Therapeutics*, vol. 6, no. 3, pp. 995–1005, 2007.
- [11] I. A. Ludwig, P. Mena, L. Calani et al., "New insights into the bioavailability of red raspberry anthocyanins and ellagitannins," *Free Radical Biology & Medicine*, vol. 89, pp. 758–769, 2015.
- [12] B. M. Burton-Freeman, A. K. Sandhu, and I. Edirisinghe, "Red raspberries and their bioactive polyphenols: cardiometabolic and neuronal health links," *Advances in Nutrition*, vol. 7, no. 1, pp. 44–65, 2016.
- [13] M. Zia-Ul-Haq, M. Riaz, V. De Feo, H. Z. Jaafar, and M. Moga, "*Rubus fruticosus* L.: constituents, biological activities and health related uses," *Molecules*, vol. 19, no. 8, pp. 10998–11029, 2014.
- [14] C. Lee, G. H. Park, E. M. Ahn, B. A. Kim, C. I. Park, and J. H. Jang, "Protective effect of *Codium fragile* against UVB-induced pro-inflammatory and oxidative damages in HaCaT cells and BALB/c mice," *Fitoterapia*, vol. 86, pp. 54–63, 2013.
- [15] E. Emanuele, J. M. Spencer, and M. Braun, "From DNA repair to proteome protection: new molecular insights for preventing non-melanoma skin cancers and skin aging," *Journal of Drugs in Dermatology*, vol. 13, no. 3, pp. 274–281, 2014.
- [16] J. Y. Fang, P. W. Wang, C. H. Huang, M. H. Chen, Y. R. Wu, and T. L. Pan, "Skin aging caused by intrinsic or extrinsic processes characterized with functional proteomics," *Proteomics*, vol. 16, no. 20, pp. 2718–2731, 2016.
- [17] S. P. Divya, X. Wang, P. Pratheeshkumar et al., "Blackberry extract inhibits UVB-induced oxidative damage and inflammation through MAP kinases and NF- $\kappa$ B signaling pathways in SKH-1 mice skin," *Toxicology and Applied Pharmacology*, vol. 284, no. 1, pp. 92–99, 2015.
- [18] S. C. Tang, P. Y. Liao, S. J. Hung et al., "Topical application of glycolic acid suppresses the UVB induced IL-6, IL-8, MCP-1 and COX-2 inflammation by modulating NF- $\kappa$ B signaling pathway in keratinocytes and mice skin," *Journal of Dermatological Science*, vol. 86, no. 3, pp. 238–248, 2017.
- [19] V. M. Adhami, D. N. Syed, N. Khan, and F. Afaq, "Phytochemicals for prevention of solar ultraviolet radiation-induced damages," *Photochemistry and Photobiology*, vol. 84, no. 2, pp. 489–500, 2008.
- [20] T. L. Pan, P. W. Wang, Y. L. Leu, T. H. Wu, and T. S. Wu, "Inhibitory effects of *Scutellaria baicalensis* extract on hepatic stellate cells through inducing G<sub>2</sub>/M cell cycle arrest and activating ERK-dependent apoptosis via Bax and caspase pathway," *Journal of Ethnopharmacology*, vol. 139, no. 3, pp. 829–837, 2012.
- [21] T. L. Pan and P. W. Wang, "Explore the molecular mechanism of apoptosis induced by tanshinone IIA on activated rat hepatic stellate cells," *Evidence-based Complementary and Alternative Medicine*, vol. 2012, Article ID 734987, 15 pages, 2012.
- [22] T. L. Pan, P. W. Wang, C. C. Huang, C. T. Yeh, T. H. Hu, and J. S. Yu, "Network analysis and proteomic identification of vimentin as a key regulator associated with invasion and metastasis in human hepatocellular carcinoma cells," *Journal of Proteomics*, vol. 75, no. 15, pp. 4676–4692, 2012.
- [23] S. Lembo, A. Balato, R. Di Caprio et al., "The modulatory effect of ellagic acid and rosmarinic acid on ultraviolet-B-induced cytokine/chemokine gene expression in skin keratinocyte (HaCaT) cells," *BioMed Research International*, vol. 2014, Article ID 346793, 8 pages, 2014.
- [24] P. W. Wang, Y. C. Hung, W. T. Li, C. T. Yeh, and T. L. Pan, "Systematic revelation of the protective effect and mechanism of Cordyceps sinensis on diethylnitrosamine-induced rat hepatocellular carcinoma with proteomics," *Oncotarget*, vol. 7, no. 37, pp. 60270–60289, 2016.
- [25] C. F. Hung, C. L. Fang, S. A. Al-Suwayeh, S. Y. Yang, and J. Y. Fang, "Evaluation of drug and sunscreen permeation via skin irradiated with UVA and UVB: comparisons of normal skin and chronologically aged skin," *Journal of Dermatological Science*, vol. 68, no. 3, pp. 135–148, 2012.
- [26] C. F. Hung, W. Y. Chen, I. A. Aljuffali, H. C. Shih, and J. Y. Fang, "The risk of hydroquinone and sunscreen over-absorption via photodamaged skin is not greater in senescent skin as compared to young skin: nude mouse as an animal model," *International Journal of Pharmaceutics*, vol. 471, no. 1–2, pp. 135–145, 2014.

- [27] T. L. Pan, P. W. Wang, I. A. Aljuffali, Y. Y. Hung, C. F. Lin, and J. Y. Fang, "Dermal toxicity elicited by phthalates: evaluation of skin absorption, immunohistology, and functional proteomics," *Food and Chemical Toxicology*, vol. 65, pp. 105–114, 2014.
- [28] J. N. McGinley and H. J. Thompson, "Quantitative assessment of mammary gland density in rodents using digital image analysis," *Biological Procedures Online*, vol. 13, no. 1, p. 4, 2011.
- [29] Y. C. Hung, P. W. Wang, and T. L. Pan, "Functional proteomics reveal the effect of *Salvia miltiorrhiza* aqueous extract against vascular atherosclerotic lesions," *Biochimica et Biophysica Acta (BBA) - Proteins and Proteomics*, vol. 1804, no. 6, pp. 1310–1321, 2010.
- [30] K. Horimukai, K. Morita, M. Narita et al., "Transepidermal water loss measurement during infancy can predict the subsequent development of atopic dermatitis regardless of filaggrin mutations," *Allergy International*, vol. 65, no. 1, pp. 103–108, 2016.
- [31] M. V. Plikus, E. N. Van Spyk, K. Pham et al., "The circadian clock in skin: implications for adult stem cells, tissue regeneration, cancer, aging, and immunity," *Journal of Biological Rhythms*, vol. 30, no. 3, pp. 163–182, 2015.
- [32] E. R. Gonzaga, "Role of UV light in photodamage, skin aging, and skin cancer: importance of photoprotection," *American Journal of Clinical Dermatology*, vol. 10, Supplement 1, pp. 19–24, 2009.
- [33] D. Mohania, S. Chandel, P. Kumar et al., "Ultraviolet radiations: skin defense-damage mechanism," *Advances in Experimental Medicine and Biology*, vol. 996, pp. 71–87, 2017.
- [34] R. P. Sahu, S. C. DaSilva, B. Rashid et al., "Mice lacking epidermal PPAR $\gamma$  exhibit a marked augmentation in photocarcinogenesis associated with increased UVB-induced apoptosis, inflammation and barrier dysfunction," *International Journal of Cancer*, vol. 131, no. 7, pp. E1055–E1066, 2012.
- [35] M. Cavinato, B. Waltenberger, G. Baraldo, C. V. C. Grade, H. Stuppner, and P. Jansen-Dürr, "Plant extracts and natural compounds used against UVB-induced photoaging," *Biogerontology*, vol. 18, no. 4, pp. 499–516, 2017.
- [36] N. Saewan and A. Jimtaisong, "Natural products as photoprotection," *Journal of Cosmetic Dermatology*, vol. 14, no. 1, pp. 47–63, 2015.
- [37] T. Yadav, S. Mishra, S. Das, S. Aggarwal, and V. Rani, "Antic-edants and natural prevention of environmental toxicants induced accelerated aging of skin," *Environmental Toxicology and Pharmacology*, vol. 39, no. 1, pp. 384–391, 2015.
- [38] E. Wineman, M. Portugal-Cohen, Y. Soroka et al., "Photo-damage protective effect of two facial products, containing a unique complex of Dead Sea minerals and Himalayan actives," *Journal of Cosmetic Dermatology*, vol. 11, no. 3, pp. 183–192, 2012.
- [39] M. R. Serafini, A. G. Guimarães, J. S. Quintans, A. A. Araújo, P. S. Nunes, and L. J. Quintans-Júnior, "Natural compounds for solar photoprotection: a patent review," *Expert Opinion on Therapeutic Patents*, vol. 25, no. 4, pp. 467–478, 2015.
- [40] A. Reich and K. Mędreń, "Effects of narrow band UVB (311 nm) irradiation on epidermal cells," *International Journal of Molecular Sciences*, vol. 14, no. 4, pp. 8456–8466, 2013.
- [41] D. Fracassetti, C. Costa, L. Moulay, and F. A. Tomás-Barberán, "Ellagic acid derivatives, ellagitannins, proanthocyanidins and other phenolics, vitamin C and antioxidant capacity of two powder products from camu-camu fruit (*Myrciaria dubia*)," *Food Chemistry*, vol. 139, no. 1–4, pp. 578–588, 2013.
- [42] F. Aqil, A. Gupta, R. Munagala et al., "Antioxidant and antiproliferative activities of anthocyanin/ellagitannin-enriched extracts from *Syzygium cumini* L. (Jamun, the Indian blackberry)," *Nutrition and Cancer*, vol. 64, no. 3, pp. 428–438, 2012.
- [43] F. Afaq, A. Malik, D. Syed, D. Maes, M. S. Matsui, and H. Mukhtar, "Pomegranate fruit extract modulates UV-B-mediated phosphorylation of mitogen-activated protein kinases and activation of nuclear factor kappa B in normal human epidermal keratinocytes paragraph sign," *Photochemistry and Photobiology*, vol. 81, no. 1, pp. 38–45, 2005.
- [44] T. Mizutani, H. Sumida, Y. Sagawa, Y. Okano, and H. Masaki, "Carbonylated proteins exposed to UVA and to blue light generate reactive oxygen species through a type I photosensitizing reaction," *Journal of Dermatological Science*, vol. 84, no. 3, pp. 314–321, 2016.
- [45] V. Lubrano and S. Balzan, "Enzymatic antioxidant system in vascular inflammation and coronary artery disease," *World Journal of Experimental Medicine*, vol. 5, no. 4, pp. 218–224, 2015.
- [46] W. Liu, S. S. Baker, R. D. Baker, and L. Zhu, "Antioxidant mechanisms in nonalcoholic fatty liver disease," *Current Drug Targets*, vol. 16, no. 12, pp. 1301–1314, 2015.
- [47] Z. Wu, H. Uchi, S. Morino-Koga, W. Shi, and M. Furue, "Z-ligustilide ameliorated ultraviolet B-induced oxidative stress and inflammatory cytokine production in human keratinocytes through upregulation of Nrf2/HO-1 and suppression of NF- $\kappa$ B pathway," *Experimental Dermatology*, vol. 24, no. 9, pp. 703–708, 2015.
- [48] D. N. Che, G. H. Xie, B. O. Cho, J. Y. Shin, H. J. Kang, and S. I. Jang, "Protective effects of grape stem extract against UVB-induced damage in C57BL mice skin," *Journal of Photochemistry and Photobiology B: Biology*, vol. 173, pp. 551–559, 2017.
- [49] K. S. Chun and R. Langenbach, "A proposed COX-2 and PGE<sub>2</sub> receptor interaction in UV-exposed mouse skin," *Molecular Carcinogenesis*, vol. 46, no. 8, pp. 699–704, 2007.
- [50] J. Y. Kwon, K. W. Lee, J. E. Kim et al., "Delphinidin suppresses ultraviolet B-induced cyclooxygenases-2 expression through inhibition of MAPKK4 and PI-3 kinase," *Carcinogenesis*, vol. 30, no. 11, pp. 1932–1940, 2009.
- [51] S. B. Kim, J. E. Kim, O. H. Kang et al., "Protective effect of ixerisoides A against UVB-induced pro-inflammatory cytokine production in human keratinocytes," *International Journal of Molecular Medicine*, vol. 35, no. 5, pp. 1411–1418, 2015.
- [52] Y. Zhai, Y. Dang, W. Gao et al., "P38 and JNK signal pathways are involved in the regulation of phlorizin against UVB-induced skin damage," *Experimental Dermatology*, vol. 24, no. 4, pp. 275–279, 2015.
- [53] J. E. Kim, J. Y. Kwon, S. K. Seo et al., "Cyanidin suppresses ultraviolet B-induced COX-2 expression in epidermal cells by targeting MKK4, MEK1, and Raf-1," *Biochemical Pharmacology*, vol. 79, no. 10, pp. 1473–1482, 2010.









# Neuroprotective Effects of Dehydroepiandrosterone Sulfate Through Inhibiting Expression of Matrix Metalloproteinase-9 from Bradykinin-Challenged Astroglia

Chian-Jiun Liou<sup>1,2</sup> · Chuen-Mao Yang<sup>3</sup> · Tsong-Hai Lee<sup>4</sup> · Pei-Shan Liu<sup>5</sup> · Hsi-Lung Hsieh<sup>1,6</sup> 

Received: 13 January 2018 / Accepted: 11 May 2018  
© Springer Science+Business Media, LLC, part of Springer Nature 2018

## Abstract

Dehydroepiandrosterone sulfate (DHEAS), one of the most important neuroactive steroids, is produced in the adrenals and the brain. DHEAS is believed to play a critical role in modulating different forms of cellular control, including processes associated with human neural systems. Its production rate and level in serum, adrenals, and brain gradually decrease with advancing age. The decline of DHEAS level was associated with age-related neuronal dysfunction and degeneration, most probably because the steroids protect the central nervous system (CNS) neurons against neurotoxic challenges. Moreover, increasing studies show that matrix metalloproteinases (MMPs), MMP-9 especially, are upregulated by proinflammatory mediators in the CNS disorders. The increased MMP-9 as an inflammatory biomarker of several CNS disorders that may participate in the CNS inflammation and neurodegeneration. Herein, we investigate the effects of DHEAS on brain inflammation by the model we have defined of bradykinin (BK)-induced MMP-9 expression in rat brain astrocyte (RBA) and its mechanism. The results showed that DHEAS significantly reduce MMP-9 induced by BK. Pretreatment with DHEAS can inhibit BK-stimulated phosphorylation of c-Src and PYK2. Moreover, DHEAS attenuated BK-stimulated NADPH oxidase (Nox)-derived reactive oxygen species (ROS) production, suggesting that DHEAS has an antioxidative effect. We further demonstrated that DHEAS blocked activation of ERK1/2, Akt, and c-Fos/AP-1 by BK. Finally, DHEAS decreased MMP-9-related events including RBA migration and neuronal apoptosis. The results will provide new insights into the anti-inflammatory action of DHEAS, supporting that DHEAS may have a neuroprotective effect in the improvement of the CNS disorders by reducing neuroinflammation.

**Keywords** Dehydroepiandrosterone sulfate · Neuroprotection · Anti-inflammation · Bradykinin · Matrix metalloproteinase-9 · Brain astrocytes

✉ Hsi-Lung Hsieh  
hlhsieh@mail.cgu.edu.tw

- <sup>1</sup> Department of Nursing, Division of Basic Medical Sciences, Research Center for Chinese Herbal Medicine, and Graduate Institute of Health Industry Technology, Chang Gung University of Science and Technology, Tao-Yuan, Taiwan
- <sup>2</sup> Division of Allergy, Asthma, and Rheumatology, Department of Pediatrics, Chang Gung Memorial Hospital, Gui-Shan, Taoyuan, Taiwan
- <sup>3</sup> Department of Physiology and Pharmacology and Health Ageing Research Center, College of Medicine, Chang Gung University, Tao-Yuan, Taiwan
- <sup>4</sup> Stroke Center and Stroke Section, Department of Neurology, Chang Gung Memorial Hospital, Linkou Medical Center and Chang Gung University College of Medicine, Tao-Yuan, Taiwan
- <sup>5</sup> Department of Microbiology, Soochow University, Taipei, Taiwan
- <sup>6</sup> Department of Neurology, Chang Gung Memorial Hospital, Tao-Yuan, Taiwan

## Introduction

Dehydroepiandrosterone sulfate (DHEAS) is the sulfated metabolite of DHEA and one of the most important natural and neuroactive steroids. It is produced in the adrenals and the brain. In human plasma, DHEA concentrations average 10 nmol/L, while DHEAS concentrations reach 10  $\mu$ mol/L in young adults 20–35 years of age [1]. The production rate and levels of DHEA and DHEAS in serum, adrenals, and brain decrease gradually with advancing age. At age 80, DHEAS levels are only about 20% those at age 25, unlike the age-independent plasma levels of cortisol [2]. The decline of its level was associated with age-related neuronal dysfunction and degeneration, most probably because these steroids protect central nervous system (CNS) neurons against noxious agents [3]. Moreover, DHEAS is the major circulating steroid in human which is known for its clinical effects on hypertension, memory disorders, and cancer

prevention [4]. In the CNS, DHEAS plays an important regulatory role in brain functions. Moreover, increasing evidence shows that DHEAS also has profound psychotropic effects, such as anxiolytic effects in animal experiments [5]. These findings suggest that DHEAS may act as endogenous neuroprotective factors. Here, we investigate and evaluate the effects of DHEAS on anti-brain inflammation and neuroprotection.

The primary role of steroids is to modulate genetic transcription through binding to their intracellular receptors, which consequently elicit different physiological responses. Many reports have indicated that some neurosteroids such as DHEAS may act on metabotropic sigma receptors like sigma-1 receptor, which coupling to Gi protein [6, 7]. Although DHEAS has well characterized effects on memory and cognitive performances [8], little is known about the underlying molecular mechanisms. Moreover, DHEAS is able to increase the immunoendocrine production of neuroprotective growth factors (e.g., IGF and VEGF), which is reduced in AD subjects, suggesting a new approach in the treatment of dementia [9]. DHEAS can prevent the toxicity of free radical and serum free culture insults by suppressing the generation of lipid peroxide and increasing the activities of antioxidant enzymes [10]. The neuroprotective effects of DHEAS may be depending on PI3K/Akt and ERK/MAPK signaling pathways [11, 12]. In brain glial cells, DHEAS can inhibit TNF production in brain astrocytic and microglial cells [13]. While DHEAS can function to protect neural system, the molecular mechanisms underlying the neuroprotective effects of DHEAS remain undefined.

Matrix metalloproteinases (MMPs), a large family of zinc-dependent endopeptidases, are a crucial molecule for the turnover of extracellular matrix (ECM) and pathophysiological processes [14]. In the CNS, MMPs, MMP-9 especially, have been demonstrated to participate in morphogenesis, wounding healing, and neurite outgrowth [15]. Expression of MMP-9 has been up-regulated by various brain injuries, which may contribute to the pathogenesis of brain diseases [16]. Moreover, cytokines and lipopolysaccharide (LPS) have been indicated to enhance MMP-9 expression and activity in culture rat brain astrocytes [17, 18]. These studies demonstrated that MMP-9 may be involved in brain inflammation and injury. Our previous studies have demonstrated that several pro-inflammatory mediators like bradykinin (BK) can induce MMP-9 expression in brain astrocytes [19]. Here, we used the model in RBA cells to evaluate the effects of DHEAS on BK-induced MMP-9 expression and MMP-9-related events such as cell migration and neuronal cell death.

Reactive oxygen species (ROS) are produced by various enzymatic and chemical processes or directly inhaled. The ROS at low level have physiological roles as signaling molecules in various cellular and developmental processes [20, 21] and killing of invading microorganisms [22]. In contrast, recent report indicated that oxidative stress plays an important

role in the progression of various diseases [22]. Moreover, ROS has been shown to interact with cellular components such as DNA that lead to cellular dysfunctions and inflammatory responses [21, 23]. Under pathological conditions, many proinflammatory factors (e.g., bradykinin) induce expression of several inflammatory genes during brain injury by enhancing ROS production [21, 24]. Recently, increasing evidence attributes the neurodegenerative diseases like Alzheimer's disease (AD) to oxidative stress (production of free radicals) that leads to brain inflammation during CNS pathogenesis [21, 24, 25]. Moreover, ROS also exert as a signaling factor mediated microglial activation induced by several proinflammatory factors [26]. The effects of BK associated with ROS generation have been indicated in several organ disorders [27]. Our recent study showed that BK induces ROS-mediated MMP-9 responses in rat brain astrocytes [28].

Based on these reports and our previous studies in the brain inflammatory responses by BK [29, 30], the experiments were performed to investigate the effects and molecular mechanisms of DHEAS on BK-induced MMP-9 expression in brain astrocytes (RBA cells). In the study, we found that DHEAS decreased BK-induced MMP-9 expression. Subsequently, BK-stimulated phosphorylation of protein kinases (e.g., c-Src and PYK2) also been inhibited by DHEAS. Moreover, DHEAS reduced BK-stimulated Nox/ROS-dependent activation of MAPKs (e.g., ERK1/2) cascade in RBA cells. Finally, we further demonstrated that DHEAS also blocked MMP-9-related events including RBA migration and neuronal apoptosis by BK. These results suggested that DHEAS may have an anti-oxidative, anti-inflammatory, and neuroprotective action in the CNS.

## Experimental Procedures

### Materials

Dulbecco's modified Eagle's medium (DMEM)/F-12 medium, fetal bovine serum (FBS), and TRIzol were from Invitrogen (Carlsbad, CA). Hybond C membrane and enhanced chemiluminescence (ECL) Western blot detection system were from GE Healthcare Biosciences (Buckinghamshire, UK). Phospho-c-Src (Tyr<sup>416</sup>) (#6943) antibodies were from Cell Signaling (Danver, MA). Phospho-PYK2 (Tyr<sup>402</sup>) (sc-101790), Phospho-ERK1/2 (Tyr<sup>204</sup>) (sc-7383), Phospho-Akt (Ser<sup>473</sup>) (sc-81433), and glyceraldehyde-3-phosphate dehydrogenase (GAPDH) antibodies were from Santa Cruz (Santa Cruz, CA). Bicinchoninic acid (BCA) protein assay reagent was from Pierce (Rockford, IL). DHEAS, BK, enzymes, and other chemicals were from Sigma (St. Louis, MO). SDS-PAGE reagents were from MDBio, Inc. (Taipei, Taiwan).

## Cell Cultures and Treatments

The rat brain astrocytic cell line (RBA, CTX TNA2) was purchased from BCRC (Hsinchu, Taiwan) and used throughout this study. Cells were plated onto 12-well culture plates and made quiescent at confluence by incubation in serum-free DMEM/F-12 for 24 h, and then incubated with BK (10 nM) at 37 °C for the indicated time intervals. When DHEAS (0.01–1 mM) or the inhibitors were used, cells were pretreated with DHEAS or the inhibitor for 1 h before exposure to BK. Treatment of RBA with DHEAS (1 mM) alone had no significant effect on cell viability determined by an XTT assay (data not shown). The SK-N-SH cells, a human neuroblastoma cell line, were purchased from American Type Culture Collection (Manassas, VA) and cultured in DMEM/F-12 supplemented with 10% FBS [31].

## MMP Gelatin Zymography

Growth-arrested cells were incubated with BK for the indicated time intervals. After treatment, the cultured media were collected and analyzed by gelatin zymography [29]. Gelatinolytic activity was manifested as horizontal white bands on a blue background. Because cleaved MMPs were not reliably detectable, only pro-form zymogens were quantified.

## Total RNA Extraction and Real-Time PCR Analysis

Total RNA was extracted from RBA cells [29]. The cDNA obtained from 0.5 µg total RNA was used as a template for PCR amplification. Oligonucleotide primers were designed on the basis of GenBank entries for rat MMP-9 and GAPDH. The primers were as follows:

MMP-9: 5'-AGTTTGGTGTCGCGGAGCAC-3' (sense).  
5'-TACATGAGCGCTTCCGGCAC-3' (antisense).

GAPDH: 5'-(AACTTTGGCATCGTGGAAGG)-3' (sense).

5'-(GTGGATGCAGGGATGATGTTTC)-3' (anti-sense).

The amplification was performed in 30 cycles at 55 °C, 30 s; 72 °C, 1 min; 94 °C, 30 s. PCR fragments were analyzed on 2% agarose 1× TAE gel containing ethidium bromide and their size was compared with a molecular weight markers. Amplification of  $\beta$ -actin, a relatively invariant internal reference RNA, was performed in parallel, and cDNA amounts were standardized to equivalent  $\beta$ -actin mRNA levels. The image densitometry analysis was quantified by an UN-SCAN-IT gel 6.1 software (Orem, UT).

## Preparation of Cell Extracts and Western Blot Analysis

Growth-arrested cells were incubated with BK at 37 °C for the indicated time intervals. The cells were washed

with ice-cold phosphate-buffered saline (PBS), scraped, and collected by centrifugation at 45,000×g for 1 h at 4 °C to yield the whole cell extract, as previously described [30]. Samples were analyzed by Western blot, transferred to nitrocellulose membrane, and then incubated overnight using a 1:1000 dilution (100 ng/ml) of anti-phospho-c-Src, phospho-PYK2, phospho-ERK1/2, phospho-Akt, or GAPDH antibody. Membranes were washed four times with TTBS for 5 min each, incubated with a 1:2000 dilution of anti-rabbit horseradish peroxidase antibody for 1 h. The immunoreactive bands were detected by ECL reagents and captured by a UVP BioSpectrum 500 Imaging System (Upland, CA). The image densitometry analysis was quantified by an UN-SCAN-IT gel 6.1 software (Orem, UT).

## Measurement of Intracellular ROS Generation

The peroxide-sensitive fluorescent probe 2',7'-dichlorofluorescein diacetate (DCF-DA) was used to assess the generation of intracellular ROS [32] with minor modifications. RBA cells on monolayers were incubated with 5 µM DCF-DA in RPMI-1640 at 37 °C for 45 min. The supernatant was removed and replaced with fresh RPMI-1640 medium before exposure to DHEAS or BK (10 nM). Relative fluorescence intensity was recorded at the indicated time by using a fluorescent plate reader (Thermo, Appliskan) at an excitation wavelength of 485 nm and emission was measured at a wavelength of 530 nm.

## Determination of NADPH Oxidase Activity by Chemiluminescence Assay

The Nox activity in intact cells was assayed by lucigenin chemiluminescence [33]. After incubation, the cells were gently scraped and centrifuged at 400×g for 10 min at 4 °C. The cell pellet was resuspended in a known volume (35 µl/well) of ice-cold RPMI 1640 medium, and the cell suspension was kept on ice. To a final 200 µl of pre-warmed (37 °C) RPMI-1640 medium containing either NADPH (1 µM) or lucigenin (20 µM), 5 µl of cell suspension ( $2 \times 10^4$  cells) was added to initiate the reaction followed by immediate measurement of chemiluminescence using an Appliskan luminometer (Thermo®) in an out-of-coincidence mode. Appropriate blanks and controls were established, and chemiluminescence was recorded. Neither NADPH nor NADH enhanced the background chemiluminescence of lucigenin alone (30–40 cpm). Chemiluminescence was continuously measured for 12 min, and the activity of Nox was expressed as counts per million cells.

## Chromatin Immunoprecipitation Assay

To detect the *in vivo* association of nuclear proteins with rat MMP-9 promoter, chromatin immunoprecipitation (ChIP) analysis was conducted as previously described [30]. Briefly, RBA cells were cross-linked with 1% formaldehyde for 10 min at 37 °C and washed thrice with ice-cold PBS containing 1 mM phenylmethylsulfonyl fluoride (PMSF) and 1% aprotinin. Soluble chromatin was prepared using a ChIP assay kit (Upstate) according to the manufacturer's recommendations and immunoprecipitated without (control) or with anti-c-Fos and normal goat immunoglobulin G (IgG). Following washes and elution, precipitates were heated overnight at 65 °C to reverse cross-linking of DNA and protein. DNA fragments were purified by phenol-chloroform extraction and ethanol precipitation. The purified DNA was subjected to PCR amplification using the primers specific for the region (− 597 to − 318) containing the distal AP-1 binding site (− 503 to − 497) present in the MMP-9 promoter region, sense primer: 5'-AGAGCCTGCTCCCAGAGGGC-3'; antisense primer: 5'-GCCAAGTCAGGCAGGACCCC-3'. PCR fragments were analyzed on 2% agarose in 1× TAE gel containing ethidium bromide and the size (279 bp) was compared to a molecular weight marker.

## Plasmid Construction, Transfection, and Luciferase Reporter Gene Assays

The upstream region (− 1280 to + 19) of the rat MMP-9 promoter was cloned to the pGL3-basic vector containing the luciferase reporter system [30]. All plasmids were prepared by using QIAGEN plasmid DNA preparation kits. These constructs were transfected into RBA cells by using a Lipofectamine reagent according to the instructions of manufacture. The transfection efficiency (~ 60%) was determined by transfection with enhanced GFP. After incubation with BK, cells were collected and disrupted by sonication in lysis buffer (25 mM Tris, pH 7.8, 2 mM EDTA, 1% Triton X-100, and 10% glycerol). After centrifugation, aliquots of the supernatants were tested for promoter activity using a luciferase assay system (Promega, Madison, WI). Firefly luciferase activities were standardized for  $\beta$ -galactosidase activity.

## Preparation of BK-Challenged Astrocytic-Conditioned Culture Medium

For collection of conditioned media, RBA cells were plated and incubated with BK for 24 h (BK-CM). Cell-free supernatant fractions were applied to human neuroblastoma SK-N-SH cells to evaluate the changes in cell viability and related parameters in the study.

## Cytotoxicity Assay

Cells were grown in 24-well culture plates at a concentration of  $5 \times 10^4$  cells/well followed by treatment. Five-microliter Cell Counting Kit-8 (CCK-8) solution (Sigma) in 500- $\mu$ l growth medium was added to each well. After incubation with CCK-8 at 37 °C for 2 h, cultured medium was collected. The water-soluble tetrazolium salt, a product of CCK-8 by the action of mitochondrial dehydrogenases, was solubilized in cultured medium and quantified spectrophotometrically at 450 nm, reference at 650 nm.

## Apoptosis Assay

Hoechst 33342 staining was performed as previously described [31], with some modifications. In brief, attached cells were washed with PBS and stained with 1  $\mu$ g/ml Hoechst 33342 in the dark for 10 min. Following rinsing with PBS and mounting on glass slides, at least 300 cells per condition were observed using a fluorescence microscope. The two cell populations (normal and apoptotic cells) were counted for Hoechst 33342 staining with chromatin. The Hoechst 33342, a kind of blue fluorescent dye, which stains the condensed chromatin in apoptotic cells, was brighter than that of normal cells. Apoptotic cells were also identified on the basis of morphology and condensation and fragmentation of nuclei.

## Statistical Analysis of Data

All data were estimated using GraphPad Prism 5 Program (GraphPad, San Diego, CA). Quantitative data were analyzed by one-way ANOVA followed by Tukey's honestly significant difference tests between individual groups. Data were expressed as mean  $\pm$  SEM. A value of  $P < 0.05$  was considered significant.

## Results

### Effects of DHEAS on BK-Induced MMP-9 Expression in Rat Brain Astrocytes

Our previous study has indicated that BK can up-regulate MMP-9 expression in brain astrocytes [29]. First, to evaluate whether DHEAS reduces BK-induced MMP-9 expression in RBA cells, cells were pretreated with DHEAS (1 mM) and then incubated with BK (10 nM) for the indicated time intervals. As shown in Fig. 1a, pretreatment with DHEAS significantly reduced (~ 65.8% at 24 h) BK-induced MMP-9 expression by the gelatin zymography. Pretreatment with DHEAS also inhibited (~ 60.8% at 24 h) BK-induced MMP-9 protein expression by Western blot analysis (Fig. 1b). Moreover, pretreated with various concentrations of DHEAS



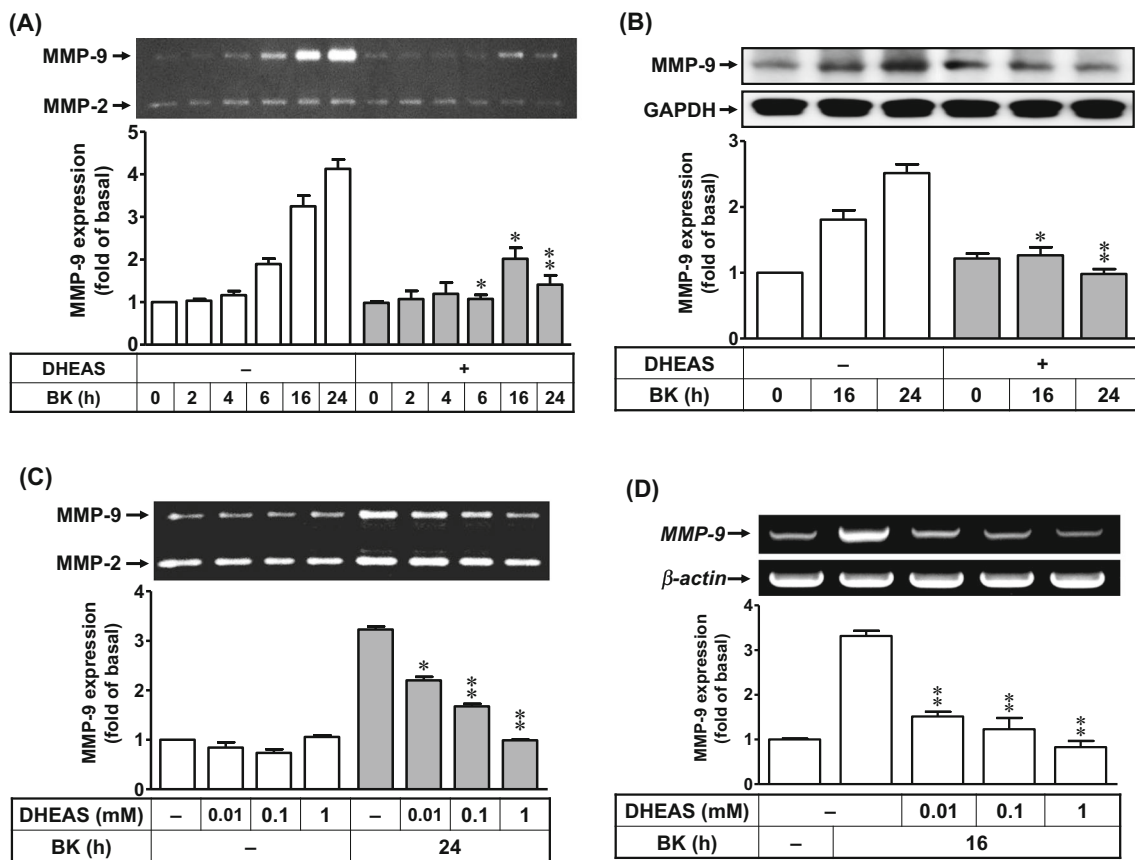


**Fig. 1** Effect of DHEAS on BK-induced MMP-9 expression in rat brain astrocytes (RBA). **a**, **b** Time dependence of DHEAS inhibited BK-induced MMP-9 activity and expression, cells were pretreated with or without DHEAS (1 mM) and then incubated with BK (10 nM) for the indicated time intervals. **c** Cells were pretreated with various concentrations of DHEAS (0.01, 0.1, and 1 mM) and then incubated with BK (10 nM) for 24 h. The conditioned media were collected and

assayed for MMP-9 expression and activity by gelatin zymography (**a**, **c**) and Western blot (**b**). **d** DHEAS concentration-dependently inhibited BK-induced MMP-9 mRNA expression. The MMP-9 mRNA was analyzed by RT-PCR as described in Methods. Data are expressed as the mean  $\pm$  SEM ( $N=3$ ). \* $P<0.05$ ; \*\* $P<0.01$ , as compared with the respective values of cells stimulated with BK only. The figure represents one of three individual experiments

(0.01, 0.1, or 1 mM) attenuated ( $\sim 32.9$ ,  $\sim 49.1$ , and  $\sim 70.1\%$ ) BK-induced MMP-9 expression in a concentration-dependent manner by the gelatin zymography (Fig. 1c). Next, to check whether DHEAS affect the BK-induced MMP-9 mRNA expression in RBA cells, cells were pretreated with various concentrations of DHEAS (0.01, 0.1, or 1 mM) for 1 h and then treated with BK for 16 h. The data showed that DHEAS concentration-dependently blocked BK-induced MMP-9 mRNA expression by RT-PCR analysis (Fig. 1d,  $\sim 54.5$ ,  $\sim 63.6$ , and  $\sim 75.8\%$ ). These results demonstrated that DHEAS can repress BK-induced MMP-9 protein and mRNA expression in RBA cells.

### DHEAS Reduces BK-Stimulated Phosphorylation of Protein Kinases, Including c-Src and PYK2 in RBA Cells

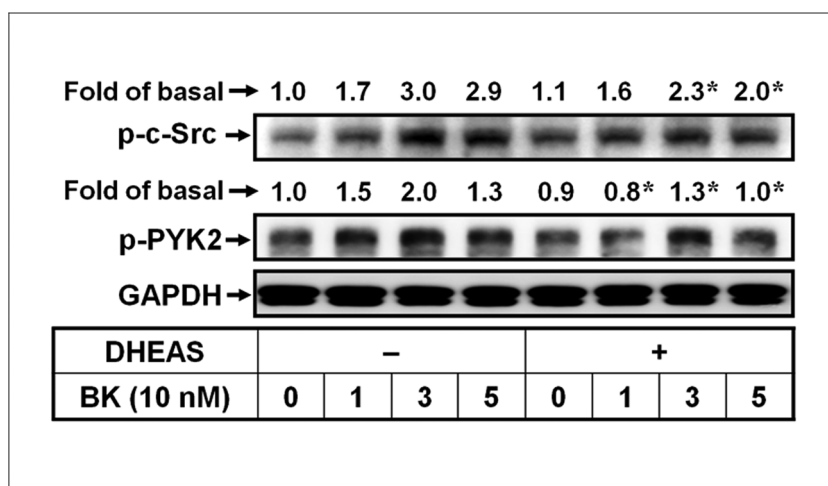
Several protein kinases, including c-Src and PYK2, have been shown to participate in MMP-9 expression in various cell types [34]. Our recent study has indicated that BK-

stimulated several protein kinases activation in brain astrocytes, including c-Src [35]. Here, we investigated whether DHEAS attenuates BK-induced MMP-9 expression via blocking activation of these related protein kinases. The cells were pretreated with DHEAS (1 mM) for 1 h and then incubated with BK for the indicated times. As shown in Fig. 2, BK stimulated time-dependently phosphorylation of c-Src and PYK2 at 1–5 min in RBA cells, which were significantly inhibited (p-c-Src:  $\sim 23.3\%$  at 3 min; p-PYK2:  $\sim 35.0\%$  at 3 min) by pretreatment with DHEAS. The results suggested that in RBA, DHEAS-reduced BK-induced MMP-9 expression may be mediated through attenuating activation of several protein kinases (i.e., c-Src and PYK2)-dependent pathways.

### Anti-Oxidative Effects of DHEAS on BK-Induced Nox-Dependent ROS Production

Recent report has indicated that ROS may contribute to MMP expression in various cell types [36]. The NADPH oxidase (Nox) is considered to be a major source of ROS in many

**Fig. 2** DHEAS inhibits BK-stimulated phosphorylation of protein kinases, including c-Src and PYK2 in RBA cells. Cells were pretreated with or without DHEAS (1 mM) and then incubated with BK (10 nM) for the indicated time intervals. The cell lysates were collected and analyzed by Western blot as described in Methods. Data are expressed as the mean  $\pm$  SEM ( $N = 3$ ). \* $P < 0.05$ ; \*\* $P < 0.01$ , as compared with the respective values of cells stimulated with BK only. The figure represents one of three individual experiments



physiological and pathological processes [22, 37]. Previous studies have demonstrated that Nox-derived ROS signaling cascade is involved in BK-induced MMP-9 expression in astrocytes [28]. Thus, to determine whether DHEAS-reduced MMP-9 induction by BK is due to decreasing Nox-dependent ROS production, the Nox activity and ROS production were detected. As shown in Fig. 3 (open bar), pretreatment with DHEAS (1 mM) markedly reduced ( $\sim 51.5\%$ ) BK-stimulated Nox activity. Next, to observe whether DHEAS also influence on BK-increased ROS production, a ROS probe DCF-DA was used. The data showed that BK-stimulated ROS production was attenuated ( $\sim 56.4\%$ ) by pretreatment with DHEAS (Fig. 3, gray bar). These data demonstrated that DHEAS can inhibit BK-stimulated Nox/ROS signal in RBA cells, suggesting that DHEAS may be possessed of anti-oxidative activity in the event.

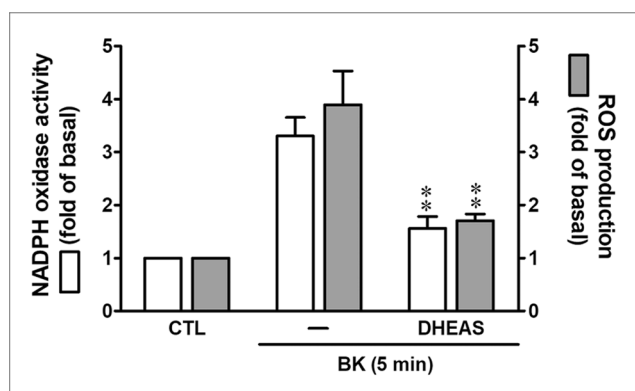


**Fig. 3** Roles of DHEAS in BK-stimulated NADPH oxidase activity and ROS generation in RBA cells. Cells were pretreated with DHEAS (1 mM) and then incubated with BK (10 nM) for 5 min. The Nox activity (open bar) was analyzed as described in Methods. Moreover, cells were incubated with the DCF-DA (5  $\mu$ M) for 45 min, followed by pretreatment with DHEAS (1 mM) and stimulation with BK for 5 min. The fluorescence intensity (gray bar: ROS generation) of cells was determined as described in Methods. Data are expressed as the mean  $\pm$  SEM ( $N = 3$ ). \*\* $P < 0.01$ , as compared with the respective values of cells stimulated with BK only

### DHEAS Attenuates BK-Stimulated ERK1/2 and Akt Activation in RBA Cells

Recently, the ROS-dependent activation of MAPKs has been indicated to participate in MMP-9 expression induced by various stimuli in brain astrocytes [38, 39]. Our previous data have also demonstrated that MAPKs such as ERK1/2 contribute to BK-induced MMP-9 expression in astrocytes [29]. Therefore, we further explained whether DHEAS affects the BK-stimulated activation of MAPKs, in particular ERK1/2, the anti-phospho-MAPKs, including ERK1/2, JNK1/2, and p38 MAPK antibodies were used. As shown in Fig. 4a, pretreatment with DHEAS (1 mM) attenuated BK-stimulated phosphorylation of ERK1/2 ( $\sim 54.2\%$  at 3 min), but not p38 MAPK and JNK1/2 (data not shown). Moreover, previous data also indicated that BK induces MMP-9 expression via Akt pathway in astrocytes [29]. Here, we also investigated the effect of DHEAS on BK-stimulated Akt phosphorylation by Western blotting. The result showed that pretreatment with DHEAS (1 mM) reduced ( $\sim 66.7\%$  at 3 min) BK-stimulated phosphorylation of Akt (Fig. 4b). These results suggested that DHEAS inhibits BK-induced MMP-9 expression that is mediated through suppressing activation of ERK1/2 and Akt in RBA cells.

### Roles of DHEAS in BK-Stimulated Activation of Transcription Factors Such as AP-1

The AP-1-dependent pathways have been demonstrated to involve in MMP-9 expression in various cell types [40]. To determine whether DHEAS-reduced BK-induced MMP-9 gene expression is mediated through blocking up-regulation of transcription factor AP-1 (i.e., c-Fos), these signals were detected by RT-PCR analysis. The results showed that pretreatment of RBA with DHEAS significantly reduced BK-stimulated c-Fos/AP-1 gene expression (Fig. 5a). Moreover, previous studies reported that MMP-9 promoter region

**Fig. 4** DHEAS attenuates BK-stimulated activation of MAPKs (e.g., ERK1/2) and PI3K/Akt cascade in RBA cells. **a, b** Cells were pretreated with or without DHEAS (1 mM) and then incubated with BK (10 nM) for the indicated time intervals. The cell lysates were collected and analyzed phosphorylation of ERK1/2 (**a**) and Akt (**b**) by Western blot as described in Methods. Data are expressed as the mean  $\pm$  SEM ( $N=3$ ). \* $P<0.05$ ; \*\* $P<0.01$ , as compared with the respective values of cells stimulated with BK only. The figure represents one of three individual experiments

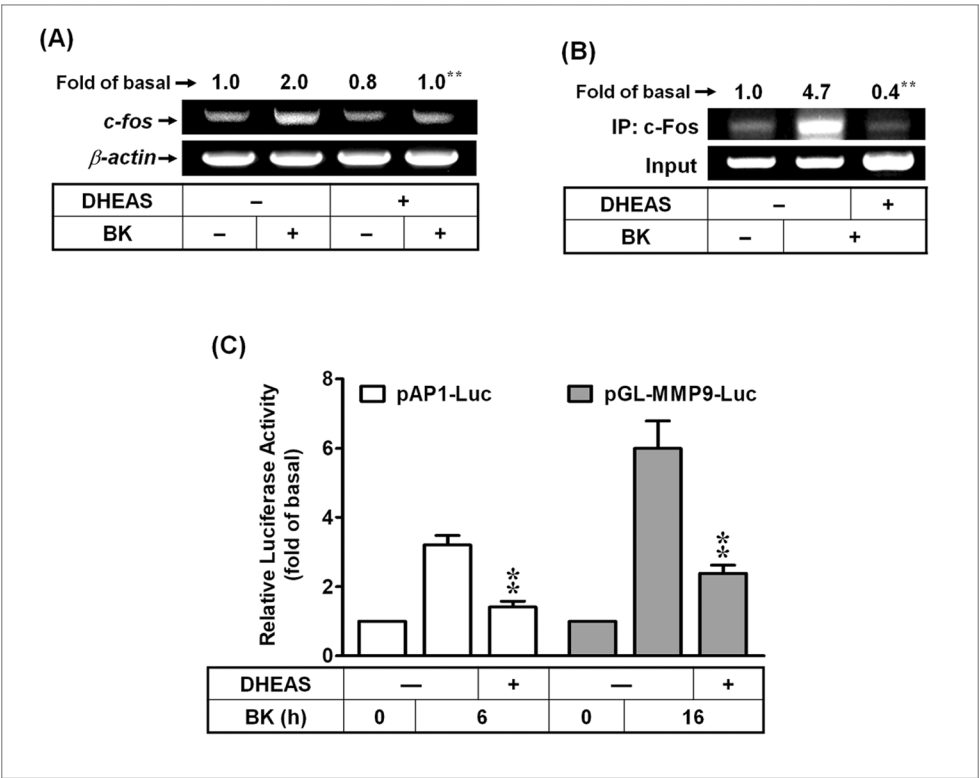
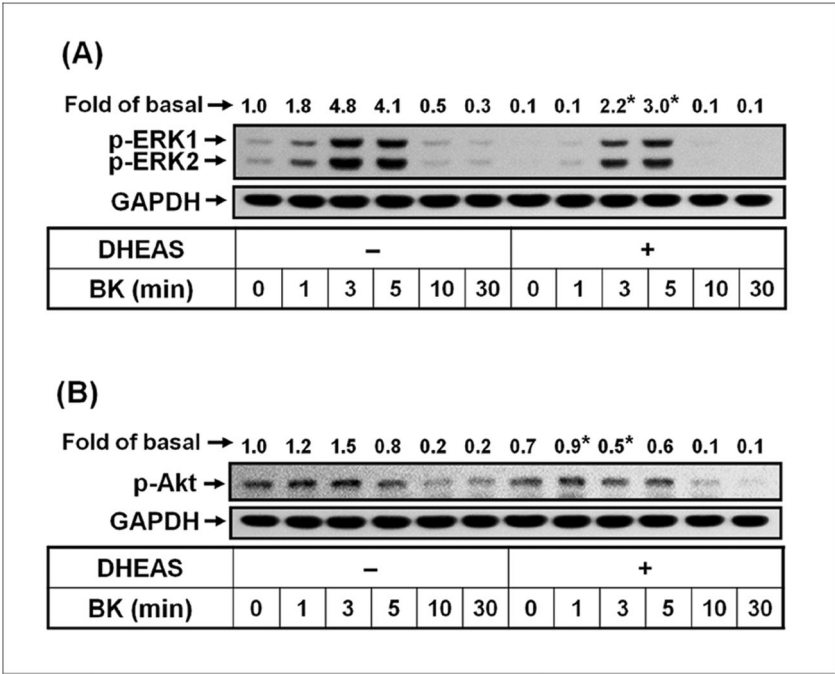


**Fig. 5** DHEAS blocks BK-upregulated the transcription factor *c-fos* expression and the recruitment of c-Fos to the MMP-9 promoter in RBA cells. **a** Cells were pretreated with DHEAS (1 mM) and then incubated with BK (10 nM) for 15 min. The total RNA was collected and analyzed *c-fos* mRNA expression by RT-PCR analysis as described in Methods. **b** BK stimulated the recruitment of c-Fos to the MMP-9 promoter, cells were pretreated with DHEAS (1 mM) and then incubated with BK (10 nM) for 30 min. The ChIP-PCR assays were performed using an anti-c-Fos antibody. **c** Cells were transiently

cotransfected with pAP1-Luc or pGL-MMP9-Luc and pGal for 24 h, pretreated with DHEAS for 1 h, and then incubated with BK for 6 or 16 h. After stimulation, luciferase activity of AP-1- or MMP-9-promoter construct were measured as relative promoter activity to that of  $\beta$ -galactosidase. Data are expressed as the mean  $\pm$  SEM ( $N=3$ ). \* $P<0.05$ ; \*\* $P<0.01$ , as compared with the respective values of cells stimulated with BK only. The figure represents one of three individual experiments

contains AP-1 binding sites [41]. Hence, we used ChIP-PCR assay to determine the effects of DHEAS on BK-stimulated recruitment of c-Fos/AP-1 to MMP-9 promoter. We designed a pair of primers for MMP-9 promoter (−597 to −318) region, containing an AP-1 binding site. Chromatin was immunoprecipitated using an anti-c-Fos antibody, and then, the MMP-9 promoter region (−597 to −318) was amplified by PCR. As shown in Fig. 5b, BK stimulated binding of c-Fos to the MMP-9 promoter at 30 min, which was blocked by pretreatment with DHEAS (1 mM), indicating that DHEAS repressed BK-enhanced recruitment of c-Fos/AP-1 to MMP-9 promoter in RBA cells. We next examined whether DHEAS also reduces BK-induced AP-1 and MMP-9 promoter activity, a promoter containing AP-1 binding sites (pAP1-Luc) and a rat MMP-9 promoter reporter constructs (pGL-MMP-9-Luc) were used [28, 41]. The data showed that pretreatment with DHEAS significantly attenuated BK-increased AP-1 (~54.8%) and MMP-9 (~60.0%) promoter activity (Fig. 5c), suggesting that DHEAS plays a suppressor in BK-induced MMP-9 expression via inhibiting c-Fos/AP-1-mediated MMP-9 transcription activity in RBA cells.

### DHEAS May Play a Neuroprotective Role via Inhibiting BK-Induced MMP-9-Related Events

MMP-9 has been reported to be elevated in various brain injuries and participates in the pathogenesis of several CNS disorders. BK-induced MMP-9 increase has been shown to involve in astrocyte migration and neuronal cell apoptosis [30, 31]. Therefore, we further investigated the effects of DHEAS on BK-induced MMP-9-mediated cellular function changes, including the RBA cell migration and neuronal cell death. First, the images of RBA cell migration induced by BK (10 nM) were observed and taken at 48 h. Pretreatment with DHEAS (1 mM) significantly blocked (~57.9%) BK-induced RBA cell migration (Fig. 6a, upper panel). The number of migratory RBA cells was counted, and the statistical data are presented in Fig. 6a (lower panel). The results demonstrated that DHEAS can block BK-induced cell migration via reducing expression of MMP-9 in brain astrocytes.

Next, to investigate the effects of DHEAS on BK-challenged astroglial MMP-9-mediated neuronal cell viability, various astrocytic conditioned culture media were preparation and a human neuroblastoma SK-N-SH cell line was used. The procedure for the experiments is shown in Fig. 6b. First, the RBA cells were pretreated with or without DHEAS (1 mM) for 1 h and treated by BK (10 nM) for 24 h, and then, the conditioned media (CM) were collected as CTL-CM, BK-CM, and DHEAS/BK-CM for the following experiments. Subsequently, the SK-N-SH cells were incubated with CTL-CM, BK-CM, or DHEAS/BK-CM for 24 h, respectively, and the cell viability was detected by XTT assay. As shown in Fig. 6c, the cell viability of SK-N-SH was reduced about 40%

(from 97 to 58%) by incubation with BK-CM. Compared to the result of BK-CM, treatment of cells with DHEAS/BK-CM was ineffective in the SK-N-SH cell viability (about 97%). Here, to demonstrate the effects of DHEAS on BK-challenged astroglial MMP-9-mediated neuronal cell apoptosis, the apoptotic events were observed and detected by a cell permeable blue-fluorescence DNA dye, Hoechst 33342 after treatment of SK-N-SH cells with CTL-CM, BK-CM, or DHEAS/BK-CM for 24 h. The statistical data of apoptotic nuclei counting are shown in Fig. 6d, indicating that BK-CM markedly induced SK-N-SH cell apoptosis about 35% (from 1 to 36%). Similarly, DHEAS/BK-CM has not significantly induced the SK-N-SH cell apoptosis (about 7%). These results suggested that the endogenous natural steroid DHEAS may play a critical role in anti-inflammation and neuroprotection through inhibiting up-regulation of MMP-9 from BK-challenged RBA cells.

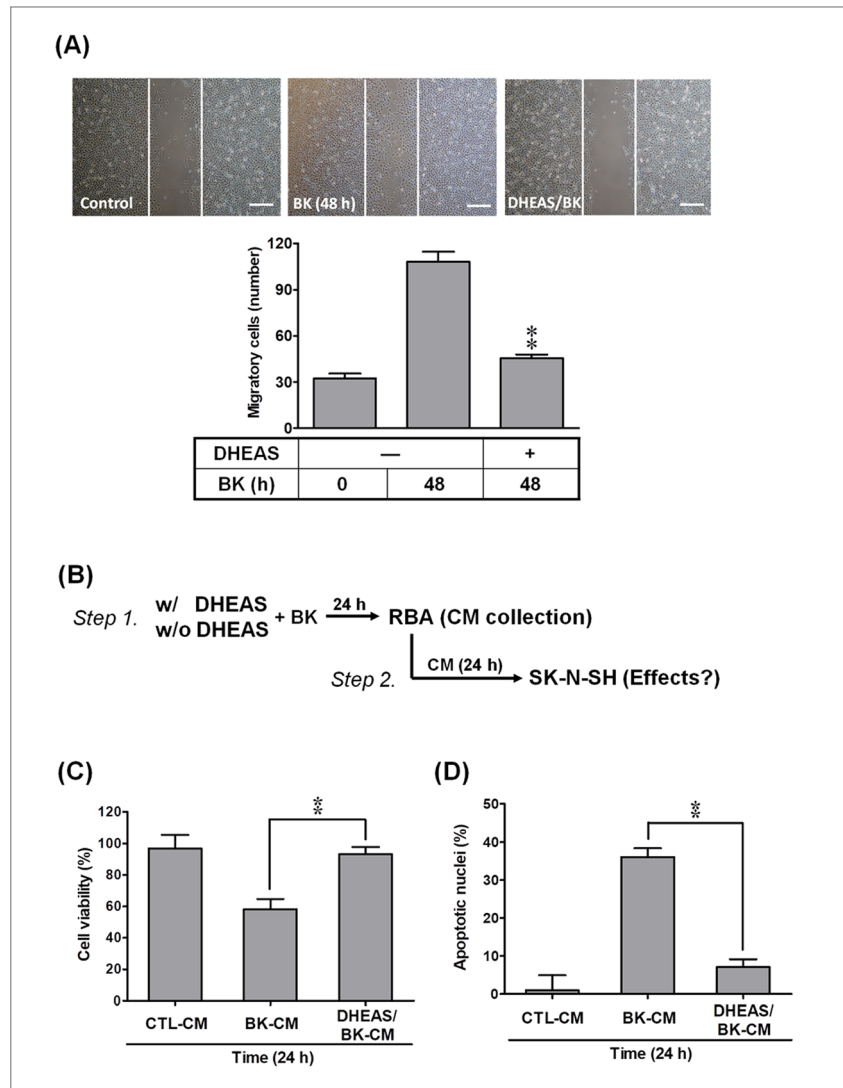
## Discussion

MMPs contribute to a wide range of biological activities in different tissues, including several CNS diseases, such as stroke, Alzheimer's disease, and malignant glioma [16]. Among MMPs, MMP-9 expression and activation play a critical role in tissue remodeling in the pathogenesis of brain diseases [16]. Reduction of MMP activity by pharmacological inhibitors or gene knock-out strategies protects the brain from advanced neuroinflammation [42]. These studies suggest that up-regulation of MMP-9 by pro-inflammatory factors may be a great effect upon brain inflammation and neurodegeneration. Moreover, BK and related peptides are simultaneously produced and released following brain injury [43]. Our previous data have demonstrated that BK induces MMP-9 expression in astrocytes which may change astrocytic functions such as cell motility and neuroinflammation [28, 31]. These findings imply that BK may play an important role in brain injury, astrogloma, or CNS diseases. Pharmacological and knockout-mouse approaches suggest that targeting MMP-9 and their upstream signaling pathways should yield useful therapeutic targets for brain injury and inflammation. Herein, we evaluate whether DHEAS possess anti-inflammatory and neuroprotective effects on BK-induced MMP-9 expression in brain astrocytes and its mechanism. In this study, we found that DHEAS is a water-soluble product, its maximum solubility of about 0.2 M, thus the highest concentration of this study used only to 1 mM. Moreover, because the collected conditioned medium is then used to treat neuronal cells, the conditioned medium is collected to maintain sterility throughout the process.

First, we found that DHEAS can inhibit BK-induced MMP-9 gene expression in RBA cells (Fig. 1). This result is the first finding that DHEAS can suppress MMP-9 up-



**Fig. 6** Effects of DHEAS on BK-regulated MMP-9-related events, including cell migration or neuronal apoptosis. **a** Cells were plated on 6-well culture plates, grew to confluence, and starved with serum-free medium for 24 h. Cells were pretreated with DHEAS for 1 h and the monolayer cells were manually scratched with a blue tip as described in Methods, and then incubated with BK (10 nM) for 48 h. Phase contrast images of cells were taken at 48 h and the number of cell migration was counted as described in Methods (scale bar = 50  $\mu$ m). **b**, **c** Cells were pretreated with or without MMP2/9 inhibitor (2/9i, 1  $\mu$ M) or DHEAS (1 mM) for 1 h before exposure to BK-CM for 24 h. The cell viability was analyzed (**b**) and the number of apoptotic nuclei was counted (**c**), and the percentage was calculated as described in the Methods. Data are expressed as mean  $\pm$  SEM of three independent experiments ( $N = 3$ ).  $**P < 0.01$ , as compared with the values of cells stimulated with BK (**a**) or BK-CM (**b**, **c**) alone



regulation by BK in brain astrocytes. Next, many reports and our previous data have indicated that several protein kinases (e.g., c-Src or PKCs) may contribute to various stimuli-induced MMP-9 expression in brain astrocytes [28, 30, 44]. Moreover, several reports also demonstrate that PYK2 is crucial for MMP-9 expression [35]. Thus, we investigated whether the inhibition of DHEAS is mediated through blocking the activation of protein kinase signals by BK in brain astrocytes. The results showed that pretreatment with DHEAS attenuated BK-stimulated phosphorylation of c-Src and PYK2 in RBA cells (Fig. 2), demonstrating that DHEAS may inhibit BK-induced MMP-9 expression via reducing protein kinases (i.e., c-Src and PYK2)-relative pathways in RBA cells.

Redox imbalance has been shown to play a causative role in numerous pathologies of degenerative diseases [25]. ROS concentration dependently exerts a key role in the normal physiological functions and the inflammatory responses [23]. In the brain, ROS also extend to the control of vascular

tone which is tightly modulated by metabolic activity within neurons [24]. Moreover, increasing ROS generation by diverse stimuli can regulate the expression of inflammatory genes in pathogenesis of brain disorders [45]. Recently, the cellular damage in neurodegenerative disorders such as Alzheimer's disease (AD) is attributed to oxidative stress in brain inflammatory disorders [21, 25]. In astrocytes, our recent data have demonstrated that in both in vitro and in vivo studies, BK induced MMP-9 expression via Nox-dependent ROS generation in brain astrocytes [28]. In the study, we further demonstrated that DHEAS may have an anti-oxidative activity function (Fig. 3). Herein, we are the first group to establish that DHEAS reduce Nox/ROS signal induced by BK in brain astrocytes. The finding is consistent with previous studies that indicated that a DHEAS analog, DHEA, has an anti-oxidative effect on endothelial cells and Leydig cells [46, 47].

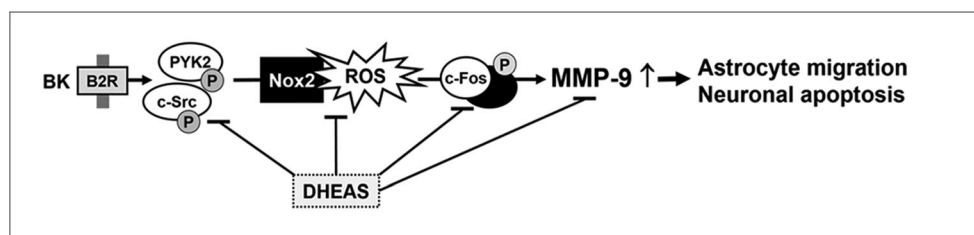


**Fig. 7** Schematic presentation of the effects of DHEAS on the BK-induced MMP-9 expression and its related events. In brain astrocytes (RBA cells), BK induces ERK1/2 activation through c-Src/PYK2, and Nox-derived ROS signals resulting in c-Fos/AP-1-dependent MMP-9 expression. This result leads to RBA cell migration and neuronal cell

death. The RBA-derived MMP-9-related events, including cell migration and neuronal apoptosis, were suppressed by DHEAS through reducing activation of c-Src/PYK2, Nox/ROS, ERK1/2, and c-Fos/AP-1 signaling pathways

Abnormal MAPK regulation might be implicated in several models of CNS inflammation and injury [18]. Moreover, BK has been reported to act as an important inflammatory mediator through activation of MAPK cascades in different cell types [48, 49]. Previously, we have demonstrated that MAPKs such as ERK were essentially required for BK-induced MMP-9 expression [28, 30]. Here, our data showed that DHEAS may reduce MMP-9 expression via inhibiting BK-stimulated ERK1/2 MAPKs activation in RBA cells (Fig. 4a). In addition to MAPKs, BK-stimulated activation of PKB/Akt has also been demonstrated in many cell types [50, 51]. Moreover, PKB/Akt has been linked to induction of MMPs such as MMP-9 [52]. The previous study has demonstrated that BK induces MMP-9 expression that is mediated through PI3K/Akt cascades in brain astrocytes [29]. Here, we found that DHEAS may inhibit MMP-9 expression through blocking BK-stimulated Akt activation in RBA cells (Fig. 4b). These findings are consistent with previous reports that showed that DHEAS can inhibit thrombin-dependent activation of Akt and ERK1/2 in platelet function [53]. Moreover, another study indicated that the antiviral activity of DHEA occurs via a mechanism independent of its ability to modulate ERK phosphorylation [54]. In contrast, the previous study showed that midazolam anesthesia protects neuronal cells from oxidative stress-induced death via activation of the MAPKs (JNK and ERK) pathway. [55]. These differences suggest that the nature of its effects may vary in a stimuli-dependent or cell-type-specific manner.

The progressive increase of oxidative stress during injuries not only causes oxidative damage to cellular macromolecules, but also modulates the pattern of gene expression through functional alterations of transcription factors. The transcription factors such as AP-1 play a key role in the regulation of several gene expressions including MMP-9 associated with physiological and pathological events [56]. In addition, several reports also indicate that AP-1 is involved in the pathogenesis of brain inflammation [40]. In the CNS, various stimuli (e.g., BK) can induce expression of several inflammatory mediators such as MMP-9 through ROS-mediated activation of AP-1 manner in astrocytes [40]. Recently, we have

demonstrated that AP-1 participates in the expression of several genes including MMP-9 by BK through ROS-dependent manner [28]. These results implicate that AP-1 play a central role in regulating MMP-9 expression and lead to inflammatory gene expression in pathological events including the CNS inflammation. Therefore, we focus on the effects of DHEAS on BK-stimulated activation of these transcription factors (e.g., AP-1) in RBA cells. The results showed that BK-stimulated activation of AP-1 (c-Fos induction), recruitment of c-Fos/AP-1 to the MMP-9 promoter, and AP-1 and MMP-9 promoter activity were inhibited by DHEAS (Fig. 5a–c). These results suggested that DHEAS may alleviate up-regulation of MMP-9 by BK through inhibiting activation of the transcription factor AP-1 in brain astrocytes.

In conclusions, our previous study showed that BK directly induces MMP-9 expression via c-Src/PYK2-mediated Nox/ROS and ERK1/2 signals, linking to activation of c-Fos/AP-1, which results in the brain astrocytes (RBA cells) migration and neuronal cell (SK-N-SH) apoptosis. Based on the observations from literatures and our findings, Fig. 7 depicts a model for the inhibitory action of DHEAS on BK-induced MMP-9-dependent events, including RBA cell migration and neuronal cell apoptosis. Herein, the results showed that in brain astrocytes, DHEAS reduced BK-induced MMP-9-dependent astrocytic migration is mediated through inhibition of the protein kinases (e.g., c-Src and PYK2)-activated Nox/ROS and ERK1/2 signals leading to induction of c-Fos/AP-1 pathways. Moreover, DHEAS can also inhibit BK-induced MMP-9-mediated neuronal cell apoptosis via the same mechanism. These findings concerning the endogenous steroid DHEAS-reduced BK-induced MMP-9 expression in brain astrocytes imply that DHEAS may play a critical role in the anti-oxidative and anti-inflammatory properties which may contribute to its protective effects in several brain inflammatory disorders. Therefore, the inhibition of MMP-9-mediated inflammatory pathways by DHEAS may provide therapeutic strategies to brain inflammation and neurodegenerative diseases. In the future, the results may be applied to clinic by increase DHEAS levels in vivo by diet or giving DHEAS

directly to brain disordered patients with low DHEAS, which might reduce or treat the brain-related inflammatory disorders.

**Acknowledgements** This work was supported by the Ministry of Science and Technology, Taiwan; Grant number: NSC102-2320-B-255-005-MY3 and MOST106-2320-B-255-005; Chang Gung Medical Research Foundation, Grant number: CMRPF1C0193, CMRPF3D0033, CMRPF1F0131, and CMRPF1F0132. We thank Ms. Yin-Chen Chen and Shu-Ching Hsu for their technical assistance. We also thank Professor Ying-Tung Lau for his support.

## Compliance with Ethical Standards

**Conflict of Interest** The authors declare that they have no conflict of interest.

## References


- Baulieu EE (1996) Dehydroepiandrosterone (DHEA): A fountain of youth? *J Clin Endocrinol Metab* 81:3147–3151
- Vermeulen A (1995) Dehydroepiandrosterone sulfate and aging. *Ann N Y Acad Sci* 774:121–127
- Charalampopoulos I, Alexaki VI, Tsatsanis C, Minas V, Dermizaki E, Lasaridis I, Vardouli L, Stourmaras C et al (2006) Neurosteroids as endogenous inhibitors of neuronal cell apoptosis in aging. *Ann N Y Acad Sci* 1088:139–152
- Chasalow FI, Blethen SL (1990) Digitalis-like materials and DHEA sulfate. In: Kalimi M, Regelson W (eds) *The biology role of Dehydroepiandrosterone (DHEA)*. Walter de Gruyter press, Berlin, pp. 317–330
- Compagnone NA, Mellon SH (2000) Neurosteroids: Biosynthesis and function of these novel neuromodulators. *Front Neuroendocrinol* 21:1–56
- Ueda H, Yoshida A, Tokuyama S, Mizuno K, Maruo J, Matsuno K, Mita S (2001) Neurosteroids stimulate G protein-coupled sigma receptors in mouse brain synaptic membrane. *Neurosci Res* 41:33–40
- Dong L, Zhu Y, Dong Y, Yang J, Zhao Y, Qi Y, Wu P, Zhu Y et al (2009) Neuroactive steroid dehydroepiandrosterone sulfate inhibits 5-hydroxytryptamine (5-HT)-evoked glutamate release via activation of sigma-1 receptors and then inhibition of 5-HT<sub>3</sub> receptors in rat prefrontal cortex. *J Pharmacol Exp Ther* 330:494–501
- Chen L, Dai XN, Sokabe M (2006) Chronic administration of dehydroepiandrosterone sulfate (DHEAS) primes for facilitated induction of long-term potentiation via sigma 1 (sigma1) receptor: Optical imaging study in rat hippocampal slices. *Neuropharmacology* 50:380–392
- Luppi C, Fioravanti M, Bertolini B, Inguscio M, Grugnetti A, Guerriero F, Rovelli C, Cantoni F et al (2009) Growth factors decrease in subjects with mild to moderate Alzheimer's disease (AD): Potential correction with dehydroepiandrosterone-sulphate (DHEAS). *Arch Gerontol Geriatr* 49(Suppl 1):173–184
- Wang Y, Rao M (1998) Effects of dehydroepiandrosterone sulfate on mimetic aging actions of cerebral cortex of fetal rats in vitro. *Yao Xue Xue Bao* 33:413–417
- Zhang L, Li B, Ma W, Barker JL, Chang YH, Zhao W, Rubinow DR (2002) Dehydroepiandrosterone (DHEA) and its sulfated derivative (DHEAS) regulate apoptosis during neurogenesis by triggering the Akt signaling pathway in opposing ways. *Brain Res Mol Brain Res* 98:58–66
- Leskiewicz M, Regulski M, Budziszewska B, Jantas D, Jaworska-Feil L, Basta-Kaim A, Kubera M, Jagla G et al (2008) Effects of neurosteroids on hydrogen peroxide- and staurosporine-induced damage of human neuroblastoma SH-SY5Y cells. *J Neurosci Res* 86:1361–1370
- Di Santo E, Foddi MC, Ricciardi-Castagnoli P, Mennini T, Ghezzi P (1996) DHEAS inhibits TNF production in monocytes, astrocytes and microglial cells. *Neuroimmunomodulation* 3:285–288
- Dollery CM, McEwan JR, Henney AM (1995) Matrix metalloproteinases and cardiovascular disease. *Circ Res* 77:863–868
- Yong VW, Krekoski CA, Forsyth PA, Bell R, Edwards DR (1998) Matrix metalloproteinases and diseases of the CNS. *Trends Neurosci* 21:75–80
- Yong VW, Power C, Forsyth P, Edwards DR (2001) Metalloproteinases in biology and pathology of the nervous system. *Nat Rev Neurosci* 2:502–511
- Gottschall PE, Yu X (1995) Cytokines regulate gelatinase a, B (matrix metalloproteinase 2 and 9) activity in cultured rat astrocytes. *J Neurochem* 64:1513–1520
- Lee WJ, Shin CY, Yoo BK, Ryu JR, Choi EY, Cheong JH, Ryu JH, Ko KH (2003) Induction of matrix metalloproteinase-9 (MMP-9) in lipopolysaccharide-stimulated primary astrocytes is mediated by extracellular signal-regulated protein kinase 1/2 (Erk1/2). *Glia* 41:15–24
- Hsieh HL, Yang CM (2013) Role of redox signaling in neuroinflammation and neurodegenerative diseases. *Biomed Res Int* 2013:484613, 1, 18.
- Demchenko IT, Oury TD, Crapo JD, Piantadosi CA (2002) Regulation of the brain's vascular responses to oxygen. *Circ Res* 91:1031–1037
- Halliwell B (2006) Oxidative stress and neurodegeneration: Where are we now? *J Neurochem* 97:1634–1658
- Chrissobolis S, Faraci FM (2008) The role of oxidative stress and NADPH oxidase in cerebrovascular disease. *Trends Mol Med* 2008(14):495–502
- Kamata H, Hirata H (1999) Redox regulation of cellular signalling. *Cell Signal* 11:1–14
- Chan PH (2001) Reactive oxygen radicals in signaling and damage in the ischemic brain. *J Cereb Blood Flow Metab* 21:2–14
- Lewén A, Matz P, Chan PH (2000) Free radical pathways in CNS injury. *J Neurotrauma* 17:871–890
- Qin L, Liu Y, Wang T, Wei SJ, Block ML, Wilson B, Liu B, Hong JS (2004) NADPH oxidase mediates lipopolysaccharide-induced neurotoxicity and proinflammatory gene expression in activated microglia. *J Biol Chem* 279:1415–1421
- Chiang WC, Chien CT, Lin WW, Lin SL, Chen YM, Lai CF, Wu KD, Chao J et al (2006) Early activation of bradykinin B2 receptor aggravates reactive oxygen species generation and renal damage in ischemia/reperfusion injury. *Free Radic Biol Med* 41:1304–1314
- Lin CC, Hsieh HL, Shih RH, Chi PL, Cheng SE, Chen JC, Yang CM (2012) NADPH oxidase 2-derived reactive oxygen species signal contributes to bradykinin-induced matrix metalloproteinase-9 expression and cell migration in brain astrocytes. *Cell Commun Signal* 10:35
- Hsieh HL, Yen MH, Jou MJ, Yang CM (2004) Intracellular signalings underlying bradykinin-induced matrix metalloproteinase-9 expression in rat brain astrocyte-1. *Cell Signal* 16:1163–1176
- Hsieh HL, Wu CY, Yang CM (2008) Bradykinin induces matrix metalloproteinase-9 expression and cell migration through a PKC- $\delta$ -dependent ERK/Elk-1 pathway in astrocytes. *Glia* 56:619–632
- Yang CM, Hsieh HL, Lin CC, Shih RH, Chi PL, Cheng SE, Hsiao LD (2013) Multiple factors from bradykinin-challenged astrocytes contribute to the neuronal apoptosis: Involvement of astroglial ROS, MMP-9, and HO-1/CO system. *Mol Neurobiol* 47:1020–1033
- LeBel CP, Ischiropoulos H, Bondy SC (1992) Evaluation of the probe 2',7'-dichlorofluorescein as an indicator of reactive oxygen

- species formation and oxidative stress. *Chem Res Toxicol* 5:227–231
33. Reinehr R, Görg B, Becker S, Qvartskhava N., Bidmon HJ, Selbach, O, Haas HL, Schliess F, Häussinger D (2007) Hypoosmotic swelling and ammonia increase oxidative stress by NADPH oxidase in cultured astrocytes and vital brain slices. *Glia* 55:758–771.
  34. Lee HS, Moon C, Lee HW, Park EM, Cho MS, Kang JL (2007) Src tyrosine kinases mediate activations of NF-kappaB and integrin signal during lipopolysaccharide-induced acute lung injury. *J Immunol* 179:7001–7011
  35. Yang CM, Yang SH, Lee TH, Fang JY, Lin CF, Jou MJ, Hsieh HL (2016) Evaluation of anti-inflammatory effects of *Helminthostachys zeylanica* extracts via inhibiting bradykinin-induced MMP-9 expression in brain astrocytes. *Mol Neurobiol* 53:5995–6005
  36. Nelson KK, Melendez JA (2004) Mitochondrial redox control of matrix metalloproteinases. *Free Radic Biol Med* 37:768–784
  37. Infanger DW, Sharma RV, Davisson RL (2006) NADPH oxidases of the brain: Distribution, regulation, and function. *Antioxid Redox Signal* 8:1583–1596
  38. Hsieh HL, Wang HH, Wu WB, Chu PJ, Yang CM (2010) Transforming growth factor- $\beta$ 1 induces matrix metalloproteinase-9 and cell migration in astrocytes: Roles of ROS-dependent ERK- and JNK-NF- $\kappa$ B pathways. *J Neuroinflammation* 7:88
  39. Ralay Ranaivo H, Hodge JN, Choi N, Wainwright MS (2012) Albumin induces upregulation of matrix metalloproteinase-9 in astrocytes via MAPK and reactive oxygen species-dependent pathways. *J Neuroinflammation* 9:68
  40. Hsieh HL, Yang CM (2013) Role of redox signaling in neuroinflammation and neurodegenerative diseases. *Biomed Res Int* 2013:484613
  41. Sato H, Seiki M (1993) Regulatory mechanism of 92 kDa type IV collagenase gene expression which is associated with invasiveness of tumor cells. *Oncogene* 8:395–405
  42. Rosenberg GA (2002) Matrix metalloproteinases in neuroinflammation. *Glia* 39:279–291
  43. Kamiya T, Katayama Y, Kashiwagi F, Terashi A (1993) The role of bradykinin in mediating ischemic brain edema in rats. *Stroke* 24:571–575
  44. Wu CY, Hsieh HL, Sun CC, Tseng CP, Yang CM (2008) IL-1 $\beta$  induces proMMP-9 expression via c-Src-dependent PDGFR/PI3K/Akt/p300 cascade in rat brain astrocytes. *J Neurochem* 105:1499–1512
  45. Floyd RA (1999) Neuroinflammatory processes are important in neurodegenerative diseases: A hypothesis to explain the increased formation of reactive oxygen and nitrogen species as major factors involved in neurodegenerative disease development. *Free Radic Biol Med* 26:1346–1355
  46. Huerta-García E, Ventura-Gallegos JL, Victoriano ME, Montiel-Dávalos A, Tinoco-Jaramillo G, López-Marure R (2012) Dehydroepiandrosterone inhibits the activation and dysfunction of endothelial cells induced by high glucose concentration. *Steroids* 77:233–240
  47. Ding X, Wang D, Li L, Ma H (2016) Dehydroepiandrosterone ameliorates H<sub>2</sub>O<sub>2</sub>-induced Leydig cells oxidation damage and apoptosis through inhibition of ROS production and activation of PI3K/Akt pathways. *Int J Biochem Cell Biol* 70:126–139
  48. Liebmann C (2001) Bradykinin signalling to MAP kinase: Cell-specific connections versus principle mitogenic pathways. *Biol Chem* 382:49–55
  49. Schwaninger M, Sallmann S, Petersen N, Schneider A, Prinz S, Libermann TA, Spranger M (1999) Bradykinin induces interleukin-6 expression in astrocytes through activation of nuclear factor- $\kappa$ B. *J Neurochem* 73:1461–1466
  50. Srivastava S, Sharma K, Kumar N, Roy P (2014) Bradykinin regulates osteoblast differentiation by Akt/ERK/NF $\kappa$ B signaling axis. *J Cell Physiol* 229:2088–2105
  51. Fu C, Li B, Sun Y, Ma G, Yao Y (2015) Bradykinin inhibits oxidative stress-induced senescence of endothelial progenitor cells through the B2R/AKT/RB and B2R/EGFR/RB signal pathways. *Oncotarget* 6:24675–22489
  52. Kim D, Kim S, Koh H, Yoon SO, Chung AS, Cho KS, Chung J (2001) Akt/PKB promotes cancer cell invasion via increased motility and metalloproteinase production. *FASEB J* 15:1953–1962
  53. Bertoni A, Rastoldo A, Sarasso C, Di Vito C, Sampietro S, Nalin M, Bagarotti A, Sinigaglia F (2012) Dehydroepiandrosterone-sulfate inhibits thrombin-induced platelet aggregation. *Steroids* 77:260–268
  54. Torres NI, Castilla V, Bruttomesso AC, Eiras J, Galagovsky LR, Wachsmann MB (2012) In vitro antiviral activity of dehydroepiandrosterone, 17 synthetic analogs and ERK modulators against herpes simplex virus type 1. *Antivir Res* 95:37–48
  55. Liu JY, Guo F, Wu HL, Wang Y, Liu JS (2017) Midazolam anesthesia protects neuronal cells from oxidative stress-induced death via activation of the JNK-ERK pathway. *Mol Med Rep* 15:169–179
  56. Haddad JJ (2002) Oxygen-sensitive pro-inflammatory cytokines, apoptosis signaling and redox-responsive transcription factors in development and pathophysiology. *Cytokines Cell Mol Ther* 7:1–14



Review

# Use of Lipid Nanocarriers to Improve Oral Delivery of Vitamins

Ching-Yun Hsu <sup>1,2,†</sup>, Pei-Wen Wang <sup>3,†</sup>, Ahmed Alalaiwe <sup>4</sup>, Zih-Chan Lin <sup>5</sup> and Jia-You Fang <sup>2,6,7,8,\*</sup> 

<sup>1</sup> Department of Nutrition and Health Sciences, Chang Gung University of Science and Technology, Kweishan, Taoyuan 33302, Taiwan; cyhsu@mail.cgu.edu.tw

<sup>2</sup> Research Center for Food and Cosmetic Safety and Research Center for Chinese Herbal Medicine, Chang Gung University of Science and Technology, Kweishan, Taoyuan 33302, Taiwan

<sup>3</sup> Department of Medical Research, China Medical University Hospital, China Medical University, Taichung 40402, Taiwan; pan@mail.cgu.edu.tw

<sup>4</sup> Department of Pharmaceutics, College of Pharmacy, Prince Sattam Bin Abdulaziz University, Al Kharj 11942, Saudi Arabia; alalaiwe@gmail.com

<sup>5</sup> Graduate Institute of Biomedical Sciences, Chang Gung University, Kweishan, Taoyuan 33302, Taiwan; jane2707@kimo.com

<sup>6</sup> Pharmaceutics Laboratory, Graduate Institute of Natural Products, Chang Gung University, Kweishan, Taoyuan 33302, Taiwan

<sup>7</sup> Chinese Herbal Medicine Research Team, Healthy Aging Research Center, Chang Gung University, Kweishan, Taoyuan 33302, Taiwan

<sup>8</sup> Department of Anesthesiology, Chang Gung Memorial Hospital, Kweishan, Taoyuan 33302, Taiwan

\* Correspondence: fajy@mail.cgu.edu.tw; Tel: +886-3-2118800; Fax: +886-3-2118236

† Equal contribution.

Received: 12 November 2018; Accepted: 3 December 2018; Published: 1 January 2019



**Abstract:** The chemical environment and enzymes in the gastrointestinal (GI) membrane limit the oral absorption of some vitamins. The GI epithelium also contributes to the poor permeability of numerous antioxidant agents. Thus, lipophilic vitamins do not readily dissolve in the GI tract, and therefore they have low bioavailability. Nanomedicine has the potential to improve the delivery efficiency of oral vitamins. In particular, the use of lipid nanocarriers for certain vitamins that are administered orally can provide improved solubility, chemical stability, epithelium permeability and bioavailability, half-life, nidus targeting, and fewer adverse effects. These lipid nanocarriers include self-emulsifying drug delivery systems (SEDDSs), nanoemulsions, microemulsions, solid lipid nanoparticles (SLNs), and nanostructured lipid carriers (NLCs). The use of nontoxic excipients and sophisticated material engineering of lipid nanosystems allows for control of the physicochemical properties of the nanoparticles and improved GI permeation via mucosal or lymphatic transport. In this review, we highlight recent progress in the development of lipid nanocarriers for vitamin delivery. In addition, the same lipid nanocarriers used for vitamins may also be effective as carriers of vitamin derivatives, and therefore enhance their oral bioavailability. One example is the incorporation of D- $\alpha$ -tocopheryl polyethylene glycol succinate (TPGS) as the emulsifier in lipid nanocarriers to increase the solubility and inhibit P-glycoprotein (P-gp) efflux. We also survey the concepts and discuss the mechanisms of nanomedical techniques that are used to develop vitamin-loaded nanocarriers.

**Keywords:** lipid nanocarrier; vitamin; nutrient; oral absorption; bioavailability

## 1. Introduction

Oral administration is often the best route for bioactive agents that have therapeutic or preventive effects in which patient compliance is important. However, oral bioactive agents experience the

harsh environment of the gastrointestinal (GI) tract, which can reduce their solubility, stability, and absorption [1]. In particular, chemical and enzymatic degradation reduces the amount that is available for absorption, the GI membrane prevents permeation into the systemic circulation, and molecules with low water solubility do not readily dissolve in the GI tract. All of these factors contribute to the low bioavailability and bioactivity of oral drugs [2].

Bioavailability, which is a major pharmacokinetic parameter, is defined as the extent and rate to which an active compound is absorbed from a product and becomes available at the target site. An individual must have adequate uptake of bioactive compounds, such as vitamins and nutrients, for these agents to provide beneficial effects. Thus, previous researchers have developed structurally sophisticated formulations to improve physical stability, protect the active ingredients from degradation, and provide controlled release during digestion to improve absorption and bioavailability [3]. The use of prodrugs, permeation enhancers, solid dispersion, polymeric complexes, and molecular encapsulation can improve oral bioavailability [4]. Colloidal delivery systems, consisting of micro-sized or nano-sized encapsulation formulations, can also improve the absorption and bioavailability of oral bioactive agents. In particular, drug formulations in the nanometer range have better pharmacokinetics than those in the micrometer range [5], because smaller carriers have a greater effective surface area. This greater surface area increases the dissolution rate and bioavailability of the active agents.

Nanoformulations can also facilitate enterocyte uptake, and thereby increase absorption. There is evidence that nanocarriers form a protective shield that maintains their stability in the GI tract [6], so that the dose can be reduced. The surface properties of nanoparticles modulate and control the release and absorption rate. Furthermore, nanocarriers can function as vehicles for delivery of a variety of chemicals, such as small-molecule drugs, antioxidants, nutrients, vitamins, peptides, proteins, antibodies, and RNAs [7]. Some nanocarriers were designed to increase oral bioavailability, such as nanocrystals, polymeric nanoparticles, dendrimers, silica nanoparticles, nanotubes, liposomes, and lipid-based nanoparticles.

Use of lipid-based nanocarriers for the oral administration of bioactive agents with poor water solubility can overcome the problems of low bioavailability. The excipients in the lipid nanoparticles, such as emulsifiers or surfactants, can also improve bioavailability [8]. Lipid-based nanodelivery systems, such as self-emulsifying drug delivery systems (SEDDSs), nanoemulsions, microemulsions, solid lipid nanoparticles (SLNs), and nanostructured lipid carriers (NLCs), encapsulate bioactive compounds and increase their solubility and bioavailability when administered by the oral route (Figure 1). Lipid nanoparticles have the characteristics of nano-sized particles and lipid solubility, leading to improved pharmacokinetic parameters and biocompatibility, reduced toxicity, and facilitating scale-up for industrial production [9]. The human body also easily takes up lipid-based nanocarriers. Their digestion involves the dispersion of fat globules into an emulsion with high surface area, enzymatic hydrolysis of the triglyceride lipid at the lipid-water interface, and the dispersion of the bioactive product into the absorbed form [10]. The encapsulation of drugs or bioactive agents by the use of lipid-based nanosystems can also reduce the influence of food intake on absorption and variability among subjects, due to their controlled release.

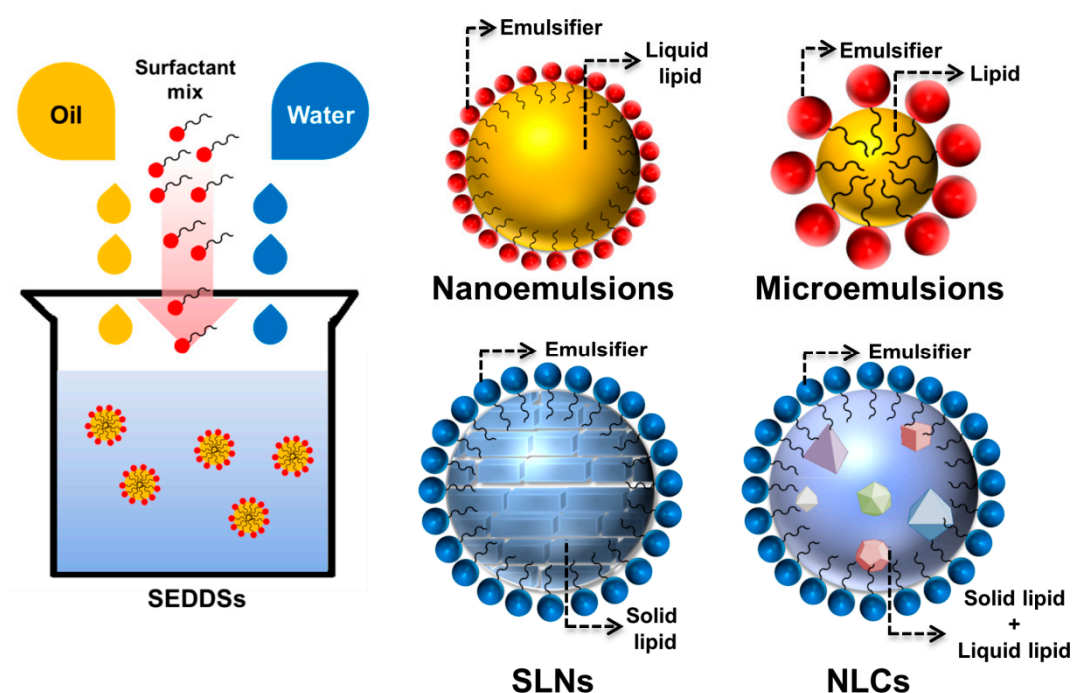


**Figure 1.** Structures of lipid-based nanoparticles: self-emulsifying drug delivery systems (SEDDSs), nanoemulsions, microemulsions, solid lipid nanoparticles (SLNs), and nanostructured lipid carriers (NLCs).

Lipid nanoparticles can improve the bioavailability of orally administered bioactive agents via various mechanisms. First, lipid nanoparticles have enhanced solubilization and rapid dissolution because of lipid inclusion within lipid nanoparticles. The administration of lipids can activate biliary and pancreatic secretion, and these assist in lipid digestion [11]. The adhesiveness of lipid nanosystems prolongs the presence of bioactive molecules in the GI tract, and this increases their absorption. For example, Peyer's patches target gut-associated lymphoid tissue and absorption by M cells, allowing lipid nanoparticle delivery. Lipids that have high solubility in triglycerides undergo lymphatic transport, leading to increased bioavailability because they are not subjected to first-pass metabolism [12]. The ability of lipids and surfactants to open tight junctions in the intestine contributes to their enhanced permeability; their ability to inhibit P-glycoprotein (P-gp) efflux from the intestinal epithelium also increases intestinal permeability [13]. In a molecular or cellular level, previous studies [14–17] have shown a facile uptake of lipid-based nanoparticles into gastric and intestinal epithelium cells. The transport of lipid nanoparticles into epithelium cells can involve in various pathways, including lipid raft-dependent endocytosis, clathrin-mediated endocytosis, and macropinocytosis [18]. Thus, lipid-based delivery systems can increase the bioavailability of oral bioactive agents by numerous mechanisms (Figure 2).

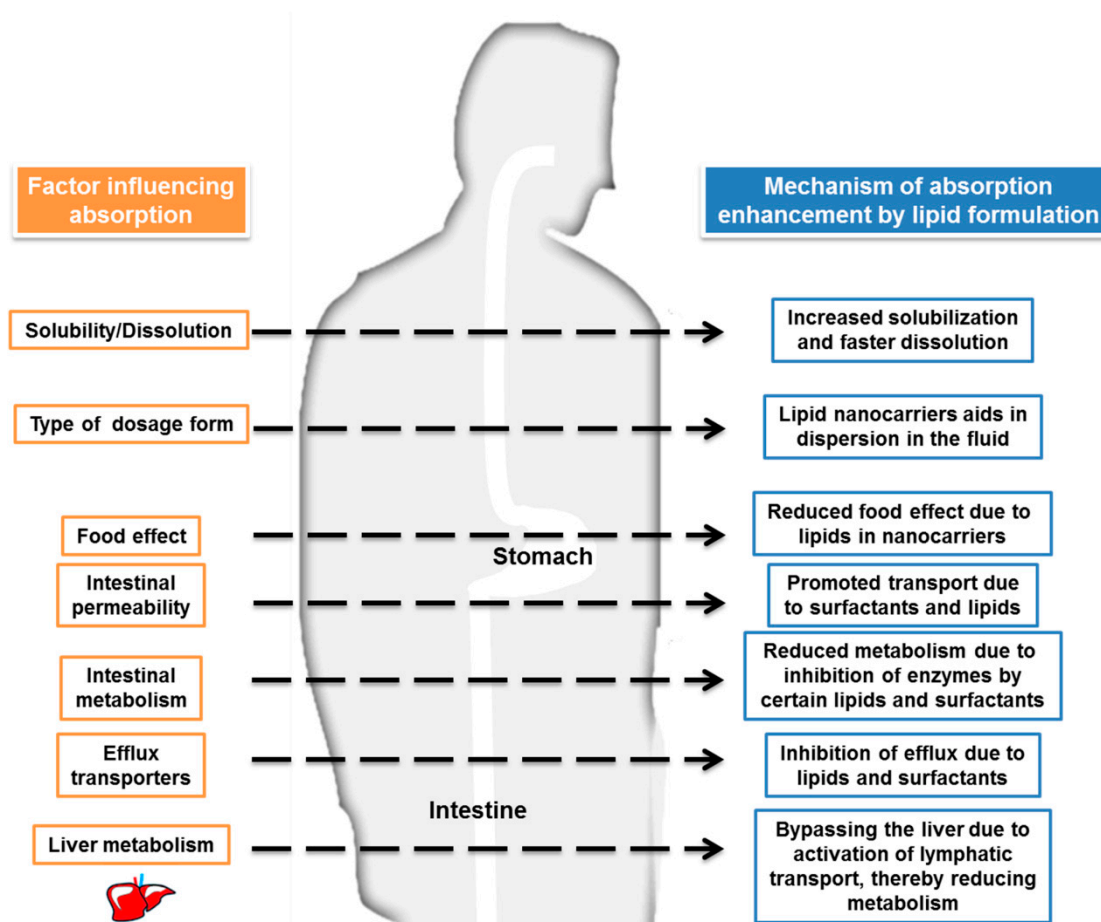


**Figure 2.** Possible mechanisms for enhancement of vitamin bioavailability using lipid-based delivery systems.

Lipid-based nanoformulations typically consist of lipids, emulsifiers/coemulsifiers, and hydrophilic solvents. Water is the most common hydrophilic solvent. The chemical properties of the individual ingredients and their proportions affect molecular entrapment, solubilization, stability, and oral absorption. Thus, different types of lipids can be formulated into lipid nanocarriers from long, medium, and short triglycerides (LCTs, MCTs, and SCTs) [19]. LCTs are digested more slowly than MCTs and SCTs, suggesting that lipase activity declines with chain length. In addition, bioactive agents are generally better maintained in a solubilized state in LCTs and MCTs than in SCTs. Due to their reduced solvent capacity, SCTs may allow the precipitation of bioactive agents. However, MCTs have increased portal vein absorption through the liver, whereas LCTs have increased lymphatic absorption and they are not subject to the first-pass effect [20]. When selecting an emulsifier system, it is also important to consider chemical stability and lipase inhibition [21]. Thus, nonionic and ionic surfactants are used to coat the oil-water interface of lipid nanoparticles. Cremophors and Pluronics are the most common emulsifiers used in lipid-based nanoparticles. The addition of cationic or anionic surfactants into lipid nanoparticles can increase the charge of the particulate surface and prevent electrostatic aggregation. The storage stability of lipid nanoparticles must also be considered, and the induction of GI irritation is an important safety issue when administering ionic surfactants. The coating of the emulsifiers with high surface charge or steric structure can avoid the aggregation between the nanoparticles. It is generally recognized that the zeta potential of  $>30$  mV or  $<-30$  mV is preferred to maintain a long-term stability for nanoparticles. The decoration of polyethylene glycol on lipid nanoparticle surface is well known to demonstrate the repulsion between particles via steric hindrance. The GI tract with harsh environment also causes the instability of nanocarriers. The



strategies of increasing surface charge and steric repulsion are also useful to increase the stability in the GI environment. In particular, some surfactants increase the viscosity of the nanosystem, leading to increased bioadhesiveness and prolonging residence time in the GI tract [22].

Inclusion of bioactive agents using lipid nanocarriers is a major technique that is used for oral delivery of nutrient-grade ingredients, such as vitamins, antioxidants, and fatty acids [23]. Vitamins are essential organic micronutrients, many of which function as enzyme cofactors. Many people worldwide take dietary supplements with vitamins to prevent obesity, cardiovascular disorders, osteoporosis, skin aging, and various cancers. Vitamins can be classified as water-soluble or lipid-soluble. The water soluble vitamins are B1 (thiamine), B2 (riboflavin), B3 (niacin), B5 (pantothenic acid), B6 (pyridoxal), B7 (biotin), B9 (folic acid), and B12 (cyanocobalamin), and C. The fat-soluble vitamins are A (retinol, retinal, and retinyl esters), D2 (ergocalciferol), D3 (cholecalciferol), E (tocopherol), K1 (phyloquinone), and K2 (menaquinone). In addition, these vitamins have many derivatives or analogs that have different bioactivities. The oral bioavailability of most vitamins is relatively low because of their low bioaccessibility, chemical instability, and poor GI absorption [24]. In addition to their low bioavailability, oral vitamins may have erratic absorption profiles, high intra- and inter-subject variations, and absorption that is not dose-dependent, all of which complicate oral administration. However, research in nanomedicine has led to the development of lipid nanocarriers that may improve the bioavailability of oral vitamins.

The objective of this review is to outline the pharmacokinetics of oral vitamins that are formulated using lipid-based nanoparticles. We focus on studies that used different lipid nanocarriers to encapsulate vitamins, such as SEDDSs, nanoemulsions, microemulsions, SLNs, and NLCs. Most of the lipid nanocarriers that we discuss are nanosystems based on oil-in-water (*o/w*). We do not consider liposomes and niosomes, because these molecules are nanovesicles with aqueous cores and lipid shells, rather than nanoparticles with a lipid matrix. We conclude with a discussion of the emerging applications of vitamin-loaded lipid nanoparticles.

## 2. Oral Delivery of Vitamins

Vitamins are organic micronutrients that are essential to the human body and important for the maintenance of normal metabolism, cellular regulation, growth, and development. Humans require 13 dietary vitamins [25]. For people at risk of vitamin deficiency, an oral supplement is generally the first treatment [26]. However, some vitamins have low oral bioavailability due to degradation, poor GI transport, and low water solubility. Thus, it is essential to develop novel forms of oral vitamins to improve absorption.

### 2.1. Vitamin A

Fat-soluble vitamins have important roles in the synthesis and degradation of nutrients, immune function, homeostasis, and growth [27]. The A vitamins are unsaturated fat-soluble organic compounds, including retinol, retinal, retinoic acid, and some provitamin A carotenoids (Figure 3A). They have important roles in vision, reproduction, bone growth, and function of the immune system and skin. Oral carotenoids, which are bioconverted to vitamin A, are often recommended for disease prevention. In particular, epidemiological studies reported that the consumption of carotenoid-rich foods is associated with decreased risk of several cancers, cardiovascular diseases, macular degeneration, and cataracts [28].  $\beta$ -carotene is the most commonly used carotenoid in functional foods and pharmaceutical products, because of its strong provitamin A and antioxidant activities.

The current recommended dietary allowance (RDA) of vitamin A is 600  $\mu\text{g}$  retinol activity equivalents (RAE) per day for adult females and 800  $\mu\text{g}$  for adult males [29]. The dose, absorption efficiency, and percentage of bioconversion of provitamin A into vitamin A impact the circulation level after intake [30]. Thus, total oral intake should consist of approximately 65% vitamin A and about 35% carotenoids. The use of vitamin A and carotenoids in the food industry is limited, due to their low oral bioavailability, poor solubility, and chemical instability. It is believed that vitamin A

transfers from foods or oral doses into lipid droplets (dietary fat emulsions) that are present in the GI lumen during ingestion. About 70% of vitamin A is stored in the liver, and the liver uptakes vitamin A chylomicron remnants through cell surface receptors, such as the low density lipoprotein (LDL) receptor, LDL receptor-related protein 1 (LRP1), and heparan sulfate proteoglycans (HSPGs) [31]. It is likely that chylomicron-remnant retinyl esters and  $\beta$ -carotene are released from hepatocytes during chylomicron remnant metabolism. Several human genetic variations can modulate vitamin A and provitamin A bioavailability and metabolism.

## 2.2. Vitamin B

Vitamins B and C are water-soluble molecules that function as cofactors for many enzymes. The vitamin B group consists of B1, B2, B3, B5, B6, B7, B9, B12, and related derivatives (Figure 3B). Among these, B1, B2, B3, B6, and B12 play important roles in disease prevention. For example, vitamin B1 is a cofactor of dehydrogenase and transketolase; polyneuritis, Alzheimer's disease, and colon cancer are linked to B1 deficiency [27]. Vitamin B2 is a precursor to flavin adenine dinucleotide (FAD) and flavin mononucleotide (FMN), which are cofactors for flavoenzymes, a large group of oxidoreductases. B2 deficiency can cause mucosal disorders, skin disorders, and anemia. Vitamin B3 is the precursor of nicotinamide adenine dinucleotide (NAD) and nicotinamide adenine dinucleotide phosphate (NADP), and B3 deficiency is associated with pellagra, depression, and dementia. Vitamin B6 is a cofactor for enzymes that function in the metabolism of amino acids, carbohydrates, and lipids [32]. The monitoring of B6 concentration is important for patients with cardiovascular diseases. Vitamin B12 has a complex structure, with a corrin ring and an embedded cobalt ion. This vitamin is important for erythrocyte formation, nerve cell maintenance, and DNA synthesis. B12 deficiency may lead to megaloblastic anemia. Dairy products are the major dietary sources of vitamin B12, although this vitamin has bioavailability of 8 to 12% from milk preparations [33], but 12 to 33% following the consumption of tofu and cheese [34].

## 2.3. Vitamin C

Vitamin C is the only water-soluble vitamin not in the vitamin B group (Figure 3C). It is one of the most essential vitamins and it has roles in many physiological processes, including immune response and iron absorption [35]. Vitamin C is abundant in many fruits and vegetables, such as mango, kiwi fruit, papaya, lettuce, tomato, and strawberry. Vitamin C is also a strong antioxidant that can reduce oxidative stress. Vitamin C may improve physiological function by increasing baroreflex sensitivity, ameliorating vascular conductance, decreasing systemic inflammation, reducing cancer cell-specific toxicity, and augmenting the inotropic response to  $\beta$ -adrenergic stimulation [36]. Oral administration is always less effective than intravenous administration because of the low bioavailability of this vitamin [37]. Sodium-dependent vitamin C transporters 1 and 2 are important for intestinal vitamin C absorption and renal reabsorption. Sodium-dependent vitamin C transporter 2 also promotes the entry of vitamin C into the most metabolically active tissues and cells [38]. Thus, the rate of intestinal absorption and renal reabsorption and excretion greatly impact the bioavailability of vitamin C.

## 2.4. Vitamin D

Vitamin D has two major forms: D2 and D3 (Figure 3D), each of which the body converts into the bioactive calcitriol (25-dihydroxyvitamin D). Ultraviolet irradiation of ergosterol in plants leads to the formation of vitamin D2, and ultraviolet radiation of 7-dehydrocholesterol in human skin leads to the formation of vitamin D3. Vitamin D is also obtained from foods, including egg yolk, fish, and milk. Vitamin D has important roles in the mineralization of bone and teeth, due to its regulation of calcium and phosphorus homeostasis [39]. There is also evidence that vitamin D supplements can prevent malignancies, cardiovascular diseases, osteoporosis, and diabetes.

Oral vitamin D absorption requires scavenger receptor class B type I (SR-BI), N-terminal Niemann-Pick C1 (NPC1), like intracellular cholesterol transporter 1 (NPC1L1), and cluster of

differentiation (CD36) [40]. These three trans-membrane proteins primarily function as cholesterol transporters in the intestine. Although use of oral vitamin D supplements is a low-cost and practical method to treat deficiency, clinical advancements of vitamin D administration are limited by its lipophilic character, low solubility in GI fluid, and low bioavailability [41]. Moreover, the facile degradation of vitamin D by light, air, and heat limits the practicability of oral vitamin D. Thus, there is an urgent need to develop new formulations of vitamin D.

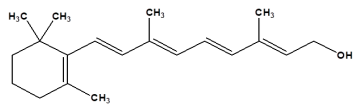
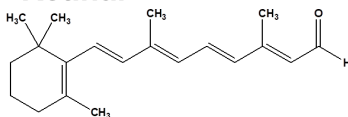
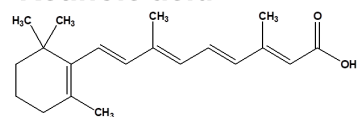
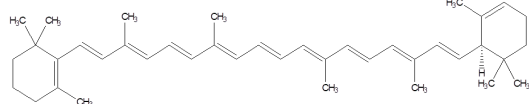
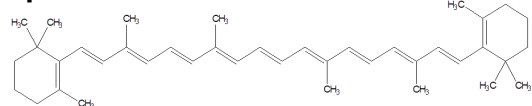
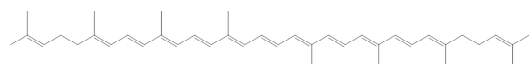
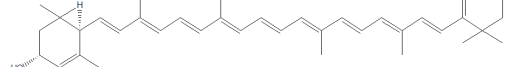
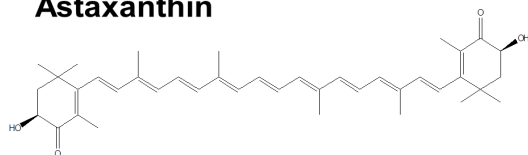
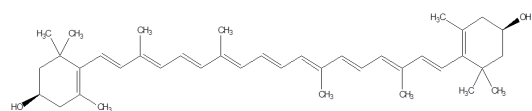
### 2.5. Vitamin E

Molecules in the vitamin E group, which function as antioxidants and free radical scavengers, include four tocopherols ( $\alpha$ ,  $\beta$ ,  $\gamma$ , and  $\delta$ ) and four corresponding unsaturated tocotrienols (Figure 3E). These compounds have anti-inflammatory activities and they are recommended for the treatment of cardiovascular disorders and cancers [42]. In general,  $\alpha$ -tocopherol has greater bioactivity than  $\beta$ - and  $\gamma$ -tocopherol (15 to 30% of  $\alpha$ -tocopherol activity), and  $\delta$ -tocopherol has very little bioactivity. Among the tocotrienols, only the  $\alpha$  and  $\beta$  forms appear to have significant activity [43]. Oral absorption of vitamin E is considered to occur by passive transport across the enterocyte apical membrane [44], predominantly in the distal region of the small intestine (distal jejunum and ileum). The three vitamin D transporters (SR-BI, NPC1L1, and CD36) also function in vitamin E absorption. Vitamin E is also absorbed through the lymphatic system, where it diffuses as lipoprotein complex [45]. In particular, the lipoprotein complex that is formed by mixing vitamin E, bile salt micelles, and chylomicron is too large to pass across blood capillary, and it is only transported via the lymphatic system.

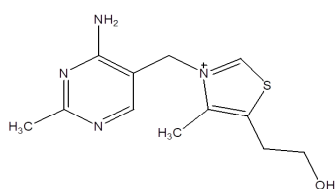
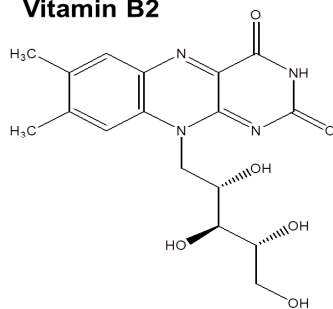
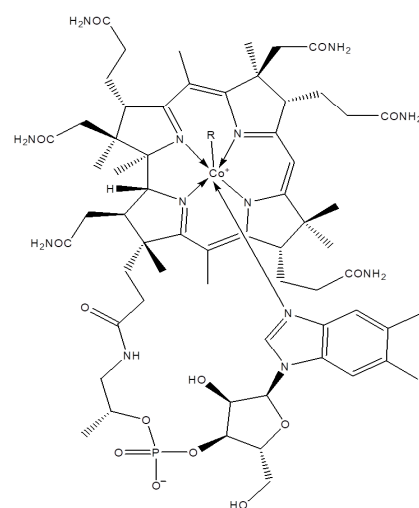
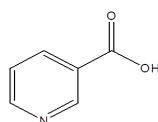
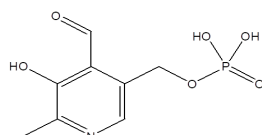
In United States, the RDA for vitamin E is 15 mg, but more than 90% of the population does not consume this amount [46]. The poor aqueous solubility and limited intestinal permeability of vitamin E account for its limited bioavailability [47]. In addition, vitamin E is highly susceptible to oxidation when exposed in oxygen, light, and heat. Thus, the oral bioavailability of tocopherol and tocotrienols ranges from 10 to 33% [44,48]. Notably,  $\alpha$ -tocopherol also competes for GI absorption with other fat-soluble vitamins, such as  $\gamma$ -tocopherol, and vitamins A, D, and K [49]. An increasing number of investigations have attempted to increase vitamin E bioavailability by the use of nanoparticles. Encapsulation of vitamin E within nanoparticles can impede its interactions with other fat-soluble vitamins, which would otherwise inhibit vitamin E absorption.

### 2.6. Vitamin K

Vitamin K is essential for the activation of specific proteins that function in bone metabolism and blood clotting. Based on its source, vitamin K is classified as plant-derived vitamin K1 (phylloquinone) or animal/bacteria-derived vitamin K2 (menaquinones) (Figure 3F). Vitamin K1 is a procoagulant that is used in cases of hemorrhage, and vitamin K2 has roles in the regulation of blood clotting factors, namely prothrombin and five other proteins (Factors VII, IX, and X, and proteins C and S) [50]. During the process of pancreatic lipolysis, vitamin K is solubilized in mixed micelles with bile salts, and is then absorbed through the proximal intestine. Vitamin K is insoluble in GI fluid, and a low blood level of vitamin K and its metabolites is often due to low dietary intake [51]. Following oral administration of vitamin K, there are large inter- and intrasubject variations in absorption, and because of this, its bioavailability can range from 10 to 63% [52].

**Retinol****Retinal****Retinoic acid** **$\alpha$ -carotene** **$\beta$ -carotene****Lycopene****Lutein****Astaxanthin****Zeaxanthin**

(A)

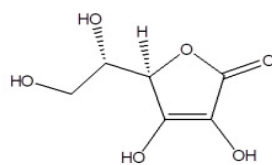
**Vitamin B1****Vitamin B2****Vitamin B12****Vitamin B3 (niacin)****Vitamin B6**

(B)

**Figure 3. Cont.**

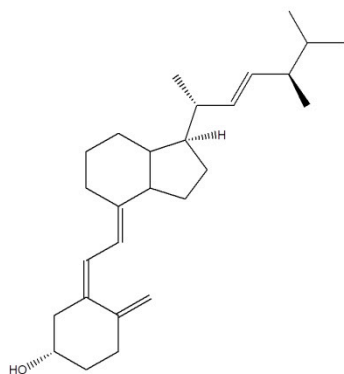


### Vitamin C

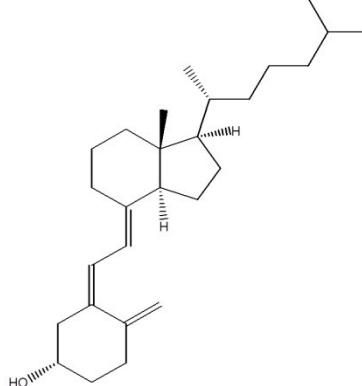


(C)

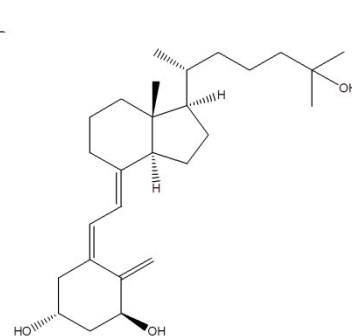
### Vitamin D2



### Vitamin D3

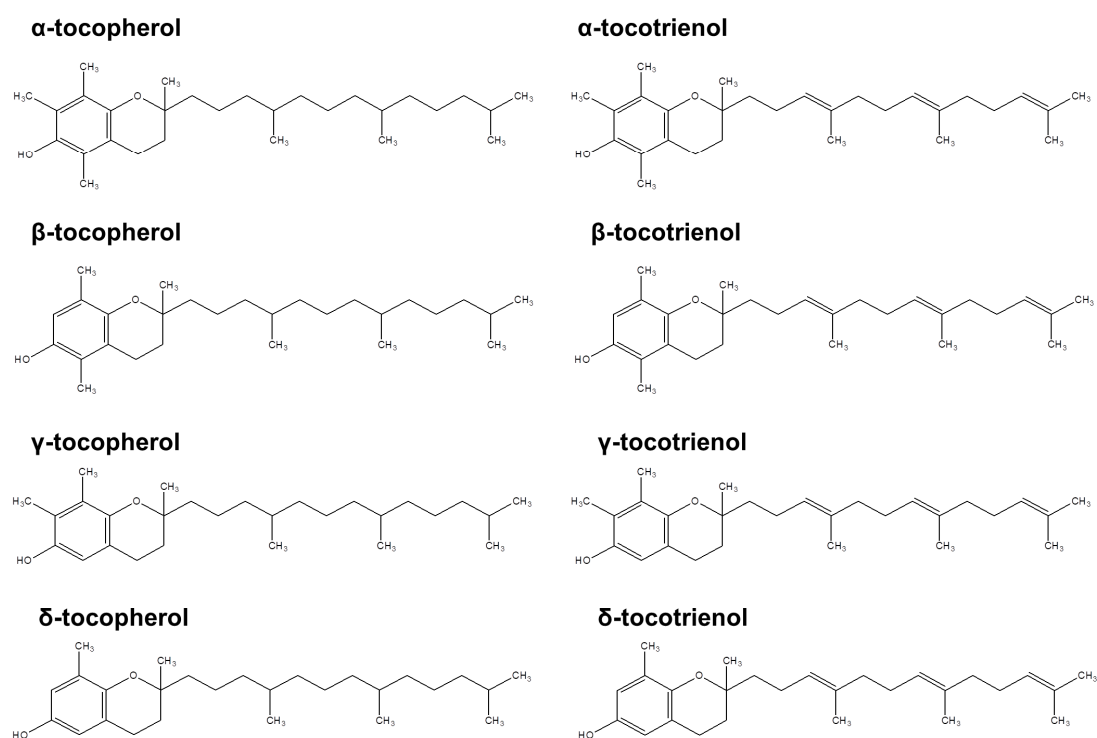


### 1,25-dihydroxyvitamin D3

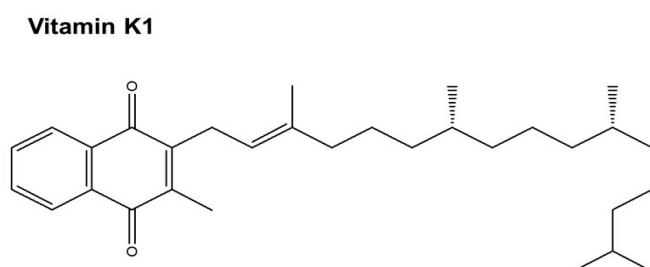


(D)

Figure 3. Cont.



(E)



(F)

**Figure 3.** Chemical structures of (A) vitamin A; (B) vitamin B; (C) vitamin C; (D) vitamin D; (E) vitamin E; and, (F) vitamin K.

### 3. Lipid Nanoparticles

Lipid-based nanodelivery systems, such as SEDDSs, nanoemulsions, microemulsions, SLNs, and NLCs, have great promise as oral vehicles for the delivery of bioactive agents because they can increase the solubility and improve bioavailability. Thus, many researchers have examined the effect of lipid nanocarriers on pharmacological or bioactive efficacy, adverse effects that are associated with conventional formulations, and compliance by patients and consumers. Orally administered lipid nanoparticles can be absorbed by several different mechanisms (Figure 4). The ingredients of lipid nanoparticles include bioactive compounds, lipids, surfactants, aqueous solvents, and cosolvents, and

the excipients are usually biocompatible and less toxic to the human body [53]. It is generally easy to scale up the production of liquid nanoparticles, and this is a major benefit when the product is to be used for commercial or clinical purposes.

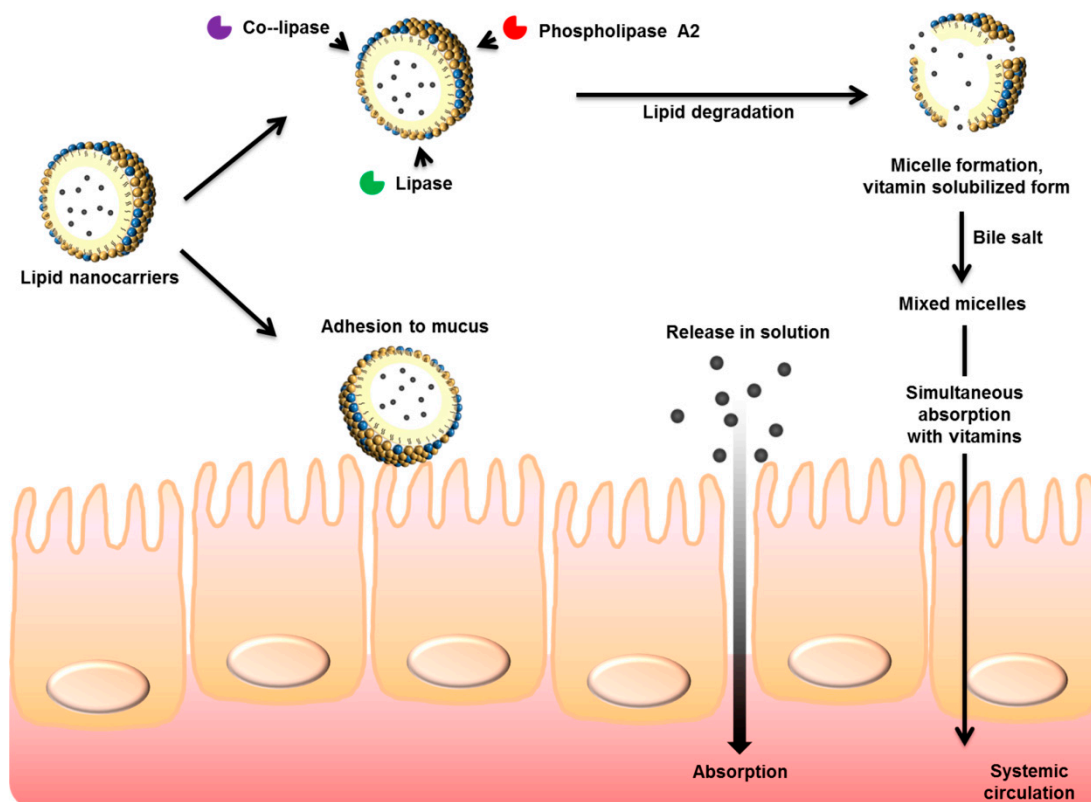


**Figure 4.** Possible pathways of gastrointestinal absorption of orally administered lipid nanoparticles.

### 3.1. Self-Emulsifying Drug Delivery Systems (SEDDSs)

SEDDSs are the most commonly employed lipid nanocarriers that are used to enhance the oral absorption of vitamins. A SEDDS consists of an anhydrous isotropic mixture of oil, emulsifier, coemulsifier, solubilizer, and active ingredient, in which spontaneously created *o/w* nanoemulsions or microemulsions with diameters below 300 nm form upon dilution with water under gentle agitation. Their unique ability of self-assembly in the GI fluid makes the drug or nutrient available as nano-sized oil droplets, and the high interfacial surface area improves dissolution in the GI environment (Figure 5) [54].

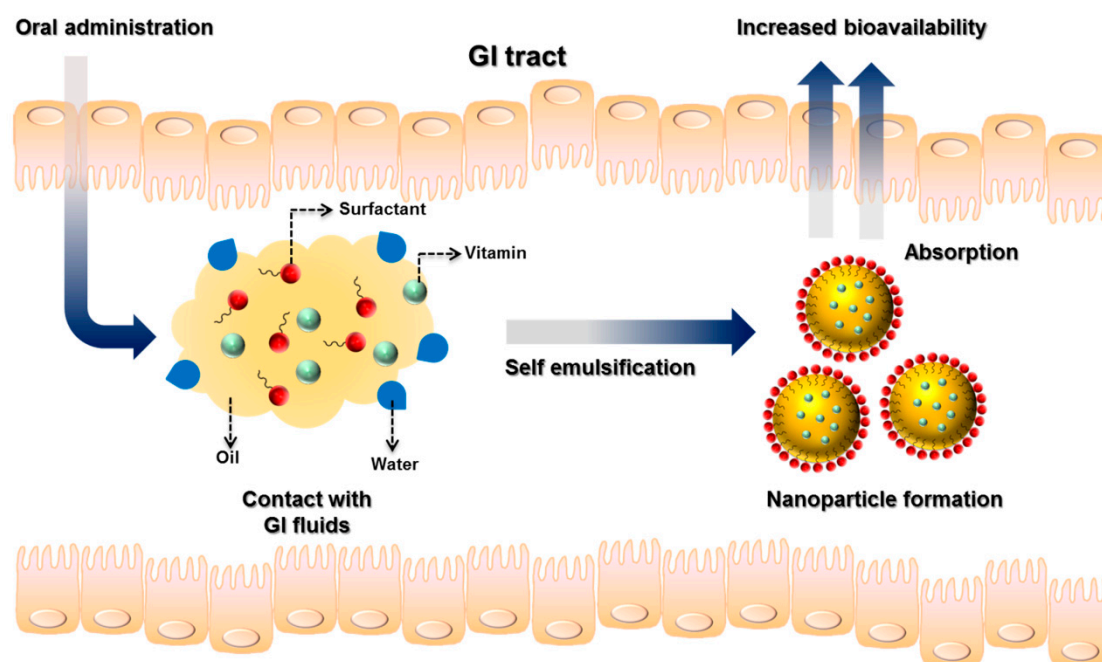


**Figure 5.** Formation of self-emulsifying drug delivery systems (SEDDSs) in the gastrointestinal tract.

The two types of SEDDs are self-nanoemulsifying drug delivery systems (SNEDDSs) and self-microemulsifying drug delivery systems (SMEDDSs). SNEDDSs are generally opaque or translucent, and the droplet diameter is below 100 nm; SMEDDSs form transparent microemulsions of thermodynamically stable systems after oral ingestion [55]. The ingredients, droplet diameter, digestibility of the lipids, and lipophilicity of the bioactive agents all affect the bioavailability of an agent from SEDDSs. The selection of suitable excipients is vital for SEDDS preparation and for increasing bioavailability. SEDDSs are generally designed using the lipids and surfactants that are generally recognized as safe (GRAS). The methods that are employed for fabrication of SEDDSs include low-energy emulsification, the phase inversion temperature method, the phase inversion composition method, and solvent displacement [56].

Large volumes of conventional emulsions must be consumed to assure the therapeutic absorption of the bioactive agents because of the need for water in these emulsions. This large amount of water may increase hydrolysis and precipitation during long-term storage, thus reducing stability and oral absorption. SEDDSs are delivery systems of emulsion preconcentrates, and no water is used in their formulation. The concerns regarding conventional emulsions can be resolved with good patient compliance. When SEDDSs are used for oral dosage, the advantages are improved physicochemical stability, a possibility of filling capsules with the vehicle, and increased patient acceptability [57]. Digestive motility provides most of the agitation that is needed for forming nanoemulsions in the GI tract. The process of self-assembly requires no input of free energy ( $\Delta G^\circ$ ) for the creation of nanoemulsions, so their development is thermodynamically spontaneous. In particular, the liquid crystalline phase formed between the oil and water phases swells, allowing for the spontaneous formation of an interface between the oil droplets and external phase [58]. Ingestion of SEDDSs increases the total amount of lipids in the GI tract, and these lipids can induce secretion of bile into the lumen. The increased bile salts, phospholipids, and cholesterol in the presence of lipids and emulsifiers provide a lipid-rich environment that favors the production of emulsion droplets. Thus, poorly soluble drugs or bioactive compounds that are initially dissolved in SEDDSs partition into the micelles. Micelle formation is an important step for increasing solubilization and absorption.

When considering oral administration, SEDDSs increase bioavailability by increasing the stability of bioactive agents in the GI environment because first-pass effects are minimal, they have increased



lymphatic transport, and they inhibit P-gp-mediated efflux [59]. Some additional advantages of SEDDSs are that they can be easily delivered by the oral route, intersubject variability and effects of food are reduced, there is a fast onset of action, lower doses can be used, and they are easy to manufacture [56]. However, a disadvantage of SEDDSs is that they must be delivered through soft or hard gelatin capsules. The material in the capsule shell might be incompatible with the excipients, leading to precipitation of the active ingredients, the need for storage at low temperatures, and the use of specific preparation methods [60]. This problem can be resolved by transforming liquid SEDDSs into the solid state. Thus, techniques, such as freeze drying, spray drying, granulation, and adsorption to carriers, can be used to produce more stable and convenient forms for handling and delivery.

In addition to their roles as bioactive agents in SEDDSs, some vitamins and their derivatives can be used as excipients in the nanocarriers to assist absorption [61]. P-gp-mediated efflux is primarily responsible for the low bioavailability of some drugs and actives. Vitamin E and D- $\alpha$ -tocopheryl polyethylene glycol succinate (TPGS) appear to counteract the effects of P-gp. In particular, vitamin E can suppress P-gp activity and TPGS is used as a surfactant in lipid nanoparticles to enhance intestinal transport due to its potent anti-P-gp activity [62].

### 3.2. Nanoemulsions

Nanoemulsions are heterogeneous mixtures of oil droplets in an aqueous medium that are stabilized by an emulsifier system. The emulsified mixture is isotropic and translucent and it is kinetically stable, in that there is no flocculation or coalescence during long-term storage. In contrast to SEDDSs, nanoemulsions are produced by directed assembly rather than self-assembly. Drugs can be loaded inside the oil cores of nanoemulsions before administration to improve absorption when administered orally. The United States Food and Drug Administration has approved some nanoemulsions of poorly soluble drugs, such as Estrasorb<sup>®</sup>, Flexogan<sup>®</sup>, and Restasis<sup>®</sup> [63]. In addition to drugs, nanoemulsions can also encapsulate nutrients and vitamins, and they have several advantages over food systems; these advantages include the ability to incorporate lipophilic entities, high physical stability, easy modulation of product texture, and rapid GI digestibility [64].

Generally, nanoemulsions are prepared from components that are GRAS or natural products. To reduce toxicity and increase stability, surfactants or cosurfactants are used in nanoemulsions, such as peptides (peptide surfactant AM1), proteins (caseinate and whey protein isolate), polysaccharides (Arabic gum and modified starch), phospholipids (egg lecithin and soybean lecithin), and small molecule nonionic surfactants (Span and Tween) [23,65]. High pressure homogenization is the major technique that is used to produce nanoemulsions. The use of rapidly diffusing, electrostatically stabilized, and low molecular weight emulsifiers can provide complete dispersivity. The other techniques used to fabricate the stable nanoemulsions are the use of a microfluidizer, a sonicator, and low energy approaches [66]. Due to their tiny droplet size and large surface area, they easily interact with the biological components of the GI tract, and are therefore efficient carriers for bioactive compounds because they provide better oral absorption than conventional emulsions. Nanoemulsions reportedly increase bioavailability because they increase solubilization, prolong gastric residence time, stimulate lymphatic absorption, reduce the effects of efflux transporters, and inhibit metabolism [67]. Vitamins, especially fat-soluble vitamins, can be loaded within the oil core of liquid droplets, where they are protected from chemical and enzymatic degradation and released after ingestion.

### 3.3. Microemulsions

Conventional emulsions are optically opaque or turbid because the coarse droplets have diameters that are similar to the wavelength of light (hundreds of nanometers), so they scatter light strongly. Nanoemulsions can be regarded as conventional emulsions with droplets of 10 to 100 nm in diameter. Conventional (coarse) emulsions and nanoemulsions are thermodynamically unstable, because the separated oil and aqueous phases have a lower total free energy than the emulsified oil and water [66]. However, microemulsions are thermodynamically stable systems, whose free energy is lower than

that of the phase-separated components, so they tend to form spontaneously or with a small input of energy [68]. Table 1 compares the properties of these three types of emulsions.

**Table 1.** Characterization of self-emulsifying drug delivery systems (SEDDSs) loaded with vitamins or their derivatives and their oral absorption.

Vitamin	Average Size	Model Animals	Outcomes Offered by Nanoparticles	Reference
Vitamins A and K2	25–200 nm	None	Good dispersity to form microemulsions	Shah et al. [69]
Vitamin A	Unknown	Rat	An increased bioavailability of 1.4-fold compared to control	Taha et al. [70]
Lutein	337 nm	Thoracic lymph-cannulated rat	An increased bioavailability of 2.5-fold compared to control	Sato et al. [71]
Lutein	92 nm	Rabbit	An increased bioavailability of 11.8-fold compared to control	Shanmugam et al. [72]
Seocalcitol	29 nm	Rat	A 45% relative bioavailability was achieved	Grove et al. [73]
$\alpha$ -tocopherol	Unknown	Human	An increased bioavailability of 2.2-fold compared to commercial capsules	Julianto et al. [74]
Tocotrienols	1.5–10.6 $\mu$ m	Human	An increased bioavailability of 2–3-fold compared to control	Yap and Yuen [75]
Tocotrienols	Unknown	Human	Improvement of arterial compliance and oral bioavailability compared to placebo	Rasool et al. [76]
Tocotrienols	211 nm	Rat	An increased bioavailability of 3–7-fold compared to commercial capsules	Alqahtani et al. [77]
$\gamma$ -tocotrienol	117 nm	Fed rat	An increased bioavailability of 2-fold compared to commercial capsules	Alqahtani et al. [78]
TPGS350 and TPGS1000	11–62 nm	Rat	An increased bioavailability of 3-fold compared to $\gamma$ -tocotrienol SEDDSs	Abu-Fayyad et al. [79]
Vitamin K1	82–263 nm	Human	An increased bioavailability of 1.7-fold compared to commercial tablets	El-Say et al. [80]

TPGS, D- $\alpha$ -tocopheryl polyethylene glycol succinate.

Microemulsions are generally optically transparent and they can be spherical, ellipsoidal, or worm-like in shape, depending on the molecular geometry of the surfactants. The different domains of microemulsions can be characterized by ternary-phase diagrams. Three basic components—two immiscible liquids and a surfactant—are needed to produce microemulsions. Most microemulsions use oil and water as immiscible liquid pairs. The relative amounts of these three components can be represented in a ternary phase diagram. Stable and transparent microemulsions only form in a specific region of the ternary phase diagram. Relative to nanoemulsions, a large amount of emulsifiers is necessary to prepare stable microemulsions.

The physicochemical characteristics and thermodynamic stability of microemulsions allow for spontaneous formation by low energy emulsification, known as the titration method. The benefits of orally applied microemulsions for drug and nutrient delivery are improved solubilization, protection from degradation, and increased GI transport [81]. The large content of surfactants in microemulsions increases GI membrane fluidity and subsequent permeability [82]. Neoral<sup>®</sup> is an example of an oral microemulsion formulation containing cyclosporine A that was approved by the United States FDA. Microemulsions are also used for solubilization and improving the bioavailability of nutraceuticals and vitamin derivatives, such as coenzyme Q10, lutein, and carotenoids [83].

### 3.4. Solid Lipid Nanoparticles (SLNs)

The pharmaceutical and food industries are devoting increasing attention to SLNs, because they are not subject to many of the deficiencies of microcapsules and conventional colloidal carrier systems [84]. SLNs are composed of melt-emulsified lipids that are solid at room temperature and in the body. Thus, they are colloidal nanosystems consisting of crystalline lipids. Because of the unique features of their particulate structure, SLNs have the advantages of controlled release, increased bioavailability, improved stability, and suitability for industrial-scale production [85]. The

avoidance of organic solvents and the use of biocompatible and biodegradable solid lipids in their preparation increase their applicability and safety. Natural and synthetic solid lipids are added into SLNs to form stable nanosystems, including triglycerides, glyceryl monostearate, glyceryl behenate, glyceryl palmitostearate, wax, fatty acids, and cholesterol [86]. SLNs can be manufactured using melt homogenization, cold homogenization, or melt microemulsification [5]. Hot homogenization is the most-used method, because the solid lipids must be melted to the liquid phase to facilitate mixing with other components in the production of small particles. Cold homogenization may be used for drugs or bioactive agents that are sensitive to heat.

Digestion of oral SLNs starts in the stomach with the action of gastric lipases. The mechanical mixing of gastric fluid with SLNs leads to a crude emulsion [87]. Intestinal fluids then further digest SLNs. The small size of SLN particles allows them to adhere to GI mucus and enter the intervillar space. The emulsifiers that coat the surface of SLNs allow increased absorption, because they reduce membrane fluidity. The solid state of the lipid nanoparticle matrix protects chemically labile bioactive agents and prolongs release of the drug or vitamin. It is also possible to load SLNs into capsules or pellets for more convenient application [69].

### 3.5. Nanostructured Lipid Carriers (NLCs)

Despite the advantages of SLNs for oral delivery of bioactive agents, several drawbacks must be resolved before their application. Due to the densely packed solid lipid matrix, there is only a small loading space for the bioactive agent. Moreover, particulate aggregation and gelation may occur during storage, and this can lead to the expulsion of the drug or bioactive agent from the nanoparticle. The “burst escape” of drugs for some oral SLNs can increase their toxicity. Thus, further research is required to improve the formulations used for SLNs. The incorporation of a liquid lipid into the crystalline matrix can increase imperfection (lattice defects) in the core, thereby increasing entrapment of the active ingredients [70].

NLCs are second-generation lipid nanoparticles composed of a mixture of liquid and solid lipids. These carriers have improved physical stability. Moreover, the release of bioactive agents from NLCs can be easily modulated by adjusting the ratio of liquid and solid lipids.

A number of preparation platforms are suitable for the production of NLCs. These include high pressure homogenization, solvent evaporation, emulsification-solvent diffusion, solvent injection, phase inversion, microemulsion, multiple emulsion, sonication, and membrane extrusion [88]. High pressure homogenization is preferred over other methods because this method has matured over many years of use in the pharmaceutical industry, and because it does not require a solvent.

NLCs are especially useful for enhancing GI absorption by lymphatic uptake via M cells and because first-pass effects can be disregarded. NLCs increase carrier transport through the stagnant layer (between the intestinal bulk fluid and brush border of enterocytes) and thereby promote absorption [71]. Surfactants on the shells of NLCs also inhibit P-gp efflux. Certain lipophilic drugs can be loaded into NLCs to improve GI transport. Research has shown that NLCs improve the bioavailability of etoposide by 3.5-fold, iloperidone by 8.3-fold, silymarin by 2.5-fold, and tamoxifen by 2.7-fold, relative to control suspensions or commercial products [72]. NLCs are also used as carriers to increase the bioavailability of water-insoluble nutrients, such as coenzyme Q10 [89].

## 4. Enhancement of Oral Bioavailability of Vitamins Using Lipid Nanocarriers

Vitamin deficiencies can adversely affect human health and even cause certain diseases. Despite significant efforts during the past few decades, the prevention and treatment of vitamin deficiency remains far from satisfactory. Conventional formulations of oral vitamins usually have insufficient bioavailability and often have adverse effects. Lipid nanocarriers can resolve many of these problems for vitamins that are administered by the oral route. In particular, lipid nanocarriers allow for modulation of the size, surface charge, ingredients, and targeting of specific ligands, and they also have greater solubility, stability, and bioactivity.

#### 4.1. Self-Emulsifying Drug Delivery Systems (SEDDSs) for Oral Vitamin Delivery

SEDDSs are the most widely used lipid nanoparticles used to improve the oral absorption of vitamins. The self-assembly of nanosystems makes them attractive for the engineering of nanomedicines with distinct physicochemical properties, and greatly simplifies the optimization of formulations. Previous research examined the use of SEDDSs for oral delivery of five nutraceuticals with poor water solubility (vitamin A, vitamin K2, coenzyme Q10, resveratrol, and quercetin) [73]. The researchers optimized the formulations to fill gelatin capsules. A dispersion test indicated that all formulations containing nutrients dispersed spontaneously to form microemulsions, with droplet diameter of 25 to 200 nm. For example, vitamin K2-loaded nanocarriers had an average diameter of about 40 nm. Thus, the development of such formulations is a feasible approach to improve the oral absorption of nutraceuticals with low solubility.

SEDDSs are the preferred formulation for incorporation into capsules or tablets for oral ingestion. There is also interest in transforming liquid SEDDSs into solid forms. Thus, previous research fabricated vitamin A SEDDSs, consisting of soybean oil, Cremophor EL, and Capmul MCM-C8, and mixed them with microcrystalline cellulose (Avicel®) to generate solid powders that can be compressed into tablets [74]. The researchers then orally administered these tablets (vitamin A dose: 7.5 mg/kg) to rats for pharmacokinetic examination. The average peak concentration ( $C_{\max}$ ) was higher for the SEDDS tablets (656 ng/mL) than the conventional tablets (421 ng/mL), indicating improved oral bioavailability.

Lutein is a naturally occurring carotenoid that can prevent cataracts and age-related macular degeneration, but it has poor water solubility. The reported oral bioavailability of lutein is only 5%, and there are large inter-individual variations [90]. Sato et al. [91] developed solid SEDDSs with lutein (droplet diameter: 337 nm) to increase its transport into the lymphatic system. They conducted thoracic lymph cannulation in rats to measure lymphatic lutein concentrations. The lutein concentration for the control powder was about 100 ng/mL at 9 h, but it was 250 ng/mL for the SEDDSs. This indicates that SEDDSs increased lutein diffusion from the intestine into the lymph stream. Shanmugan et al. [75] prepared SEDDSs containing phosphatidylcholine as the oil phase to promote oral lutein absorption by spray-drying liquid SEDDSs to form a solid powder. These SEDDSs had a droplet diameter of 92 nm and a polydispersity index (PDI) of 0.208. The lutein dissolution from SEDDSs was 79% within 30 min. Analysis of the pharmacokinetic parameters following oral administration to rabbits at a lutein dose of 5 mg/kg indicated that the SEDDSs had  $C_{\max}$  values that were about 21-fold greater than lutein powder, and eight-fold greater than the commercial product.

Based on the literature [76], MCTs are preferred over LCTs for SEDDSs because they have higher fluidity, better solubilization, and the ability to self-emulsify. Grove et al. [77] compared the pharmacokinetics of two SEDDSs, one containing MCT and the other containing LCT, for oral delivery of seocalcitol (a vitamin D analog) by giving rats 47 µg/kg of oral  $^3\text{H}$ -seocalcitol. The bioavailability was 45% for the MCT-SEDDSs and 18% for the LCT-SEDDSs, thus confirming the superiority of MCTs for use in the oil phase.

Vitamin E can be absorbed via lymph, where it is transported as a lipoprotein complex, and SEDDSs are ideal carriers for vitamin E because they enhance lymphatic absorption. Thus, a pharmacokinetic study in eight healthy humans compared vitamin E-loaded SEDDSs (400 IU of  $\alpha$ -tocopherol) with commercial capsules (Natopherol®) [78]. The SEDDSs had a 2.2-fold greater bioavailability than the capsules (control). The SEDDSs also had a lag time of 2.1 h, shorter than that of capsules (5.0 h). These results indicated that SEDDSs provided more rapid delivery of  $\alpha$ -tocopherol.

Tocotrienols, compounds in the vitamin E family that have a chromanol head and a 16-C phytyl chain, have some bioactivities that are not present in the tocopherols, including lowering of cholesterol, suppression of tumors, and neuroprotection [92]. However, the oral bioavailability of tocotrienols is low due to their poor GI absorption. In addition, the biological half-life ( $t_{1/2}$ ) of tocotrienols is four- to five-fold shorter than  $\alpha$ -tocopherol [79]. Yap and Yuen [80] produced two different tocotrienol-loaded SEDDSs that were easily lipolyzed under in vitro conditions, and they had a finer dispersion with



negligible lipolysis. A single dose bioavailability test in six healthy subjects indicated that the area-under-curve (AUC) of each SEDDS was two to three times greater than a soybean oil solution. The two nanosystems also had comparable absorption and faster onset of GI absorption.

Supplementary vitamin E can slow the progression of atherosclerosis. Thus, Rasool et al. [93] prepared tocotrienol-loaded SEDDSs and conducted a randomized, placebo-controlled, clinical study to evaluate arterial compliance and vitamin E blood level. They assessed arterial compliance using carotid femoral pulse wave velocity and the augmentation index. The results indicated a linear dose response with circulatory tocotrienol concentration for oral doses of 50, 100, and 200 mg. In addition, the SEDDSs provided greater plasma tocotrienol level than the placebo. The SEDDSs also had improved arterial compliance within two months of treatment.

Alqahtani et al. [94] compared the oral bioavailability of  $\gamma$ -tocotrienol-SEDDS and  $\delta$ -tocotrienol-SEDDS with commercial capsules (Unique E<sup>®</sup>). The nanocarriers had a mean diameter of 211 nm and a mean PDI of 0.5. Measurement of cellular uptake by human epithelial colorectal adenocarcinoma (Caco-2) cells indicated that the SEDDSs provided three-fold greater tocotrienol permeability than the commercial product (control). Moreover, SEDDSs significantly increased the bioavailability of the  $\gamma$  and  $\delta$  forms in rats. Relative to the capsules, the AUC of  $\delta$ -tocotrienol-SEDDS was seven-fold greater for 0.5 mg/kg doses and three-fold greater for 2.5 mg/kg doses. Nevertheless, this effect was self-limiting, because a corresponding increase in the free surfactant level negatively impacted tocotrienol transport via NPC1L1. Alqahtani et al. [95] compared the lipolysis and oral bioavailability of  $\gamma$ -tocotrienol in SEDDSs to Tocovid<sup>®</sup>, a soft gelatin capsule formulation that is used to enhance tocotrienol absorption. The nanocarriers had a diameter of 117 nm and a PDI of 0.5. Analysis of in vitro lipolysis indicated the SEDDS provided a two-fold increased  $\gamma$ -tocotrienol solubilization. They also determined the plasma  $\gamma$ -tocotrienol level following oral administration to rats. The SEDDSs had a two-fold greater bioavailability at 10, 25, and 50 mg/kg doses.

Other researchers developed a polyethylene glycol conjugate of an  $\alpha$ -tocopherol isomer (TPGS) that was water-soluble to be used for treating low birth weight infants and cholestasis [96]. Because of the surfactant, TPGS can self-assemble to form lipid nanoparticles. Another study examined the oral absorption of TPGS-SEDDSs with molecular weights of 350 Da (diameter: 10.8 nm) and 1000 Da (diameter: 61.6 nm) in rats [97]. Following oral dosing at 1 mg/kg, the absolute bioavailability of TPGS350 was 18.2% and that of TPGS1000 was 16.6%; these values were three-fold higher than that of  $\gamma$ -tocotrienol in SEDDSs.

Other researchers encapsulated vitamin K1 into SEDDSs to develop lyophilized tablets for and examined oral delivery [98]. They prepared these SEDDSs using Labrasol and Transcutol as the excipients. The droplet diameters size of a series of SEDDSs was 92 to 263 nm, depending on the mixture. An in vitro release study indicated that the commercial tablets released 28% of vitamin K1 after 1 h; the optimized SEDDSs tablets released 99% of vitamin K, which is due to the smallest droplet size of 82 nm. Analysis of the pharmacokinetics of vitamin K1 from SEDDSs and commercial tablets in human volunteers indicated that SEDDSs increased vitamin K1 absorption, with a bioavailability that was 170% of that provided by the commercial products. The AUC of these oral SEDDSs was similar to that obtained from intramuscular injection. Table 1 summarizes the profiles of SEDDSs formulations used for oral vitamin delivery.

Vitamin E and its derivatives can also function as additives, rather than the active ingredient, in lipid nanocarriers, because vitamin E is a strong antioxidant that can stabilize oxygen-sensitive drugs or bioactive agents in lipid nanosystems [61,99]. TPGS is a non-ionic surfactant that can prevent drug precipitation and promote supersaturation in lipid nanosystems [100]; it can also interact with drugs by hydrogen bonding, thereby accelerating drug dissolution [101]. Previous research reported that TPGS could inhibit presystemic drug metabolism and intestinal efflux mediated by P-gp, and increase oral drug bioavailability [62,102]. Yang et al. [103] evaluated the oral pharmacokinetics of paclitaxel (an anti-cancer agent) in SEDDSs with TPGS1000 as a P-gp inhibitor. Because of the high affinity for P-gp and the first-pass effect by cytochrome P450 enzymes, oral administration of paclitaxel is not very

effective [104]. An aqueous dilution of paclitaxel-loaded SEDDSs led to droplet diameters of only 2 nm. Oral administration of these SEDDSs to rats at 2, 5, and 10 mg/kg indicated that the SEDDSs increased the bioavailability by 29% to 53% (depending on the dose) relative to commercial Taxol<sup>®</sup>. This result suggests that TPGS have great potential for increasing drug absorption. Other research examined paclitaxel-loaded SEDDSs in patients with advanced cancers to determine the oral efficiency [105]. The results indicated that TPGS1000 increased paclitaxel solubility. In these experiments, all of the patients received 160 mg on days 1, 8, and 15. The AUC was similar for oral SEDDSs ( $2.06 \mu\text{g}\cdot\text{h mL}^{-1}$ ) and Taxol<sup>®</sup> ( $1.97 \mu\text{g}\cdot\text{h mL}^{-1}$ ). However, oral SEDDSs had a shorter  $t_{\text{max}}$  (2 h) than Taxol<sup>®</sup> (4 h), suggesting that TPGS increased the absorption rate of paclitaxel.

Docetaxel is a second-generation of taxoid with greater anticancer potency than paclitaxel. Valicherla et al. [106] developed docetaxel-loaded SEDDSs containing TPGS1000 (droplet diameter: 160 to 180 nm), and evaluated oral absorption and therapeutic activity. The SEDDSs had a 25-fold increased cytotoxicity against breast cancer (MCF-7) cells relative to the free drug. The absolute bioavailability of SEDDSs in rats (22%) was higher than that of Taxotere<sup>®</sup> (7%). The chylomicron flow blocking and tissue distribution indicated the importance of lymphatic transport of SEDDSs, and that this accounted for its greater tumor accumulation than Taxotere<sup>®</sup>.

Cyclosporine A is a lipophilic cyclic polypeptide used as an immunosuppressant drug for immunomodulation in transplant recipients. Oral dosing has limited effectiveness, because of its limited aqueous solubility, low intestinal permeation, and P-g efflux [107]. Thus, researchers incorporated TPGS1000 in SEDDSs as an efflux inhibitor to increase the intestinal absorption of oral cyclosporine A [108]. The optimized nanocarriers had good stability in simulated GI fluids. These SEDDSs had faster drug release and 4.5-fold greater oral bioavailability than the commercial product (Bioral<sup>®</sup>). The nephrotoxicity of these SEDDSs was negligible, based on measurements of blood urea nitrogen and plasma creatinine.

Sirolimus (rapamycin) is a triene macrolide with potent immunosuppressive effects due to its inhibition of T-cell activation. However, the poor water solubility and low stability of this drug limit its use as an oral agent. Cho et al. [109] designed solid SEDDSs (mean droplet diameter: 108 nm) for sirolimus to improve its dissolution, stability, and GI absorption. Based on surfactant screening, TPGS1000 was a more effective stabilizer in simulated gastric fluid than Poloxamer, Gelucire, and Sucroester. The addition of TPGS1000 also increased the  $t_{1/2}$  of sirolimus from 5.2 to 100.3 min. These researchers also administered oral sirolimus to rats at a dose of 5 mg/kg for the analysis of its pharmacokinetics. Relative to the commercial Rapamune<sup>®</sup> solution, the SEDDS had a greater AUC (363 vs. 484  $\mu\text{g}\cdot\text{h mL}^{-1}$ ) and a shorter  $t_{\text{max}}$  (2.4 vs. 1.0 h).

Cefpodoxime is an oral, third-generation cephalosporin antibiotic. Previous research attempted to improve its solubility, GI permeation, and oral bioavailability by use of SEDDSs, with TPGS and Tween 80 as surfactants and Capmul as the oil phase (average diameter: 55 to 60 nm) [110]. An in vitro permeability test, performed in a Franz diffusion cell using goat intestine as the diffusion barrier, indicated that the drug flux was much greater for the SEDDSs than the free control (0.985 vs. 0.104  $\mu\text{g}/\text{cm}^2/\text{min}$ ). Administration of oral formulations to rats at a dose of 100 mg/kg indicated the SEDDSs provided a 5.4-fold increased AUC relative to the plain cefpodoxime.

Fenofibrate is a cholesterol-lowering drug with a high lipophilicity, whose oral bioavailability in hard gelatin capsules is about 60%, but highly variable among individuals [111]. Wei et al. [112] investigated the oral bioavailability of fenofibrate formulated with SEDDSs, consisting of TPGS1000 and Tween 20 or Tween 80 as surfactants. Fenofibrate release from the SEDDSs was complete within 30 min, but release from the commercial product (Tricor<sup>®</sup>) was limited. A pharmacokinetic study of healthy volunteers examined the effect of different forms of oral fenofibrate at a dose of 54 mg. Tricor<sup>®</sup> had the greatest AUC (87  $\mu\text{g}\cdot\text{h mL}^{-1}$ ), followed by SEDDSs containing Tween 20 (53  $\mu\text{g}\cdot\text{h mL}^{-1}$ ) and SEDDSs containing Tween 80 (52  $\mu\text{g}\cdot\text{h mL}^{-1}$ ). Consumption of water with oral SEDDSs and the agitation of GI tract may be insufficient to enhance the self-emulsifying process that is necessary for in vivo dissolution. Another study examined the oral absorption of SEDDSs (droplet diameter: 205

to 379 nm, depending on the oil:surfactant ratio) loaded with fenofibrate that were composed of Myritol (oil phase) and TPGS1000 (surfactant) [113]. These researchers then selected two optimized SEDDSs for analysis of the pharmacokinetics in healthy subjects receiving oral fenofibrate containing Tween 80 or with a high oil:surfactant ratio. The  $t_{\max}$  was greatest for Tricor<sup>®</sup> (2.8 h), followed by Tween 80 SEDDSs (2.0 h) and high-oil SEDDSs (1.8 h). The bioavailability was also 1.2-fold greater for high-oil SEDDSs than Tricor<sup>®</sup>. However, loading fenofibrate into Tween 80 SEDDSs reduced the AUC. Table 2 summarizes the pharmacokinetic parameters of oral drug delivery assisted by TPGS-containing SEDDSs that were designed to increase bioavailability.

**Table 2.** Characterization of self-emulsifying drug delivery systems (SEDDSs) incorporated with D- $\alpha$ -tocopheryl polyethylene glycol succinate (TPGS) as the surfactants for enhancing the oral absorption of drugs.

Active Ingredient	Average Size	Model Animals	Outcomes Offered by Nanoparticles	Reference
Paclitaxel	2 nm	Rat	An increased bioavailability of 1.3–1.5-fold compared to Taxol <sup>®</sup>	Yang et al. [97]
Paclitaxel	Unknown	Patients with cancers	A decreased $t_{\max}$ of 2-fold compared to Taxol <sup>®</sup>	Veltkamp et al. [99]
Docetaxel	160–180 nm	Rat	An increased bioavailability of 3.2-fold compared to Taxotere <sup>®</sup>	Valicherla et al. [100]
Cyclosporine A	72 nm	Rat	An increased bioavailability of 4.5-fold compared to Bioral <sup>®</sup>	Jain et al. [102]
Sirolimus	108 nm	Rat	An increased bioavailability of 1.3-fold compared to Rapamune <sup>®</sup>	Cho et al. [103]
Cefpodoxime	55–60 nm	Rat	An increased bioavailability of 5.4-fold compared to plain drug	Bajaj et al. [104]
Fenofibrate	Unknown	Human	The bioavailability was reduced by SEDDSs	Wei et al. [106]
Fenofibrate	205–379 nm	Human	An increased bioavailability of 1.2-fold compared to Tricor <sup>®</sup>	Lin et al. [107]

TPGS, D- $\alpha$ -tocopheryl polyethylene glycol succinate.

#### 4.2. Nanoemulsions/Microemulsions for Oral Vitamin Delivery

Nanoemulsions and microemulsions are other approaches used to improve the solubility and GI transport of vitamins [114]. Vitamins that are formulated in nanoemulsions have better physical stability in electrolyte dispersions and plasma [115]. The group of Dr. McClements (University of Massachusetts) performed a series of experiments to investigate the effect of different nanoemulsion formulations on the GI bioaccessibility of  $\beta$ -carotene (a provitamin A). More specifically, they examined the influence of the oil matrix of nanoemulsions on the GI diffusion of  $\beta$ -carotene [116]. They created nanoemulsions consisting of Tween 20 as an emulsifier, with LCTs, MCTs, or orange oil as the carrier oils, and then measured bioaccessibility across a GI membrane using an in vitro model to simulate the gastric and intestinal phases. The bioaccessibility significantly depended on the type of oil in the nanoemulsion. Thus, the bioaccessibility of  $\beta$ -carotene was near 0 in orange oil (due to an inability to form mixed micelles that solubilize  $\beta$ -carotene). However, the bioaccessibility was relatively high for LCTs (66%), but it was low for MCTs (2%), indicating that the mixed micelles with MCTs were too small to solubilize  $\beta$ -carotene.

The team of Dr. McClements also compared the bioaccessibility of  $\beta$ -carotene from predissolved nanoemulsions, a physical mixture with nanoemulsions, and phosphate buffered saline [117]. They constructed the *o/w* nanoemulsions using corn oil as the lipid core. Measurement of bioaccessibility using a simulated GI model indicated that the  $\beta$ -carotene crystals in PBS had the lowest transport, which they attributed to the small number of mixed micelles that are available for the solubilization of  $\beta$ -carotene. The solubilized  $\beta$ -carotene in nanoemulsions was transferred from the oil droplets into mixed micelles in the lipid digestion step, leading to a bioaccessibility of 69%. The interfacial layer surrounding the oil droplets in nanoemulsions is essential to maintain the long-term stability of

nanosystems [118]. Thus, Liu et al. [119] utilized ternary conjugates of covalent polyphenol, protein, and carbohydrate cross-links to stabilize the oil drop surface of  $\beta$ -carotene-loaded nanoemulsions. The nanoparticles that were coated with surface-active chlorogenic acid-lactoferrin-polydextrose had better stability in terms of droplet fusion in the GI tract, and therefore increased  $\beta$ -carotene bioaccessibility. Their interpretation was that this was because the formation of a thick interfacial layer by the conjugates suppressed the ability of lipase to adsorb to the oil droplets. Mun et al. [120] incorporated  $\beta$ -carotene-loaded nanoemulsions into rice starch hydrogels and then determined the in vitro bioaccessibility in simulated GI tract. The oil droplets were stable in the simulated stomach, but they aggregated in the simulated small intestine. Moreover, when they added  $\beta$ -carotene into the nanoemulsions, the bioaccessibility increased from 1% to 23% due to the formation of mixed micelles in the simulated small intestine fluid. The further incorporation of hydrogels increased the bioaccessibility to about 50%, presumably because the hydrogel matrix protected the oil droplets from coalescence in the gastric phase.

*Rhinacanthus nasutus* is a medicinal herb rich in carotenoids that has anticancer activity [121]. Ho et al. [122] isolated the carotenoids from *R. nasutus* to prepare microemulsions with enhanced oral bioavailability in rats. The microemulsions were prepared using Capryol 90, Transcutol, and Tween 80, and the mean size was 10.4 nm. A carotenoid suspension or microemulsions were fed to rats at a dose of 20 mg/kg. The absolute bioavailability of carotenoids was 0.11% for the aqueous dispersion and 0.45% for the microemulsions.

Other researchers examined the anti-inflammatory effect of vitamin D-loaded nanoemulsions in ovalbumin-activated asthmatic mice [123]. The nanoemulsions contained Miglyol 812, Cremophor RH40, Tween 80, and Transcutol and the Balb/c mice received oral vitamin D at a dose of 2000 IU/kg. The nanoemulsions had a greater  $C_{\max}$  (26.3 vs. 38.3 ng/mL) and a shorter  $t_{\max}$  (5.22 vs. 3.56 h). Treatment with nanoemulsions also decreased the myeloperoxidase activity,  $O_2^-$  level, and cytokine production, and attenuated asthma. Salvia-Trujillo et al. [124] evaluated the impact of nanoemulsion droplet size on the in vitro vitamin D2 bioaccessibility and in vivo absorption in humans. The nanoemulsions had mean droplet diameters of 112, 530, and 14,500 nm. The in vitro lipid digestion experiments indicated the complete digestion of the small- and medium-sized nanoemulsions, but not the large ones (83%). However, in vivo oral absorption was greatest for the largest emulsions. Differences between the simulated GI tract and the actual GI tract may partly explain the poor correlation of the in vitro and in vivo results.

Parthasarathi et al. [125] examined the impact of droplet size on vitamin E absorption by preparing nanoemulsions (diameter: 277 nm) with conventional emulsions (diameter: 1285 nm). The saponin-coated nanoemulsions had greater stability when subjected to heating, long-term storage, and mechanical stress. They also administered the vitamin E to rats at a dose of 100 mg/kg. The nanoemulsions had a greater  $C_{\max}$  (11.6 vs. 2.6  $\mu$ g/mL) and a shorter  $t_{1/2}$  (0.85 vs. 1.11 h). Natural vitamin E can be derived from crops (nuts, grains, and vegetables) and nanoemulsions can be an excellent system for the oral absorption of natural vitamin E [47]. Fabrication of vitamin E-loaded nanoemulsions led to an average diameter of 88 nm, and the AUC of vitamin E in nanoemulsions was 1.6-fold greater than commercial soft capsules in rats. The nanoemulsions were also stronger antioxidants than soft capsules in rats with oxidative damage due to d-Galactosamine.

As with SEDDSs, vitamin E derivatives may be used in nanoemulsions to improve oral drug absorption. Thus, previous researchers used nanoemulsions containing TPGS1000 with paclitaxel to enhance oral absorption in rats [126]. These nanoemulsions had a diameter of 21.6 nm and a PDI of 0.13. Upon oral administration, the commercial product (Taxol) had plasma below 300 ng/mL and a bioavailability of 10.6%. Paclitaxel from nanoemulsions was rapidly absorbed, and it had a  $C_{\max}$  of 3.5  $\mu$ g/mL within 30 min and a bioavailability of 70.6%.

Acetylpuerarin is a promising agent for the amelioration of coronary heart disorder and arrhythmia, because it decreases myocardial oxygen consumption [127]. Sun et al. [128] tried to develop nanoemulsions to enhance oral acetylpuerarin delivery and to improve its therapeutic



potential. Their nanoemulsions had an average diameter of 150 nm and were stabilized by TPGS1000 with acetylpuerarin encapsulation. The AUC of oral acetylpuerarin nanoemulsions in rats was  $5.76 \mu\text{g}\cdot\text{h mL}^{-1}$ ; this value was 2.6-fold greater than the suspension and 1.7-fold greater than the oil solution. They also used the chylomicron flow-blocking rat model to examine the role of lymphatic transport. The results showed a lower AUC in the blocking model than the control model, indicating the importance of lymphatic absorption for oral nanoemulsions. Table 3 shows the profiles for oral vitamin delivery by nanoemulsions and microemulsions.

**Table 3.** Characterization of nanoemulsions and microemulsions loaded with vitamins or their derivatives and their oral absorption.

Vitamin	Average Size	In Vitro or In Vivo Model	Outcomes Offered by Nanoparticles	Reference
$\beta$ -carotene	140~170 nm	In vitro bioaccessibility	Increased bioaccessibility in simulated GI environment (66%)	Qian et al. [110]
$\beta$ -carotene	About 200 nm	In vitro bioaccessibility	Increased bioaccessibility in simulated GI environment (69%)	Xia et al. [111]
$\beta$ -carotene	About 400 nm	In vitro bioaccessibility	Increased $\beta$ -carotene stability and bioaccessibility in simulated GI environment	Liu et al. [113]
$\beta$ -carotene	260 nm	In vitro bioaccessibility	Increased bioaccessibility in simulated GI environment (about 50%)	Mun et al. [114]
Carotenoids	10.4 nm	In vivo bioavailability in rat	An increased bioavailability of 4-fold compared to aqueous suspension	Ho et al. [116]
Vitamin D	Unknown	In vivo bioavailability in mouse	An increased bioavailability of 1.3-fold with asthma attenuation	Tang et al. [117]
Vitamin D2	112, 530, and 14,500 nm	In vitro bioaccessibility and in vivo bioavailability	Increased bioavailability following the increase of droplet size	Salvia-Trujillo et al. [118]
Vitamin E	227 nm	In vivo bioavailability in rat	An increased bioavailability of 3-fold compared to conventional emulsions	Parthasarathi et al. [119]
Natural vitamin E	88 nm	In vivo bioavailability in rat	An increased bioavailability of 1.6-fold compared to soft capsules	Gong et al. [120]
TPGS as surfactant	21.6 nm	In vivo bioavailability in rat	An increased bioavailability of 6.7-fold compared to Taxol	Khandavilli and Panchagnula [121]
TPGS as surfactant	150 nm	In vivo bioavailability in rat	An increased bioavailability of 2.6-fold compared to aqueous suspension	Sun et al. [123]

TPGS, D- $\alpha$ -tocopheryl polyethylene glycol succinate.

#### 4.3. SLNs for Oral Vitamin Delivery

Some investigations have examined the use of SLNs as oral delivery systems for vitamins and their analogs because they are biocompatible with the lipid matrix (consisting of triglycerides, fatty acids, or glycerol esters) and are readily degraded in vivo. Astaxanthin is a naturally occurring carotenoid that is abundant in salmon, shellfish, and shrimp, which has activity against several cancers and cardiovascular disorders, with greater potency than vitamin E and  $\beta$ -carotene [129]. However, its poor water solubility, light sensitivity, and decomposition in the presence of oxygen have limited its use in oral formulations. Thus, researchers have entrapped astaxanthin into SLNs composed of glycerol esters and Tween 20 [130]. These SLNs had a mean diameter of 163 to 167 nm and the encapsulation percentage was approximately 89%. The results showed that SLNs provided prolonged astaxanthin release in simulated GI juices.

The saturable process of intestinal  $\gamma$ -tocotrienol absorption (mediated by NPC1L1) leads to an oral bioavailability of only 9% [131]. Thus, researchers have also examined the use of SLNs to increase  $\gamma$ -tocotrienol permeation and bioavailability in human liver (HepG2) cells [132]. The results indicated that the SLN provided a two-fold increased uptake relative to mixed micelles. In addition, an in

situ perfusion study, in which rats were given oral  $\gamma$ -tocotrienol (10 mg/kg) as SLNs or as mixed micelles, demonstrated that SLNs provided a 10-fold greater permeability. The AUC for SLNs was  $12.1 \mu\text{g}\cdot\text{h mL}^{-1}$  and that for mixed micelles was  $3.9 \mu\text{g}\cdot\text{h mL}^{-1}$ .

Other researchers, in an attempt to increase the bioavailability of docetaxel (an anticancer agent), compared TPGS 1000-coated docetaxel-loaded SLNs (diameter: 189 nm) with Tween 80-coated docetaxel-loaded SLNs (diameter: 215 nm) [133]. The SLNs provided a more sustained release of docetaxel than the marketed product Taxotere®. In particular, after oral delivery, the AUC was  $12.9 \mu\text{g}\cdot\text{min/mL}$  for TPGS-coated SLNs  $7.0 \mu\text{g}\cdot\text{min/mL}$  for Tween 80-coated LNs, but only  $3.9 \mu\text{g}\cdot\text{min/mL}$  for Taxotere®. This result confirmed that TPGS inhibited docetaxel efflux.

Other researchers used TPGS 1000-coated SLNs with curcumin to increase its GI absorption [134]. Curcumin is a natural compound that has an antioxidant, anti-inflammatory, chemopreventative, and anti-viral properties [135], but its clinical use is limited due to its low aqueous solubility, instability in GI fluid, and rapid elimination [136]. Thus, the application of *N*-trimethyl chitosan to the SLN surface formed an acid-resistant shell, which increased the stability. An oral curcumin suspension (50 mg/kg) had a  $C_{\text{max}}$  of  $0.24 \mu\text{g/mL}$  and an AUC of  $0.27 \mu\text{g}\cdot\text{h mL}^{-1}$ ; however, oral SLNs with curcumin had a  $C_{\text{max}}$  of  $1.21 \mu\text{g/mL}$  and an AUC of  $6.23 \mu\text{g}\cdot\text{h mL}^{-1}$ . SLNs also improved curcumin targeting in the rat brain. Ji et al. [137] formulated curcumin into SLNs coated with TPGS and Brij® 78. The optimized SLNs had an average diameter of 135 nm with 91% curcumin encapsulation. These SLNs exhibited no “burst release”, suggesting homogeneous curcumin distribution in the lipid core. An in situ GI absorption test, in which a curcumin suspension and SLNs were dosed at 50 mg/kg, found that SLN loading increased curcumin permeability across jejunum from  $0.81 \times 10^{-4}$  to  $1.56 \times 10^{-4}$  cm/s. The AUC of SLNs was 12.3-fold higher than the suspension.

#### 4.4. NLCs for Oral Vitamin Delivery

It is also feasible to use NLCs as carriers to improve the oral absorption of lipid-soluble vitamins [89]. For example, previous researchers used hot pressure homogenization to develop NLCs that entrapped the lipophilic vitamin D3 [138]. These NLCs were stable and had a mean diameter of 133 nm. The diameter remained unchanged in simulated gastric fluid, but it increased to 216 nm in simulated intestinal fluid. An in vitro digestion test demonstrated that NLCs provided controlled release of vitamin D3, in that they were not degraded in simulated stomach fluid, but they released more than 90% of the vitamin D3 into intestinal fluid.

Dacarbazine is a highly lipophilic and light-sensitive anticancer drug with very low oral absorption [139]. Almousallam et al. [140] fabricated NLCs that were coated with TPGS to improve dacarbazine absorption. These NLCs encapsulated about 99% of this drug and the diameter of the nanoformulations was 155 nm. The in vitro release of the drug was biphasic, with 50% released during the first 2 h and sustained release for up to 30 h. Other researchers used TPGS-coated NLCs to encapsulate sulforaphane, a natural anti-cancer agent derived from broccoli, cauliflower, and cabbage, to improve oral bioavailability [141]. Sulforaphane has documented effectiveness against pancreatic, breast, hepatic, melanoma, and prostate malignancies [142]. The particle diameter was 145 nm and the encapsulation efficiency was 85%. Measurements of intestinal transport in vitro showed that NLC loading increased the permeability coefficient from  $0.67 \times 10^{-4}$  to  $4.82 \times 10^{-4}$  cm/min. In addition, examination of the in vivo pharmacokinetics in rats indicated that NLCs provided a five-fold enhancement of oral bioavailability relative to the control suspension. The sustained release of sulforaphane from NLCs also increased the  $t_{\text{max}}$  from 2.5 to 7.5 h.

## 5. Conclusions

When designing different formulations to improve the bioavailability of an oral vitamin, it is essential that the carrier stabilizes the vitamin and improves its transport into circulation. This review summarized recent advances in the use of vitamin-loaded lipid-based nanocarriers that were designed to enhance oral bioavailability. The selection of the carrier is important, and it should ideally provide

maximal activity and minimal side effects. The use of lipid nanoparticles has numerous advantages over conventional formulations for dosing of vitamins, because they are more stable, they can provide sustained release, they can target different tissues, and they provide increased bioavailability. Some important limitations of conventional formulations, such as low solubility and poor epithelium permeation, can also be resolved by the use of lipid nanocarriers. Self-assembled lipid nanoparticles are frequently utilized to improve the oral delivery of vitamins. The type of emulsifier, particle size, interfacial composition, and vitamin concentration are the major factors that impact oral absorption. The comparison of different lipid-based nanoparticles used for enhancing oral vitamin delivery is summarized in Table 4. Our introduction and description of the lipid-based nanocarriers that are used for vitamin delivery provide an overview for investigators who are attempting to design feasible and efficient delivery systems for vitamins and other bioactive agents. In the near future, it may be possible to extend the use of lipid nanoparticles by using them as vehicles for other functional nutrients.

**Table 4.** The comparison of different lipid nanocarriers for enhancing oral vitamin delivery.

Lipid Nanosystem	Nanoparticle Structure	Vitamins and Related Compounds Loaded
SEDDS	An anhydrous isotropic mixture of oil and emulsifier to spontaneously create nanoparticles in GI tract	Vitamin A, vitamin K1, vitamin K2, coenzyme Q10, lutein, and tocotrienols
Nanoemulsions/ microemulsions	The isotropic or heterogeneous mixtures to form oil droplets in an aqueous system stabilized by emulsifiers	Carotenoids, vitamin D, vitamin D2, and vitamin E
SLNs	The crystalline lipid structure in nanoparticles composed of melt-emulsified lipids that are solid at room temperature	Astaxanthin and tocotrienols
NLCs	The second-generation lipid nanoparticles composed of a mixture of liquid and solid lipids for improving physical stability	Vitamin D3

SEDDS, self-emulsifying drug delivery systems; SLNs, solid lipid nanoparticles; NLCs, nanostructured lipid carriers; GI, gastrointestinal.

**Author Contributions:** For research articles with several authors, a short paragraph specifying their individual contributions must be provided. The following statements should be used “Conceptualization, C.-Y.H. and J.-Y.F.; Methodology, C.-Y.H.; Data Collection, P.-W.W. and Z.-C.L.; Writing-Original Draft Preparation, C.-Y.H. and P.-W.W.; Writing-Review & Editing, A.A. and J.-Y.F.; Supervision, J.-Y.F.; Funding Acquisition, J.-Y.F.”, please turn to the CRediT taxonomy for the term explanation. Authorship must be limited to those who have contributed substantially to the work reported.

**Funding:** The authors are grateful for financial support from Ministry of Science and Technology of Taiwan (MOST-105-2320-B-182-010-MY3) and Chang Gung Memorial Hospital (CMRPG6G0221).

**Conflicts of Interest:** The authors declare no conflict of interest. The funders had no role in the design of the study; in the collection, analyses, or interpretation of data; in the writing of the manuscript, and in the decision to publish the results.

## References

- Choonara, B.F.; Choonara, Y.E.; Kumar, P.; Bijukumar, D.; du Toit, L.C.; Pillay, V. A review of advanced oral drug delivery technologies facilitating the protection and absorption of protein and peptide molecules. *Biotechnol. Adv.* **2014**, *32*, 1269–1282. [[CrossRef](#)] [[PubMed](#)]
- Tyagi, P.; Pechenov, S.; Anand Subramony, J. Oral peptide delivery: Translational challenges due to physiological effects. *J. Control. Release* **2018**, *287*, 167–176. [[CrossRef](#)] [[PubMed](#)]
- Rein, M.J.; Renouf, M.; Cruz-Hernandez, C.; Actis-Goretta, L.; Thakkar, S.K.; da Silva Pinto, M. Bioavailability of bioactive food compounds: A challenging journey to bioefficacy. *Br. J. Clin. Pharmacol.* **2013**, *75*, 588–602. [[CrossRef](#)] [[PubMed](#)]
- Rumondor, A.C.F.; Dhareshwar, S.S.; Kesisoglou, F. Amorphous solid dispersions or prodrugs: Complementary strategies to increase drug absorption. *J. Pharm. Sci.* **2016**, *105*, 2498–2508. [[CrossRef](#)] [[PubMed](#)]
- Weiss, J.; Decker, E.A.; McClements, D.J.; Kristbergsson, K.; Helgason, T.; Awad, T. Solid lipid nanoparticles as delivery systems for bioactive food components. *Food Biophys.* **2008**, *3*, 146–154. [[CrossRef](#)]

6. Suchaoain, W.; Bernkop-Schnürch, A. Nanocarriers protecting toward an intestinal pre-uptake metabolism. *Nanomedicine* **2017**, *12*, 255–269. [[CrossRef](#)] [[PubMed](#)]
7. Tagami, T.; Ozeki, T. Recent trends in clinical trials related to carrier-based drugs. *J. Pharm. Sci.* **2017**, *106*, 2219–2226. [[CrossRef](#)]
8. Chakraborty, S.; Shukla, D.; Mishra, B.; Singh, S. Lipid-an emerging platform for oral delivery of drugs with poor bioavailability. *Eur. J. Pharm. Biopharm.* **2009**, *73*, 1–15. [[CrossRef](#)]
9. Dumont, C.; Bourgeois, S.; Fessi, H.; Jannin, V. Lipid-based nanosuspensions for oral delivery of peptides, a critical review. *Int. J. Pharm.* **2018**, *541*, 117–135. [[CrossRef](#)]
10. Joyce, P.; Whitby, C.P.; Prestidge, C.A. Nanostructuring biomaterials with specific Activities towards digestive enzymes for controlled gastrointestinal absorption of lipophilic bioactive molecules. *Adv. Colloid Interface Sci.* **2016**, *237*, 52–75. [[CrossRef](#)]
11. Akula, S.; Gurram, A.K.; Devireddy, S.R. Self-microemulsifying drug delivery systems: An attractive strategy for enhanced therapeutic profile. *Int. Sch. Res. Notices* **2014**, *2014*, 964051. [[CrossRef](#)] [[PubMed](#)]
12. Managuli, R.S.; Raut, S.Y.; Reddy, M.S.; Mutalik, S. Targeting the intestinal lymphatic system: A versatile path for enhanced oral bioavailability of drugs. *Expert Opin. Drug Deliv.* **2018**, *15*, 787–804. [[CrossRef](#)] [[PubMed](#)]
13. Negi, L.M.; Tariq, M.; Talegaonkar, S. Nano scale self-emulsifying oil based carrier system for improved oral bioavailability of camptothecin derivative by P-Glycoprotein modulation. *Colloids Surf. B Biointerfaces* **2013**, *111*, 346–353. [[CrossRef](#)] [[PubMed](#)]
14. Roger, E.; Lagarce, F.; Garcion, E.; Benoit, J.P. Lipid nanocarriers improve paclitaxel transport throughout human intestinal epithelial cells by using vesicle-mediated transcytosis. *J. Control. Release* **2009**, *140*, 174–181. [[CrossRef](#)] [[PubMed](#)]
15. Howe, S.E.; Lickteig, D.J.; Plunkett, K.N.; Ryerse, J.S.; Konjufca, V. The uptake of soluble and particulate antigens by epithelial cells in the mouse small intestine. *PLoS ONE* **2014**, *9*, e86656. [[CrossRef](#)] [[PubMed](#)]
16. Shi, L.L.; Xie, H.; Lu, J.; Cao, Y.; Liu, J.Y.; Zhang, X.X.; Zhang, H.; Cui, J.H.; Cao, Q.R. Positively charged surface-modified solid lipid nanoparticles promote the intestinal transport of docetaxel through multifunctional mechanisms in rats. *Mol. Pharm.* **2016**, *13*, 2667–2676. [[CrossRef](#)]
17. Xu, Y.; Zheng, Y.; Wu, L.; Zhu, X.; Zhang, Z.; Huang, Y. Novel solid lipid nanoparticle with endosomal escape function for oral delivery of insulin. *ACS Appl. Mater. Interfaces* **2018**, *10*, 9315–9324. [[CrossRef](#)]
18. Li, Q.; Xia, D.; Tao, J.; Shen, A.; He, Y.; Gan, Y.; Wang, C. Self-assembled core-shell-type lipid-polymer hybrid nanoparticles: Intracellular trafficking and relevance for oral absorption. *J. Pharm. Sci.* **2017**, *106*, 3120–3130. [[CrossRef](#)]
19. Pouton, C.W.; Porter, C.J. Formulation of lipid-based delivery systems for oral administration: Materials, methods and strategies. *Adv. Drug Deliv. Rev.* **2008**, *60*, 625–637. [[CrossRef](#)]
20. Kollipara, S.; Gandhi, R.K. Pharmacokinetic aspects and in vitro-in vivo correlation potential for lipid-based formulations. *Acta Pharm. Sin. B* **2014**, *4*, 333–349. [[CrossRef](#)]
21. Chatzidaki, M.D.; Mateos-Diaz, E.; Leal-Calderon, F.; Xenakis, A.; Carrière, F. Water-in-oil microemulsions versus emulsions as carriers of hydroxytyrosol: An in vitro gastrointestinal lipolysis study using the pHstat technique. *Food Funct.* **2016**, *7*, 2258–2269. [[CrossRef](#)] [[PubMed](#)]
22. Fonte, P.; Nogueira, T.; Gehm, C.; Ferreira, D.; Sarmiento, B. Chitosan-coated solid lipid nanoparticles enhance the oral absorption of insulin. *Drug Deliv. Transl. Res.* **2011**, *1*, 299–308. [[CrossRef](#)] [[PubMed](#)]
23. Kumar, D.H.L.; Sarkar, P. Encapsulation of bioactive compounds using nanoemulsions. *Environ. Chem. Lett.* **2018**, *16*, 59–70. [[CrossRef](#)]
24. Lopes, C.M.; Martins-Lopes, P.; Souto, E.B. Nanoparticulate carriers (NPC) for oral pharmaceuticals and nutraceuticals. *Pharmazie* **2010**, *65*, 75–82. [[PubMed](#)]
25. Zhang, Y.; Zhou, W.E.; Yan, J.Q.; Liu, M.; Zhou, Y.; Shen, X.; Ma, Y.L.; Feng, X.S.; Yang, J.; Li, G.H. A review of the extraction and determination methods of thirteen essential vitamins to the human body: An update from 2010. *Molecules* **2018**, *23*, 1484. [[CrossRef](#)] [[PubMed](#)]
26. Eggersdorfer, M.; Laudert, D.; Létinois, U.; McClymont, T.; Medlock, J.; Netscher, T.; Bonrath, W. One hundred years of vitamins-a success story of the natural sciences. *Angew Chem. Int. Ed. Engl.* **2012**, *51*, 12960–12990. [[CrossRef](#)] [[PubMed](#)]
27. Karaźniewicz-Łada, M.; Głowska, A. A review of chromatographic methods for the determination of water- and fat-soluble vitamins in biological fluids. *J. Sep. Sci.* **2016**, *39*, 132–148. [[CrossRef](#)] [[PubMed](#)]



28. Langi, P.; Kiokias, S.; Varzakas, T.; Proestos, C. Carotenoids: From plants to food and feed industries. *Methods Mol. Biol.* **2018**, *1852*, 57–71. [[PubMed](#)]
29. Weber, D.; Grune, T. The contribution of  $\beta$ -carotene to vitamin A supply of humans. *Mol. Nutr. Food Res.* **2012**, *56*, 251–258. [[CrossRef](#)]
30. Borel, P.; Desmarchelier, C. Genetic variations associated with vitamin A status and vitamin A bioavailability. *Nutrients* **2017**, *9*, 246. [[CrossRef](#)]
31. O’Byrne, S.M.; Blaner, W.S. Retinol and retinyl esters: Biochemistry and physiology. *J. Lipid Res.* **2013**, *54*, 1731–1743. [[CrossRef](#)] [[PubMed](#)]
32. Vrolijk, M.F.; Opperhuizen, A.; Jansen, E.H.J.M.; Hageman, G.J.; Bast, A.; Haenen, G.R.M.M. The vitamin B6 paradox: Supplementation with high concentrations of pyridoxine leads to decreased vitamin B6 function. *Toxicol. Vitro* **2017**, *44*, 206–212. [[CrossRef](#)] [[PubMed](#)]
33. Matte, J.J.; Guay, F.; Christiane, L. Bioavailability of vitamin B<sub>12</sub> in cow’s milk. *Br. J. Nutr.* **2012**, *107*, 61–66. [[CrossRef](#)]
34. Bueno Dalto, D.; Audet, I.; Girard, C.L.; Matte, J.J. Bioavailability of vitamin B<sub>12</sub> from dairy products using a pig model. *Nutrients* **2018**, *10*, 1134. [[CrossRef](#)] [[PubMed](#)]
35. Jacob, R.A.; Sotoudeh, G. Vitamin C function and status in chronic disease. *Nutr. Clin. Care* **2002**, *5*, 66–74. [[CrossRef](#)] [[PubMed](#)]
36. Carr, A.C.; Maggini, S. Vitamin C and immune function. *Nutrients* **2017**, *9*, 1211. [[CrossRef](#)]
37. Davis, J.L.; Paris, H.L.; Beals, J.W.; Binns, S.E.; Giordano, G.R.; Scalzo, R.L.; Schweder, M.M.; Blair, E.; Bell, C. Liposomal-encapsulated ascorbic acid: Influence on vitamin C bioavailability and capacity to protect against ischemia-reperfusion injury. *Nutr. Metab. Insights* **2016**, *9*, 25–30. [[CrossRef](#)]
38. Muñoz-Montesino, C.; Roa, F.J.; Peña, E.; González, M.; Sotomayor, K.; Inostroza, E.; Muñoz, C.A.; González, I.; Maldonado, M.; Soliz, C.; et al. Mitochondrial ascorbic acid transport is mediated by a low-affinity form of the sodium-coupled ascorbic acid transporter-2. *Free Radic. Biol. Med.* **2014**, *70*, 241–254. [[CrossRef](#)]
39. Bouillon, R.; Suda, T. Vitamin D: Calcium and bone homeostasis during evolution. *Bonekey Rep.* **2014**, *3*, 480. [[CrossRef](#)]
40. Reboul, E.; Goncalves, A.; Comera, C.; Bott, R.; Nowicki, M.; Landrier, J.F.; Jourdeuil-Rahmani, D.; Dufour, C.; Collet, X.; Borel, P. Vitamin D intestinal absorption is not a simple passive diffusion: Evidences for involvement of cholesterol transporters. *Mol. Nutr. Food Res.* **2011**, *55*, 691–702. [[CrossRef](#)]
41. Hodgkinson, A.J.; Wallace, O.A.M.; Kruger, M.C.; Prosser, C.G. Effect of the dietary delivery matrix on vitamin D3 bioavailability and bone mineralisation in vitamin-D3-deficient growing male rats. *Br. J. Nutr.* **2018**, *119*, 143–152. [[CrossRef](#)] [[PubMed](#)]
42. Szymańska, R.; Nowicka, B.; Kruk, J. Vitamin E-occurrence, biosynthesis by plants and functions in human nutrition. *Mini Rev. Med. Chem.* **2017**, *17*, 1039–1052. [[CrossRef](#)] [[PubMed](#)]
43. Azzi, A. Many tocopherols, one vitamin E. *Mol. Aspects Med.* **2018**, *61*, 92–103. [[CrossRef](#)] [[PubMed](#)]
44. Reboul, E. Vitamin E bioavailability: Mechanisms of intestinal absorption in the spotlight. *Antioxidants* **2017**, *6*, 95. [[CrossRef](#)] [[PubMed](#)]
45. Zou, W.; Noh, S.K.; Owen, K.Q.; Koo, S.I. Dietary L-carnitine enhances the lymphatic absorption of fat and alpha-tocopherol in ovariectomized rats. *J. Nutr.* **2005**, *135*, 753–756. [[CrossRef](#)] [[PubMed](#)]
46. Traber, M.G. Vitamin E inadequacy in humans: Causes and consequences. *Adv. Nutr.* **2014**, *5*, 503–514. [[CrossRef](#)] [[PubMed](#)]
47. Gong, Y.; Wu, Y.; Zheng, C.; Fan, L.; Xiong, F.; Zhu, J. An excellent delivery system for improving the oral bioavailability of natural vitamin E in rats. *AAPS PharmSciTech* **2012**, *13*, 961–966. [[CrossRef](#)]
48. Bruno, R.S.; Leonard, S.W.; Park, S.I.; Zhao, Y.; Traber, M.G. Human vitamin E requirements assessed with the use of apples fortified with deuterium-labeled alpha-tocopheryl acetate. *Am. J. Clin. Nutr.* **2006**, *83*, 299–304. [[CrossRef](#)]
49. Goncalves, A.; Roi, S.; Nowicki, M.; Dhaussy, A.; Huertas, A.; Amiot, M.J.; Reboul, E. Fat-soluble vitamin intestinal absorption: Absorption sites in the intestine and interactions for absorption. *Food Chem.* **2015**, *172*, 155–160. [[CrossRef](#)]
50. Shearer, M.J.; Okano, T. Key pathways and regulators of vitamin K function and intermediary metabolism. *Annu. Rev. Nutr.* **2018**, *38*, 127–151. [[CrossRef](#)]

51. van Hasselt, P.M.; Janssens, G.E.; Slot, T.K.; van der Ham, M.; Minderhoud, T.C.; Talelli, M.; Akkermans, L.M.; Rijcken, C.J.; van Nostrum, C.F. The influence of bile acids on the oral bioavailability of vitamin K encapsulated in polymeric micelles. *J. Control. Release* **2009**, *133*, 161–168. [[CrossRef](#)] [[PubMed](#)]
52. Øie, S.; Trenk, D.; Guentert, T.W.; Mosberg, H.; Jähnchen, E. Disposition of vitamin K<sub>1</sub> after intravenous and oral administration to subjects on phenprocoumon therapy. *Int. J. Pharm.* **1988**, *48*, 223–230. [[CrossRef](#)]
53. Weber, S.; Zimmer, A.; Pardeike, J. Solid lipid nanoparticles (SLN) and nanostructured lipid carriers (NLC) for pulmonary application: A review of the state of the art. *Eur. J. Pharm. Biopharm.* **2014**, *86*, 7–22. [[CrossRef](#)] [[PubMed](#)]
54. Pathak, K.; Raghuvanshi, S. Oral bioavailability: Issues and solutions via nanoformulations. *Clin. Pharmacokinet.* **2015**, *54*, 325–357. [[CrossRef](#)] [[PubMed](#)]
55. Dokania, S.; Joshi, A.K. Self-microemulsifying drug delivery system (SMEDDS)-challenges and road ahead. *Drug Deliv.* **2015**, *22*, 675–690. [[CrossRef](#)] [[PubMed](#)]
56. Date, A.A.; Desai, N.; Dixit, R.; Nagarsenker, M. Self-nanoemulsifying drug delivery systems: Formulation insights, applications and advances. *Nanomedicine* **2010**, *5*, 1595–1616. [[CrossRef](#)] [[PubMed](#)]
57. Chen, C.H.; Chen, C.J.; Elzoghby, A.O.; Yeh, T.S.; Fang, J.Y. Self-assembly and directed assembly of lipid nanocarriers for prevention of liver fibrosis in obese rats: A comparison with the therapy of bariatric surgery. *Nanomedicine* **2018**, *13*, 1551–1566. [[CrossRef](#)] [[PubMed](#)]
58. Khan, A.W.; Kotta, S.; Ansari, S.H.; Sharma, R.K.; Ali, J. Potentials and challenges in self-nanoemulsifying drug delivery systems. *Expert Opin. Drug Deliv.* **2012**, *9*, 1305–1317. [[CrossRef](#)] [[PubMed](#)]
59. Rehman, F.U.; Shah, K.U.; Shah, S.U.; Khan, I.U.; Khan, G.M.; Khan, A. From nanoemulsions to self-nanoemulsions, with recent advances in self-nanoemulsifying drug delivery systems (SNEDDS). *Expert Opin. Drug Deliv.* **2017**, *14*, 1325–1340. [[CrossRef](#)] [[PubMed](#)]
60. Cole, E.T.; Cadé, D.; Benameur, H. Challenges and opportunities in the encapsulation of liquid and semi-solid formulations into capsules for oral administration. *Adv. Drug Deliv. Rev.* **2008**, *60*, 747–756. [[CrossRef](#)] [[PubMed](#)]
61. Tsai, M.J.; Wu, P.C.; Huang, Y.B.; Chang, J.S.; Lin, C.L.; Tsai, Y.H.; Fang, J.Y. Baicalein loaded in tocol nanostructured lipid carriers (tocol NLCs) for enhanced stability and brain targeting. *Int. J. Pharm.* **2012**, *423*, 461–470. [[CrossRef](#)] [[PubMed](#)]
62. Guo, Y.; Luo, J.; Tan, S.; Otieno, B.O.; Zhang, Z. The applications of Vitamin E TPGS in drug delivery. *Eur. J. Pharm. Sci.* **2013**, *49*, 175–186. [[CrossRef](#)] [[PubMed](#)]
63. Gao, F.; Zhang, Z.; Bu, H.; Huang, Y.; Gao, Z.; Shen, J.; Zhao, C.; Li, Y. Nanoemulsion improves the oral absorption of candesartan cilexetil in rats: Performance and mechanism. *J. Control. Release* **2011**, *149*, 168–174. [[CrossRef](#)] [[PubMed](#)]
64. Salvia-Trujillo, L.; Martín-Belloso, O.; McClements, D.J. Excipient nanoemulsions for improving oral bioavailability of bioactives. *Nanomaterials* **2016**, *6*, 17. [[CrossRef](#)] [[PubMed](#)]
65. Wibowo, D.; Zhao, C.X.; Middelberg, A.P. Emulsion-templated silica nanocapsules formed using bio-inspired silicification. *Chem. Commun.* **2014**, *50*, 11325–11328. [[CrossRef](#)] [[PubMed](#)]
66. McClements, D.J. Edible nanoemulsions: Fabrication, properties, and functional performance. *Soft Matter* **2011**, *7*, 2297–2316. [[CrossRef](#)]
67. Salvia-Trujillo, L.; Soliva-Fortuny, R.; Rojas-Gratü, M.A.; McClements, D.J.; Martín-Belloso, O. Edible nanoemulsions as carriers of active ingredients: A review. *Annu. Rev. Food Sci. Technol.* **2017**, *8*, 439–466. [[CrossRef](#)]
68. Callender, S.P.; Mathews, J.A.; Kobernyk, K.; Wettig, S.D. Microemulsion utility in pharmaceuticals: Implications for multi-drug delivery. *Int. J. Pharm.* **2017**, *526*, 425–442. [[CrossRef](#)]
69. Ezzati Nazhad Dolatabadi, J.; Valizadeh, H.; Hamishehkar, H. Solid lipid nanoparticles as efficient drug and gene delivery systems: Recent breakthroughs. *Adv. Pharm. Bull.* **2015**, *5*, 151–159. [[CrossRef](#)]
70. Garcês, A.; Amaral, M.H.; Sousa Lobo, J.M.; Silva, A.C. Formulations based on solid lipid nanoparticles (SLN) and nanostructured lipid carriers (NLC) for cutaneous use: A review. *Eur. J. Pharm. Sci.* **2018**, *112*, 159–167. [[CrossRef](#)]
71. Zhou, X.; Zhang, X.; Ye, Y.; Zhang, T.; Wang, H.; Ma, Z.; Wu, B. Nanostructured lipid carriers used for oral delivery of oridonin: An effect of ligand modification on absorption. *Int. J. Pharm.* **2015**, *479*, 391–398. [[CrossRef](#)] [[PubMed](#)]

72. Beloqui, A.; Solinís, M.Á.; Rodríguez-Gascón, A.; Almeida, A.J.; Préal, V. Nanostructured lipid carriers: Promising drug delivery systems for future clinics. *Nanomed. Nanotechnol. Biol. Med.* **2016**, *12*, 143–161. [[CrossRef](#)] [[PubMed](#)]
73. Shah, A.V.; Desai, H.H.; Thool, P.; Dalrymple, D.; Serajuddin, A.T.M. Development of self-microemulsifying drug delivery system for oral delivery of poorly water-soluble nutraceuticals. *Drug Dev. Ind. Pharm.* **2018**, *44*, 895–901. [[CrossRef](#)] [[PubMed](#)]
74. Taha, E.I.; Al-Suwayeh, S.A.; Anwer, M.K. Preparation, in vitro and in vivo evaluation of solid-state self-nanoemulsifying drug delivery system (SNEDDS) of vitamin A acetate. *J. Drug Target.* **2009**, *17*, 468–473. [[CrossRef](#)] [[PubMed](#)]
75. Shanmugam, S.; Baskaran, R.; Balakrishnan, P.; Thapa, P.; Yong, C.S.; Yoo, B.K. Solid self-nanoemulsifying drug delivery system (S-SNEDDS) containing phosphatidylcholine for enhanced bioavailability of highly lipophilic bioactive carotenoid lutein. *Eur. J. Pharm. Biopharm.* **2011**, *79*, 250–257. [[CrossRef](#)] [[PubMed](#)]
76. Shah, N.H.; Carvajal, M.T.; Patel, C.I.; Infeld, M.H.; Malick, A.W. Self-emulsifying drug delivery systems (SEDDS) with polyglycolized glycerides for improving in vitro dissolution and oral absorption of lipophilic drugs. *Int. J. Pharm.* **1994**, *106*, 15–23. [[CrossRef](#)]
77. Grove, M.; Müllertz, A.; Nielsen, J.L.; Pedersen, G.P. Bioavailability of seocalcitol II: Development and characterisation of self-microemulsifying drug delivery systems (SMEDDS) for oral administration containing medium and long chain triglycerides. *Eur. J. Pharm. Sci.* **2006**, *28*, 233–242. [[CrossRef](#)] [[PubMed](#)]
78. Julianto, T.; Yuen, K.H.; Noor, A.M. Improved bioavailability of vitamin E with a self emulsifying formulation. *Int. J. Pharm.* **2000**, *200*, 53–57. [[CrossRef](#)]
79. Yap, S.P.; Yuen, K.H.; Wong, J.W. Pharmacokinetics and bioavailability of  $\alpha$ -,  $\gamma$ -, and  $\delta$ -tocotrienols under different food status. *J. Pharm. Pharmacol.* **2001**, *53*, 1–5. [[CrossRef](#)]
80. Yap, S.P.; Yuen, K.H. Influence of lipolysis and droplet size on tocotrienol absorption from self-emulsifying formulations. *Int. J. Pharm.* **2004**, *281*, 67–78. [[CrossRef](#)]
81. Mukhija, K.; Singhal, K.; Angmo, S.; Yadav, K.; Yadav, H.; Sandhir, R.; Singhal, N.K. Potential of alginate encapsulated ferric saccharate microemulsions to ameliorate iron deficiency in mice. *Biol. Trace Elem. Res.* **2016**, *172*, 179–192. [[CrossRef](#)]
82. Gibaud, S.; Attivi, D. Microemulsions for oral administration and their therapeutic applications. *Expert Opin. Drug Deliv.* **2012**, *9*, 937–951. [[CrossRef](#)] [[PubMed](#)]
83. Bali, V.; Bhavna; Ali, M.; Baboota, S.; Ali, J. Potential of microemulsions in drug delivery and therapeutics: A patent review. *Recent Pat. Drug Deliv. Formul.* **2008**, *2*, 136–144. [[CrossRef](#)] [[PubMed](#)]
84. Salminen, H.; Gömmel, C.; Leuenberger, B.H.; Weiss, J. Influence of encapsulated functional lipids on crystal structure and chemical stability in solid lipid nanoparticles: Towards bioactive-based design of delivery systems. *Food Chem.* **2016**, *190*, 928–937. [[CrossRef](#)] [[PubMed](#)]
85. Lin, Y.K.; Chou, W.L.; Wang, P.W.; Yang, S.C.; Fang, J.Y. The use of therapeutic nanoparticulate systems for treating atopic dermatitis. *Curr. Nanosci.* **2018**, *14*, 3–16. [[CrossRef](#)]
86. Das, S.; Chaudhury, A. Recent advances in lipid nanoparticle formulations with solid matrix for oral drug delivery. *AAPS PharmSciTech* **2011**, *12*, 62–76. [[CrossRef](#)] [[PubMed](#)]
87. Lin, C.H.; Chen, C.H.; Lin, Z.C.; Fang, J.Y. Recent advances in oral delivery of drugs and bioactive natural products using solid lipid nanoparticles as the carriers. *J. Food Drug Anal.* **2017**, *25*, 219–234. [[CrossRef](#)] [[PubMed](#)]
88. Khosa, A.; Reddi, S.; Saha, R.N. Nanostructured lipid carriers for site-specific drug delivery. *Biomed. Pharmacother.* **2018**, *103*, 598–613. [[CrossRef](#)]
89. Liu, G.Y.; Wang, J.M.; Xia, Q. Application of nanostructured lipid carrier in food for the improved bioavailability. *Eur. Food Res. Technol.* **2012**, *234*, 391–398. [[CrossRef](#)]
90. Sato, Y.; Kobayashi, M.; Itagaki, S.; Hirano, T.; Noda, T.; Mizuno, S.; Sugawara, M.; Iseki, K. Pharmacokinetic properties of lutein emulsion after oral administration to rats and effect of food intake on plasma concentration of lutein. *Biopharm. Drug Dispos.* **2011**, *32*, 151–158. [[CrossRef](#)]
91. Sato, Y.; Joumura, T.; Nashimoto, S.; Yokoyama, S.; Takekuma, Y.; Yoshida, H.; Sugawara, M. Enhancement of lymphatic transport of lutein by oral administration of a solid dispersion and a self-microemulsifying drug delivery system. *Eur. J. Pharm. Biopharm.* **2018**, *127*, 171–176. [[CrossRef](#)] [[PubMed](#)]
92. Sen, C.K.; Khanna, S.; Rink, C.; Roy, S. Tocotrienols: The emerging face of natural vitamin E. *Vitam. Horm.* **2007**, *76*, 203–261.

93. Rasool, A.H.; Rahman, A.R.; Yuen, K.H.; Wong, A.R. Arterial compliance and vitamin E blood levels with a self-emulsifying preparation of tocotrienol rich vitamin E. *Arch. Pharm. Res.* **2008**, *31*, 1212–1217.
94. Alqahtani, S.; Alayoubi, A.; Nazzal, S.; Sylvester, P.W.; Kaddoumi, A. Nonlinear absorption kinetics of self-emulsifying drug delivery systems (SEDDS) containing tocotrienols as lipophilic molecules: In vivo and in vitro studies. *AAPS J.* **2013**, *15*, 684–695. [[CrossRef](#)] [[PubMed](#)]
95. Alqahtani, S.; Alayoubi, A.; Nazzal, S.; Sylvester, P.W.; Kaddoumi, A. Enhanced solubility and oral bioavailability of  $\gamma$ -tocotrienol using a self-emulsifying drug delivery system (SEDDS). *Lipids* **2014**, *49*, 819–829. [[CrossRef](#)] [[PubMed](#)]
96. Westergren, T.; Kalikstad, B. Dosage and formulation issues: Oral vitamin E therapy in children. *Eur. J. Clin. Pharmacol.* **2010**, *66*, 109–118. [[CrossRef](#)] [[PubMed](#)]
97. Abu-Fayyad, A.; Behery, F.; Sallam, A.A.; Alqahtani, S.; Ebrahim, H.; El Sayed, K.A.; Kaddoumi, A.; Sylvester, P.W.; Carroll, J.L.; Cardelli, J.A.; et al. PEGylated  $\gamma$ -tocotrienol isomer of vitamin E: Synthesis, characterization, in vitro cytotoxicity, and oral bioavailability. *Eur. J. Pharm. Biopharm.* **2015**, *96*, 185–195. [[CrossRef](#)]
98. El-Say, K.M.; Ahmed, T.A.; Ahmed, O.A.A.; Hosny, K.M.; Abd-Allah, F.I. Self-nanoemulsifying lyophilized tablets for flash oral transmucosal delivery of vitamin K: Development and clinical evaluation. *J. Pharm. Sci.* **2017**, *106*, 2447–2456. [[CrossRef](#)]
99. Wu, Q.; Uluata, S.; Cui, L.; Wang, C.; Li, D.; McClements, J.; Decker, E.A. Physical and oxidation stability of self-emulsifying krill oil-in-water emulsions. *Food Funct.* **2016**, *7*, 3590–3598. [[CrossRef](#)]
100. Mannina, P.; Segale, L.; Giovannelli, L.; Bonda, A.F.; Pattarino, F. Self-emulsifying excipient platform for improving technological properties of alginate-hydroxypropylcellulose pellets. *Int. J. Pharm.* **2016**, *499*, 74–80. [[CrossRef](#)]
101. Raut, S.; Karzuon, B.; Atef, E. Using in situ Raman spectroscopy to study the drug precipitation inhibition and supersaturation mechanism of Vitamin E TPGS from self-emulsifying drug delivery systems (SEDDS). *J. Pharm. Biomed. Anal.* **2015**, *109*, 121–127. [[CrossRef](#)] [[PubMed](#)]
102. Wempe, M.F.; Wright, C.; Little, J.L.; Lightner, J.W.; Large, S.E.; Caflisch, G.B.; Buchanan, C.M.; Rice, P.J.; Wachter, V.J.; Ruble, K.M.; et al. Inhibiting efflux with novel non-ionic surfactants: Rational design based on vitamin E TPGS. *Int. J. Pharm.* **2009**, *370*, 93–102. [[CrossRef](#)] [[PubMed](#)]
103. Yang, S.; Gursay, R.N.; Lambert, G.; Benita, S. Enhanced oral absorption of paclitaxel in a novel self-microemulsifying drug delivery system with or without concomitant use of P-glycoprotein inhibitors. *Pharm. Res.* **2004**, *21*, 261–270. [[CrossRef](#)] [[PubMed](#)]
104. Hendriks, J.J.; Lagas, J.S.; Rosing, H.; Schellens, J.H.; Beijnen, J.H.; Schinkel, A.H. P-glycoprotein and cytochrome P450 3A act together in restricting the oral bioavailability of paclitaxel. *Int. J. Cancer.* **2013**, *132*, 2439–2447. [[CrossRef](#)] [[PubMed](#)]
105. Veltkamp, S.A.; Thijssen, B.; Garrigue, J.S.; Lambert, G.; Lallemand, F.; Binlich, F.; Huitema, A.D.; Nuijen, B.; Nol, A.; Beijnen, J.H.; et al. A novel self-microemulsifying formulation of paclitaxel for oral administration to patients with advanced cancer. *Br. J. Cancer* **2006**, *95*, 729–734. [[CrossRef](#)] [[PubMed](#)]
106. Valicherla, G.R.; Dave, K.M.; Syed, A.A.; Riyazuddin, M.; Gupta, A.P.; Singh, A.; Wahajuddin; Mitra, K.; Datta, D.; Gayen, J.R. Formulation optimization of docetaxel loaded self-emulsifying drug delivery system to enhance bioavailability and anti-tumor activity. *Sci. Rep.* **2016**, *6*, 26895. [[CrossRef](#)] [[PubMed](#)]
107. Ansermot, N.; Rebsamen, M.; Chabert, J.; Fathi, M.; Gex-Fabry, M.; Daali, Y.; Besson, M.; Rossier, M.; Rudaz, S.; Hochstrasser, D.; et al. Influence of ABCB1 gene polymorphisms and P-glycoprotein activity on cyclosporine pharmacokinetics in peripheral blood mononuclear cells in healthy volunteers. *Drug Metab. Lett.* **2008**, *2*, 76–82. [[CrossRef](#)]
108. Jain, S.; Kambam, S.; Thanki, K.; Jain, A.K. Cyclosporine A loaded self-nanoemulsifying drug delivery system (SNEDDS): Implication of a functional excipient based co-encapsulation strategy on oral bioavailability and nephrotoxicity. *RSC Adv.* **2015**, *5*, 49633–49642. [[CrossRef](#)]
109. Cho, W.; Kim, M.S.; Kim, J.S.; Park, J.; Park, H.J.; Cha, K.H.; Park, J.S.; Hwang, S.J. Optimized formulation of solid self-microemulsifying sirolimus delivery systems. *Int. J. Nanomed.* **2013**, *8*, 1673–1682.
110. Bajaj, A.; Rao, M.R.; Khole, I.; Munjapara, G. Self-nanoemulsifying drug delivery system of cefpodoxime proxetil containing tocopherol polyethylene glycol succinate. *Drug Dev. Ind. Pharm.* **2013**, *39*, 635–645. [[CrossRef](#)]



111. Miller, D.B.; Spence, J.D. Clinical pharmacokinetics of fibric acid derivatives (fibrates). *Clin. Pharmacokinet.* **1998**, *34*, 155–162. [[CrossRef](#)] [[PubMed](#)]
112. Wei, J.D.; Ho, H.O.; Chen, C.H.; Ke, W.T.; Chen, E.T.; Sheu, M.T. Characterisation of fenofibrate dissolution delivered by a self-microemulsifying drug-delivery system. *J. Pharm. Pharmacol.* **2010**, *62*, 1685–1696. [[CrossRef](#)] [[PubMed](#)]
113. Lin, Y.M.; Wu, J.Y.; Chen, Y.C.; Su, Y.D.; Ke, W.T.; Ho, H.O.; Sheu, M.T. In situ formation of nanocrystals from a self-microemulsifying drug delivery system to enhance oral bioavailability of fenofibrate. *Int. J. Nanomed.* **2011**, *6*, 2445–2457.
114. Goh, P.S.; Ng, M.H.; Choo, Y.M.; Amru, N.B.; Chuah, C.H. Production of nanoemulsions from palm-based tocotrienol rich fraction by microfluidization. *Molecules* **2015**, *20*, 19936–19946. [[CrossRef](#)] [[PubMed](#)]
115. Alayoubi, A.; Ayoub, N.M.; Malaviya, A.; Sylvester, P.W.; Nazzal, S. Entrapment into nanoemulsions potentiates the anticancer activity of tocotrienols against the highly malignant (+SA) mouse mammary epithelial cells. *J. Nanosci. Nanotechnol.* **2014**, *14*, 4002–4005. [[CrossRef](#)]
116. Qian, C.; Decker, E.A.; Xiao, H.; McClements, D.J. Nanoemulsion delivery systems: Influence of carrier oil on  $\beta$ -carotene bioaccessibility. *Food Chem.* **2012**, *135*, 1440–1447. [[CrossRef](#)] [[PubMed](#)]
117. Xia, Z.; McClements, D.J.; Xiao, H. Influence of physical state of  $\beta$ -carotene (crystallized versus solubilized) on bioaccessibility. *J. Agric. Food Chem.* **2015**, *63*, 990–997. [[CrossRef](#)]
118. Evans, M.; Ratcliffe, I.; Williams, P.A. Emulsion stabilisation using polysaccharide-protein complexes. *Curr. Opin. Colloid Interf. Sci.* **2013**, *18*, 272–282. [[CrossRef](#)]
119. Liu, F.; Ma, C.; Zhang, R.; Gao, Y.; McClements, D.J. Controlling the potential gastrointestinal fate of  $\beta$ -carotene emulsions using interfacial engineering: Impact of coating lipid droplets with polyphenol-protein-carbohydrate conjugate. *Food Chem.* **2017**, *221*, 395–403. [[CrossRef](#)]
120. Mun, S.; Kim, Y.R.; McClements, D.J. Control of  $\beta$ -carotene bioaccessibility using starch-based filled hydrogels. *Food Chem.* **2015**, *173*, 454–461. [[CrossRef](#)]
121. Huang, R.T.; Lu, J.F.; Inbaraj, B.S.; Chen, B.H. Determination of phenolic acids and flavonoids in *Rhinacanthus nasutus* (L.) kurz by high-performance-liquid-chromatography with photodiode-array detection and tandem mass spectrometry. *J. Funct. Foods* **2015**, *12*, 498–508. [[CrossRef](#)]
122. Ho, N.H.; Inbaraj, B.S.; Chen, B.H. Utilization of microemulsions from *Rhinacanthus nasutus* (L.) Kurz to improve carotenoid bioavailability. *Sci. Rep.* **2016**, *6*, 25426. [[CrossRef](#)] [[PubMed](#)]
123. Tang, W.H.; Guan, M.C.; Xu, Z.; Sun, J. Pharmacological and pharmacokinetic studies with vitamin D-loaded nanoemulsions in asthma model. *Inflammation* **2014**, *37*, 723–728.
124. Salvia-Trujillo, L.; Fumiaki, B.; Park, Y.; McClements, D.J. The influence of lipid droplet size on the oral bioavailability of vitamin D<sub>2</sub> encapsulated in emulsions: An in vitro and in vivo study. *Food Funct.* **2017**, *8*, 767–777. [[CrossRef](#)] [[PubMed](#)]
125. Parthasarathi, S.; Muthukumar, S.P.; Anandharamakrishnan, C. The influence of droplet size on the stability, in vivo digestion, and oral bioavailability of vitamin E emulsions. *Food Funct.* **2016**, *7*, 2294–2302. [[CrossRef](#)] [[PubMed](#)]
126. Khandavilli, S.; Panchagnula, R. Nanoemulsions as versatile formulations for paclitaxel delivery: Peroral and dermal delivery studies in rats. *J. Invest. Dermatol.* **2007**, *127*, 154–162. [[CrossRef](#)] [[PubMed](#)]
127. Zhou, Y.X.; Zhang, H.; Peng, C. Puerarin: A review of pharmacological effects. *Phytother. Res.* **2014**, *28*, 961–975. [[CrossRef](#)]
128. Sun, D.; Wei, X.; Xue, X.; Fang, Z.; Ren, M.; Lou, H.; Zhang, X. Enhanced oral absorption and therapeutic effect of acetylpuerarin based on D- $\alpha$ -tocopheryl polyethylene glycol 1000 succinate nanoemulsions. *Int. J. Nanomed.* **2014**, *9*, 3413–3423.
129. Higuera-Ciapara, I.; Félix-Valenzuela, L.; Goycoolea, F.M. Astaxanthin: A review of its chemistry and applications. *Crit. Rev. Food Sci. Nutr.* **2006**, *46*, 185–196. [[CrossRef](#)]
130. Li, M.; Zahi, M.R.; Yuan, Q.; Tian, F.; Liang, H. Preparation and stability of astaxanthin solid lipid nanoparticles based on stearic acid. *Eur. J. Lipid Sci. Technol.* **2016**, *118*, 592–602. [[CrossRef](#)]
131. Yap, S.P.; Yuen, K.H.; Lim, A.B. Influence of route of administration on the absorption and disposition of  $\alpha$ -,  $\gamma$ - and  $\delta$ -tocotrienols in rats. *J. Pharm. Pharmacol.* **2003**, *55*, 53–58. [[CrossRef](#)] [[PubMed](#)]
132. Abuasal, B.S.; Lucas, C.; Peyton, B.; Alayoubi, A.; Nazzal, S.; Sylvester, P.W.; Kaddoumi, A. Enhancement of intestinal permeability utilizing solid lipid nanoparticles increases  $\gamma$ -tocotrienol oral bioavailability. *Lipids* **2012**, *47*, 461–469. [[CrossRef](#)] [[PubMed](#)]

133. Cho, H.J.; Park, J.W.; Yoon, I.S.; Kim, D.D. Surface-modified solid lipid nanoparticles for oral delivery of docetaxel: Enhanced intestinal absorption and lymphatic uptake. *Int. J. Nanomed.* **2014**, *9*, 495–504.
134. Ramalingam, P.; Ko, Y.T. Enhanced oral delivery of curcumin from N-trimethyl chitosan surface-modified solid lipid nanoparticles: Pharmacokinetic and brain distribution evaluations. *Pharm. Res.* **2015**, *32*, 389–402. [[CrossRef](#)] [[PubMed](#)]
135. Rahmani, A.H.; Alsahli, M.A.; Aly, S.M.; Khan, M.A.; Aldebasi, Y.H. Role of curcumin in disease prevention and treatment. *Adv. Biomed. Res.* **2018**, *7*, 38. [[CrossRef](#)] [[PubMed](#)]
136. Adiwidjaja, J.; McLachlan, A.J.; Boddy, A.V. Curcumin as a clinically-promising anti-cancer agent: Pharmacokinetics and drug interactions. *Expert Opin. Drug Metab. Toxicol.* **2017**, *13*, 953–972. [[CrossRef](#)] [[PubMed](#)]
137. Ji, H.; Tang, J.; Li, M.; Ren, J.; Zheng, N.; Wu, L. Curcumin-loaded solid lipid nanoparticles with Brij78 and TPGS improved in vivo oral bioavailability and in situ intestinal absorption of curcumin. *Drug Deliv.* **2016**, *23*, 459–470. [[CrossRef](#)] [[PubMed](#)]
138. Park, S.J.; Garcia, C.V.; Shin, G.H.; Kim, J.T. Development of nanostructured lipid carriers for the encapsulation and controlled release of vitamin D3. *Food Chem.* **2017**, *225*, 213–219. [[CrossRef](#)]
139. Ohshio, G.; Hosotani, R.; Imamura, M.; Sakahara, H.; Ochi, J.; Kubota, N. Gastrinoma with multiple liver metastases: Effectiveness of dacarbazine (DTIC) therapy. *J. Hepatobiliary Pancreat. Surg.* **1998**, *5*, 339–343. [[CrossRef](#)]
140. Almousallam, M.; Moia, C.; Zhu, H. Development of nanostructured lipid carrier for dacarbazine delivery. *Int. Nano Lett.* **2015**, *5*, 241–248. [[CrossRef](#)]
141. Soni, K.; Rizwanullah, M.; Kohli, K. Development and optimization of sulforaphane-loaded nanostructured lipid carriers by the Box-Behnken design for improved oral efficacy against cancer: In vitro, ex vivo and in vivo assessments. *Artif. Cells Nanomed. Biotechnol.* **2017**. [[CrossRef](#)] [[PubMed](#)]
142. Ullah, M.F. Sulforaphane (SFN): An isothiocyanate in a cancer chemoprevention paradigm. *Medicines* **2015**, *2*, 141–156. [[CrossRef](#)] [[PubMed](#)]



© 2019 by the authors. Licensee MDPI, Basel, Switzerland. This article is an open access article distributed under the terms and conditions of the Creative Commons Attribution (CC BY) license (<http://creativecommons.org/licenses/by/4.0/>).

# Curcumin nanoparticles are a promising anti-bacterial and anti-inflammatory agent for treating periprosthetic joint infections

This article was published in the following Dove Medical Press journal:  
International Journal of Nanomedicine

Kuo-Ti Peng,<sup>1,2</sup> Yao-Chang Chiang,<sup>3,4</sup> Tsung-Yu Huang,<sup>5,6</sup> Pei-Chun Chen,<sup>1</sup> Pey-Jium Chang,<sup>6,7</sup> Chiang-Wen Lee<sup>3,4,8,9</sup>

<sup>1</sup>Department of Orthopaedic Surgery, Chang Gung Memorial Hospital, Puzi City, Chiayi County 61363, Taiwan; <sup>2</sup>College of Medicine, Chang Gung University, Guishan District, Taoyuan City 33303, Taiwan; <sup>3</sup>Department of Nursing, Chang Gung University of Science and Technology, Puzi City, Chiayi County 61363, Taiwan; <sup>4</sup>Division of Basic Medical Sciences, and Chronic Diseases and Health Promotion Research Center, Chang Gung University of Science and Technology, Puzi City, Chiayi County 61363, Taiwan; <sup>5</sup>Division of Infectious Diseases, Department of Internal Medicine, Chang Gung Memorial Hospital, Chiayi, Taiwan; <sup>6</sup>Graduate Institute of Clinical Medical Sciences, College of Medicine, Chang-Gung University, Taoyuan, Taiwan; <sup>7</sup>Department of Nephrology, Chang Gung Memorial Hospital, Chiayi, Taiwan; <sup>8</sup>Research Center for Industry of Human Ecology and Research Center for Chinese Herbal Medicine, Chang Gung University of Science and Technology, Guishan District, Taoyuan City 33303, Taiwan; <sup>9</sup>Department of Rehabilitation, Chang Gung Memorial Hospital, Puzi City, Chiayi County 61363, Taiwan

**Background:** Periprosthetic joint infections (PJIs) have a high incidence of recurrence after total joint replacement and are difficult to treat by debridement or antibiotic treatment. Curcumin is a natural product with anti-inflammatory and anti-bacterial properties. The low bioactivity of curcumin in water restricts its clinical application. Curcumin nanoparticles (CURN) were developed to overcome this limitation.

**Methods:** In this study, the therapeutic effects of CURN and their anti-inflammatory functions were investigated in a *Staphylococcus aureus* biofilm-induced PJIs model.

**Results:** CURN first attenuated the biofilm-induced expansion of myeloid-derived suppressor cells (MDSCs) and then regulated M1- and M2-phenotypic MDSC expression. Down-regulation of cytokines and reactive oxygen species was considered as the mechanism of CURN in reversing the suppression of T cell proliferation. The recovery of bone permeative destruction demonstrated that CURN enhanced therapeutic potency of vancomycin in vivo.

**Conclusion:** This is the first study to demonstrate that CURN may be useful for treating PJIs.

**Keywords:** periprosthetic joint infections, osteomyelitis, *Staphylococcus aureus*, myeloid-derived suppressor cells

## Introduction

Joint replacement is the most common elective orthopedic surgeries, which improves the lives of millions of people worldwide.<sup>1</sup> According to statistical data from 2010, 332,000 total hip and 719,000 total knee arthroplasties were performed in the United States,<sup>1</sup> and the predicted numbers of total hip and total knee arthroplasties may increase to 137% and 601%, respectively, reaching 572,000 and 3,480,000 by 2030.<sup>2</sup>

Periprosthetic joint infections (PJIs) are a huge financial burden for individual patients and the global health care industry.<sup>1,3–5</sup> The incidence of PJIs is 1%–2% for primary total joint arthroplasties and 2%–6% for revision joint arthroplasties.<sup>6</sup> Although treatment strategies such as radical debridement with retention of the implants or one-stage (or immediate) or two-stage (or delayed) revisions and excision arthroplasty are applied in the clinic,<sup>7,8</sup> the treatment failure rate of PJIs remains high at 30%–50% after surgical debridement and over 10% after one-stage or two-stage surgical treatment in follow-up.<sup>9–14</sup>

PJIs and osteomyelitis (OM) are typically caused by *Staphylococcus aureus* (*S. aureus*), a Gram-positive microorganism,<sup>14,15</sup> which is a major pathogen that causes community-associated nosocomial infections.<sup>16,17</sup> The biofilm produced by *S. aureus*, a self-produced matrix of hydrated extracellular polymeric substances composed of polysaccharides, proteins, lipids, and extracellular nucleic acids, can contaminate

Correspondence: Chiang-Wen Lee  
Department of Nursing, Chang Gung University of Science and Technology, Puzi City, Chiayi County 61363, Taiwan  
Tel +886 5 362 8800 ext 2620  
Fax +886 5 362 8866  
Email cwlee@mail.cgu.edu.tw

Kuo-Ti Peng  
Department of Orthopaedic Surgery, Chang Gung Memorial Hospital, Puzi City, Chiayi County 61363, Taiwan  
Tel +886 5362 1000 ext 2004  
Email mr3497@cgmh.org.tw

internal medical devices and orthopedic implants and surgeries, resulting in serious health care concerns because of their resistance to antibiotics.<sup>18</sup> Additionally, methicillin-resistant *S. aureus* (MRSA) has gradually increased in proportion among the clinical isolates of *S. aureus*,<sup>19</sup> showing >50% prevalence among hospital pathogens in several Asian countries<sup>20</sup> and increases in the human population.<sup>21</sup> Thus, MRSA is a serious therapeutic problem,<sup>21</sup> and treatment of *S. aureus* and MRSA-related biofilm infections are an urgent issue for PJIs and public health.<sup>14–17,20–22</sup>

Studies of cellular pathologic changes have suggested that myeloid-derived suppressor cells (MDSCs) and M2-macrophages are involved in *S. aureus* biofilm-infected PJIs.<sup>23,24</sup> Previously, we established a *S. aureus* biofilm-infected animal model to simulate PJIs, and further demonstrated that *S. aureus* biofilm-induced bone marrow cells (BMCs) preferentially promoted the expansion of monocytic but not granulocytic MDSCs, as well as increased the immunosuppressive activity of T cells of overall MDSCs and conversion of monocytic MDSCs into M2-macrophages in vitro and in vivo.<sup>25</sup> Hence, drugs that influence *S. aureus* biofilm-mediated MDSCs change are candidate agents for treating PJIs.

Conventional curcumin (CUR), a nature polyphenol product, was first identified in 1910 in the rhizome of the medicinal plant *Curcuma longa*.<sup>26</sup> Several studies demonstrated that CUR has potential anti-oxidant, anti-inflammatory, anti-bacterial, and anti-tumour growth activities.<sup>27–30</sup> In cells, CUR regulates the expression of multiple enzymes, kinases, cytokines, growth factors, and transcription factors.<sup>31–33</sup> Although CUR has numerous cellular functions, it shows low bioavailability which may attributable to its low aqueous solubility and dissolution properties.<sup>27,34</sup> In general, dimethyl sulfoxide (DMSO) is a useful solvent for solubilising poorly soluble drugs in biochemical and animal experiments. Unfortunately, DMSO is toxic toward normal cells and been rarely used as a solvent in clinical applications.<sup>35–38</sup> In recent years, nanoparticle formations have been developed to improve the solubility of CUR to increase its bioavailability and pharmacological effects.<sup>27,28,34,39</sup> A polyvinylpyrrolidone (PVP)-based novel curcumin nanoparticle (CURN) system was developed in our previous study.<sup>34</sup> The physicochemical properties (including the reduction of particle size and formation of a high-energy amorphous state) of CURN promoted its water solubility and drug release.<sup>34</sup> Furthermore, CURN improved cellular functions, such as by enhancing anti-oxidant and anti-cancer activities in hepatocytes<sup>34</sup> and reducing tumour necrosis factor-alpha (TNF- $\alpha$ )-induced in tercellular adhesion

molecule-1 expression in human lung epithelial cells as compared to the CUR water preparation.<sup>39</sup>

In the current study, we utilized the *S. aureus* biofilm-infected model to evaluate the therapeutic function of CURN. The anti-inflammatory effects of CURN on *S. aureus* biofilm-induced changes in MDSCs, M1- and M2-phenotypic MDSCs, cytokine expression, T-cell proliferation, and recovery of osteolytic lesion were investigated.

## Materials and methods

### Materials

The MRSA strain of *S. aureus* (ATCC43300) was purchased from the Bioresource Collection and Research Center (Hsinchu, Taiwan). CURN was provided by Feng-Lin Yen (Kaohsiung Medical University). The preparation methods were described in previously.<sup>34</sup> CURN was powdered and stored in a black bottle at  $-20^{\circ}\text{C}$ . CURN was dissolved in PBS before the experiments were performed. RPMI 1640 medium was obtained from Thermo Fisher Scientific (Waltham, MA, USA). Brain heart infusion (BHI) was obtained from Bacto (Detroit, MI, USA).

### Curcumin nanoparticle synthesis

The synthesis protocol of PVP-based CURN was developed in a previous study.<sup>34</sup> Briefly, 50 mg of curcumin was dissolved in 25 mL of ethanol. The 75 mL 300 mg PVP contained aqueous solution were quickly injected into the organic phase which was isolated from the curcumin ethanol solution. This mixed solution was homogenized at 22,000 rpm for 25 minutes during the injection process. After that, excess ethanol was completely removed from the mixed solution by rotary vacuum evaporation at  $40^{\circ}\text{C}$ . The remaining fraction, which consists of the nanoparticle of curcumin, was lyophilized and stored until use.

### Animals

Male C57BL/6 mice (National Laboratory Animal Center, Taipei, Taiwan), weighing 22–30 g, were acclimatized to a room with a controlled temperature ( $25^{\circ}\text{C}$ ) and humidity ( $50\%\pm 10\%$ ) with a 12-hour day–night cycle (light on 07:00–19:00 hours) for 24 hours before performing the experiments. After surgery, the mice were kept individually in separate cages and provided with food (LabDiet 5053; PMI Nutrition International, St Louis, MO, USA) and water ad libitum. Infection with *S. aureus* biofilm was performed on mice aged 12 weeks. Ethical guidelines established by the Chang Gung Memorial Hospital Animal Care were followed throughout the study protocol. The animal studies were



approved by Institutional Animal Care and Use Committee of Chang Gung Memorial Hospital (IACUC number: 2015120302 and 2016122119).

### ***S. aureus* and biofilm preparation**

The *S. aureus* bacteria were cultured in BHI media (Bacto) for 4 days to form the biofilm as previously described.<sup>25,40</sup> Briefly, the biofilm was collected by centrifugation at 3,900× *g* for 15 minutes, and then sterilized by autoclaving or pre-treatment with vancomycin (20 µg/mL) and UV for 12 hours. The pellets of biofilm were redissolved in RPMI 1640 medium (Thermo Fisher Scientific) for in vitro experiments and the concentration was measured using the bicinchoninic acid assay (Thermo Fisher Scientific). For experimental use, *S. aureus* was pelleted, washed three times with cooled PBS, and resuspended in cooled PBS until use. The concentration of *S. aureus* was estimated by spectrophotometry at an absorbance wavelength of 600 nm ( $A_{600}$ ).

### **Isolation of specific cell populations from mice bone marrow**

BMCs were collected from the bone marrow of the mouse femur. The MDSC population (CD11b<sup>+</sup>Gr1<sup>+</sup>) was sorted from the CD11b-FITC, Gr1-PE double-positive population by using a FACS Aria Fusion cell sorter (BD Biosciences, Franklin Lakes, NJ, USA). The purity of the isolated cell population was verified by flow cytometry.

### **Coculture of isolated cell populations with *S. aureus* biofilm and CURN in vitro**

Mouse BMCs were seeded into a 24-well plate and cocultured with 0.2 mg/mL *S. aureus* biofilm loaded in a transwell cell culture insert (0.4 µm pore size) and treated with different concentrations of CURN. All cell populations were cultured in RPMI 1640 (Thermo Fisher Scientific) containing 10% FBS. After 48 hours, the cells were analyzed by flow cytometry (BD FACSCanto II) using specific antibodies.

### **Flow cytometry analysis**

For flow cytometry analysis, 50 µL blood samples were collected to determine the dynamic changes in the immune cell populations in the peripheral blood of mice. After lysing the red blood cells, the remaining leukocytes were resuspended in PBS containing 2% FBS, and then stained with CD11b-FITC (BD Biosciences) or Gr1-PE (BD Biosciences) for 30 minutes at 4°C. Mouse cells were analyzed by staining with CD11b-FITC (BD Biosciences), Gr1-PE (BD Biosciences), CD80-APC (#104714; Biolegend, San Diego, CA, USA),

and dectin-1-APC (eBioscience; Thermo Fisher Scientific). Flow cytometry data from the BD FACSCantoII flow cytometer were evaluated using FACSDiva software (BD Biosciences). The number of events analyzed was 10,000 per sample. Analysis was performed using FlowJo software (Tree Star, Ashland, OR, USA).

### **Measurement of cytokines in cell culture supernatants**

Cell culture supernatants of mouse BMC with/without *S. aureus* biofilm treated with different concentrations of CURN for 48 hours were used for measuring the levels of cytokines. Cytokines were detected with a BD Cytometric Bead Array Mouse Inflammation kit (#552364; BD Biosciences) according to the manufacturer's instructions. Briefly, 50 µL of the cell culture supernatant was prepared and mixed with capture beads and mouse inflammation PE detection reagent, and then washed with wash buffer. Flow cytometry data from the BD FACSCantoII flow cytometer were acquired using FACSDiva software (BD Biosciences).

### **Measurement of ROS production**

Reactive oxygen species (ROS) production from mouse BMC with/without *S. aureus* biofilm treated with different concentrations of CURN for 48 hours were measured using 2',7'-dichlorofluorescein diacetate (DCFDA) (D6883; Sigma-Aldrich Co., St Louis, MO, USA). The cells were incubated at 25°C for 30 minutes in 20 µM DCFDA. After incubation, the cells were washed twice with PBS and analyzed by flow cytometry (BD FACSCanto II).

### **T-cell proliferation assays**

Mice BMCs were seeded into 24-well plates with untreated or *S. aureus* biofilm treated with different concentrations of CURN for 48 hours. The isolated MDSC populations (CD11b/Gr1 double-positive cells) were subsequently cocultured with 5(6)-carboxyfluorescein N-hydroxysuccinimidyl ester-labeled spleen T cells stimulated by Dynabeads Mouse T-Activator CD3/CD28 (Thermo Fisher Scientific) for 48 hours. The ratio of the tested cell populations to T cells ( $2 \times 10^5$  cells/well in a 96-well round bottom plate in RPMI 1640 with 10% FBS) was 0.25:1 in the study. To isolate spleen T cells, spleens were gently pressed through a strainer using the plunger end of a syringe to obtain single cells. These cells were washed with PBS buffer and ACK lysing buffer (Thermo Fisher Scientific). Cells in warm RPMI (2 mL) were injected into the nylon wool column and washed with RPMI. The column was sealed and

incubated at 37°C and 5% CO<sub>2</sub> for 45 minutes. Cells were then eluted with 10 mL of warm RPMI medium.

### *S. aureus* biofilm infection in mice

Male C57BL/6J mice were anesthetised with 50% Zoletil (1 mL/kg) and 2% rompun mixture solution. The skin near the right knee was disinfected with povidone-iodine and then an incision was made. A 26-gauge needle was utilized to make a burr hole in the femoral intercondylar notch extending into the intramedullary canal, and then a pre-cut 0.5 cm orthopedic grade Kirschner (K) wire (0.6 mm diameter; Synthes GmbH, Solothurn, Switzerland) was implanted into the intramedullary canal. The *S. aureus* (2×10<sup>3</sup> CFU) biofilm was inoculated into the intramedullary canal containing the implant, the burr hole was sealed with bone wax, and the surgical site was closed with coated Vicryl\* 4–0 sutures (Ethicon Inc., Bridgewater, NJ, USA). Sterile implants were used for the sham-operated group. Ketorolac (0.5–1 mg/kg, intramuscularly) was used to treat the mice immediately after surgery and 24 hours later for the PJI model to evaluate relief from pain. The C57BL/6J mice were divided into seven groups, including the sham group and six different treated groups (n=4 for each group). The six experimental groups were the following: 1) the group administered CURN (20 mg/kg) only; 2) the group infected with *S. aureus* only; 3) the group injected intraperitoneally with vancomycin (2 mg/kg) only after infection with *S. aureus* for 7 days; 4–6) the groups injected intraperitoneally with different concentrations of CURN (5, 10, and 20 mg/kg in PBS, respectively) and vancomycin (2 mg/kg) every day after infection with *S. aureus* for 7 days. Mice containing sterile implants served as the sham-operated group. At 2 weeks after injection, the mice were sacrificed and the femurs were fixed in 10% formalin.

### Data analyses and statistics

All data were evaluated and graphed with Microsoft Excel software (Microsoft, Redmond, WA, USA). The results were expressed as the mean ± SD. The results were tested using one-way ANOVA with the post-hoc Tukey's correction and GraphPad Prism software (GraphPad, San Diego, CA, USA). A *P*-value <0.05 was considered significant.

## Results

### Effects of CURN on *S. aureus* biofilm-induced BMCs in regulating MDSC expansion

We examined whether CURN affects *S. aureus* biofilm infection-induced expansion of BMCs to MDSCs in the PJI model.

For establishing the biofilm-stimulated BMC system, several methods were tested, which included autoclaving and pretreatment with antibiotic or UV for 12 hours. Results showed that pre-treatment with antibiotic or UV failed to reduce the *S. aureus* growth rate compared to sterilization by using an autoclave; thus, autoclaving method was found to be the optimal method in our system (Figure S1). A previous study has demonstrated that even after autoclaving, biofilm still shows stimulated effects on BMC cells.<sup>25</sup> As shown in Figure 1A, after treating the mouse BMCs with *S. aureus* biofilm for 48 hours, the expansion of MDSCs was increased by nearly 1.6-fold (41.6% without and 62.6% with biofilm exposure). After adjusting for each control group, CURN notably suppressed biofilm-induced MDSC expansion in a dose-dependent manner (Figure 1B), while no effects were observed in the non-biofilm treatment groups. Interestingly, CUR dissolved in PBS did not affect MDSC expansion in the biofilm or non-biofilm groups (Figure 1C). This indicates the CURN, which has higher water solubility, effectively reduced biofilm-induced MDSC expansion but did not change the normal MDSC expansion rate under non-infected state.

### Effects of CURN on the conversion of MDSCs to M1- and M2-phenotypic MDSCs upon exposure to *S. aureus* biofilm

Because M1 and M2 cells play different roles, we next evaluated the effects of CURN on M1- and M2-phenotypic MDSC expression with/without biofilm treatment. In general, M1-phenotypic MDSCs play a pro-inflammatory role, while anti-inflammatory M2-phenotypic MDSCs are involved in adaptive immunity and the inflammatory circuit.<sup>41,42</sup> As shown in Figure 2A, CURN slightly but effectively decreased M1-phenotypic marker expression after biofilm exposure. In contrast, biofilm-induced M2-phenotypic marker expression was enhanced by treatment with CURN in a dose-dependent manner (Figure 2B). This result suggests a prominent anti-inflammatory effect of CURN as a result of *S. aureus* biofilm infection.

### Effects of CURN on *S. aureus* biofilm-induced inflammatory factors

Several inflammatory factors, such as IL-6, TNF-α, and monocyte chemoattractant protein-1 (MCP-1), are highly associated with PJIs.<sup>43,44</sup> Thus, the levels of these proteins were evaluated after CURN treatment. CURN dose-dependently reduced the expression of biofilm-induced IL-6

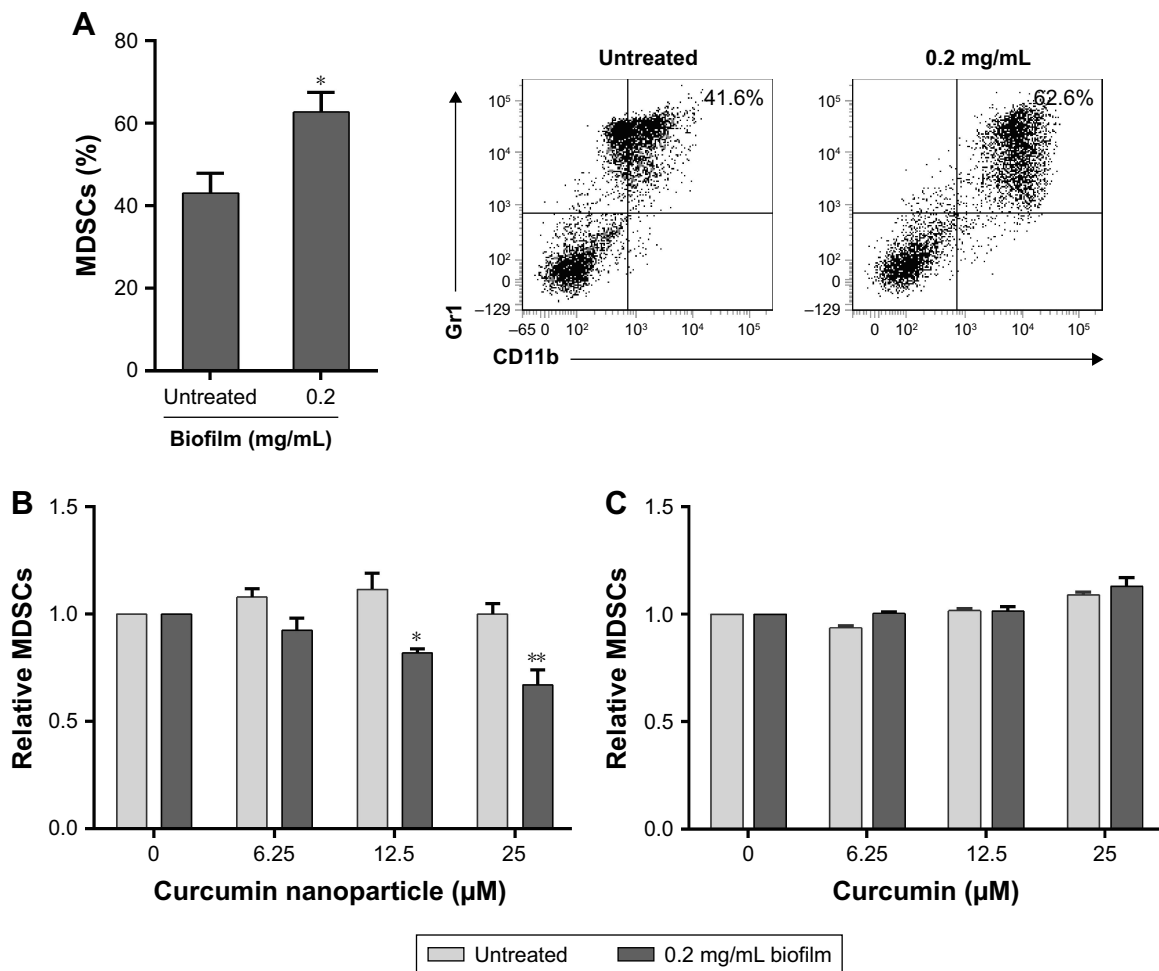


**Figure 1** (A) MDSC expression in *S. aureus* biofilm exposure. The bar graph (left panel) was illustrated and converted based on the flow cytometry results (right panel). (B) CURN suppressed biofilm-induced MDSC expansion in a dose-dependent manner. (C) CUR dissolved in PBS did not affect MDSC expansion. Data are expressed as the mean  $\pm$  SD. \* $P < 0.05$  compared to biofilm-untreated group in (A). \* $P < 0.05$  and \*\* $P < 0.01$  compared to the biofilm-induced but no CURN treated group.

**Abbreviations:** CUR, curcumin; CURN, CUR nanoparticles; MDSCs, myeloid-derived suppressor cells; *S. aureus*, *Staphylococcus aureus*.

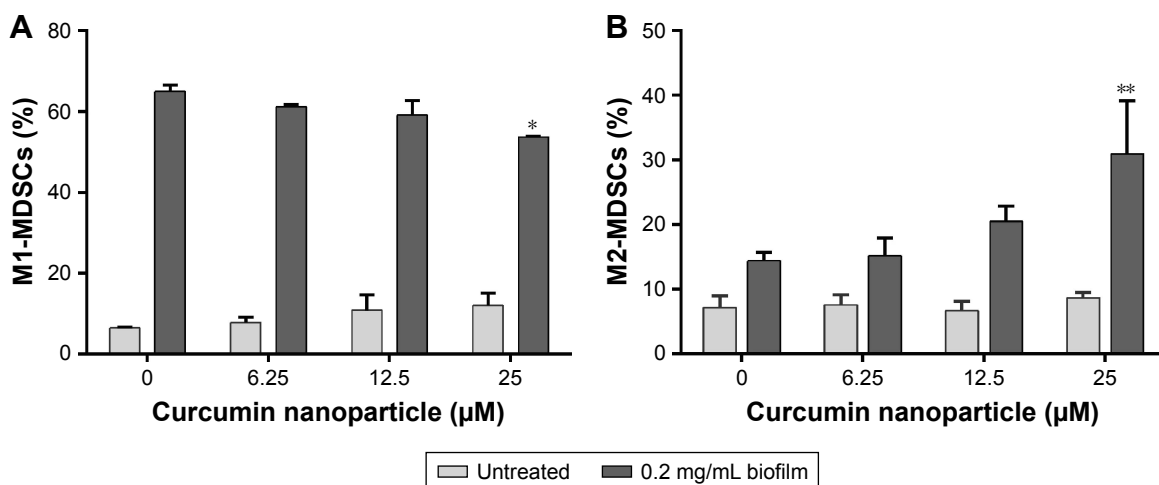


**Figure 2** CURN induced expansion of MDSCs to M1- (A) and M2-phenotypic (B) MDSCs upon exposure to *S. aureus* biofilm via its anti-inflammatory activity.

**Notes:** Data are expressed as the mean  $\pm$  SD. \* $P < 0.05$  and \*\* $P < 0.01$  compared to the biofilm-induced but no CURN treated group.

**Abbreviations:** CURN, curcumin nanoparticles; MDSCs, myeloid-derived suppressor cells; *S. aureus*, *Staphylococcus aureus*.

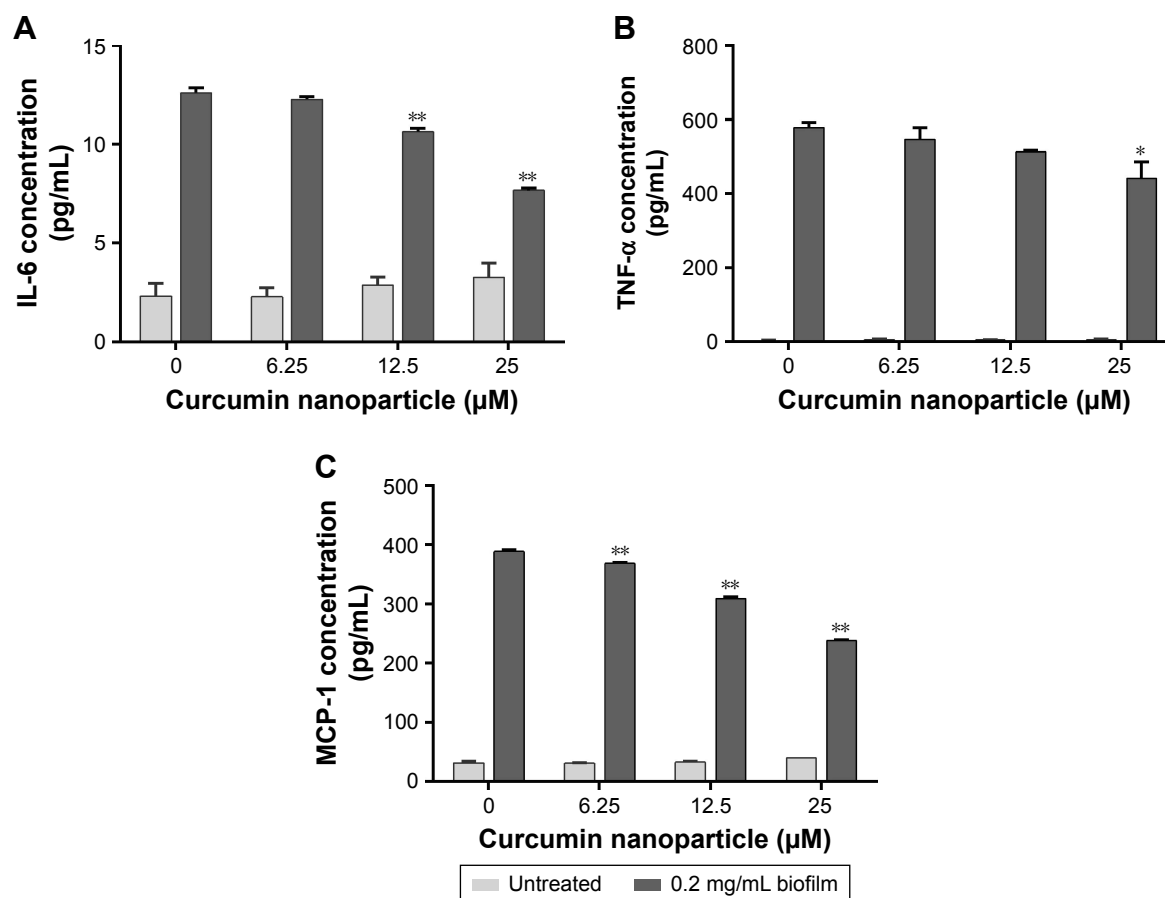


**Figure 3** Cytokines including IL-6 (A), TNF- $\alpha$  (B), and MCP-1 (C) were downregulated by CURN in the mouse BMC culture supernatants of *S. aureus* biofilm-stimulated MDSCs.

**Notes:** Data are expressed as the mean  $\pm$  SD. \* $P < 0.05$  and \*\* $P < 0.01$  compared to the biofilm-induced but no CURN treated group.

**Abbreviations:** BMCs, bone marrow cells; CURN, curcumin nanoparticles; MCP-1, monocyte chemoattractant protein-1; MDSCs, myeloid-derived suppressor cells; TNF- $\alpha$ , tumour necrosis factor-alpha; *S. aureus*, *Staphylococcus aureus*.

(39.2% at 25  $\mu$ M), MCP-1 (38.7% at 25  $\mu$ M), and TNF- $\alpha$  (18% at 25  $\mu$ M), while no significant effects were observed in the biofilm-negative groups (Figure 3A–C). Additionally, ROS play a key signaling role in the progression of inflammatory disorders.<sup>45</sup> Biofilm caused increases in ROS, which were also dose-dependently suppressed by CURN. At the highest CURN dose (25  $\mu$ M), ROS production was notably suppressed by more than 50% (Figure 4). These results suggest that CURN can reverse the inflammatory status triggered by *S. aureus* biofilm.

### Effects of CURN on *S. aureus* biofilm-treated MDSC and T-cell proliferation

T cells play important roles in anti-bacterial infections.<sup>46,47</sup> It is well-known that MDSCs are potent inhibitors of T-cell activation in *S. aureus* infection.<sup>48–50</sup> We previously showed that *S. aureus* biofilm increased MDSC expansion and subsequent T-cell suppression.<sup>25</sup> Compared to non-MDSC controls, coculture with MDSCs decreased T-cell proliferation by

41.4%, while treatment with biofilm reduced the proliferation by up to 62.8% (Figure 5). CURN reversed T-cell proliferation in a dose-dependent manner. The reversal effects of CURN on MDSCs suppressed T-cell proliferation not only in the biofilm-exposed groups but also in the control groups. However, the recovery rate rapidly increased in the biofilm groups. This result indicates that CURN effectively recovered the biofilm-mediated decrease in T-cell activity.

### Biofilm formation in a *S. aureus*-infected PJI model

To evaluate whether CURN is useful as a therapeutic agent for treating PJIs, in vivo analysis was performed. A mouse PJI model, which we established previously,<sup>25</sup> was utilized to mimic *S. aureus* biofilm infection in vivo. As shown in Figure 6, sham-operated and CURN-treated mice showed no changes in bone formation according to micro-computed tomography (CT) images. Bone in the *S. aureus* biofilm infection groups showed severe permeated pathologic



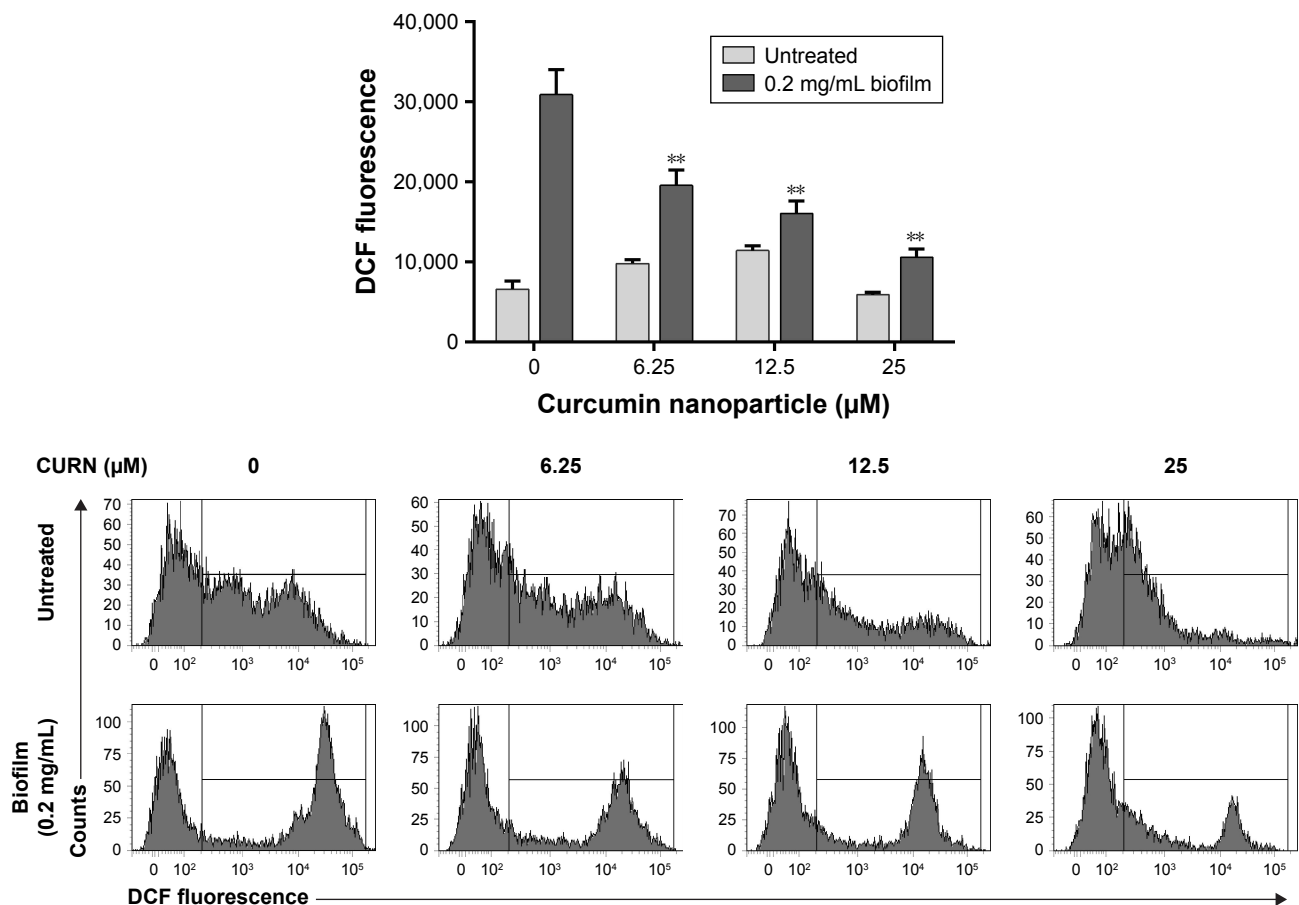


**Figure 4** ROS generation from biofilm induced in mouse BMCs was suppressed by CURN in vitro.

**Notes:** DCF fluorescence was measured by flow cytometry. The bar graphs illustrate the signals of DCF fluorescence. Data are expressed as the mean  $\pm$  SD. \*\* $P < 0.01$  compared to the biofilm-induced but no CURN treated group.

**Abbreviations:** BMCs, bone marrow cells; CURN, curcumin nanoparticles; DCF, dichlorofluorescein; ROS, reactive oxygen species.

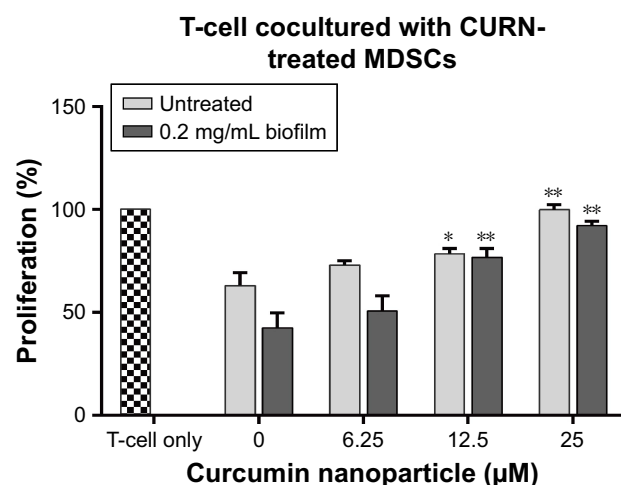


**Figure 5** CURN reversed the immunosuppressive activity of *S. aureus* biofilm-treated MDSCs on T cells.

**Notes:** The differentiation rate of naive T cells after receiving CD3/CD28 beads stimulation was set as 100% (the mosaic bar). The changes in T-cell differentiation rate were measured after coculturing with MDSCs, which were pretreated with different concentrations of CURN and biofilm. Data are expressed as the mean  $\pm$  SD. \* $P < 0.05$  and \*\* $P < 0.01$  compared to the biofilm-induced but no CURN treated group.

**Abbreviations:** CURN, curcumin nanoparticles; MDSCs, myeloid-derived suppressor cells; *S. aureus*, *Staphylococcus aureus*.

fracture and was recovered with the general clinical treatment strategy, that is, vancomycin treatment. Osteolytic destructions were lower after cotreatment with CURN and vancomycin compared to the group treated with vancomycin alone, both showing a dose-dependent effect. Furthermore, the structures stained by H&E staining were consistent with the results of micro-CT imaging (Figure 7). Vancomycin decreased inflammation levels (swollen tissues and broken bones) and lymphocyte expression, but was more effective in reducing inflammation levels and lymphocytes in the vancomycin–CURN cotreated groups. Additionally, to confirm whether the CURN-suppressed MDSC expansion occurred in the PJI in vivo model, blood MDSC levels were measured. The MDSC levels were increased after *S. aureus* biofilm infection (increased by 117.5% compared to the sham group), while the rate of MDSC expansion was reduced after vancomycin treatment (decreased by 10.3% compared to the infected group). Cotreatment with vancomycin and CURN notably affected MDSC expansion compared to vancomycin

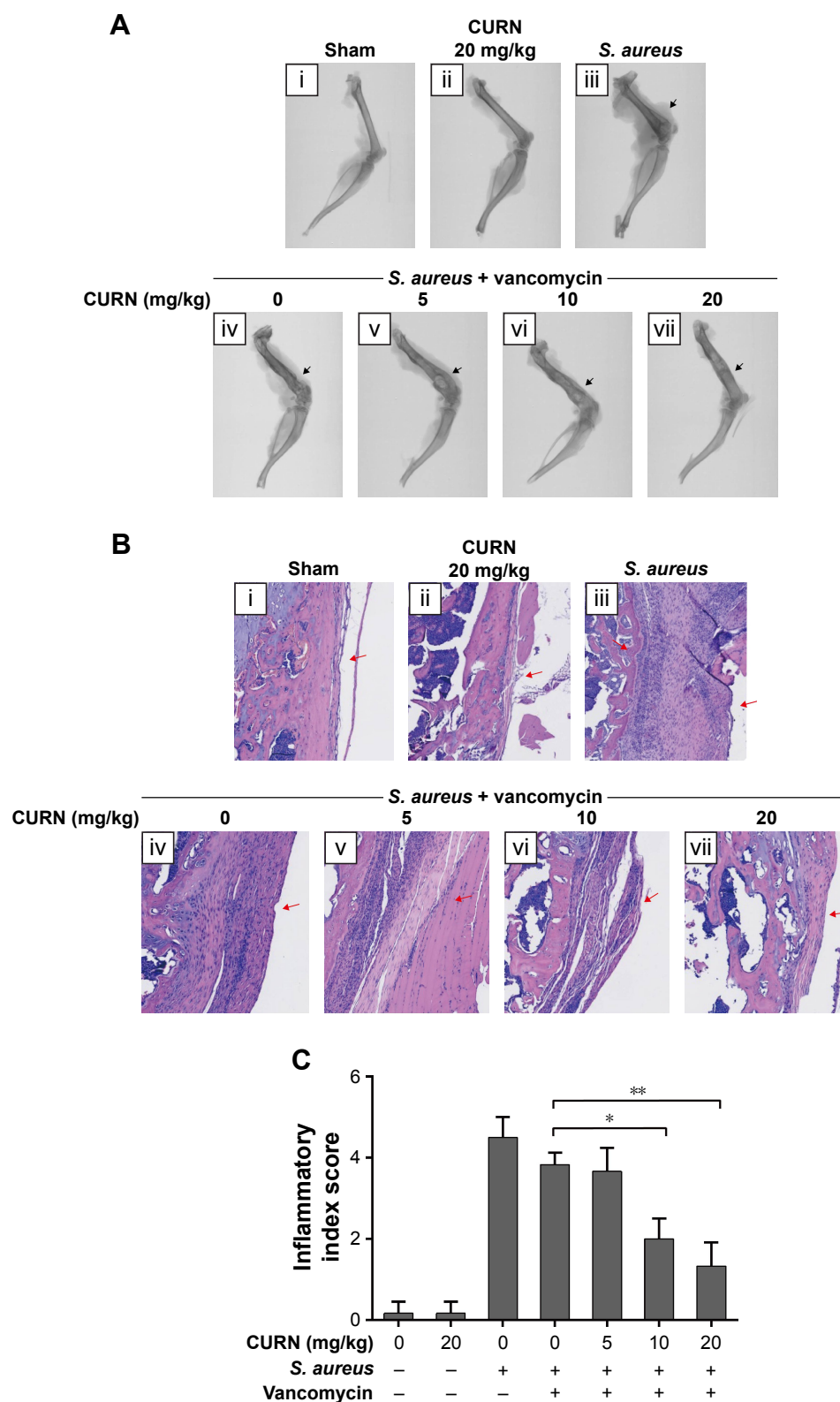


**Figure 6** Evaluation of infection level in mouse femur.

**Notes:** (A) Micro-CT images, in which black arrows indicate the grade of severity in bone destruction: (i) sham group, (ii) CURN only, (iii) permeative destruction with *S. aureus* implantation, (iv) pathologic fracture after vancomycin (2 mg/kg) treatment, and (v–vii) the less osteolytic size in the gradient concentration of CURN. (B) Histological analysis by H&E staining showed that CURN was effective for treating PJIs cotreated with vancomycin (2 mg/kg). The labeling of figures is the same as that of micro-CT images. Red arrows indicate infiltrating mononuclear immune cells. (C) The inflammatory index score was evaluated based on the levels of inflammatory cell infiltration in the femur ( $n=3$  for each group). Red arrows indicate infiltrating mononuclear immune cells. Data are expressed as the mean  $\pm$  SD. \* $P<0.05$  and \*\* $P<0.01$  compared to the group of *S. aureus* infection treated with vancomycin alone.

**Abbreviations:** CT, computed tomography; CURN, curcumin nanoparticles; PJI, periprosthetic joint infection; *S. aureus*, *Staphylococcus aureus*.

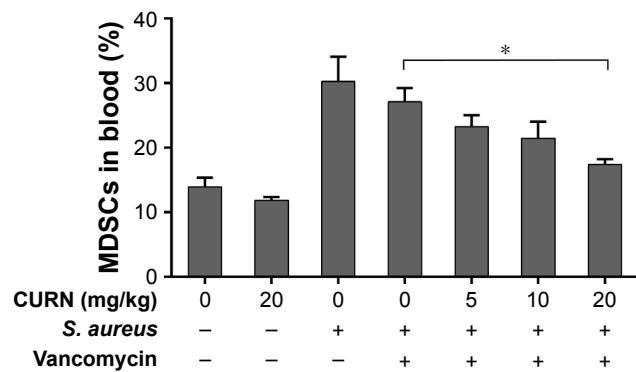


**Figure 7** CURN reduces the expansion of MDSCs in the peripheral blood from mice infected with *S. aureus*.

**Notes:** Data are expressed as the mean  $\pm$  SD. \* $P < 0.05$  compared to the group of *S. aureus* infection treated with vancomycin (2 mg/kg) alone.

**Abbreviations:** CURN, curcumin nanoparticles; MDSCs, myeloid-derived suppressor cells; *S. aureus*, *Staphylococcus aureus*.

treatment alone (5, 10, and 20 mg/kg CURN: 23.2%, 29%, and 42.4% respectively, decrease compared to the infected group). These results strongly suggest that CURN decreased MDSC expansion and is a potential therapeutic agent for use with antibiotics to treat *S. aureus* biofilm-infected PJIs.

## Discussion

In the current study, we clearly demonstrated that CURN is a useful assistant agent for treating PJIs and OM through in vitro and in vivo experiments. CURN significantly suppressed *S. aureus* biofilm-triggered MDSC expansion and bilaterally regulated the conversion rates of MDSCs to M1- or M2-phenotypic cell expression. This indicates that CURN can reverse the *S. aureus* biofilm-induced immune imbalance. To characterize the possible cellular mechanisms of CURN, we analyzed the levels of PJI-associated inflammatory cytokines and ROS. Our results suggest that CURN notably reduced *S. aureus* biofilm-enhanced IL-6, TNF- $\alpha$ , and MCP-1 concentrations and ROS production in cultured MDSCs. Furthermore, the proliferation value and rate of T-cell suppression by *S. aureus* biofilm infection were recovered by CURN treatment. An in vivo animal PJI model was used to confirm our in vitro findings. The results clearly showed that CURN improved the effects of traditional clinical strategy – vancomycin treatment – on the inflammatory site and structure formation and on MDSCs in the blood.

PJI is an increasing and difficult-to-treat infection caused by *S. aureus* or MRSA biofilm.<sup>19–21</sup> PJIs show a high risk to progress to chronic OM.<sup>7,51</sup> The antimicrobial therapy is not very effective in treating bone and joint infections because of the physiological and anatomical characteristics of these infections, and surgical debridement is often necessary.<sup>51</sup>

However, the success rate of treating PJIs is low, with failure rates being in the range 30%–50%.<sup>9–14</sup> The overuse of antibiotics leads to the development of multi-resistant bacteria and harms human health. Thus, natural bioactive compounds may be useful for developing therapeutic agents for treating bacterial infections as alternatives to synthetic drugs.

Conventional CUR is a natural product identified more than 100 years ago.<sup>26</sup> The systemic functions of CUR include anti-inflammation, anti-cancer, anti-oxidant, bacterial growth suppression, and regulation of gut microbiota composition,<sup>27–30,52</sup> and CUR plays cellular roles in regulating multiple enzymes, kinases, cytokine growth factors, and transcription factors release.<sup>31–33</sup> While CUR is a potential antibacterial agent, it is difficult to apply in the clinical setting because of its low bioavailability, solubility, and dissolution properties in water.<sup>27,34</sup> Owing to the advances in nanochemistry, the potential for using CUR in the clinic has increased.

Since hematopoiesis is altered in chronic infections and cancer, MDSCs are found to expand greatly.<sup>53</sup> Thus, PVP-based CURN, developed in our previous study, may suppress the expansion to decrease infection levels. Under pathological conditions, several inflammatory factors are involved in MDSC expansion, such as pro-inflammatory cytokines like TNF- $\alpha$ , IL-6, prostaglandin E2, etc.<sup>49</sup> Moreover, IL-6, TNF- $\alpha$ , and MCP-1 are involved in inflammation and are sensitive markers for PJIs or deep implants.<sup>43,44</sup> *S. aureus* biofilm infection induced the upregulation of TNF- $\alpha$ , IL-6, and MCP-1, which were reduced by CURN treatment in this study. This suppression agrees with the results of previous studies on inflammation<sup>29</sup> and indicates that CURN reduced MDSC expansion by downregulating the expression of inflammatory cytokines.

Traditionally, MDSCs can be classified as monocytic (M-MDSC, CD11b<sup>+</sup>Ly6C<sup>+</sup>Ly6G<sup>low</sup>) and granulocytic (G-MDSC, CD11b<sup>+</sup>Ly6C<sup>low</sup>Ly6G<sup>+</sup>) based on the expression levels of Ly6C and Ly6G.<sup>49</sup> *S. aureus* biofilm infections preferentially promote M-MDSC expansion in PJI models and other infectious diseases.<sup>25,54</sup> M-MDSCs generated high levels of inducible nitric oxide, which can cause T-cell receptor nitration and prevent its interaction with antigen–major histocompatibility complex. Additionally, high levels of inducible nitric oxide synthase could restrict the availability of amino acid—L-arginine, which is essential for T cell proliferation, subsequent to suppress T cell activity.<sup>49</sup> CUR was also reported to play a role in macrophage polarization. Previous studies showed that CUR inhibited M1 macrophage polarization and TNF- $\alpha$ , IL-6, and IL-12B production in a dose-dependent manner<sup>55</sup> and

induced M2 macrophage polarization via the secretion of IL-4 and/or IL-13.<sup>56</sup> Furthermore, M1 macrophages respond to inflammatory signaling by playing a pro-inflammatory role, while M2 macrophages participate in the resolution of the inflammatory process by playing an anti-inflammatory role and produce anti-inflammatory cytokines to facilitate tissue healing.<sup>41</sup> Our results showed that CURN decreased M1- and increased M2-phenotypic expression, which may improve the anti-inflammatory effects and promote tissue recovery.

The anti-inflammatory effects of CUR or CURN may occur through the reduction of ROS production.<sup>34,39</sup> Nicotinamide adenine dinucleotide phosphate (NADP) oxidases are ROS generators and have been identified in phagocytes for bacterial killing.<sup>45</sup> In cancer, tissue damage, and inflammation, ROS production is increased because MDSCs express the NADPH oxidase (Nox2) components p47<sup>phox</sup> and gp91<sup>phox</sup> and upregulate Nox2 activity. Consistently, deficits in p47<sup>phox</sup> or Nox2 protect against damages from TNF- $\alpha$  induced inflammatory response.<sup>45</sup> In general, MDSCs exhibit strong immunosuppressive activities rather than immunostimulation functions.<sup>57</sup> Furthermore, suppression of ROS production reverses the immunosuppressive function of MDSCs to T-cell responses.<sup>53,58</sup> Not only ROS, but also MDSCs inhibit T-cell responses through multiple pathways, such as NO production, amino acid metabolism, and cytokines, among others. A previous study suggested that T-cell suppression of MDSCs is related to cancer-derived IL-6, and inhibition of IL-6-mediated signals improved the prognosis of cancer.<sup>59</sup> T-cell function is gradually decreased in *S. aureus*-induced chronic abscess and is associated with infection progression.<sup>48</sup> T cells also kill bacteria during infection.<sup>47</sup> Thus, reversing the suppression of T-cell function is beneficial for treating PJIs. Our results indicate that *S. aureus* biofilm in MDSCs showed greater immunosuppressive effects on T-cell proliferation, but this may be reversed by CURN treatment, which decreases MDSC-triggered ROS production and cytokine expression. This finding strongly suggests that CURN is useful as an immunoactivity enhancer for treating *S. aureus* biofilm infection-related diseases, such as PJIs or OM.

Local treatment with nano-formulated CUR effectively inhibited inflammation and bone resorption in an experimental periodontal disease model.<sup>60</sup> This finding and our results following CURN administration in the PJI model suggest that CURN had anti-inflammation effects and improved bone absorption. After cotreatment with vancomycin, CURN recovered *S. aureus* biofilm-induced serious

bone destruction, while CUR in PBS was not effective (data not shown). Furthermore, suppression of the expansion of MDSCs by CURN in the blood provides cellular evidence for the recovery of bone destruction.

In conclusion, this is the first study to demonstrate that CURN is useful for treating PJIs based on in vitro and in vivo analysis. CURN reduced cytokine expression and ROS production to suppress *S. aureus* biofilm-induced MDSCs expansion and increased the expression levels of M2-phenotypic cells to reverse the proliferation of T cells. Furthermore, the permeative destruction caused by *S. aureus* biofilm infection was effectively recovered by cotreatment with CURN and vancomycin. Therefore, CURN can be considered as a potential additive anti-infective agent in the treatment of PJIs and OM.

## Acknowledgments

We thank Feng-Lin Yen (Kaohsiung Medical University) for providing curcumin-loaded PVP nanoparticles for this study. This work was supported by the Chang Gung Medical Research Program Foundation (grant numbers CMRPG6F0341, CMRPG6F0342, CMRPG6G0231, and CMRPG6H0401 from the Chang-Gung Memorial Hospital, Taiwan), and the Ministry of Science and Technology (ROC) (grant numbers NMRPG6G6011 and NMRPG6G6012).

## Disclosure

The authors report no conflicts of interest in this work.

## References

1. Tande AJ, Patel R. Prosthetic joint infection. *Clin Microbiol Rev.* 2014; 27(2):302–345.
2. Kurtz S, Ong K, Lau E, Mowat F, Halpern M. Projections of primary and revision hip and knee arthroplasty in the United States from 2005 to 2030. *J Bone Joint Surg Am.* 2007;89(4):780–785.
3. Kurtz SM, Lau E, Watson H, Schmier JK, Parvizi J. Economic burden of periprosthetic joint infection in the United States. *J Arthroplasty.* 2012;27(8 Suppl):61–65.
4. Peel TN, Dowsey MM, Buisson KL, Liew D, Choong PF. Cost analysis of debridement and retention for management of prosthetic joint infection. *Clin Microbiol Infect.* 2013;19(2):181–186.
5. McConoughey SJ, Howlin R, Granger JF, et al. Biofilms in periprosthetic orthopedic infections. *Future Microbiol.* 2014;9(8):987–1007.
6. Gallo J, Kolar M, Novotny R, Rihakova P, Ticha V. Pathogenesis of prosthesis-related infection. *Biomed Pap Med Fac Univ Palacky Olomouc Czech Repub.* 2003;147(1):27–35.
7. Rao N, Ziran BH, Lipsky BA. Treating osteomyelitis: antibiotics and surgery. *Plast Reconstr Surg.* 2011;127(Suppl 1):177S–187S.
8. Fagotti L, Tatka J, Salles MJC, Queiroz MC. Risk factors and treatment options for failure of a two-stage exchange. *Curr Rev Musculoskelet Med.* 2018;420–427.
9. Vilchez F, Martínez-Pastor JC, García-Ramiro S, et al. Outcome and predictors of treatment failure in early post-surgical prosthetic joint infections due to *Staphylococcus aureus* treated with debridement. *Clin Microbiol Infect.* 2011;17(3):439–444.



10. Byren I, Bejon P, Atkins BL, et al. One hundred and twelve infected arthroplasties treated with 'DAIR' (debridement, antibiotics and implant retention): antibiotic duration and outcome. *J Antimicrob Chemother.* 2009;63(6):1264–1271.
11. Bryan AJ, Abdel MP, Sanders TL, Fitzgerald SF, Hanssen AD, Berry DJ. Irrigation and debridement with component retention for acute infection after hip arthroplasty: improved results with contemporary management. *J Bone Joint Surg Am.* 2017;99(23):2011–2018.
12. Lora-Tamayo J, Murillo O, Iribarren JA, et al. A large multicenter study of methicillin-susceptible and methicillin-resistant *Staphylococcus aureus* prosthetic joint infections managed with implant retention. *Clin Infect Dis.* 2013;56(2):182–194.
13. Nodzo SR, Boyle KK, Spiro S, Nocon AA, Miller AO, Westrich GH. Success rates, characteristics, and costs of articulating antibiotic spacers for total knee periprosthetic joint infection. *Knee.* 2017;24(5):1175–1181.
14. Ricciardi BF, Muthukrishnan G, Masters E, Ninomiya M, Lee CC, Schwarz EM. *Staphylococcus aureus* evasion of host immunity in the setting of prosthetic joint infection: biofilm and beyond. *Curr Rev Musculoskelet Med.* Epub 2018 Jul 9.
15. Gbejuade HO, Lovering AM, Webb JC. The role of microbial biofilms in prosthetic joint infections. *Acta Orthop.* 2015;86(2):147–158.
16. Jones M, Ying J, Huttner B, et al. Relationships between the importation, transmission, and nosocomial infections of methicillin-resistant *Staphylococcus aureus*: an observational study of 112 Veterans Affairs Medical Centers. *Clin Infect Dis.* 2014;58(1):32–39.
17. Keynan Y, Rubinstein E. *Staphylococcus aureus* bacteremia, risk factors, complications, and management. *Crit Care Clin.* 2013;29(3):547–562.
18. Flemming HC, Wingender J. The biofilm matrix. *Nat Rev Microbiol.* 2010;8(9):623–633.
19. Hiramatsu K, Katayama Y, Yuzawa H, Ito T. Molecular genetics of methicillin-resistant *Staphylococcus aureus*. *Int J Med Microbiol.* 2002;292(2):67–74.
20. Grundmann H, Aires-de-Sousa M, Boyce J, Tiemersma E. Emergence and resurgence of methicillin-resistant *Staphylococcus aureus* as a public-health threat. *Lancet.* 2006;368(9538):874–885.
21. Drago L, De Vecchi E, Nicola L, Gismondo MR. In vitro evaluation of antibiotics' combinations for empirical therapy of suspected methicillin resistant *Staphylococcus aureus* severe respiratory infections. *BMC Infect Dis.* 2007;7(1):111.
22. Hanke ML, Heim CE, Angle A, Sanderson SD, Kielian T. Correction: targeting macrophage activation for the prevention and treatment of *Staphylococcus aureus* biofilm infections. *J Immunol.* 2013;190(12):6709–6710.
23. Gabrilovich DI, Nagaraj S. Myeloid-derived suppressor cells as regulators of the immune system. *Nat Rev Immunol.* 2009;9(3):162–174.
24. Peranzoni E, Zilio S, Marigo I, et al. Myeloid-derived suppressor cell heterogeneity and subset definition. *Curr Opin Immunol.* 2010;22(2):238–244.
25. Peng KT, Hsieh CC, Huang TY, et al. *Staphylococcus aureus* biofilm elicits the expansion, activation and polarization of myeloid-derived suppressor cells in vivo and in vitro. *PLoS One.* 2017;12(8):e0183271.
26. Miłobędzka J, Kostanecki SV, Lampe V. Zur Kenntnis des Curcumins. [Structure of curcumin]. *Berichte der Deutschen Chemischen Gesellschaft.* 1910;43(2):2163–2170. German.
27. Gera M, Sharma N, Ghosh M, et al. Nanoformulations of curcumin: an emerging paradigm for improved remedial application. *Oncotarget.* 2017;8(39):66680–66698.
28. Yallapu MM, Jaggi M, Chauhan SC. Curcumin nanoformulations: a future nanomedicine for cancer. *Drug Discov Today.* 2012;17(1–2):71–80.
29. Chainani-Wu N. Safety and anti-inflammatory activity of curcumin: a component of tumeric (*Curcuma longa*). *J Altern Complement Med.* 2003;9(1):161–168.
30. Li B, Li X, Lin H, Zhou Y. Curcumin as a promising antibacterial agent: effects on metabolism and biofilm formation in *S. mutans*. *Biomed Res Int.* 2018;2018(3):1–11.
31. Jin CY, Lee JD, Park C, Choi YH, Kim GY. Curcumin attenuates the release of pro-inflammatory cytokines in lipopolysaccharide-stimulated BV2 microglia. *Acta Pharmacol Sin.* 2007;28(10):1645–1651.
32. Yadav R, Jee B, Awasthi SK. Curcumin suppresses the production of pro-inflammatory cytokine interleukin-18 in lipopolysaccharide stimulated murine macrophage-like cells. *Indian J Clin Biochem.* 2015;30(1):109–112.
33. Shishodia S. Molecular mechanisms of curcumin action: gene expression. *Biofactors.* 2013;39(1):37–55.
34. Yen FL, Wu TH, Tzeng CW, Lin LT, Lin CC. Curcumin nanoparticles improve the physicochemical properties of curcumin and effectively enhance its antioxidant and antihepatoma activities. *J Agric Food Chem.* 2010;58(12):7376–7382.
35. de Abreu Costa L, Henrique Fernandes Ottoni M, Dos Santos M, et al. Dimethyl sulfoxide (DMSO) decreases cell proliferation and TNF- $\alpha$ , IFN- $\gamma$ , and IL-2 cytokines production in cultures of peripheral blood lymphocytes. *Molecules.* 2017;22(11):1789.
36. Maral S, Albayrak M, Pala C, Yildiz A, Sahin O, Ozturk HB. Dimethyl sulfoxide-induced tonic-clonic seizure and cardiac arrest during infusion of autologous peripheral blood stem cells. *Cell Tissue Bank.* 2018;19(4):831–832.
37. Morris C, de Wreede L, Scholten M, et al. Should the standard dimethyl sulfoxide concentration be reduced? Results of a European Group for Blood and Marrow Transplantation prospective noninterventive study on usage and side effects of dimethyl sulfoxide. *Transfusion.* 2014;54(10):2514–2522.
38. Windrum P, Morris TC, Drake MB, Niederwieser D, Ruutu T, Subcommittee E, EBMT Chronic Leukaemia Working Party Complications Subcommittee. Variation in dimethyl sulfoxide use in stem cell transplantation: a survey of EBMT centres. *Bone Marrow Transplant.* 2005;36(7):601–603.
39. Yen FL, Tsai MH, Yang CM, et al. Curcumin nanoparticles ameliorate ICAM-1 expression in TNF- $\alpha$ -treated lung epithelial cells through p47 (phox) and MAPKs/AP-1 pathways. *PLoS One.* 2013;8(5):e63845.
40. Thurlow LR, Hanke ML, Fritz T, et al. *Staphylococcus aureus* biofilms prevent macrophage phagocytosis and attenuate inflammation in vivo. *J Immunol.* 2011;186(11):6585–6596.
41. Saqib U, Sarkar S, Suk K, Mohammad O, Baig MS, Savai R. Phytochemicals as modulators of M1-M2 macrophages in inflammation. *Oncotarget.* 2018;9(25):17937–17950.
42. Mantovani A, Sozzani S, Locati M, Allavena P, Sica A. Macrophage polarization: tumor-associated macrophages as a paradigm for polarized M2 mononuclear phagocytes. *Trends Immunol.* 2002;23(11):549–555.
43. Bottner F, Wegner A, Winkelmann W, Becker K, Erren M, Götze C. Interleukin-6, procalcitonin and TNF-alpha: markers of peri-prosthetic infection following total joint replacement. *J Bone Joint Surg Br.* 2007;89(1):94–99.
44. Shahi A, Parvizi J. The role of biomarkers in the diagnosis of periprosthetic joint infection. *EFORT Open Rev.* 2016;1(7):275–278.
45. Mittal M, Siddiqui MR, Tran K, Reddy SP, Malik AB. Reactive oxygen species in inflammation and tissue injury. *Antioxid Redox Signal.* 2014;20(7):1126–1167.
46. González JF, Hahn MM, Gunn JS. Chronic biofilm-based infections: skewing of the immune response. *Pathog Dis.* 2018;76(3).
47. Kerkisiek KM, Pamer EG. T cell responses to bacterial infection. *Curr Opin Immunol.* 1999;11(4):400–405.
48. Ziegler C, Goldmann O, Hobeika E, Geffers R, Peters G, Medina E. The dynamics of T cells during persistent *Staphylococcus aureus* infection: from antigen-reactivity to *in vivo* anergy. *EMBO Mol Med.* 2011;3(11):652–666.
49. Medina E, Hartl D. Myeloid-derived suppressor cells in infection: a general overview. *J Innate Immun.* 2018;1–7.
50. Heim CE, Vidlak D, Odvody J, Hartman CW, Garvin KL, Kielian T. Human prosthetic joint infections are associated with myeloid-derived suppressor cells (MDSCs): Implications for infection persistence. *J Orthop Res.* 2018;36(6):1605–1613.
51. Lew DP, Waldvogel FA. Osteomyelitis. *Lancet.* 2004;364(9431):369–379.

52. Dudek-Wicher RK, Junka A, Bartoszewicz M. The influence of antibiotics and dietary components on gut microbiota. *Prz Gastroenterol*. 2018;13(2):85–92.
53. Tamadao RSE, Hoerauf A, Layland LE. Immunomodulatory effects of myeloid-derived suppressor cells in diseases: Role in cancer and infections. *Immunobiology*. 2018;223(4–5):432–442.
54. Dorhoi A, Du Plessis N. Monocytic myeloid-derived suppressor cells in chronic infections. *Front Immunol*. 2017;8:1895.
55. Zhou Y, Zhang T, Wang X, et al. Curcumin modulates macrophage polarization through the inhibition of the Toll-like receptor 4 expression and its signaling pathways. *Cell Physiol Biochem*. 2015;36(2):631–641.
56. Gao S, Zhou J, Liu N, et al. Curcumin induces M2 macrophage polarization by secretion IL-4 and/or IL-13. *J Mol Cell Cardiol*. 2015;85:131–139.
57. Pastuła A, Marcinkiewicz J. Myeloid-derived suppressor cells: a double-edged sword? *Int J Exp Pathol*. 2011;92(2):73–78.
58. Condamine T, Gabrilovich DI. Molecular mechanisms regulating myeloid-derived suppressor cell differentiation and function. *Trends Immunol*. 2011;32(1):19–25.
59. Jiang M, Chen J, Zhang W, et al. Interleukin-6 trans-signaling pathway promotes immunosuppressive myeloid-derived suppressor cells via suppression of suppressor of cytokine signaling 3 in breast cancer. *Front Immunol*. 2017;8:1840.
60. Zambrano LMG, Brandao DA, Rocha FRG, et al. Local administration of curcumin-loaded nanoparticles effectively inhibits inflammation and bone resorption associated with experimental periodontal disease. *Sci Rep*. 2018;8(1):6652.

## Supplementary material

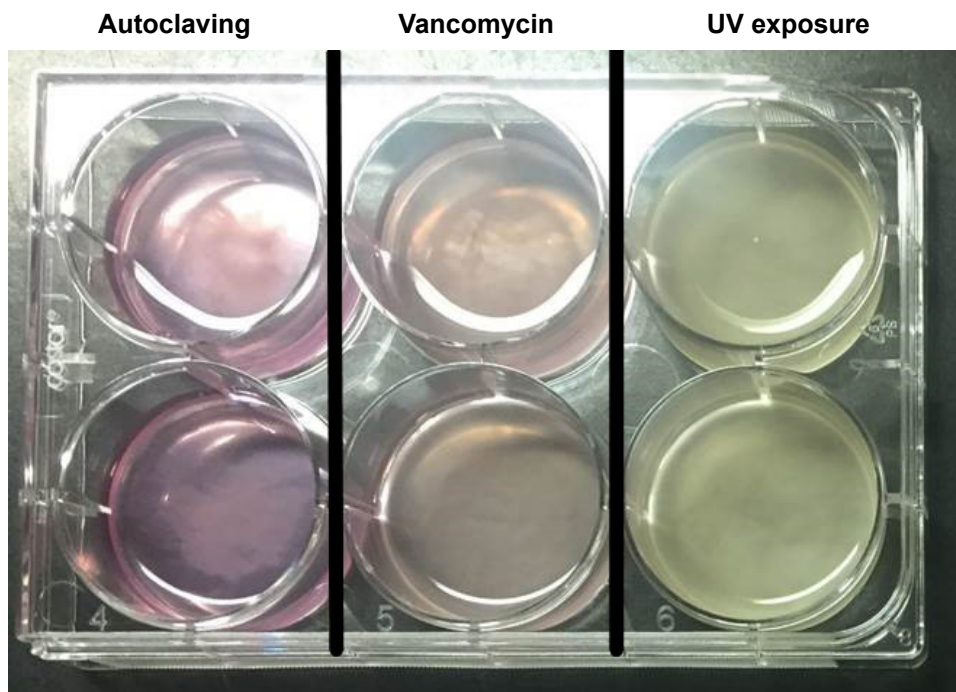


**Figure S1** The supplementary data demonstrated that the autoclaving method for biofilm is the optimal method in our system.

**Notes:** *S. aureus* and its biofilm were collected by centrifugation at  $3,900\times g$  for 15 minutes, and then the pellet was sterilized by autoclaving or pre-treatment with vancomycin or UV for 12 hours (from lane 1 to lane 3) before adding to BMC culture. Both pre-treatment with vancomycin (lane 2) and UV for 12 hours (lane 3) failed to reduce the *S. aureus* growth rate. If the collected pellet was not autoclaved, the growth of *S. aureus* was rapid and resulted in the death of BMCs within 48 hours.

**Abbreviations:** BMCs, bone marrow cells; *S. aureus*, *Staphylococcus aureus*.

International Journal of Nanomedicine

**Publish your work in this journal**

The International Journal of Nanomedicine is an international, peer-reviewed journal focusing on the application of nanotechnology in diagnostics, therapeutics, and drug delivery systems throughout the biomedical field. This journal is indexed on PubMed Central, MedLine, CAS, SciSearch®, Current Contents®/Clinical Medicine,

Submit your manuscript here: <http://www.dovepress.com/international-journal-of-nanomedicine-journal>

Journal Citation Reports/Science Edition, EMBase, Scopus and the Elsevier Bibliographic databases. The manuscript management system is completely online and includes a very quick and fair peer-review system, which is all easy to use. Visit <http://www.dovepress.com/testimonials.php> to read real quotes from published authors.

Dovepress

## Research Paper

# MicroRNA-29a is a key regulon that regulates BRD4 and mitigates liver fibrosis in mice by inhibiting hepatic stellate cell activation

Ying-Hsien Huang<sup>1</sup>, Hsing-Chun Kuo<sup>2,3,4,5</sup>, Ya-Ling Yang<sup>6</sup>✉, Feng-Sheng Wang<sup>7</sup>✉

1. Department of Pediatrics, Kaohsiung Chang Gung Memorial Hospital and Chang Gung University College of Medicine, Kaohsiung, Taiwan
2. Department of Nursing, Chang Gung University of Science and Technology, Chiayi, Taiwan
3. Research Fellow, Chiayi Chang Gung Memorial Hospital, Chiayi, Taiwan
4. Research Center for Industry of Human Ecology and Research Center for Chinese Herbal Medicine, College of Human Ecology, Chang Gung University of Science and Technology, Taoyuan, Taiwan
5. Chronic Diseases and Health Promotion Research Center, CGUST, Chiayi, Taiwan
6. Department of Anesthesiology, Kaohsiung Chang Gung Memorial Hospital and Chang Gung University College of Medicine, Kaohsiung, Taiwan, 833
7. Core Laboratory for Phenomics & Diagnostics, Department of Medical Research, Kaohsiung Chang Gung Memorial Hospital and Chang Gung University College of Medicine, Kaohsiung, Taiwan, 833

✉ Corresponding authors: Ya-Ling Yang, M.D., Department of Anesthesiology, Kaohsiung Chang Gung Memorial Hospital and Chang Gung University College of Medicine, Kaohsiung, Taiwan, 833, 123 Ta-Pei Road, Niao-Sung District, Kaohsiung, Taiwan 833, R.O.C. E-mail: yaling453@yahoo.com.tw. Feng-Sheng Wang, PhD, Department of Medical Research, Kaohsiung Chang Gung Memorial Hospital, 123 Ta-Pei Road, Niao-Sung District, Kaohsiung, Taiwan 833, R.O.C. Tel: +886-7-7317123 ext. 8795; Fax: +886-7-7338009; E-mail: wangfs@ms33.hinet.net

© Ivyspring International Publisher. This is an open access article distributed under the terms of the Creative Commons Attribution (CC BY-NC) license (<https://creativecommons.org/licenses/by-nc/4.0/>). See <http://ivyspring.com/terms> for full terms and conditions.

Received: 2018.09.14; Accepted: 2018.12.05; Published: 2019.01.01

## Abstract

MicroRNA-29a is a key regulon that regulates hepatic stellate cells (HSCs) and mitigates liver fibrosis. However, the mechanism by which it does so remains largely undefined. The inhibition of bromodomain-4 protein (BRD4) represents a novel therapeutic target in hepatic fibrosis. Therefore, the purpose of this study is to investigate the miR-29a regulation of BRD4 signaling in a bile duct-ligation (BDL) animal model with regard to developing cholestatic liver fibrosis. Hepatic tissue in miR-29a transgenic mice (miR-29aTg mice) displayed weak fibrotic matrix, as shown by  $\alpha$ -smooth muscle actin staining within affected tissues compared to wild-type mice. miR-29a overexpression reduced the BDL exaggeration of BRD4 and SNAIL expression. Increased miR-29a signaling caused the downregulation of EZH2, MeCP2, and SNAIL, as well as the upregulation of PPAR- $\gamma$  expression, in primary HSCs. We further demonstrated that the administration of JQ1, a BRD4 inhibitor, could inhibit BRD4, C-MYC, EZH2, and SNAIL expression, while both JQ1 and a miR-29a mimic could inhibit the migration and proliferation of HSCs. In short, our research demonstrates that miR-29a negatively regulates HSC activation by inhibiting BRD4 and EZH2 function, thus making it a promising target for the pharmacologic treatment of hepatic fibrosis.

Key words: miR-29a, bile duct ligation, cholestasis, liver fibrosis, BRD4

## Introduction

Chronic liver damage caused by any form of hepatitis or cholestasis can cause liver fibrosis, which is a complex process controlled by a series of signaling pathways [1]. When hepatic stellate cells (HSC) are activated and undergo morphologic and functional trans-differentiation [1-3], they not only secrete profibrogenic mediators, such as transforming growth factor- $\beta$  (TGF- $\beta$ ) signaling, but also generate ECM components.

MicroRNAs (miRNAs) are small single-stranded non-coding RNAs that can suppress endogenous

mRNA transcripts [4]. Cumulative evidence has shown that miR-29 levels are significantly decreased in fibrotic livers and that their downregulation influences HSC activation [5-7]. Furthermore, an increase in miR-29 in murine HSCs has been shown to inhibit collagen expression [6, 8] by directly targeting the mRNA expression of ECM genes. In our previous studies [9-15], we have already demonstrated that miR-29a overexpression in cholestatic mice significantly inhibited hepatocellular damage and liver fibrosis, and the multiple pathways of apoptosis,



autophagy, endoplasmic reticulum stress, and toll-like receptors were all included.

The field of epigenetics consists of changing both the chromatin structure and the DNA methylation and acetylation patterns of a genome [16]. Histones require the addition of a functional group, such as methylation, acetylation, phosphorylation, sumoylation, or ubiquitination [17]. We have previously found that miR-29a normalizes histone deacetylase 4 expression, increases the acetylation status of H3K9 in HSCs, and mitigates HSC activation [11]. However, histone methylation is reversible, and its dynamic nature is controlled by a balance between histone methyltransferases and demethylases [18]. A growing amount of evidence has implied that inhibiting the function of Enhancer of Zeste Homolog 2 (EZH2), a catalytic sub-unit of the Polycomb Repressive Complex 2 and histone methyltransferases that catalyze the addition of methyl groups to histone H3 at lysine 27 [18], can lessen liver fibrosis by blocking HSC function [19, 20]. Furthermore, suppression of BRD4 has been demonstrated to decrease the expression of EZH2 through the upregulation of C-MYC [21]. In a recent study, TGF- $\beta$ 1 was observed to promote HSC activation via the BRD4/C-MYC/EZH2 pathway in liver fibrosis [22]. The interaction of SNAI1 and EZH2 can also repress E-cadherin expression, which is essential for triggering epithelial-mesenchymal transition (EMT) [23]. Therefore, in this study, we decided to investigate the miR-29a regulation of BRD4/ EZH2 signaling in a cholestatic animal with regard to liver fibrosis and HSC activation.

## Materials and Methods

### Ethics statement

The Institutional Animal Care and Use Committee of Chang Gung Memorial Hospital reviewed and approved all protocols related to animal uses (#2017091801). We acquired male C57BL/6 mice (body weight 25- 35 g) from BioLASCO Taiwan Co., Ltd. and housed them in an animal facility at 22 °C, with a relative humidity of 55%, in a 12 h light/12 h dark cycle, where they were given both sterile tap water and food *ad libitum*.

### Construction and breeding of the miR-29a transgenic mouse colony

Transgenic mice that overexpressed miR-29a driven by the PGK promoter were bred and housed in a specific pathogen-free rodent barrier, as described in a previous study [14]. The genotype of the transgenic mice was typed with PCR and primers (forward: 5'-GAGGATCCCCTCAAGGATACCAAGGGATGA AT-3' and reverse 5'-CTTCTAGAAGGAGTGTTC

TAGGTATCCGTCA-3'). We obtained wild-type mice from littermates that did not carry the construct.

### Animal model and experimental protocol

Six to eight mice were used for each of our experiments. The mice were categorized into either the "BDL" group or the "sham" group in accordance with whether it had received an actual ligation or a sham ligation of the common bile duct, the method of which has been previously described [11]. All the mice were euthanized one week after the operation, at which point liver tissues were dissected, snap-frozen, and processed to isolate total RNA and proteins. All specimens were stored at -80 °C until biochemical analysis.

### Primary HSC isolation and culture

We isolated primary HSCs from fresh livers in mice using the following procedure: Hepatic specimens were digested by pronase and collagenase. The digested mixtures were subjected to density gradient centrifugation in 8.5% Nycodenz (Sigma-Aldrich, St. Louis, MO) as previously described in another study [24, 25]. HSCs expressed autofluorescence of retinoids in the lipid droplets of cell cultures, and HSC lipid droplets were verified under a fluorescence microscope. Trypan blue exclusion assays demonstrated that the viability of cell culture was more than 95%. 95-99% cells were positive for Oil red O staining [25]. Cells were incubated in Dulbecco's modified Eagle's medium supplemented with 5% newborn calf serum. After one day in culture, the HSCs exhibited a dormant phenotype, which was followed by an activated phenotype 7-14 days after incubation. The cell cultures were incubated until confluence, and those within 2-6 passages were used for study.

### RNAi transfection

The hepatic stellate cells (HSCs) were maintained in DMEM supplemented with 10% fetal bovine serum, glutamax, and antibiotic-antimycotic in a 5% CO<sub>2</sub> humidified incubator at 37°C. Cells were seeded at a density of  $9 \times 10^5$  cells per 6-cm culture dish for western blot,  $3 \times 10^4$  cells/well in the ibidi Culture-Insert 2 Well for wound healing assay, and  $8 \times 10^3$  cells/well in the 96-well culture microplate for cell proliferation assay. Twenty-four hours after initial seeding, we transfected the HSCs with a concentration of 25 nM of miR-29a precursor (mimic-miR-29a, GE Healthcare Dharmacon, IN), miR control (GE Healthcare Dharmacon, IN), or miR-29a antisense oligonucleotide inhibitor (inhibitor-miR-29a GE Healthcare Dharmacon, IN) for 24 h with Lipofectamine™ RNAiMAX Transfection Reagent (Invitrogen, CA) according to the manufacturer's

instructions. Infected cells were incubated for 24 h at 37°C and then used for further experiments [26].

### Immunohistological Analysis

For immunohistochemical analysis, formalin-fixed paraffin-embedded blocks of the mice's liver tissues were cut into 2-µm sections. After deparaffinization and rehydration, we heated sections in a citrate buffer (10 mM, pH 6, Thermo Fisher Scientific, Waltham, MA, USA) in a microwave for 30 min to retrieve the antigens. Endogenous peroxidase activity was blocked with a 3% hydrogen peroxide (UltraVision Hydrogen Peroxide Block; Thermo Fisher Scientific) for 10 min. The sections were incubated with α-SMA antibody (ab5694, abcam, JHY) for 1 h at room temperature and then visualized using HRP polymer (UltraVision Quanto Detection System; Thermo Fisher Scientific) and DAB chromogen (DAB Peroxidase Substrate Kit; Vector Laboratories, Burlingame, CA, USA). The sections were counterstained with Mayer's hematoxylin (ScyTek Laboratories, Logan, UT, USA), dehydrated, and then mounted using a mounting medium. The staining intensity of sections was measured by independent color channel of an image J analysis [27]. Each group had six to eight samples.

### JQ1 treatment for hepatic stellate cells

The HSCs were seeded in a 10-cm culture dish with a density of  $1.5 \times 10^6$  cells /dish and incubated overnight at 37°C. Cells were then maintained in DMEM medium with JQ1 (100 nM) for 24 h. Proteins were extracted from the cells for western blot analysis.

### Western blot analysis

We used approximately 20 mg of liver tissue in a 500 ml protein lysis buffer (iNtRON, Seongnam-si), homogenized by the MagNA Lyser system (Roche, Germany). The extraction protein (40 µg) from the supernatant of each sample was mixed with 4x sample buffer (Bio-Rad) and boiled for 10 min. All samples, including protein markers (TM-PM10170, TOOLS, NTPC), were fractionated by 6~15 % SDS-PAGE and transferred to a PVDF membrane. After incubation with 10 % nonfat milk in TBST (10 mM Tris, pH 8.0, 150 mM NaCl, 0.05 % Tween 20) for 60 min at room temperature, they were washed with TBST and incubated with primary antibodies against BRD4 (ab128874, abcam, JHY), SNAI1 (#3895, cell signaling, MA), EZH2 (#4905, cell signaling, MA), MeCP2 (#10861-1-AP, PROTEINTECH, IL), or PPAR-γ (#16643-1-AP, PROTEINTECH, IL), as well as Nucleolin (ab134164, abcam, JHY) or GAPDH, used as the internal control (#60004-1-Ig, PROTEINTECH, IL) at 4 °C overnight. We washed membranes three times for 10 min and incubated them with horseradish

peroxidase-coupled anti-rabbit immunoglobulin-G antibodies (dilution: 1:5000) and HRP anti-mouse immunoglobulin-G antibodies (dilution: 1:10,000) at room temperature for 1 h. Blots were washed with TBST three times and developed with enhanced chemiluminescence detection (GE Healthcare Biosciences AB, Uppsala, Sweden) and exposed to film, and we quantified the signals using densitometry.

### Cell proliferation analysis

Cell proliferation was determined by the WST-1 assay. After infection by the miR-29a precursor or being treated with 100 nM JQ1 (Sigma-Aldrich Chemie GmbH) for 24 h, we added 10 µL WST-1 reagent (Roche Diagnostics, Laval, Quebec, Canada) to each well and incubated for another 60 minutes at 37° C. The absorbance was determined using a microplate reader (Hidex Sense microplate reader) at a test wavelength of 450 nm and reference wavelength of 630 nm.

### Wound healing assay

We adopted the wound healing assay to detect cell migration. HSCs were seeded in a culture-insert (ibidi culture-insert 2 well, ibidi GmbH, Martinsried, Germany) at a density of  $3 \times 10^4$  cells per well. After allowing the cells to attach overnight, we removed the culture-insert and washed the cells with PBS to remove non-adherent cells. We then provided fresh medium containing JQ1 (100nM) or miR-29a (25nM) mimic and photographed the plate at 0, 5, and 8 h to capture the two different fields at each time point on each plate. The number of cells that migrated into the wound space were manually counted in three fields per well under a light microscope at 50× magnification. We then quantified the areas using image J analysis.

### Statistical analysis

All values in the figures and tables are expressed as mean ± standard error. Quantitative data were analyzed using the one-way analysis of variance [28] when appropriate, and we adopted the least significant difference (LSD) test for post-hoc testing. A two-sided p-value less than 0.05 was considered statistically significant.

## Results

### Overexpression of miR-29a considerably decreases liver fibrosis in cholestatic livers

To determine the influence of overexpressed miR-29a on the cholestatic liver injury process, we studied α-SMA expression by immunohistochemistry. As shown in Figure 1, α-SMA expression revealed

abundant brown staining around the portal regions in the BDL-affected liver specimens in the wild-type mice compared to the sham group ( $p < 0.001$ ). This histopathology was clearly alleviated in the BDL-affected miR-29Tg mice ( $p < 0.001$ ) (Figure 1).

### miR-29a overexpression reduced hepatic BRD4 and SNAI1 expression in cholestatic livers

We first examined whether miR-29a signaling could alter BRD4, EZH2, and SNAI1 expressions in liver tissues injured by BDL. In the wild-type group,

BRD4 ( $p = 0.011$ ) and SNAI1 ( $p < 0.001$ ) were significantly increased after BDL (Fig. 2). The BDL increase of BRD4 ( $p=0.029$ ) and SNAI1 ( $p=0.014$ ) levels was significantly reduced in the miR-29aTg mice (Fig. 2). However, the signal intensity of EZH2 was too weak to detect between the two groups.

### Increased miR-29a function reduced EZH2, MeCP2, and SNAI1 and increased PPAR- $\gamma$ expressions in HSCs

In a previous study, we found that the expressions in BRD4 were significantly reduced in the

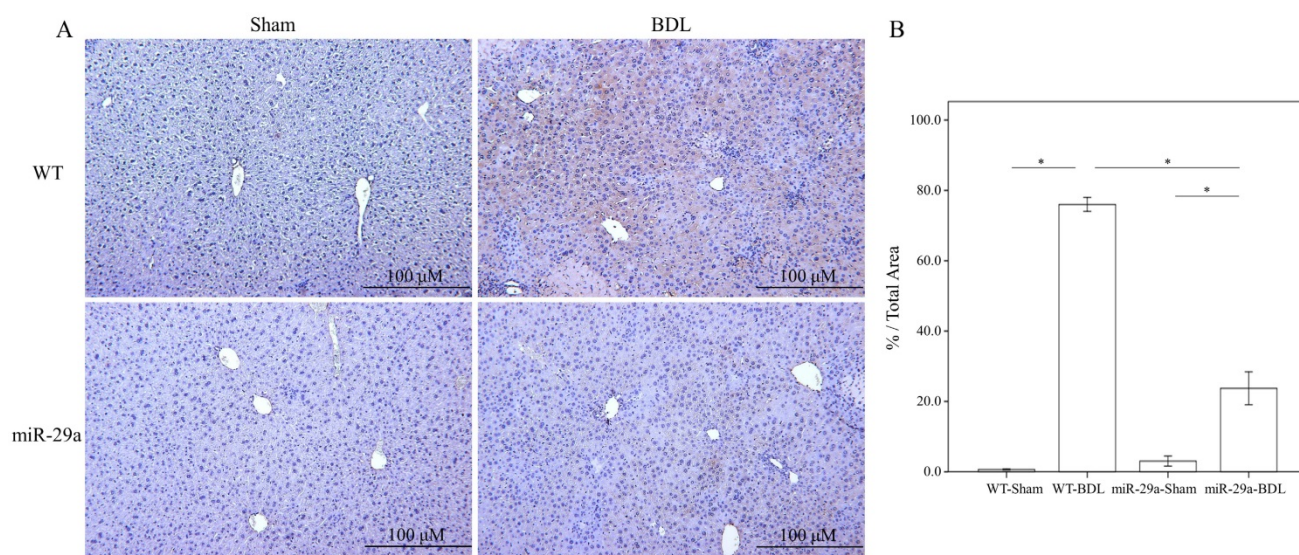


**Figure 1.** Overexpression of miR-29a in the murine model resulted in the downregulation of fibrosis in mice livers after BDL. (A) Histomorphometric analyses of alpha-smooth muscle actin ( $\alpha$ -SMA) demonstrated strong  $\alpha$ -SMA immunoreactivity (brown staining) in wild-type (WT) mice compared to those in miR-29aTg mice. (B) We measured the histomorphometric analyses of alpha-smooth muscle actin by independent color channel of an image J analysis. Data are expressed as the mean  $\pm$  SE of six to eight samples per group. \*indicates a  $p < 0.05$  between the groups.

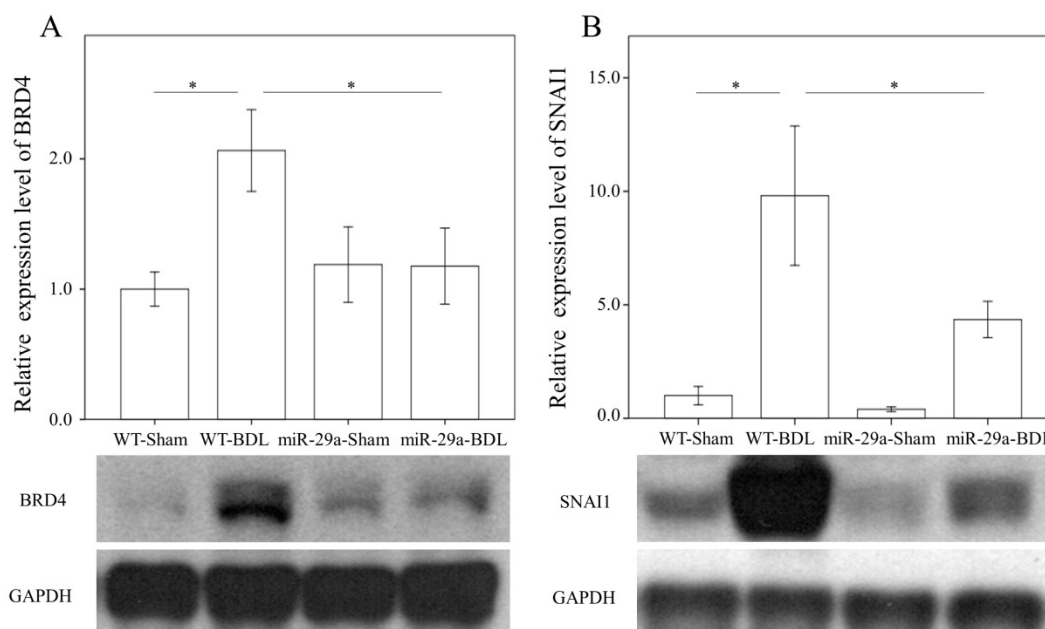


**Figure 2.** Comparison of the protein expression of BRD4 (A) and SNAI1 (B) in WT and miR-29Tg mice livers following BDL. Data from the six to eight samples per group are expressed as mean  $\pm$  SE. \*indicates a  $p < 0.05$  between the groups.



miR-29 mimic-transfected HSCs [14]. Therefore, we examined whether miR-29a signaling could regulate EZH2, MeCP2, SNAI1, and PPAR- $\gamma$  expressions in primary HSCs. As shown in Figure 3 A, B, and C, the expressions in EZH2, MeCP2, and SNAI1 were significantly reduced in the miR-29 mimic-transfected cell cultures ( $p = 0.007$ ;  $p = 0.048$ ; and  $p = 0.016$ , respectively). In contrast, after treatment with a miR-29 mimic, PPAR- $\gamma$  expression was significantly upregulated in the HSCs ( $p = 0.012$ , Fig. 3D).

### Administering JQ1 reduced BRD4, C-MYC, EZH2, and SNAI1 expressions in HSCs

To examine the effects of JQ1 on the expression of BRD4, C-MYC, EZH2, and SNAI1, we treated primary HSCs with JQ1, which is a BRD4 inhibitor. As expected, JQ1 significantly downregulated the

expression of BRD4, C-MYC, EZH2, and SNAI1 in primary HSCs ( $p = 0.05$ ;  $p = 0.035$ ;  $p = 0.033$  and  $p = 0.005$ , Fig. 4).

### Administering JQ1 and miR-29a inhibits HSC migration and proliferation

To evaluate whether JQ1 may regulate HSC migration, a wound healing assay was performed using primary HSCs. The results of the present study showed that both JQ1 and miR-29a mimic were capable of inhibiting the migration of primary HSCs (both  $p < 0.001$ ; Fig. 5A, B). We then conducted a cell proliferation assay to examine the effects of JQ1 and miR-29a on cell proliferation. As shown in Fig. 5C, either a JQ1 or miR-29a mimic could inhibit the proliferation of primary HSCs (both  $p < 0.001$ ).

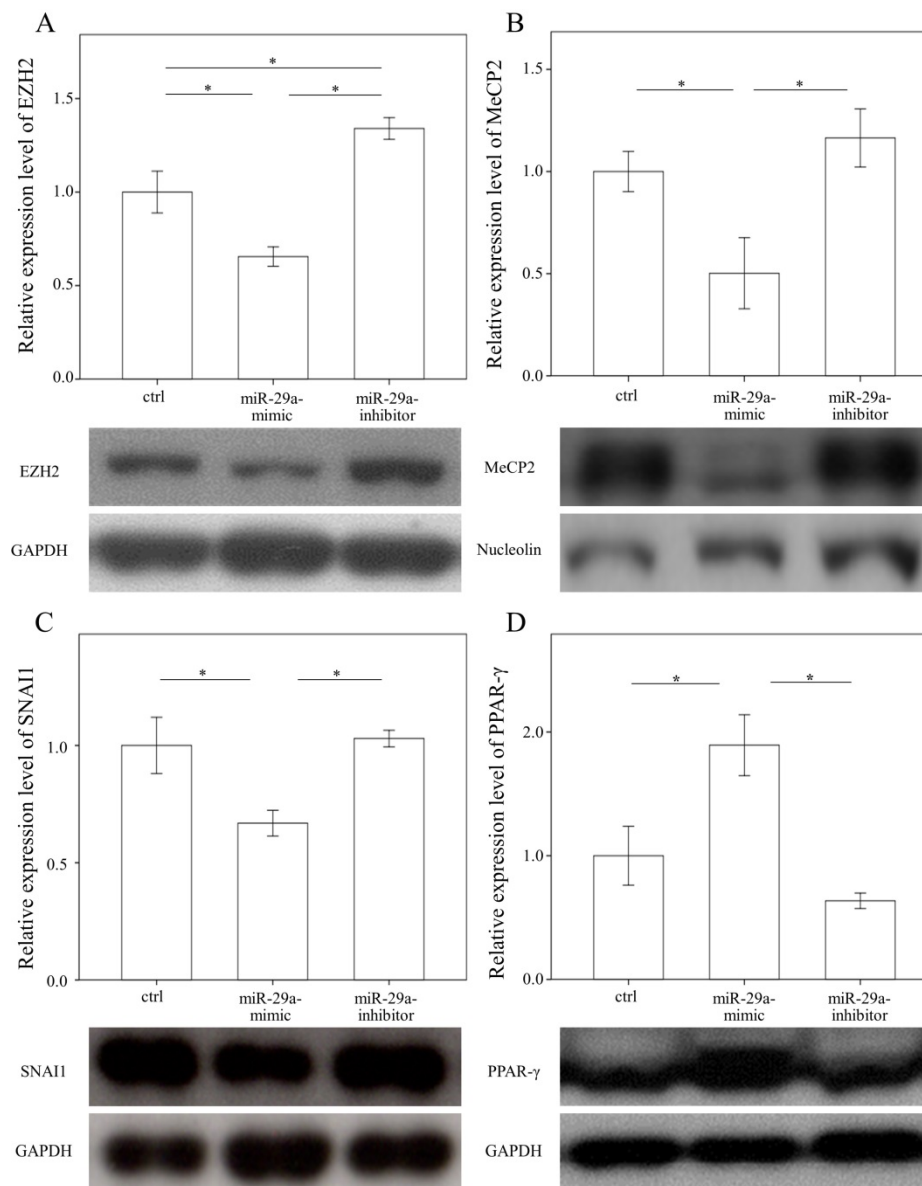


**Figure 3.** Comparison of protein expression of EZH2 (A), MeCP2(B), SNAI1 (C), and PPAR- $\gamma$  (D) in primary hepatic stellate cells after being treated with or without a miR-29a mimic or inhibitor or only a miRNA scramble for 24 hours. Data are expressed as mean  $\pm$  SE of the four to six samples per group. \*indicates a  $p < 0.05$  between the groups.



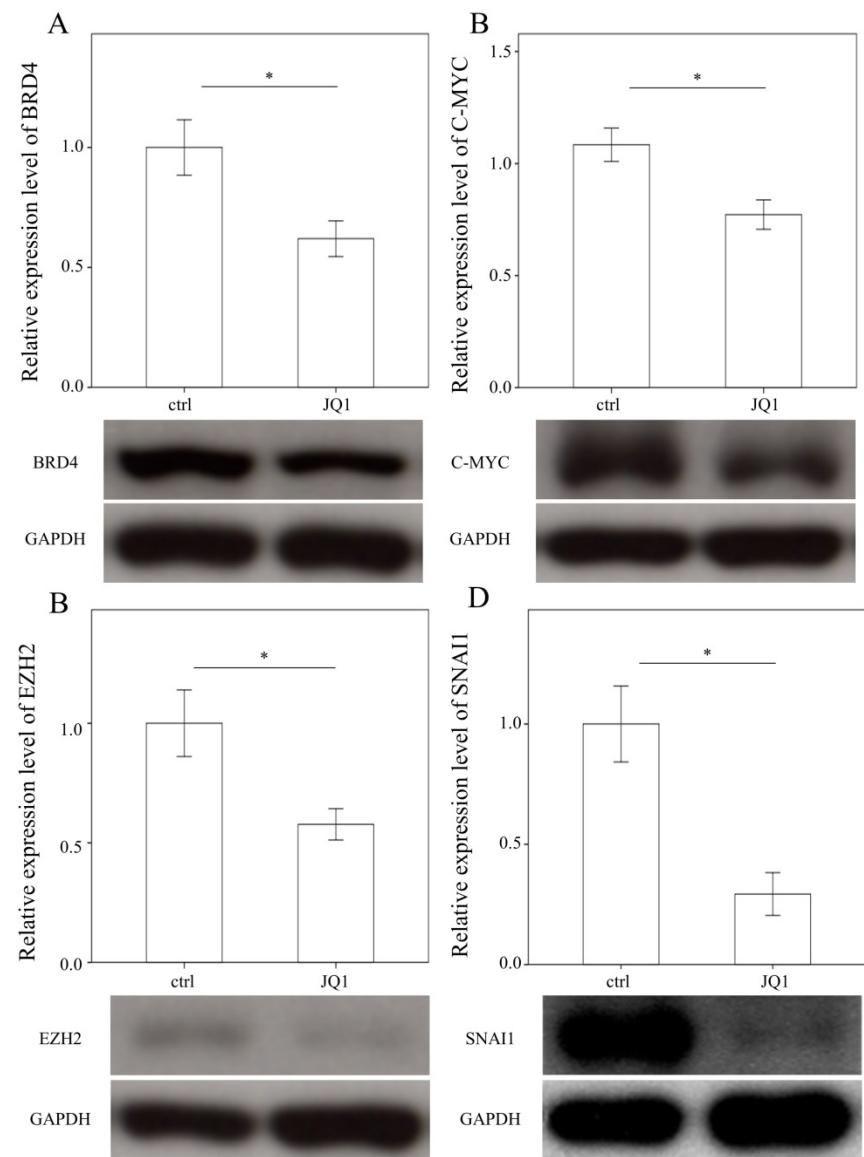


**Figure 4.** Comparison of protein expression of BRD4 (A), C-MYC (B), EZH2 (C), and SNAI1 (D) in primary hepatic stellate cells after being treated with JQ1 for 24 hours. Data are expressed as mean  $\pm$  SE of the four to five samples per group. \*indicates a  $p < 0.05$  between the groups.

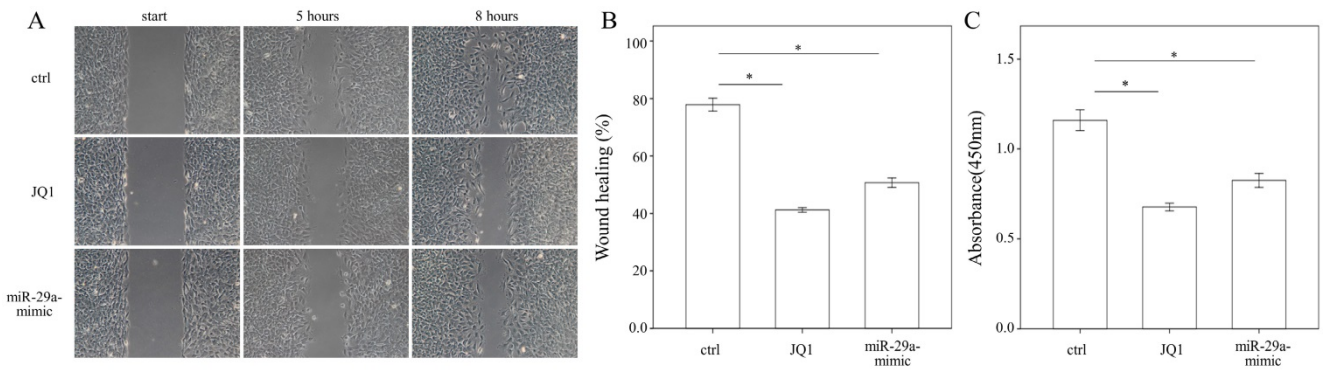


**Figure 5.** We measured the migration and proliferation of primary activated HSCs using wound healing and WST-I assay, respectively. A miR-29a mimic or JQ1 significantly inhibited the migration of primary HSCs of WT mice. Data are expressed as the mean  $\pm$  SE of three independent experiments. \*indicates a  $p < 0.05$  between the groups.

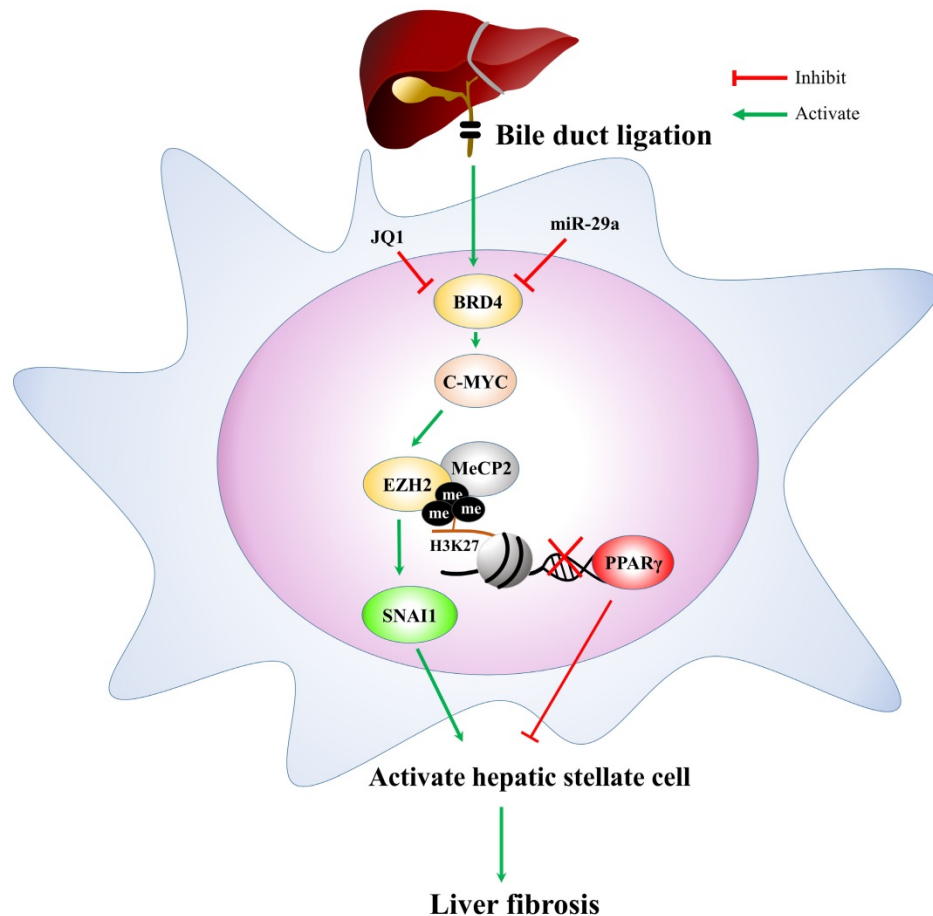


**Figure 6.** The proposed miR-29a signaling protection model in liver fibrosis by inhibiting BRD4/EZH2/SNAI1. miR-29a is a vital regulator of the profibrogenic phenotype of HSCs. Increased miR-29a function hinders BRD4, EZH2, SNAI1, and PPAR- $\gamma$  expressions, thus inhibiting HSC activation.

## Discussion

The trans-differential activation of liver injury and HSCs is responsible for the pathogenesis of liver fibrosis. Increased miR-29a function in cholestatic mice significantly inhibited liver fibrosis, and this study is the first to report that miR-29a could directly modulate BRD4 expression of the profibrogenic phenotype of HSCs in an obstructive jaundice mouse model. Furthermore, we discovered that the expression of BRD4 is associated miR-29a, along with EZH2, MeCP2, and SNAI1, as well as upregulation of PPAR- $\gamma$  expression, in activating primary HSCs. Finally, we have demonstrated that overexpression of miR29a or inhibition of BRD4 can significantly weaken activated HSC migration and proliferation.

Although studies have implicated BRD4, a bromodomain protein and extra-terminal member, can delicately control inflammatory gene expression through epigenetic pathways [29]. We have also uncovered that overexpression of miR-29a in cholestatic mice significantly obstructed TLR2 and TLR4 signaling in liver tissues while significantly decreasing the proinflammatory cytokines expression [30]. Sun et al. also showed that inhibition of BRD4

with JQ1 suppressed activation of TLR4 signaling and decreased acute myocardial infarction damage [31]. Meanwhile, JQ1 has been clearly shown to effectively suppress HSC proliferation and differentiation into myofibroblasts and to ameliorate pathological fibrotic responses [32]. EZH2 is the key catalytic sub-unit of Polycomb repressive complex 2 and has emerged as a crucial regulator of EMT, wound healing, fibrogenesis, and tumor metastasis [33, 34]. In this study, we demonstrated that miR-29a positively regulated EZH2 expression by upregulating C-MYC in primary HSCs. In line with our study, overexpression of miR-29a inhibits BDL-provoked excessive fibrogenesis, which is partially mediated by the inhibition of BRD4/C-MYC/EZH2 signaling. SNAI1 is the key transcription factor best known for its ability to trigger EMT to influence fibrosis development [35]. Scarpa et al. demonstrated an upregulated expression of SNAI1 in human hepatic fibrosis and murine experimental models of liver injury [36]. SNAI1 knockdown resulted in the improvement of hepatic fibrosis and its involvement in the HSC trans-differentiation process [36]. Furthermore, SNAI1 has been reported to recruit

Polycomb Repressive Complex 2 to the E-cadherin promoter to repress E-cadherin expression [23]. Recently, Oh et al. also reported that high glucose levels enhance the formation of EZH2/Snai1 complex to facilitate E-cadherin repression and stimulate human mesenchymal stem cell migration [37]. All of these studies agree with our finding that increased miR-29a function significantly inhibits the upregulation of SNAI1 in cholestatic liver and primary HSCs.

The MeCP2 (methyl CpG binding protein 2) dependent epigenetic pathway facilitates the activation of HSCs by regulating the suppression of PPAR $\gamma$ , which opposes myofibroblast trans-differentiation expression by targeting DNA methyltransferases to maintain the HSCs in a quiescent stage [38]. MeCP2 also promotes EZH2 expression and H3K27 methylation to constitute a repressive chromatin structure in the promoter of PPAR $\gamma$  [5]. Meanwhile, the inhibition of EZH2 or the activation of PPAR $\gamma$  blocked the exacerbation of liver fibrosis in mice [20]. Therefore, the EZH2-mediated repression of PPAR $\gamma$  may be involved in the aggravated liver fibrosis driven by increased miR-29a in HSCs. In short, our data suggest that miR-29a plays an essential role in guiding the transition of HSC phenotypes and contributing to the regulation of cellular proliferation and the migration of activated HSCs.

In conclusion, based on the miR-29a signaling protection model (miR-29aTg mice) in liver fibrosis, we demonstrated a new mechanism for liver damage via inhibiting BRD4/EZH2/SNAI1 pathway. The bile duct-ligation model and liver fibrosis correspond to the effects of BRD4, EZH2, SNAI1, and PPRP- $\gamma$  expressions at cholestatic liver locations, thereby triggering livers injury. Increased miR-29a function hinders BRD4, EZH2, SNAI1, and PPRP- $\gamma$  expressions, thus inhibiting HSC activation (Fig. 6). This study provides additional evidence that the possibility of finding novel therapeutic agents targeting miR-29a-based BRD4 for the improvement of hepatic fibrosis would play an important role in liver injury diseases. This study highlights that the epigenetic mechanism by miR-29a signaling may modulate their profibrogenic phenotype in the activation of HSCs. Further studies are required in the future to delineate the use of miR-29a agonists as novel therapeutics for treating liver fibrosis.

## Acknowledgments

The authors would like to thank Miss Yuan-Ting Chuang and Chia-Ling Wu for assisting with this article.

## Funding

This study was supported by grants from the National Health Research Institute (NHRI-EX107-10736SI), Ministry of Science and Technology, Taiwan (106-2314-B-182A-141 -MY3) and Chang Gung Memorial Hospital, Taiwan (CMRPG8G1341, 8G1342 and 8F1562). However, these organizations had no part in the study design, data collection and analysis, publication decisions, or preparation of the manuscript.

## Competing Interests

The authors have declared that no competing interest exists.

## References

- Friedman SL. Evolving challenges in hepatic fibrosis. *Nature reviews Gastroenterology & hepatology*. 2010; 7: 425-36.
- Battaller R, Brenner DA. Liver fibrosis. *The Journal of clinical investigation*. 2005; 115: 209-18.
- Friedman SL. Mechanisms of hepatic fibrogenesis. *Gastroenterology*. 2008; 134: 1655-69.
- Cha W, Fan R, Miao Y, Zhou Y, Qin C, Shan X, et al. MicroRNAs as novel endogenous targets for regulation and therapeutic treatments. *Medchemcomm*. 2018; 9: 396-408.
- Mann J, Chu DC, Maxwell A, Oakley F, Zhu NL, Tsukamoto H, et al. MeCP2 controls an epigenetic pathway that promotes myofibroblast transdifferentiation and fibrosis. *Gastroenterology*. 2010; 138: 705-14, 14 e1-4.
- Roderburg C, Urban GW, Bettermann K, Vucur M, Zimmermann H, Schmidt S, et al. Micro-RNA profiling reveals a role for miR-29 in human and murine liver fibrosis. *Hepatology*. 2011; 53: 209-18.
- Sekiya Y, Ogawa T, Yoshizato K, Ikeda K, Kawada N. Suppression of hepatic stellate cell activation by microRNA-29b. *Biochemical and biophysical research communications*. 2011; 412: 74-9.
- Bandyopadhyay S, Friedman RC, Marquez RT, Keck K, Kong B, Icardi MS, et al. Hepatitis C virus infection and hepatic stellate cell activation downregulate miR-29: miR-29 overexpression reduces hepatitis C viral abundance in culture. *J Infect Dis*. 2011; 203: 1753-62.
- Ghavami S, Hashemi M, Ande SR, Yeganeh B, Xiao W, Eshraghi M, et al. Apoptosis and cancer: mutations within caspase genes. *Journal of medical genetics*. 2009; 46: 497-510.
- Li SC, Wang FS, Yang YL, Tiao MM, Chuang JH, Huang YH. Microarray Study of Pathway Analysis Expression Profile Associated with MicroRNA-29a with Regard to Murine Cholestatic Liver Injuries. *International journal of molecular sciences*. 2016; 17: 324.
- Tiao MM, Wang FS, Huang LT, Chuang JH, Kuo HC, Yang YL, et al. MicroRNA-29a protects against acute liver injury in a mouse model of obstructive jaundice via inhibition of the extrinsic apoptosis pathway. *Apoptosis*. 2014; 19: 30-41.
- Huang YH, Yu-Hsieh H, Huang CC, Shin-Mu VT, Tai MH, Chen CL, et al. Liver hepcidin and stainable iron expression in biliary atresia. *Pediatr Res*. 2006; 59: 662-6.
- Huang YH, Shih HH, Tiao MM, Huang CC, Kuo KC, Huang FC, et al. Toll-like receptor 7 agonist induces hypoplasia of the biliary system in a neonatal mouse model. *J Microbiol Immunol Infect*. 2018; 51: 166-73.
- Huang YH, Yang YL, Huang FC, Tiao MM, Lin YC, Tsai MH, et al. MicroRNA-29a mitigation of endoplasmic reticulum and autophagy aberrance counteracts in obstructive jaundice-induced fibrosis in mice. *Exp Biol Med* (Maywood). 2018; 243: 13-21.
- Huang YH, Yang YL, Wang FS. The Role of miR-29a in the Regulation, Function, and Signaling of Liver Fibrosis. *International journal of molecular sciences*. 2018; 19.
- Vallejo D, Crespo I, San-Miguel B, Alvarez M, Prieto J, Tunon MJ, et al. Autophagic response in the Rabbit Hemorrhagic Disease, an animal model of virally-induced fulminant hepatic failure. *Veterinary research*. 2014; 45: 15.
- Sano R, Reed JC. ER stress-induced cell death mechanisms. *Biochim Biophys Acta*. 2013; 1833: 3460-70.
- Iredale JP. Models of liver fibrosis: exploring the dynamic nature of inflammation and repair in a solid organ. *The Journal of clinical investigation*. 2007; 117: 539-48.
- Zhao H, Wang Z, Tang F, Zhao Y, Feng D, Li Y, et al. Carnosol-mediated Sirtuin 1 activation inhibits Enhancer of Zeste Homolog 2 to attenuate liver fibrosis. *Pharmacological research : the official journal of the Italian Pharmacological Society*. 2018; 128: 327-37.
- Li M, Hong W, Hao C, Li L, Wu D, Shen A, et al. SIRT1 antagonizes liver fibrosis by blocking hepatic stellate cell activation in mice. *FASEB journal* :

- official publication of the Federation of American Societies for Experimental Biology. 2018; 32: 500-11.
21. Wu X, Liu D, Tao D, Xiang W, Xiao X, Wang M, et al. BRD4 Regulates EZH2 Transcription through Upregulation of C-MYC and Represents a Novel Therapeutic Target in Bladder Cancer. *Mol Cancer Ther.* 2016; 15: 1029-42.
  22. Cai X, Li Z, Zhang Q, Qu Y, Xu M, Wan X, et al. CXCL6-EGFR-induced Kupffer cells secrete TGF-beta1 promoting hepatic stellate cell activation via the SMAD2/BRD4/C-MYC/EZH2 pathway in liver fibrosis. *J Cell Mol Med.* 2018; 22: 5050-61.
  23. Herranz N, Pasini D, Diaz VM, Franci C, Gutierrez A, Dave N, et al. Polycomb complex 2 is required for E-cadherin repression by the Snail1 transcription factor. *Mol Cell Biol.* 2008; 28: 4772-81.
  24. Friedman SL, Roll FJ, Boyles J, Bissell DM. Hepatic lipocytes: the principal collagen-producing cells of normal rat liver. *Proc Natl Acad Sci U S A.* 1985; 82: 8681-5.
  25. Chou MH, Huang YH, Lin TM, Du YY, Tsai PC, Hsieh CS, et al. Selective activation of Toll-like receptor 7 in activated hepatic stellate cells may modulate their profibrogenic phenotype. *Biochem J.* 2012; 447: 25-34.
  26. Kwiecinski M, Noetel A, Elfimova N, Trebicka J, Schievenbusch S, Strack I, et al. Hepatocyte growth factor (HGF) inhibits collagen I and IV synthesis in hepatic stellate cells by miRNA-29 induction. *PLoS One.* 2011; 6: e24568.
  27. Chung YH, Huang YH, Chu TH, Chen CL, Lin PR, Huang SC, et al. BMP-2 restoration aids in recovery from liver fibrosis by attenuating TGF-beta1 signaling. *Lab Invest.* 2018.
  28. Wang H, Bloom O, Zhang M, Vishnubhakat JM, Ombrellino M, Che J, et al. HMG-1 as a late mediator of endotoxin lethality in mice. *Science.* 1999; 285: 248-51.
  29. Bao Y, Wu X, Chen J, Hu X, Zeng F, Cheng J, et al. Brd4 modulates the innate immune response through Mnk2-eIF4E pathway-dependent translational control of IkappaBalpha. *Proc Natl Acad Sci U S A.* 2017; 114: E3993-E4001.
  30. Lin YC, Wang FS, Yang YL, Chuang YT, Huang YH. MicroRNA-29a mitigation of toll-like receptor 2 and 4 signaling and alleviation of obstructive jaundice-induced fibrosis in mice. *Biochem Biophys Res Commun.* 2018; 496: 880-6.
  31. Sun Y, Huang J, Song K. BET protein inhibition mitigates acute myocardial infarction damage in rats via the TLR4/TRAF6/NF-kappaB pathway. *Exp Ther Med.* 2015; 10: 2319-24.
  32. Ding N, Hah N, Yu RT, Sherman MH, Benner C, Leblanc M, et al. BRD4 is a novel therapeutic target for liver fibrosis. *Proc Natl Acad Sci U S A.* 2015; 112: 15713-8.
  33. Liu CA, Chang CY, Hsueh KW, Su HL, Chiou TW, Lin SZ, et al. Migration/Invasion of Malignant Gliomas and Implications for Therapeutic Treatment. *International journal of molecular sciences.* 2018; 19.
  34. Zhang Q, Dong P, Liu X, Sakuragi N, Guo SW. Enhancer of Zeste homolog 2 (EZH2) induces epithelial-mesenchymal transition in endometriosis. *Scientific reports.* 2017; 7: 6804.
  35. Zhang J, Tian XJ, Xing J. Signal Transduction Pathways of EMT Induced by TGF-beta, SHH, and WNT and Their Crosstalks. *J Clin Med.* 2016; 5.
  36. Scarpa M, Grillo AR, Brun P, Macchi V, Stefani A, Signori S, et al. Snail1 transcription factor is a critical mediator of hepatic stellate cell activation following hepatic injury. *Am J Physiol Gastrointest Liver Physiol.* 2011; 300: G316-26.
  37. Oh JY, Choi GE, Lee HJ, Jung YH, Ko SH, Chae CW, et al. High Glucose-Induced Reactive Oxygen Species Stimulates Human Mesenchymal Stem Cell Migration Through Snail and EZH2-Dependent E-Cadherin Repression. *Cellular physiology and biochemistry : international journal of experimental cellular physiology, biochemistry, and pharmacology.* 2018; 46: 1749-67.
  38. Yang MD, Chiang YM, Higashiyama R, Asahina K, Mann DA, Mann J, et al. Rosmarinic acid and baicalin epigenetically derepress peroxisomal proliferator-activated receptor gamma in hepatic stellate cells for their antifibrotic effect. *Hepatology.* 2012; 55: 1271-81.





## Protective mechanisms of resveratrol derivatives against TNF- $\alpha$ -induced inflammatory responses in rat mesangial cells

I-Ta Lee<sup>a</sup>, Chwan-Fwu Lin<sup>b,c,d</sup>, Yu-Ling Huang<sup>b,e</sup>, Kowit-Yu Chong<sup>f,g</sup>, Ming-Fa Hsieh<sup>h</sup>, Tse-Hung Huang<sup>i,j</sup>, Ching-Yi Cheng<sup>d,i,j,k,\*</sup>

<sup>a</sup> Department of Medical Research, Taichung Veterans General Hospital, Taichung, Taiwan

<sup>b</sup> Department of Cosmetic Science, Chang Gung University of Science and Technology, Taoyuan, Taiwan

<sup>c</sup> Department of Anesthesiology, Chang Gung Memorial Hospital at Linkou, Taoyuan, Taiwan

<sup>d</sup> Research Center for Food and Cosmetic Safety, and Research Center for Chinese Herbal Medicine, College of Human Ecology, Chang Gung University of Science and Technology, Taoyuan, Taiwan

<sup>e</sup> National Research Institute of Chinese Medicine, Taipei, Taiwan

<sup>f</sup> Department of Medical Biotechnology and Laboratory Science, College of Medicine, Chang Gung University, Taoyuan, Taiwan

<sup>g</sup> Department of Thoracic Medicine, Chang Gung Memorial Hospital at Linkou, Taoyuan, Taiwan

<sup>h</sup> Department of Biomedical Engineering, Chung Yuan Christian University, Taoyuan, Taiwan

<sup>i</sup> Department of Traditional Chinese Medicine, Chang Gung Memorial Hospital, Keelung, Taiwan

<sup>j</sup> Graduate Institute of Health Industry Technology, Chang Gung University of Science and Technology, Taoyuan, Taiwan

<sup>k</sup> Department of Ophthalmology, Chang Gung Memorial Hospital at Linkou, Taoyuan, Taiwan

### ARTICLE INFO

#### Keywords:

Mesangial cells  
Resveratrol derivatives  
Inflammation  
Cyclooxygenase 2  
Cytokine

### ABSTRACT

**Introduction:** Resveratrol has been reported to alleviate inflammatory responses and oxidative stress in mesangial cells and in several types of renal injury in animal models. Previously, the active resveratrol derivatives from the roots of *Vitis thunbergii* Sieb. & Zucc. (Vitaceae) were shown to have significant anti-platelet and anti-oxidative activities. However, the anti-inflammatory mechanisms of these resveratrol derivatives in rat mesangial cells (RMCs) have not been clarified fully.

**Methods:** The protective mechanisms of resveratrol derivatives involved in tumor necrosis factor- $\alpha$  (TNF- $\alpha$ )-induced inflammatory responses were assessed by Western blot analysis, real-time PCR, and RT-PCR. The involvement of various signaling molecules in these responses was investigated using selective pharmacological inhibitors.

**Results:** Nontoxic concentrations of the resveratrol derivatives significantly attenuated cytosolic phospholipase A<sub>2</sub> (cPLA<sub>2</sub>) and cyclooxygenase 2 (COX-2) expression in RMCs challenged by TNF- $\alpha$ . These resveratrol derivatives inhibited TNF- $\alpha$ -activated ERK1/2 and JNK1/2 without affecting p38 phosphorylation. Next, we demonstrated that TNF- $\alpha$  induced NF- $\kappa$ B activation, translocation, and promoter activity, which was inhibited by pretreatment with resveratrol derivatives in RMCs.

**Conclusion:** The protective mechanisms of resveratrol derivatives against TNF- $\alpha$ -stimulated inflammatory responses via cPLA<sub>2</sub>/COX-2/PGE<sub>2</sub> inhibition was caused by the attenuation of the JNK1/2, ERK1/2, and NF- $\kappa$ B signaling pathways in RMCs.

### 1. Introduction

The tumor necrosis factor- $\alpha$  (TNF- $\alpha$ ) is a major proinflammatory cytokine in kidney pathogenesis that damages the glomerular permeability barrier with the development of albuminuria [1,2]. Blocking TNF- $\alpha$  activity with a recombinant TNF- $\alpha$ -binding protein reduced

neutrophil infiltration and ameliorated ischemic injury in kidneys [3]. As an extrinsic source or positive feedback loop, binding of TNF- $\alpha$  to its membrane receptors can reactivate signaling pathways and further augment TNF- $\alpha$  production and the expression of inflammatory mediators in renal resident cells [1]. Some studies have shown that TNF- $\alpha$  is implicated in inflammation by upregulating inflammatory genes such

**Abbreviations:** COX, cyclooxygenase; cPLA<sub>2</sub>, cytosolic phospholipase A<sub>2</sub>; PGE<sub>2</sub>, prostaglandin E<sub>2</sub>; RMCs, rat mesangial cells; TNF- $\alpha$ , Tumor necrosis factor  $\alpha$

\* Corresponding author at: Graduate Institute of Health Industry Technology, Research Center for Chinese Herbal Medicine and Research Center for Food and Cosmetic Safety, Chang Gung University of Science and Technology, No. 261, Wenhua 1st Rd., Guishan Dist., Taoyuan City 33303, Taiwan.

E-mail address: [Jennycheng@mail.cgu.edu.tw](mailto:Jennycheng@mail.cgu.edu.tw) (C.-Y. Cheng).

<https://doi.org/10.1016/j.cyto.2018.10.008>

Received 2 April 2018; Received in revised form 18 August 2018; Accepted 8 October 2018

1043-4666/ © 2018 Elsevier Ltd. All rights reserved.

as cyclooxygenase 2 (COX-2) and cytosolic phospholipase A<sub>2</sub> (cPLA<sub>2</sub>) [4]. In addition, prostaglandin E<sub>2</sub> (PGE<sub>2</sub>), which is one of the most abundant metabolites of arachidonic acid (AA), is generated through an enzymatic cascade controlled by COX enzymes and is a principal mediator of inflammation in diseases [4]. Therefore, cPLA<sub>2</sub> and COX-2 may play a crucial role in the development of a variety of renal inflammatory diseases. However, the molecular mechanisms underlying TNF- $\alpha$  stimulation of cPLA<sub>2</sub> and COX-2 in renal mesangial cells remain largely unknown.

Mitogen-activated protein kinases (MAPKs) are a type of serine/threonine protein kinases. They are phosphorylated by many stimuli, such as cytokines and growth factors [5]. It was found that inflammation elicited by various external stimuli activates NF- $\kappa$ B, which regulates the expression of many inflammatory-related genes, such as cPLA<sub>2</sub> and COX-2. NF- $\kappa$ B activity is regulated by several pathways, including the activation of various MAPKs [4]. Thus, we explored the roles of NF- $\kappa$ B and MAPKs in cPLA<sub>2</sub> and COX-2 induction in rat mesangial cells (RMCs) challenged with TNF- $\alpha$ .

Resveratrol has been reported to ameliorate the increase in vasoconstrictors and intracellular calcium in mesangial cells and in several types of renal injury in animal models, including diabetic nephropathy and hyperuricemia [6]. Recently, many reports have described resveratrol derivatives that are more effective than resveratrol itself and inhibit tumor cell proliferation and inflammation [7,8]. Previously, active resveratrol derivatives, such as ampelopsin C (AC) and ampelopsin F (AF) from the roots of *Vitis thunbergii* Sieb. & Zucc. (Vitaceae), were shown to have significant anti-platelet and anti-oxidative activities [9,10]. Moreover, both AC and AF are stilbene oligomers; AC is a trimer form of resveratrol, whereas AF is a dimer form of resveratrol [8]. Polydatin (PD) is the glycoside form of resveratrol [11]. Accumulating evidence indicates that resveratrol derivatives may attenuate inflammatory signaling pathways [7,12,13]. PD has been shown to possess strong anti-oxidative bioactivity [14] and to alleviate experimental-diabetes-induced extracellular matrix accumulation through anti-inflammatory mechanisms in rat glomerular mesangial cells [15]. The nephroprotective effects of PD were attributed to its anti-inflammatory cascade, including the inhibition of the expression of the NF- $\kappa$ B (p65), COX-2, and inducible nitric oxide synthase (iNOS) proteins and the production of TNF- $\alpha$ , PGE<sub>2</sub>, and IL-1 $\beta$  [16]. Qi et al. reported that ampelopsin has anti-inflammatory effects via the inhibition of the Phosphoinositide 3-kinase, Protein kinase B, and NF- $\kappa$ B signaling cascades in RAW264.7 murine macrophage-like cells [17]. Ampelopsin can inhibit LPS-induced inflammatory responses via the NF- $\kappa$ B and JAK2/STAT3 signaling pathways in microglial cells [18]. However, the anti-inflammatory mechanisms of ampelopsin in renal diseases *in vivo* or *in vitro* have not been reported.

Therefore, we investigated whether resveratrol derivatives inhibit TNF- $\alpha$ -induced cPLA<sub>2</sub> and COX-2 expression and elucidated the underlying mechanisms. Currently, our laboratory uses RMCs as an *in vitro* cell culture model to examine the effects of AC, AF, and PD on TNF- $\alpha$ -induced inflammatory responses. Here, we established for the first time in RMCs that resveratrol derivatives reduced cPLA<sub>2</sub>/COX-2 expression and PGE<sub>2</sub> production via the JNK1/2, ERK1/2, and NF- $\kappa$ B signaling pathways in response to TNF- $\alpha$ .

## 2. Materials and methods

### 2.1. Plant materials

The roots of *V. thunbergii* were purchased in Taipei and identified by Mr. Jun-Chih Ou, a taxonomist previously with the National Research Institute of Chinese Medicine. The specimen (NRICM-05-018) is preserved at the National Research Institute of Chinese Medicine, Republic of China. AC and AF were isolated from the EtOH extracts of *V. thunbergii*, as described previously [10], and the purities of AC and AF were determined to be greater than 97% by high-performance liquid

chromatography analysis. Their structures were determined by spectroscopic analyses and by comparison with those available in the literature [10]. PD was from Sigma-Aldrich (St. Louis, MO, USA). AC, AF, or PD was dissolved in dimethylsulfoxide (DMSO) and then further diluted with the assay medium (2, 5, 10  $\mu$ g/ml). Solvent controls with DMSO were used in each assay.

### 2.2. Materials

The anti-phospho-c-Jun, anti-phospho-p65, anti-phospho-ERK1/2, anti-phospho-p38, anti-phospho-JNK1/2, anti-COX-2, and anti-cPLA<sub>2</sub> antibodies were from Cell Signaling Technology (Danvers, MA, USA). The anti-p65 and anti-lamin B antibodies were from Santa Cruz Biotechnology (Santa Cruz, CA, USA). AACOCF<sub>3</sub>, Bay 11-7082, SP600125, SB202190, and U0126 were from Enzo Life Sciences (Farmingdale, NY, USA). Human recombinant TNF- $\alpha$  was from R&D Systems (Minneapolis, MN, USA). The anti-GAPDH antibody, enzymes, and other chemicals were from Sigma-Aldrich.

### 2.3. Cell culture

The rat mesangial cell line was bought from the American Type Culture Collection (ATCC; Rockville, MD, USA) and used according to the instructions provided. In experiments, cells were cultured with resveratrol derivatives or inhibitors of kinases for 1 h prior to TNF- $\alpha$  treatment in a 5% CO<sub>2</sub>-humidified incubator at 37 °C.

### 2.4. 3-(4,5-dimethylthiazol-2-yl)-2,5-diphenyltetrazolium bromide (MTT) assay

RMCs (2.5  $\times$  10<sup>5</sup> cells per well) were incubated at 37 °C with varying concentrations of AC, AF, and PD, followed by the addition of the MTT solution (0.25 mg/ml) for 30 min. After incubation, the DMSO solution was added to dissolve the formazan crystals, and the supernatants were surveyed at A540 nm on a microplate reader (SpectraMax 250, Molecular Device, CA, USA). The results were determined by comparing the optical density of the drug-treated group with that of the vehicle-treated group (1% DMSO).

### 2.5. Isolation of cell fractions

After treatment, cells were harvested, sonicated, and centrifuged and the cytoplasmic and nuclear proteins separated, as per the workflow steps described previously [19]. The translocation of NF- $\kappa$ B (p65) from the cytoplasm into the nucleus was analyzed by Western blotting.

### 2.6. Immunofluorescence staining

Growth-arrested RMCs were stimulated with TNF- $\alpha$  at different time points. In addition, cells were treated with inhibitors of kinases for 1 h prior to TNF- $\alpha$  treatment. After treatment, cells were washed with phosphate buffered saline, fixed with 4% paraformaldehyde, permeabilized with 0.1% Triton X-100, blocked with blocking buffer (Visual Protein Biotech Corporation, Taipei, Taiwan), and stained with an anti-NF- $\kappa$ B (p65) antibody, as per the workflow steps described previously [19]. The distribution of NF- $\kappa$ B (p65) movement and the nucleus were observed using a fluorescence microscope (DFC310 FX; Leica, Wetzlar, Germany).

### 2.7. Western blotting

After the treatment of cells with drugs and TNF- $\alpha$ , cell lysates were collected and the protein concentrations were adjusted, as described previously [19]. Briefly, samples were separated on sodium dodecyl sulphate-polyacrylamide gels and transferred to polyvinylidene fluoride (PVDF) membranes (Millipore, Bedford, MA, USA), which were

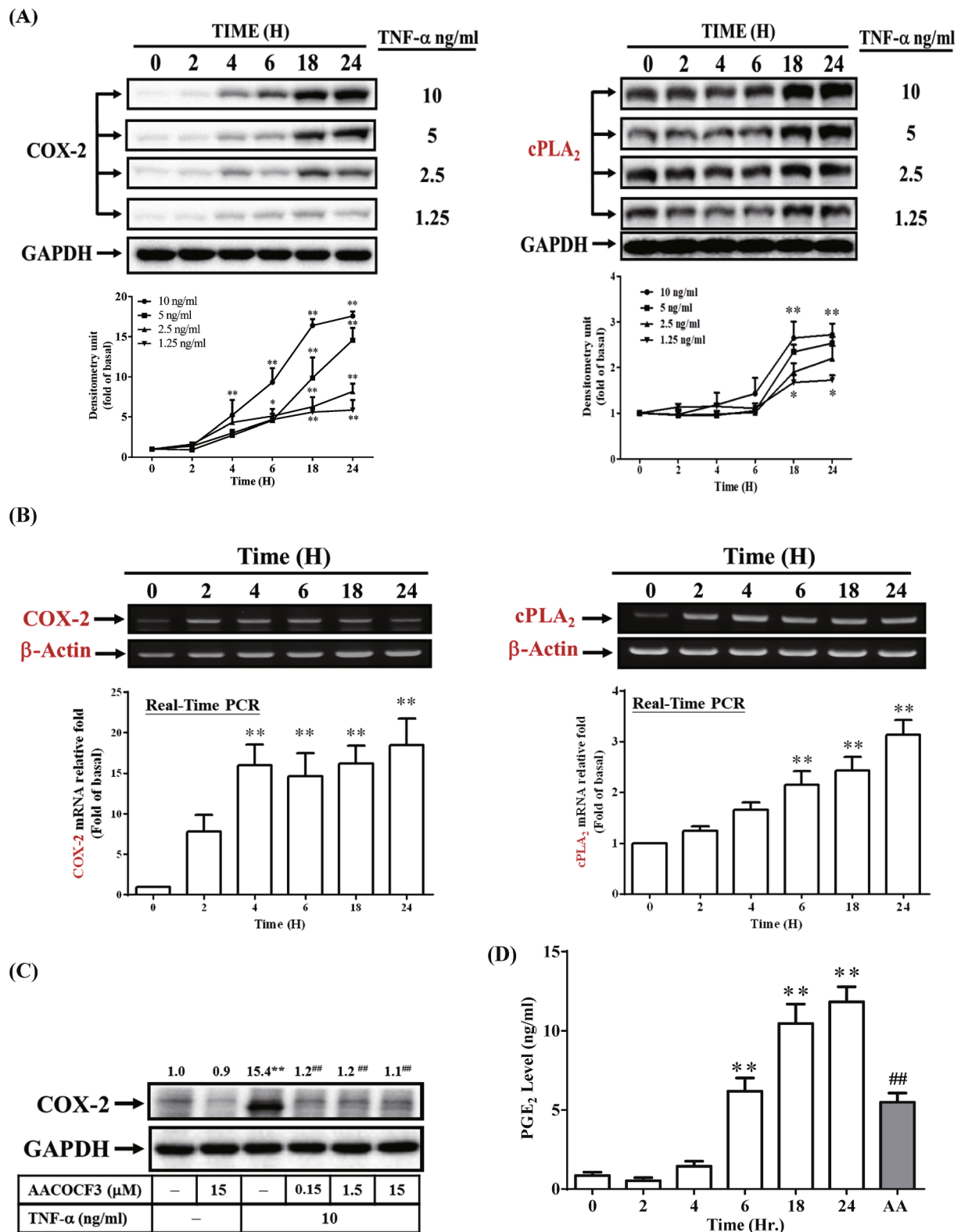


**Fig. 1.** Time and concentration dependence of TNF- $\alpha$ -stimulated COX-2 and cPLA<sub>2</sub> expression in RMCs. Cells were incubated with different concentrations of TNF- $\alpha$  (10, 5, 2.5, or 1.25 ng/ml) for various times. The expression of the COX-2 and cPLA<sub>2</sub> proteins was determined by Western blotting (A). The mRNA levels of COX-2 and cPLA<sub>2</sub> were determined by RT-PCR and real-time PCR (B). (C) Cells were pretreated with AACOCF3 for 1 h and then incubated with TNF- $\alpha$  (10 ng/ml) for 24 h. The expression of the COX-2 protein was determined by Western blotting. (D) Cells were treated with TNF- $\alpha$  (10 ng/ml) for the indicated times or pretreated with AACOCF3 for 1 h, followed by incubation with TNF- $\alpha$  (10 ng/ml) for 24 h. The media were collected and analyzed for PGE<sub>2</sub> release. Data are expressed as the mean  $\pm$  S.E.M. of three independent experiments. \* $P$  < 0.05; \*\* $P$  < 0.01 compared with cells exposed to the vehicle. ### $P$  < 0.01 compared with cells exposed to TNF- $\alpha$  alone.

then blocked and incubated with primary and secondary antibodies. Between this two-step process, membranes were washed with Tris buffered saline with Tween-20 solution. Immunofluorescent signals were developed using the LumiFlash Ultima chemiluminescent substrate HRP system (Visual Protein Biotech Corporation). The levels of specific proteins were quantified using Image Lab™ 5.0 Software (Bio-Rad Laboratories, Inc., Hercules, CA, USA) and normalized to GAPDH levels (which was used as a control).

## 2.8. RT-PCR and real-time PCR

Total RNA was extracted with TRIzol reagent (Invitrogen, CA, USA) and used as a template for cDNA synthesis. RNA concentration and purity were determined spectrophotometrically. The expression of

inflammatory genes was measured using RT-PCR and real-time PCR system kits (Bio-Rad Laboratories). The PCR conditions were as follows: one cycle of initial denaturation at 94 °C for 5 min; 35 cycles of denaturation at 94 °C for 1 min, primer annealing at 58 °C for 1 min, and extension at 72 °C for 2 min; and one cycle of final extension at 72 °C for 12 min. The expression of  $\beta$ -actin was used as an internal control for the assay of a constitutively expressed gene. The primers used for RT-PCR were as follows: 5'-GAACCTAAGGCAACCGTG-3' (forward) and 5'-TGGCATAGAGGTCTTTACGG-3' (reverse) for  $\beta$ -actin; 5'-TGTTCAACA GAGTTTGG-3' (forward) and 5'-AACAGAGCAACGAGATGG-3' (reverse) for cPLA<sub>2</sub>; and 5'-CTGTATCCCGCCGCTGTGGTG-3' (forward) and 5'-ACTTGCCTGATGGTGGCTGTCT-3' (reverse) for COX-2. Real-time PCR was performed using the CFX Connect Real-time PCR Detection System (Bio-Rad Laboratories). Standard thermal conditions

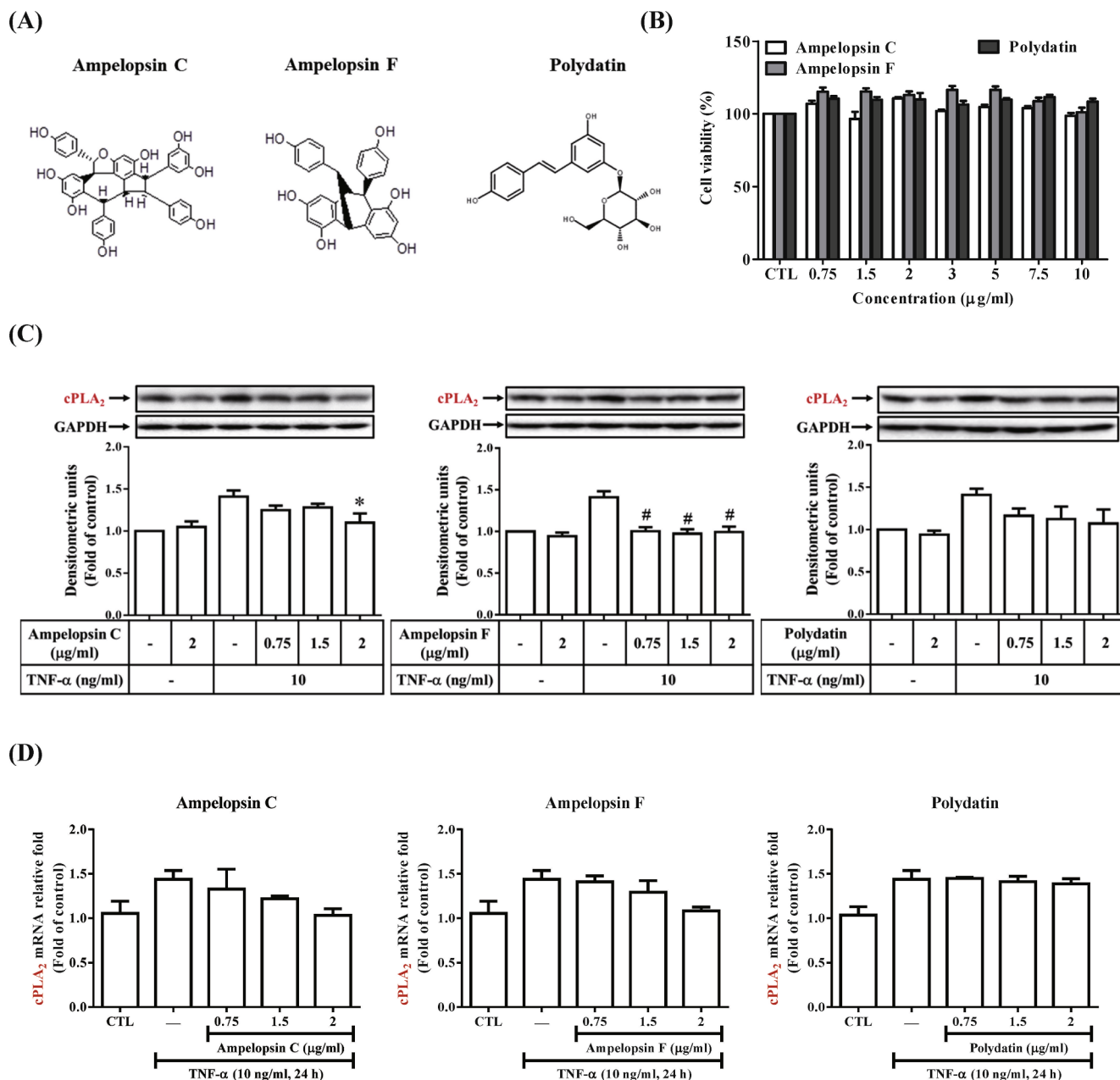


**Fig. 2.** Effects of AC, AF, and PD on TNF- $\alpha$ -induced cPLA<sub>2</sub> expression in RMCs. (A) Chemical structure of AC, AF, and PD. (B) Cells were treated with various concentrations of AC, AF, or PD for 24 h. Cell viability was assayed using the MTT assay. (C) Cells were pretreated with AC, AF, or PD for 1 h, and then exposed to TNF- $\alpha$  (10 ng/ml) for 24 h. The expression of the cPLA<sub>2</sub> protein was determined by Western blotting. (D) Cells were pretreated with AC, AF, or PD for 1 h, and then incubated with TNF- $\alpha$  for 6 h. The mRNA levels of cPLA<sub>2</sub> were analyzed by real-time PCR. Data are expressed as the mean  $\pm$  S.E.M. of three independent experiments. \* $P$  < 0.05; # $P$  < 0.01 compared with cells exposed to TNF- $\alpha$  alone.



(3 min at 95 °C, 40 cycles of 10 s at 95 °C and 30 s at 58 °C) were used. Relative gene expression was determined by the  $2^{-\Delta\Delta C_t}$  method, where  $C_t$  is the threshold cycle. Gene expression was normalized relative to unstimulated cells and fold variation was normalized to  $\beta$ -actin (an endogenous control). The primers used for real-time PCR were as follows: 5'-CGTGAAAAGATGACCCAGATCA-3' (forward) and 5'-CTCCG GAGTCCATCACAATG-3' (reverse) for  $\beta$ -actin; 5'-ACATTCAGGCAGCA GAGGA-3' (forward) and 5'-CCACCACAGGCACATCAC-3' (reverse) for cPLA<sub>2</sub>; and 5'-CAAGAATCAAATTACCGCTGAAG-3' (forward) and 5'-CGAAGGAAGGAATGTTGTT-3' (reverse) for COX-2.

## 2.9. Measurement of NF- $\kappa$ B-luciferase activity

Cells were transiently transfected with an NF- $\kappa$ B-luciferase reporter plasmid using the Gene Pulser Xcell Electroporation System (Bio-Rad

Laboratories). Cells ( $1.0 \times 10^6$  cells/ml) were washed, suspended in Opti-MEM medium, and placed into a 2 mm electroporation cuvette (Bio-Rad Laboratories). A reporter gene (10  $\mu$ g) was added into the cuvette containing the cells, which was subjected to a high-voltage electrical pulse at 260 V, 950  $\mu$ F,  $\infty \Omega$ , exponential decay pulse. After electroporation, cell suspensions were immediately transferred to 10% FBS growth medium (without antibiotics) and incubated for 24 h. The luciferase assay was performed after the electroporation. The medium was changed to fresh 10% FBS growth medium (without antibiotics) before RMCs were treated with or without resveratrol derivatives (10  $\mu$ g/ml) for 1 h prior to TNF- $\alpha$  treatment. NF- $\kappa$ B-luc activity was analyzed using a luciferase assay system (Promega, Madison, WI, USA) and read using a SpectraMax i3x microplate reader. The luciferase activity was normalized to the  $\beta$ -galactosidase activity.

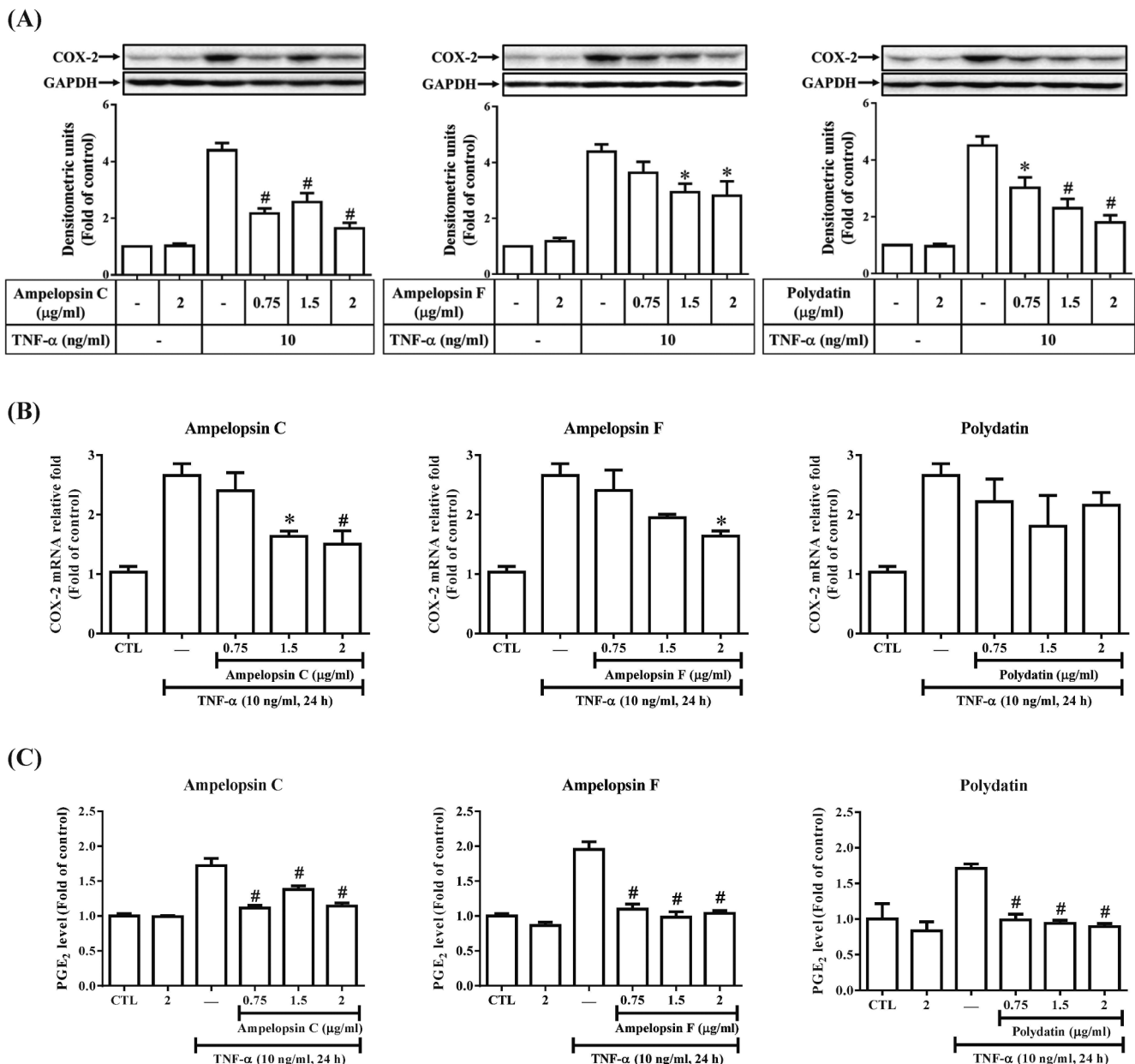


**Fig. 3.** Effects of AC, AF, and PD on TNF- $\alpha$ -induced COX-2 expression and PGE<sub>2</sub> production in RMCs. (A) Cells were pretreated with AC, AF, or PD for 1 h, and then exposed to TNF- $\alpha$  (10 ng/ml) for 24 h. The expression of the COX-2 protein was determined by Western blotting. (B) Cells were pretreated with AC, AF, or PD for 1 h, and then incubated with TNF- $\alpha$  for 6 h. The mRNA levels of COX-2 were analyzed by real-time PCR. (C) Cells were pretreated with AC, AF, or PD for 1 h, and then exposed to TNF- $\alpha$  (10 ng/ml) for 24 h. The media were collected and analyzed for PGE<sub>2</sub> release. Data are expressed as the mean  $\pm$  S.E.M. of three independent experiments.  $^{\#}P < 0.01$  compared with cells exposed to TNF- $\alpha$  alone.

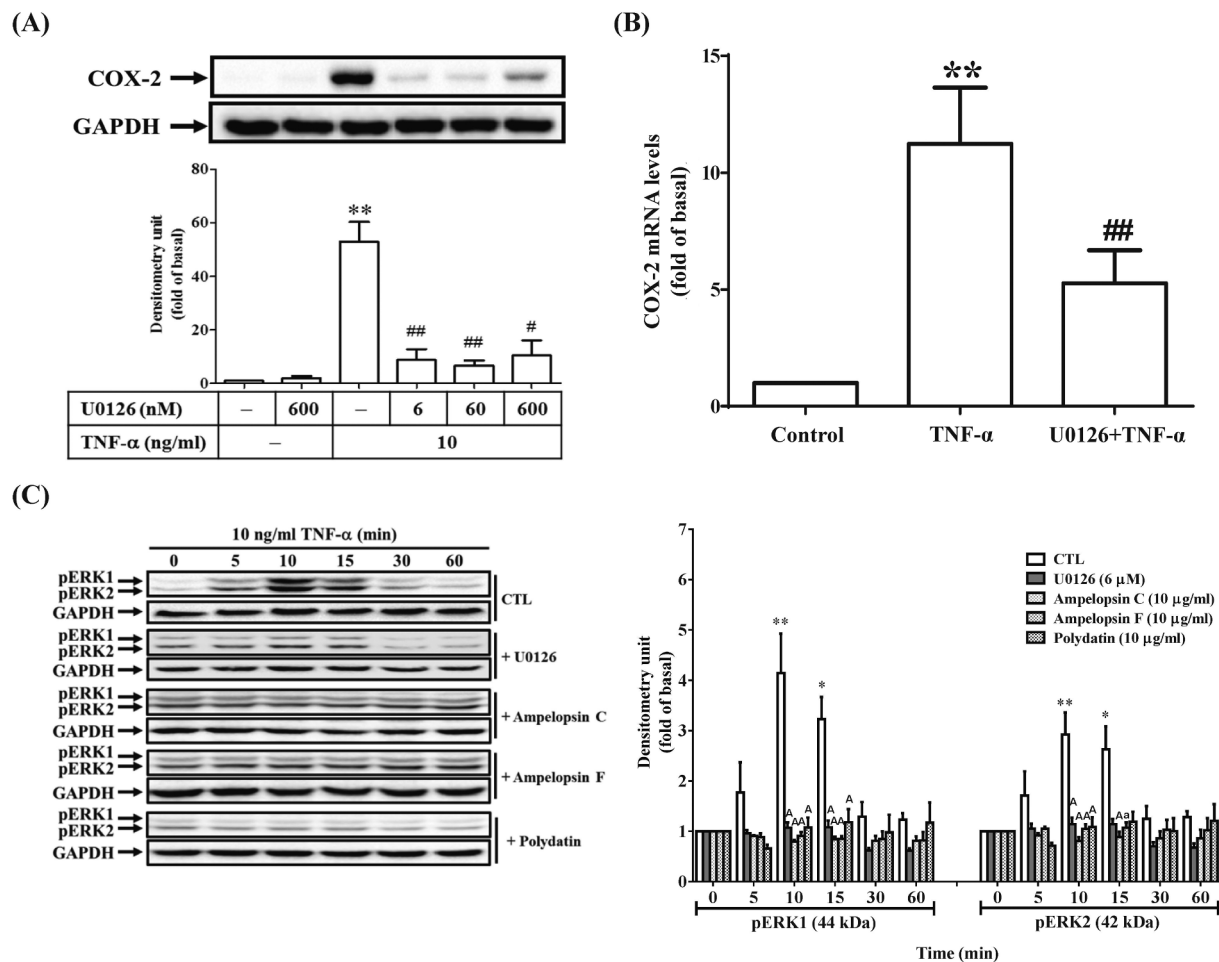


**Fig. 4.** AC, AF, and PD inhibit TNF- $\alpha$ -induced COX-2 expression via the inhibition of ERK1/2 activation in RMCs. (A) RMCs were pretreated with U0126 (6, 60, or 600 nM) for 1 h, and then incubated with TNF- $\alpha$  for 24 h. The expression of the COX-2 protein was determined by Western blotting. (B) Cells were pretreated with U0126 for 1 h, and then incubated with TNF- $\alpha$  for 6 h. The mRNA levels of COX-2 were analyzed by real-time PCR. (C) Cells were pretreated with or without U0126 (600 nM), AC (10  $\mu$ g/ml), AF (10  $\mu$ g/ml), or PD (10  $\mu$ g/ml) for 1 h, and then treated with TNF- $\alpha$  for the indicated time. The expression of phospho-ERK1/2 was determined by Western blotting. Data are expressed as the mean  $\pm$  S.E.M. of three independent experiments. \* $P$  < 0.05; \*\* $P$  < 0.01 compared with the cells exposed to the vehicle. # $P$  < 0.05; ## $P$  < 0.01 compared with cells exposed to TNF- $\alpha$  alone for 24 h.  $^aP$  < 0.05;  $^AP$  < 0.01 compared with the cells exposed to TNF- $\alpha$  alone for 10 or 15 min.

## 2.10. Determination of PGE<sub>2</sub> release

Confluent RMCs were treated with or without resveratrol derivatives for 1 h, followed by incubation with TNF- $\alpha$  for 24 h. The supernatants were then collected for PGE<sub>2</sub> production analysis. The expression of PGE<sub>2</sub> was measured using a PGE<sub>2</sub> ELISA kit (Enzo Life Sciences) according to the manufacturer's instructions.

## 2.11. Statistical analysis

Results were statistically analyzed using GraphPad Prism 6 Software (GraphPad Software, Inc., CA, USA). Quantitative data were analyzed by two-way ANOVA followed by Bonferroni's honestly significant difference between individual groups. Data are presented as the mean  $\pm$  S.E.M. of at least three independent experiments.  $P$  < 0.05 was considered statistically significant.

## 3. Results

### 3.1. TNF- $\alpha$ induced proinflammatory cytokine expression in RMCs

The literature shows that TNF- $\alpha$  is implicated in the pathogenesis of

kidney injury and glomerular permeability barrier damage by upregulating proinflammatory cytokines [1,2]. To determine the effects of TNF- $\alpha$ , RMCs were challenged with different concentrations of this molecule. As shown in Fig. 1A, TNF- $\alpha$  induced COX-2 and cPLA<sub>2</sub> expression in time- and concentration-dependent manners. In addition, cells were treated with TNF- $\alpha$  (10 ng/ml) for the indicated time intervals, and the mRNA expression of COX-2 and cPLA<sub>2</sub> was determined by RT-PCR and real-time PCR. As shown in Fig. 1B, TNF- $\alpha$  markedly enhanced COX-2 and cPLA<sub>2</sub> mRNA expression in a time-dependent manner in RMCs. PGE<sub>2</sub>, which is one of the most abundant metabolites of AA, is generated through an enzymatic cascade controlled by COX enzymes and is a principal mediator of inflammation in diseases [4]. Thus, we further assessed whether TNF- $\alpha$  induces PGE<sub>2</sub> generation mediated by cPLA<sub>2</sub> and COX-2 upregulation. As shown in Fig. 1C, pretreatment with an inhibitor of cPLA<sub>2</sub> (AACOCF3) [20] significantly attenuated COX-2 expression in RMCs in response to TNF- $\alpha$ . In addition, TNF- $\alpha$  markedly induced PGE<sub>2</sub> release in a time-dependent manner (Fig. 1D). However, pretreatment with AACOCF3 also significantly attenuated TNF- $\alpha$ -induced PGE<sub>2</sub> production (Fig. 1D). These results suggest that TNF- $\alpha$  enhances PGE<sub>2</sub> generation via cPLA<sub>2</sub>/COX-2 upregulation in RMCs.

### 3.2. Inhibitory effects of resveratrol derivatives on TNF- $\alpha$ -induced cPLA<sub>2</sub>/COX-2 expression and PGE<sub>2</sub> release in RMCs

Fig. 2A shows the chemical structures of resveratrol derivatives (AC, AF, and PD). Here, we examined the effects of AC, AF, and PD on the viability of RMCs using an MTT assay. As shown in Fig. 2B, AC, AF, and PD (0.75–10  $\mu$ g/ml) had no effects on the viability of RMCs. Therefore, we used AC, AF, and PD at a concentration < 10  $\mu$ g/ml in this study and evaluated their potential anti-inflammatory and pharmacological properties in TNF- $\alpha$ -stimulated RMCs. Next, we investigated the effects of resveratrol derivatives on TNF- $\alpha$ -induced cPLA<sub>2</sub> expression. As shown in Fig. 2C, pretreatment with AC or AF at 2  $\mu$ g/ml significantly attenuated TNF- $\alpha$ -induced cPLA<sub>2</sub> protein expression, but did not affect cPLA<sub>2</sub> mRNA levels significantly (Fig. 2D). In addition, pretreatment with PD did not affect TNF- $\alpha$ -induced cPLA<sub>2</sub> expression. We further evaluated the effects of AC, AF, and PD on TNF- $\alpha$ -induced COX-2 expression and PGE<sub>2</sub> release in RMCs. Cells were pretreated with AC, AF, or PD for 1 h, and then incubated with TNF- $\alpha$  for 24 h. As shown in Fig. 3A, pretreatment with AC, AF, or PD significantly attenuated TNF- $\alpha$ -induced COX-2 expression in a concentration-dependent manner. In addition, both AC and AF at 2  $\mu$ g/ml significantly inhibited COX-2 mRNA levels (Fig. 3B). Finally, we demonstrated that TNF- $\alpha$ -induced PGE<sub>2</sub> release was reduced by pretreatment with AC, AF, or PD in RMCs (Fig. 3C), although increased concentrations (up to 2  $\mu$ g/ml) did not yield an increase in the inhibitory effect. Taken together, these results showed that resveratrol derivatives (AC, AF, and PD) have an inhibitory effect on TNF- $\alpha$ -induced cPLA<sub>2</sub>/COX-2 expression and PGE<sub>2</sub> production in RMCs.

### 3.3. Resveratrol derivatives inhibited TNF- $\alpha$ -induced COX-2 expression via the downregulation of ERK1/2 activation in RMCs

To investigate whether MAPKs are involved in TNF- $\alpha$ -induced COX-2 expression, cells were pretreated with an inhibitor of MEK1/2 (U0126) [21] for 1 h, and then incubated with TNF- $\alpha$  for 24 h. As shown in Fig. 4A, pretreatment with U0126 attenuated TNF- $\alpha$ -induced COX-2 expression in a concentration-dependent manner. In addition, TNF- $\alpha$ -induced COX-2 mRNA levels were also reduced by pretreatment with U0126 (Fig. 4B). We further showed that TNF- $\alpha$  markedly induced ERK1/2 activation in RMCs in a time-dependent manner (Fig. 4C). Finally, we investigated whether resveratrol derivatives (AC, AF, and PD) inhibited TNF- $\alpha$ -induced ERK1/2 activation. As shown in Fig. 4C, pretreatment with AC, AF, or PD significantly attenuated TNF- $\alpha$ -stimulated ERK1/2 phosphorylation. Taken together, these results indicate that, in RMCs, these resveratrol derivatives inhibited TNF- $\alpha$ -induced COX-2 expression via the downregulation of ERK1/2 activation.

### 3.4. Resveratrol derivatives inhibited TNF- $\alpha$ -induced COX-2 expression via a p38 MAPK-independent pathway

We determined whether p38 MAPK phosphorylation was required for TNF- $\alpha$ -induced COX-2 expression in RMCs. However, in this study, we found that pretreatment with SB202190 (a p38 MAPK inhibitor) [22] did not inhibit TNF- $\alpha$ -induced COX-2 mRNA accumulation (Fig. 5A). We further showed that TNF- $\alpha$  markedly induced p38 MAPK activation in RMCs in a time-dependent manner, which was reduced by pretreatment with SB202190 (Fig. 5B). Finally, we investigated

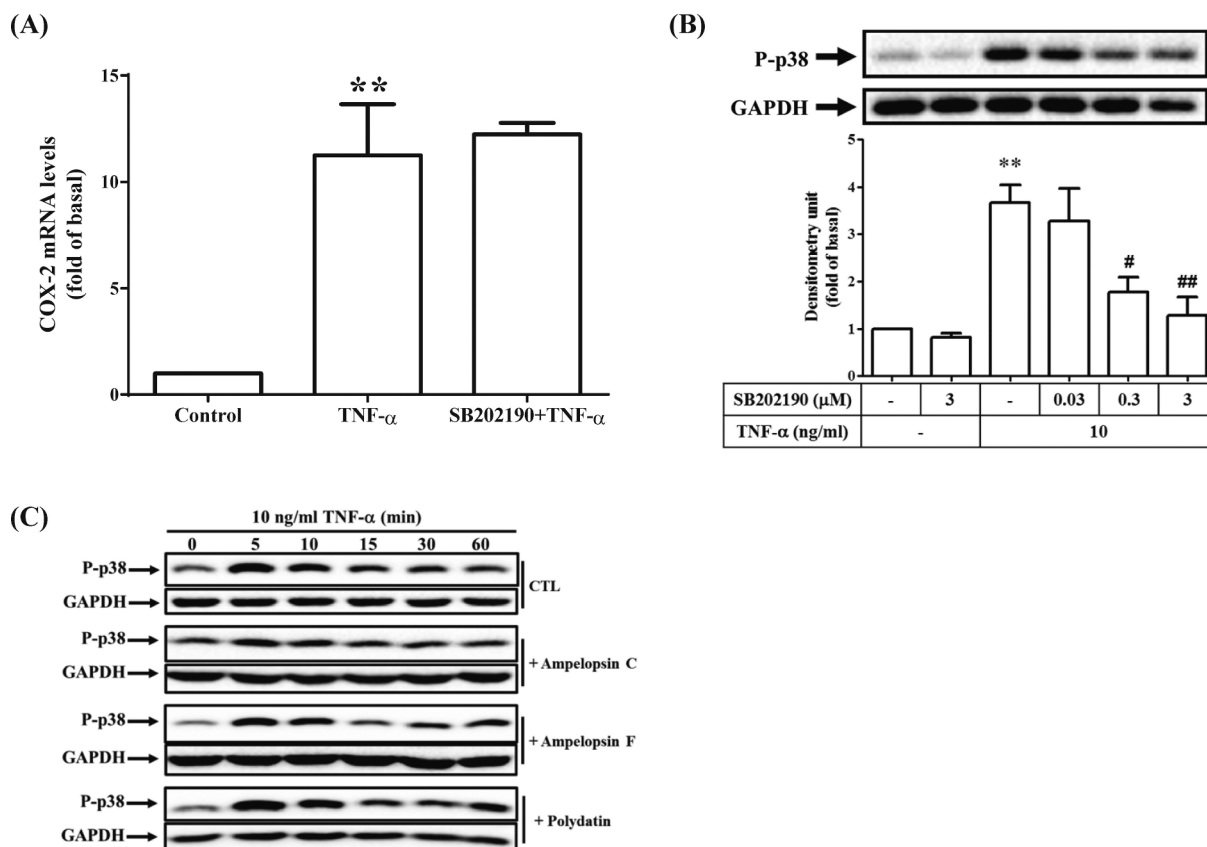


**Fig. 5.** AC, AF, and PD have no effects on TNF- $\alpha$ -induced p38 activation. (A) Cells were pretreated with SB202190 for 1 h, and then incubated with TNF- $\alpha$  for 6 h. The mRNA levels of COX-2 were analyzed by real-time PCR. (B) RMCs were pretreated with SB202190 (0.03, 0.3, or 3  $\mu$ M) for 1 h, and then incubated with TNF- $\alpha$  for 5 min. The expression of phospho-p38 MAPK was determined by Western blotting. (C) Cells were pretreated with or without AC (10  $\mu$ g/ml), AF (10  $\mu$ g/ml), or PD (10  $\mu$ g/ml) for 1 h, and then treated with TNF- $\alpha$  for the indicated time. The expression of phospho-p38 MAPK was determined by Western blotting. Data are expressed as the mean  $\pm$  S.E.M. of three independent experiments. \*\* $P$  < 0.01 compared with cells exposed to the vehicle. # $P$  < 0.05; ## $P$  < 0.01 compared with cells exposed to TNF- $\alpha$  alone for 5 min.

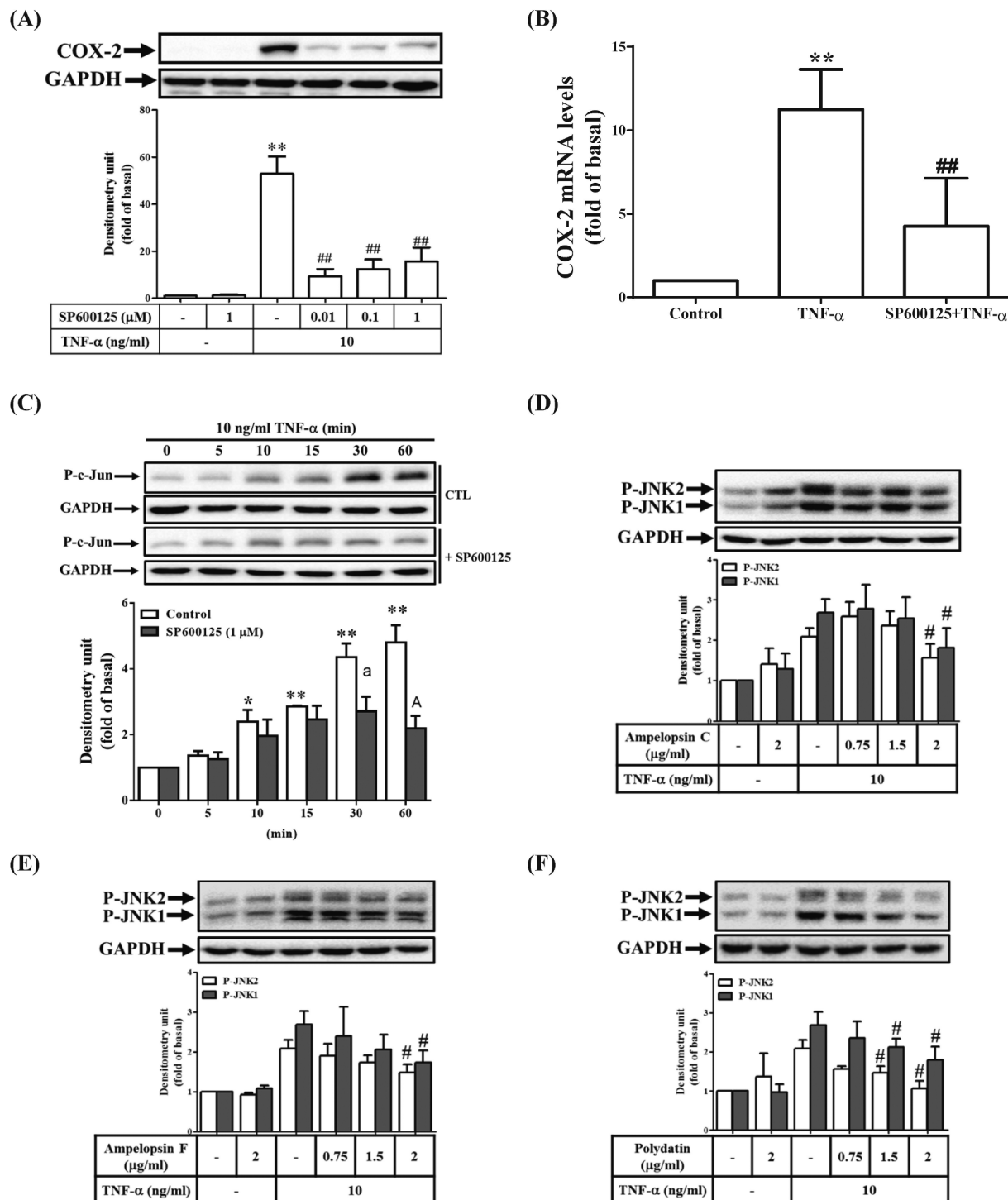


**Fig. 6.** AC, AF, and PD inhibit TNF- $\alpha$ -induced COX-2 expression via the reduction of JNK1/2 activation in RMCs. (A) RMCs were pretreated with SP600125 (0.01, 0.1, or 1  $\mu$ M) for 1 h, and then incubated with TNF- $\alpha$  for 24 h. The expression of the COX-2 protein was determined by Western blotting. (B) Cells were pretreated with SP600125 for 1 h, and then incubated with TNF- $\alpha$  for 6 h. The mRNA levels of COX-2 were analyzed by real-time PCR. (C) Cells were pretreated with or without SP600125 for 1 h, and then incubated with TNF- $\alpha$  for the indicated time. The expression of phospho-c-Jun was determined by Western blotting. (D–F) Cells were pretreated with AC, AF, or PD for 1 h, and then incubated with TNF- $\alpha$  for 15 min. The expression of phospho-JNK1/2 was determined by Western blotting. Data are expressed as the mean  $\pm$  S.E.M. of three independent experiments. \* $P$  < 0.05; \*\* $P$  < 0.01 compared with cells exposed to the vehicle. # $P$  < 0.05; ## $P$  < 0.01 compared with cells exposed to TNF- $\alpha$  alone. <sup>a</sup> $P$  < 0.05; <sup>A</sup> $P$  < 0.01 compared with cells exposed to TNF- $\alpha$  alone for 30 or 60 min.

whether resveratrol derivatives (AC, AF, and PD) inhibited TNF- $\alpha$ -induced p38 MAPK activation. As shown in Fig. 5C, pretreatment with AC, AF, or PD did not attenuate TNF- $\alpha$ -stimulated p38 MAPK

phosphorylation. Taken together, these results indicate that, in RMCs, AC, AF, and PD inhibited TNF- $\alpha$ -induced COX-2 expression via a p38 MAPK-independent pathway.



### 3.5. Resveratrol derivatives inhibited TNF- $\alpha$ -induced COX-2 expression via the reduction of JNK1/2 activation in RMCs

JNK1/2 has been shown to regulate COX-2 expression in various cell types [23–25]. Here, we investigated whether JNK1/2 is involved in TNF- $\alpha$ -induced COX-2 expression. Cells were pretreated with an inhibitor of JNK1/2 (SP600125) [26] for 1 h, and then incubated with TNF- $\alpha$  for 24 h. As shown in Fig. 6A, pretreatment with SP600125 attenuated TNF- $\alpha$ -induced COX-2 expression. In addition, TNF- $\alpha$ -induced COX-2 mRNA levels were also reduced by pretreatment with SP600125 (Fig. 6B). We further showed that TNF- $\alpha$  markedly induced c-Jun activation in RMCs in a time-dependent manner, which was inhibited by pretreatment with SP600125 (Fig. 6C). Finally, we investigated whether resveratrol derivatives (AC, AF, and PD) inhibited TNF- $\alpha$ -induced JNK1/2 activation. As shown in Fig. 6D–F, pretreatment with AC, AF, or PD significantly attenuated TNF- $\alpha$ -stimulated JNK1/2 phosphorylation. Taken together, these results indicate that, in RMCs, resveratrol derivatives inhibited TNF- $\alpha$ -induced COX-2 expression via the down-regulation of JNK1/2 activation.

### 3.6. Resveratrol derivatives inhibited TNF- $\alpha$ -induced COX-2 expression via the reduction of NF- $\kappa$ B (p65) activation in RMCs

NF- $\kappa$ B has been shown to be involved in COX-2 induction in various cell types [27–29]. Here, we investigated whether NF- $\kappa$ B is involved in TNF- $\alpha$ -induced COX-2 expression. Cells were pretreated with an inhibitor of NF- $\kappa$ B (Bay 11-7082) [30] for 1 h, and then incubated with TNF- $\alpha$  for 24 h. As shown in Fig. 7A, pretreatment with Bay11-7082

attenuated TNF- $\alpha$ -induced COX-2 expression. In addition, TNF- $\alpha$ -induced COX-2 mRNA levels were also reduced by pretreatment with Bay11-7082 (Fig. 7B). We further showed that TNF- $\alpha$  markedly induced NF- $\kappa$ B (p65) activation in RMCs in a time-dependent manner, which was inhibited by pretreatment with Bay11-7082 (Fig. 7C). Finally, we investigated whether resveratrol derivatives (AC, AF, and PD) inhibited TNF- $\alpha$ -induced NF- $\kappa$ B (p65) activation. As shown in Fig. 7C, pretreatment with AC, AF, or PD significantly attenuated TNF- $\alpha$ -stimulated NF- $\kappa$ B (p65) phosphorylation. NF- $\kappa$ B activity is regulated by multiple mechanisms, including phosphorylation by various MAPKs [4]. Interestingly, in our study, we found that pretreatment of RMCs with U0126, SB202190, or SP600125 did not attenuate the TNF- $\alpha$ -induced phosphorylation of NF- $\kappa$ B (p65) (Fig. 7D). Thus, these results indicate that, in RMCs, these resveratrol derivatives reduced TNF- $\alpha$ -induced COX-2 expression via the inhibition of MAPK-independent NF- $\kappa$ B activation.

### 3.7. Resveratrol derivatives inhibited TNF- $\alpha$ -induced COX-2 expression via the reduction of NF- $\kappa$ B (p65) translocation

Here, we determined whether TNF- $\alpha$  induces NF- $\kappa$ B (p65) translocation in RMCs. As shown in Fig. 8A and B, TNF- $\alpha$  markedly induced NF- $\kappa$ B (p65) translocation from the cytosol to the nucleus in these cells in a time-dependent manner. We further investigated whether the resveratrol derivatives (AC, AF, and PD) inhibited TNF- $\alpha$ -induced NF- $\kappa$ B (p65) translocation. As shown in Fig. 8C, pretreatment with AC, AF, or PD partially attenuated TNF- $\alpha$ -stimulated NF- $\kappa$ B (p65) translocation. Moreover, we found that pretreatment of RMCs with U0126, SB202190, or SP600125, but not Bay11-7082, did not attenuate the TNF- $\alpha$ -induced

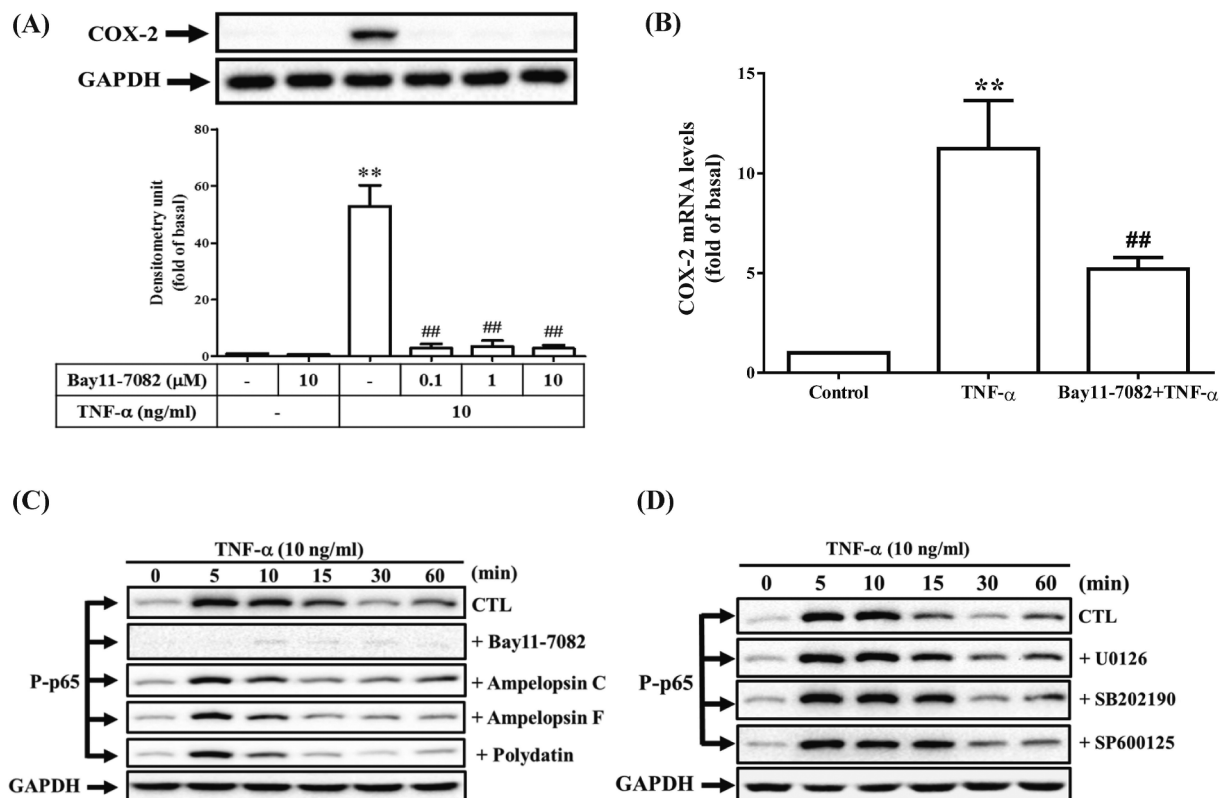


**Fig. 7.** AC, AF, and PD inhibit TNF- $\alpha$ -induced NF- $\kappa$ B (p65) phosphorylation. (A) RMCs were pretreated with Bay11-7082 (0.1, 1, or 10 μM) for 1 h, and then incubated with TNF- $\alpha$  for 24 h. The expression of the COX-2 protein was determined by Western blotting. (B) Cells were pretreated with Bay11-7082 for 1 h, and then incubated with TNF- $\alpha$  for 6 h. The mRNA levels of COX-2 were analyzed by real-time PCR. (C, D) Cells were pretreated with or without Bay11-7082 (10 μM), AC (10 μg/ml), AF (10 μg/ml), PD (10 μg/ml), U0126 (600 nM), SB202190 (3 μM), or SP600125 (1 μM) for 1 h, and then incubated with TNF- $\alpha$  for the indicated time. The expression of phospho-p65 was determined by Western blotting. Data are expressed as the mean  $\pm$  S.E.M. of three independent experiments. \*\* $P$  < 0.01 compared with cells exposed to the vehicle. ## $P$  < 0.01 compared with cells exposed to TNF- $\alpha$  alone.

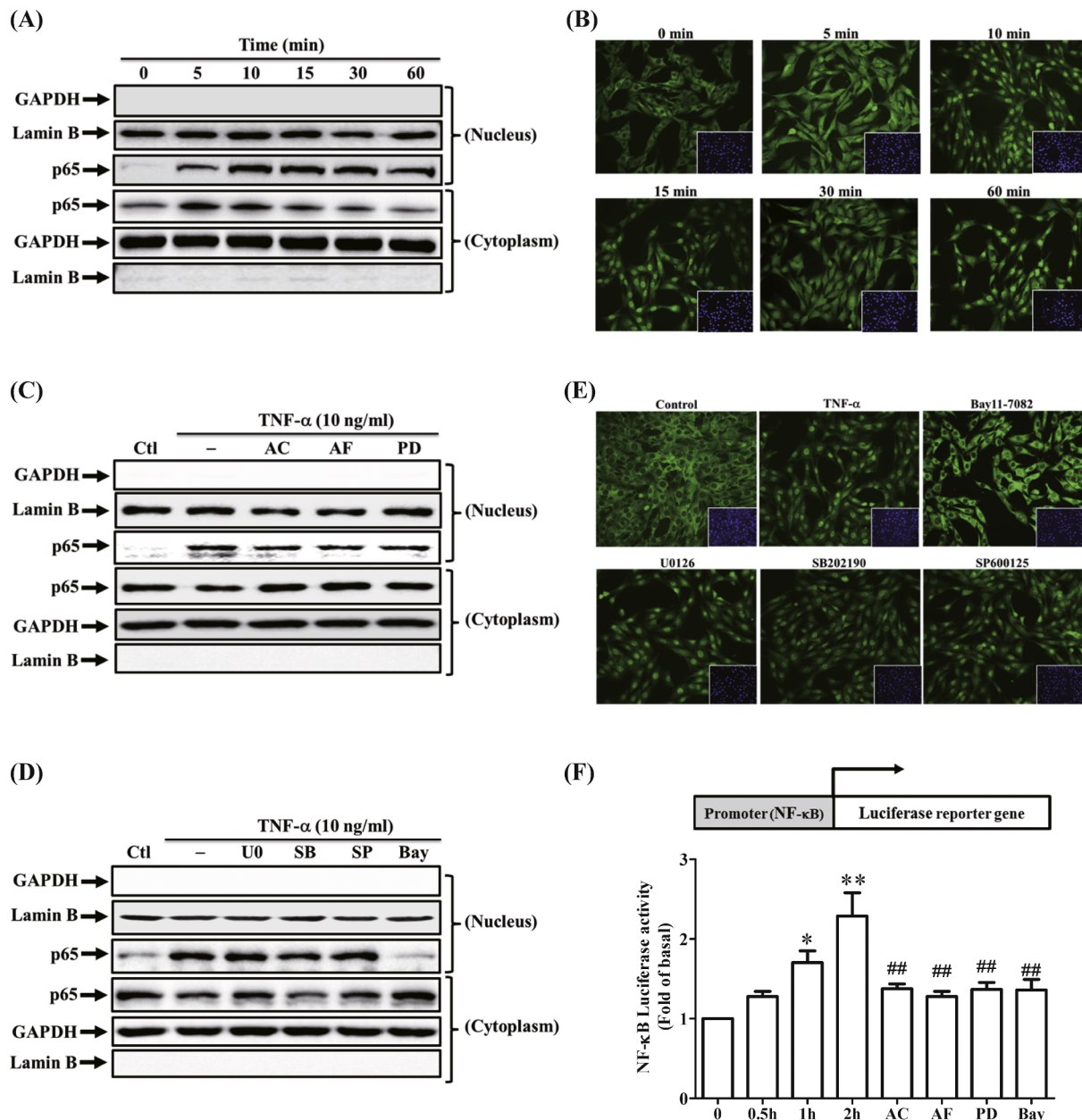


**Fig. 8.** AC, AF, and PD inhibit TNF- $\alpha$ -induced NF- $\kappa$ B (p65) translocation in RMCs. Cells were treated with TNF- $\alpha$  for the indicated time. The nuclear and cytosolic fractions were prepared and subjected to Western blotting using an anti-p65 antibody. Lamin B and GAPDH were used as marker proteins of the nuclear and cytosolic fractions, respectively (A). The translocation of NF- $\kappa$ B (p65) was observed using fluorescence microscopy (B). (C, D) Cells were pretreated without or with AC, AF, PD, U0126, SB202190, SP600125, or Bay11-7082 for 1 h, and then stimulated with 10 ng/ml TNF- $\alpha$  for 10 min. The nuclear and cytosolic fractions were prepared and subjected to Western blotting using an anti-p65 antibody. Lamin B and GAPDH were used as marker proteins of the nuclear and cytosolic fractions, respectively. (E) Cells were pretreated with or without U0126, SB202190, SP600125, or Bay11-7082 for 1 h, and then stimulated with 10 ng/ml TNF- $\alpha$  for 10 min. The translocation of NF- $\kappa$ B (p65) was observed using fluorescence microscopy. (F) Cells were treated with TNF- $\alpha$  for the indicated time or pretreated with AC, AF, PD, or Bay 11-7082 for 1 h, and then incubated with TNF- $\alpha$  for 2 h. NF- $\kappa$ B promoter activity was measured. Data are expressed as the mean  $\pm$  S.E.M. of three independent experiments. \* $P$  < 0.05; \*\* $P$  < 0.01 compared with cells exposed to the vehicle. ## $P$  < 0.01 compared with cells exposed to TNF- $\alpha$  alone.

translocation of NF- $\kappa$ B (p65) (Fig. 8D and E). Finally, we showed that TNF- $\alpha$  markedly induced NF- $\kappa$ B promoter activity in a time-dependent manner, which was reduced by pretreatment with the resveratrol derivatives (AC, AF, and PD) (Fig. 8F). These results indicate that resveratrol derivatives attenuated TNF- $\alpha$ -induced COX-2 expression via the inhibition of MAPK-independent NF- $\kappa$ B translocation.

#### 4. Discussion

cPLA<sub>2</sub> and COX-2, which are regulated by various stimuli, are important in renal inflammation and may lead to several renal diseases.

The inhibition of COX-2 can limit renal damage and inflammation [31]. Resveratrol has been reported to suppress inflammatory responses in mesangial cells and in several types of renal injury in animal models [32,33]. Moreover, resveratrol derivatives were shown to inhibit inflammatory pathways (COX activity), in part more effectively than resveratrol itself [7,8,12,13]. Previously, the active resveratrol derivatives from the roots of *V. thunbergii* Sieb. & Zucc. (Vitaceae) were shown to have significant anti-platelet and anti-oxidative activities. However, the anti-inflammatory mechanisms of these resveratrol derivatives in RMCs have not been clearly explained. In the present study, we found that resveratrol derivatives (AC, AF, and PD) can reduce cPLA<sub>2</sub>/COX-2/

PGE<sub>2</sub> expression via the inhibition of JNK1/2, ERK1/2 and attenuate the NF- $\kappa$ B activation induced by TNF- $\alpha$  in RMCs. TNF- $\alpha$  induces JNK1/2- and ERK1/2-independent NF- $\kappa$ B activation and translocation in RMCs. Activated NF- $\kappa$ B is recruited to the promoter regions of COX-2, leading to an increase in COX-2 mRNA levels and protein expression. These responses may further lead to kidney inflammatory diseases. The results of the present study suggest that resveratrol derivatives from the roots of *V. thunbergii* Sieb. & Zucc. (Vitaceae) exerted a protective effect on renal inflammation by inhibiting cPLA<sub>2</sub>/COX-2/PGE<sub>2</sub> expression.

TNF- $\alpha$ , which was initially reported to induce tumor cell apoptosis and cachexia, is now considered a central mediator of a broad range of biological activities, from cell proliferation, cell death, and differentiation to the induction of inflammation and immune modulation [34]. TNF- $\alpha$  exerts its biological responses via interaction with two cell surface receptors: TNFR1 and TNFR2 [35]. These receptors trigger shared and distinct signaling pathways upon TNF- $\alpha$  binding, which in turn results in cellular outputs that may promote tissue injury, but may also induce protective, beneficial responses [36]. Multiple studies have investigated the role of TNFRs in the development of early and late renal failure (diabetic nephropathy, nephroangiosclerosis, acute kidney transplant rejection, renal cell carcinoma, glomerulonephritis, sepsis, and obstructive renal injury) [37]. Renal expression and circulating levels of bioactive TNF- $\alpha$  are increased during clinical and experimental lupus nephritis and correlate with disease activity [38]. Low levels of the TNF- $\alpha$  mRNA can be detected in lupus-prone mice prior to renal injury [39]. Renal mesangial cells are responsible for glomerular PAF generation and, ultimately, are the victims of its excessive production [40]. The mesangial pathology is widely acknowledged to reflect glomerular damage, which culminates in glomerulosclerosis and proteinuria. Therefore, the modulation of mesangial cell responses would offer a pathophysiology-based therapeutic approach to prevent glomerular injury.

Plants contain numerous polyphenols, which have been shown to reduce inflammation and increase resistance to disease. Although resveratrol, a natural polyphenolic molecule with several biological activities, is a well-recognized anti-inflammation, anti-oxidant, anti-aging, and cancer chemopreventive agent [41,42], some resveratrol derivatives have been shown to inhibit inflammatory pathways (COX activity), in part more effectively than resveratrol itself [7,8]. Active resveratrol derivatives from the roots of *V. thunbergii* Sieb. & Zucc. (Vitaceae) are well-known folk medicines for the treatment of hepatitis and diarrhea in Taiwan [8]. Previously, active resveratrol derivatives, such as AC and AF, from the roots of *V. thunbergii* Sieb. & Zucc. (Vitaceae) have been shown to have significant anti-platelet and anti-oxidative activities [9,10]. Ampelopsin, a plant flavonoid, has potent anti-inflammatory properties *in vitro* and *in vivo*. It has been reported that ampelopsin inhibited NO production in LPS-stimulated RAW264.7 macrophages and reduced carrageenan-induced acute inflammation *in vivo* [43], which is consistent with another report that ampelopsin played an important role not only in reducing the production of pro-inflammatory mediators, such as IL-1 $\beta$ , IL-6, and TNF- $\alpha$ , but also in inhibiting the activity of iNOS. The nephroprotective effects of PD were attributed to its anti-inflammatory cascade, including the inhibition of the expression of NF- $\kappa$ B (p65), COX-2, and iNOS proteins and the production of TNF- $\alpha$ , PGE<sub>2</sub> and IL-1 $\beta$  [16]. PD has been reported to alleviate high-glucose-induced extracellular matrix accumulation through anti-inflammatory mechanisms in rat glomerular mesangial cells *in vitro* [15]. Here, we found that pretreatment with resveratrol derivatives inhibited cPLA<sub>2</sub> and COX-2 expression and PGE<sub>2</sub> release in RMCs. Moreover, the inhibitory effects of TNF- $\alpha$ -induced cPLA<sub>2</sub> and COX-2 expression detected in the AC and AF groups were stronger than those observed in the PD group. This may be because both AC and AF

are stilbene oligomers (AC is a trimer form of resveratrol, whereas AF is a dimer form of resveratrol [8]). By contrast, PD is a glycoside form of resveratrol [11], which is the most abundant form of resveratrol in nature [44]. Therefore, in our study, both AC and AF were shown to inhibit cPLA<sub>2</sub>/COX-2/PGE<sub>2</sub> activity more effectively than resveratrol itself (PD).

In addition, we also found that the cells treated with TNF- $\alpha$  prior to the administration of these inhibitors and resveratrol derivatives exhibited higher expression levels of cPLA<sub>2</sub> and COX-2 than did the cells that had been exposed to TNF- $\alpha$  alone (Supplementary data 1). This may be because the cells stimulated by TNF- $\alpha$  release many factors, including inflammatory cytokines, which might worsen the inflammatory responses. Therefore, when these inhibitors and resveratrol derivatives were added after the cells had already been exposed to TNF- $\alpha$ , they may not have reduced or inhibited inflammatory responses. Taken together, these results suggest that resveratrol derivatives might be useful as anti-inflammatory modulators of kidney inflammation.

Supplementary data associated with this article can be found, in the online version, at <https://doi.org/10.1016/j.cyto.2018.10.008>.

The compromised MAPK signaling pathways, which include JNK1/2, p38 MAPK, and ERK1/2, contribute to the pathology of diverse human diseases [45,46]. The JNK1/2 and p38 MAPK signaling pathways are activated by various types of cellular stresses, such as oxidative, genotoxic, and osmotic, as well as by proinflammatory cytokines, such as TNF- $\alpha$  and IL-1 $\beta$  [46]. Renal ERK1/2 and JNK1/2 activation was also increased in the glycerol model of myoglobinuric acute renal injury [47]. It seems that MAPK signaling pathways represent a potential target for therapeutic intervention. Here, we found that TNF- $\alpha$ -induced COX-2 expression was downregulated by an inhibitor of JNK1/2 or ERK1/2, but not of p38 MAPK, in RMCs. In addition, pretreatment with the resveratrol derivatives reduced TNF- $\alpha$ -induced ERK1/2, JNK1/2, and c-Jun activation in RMCs. Thus, we consider that the resveratrol derivatives inhibit TNF- $\alpha$ -induced inflammatory responses via the inhibition of ERK1/2 and JNK1/2 activation in RMCs.

NF- $\kappa$ B regulates the expression of cytokines, growth factors, and effector enzymes in response to the ligation of many receptors involved in immunity, including TNFR, CD40, and the TIR family [48]. NF- $\kappa$ B also regulates the expression of genes outside of the immune system and, hence, can influence multiple aspects of normal and disease physiology [49]. Moreover, we established that NF- $\kappa$ B played a key role in mediating TNF- $\alpha$ -induced inflammatory responses in RMCs. In addition, NF- $\kappa$ B activity is regulated by multiple mechanisms, including phosphorylation by various MAPKs [4]. Interestingly, we found that TNF- $\alpha$  induced NF- $\kappa$ B activation via a JNK1/2- and ERK1/2-independent pathway in RMCs. In the future, we will investigate the detailed signaling pathways involved in TNF- $\alpha$ -stimulated NF- $\kappa$ B activation in these cells. Moreover, we also showed that the resveratrol derivatives inhibited TNF- $\alpha$ -induced NF- $\kappa$ B (p65) activation and translocation. Thus, we also consider that the resveratrol derivatives inhibit TNF- $\alpha$ -induced inflammatory responses via the inhibition of NF- $\kappa$ B activation in RMCs.

In summary, as shown in Fig. 9, our results demonstrate that TNF- $\alpha$  induces JNK1/2- and ERK1/2-independent NF- $\kappa$ B activation and translocation in RMCs. Activated NF- $\kappa$ B is recruited to the promoter regions of COX-2, leading to the upregulation of the COX-2 mRNA and protein. Resveratrol derivatives (AC, AF, and PD) can reduce cPLA<sub>2</sub>/COX-2/PGE<sub>2</sub> expression via the inhibition of the JNK1/2, ERK1/2, and NF- $\kappa$ B activation induced by TNF- $\alpha$  in RMCs.

## 5. Notes

The authors declare that there is no conflict of interest.



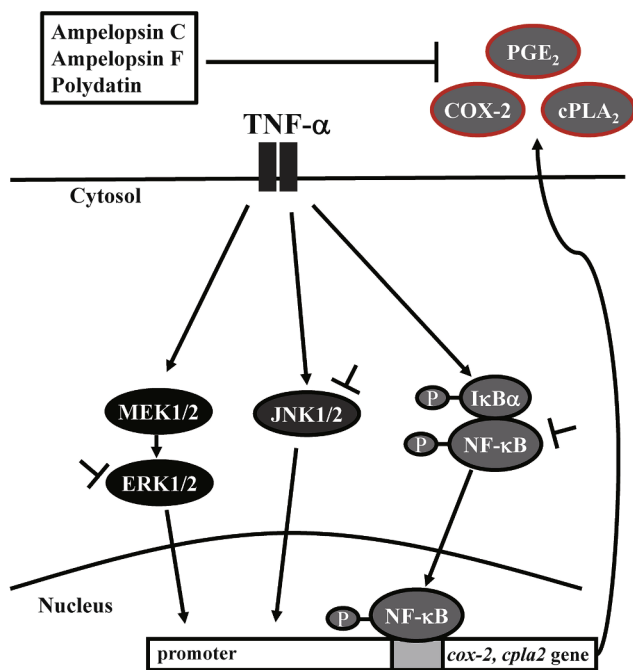


**Fig. 9.** Schematic diagram of the proposed signaling pathway involved in TNF- $\alpha$ -induced cPLA<sub>2</sub>/COX-2 expression in RMCs. TNF- $\alpha$  induces JNK1/2- and ERK1/2-independent NF- $\kappa$ B activation and translocation in RMCs. The activated NF- $\kappa$ B is recruited to the promoter regions of COX-2, leading to the up-regulation of the COX-2 mRNA and protein. Resveratrol derivatives (AC, AF, and PD) downregulate cPLA<sub>2</sub>/COX-2/PGE<sub>2</sub> expression via the inhibition of TNF- $\alpha$ -induced JNK1/2, ERK1/2, and NF- $\kappa$ B activation in RMCs.

## Acknowledgments

This work was supported by the Ministry of Science and Technology, Taiwan, grant number MOST 101-2320-B-255-003-MY3; the Chang Gung Medical Research Foundation, grant number CMRPF3E0051, CMRPF3E0052, CMRPF3G0011, CMRPF3G0012 and BMRPD16; Chang Gung University of Science and Technology, grant number EZRPF3E0601, EZRPF3E0161, EZRPF3E0201, EZRPF3E0191, EZRPF3E0181 and EZRPF3E0171, EZRPF3G0551.

## References

- [1] V. Vielhauer, T.N. Mayadas, Functions of TNF and its receptors in renal disease: distinct roles in inflammatory tissue injury and immune regulation, *Semin. Nephrol.* 27 (2007) 286–308.
- [2] J.F. Navarro, C. Mora-Fernandez, The role of TNF- $\alpha$  in diabetic nephropathy: pathogenic and therapeutic implications, *Cytokine Growth Factor Rev.* 17 (2006) 441–450.
- [3] K.K. Donnahoo, X. Meng, A. Ayala, et al., Early kidney TNF- $\alpha$  expression mediates neutrophil infiltration and injury after renal ischemia-reperfusion, *Am. J. Physiol.* 277 (1999) R922–R929.
- [4] I.T. Lee, C.M. Yang, Inflammatory signalings involved in airway and pulmonary diseases, *Mediators Inflamm.* 2013 (2013) 791231.
- [5] C.M. Yang, I.T. Lee, R.C. Hsu, et al., NADPH oxidase/ROS-dependent PYK2 activation is involved in TNF- $\alpha$ -induced matrix metalloproteinase-9 expression in rat heart-derived H9c2 cells, *Toxicol. Appl. Pharmacol.* 272 (2013) 431–442.
- [6] G. Albertoni, N. Schor, Resveratrol plays important role in protective mechanisms in renal disease—mini-review, *Jornal brasileiro de nefrologia: 'orgao oficial de Sociedades Brasileira e Latino-Americana de Nefrologia* 37 (2015) 106–114.
- [7] T. Szekeres, P. Saiko, M. Fritzer-Szekeres, et al., Chemopreventive effects of resveratrol and resveratrol derivatives, *Ann. NY Acad. Sci.* 1215 (2011) 89–95.
- [8] M.H. Keyrol, B.S. Matsuura, C.R. Stephenson, Chemistry and biology of resveratrol-derived natural products, *Chem. Rev.* 115 (2015) 8976–9027.
- [9] W.F. Chiou, C.C. Shen, C.C. Chen, et al., Oligostilbenes from the roots of *Vitis thunbergii*, *Planta Medica* 75 (2009) 856–859.
- [10] Y.L. Huang, W.J. Tsai, C.C. Shen, et al., Resveratrol derivatives from the roots of *Vitis thunbergii*, *J. Nat. Prod.* 68 (2005) 217–220.
- [11] Q.H. Du, C. Peng, H. Zhang, Polydatin: a review of pharmacology and pharmacokinetics, *Pharm. Biol.* 51 (2013) 1347–1354.
- [12] N. Calabriso, E. Scoditti, M. Massaro, et al., Multiple anti-inflammatory and anti-

- atherosclerotic properties of red wine polyphenolic extracts: differential role of hydroxycinnamic acids, flavonols and stilbenes on endothelial inflammatory gene expression, *Eur. J. Nutr.* 55 (2016) 477–489.
- [13] G. Kaur, M. Roberti, F. Raul, et al., Suppression of human monocyte tissue factor induction by red wine phenolics and synthetic derivatives of resveratrol, *Thromb. Res.* 119 (2007) 247–256.
- [14] Y. Gao, Z. Zeng, T. Li, et al., Polydatin inhibits mitochondrial dysfunction in the renal tubular epithelial cells of a rat model of sepsis-induced acute kidney injury, *Anesth. Analg.* 121 (2015) 1251–1260.
- [15] X. Xie, J. Peng, K. Huang, et al., Polydatin ameliorates experimental diabetes-induced fibronectin through inhibiting the activation of NF- $\kappa$ B signaling pathway in rat glomerular mesangial cells, *Mol. Cell. Endocrinol.* 362 (2012) 183–193.
- [16] L. Chen, Z. Lan, Q. Lin, et al., Polydatin ameliorates renal injury by attenuating oxidative stress-related inflammatory responses in fructose-induced urate nephropathic mice, *Food Chem. Toxicol.: Int. J. Published British Ind. Biol. Res. Assoc.* 52 (2013) 28–35.
- [17] S. Qi, Y. Xin, Y. Guo, et al., Ampelopsin reduces endotoxin inflammation via repressing ROS-mediated activation of PI3K/Akt/NF- $\kappa$ B signaling pathways, *Int. Immunopharmacol.* 12 (2012) 278–287.
- [18] L. Weng, H. Zhang, X. Li, et al., Ampelopsin attenuates lipopolysaccharide-induced inflammatory response through the inhibition of the NF- $\kappa$ B and JAK2/STAT3 signaling pathways in microglia, *Int. Immunopharmacol.* 44 (2017) 1–8.
- [19] C.Y. Cheng, C.T. Kuo, C.C. Lin, et al., IL-1 $\beta$  induces expression of matrix metalloproteinase-9 and cell migration via a c-Src-dependent, growth factor receptor transactivation in A549 cells, *Br. J. Pharmacol.* 160 (2010) 1595–1610.
- [20] I.P. Street, H.K. Lin, F. Laliberte, et al., Slow- and tight-binding inhibitors of the 85-kDa human phospholipase A2, *Biochemistry* 32 (1993) 5935–5940.
- [21] M.F. Favata, K.Y. Horiuchi, E.J. Manos, et al., Identification of a novel inhibitor of mitogen-activated protein kinase kinase, *J. Biol. Chem.* 273 (1998) 18623–18632.
- [22] P.R. Young, M.M. McLaughlin, S. Kumar, et al., Pyridinyl imidazole inhibitors of p38 mitogen-activated protein kinase bind in the ATP site, *J. Biol. Chem.* 272 (1997) 12116–12121.
- [23] W.C. Chen, C.K. Tseng, Y.H. Chen, et al., HCV NS5 A up-regulates COX-2 expression via IL-8-mediated activation of the ERK/JNK MAPK pathway, *PLoS One* 10 (2015) e0133264.
- [24] Y.F. Chuang, M.C. Chen, S.W. Huang, et al., Protein phosphatase 2A in lipopolysaccharide-induced cyclooxygenase-2 expression in murine lymphatic endothelial cells, *PLoS One* 10 (2015) e0137177.
- [25] Y. Zhai, Y. Dang, W. Gao, et al., P38 and JNK signal pathways are involved in the regulation of phlorizin against UVB-induced skin damage, *Exp. Dermatol.* 24 (2015) 275–279.
- [26] B.L. Bennett, D.T. Sasaki, B.W. Murray, et al., SP600125, an anthracycline inhibitor of Jun N-terminal kinase, *Proc. Natl. Acad. Sci. USA* 98 (2001) 13681–13686.
- [27] H.L. Hsieh, C.B. Wu, C.C. Sun, et al., Sphingosine-1-phosphate induces COX-2 expression via PI3K/Akt and p42/p44 MAPK pathways in rat vascular smooth muscle cells, *J. Cell Physiol.* 207 (2006) 757–766.
- [28] H.L. Hsieh, H.H. Wang, C.Y. Wu, et al., BK-induced COX-2 expression via PKC- $\delta$ -dependent activation of p42/p44 MAPK and NF- $\kappa$ B in astrocytes, *Cell Signal* 19 (2007) 330–340.
- [29] H.L. Hsieh, C.C. Sun, T.S. Wang, et al., PKC- $\delta$ /c-Src-mediated EGF receptor transactivation regulates thrombin-induced COX-2 expression and PGE(2) production in rat vascular smooth muscle cells, *Biochim. Biophys. Acta* 1783 (2008) 1563–1575.
- [30] J.W. Pierce, R. Schoenleber, G. Jesmok, et al., Novel inhibitors of cytokine-induced I $\kappa$ B $\alpha$  phosphorylation and endothelial cell adhesion molecule expression show anti-inflammatory effects in vivo, *J. Biol. Chem.* 272 (1997) 21096–21103.
- [31] R. Mohamed, C. Jayakumar, P.V. Ranganathan, et al., Kidney proximal tubular epithelial-specific overexpression of netrin-1 suppresses inflammation and albuminuria through suppression of COX-2-mediated PGE2 production in streptozotocin-induced diabetic mice, *Am. J. Pathol.* 181 (2012) 1991–2002.
- [32] F. Xu, Y. Wang, W. Cui, et al., Resveratrol prevention of diabetic nephropathy is associated with the suppression of renal inflammation and mesangial cell proliferation: possible roles of Akt/NF- $\kappa$ B pathway, *Int. J. Endocrinol.* 2014 (2014) 289327.
- [33] J. Li, L. Li, S. Wang, et al., Resveratrol alleviates inflammatory responses and oxidative stress in rat kidney ischemia-reperfusion injury and H2O2-induced NRK-52E cells via the Nrf2/TLR4/NF- $\kappa$ B pathway, *Cell. Physiol. Biochem.: Int. J. Exp. Cell. Physiol., Biochem. Pharmacol.* 45 (2018) 1677–1689.
- [34] R.S. Al-Lamki, T.N. Mayadas, TNF receptors: signaling pathways and contribution to renal dysfunction, *Kidney Int.* 87 (2015) 281–296.
- [35] I.T. Lee, S.F. Luo, C.W. Lee, et al., Overexpression of HO-1 protects against TNF- $\alpha$ -mediated airway inflammation by down-regulation of TNFR1-dependent oxidative stress, *Am. J. Pathol.* 175 (2009) 519–532.
- [36] C.K. Hsu, I.T. Lee, C.C. Lin, et al., Nox2/ROS-dependent human antigen R translocation contributes to TNF- $\alpha$ -induced SOCS-3 expression in human tracheal smooth muscle cells, *Am. J. Physiol. Lung Cell Mol. Physiol.* 306 (2014) L521–L533.
- [37] M.M. Speckaert, R. Speckaert, M. Laute, et al., Tumor necrosis factor receptors: biology and therapeutic potential in kidney diseases, *Am. J. Nephrol.* 36 (2012) 261–270.
- [38] S. Yung, K.F. Cheung, Q. Zhang, et al., Mediators of inflammation and their effect on resident renal cells: implications in lupus nephritis, *Clin. Dev. Immunol.* 2013 (2013) 317682.
- [39] J.M. Boswell, M.A. Yui, D.W. Burt, et al., Increased tumor necrosis factor and IL-1  $\beta$  gene expression in the kidneys of mice with lupus nephritis, *J. Immunol.* 141



- (1988) 3050–3054.
- [40] A. Reznichenko, R. Korstanje, The role of platelet-activating factor in mesangial pathophysiology, *Am. J. Pathol.* 185 (2015) 888–896.
  - [41] S. Bengmark, M.D. Mesa, A. Gil, Plant-derived health: the effects of turmeric and curcuminoids, *Nutr. Hosp.* 24 (2009) 273–281.
  - [42] E. Conte, E. Fagone, M. Fruciano, et al., Anti-inflammatory and antifibrotic effects of resveratrol in the lung, *Histol. Histopathol.* 30 (2015) 523–529.
  - [43] K.T. Ku, Y.L. Huang, Y.J. Huang, et al., Miyabenol A inhibits LPS-induced NO production via IKK/IkappaB inactivation in RAW 264.7 macrophages: possible involvement of the p38 and PI3K pathways, *J. Agric. Food Chem.* 56 (2008) 8911–8918.
  - [44] G. Regev-Shoshani, O. Shoseyov, I. Bilkis, et al., Glycosylation of resveratrol protects it from enzymic oxidation, *Biochem. J.* 374 (2003) 157–163.
  - [45] E.K. Kim, E.J. Choi, Pathological roles of MAPK signaling pathways in human diseases, *Biochim. Biophys. Acta* 2010 (1802) 396–405.
  - [46] E.K. Kim, E.J. Choi, Compromised MAPK signaling in human diseases: an update, *Arch. Toxicol.* 89 (2015) 867–882.
  - [47] S. Ishizuka, T. Yano, K. Hagiwara, et al., Extracellular signal-regulated kinase mediates renal regeneration in rats with myoglobinuric acute renal injury, *Biochem. Biophys. Res. Commun.* 254 (1999) 88–92.
  - [48] R.L. Cho, C.C. Yang, I.T. Lee, et al., Lipopolysaccharide induces ICAM-1 expression via a c-Src/NADPH oxidase/ROS-dependent NF-kappaB pathway in human pulmonary alveolar epithelial cells, *Am. J. Physiol. Lung Cell Mol. Physiol.* 310 (2016) L639–657.
  - [49] S.E. Cheng, I.T. Lee, C.C. Lin, et al., Thrombin induces ICAM-1 expression in human lung epithelial cells via c-Src/PDGFR/PI3K/Akt-dependent NF-kappaB/p300 activation, *Clin. Sci. (Lond)* 127 (2014) 171–183.

Original Paper

# ***Garcinia Multiflora* Inhibits FPR1-Mediated Neutrophil Activation and Protects Against Acute Lung Injury**

Yung-Fong Tsai<sup>a,b,c</sup> Shun-Chin Yang<sup>a,d</sup> Wen-Yi Chang<sup>a</sup> Jih-Jung Chen<sup>e,f</sup>  
Chun-Yu Chen<sup>a,b,c</sup> Shih-Hsin Chang<sup>a,g</sup> Tsong-Long Hwang<sup>a,b,g,h</sup>

<sup>a</sup>Graduate Institute of Natural Products, College of Medicine, Chang Gung University, Taoyuan, <sup>b</sup>Department of Anesthesiology, Chang Gung Memorial Hospital, Taoyuan, <sup>c</sup>Graduate Institute of Clinical Medical Sciences, College of Medicine, Chang Gung University, Taoyuan, <sup>d</sup>Department of Anesthesiology, Taipei Veterans General Hospital and National Yang-Ming University, Taipei, <sup>e</sup>Faculty of Pharmacy, School of Pharmaceutical Sciences, National Yang-Ming University, Taipei, <sup>f</sup>Department of Medical Research, China Medical University Hospital, Taichung, <sup>g</sup>Research Center for Chinese Herbal Medicine, Research Center for Food and Cosmetic Safety, Graduate Institute of Health Industry Technology, College of Human Ecology, Chang Gung University of Science and Technology, Taoyuan, <sup>h</sup>Chinese Herbal Medicine Research Team, Healthy Aging Research Center, Chang Gung University, Taoyuan, Taiwan

## **Key Words**

Acute lung injury • Elastase • Formyl peptide receptor 1 • *Garcinia multiflora* • Neutrophil • Superoxide anion

## **Abstract**

**Background/Aims:** Formyl peptide receptors (FPRs) recognize different endogenous and exogenous molecular stimuli and mediate neutrophil activation. Dysregulation of excessive neutrophil activation and the resulting immune responses can induce acute lung injury (ALI) in the host. Accordingly, one promising approach to the treatment of neutrophil-dominated inflammatory diseases involves therapeutic FPR1 inhibition. **Methods:** We extracted a potent FPR1 antagonist from *Garcinia multiflora* Champ. (GMC). The inhibitory effects of GMC on superoxide anion release and elastase degranulation from activated human neutrophils were determined with spectrophotometric analysis. Reactive oxygen species (ROS) production and the FPR1 binding ability of neutrophils were assayed by flow cytometry. Signaling transduction mediated by GMC in response to chemoattractants was assessed with a calcium influx assay and western blotting. A lipopolysaccharide (LPS)-induced ALI mouse model was used to determine the therapeutic effects of GMC *in vivo*. **Results:** GMC significantly reduced superoxide anion release, the reactive oxidants derived therefrom, and elastase degranulation mediated through selective, competitive FPR1 blocking in *N*-formyl-L-methionyl-L-leucyl-L-phenylalanine (fMLF)-stimulated human neutrophils. In cell-free systems, GMC was unable

Tsong-Long Hwang

Graduate Institute of Natural Products, Chang Gung University  
259 Wen-Hwa 1st Road, Kweishan, Taoyuan (Taiwan)  
Tel. 886-3-2118506, Fax 886-3-2118506, E-Mail [htl@mail.cgu.edu.tw](mailto:htl@mail.cgu.edu.tw)

to scavenge superoxide anions or suppress elastase activity. GMC produced a right shift in fMLF-activated concentration-response curves and was confirmed to be a competitive FPR1 antagonist. GMC binds to FPR1 not only in neutrophils, but also FPR1 in neutrophil-like THP-1 and hFPR1-transfected HEK293 cells. Furthermore, the mobilization of calcium and phosphorylation of mitogen-activated protein kinases and Akt, which are involved in FPR1-mediated downstream signaling, was competitively blocked by GMC. In an *in vivo* study, GMC significantly reduced pulmonary edema, neutrophil infiltration, and alveolar damage in LPS-induced ALI mice. **Conclusion:** Our findings demonstrate that GMC is a natural competitive FPR1 inhibitor, which makes it a possible anti-inflammatory treatment option for patients critically inflicted with FPR1-mediated neutrophilic lung damage.

© 2018 The Author(s)  
Published by S. Karger AG, Basel

## Introduction

Inflammation is a physical defense response to microorganism infection and pathologic progression that is largely mediated by neutrophil recruitment and activation [1]. However, dysregulation of neutrophil activation can be harmful to major organs and has been associated with the pathogenesis of many clinical diseases, such as acute lung injury (ALI), acute respiratory distress syndrome (ARDS), Alzheimer's disease, autoimmune diabetes, and rheumatoid arthritis [2-5]. As ALI and ARDS develop, a large number of neutrophils are activated and recruited into inflamed lungs. Poorly regulated neutrophils release massive quantities of superoxide anions and proteolytic enzymes, which can damage the alveolar capillary barrier and hinder pulmonary gas exchange [6]. Despite the development of numerous therapeutic strategies, mortality rates remain high among patients with ALI and ARDS [7].

G protein-coupled formyl peptide receptor 1 (FPR1) is a transmembrane receptor primarily found in neutrophils. These receptors are responsible for sensing various endogenous and exogenous molecular stimuli to mediate neutrophil activation during inflammation [8, 9]. *N*-formyl peptides derived from invading microorganisms or endogenous host mitochondria strongly bind to FPR1 to trigger septic or sterile inflammatory responses [10, 11]. The binding of *N*-formyl peptides to FPR1 activates neutrophils and guides their migration into infected or injured tissues. Recent cellular and animal studies have proven the therapeutic effects of FPR1 antagonists [12, 13]. Blockade of FPR1 reduces many of the essential functions of neutrophils associated with defense, such as superoxide anion generation, elastase release, chemotaxis, and phagocytosis [14]. One previous study reported that trauma hemorrhagic shock-induced lung damage and systemic inflammatory response syndrome in rats are associated with endogenous mitochondrial *N*-formyl peptides, which can be alleviated by the administration of FPR inhibitors [15]. Grommes [16] revealed that exogenous endotoxin induced FPR1-mediated lung neutrophil infiltration, with relief provided by FPR1 knockout. FPR1 antagonists also decrease neutrophil infiltration in cases of lipopolysaccharide (LPS)-induced ALI [13].

FPR1 antagonists are an emerging therapeutic target in the development of drugs to combat neutrophilic lung inflammation. However, only a few FPR1 antagonists have been studied [12]. Our research team examined the anti-inflammatory effects of extracts from the fruit of the evergreen *Garcinia multiflora* Champ., which is endemic to Taiwan, Hong Kong, and southern China. We named the fruit extraction from *Garcinia multiflora* Champ. as GMC. Studies have reported that *G. multiflora* has anti-inflammatory [17] and anti-HIV activity [18]. We previously reported that pure compounds from *G. multiflora* inhibit the generation of superoxide anions and elastase release in fMLF-stimulated neutrophils [17, 19]. Nonetheless, the pharmacological mechanisms and therapeutic effects of GMC remain to be elucidated.

In this study, we investigated the anti-inflammatory roles of GMC by conducting *in vitro* studies of neutrophil activation and an *in vivo* study of LPS-induced ALI in mice. Our results revealed that GMC significantly suppresses superoxide anion production, the reactive

oxidants derived therefrom, and elastase degranulation in *N*-formyl peptide-stimulated neutrophils by selectively binding to FPR1 to block calcium mobilization as well as mitogen-activated protein kinase (MAPK) and Akt activation. Administration of GMC also greatly reduced endotoxin-induced ALI in mice, indicating GMC as a clinical therapeutic option for the treatment of neutrophil-related pulmonary inflammation.

## Materials and Methods

### *Plant extraction*

The dried fruit of *G. multiflora* (3 kg) was cut into small pieces and immersed in MeOH (3 × 10 L) for 3 days for sequential extraction. Residue (330 g) was concentrated from MeOH extracts under vacuum and then partitioned into EtOAc and H<sub>2</sub>O. Residue Fraction A (167 g) was concentrated from the EtOAc layer. After obtaining chromatographs from samples on silica gel, we subjected 120 g of Fraction A to elution using CH<sub>2</sub>Cl<sub>2</sub>, which yielded 77 mg of GMC.

### *Reagents*

Trp-Lys-Tyr-Met-Val-D-Met-NH<sub>2</sub> (WKYMVm) was obtained from Tocris Bioscience (Ellisville, MO). Fluo-3/AM and *N*-formyl-Nle-Leu-Phe-Nle-Tyr-Lys-fluorescein (FNLFNKYK) were obtained from Molecular Probes (Eugene, OR). Methoxysuccinyl-Ala-Ala-Pro-Val-nitroanilide, rolipram, and N-[2-(p-Bromocinnamylamino)ethyl]-5-isoquinolinesulfonamide (H89) were purchased from Calbiochem (San Diego, CA). Water soluble tetrazolium-1 (WST-1) was purchased from Dojindo Laboratories (Kumamoto, Japan). Cyclic adenosine monophosphate (cAMP) immunoassay kits were obtained from GE Healthcare (Uppsala, Sweden). The antibody for p38 MAPK was purchased from Santa Cruz Biotechnology (Santa Cruz, CA), and other antibodies were obtained from Cell Signaling Technology (Danvers, MA). All other pharmacologic materials were purchased from Sigma-Aldrich (St. Louis, MO).

### *Human neutrophil preparation*

All human research protocols were examined by the Institutional Review Board of Chang Gung Medical Foundation. Healthy volunteers who had not been taking any medication within at least the 2 previous weeks provided informed consent prior to enrollment in the study. Blood samples were donated only from healthy young people (20–30 years of age). Buffy coats containing neutrophils were obtained from donated whole blood using a dextran sedimentation assay, as described in [20]. The buffy coats were then collected using differential centrifugation in a Ficoll Hypaque. Erythrocytes were lysed using a hypotonic solution on ice. Samples were washed and resuspended in iced Hank's balanced salts solution (HBSS) to obtain viable neutrophils of no less than 98% purity.

### *Cell culture*

THP-1 cells were grown in Roswell Park Memorial Institute medium 1640 supplemented with glutamine (2 mM), fetal bovine serum (FBS, 10%), and antibiotics. THP-1 cells then underwent induced cell differentiation using dibutyl cAMP (300 μM) for 2 days before being centrifuged and resuspended in growth medium [13].

HEK293 cells were cultured in Dulbecco's modified Eagle's medium containing FBS (10%), glutamine (2 mM), and antibiotics. HEK293 cells were transfected with the human FPR1 gene (NM\_002029; OriGene, Rockville, MD) using a pCMV6-AC vector for 3 days in accordance with the manufacturer's instructions [13].

### *Determination of superoxide anion and reactive oxygen species production*

The extracellular superoxide anion levels in neutrophils were determined using a spectrophotometer (U-3010; Hitachi, Tokyo) and are expressed as the reduction in the quantity of ferricytochrome *c*. Following pre-incubation with ferricytochrome *c*, neutrophils were primed with or without cytochalasin B at 37°C for 3 min. For cell activation, neutrophils were pretreated with vehicle (dimethyl sulfoxide [DMSO]) or GMC for 5 min followed by a 10-min stimulation with fMLF (FPR1 agonist), WKYMVm (FPR1/FPR2 agonist), NaF (G protein activator), or PMA (protein kinase C activator). The changes in absorbance were analyzed continuously at 550 nm by a spectrophotometer. DHR123 dye was used to probe reactive oxygen species



(ROS) levels in the neutrophils. ROS is a reactive oxidant derived from superoxide anion. Following incubation with DHR123 dye for 12 min and DMSO or GMC for 5 min, neutrophils were induced via fMLF. The fluorescence intensity was determined as an indication of ROS levels using flow cytometry (FACSCalibur™; BD Bioscience, San Jose, CA) [20].

## *Measurement of elastase release*

Elastase release is expressed as the eliminating ability for the substrate methoxysuccinyl-Ala-Ala-Pro-Val-p-nitroanilide determined by spectrophotography at 405 nm. Neutrophils pre-mixed with elastase substrate (0.1 mM) were incubated with DMSO or GMC at 37°C for 5 min and stimulated using fMLF, WKYMVm, NaF, or leukotriene B<sub>4</sub> (LTB<sub>4</sub>, BLT1 receptor agonist). Neutrophils were primed using cytochalasin B for 3 min prior to cell activation. Data are presented as the percentages of the levels obtained from the control group [20].

## *Assays of the scavenging effects of superoxide anions and diphenyl picryl hydrazyl radicals*

A xanthine/xanthine oxidase system was used to evaluate the scavenging effects of superoxide anions. Test samples were incubated with WST-1 (300 µM), Tris (pH 7.4, 50 mM), and xanthine oxidase (0.02 U/ml). Following the administration of xanthine (0.1 mM) to the sample solution, WST-1 was eliminated using superoxide anions. The radical scavenging effects are presented as the change in absorbance as determined using spectrophotography at 450 nm at 30°C. In diphenyl picryl hydrazyl (DPPH) scavenging assays, DMSO or GMC were added to the ethanol buffer of DPPH (0.1 mM). The change in absorbance was measured at 30°C at 517 nm, and the data were compared with the data obtained from the control [20].

## *Analysis of the lactate dehydrogenase level*

Lactate dehydrogenase (LDH) levels were detected using a commercial kit (Promega, Madison, WI). LDH levels are presented as the relative percentage of the total LDH. Total LDH levels were measured by lysing the cells using Triton X-100 (0.1%) [21].

## *Receptor binding assay*

Fluorescence-activated cell sorting (FACS) assays were used to characterize receptor binding [13]. A fluorescent analog of fMLF (FNLFNKYK) was adopted for the analysis of binding ability to FPR1. All sample cells were pretreated for 5 min with DMSO, GMC, or fMLF and stained with FNLFNKYK at 4°C. Cells were then resuspended in HBSS and analyzed using flow cytometry with fMLF as positive control.

## *Determination of cAMP concentrations*

Neutrophils were treated with DMSO or GMC for 5 min before stimulation with fMLF, with rolipram as positive control. The assay was blocked by the administration of dodecyltrimethylammonium bromide (0.5%). Following centrifugation at 3,000 × g, the supernatant of the samples was obtained to measure cAMP levels using a commercial enzyme immunoassay kit (Amersham Biosciences, Buckinghamshire, UK) [21].

## *Determination of calcium concentrations in neutrophils*

Neutrophils stained with Fluo-3/AM dye (2 µM) were used to assess calcium influx in response to chemoattractants. Cytoplasmic calcium concentrations were assayed using a spectrofluorometer at 37°C. The excitation and emission wavelengths were 488 and 520 nm, respectively. Following treatment with DMSO or GMC, fMLF, WKYMVm, or LTB<sub>4</sub> were administered to induce calcium mobilization. The peak intracellular calcium concentration ([Ca<sup>2+</sup>]<sub>i</sub>) was calculated by determination of the fluorescence intensity based on the protocol described in our previous study [21].

## *Western immunoblotting analysis*

Following incubation with the vehicle control (DMSO) or GMC, neutrophils were stimulated with fMLF for 30 s or with WKYMVm, PMA, or LTB<sub>4</sub> for 60 s. Lysates of neutrophils were obtained for western blotting analysis after separation via centrifugation at 14,000 × g. We used 12% sodium dodecyl sulfate-polyacrylamide gel electrophoresis to determine the levels of each protein target in each of the cytoplasmic extracts. The separated proteins were blotted onto transfer membrane and treated with primary antibodies

and anti-rabbit horseradish peroxidase-conjugated secondary antibodies (Cell Signaling Technology). The intensity of the blotted proteins was determined using a chemiluminescence substrate (Amersham Biosciences, Piscataway, NJ) on a UVP Biospectrum imager (UVP, Upland, CA) [13, 20].

#### *Experimental animals*

The protocol of this study protocol was based on the instructions found in *The Guide for Care and Use of Laboratory Animals* issued by the Taiwanese government. C57BL/6 mice (BioLasco, Ilan, Taiwan) underwent environmental adaptation for a period of 7 days prior to the animal study.

#### *LPS-induced ALI mouse model*

Twenty-four male mice (20–25 g, 7–8 weeks old) underwent general anesthesia through the intraperitoneal administration of Zoletil 50 (30 µg/g) and Xylazine (6 µg/g). After being anesthetized, the mice were intratracheally instilled with an LPS spray (160 ng/g; Sigma-Aldrich) from *E. coli* (serotype 0111:B4) [13, 20]. Animals were randomly separated into groups to receive GMC (100 mg/kg) or vehicle via the intraperitoneal route 1 h prior to the induction of lung injury. The animals were divided into four groups: sham, GMC only, LPS only, and LPS+GMC. Mouse lungs were removed under anesthesia after 6 h. The left lung was fixed in buffered formalin (10%) for histologic examination. The right upper lobes were analyzed for lung water content, and the other lobes of the right lung were assayed for myeloperoxidase (MPO) activity. Water content in the lungs was characterized by the wet-to-dry weight ratio.

#### *Measurement of MPO levels*

Harvested organs were homogenized in ice-cold PBS buffer (50 mM, pH 6.0) using a homogenizer. The homogenate was centrifuged at  $12,000 \times g$  (4°C) for 20 min and the supernatant was recovered. The level of MPO in the supernatant was characterized as the degree of oxidation of *o*-dianisidine dihydrochloride (Sigma-Aldrich) using a spectrophotometer at 405 nm. The results were normalized to the protein content of the samples as determined using the Bradford method (Bio-Rad Laboratories, Hercules, CA) [20].

#### *Histopathology examination*

Lung samples were immersed in formalin (10%) for 1 day and embedded in paraffin blocks before being cut into 5-µm-thick pieces. Tissue sections were stained using hematoxylin and eosin or immunohistochemistry as described previously [20]. Formalin-fixed sections embedded in paraffin underwent immunohistochemical analysis using Ly-6G (Gr-1) protein. Ly-6G (Gr-1) is a myeloid differentiation antigen and a good indicator for the identification of peripheral neutrophils. In this experiment, we used rat anti-mouse-Ly-6G (Gr-1) monoclonal primary antibodies (eBioscience, San Diego, CA) at a 1:200 dilution for staining. Microscopic images were obtained under a light microscope.

#### *Statistical analysis*

Experiment data are presented as the mean  $\pm$  standard error of the mean (SEM). Statistical analysis included the Student's *t*-test, one- or two-way analysis of variance, and Bonferroni's multiple-comparison test (SigmaPlot software, Systat Software, Inc., San Jose, CA). A *p* value < 0.05 was considered to indicate a significant difference between two groups.

## Results

### *GMC reduces superoxide anion release, elastase degranulation, and ROS production in fMLF-stimulated human neutrophils*

Respiratory burst and degranulation are the basic inflammatory responses observed in neutrophils. Our data revealed that GMC greatly reduced superoxide anion generation and elastase degranulation in fMLF-stimulated neutrophils, with half-maximal inhibitory concentration ( $IC_{50}$ ) values of  $3.89 \pm 1.17$  and  $4.33 \pm 0.95$  ng/ml, respectively (Fig. 1A and B). fMLF is a selective FPR1 agonist. In flow cytometric analysis, GMC decreased intracellular ROS production in fMLF-stimulated human neutrophils (Fig. 1C). Because GMC did not induce LDH release, even at a concentration of 2 µg/ml (data not shown), GMC is not likely

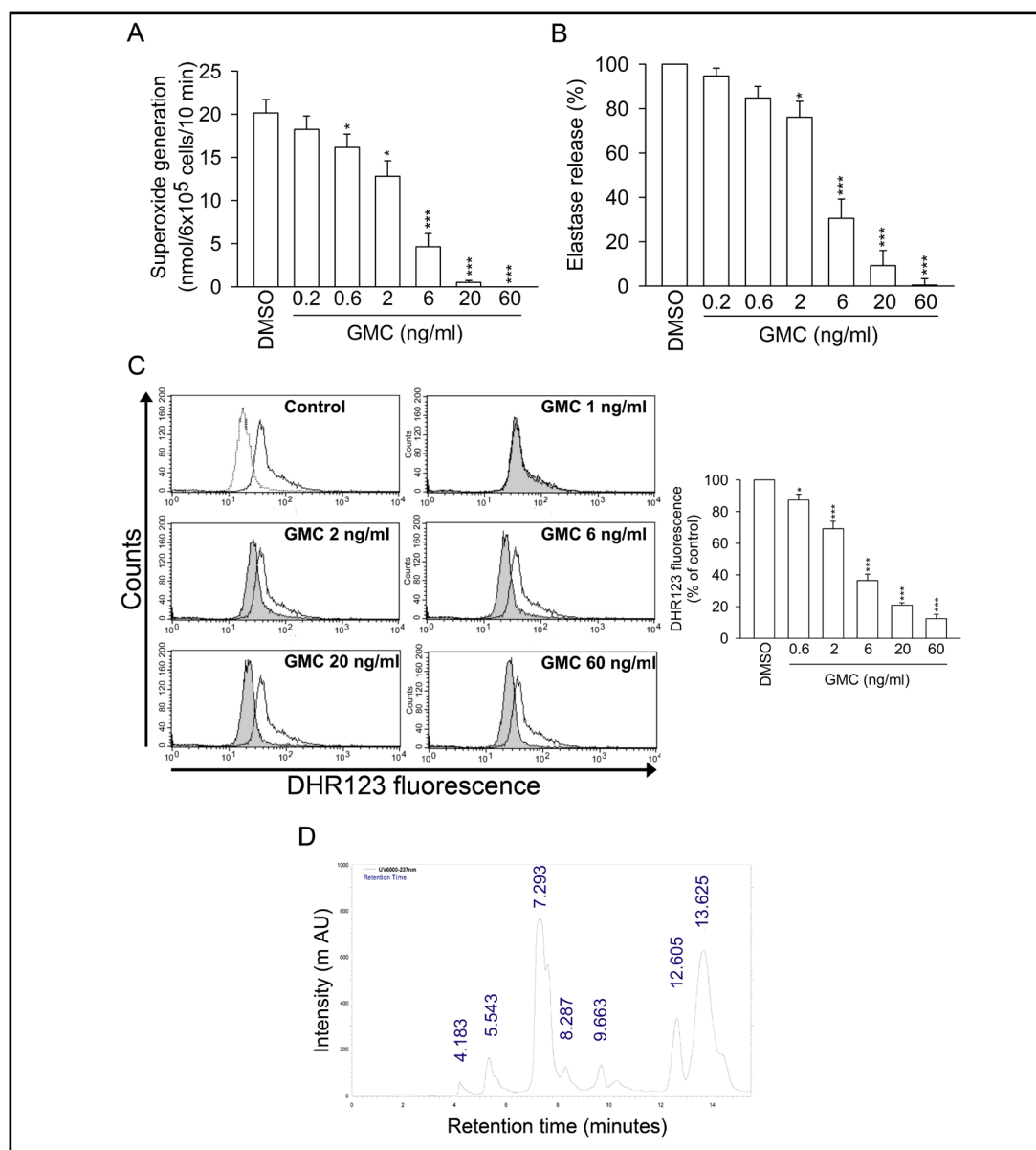


**Fig. 1.** GMC inhibits superoxide anion release, elastase degranulation, and ROS production in fMLF-stimulated human neutrophils. Neutrophils were treated with or without GMC (0.2–60 ng/ml) prior to being activated with fMLF (100 nM). The levels of (A) superoxide anion release and elastase degranulation were determined via spectrophotometric analysis. (C) Neutrophils stained with DHR123 dye were treated with or without GMC (0.6–60 ng/ml) followed by stimulation with fMLF (100 nM) and flow cytometry monitoring. The gray area indicates the basal group comprising neutrophils without any fMLF or GMC treatment. The black lines indicate the treatment groups. (D) Chromatographic analysis of GMC. Experiments were conducted independently eight times for A and B and five times for C. Values are expressed as mean  $\pm$  SEM. \* $p < 0.05$ , \*\*\* $p < 0.001$  compared with the control.

to be cytotoxic to human neutrophils. GMC was obtained via ethyl acetate extraction from a novel active fraction of a medicinal herb in conjunction with high-performance liquid chromatography (HPLC) to ensure quality control. A fingerprint chromatogram of GMC is shown in Fig. 1D. The full-scan assay revealed that separation at a wavelength of 237 nm was superior to that at other wavelengths. A group of peaks and a characteristic peak at 7.293 min of retention time were observed in the fingerprint chromatogram (Fig. 1D).

*GMC fails to directly scavenge superoxide anions or suppress elastase activity*

We used a xanthine/xanthine oxidase system and DPPH assays to evaluate the direct effects of superoxide anion-scavenging and anti-oxidation. Even at a high dose (2  $\mu\text{g/ml}$ ), GMC remained non-reactive in these cell-free systems (Fig. 2A and B). Superoxide dismutase and  $\alpha$ -tocopherol were used as positive controls. As shown in Fig. 2C, GMC did not have a direct effect on the inhibition of elastase activity.

*GMC does not inhibit superoxide anion release or elastase degranulation in non-FPR1 agonist-activated neutrophils*

To examine the anti-inflammatory effects of GMC in non-FPR1 agonist-activated neutrophils, we used WKYMVm (dual FPR1/FPR2 agonist), PMA (protein kinase C activator), LTB<sub>4</sub> (BLT1 receptor agonist), or NaF (direct G protein activator) to trigger neutrophil functions. GMC failed to reduce superoxide anion release or elastase degranulation in non-FPR1 agonist-stimulated cells (Fig. 3).

*GMC competes with the receptor binding of the FPR1-specific ligand FNLFNKY in neutrophils*

Receptor binding analysis based on flow cytometry was used to assay the FPR1 binding affinity of GMC. FNLFNKY (a fluorescently labeled FPR1 ligand) is an fMLF analog. fMLF (used as a positive control) almost entirely blocked the binding affinity of FNLFNKY to neutrophils at a dose of 10  $\mu\text{M}$ . GMC notably reduced the linkage of FNLFNKY to FPR1 in a dose-dependent manner, as did the positive control fMLF (Fig. 4A and B). The concentration-response curve of fMLF in superoxide production is shown in Fig. 4C. GMC showed a distinct right shift in the concentration-response curves of fMLF for superoxide anion release, confirming GMC as a competitive FPR1 inhibitor.

*GMC binds FPR1 in non-neutrophil cells*

The inhibition of FPR1 by GMC was reproduced in non-neutrophil cells, including dibutyryl cAMP-differentiated THP-1 and hFPR1-transfected HEK293 cells. Again, GMC dose-dependently reduced the FPR1 binding of FNLFNKY in THP-1 and HEK293 cells (Fig. 5). GMC showed specificity for FPR1 binding in FPR1-expressing cells.

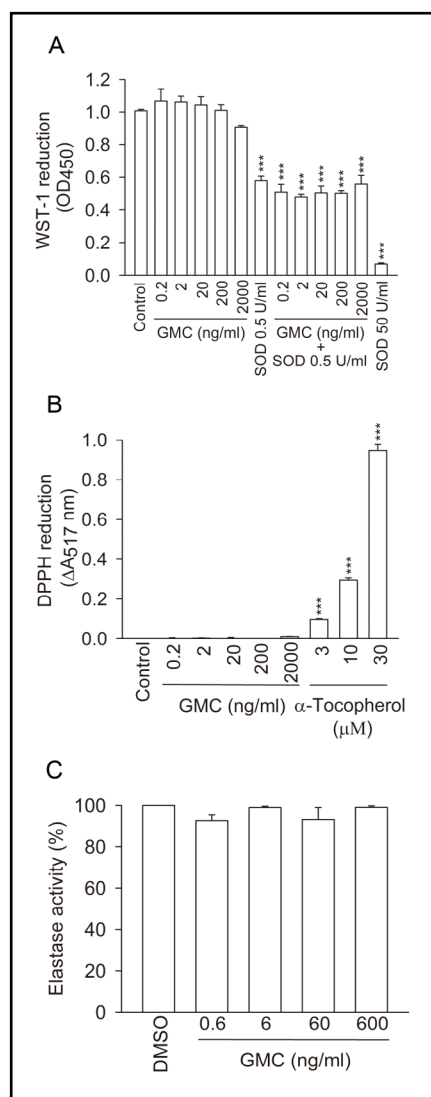


**Fig. 2.** GMC does not have inhibitory effects in cell-free systems. Reductions in (A) WST-1 and (B) DPPH were assayed spectrophotometrically at 450 and 517 nm, respectively. (C) Conditioned medium was produced from the supernatant of activated neutrophils, followed by treatment with or without GMC prior to substrate addition. All experiments were conducted independently three times. Values are expressed as mean  $\pm$  SEM. \*\*\* $p < 0.001$  compared with the control. SOD, superoxide dismutase.



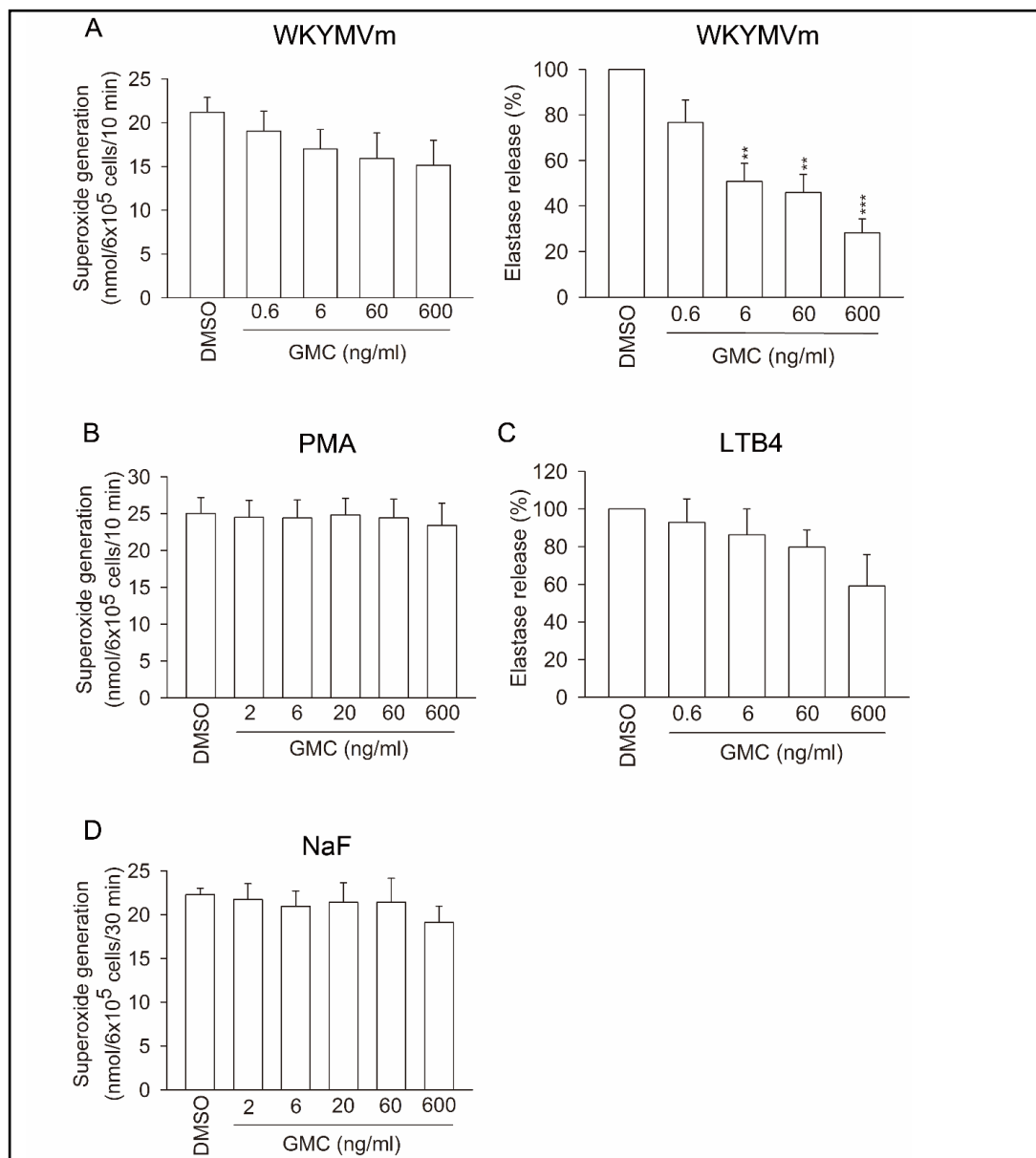


**Fig. 3.** GMC fails to inhibit superoxide anion release and elastase degranulation in non-FPR1 agonist-stimulated neutrophils. Neutrophils were treated with or without GMC (0.6–600 ng/ml) and activated with (A) WKYMVm (2 nM), (B) PMA (5 nM), (C) LTB<sub>4</sub> (100 nM), or (D) NaF (20 mM). Superoxide anion production or elastase release was determined using spectrophotometric analysis. Experiments were conducted independently four times for A and B, five times for C, and three times for D. Values are expressed as mean ± SEM. \*\*p<0.01, \*\*\*p<0.001 compared with the control.

#### *The inhibitory effects of GMC are not mediated through protein kinase A signaling*

cAMP/PKA has been closely associated with negative regulatory effects in human neutrophils [20]. The protein kinase A (PKA) antagonist H89 was unable to abolish the inhibitory effects of GMC on superoxide anion release and elastase degranulation (Fig. 6A and B). As shown in Fig. 6C, rolipram (phosphodiesterase 4 inhibitor), but not GMC, elevated intracellular cAMP concentrations in fMLF-stimulated neutrophils. Collectively, our results confirm that the suppressive effects of GMC are not associated with the cAMP/PKA signaling pathway.

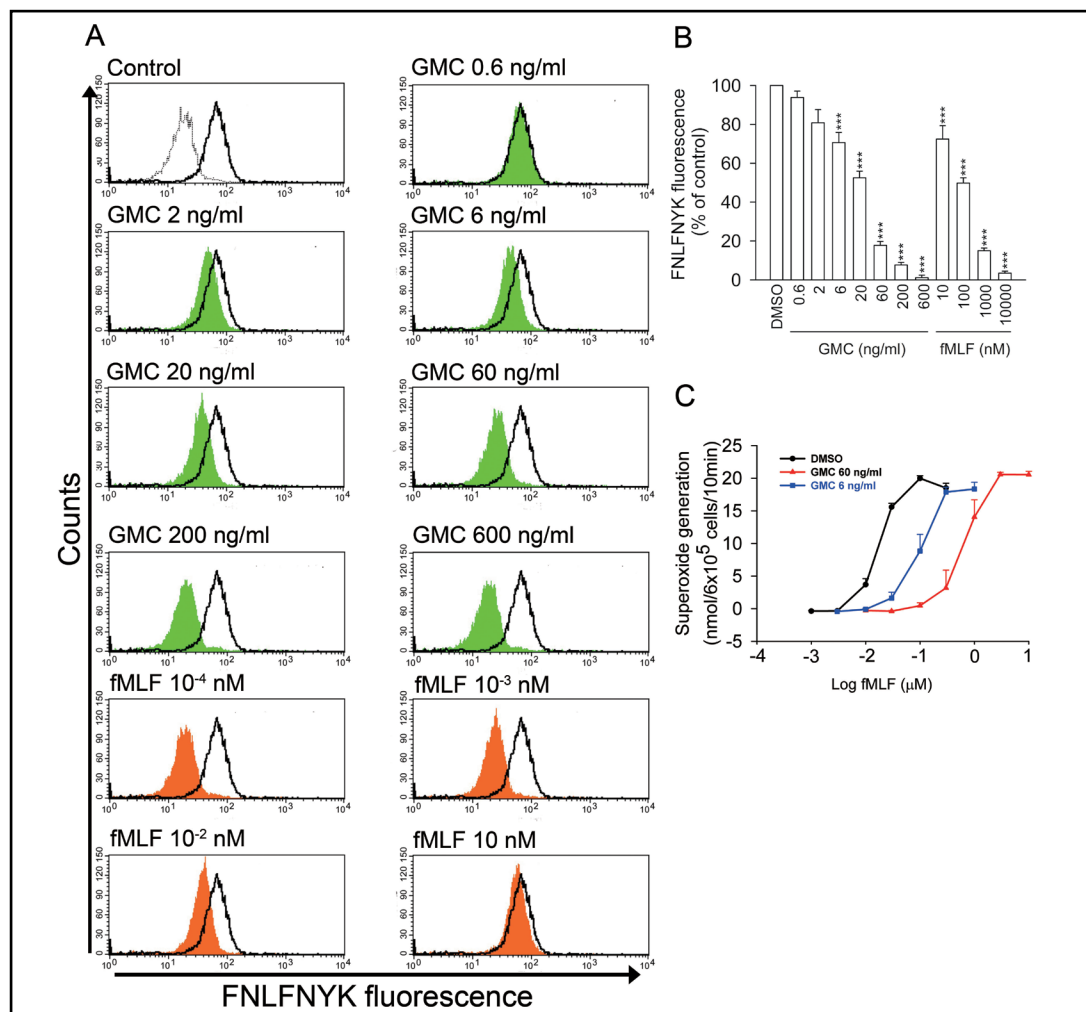


**Fig. 4.** GMC blocks receptor binding of FNLFNK and exerts competitive inhibitory effects in human neutrophils. (A) Neutrophils were treated with GMC or fMLF (10  $\mu$ M) for 5 min and then stained with the fluorescent FPR1 ligand FNLFNK (4 nM). The green or orange area indicates DMSO alone in the absence of FNLFNK. The black lines indicate testing groups with GMC or fMLF in the presence of FNLFNK. (B) The mean fluorescence intensity (MFI) was compared by reference to the control group (100%) (C) Neutrophils were treated with GMC (6 and 60 ng/ml) for 5 min. Superoxide anion production was activated using increasing concentrations of fMLF (1.0–10000 nM). All experiments were conducted independently three or four times. \*\*\* $p < 0.001$  compared with the control.

#### *GMC specifically reduces fMLF-induced $Ca^{2+}$ mobilization in neutrophils*

$Ca^{2+}$  mobilization is associated with numerous inflammation-related reactions in neutrophils. Activation of G protein-coupled receptors results in two phases of calcium mobilization in neutrophils. Initially, activation of G protein-coupled receptors induces phospholipase C $\beta$  and IP $_3$  to trigger rapid calcium release from intracellular endoplasmic reticulum. Then, a prolonged  $Ca^{2+}$  influx develops after  $Ca^{2+}$  release-activated  $Ca^{2+}$  channels are activated [22]. The cytosolic  $Ca^{2+}$  elevation will rapidly diminish to reach basal values within several minutes [23]. We examined the effects of GMC on  $Ca^{2+}$  signaling in activated neutrophils. GMC significantly reduced the  $[Ca^{2+}]_i$  peak induced by fMLF in a dose-dependent manner (Fig. 7A). In contrast, the  $[Ca^{2+}]_i$  peak induced by other stimulants (WKYMVm and LTB $_4$ ) was unaffected by GMC (Fig. 7B and C). These findings indicate that GMC specifically suppresses  $Ca^{2+}$  signals in FPR1 agonist-stimulated neutrophils.

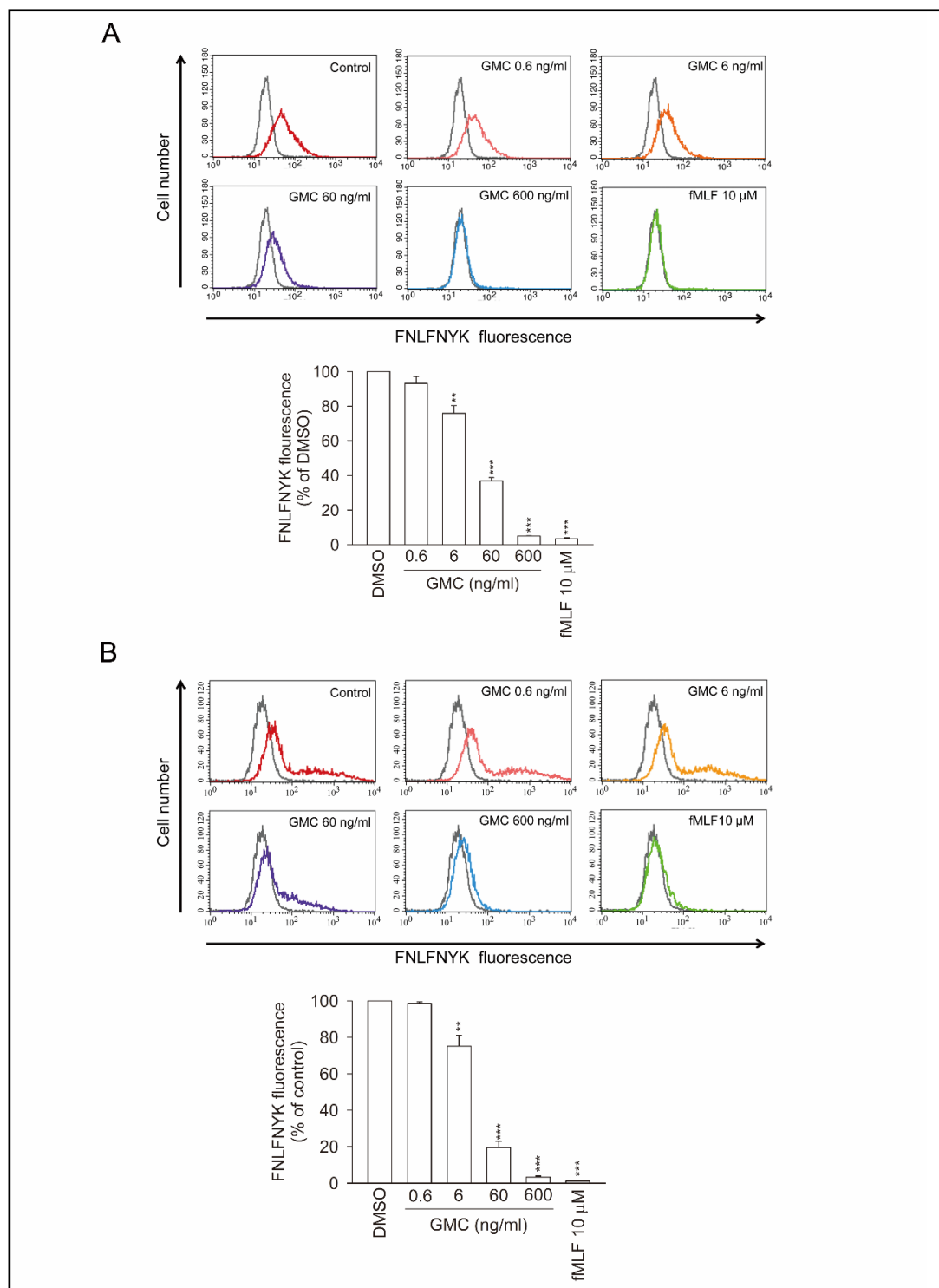
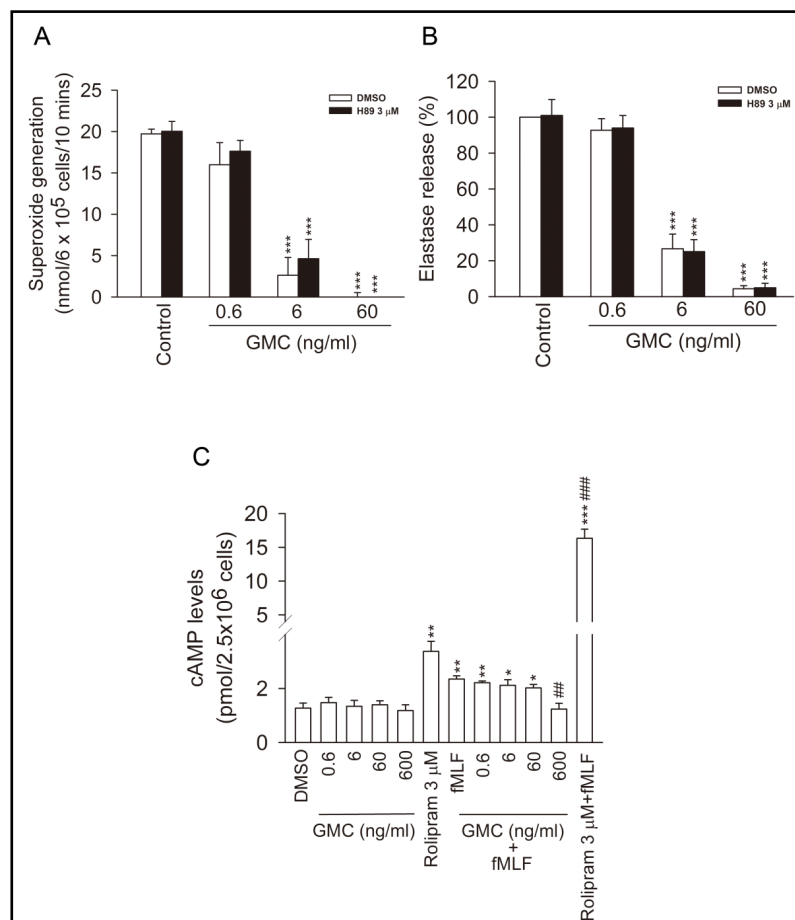


**Fig. 5.** GMC blocks the binding of FNLFNK to FPR1 in non-neutrophil cultured cells. (A) Differentiated THP-1 and (B) hFPR1-transfected HEK293 cells were treated with GMC (0.6–600 ng/ml) or fMLF (10 μM) for 5 min and then stained with the fluorescent FPR1 ligand FNLFNK (4 nM). The black line denotes the basal group, which was incubated using DMSO only in the absence of FNLFNK. The colored lines denote the test groups, which were administered DMSO, GMC, or fMLF in the presence of FNLFNK. The MFI was compared with a reference control group (100%). All experiments were conducted independently three times. \*\*p < 0.01, \*\*\*p < 0.001 compared with the control.

**Fig. 6.** cAMP/PKA signaling does not mediate the inhibitory effects of GMC. Neutrophils were pretreated with a PKA inhibitor, H89 (3  $\mu$ M), prior to the addition of GMC. (A) Superoxide production and (B) elastase degranulation were stimulated using fMLF. (C) Cells were incubated with GMC (0.6–600 ng/ml) or rolipram (3  $\mu$ M, positive control) with or without fMLF (100 nM). cAMP levels were measured using ELISA kits. All experiments were conducted independently three or four times. Values are expressed as mean  $\pm$  SEM. \* $p$ <0.05, \*\* $p$ <0.01, \*\*\* $p$ <0.001 compared with the control. ## $p$ <0.01 versus fMLF alone.



#### GMC attenuates MAPK and Akt phosphorylation with high specificity in fMLF-stimulated neutrophils

In the next experiments, we evaluated the effects of GMC on the phosphorylation of MAPK and Akt proteins. Our results revealed the rapid phosphorylation of MAPKs and Akt in fMLF-, WKYMVm-, PMA-, and LTB<sub>4</sub>-activated neutrophils. GMC specifically inhibited the fMLF-induced phosphorylation of MAPKs and Akt in human neutrophils (Fig. 8A). GMC did not inhibit the phosphorylation of MAPKs or Akt in WKYMVm-, PMA-, or LTB<sub>4</sub>-activated human neutrophils (Fig. 8B and C).

#### GMC ameliorates lung inflammation in an LPS-induced ALI mouse in vivo

Histological analysis of LPS-induced ALI in mice revealed neutrophil infiltration (Ly6G<sup>+</sup> cells), interstitial edema, and alveolar wall thickening. GMC treatment reduced neutrophil infiltration and thickening of the alveolar wall in the presence of LPS. GMC alone and sham groups showed no signs of airspace inflammation or a reduction in neutrophil infiltration. Thus, GMC reduced the effects of lung injury in an LPS-induced ALI mouse model (Fig. 9A).

The wet-to-dry weight ratio of mouse lungs was used to indicate the degree of pulmonary edema. The calculated ratios in LPS-treated lung exceeded those of the sham groups. GMC treatment clearly mediated the increase in the wet-to-dry weight ratios in LPS-treated lungs (Fig. 9B). Moreover, MPO activity mirrors neutrophil infiltration [24]. LPS treatment significantly increased MPO activity compared with the sham group while GMC administration significantly suppressed the increase in MPO activity in the LPS-treated groups (Fig. 9C).



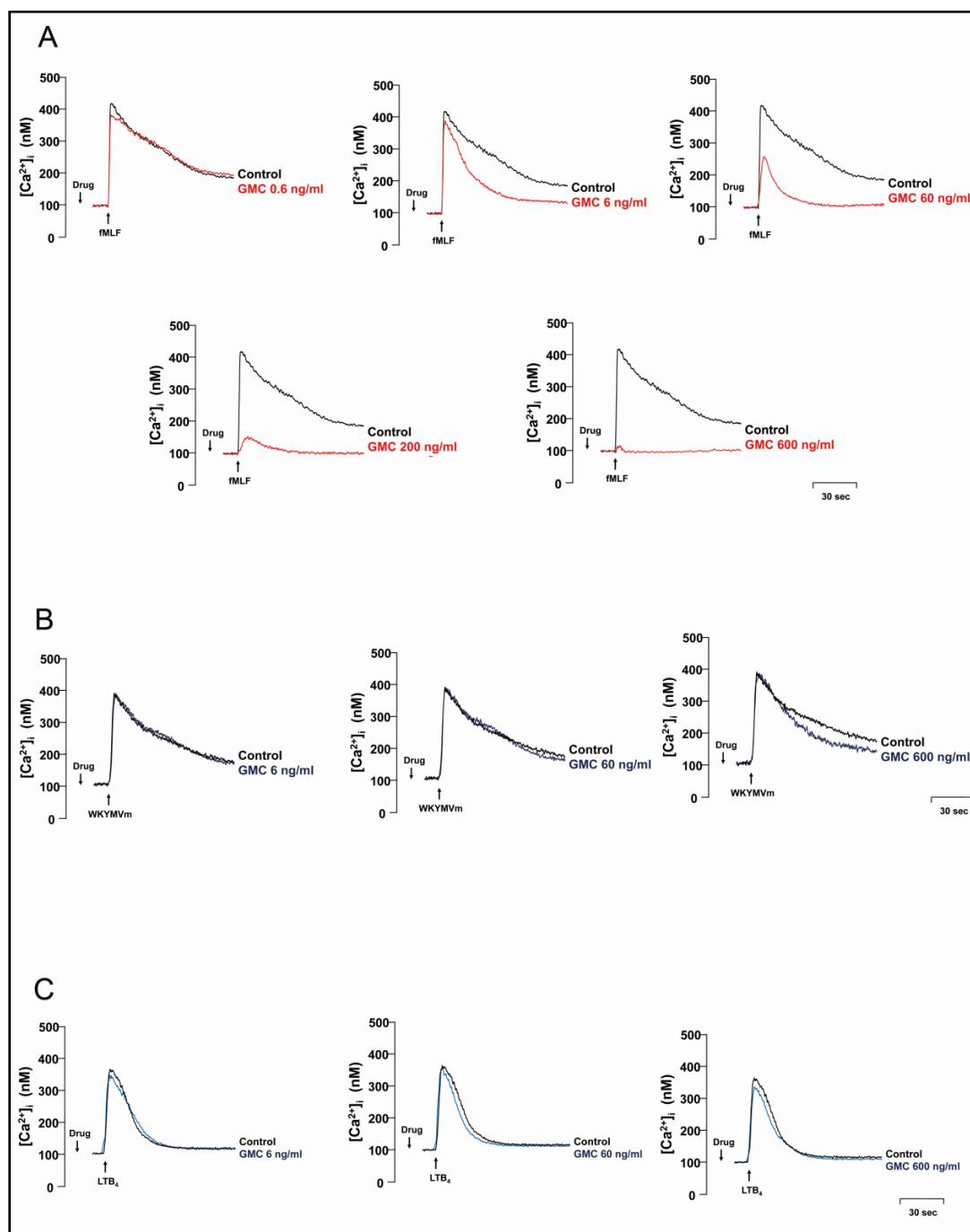


**Fig. 7.** GMC inhibits intracellular calcium mobilization specifically in fMLF-stimulated neutrophils. Neutrophils stained with fluo-3/AM (2  $\mu$ M) were treated with GMC and induced using (A) fMLF (100 nM), (B) WKYMVm (2 nM), or (C) LTB<sub>4</sub> (100 nM). All experiments were conducted independently three to six times.

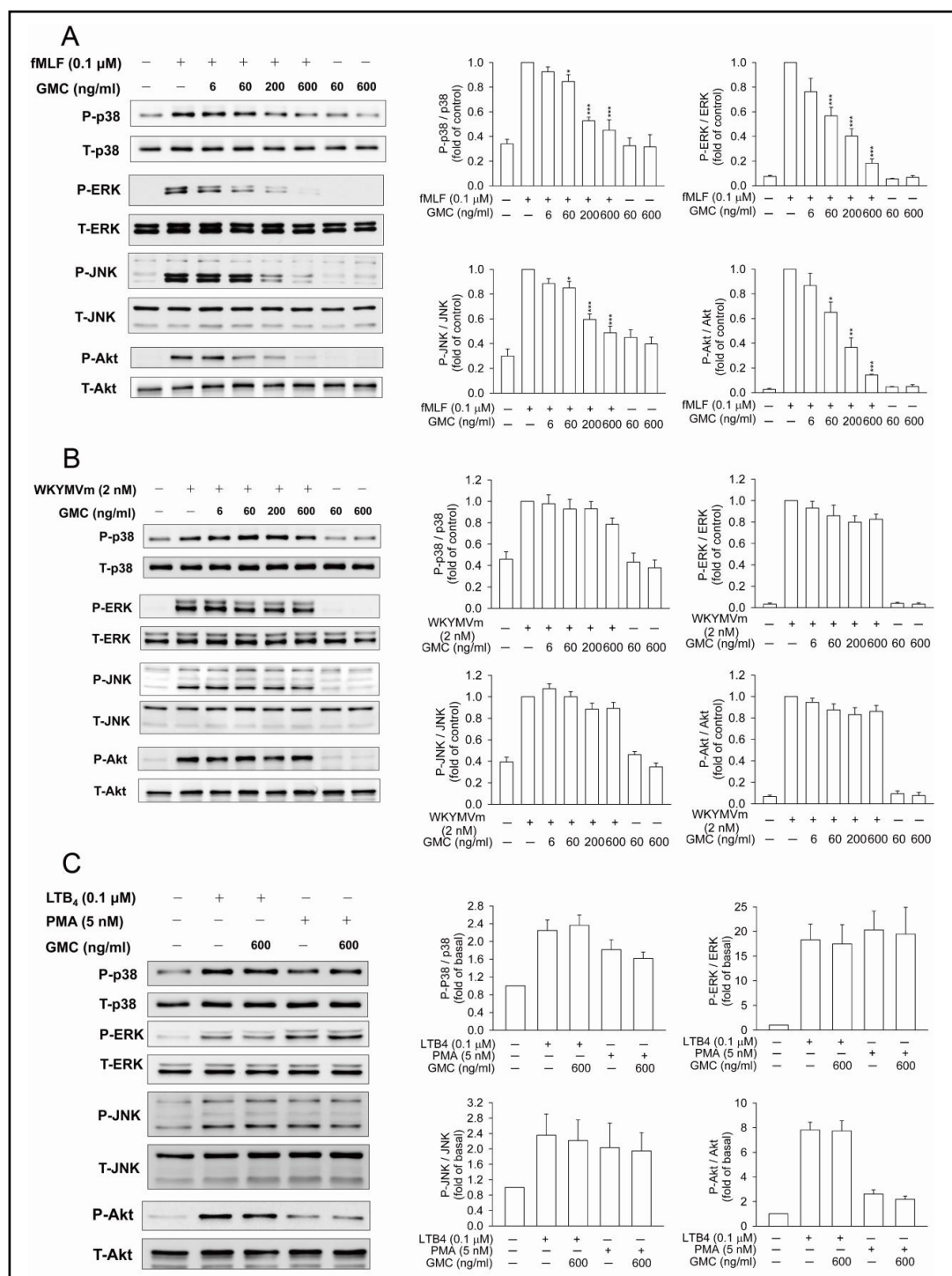
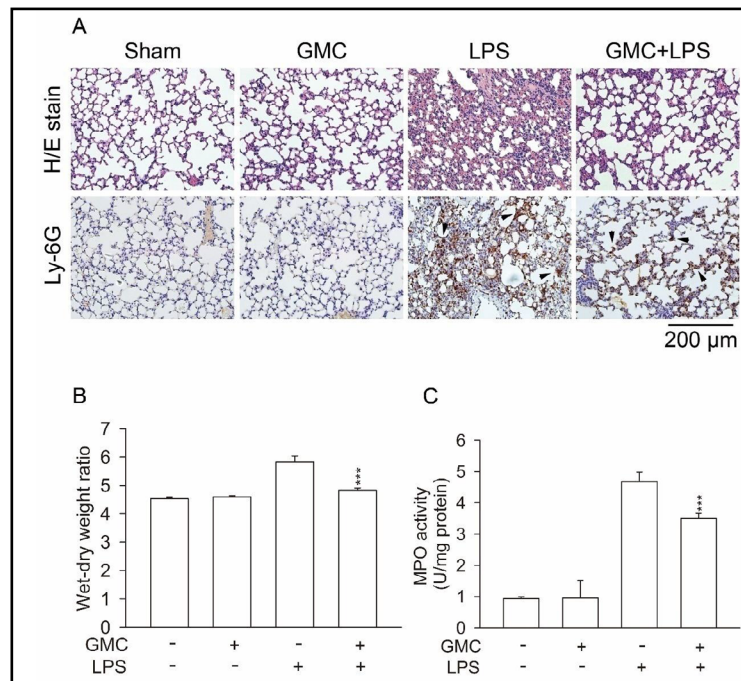


**Fig. 8.** GMC significantly suppresses the phosphorylation of MAPK and Akt protein in fMLF-stimulated neutrophils. Neutrophils were treated with GMC for 5 min and then stimulated for 1 min using (A) fMLF (100 nM), (B) WKYMVm (2 nM), (C) LTB<sub>4</sub> (100 nM), or PMA (5 nM). Phosphorylation of p38, ERK, JNK, and Akt was assessed by immunoblotting using antibodies corresponding to the target proteins. The intensity of blotted proteins was determined using a densitometer and normalized to reference values obtained from the corresponding total protein values. All experiments were conducted independently four or five times. All data are summarized as mean  $\pm$  SEM compared with the control. \*p<0.05, \*\*p<0.01, \*\*\*p<0.001 versus the corresponding control group.

**Fig. 9.** GMC ameliorates lung inflammation in LPS-induced ALI mice. C57BL/6 male animals were intraperitoneally administered the vehicle or GMC (100 mg/kg) 1 h before LPS (160 ng/g) was sprayed into the trachea to induce ALI. All mice were divided into four groups: sham, GMC only, LPS only, and LPS+GMC. (A) Photomicrographic image showing hematoxylin & eosin-stained lung sections obtained using a light microscope with a 200× objective lens. Immunohistochemical staining of neutrophilic Ly-6G proteins indicated by arrows was also present in tissues. (B) Wet-to-dry weight ratios of lung samples and (C) MPO activity. Values are expressed as mean ± SEM from six mice in each group. \*\*\*p<0.001 versus the LPS group.



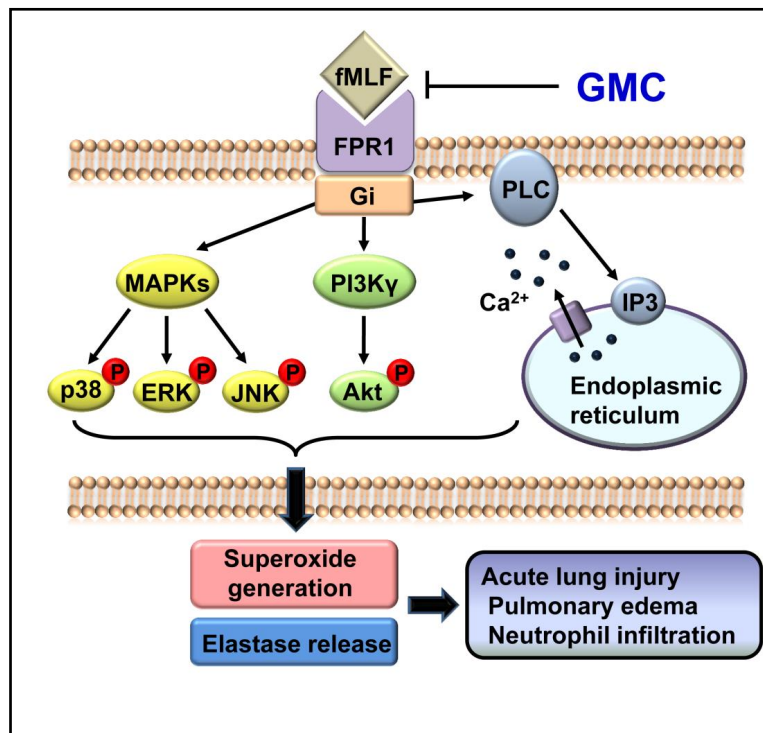
## Discussion

Exogenous pathogen infection or endogenous tissue damage induces neutrophil activation and the subsequent release of inflammatory mediators, thereby contributing to acute inflammatory responses [25, 26]. Uncontrolled or poorly regulated acute inflammation in the lung can lead to lethal ALI and ARDS. Dysregulation of excess neutrophil activation and the resulting immune responses greatly impair pulmonary endothelial function and occupy airway space during inflammation [27]. FPRs, particularly FPR1, are responsible for recognizing different endogenous or exogenous molecular stimuli in neutrophils and play a critical role in mediating neutrophil activation. A growing body of evidence supports claims that FPR1 antagonists have promising anti-inflammatory effects [28, 29]. In the present study, we demonstrate that a natural constituent extracted from *G. multiflora* Champ. strongly inhibits superoxide generation, elastase release, and ROS production by selectively and competitively blocking FPR1 in *N*-formyl peptide-stimulated cells. GMC also prevented LPS-induced ALI in our animal study. These findings suggest GMC as a novel FPR1 inhibitor that could help in the regulation of neutrophil-dominated inflammation.

GMC had concentration-dependent inhibitory effects on respiratory burst and elastase degranulation in fMLF-activated neutrophils. GMC decreased oxidative stress by limiting the extracellular release of superoxides and the intracellular generation of superoxides. In cell-free assays, we found that none of the aforementioned inhibitory effects were associated with free radical scavenging ability or drug cytotoxicity. The effects were clearly associated with FPR1-mediated downstream signaling pathways.

FPRs are G protein-coupled receptors that are expressed primarily on the cell membrane of phagocytes [8]. FPR1 and FPR2 are homologous receptors that are activated by binding to an *N*-formyl methionine motif, which is generated from bacterial membrane components or from endogenous mitochondria [10, 30]. Infectious and sterile inflammation can both be initiated through FPR-mediated neutrophil activation. We used the well-known synthetic *N*-formyl peptide, fMLF, to study the involvement of FPR1 signaling transduction in neutrophil

**Fig. 10.** Schema demonstrating that GMC inhibits superoxide release and elastase degranulation in fMLF-stimulated human neutrophils and protects against LPS-induced ALI. GMC is a selective antagonist of FPR1. The anti-inflammatory effects of GMC are mediated by the blockage of formyl peptide binding to FPR1, resulting in a reduction in calcium mobilization and the activation of MAPK and Akt signaling. GMC protects mice from LPS-induced ALI.



activation. Hexapeptide WKYMVm was used to assay FPR1- and FPR2-mediated neutrophil activation [31]. PMA, LTB<sub>4</sub>, and NaF were used as non-FPR agonists for neutrophils. Our results revealed that GMC exhibits inhibitory effects only in fMLF- or WKYMVm-activated neutrophils but not in other non-FPR agonist-activated neutrophils. Moreover, receptor binding assays revealed that GMC significantly inhibited the binding of fMLF to FPR1 in activated neutrophils. GMC also presented competitive binding to FPR1 with FNLFNKYK in THP-1 and hFPR1-transfected HEK293 cells. These findings suggest that GMC is a potentially competitive FPR1 antagonist.

Many downstream signaling pathways are transduced by FPR1, including cAMP/PKA, calcium mobilization, MAPK, and Akt signaling [11]. The PKA inhibitor H89 is unable to abolish the inhibitory effects of GMC on fMLF-induced superoxide anion production and elastase release. FPR1-mediated neutrophil activation increases intracellular cAMP concentrations, thereby reducing respiratory burst and elastase degranulation [20, 21]. Agents mediated by PKA signaling, such as PDE4 inhibitors, synergistically increase cAMP levels in fMLF-stimulated neutrophils [20, 21]. In our study, GMC showed inhibitory rather than synergistic effects in fMLF-induced increases in cAMP levels. Taken together, we can deduce that the cAMP/PKA signaling pathway is not involved in these inhibitory effects of GMC in neutrophils. We subsequently assessed the effects of the FPR1-mediated downstream signaling pathway on neutrophil activation to identify the mechanisms underlying the protective effects of GMC, including intracellular calcium mobilization, MAPK, and PI3K/Akt pathways [32]. All of these signaling pathways mediate diverse immune responses in FPR1-stimulated neutrophils [23, 32, 33]. GMC dose-dependently decreased the concentration of the peak calcium influx in fMLF-stimulated neutrophils but not in non-FPR1 agonist-stimulated neutrophils. In western blot assays, GMC had concentration-dependent inhibitory effects on MAPK and Akt phosphorylation in fMLF-stimulated neutrophils but not in WKYMVm- or LTB<sub>4</sub>-activated cells. Our results support our hypothesis that GMC inhibits fMLF-induced superoxide anion release, elastase degranulation, and ROS production in human neutrophils. The mediation of these inhibitory effects is enabled by blockade of the downstream pathways of FPR1.

N-formyl peptides may facilitate neutrophil mobilization and recruitment to sites of inflammation, resulting in lung damage [34, 35]. Chemotaxis and the migration of fMLF-



stimulated neutrophils are both absent in FPR knockout mice [36]. FPR1 signaling facilitates neutrophil activation and infiltration in endotoxin-induced ALI, and FPR1 antagonists alleviate pulmonary damage and edema [13, 16]. In the present study, we evaluated the anti-inflammatory effects and therapeutic value of GMC in a mouse model of LPS-induced ALI. LPS and fMLF are components of bacterial membranes that chemotactically attract neutrophils into inflamed lung tissue during the progression of pathogenesis. LPS triggers marked immune reactions, leading to ALI or septic shock, which have high mortality rates [37]. The severity of LPS-induced ALI is closely related to neutrophil activation and infiltration in the lung [38]. Our findings suggest that GMC decreases alveolar wall disruption, pulmonary hemorrhage and edema, and neutrophil infiltration among mice with ALI-induced LPS. Our results indicate GMC as a novel FPR1 inhibitor, with the potential to cure neutrophil-related inflammation.

## Conclusion

The results obtained in this study demonstrate that GMC acts as a natural selective FPR1 inhibitor. GMC markedly suppresses the expressions of superoxide anion, reactive oxidants derived therefrom, and elastase in fMLF-stimulated human neutrophils. All inhibitory effects are mediated by blockade of FPR1 binding, which also reduces calcium mobilization and MAPK and Akt activation (Fig. 10). Our results suggest the potential development of GMC as a therapeutic treatment for critically lethal ALI.

## Abbreviations

ALI (acute lung injury); Akt (protein kinase B); ARDS (acute respiratory distress syndrome); cAMP (cyclic adenosine monophosphate); CB (cytochalasin B); DMSO (dimethyl sulfoxide); FBS (fetal bovine serum); DPPH (diphenyl picrylhydrazyl); FACS (fluorescence-activated cell sorting); fMLF (*N*-formyl-L-methionyl-L-leucyl-L-phenylalanine); FNLFNKYK (*N*-formyl-Nle-Leu-Phe-Nle-Tyr-Lys-fluorescein); FPR (formyl peptide receptor); GMC (fruit extraction from *Garcinia multiflora* Champ); H89 (N-[2-(p-Bromocinnamylamino) ethyl]-5-isoquinolinesulfonamide); HBSS (Hank's balanced salts solution); HPLC (high performance liquid chromatography); IC50 (half maximal inhibitory concentration); LDH (lactate dehydrogenase); LPS (lipopolysaccharide); LTB4 (leukotriene B4); MAPK (mitogen-activated protein kinase); MFI (mean fluorescence intensity); MPO (myeloperoxidase); NAF (sodium fluoride); PAF (platelet-activating factor); PKA; protein (kinase A); PMA (phorbol myristate acetate); RPMI (Roswell Park Memorial Institute); ROS (reactive oxygen species); SEM (standard error of the mean); SOD (superoxide dismutase); WKYMVm (Trp-Lys-Tyr-Met-Val-D-Met); WST-1 (water soluble tetrazolium-1.).

## Acknowledgements

This study was supported by the grants from the Ministry of Science Technology (MOST 106-2320-B-255-003-MY3, MOST 104-2320-B-255-004-MY3, and MOST 106-2320-B-182A-002-MY2), Ministry of Education (EMRPD1G0231), and Chang Gung Memorial Hospital (CMRPF1F0011~3, CMRPF1F0061~3, CMRPG3G1201, and BMRP450), Taiwan.

## Disclosure Statement

The authors declare that no conflicts of interest exist.

## References

- 1 von Andrian UH, Berger EM, Ramezani L, Chambers JD, Ochs HD, Harlan JM, Paulson JC, Etzioni A, Arfors KE: *In vivo* behavior of neutrophils from two patients with distinct inherited leukocyte adhesion deficiency syndromes. *J Clin Invest* 1993;91:2893-2897.
- 2 Bai J, Tang L, Lomas-Neira J, Chen Y, McLeish KR, Uriarte SM, Chung CS, Ayala A: TAT-SNAP-23 treatment inhibits the priming of neutrophil functions contributing to shock and/or sepsis-induced extra-pulmonary acute lung injury. *Innate Immun* 2015;21:42-54.
- 3 Tsai YF, Hwang TL: Neutrophil elastase inhibitors: a patent review and potential applications for inflammatory lung diseases (2010 - 2014). *Expert Opin Ther Pat* 2015;25:1145-1158.
- 4 Wang Y, Xiao Y, Zhong L, Ye D, Zhang J, Tu Y, Bornstein SR, Zhou Z, Lam KS, Xu A: Increased neutrophil elastase and proteinase 3 and augmented NETosis are closely associated with beta-cell autoimmunity in patients with type 1 diabetes. *Diabetes* 2014;63:4239-4248.
- 5 Wiener-Kronish JP, Gropper MA, Matthay MA: The adult respiratory distress syndrome: definition and prognosis, pathogenesis and treatment. *Br J Anaesth* 1990;65:107-129.
- 6 Davey A, McAuley DF, O'Kane CM: Matrix metalloproteinases in acute lung injury: mediators of injury and drivers of repair. *Eur Respir J* 2011;38:959-970.
- 7 Tiruvoipati R, Botha J, Peek G: Effectiveness of extracorporeal membrane oxygenation when conventional ventilation fails: valuable option or vague remedy? *J Crit Care* 2012;27:192-198.
- 8 Le Y, Murphy PM, Wang JM: Formyl-peptide receptors revisited. *Trends Immunol* 2002;23:541-548.
- 9 Migeotte I, Communi D, Parmentier M: Formyl peptide receptors: a promiscuous subfamily of G protein-coupled receptors controlling immune responses. *Cytokine Growth Factor Rev* 2006;17:501-519.
- 10 Carp H: Mitochondrial N-formylmethionyl proteins as chemoattractants for neutrophils. *J Exp Med* 1982;155:264-275.
- 11 Dorward DA, Lucas CD, Chapman GB, Haslett C, Dhaliwal K, Rossi AG: The role of formylated peptides and formyl peptide receptor 1 in governing neutrophil function during acute inflammation. *Am J Pathol* 2015;185:1172-1184.
- 12 Tsai YF, Yang SC, Hwang TL: Formyl peptide receptor modulators: a patent review and potential applications for inflammatory diseases (2012-2015). *Expert Opin Ther Pat* 2016;10.1080/13543776.2016.12165461-18.
- 13 Yang SC, Chang SH, Hsieh PW, Huang YT, Ho CM, Tsai YF, Hwang TL: Dipeptide HCH6-1 inhibits neutrophil activation and protects against acute lung injury by blocking FPR1. *Free Radic Biol Med* 2017;106:254-269.
- 14 Selvatici R, Falzarano S, Mollica A, Spisani S: Signal transduction pathways triggered by selective formylpeptide analogues in human neutrophils. *Eur J Pharmacol* 2006;534:1-11.
- 15 Wenceslau CF, McCarthy CG, Szasz T, Gouloupoulou S, Webb RC: Mitochondrial N-formyl peptides induce cardiovascular collapse and sepsis-like syndrome. *Am J Physiol Heart Circ Physiol* 2015;308:H768-777.
- 16 Grommes J, Drechsler M, Soehnlein O: CCR5 and FPR1 mediate neutrophil recruitment in endotoxin-induced lung injury. *J Innate Immun* 2014;6:111-116.
- 17 Ting CW, Hwang TL, Chen IS, Cheng MJ, Sung PJ, Yen MH, Chen JJ: Garcimultiflorone G, a novel benzoylphloroglucinol derivative from *Garcinia multiflora* with inhibitory activity on neutrophil pro-inflammatory responses. *Chem Biodivers* 2014;11:819-824.
- 18 Lin YM, Anderson H, Flavin MT, Pai YH, Mata-Greenwood E, Pengsuparp T, Pezzuto JM, Schinazi RF, Hughes SH, Chen FC: *In vitro* anti-HIV activity of biflavonoids isolated from *Rhus succedanea* and *Garcinia multiflora*. *J Nat Prod* 1997;60:884-888.
- 19 Ting CW, Hwang TL, Chen IS, Yen MH, Chen JJ: A new benzoylphloroglucinol derivative with an adamantyl skeleton and other constituents from *Garcinia multiflora*: effects on neutrophil pro-inflammatory responses. *Chem Biodivers* 2012;9:99-105.
- 20 Tsai YF, Chu TC, Chang WY, Wu YC, Chang FR, Yang SC, Wu TY, Hsu YM, Chen CY, Chang SH, Hwang TL: 6-Hydroxy-5, 7-dimethoxy-flavone suppresses the neutrophil respiratory burst via selective PDE4 inhibition to ameliorate acute lung injury. *Free Radic Biol Med* 2017;106:379-392.
- 21 Tsai YF, Yu HP, Chung PJ, Leu YL, Kuo LM, Chen CY, Hwang TL: Osthol attenuates neutrophilic oxidative stress and hemorrhagic shock-induced lung injury via inhibition of phosphodiesterase 4. *Free Radic Biol Med* 2015;89:387-400.

- 22 Gupta AK, Giaglis S, Hasler P, Hahn S: Efficient neutrophil extracellular trap induction requires mobilization of both intracellular and extracellular calcium pools and is modulated by cyclosporine A. *PLoS One* 2014;9:e97088.
- 23 Tintinger G, Steel HC, Anderson R: Taming the neutrophil: calcium clearance and influx mechanisms as novel targets for pharmacological control. *Clin Exp Immunol* 2005;141:191-200.
- 24 Arnhold J: Properties, functions, and secretion of human myeloperoxidase. *Biochemistry (Mosc)* 2004;69:4-9.
- 25 Boulay F, Tardif M, Bouchon L, Vignais P: Synthesis and use of a novel N-formyl peptide derivative to isolate a human N-formyl peptide receptor cDNA. *Biochem Biophys Res Commun* 1990;168:1103-1109.
- 26 Hazeldine J, Hampson P, Lord JM: The impact of trauma on neutrophil function. *Injury* 2014;45:1824-1833.
- 27 Tate MD, Deng YM, Jones JE, Anderson GP, Brooks AG, Reading PC: Neutrophils ameliorate lung injury and the development of severe disease during influenza infection. *J Immunol* 2009;183:7441-7450.
- 28 Kao W, Gu R, Jia Y, Wei X, Fan H, Harris J, Zhang Z, Quinn J, Morand EF, Yang YH: A formyl peptide receptor agonist suppresses inflammation and bone damage in arthritis. *Br J Pharmacol* 2014;171:4087-4096.
- 29 Schepetkin IA, Kirpotina LN, Khlebnikov AI, Cheng N, Ye RD, Quinn MT: Antagonism of human formyl peptide receptor 1 (FPR1) by chromones and related isoflavones. *Biochem Pharmacol* 2014;92:627-641.
- 30 Marasco WA, Phan SH, Krutzsch H, Showell HJ, Feltner DE, Nairn R, Becker EL, Ward PA: Purification and identification of formyl-methionyl-leucyl-phenylalanine as the major peptide neutrophil chemotactic factor produced by *Escherichia coli*. *J Biol Chem* 1984;259:5430-5439.
- 31 Christophe T, Karlsson A, Dugave C, Rabiet MJ, Boulay F, Dahlgren C: The synthetic peptide Trp-Lys-Tyr-Met-Val-Met-NH<sub>2</sub> specifically activates neutrophils through FPRL1/lipoxin A<sub>4</sub> receptors and is an agonist for the orphan monocyte-expressed chemoattractant receptor FPRL2. *J Biol Chem* 2001;276:21585-21593.
- 32 Korkmaz S, Erturan I, Naziroglu M, Uguz AC, Cig B, Ovey IS: Colchicine modulates oxidative stress in serum and neutrophil of patients with Behcet disease through regulation of Ca<sup>2+</sup>(+) release and antioxidant system. *J Membr Biol* 2011;244:113-120.
- 33 Chen LW, Lin MW, Hsu CM: Different pathways leading to activation of extracellular signal-regulated kinase and p38 MAP kinase by formyl-methionyl-leucyl-phenylalanine or platelet activating factor in human neutrophils. *J Biomed Sci* 2005;12:311-319.
- 34 Bleyl JU, Heller AR, Fehrenbach A, Heintz M, Fehrenbach H, Klenz G, Gama de Abreu M, Hubler M, Spieth PM, Koch T: Pretreatment with perfluorohexane vapor attenuates fMLP-induced lung injury in isolated perfused rabbit lungs. *Exp Lung Res* 2010;36:342-351.
- 35 Schiffmann E, Showell HV, Corcoran BA, Ward PA, Smith E, Becker EL: The isolation and partial characterization of neutrophil chemotactic factors from *Escherichia coli*. *J Immunol* 1975;114:1831-1837.
- 36 Gao JL, Lee EJ, Murphy PM: Impaired antibacterial host defense in mice lacking the N-formylpeptide receptor. *J Exp Med* 1999;189:657-662.
- 37 Michie HR, Manogue KR, Spriggs DR, Revhaug A, O'Dwyer S, Dinarello CA, Cerami A, Wolff SM, Wilmore DW: Detection of circulating tumor necrosis factor after endotoxin administration. *N Engl J Med* 1988;318:1481-1486.
- 38 Yoshikawa T, Takano H, Takahashi S, Ichikawa H, Kondo M: Changes in tissue antioxidant enzyme activities and lipid peroxides in endotoxin-induced multiple organ failure. *Circ Shock* 1994;42:53-58.

## Research Article

# Nanobubbles Water Curcumin Extract Reduces Injury Risks on Drop Jumps in Women: A Pilot Study

I-Lin Wang <sup>1</sup>, Chien-Yu Hsiao,<sup>2,3,4</sup> Yu-Heng Li,<sup>1</sup> Fan-Bo Meng,<sup>5</sup>  
Chi-Chang Huang <sup>6</sup> and Yi-Ming Chen <sup>1</sup>

<sup>1</sup>Health Technology College, Jilin Sport University, Changchun 130022, Jilin, China

<sup>2</sup>Department of Nutrition and Health Sciences, Chang Gung University of Science and Technology, Taoyuan 33301, Taiwan

<sup>3</sup>Research Center for Industry of Human Ecology and Research Center for Chinese Herbal Medicine, College of Human Ecology, Chang Gung University of Science and Technology, Taoyuan 33301, Taiwan

<sup>4</sup>Aesthetic Medical Center, Department of Dermatology, Chang Gung Memorial Hospital, Taoyuan 33301, Taiwan

<sup>5</sup>Cardiovascular Department, China-Japan Union Hospital, Jilin University, Changchun 130033, China

<sup>6</sup>Graduate Institute of Sports Science, National Taiwan Sport University, Taoyuan 33301, Taiwan

Correspondence should be addressed to Chi-Chang Huang; [john5523@ntsus.edu.tw](mailto:john5523@ntsus.edu.tw) and Yi-Ming Chen; [1021302@ntsus.edu.tw](mailto:1021302@ntsus.edu.tw)

Received 28 November 2018; Revised 14 February 2019; Accepted 20 February 2019; Published 1 April 2019

Academic Editor: Francesca Mancianti

Copyright © 2019 I-Lin Wang et al. This is an open access article distributed under the Creative Commons Attribution License, which permits unrestricted use, distribution, and reproduction in any medium, provided the original work is properly cited.

**Purpose.** To verify the beneficial effects of Nanobubbles water curcumin extract (NCE) supplementation on health promotion and to demonstrate the application of NCE in reducing the risk of musculoskeletal injury. **Methods.** In the current study, 12 females were randomly assigned to NCE (15g/day) and maltodextrin groups. Performance and related body composition were evaluated at 2 time points—presupplementation (pre-) and after 4 weeks of postsupplementation (post-). The posttest consists of a set of biochemical parameters for antifatigue activity and injury status evaluation. **Results.** NCE group exhibited significantly lower levels of alanine aminotransferase (ALT), alkaline phosphatase (ALP), triglycerides (TG), and higher high-density lipoprotein (HDL) after a 4-week supplementation, compared with the placebo group. After a 15-minute session on the spinning bike, serum lactate and ammonia levels were decreased and glucose was economized in the NEC group. 4-week-NCE supplementation was also able to reduce the peak vertical ground reaction force (PVGRF) during drop jump. Therefore, the risk of musculoskeletal system in lower extremity could be reduced. **Conclusion.** We demonstrate that 4-week-NCE supplementation can also be used in explosiveness exercise for better physiological adaptation. Thus, NCE has potential for use with nutrient supplements toward a variety of benefits for athletics.

## 1. Introduction

The nanobubbles (NBs) or microbubbles (MBs) technology in combination with the coagulation/flocculation process has been used effectively to improve the efficiency of drug delivery [1]. Nanobubbles is produced by collapsing microbubble (less or equal to 50  $\mu\text{m}$  in diameter) in the electrolyte under ultra-high temperature and pressure to form gas nuclei <100 nm in diameter [2]. Several studies have shown the use of these NBs water in medical applications: NB water increases blood-brain barrier permeability [3], is used as an adjunct to periodontal treatment due to its potent antimicrobial effect [2], and has been reported to help in the prevention of kidney stones [4].

The main constituent of turmeric (*Curcuma longa*), curcumin, has been extensively used as a spice, food preservative, and coloring material in China, India, and South East Asia [5]. Also used in traditional medicine, curcumin has a broad range of exercise-related bioactivities including being used as an ergogenic aid for exercise performance [6], reducing endurance exercise-induced inflammation [7], and mitigating the negative effects associated with eccentric exercise-induced muscle damage [8, 9]. In this study, we attempt to use the unique NBs technology in the development of a nanobubble water curcumin extract (NCE) for use as an ergogenic aid.

Certain substances or drugs are termed ergogenic; i.e., they are able to enhance performance by improving exercise energy efficiency, strength, condition, and endurance [10].



Ergogenic aids have been used for centuries, although there has been growing scientific evidence and support for their effects. Athletes are increasingly turning to supplement to improve exercise performance. Their most common motivation is to improve attention, reduce reaction time and delay fatigue, reduce sensitivity to pain, and increase strength, training endurance, and alertness [11]. The performance of sports is broadly affected by neuromuscular functions (muscle strength, explosiveness, coordination, energy output (anaerobic, aerobic capacity), and joint mobility (muscle ductility) [12]. The use of these supplements is to be able to enhance both muscle function and motor performance. In order to achieve the highest performance in competitions, athletes need to shorten the compensatory period during long-term continuous exercise so as to accelerate or promote the body's recovery process. Ergogenic substances are able to reduce energy consumption, restore the internal dynamic balance environment, restore body mechanisms for nutrient regeneration, and optimize functional parameters to improve performance [13].

In our previous study of animal study, we demonstrated that curcumin could significantly increase exercise performance and mitigate the increase of physiological biomarkers induced by intensive aerobic training [6]. In the current clinical trial, we examine the antifatigue activity and beneficial effects of nanobubbles water applied on curcumin extract to enhance explosiveness without a training program. NCE supplementation may be helpful for athletes performing explosiveness-type exercises, as well as for overall physiological protective effects.

## 2. Materials and Methods

**2.1. Preparation of Nanobubble Water Curcumin Extract (NCE).** Nanobubbles (NBs) were generated by using a controllable platform of instant high pressure based on high speed grinding and cutting of water molecules in the presence of a magnet at 3000-4000 E. The NCE extraction process and formula (Leading curcumin®) was provided by Leading Auto. Bio Co. Ltd. (Hsinchu, Taiwan). Curcumin powder was soaked in NBs for 3-5 min until the NBs impacted all curcumin particles. After the NBs process, the sample was dried and stored at room temperature in a dark and dry cabinet. NCE was freshly prepared before each daily administration. The main constituents of curcumin, bisdemethoxycurcumin, and demethoxycurcumin were determined by high-performance liquid chromatography (HPLC) [14, 15]. The nutritional content and total amount of curcumin in NCE were analyzed by SGS Taiwan, Ltd. (New Taipei City, Taiwan).

**2.2. Experimental Design.** This single center, randomized, placebo-controlled double-blind, parallel group trial was approved by the Joint Institutional Review Board of Jilin Sport University (Changchun, China; JLSU-IRB no. 2018001). Subjects used in this study were volunteers from Jilin Sport University (JLSU). The subjects gave informed consent for inclusion before enrolment into the study which was conducted in accordance with the Declaration of Helsinki. After

enrolment, subjects were randomly allocated to 2 groups: nanobubbles water curcumin extract (NCE) or placebo (maltodextrin). Each group (n=6) consumed NCE (containing 230.9 mg curcumin) or placebo at 15 g/day daily before breakfast for 4 consecutive weeks. Both NCE and placebo were isocaloric at 43 kcal/day. Subjects attended 2 study visits on Day 0 (pretest) and Day 28 (posttest). The posttest visit was arranged after the last supplementation. Body composition and effects on exercise performance were measured at these visits [16].

**2.3. Subjects.** Twelve female Jilin Sport University students volunteered to participate in this study. All subjects have no regular exercise habit and individuals were excluded from the study if they had any known metabolic disorders, heart/cardiopulmonary diseases, diabetes, thyroid disease, hypogonadism, hepatorenal disease, musculoskeletal disorders, neuromuscular/neurological diseases, autoimmune diseases, cancer, peptic ulcers, or anemia. Subjects were asked to refrain from any aerobic or anaerobic exercise training while keeping their normal dietary pattern and daily caloric intake under control during the experimental period. Nutritional supplements including certain types of protein, antioxidants, creatine, and steroid supplementation were disallowed. Subjects were randomly assigned to the placebo or NCE group and the basic characteristics of age ( $21.2 \pm 1.1$  years), height ( $166.3 \pm 4.5$  vs.  $165.2 \pm 5.0$  cm), and weight ( $57.1 \pm 5.1$  vs.  $56.5 \pm 7.6$  kg) did not significantly differ before and after the study.

**2.4. Drop Jumps with Kinetic and Kinematic Analysis.** All subjects had to first complete the familiarization day to familiarize themselves with the test protocol and specific jumping techniques. The subjects were attired in shorts, sports bras, and indoor sneakers. Prior to the test protocol, the subjects had to warm up by stretching their high knees and lower jaw, performing gait swings and running for 20 minutes. After the warm-ups, there was a 3-minute rest before the subjects had to carry out 3 repeated counter-movement jumps (CMJs) tests [17]. The subject stood on the force plate and immediately leaped up vertically with maximum force as quickly as possible. There is a 60-second static recovery between each iteration. The highest jump height is defined as 100% high (H). The drop jumps high (DJH) 70%, DJH 100%, and DJH 130% tests were performed three times consecutively with a minute static rest within each DJH repetition and three minutes of interval rest (whereby the subject sat on a chair) between the DJHs. Each subject repeated this entire CMJs test three times. The schematic of DJs is as shown in Figure 1. Subjects are at the top of a raised platform box and step off the platform using their leg of choice. Subjects need to land on their feet at the same time, touch the ground as little as possible, and bounce as quickly as possible to jump to the maximum height. The results are expressed as the average of three performances. The kinetic and kinematic data were collected using the BTS motion capture and analog data acquisition system (Bioengineering, Milano, Italy). Ten infrared Qualisys motion capture cameras

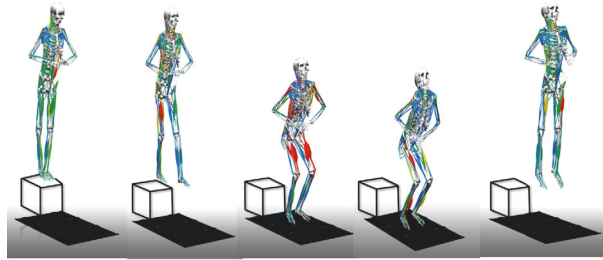


FIGURE 1: Schematic of the study design on drop jumps (DJs). Subjects had their hands on their waist and performed the DJs by stepping off a raised platform with their dominant leg sticking out from the platform. The body leans forward naturally to drop onto 2 force plates with each foot on separate plates. They were instructed to jump up from the ground with maximum effort after the first landing.

(SMART-DX400, BTS Bioengineering, Milano, Italy) at a 200-Hz sampling rate and 4 force platforms (BTS P6000, BTS Bioengineering, Milano, Italy) at a 400-Hz sampling rate were used. Cameras and force platforms were synchronized using a BTS A/D board. A modified Helen Hayes marker set was used to identify the 7-segment rigid link model of the lower extremities.

**2.5. Acute Spinning Bike Challenge Followed by Biochemical Analyses.** Subjects were pretreated with placebo or NCE for 4 weeks before being given the postexercise performance test, given 1 h after the last consumption of study product. Twelve subjects performed a 15-minute test on a spinning bike (Keiser M3i Indoor Cycle, Keiser®, Fresno, California, USA). All subjects wore a Polar T31 heart rate sensor (Polar Electro, Kempele, Finland) while being tested on the spinning bike. The heart rate was under the 60–65% maximum heart rate. The intensity of spinning bike was  $85.5 \pm 1.7$  RPM,  $26.9 \pm 1.6$  Watts,  $6.4 \pm 0.1$  km. After the 15min spinning bike challenge, the biochemical levels of lactate, ammonia ( $\text{NH}_3$ ), creatine kinase (CK), and glucose were assessed using the Selectra Pro XL analyzer (Vita lab, Netherlands).

**2.6. Clinical Biochemistry.** At the end of experiment, blood samples were taken after subjects had fasted for at least 8 hours. Biochemical levels of aspartate aminotransferase (AST), alanine aminotransferase (ALT), alkaline phosphatase (ALP), lactic dehydrogenase (LDH), creatine kinase (CK), albumin, total protein (TP), blood urea nitrogen (BUN), uric acid (UA), glucose, total cholesterol (TC), triglycerides (TG), high-density lipoprotein (HDL), and low-density lipoprotein (LDL) were assessed using a Beckman Coulter AU5800 autoanalyzer (Beckman Coulter Inc., Brea CA, USA).

**2.7. Anthropometric Measurements.** In the beginning of experiment and at the end of experiment, all subjects arrived at the laboratory in the morning for anthropometric measurements including body height (cm), body weight (kg), body mass index (BMI;  $\text{kg}/\text{m}^2$ ), basal metabolic rates (BMR), free fat mass (FFM, kg), body fat percentage (%), water content percentage (%), and bone salts (kg). Standing body height without shoes or socks was measured to the nearest 0.1 cm with a height meter mounted on a wall. BW, FFM,

body fat, water content, and bone salts were measured by a bioelectrical impedance instrument (CH18, HUAWEI Technologies Co., Ltd., Shenzhen, China) using standard methods to assess the body composition.

**2.8. Statistical Analysis.** Statistical analyses were performed using SPSS version 18.0 software (SPSS, Chicago, IL, USA). Data is expressed as the mean  $\pm$  SEM. A mixed design two-way analysis of variance (ANOVA) (supplementation  $\times$  time) was used to compare the variables of biochemistry, body compositions, and exercise performance. A  $p$ -value  $< 0.05$  was considered statistically significant. A post-hoc independent-repeated t-test was used when the main effect or interaction effect was significant. Kinematic and GRF data were filtered using a fourth-order, zero-lag, low-pass Butterworth filter with cutoff frequencies of 10 and 50 Hz, respectively. Initial contact was identified with a vertical GRF threshold of 20 N. The jumping height (H) was calculated using the formula:  $H = gT^2/8$ . The reactive strength index (RSI) was calculated using the following formula:  $\text{RSI} = H/\text{ground contact time}$ . The ground contact time was calculated as the time from the foot leaving the ground to the time of the foot contacting the ground. The peak vertical ground reaction force (PVGRF) was defined as the maximum PVGRF during the first landing phase and the PVGRF was normalized by body weight (BW).

### 3. Results

**3.1. The Nutritional Content of Nanobubbles Curcumin Extract (NCE).** Total calories of NCE were 43 kcal/15g. The 15g NCE had protein, fat, saturated fat, transfat, carbohydrate, sugar, fiber, and sodium were 1.15 g, 0.21g, 0.06g, 0 g, 10.8 g, 0.22g, 3.46g, and 176.1 mg. The contents of curcumin, bis-demethoxycurcumin, and demethoxycurcumin were 230.9 mg, 56.2 mg, and 75.6 mg in 15g NCE.

**3.2. Effects of Supplements on Biochemical Variables.** Biochemical analyses at the indicated points of the experiment can provide clinical information about the physiological adaptation status of subject. To this end, we categorized different parameters according to physiological functions (Table 1). At the posttest assessment, both hepatic indexes ALT and ALP were significantly decreased in the NCE vs placebo groups by 35.66% ( $p=0.0002$ ) and 28.65%

TABLE 1: Effect of supplementation on the biochemical serum profile levels during posttest assessment.

Parameter	Placebo	NCE	<i>p</i> -value
AST (U/L)	16.4 ± 0.4	15.6 ± 0.3	0.1590
ALT (U/L)	9.5 ± 0.3	6.1 ± 0.5*	0.0002
ALP (U/L)	89.4 ± 5.3	63.8 ± 2.3*	0.0013
LDH (U/L)	176.4 ± 4.07	176.4 ± 4.01	0.9991
CK (U/L)	73.6 ± 6.5	63.7 ± 3.6	0.2136
Albumin (g/L)	45.6 ± 0.2	45.7 ± 0.3	0.6469
TP (g/L)	74.5 ± 0.8	74.9 ± 0.8	0.7461
BUN (mmol/L)	13.1 ± 0.2	12.4 ± 0.4	0.1253
UA (mmol/L)	4.8 ± 0.1	4.9 ± 0.1	0.3051
Glucose (mg/dL)	77.6 ± 1.8	78.4 ± 1.8	0.7744
TC (mg/dL)	164 ± 6	153 ± 7	0.2411
TG (mg/dL)	82 ± 4	56 ± 4*	0.0006
HDL (mg/dL)	48 ± 1	57 ± 2*	0.0017
LDL (mg/dL)	105 ± 10	86 ± 6	0.1450

Data are mean ± SEM and *n* = 6 subjects/group. The asterisk (\*) in the same row indicates a significant difference at *p* < 0.05 by One-Way ANOVA. AST: aspartate aminotransferase; ALT: alanine aminotransferase; ALP: alkaline phosphatase; LDH: lactic dehydrogenase; CK: creatine kinase; TP: total protein; BUN: blood urea nitrogen; UA: uric acid; TC: total cholesterol; TG: triglycerides; HDL: high-density lipoprotein; LDL: low-density lipoprotein

TABLE 2: General characteristics of the body composition.

Characteristic	Treatment	Pre-test	Post-test	Main effect (Sup)	<i>p</i> values	
					Main effect (Times)	Interaction (Sup x Times)
Weight (kg)	Placebo	57.1 ± 5.1	56.8 ± 5.2	0.8554	0.9262	0.9785
	NCE	56.5 ± 7.6	56.4 ± 8.5			
BMI (kg/m <sup>2</sup> )	Placebo	20.7 ± 2.5	20.6 ± 2.5	0.9602	0.9602	0.9829
	NCE	20.8 ± 2.9	56.7 ± 3.3			
BMR (kcal/day)	Placebo	1265 ± 121	1261 ± 97	0.5452	0.9304	0.9944
	NCE	1237 ± 112	1232 ± 129			
FFM (kg)	Placebo	38.8 ± 3.6	38.5 ± 3.0	0.3989	0.8706	0.9567
	NCE	37.6 ± 3.2	37.4 ± 3.6			
Fat Mass (%)	Placebo	26.7 ± 2.6	26.5 ± 2.8	0.6386	0.9374	0.9922
	NCE	27.5 ± 5.2	27.4 ± 5.1			
Water content (%)	Placebo	50.2 ± 0.9	50.1 ± 0.9	0.5213	0.9067	0.9533
	NCE	49.8 ± 1.8	49.7 ± 1.7			
Bone salts (kg)	Placebo	2.98 ± 0.53	3.07 ± 0.33	0.4771	0.8116	0.8116
	NCE	3.15 ± 0.46	3.15 ± 0.46			

The main effect of supplementation (Sup) refers to the NCE and placebo treatment and the main effect of time refers to the two-time point assessments (pre-test, post-test). Data are presented as the mean ± SEM for *n*=6 in each group. A two-way ANOVA was used and a *p* value < 0.05 was considered significantly different. The *post-hoc* test was performed by a repeated Student's *t*-test between groups at the same time point and significance (\*) was set to an alpha level of 0.05.

(*p*=0.0013), respectively. For lipid-related parameters, TG showed a significant decrease of 31.96% (*p*=0.0006) in the NCE group compared with the placebo group. The NCE group had significantly increased HDL by 1.17-fold (*p*=0.0017) compared to the placebo group after the 4-week NCE supplementation. The remaining biochemical parameters including AST, LDH, CK, albumin, TP, BUN UA, glucose, TC, and LDL showed no significant difference in the 2 groups.

**3.3. Effects of Supplementation on Body Composition Profiles.** Table 2 shows the body weight (BW), body mass index (BMI), free fat mass (FFM), fat mass, water content, and bone salts content for the NCE and placebo groups as assessed before and after test. The mean height of the subjects in the placebo and NCE group was 166.3 ± 4.5 cm and 165.2 ± 5.0 cm, respectively. At the pretest assessment, the body composition parameters of the subjects in the NCE group were not significantly different from the placebo group for BW (*p*=0.8788),

TABLE 3: Effect of NCE supplementation on drop jumps (DJs) with kinetic and kinematic data.

Characteristic	Treatment	Pre-test	Post-test	Main effect (Sup)	<i>p</i> values Main effect (Times)	Interaction (Sup x Times)
Jump High (cm)	Placebo	18.6 ± 1.46	19.0 ± 0.62	0.2571	0.1613	0.2342
DJH 70%	NCE	18.6 ± 1.97	22.7 ± 1.72			
Jump High (cm)	Placebo	19.3 ± 0.92	19.3 ± 0.84	0.4860	0.4095	0.4068
DJH 100%	NCE	19.1 ± 1.73	21.5 ± 1.94			
Jump High (cm)	Placebo	17.7 ± 1.11	18.1 ± 0.8	0.1191	0.3242	0.4871
DJH 130%	NCE	19.0 ± 1.83	21.5 ± 1.68			
RSI (cm/s)	Placebo	49.0 ± 3.27	44.8 ± 5.15	0.0895	0.2911	0.8004
DJH 70%	NCE	41.2 ± 6.51	34.4 ± 4.87			
RSI (cm/s)	Placebo	51.1 ± 2.53	43.8 ± 5.67	0.1604	0.5553	0.3527
DJH 100%	NCE	39.8 ± 5.7	41.4 ± 4.23			
RSI (cm/s)	Placebo	47.0 ± 3.59	40.1 ± 4.74	0.4327	0.5115	0.3488
DJH 130%	NCE	39.5 ± 4.35	40.8 ± 4.2			
Contact Time (ms)	Placebo	0.38 ± 0.02	0.45 ± 0.05	0.0799	0.1283	0.3224
DJH 70%	NCE	0.48 ± 0.05	0.80 ± 0.23			
Contact Time (ms)	Placebo	0.38 ± 0.03	0.47 ± 0.05	0.0379	0.1238	0.4630
DJH 100%	NCE	0.50 ± 0.03	0.53 ± 0.03 *			
Contact Time (ms)	Placebo	0.39 ± 0.04	0.48 ± 0.05	0.0600	0.1112	0.5939
DJH 130%	NCE	0.49 ± 0.04	0.54 ± 0.03			
PVGRF (BW)	Placebo	3.1 ± 0.51	2.6 ± 0.29	0.2849	0.1383	0.8394
DJH 70%	NCE	2.8 ± 0.33	2.2 ± 0.07 *			
PVGRF (BW)	Placebo	3.7 ± 0.95	2.7 ± 0.29	0.5291	0.1338	0.6413
DJH 100%	NCE	3.1 ± 0.35	2.6 ± 0.2			
PVGRF (BW)	Placebo	4.2 ± 0.65	3.2 ± 0.22	0.4605	0.0662	0.6376
DJH 130%	NCE	3.7 ± 0.42	3.1 ± 0.28			

(1) The posttest was assessed after 4 weeks of supplementation.

(2) The main effect of supplementation (sup) refers to the NCE and placebo treatment and the main effect of time is the distance recorded at 2 points (pre- and post-). Data are presented as the mean ± SEM for  $n=6$  in each group. Statistical analysis was using a Two-Way ANOVA. A  $p$  value  $<0.05$  was considered significantly different. The *post-hoc* test was performed by repeated Student's  $t$ -test between groups at the same time point and significance (\*) set at an alpha level of 0.05. Drop jumps high (DJH); reactive strength index (RSI); peak vertical ground reaction force (PVGRF).

BMI ( $p=0.9836$ ), FFM ( $p=0.5370$ ), fat mass ( $p=0.7762$ ), water content ( $p=0.5350$ ), and bone salts ( $p=0.5294$ ). At the end of the 4-week supplementation, both NCE and placebo groups were assessed again for the same parameters. The posttest BW ( $p=0.9170$ ), BMI ( $p=0.9615$ ), FFM ( $p=0.5755$ ), fat mass ( $p=0.7327$ ), water content ( $p=0.8376$ ), and bone salts ( $p=0.7264$ ) were again no different in the 2 groups. The data also showed no significant difference in main (supplementation, times) or interaction effects (supplementation x times). The results suggest that NCE did not significantly affect body composition.

#### 3.4. Effects of Supplementation on Exercise Performance.

Drop jumps (DJs) from different heights have been commonly used in plyometric training programs. Our results show that NCE groups cannot increase the jumps high (Table 3). Ground reaction force is an important factor affecting ground load. If the landing period results in a large ground reaction force, it will increase the risk of lower

extremity and knee injuries [18, 19]. For the muscle strength indexes (contact time), the statistical analysis demonstrated significant supplementation main effects ( $p=0.0379$ ), time main effects ( $p=0.1238$ ), and interaction effects ( $p=0.4630$ ). The posttest analysis showed that the contact time at drop jumps high 100% was significantly increased ( $p=0.0487$ ) by NCE supplementation. The increase in contact times was due to the enhancement of muscle strength by NCE supplementation. The knee injury index (peak vertical ground reaction force, PVGRF) in the posttest DJH 70% was significantly decreased by 15.38% ( $p=0.0467$ ) in the NCE group compared with placebo group. Taken together, our results suggest that 4-week NCE supplementation increased drop jumps' ground contact times and decreased ground reaction force to reduce the risk of injury on drop jumps.

#### 3.5. Effects of Supplementation on Serum Lactate, Ammonia, Glucose, and CK Levels after Spinning Bike Challenge.

Muscle fatigue after exercise can be evaluated by biochemical



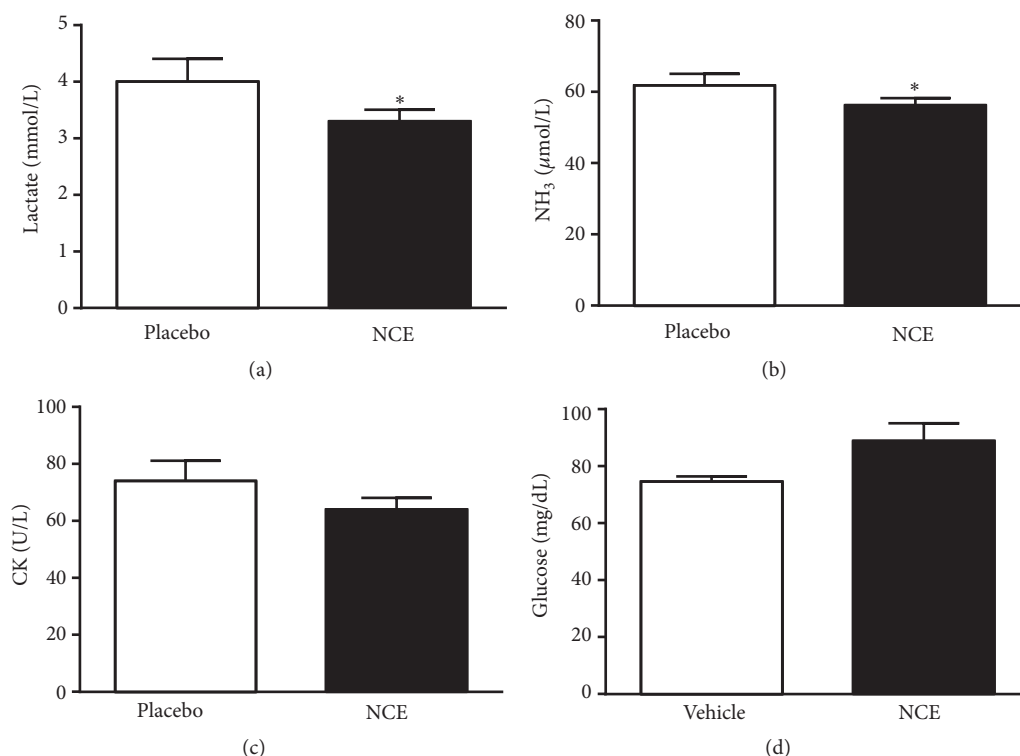


FIGURE 2: Effect of 4-week-NCE supplementation on serum levels of (a) lactate, (b) ammonia, (c) creatine kinase (CK), and (d) glucose after an acute exercise challenge. Subjects consumed either NCE or placebo for 4 weeks and, one hour following the last administration, a 15-minute spinning bike test was carried out. Data are expressed as mean  $\pm$  SEM with six subjects in each group. Significance (\*) was set at  $p < 0.05$  by a One-Way ANOVA.

indicators including lactate, ammonia, glucose and CK levels [20]. Lactate is an oxidizable substrate in skeletal muscle and a precursor to gluconeogenesis in muscles or liver after exercise [21]. In the present study, lactate levels in the placebo and NCE groups were  $4.02 \pm 0.43$  and  $3.27 \pm 0.18$  mmol/L, respectively, with the NCE treatment leading to significantly lower levels (18.67%,  $p = 0.0057$ ) (Figure 2(a)) than the placebo treatments. Peripheral and central fatigue levels are related to increased ammonia level during exercise. Serum ammonia levels in the NCE group were significantly lower (9.02%,  $p = 0.0048$ ) than the placebo group at  $61.9 \pm 3.2$  vs  $56.3 \pm 1.9$   $\mu$ mol/L (Figure 2(b)). Once muscle glycogen is depleted or near depletion, fatigue sets in and exercise capacity is compromised [22]. Therefore, blood glucose level is an important index for performance maintenance during exercise [23]. Serum CK is an important clinical biomarker for muscle damage such as muscular dystrophy, severe muscle breakdown, myocardial infarction, autoimmune myositis, and acute renal failure. CK activities in the placebo and NCE groups were not significantly different at  $74 \pm 7$  and  $64 \pm 4$  U/L, respectively (Figure 2(c)). Serum glucose levels in the placebo and NCE groups were  $74.5 \pm 1.9$  and  $88.9 \pm 6.1$  mg/dL, respectively, with the NCE group higher by 1.19-fold ( $p = 0.0474$ ) than the placebo group (Figure 2(d)). Our results indicate that NCE supplementation is able to ameliorate skeletal muscle injury induced by acute exercise challenge. Compared to the placebo, NCE supplementation

was able to reduce serum lactate, ammonia, and CK levels after the spinning bike challenge, possibly acting as an ergogenic supplement for fatigue recovery and reducing muscle damage.

#### 4. Discussion

In the current clinical study, we found that NCE could significantly mitigate ALT, ALP, and TG levels. In addition, NCE also increases serum HDL content (Table 1). NCE supplementation demonstrated functional activities in terms of physiological protection and recovery promotion. NCE supplementation had no adverse effect on body composition with 4-week supplementation (Table 2) and could improve fatigue after a 15-minute spinning bike test as assessed by the biochemical markers. The combination of physiological protection and antifatigue activity can contribute to significant improvement in exercise performance.

In the presence of nanobubbles, the porous nature of the material increases drastically and causes changes in the original properties of the material. As the density of the material changes, its fluidity and other properties are changed [24]. In recent years, nanobubbles (NBs) are spontaneously generated by using a controllable platform of superfast microvortices, based on turbulent jet flows in the presence of graphene oxide sheets [25]. This process is costly and space inefficient; we were able to overcome these problems to develop a rapid

and continuous process for application in the nanobubble extraction technology.

Our data suggests that NCE can be applied to a living body for use in fatigue recovery. During high jumps or exhaustive exercises, membrane permeability is altered and large amounts of enzymes such as CK, LDH, AST, and ALT can leak out due to muscle damage [26]. Previous studies have demonstrated the functional bioactivities of curcumin in preventing joint inflammation [27], attenuating exercise-induced oxidative stress by increasing blood antioxidant capacity [28, 29] and reducing delayed onset muscle soreness [30]. In the current study, we also found that 4 weeks of NCE supplementation were able to ameliorate the increase in indexes related to muscle damage. A study of lipids and lipid proteins in aerobic athletes showed characteristics of low TG, low LDL, and high HDL-cholesterol compared to those with a sedentary lifestyle [31]. In the current study, NCE supplementation also significantly decreased TG and increased HDL levels compared to the placebo group, even without exercise training.

Physiological fatigue resulting from inadequate rest, physical loading or mental strain/pressure and is further classified as central or peripheral fatigue [32]. Peripheral fatigue can be assessed by important serum indicators such as lactate, ammonia, glucose, CK, BUN, ALT, and ALT that are related to exercise fatigue or injury [33]. We found that after 4 weeks of supplementation, the NCE group exhibited significantly lower lactate, ammonia, and economic glucose levels after the 15-minute spinning bike challenge compared with the placebo group, indicating that the NCE group maintained a lower peripheral fatigue status.

A previous study demonstrated that an electrokinetically modified water (EMW) beverage can improve skeletal muscle function [34]. The source of bioactivity in EMW is thought to involve the presence of charge-stabilized nanostructures (CSNs), which by virtue of their size, charge, and stability affect constituents of the cell membrane [35, 36]. During exercise, increased lactate levels in exercising muscle and blood may trigger sensations of pain and discomfort, thus elevating perceptions of exertion [20, 37]. Ammonia is fatigue factor, whereby reduction of blood ammonia could prevent muscle catabolism and muscle damage [20]. Glucose is the main energy source during exercise and the glucose amount in the serum, liver, or muscle can greatly affect the body's exercise fatigue resistance [38]. In the current study, NCE is able to reduce lactate and ammonia accumulation while improving glucose utilization. This implies that NCE supplementation can ameliorate exercise fatigue and promote recovery.

Although studies on the effect of curcumin in reducing muscle damage are common, there is a lack of study reflecting evidence of its effect on exercise performance. One recent study showed that curcumin supplementation for 6 weeks in Wistar rats on a treadmill training model is able to affect exercise performance by regulating the NF- $\kappa$ B and Nrf2 pathways [39]. In our study, we found that the PVGRF in the NCE group was lower than the placebo group after 4 weeks of supplementation. This finding could imply that the NCE group in DJH 70% drop height lightly loaded the

lower extremities. NCE groups could reduce peak vertical ground reaction force at drop jumps. This implies that NCE may have the potential to reduce the risk of musculoskeletal system injury at this height (DJH 70%) in drop jumps. NCE supplementation also increases the ground contact time at DJH 100%, suggesting that the lower body muscle strength increased after 4-week treatment. These findings are consistent with our previous animal study showing that curcumin supplementation reduced fatigue after exercise [6]. However, this approach carries limitations and cannot show direct causative relationships between NCE supplementation effects on whole exercise system or systemic variables. Nevertheless, future clinical studies on programmed exercise prescriptions in combination with NCE supplementation would be important.

## 5. Conclusions

Curcumin is an important nutrient supplement with applications in reducing muscle damage associated with exercise training. There is much interest in generating nanobubbles, which can enable new uses of ultrasound contrast agents in molecular imaging and drug delivery, particularly for cancer applications [40]. To our knowledge, our study is the first using NBs on curcumin extraction. In the current study, we find that NCE can also play a role in physiological protection from the risk of musculoskeletal system injury due to explosiveness exercise. Fitness training has become popular in recent years because people recognize the positive effects of aerobic and endurance exercise on health promotion and physiological maintenance. Our data shows that NCE is beneficial for the reduction of fatigue and musculoskeletal system injury. Taken together, our results suggest that NCE, high quality form of curcumin, may be a potential nutrient supplement option to be used with aerobic and anaerobic exercises.

## Data Availability

The data used to support the findings of this study are included within the article.

## Disclosure

This work was supported by Chang Gung Memorial Hospital Grants (CMRPF1G0172). The results of the study are presented clearly, honestly, and without fabrication, falsification, or inappropriate data manipulation.

## Conflicts of Interest

All authors declare that they have no conflicts of interest with regard to the contents of this article.

## Acknowledgments

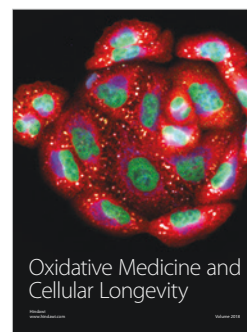
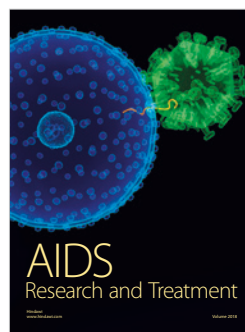
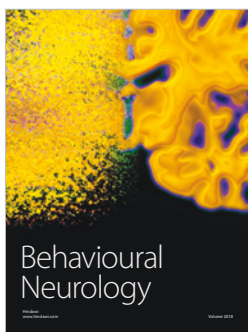
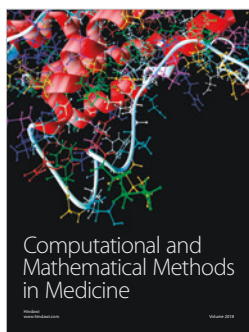
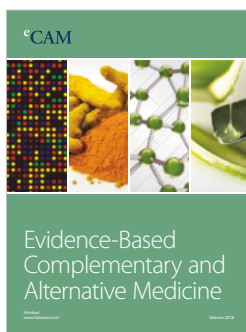
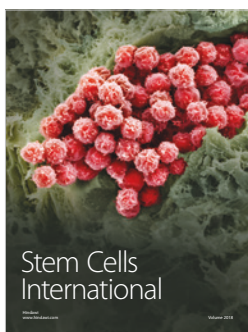
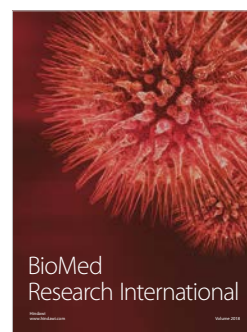
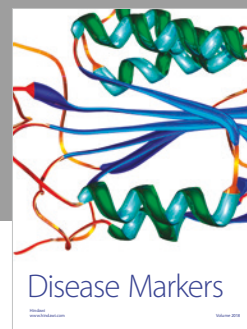
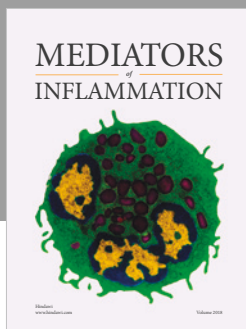
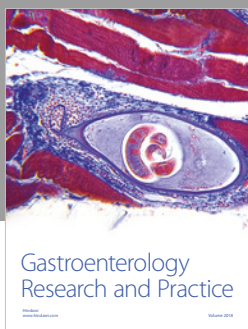
The NBs technology was provided by Yung-hsiang Tseng (Leading Auto. Bio Co. Ltd.). The authors thank Qing-Hong Shi for conducting the biochemical examination.

## References

- [1] H. H. Peng, C. H. Wu, S. T. Kang et al., "Real-time monitoring of inertial cavitation effects of microbubbles by using MRI: In vitro experiments," *Magnetic Resonance in Medicine*, vol. 77, no. 1, pp. 102–111, 2017.
- [2] S. Hayakumo, S. Arakawa, Y. Mano, and Y. Izumi, "Clinical and microbiological effects of ozone nano-bubble water irrigation as an adjunct to mechanical subgingival debridement in periodontitis patients in a randomized controlled trial," *Clinical Oral Investigations*, vol. 17, no. 2, pp. 379–388, 2013.
- [3] K. Hynynen, N. McDannold, N. Vykhodtseva et al., "Focal disruption of the blood-brain barrier due to 260-kHz ultrasound bursts: a method for molecular imaging and targeted drug delivery," *Journal of Neurosurgery*, vol. 105, no. 3, pp. 445–454, 2006.
- [4] Y. Hirose, T. Yasui, K. Taguchi et al., "Oxygen nano-bubble water reduces calcium oxalate deposits and tubular cell injury in ethylene glycol-treated rat kidney," *Urolithiasis*, vol. 41, no. 4, pp. 279–294, 2013.
- [5] I. Chattopadhyay, K. Biswas, U. Bandyopadhyay, and R. K. Banerjee, "Turmeric and curcumin: biological actions and medicinal applications," *Current Science*, vol. 87, pp. 44–53, 2004.
- [6] W. C. Huang, W. C. Chiu, H. L. Chuang et al., "Effect of curcumin supplementation on physiological fatigue and physical performance in mice," *Nutrients*, vol. 7, no. 2, pp. 905–921, 2015.
- [7] J. N. Sciberras, S. Galloway, A. Fenech et al., "The effect of turmeric (Curcumin) supplementation on cytokine and inflammatory marker responses following 2 hours of endurance cycling," *Journal of the International Society of Sports Nutrition*, vol. 12, no. 1, p. 5, 2015.
- [8] F. Drobnic, J. Riera, G. Appendino et al., "Reduction of delayed onset muscle soreness by a novel curcumin delivery system (Meriva®): A randomised, placebo-controlled trial," *Journal of the International Society of Sports Nutrition*, vol. 11, no. 1, p. 31, 2014.
- [9] Y. Tanabe, S. Maeda, N. Akazawa et al., "Attenuation of indirect markers of eccentric exercise-induced muscle damage by curcumin," *European Journal of Applied Physiology*, vol. 115, no. 9, pp. 1949–1957, 2015.
- [10] I. Garthe and R. J. Maughan, "Athletes and Supplements: Prevalence and Perspectives," *International Journal of Sport Nutrition and Exercise Metabolism*, vol. 28, no. 2, pp. 126–138, 2018.
- [11] D. E. Scofield and S. Unruh, "Dietary supplement use among adolescent athletes in central Nebraska and their sources of information," *The Journal of Strength and Conditioning Research*, vol. 20, no. 2, pp. 452–455, 2006.
- [12] P. M. Jakeman, E. M. Winter, and J. Doust, "A review of research in sports physiology," *Journal of Sports Sciences*, vol. 12, no. 1, pp. 33–60, 1994.
- [13] M. Apostu, "The effect of ergogenic substances over sports performance," *Procedia - Social and Behavioral Sciences*, vol. 117, pp. 329–334, 2014.
- [14] K. V. Nagappan, S. Meyyanathan, R. B. Raja, and E. Kannan, "A liquid chromatography method for the simultaneous determination of curcumin and piperine in food products using diode array detection," *Asian Journal of Research in Chemistry*, vol. 2, no. 2, pp. 115–118, 2009.
- [15] W. Wichitnithad, N. Jongaroonngamsang, S. Pummangura, and P. Rojsitthisak, "A simple isocratic HPLC method for the simultaneous determination of curcuminoids in commercial turmeric extracts," *Phytochemical Analysis*, vol. 20, no. 4, pp. 314–319, 2009.
- [16] W. C. Huang, Y. C. Chang, Y. M. Chen et al., "Whey protein improves marathon-induced injury and exercise performance in elite track runners," *International Journal of Medical Sciences*, vol. 14, no. 7, pp. 648–654, 2017.
- [17] J. T. Weinhandl, B. S. Irmischer, and Z. A. Sievert, "Sex differences in unilateral landing mechanics from absolute and relative heights," *The Knee*, vol. 22, no. 4, pp. 298–303, 2015.
- [18] T. E. Hewett, G. D. Myer, K. R. Ford et al., "Biomechanical measures of neuromuscular control and valgus loading of the knee predict anterior cruciate ligament injury risk in female athletes: a prospective study," *The American Journal of Sports Medicine*, vol. 33, no. 4, pp. 492–501, 2005.
- [19] S. N. Zhang, B. T. Bates, and J. S. Dufek, "Contributions of lower extremity joints to energy dissipation during landings," *Medicine & Science in Sports & Exercise*, vol. 32, no. 4, pp. 812–819, 2000.
- [20] Y. M. Chen, H. C. Lee, M. T. Chen, C. C. Huang, and W. C. Chen, "Dehydroepiandrosterone supplementation combined with weight-loading whole-body vibration training (WWBV) affects exercise performance and muscle glycogen storage in middle-aged C57BL/6 mice," *International Journal of Medical Sciences*, vol. 15, no. 6, pp. 564–573, 2018.
- [21] G. A. Brooks, "Intra- and extra-cellular lactate shuttles," *Medicine & Science in Sports & Exercise*, vol. 32, no. 4, pp. 790–799, 2000.
- [22] J. Carvalho-Peixoto, R. C. Alves, and L.-C. Cameron, "Glutamine and carbohydrate supplements reduce ammonemia increase during endurance field exercise," *Applied Physiology, Nutrition, and Metabolism*, vol. 32, no. 6, pp. 1186–1190, 2007.
- [23] M. A. Hearris, K. M. Hammond, J. M. Fell, and J. P. Morton, "Regulation of muscle glycogen metabolism during exercise: implications for endurance performance and training adaptations," *Nutrients*, vol. 10, no. 3, 2018.
- [24] G. Senthilkumar, C. Rameshkumar, M. N. Nikhil, and J. N. Kumar, "An investigation of nanobubbles in aqueous solutions for various applications," *Applied Nanoscience*, vol. 8, no. 6, pp. 1557–1567, 2018.
- [25] M. Jannesari, O. Akhavan, and H. R. Madaah Hosseini, "Graphene oxide in generation of nanobubbles using controllable microvortices of jet flows," *Carbon*, vol. 138, pp. 8–17, 2018.
- [26] K. C. Huang, W. T. Wu, F. L. Yang et al., "Effects of freshwater clam extract supplementation on time to exhaustion, muscle damage, pro/anti-inflammatory cytokines, and liver injury in rats after exhaustive exercise," *Molecules*, vol. 18, no. 4, pp. 3825–3838, 2013.
- [27] A. Shehzad, G. Rehman, and Y. S. Lee, "Curcumin in inflammatory diseases," *BioFactors*, vol. 39, no. 1, pp. 69–77, 2013.
- [28] M. Takahashi, K. Suzuki, H. K. Kim et al., "Effects of curcumin supplementation on exercise-induced oxidative stress in humans," *International Journal of Sports Medicine*, vol. 35, no. 6, pp. 469–475, 2014.
- [29] N. Kawanishi, K. Kato, M. Takahashi et al., "Curcumin attenuates oxidative stress following downhill running-induced muscle damage," *Biochemical and Biophysical Research Communications*, vol. 441, no. 3, pp. 573–578, 2013.
- [30] L. M. Nicol, D. S. Rowlands, R. Fazakerly, and J. Kellett, "Curcumin supplementation likely attenuates delayed onset muscle soreness (DOMS)," *European Journal of Applied Physiology*, vol. 115, no. 8, pp. 1769–1777, 2015.

- [31] G. C. Cardoso Saldana, S. Hernandez de, J. Leon, and C. Posadas Romero, "Lipid and lipoprotein levels in athletes in different sports disciplines," *Arch Inst Cardiol Mex*, vol. 65, no. 3, pp. 229–235, 1995.
- [32] M. J. Zwartz, G. Bleijenberg, and B. G. M. van Engelen, "Clinical neurophysiology of fatigue," *Clinical Neurophysiology*, vol. 119, no. 1, pp. 2–10, 2008.
- [33] H. K. Antunes, G. S. Leite, K. S. Lee et al., "Exercise deprivation increases negative mood in exercise-addicted subjects and modifies their biochemical markers," *Physiology & Behavior*, vol. 156, pp. 182–190, 2016.
- [34] P. A. Borsa and K. A. Larkin-Kaiser, "Daily controlled consumption of an electrokinetically modified water alters the fatigue response as a result of strenuous resistance exercise," *Physiology Journal*, vol. 2014, Article ID 673530, 7 pages, 2014.
- [35] S. Khasnavis, A. Roy, S. Ghosh, R. Watson, and K. Pahan, "Protection of dopaminergic neurons in a mouse model of Parkinson's disease by a physically-modified saline containing charge-stabilized nanobubbles," *Journal of Neuroimmune Pharmacology*, vol. 9, no. 2, pp. 218–232, 2014.
- [36] S. Mondal, J. A. Martinson, S. Ghosh, R. Watson, and K. Pahan, "Protection of tregs, suppression of Th1 and Th17 cells, and amelioration of experimental allergic encephalomyelitis by a physically-modified saline," *PLoS ONE*, vol. 7, no. 12, Article ID e51869, 2012.
- [37] A. Kantanista, K. Kusy, E. Zarębska, M. Włodarczyk, M. Ciekot-Sołtysiak, and J. Zieliński, "Blood ammonia and lactate responses to incremental exercise in highly-trained male sprinters and triathletes," *Biomedical Human Kinetics*, vol. 8, no. 1, pp. 32–38, 2016.
- [38] C. Y. Hsiao, Y. M. Chen, Y. J. Hsu, C. C. Huang, H. C. Sung, and S. S. Chen, "Supplementation with Hualian No. 4 wild bitter gourd (*Momordica charantia* Linn. var. *abbreviata* ser.) extract increases anti-fatigue activities and enhances exercise performance in mice," *Journal of Veterinary Medical Science*, vol. 79, no. 6, pp. 1110–1119, 2017.
- [39] K. Sahin, R. Pala, M. Tuzcu et al., "Curcumin prevents muscle damage by regulating NF- $\kappa$ B and Nrf2 pathways and improves performance: an in vivo model," *Journal of Inflammation Research*, vol. 9, pp. 147–154, 2016.
- [40] C. Hernandez, S. Gulati, G. Fioravanti, P. L. Stewart, and A. A. Exner, "Cryo-EM visualization of lipid and polymer-stabilized perfluorocarbon gas nanobubbles - a step towards nanobubble mediated drug delivery," *Scientific Reports*, vol. 7, no. 1, p. 13517, 2017.







## FULL PAPER

Physiology

# ***Ludwigia octovalvis* (Jacq.) raven extract supplementation enhances muscle glycogen content and endurance exercise performance in mice**

Yi-Ming CHEN<sup>1)†</sup>, Chi-Chang HUANG<sup>2)</sup>, Chien-Yu HSIAO<sup>3–5)†</sup>, Sindy HU<sup>5–7)</sup>, I-Lin WANG<sup>1)</sup> and Hsin-Ching SUNG<sup>5,8)\*</sup>

<sup>1)</sup>Health Technology College, Jilin Sport University, Changchun 130022, Jilin, China

<sup>2)</sup>Graduate Institute of Sports Science, National Taiwan Sport University, Taoyuan 33301, Taiwan

<sup>3)</sup>Department of Nutrition and Health Sciences, Chang Gung University of Science and Technology, Taoyuan 33301, Taiwan

<sup>4)</sup>Research Center for Industry of Human Ecology and Research Center for Chinese Herbal Medicine, College of Human Ecology, Chang Gung University of Science and Technology, Taoyuan 33301, Taiwan

<sup>5)</sup>Aesthetic Medical Center, Department of Dermatology, Chang Gung Memorial Hospital, Taoyuan 33301, Taiwan

<sup>6)</sup>Department of Cosmetic Science, Chang Gung University of Science and Technology, Taoyuan 33301, Taiwan

<sup>7)</sup>College of Medicine, Chang Gung University, Taoyuan 33301, Taiwan

<sup>8)</sup>Department of Anatomy, College of Medicine, Chang Gung University, Taoyuan 33301, Taiwan

**ABSTRACT.** *Ludwigia octovalvis* extract (LOE) is a widely used traditional Chinese herbal medicine. To date, few studies have demonstrated the effect of LOE supplementation on exercise performance, physical fatigue and biochemical profile. The purpose of this study is to evaluate the potential beneficial effects of LOE extract on fatigue and ergogenic functions following physiological challenge. Male ICR mice from 3 groups ( $n=8$  per group) were orally administered LOE for 4 weeks at 0 (vehicle), 61.5 (LOE-1X) or 307.5 (LOE-5X) mg/kg/day. LOE supplementation was able to dose-dependently increase endurance swimming time ( $P<0.0001$ ) and decrease levels of serum lactate ( $P=0.0022$ ), ammonia ( $P<0.0001$ ), creatine kinase ( $P<0.0001$ ), blood urea nitrogen ( $P<0.0001$ ) and glucose utilization ( $P<0.0001$ ) after acute exercise challenge. The glycogen in gastrocnemius muscle also increased with LOE treatment in a dose-dependent manner ( $P<0.0001$ ). Biochemically, AST, ALT, LDH, CK, BUN, creatinine and UA levels were decreased with LOE treatment. Our study shows that 4-week supplementation with LOE increases muscle glycogen content storage to enhance exercise performance and anti-fatigue effects.

**KEY WORDS:** anti-fatigue, exercise performance, glycogen

*J. Vet. Med. Sci.*

81(5): 667–674, 2019

doi: 10.1292/jvms.18-0165

Received: 14 May 2018

Accepted: 12 June 2018

Published online in J-STAGE:  
29 June 2018

*Ludwigia octovalvis* (Jacq.) P. H. Raven (Family: Onagraceae) is an aquatic plant commonly grown in the wet areas of Taiwan (Fig. 1). *L. octovalvis* extract (LOE) is widely consumed as a healthful drink in a number of countries [15] and has been extensively used in traditional Chinese medicine to provide immunoregulatory, hepatoprotective, cardiovascular-protective properties and anti-aging effects [20]. Numerous antioxidative flavonoids, such as quercetin, luteolin, apigenin, and gallic acid, have been isolated from *L. octovalvis* [15]. In previous studies, LOE has been shown to contain high levels of polyphenols, flavonoids and  $\beta$ -sitosterol [18, 20, 28]. Quercetin is one of the active components of flavonoids which exist in natural plants, particularly in LOE [29]. Intake of quercetin has been inversely associated with coronary heart disease [2]. In addition to antibacterial activity, quercetin also contains antioxidant activity, preventing oxidation of low density lipoproteins *in vitro*. Besides quercetin, LOE's active ingredient,  $\beta$ -sitosterol, has been shown to significantly extend the lifespan of fruit flies [21] and activate the AMP-activated protein kinase (AMPK) pathway [21, 27]. AMPK is a major cellular energy sensor and metabolic regulator, and is considered to be a therapeutic target for treatment of diabetes mellitus via glucose handling [7]. AMPK also plays a major role in the physiological effects of energy metabolism and metabolic adaptation to fasting and exercise in skeletal muscle [3]. Based on these, there is potential for LOE to be used as a sport nutrition supplementation to enhance exercise performance or to counteract fatigue. Given there are very few studies that directly

\*Correspondence to: Sung, H.-C.: hcs@mail.cgu.edu.tw

†These authors contributed equally to this work.

©2019 The Japanese Society of Veterinary Science



This is an open-access article distributed under the terms of the Creative Commons Attribution Non-Commercial No Derivatives (by-nc-nd) License. (CC-BY-NC-ND 4.0: <https://creativecommons.org/licenses/by-nc-nd/4.0/>)

address LOE's anti-fatigue properties and ability to improve exercise performance, this study seeks to evaluate the potential ergogenic, anti-fatigue and beneficial health effects of LOE supplementation in mice after 28 days by using our previously established *in vivo* platform [12].

## MATERIALS AND METHODS

### *Preparation of L. octovalvis extract (LOE)*

Air-dried whole plants of *L. octovalvis* were obtained from the Taiwan Herbal Biopharma Co., Ltd. (Tainan, Taiwan). Briefly, 100 g of dry *L. octovalvis* powder was soaked in 400 ml of 95% ethanol overnight for 4 hr, extracted and then concentrated in a rotary evaporator at 55°C for 30 min. The extract was decanted and filtered through Whatman No. 2 filter paper to remove debris and lyophilized for 40 hr. The lyophilized powder was dried in oven at 55°C. The yield of LOE was 2.5% (2.5/100 g  $\times$  100%).

### *Materials, animals, and experiment design*

Male ICR mice (8-weeks old) grown under specific pathogen-free conditions were purchased from BioLASCO (Yi-Lan, Taiwan). All mice were provided a standard laboratory diet (No. 5001; PMI Nutrition International, Brentwood, MO, U.S.A.), distilled water *ad libitum* and housed at 12-hr light/12-hr dark cycle at room temperature ( $22 \pm 1^\circ\text{C}$ ) and 50–60% humidity. The Institutional Animal Care and Use Committee (IACUC) of National Taiwan Sport University (NTSU) inspected all animal experiments, and this study conformed to the guidelines of protocol IACUC-10502 approved by the IACUC ethics committee. The 1X dose of LOE extract used for humans is typically 300 mg per day. The 1X mouse dose (61.5 mg/kg) we used was converted from a human-equivalent dose (HED) based on body surface area according to the US Food and Drug Administration formula: Assuming a human weight of 60 kg, the HED for 300 (mg)/60 (kg) =  $5 \times 12.3 = 61.5$  mg/kg; the conversion coefficient 12.3 is used to account for differences in body surface area between mice and human as previously described [5]. In total, 24 mice were randomly assigned to 3 groups (8 mice/group) for daily oral LOE treatment for 4 weeks: vehicle; 61.5 mg/kg (LOE-1X); and 307.5 mg/kg (LOE-5X). The vehicle group received the same volume of solution equivalent to individual body weight (BW). Mice were randomly housed in groups of 4 per cage.

### *Forelimb grip strength test*

A low-force testing system (Model-RX-5, Aikoh Engineering, Nagoya, Japan) was used to measure the forelimb grip strength of treated mice as previously described [6].

### *Swimming exercise performance test*

The swim-to-exhaustion test involved loads corresponding to 5% of the mouse BW attached to the tails to evaluate endurance times as previously described [5]. The swimming endurance time of each mouse was recorded from beginning to exhaustion, which is determined by observing loss of coordinated movements and failure to return to the surface within 7 sec.

### *Determination of fatigue-associated biochemical variables*

The effect of LOE supplementation on fatigue-associated biochemical indices was evaluated after exercise as previously described [22]. One hour after LOE supplementation, all mice underwent a 15-min swim exercise without weight loading. After the 15-min swim exercise, blood samples were immediately collected and centrifuged at  $1,500 \times g$  at  $4^\circ\text{C}$  for 10 min to obtain the serum. Serum lactate, ammonia, glucose, creatine kinase (CK) and blood urea nitrogen (BUN) levels were determined by using an autoanalyzer (Hitachi 7060, Hitachi, Tokyo, Japan).

### *Clinical biochemical profiles*

At the end of the experimental period, mice were euthanized by 95% CO<sub>2</sub> asphyxiation and blood collected immediately. Serum was separated by centrifugation and levels of the clinical biochemical variables, including aspartate aminotransferase (AST), alanine aminotransferase (ALT), lactic dehydrogenase (LDH), creatine kinase (CK), total protein (TP), albumin, blood urea nitrogen (BUN), creatinine, uric acid (UA), total cholesterol (TC), triacylglycerols (TG) and glucose, were measured by using an autoanalyzer (Hitachi 7060).

### *Tissue glycogen determination and visceral organ weight*

The stored form of glucose is glycogen, which exists mostly in liver and muscle tissue. Liver and muscle tissues were excised after the mice were euthanized and weighed for glycogen content analysis as described previously [6, 22]. The weights of the liver, kidney, heart, lung, muscle and epididymal fat pad (EFP) related visceral organs were recorded.

### *Histology of tissues*

All tissues were carefully removed, minced and fixed in 10% formalin. Samples were embedded in paraffin and cut into 4- $\mu\text{m}$

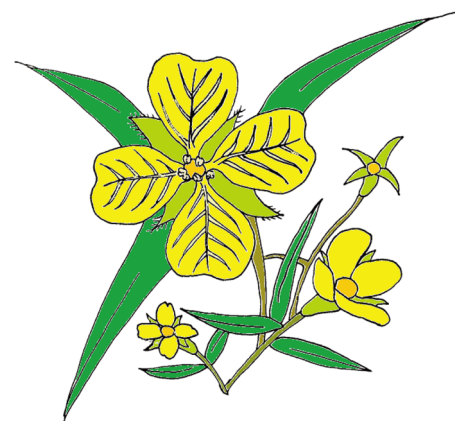


**Fig. 1.** Schematic diagram of wild *Ludwigia octovalvis* (Jacq.) P. H. Raven.



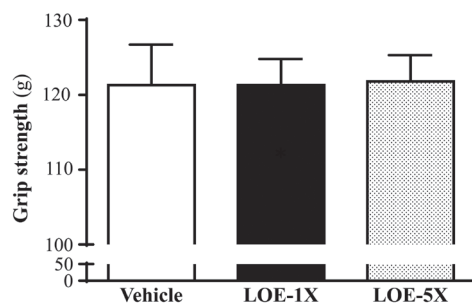


**Fig. 2.** Effect of LOE (*L. octovalvis* extract) supplementation for 4 weeks on forelimb grip strength. Mice were treated with vehicle, LOE-1X, or LOE-5X for 4 weeks before the forelimb grip strength test was administered. Data is shown as mean  $\pm$  SEM,  $n=8$  mice/group. Analysis is using one-way ANOVA, with different letters (a, b) indicating a significant difference at  $P<0.05$ .

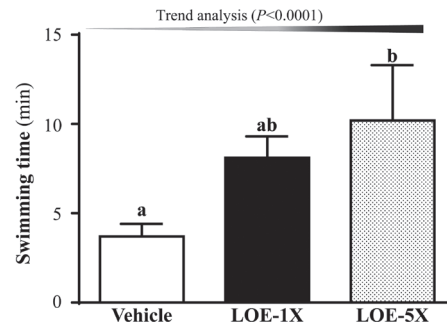


**Fig. 3.** Effect of LOE supplementation on swimming exercise performance. Mice were treated with vehicle, LOE-1X or LOE-5X for 4 weeks. One hr after the last treatment, the exhaustive swimming test was performed. Loads used for the tests were attached to the tails of the mice and equivalent to 5% of the body weight. Data is shown as mean  $\pm$  SEM,  $n=8$  mice/group. Analysis is using one-way ANOVA with different letters (a, b) indicating a significant difference at  $P<0.05$ .

thick slices for morphological and pathological evaluations. Tissue was stained with hematoxylin and eosin (H&E) and examined by a veterinary pathologist using an optical microscope equipped with a CCD camera (BX-51, Olympus, Tokyo, Japan).

### Statistical analysis

All data are expressed as mean  $\pm$  SEM,  $n=8$  mice/group. Statistical differences among groups were analyzed by a one-way analysis of variance (ANOVA) and the Cochran-Armitage test for dose-effect trend analysis with SAS 9.0 (SAS Inst., Cary, NC, U.S.A.). Differences between groups were analyzed by one-way analysis of variance (ANOVA) and using Duncan's *post-hoc* test. All  $P$ -values  $<0.05$  were considered significant.

## RESULTS

### Effects of LOE on exercise performance in forelimb grip strength and weight-loaded swimming test

After supplementation of LOE for 4 weeks, we examined the effect of LOE on forelimb grip strength in the mice. The forelimb grip strengths for the vehicle, LOE-1X and LOE-5X groups were found to be  $121 \pm 5$ ,  $121 \pm 4$  and  $121 \pm 8$  g, respectively (Fig. 2). The difference in forelimb grip strength was shown to be statistically insignificant with the LOE supplementation. We further evaluated the anti-fatigue effects of LOE supplementation using exercise endurance as an index. Endurance swimming times were  $3.7 \pm 0.7$ ,  $8.1 \pm 1.2$  and  $10.2 \pm 3.1$  min with the vehicle, LOE-1X and LOE-5X treatment groups, respectively (Fig. 3). The exhaustive swimming time was higher by 2.72-fold in the LOE-5X group than vehicle group ( $P=0.0295$ ). In the trend analysis, absolute exhaustive swimming time dose-dependently increased with LOE supplementation ( $P<0.0001$ ).

### Effect of LOE supplementation on serum lactate, ammonia, glucose, CK and BUN levels after acute exercise challenge

Lactate levels in vehicle, LOE-1X, and LOE-5X groups were  $7.5 \pm 0.3$ ,  $5.5 \pm 0.4$  and  $4.7 \pm 0.2$  mmol/l. Compared with the vehicle group, lactate level was decreased by 27.24% ( $P=0.0005$ ) and 38.21% ( $P<0.0001$ ) in the LOE-1X and LOE-5X groups, respectively (Fig. 4A). In the trend analysis, serum lactate levels decreased in a dose-dependent manner with increased LOE dose ( $P<0.0001$ ). These results indicate that LOE supplementation may have the potential for clearance or utilization of blood lactate during exercise.

Serum ammonia levels of the vehicle, LOE-1X and LOE-5X groups were  $129 \pm 6$ ,  $61 \pm 7$  and  $56 \pm 5$   $\mu$ mol/l, respectively (Fig. 4B). The ammonia levels of LOE-1X and LOE-5X groups were significantly lower by 52.52% ( $P<0.0001$ ) and 56.41% ( $P<0.0001$ ), compared with vehicle group. Trend analysis revealed that serum ammonia level dose-dependently decreased with increasing LOE dose ( $P<0.0001$ ), suggesting that continuous supplementation with LOE for 4 weeks could decrease ammonia accumulation during exercise.

Serum CK level is an important clinical biomarker of muscle damage with lower CK levels representing greater recovery capacity from exercise-induced muscle damage. The serum CK levels of vehicle, LOE-1X and LOE-5X groups were shown to be  $1097 \pm 191$ ,  $518 \pm 51$  and  $302 \pm 30$  (mg/dl), respectively (Fig. 4D). Compared with vehicle treatment, the CK level was decreased by 52.79% ( $P=0.0046$ ) and 72.45% ( $P=0.0003$ ) for the LOE-1X and LOE-5X groups, respectively. Our findings suggest that LOE supplementation could ameliorate skeletal muscle injury induced by acute exercise challenge. Trend analysis showed that LOE treatment had a significant dose-dependent effect on CK level ( $P<0.0001$ ).

Blood glucose level is an important index for performance maintenance during exercise. As exercise continues, there is an increase in glucose uptake and a decrease in intramuscular glucose concentration as the hexokinase inhibition is relieved by a lower glucose 6-phosphate (G-6-P) concentration [17]. Serum glucose levels in the vehicle, LOE-1X and LOE-5X groups were  $123 \pm$



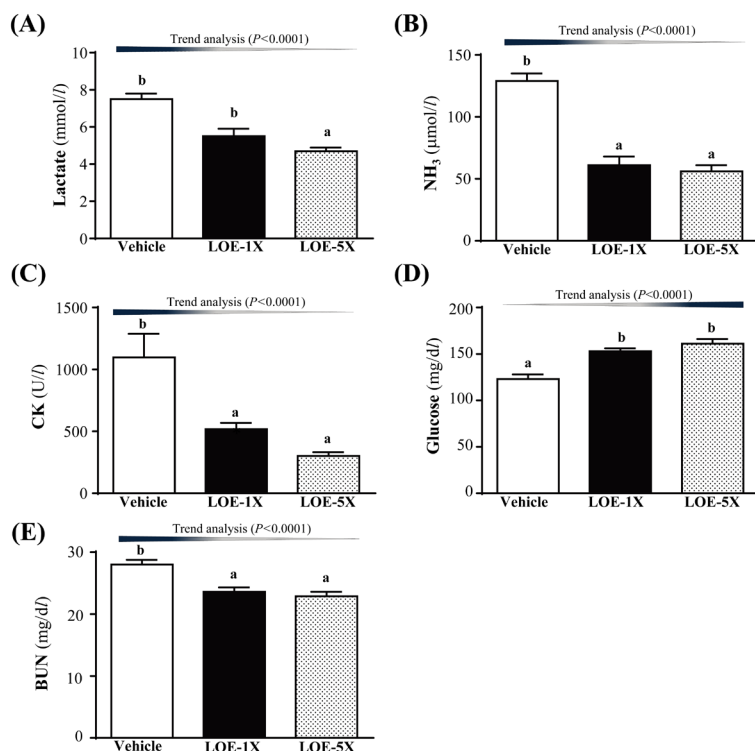


**Fig. 4.** Effect of LOE supplementation on serum levels of (A) lactate, (B) ammonia, (C) creatine kinase (CK), (D) glucose and (E) blood urea nitrogen (BUN) after acute exercise challenge. Data is expressed as mean  $\pm$  SEM,  $n=8$  mice/group. Analysis is using one-way ANOVA. Different letters (a, b) indicate a significant difference at  $P<0.05$ .

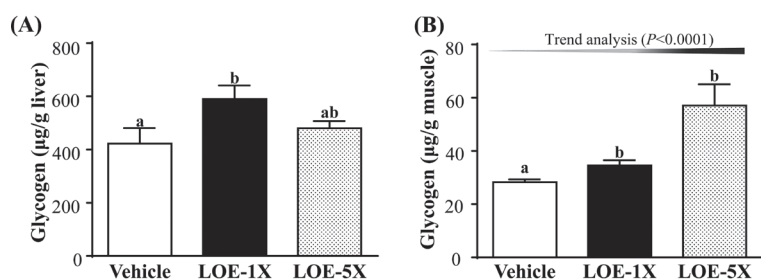


**Fig. 5.** Effect of LOE supplementation on glycogen levels in (A) liver and (B) muscle. Data is expressed as mean  $\pm$  SEM,  $n=8$  mice/group, by one-way ANOVA. Different letters (a, b) indicate a significant difference at  $P<0.05$ .

5,  $153 \pm 3$  and  $161 \pm 5$  mg/dl, respectively (Fig. 4C). The glucose levels of the LOE-1X and LOE-5X group were higher by 1.24- ( $P=0.0004$ ) and 1.31-fold ( $P<0.0001$ ) compared with the vehicle group. Trend analysis showed dose-dependent serum glucose level increase with increased LOE supplementation ( $P<0.0001$ ). Taken together, our data indicates that continuous supplementation with LOE for 4 weeks could increase serum glucose levels and improve glucose uptake capacity toward beneficial anti-fatigue activity.

BUN is an important biochemical parameter related to fatigue and BUN level measures the amount of nitrogen in blood from the waste product of urea. Urea serves an important role in the metabolism of nitrogen-containing compounds. Serum BUN levels of the vehicle, LOE-1X and LOE-5X were  $28.0 \pm 0.8$ ,  $23.6 \pm 0.7$  and  $22.9 \pm 0.7$  (mg/dl), respectively (Fig. 4E). Compared with vehicle group, the BUN level of the LOE-1X and LOE-5X was significantly decreased by 15.63% ( $P=0.0009$ ) and 18.81% ( $P=0.0002$ ), respectively. The trend analysis revealed that LOE treatment had a significant dose-dependent effect on BUN level ( $P<0.0001$ ).

#### Effect of LOE supplementation for 4 weeks on hepatic and muscle glycogen level

We measured glycogen content of liver and muscle tissues (Fig. 5A and 5B). The liver glycogen levels in the vehicle, LOE-1X and LOE-5X groups were  $4.22 \pm 0.59$ ,  $5.90 \pm 0.51$  and  $4.80 \pm 0.27$  mg/g liver, respectively. The LOE-1X group showed a significantly higher (1.40-fold,  $P=0.0214$ ) liver glycogen level compared to the vehicle control group. The muscle glycogen in vehicle, LOE-1X and LOE-5X groups were  $0.28 \pm 0.01$ ,  $0.35 \pm 0.02$  and  $0.57 \pm 0.08$  mg/g muscle, respectively. The muscle glycogen content for the LOE-5X group was significantly higher (2.02-fold,  $P=0.0004$ ) than the vehicle group, suggesting that LOE supplementation could help increase muscle glycogen storage in the mice leading to enhanced energy utilization. In the trend analysis, muscle glycogen increased with the LOE dosage ( $P<0.0001$ ).

#### General characteristics of mice with LOE supplementation for 4 weeks

Initial BW and final BW of the mice did not differ among the vehicle, LOE-1X and LOE-5X groups (Table 1). Similarly, daily

**Table 1.** General characteristics of mice with *L. octovalvis* extract (LOE) supplementation

Characteristic	Vehicle	LOE-1X	LOE-5X	Trend analysis
Initial BW (g)	34.59 ± 0.32	34.48 ± 0.48	34.53 ± 0.32	0.9721
Final BW (g)	37.61 ± 0.49	37.88 ± 0.38	38.00 ± 0.31	0.5334
Food intake (g/day)	7.59 ± 0.12	7.69 ± 0.13	7.71 ± 0.20	0.5726
Water intake (ml/day)	7.97 ± 0.13	7.90 ± 0.26	8.02 ± 0.13	0.5999
Liver (g)	1.82 ± 0.08	1.87 ± 0.02	1.81 ± 0.02	0.2179
Kidney (g)	0.60 ± 0.00	0.60 ± 0.02	0.62 ± 0.01	0.1561
Heart (g)	0.22 ± 0.01	0.21 ± 0.01	0.22 ± 0.01	0.9788
Lung (g)	0.21 ± 0.00	0.22 ± 0.00	0.22 ± 0.00	0.4959
Muscle (g)	0.38 ± 0.01	0.39 ± 0.00	0.38 ± 0.01	0.6695
EFP (g)	0.36 ± 0.02	0.36 ± 0.02	0.37 ± 0.02	0.8280
BAT (g)	0.075 ± 0.009 <sup>a</sup>	0.094 ± 0.003 <sup>b</sup>	0.090 ± 0.004 <sup>a,b</sup>	0.1720
Relative liver weight (%)	4.83 ± 0.17	4.93 ± 0.08	4.78 ± 0.07	0.4016
Relative Kidney weight (%)	1.60 ± 0.02	1.58 ± 0.04	1.63 ± 0.03	0.3901
Relative Heart weight (%)	0.58 ± 0.03	0.56 ± 0.02	0.57 ± 0.02	0.9419
Relative Lung weight (%)	0.57 ± 0.02	0.57 ± 0.01	0.58 ± 0.02	0.7591
Relative Muscle weight (%)	1.00 ± 0.02	1.04 ± 0.02	1.00 ± 0.02	0.9404
Relative EFP weight (%)	0.95 ± 0.05	0.95 ± 0.05	0.97 ± 0.06	0.9576
Relative BAT weight (%)	0.20 ± 0.02 <sup>a</sup>	0.25 ± 0.01 <sup>b</sup>	0.24 ± 0.01 <sup>a,b</sup>	0.1760

Data are mean ± SEM, n=8 mice/group. Different letters (a, b) in the same row indicate a significant difference at  $P<0.05$ . Food efficiency ratio: body weight (BW) gain (g/day)/food intake (g/day). Muscle mass includes both gastrocnemius and soleus muscles in the back part of the lower legs. BAT: brown adipose tissue; EFP: epididymal fat pad. Mice were treated with vehicle, LOE-1X, or LOE-5X for 4 weeks.

intake of diet and water were no different between the vehicle and treatment groups. We observed that LOE treatment did not affect water intake, diet or BW. The BW of the mice in each group steadily increased throughout the experimental period (Table 1). Analyses of the mice body compositions after 4-week LOE supplementation showed no significant difference in weights of liver, kidney, heart, lung, muscle and epididymal fat pad (EFP). Only the brown adipose fat (BAT) saw slight increase (1.25-fold,  $P=0.0396$ ) in the LOE-1X group compared with vehicle treatment. We also examined the relative tissue weights at the end of 4 weeks LOE supplementation, which is calculated by the different tissue weights adjusted for by individual BW %. The relative BAT weight with the LOE-1X group was higher by 1.24-fold ( $P=0.0396$ ) than vehicle group, suggesting a slight beneficial effect of LOE supplementation on BAT weight. Besides that, all relative weight of all other tissues did not differ significantly among the vehicle, LOE-1X and LOE-5X groups.

#### Effect of LOE supplementation on biochemical variables

We observed that 4-weeks LOE supplementation increased exhaustive exercise challenge time and optimized anti-fatigue indicators including lactate, ammonia, glucose, CK and BUN levels. Both liver and muscle glycogen storage capacity could also be increased by LOE supplementation. We further investigated whether the 4-week LOE treatment could affect other biochemical markers in the healthy mice by examining tissue- and health status-related biochemical variables and major organs including the skeletal muscle, heart, kidney and lung (Table 2).

Total protein and albumin levels did not differ among the groups ( $P>0.05$ , Table 2). Serum AST levels were lower by 24.28% ( $P=0.0003$ ) and 27.43% ( $P<0.0001$ ) with the LOE-1X and LOE-5X group respectively, compared with the vehicle group. Similarly, ALT levels were reduced by 28.31% ( $P=0.0214$ ) and 24.62% ( $P=0.0422$ ) with LOE-1X and LOE-5X, respectively. LDH levels were also significantly lower in the LOE-1X (30.44%,  $P=0.0046$ ) and LOE-5X (28.09%,  $P=0.0081$ ) than vehicle group. The serum CK of the mice in the LOE-1X and LOE-5X groups were lower by 46.78% ( $P<0.0001$ ) and 54.78% ( $P<0.0001$ ), respectively. BUN levels in LOE-1X and LOE-5X were significantly lowered by 19.18% ( $P=0.0030$ ) and 20.74% ( $P=0.0016$ ), respectively, compared with vehicle treatment. Serum creatinine levels in LOE-5X group was 17.49% ( $P=0.0074$ ) lower than in vehicle group. The serum UA of the mice in the LOE-1X and LOE-5X groups were reduced by 20.38% ( $P=0.0014$ ) and 38.86% ( $P<0.0001$ ), respectively, while the serum TC and TG of the mice in the LOE-5X group were lowered by 14.73% ( $P=0.0063$ ) and 27.11% ( $P<0.0005$ ), respectively, compared to the vehicle group.

Trend analysis revealed that LOE treatment had significant dose-dependent reduction in levels of AST ( $P<0.0001$ ), ALT ( $P=0.0450$ ), LDH ( $P=0.0016$ ), CK ( $P<0.0001$ ), BUN ( $P<0.0001$ ), creatinine ( $P=0.0021$ ), UA ( $P<0.0001$ ), TC ( $P=0.0034$ ) and TG ( $P<0.0001$ ). In addition, serum glucose was shown to be 1.11-fold higher ( $P=0.0243$ ) in the LOE-5X compared to the vehicle group. Trend analysis also revealed significant ( $P=0.0108$ ) dose-dependent increase on serum glucose levels. Taken together, our findings indicate that long-term daily supplementation with LOE may potentially protect muscle damage by decreasing AST, ALT, LDH, CK, BUN, creatinine and UA levels. Additionally, our results also suggest that LOE supplementation may have the potential to prevent lipid accumulation through reduced TC and TG.

**Table 2.** Biochemical analysis with LOE supplementation at the end of the experiment

Parameter	Vehicle	LOE-1X	LOE-5X	Trend analysis
AST (U/l)	135 ± 5 <sup>b</sup>	102 ± 5 <sup>a</sup>	98 ± 4 <sup>a</sup>	<0.0001 (↓)
ALT (U/l)	75 ± 5 <sup>b</sup>	54 ± 5 <sup>a</sup>	56 ± 6 <sup>a</sup>	0.0450 (↓)
LDH (U/l)	766 ± 71 <sup>b</sup>	533 ± 30 <sup>a</sup>	551 ± 24 <sup>a</sup>	0.0016 (↓)
CK (U/l)	835 ± 22 <sup>b</sup>	444 ± 24 <sup>a</sup>	377 ± 61 <sup>a</sup>	<0.0001 (↓)
TP (g/dl)	5.1 ± 0.0 <sup>a</sup>	5.1 ± 0.0 <sup>a</sup>	5.1 ± 0.1 <sup>a</sup>	0.9224
Albumin (g/dl)	3.1 ± 0.0 <sup>a</sup>	3.2 ± 0.0 <sup>a</sup>	3.1 ± 0.0 <sup>a</sup>	0.7858
BUN (mg/dl)	25.7 ± 1.4 <sup>b</sup>	20.8 ± 0.6 <sup>a</sup>	20.4 ± 0.5 <sup>a</sup>	<0.0001 (↓)
Creatinine (mg/dl)	0.28 ± 0.01 <sup>b</sup>	0.25 ± 0.01 <sup>b</sup>	0.23 ± 0.01 <sup>a</sup>	0.0021 (↓)
UA (mg/dl)	2.6 ± 0.1 <sup>b</sup>	2.1 ± 0.1 <sup>a</sup>	1.6 ± 0.1 <sup>a</sup>	<0.0001 (↓)
TC (mg/dl)	141 ± 4 <sup>b</sup>	143 ± 4 <sup>b</sup>	120 ± 4 <sup>a</sup>	0.0034 (↓)
TG (mg/dl)	145 ± 6 <sup>c</sup>	131 ± 6 <sup>b,c</sup>	106 ± 7 <sup>a</sup>	<0.0001 (↓)
Glucose (mg/dl)	147 ± 3 <sup>a</sup>	161 ± 4 <sup>a,b</sup>	164 ± 6 <sup>b</sup>	0.0108 (↑)

Data are mean ± SEM, n=8 mice/group. Different letters (a, b) in the same row indicate a significant difference at  $P < 0.05$  by one-way ANOVA. AST, aspartate aminotransferase; ALT, alanine aminotransferase; LDH, lactic dehydrogenase; CK, creatine kinase; TP, total protein; BUN, blood urea nitrogen; UA, uric acid; TC, total cholesterol; TG, triglycerides.

### *Effect of LOE supplementation on histological examinations at the end of the experiment*

LOE supplementation for 4 weeks in the mice had no adverse effects on major organs such as the liver, skeletal muscle, heart, kidney, lung and EFP based on tissue morphology (Fig. 6). This suggests that the dose for LOE supplementation used in this study was safe.

## DISCUSSION

According to previous studies, LOE has been shown to be an AMP activated protein kinase (AMPK) activator. AMPK is a major cellular energy sensor and metabolic regulator, and is considered to be a therapeutic target for treatment of diabetes mellitus [21]. Additionally, AMPK is a sensor of cellular energy status and plays a central role in skeletal muscle metabolism [14]. Either nutritional supplementation or exercise is able to activate AMPK in the heart [8]. Activation AMPK could increase skeletal muscle strength and cardiac function, especially during endurance exercise [19]. In our study, although the mice did not undergo a training intervention, LOE supplementation was able to extend endurance exercise times to improve exercise performance, possibly through LOE's activation of the AMPK pathway [20, 23, 29].

Exercise-induced muscle fatigue can be evaluated by various biochemical indicators, of which the most well-known biomarkers include lactate, ammonia, glucose, CK and BUN levels [13, 24]. Lactate threshold is a useful measure for deciding exercise intensity for training and racing in endurance exercise, with lactate accumulation being caused by changes in extracellular pH. A decrease in pH is required for lactate to efflux from the muscle [1]. Lactate clearance is expected to reduce peripheral neuromuscular fatigue and has positive effects on muscle function [26].

During exercise, the consumption of ATP exceeds the ATP supply, causing ATP/ADP (adenosine diphosphate) ratio decreases. The production of ammonia during exercise is the result of adenylate kinase transferring one energy-rich phosphate group from one ADP molecule to another, resulting in the formation of one ATP and one AMP molecule. AMP is deaminated to inosine monophosphate (IMP) and ammonia via the enzyme AMP deaminase [10]. Ammonia accumulation in blood has been observed in endurance athletes and exercise-related increase in blood ammonia is almost linear, regardless of the exercise intensity [16]. In previous studies, lower ammonia accumulation has been observed in endurance athletes [9]. Both serum lactate and ammonia concentration are useful biomarkers for exercise-related metabolic responses in competitive explosive force, as well as in endurance-trained athletes [16]. In this respect, LOE may have potential as an ergogenic supplement by improving the removal of these metabolic wastes during exercise.

Oleanolic acid and related derivatives such as triterpene acids and ursolic acid have been isolated from LOE [4]. Synthesis and biological evaluation of oleanolic acid and related derivatives have shown them to be novel inhibitors of glycogen phosphorylase [25]. Inhibition of glycogen phosphorylase leads to inhibition of glycogenolysis. ATP and glucose are also known glycogen phosphorylase inhibitors, but high concentrations of AMP can activate previously inactive glycogen phosphorylase to accelerate glycogenolysis [11]. Our findings suggest that LOE could increasing blood glucose and muscle glycogen breakdown redirecting blood flow toward skeletal muscle for enhanced performance, especially in enhance glucose storage in muscle, concomitantly enhancing endurance exercise performance.

In this study, we found that a 4-week supplementation with LOE extract could significantly improve performance of endurance exercise, with the mice showing extended swimming times to exhaustion. LOE's anti-fatigue activity is reflected by the decrease in plasma lactate, ammonia, CK, BUN and increased glucose levels, after acute exercise in mice. LOE also had positive effects on the liver, kidney, muscle protection and prevention of lipid accumulation by decreasing AST, ALT, LDH, CK, BUN, creatinine, UA levels, as well as TC and TG levels. In terms of glycogen storage capacity, our data clearly indicates that muscle glycogen increased with 4-week LOE-supplementation in a dose-dependent manner, suggesting that enhanced muscle glycogen storage was the main reason for extended swimming time to exhaustion.



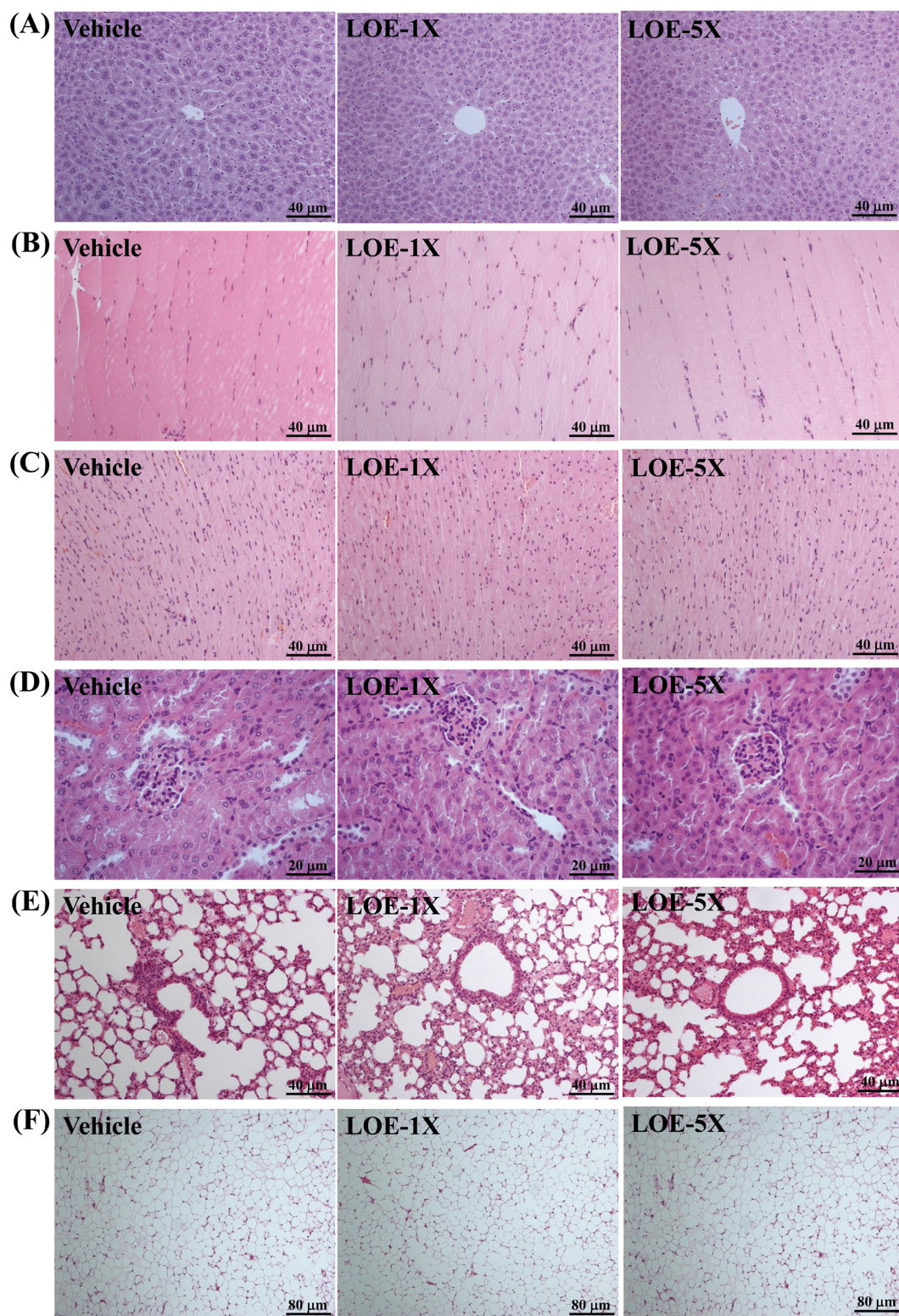


**Fig. 6.** Effect of LOE supplementation on morphology of (A) liver, (B) skeletal muscle, (C) heart, (D) kidney, (E) lungs and (F) epididymal fat pad (EFP). Specimens were photographed by light microscopy and stained with H&E. Magnification:  $\times 200$  (A–E) and  $\times 100$  (F).

In conclusion, our study has found that LOE supplementation for 4 weeks is able to considerably enhance endurance exercise performance, improve fatigue as assessed by the biochemical markers, as well as increase muscle glycogen. This suggests that LOE could potentially serve well as a nutrient supplement or healthy ergogenic aid to enhance muscle glycogen storage and maximize energy utilization during exercise.



CONFLICTS OF INTEREST. The authors declare no conflict of interest.

ACKNOWLEDGMENTS. This work was supported by Chang Gung Memorial Hospital Grants (CMRPF1G0171). The authors thank Dr. Chien-Chao Chiu for conducting the histological examination.

## REFERENCES

- Banister, E. W., Allen, M. E., Mekjavic, I. B., Singh, A. K., Legge, B. and Mutch, B. J. C. 1983. The time course of ammonia and lactate accumulation in blood during bicycle exercise. *Eur. J. Appl. Physiol.* **51**: 195–202. [\[CrossRef\]](#)
- Boots, A. W., Haenen, G. R. M. M. and Bast, A. 2008. Health effects of quercetin: from antioxidant to nutraceutical. *Eur. J. Pharmacol.* **585**: 325–337. [\[Medline\]](#) [\[CrossRef\]](#)
- Cantó, C., Jiang, L. Q., Deshmukh, A. S., Matak, C., Coste, A., Lagouge, M., Zierath, J. R. and Auwerx, J. 2010. Interdependence of AMPK and SIRT1 for metabolic adaptation to fasting and exercise in skeletal muscle. *Cell Metab.* **11**: 213–219. [\[Medline\]](#) [\[CrossRef\]](#)
- Chang, C. I., Kuo, C. C., Chang, J. Y. and Kuo, Y. H. 2004. Three new oleanane-type triterpenes from *Ludwigia octovalvis* with cytotoxic activity against two human cancer cell lines. *J. Nat. Prod.* **67**: 91–93. [\[Medline\]](#) [\[CrossRef\]](#)
- Chen, Y. M., Lee, H. C., Chen, M. T., Huang, C. C. and Chen, W. C. 2018. Dehydroepiandrosterone supplementation combined with Weight-Loading Whole-Body Vibration Training (WWBV) affects exercise performance and muscle glycogen storage in middle-aged C57BL/6 mice. *Int. J. Med. Sci.* **15**: 564–573. [\[Medline\]](#) [\[CrossRef\]](#)
- Chen, Y. M., Wei, L., Chiu, Y. S., Hsu, Y. J., Tsai, T. Y., Wang, M. F. and Huang, C. C. 2016. *Lactobacillus plantarum* TWK10 supplementation improves exercise performance and increases muscle mass in mice. *Nutrients* **8**: 205. [\[Medline\]](#) [\[CrossRef\]](#)
- Coughlan, K. A., Valentine, R. J., Ruderman, N. B. and Saha, A. K. 2014. AMPK activation: a therapeutic target for type 2 diabetes? *Diabetes Metab. Syndr. Obes.* **7**: 241–253. [\[Medline\]](#)
- Dolinsky, V. W., Jones, K. E., Sidhu, R. S., Haykowsky, M., Czubyrt, M. P., Gordon, T. and Dyck, J. R. 2012. Improvements in skeletal muscle strength and cardiac function induced by resveratrol during exercise training contribute to enhanced exercise performance in rats. *J. Physiol.* **590**: 2783–2799. [\[Medline\]](#) [\[CrossRef\]](#)
- Graham, T. E., Turcotte, L. P., Kiens, B. and Richter, E. A. 1997. Effect of endurance training on ammonia and amino acid metabolism in humans. *Med. Sci. Sports Exerc.* **29**: 646–653. [\[Medline\]](#) [\[CrossRef\]](#)
- Hancock, C. R., Janssen, E. and Terjung, R. L. 2006. Contraction-mediated phosphorylation of AMPK is lower in skeletal muscle of adenylate kinase-deficient mice. *J. Appl. Physiol.* **100**: 406–413. [\[Medline\]](#) [\[CrossRef\]](#)
- Henke, B. R. and Sparks, S. M. 2006. Glycogen phosphorylase inhibitors. *Mini Rev. Med. Chem.* **6**: 845–857. [\[Medline\]](#) [\[CrossRef\]](#)
- Hsiao, C. Y., Chen, Y. M., Hsu, Y. J., Huang, C. C., Sung, H. C. and Chen, S. S. 2017. Supplementation with Hualian No. 4 wild bitter gourd (*Momordica charantia* Linn. var. *abbreviata* ser.) extract increases anti-fatigue activities and enhances exercise performance in mice. *J. Vet. Med. Sci.* **79**: 1110–1119. [\[Medline\]](#) [\[CrossRef\]](#)
- Izquierdo, M., González-Izal, M., Navarro-Amezqueta, I., Calbet, J. A., Ibañez, J., Malanda, A., Mallor, F., Häkkinen, K., Kraemer, W. J. and Gorostiaga, E. M. 2011. Effects of strength training on muscle fatigue mapping from surface EMG and blood metabolites. *Med. Sci. Sports Exerc.* **43**: 303–311. [\[Medline\]](#) [\[CrossRef\]](#)
- Jäger, S., Handschin, C., St-Pierre, J. and Spiegelman, B. M. 2007. AMP-activated protein kinase (AMPK) action in skeletal muscle via direct phosphorylation of PGC-1 $\alpha$ . *Proc. Natl. Acad. Sci. U.S.A.* **104**: 12017–12022. [\[Medline\]](#) [\[CrossRef\]](#)
- Kadam Yakob, H., Manaf Uyub, A. and Fariza Sulaiman, S. 2012. Toxicological evaluation of 80% methanol extract of *Ludwigia octovalvis* (Jacq.) P.H. Raven leaves (*Onagraceae*) in BALB/c mice. *J. Ethnopharmacol.* **142**: 663–668. [\[Medline\]](#) [\[CrossRef\]](#)
- Kantanista, A., Kusy, K., Zarebska, E., Włodarczyk, M., Ciekot-Soltysiak, M. and Zieliński, J. 2016. Blood ammonia and lactate responses to incremental exercise in highly-trained male sprinters and triathletes. *Biomed. Hum. Kinetics* **8**: 32–38. [\[CrossRef\]](#)
- Kawanaka, K., Nolte, L. A., Han, D. H., Hansen, P. A. and Holloszy, J. O. 2000. Mechanisms underlying impaired GLUT-4 translocation in glycogen-supercompensated muscles of exercised rats. *Am. J. Physiol. Endocrinol. Metab.* **279**: E1311–E1318. [\[Medline\]](#) [\[CrossRef\]](#)
- Kritchevsky, D. and Chen, S. C. 2005. Phytochemicals –health benefits and potential concerns: A review. *Nutr. Res.* **25**: 413–428. [\[CrossRef\]](#)
- Lantier, L., Fentz, J., Mounier, R., Leclerc, J., Tebbak, J. T., Pehmoller, C., Sanz, N., Sakakibara, I., Saint-Amand, E., Rimbaud, S., Maire, P., Marette, A., Ventura-Clapier, R., Ferry, A., Wojtaszewski, J. F., Foretz, M. and Viollet, B. 2014. AMPK controls exercise endurance, mitochondrial oxidative capacity, and skeletal muscle integrity. *FASEB J.* **28**: 3211–3224. [\[Medline\]](#) [\[CrossRef\]](#)
- Lin, W. S., Chen, J. Y., Wang, J. C., Chen, L. Y., Lin, C. H., Hsieh, T. R., Wang, M. F., Fu, T. F. and Wang, P. Y. 2014. The anti-aging effects of *Ludwigia octovalvis* on *Drosophila melanogaster* and AMPK mice. *Age (Dordr.)* **36**: 689–703. [\[Medline\]](#) [\[CrossRef\]](#)
- Lin, W. S., Lo, J. H., Yang, J. H., Wang, H. W., Fan, S. Z., Yen, J. H. and Wang, P. Y. 2017. *Ludwigia octovalvis* extract improves glycemic control and memory performance in diabetic mice. *J. Ethnopharmacol.* **207**: 211–219. [\[Medline\]](#) [\[CrossRef\]](#)
- Ma, G. D., Chiu, C. H., Hsu, Y. J., Hou, C. W., Chen, Y. M. and Huang, C. C. 2017. Changbai Mountain ginseng (*Panax ginseng* CA Mey) extract supplementation improves exercise performance and energy utilization and decreases fatigue-associated parameters in mice. *Molecules* **22**: 237. [\[CrossRef\]](#)
- Narkar, V. A., Downes, M., Yu, R. T., Emblar, E., Wang, Y. X., Banayo, E., Mihaylova, M. M., Nelson, M. C., Zou, Y., Juguilon, H., Kang, H., Shaw, R. J. and Evans, R. M. 2008. AMPK and PPAR $\delta$  agonists are exercise mimetics. *Cell* **134**: 405–415. [\[Medline\]](#) [\[CrossRef\]](#)
- Strojnik, V. and Komi, P. V. 2000. Fatigue after submaximal intensive stretch-shortening cycle exercise. *Med. Sci. Sports Exerc.* **32**: 1314–1319. [\[Medline\]](#) [\[CrossRef\]](#)
- Sultana, N. and Ata, A. 2008. Oleanolic acid and related derivatives as medicinally important compounds. *J. Enzyme Inhib. Med. Chem.* **23**: 739–756. [\[Medline\]](#) [\[CrossRef\]](#)
- White, G. E. and Wells, G. D. 2015. The effect of on-hill active recovery performed between runs on blood lactate concentration and fatigue in alpine ski racers. *J. Strength Cond. Res.* **29**: 800–806. [\[Medline\]](#) [\[CrossRef\]](#)
- Wu, S. J., Ng, L. T., Wang, G. H., Huang, Y. J., Chen, J. L. and Sun, F. M. 2010. Chlorophyll a, an active anti-proliferative compound of *Ludwigia octovalvis*, activates the CD95 (APO-1/CD95) system and AMPK pathway in 3T3-L1 cells. *Food Chem. Toxicol.* **48**: 716–721. [\[Medline\]](#) [\[CrossRef\]](#)
- Yakob, H. K., Sulaiman, S. F. and Uyub, A. M. 2012. Antioxidant and antibacterial activity of *Ludwigia octovalvis* on *Escherichia coli* O157: H7 and some pathogenic bacteria. *World Appl. Sci. J.* **16**: 22–29.
- Yan, J. and Yang, X. W. 2005. [Studies on the chemical constituents in herb of *Ludwigia octovalvis*]. *Zhongguo Zhongyao Zazhi* **30**: 1923–1926 (in Chinese). [\[Medline\]](#)

## Article

# Chemical Constituents of *Vigna luteola* and Their Anti-inflammatory Bioactivity

Sio-Hong Lam <sup>1,†</sup>, Yue-Chiun Li <sup>2,†</sup>, Ping-Chung Kuo <sup>1,\*</sup> , Tsong-Long Hwang <sup>3,4,5</sup> ,  
Mei-Lin Yang <sup>1</sup>, Chien-Chiao Wang <sup>3</sup> and Jason T. C. Tzen <sup>2,\*</sup>

<sup>1</sup> School of Pharmacy, College of Medicine, National Cheng Kung University, Tainan 701, Taiwan; shlam@mail.ncku.edu.tw (S.-H.L.); L3891104@nckualumni.org.tw (M.-L.Y.)

<sup>2</sup> Graduate Institute of Biotechnology, National Chung-Hsing University, Taichung 402, Taiwan; ycli0126@gmail.com

<sup>3</sup> Graduate Institute of Natural Products, College of Medicine, Chang Gung University, Taoyuan 333, Taiwan; htl@mail.cgu.edu.tw (T.-L.H.); D0501502@cgu.edu.tw (C.-C.W.)

<sup>4</sup> Research Center for Industry of Human Ecology, Research Center for Chinese Herbal Medicine, and Graduate Institute of Health Industry Technology, Chang Gung University of Science and Technology, Taoyuan 333, Taiwan

<sup>5</sup> Department of Anesthesiology, Chang Gung Memorial Hospital, Taoyuan 333, Taiwan

\* Correspondence: z10502016@email.ncku.edu.tw (P.-C.K.); tctzen@dragon.nchu.edu.tw (J.T.C.T.); Tel.: +886-6-2353535 (ext. 6806) (P.-C.K.); +886-4-22840328 (J.T.C.T.)

† These authors contributed equally to this work.

Received: 18 March 2019; Accepted: 7 April 2019; Published: 8 April 2019



**Abstract:** Seventy-three compounds were identified from the methanol extract of *V. luteola*, and among these, three new (1–3) were characterized by spectroscopic and mass spectrometric analyses. The isolated constituents were assessed for anti-inflammatory potential evaluation, and several purified principles exhibited significant superoxide anion and elastase inhibitory effects.

**Keywords:** fabaceae; sesquiterpenoid; superoxide anion generation; elastase release

## 1. Introduction

Plenty of phytochemicals isolated from dietary and medicinal plants, such as epigallocatechin gallate [1], soy isoflavones [2], and curcumin [3,4], have been considered as promising sources of potential anticancer agents [5,6], and are one of the important sources for cancer treatment [7]. As of a thousand years ago, legumes had become essential for the protein supplements in the world. In addition, legumes are a considerable target for scientists to develop new foods, so that various seeds including the wild relatives and cultivated legumes attracted much attention. Many studies have reported that legumes possess various bioactivities [8–10]. Therefore, our team continued to explore edible wild beans as new natural health food supplements in the recent years.

Inflammation is the first response of the immune system to infection or irritation due to bacteria, virus, wound, or other various environmental factors resulting in injuring. Recently, the overexpression of neutrophils has been demonstrated to be related with various human diseases and causing serious threat to human health [11–15]. A response to diverse stimuli of the immune system is the activation of neutrophils to secrete a series of cytotoxins, such as superoxide anion and elastase [16]. Therefore, equilibrium of superoxide anion production and elastase release in infected tissues and organs is important. Furthermore, only a few available agents could directly modulate neutrophil proinflammatory responses in clinical practice. Chemoprevention is the idea of feeding natural sources to protect the human body from various diseases. Thus, utilization of anti-inflammatory health food supplements is important for the reduction of some diseases such as cancer.

*V. luteola* (Jacq.) Benth. is a trailing or twining herb belonging to the *Vigna* genus usually distributed in the tropical regions. In Taiwan, *V. luteola* is grown in the open seaside at elevation below 100 m and spread over the island [17]. The *Vigna* genus has been reported to show antioxidant [18,19], antifungal [20], antitumor [21,22], deworming [23,24], hypoglycemic [25,26], hepatoprotective [27,28], kidney protection [29,30], antibacterial [31,32], hypotensive [33,34], and hypolipidemic [35,36] bioactivities. In our previous research, the constituents and anti-inflammatory bioactivity of *V. vexillata* were investigated and the results exhibited potent inhibitory activity of superoxide generation and elastase release [37]. Preliminary bioassay data indicated that the methanol extract and fractions of *V. luteola* (at 10 µg/mL) also displayed significant superoxide and elastase inhibition by human neutrophils in response to *N*-formyl-L-methionyl-phenylalanine/cytochalasin B (fMLP/CB) (Table 1). Therefore, the present study aimed to characterize the chemical constituents and anti-inflammatory bioactivity of *V. luteola*. In total, seventy-three compounds were identified and, among these, one sesquiterpenoid (1), one alkaloid (2), and one  $\alpha$ -pyranone (3) were characterized based on spectroscopic and spectrometric analyses. Moreover, some of the isolated compounds were evaluated for their inhibitory activity of superoxide anion generation and elastase release.

**Table 1.** Inhibitory percentages of crude extract and partial purified fractions of *V. luteola* on superoxide anion generation and elastase release by human neutrophils in response to *N*-formyl-L-methionyl-phenylalanine/cytochalasin B (fMLP/CB).

Samples	Inh % <sup>a</sup>	
	Superoxide Anion Generation	Elastase Release
methanol extract	51.8 ± 6.8 ***	108.4 ± 6.9 ***
chloroform fraction	91.2 ± 3.8 ***	118.0 ± 5.0 ***
water fraction	18.3 ± 6.1 *	34.6 ± 3.6 ***

<sup>a</sup> Percentage of inhibition (Inh %) at 10 µg/mL concentration. Results are presented as mean ± S.E.M. (n = 3). \*  $p < 0.05$ , \*\*\*  $p < 0.001$  compared with the control value (DMSO).

## 2. Results and Discussion

### 2.1. Purification and Characterization

The whole-plants of *V. luteola* were air-dried, powdered, and extracted with methanol under reflux. The methanol extract was concentrated under reduce pressure to give a deep brown syrup extract. This extract was partitioned with water and chloroform to provide two soluble layers, i.e., chloroform soluble and water soluble layers, respectively. With the assistance of a combination of conventional chromatographic techniques, one sesquiterpenoid viglutin (1), one alkaloid viglutoside (2), one  $\alpha$ -pyranone viglutanone (3), along with two salts sodium phaseate (4) and sodium *p*-coumarate (5), were characterized and their structures were constructed from the nuclear magnetic resonance (NMR) spectral elucidation and mass (MS) spectrometric analysis. Moreover, sixty-eight known compounds, including eight sesquiterpenoids, loliolide (6), isolololide (7), blumenol A (8), kiwiionol (9), (+)-(*S*)-dehydrovomifoliol (10), (6*S*,9*R*)-roseoside (11), (3*S*,5*R*,6*S*,7*E*,9*R*)-megastigman-7-en-3,6,9-triol (12), (3*S*,5*R*,6*R*,7*E*)-3,5,6-trihydroxymegastigman-7-en-9-one (13); two sesquiterpenoids, abscisic acid (14) and machilusoxide A (15); one diterpenoid, 3(17)-phytene-1,2-diol (16); two triterpenoids, lupeol (17) and simiarenol (18); seven steroids, mixture of  $\beta$ -sitosterol (19) and stigmasterol (20), mixture of  $\beta$ -sitosteryl-3-*O*- $\beta$ -D-glucoside (21), and stigmasteryl-3-*O*- $\beta$ -D-glucoside (22), mixture of stigmast-4-en-3-one (23) and stigmast-4,22-dien-3-one (24), ergosterol peroxide (25); one lignan, (+)-pinorezinol (26); eight alkaloids, uracil (27), uridine (28), 6-hydroxymethyl-3-pyridinol (29), thymine (30), adenine (31), nicotinamide (32), potassium nicotinate (33), 6-hydroxynicotinic acid (34); nineteen benzenoids, *p*-hydroxybenzoic acid (35), methylparaben (36), *trans*-methyl *p*-coumarate (37), (*E*)-methyl ferulate (38), *trans*-isoferulic acid (39), *trans*-ferulic acid (40), isovanillic acid (41), methyl vanillate (42), vanillic acid (43), 4-hydroxybenzaldehyde (44), syringic acid (45), gentisic acid (46),

sodium salicylate (47), benzoic acid (48), methyl 2-O- $\beta$ -D-glucopyranosylsalicylate (49), protocatechuic acid (50), phenylacetic acid (51), benzyl alcohol  $\beta$ -D-glucopyranosyl(1 $\rightarrow$ 6)- $\beta$ -D-glucopyranoside (52), gentisic acid 5-O- $\beta$ -D-xylopyranoside (53); nine flavonoids, kaempferol (54), liquiritigenin (55), kaempferol 3-O-[ $\alpha$ -L-rhamnopyranosyl(1 $\rightarrow$ 6)]- $\beta$ -D-galactopyranoside (56), chrysoeriol (57), astragalin (58), kaempferol-3-O-sophorose (59), kaempferol 3-O-sophorose-7-O-rhamnoside (60), robinin (61), isorhamnetin 3-O-[ $\alpha$ -L-rhamnopyranosyl(1 $\rightarrow$ 6)]- $\beta$ -D-galactopyranoside 7-O- $\alpha$ -L-rhamnopyranoside (62); eight isoflavonoids, daidzein (63), 8-O-methylretusin (64), 5,7,4'-trihydroxyisoflavone (65), 7,2',4'-trihydroxyisoflavone (66), tectorigenin (67), afromosin (68), 3'-methoxydaidzein (69), 7,4'-dihydroxy-8-methoxyisoflavone (70); three others, 2-furanoic acid (71), maltol glucoside (72), sodium 5-hydroxymethylfuran-2-carboxylate (73), respectively, were verified by inspection of their reported spectroscopic data (references of known compounds were provided in Supplementary Materials).

## 2.2. Structural Elucidations of 1–5

Compound 1 was isolated as optically active yellow powder, and the molecular formula was assigned as  $C_{13}H_{22}O_3$  with a sodium adduct ion peak at  $m/z$  249.1460 in high-resolution electrospray ionization mass spectrometry (HR-ESI-MS) analysis. The infrared (IR) absorption bands at 3416 and 1647  $cm^{-1}$  were in agreement with the presences of hydroxy and carbon–carbon double bond functionalities, respectively. In the  $^1H$ -NMR spectrum, there were proton signals for two methyl singlets at  $\delta$  0.96 (3H, s,  $CH_3$ -11), 1.06 (3H, s,  $CH_3$ -12), one methyl doublet of doublets 1.73 (3H, dd,  $J$  = 6.5, 1.5 Hz,  $CH_3$ -10), two oxymethylene protons at  $\delta$  3.61 (1H, dd,  $J$  = 11.0, 7.0 Hz, H-13a) and 3.81 (1H, m, H-13b), two oxymethine at  $\delta$  3.80 (1H, dddd,  $J$  = 12.0, 7.5, 5.0, 3.5 Hz, H-3) and 4.18 (1H, d,  $J$  = 8.5 Hz, H-7), three methines at  $\delta$  1.36 (1H, ddd,  $J$  = 12.6, 5.0, 1.5 Hz, H-2b), 1.51 (1H, ddd,  $J$  = 12.0, 12.0, 11.5 Hz, H-4a), 2.44 (1H, m, H-5), and two trans olefinic protons at  $\delta$  5.67 (1H, ddd,  $J$  = 15.5, 8.5, 1.5 Hz, H-8) and 5.78 (1H, dq,  $J$  = 15.5, 6.5 Hz, H-9). The  $^{13}C$ -NMR and distortionless enhancement by polarization transfer (DEPT) spectra exhibited three methyl carbons at  $\delta$  18.2 (C-10), 24.0 (C-12) and 25.9 (C-11); three methylene carbons at  $\delta$  31.6 (C-4), 46.8 (C-2), and 69.7 (C-13); five methines at  $\delta$  43.7 (C-5), 68.5 (C-3), 84.4 (C-7), 129.6 (C-8), and 132.1 (C-9); and two quaternary carbons at  $\delta$  37.7 (C-1) and 81.2 (C-6). The correlation spectroscopy (COSY) indicated the linkage of H-2/H-3/H-4/H-5/H-13 and H-7/H-8/H-9/H-10 (Figure 1). The  $^2J$ - and  $^3J$ - correlation peaks from H-2 to C-4 and C-6; from H-3 to C-5; from H-7 to C-8 and C-9; from H-8 to C-10; from H-13 to C-6 and C-7; and from  $CH_3$ -11 to C-1, C-2, C-6, and  $CH_3$ -12, respectively, were observed in the 2-dimensions (2D) heteronuclear multiple bond correlation (HMBC) spectrum (Figure 1). In addition, the index of hydrogen deficiency (IHD = 3) of 1 suggested the presences of one double bond and two rings in 1. According to this spectral evidence, the planar structure of 1 was constructed as shown (Figure 1). Furthermore, the large coupling constant of H-3 (12.0 Hz) revealed its axial orientation, and the correlations of H-3/H-5, H-5/H-13, and  $CH_3$ -12/H-7 in the Nuclear Overhauser Effect spectroscopy (NOESY) established its relative stereochemistry configuration (Figure 1). All the proton and carbon signals assignments were achieved by the combination of 2D NMR experiments (see Supplementary Materials). Conclusively, the structure of 1 was assigned as shown based on the experimental results which mentioned above and named trivially as viglutin.



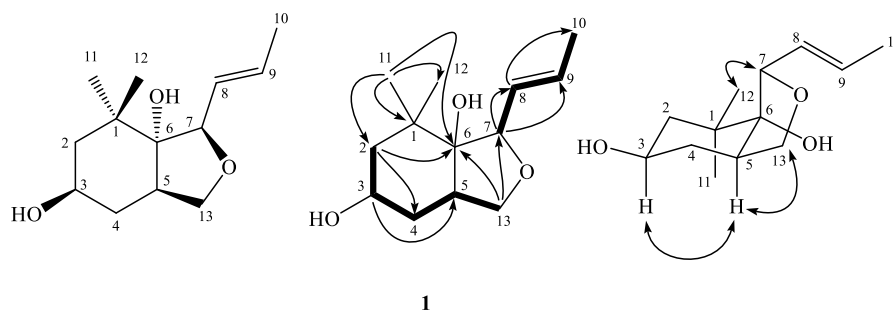


Figure 1. Key COSY (■), HMBC (→), and NOESY (↔) correlations of **1**.

Compound **2** was assigned a molecular formula of  $C_{12}H_{17}NO_6$  from its HR-ESI-MS analytical data ( $m/z$  294.0952, calc. for  $C_{12}H_{17}NNaO_6$ , 294.0954). The UV absorption maxima at 274 and 221 nm were indication of the heteroaromatic chromophore [38], and it was further supported by the downfield ABX-coupled aromatic protons at  $\delta$  7.21 (1H, dd,  $J = 8.5, 2.5$  Hz, H-4), 7.32 (1H, d,  $J = 8.5$  Hz, H-5), and 8.03 (1H, d,  $J = 2.5$  Hz, H-2). The existence of hydroxyl and carbon–carbon double bond functionalities could be determined from the IR absorption bands at 3430 and 1637  $cm^{-1}$ . One methylene group at  $\delta$  4.51 (1H, d,  $J = 12.0$  Hz, H-7a) and 4.65 (1H, d,  $J = 12.0$  Hz, H-7b), and one set of rhamnose protons at  $\delta$  1.25 (3H, d,  $J = 6.0$  Hz, H-6'), 3.38 (1H, dd,  $J = 9.5, 9.5$  Hz, H-4'), 3.60 (1H, dd,  $J = 9.5, 6.0$  Hz, H-5'), 3.67 (1H, dd,  $J = 9.5, 3.5$  Hz, H-3'), 3.85 (1H, dd,  $J = 3.5, 2.0$  Hz, H-2'), and 4.78 (1H, d,  $J = 2.0$  Hz, H-1') appeared in the  $^1H$ -NMR spectrum of **2**. In its  $^{13}C$ -NMR spectrum, a set of signals at  $\delta$  18.0 (C-6'), 70.1 (C-5'), 72.3 (C-2'), 72.4 (C-3'), 74.0 (C-4'), and 101.4 (C-1') also evidenced the presence of rhamnoside [39]. The observed HMBC correlations from H-2 to C-3, C-4, and C-6; from H-4 to C-6; from H-5 to C-3 and C-6; from H-7 to C-5, C-6, and C-1'; from H-1' to C-3' and C-5', respectively, established the structure of **2** as 6-( $\alpha$ -rhamnosyloxymethyl)-3-pyridinol (Figure 2) and assigned the trivial name as viglutoside.

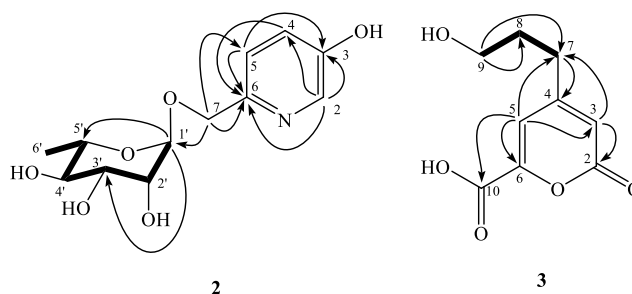


Figure 2. Key COSY (■) and HMBC (→) correlations of **2** and **3**.

Viglutanone (**3**) was isolated as brown syrup, and the molecular formula was determined as  $C_9H_{10}O_5$  by a deprotonated molecular ion peak at  $m/z$  197.0449 in the HR-ESI-MS analysis. The UV absorption maximum at 299 nm and IR absorption bands at 3493, 1703, and 1631  $cm^{-1}$ , along with the consideration of IHD value (5) proposed the presence of an  $\alpha$ -pyranone basic structure with a carboxylic acid group. It was further evidenced by the proton signals for two vinyl singlets at  $\delta$  6.25 (1H, H-3) and 6.97 (1H, H-5) in  $^1H$ -NMR, and the carbon peaks for two vinyl groups at  $\delta$  110.4 (C-5), 114.8 (C-3), 156.4 (C-6), and 162.3 (C-4), and two carbonyls at  $\delta$  164.8 (C-2) and 165.8 (C-10), respectively. In addition, three methylene groups responsible for the propyloxyl substituent at  $\delta$  1.84 (2H, tt,  $J = 8.0, 6.4$  Hz, H-8), 2.60 (2H, t,  $J = 8.0$  Hz, H-7), and 3.60 (2H, t,  $J = 6.4$  Hz, H-9) were observed in the  $^1H$ -NMR spectrum of **3**. The  $^2J$ - and  $^3J$ -HMBC correlations from H-3 to C-2 and C-7; from H-5 to C-3, C-6, C-7, and C-10; from H-7 to C-4; and from H-9 to C-7 and C-8 concluded the structure of **3** as the  $\alpha$ -pyranone basic skeleton substituted with a propyloxyl fragment at C-4 and a carboxyl group at C-6 as shown (Figure 2).

In addition to new compounds **1–3**, two sodium salts **4** and **5** were also characterized from the methanol extract of *V. luteola*. Compound **4** was obtained as optically active white powder, and exhibited a protonated molecular at  $m/z$  279.1234 in the HR-ESI-MS experiment. The ultraviolet (UV) absorption maxima at 249 nm and the IR absorption bands at 3424, 1713, and  $1644\text{ cm}^{-1}$  suggested the occurrences of hydroxyl, carbonyl, and conjugated carbonyl groups in the molecule. The  $^1\text{H}$ -NMR spectrum of **4** exhibited signals for two *trans* olefinic protons at  $\delta$  6.20 (1H, d,  $J = 16.0$  Hz, H-7) and 7.87 (1H, d,  $J = 16.0$  Hz, H-8); one vinyl proton at  $\delta$  5.86 (1H, br s, H-10); three methyl singlets at  $\delta$  1.00 (3H,  $\text{CH}_3$ -13), 1.22 (3H,  $\text{CH}_3$ -14), and 1.95 (3H,  $\text{CH}_3$ -15); and three methylene groups at  $\delta$  2.37 (1H, dd,  $J = 18.0, 2.4$  Hz, H-2a), 2.45 (1H, dd,  $J = 18.0, 2.4$  Hz, H-4a), 2.71 (1H, dd,  $J = 18.0, 2.4$  Hz, H-2b), 2.81 (1H, d,  $J = 18.0$  Hz, H-4b), 3.65 (1H, d,  $J = 7.2$  Hz, H-12a), and 3.93 (1H, dd,  $J = 7.2, 2.8$  Hz, H-12b). The  $^{13}\text{C}$ -NMR spectrum also displayed one carbonyl carbon at  $\delta$  211.3 (C-3); one carboxyl signal at  $\delta$  175.0 (C-11); three methyl carbons at  $\delta$  15.8 (C-13), 19.4 (C-14), and 20.5 (C-15); three methylene carbons at  $\delta$  53.2 (C-2), 54.0 (C-4), and 78.5 (C-12); three methines at  $\delta$  127.9 (C-10), 129.2 (C-7), and 134.1 (C-8); and four quaternary carbons at  $\delta$  49.0 (C-1), 82.8 (C-6), 87.8 (C-5), and 141.6 (C-9), respectively. The  $^2J$ - and  $^3J$ -HMBC correlations from H-2 to C-3, C-6; from H-7 to C-6, C-8, and C-9; from H-8 to C-10, and  $\text{CH}_3$ -15; from H-10 to C-11 and  $\text{CH}_3$ -15; from H-12 to C-1, C-2, C-6, and  $\text{CH}_3$ -13; and from  $\text{CH}_3$ -14 to C-4 and C-6, respectively, provided the possible planar structure as shown (Figure 3). Compared the spectral data of **4** with those of (–)-phaseic acid [40], the upfield shift of H-5 ( $\delta$  8.11 to 7.87) and  $^{13}\text{C}$  NMR signal of the carboxylate at  $\delta$  175.0 (C-11) further indicated the occurrence of sodium carboxylate. The presence of **4** as a sodium salt was evidenced by the inductively coupled plasma (ICP) MS analytical data, in which  $[\text{Na}^+]$  was equal to 0.8 ppm in the 10 ppm sample. After acidification of **4** with 0.1 M HCl, the spectral data was changed to be the same as that of (–)-phaseic acid [40]. Furthermore, the NOE correlations of H-7 and  $\text{CH}_3$ -13, H-7 and  $\text{CH}_3$ -15, and H-10 and  $\text{CH}_3$ -15, confirmed the relative stereochemical structure of **4** as sodium phaseate (Figure 3).

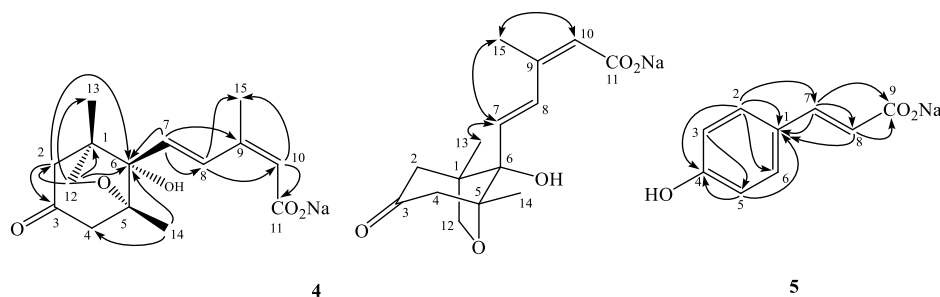


Figure 3. Key HMBC ( $\rightarrow$ ) and NOESY ( $\leftrightarrow$ ) correlations of **4** and **5**.

Compound **5** was purified as colorless powder and its molecular formula was characterized as  $\text{C}_9\text{H}_7\text{O}_3$  according to the HR-ESI-MS data. The UV absorption maxima at 282 nm and the IR absorption bands at 3403 and  $1550\text{ cm}^{-1}$  suggested the occurrence of hydroxyl and carboxyl groups in the molecule. Only  $\text{A}_2\text{B}_2$ -coupled aromatic protons at  $\delta$  6.75 (2H, d,  $J = 8.8$  Hz, H-3, 5) and 7.36 (2H, d,  $J = 8.8$  Hz, H-2, 6), and two *trans* olefinic protons at  $\delta$  6.33 (1H, d,  $J = 15.6$  Hz, H-8) and 7.33 (1H, d,  $J = 15.6$  Hz, H-7) could be observed in its  $^1\text{H}$ -NMR spectrum. Compared the spectral data of **5** with those of *p*-coumaric acid [41], the upfield shift of H-7 ( $\delta$  7.60 to 7.33) and  $^{13}\text{C}$  NMR signal of the carboxylate at  $\delta$  176.4 (C-9) further indicated the occurrence of sodium carboxylate in **5**. The  $^2J$ - and  $^3J$ -HMBC correlations from H-2 to C-1, C-4, C-6, and C-7; from H-3 to C-5; from H-5 to C-1 and C-4; from H-7 to C-1, C-8, and C-9; and from H-8 to C-1 and C-9, respectively, evidenced the planar structure of **5** (Figure 3). The presence of **5** as a sodium salt was evidenced by the ICPMS analytical data, in which  $[\text{Na}^+]$  was equal to 2 ppm in the 10 ppm sample. After acidification of **5** with 0.1 M HCl, the spectral data was changed to be the same as that of *p*-coumaric acid [41]. These data determined the structure of **5** as sodium *p*-coumarate. Although compound **5** was already reported in 2012 [42], the present research is the first report of **5** from the natural sources.

### 2.3. Anti-Inflammatory Activity

Most of the purified compounds were examined for their inhibitory activity against the superoxide anion and elastase release by human neutrophils in response to fMLP/CB [43] (Table S1), and only those compounds with  $IC_{50}$  values lower than 10  $\mu$ M are listed in Table 2. The experimental data indicated **26**, **54**, **55**, **57**, **63**, **65**, **67**, and **70** displayed significant inhibition of superoxide anion generation with  $IC_{50}$  values ranged from  $1.9 \pm 0.2$  to  $9.3 \pm 0.3$   $\mu$ M, as compared with the positive control LY294002 ( $IC_{50}$   $1.0 \pm 0.2$   $\mu$ M). In addition, **55**, **57**, **63**, **65**, **66**, and **67** exhibited significant inhibition of elastase release with  $IC_{50}$  values ranged from  $3.8 \pm 0.1$  to  $7.7 \pm 0.5$   $\mu$ M, as compared with the positive control LY294002 ( $IC_{50}$   $3.1 \pm 0.7$   $\mu$ M). These experimental results indicated that flavonoids and isoflavonoids in *Vigna* species displayed significant chemoprevention potentials. According to the anti-inflammatory activity examinations performed in this study, the crude extract and purified constituents of *V. luteola* could be developed as new lead compounds or health food ingredients in the future.

**Table 2.** Inhibitory effects of purified compounds on superoxide anion generation and elastase release by human neutrophils in response to fMLP/CB.

Compound	Superoxide Anion Generation		Elastase Release	
	$IC_{50}$ ( $\mu$ M) <sup>a</sup>	Inh % <sup>b</sup>	$IC_{50}$ ( $\mu$ M)	Inh %
<b>26</b>	$6.1 \pm 0.3$	$69.9 \pm 4.4$ ***	– <sup>c</sup>	$11.8 \pm 2.1$ **
<b>54</b>	$4.5 \pm 0.3$	$93.6 \pm 3.3$ ***	–	$23.7 \pm 1.1$ ***
<b>55</b>	$4.1 \pm 0.2$	$99.0 \pm 1.9$ ***	$3.8 \pm 0.1$	$89.4 \pm 4.5$ ***
<b>57</b>	$5.0 \pm 0.4$	$88.4 \pm 5.3$ ***	$4.7 \pm 0.4$	$89.9 \pm 2.2$ ***
<b>63</b>	$9.3 \pm 0.3$	$52.5 \pm 1.2$ ***	$4.9 \pm 0.2$	$75.2 \pm 3.2$ ***
<b>65</b>	$1.9 \pm 0.2$	$89.3 \pm 2.9$ ***	$6.4 \pm 0.7$	$61.3 \pm 4.7$ ***
<b>66</b>	–	$27.4 \pm 7.5$ *	$7.7 \pm 0.5$	$60.4 \pm 2.3$ ***
<b>67</b>	$3.2 \pm 0.1$	$100.0 \pm 1.3$ ***	$4.1 \pm 0.7$	$99.6 \pm 7.6$ ***
<b>70</b>	$5.6 \pm 0.9$	$85.2 \pm 9.7$ ***	–	$46.5 \pm 2.2$ ***
LY294002 <sup>d</sup>	$1.0 \pm 0.2$		$3.1 \pm 0.7$	

Results are presented as mean  $\pm$  SEM (n = 3). \*  $p < 0.05$ , \*\*  $p < 0.01$ , \*\*\*  $p < 0.001$  compared with the control (DMSO).

<sup>a</sup> Concentration necessary for 50 % inhibition ( $IC_{50}$ ). <sup>b</sup> Percentage of inhibition (Inh %) at 10  $\mu$ M concentration. <sup>c</sup> Not determined. <sup>d</sup> A phosphatidylinositol-3-kinase inhibitor was used as a positive control.

## 3. Experimental Section

### 3.1. General

The spectroscopic data of the purified compounds including optical rotations ( $[\alpha]_D^{25}$ ) and UV and IR spectra were recorded on a Jasco P-2000 digital polarimeter (Jasco, Tokyo, Japan), a Hitachi U-0080D diode array spectrophotometer (Hitachi, Tokyo, Japan), and a Jasco FT/IR-4100 spectrophotometer (Jasco, Tokyo, Japan), respectively. The mass spectra were collected on a Shimadzu LC-MS 8040 spectrometer (Shimadzu, Kyoto, Japan). The HRMS data were obtained on a JMS-T100LP spectrometer (Jeol, Tokyo, Japan). ICPMS examination was performed on a Thermo-Element XR ICPMS spectrometer, and three elements (Na, K, and Ca) were examined for their concentration by comparison with the standard curves.  $^1H$ -,  $^{13}C$ -, and 2D NMR spectra were recorded on the Bruker AV-500 and Avance III-400 NMR spectrometers (Bruker, Billerica, MA, USA) using tetramethylsilane as the internal standard, and all NMR experiments were detected on standard pulse sequences and parameters with all chemical shifts reported in parts per million (ppm,  $\delta$ ). The deuterated solvents were purchased from Sigma-Aldrich (St. Louis, MO, USA). Other chemicals used in this study were provided by Merck KGaA (Darmstadt, Germany). Column chromatography was performed on silica gels in different mesh sizes (70–230 and 230–400 mesh, Kieselgel 60, Merck KGaA, Darmstadt, Germany). Thin-layer chromatography (TLC) was conducted on precoated Kieselgel 60 F 254 plates (Merck KGaA, Darmstadt, Germany). The spots on TLC were detected by UV light or spraying with 10 % (v/v)  $H_2SO_4$  followed by heating at 110  $^{\circ}C$  for 10 min.

### 3.2. Plant Materials

The plant material *Vigna luteola* (Jacq.) Benth. was gathered in the side of Ching-Shui River, Nantou, Taiwan (March 2006), and it was authenticated by Prof. C. S. Kuoh (Department of Life Science, National Cheng Kung University, Tainan, Taiwan). A voucher specimen (PCKuo\_2006002) was deposited in the herbarium of School of Pharmacy, National Cheng Kung University, Tainan, Taiwan.

### 3.3. Extraction and Isolation

The herbs of *V. luteola* (dried weight: 3.5 kg) were grounded and extracted with methanol (20 L) exhaustively under reflux (85 °C) for 8 hours, and the resulting liquid was concentrated in vacuo to give a dark brown syrup (640 g). The methanol extract was partitioned between chloroform and water to produce chloroform soluble layer (190 g) and water soluble layer (450 g), respectively.

The chloroform layer was subjected to a silica gel column eluted with a step gradient of *n*-hexane and acetone (100:1 to 1:1) to afford seven fractions (CF 1–7), as monitored by TLC. CF 3 was further column chromatographed on silica gel with a mixture of *n*-hexane and ethyl acetate (step gradient from 50:1 to 1:1) to afford fourteen subfractions (CF 3-1–3-14). CF 3-2 was purified by silica gel column chromatography (SiO<sub>2</sub> CC) and the minor fraction was recrystallized from chloroform to give **18** (0.3 g). CF 3-3 was isolated by SiO<sub>2</sub> CC to yield **16** (0.8 mg), **17** (1.1 mg), **40** (1.8 mg), a mixture of **19** and **20** (2.5 mg), and a mixture of **23** and **24** (2.2 mg), respectively. CF 3-5 was separated by SiO<sub>2</sub> CC and further preparative thin-layer chromatography (pTLC) purification afforded compounds **6** (1.6 mg), **7** (4.3 mg), **37** (4.2 mg), **69** (0.6 mg), **8** (5.4 mg), **14** (1.2 mg), **55** (1.8 mg), and **63** (2.0 mg), respectively. CF 6 was further subjected on a silica gel column and eluted with a chloroform and methanol mixture (step gradient from 50:1 to 1:1) to produce thirteen subfractions (CF 6-1–6-13). A mixture of **21** and **22** (4.3 mg) was obtained from CF 6-7 by recrystallization of ethyl acetate. CF 6-8 was purified by SiO<sub>2</sub> CC and the minor fraction was further isolated by pTLC with a solvent mixture of chloroform and acetone (10:1) to obtain **41** (1.0 mg). CF 7 was isolated on a SiO<sub>2</sub> CC eluted with chloroform and methanol (step gradient from 50:1 to 1:1) to give twelve subfractions (CF 7-1–7-12). CF 7-3, 7-4, 7-5, and 7-8 were purified by SiO<sub>2</sub> CC and the resulting minor fractions were subjected to pTLC to yield **68** (2.3 mg), **25** (1.9 mg) and **64** (1.5 mg), **10** (1.6 mg) and **43** (5.1 mg), and **36** (2.2 mg), respectively.

The water soluble layer was resolved on a Diaion HP-20 column and eluted with a step gradient mixture of water and methanol (10:0, 7:3, 5:5, 3:7, and 0:10) to result in sixteen fractions (WF 1–16). WF 1 was subjected to Diaion HP-20 CC eluted with the same program as mentioned above to obtain nine subfractions (WF 1-1–1-9). WF 1-3 was purified by pTLC with a solvent mixture of chloroform and methanol (50:1) to give **26** (3.1 mg) and **38** (1.5 mg). WF 1-4 was separated by SiO<sub>2</sub> CC and further purified by pTLC to afford **65** (2.2 mg), **67** (6.0 mg), **35** (24.0 mg), and **54** (2.7 mg). WF 3 was purified by Sephadex LH-20 CC eluted with a step gradient mixture of water and methanol (10:0, 7:3, 5:5, 3:7, and 0:10) to produce thirteen subfractions (WF 3-1–3-13). WF 3-4 and 3-9 were separated by pTLC to yield **70** (1.3 mg), **48** (2.4 mg), and **56** (7.3 mg). WF 3-10 was purified by SiO<sub>2</sub> CC eluted with a step gradient mixture of chloroform and methanol (50:1 to 1:1) to produce eight minor fractions (WF 3-10-1–3-10-8). WF 3-10-2 was isolated by reversed-phase HPLC with a Gemini 5u C18 column (250 × 4.6 mm, 5µm) eluted with a MeOH-H<sub>2</sub>O mixture (40:60, 0.4 mL/min) to yield **61** (2.7 mg) and **62** (3.5 mg). WF 5 was isolated by Diaion HP-20 CC to give six subfractions (WF 5-1 ~ 5-6). WF 5-4 was subjected on a Sephadex LH-20 column eluted with a mixture of water and methanol (10:0, 7:3, 5:5, 3:7, and 0:10), and then recrystallization of the resulting minor fractions afforded **66** (2.2 mg), **71** (1.1 mg), **4** (3.7 mg), **39** (1.6 mg), **44** (1.8 mg), and **57** (5.0 mg), respectively. WF 5-5 was purified by reversed-phase HPLC with a Gemini 5u C18 column (250 × 4.6 mm, 5µm) eluted with a MeOH-H<sub>2</sub>O mixture (20:80, 0.6 mL/min) to afford **52** (4.2 mg). WF 6 was subjected to Diaion HP-20 CC eluted with water and a step gradient of methanol (10:0 to 0:10) to afford six subfractions (WF 6-1–6-6). WF 6-2 and 6-6 were further purified by SiO<sub>2</sub> CC and pTLC to obtain **5** (4.0 mg), **12** (2.6 mg), **49** (3.3 mg), **15** (3.5 mg), and **58** (0.4 g). WF 7 was purified by Diaion HP-20 CC eluted with water and a step gradient of methanol (10:0 to 0:10) to obtain seven subfractions (WF 7-1–7-7). WF 7-6 was separated by repeated



Sephadex LH-20 CC eluted with a step gradient mixture of water and methanol (10:0 to 0:10) to yield **1** (2.8 mg), **9** (17.0 mg), **11** (5.2 mg), **47** (2.6 g), **59** (1.5 g), and **60** (0.5 g). WF 8 was purified by SiO<sub>2</sub> CC eluted by chloroform and a step gradient with methanol and water (100:1:0.1 to 1:1:0.1) to obtain seven subfractions (WF 8-1–8-7). WF 8-4 was isolated by SiO<sub>2</sub> CC and pTLC to give **45** (2.7 mg), **13** (1.1 mg), and **72** (1.9 mg). WF 10 was subjected to Sephadex LH-20 CC eluted with water and a step gradient of methanol (10:0 to 0:10) to obtain ten subfractions (WF 10-1–10-10). WF 10-3, 10-6, and 10-9 were further purified by pTLC to yield **42** (0.8 mg); **31** (4.2 mg), **46** (12.3 mg), and **50** (11.0 mg), and **51** (1.3 mg) and **53** (2.2 mg), respectively. WF 12 was subjected to Diaion HP-20 CC eluted with a mixture of water and methanol (step gradient from 10:0 to 0:10) to afford seven subfractions (WF 12-1–12-7). WF 12-3 was purified by Sephadex LH-20 CC and further resolved on pTLC to produce **30** (1.9 mg), **34** (2.1 mg), and **73** (1.4 mg). WF 12-6 was isolated by repeated SiO<sub>2</sub> CC yield **2** (4.2 mg). WF 13 was resolved on a Sephadex LH-20 column eluted with water and methanol (step gradient from 10:0 to 0:10) to produce eight subfractions (WF 13-1–13-8). WF 13-3 was separated by SiO<sub>2</sub> CC and pTLC to obtain **32** (1.6 mg) and **33** (40.0 mg). WF 13-7 was resolved on Sephadex LH-20 CC and the minor fraction was isolated by repeated SiO<sub>2</sub> CC to result in **3** (6.3 mg), **27** (33.0 mg), and **28** (43.3 mg). WF 14 was subjected to SiO<sub>2</sub> CC eluted with ethyl acetate and methanol (step gradient from 300:1 to 1:1) to give nine subfractions (WF 14-1–14-9). Compound **29** (7.5 mg) was obtained from the WF 14-7 by repeated SiO<sub>2</sub> CC followed by recrystallization.

### 3.3.1. Viglutin (1)

Colorless powder;  $[\alpha]_D^{25} + 36.9$  (c 0.1, MeOH); IR (neat)  $\nu_{\max}$ : 3416, 2928, 1647, 1580, 1383, 1045 cm<sup>−1</sup>; ESI-MS (*rel. int.* %)  $m/z$  227 ([M + H]<sup>+</sup>, 100), 209 (43); HR-ESI-MS  $m/z$  249.1460 ([M + Na]<sup>+</sup>) (Calcd for C<sub>13</sub>H<sub>22</sub>NaO<sub>3</sub>: 249.1467); <sup>1</sup>H-NMR (CD<sub>3</sub>OD, 500 MHz)  $\delta$  5.78 (1H, dq,  $J$  = 15.5, 6.5 Hz, H-9), 5.67 (1H, ddd,  $J$  = 15.5, 8.5, 1.5 Hz, H-8), 4.18 (1H, d,  $J$  = 8.5 Hz, H-7), 3.81 (1H, m, H-13b), 3.80 (1H, dddd,  $J$  = 12.0, 7.5, 5.0, 3.5 Hz, H-3), 3.61 (1H, dd,  $J$  = 11.0, 7.0 Hz, H-13a), 2.44 (1H, m, H-5), 1.73 (1H, m, H-4b), 1.73 (3H, dd,  $J$  = 6.5, 1.5 Hz, CH<sub>3</sub>-10), 1.51 (1H, ddd,  $J$  = 12.0, 12.0, 11.5 Hz, H-4a), 1.36 (1H, ddd,  $J$  = 12.6, 5.0, 1.5 Hz, H-2b), 1.31 (1H, m, H-2a), 1.06 (3H, s, CH<sub>3</sub>-12), 0.96 (3H, s, CH<sub>3</sub>-11); <sup>13</sup>C-NMR (CD<sub>3</sub>OD, 125 MHz)  $\delta$  132.1 (C-9), 129.6 (C-8), 84.4 (C-7), 81.2 (C-6), 69.7 (C-13), 68.5 (C-3), 46.8 (C-2), 43.7 (C-5), 37.7 (C-1), 31.6 (C-4), 25.9 (C-11), 24.0 (C-12), 18.2 (C-10).

### 3.3.2. Viglutoside (2)

Yellowish amorphous powder;  $[\alpha]_D^{25} - 23.6$  (c 0.3, MeOH); UV (MeOH)  $\lambda_{\max}$  (log  $\epsilon$ ): 221 (3.78), 274 (3.38) nm; IR (neat)  $\nu_{\max}$ : 3430, 2924, 1637 cm<sup>−1</sup>; ESI-MS (*rel. int.* %)  $m/z$  272 ([M + H]<sup>+</sup>, 100); HR-ESI-MS  $m/z$  294.0952 ([M + Na]<sup>+</sup>) (Calcd for C<sub>12</sub>H<sub>17</sub>NNaO<sub>6</sub>: 294.0954); <sup>1</sup>H-NMR (CD<sub>3</sub>OD, 500 MHz)  $\delta$  8.03 (1H, d,  $J$  = 2.5 Hz, H-2), 7.32 (1H, d,  $J$  = 8.5 Hz, H-5), 7.21 (1H, dd,  $J$  = 8.5, 2.5 Hz, H-4), 4.78 (1H, d,  $J$  = 2.0 Hz, H-1'), 4.65 (1H, d,  $J$  = 12.0 Hz, H-7b), 4.51 (1H, d,  $J$  = 12.0 Hz, H-7a), 3.85 (1H, dd,  $J$  = 3.5, 2.0 Hz, H-2'), 3.67 (1H, dd,  $J$  = 9.5, 3.5 Hz, H-3'), 3.60 (1H, dd,  $J$  = 9.5, 6.0 Hz, H-5'), 3.38 (1H, dd,  $J$  = 9.5, 9.5 Hz, H-4'), 1.25 (1H, d,  $J$  = 6.0 Hz, H-6'); <sup>13</sup>C-NMR (CD<sub>3</sub>OD, 125 MHz)  $\delta$  155.9 (C-3), 148.6 (C-6), 138.1 (C-2), 125.0 (C-4), 124.8 (C-5), 101.4 (C-1'), 74.0 (C-4'), 72.4 (C-3'), 72.3 (C-2'), 70.3 (C-7), 70.1 (C-5'), 18.0 (C-6').

### 3.3.3. Viglutanone (3)

Colorless syrup; UV (MeOH)  $\lambda_{\max}$  (log  $\epsilon$ ): 299 (3.44) nm; IR (neat)  $\nu_{\max}$ : 3493, 2953, 2133, 1703, 1631, 1387, 1054 cm<sup>−1</sup>; ESI-MS (*rel. int.* %)  $m/z$  197 ([M-H]<sup>−</sup>, 100); HR-ESI-MS  $m/z$  197.0449 ([M − H]<sup>−</sup>) (Calcd for C<sub>9</sub>H<sub>9</sub>O<sub>5</sub>: 197.0450); <sup>1</sup>H-NMR (CD<sub>3</sub>OD, 400 MHz)  $\delta$  6.97 (1H, s, H-5), 6.25 (1H, s, H-3), 3.60 (1H, t,  $J$  = 6.4 Hz, H-9), 2.60 (1H, t,  $J$  = 8.0 Hz, H-7), 1.84 (1H, tt,  $J$  = 8.0, 6.4 Hz, H-8); <sup>13</sup>C-NMR (CD<sub>3</sub>OD, 100 MHz)  $\delta$  165.8 (C-10), 164.8 (C-2), 162.3 (C-4), 156.4 (C-6), 114.8 (C-3), 110.4 (C-5), 61.7 (C-9), 32.6 (C-7), 32.1 (C-8).

### 3.3.4. Sodium Phaseate (4)

Colorless powder;  $[\alpha]_D^{25} - 9.1$  (c 0.5, MeOH); UV (MeOH)  $\lambda_{\max}$  (log  $\epsilon$ ): 249 (3.55) nm; IR (neat)  $\nu_{\max}$ : 3424, 2937, 1713, 1644, 1636, 1550, 1401, 1334, 1254  $\text{cm}^{-1}$ ; HR-ESI-MS  $m/z$  279.1234 ( $[\text{M} - \text{Na}]^-$ ) (Calcd for  $\text{C}_{15}\text{H}_{19}\text{O}_5$ : 279.1233);  $^1\text{H-NMR}$  ( $\text{CD}_3\text{OD}$ , 400 MHz)  $\delta$  7.87 (1H, d,  $J = 16.0$  Hz, H-8), 6.20 (1H, d,  $J = 16.0$  Hz, H-7), 5.86 (1H, br s, H-10), 3.93 (1H, dd,  $J = 7.2, 2.8$  Hz, H-12b), 3.65 (1H, d,  $J = 7.2$  Hz, H-12a), 2.81 (1H, d,  $J = 18.0$  Hz, H-4b), 2.71 (1H, dd,  $J = 18.0, 2.4$  Hz, H-2b), 2.45 (1H, dd,  $J = 18.0, 2.4$  Hz, H-4a), 2.37 (1H, dd,  $J = 18.0, 2.4$  Hz, H-2a), 1.95 (3H, s,  $\text{CH}_3$ -15), 1.22 (3H, s,  $\text{CH}_3$ -14), 1.00 (3H, s,  $\text{CH}_3$ -13);  $^{13}\text{C-NMR}$  ( $\text{CD}_3\text{OD}$ , 100 MHz)  $\delta$  211.3 (C-3), 175.0 (C-11), 141.6 (C-9), 134.1 (C-8), 129.2 (C-7), 127.9 (C-10), 87.8 (C-5), 82.8 (C-6), 78.5 (C-12), 54.0 (C-4), 53.2 (C-2), 49.0 (overlapped by MeOH, C-1), 20.5 (C-15), 19.4 (C-14), 15.8 (C-13).

### 3.3.5. Sodium *p*-Coumarate (5)

Colorless powder; UV (MeOH)  $\lambda_{\max}$  (log  $\epsilon$ ): 282 (3.83) nm; IR (neat)  $\nu_{\max}$ : 3403, 2941, 1550, 1414, 1389, 1250, 1085  $\text{cm}^{-1}$ ; ESI-MS (*rel. int.* %)  $m/z$  163 ( $[\text{M}-\text{Na}]^-$ , 100); HR-ESI-MS  $m/z$  163.0396 ( $[\text{M} - \text{Na}]^-$ ) (Calcd for  $\text{C}_9\text{H}_7\text{O}_3$ : 163.0395);  $^1\text{H-NMR}$  ( $\text{CD}_3\text{OD}$ , 400 MHz)  $\delta$  7.36 (2H, d,  $J = 8.8$  Hz, H-2, 6), 7.33 (1H, d,  $J = 15.6$  Hz, H-7), 6.75 (2H, d,  $J = 8.8$  Hz, H-3, 5), 6.33 (1H, d,  $J = 15.6$  Hz, H-8);  $^{13}\text{C-NMR}$  ( $\text{CD}_3\text{OD}$ , 100 MHz)  $\delta$  176.4 (C-9), 160.0 (C-4), 141.0 (C-7), 130.1 (C-2 and -6), 128.6 (C-1), 123.2 (C-8), 116.6 (C-3 and -5).

## 3.4. Anti-Inflammatory Bioactivity Examination

The assays of the generation of superoxide anion and elastase release inhibition examinations were determined as described previously [43]. The experimental details were provided in the Supplementary Materials.

**Supplementary Materials:** The following are available online, S1: Complete extraction and isolation procedures; S2: References of the known compounds; S3: Anti-inflammatory bioactivity experimental procedures; Table S1: Inhibitory effects of isolated compounds; Figures S1–37: NMR spectra of compounds 1–5.

**Author Contributions:** Conceptualization, P.-C.K. and J.T.C.T.; Data Curation and Investigation, S.-H.L., Y.-C.L., and M.-L.Y.; Methodology, T.-L.H. and C.-C.W.; Resources, M.-L.Y. and P.-C.K.; Writing—Original Draft, Y.-C.L.; Writing—Review & Editing, S.-H.L., P.-C.K., and J.T.C.T. All authors read and approved the final manuscript.

**Funding:** This research is sponsored by the Ministry of Science and Technology (MOST), Taiwan, granted to P.-C.K. and J.T.C.T. The authors are also thankful for partial financial support from Chang Gung Memorial Hospital (CMRPF1G0241~3, CMRPF1F0061~3, and BMRP450 granted to T.-L.H.).

**Conflicts of Interest:** The authors declare no conflict of interest.

## References

- Na, H.K.; Kim, E.H.; Jung, J.H.; Lee, H.H.; Hyun, J.W.; Surh, Y.J. (–)-Epigallocatechin gallate induces Nrf2-mediated antioxidant enzyme expression via activation of PI3K and ERK in human mammary epithelial cells. *Arch. Biochem. Biophys.* **2008**, *476*, 171–177. [[CrossRef](#)]
- Swami, S.; Krishnan, A.V.; Moreno, J.; Bhattacharyya, R.S.; Gardner, C.; Brooks, J.D.; Peehl, D.M.; Feldman, D. Inhibition of prostaglandin synthesis and actions by genistein in human prostate cancer cells and by soy isoflavones in prostate cancer patients. *Int. J. Cancer* **2009**, *124*, 2050–2059. [[CrossRef](#)] [[PubMed](#)]
- Bar-Sela, G.; Epelbaum, R.; Schaffer, M. Curcumin as an anti-cancer agent: Review of the gap between basic and clinical applications. *Curr. Med. Chem.* **2010**, *17*, 190–197. [[CrossRef](#)] [[PubMed](#)]
- Kuo, P.C.; Yang, C.J.; Lee, Y.C.; Chen, P.C.; Liu, Y.C.; Wu, S.N. The comprehensive electrophysiological study of curcuminoids on delayed-rectifier  $\text{K}^+$  currents in insulin-secreting cells. *Eur. J. Pharmacol.* **2018**, *819*, 233–247. [[CrossRef](#)]
- Shu, L.; Cheung, K.L.; Khor, T.O.; Chen, C.; Kong, A.N. Phytochemicals: Cancer chemoprevention and suppression of tumor onset and metastasis. *Cancer Metastasis Rev.* **2010**, *29*, 483–502. [[CrossRef](#)] [[PubMed](#)]

6. Johnson, S.M.; Wang, X.; Evers, B.M. Triptolide inhibits proliferation and migration of colon cancer cells by inhibition of cell cycle regulators and cytokine receptors. *J. Surg. Res.* **2011**, *168*, 197–205. [[CrossRef](#)] [[PubMed](#)]
7. Newman, D.J.; Cragg, G.M.; Snader, K.M. The influence of natural products upon drug discovery. *Nat. Prod. Rep.* **2000**, *17*, 215–234. [[CrossRef](#)] [[PubMed](#)]
8. Boudjou, S.; Oomah, B.D.; Zaidi, F.; Hosseini, F. Phenolics content and antioxidant and anti-inflammatory activities of legume fractions. *Food Chem.* **2013**, *138*, 1543–1550. [[CrossRef](#)]
9. Lima, A.I.; Mota, J.; Monteiro, S.A.; Ferreira, R.M. Legume seeds and colorectal cancer revisited: Protease inhibitors reduce MMP-9 activity and colon cancer cell migration. *Food Chem.* **2016**, *197*, 30–38. [[CrossRef](#)]
10. Hu, X.R.; Chou, G.X.; Zhang, C.G. Flavonoids, alkaloids from the seeds of *Crotalaria pallida* and their cytotoxicity and anti-inflammatory activities. *Phytochemistry* **2017**, *143*, 64–71. [[CrossRef](#)] [[PubMed](#)]
11. Malech, H.L.; Gallin, J.I. Neutrophils in human diseases. *N. Engl. J. Med.* **1987**, *317*, 687–694. [[CrossRef](#)] [[PubMed](#)]
12. Witko-Sarsat, V.; Rieu, P.; Descamps-Latscha, B.; Lesavre, P.; Halbwachs-Mecarelli, L. Neutrophils: Molecules, functions and pathophysiological aspects. *Lab. Investig.* **2000**, *80*, 617–653. [[CrossRef](#)]
13. Okajima, K.; Harada, N.; Uchiba, M. Ranitidine reduces ischemia/reperfusion-induced liver injury in rats by inhibiting neutrophil activation. *J. Pharmacol. Exp. Ther.* **2002**, *301*, 1157–1165. [[CrossRef](#)]
14. Ennis, M. Neutrophils in asthma pathophysiology. *Curr. Allergy Asthma Rep.* **2003**, *3*, 159–165. [[CrossRef](#)]
15. Vinten-Johansen, J. Involvement of neutrophils in the pathogenesis of lethal myocardial reperfusion injury. *Cardiovasc. Res.* **2004**, *61*, 481–497. [[CrossRef](#)] [[PubMed](#)]
16. Hwang, T.L.; Li, G.L.; Lan, Y.H.; Chia, Y.C.; Hsieh, P.W.; Wu, Y.H.; Wu, Y.C. Potent inhibition of superoxide anion production in activated human neutrophils by isopedicin, a bioactive component of the Chinese medicinal herb *Fissistigma Oldhamii*. *Free Radic. Biol. Med.* **2009**, *46*, 520–528. [[CrossRef](#)] [[PubMed](#)]
17. Huang, T.C.; Ohashi, H. *Flora of Taiwan*, 2nd ed.; Editorial Committee of Flora of Taiwan: Taipei, Taiwan, 1993; Volume 3, p. 385.
18. Sreerama, Y.N.; Sashikala, V.B.; Pratapa, V.M. Phenolic compounds in cowpea and horse gram flours in comparison to chickpea flour: Evaluation of their antioxidant and enzyme inhibitory properties associated with hyperglycemia and hypertension. *Food Chem.* **2012**, *133*, 156–162. [[CrossRef](#)]
19. Silva, L.R.; Pereira, M.J.; Azevedo, J.; Gonçalves, R.F.; Valentão, P.; de Pinho, P.G.; Andrade, P.B. *Glycine max* (L.) Merr., *Vigna radiata* L. and *Medicago sativa* L. sprouts: A natural source of bioactive compounds. *Food Res. Int.* **2013**, *50*, 167–175. [[CrossRef](#)]
20. Seneviratne, G.I.; Harborne, J.B. Constitutive flavonoids and induced isoflavonoids as taxonomic markers in the genus *Vigna*. *Biochem. Syst. Ecol.* **1992**, *20*, 459–467. [[CrossRef](#)]
21. Soucek, J.; Skvor, J.; Pouckova, P.; Matousek, J.; Slavik, T.; Matousek, J. Mung bean (*Phaseolus aureus*) nuclease and its biological and antitumor effects. *Neoplasma* **2006**, *53*, 402–409.
22. Joanitti, G.A.; Azevedo, R.B.; Freitas, S.M. Apoptosis and lysosome membrane permeabilization induction on breast cancer cells by an anticarcinogenic Bowman-Birk protease inhibitor from *Vigna unguiculata* seeds. *Cancer Lett.* **2010**, *293*, 73–81. [[CrossRef](#)]
23. Lattanzio, V.; Arpaia, S.; Cardinali, A.; Venere, D.D.; Linsalata, V. Role of endogenous flavonoids in resistance mechanism of *Vigna* to aphids. *J. Agric. Food Chem.* **2000**, *48*, 5316–5320. [[CrossRef](#)]
24. Franco, O.L.; dos Santos, R.C.; Batista, J.A.N.; Mendes, A.C.M.; de Araújo, M.A.M.; Monnerat, R.G.; Grossi-de-Sá, M.F.; de Freitas, S.M. Effects of black-eyed pea trypsin/chemotrypsin inhibitor on proteolytic activity and on development of *Anthonomus grandis*. *Phytochemistry* **2003**, *63*, 343–349. [[CrossRef](#)]
25. Yao, Y.; Cheng, X.Z.; Wang, L.X.; Wang, S.H.; Ren, G. Major phenolic compounds, antioxidant capacity and antidiabetic potential of rice bean (*Vigna umbellata* L.) in China. *Int. J. Mol. Sci.* **2012**, *13*, 2707. [[CrossRef](#)]
26. Yao, Y.; Cheng, X.; Wang, S.; Wang, L.; Ren, G. Influence of altitudinal variation on the antioxidant and antidiabetic potential of adzuki bean (*Vigna angularis*). *Int. J. Food Sci. Nutr.* **2012**, *63*, 117–124. [[CrossRef](#)]
27. Han, K.H.; Fukushima, M.; Ohba, K.; Shimada, K.I.; Sekikawa, M.; Chiji, H.; Lee, C.H.; Nakano, M. Hepatoprotective effects of the water extract from adzuki bean hulls on acetaminophen-induced damage in rat liver. *J. Nutr. Sci. Vitaminol.* **2004**, *50*, 380–383. [[CrossRef](#)]
28. Kojima, M.; Yamashita, S.; Nishi, S.; Saito, Y.; Maeda, R. Antioxidative effect and liver protective action of adzuki polyphenol. *Nippon Shokuhin Kagaku Kogaku Kaishi* **2006**, *53*, 386–392. [[CrossRef](#)]

29. Sato, S.; Mukai, Y.; Yamate, J.; Kato, J.; Kurasaki, M.; Hatai, A.; Sagai, M. Effect of polyphenol-containing adzuki bean (*Vigna angularis*) extract on blood pressure elevation and macrophage infiltration in the heart and kidney of spontaneously hypertensive rats. *Clin. Exp. Pharmacol. Physiol.* **2008**, *35*, 43–49. [CrossRef]
30. Sato, S.; Mukai, Y.; Yamate, J. Beneficial effects of adzuki bean (*Vigna angularis*) extract: Anti-oxidant, anti-hypertension and treatment for renal damage. *Curr. Nutr. Food Sci.* **2009**, *5*, 217–222. [CrossRef]
31. Franco, O.L.; Murad, A.M.; Leite, J.R.; Mendes, P.A.M.; Prates, M.V.; Jr, C.B. Identification of a cowpea  $\gamma$ -thionin with bactericidal activity. *FEBS J.* **2006**, *273*, 3489–3497. [CrossRef]
32. Thembo, K.M.; Vismer, H.F.; Nyazema, N.Z.; Gelderblom, W.C.A.; Katerere, D.R. Antifungal activity of four weedy plant extracts against selected mycotoxigenic fungi. *J. Appl. Microbiol.* **2010**, *109*, 1479–1486. [CrossRef]
33. Mukai, Y.; Sato, S. Polyphenol-containing adzuki bean (*Vigna angularis*) extract attenuates blood pressure elevation and modulates nitric oxide synthase and caveolin-1 expressions in rats with hypertension. *Nutr. Metab. Cardiovasc. Dis.* **2009**, *19*, 491–497. [CrossRef]
34. Mukai, Y.; Sato, S. Polyphenol-containing adzuki bean (*Vigna angularis*) seed coats attenuate vascular oxidative stress and inflammation in spontaneously hypertensive rats. *J. Nutr. Biochem.* **2011**, *22*, 16–21. [CrossRef]
35. Itoh, T.; Furuichi, Y. Lowering serum cholesterol level by feeding a 40% ethanol-eluted fraction from HP-20 resin treated with hot water extract of adzuki beans (*Vigna angularis*) to rats fed a high-fat cholesterol diet. *Nutrition* **2009**, *25*, 318–321. [CrossRef]
36. Solanki, Y.B.; Jain, S.M. Antihyperlipidemic activity of *Clitoria ternatea* and *Vigna mungo* in rats. *Pharm. Biol.* **2010**, *48*, 915–923. [CrossRef]
37. Leu, Y.L.; Hwang, T.L.; Kuo, P.C.; Liou, K.P.; Huang, B.S.; Chen, G.F. Constituents from *Vigna vexillata* and their anti-inflammatory activity. *Int. J. Mol. Sci.* **2012**, *13*, 9754–9768. [CrossRef]
38. Miyake, Y.; Ebata, M. The structures of a  $\beta$ -galactosidase inhibitor, galactostatin, and its derivatives. *Agric. Biol. Chem.* **1988**, *52*, 661–666.
39. Kashman, Y.; Yosief, T.; Carmeli, S. New triterpenoids from the Red Sea sponge *Siphonochalina siphonella*. *J. Nat. Prod.* **2001**, *64*, 175–180. [CrossRef]
40. Arai, S.; Todoroki, Y.; Ibaraki, S.; Naoe, Y.; Hirai, N.; Ohigashi, H. Synthesis and biological activity of 3'-chloro-, -bromo, and -iodoabscisic acids, and biological activity of 3'-fluoro-8'-hydroxyabscisic acid. *Phytochemistry* **1999**, *52*, 1185–1193. [CrossRef]
41. Liao, C.R.; Kuo, Y.H.; Ho, Y.L.; Wang, C.Y.; Yang, C.S.; Lin, C.W.; Chang, Y.S. Studies on cytotoxic constituents from the leaves of *Elaeagnus oldhamii* Maxim. in non-small cell lung cancer A549 cells. *Molecules* **2014**, *19*, 9515–9534. [CrossRef]
42. Swisłocka, R.; Kowczyk-Sadowy, M.; Kalinowska, M.; Lewandowski, W. Spectroscopic (FT-IR, FT-Raman,  $^1\text{H}$  and  $^{13}\text{C}$  NMR) and theoretical studies of *p*-coumaric acid and alkali metal *p*-coumarates. *Spectroscopy* **2012**, *27*, 35–48. [CrossRef]
43. Yu, H.P.; Hsieh, P.W.; Chang, Y.J.; Chung, P.J.; Kuo, L.M.; Hwang, T.L. 2-(2-Fluorobenzamido)benzoate ethyl ester (EFB-1) inhibits superoxide production by human neutrophils and attenuates hemorrhagic shock-induced organ dysfunction in rats. *Free Radic. Biol. Med.* **2011**, *50*, 1737–1748. [CrossRef]

**Sample Availability:** Samples of all the isolated compounds are available from the authors.



© 2019 by the authors. Licensee MDPI, Basel, Switzerland. This article is an open access article distributed under the terms and conditions of the Creative Commons Attribution (CC BY) license (<http://creativecommons.org/licenses/by/4.0/>).



REVIEW

Open Access



# Probiotics, prebiotics and amelioration of diseases

Yu-Ling Tsai<sup>2†</sup>, Tzu-Lung Lin<sup>2†</sup>, Chih-Jung Chang<sup>2,3†</sup>, Tsung-Ru Wu<sup>8</sup>, Wei-Fan Lai<sup>7</sup>, Chia-Chen Lu<sup>9\*</sup> and Hsin-Chih Lai<sup>1,2,3,4,5,6\*</sup>

## Abstract

Dysbiosis of gut microbiota is closely related to occurrence of many important chronic inflammations-related diseases. So far the traditionally prescribed prebiotics and probiotics do not show significant impact on amelioration of these diseases in general. Thus the development of next generation prebiotics and probiotics designed to target specific diseases is urgently needed. In this review, we first make a brief introduction on current understandings of normal gut microbiota, microbiome, and their roles in homeostasis of mucosal immunity and gut integrity. Then, under the situation of microbiota dysbiosis, development of chronic inflammations in the intestine occurs, leading to leaky gut situation and systematic chronic inflammation in the host. These subsequently resulted in development of many important diseases such as obesity, type 2 diabetes mellitus, liver inflammations, and other diseases such as colorectal cancer (CRC), obesity-induced chronic kidney disease (CKD), the compromised lung immunity, and some on brain/neuro disorders. The strategy used to optimally implant the effective prebiotics, probiotics and the derived postbiotics for amelioration of the diseases is presented. While the effectiveness of these agents seems promising, additional studies are needed to establish recommendations for most clinical settings.

**Keywords:** Prebiotics, Probiotics, Leaky gut, Inflammation

## Introduction

### Gut microbiota and microbiome

The luminal surface of the intestines contains billions of live bacteria whose total number is expected to be up to  $10^{14}$  in colon, that is 1–100 times higher than the number of cells in an adult person [1, 2]. These bacteria form a populational density gradient, ranging from a lower density at about  $10^2$ /ml in the stomach, to about  $10^{11}$ /ml located in the colon. Based on the results of targeted 16S rRNA gene sequencing, there are currently 52 recognized bacterial phyla reported, with approximately five to seven phyla known to reside in the mammalian gastrointestinal tracts [3]. Among these, 4 major phyla Firmicutes, Bacteroidetes, Actinobacteria, and Proteobacteria dominate and occupy up to 97% of the total

bacteria [4]. A complete and balanced bacterial ecosystem forms due to optimal interactions among the different bacterial phyla [5].

Besides the targeted 16S rRNA gene sequencing, use of the shotgun sequencing strategy provides more detailed information. All DNAs existing in the gut microbiota are sequenced. Subsequently, the open reading frames (ORFs) or genes are annotated and their functions are predicted through Gene Ontology (GO) or Kyoto Encyclopedia of Genes and Genomes (KEGG) bioinformatics resources. These may link their DNA sequences to potential biochemical metabolic pathways and functions highlighted in these bacteria [6–8]. In contrast to the term “Microbiota” that are basically phylogenetically analyzed by targeted 16S rRNA gene (mostly V3–V4 domain) sequencing, results obtained from the shotgun sequencing approach (the metagenomics approach) are named as “Microbiome”. Through metagenomics analysis, the total number of genes of the microbiota, which is predicted to be ca. 3.3 million is far more than the 25,000 from humans [9]. Thus the messages obtained from microbiome provide much more

\* Correspondence: 082385@mail.fju.edu.tw; hclai@mail.cgu.edu.tw

<sup>†</sup>Yu-Ling Tsai, Tzu-Lung Lin and Chih-Jung Chang contributed equally to this work.

<sup>2</sup>Department of Respiratory Therapy, Fu Jen Catholic University, Xinzhuang, New Taipei City 24205, Taiwan

<sup>1</sup>Department of Medical Biotechnology and Laboratory Science, College of Medicine, Chang Gung University, Gueishan, Taoyuan 33302, Taiwan

Full list of author information is available at the end of the article



information than those from the microbiota. On top of the gut microbiome, the gastrointestinal tracts are also colonized by fungi and virus to form the gut mycobiome and the gut virome, respectively [10].

Along the life span of the humans, microbiota colonize the intestines from birth, and start to stabilize in the early first years [11]. In healthy adults, microbiota show higher complexity and diversity. By contrast, microbiota reduces diversity at elder stage [12]. There are many environmental factors influencing the microbiota composition, the most important ones being diet, way of delivery, drugs (antibiotics) usage and ageing [13].

### Gut microbiota normobiosis, dysbiosis and systemic inflammations

Gut microbiota play important roles in maintaining intestinal homeostasis, including metabolism of nutrients, synthesis of vitamin K and B12, metabolism of xenobiotics, and normal commensal bacteria prevent pathobiotic invasion and maintain barrier functions [14].

The composition of intestinal microbiota changes dynamically from birth to adulthood. Among the different phyla, Proteobacteria proliferate as a dominant phylum in newborn mice. Its number is subsequently suppressed in normal adult microbiota. The B cells and Proteobacteria-specific IgA plays an important role in the regulation of microbiota maturation and maintenance of the relative bacterial number [15]. As human beings become ageing, the percentage of Proteobacteria also increase [3]. The phylum Proteobacteria contains alpha-, beta-, gamma-, delta-, epsilon-, and zeta-proteobacteria classes. Many common human pathogens, for example, the pathogens *Escherichia*, *Shigella*, *Salmonella*, and *Yersinia* belong to the gamma-Proteobacteria [16]. On the other hand, many important gut commensals responsible for enhancing the intestinal immunity also belong to this phylum [17, 18].

Alterations in the microbiota, or the term dysbiosis, are found to be closely related to systematic inflammations and the metabolic syndromes. Among these, in adults the Proteobacteria are frequently identified to increase in many chronic inflammations-related diseases such as diabetes [19, 20], nonalcoholic fatty liver disease (NAFLD) and nonalcoholic steatohepatitis (NASH) [21], mental behaviors [22], children's dietary behaviors [23], cardiovascular diseases [24], and colitis [25]. For example, in contrast to Firmicutes and Bacteroidetes, in liver inflammations and the prediabetes, a significant increase in the members of Enterobacteriaceae belonging to gamma-Proteobacteria was observed [26, 27].

Due to the aberrant diet habitats which are among the many causative environmental factors that lead to the situation of intestinal dysbiosis such as the over-growth of the Proteobacteria, and/or reduced Bacteroidetes, a compromised host ability to maintain a balanced gut

microbial community is observed [28]. These are closely related to defective resistance of the gut commensals to colonization by enteropathogens [3]. Based on the current evidences gathered, abnormal expansion of Proteobacteria may lead to energy disequilibrium among the different bacterial species and suppression of the growth of other bacterial species. The proliferation of some bacterial species belonging to Proteobacteria may cause the development of diseases. For example, a single *Enterobacter spp.* only was reported to play a causative role in metabolic disorder. The *Enterobacter cloacae* B29 isolated from the obese human faeces, can induce obesity and insulin resistance in germ-free mice model at a monocolonization manner [29].

The change of relative abundances between different phyla may result in development of chronic inflammation. Among these, the increased Proteobacteria number may enhance chronic and systemic inflammations, leading to increased permeability of the intestine (leaky gut) and systematic inflammations in host [3]. Thus an increased prevalence of Proteobacteria may be a potential diagnostic signature of dysbiosis and the risks of disease. How to maintain the balance between these bacterial phyla to achieve immune balance is an essential issue. Basically there are many bacterial derived components that are involved in immune modulation. Among these, the increased lipopolysaccharides (LPS) derived from Proteobacteria may induce enhanced inflammations, and innate and adaptive immunity [3]. By contrast, LPS produced from Bacteroidetes generally show non-stimulating effects on immune cells, and may even present antagonistic effects on the LPS derived from Proteobacteria [30–32]. Such close interactions between the two bacterial phyla participate in homeostasis of the ecosystem, and are essential for the maintenance of optimal immunity, intestinal integrity and the host health.

### Traditional probiotics

Traditionally, the fermented dairy products such as the sour milk are known to show the effects of amelioration of gastroenteritis, and even the longevity [33]. Subsequently, the underlying effect and mechanism are identified to be closely related to the existence of bacteria such as lactobacilli whose fermentation products can inhibit the toxins produced by intestinal pathogens, and promote the health of cells in the host [34]. Gradually, the bacterium *Lactobacillus acidophilus* together other species and strains were shown to colonize on the surface of the human bowel, showing close interaction with the intestinal epithelial cells [35]. These issues lead to development of health-promotion bacteria called probiotics.

The initial definition of probiotics was proposed as early as in 1965 [36]. Subsequently, the WHO define

that “probiotic” refers to live microorganisms that show beneficial effects on the health of the host [37]. According to the descriptions from International Scientific Association for Probiotics and Prebiotics (ISAPP), the spectrum of products that can be classified as probiotics comprise not only beneficial bacteria, but also others. These include drugs and enteral feedings for amelioration of diseases, food supplements for promotion of the benefits of health, infant formula such as the milk powders, and even the animal feedings [38].

The current definition of a probiotic indicates specific bacterial strain(s) that can effectively promote the health of humans [39]. The underlying mechanisms on how and why the bacterial strain(s) work to achieve such effects have been under intensive study [40]. Generally speaking, it is not necessary that probiotics colonize the target organ such as the intestine. However, at least certain amount of live bacteria have to reach the colon where they can affect the local intestinal ecology, physiology and metabolisms [41]. By definition, probiotics should be safe in animal, resistant to acidity and bile acids, and able to adhere and colonize in the intestine [42].

Traditionally, there are many different species of probiotics widely used. The *Saccharomyces cerevisiae* (boulardii) is the most widely used yeast strain. Other bacterial probiotics mainly comprise of *Lactobacillus species* and *Bifidobacterium species*. These include *L. rhamnosus*, *L. plantarum*, *L. sporogens*, *L. reuteri*, *L. casei*, *L. bulgaricus*, *L. delbrueckii*, *L. salivarius*, *L. johnsonii*, and *L. acidophilus*...etc. On top of these, *B. bifidum*, *B. bifidus*, *B. lactis*, *B. longum*, *B. breve* (Yakult), and *B. infantis* are also commonly used. Other probiotics commercially available include *Streptococcus thermophilus*, *Streptococcus acidophilus*, *Lactococcus lactis*, *Enterococcus SF68*, and *Escherichia coli* Nissle 1917 (serotype O6:K5:H1) [37]. The functions of these probiotics vary significantly within the same species, mostly up to and dependent on some specific strain. Thus in evaluating the functions of the probiotics, it is essential to characterize the functions of each probiotic to the specific strain. So far the functions and effects of these probiotics in the prevention or amelioration of diseases, or in the combinational immuno-therapy basically remain controversial and need further and continuous validation. On the other hand, it is urgently needed that next generation probiotics be screened and isolated by next generation sequencing and bioinformatics platforms. These beneficial bacteria will aim for amelioration of specific and targeted diseases.

#### Prebiotics and short chain fatty acids

In the 1980s, it was postulated that some components of the diet could promote the growth of certain bacterial strains present in the intestine, which are closely

associated with benefits for host health [43]. Subsequently, the term “prebiotic” was generally accepted to selectively refer to food ingredients that are non-digestible and show beneficial effects on the host by stimulating the growth and/or activity of probiotics in the colon after fermentation [44]. Under this definition, there are many different kinds of food ingredients reckoned as the prebiotics. Among these, many dietary fibers which are composed of carbohydrates (polymers of mono-sugars) are most emphasized and highlighted as prebiotics. Dietary fibers basically resist the hydrolysis by human digestive enzymes in the small intestine; however, they can be fermented by colonic microbiota bacteria. Many different kinds of carbohydrates belong to dietary fibers. These include resistant starch (starch and starch degradation products), non-starch polysaccharides (celluloses, hemicelluloses, pectins, gums, and mucilages), inulin, and oligosaccharides such as fructooligosaccharides (FOS, a subgroup of inulin with the degree of polymerization (DP)  $\leq 10$ ), galactooligosaccharides (GOS, DP 2–8), and xylooligosaccharides (XOS, DP 2–10) [45].

Among the fermentative products of prebiotics produced from the microbiota, short chain fatty acids (SCFAs) are studied most intensively, though they may not be the only biologically active products derived from microbiota fermentation. SCFAs are mainly composed of acetate, propionate and butyrate, and many other metabolites and gases are produced after fermentation of prebiotics by microbiota bacteria [46]. SCFAs can act as energy sources absorbed through colonic mucosa [47]. Among these, acetate is mainly metabolized in muscle, kidneys, heart, and brain. Propionate undergoes metabolism in the liver and is a neoglucogenic substrate that may inhibit cholesterol synthesis and regulate lipogenesis in adipose tissue. By contrast, butyrate is mainly metabolized by the colonic commensal bacteria, where it acts as a preferential substrate and regulates cell growth and differentiation by different mechanisms [48].

Besides the energy source, SCFAs also presented many important physiological functions, including maintaining the luminal pH, inhibiting the growth of pathogens, influencing the bowel motility, and reducing colon cancer by stimulating cancer cells apoptosis [49]. Besides, SCFAs also act as signaling molecules reducing production of proinflammatory cytokines and increasing the population of regulatory T (Treg) cells in the large intestine, through G-protein coupled receptors (GPCRs) [50]. Due to the conditions that different prebiotics produce differential amount and composition of SCFAs and gas after microbiota fermentation, for prevention or treatment for some specific inflammatory diseases, different prebiotic fibers have to be preferentially selected for administration based on their metabolic situations in the colon.

### Synbiotics

To improve the therapeutic efficacy, the “synbiotics” are sometimes used. Synbiotics refer to food ingredients or dietary supplements composed of both probiotics and prebiotics in a form of synergism [51]. The function of synbiotics can be either complementary or synergistic. Being complementary indicates each component within the symbiotic is independently chosen for its potential health-promotion effect on host health. For example, the combination of FOS with *L. casei* in which functions from both reagents are complementary. On the other hand, being synergistic means the chosen prebiotic component is to support the activity of the specific probiotic. For example, FOS together with Bifidobacterium. More studies are needed to evaluate the optimal composition and efficacy of synbiotics, and the most optimal combination is known as “optibiotics” [52]. There are already some synbiotics used in clinical practice. These include OAT fiber/*L. plantarum*, and FOS/*L. sporogens* [51].

### Mechanisms of probiotics and prebiotics administration

The consensus of the ISAPP describes the potential underlying mechanisms of health-promotion effects from prebiotics and probiotics. These range from conserved to very unique mechanisms. General ameliorative effects include maintaining intestinal homeostasis and integrity, competitive exclusion to colonization from many other pathobionts, production of SCFAs and vitamins, metabolism of primary to secondary bile salts, regulation of gastrointestinal transit, increasing enterocyte regeneration from activation of stem cells, providing enzymes digestion activities for degradation of undigested fibers, and neutralization of carcinogens or xenobiotics....etc. [53]. These factors coming together result in enhanced integrity of the intestine and thus reduce the phenomenon of leaky gut. As the maintenance of the optimal intestinal immunity is essential, in the intestinal ecosystem, there should be neither too much inflammation nor compromised immunity in the local intestinal environment. The optimal immunity balance is achieved by maintaining the relative bacterial numbers among Bacteroidetes, Firmicutes, Proteobacteria and Actinobacteria....etc. [54]. Thus one of the main effects of administration of prebiotics and probiotics is to achieve the homeostasis of the bacterial numbers among these phyla [55]. Based on this assumption, treatment of the prebiotics and probiotics may not just revert the imbalanced microbiota back to the same composition of the healthy subjects. Effects did present that for effective treatment from some prebiotics, probiotics or synbiotics, the compositions of microbiota are shifted towards more balanced structure [51]. This may ameliorate not only the imbalanced bacterial community, but also the

aberrant blood metabolomics or cellular transcriptomics pattern of the host tissues [56].

There are also more specific mechanisms corresponding to the function of each different strain. These included modulation of neurological and brain behavior effects [57], immune-enhancing or inhibitory effects, endocrine-modulation effects, bioactive substances production, and prevention and amelioration of acute diarrhea, colitis and antibiotics associated diarrhea (AAD). Though not totally understood, it seems to adjust the intestinal back to homeostasis plays a most important role.

### Controversial effects of prebiotics and probiotics in amelioration of diseases

The effects of current prebiotics/probiotics/synbiotics on amelioration of diseases such as AAD, inflammatory bowel disease (IBD), CRC, necrotizing enterocolitis (NEC) NAFLD, encephalopathy, and ventilator-associated pneumonia (VAP) in intensive care units (ICU)...etc. remain controversial. Study results obtained are very heterogeneous and not consistent.

Among these diseases, the AAD is a very serious global clinical issue and is closely related to the *Clostridium difficile* infection after antibiotics treatment that induced gut microbiota dysbiosis [58]. Though the use of probiotics may somewhat restore intestinal microflora, the current best strategy for treatment of AAD is still through translocation of faecal microbiota (fecal microbiota transplantation, FMT) from healthy donors to the patients [59]. There are already more than 10,000 FMT cases occurring worldwide, and the number is rapidly increasing [60]. Results obtained are very positive [60]. The national clinical regulations on FMT are currently formulated and approved in many countries and it is expected that soon patients suffered from AAD are to be benefited from FMT. For some other clinical applications of probiotics and prebiotics, effects on reducing the syndromes of autism spectrum diseases (ASD) and also on the efficacy of cancer immune checkpoints therapies (ICI) [61] started to show promising results [62]. Even so, more detailed and independent basic and clinical studies are warranted.

Many other potentially deleterious effects from administration of prebiotics and probiotics were also reported. These mostly applied to patients under serious disease situations. In patients with multiorgan failure, the use of probiotics was shown to increase bacterial translocation, due to serious immunocompromised situation [63]. Furthermore, it has been indicated that the jejunal administration of probiotics with prebiotic fiber (synbiotic) in severely ill patients may possibly have negative effects on intestinal perfusion, promoting multiorgan failure, bowel necrosis, and even death [64]. Thus for the moment, it is suggested not to infuse probiotics using the jejunal



administration route in critically ill patients as a standard clinical practice. More well designed and randomized studies have to be performed for detailed evaluation.

Another important issue to be mentioned is that data obtained from one study through use of the same species of probiotics or synbiotics cannot be directly extrapolated into other study. For example, *S. cerevisiae* boulardii is a widely used and studied probiotic; however, it does not show the significant activities of decreasing the risk of AAD-associated *C. difficile* infection in older patients [65]. Furthermore, effects from use of some other probiotics such as *Lactobacillus*, *Bifidobacterium*, *Streptococcus*, *Enterococcus*, and *Bacillus*, alone or in combination, also reported not to be effective for the elder patients suffering from AAD. A significant heterogeneity and controversy were also observed in other studies [37].

The effects of many commercial combinations of prebiotics and probiotics are also evaluated in the aspect of diarrhea. For example, *L. acidophilus*/*L. bulgaricus* 3 g/day, VSL#3 ( $9 \times 10^{11}$  CFU/day), *S. boulardii* (2 g/day), *L. rhamnosus* GG ( $2 \times 10^{10}$  CFU/day)/inulin 560 mg/day, *Ergyphilus* ( $2 \times 10^{10}$  CFU/day), *L. paracasei*/*B. longum*/FOS/inulin/acacia gum, *B. breve*  $1 \times 10^8$ /*L. casei* Shirota  $1 \times 10^8$ /GOS 15 g, and a mixture of bifidobacteria with enteral nutrition with mixed fibers and other immunonutrients [51]. However, their effects on benefits in terms of diarrhea reduction are still not impressive. More well designed researches have to be performed to validate the effects of these treatments.

NEC is the most common serious gastrointestinal disease in preterm infants and causes the death in extremely preterm infants from 2 weeks to 2 months of age [66]. Several studies have reported the early dysbiosis with an overgrowth of intestinal *Gammaproteobacteria* in many preterm infants [67, 68]. Previous studies have shown that *Bifidobacteria* species are enhanced by human milk oligosaccharides in breast-fed term infants [69, 70]. By contrast, these bacteria are less common in premature infants and even less abundant in preterm infants who go on to develop NEC compared to controls [69]. Further studies utilizing *Bifidobacterium* species, *Lactobacillus* species or a combination of the two bacteria showed a strong treatment effect in reduction of NEC by cumulative meta-analysis [71, 72]. On top of these, the effects of many commercial probiotic products such as BioGaia, Culturelle...etc. that contain *Lactobacillus reuteri* and *Lactobacillus rhamnosus* GG (LGG) are also used to reduce NEC [73]. Even so, the group at greatest risk of NEC, especially those with a birthweight of < 1000 g, is relatively underrepresented in these probiotic treatment. So far we do not have adequate evidences of either efficacy or safety to recommend universal prophylactic administration of probiotics to

premature infants. Hence, the effect of routine probiotics administration is controversial.

IBD classically comprising two distinct subtypes, ulcerative colitis (UC) and Crohn's disease (CD), is characterized by chronic and relapsing inflammatory diseases of the intestines. UC by definition is continuous inflammation starting in the rectum and restricted to the colon while CD inflammation can occur anywhere in the gastrointestinal tract [74]. The microbiota composition in patients with IBD is reported to be different from that of normal individuals [75]. There are some *Clostridium* species producing short-chain fatty acids such as butyrate which can decrease inflammation via induction of regulatory T cells [75]. Besides, *E. coli* Nissle 1917 and the combination probiotic cocktail VSL#3 have been found to be most beneficial for UC prevention and treatment. Synbiotic, *Bifidobacterium breve* combining with galacto-oligosaccharide, and *Bifidobacterium longum* mixing with inulinoligofructose (synergy 1) also ameliorate UC [76, 77]. Even though there are many studies, the magnitude of the effect of probiotics needs further validation.

The current studies indicate a different composition of gut microbiota between the healthy controls and many chronic inflammation-related diseases. These include obesity, diabetes, NAFLD and cardiovascular and renal diseases [78]. Changes in the composition and activity of gut microbiota after the administration of nutrients with prebiotics or probiotics may systematically change gene expression pattern (transcriptomics) and metabolism (metabolomics) of many organs in host. Organs affected many include adipose tissues, muscle, liver, pancreas, brains/neuros, lung, heart and vessels and even physiologically the modulation of satiety [79]. Administration of some prebiotics and probiotics may ameliorate the metabolic changes associated with obesity and diabetes such as insulin resistance, hyperglycemia, inflammation, dyslipidemia or NAFLD in animals [80]. However, these results have to be further confirmed in humans in well-designed, controlled clinical studies. For example, the administration of probiotics (many were conducted with different strains of *Lactobacillus* spp.) may contribute to modest improvement in blood glucose control [81]. Similarly, some other reports also show that the use of prebiotics (such as GOS, FOS, inulin... etc.), probiotics, and synbiotics is associated with slight improvements in lipid control [82]. Many effects reported are still poorly relevant for clinical practice [83].

The underlying reasons that may cause heterogeneity of study results may include different populations such as adults or children, the different types and duration of antibiotics administered, the different ingredients of probiotic preparation, the different dosages used and time for each prescription, different specific strains tested,

and the differential contents of the nutritional formula [84]. More evidence-based recommendations are urgently needed for administration of patients in urgent need.

### Safety of probiotics in clinical practice

The safety issue on prescription of probiotics is most important, due to the trend of rapid increase in the use of probiotics in recent years under different clinical circumstances. This is because different strains of probiotics may potentially have different safety characteristics. This issue is becoming more and more important as there may be novel probiotics to be developed soon in the near future.

So far, few situations of bacteremia, sepsis, or endocarditis are reported to be caused by lactobacilli *L. rhamnosus* GG or *L. casei* [85]. Infections by bifidobacteria are rare in the literature. However, bacteremia, sepsis, and cholangitis induced by *Bacillus subtilis* have been reported [86]. On the other hand, fungal sepsis caused by *S. boulardii* has also been reported [55]. Basically, the risk of infection from the administration of probiotics is low and is similar to that of infection by commensal bacterial strains. Generally speaking, more benefits are observed in contrast to the risks after probiotics treatment.

Even though the probiotics generally show safety; however, for some selected groups of patients, especially for some immuno-suppressed patients, care has to be taken in use of probiotics. A number of factors predisposing to sepsis induced by administration of probiotics is proposed. Special care has to be taken for patients of severe immuno-deficiency, malnutrition or suffering from cancer [86]. For some patients who are under special treatment regime, caution also has to be taken. For example, patients who have to uptake probiotics via jejunostomy, or shows symptoms of incompetent intestinal epithelial barrier (severe diarrhea) or concomitant administration of wide spectrum antibiotics [86]. All the strategies highlighted are to reduce the risks of sepsis caused by probiotics and infections by other potential pathogenic bacteria, or other diseases such as necrotizing enterocolitis in newborns [86].

### Conclusions

The use of probiotics, prebiotics, and synbiotics have been emerging as a promising therapy strategy which is generally safe in different clinical settings. While their efficacy for the prevention of diseases such as AAD, the reduction of the incidence of NEC in preterm newborns, and the prevention and treatment of UC appears to be effective, their effects are mostly marginal. More specific and disease-oriented, next generation probiotics are urgently needed. Further researches are needed before any final recommendations can be achieved.

### Acknowledgements

Microbiota Research Center from Chang Gung University, and the Research Center for Emerging Viral Infections from The Featured Areas Research Center Program within the framework of the Higher Education Sprout Project by the Ministry of Education (MOE) and MOST, Taiwan.

### Funding

CORPD1F0013 and CMRPD1F0123 from Chang Gung Memorial Hospital 108-2320-B-182-002-MY2, 107-2321-B-182-002 and MOST 107-3017-F-182-001 from Ministry of Science and Technology (MOST).

### Availability of data and materials

NA

### Authors' contributions

Guarantor of integrity of entire manuscript, HCL manuscript drafting and revision for important intellectual content, literature research, and manuscript final version approval: YLT, TLL, CJC, TRW, WFL, CCL and HCL.

### Ethics approval and consent to participate

NA

### Consent for publication

NA

### Competing interests

I declare that there is no competing interest.

### Publisher's Note

Springer Nature remains neutral with regard to jurisdictional claims in published maps and institutional affiliations.

### Author details

<sup>1</sup>Department of Medical Biotechnology and Laboratory Science, College of Medicine, Chang Gung University, Gueishan, Taoyuan 33302, Taiwan. <sup>2</sup>Microbiota Research Center and Emerging Viral Infections Research Center, Chang Gung University, Gueishan, Taoyuan 33302, Taiwan. <sup>3</sup>Chang Gung Immunology Consortium, Linkou Chang Gung Memorial Hospital, Gueishan, Taoyuan 33305, Taiwan. <sup>4</sup>Department of Laboratory Medicine, Linkou Chang Gung Memorial Hospital, Gueishan, Taoyuan 33305, Taiwan. <sup>5</sup>Research Center for Chinese Herbal Medicine, College of Human Ecology, Chang Gung University of Science and Technology, Gueishan, Taoyuan 33303, Taiwan. <sup>6</sup>Research Center for Food and Cosmetic Safety, College of Human Ecology, Chang Gung University of Science and Technology, Gueishan, Taoyuan 33303, Taiwan. <sup>7</sup>Department of Medicine, College of Medicine, Chang Gung University, Gueishan, Taoyuan 33302, Taiwan. <sup>8</sup>Institute of Biomedical Sciences, Academia Sinica, Taipei 115, Taiwan. <sup>9</sup>Department of Respiratory Therapy, Fu Jen Catholic University, Xinzhuang, New Taipei City 24205, Taiwan.

Received: 18 October 2018 Accepted: 13 December 2018

Published online: 04 January 2019

### References

1. Sender R, Fuchs S, Milo R. Are we really vastly outnumbered? Revisiting the ratio of bacterial to host cells in humans. *Cell*. 2016;164(3):337–40.
2. Kau AL, et al. Human nutrition, the gut microbiome and the immune system. *Nature*. 2011;474(7351):327–36.
3. Shin NR, Whon TW, Bae JW. Proteobacteria: microbial signature of dysbiosis in gut microbiota. *Trends Biotechnol*. 2015;33(9):496–503.
4. Khanna S, Tosh PK. A clinician's primer on the role of the microbiome in human health and disease. *Mayo Clin Proc*. 2014;89(1):107–14.
5. Trosvik P, de Muinck EJ. Ecology of bacteria in the human gastrointestinal tract—identification of keystone and foundation taxa. *Microbiome*. 2015;3:44.
6. Kunin, V, et al. A bioinformatician's guide to metagenomics. *Microbiol Mol Biol Rev*. 2008. 72(4): p. 557–78, Table of Contents.
7. Oulas A, et al. Metagenomics: tools and insights for analyzing next-generation sequencing data derived from biodiversity studies. *Bioinform Biol Insights*. 2015;9:75–88.

8. Mitra S, et al. Analysis of the intestinal microbiota using SOLiD 16S rRNA gene sequencing and SOLiD shotgun sequencing. *BMC Genomics*. 2013; 14(Suppl 5):S16.
9. Qin J, et al. A human gut microbial gene catalogue established by metagenomic sequencing. *Nature*. 2010;464(7285):59–65.
10. Lopetuso LR, et al. Gut Virome and inflammatory bowel disease. *Inflamm Bowel Dis*. 2016;22(7):1708–12.
11. Koenig JE, et al. Succession of microbial consortia in the developing infant gut microbiome. *Proc Natl Acad Sci U S A*. 2011;108(Suppl 1):4578–85.
12. Biagi E, et al. Through ageing, and beyond: gut microbiota and inflammatory status in seniors and centenarians. *PLoS One*. 2010;5(5): e10667.
13. Backhed F, et al. Host-bacterial mutualism in the human intestine. *Science*. 2005;307(5717):1915–20.
14. Jandhyala SM, et al. Role of the normal gut microbiota. *World J Gastroenterol*. 2015;21(29):8787–803.
15. Mripuri J, et al. Blood bacteria-specific IgA regulates maturation of the intestinal microbiota. *Gut Microbes*. 2014;5(1):28–39.
16. Human Microbiome Project, C. Structure, function and diversity of the healthy human microbiome. *Nature*. 2012;486(7402):207–14.
17. Poole LB, Schoneich C. Introduction: what we do and do not know regarding redox processes of thiols in signaling pathways. *Free Radic Biol Med*. 2015;80:145–7.
18. Krajmalnik-Brown R, et al. Effects of gut microbes on nutrient absorption and energy regulation. *Nutr Clin Pract*. 2012;27(2):201–14.
19. Sen T, et al. Diet-driven microbiota dysbiosis is associated with vagal remodeling and obesity. *Physiol Behav*. 2017;173:305–17.
20. Qin J, et al. A metagenome-wide association study of gut microbiota in type 2 diabetes. *Nature*. 2012;490(7418):55–60.
21. Michail S, et al. Altered gut microbial energy and metabolism in children with non-alcoholic fatty liver disease. *FEMS Microbiol Ecol*. 2015;91(2):1–9.
22. Vaughn AC, et al. Energy-dense diet triggers changes in gut microbiota, reorganization of gut-brain vagal communication and increases body fat accumulation. *Acta Neurobiol Exp (Wars)*. 2017;77(1):18–30.
23. De Filippo C, et al. Impact of diet in shaping gut microbiota revealed by a comparative study in children from Europe and rural Africa. *Proc Natl Acad Sci U S A*. 2010;107(33):14691–6.
24. Amar J, et al. Blood microbiota dysbiosis is associated with the onset of cardiovascular events in a large general population: the D.E.S.I.R. study. *PLoS One*. 2013;8(1):e54461.
25. Selvanantham T, et al. NKT cell-deficient mice harbor an altered microbiota that fuels intestinal inflammation during chemically induced colitis. *J Immunol*. 2016;197(11):4464–72.
26. American Diabetes A. Diagnosis and classification of diabetes mellitus. *Diabetes Care*. 2014;37(Suppl 1):S81–90.
27. Lambeth SM, et al. Composition, diversity and abundance of gut Microbiome in prediabetes and type 2 Diabetes. *J Diabetes Obes*. 2015;2(3):1–7.
28. Ley RE, et al. Microbial ecology: human gut microbes associated with obesity. *Nature*. 2006;444(7122):1022–3.
29. Fei N, Zhao L. An opportunistic pathogen isolated from the gut of an obese human causes obesity in germfree mice. *ISME J*. 2013;7(4):880–4.
30. Belkaid Y, Hand TW. Role of the microbiota in immunity and inflammation. *Cell*. 2014;157(1):121–41.
31. Jacobson AN, Choudhury BP, Fischbach MA. The biosynthesis of Lipooligosaccharide from *Bacteroides thetaiotaomicron*. *MBio*. 2018;9(2).
32. Vatanen T, et al. Variation in Microbiome LPS immunogenicity contributes to autoimmunity in humans. *Cell*. 2016;165(6):1551.
33. Fioramonti J, Theodorou V, Bueno L. Probiotics: what are they? What are their effects on gut physiology? *Best Pract Res Clin Gastroenterol*. 2003; 17(5):711–24.
34. Canny GO, McCormick BA. Bacteria in the intestine, helpful residents or enemies from within? *Infect Immun*. 2008;76(8):3360–73.
35. Segers ME, Lebeer S. Towards a better understanding of lactobacillus rhamnosus GG–host interactions. *Microb Cell Factories*. 2014;13(Suppl 1):S7.
36. Sirisinha S. The potential impact of gut microbiota on your health: current status and future challenges. *Asian Pac J Allergy Immunol*. 2016;34(4):249–64.
37. Fijan S. Microorganisms with claimed probiotic properties: an overview of recent literature. *Int J Environ Res Public Health*. 2014;11(5):4745–67.
38. Hill C, et al. Expert consensus document. The international scientific Association for Probiotics and Prebiotics consensus statement on the scope and appropriate use of the term probiotic. *Nat Rev Gastroenterol Hepatol*. 2014;11(8):506–14.
39. Senok AC, Ismaeel AY, Botta GA. Probiotics: facts and myths. *Clin Microbiol Infect*. 2005;11(12):958–66.
40. Nagpal R, et al. Probiotics, their health benefits and applications for developing healthier foods: a review. *FEMS Microbiol Lett*. 2012;334(1):1–15.
41. Bourlioux P, et al. The intestine and its microflora are partners for the protection of the host: report on the Danone symposium "the intelligent intestine," held in Paris, June 14, 2002. *Am J Clin Nutr*. 2003;78(4):675–83.
42. Papadimitriou K, et al. Discovering probiotic microorganisms: in vitro, in vivo genetic and omics approaches. *Front Microbiol*. 2015;6:58.
43. Janssen AW, Kersten S. The role of the gut microbiota in metabolic health. *FASEB J*. 2015;29(8):3111–23.
44. Slavin J. Fiber and prebiotics: mechanisms and health benefits. *Nutrients*. 2013;5(4):1417–35.
45. *Xylooligosaccharides (XOS) as an Emerging Prebiotic: Microbial Synthesis, Utilization, Structural Characterization, Bioactive Properties, and Applications*. *Compr Rev Food Sci Food Saf*. 2010. 10.
46. Rios-Covian D, et al. Intestinal short chain fatty acids and their link with diet and Human health. *Front Microbiol*. 2016;7:185.
47. Janout V, Kollarova H. Epidemiology of colorectal cancer. *Biomed Pap Med Fac Univ Palacky Olomouc Czech Repub*. 2001;145(1):5–10.
48. Ahmad MS, et al. Butyrate and glucose metabolism by colonocytes in experimental colitis in mice. *Gut*. 2000;46(4):493–9.
49. Sun Y, O'Riordan MX. Regulation of bacterial pathogenesis by intestinal short-chain fatty acids. *Adv Appl Microbiol*. 2013;85:93–118.
50. Correa-Oliveira R, et al. Regulation of immune cell function by short-chain fatty acids. *Clin Transl Immunology*. 2016;5(4):e73.
51. Pandey KR, Naik SR, Vakil BV. Probiotics, prebiotics and synbiotics- a review. *J Food Sci Technol*. 2015;52(12):7577–87.
52. Ma J, Zhou Q, Li H. Gut microbiota and nonalcoholic fatty liver disease: insights on mechanisms and therapy. *Nutrients*. 2017;9(10).
53. Sivaprakasam S, Prasad PD, Singh N. Benefits of short-chain fatty acids and their receptors in inflammation and carcinogenesis. *Pharmacol Ther*. 2016; 164:144–51.
54. Clarke SF, et al. The gut microbiota and its relationship to diet and obesity: new insights. *Gut Microbes*. 2012;3(3):186–202.
55. Hemarajata P, Versalovic J. Effects of probiotics on gut microbiota: mechanisms of intestinal immunomodulation and neuromodulation. *Therap Adv Gastroenterol*. 2013;6(1):39–51.
56. Rooks MG, Garrett WS. Gut microbiota, metabolites and host immunity. *Nat Rev Immunol*. 2016;16(6):341–52.
57. Schachter J, et al. Effects of obesity on depression: a role for inflammation and the gut microbiota. *Brain Behav Immun*. 2018;69:1–8.
58. Johanesen PA, et al. Disruption of the gut Microbiome: *Clostridium difficile* infection and the threat of antibiotic resistance. *Genes (Basel)*. 2015;6(4): 1347–60.
59. Borody TJ, Paramsothy S, Agrawal G. Fecal microbiota transplantation: indications, methods, evidence, and future directions. *Curr Gastroenterol Rep*. 2013;15(8):337.
60. Rohlke F, Stollman N. Fecal microbiota transplantation in relapsing *Clostridium difficile* infection. *Therap Adv Gastroenterol*. 2012;5(6):403–20.
61. Navarro F, Liu Y, Rhoads JM. Can probiotics benefit children with autism spectrum disorders? *World J Gastroenterol*. 2016;22(46):10093–102.
62. Gopalakrishnan V, et al. The influence of the gut Microbiome on Cancer, immunity, and Cancer immunotherapy. *Cancer Cell*. 2018;33(4):570–80.
63. Knopp RH, Paramsothy P. Oxidized LDL and abdominal obesity: a key to understanding the metabolic syndrome. *Am J Clin Nutr*. 2006;83(1):1–2.
64. Ackland G, Grocott MP, Mythen MG. Understanding gastrointestinal perfusion in critical care: so near, and yet so far. *Crit Care*. 2000;4(5):269–81.
65. Xie C, et al. Probiotics for the prevention of antibiotic-associated diarrhoea in older patients: a systematic review. *Travel Med Infect Dis*. 2015;13(2):128–34.
66. Patel RM, et al. Causes and timing of death in extremely premature infants from 2000 through 2011. *N Engl J Med*. 2015;372(4):331–40.
67. Pammi M, et al. Intestinal dysbiosis in preterm infants preceding necrotizing enterocolitis: a systematic review and meta-analysis. *Microbiome*. 2017;5(1):31.
68. Warner BB, et al. Gut bacteria dysbiosis and necrotizing enterocolitis in very low birthweight infants: a prospective case-control study. *Lancet*. 2016; 387(10031):1928–36.
69. Underwood MA, et al. *Bifidobacterium longum* subspecies infantis: champion colonizer of the infant gut. *Pediatr Res*. 2015;77(1–2):229–35.

70. Torrazza RM, et al. Intestinal microbial ecology and environmental factors affecting necrotizing enterocolitis. *PLoS One*. 2013;8(12):e83304.
71. Rees CM, et al. Probiotics for the prevention of surgical necrotising enterocolitis: systematic review and meta-analysis. *BMJ Paediatr Open*. 2017; 1(1):e000066.
72. Patel RM, Denning PW. Therapeutic use of prebiotics, probiotics, and postbiotics to prevent necrotizing enterocolitis *what is the current evidence?* *Clin Perinatol*. 2013;40(1):11–25.
73. Patel RM, Underwood MA. Probiotics and necrotizing enterocolitis. *Semin Pediatr Surg*. 2018;27(1):39–46.
74. Mack DR. Probiotics in inflammatory bowel diseases and associated conditions. *Nutrients*. 2011;3(2):245–64.
75. Sartor RB. The intestinal microbiota in inflammatory bowel diseases. *Nestle Nutr Inst Workshop Ser*. 2014;79:29–39.
76. Ishikawa H, et al. Beneficial effects of probiotic bifidobacterium and galacto-oligosaccharide in patients with ulcerative colitis: a randomized controlled study. *Digestion*. 2011;84(2):128–33.
77. Furrie E, et al. Synbiotic therapy (Bifidobacterium longum/synergy 1) initiates resolution of inflammation in patients with active ulcerative colitis: a randomised controlled pilot trial. *Gut*. 2005;54(2):242–9.
78. Boulange CL, et al. Impact of the gut microbiota on inflammation, obesity, and metabolic disease. *Genome Med*. 2016;8(1):42.
79. Pluznick JL, et al. Olfactory receptor responding to gut microbiota-derived signals plays a role in renin secretion and blood pressure regulation. *Proc Natl Acad Sci U S A*. 2013;110(11):4410–5.
80. Bashiardes S, et al. Non-alcoholic fatty liver and the gut microbiota. *Mol Metab*. 2016;5(9):782–94.
81. Festi D, et al. Gut microbiota and metabolic syndrome. *World J Gastroenterol*. 2014;20(43):16079–94.
82. Saez-Lara MJ, et al. Effects of probiotics and Synbiotics on obesity, insulin resistance syndrome, type 2 Diabetes and non-alcoholic fatty liver disease: a review of Human clinical trials. *Int J Mol Sci*. 2016;17(6).
83. Markowiak P, Slizewska K. Effects of probiotics, prebiotics, and Synbiotics on Human health. *Nutrients*. 2017;9(9).
84. Schechner V, et al. Epidemiological interpretation of studies examining the effect of antibiotic usage on resistance. *Clin Microbiol Rev*. 2013;26(2):289–307.
85. Doron S, Snyderman DR. Risk and safety of probiotics. *Clin Infect Dis*. 2015; 60(Suppl 2):S129–34.
86. Boyle RJ, Robins-Browne RM, Tang ML. Probiotic use in clinical practice: what are the risks? *Am J Clin Nutr*. 2006;83(6):1256–64 quiz 1446-7.

**Ready to submit your research? Choose BMC and benefit from:**

- fast, convenient online submission
- thorough peer review by experienced researchers in your field
- rapid publication on acceptance
- support for research data, including large and complex data types
- gold Open Access which fosters wider collaboration and increased citations
- maximum visibility for your research: over 100M website views per year

**At BMC, research is always in progress.**

Learn more [biomedcentral.com/submissions](https://biomedcentral.com/submissions)





# Large-Scale Proteomic Identification of Targets of Cellular miR-197 Downregulated by Enterovirus A71

Wen-Fang Tang,<sup>†,§,¶</sup> Ru-Ting Huang,<sup>†,§</sup> Kun-Yi Chien,<sup>†,§,¶</sup> Petrus Tang,<sup>||,⊥</sup>  
and Jim-Tong Horng<sup>\*,†,⊥,▽,¶</sup>

<sup>†</sup>Department of Biochemistry and Molecular Biology, College of Medicine, Chang Gung University, Taoyuan 333, Taiwan

<sup>‡</sup>Clinical Proteomics Core Laboratory, Chang Gung Memorial Hospital, Taoyuan 333, Taiwan

<sup>||</sup>Bioinformatics Center, Chang Gung University, Chang Gung University, Taoyuan 333, Taiwan

<sup>⊥</sup>Molecular Infectious Disease Research Center, Chang Gung Memorial Hospital, Taoyuan 333, Taiwan

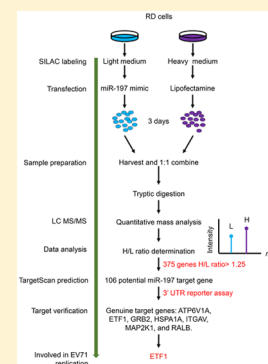
<sup>▽</sup>Research Center for Chinese Herbal Medicine, Research Center for Food and Cosmetic Safety and Graduate Institute of Health Industry Technology, College of Human Ecology, Chang Gung University of Science and Technology, Taoyuan 333, Taiwan

<sup>¶</sup>Research Center for Emerging Viral Infections, Chang Gung University, Taoyuan 333, Taiwan

## Supporting Information

**ABSTRACT:** MicroRNAs are noncoding RNA species comprising 18–23 nucleotides that regulate host–virus interaction networks. Here, we show that enterovirus A71 infection in human rhabdomyosarcoma (RD) is regulated by miR-197 expression. Transfection of miR-197 mimic into RD cells inhibited virus replication by interfering with the viral RNA synthesis. We employed a combination of mass-spectrometry-based quantitative proteomics with the stable isotope labeling with amino acids in cell culture (SILAC) approach for the identification of the miR-197 target genes in RD cells and to investigate the differential expression of the prospective target proteins. A total of 1822 proteins were repeatedly identified in miR-197-transfected RD cells, 106 of which were predicted to have seed sites by TargetScan. Notably, seven of eight selected genes potentially related to viral replication and immune response were validated as direct miR-197 targets, using a luciferase 3′-untranslated region (UTR) reporter assay. The expression levels of three selected endogenous molecules (ITGAV, ETF1, and MAP2K1/MEK1) were significantly reduced when RD cells were transfected with a miR-197 mimic. Our results provide a comprehensive database of miR-197 targets, which might provide better insights into the understanding of host–virus interaction.

**KEYWORDS:** enterovirus A71, microRNA, miR-197, SILAC, TargetScan, viral replication



## INTRODUCTION

Enterovirus A71 (EV-A71) is a (+)sense RNA virus belonging to the Picornaviridae family.<sup>1</sup> It was first isolated from a child with encephalitis in 1969 and causes a highly contagious infection among children younger than 5 years. The symptoms of EV-A71 infection are fever, hand-foot-and-mouth disease (HFMD), herpangina, and occasionally serious neurological diseases, including brainstem encephalitis, meningitis, poliomyelitis-like paralysis, and cardiopulmonary failure.<sup>2,3</sup> The EV-A71 genome is ~7.5 kb in length, accommodating an open reading frame (ORF) flanked by 5′ and 3′ untranslated regions (UTR). A variable-length poly(A) tail is present in the 3′ end. The 5′UTR of the EV-A71 genome is highly structured and includes an internal ribosomal entry site (IRES) that facilitates viral protein translation. The ORF is translated into a polyprotein by host translation machinery, and the viral polyprotein undergoes a self-cleaving process by virus-encoded proteinases, 2A<sup>pro</sup> and 3C<sup>pro</sup>, to generate 11 mature proteins. VP1–VP4 constitute the virus capsid, while 2A–C and 3A–D are involved in virus replication.<sup>3</sup>

microRNAs are a group of small noncoding RNAs approximately 21–23 nucleotides in length. They play a critical role in gene regulation to modulate physiological processes like apoptosis, cell cycle, sex determination, cell differentiation and proliferation, and development of cancer.<sup>4</sup> Extensive studies have revealed the presence of at least 2654 mature miRNAs in the human genome (miRBase; <http://www.mirbase.org/>). The primary miRNA transcript may originate from diverse resources, including specific miRNA genes, noncoding genes, the intronic region, or even exons of long noncoding transcripts.<sup>5</sup> The majority of primary miRNAs are transcribed by RNA polymerase II and recognized by microprocessor protein complex, following series of posttranscriptional processing to generate functional and mature miRNAs.<sup>6</sup> The complementarity between an miRNA and the 3′UTR of its target gene influences the action of gene silencing.<sup>7–9</sup> The perfect complementarity between the 3′UTR of the mRNA and the miRNA directs the target mRNA to

**Received:** September 26, 2018

**Published:** October 18, 2018

degradation via Ago2 cleavage, a component of RNA-induced silencing complex (RISC), whereas incomplete complementary base pairing between the miRNA and the 3'UTR of the mRNA interferes with target mRNA translation. The target complementarity is crucially determined by the 5' end of the miRNA bases 2–8, or at least, bases 2–7 which is also known as the “seed (nucleus) region”.<sup>10</sup> The stretch of six continuous nucleotides of the seed region thus complementarily pairs with the corresponding mRNA to form the miRNA–mRNA complex.<sup>11,12</sup>

Having simple components like virus capsids and genomic RNA, EV-A71 needs to utilize the host cellular machinery to sustain virus replication. EV-A71 has been described to modulate cellular miRNAs to support its replication and evade the host immune response. The transcription factor EGR1 expression elevates in response to EV-A71 infection to transactivate miR-141 transcription.<sup>13</sup> The expression level of the miR141 target gene, eIF4E, is thus inhibited to assist viral protein synthesis by switching cap-dependent translation to IRES-dependent translation.<sup>13</sup> We observed that miR-197 is downregulated in EV-A71-infected RD cells, thus leading to upregulated levels of ras-related nuclear protein (RAN), one of the miR-197 target genes, in order to sustain the nuclear traffic of crucial proteins, including host protein hnRNP K and viral proteins 3D/3CD, for virus replication.<sup>14</sup> Interestingly, miR-134 modulates poliovirus replication by targeting RAN. It also inhibited the replication of viruses belonging to Picornaviridae family, including EV-A71.<sup>15</sup> Another study showed upregulated miR-21 in EV-A71-infected cells, which in turn targets myeloid differentiation factor 88 (MyD88) and interleukin-1 receptor-associated kinase 1 (IRAK1) to repress type I interferons production. This facilitates the virus to escape the host immune system.<sup>16</sup> In addition, miR-296–5p and miR-23b restrict EV-A71 replication by directly targeting its genome.<sup>17,18</sup>

Stable isotope labeling with amino acids in cell culture (SILAC) has been reported as a popular quantitative proteomic method for screening miRNA targets.<sup>19,20</sup> Heavy- and light-stable isotope (nonradioactive) labeled essential amino acids are added into the culture medium, and cellular proteins are metabolically incorporated with nonradioactive isotopes after a few passages. The peptides are incorporated with heavy amino acids creating a mass shift. The peptide abundance ratio calculated by mass spectrometry from the intensity differences enable the quantification of relative protein changes.<sup>21</sup>

In our study, we used mass spectrometry (MS)-based SILAC approach to screen for the miR-197 targets by analyzing the protein expression changes in miR-197-transfected RD cells. We subsequently combined a miRNA target prediction tool, TargetScan, and 3'UTR reporter assays to identify novel miRNA targets and investigate their biological significance in viral pathogenesis.

## ■ EXPERIMENTAL PROCEDURES

### Cells Culture, Viruses, and Antibodies

Human rhabdomyosarcoma (RD) cells were obtained from the Food Industry Research and Development Institute (Hsinchu, Taiwan). The cells were cultured in Dulbecco's modified Eagle's medium (DMEM) (Gibco, Thermo Fisher Scientific, Waltham, MA) supplemented with 10% fetal bovine serum (FBS) (Gibco) and incubated at 37 °C in a humidified

incubator with 5% CO<sub>2</sub>. The EV-A71 strain 98/2231/TW was expanded from an infectious clone plasmid received from Dr. Mei-Shang Ho of Academia Sinica (Taipei, Taiwan). The antibodies used in this study are anti-GAPDH (H00002597-M01, Abnova, Taipei, Taiwan), anti-FLAG (F-3165, Sigma-Aldrich, St. Louis, MO), polyclonal antibodies against MAP2K1 (GTX102391, GeneTex, Irvine, CA), ITGAV (GTX100789, GeneTex), ETF1 (GTX108271, GeneTex). The polyclonal antibody against full-length 3A was prepared in-house.<sup>22</sup>

### Virus Infection and Plaque Assay

RD cells were plated in dishes and incubated at 37 °C overnight. For virus infection, the culture medium was removed, and the cells were washed with PBS. The cells were then adsorbed with EV-A71 at a multiplicity of infection (M.O.I.) of 10 diluted in serum-free DMEM for 1 h (between –1 and 0 h post infection (p.i.)) at 37 °C. After adsorption, the unbound viruses were removed by PBS wash, and the cells were maintained in DMEM containing 2% FBS before harvesting. The viral titer was determined by plaque assay in RD cells using the procedure described in a previous study.<sup>14</sup>

### miRNA Expression Array

Analysis of miRNA expression by microarray was carried out as described previously.<sup>14</sup> The entire set of miRNA microarray data was uploaded to the Gene Expression Omnibus database (GEO accession: GSE75455).

### RNA Extraction, Reverse Transcription, and Quantitative Polymerase Chain Reaction (qPCR)

Total RNA extraction was performed using TRIzol (Invitrogen, Thermo Fisher Scientific, Carlsbad, CA) method according to the manufacturer's protocol, and the samples were treated with DNase (Promega, Madison, WI) to remove the DNA contaminants. The procedures of reverse transcription and qPCR are described in a previous study.<sup>14</sup> The primers used in this study are listed in Table S1.

### Synthetic miRNAs, siRNAs, and Transfection

Synthetic miRNA hairpin inhibitors or double-strand mimics and the respective negative controls were purchased from Dharmacon (Thermo Fisher Scientific, Lafayette, CO). The siRNA oligomers (siETF1, siMAP2K1, siITGAV, and scrambled siRNA (SC)) were obtained from Invitrogen. The sequences of miRNA inhibitors/mimics and the siRNAs are listed in Table S1. Lipofectamine 2000 (Life Technologies, Carlsbad, CA) was used for transfection in RD cells. Post-transfection 48 h, RD cells were seeded in culture dishes or plates and incubated at 37 °C overnight. Transfected cells were then subjected to EV-A71 infection, EV-A71 replicon RNA transfection, or EV-A71 2231 internal ribosome entry site (IRES) plasmid transfection.

### SILAC Labeling of Cells

The Pierce SILAC Protein Quantitation Kit (Thermo Fisher Scientific, Rockford, IL) was used to label RD cells with heavy- and light-stable isotopes. The cell labeling and sample preparation were performed as mentioned elsewhere.<sup>14</sup>

### Online 2D LC System, MS, and Data Analysis

The SILAC samples were separated by the comprehensive 2D SCX-RP (reverse phase) LC system (UltiMate 3000, Thermo Fisher Scientific, Waltham, MA) according to the manufacturer's protocols. Each fraction was inspected using an LTQ Orbitrap mass spectrometer equipped with a nanoelectrospray

ion source (Thermo Fisher Scientific), and the mass spectrometry data were obtained in a data-dependent mode using Xcalibur software (version 2.0.7 SR 2, Thermo Fisher Scientific). The identification and quantification of proteins were performed using the MaxQuant v1.0.13.13 software package developed by Jürgen Cox and Matthias Mann (Max Planck Institute of Biochemistry, Planegg, Germany). A more detailed protocol is provided in the [Supporting Information](#). The mass spectrometry data have been deposited in the PRIDE Archive (<http://www.ebi.ac.uk/pride/archive/>) via the PRIDE partner repository with the data set identifier PXD010585 and 10.6019/PXD010585.

### Plasmid Construction and Primer Sequences

The 3'UTR fragments of candidate target genes containing wild-type (WT) or mutated miR-197 seed region were amplified by PCR using specific primers with incorporated restriction sites (listed in [Supplementary Table S1](#)). The PCR products were digested with *PmeI*, *SmaI*, or *EcoRV* enzymes and ligated to a *PmeI*-digested firefly luciferase (Fluc) reporter plasmid, as described in a previous study.<sup>14</sup> The *Renilla* luciferase (Rluc)-expressing plasmid was used as an internal control, and the EV-A71 2231 replicon was used to study EV-A71 replication as described in a previous study.<sup>14</sup> In order to construct an ETF1-overexpressing plasmid (pFLAG-CMV2-2-ETF1), ETF1 was cloned in pFLAG-CMV-2 (Sigma-Aldrich) between *NheI* and *BamHI* restriction sites. The silent mutant pFLAG-CMV-2-ETF1simut, which was refractory to siETF1, was constructed by modifying three nucleotides of ETF1 in the region complementary to the siETF1 sequence (underlined in [Table S1](#)).

### Protein Extraction and Western Blotting

Protein extraction and immunoblotting were performed as described in a previous study.<sup>14</sup> The intensity of the protein bands was first normalized to GAPDH, and the ratios of miR-197 mimic-treated samples or siRNA-treated samples were normalized to the respective controls (arbitrarily set as 1).

### Reporter Assay

The 3'UTR reporter assays were performed by transfection of 8  $\mu$ g of 3'UTR-Fluc reporter plasmid and 2  $\mu$ g of Rluc plasmid (as an internal control) using Lipofectamine 2000. The relative luciferase activity was determined by the ratio of Fluc to Rluc activity. The relative luciferase activity of a miR-197 mimic-transfected sample was normalized to that of the NC mimic-transfected control (NC mimic) (arbitrarily set as 1). The luciferase activities of the 3'UTR reporter after EV-A71 infection, EV-A71 replicon replication, and EV-A71 IRES reporter activity in miR-197 target gene silencing cells were detected as previously described.<sup>14</sup>

### Statistical Analysis

Student's two-tailed *t*-test was used for statistical analysis, and a *p*-value <0.05 was considered to indicate statistically significant differences.

## RESULTS

### EV-A71 Infection Alters the Expression Profile of Host Cellular miRNAs

To systematically study the EV-A71-induced miRNA expression levels, we infected RD cells with EV-A71 (M.O.I. of 10) and the differential expression of miRNAs was compared between 5 and 10 h p.i. These time points are considered to

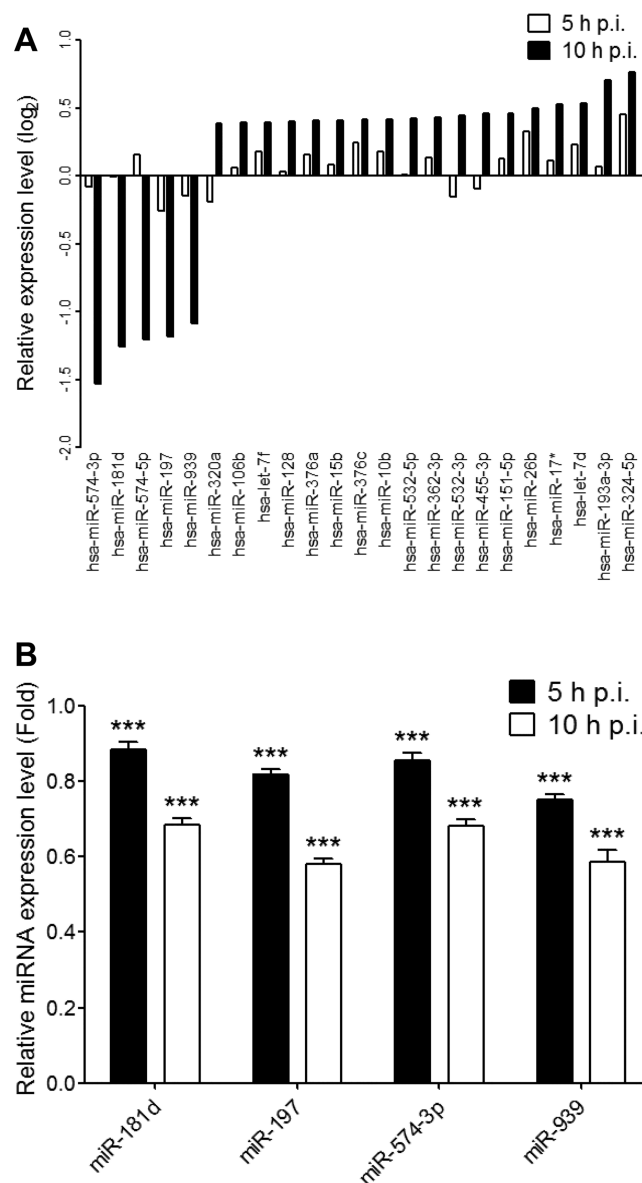


**Figure 1.** EV-A71 infection alters the host cellular miRNA expression. Total RNA extracted from EV-A71-infected RD cells (M.O.I. 10) was analyzed by miRNA microarrays and qPCR. (A) Relative expression profile of EV-A71-infection-responsive miRNAs. The gene signals expression in EV-A71-infected cells were normalized to those of mock-infected cells at the indicated times. (B) Evaluation of the relative expression level of miR-197, -181d, -574-3p, and -939 by qPCR. The yield of each miRNAs was first normalized to that of miR-16, and the relative miRNA expression level of virus groups was then normalized to that of the mock group (arbitrarily set as 1) at indicated time points. Results are presented as means  $\pm$  SEM ( $n = 3$ , \*\*\**p* < 0.005).

indicate the key replication steps, namely, active replication and viral shedding. Previous studies demonstrated the virus induced cytopathic effects (CPEs) as early as 6 h p.i., followed by virus release.<sup>23</sup> The differential expression of miRNAs at these time points was analyzed using miRNA microarray and GeneSpring 7.3.1 normalized using the 75th percentile method (Agilent Technologies, Santa Clara, CA).<sup>14,24</sup> Using this array, 101 miRNAs were sufficiently detectable in at least 1 of 4 RNA samples prepared from the RD cells (mock-5h, virus-5h, mock-10h, and virus-10h) and were adequate enough to be



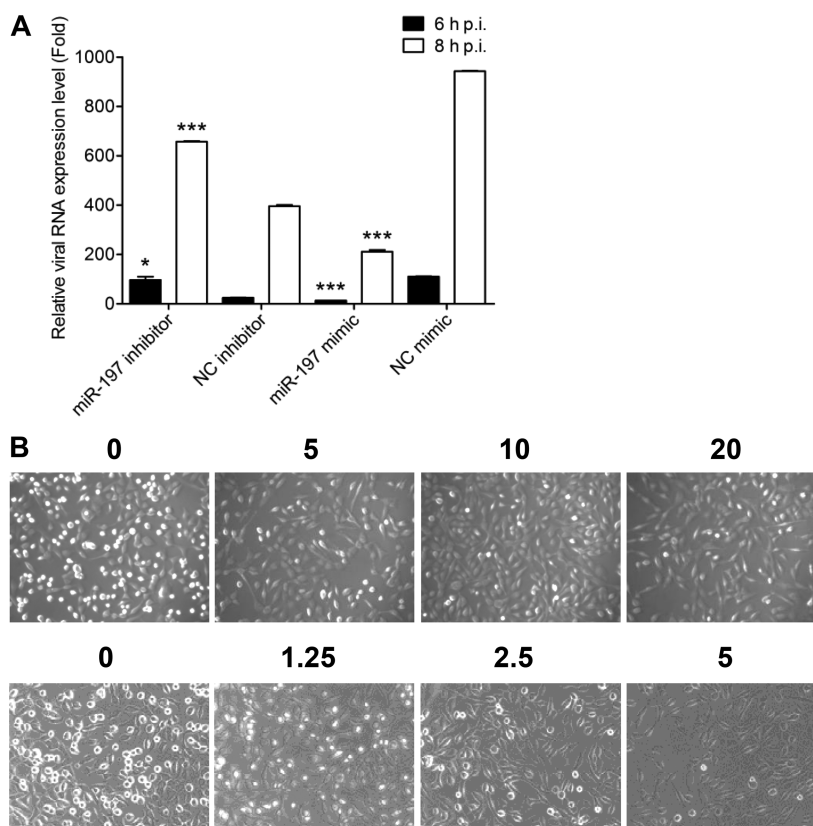


**Figure 2.** Examination of viral RNA expression and CPE regulated by miR-197 mimic or inhibitor. RD cells were transfected with miR-197 mimic or inhibitor. Three days post-transfection, the cells were infected with EV-A71 at an M.O.I. of 10. (A) miR-197 mimic was inhibitory to viral RNA expression. The yield of EV-A71 RNA was first normalized to GAPDH mRNA, and the ratios were normalized to the control at 0 h p.i. (arbitrarily set as 1) at the indicated times p.i. (B) miR-197 inhibits virus-induced CPE in a dose-dependent manner. RD cells were transfected with 1.25–20 nM miR-197 mimic, and CPE was evaluated at 8 h p.i. using a Zeiss Axiovert 200 microscope (Oberkochen, Germany).

confirmed by qPCR. We observed that five miRNAs (miR-574–5p, miR-574–3p, miR-181d, miR-197, and miR-939) were downregulated by >50% ( $\log_2 < -1$ ), and 18 miRNAs were upregulated by 30–70% ( $\log_2 \leq 1$ ) in EV-A71 infected cells compared with those in mock infected cells at 10 h p.i. (Figure 1A). qPCR was used to corroborate the expression of these decreased miRNAs detected by microarray analysis, and the results suggested the downregulation of miR-574–3p, miR-181d, miR-197, and miR-939 by 30–40% in the virus-10h group compared to that in the mock-10h group (Figure 1B). Because of its highly repetitive GU elements, the probe for miR-574–5p was not commercially available and hence excluded from the analysis. We chose miR-197 for further studies because our previous studies suggested that viral replication was consistently and more efficiently inhibited upon transfection with a miR-197 mimetic, and the viral replication was increased when cells were transfected with a miR-197 inhibitor.<sup>14</sup>

#### Overexpression of miR-197 Inhibits EV-A71 Replication

To investigate the function of miR-197 in EV-A71 replication, we transiently transfected a miR-197 mimetic or antagonist into RD cells (Figure 2). Transfection of miR-197 mimics significantly reduced the viral RNA synthesis compared to that in the NC mimic control (Figure 2A). Conversely, the levels of viral RNA were considerably elevated upon transfection of miR-197 inhibitors (Figure 2B). Our previous study indicated that the viral protein expression significantly reduced after transfection with miR-197 mimics.<sup>14</sup> Results from the CPE

assay demonstrated that miR-197 mimics possess potent antiviral activity in a dose-dependent manner (1.25–20 nM) (Figure 2B). Our previous study showed 5 nM of miR-197-mediated inhibition of viral RNA synthesis (Figure 2A) and protein expression,<sup>14</sup> and hence, we used this concentration for the subsequent experiments in the present study.

#### Identification of Genes Targeted by miR-197 Using a High-Throughput MS-Based SILAC Method

We hypothesized that reduction of miRNA expression induced by EV-A71 may conversely increase the level of host proteins required for viral pathogenesis. To identify the target genes modulated by miR-197, we employed a SILAC assay in combination with MS-based quantitative proteomics (Figure 3A). RD cells incorporated with a light-stable isotope (light cells) were transfected with miR-197 mimic, whereas cells incorporated with a heavy stable isotope (heavy cells) were mock-transfected with only Lipofectamine. After incubation for 3 days, cell lysates were prepared for MS analysis. The light cells had an increase in miR-197 levels by >40-fold relative to that in heavy cells, indicating that miR-197 was sufficiently overexpressed to sequester its targets in RD cells (Figure 3B). We identified 5475, 5252, and 5029 proteins in three independent experiments. Among these, we reproducibly identified 1822 proteins that had three or more unique peptides (Table S2), 375 of which were differentially expressed with an average heavy/light (H/L) ratio  $\geq 1.25$  (Table S2). As expected, miR-197 transfection yielded a mild change in the most unique proteins (Figure 3C). Examination of the



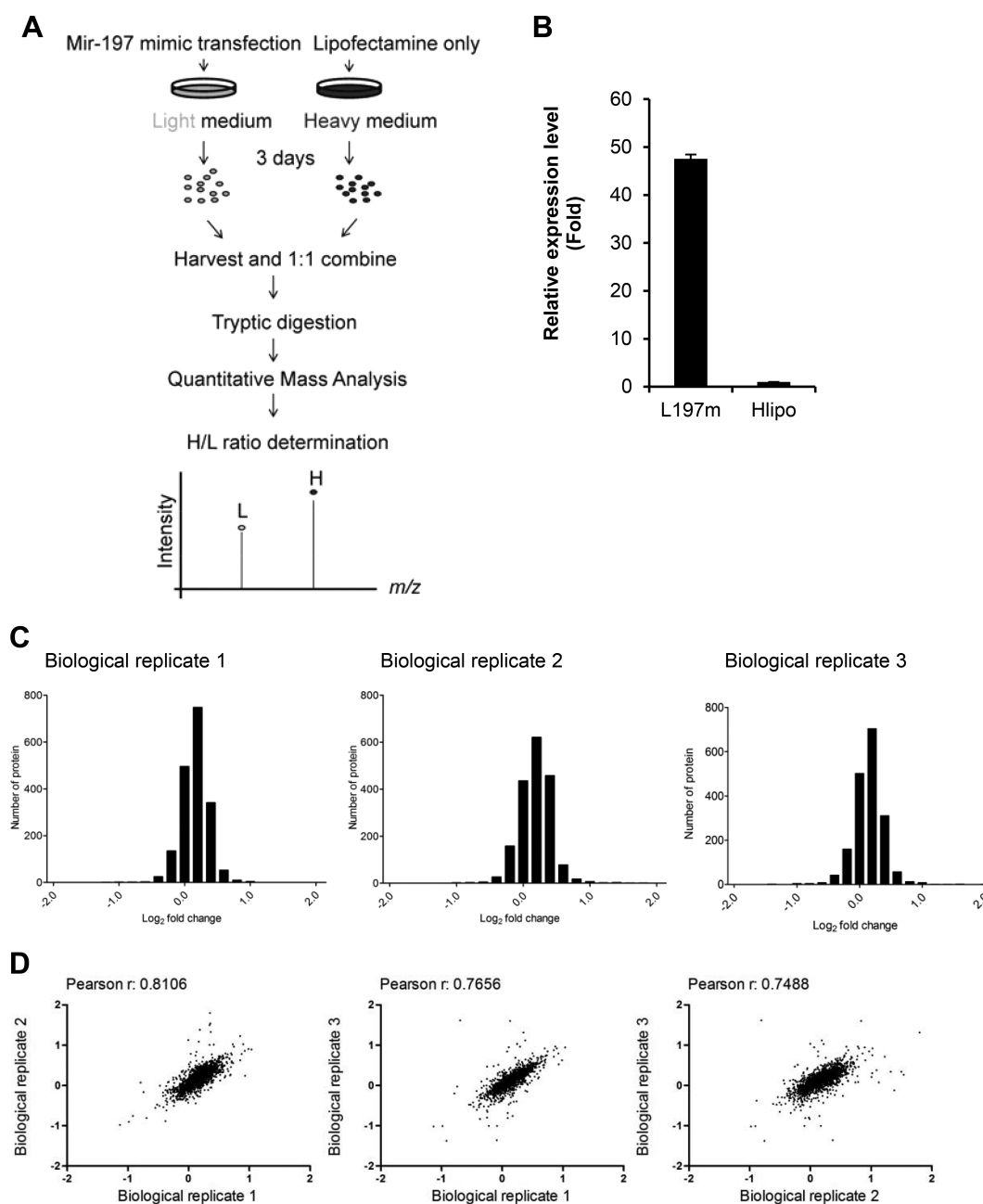


**Figure 3.** Large-scale analysis of changes in the protein expression in miR-197-transfected RD cells by MS-based SILAC. (A) Cells were metabolically labeled in culture medium containing essential amino acids incorporated with heavy- and light-stable (nonradioactive) isotopes. The peptides containing heavy amino acids generated a shift in mass. The intensities of peptide pairs with the predicted mass difference revealed their abundance. (B) Relative expression level of miR-197 in metabolic-labeled RD cells transfected with miR-197 mimic or NC mimic. (C) Histograms depicting the changes in the protein levels of each replicate with three or more unique peptides identified in RD cells after miR-197 overexpression. (D) Reproducibility of three independent biological replicates of SILAC experiments.

reproducibility of the results revealed a strong association (Pearson's correlation coefficient, 0.749–0.811) between any two experimental replicates in the entire dynamic range (Figure 3D). This led to the identification of 106 potential genes from SILAC analysis which have at least one consensus seed sequence at 3'UTR as predicted by TargetScan (Release 7.1; <http://www.targetscan.org/>). Pathway analysis of the 375 differentially expressed genes indicated that most of them are involved in metabolic pathways, viral infection, and pathogenesis (Table S4).

### Target Gene Verification

To confirm the authenticity of the candidate target genes that were identified by coupling SILAC with the TargetScan algorithm, eight selected candidates involved in viral replication, cellular signaling pathways, and immune response regulation, as indicated by a literature search,<sup>25–35</sup> and bioinformatic analysis (Table S4), were further examined (Table 1). The 3'UTR reporter assay was conducted to verify these miR-197 targets, where the 3'UTR containing the seed sequence of the prospective genes were cloned downstream to the Fluc reporter. The Fluc/Rluc ratio of the reporter

Table 1. Candidate Target Genes Identified Using SILAC and TargetScan

gene name	full name	H/L ratio <sup>a</sup>	repression fold (miR-197mimic/Lipo, log <sub>2</sub> )	target sites			context score	references <sup>b</sup>
				8mer	7mer-m8	7mer-1A		
ATP6 V1A	ATPase, H <sup>+</sup> transporting, lysosomal 70 kDa, V1 subunit A	1.6337	−0.7081	1	0	0	−0.41	28,32
ETF1	eukaryotic translation termination factor 1	1.4007	−0.4861	1	1	1	−0.49	33,34
GRB2	growth factor receptor-bound protein 2	1.3429	−0.4254	0	1	1	−0.17	27
HSPA1A	heat shock 70 kDa protein 1A	1.5621	−0.6435	0	0	1	−0.16	25
ITGAV	integrin, alpha V (vitronectin receptor, alpha polypeptide, antigen CD51)	1.6053	−0.6828	1	0	0	−0.07	29,30
MAP2K1	mitogen-activated protein kinase kinase 1	1.9460	−0.9605	0	1	1	−0.32	26,27
RALB	v-ral simian leukemia viral oncogene homologue B (ras related; GTP binding protein)	1.7268	−0.7881	1	0	0	−0.22	31
ZRANB2	zinc finger, RAN-binding domain containing 2	1.3969	−0.4822	0	0	1	−0.05	35

<sup>a</sup>average from 3 independent experiments. <sup>b</sup>functions related to immune or viral replication.

constructs was observed to be downregulated by 20–40% compared with the respective controls (Figure 4B). Except for ZRANB2, reduction of luciferase activity was not noticed for reporter constructs with reverse-oriented 3'UTRs or for the Fluc vector alone, demonstrating that ATP6 V1A, ETF1, GRB2, HSPA1A, ITGAV, MAP2K1, and RALB are *bona fide* candidate targets of miR-197. Because of their potential involvement in viral replication, we closely examined the molecular functions of ETF1, ITGAV, and MAP2K1.<sup>26,27,29,30,33,34</sup> According to the TargetScan algorithm, the canonical seed regions located in the 3'UTR of ITGAV had one 8mer seed, whereas MAP2K1 contained one 7mer-m8 and one 7mer-A1 seed (Figure 4A). Interestingly, ETF1 contained three seeds, including one 8mer site, one 7mer-m8 site, and one 7mer-A1 site. To investigate the authenticity of each of these seed regions, Fluc reporter plasmids with 3'UTR sequences carrying point mutations in the respective seed regions were generated. The relative luciferase activity of WT ITGAV<sup>+</sup> was downregulated by >40% after miR-197 mimic treatment, whereas that of ITGAV-mut and ITGAV<sup>−</sup> was barely changed following the treatment (Figure 4B). The Fluc/Rluc ratio of ETF1<sup>+</sup> was downregulated by 35%, whereas the inhibition of ETF1<sup>−</sup> and ETF1-mut2 (carrying a mutated 8mer site) was completely abolished (Figure 4B). The ratio of ETF1-mut1 carrying a mutated 7mer-A1 site was reduced by ~25% and that of ETF1-mut3 carrying a mutated 7mer-m8 site was inhibited by ~25% after transfection with miR-197 mimic, indicating that the seed sequence containing an 8mer in mut2 is the *bona fide* target site (Figure 4B). In the case of MAP2K1, the relative luciferase activity of MAP2K1<sup>+</sup> was downregulated, in contrast with that of MAP2K1<sup>−</sup>, which was marginally, if at all, repressed. However, MAP2K1-mut1 (with a 7mer-1A seed) and MAP2K1-mut2 (with a 7mer-m8 seed) did not show rescue of luciferase activity, indicating that both target sites were genuine (Figure 4B). We further used Western blot analysis to confirm the data obtained from 3'UTR reporter assay. ETF1, ITGAV, and MAP2K1 proteins were significantly downregulated by miR-197 compared to that of NC mimic ( $p < 0.05$ , Figure 4C). These observations from 3'UTR reporter assay and Western blotting analysis confirm that ATP6 V1A, ETF1, GRB2, HSPA1A, ITGAV, MAP2K1, and RALB are valid targets of miR-197.

### Involvement of miR-197 Target Genes in Viral Replication

To investigate the importance of miR-197 target genes during EV-A71 replication, siRNAs targeting *ETF1* (siETF1), *ITGAV*

(siITGAV), and *MAP2K1* (siMAP2K1) were transfected independently into RD cells, and the viral protein expression and viral titer were examined (Figure 5A–C). Our results indicated that the viral protein expression was inhibited in *ETF1*-silenced cells (Figure 5A), and the inhibition was recovered by the overexpression of the nondegradable mutant, FLAG-ETF1simut. However, in cells silenced for *MAP2K1* or *ITGAV*, 3A expression did not show any significant change compared to scrambled control (Figure 5B), suggesting that *ETF1*, but not *ITGAV* and *MAP2K1*, is necessary for viral protein production. Moreover, the viral titer was significantly reduced in siETF1 but not in siMAP2K1- or siITGAV-transfected cells, consistent with the Western blotting data (Figure 5C). *ETF1* might be associated with replication because its knockdown resulted in roughly 40% reduction of viral replicon activity (Figure 5D). However, the replicon activity remained unchanged between siETF1- and SC-transfected cells in the presence of GnHCl, an RNA replication inhibitor, indicating that *ETF1* might not play a role in the initial translation of the EV-A71 replicon (Figure 5D). The finding that viral protein synthesis was attenuated by specific targets of miR-197 led us to investigate whether they target the IRES activity of EV-A71. The intrinsic IRES activity present in the 5'UTR of EV-A71 in a dicistronic system was measured after silencing *ETF1* (Figure 5E). The relative luciferase activity in siETF1-transfected cells was not different compared to SC-transfected cells (Figure 5F), demonstrating that *ETF1*-mediated inhibition of viral protein expression did not result from the reduced IRES-dependent translation. As expected, silencing of *MAP2K1* and *ITGAV* did not affect the IRES activity, which agrees with the findings in Figure 5D.

The decrease in miR-197 expression during viral infection may be associated with increased expression of target genes to regulate viral replication. Hence, we examined the expression levels of the three target proteins at different time points during a replication cycle of EV-A71 infection (Figure 6A). The protein levels of the target genes, with the exception of *ITGAV*, were retained at ~70% compared to the mock-infected cells. eIF4G, whose cleavage by enterovirus was shown to be responsible for the virus-induced translation attenuation,<sup>36</sup> was markedly cleaved at 10 h p.i. These data suggest that these miRNA target genes were barely altered during EV-A71 infection. In addition, the expression of 3'UTR reporter constructs carrying WT or mutated seeds (Figure 4A,B) was examined in EV-A71-infected RD cells (Figure 6B). RD cells were transfected with Fluc reporter and the control plasmid Rluc, followed by infection with EV-A71 and luciferase assay.

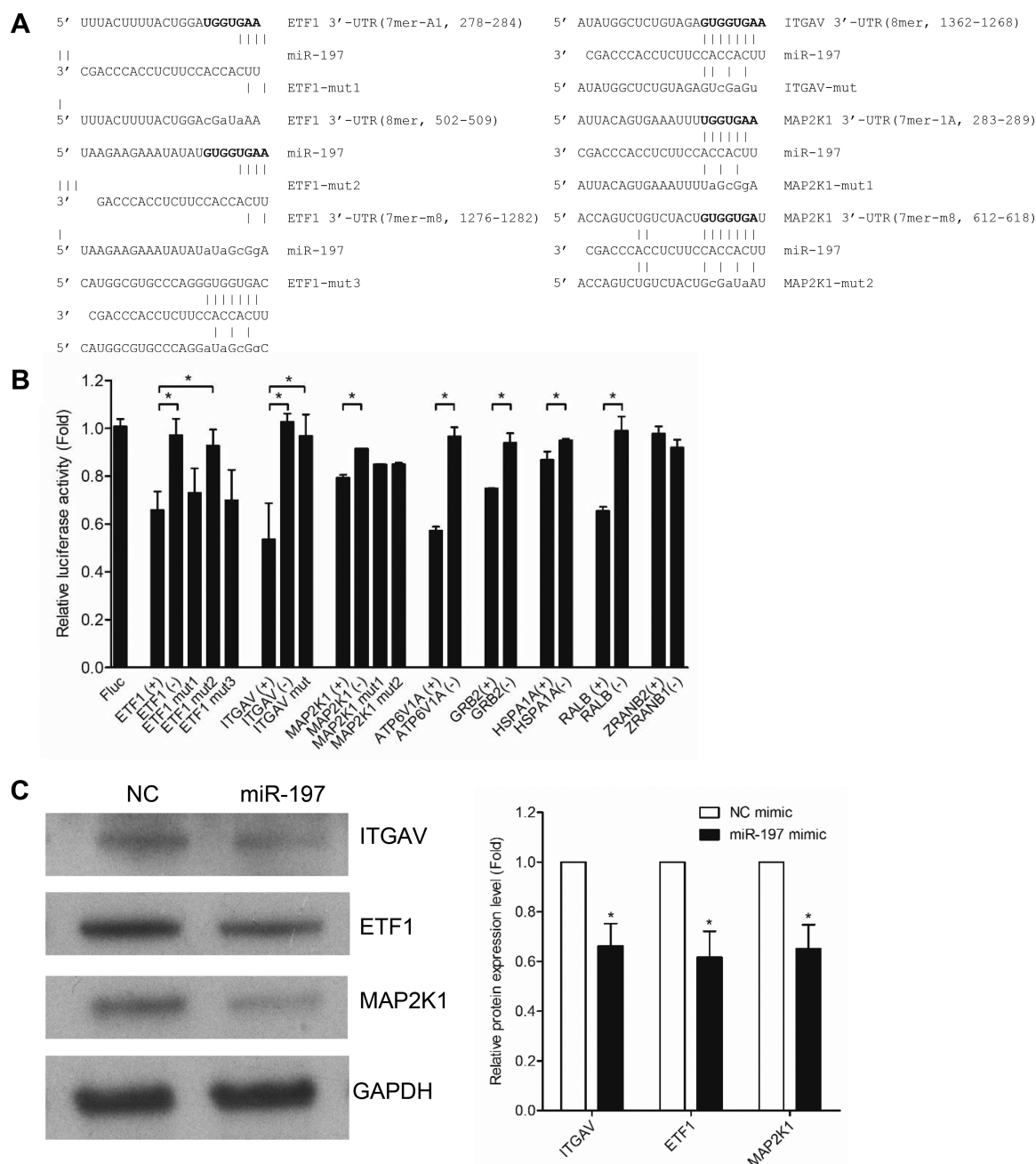


**Figure 4.** Genes identified by SILAC as being downregulated by miR-197 overexpression were verified using a 3'UTR reporter assay and immunoblotting. (A) Seed region of the 3'UTR-Fluc reporters of *ETF1*, *ITGAV*, and *MAP2K1*. (B) Mutational analysis of the seed regions of targets. RD cells were transfected with Fluc vector only, wild type (+), or reverse (–)-3'UTR-Fluc reporters of candidate genes together with a control Rluc plasmid for 24 h prior to transfection with 5 nM miR-197 mimic or NC mimic. The changes of Fluc/Rluc activity were individually determined, and the relative Fluc/Rluc of miR-197-transfected cells was normalized to that of NC mimic transfected cells (arbitrarily set as 1). (C) Western blot analysis of target protein expression in 5 nM miR-197 mimic-transfected cells. Western blotting was performed using antibodies specific for *ETF1*, *ITGAV*, and *MAP2K1*. Error bars represent means  $\pm$  SEM ( $n = 3$ , \* $p < 0.05$ ).

*MAP2K1*<sup>+</sup>, *ITGAV*<sup>+</sup>, and *ETF1*<sup>+</sup> reporter activities were significantly upregulated (by 20–30%) at 8 h p.i., while the reverse or mutated controls did not show any significant changes (Figure 6B). Thus, the viral infection resulted in the downregulation of miR-197, consequently upregulating the three miR-197 target genes to counteract the virus-induced translation attenuation. In addition, the half-life of *ETF1* was below 2 h after the treatment with cycloheximide (CHX), a eukaryotic protein synthesis inhibitor, suggesting that the diminished expression of miR-197 during EV-A71 infection

might lead to the upregulation of its target genes, such as *ETF1*, to facilitate viral replication (Figure 6C).

## DISCUSSION

In this study, we used the SILAC method to determine the target genes for miR-197 and to investigate the role of these targets in EV-A71 replication. This work not only identified a set of direct targets for miR-197 that might play crucial roles in EV-A71 replication and other physiological functions but also showed that EV-A71 has evolved a highly sophisticated

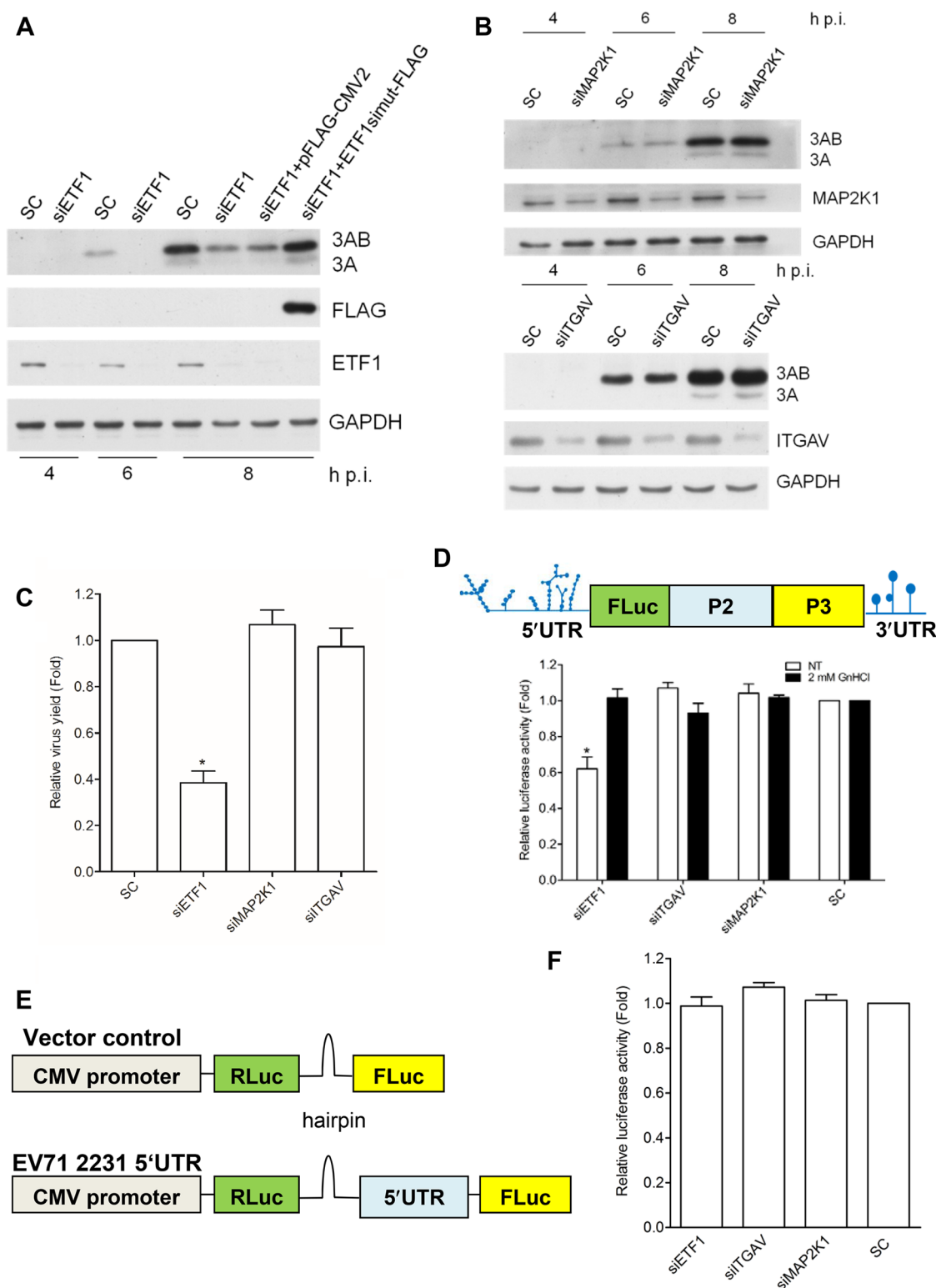


**Figure 5.** Effect of miR-197 target genes on viral replication. (A–B) Immunoblotting analysis of target genes by siRNA transfection. RD cells were infected with EV-A71 (M.O.I. 10) after transfection with siITGAV (80 nM), siMAP2K1 (20 nM), or siETF1 (20 nM) and/or ETF1simut-FLAG for 24 h. Cells were harvested and lysed for immunoblotting at indicated h p.i. SC, scrambled siRNA control. pFLAG-CMV2 served as the vector control for ETF1. The doublet bands recognized by anti-3A antibody represented 3A and its precursor 3AB. (C) Viral titration determination in siRNA-transfected RD cells. Viral titer was determined by plaque assay at 8 h p.i. Normalization was done using the SC control (arbitrarily set as 1). Error bar represents mean  $\pm$  SEM of three reproducible experiments (\* $p < 0.05$ ). (D) The effect of GnHCl on viral replicon activity. Illustration showing construction of the replicon by replacing the P1 region with FLuc in the infectious cDNA clone. Data were normalized to that of SC-treated cells (arbitrarily set as 1) and expressed as the mean  $\pm$  SEM of three independent experiments (\* $p < 0.05$ ). (E) Structural diagram of the EV-A71 IRES reporter plasmid. (F) IRES reporter assay after knockdown of target genes. The changes of Fluc/Rluc ratio were first normalized to SC-treated cells, and then to the vector control. Error bars represent means  $\pm$  SEM ( $n = 3$ ).



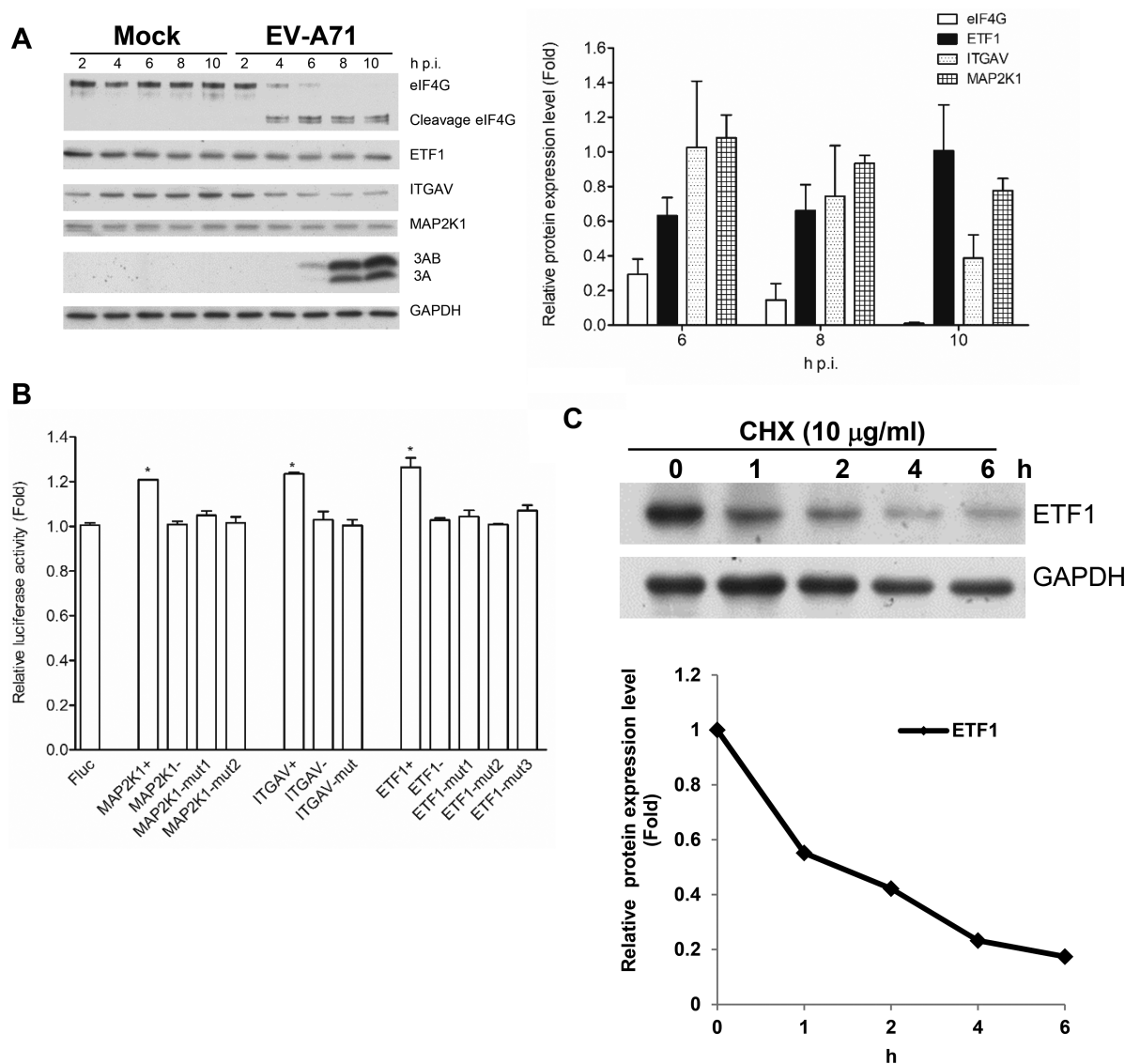


**Figure 6.** Effect of target genes of miR-197 during EV-A71 infection. (A) Target gene expression during EV-A71 infection. RD cells were infected with EV-A71 at an M.O.I. of 10 and harvested at the times indicated. (B) Reporter assay of wild type and mutant MAP2K1-, ITGAV-, and ETF1-3'UTR during viral infection. Cells were transfected with reporter plasmids followed by infection of EV-A71. At 8 h p.i., the cells were collected for reporter assay. The activity of each Fluc was normalized to Rluc activity, then to that of the mock-infected control, and the Fluc-only control (arbitrarily set as 1). Error bars represent means  $\pm$  SEM,  $n = 3$ . \* $p < 0.05$ . (C) Evaluation of the stability of ETF1. RD cells were incubated with 10  $\mu$ g/mL cycloheximide (CHX) for 0, 1, 2, 4, and 6 h, and were then harvested and lysed. Protein stability was measured via Western blotting using antibodies against ETF1 and GAPDH. Quantification of protein expression is shown in the bottom panel. Data are representative of three independent experiments.

mechanism to sustain virus-diverted cellular protein levels to promote its virulence by downregulating host miRNAs. The regulation of the cellular miRNA species for RNA virus replication has been documented. Liver-specific miR-122 can bind to the 5' end of the viral genome to enhance hepatitis C virus replication.<sup>37</sup> miR-221 and other miRNA species were downregulated by respiratory syncytial virus, and the transfection of miR-221 significantly inhibited viral replication in the bronchial epithelial cells.<sup>38</sup> Recently, miR-141 induced by EV-A71 infection was shown to target the cap-dependent translation initiation factor eIF4E. miR-197 may play an inhibitory role in viral replication because EV-A71 mediated repression of miR-197 and the overexpression of its mimic in RD cell clearly inhibited viral protein and RNA expression. A comprehensive investigation of the 375 genes obtained in

large-scale SILAC-based MS analysis coupled with TargetScan analysis showed that 106 genes possessed seed sequences. Examination of a panel of eight putative target genes by 3'UTR reporter assay revealed that seven were *bona fide* targets, indicating that the coupling of SILAC analysis with the TargetScan algorithm yielded highly accurate target identification. Interestingly, we identified two miR-197 target molecules involved in the receptor tyrosine kinase signaling transduction, namely, GRB2 and MAP2K1. GRB2 is an adaptor protein that is involved in receptor tyrosine kinase signaling by activating MAP kinase and other signaling pathways.<sup>39</sup> Although miRNAs have only a moderate effect on their target genes, they might target more than one molecule in a certain signaling/biochemical pathway and exacerbate their effect. We also identified a small GTPase,

RalB, out of the eight putative targets. RalB belongs to the Ras superfamily and has been implicated in increasing the innate immune response to viral infection.<sup>31</sup> Unraveling the significance of GRB2 and RalB in EV-A71 replication is under investigation.

IGTAV encodes the integrin alpha chain V subunit. Mammalian integrin is a heterodimer composed of an  $\alpha$  and a  $\beta$  subunit. Integrin alpha V subunit combined with different  $\beta$  chains facilitates infection of two picornaviruses (echovirus 9 and coxsackievirus B1).<sup>29,30</sup> However, knockdown of *ITGAV* did not affect EV-A71 replication, although it was upregulated during infection (Figure 5), suggesting that *ITGAV* is not essential for EV-A71 replication. We also demonstrated that MAP2K1 is dispensable for the virus replication cycle (Figure 5). Intriguingly, EV-A71 replication is inhibited by the chemical inhibitor U0126, which targeted both MAP2K1 and MAP2K2 in a neuroblastoma cell line (SK-N-SH).<sup>26</sup> In contrast, we demonstrated that the knockdown of *MAP2K1* did not abolish extracellular signal-regulated kinase 1/2 (ERK1/2) phosphorylation induced by viral infection, suggesting that the activation of ERK1/2 signaling or its effect on viral replication potentially results from other MEK isoforms (data not shown).

The translation termination at the stop codon in eukaryotes is mediated by a protein complex comprising ETF1 (also known as eRF1) and eRF3.<sup>40</sup> It has been shown that ETF1 can interact with different viral proteins for viral replication.<sup>34</sup> For example, the polymerase gene of the murine leukemia viruses is expressed by the translational read-through of the stop codon at the *gag-pol* border to synthesize a large Gag-Pol fusion protein.<sup>33</sup> ETF1 and eRF3 function to terminate the translation by ribosomes and release Gag, but a small portion of ribosomes read through the stop codon, and a large precursor of Gag-Pol is thus translated. The interaction of the viral reverse transcriptase (RT) with cellular ETF1 is important for controlling the translation of the Gag-Pol protein because RT blocks ETF1 and increases the probability of translational read-through.<sup>33</sup> It has been reported that ETF1 could be involved in mRNA stability via the interaction between eRF3 and poly(A)-binding protein (PABP).<sup>41</sup> PABP brings the 5'- and 3'UTRs of mRNAs into close proximity and binds eIF4G to act synergistically in the recruitment of the initiation complex.<sup>42</sup> The cleavage of eIF4G and PABP by proteases 2A and 3C of enteroviruses, respectively, is a well-known mechanism for attenuation of host translation.<sup>43,44</sup> EV-A71-induced ETF1 overexpression via downregulation of miR-197 may stabilize the viral RNA (also a mRNA), benefiting viral replication. This hypothesis is currently under active investigation.

## CONCLUSIONS

We generated a comprehensive panel of miR-197 target genes using SILAC and TargetScan. Seven of eight selected genes were confirmed to be genuine targets by 3'UTR reporter assay, demonstrating a high accuracy of the combination of SILAC and TargetScan for miRNA target prediction. Further studies on the physiological pathways regulated by miR-197 and required for viral replication and the proteins involved in these pathways may serve to identify potential therapeutic targets.

## ASSOCIATED CONTENT

### Supporting Information

The Supporting Information is available free of charge on the ACS Publications website at DOI: 10.1021/acs.jproteome.8b00762.

Experimental procedures (PDF)

Supporting Table 1. Oligonucleotides used for qPCR, 3'UTR reporter construction, wild type and silenced mutant of ETF1 construction, and siRNA interference (PDF)

Supporting Table 2. List of 1,822 proteins with unique peptides >3 based on 3 rounds of SILAC analysis (XLSX)

Supporting Table 3. Changes in miR-197 target genes with a ratio >1.25-fold (XLSX)

Supporting Table 4. Pathway analysis of 375 target genes of miR-197 identified by SILAC (XLSX)

## AUTHOR INFORMATION

### Corresponding Author

\*E-mail: jimtong@mail.cgu.edu.tw. Tel./Fax: +886-3-2118407.

### ORCID

Wen-Fang Tang: 0000-0002-3937-9092

Kun-Yi Chien: 0000-0002-1723-0406

### Author Contributions

§(W.-F.T., R.-T.H., K.-Y.C.) These authors contributed equally to this work.

### Notes

The authors declare no competing financial interest.

## ACKNOWLEDGMENTS

This work was supported by Chang Gung Memorial Hospital, Taoyuan, Taiwan (BMRP416, CMRPD1E0041-3, CMRPD1G0301-3, CMRPD1F0581-3, and CMRPD1D0321-3), the Ministry of Science and Technology of Taiwan (106-2320-B-182-004-MY3, 106-2811-B-182-011, 106-2632-B-182-001, and 107-3017-F-182-001), and the Research Center for Emerging Viral Infections from The Featured Areas Research Center Program within the framework of the Higher Education Sprout Project by the Ministry of Education (MOE) in Taiwan and the Ministry of Science and Technology (MOST), Taiwan (MOST 107-3017-F-182-001).

## REFERENCES

- (1) Schmidt, N. J.; Lennette, E. H.; Ho, H. H. An apparently new enterovirus isolated from patients with disease of the central nervous system. *J. Infect. Dis.* **1974**, *129* (3), 304–9.
- (2) Hayward, J. C.; Gillespie, S. M.; Kaplan, K. M.; Packer, R.; Pallansch, M.; Plotkin, S.; Schonberger, L. B. Outbreak of poliomyelitis-like paralysis associated with enterovirus 71. *Pediatr Infect Dis J.* **1989**, *8* (9), 611–6.
- (3) McMinn, P. C. An overview of the evolution of enterovirus 71 and its clinical and public health significance. *FEMS microbiology reviews* **2002**, *26* (1), 91–107.
- (4) Bushati, N.; Cohen, S. M. microRNA functions. *Annu. Rev. Cell Dev. Biol.* **2007**, *23*, 175–205.
- (5) Rodriguez, A.; Griffiths-Jones, S.; Ashurst, J. L.; Bradley, A. Identification of mammalian microRNA host genes and transcription units. *Genome Res.* **2004**, *14* (10A), 1902–1910.
- (6) Gregory, R. I.; Yan, K. P.; Amuthan, G.; Chendrimada, T.; Doratotaj, B.; Cooch, N.; Shiekhattar, R. The Microprocessor

complex mediates the genesis of microRNAs. *Nature* **2004**, 432 (7014), 235–40.

(7) Mourelatos, Z.; Dostie, J.; Paushkin, S.; Sharma, A.; Charroux, B.; Abel, L.; Rappsilber, J.; Mann, M.; Dreyfuss, G. miRNPs: a novel class of ribonucleoproteins containing numerous microRNAs. *Genes Dev.* **2002**, 16 (6), 720–728.

(8) Yi, R.; Qin, Y.; Macara, I. G.; Cullen, B. R. Exportin-5 mediates the nuclear export of pre-microRNAs and short hairpin RNAs. *Genes Dev.* **2003**, 17 (24), 3011–3016.

(9) Berkhout, B.; Jeang, K. T. RISCy business: MicroRNAs, pathogenesis, and viruses. *J. Biol. Chem.* **2007**, 282 (37), 26641–5.

(10) Brennecke, J.; Stark, A.; Russell, R. B.; Cohen, S. M. Principles of microRNA–target recognition. *PLoS Biol.* **2005**, 3 (3), e85.

(11) Lewis, B. P.; Burge, C. B.; Bartel, D. P. Conserved seed pairing, often flanked by adenosines, indicates that thousands of human genes are microRNA targets. *Cell* **2005**, 120 (1), 15–20.

(12) Lewis, B. P.; Shih, I. H.; Jones-Rhoades, M. W.; Bartel, D. P.; Burge, C. B. Prediction of mammalian microRNA targets. *Cell* **2003**, 115 (7), 787–98.

(13) Ho, B. C.; Yu, S. L.; Chen, J. J.; Chang, S. Y.; Yan, B. S.; Hong, Q. S.; Singh, S.; Kao, C. L.; Chen, H. Y.; Su, K. Y.; Li, K. C.; Cheng, C. L.; Cheng, H. W.; Lee, J. Y.; Lee, C. N.; Yang, P. C. Enterovirus-induced miR-141 contributes to shutoff of host protein translation by targeting the translation initiation factor eIF4E. *Cell Host Microbe* **2011**, 9 (1), 58–69.

(14) Tang, W. F.; Huang, R. T.; Chien, K. Y.; Huang, J. Y.; Lau, K. S.; Jheng, J. R.; Chiu, C. H.; Wu, T. Y.; Chen, C. Y.; Horng, J. T. Host MicroRNA miR-197 Plays a Negative Regulatory Role in the Enterovirus 71 Infectious Cycle by Targeting the RAN Protein. *J. Virol.* **2016**, 90 (3), 1424–38.

(15) Orr-Burks, N. L.; Shim, B. S.; Wu, W.; Bakre, A. A.; Karpilow, J.; Tripp, R. A. MicroRNA screening identifies miR-134 as a regulator of poliovirus and enterovirus 71 infection. *Sci. Data* **2017**, 4, 170023.

(16) Feng, N.; Zhou, Z.; Li, Y.; Zhao, L.; Xue, Z.; Lu, R.; Jia, K. Enterovirus 71-induced has-miR-21 contributes to evasion of host immune system by targeting MyD88 and IRAK1. *Virus Res.* **2017**, 237, 27–36.

(17) Zheng, Z.; Ke, X.; Wang, M.; He, S.; Li, Q.; Zheng, C.; Zhang, Z.; Liu, Y.; Wang, H. Human microRNA hsa-miR-296–5p suppresses enterovirus 71 replication by targeting the viral genome. *J. Virol.* **2013**, 87 (10), 5645–56.

(18) Wen, B. P.; Dai, H. J.; Yang, Y. H.; Zhuang, Y.; Sheng, R. MicroRNA-23b inhibits enterovirus 71 replication through down-regulation of EV71 VP1 protein. *Intervirology* **2013**, 56 (3), 195–200.

(19) Ong, S. E.; Blagoev, B.; Kratchmarova, I.; Kristensen, D. B.; Steen, H.; Pandey, A.; Mann, M. Stable isotope labeling by amino acids in cell culture, SILAC, as a simple and accurate approach to expression proteomics. *Mol. Cell. Proteomics* **2002**, 1 (5), 376–86.

(20) Vinther, J.; Hedegaard, M. M.; Gardner, P. P.; Andersen, J. S.; Arctander, P. Identification of miRNA targets with stable isotope labeling by amino acids in cell culture. *Nucleic Acids Res.* **2006**, 34 (16), e107.

(21) Zhu, H.; Pan, S.; Gu, S.; Bradbury, E. M.; Chen, X. Amino acid residue specific stable isotope labeling for quantitative proteomics. *Rapid Commun. Mass Spectrom.* **2002**, 16 (22), 2115–23.

(22) Tang, W. F.; Yang, S. Y.; Wu, B. W.; Jheng, J. R.; Chen, Y. L.; Shih, C. H.; Lin, K. H.; Lai, H. C.; Tang, P.; Horng, J. T. Reticulon 3 binds the 2C protein of enterovirus 71 and is required for viral replication. *J. Biol. Chem.* **2007**, 282 (8), 5888–98.

(23) Lu, J.; He, Y. Q.; Yi, L. N.; Zan, H.; Kung, H. F.; He, M. L. Viral kinetics of enterovirus 71 in human abdomyosarcoma cells. *World J. Gastroenterol* **2011**, 17 (36), 4135–4142.

(24) Lopez-Romero, P.; Gonzalez, M. A.; Callejas, S.; Dopazo, A.; Irizarry, R. A. Processing of Agilent microRNA array data. *BMC Res. Notes* **2010**, 3, 18.

(25) Macejak, D. G.; Sarnow, P. Association of heat shock protein 70 with enterovirus capsid precursor P1 in infected human cells. *J. Virol* **1992**, 66 (3), 1520–1527.

(26) Tung, W. H.; Hsieh, H. L.; Yang, C. M. Enterovirus 71 induces COX-2 expression via MAPKs, NF-kappaB, and AP-1 in SK-N-SH cells: Role of PGE(2) in viral replication. *Cell. Signalling* **2010**, 22 (2), 234–46.

(27) Tung, W. H.; Hsieh, H. L.; Lee, I. T.; Yang, C. M. Enterovirus 71 modulates a COX-2/PGE2/cAMP-dependent viral replication in human neuroblastoma cells: role of the c-Src/EGFR/p42/p44 MAPK/CREB signaling pathway. *J. Cell. Biochem.* **2011**, 112 (2), 559–70.

(28) Konig, R.; Stertz, S.; Zhou, Y.; Inoue, A.; Hoffmann, H. H.; Bhattacharyya, S.; Alamares, J. G.; Tscherne, D. M.; Ortigoza, M. B.; Liang, Y.; Gao, Q.; Andrews, S. E.; Bandyopadhyay, S.; De Jesus, P.; Tu, B. P.; Pache, L.; Shih, C.; Orth, A.; Bonamy, G.; Miraglia, L.; Ideker, T.; Garcia-Sastre, A.; Young, J. A.; Palese, P.; Shaw, M. L.; Chanda, S. K. Human host factors required for influenza virus replication. *Nature* **2010**, 463 (7282), 813–7.

(29) Agrez, M. V.; Shafren, D. R.; Gu, X.; Cox, K.; Sheppard, D.; Barry, R. D. Integrin alpha v beta 6 enhances coxsackievirus B1 lytic infection of human colon cancer cells. *Virology* **1997**, 239 (1), 71–7.

(30) Nelsen-Salz, B.; Eggers, H. J.; Zimmermann, H. Integrin alpha(v)beta3 (vitronectin receptor) is a candidate receptor for the virulent echovirus 9 strain Barty. *J. Gen. Virol.* **1999**, 80 (9), 2311–2313.

(31) Chien, Y.; Kim, S.; Bumeister, R.; Loo, Y. M.; Kwon, S. W.; Johnson, C. L.; Balakireva, M. G.; Romeo, Y.; Kopelovich, L.; Gale, M., Jr.; Yeaman, C.; Camonis, J. H.; Zhao, Y.; White, M. A. RalB GTPase-mediated activation of the IkkappaB family kinase TBK1 couples innate immune signaling to tumor cell survival. *Cell* **2006**, 127 (1), 157–70.

(32) Liberman, R.; Bond, S.; Shainheit, M. G.; Stadecker, M. J.; Forgac, M. Regulated assembly of vacuolar ATPase is increased during cluster disruption-induced maturation of dendritic cells through a phosphatidylinositol 3-kinase/mTOR-dependent pathway. *J. Biol. Chem.* **2014**, 289 (3), 1355–63.

(33) Orlova, M.; Yueh, A.; Leung, J.; Goff, S. P. Reverse transcriptase of Moloney murine leukemia virus binds to eukaryotic release factor 1 to modulate suppression of translational termination. *Cell* **2003**, 115 (3), 319–31.

(34) Walsh, D.; Mohr, I. Viral subversion of the host protein synthesis machinery. *Nat. Rev. Microbiol.* **2011**, 9 (12), 860–75.

(35) Loughlin, F. E.; Mansfield, R. E.; Vaz, P. M.; McGrath, A. P.; Setiyaputra, S.; Gamsjaeger, R.; Chen, E. S.; Morris, B. J.; Guss, J. M.; Mackay, J. P. The zinc fingers of the SR-like protein ZRANB2 are single-stranded RNA-binding domains that recognize 5' splice site-like sequences. *Proc. Natl. Acad. Sci. U. S. A.* **2009**, 106 (14), 5581–6.

(36) Krausslich, H. G.; Nicklin, M. J.; Toyoda, H.; Etchison, D.; Wimmer, E. Poliovirus proteinase 2A induces cleavage of eucaryotic initiation factor 4F polypeptide p220. *J. Virol* **1987**, 61 (9), 2711–2718.

(37) Jopling, C. L.; Yi, M.; Lancaster, A. M.; Lemon, S. M.; Sarnow, P. Modulation of hepatitis C virus RNA abundance by a liver-specific MicroRNA. *Science (Washington, DC, U. S.)* **2005**, 309 (5740), 1577–1581.

(38) Othumpangat, S.; Walton, C.; Piedimonte, G. MicroRNA-221 modulates RSV replication in human bronchial epithelium by targeting NGF expression. *PLoS One* **2012**, 7 (1), e30030.

(39) Rozakis-Adcock, M.; McGlade, J.; Mbamalu, G.; Pelicci, G.; Daly, R.; Li, W.; Batzer, A.; Thomas, S.; Brugge, J.; Pelicci, P. G.; Schlessinger, J.; Pawson, T.; et al. Association of the Shc and Grb2/Sem5 SH2-containing proteins is implicated in activation of the Ras pathway by tyrosine kinases. *Nature* **1992**, 360 (6405), 689–92.

(40) Kisselev, L. L.; Buckingham, R. H. Translational termination comes of age. *Trends Biochem. Sci.* **2000**, 25 (11), 561–6.

(41) Jacobson, A.; Peltz, S. W. Interrelationships of the pathways of mRNA decay and translation in eukaryotic cells. *Annu. Rev. Biochem.* **1996**, 65, 693–739.

(42) Gray, N. K.; Collier, J. M.; Dickson, K. S.; Wickens, M. Multiple portions of poly(A)-binding protein stimulate translation in vivo. *EMBO journal* **2000**, 19 (17), 4723–4733.

(43) Gradi, A.; Svitkin, Y. V.; Imataka, H.; Sonenberg, N. Proteolysis of human eukaryotic translation initiation factor eIF4GII, but not eIF4GI, coincides with the shutoff of host protein synthesis after poliovirus infection. *Proc. Natl. Acad. Sci. U. S. A.* **1998**, 95 (19), 11089–94.

(44) Kuyumcu-Martinez, N. M.; Van Eden, M. E.; Younan, P.; Lloyd, R. E. Cleavage of poly(A)-binding protein by poliovirus 3C protease inhibits host cell translation: a novel mechanism for host translation shutoff. *Molecular and cellular biology* **2004**, 24 (4), 1779–90.



## Article

# Chemical Constituents of the Leaves of *Peltophorum pterocarpum* and Their Bioactivity

Yue-Chiun Li <sup>1</sup>, Ping-Chung Kuo <sup>2,\*</sup>, Mei-Lin Yang <sup>3</sup>, Tzu-Yu Chen <sup>3</sup>, Tsong-Long Hwang <sup>4,5,6</sup>, Chih-Chao Chiang <sup>7</sup>, Tran Dinh Thang <sup>8,9</sup>, Nguyen Ngoc Tuan <sup>10</sup> and Jason T.C. Tzen <sup>1,\*</sup>

<sup>1</sup> Graduate Institute of Biotechnology, National Chung-Hsing University, Taichung 402, Taiwan; ycli0126@gmail.com

<sup>2</sup> School of Pharmacy, College of Medicine, National Cheng Kung University, Tainan 701, Taiwan

<sup>3</sup> Department of Biotechnology, National Formosa University, Yunlin 632, Taiwan; L3891104@nckualumni.org.tw (M.-L.Y.); black4635@gmail.com (T.-Y.C.)

<sup>4</sup> Graduate Institute of Natural Products, College of Medicine, Chang Gung University, Taoyuan 333, Taiwan; htl@mail.cgu.edu.tw

<sup>5</sup> Research Center for Industry of Human Ecology, Research Center for Chinese Herbal Medicine, and Graduate Institute of Health Industry Technology, Chang Gung University of Science and Technology, Taoyuan 333, Taiwan

<sup>6</sup> Department of Anesthesiology, Chang Gung Memorial Hospital, Taoyuan 333, Taiwan

<sup>7</sup> Graduate Institute of Clinical Medical Sciences, College of Medicine, Chang Gung University, Taoyuan 333, Taiwan; moonlight0604@hotmail.com

<sup>8</sup> School of Chemistry, Biology and Environment, Vinh University, Vinh City 43159, Vietnam; thangtd@vinhuni.edu.vn

<sup>9</sup> NTT Institute of High Technology, Nguyen Tat Thanh University, Ho Chi Minh City 72820, Vietnam

<sup>10</sup> Institute of Biotechnology and Food Technology, Industrial University of Ho Chi Minh City, Ho Chi Minh City 71408, Vietnam; nguyenngoctuan@iuh.edu.vn

\* Correspondence: z10502016@email.ncku.edu.tw (P.-C.K.); tctzen@dragon.nchu.edu.tw (J.T.C.T.); Tel.: +886-6-2353535 (ext. 6806) (P.-C.K.); +886-4-22840328 (J.T.C.T.)

Academic Editor: Ericsson Coy-Barrera

Received: 20 December 2018; Accepted: 9 January 2019; Published: 10 January 2019



**Abstract:** Two new sesquiterpenoids peltopterins A and B (compounds **1** and **2**) and fifty-two known compounds were isolated from the methanol extract of *P. pterocarpum* and their chemical structures were established through spectroscopic and mass spectrometric analyses. The isolates **40**, **43**, **44**, **47**, **48**, **51** and **52** exhibited potential inhibitory effects of superoxide anion generation or elastase release.

**Keywords:** Fabaceae; sesquiterpenoid; superoxide anion generation; elastase release

## 1. Introduction

*Peltophorum pterocarpum* (DC.) Backer ex K. Heyne (Fabaceae) is a deciduous tree originated from the tropical regions, ex. Sri Lanka, the Andamans, the Malay Peninsula and North Australia [1]. Traditionally, its flowers are used for slowing intestinal diseases and childbirth pain, treating muscle sprains, bruises, swelling and pain [2]. Roots and barks are also used to cure abdominal colic, joint and back pain, and ascites [3]. Reports on *Peltophorum* species have described antibacterial [4,5], antifungal [6,7], antiviral [8,9], antioxidant [10], antitumor [10,11], deworming [12,13], hypoglycemic [2,14], cardioprotective [15], hepatoprotective [16] and leukoagglutinating bioactivities [17]. However, there are only a few studies related to the chemical composition of the *Peltophorum* species. A preliminary examination showed that the methanol extract and fractions of leaves of *P. pterocarpum* displayed significant superoxide anion and elastase inhibition at 10 µg/mL (Table 1). Therefore, we sought to purify the constituents from the leaf extract and

examine the anti-inflammatory potential of the isolated compounds to identify new anti-inflammatory leads from natural sources. In this study the chemical profiles of leaves of *P. pterocarpum* were comprehensively investigated and a total of fifty-four compounds were identified. Among these, two new sesquiterpenoids **1** and **2** were characterized and the structures were established by spectroscopic and spectrometric analyses. In addition, the purified compounds were examined for their superoxide anion and elastase inhibitory effects.

**Table 1.** Inhibition of *P. pterocarpum* leave extract and fractions on superoxide anion generation and elastase release in human neutrophils.

Samples	Inhibition Percentage (%) <sup>a</sup>	
	Superoxide Anion Generation	Elastase Release
Methanol extract	53.4 ± 4.3 ***	112.3 ± 5.0 ***
Chloroform fraction	60.7 ± 5.9 ***	113.6 ± 5.9 ***
Water fraction	49.4 ± 0.7 ***	50.8 ± 5.0 ***

<sup>a</sup> Percentage of inhibition (Inh %) at 10 µg/mL concentration. Results are presented as mean ± S.E.M. (*n* = 3).

\*\*\* *p* < 0.001 compared with the control value.

## 2. Results and Discussion

### 2.1. Isolation and Identification

Air-dried and powdered leaves of *P. pterocarpum* were refluxed with methanol, and the combined extracts were concentrated in vacuo to produce a brownish syrup. This syrup was suspended into water and partitioned with chloroform to afford a chloroform layer and a water soluble fraction respectively. After isolation using a combination of continuous conventional chromatographic techniques, two new compounds, named peltopterins A (**1**) and B (**2**), were isolated and their structures established by nuclear magnetic resonance (NMR) and mass spectrometric analyses. Moreover, fifty-two known compounds, including six sesquiterpenoids: rel-5-(3*S*,8*S*-dihydroxy-1*R*,5*S*-dimethyl-7-oxa-6-oxobicyclo[3,2,1]-oct-8-yl)-3-methyl-2*Z*,4*E*-pentadienoic acid (**3**) [18], 3,6-dihydroxy-5,6-dihydro-β-ionol (**4**) [19], (−)-boscianin (**5**) [20], (3*S*,5*R*,6*R*,7*E*,9*S*)-3,5,6,9-tetrahydroxy-7-megastigmen (**6**) [21], 2,6,6-trimethyl-4-oxo-2-cyclohexene-1-acetic acid (**7**) [22], (3*S*,5*R*,6*S*,9*S*)-megastigmane-3,9,13-triol (**8**) [23]; nine benzenoids, *p*-hydroxybenzoic acid (**9**) [24], isovanillic acid (**10**) [25], *trans*-methyl *p*-coumarate (**11**) [24], *trans*-ferulic acid (**12**) [26], methyl ferulate (**13**) [27], benzoic acid (**14**) [28], vanillic acid (**15**) [29], syringic acid (**16**) [30], sodium salicylate (**17**) [31]; two coumarins: scopoletin (**18**) [32], scopolin (**19**) [33]; two lignans: dihydrodehydrodiconiferyl alcohol (**20**) [34], (7'*S*,8'*R*)-7',8'-dihydro-8'-hydroxymethyl-3-hydroxy-7'-(4'-hydroxy-3'-methoxyphenyl)-1-benzofuranpropanol 9'-*O*-β-D-glucoside (**21**) [18]; one alkaloid: 4(1*H*)-quinolinone (**22**) [35]; one diterpene: 3(17)-phytene 1,2-diol (**23**) [36]; thirteen steroids: a mixture of β-sitosterol (**24**) and stigmastrol (**25**) [37,38], a mixture of 6β-hydroxystigmast-4-en-3-one (**26**) and 6β-hydroxystigmast-4,22-dien-3-one (**27**) [39,40], a mixture of 7-ketositosterol (**28**) and 3β-hydroxystigmast-5,22-dien-7-one (**29**) [41,42], a mixture of stigmast-4-en-3-one (**30**) and stigmast-4,22-dien-3-one (**31**) [43,44], β-sitosteryl-3-*O*-β-D-glucoside (**32**) [45], ergosterol peroxide (**33**) [46], ergosta-4,6,8(14),22-tetraen-3-one (**34**) [47], 9,11-dehydroergosterol peroxide (**35**) [48], 20-hydroxy-ecdysone (**36**) [49]; six triterpenes: friedelin (**37**) [50], lupenone (**38**) [51], 24,25-dihydrocimicifugeuol (**39**) [52], cyclotirucanone (**40**) [53], cycloart-25-ene-3β,24-diol (**41**) [54], cycloeucalenol (**42**) [55]; and twelve flavonoids: kaempferol 3-*O*-α-L-rhamnoside (**43**) [56], quercetin 3-*O*-α-L-rhamnoside (**44**) [57], kaempferol 3-*O*-β-D-glucoside (**45**) [58], kaempferol 3-rutinoside (**46**) [59], quercetin 3-*O*-β-D-glucoside (**47**) [57], quercetin 3-*O*-α-L-arabinofuranoside (**48**) [60], kaempferol 3-*O*-[α-L-rhamnopyranosyl(1→6)]-β-D-galactopyranoside (**49**) [61], kaempferol 3-*O*-[α-L-rhamnopyranosyl(1→3)]-β-D-glucopyranoside

(50) [62], quercetin 3-O-[ $\alpha$ -L-rhamnopyranosyl(1 $\rightarrow$ 3)]- $\beta$ -D-glucopyranoside (51) [63], quercetin 3-O-[ $\alpha$ -L-rhamnopyranosyl(1 $\rightarrow$ 2)]- $\beta$ -D-xylopyranoside (52) [64], kaempferol 3-O-[ $\alpha$ -L-rhamnopyranosyl(1 $\rightarrow$ 2)]- $\beta$ -D-xylopyranoside (53) [65], kaempferol 3-O-[ $\alpha$ -L-rhamnopyranosyl(1 $\rightarrow$ 2)- $\alpha$ -L-rhamnopyranosyl(1 $\rightarrow$ 6)]- $\beta$ -D-galactopyranoside (54) [66], respectively, were characterized by comparison of their physical and spectroscopic data with those published previously.

## 2.2. Structural Determination of **1** and **2**

Compound **1** was obtained as white powder with m.p. 116–118 °C and  $[\alpha]_D^{25} = -73$ . The molecular formula was determined as  $C_{11}H_{18}O_3$  by a sodium adduct ion peak at  $m/z$  221.1150 in high resolution electrospray ionization mass spectrometry (HR-ESI-MS) analysis. The infrared (IR) absorption bands at 3430 and 1709  $cm^{-1}$  corresponded with the presence of a hydroxy and a carbonyl groups, respectively. In its  $^1H$ -NMR analysis, there were proton signals for two methyl singlets at  $\delta$  0.87 (3H,  $CH_3$ -11) and 0.95 (3H,  $CH_3$ -10), one methylene group at  $\delta$  2.20 (1H, dd,  $J = 18.1, 12.2$  Hz, H-7) and 2.68 (1H, dd,  $J = 18.1, 5.6$  Hz, H-7), two oxymethylene protons at  $\delta$  3.88 (1H, m, H-9a) and 4.34 (1H, dd,  $J = 11.1, 4.8$  Hz, H-9b), one oxymethine at  $\delta$  3.88 (1H, m, H-3), and two methines at  $\delta$  1.21 (1H, dd,  $J = 12.1, 6.7$  Hz, H-2) and 0.89 (1H, m, H-4). The  $^{13}C$ -NMR and distortionless enhancement by polarization transfer (DEPT) spectra exhibited a ester carbonyl signal at  $\delta$  171.2 (C-8), two methyl carbons at  $\delta$  20.2 (C-11) and 29.2 (C-10), four methylene carbons at  $\delta$  30.8 (C-7), 36.8 (C-4), 50.0 (C-2) and 73.8 (C-9), three methines at  $\delta$  32.3 (C-5), 44.2 (C-6) and 65.8 (C-3), and a quaternary carbon at  $\delta$  34.0 (C-1). The correlation spectroscopy (COSY) correlations of H-2/H-3/H-4, H-5/H-6/H-7, and H-9/H-5 suggested the presence of the partial structures  $-CH_2CH(OH)CH_2-$ ,  $-CH_2CHCH-$ , and  $-CHCH_2-$ , respectively. The  $^2J$ - and  $^3J$ -correlations from H-2 to C-4, C-6, C-10, and C-11; from H-3 to C-5; from H-6 to C-5 and C-9; from H-7 to C-1, C-5, and C-8; and from H-9 to C-4, C-5, and C-8, respectively, could be observed in the heteronuclear multiple bond correlation (HMBC) spectrum (Figure 1). According to these spectral analyses and the index of hydrogen deficiency (IHD = 3), it indicated the presence of two rings and a carbonyl group in **1** and these analytical results constructed the planar structure of **1** (Figure 1). Furthermore, the coupling pattern of full width at half maximum (FWHM) of H-3 (12.3 Hz) revealed its axial orientation. The nuclear overhauser effect spectroscopy (NOESY) showed NOE correlations between H-3 and H-5 but no correlations were observed between H-5 and H-6. These experimental data established the relative stereochemistry configuration of **1** as shown (Figure 1) and assigned the trivial name peltopterin A.

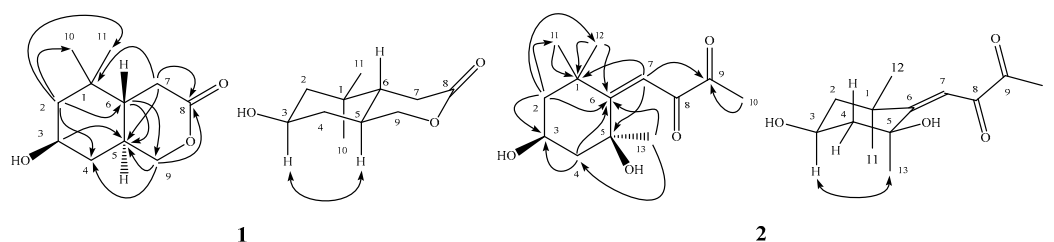


Figure 1. Significant HMBC ( $\rightarrow$ ) and NOESY ( $\leftrightarrow$ ) correlations of **1** and **2**.

Peltopterin B (**2**) was assigned a molecular formula of  $C_{13}H_{20}O_4$  from HR-ESI-MS analysis. The ultraviolet (UV) absorption maxima at 232 nm and the IR absorption bands at 3414 and 1677  $cm^{-1}$  indicated the occurrence of hydroxyl and conjugated carbonyl groups. The  $^1H$ -NMR spectrum of **2** revealed signals for one vinyl proton at  $\delta$  5.84 (1H, s, H-7); four methyl singlets at  $\delta$  1.15 (3H,  $CH_3$ -12), 1.37 (3H,  $CH_3$ -11), 1.42 (3H,  $CH_3$ -13) and 2.17 (3H,  $CH_3$ -10); one oxymethine at  $\delta$  4.33 (1H, dddd,  $J = 11.5, 11.5, 4.0, 4.0$  Hz, H-3); and two methylene groups at  $\delta$  1.36 (1H, m, H-2<sub>ax</sub>), 1.43 (1H, m, H-4<sub>ax</sub>), 1.98 (1H, ddd,  $J = 11.5, 4.0, 2.5$  Hz, H-2<sub>eq</sub>), and 2.29 (1H, ddd,  $J = 11.5, 4.0, 2.5$  Hz, H-4<sub>eq</sub>). The  $^{13}C$ -NMR spectrum also displayed two carbonyl signals at  $\delta$  198.5 (C-9) and 209.8 (C-8), three methyl carbons at  $\delta$  26.5 (C-10), 29.2 (C-11), and 31.1 (C-13), two methylene carbons at  $\delta$  49.1 (C-2) and

48.8 (C-4), two methines at  $\delta$  63.4 (C-3) and 100.9 (C-7), and four quaternary carbons at  $\delta$  36.3 (C-1), 72.5 (C-5), 118.6 (C-6), and 31.8 (C-12), respectively. The  $^2J$ - and  $^3J$ -HMBC correlations from H-2 to C-3, C-6, C-11, and C-12; from H-4 to C-3, and C-6; from H-7 to C-1, C-5, C-6 and C-9; from CH<sub>3</sub>-10 to C-9; from CH<sub>3</sub>-11 to C-1; from CH<sub>3</sub>-12 to C-1 and C-6; and from CH<sub>3</sub>-13 to C-4 and C-6, respectively, evidenced the planar structure of **2** as (3,5-dihydroxy-1,1,5-trimethylcyclohexylidene)butan-8,9-dione (Figure 1). The NOE correlation between H-3 and CH<sub>3</sub>-13 (see Supplementary Materials) determined the relative stereochemistry at C-5 (Figure 1) and the structure **2** was characterized accordingly. However, the absolute configurations of the two new compounds remained to be determined. Among the purified flavonoid glycosides, compounds **51** and **52** had been reported without NMR spectral data recorded in MeOH-*d*<sub>4</sub> [63,64]. In the present study, these compounds were identified through 1D and 2D NMR spectroscopic analysis and the fully assigned NMR data in MeOH-*d*<sub>4</sub> were listed in Section 3.

### 2.3. Anti-inflammatory Activity

Among these isolates, numerous compounds were selected to be evaluated for the superoxide anion generation and elastase release inhibition by human neutrophils in response to *N*-formyl-L-methionyl-phenylalanine/cytochalasin B (fMLP/CB) (Table 2).

**Table 2.** Superoxide anion and elastase inhibitory effects of isolated compounds in human neutrophils.

Compound	Superoxide Anion	Elastase
	Inh % <sup>a</sup>	Inh % <sup>a</sup>
<b>1</b>	7.0 ± 3.4	−2.1 ± 3.4
<b>2</b>	0.9 ± 2.2	1.5 ± 3.1
<b>3</b>	2.5 ± 1.6	−2.1 ± 3.1
<b>4</b>	5.5 ± 0.2 ***	1.7 ± 3.5
<b>5</b>	4.8 ± 1.4 *	8.3 ± 1.3
<b>6</b>	5.4 ± 0.5 ***	6.5 ± 1.3 **
<b>7</b>	7.2 ± 2.5 *	3.9 ± 4.1
<b>8</b>	3.0 ± 0.6 **	5.3 ± 5.6
<b>19</b>	2.2 ± 0.8	7.5 ± 4.1
<b>20</b>	10.6 ± 2.6 *	1.7 ± 3.6
<b>21</b>	9.2 ± 0.1 ***	9.3 ± 2.9 *
<b>36</b>	10.4 ± 6.9	3.0 ± 2.3
<b>39</b>	14.0 ± 0.1 ***	− <sup>b</sup>
<b>40</b>	13.4 ± 2.5 **	24.9 ± 3.1 **
<b>41</b>	17.1 ± 2.3 **	− <sup>b</sup>
<b>43</b>	42.3 ± 4.3 ***	22.1 ± 6.8 *
<b>44</b>	48.5 ± 1.0 ***	12.6 ± 4.0 *
<b>45</b>	20.4 ± 4.2 **	14.6 ± 5.9
<b>46</b>	−6.8 ± 3.0	−3.5 ± 4.2
<b>47</b>	45.7 ± 0.5 ***	22.1 ± 5.4 *
<b>48</b>	44.2 ± 4.4 ***	25.5 ± 7.6 *
<b>49</b>	−9.1 ± 7.5	17.6 ± 4.4 *
<b>50</b>	10.6 ± 1.1 ***	13.2 ± 2.7 **
<b>51</b>	46.4 ± 2.7 ***	15.8 ± 3.0 **
<b>52</b>	43.7 ± 4.9 ***	32.3 ± 6.8 **
<b>53</b>	6.8 ± 2.3 *	17.0 ± 4.9 *
<b>54</b>	6.9 ± 1.8 *	18.2 ± 2.9 **

<sup>a</sup> Percentage of inhibition (Inh %) at 10  $\mu$ M concentration. Results are presented as mean  $\pm$  S.E.M. ( $n = 3$ ). \*  $p < 0.05$ , \*\*  $p < 0.01$ , \*\*\*  $p < 0.001$  compared with the control (DMSO). <sup>b</sup> The enhance of elastase release was observed at tested concentration.

The results indicated that **43**, **44**, **47**, **48**, **51** and **52** show a significant inhibition of superoxide anion generation, with the inhibitory percentages ranged from 42.3  $\pm$  4.3 to 48.5  $\pm$  1.0% at 10  $\mu$ M. In addition, **40**, **43**, **47**, **48** and **52** presented inhibition of elastase release, with inhibitory percentages that ranged from 22.1  $\pm$  5.4 to 32.3  $\pm$  6.8% at 10  $\mu$ M. Inflammation is a defense mechanism response



to bacteria, virus, wound or other various environmental factors resulting in injury. It is also a first response of the immune system to infection and stimulation. In response to diverse stimuli, activated neutrophils secrete a series of cytotoxins, such as superoxide anion and elastase [67]. Therefore, inhibition of superoxide anion production and elastase release in infected tissues and organs could directly modulate neutrophil pro-inflammatory responses. Therefore, the crude extract and purified constituents of *P. pterocarpum* have potential to be developed as new anti-inflammatory lead drugs or health food ingredients. In comparison, **39** and **41** enhanced the elastase release in CB-priming human neutrophils with values of  $73.0 \pm 9.8$  and  $86.8 \pm 3.0$  % at 10  $\mu$ M. It had been reported that an increasing elastase release effect promoted the immune response [68,69]. These results are interesting for the further studies related to the bioactivity and mechanism.

### 3. Materials and Methods

#### 3.1. General

All the chemicals, unless specifically indicated otherwise, were bought from Merck KGaA (Darmstadt, Germany). The melting points, optical rotations, UV and IR spectra were recorded on an MP-S3 micromelting point apparatus (Yanagimoto, Kyoto, Japan), a P-2000 digital polarimeter (Jasco, Tokyo, Japan), a U-0080D diode array spectrophotometer (Hitachi, Tokyo, Japan), and a FT-IR Spectrum RX1 spectrophotometer (PerkinElmer, Waltham, MA, USA), respectively. The ESI-MS and HR-ESI-MS spectra were obtained on a Bruker Daltonics APEX II 30e spectrometer (Bruker, Billerica, MA, USA).  $^1\text{H}$ -,  $^{13}\text{C}$ -, and all 2D NMR (COSY, NOESY, HMQC, and HMBC) spectra were recorded on Bruker AV-500 and Avance III-400 NMR spectrometers (Bruker, Billerica, MA, USA) with tetramethylsilane as the internal standard using deuterated solvents purchased from Sigma-Aldrich (St. Louis, MO, USA). Chemical shifts are reported in parts per million (ppm,  $\delta$ ). Column chromatography and thin layer chromatography (TLC) were conducted on silica gels (Kieselgel 60, 70–230 mesh and 230–400 mesh) and precoated Kieselgel 60 F 254 plates (Merck KGaA), and the compounds were detected by UV light or 10% (v/v)  $\text{H}_2\text{SO}_4/\text{EtOH}$  reagent.

#### 3.2. Plant Materials

The leaves of *P. pterocarpum* were collected in Vietnam (August 2009) and the plant material was authenticated by Assoc. Prof. Dr. Tran Huy Thai, Institute of Ecology and Biological Resources, Vietnamese Academy of Science and Technology.

#### 3.3. Extraction and Isolation

The leaves of *P. pterocarpum* (dried weight 10.0 kg) were powdered, refluxed with methanol and the combined extracts then concentrated *in vacuo* to give a brownish syrup (1.2 kg). The crude extract was further separated into chloroform (350 g) and water soluble layers (850 g) by partition between chloroform and water.

The chloroform layer was purified on a silica gel column eluted with *n*-hexane and a step gradient of ethyl acetate (300:1 to 1:1) to afford nine fractions as monitored by TLC. Fraction 4 was column chromatographed on silica gel with a step gradient mixture of *n*-hexane and ethyl acetate (100:1 to 1:1) to afford 13 subfractions. Subfraction 4.2 was further purified by preparative TLC eluted with a *n*-hexane and ethyl acetate solvent mixture (100:1) to yield **38** (0.8 mg) and **40** (4.2 mg). Subfraction 4.5 was further resolved on a silica gel column eluted with a step gradient mixture of *n*-hexane and acetone (100:1 to 1:1) to produce eight minor fractions (4.5.1–4.5.8). Minor fraction 4.5.2 was purified with pTLC using *n*-hexane and ethyl acetate (50:1) to yield **37** (7.8 mg). Minor fraction 4.5.4 was isolated with silica gel column chromatography with a mixture of benzene and acetone (300:1) and further recrystallization of the resulting fractions afforded **23** (5.5 mg), a mixture of **26** and **27** (6.5 mg), a mixture of **30** and **31** (4.4 mg), **39** (2.7 mg), and **42** (5.6 mg), respectively. Minor fraction 4.5.7 was performed pTLC purification with a mixture of benzene and acetone (50:1) and produced **41** (4.5 mg).

Subfraction 4.6 was isolated by silica gel column chromatography eluted with a mixture of benzene and acetone (300:1) and further recrystallization of the minor fractions produced a mixture of **24** and **25** (15.1 mg), a mixture of **28** and **29** (3.2 mg), and **34** (1.5 mg). Subfraction 4.7 was separated by silica gel column chromatography eluted with a chloroform and acetone solvent mixture (300:1) to yield **12** (2.8 mg) and **35** (1.5 mg). Fraction 5 was further separated by repeated column chromatography over silica gel eluted with *n*-hexane and a step gradient of acetone (200:1 to 1:1) followed by purification of the resulting subfractions by recrystallization to afford **1** (2.2 mg), **2** (1.6 mg), **5** (2.7 mg), **11** (2.2 mg), **18** (2.2 mg), and **33** (0.8 mg). Fraction 6 was subjected to silica gel column chromatography eluted with chloroform and a step gradient of methanol (200:1 to 1:1) to produce 13 subfractions. Subfraction 6.6 was further silica gel column chromatographed with a mixture of *n*-hexane and acetone (20:1) to yield **4** (9.0 mg), **7** (4.3 mg) and **20** (7.8 mg). Fraction 7 was resolved on silica gel column eluted with a step gradient mixture of chloroform and methanol (200:1 to 1:1) to give 17 subfractions. Subfraction 7.10 was further separated by silica column chromatography with a mixture of chloroform and acetone (20:1) to result in **10** (1.5 mg). Subfraction 7.11 was isolated by pTLC with a mixture of chloroform and acetone (20:1) to yield **9** (3.1 mg).

The water soluble layer was applied to a reverse-phase Diaion HP-20 column and eluted with a step gradient of water and methanol (10:0, 7:3, 5:5, 3:7, 0:10) to afford nine fractions. Fraction 4 was further purified with Diaion HP-20 column chromatography eluted with water and a step gradient of methanol (10:0 to 0:10) to afford eight subfractions. Subfraction 4.2 was separated by Diaion HP-20 gel column chromatography as previously described to obtain nine minor fractions. The first minor fraction 4.2.1 was further purified by silica gel column chromatography with a mixture of chloroform and methanol (100:1) to produce **6** (2.3 mg) and **14** (4.5 mg). Minor fraction 4.2.4 was further isolated by repeated column chromatography over silica gel eluted with a step gradient mixture of ethyl acetate and methanol (100:1 to 1:1) to result in **3** (4.0 mg), **16** (2.1 mg), **19** (8.2 mg), and **22** (4.8 mg). Minor fraction 4.2.6 was applied to pTLC with a mixture of ethyl acetate, methanol and water (30:1:0.1) to give **54** (7.2 mg). Fraction 5 was resolved on Diaion HP-20 gel column eluted with water and a step gradient of methanol (10:0 to 0:10) to produce eight subfractions. Subfraction 5.4 was further purified by silica gel column chromatography with a mixture of chloroform and methanol (50:1) to yield six minor fractions. Minor fraction 5.4.1 was subjected to pTLC purification with a mixture of chloroform and methanol (100:1) to obtain **15** (9.1 mg). Minor fraction 5.4.2 was further separated by silica gel column chromatography with a mixture of chloroform, methanol and water (10:1:0.1) to result in **50** (14.1 mg), **51** (2.2 mg), and **52** (4.9 mg). Subfraction 5.5 was separated by repeated column chromatography over silica gel eluted with a step gradient mixture of ethyl acetate and methanol (300:1 to 1:1) followed by recrystallization of the resulting minor fractions to yield **8** (7.4 mg), **17** (1.4 mg), **47** (1.9 mg), and **53** (22.4 mg). Fraction 6 was column chromatographed with Diaion HP-20 gel to give 11 subfractions. Subfraction 6.6 was purified by silica gel column chromatography eluted with a step gradient mixture of chloroform, methanol and water (100:1:0.1 to 1:1:0.1) to produce five minor fractions. Minor fraction 6.6.1 was purified by pTLC with a mixture of chloroform, methanol and water (8:1:0.1) to obtain **44** (2.2 g) and **48** (17.3 mg). Subfraction 6.6.2 was purified by repeated column chromatography over silica gel eluted with a step gradient mixture of ethyl acetate, methanol and water (300:1:0.1 to 1:1:0.1) to yield **36** (3.8 mg), **45** (1.5 mg), **46** (12.6 mg), and **49** (2.8 mg). Subfraction 6.7 was further isolated by silica gel column chromatography eluted with a mixture of chloroform, methanol and water (50:1:0.1) to give six minor fractions. The minor fractions 6.7.4 and 6.7.6 were purified by pTLC with a mixture of chloroform, methanol and water (5:1:0.1) to afford **21** (1.6 mg), **43** (6.3 mg); and **13** (4.2 mg), respectively. Fraction 9 was resolved repeatedly on silica gel column chromatography eluted with a step gradient mixture of ethyl acetate and methanol (300:1 to 1:1) followed by recrystallization of the resulting fractions to obtain **32** (1.5 mg).

### 3.3.1. Peltopterin A (1)

White powder, m.p. 116–118 °C (CHCl<sub>3</sub>);  $[\alpha]_D^{25} = -73$  (c 0.1, CHCl<sub>3</sub>); IR (KBr)  $\nu_{\max}$  3430, 2949, 2924, 1709, 1469, 1299, 1239, 1219, 1092, 1026 cm<sup>-1</sup>; ESI-MS (*rel. int.* %)  $m/z$  221 ([M + Na]<sup>+</sup>, 100); HR-ESI-MS  $m/z$  221.1150 [M + Na]<sup>+</sup> (calcd for C<sub>11</sub>H<sub>18</sub>NaO<sub>3</sub>, 221.1154); <sup>1</sup>H-NMR (CDCl<sub>3</sub>, 400 MHz)  $\delta$  4.34 (1H, dd,  $J = 11.1, 4.8$  Hz, H-9b), 3.88 (1H, m, H-9a), 3.88 (1H, FWHM = 23.2 Hz, H-3), 2.68 (1H, dd,  $J = 18.1, 5.6$  Hz, H-7), 2.20 (1H, dd,  $J = 18.1, 12.2$  Hz, H-7), 1.99 (1H, m, H-4), 1.82 (2H, m, H-2, 5), 1.38 (1H, ddd,  $J = 12.2, 12.1, 5.6$  Hz, H-6), 1.21 (1H, dd,  $J = 12.1, 6.7$  Hz, H-2), 0.95 (3H, s, CH<sub>3</sub>-10), 0.89 (1H, m, H-4), 0.87 (3H, s, CH<sub>3</sub>-11); <sup>13</sup>C-NMR (CDCl<sub>3</sub>, 100 MHz)  $\delta$  171.2 (C-8), 73.8 (C-9), 65.8 (C-3), 50.0 (C-2), 44.2 (C-6), 36.8 (C-4), 34.0 (C-1), 32.3 (C-5), 30.8 (C-7), 29.2 (C-10), 20.2 (C-11).

### 3.3.2. Peltopterin B (2)

Colorless syrup,  $[\alpha]_D^{25} = -29$  (c 0.4, CH<sub>3</sub>OH); UV (MeOH)  $\lambda_{\max}$  (log  $\epsilon$ ) 232 (4.00) nm; IR (KBr)  $\nu_{\max}$  3417, 2963, 1938, 1667, 1455, 1366, 1243, 1157, 1040, 955, 820 cm<sup>-1</sup>; HR-ESI-MS  $m/z$  241.1434 ([M + H]<sup>+</sup>) (calcd for C<sub>13</sub>H<sub>21</sub>O<sub>4</sub>: 241.1440); <sup>1</sup>H-NMR (CDCl<sub>3</sub>, 500 MHz)  $\delta$  5.84 (1H, s, H-7), 4.33 (1H, dddd,  $J = 11.5, 11.5, 4.0, 4.0$  Hz, H-3), 2.29 (1H, ddd,  $J = 11.5, 4.0, 2.5$  Hz, H-4<sub>eq</sub>), 2.17 (3H, s, CH<sub>3</sub>-10), 1.98 (1H, ddd,  $J = 11.5, 4.0, 2.5$  Hz, H-2<sub>eq</sub>), 1.43 (1H, m, H-4<sub>ax</sub>), 1.42 (3H, s, CH<sub>3</sub>-13), 1.37 (3H, s, CH<sub>3</sub>-11), 1.36 (1H, m, H-2<sub>ax</sub>), 1.15 (3H, s, CH<sub>3</sub>-12); <sup>13</sup>C-NMR (CDCl<sub>3</sub>, 125 MHz)  $\delta$  209.8 (C-8), 198.5 (C-9), 118.8 (C-6), 100.9 (C-7), 72.5 (C-5), 63.4 (C-3), 49.1 (C-2), 48.8 (C-4), 36.3 (C-1), 31.8 (C-12), 31.1 (C-13), 29.2 (C-11), 26.5 (C-10).

### 3.3.3. Quercetin-3-O-[ $\alpha$ -L-rhamnopyranosyl(1→3)]- $\beta$ -D-glucopyranoside (51)

Yellow powder; <sup>1</sup>H-NMR (CD<sub>3</sub>OD, 500 MHz)  $\delta$  7.69 (1H, d,  $J = 2.0$  Hz, H-2'), 7.58 (1H, dd,  $J = 8.5, 2.0$  Hz, H-5'), 6.87 (1H, d,  $J = 8.5$  Hz, H-6'), 6.35 (1H, d,  $J = 2.0$  Hz, H-8), 6.17 (1H, d,  $J = 2.0$  Hz, H-6), 5.74 (1H, d,  $J = 7.5$  Hz, H-1''), 5.21 (1H, d,  $J = 1.5$  Hz, H-1'''), 4.02 (1H, dd,  $J = 10.0, 6.5$  Hz, H-5'''), 3.99 (1H, dd,  $J = 3.5, 1.5$  Hz, H-2'''), 3.96 (1H, dd,  $J = 10.0, 8.0$  Hz, H-3''), 3.85 (1H, m, H-4''), 3.78 (1H, dd,  $J = 10.0, 3.5$  Hz, H-3'''), 3.71 (1H, dd,  $J = 8.0, 7.5$  Hz, H-2''), 3.65 (1H, dd,  $J = 11.5, 6.0$  Hz, H-6''b), 3.61 (1H, dd,  $J = 11.5, 6.5$  Hz, H-6''a), 3.49 (1H, dd,  $J = 6.5, 6.0$  Hz, H-5''), 3.34 (1H, m, H-4'''), 0.93 (3H, d,  $J = 6.5$  Hz, CH<sub>3</sub>-6'''); <sup>13</sup>C-NMR (CD<sub>3</sub>OD, 125 MHz)  $\delta$  179.4 (C-4), 168.8 (C-7), 163.2 (C-5), 158.4 (C-9), 158.1 (C-2), 149.6 (C-4'), 145.9 (C-3'), 134.6 (C-3), 123.4 (C-6'), 123.0 (C-1'), 117.3 (C-2'), 116.1 (C-5'), 105.8 (C-10), 102.6 (C-1'''), 100.8 (C-1''), 99.9 (C-6), 94.6 (C-8), 77.6 (C-3''), 77.1 (C-5''), 75.8 (C-2''), 74.1 (C-4'''), 72.4 (C-3'''), 72.3 (C-2'''), 70.9 (C-4''), 69.9 (C-5'''), 62.1 (C-6''), 17.4 (C-6''').

### 3.3.4. Quercetin 3-O-[ $\alpha$ -L-rhamnopyranosyl(1→2)]- $\beta$ -D-xylopyranoside (52)

Yellow powder; <sup>1</sup>H-NMR (CD<sub>3</sub>OD, 500 MHz)  $\delta$  7.59 (1H, dd,  $J = 8.5, 2.5$  Hz, H-6'), 7.58 (1H, d,  $J = 2.5$  Hz, H-2'), 6.87 (1H, d,  $J = 8.5$  Hz, H-5'), 6.34 (1H, d,  $J = 2.0$  Hz, H-8), 6.16 (1H, d,  $J = 2.0$  Hz, H-6), 5.59 (1H, d,  $J = 7.0$  Hz, H-1''), 5.02 (1H, d,  $J = 1.0$  Hz, H-1'''), 4.08 (1H, qd,  $J = 10.0, 6.0$  Hz, H-5'''), 4.00 (1H, dd,  $J = 3.5, 1.0$  Hz, H-2'''), 3.79 (1H, dd,  $J = 9.5, 3.5$  Hz, H-3'''), 3.75 (1H, dd,  $J = 12.5, 4.5$  Hz, H-5''b), 3.70 (1H, dd,  $J = 9.0, 7.0$  Hz, H-2''), 3.51 (1H, m, H-4''), 3.51 (1H, m, H-3''), 3.36 (1H, dd,  $J = 10.0, 9.5$  Hz, H-4'''), 3.10 (1H, dd,  $J = 12.5, 9.0$  Hz, H-5''a), 1.07 (3H, d,  $J = 6.0$  Hz, CH<sub>3</sub>-6'''); <sup>13</sup>C-NMR (CD<sub>3</sub>OD, 125 MHz)  $\delta$  179.1 (C-4), 167.5 (C-7), 163.1 (C-5), 158.5 (C-9), 158.4 (C-2), 149.8 (C-4'), 146.2 (C-3'), 134.4 (C-3), 123.3 (C-6'), 123.2 (C-1'), 117.0 (C-2'), 116.0 (C-5'), 105.4 (C-10), 102.7 (C-1'''), 101.3 (C-1''), 100.3 (C-6), 95.0 (C-8), 79.6 (C-2''), 77.9 (C-3''), 74.1 (C-4'''), 72.4 (C-3'''), 72.3 (C-2'''), 71.5 (C-4''), 70.1 (C-5'''), 67.1 (C-5''), 17.6 (C-6''').

## 3.4. Anti-Inflammatory Bioactivity Examination

The human neutrophils study (No. 1612200032) was approved by the Chang Gung Memorial Hospital Institutional Review Board (Taoyuan, Taiwan) and was conducted according to the Declaration of Helsinki (2013). The examination for the superoxide anion and elastase release inhibition was based on the superoxide dismutase (SOD)-inhibitable reduction of ferricytochrome c

and degranulation of azurophilic granules as reported [67]. The experimental details were attached in the file of Supplementary Materials.

**Supplementary Materials:** The following are available online, S1: Extraction and isolation schemes; S2: Anti-inflammatory bioactivity experimental procedures; Figures S1–S14: 1D, 2D-NMR and MS spectra of new compounds **1** and **2**; Figures S15–S18: <sup>1</sup>H- and <sup>13</sup>C-NMR spectra of compounds **51** and **52**.

**Author Contributions:** Conceptualization, P.-C.K. and J.T.C.T.; Data curation and Investigation, Y.-C.L., M.-L.Y., and T.-Y.C.; Methodology, T.-L.H. and C.-C.C.; Resources, T.-D.T. and N.N.T.; Writing-original draft, Y.-C.L.; Writing-review & editing, P.-C.K. and J.T.C.T. All authors read and approved the final manuscript.

**Funding:** This research is sponsored by the Ministry of Science and Technology (MOST), Taiwan, granted to P.-C.K. and J.T.-C.T. The authors are also thankful for partial financial support from Chang Gung Memorial Hospital (CMRPF1G0241~3, CMRPF1F0061~3, and BMRP450 granted to T.-L.H.).

**Acknowledgments:** We appreciate T.S. Wu's valuable suggestions.

**Conflicts of Interest:** The authors declare no conflict of interest.

## References

- Sukumaran, S.; Kiruba, S.; Mahesh, M.; Nisha, S.R.; Miller, P.Z.; Ben, C.P.; Jeeva, S. Phytochemical constituents and antibacterial efficacy of the flowers of *Peltophorum pterocarpum* (DC.) Baker ex Heyne. *Asian Pac. J. Trop. Med.* **2011**, *4*, 735–738. [\[CrossRef\]](#)
- Manaharan, T.; Teng, L.L.; Appleton, D.; Ming, C.H.; Masilamani, T.; Palanisamy, U.D. Antioxidant and antiglycemic potential of *Peltophorum pterocarpum* plant parts. *Food Chem.* **2011**, *129*, 1355–1361. [\[CrossRef\]](#)
- Bizimenyera, E.S.; Aderogba, M.A.; Eloff, J.N.; Swan, G.E. Potential of neuroprotective antioxidant-based therapeutics from *Peltophorum africanum* Sond. (Fabaceae). *Afr. J. Trad. CAM* **2007**, *4*, 99–106. [\[CrossRef\]](#)
- Dandapat, R.; Jena, B.S.; Negi, P.S. Antimutagenic and antibacterial activities of *Peltophorum ferrugineum* flower extracts. *Asian Pac. J. Trop. Dis.* **2012**, *2*, S778–S782. [\[CrossRef\]](#)
- Jain, S.C.; Pancholi, B.; Jain, R. Antimicrobial, free radical scavenging activities and chemical composition of *Peltophorum pterocarpum* Baker ex K. Heyne stem extract. *Der. Pharm. Chem.* **2012**, *4*, 2073–2079.
- Jain, S.C.; Pancholi, B.; Jain, R. *Peltophorum pterocarpum* (DC.) Baker ex. K. Heyne flowers: Antimicrobial and antioxidant efficacies. *J. Med. Plants Res.* **2011**, *5*, 274–280. [\[CrossRef\]](#)
- Raj, M.K.; Duraipandian, V.; Agustin, P.; Ignacimuthu, S. Antimicrobial activity of bergenin isolated from *Peltophorum pterocarpum* DC. flowers. *Asian Pac. J. Trop. Biomed.* **2012**, *2*, S901–S904. [\[CrossRef\]](#)
- Lam, S.K.; Ng, T.B. First report of an antifungal amidase from *Peltophorum pterocarpum*. *Biomed. Chromatogr.* **2010**, *24*, 458–464. [\[CrossRef\]](#) [\[PubMed\]](#)
- Manosroi, J.; Boonpisuttinant, K.; Manosroi, W.; Manosroi, A. Anti-proliferative activities on HeLa cancer cell line of Thai medicinal plant recipes selected from MANOSROI II database. *J. Ethnopharmacol.* **2012**, *142*, 422–431. [\[CrossRef\]](#) [\[PubMed\]](#)
- Raj, M.K.; Balachandran, C.; Duraipandian, V.; Agastian, P.; Ignacimuthu, S.; Vijayakumar, A. Isolation of terrestribisamide from *Peltophorum pterocarpum* (DC.) Baker ex. K. Heyne and its antimicrobial, antioxidant, and cytotoxic activities. *Med. Chem. Res.* **2013**, *22*, 3823–3830.
- Polasek, J.; Queiroz, E.F.; Marcourt, L.; Meligova, A.K.; Halabalaki, M.; Skaltsounis, A.L.; Alexis, M.N.; Prajogo, B.; Wolfender, J.L.; Hostettmann, K. Peltogynoids and 2-phenoxychromones from *Peltophorum pterocarpum* and evaluation of their estrogenic activity. *Planta Med.* **2013**, *79*, 480–486. [\[CrossRef\]](#) [\[PubMed\]](#)
- Bizimenyera, E.S.; Githiori, J.B.; Swan, G.E.; Eloff, J.N. In vitro ovidal and larvicidal activity of the leaf, bark and root extracts of *Peltophorum africanum* Sond. (Fabaceae) on *Haemonchus contortus*. *J. Anim. Vet. Adv.* **2006**, *5*, 608–614.
- Bizimenyera, E.S.; Meyer, S.; Naidoo, V.; Eloff, J.N.; Swan, G.E. Efficacy of *Peltophorum africanum* Sond. (Fabaceae) extracts on *Haemonchus contortus* and *Trichostrongylus colubriformis* in sheep. *J. Anim. Vet. Adv.* **2008**, *7*, 364–371.
- Islam, M.S.; Ali, S.; Rahman, M.; Islam, R.; Ali, A.; Azad, A.K.; Islam, M.R. Antidiabetic, cytotoxic activities and phytochemical screening of *Peltophorum pterocarpum* (DC.) K. Heyne root. *J. Med. Plants Res.* **2011**, *5*, 3745–3750.



15. Raju, B.; Vijaya, C.; Ramu, A. Evaluation of cardiogenic activity of *Peltophorum pterocarpum*. *Int. J. Phytopharmacol.* **2011**, *2*, 1–6.
16. Biswas, K.; Kumar, A.; Babaria, B.A.; Prabhu, K.; Setty, S.R. Hepatoprotective effect of leaves of *Peltophorum pterocarpum* against paracetamol induced acute liver damage in rats. *J. Basic Clin. Pharm.* **2010**, *1*, 10–15.
17. Agrawal, S.; Agarwal, S.S. Preliminary observations on leukaemia specific agglutinins from seeds. *Indian J. Med. Res.* **1990**, *92*, 38–42. [[PubMed](#)]
18. Kikuzaki, H.; Kayano, S.; Fukutsuka, N.; Aoki, A.; Kasamatsu, K.; Yamasaki, Y.; Mitani, T.; Nakatani, N. Abscissic acid related compounds and lignans in prunes (*Prunus domestica* L.) and their oxygen radical absorbance capacity (ORAC). *J. Agric. Food Chem.* **2004**, *52*, 344–349. [[CrossRef](#)]
19. Yu, Q.; Otsuka, H.; Hirata, E.; Shinzato, T.; Takeda, Y. Turpinionosides A—E: Megastigmane glucosides from leaves of *Turpinia ternata* Nakai. *Chem. Pharm. Bull.* **2002**, *50*, 640–644. [[CrossRef](#)]
20. Busch, J.; Grether, Y.; Ochs, D.; Séquin, U. Total synthesis and biological activities of (+)- and (–)-boscinalin and their 1'-epimers. *J. Nat. Prod.* **1998**, *61*, 591–597. [[CrossRef](#)]
21. Takeda, Y.; Okada, Y.; Masuda, T.; Hirata, E.; Shinzato, T.; Takushi, A.; Yu, Q.; Otsuka, H. New megastigmane and tetraketide from the leaves of *Euscaphis japonica*. *Chem. Pharm. Bull.* **2000**, *48*, 752–754. [[CrossRef](#)] [[PubMed](#)]
22. Wang, C.Y.; Liu, X.; Guo, L.M.; Shao, C.L.; Fang, Y.C.; Wei, Y.X.; Zheng, C.J.; Gu, Q.Q.; Zhu, W.M.; Guan, H.S. Two new natural keto-acid derivatives from *Sargassum pallidum*. *Chem. Nat. Compd.* **2010**, *46*, 292–294. [[CrossRef](#)]
23. Takeshige, Y.; Kawakami, S.; Matsunami, K.; Otsuka, H.; Lhieochaiphant, D.; Lhieochaiphant, S. Oblongionosides A—F, megastigmane glycosides from the leaves of *Croton oblongifolius* Roxburgh. *Phytochemistry* **2012**, *80*, 132–136. [[CrossRef](#)] [[PubMed](#)]
24. Chen, C.Y.; Chang, F.R.; Teng, C.M.; Wu, Y.C. Cheritamine, a new N-fatty acyl tryptamine and other constituents from the stems of *Annona cherimola*. *J. Chin. Chem. Soc.* **1999**, *46*, 77–86. [[CrossRef](#)]
25. Kobayashi, S.; Ozawa, T.; Imagawa, H. Dehydrochorismic acid from *Pinus densiflora* pollen. *Agric. Biol. Chem.* **1982**, *46*, 845–847. [[CrossRef](#)]
26. Han, T.; Li, H.; Zhang, Q.; Zheng, H.; Qin, L. New thiazinediones and other components from *Xanthium strumarium*. *Chem. Nat. Compd.* **2006**, *42*, 567–570. [[CrossRef](#)]
27. Gopalakrishnan, S.; Subbarao, G.V.; Nakahara, K.; Yoshihashi, T.; Ito, O.; Maeda, I.; Ono, H.; Yoshida, M. Nitrification inhibitors from the root tissues of *Brachiaria humidicola*, a tropical grass. *J. Agric. Food Chem.* **2007**, *55*, 1385–1388. [[CrossRef](#)]
28. Laurent, P.; Lebrun, B.; Braekman, J.C.; Daloze, D.; Pasteels, J.M. Biosynthetic studies on adaline and adalidine, two alkaloids from ladybird beetles (Coleoptera: Coccinellidae). *Tetrahedron* **2001**, *57*, 3403–3412. [[CrossRef](#)]
29. Chung, C.P.; Hsia, S.M.; Lee, M.Y.; Chen, H.J.; Cheng, F.; Chan, L.C.; Kuo, Y.H.; Lin, Y.L.; Chiang, W. Gastroprotective activities of adlay (*Coix lacryma-jobi* L. var. *ma-yuen* Stapf) on the growth of the stomach cancer AGS cell line and indomethacin-induced gastric ulcers. *J. Agric. Food Chem.* **2011**, *59*, 6025–6033. [[CrossRef](#)]
30. Tan, J.; Bednarek, P.; Liu, J.; Schneider, B.; Svatoš, A.; Hahlbrock, K. Universally occurring phenylpropanoid and species-specific indolic metabolites in infected and uninfected *Arabidopsis thaliana* roots and leaves. *Phytochemistry* **2004**, *65*, 691–699. [[CrossRef](#)]
31. Manohar, C.; Rao, U.R.K.; Valaulikar, B.S.; Iyer, R.M. On the Origin of viscoelasticity in micellar solutions of cetyltrimethylammonium bromide and sodium salicylate. *J. Chem. Soc. Chem. Commun.* **1986**, *5*, 379–381. [[CrossRef](#)]
32. Begum, T.; Rahman, M.S.; Rashid, M.A. Phytochemical and biological investigations of *Phyllanthus reticulatus*. *Dhaka Univ. J. Pharm. Sci.* **2006**, *5*, 21–23. [[CrossRef](#)]
33. Teh, C.H.; Morita, H.; Shiota, O.; Chan, K.L. 2,3-Dehydro-4 $\alpha$ -hydroxylongilactone, a novel quassinoid and two known phenyl propanoids from *Eurycoma longifolia* Jack. *Food Chem.* **2010**, *120*, 794–798. [[CrossRef](#)]
34. Shen, Y.C.; Hsieh, P.W.; Kuo, Y.H. Neolignan glucosides from *Jasminum urophyllum*. *Phytochemistry* **1998**, *48*, 719–723. [[CrossRef](#)]
35. Shi, P.; Wang, L.; Chen, K.; Wang, J.; Zhu, J. Co(III)-catalyzed enamionone-directed C-H amidation for quinolone synthesis. *Org. Lett.* **2017**, *19*, 2418–2421. [[CrossRef](#)]

36. Rodríguez, A.D.; Acosta, A.L. New cembranoid diterpenes and a geranylgeraniol derivative from the common Caribbean sea whip *Eunicea succinea*. *J. Nat. Prod.* **1997**, *60*, 1134–1138. [[CrossRef](#)]
37. Ahmad, F.; Ali, M.; Alam, P. New phytoconstituents from the stem bark of *Tinospora cordifolia* Miers. *Nat. Prod. Res.* **2010**, *24*, 926–934. [[CrossRef](#)]
38. Bibi, N.; Tanoli, S.A.K.; Farheen, S.; Afza, N.; Siddiqi, S.; Zhang, Y.; Kazmi, S.U.; Malik, A. In vitro antituberculosis activities of the constituents isolated from *Haloxylon salicornicum*. *Bioorg. Med. Chem. Lett.* **2010**, *20*, 4173–4176. [[CrossRef](#)]
39. Kuo, Y.H.; Chu, P.H. Studies on the constituents from the bark of *Bauhinia purpurea*. *J. Chin. Chem. Soc.* **2002**, *49*, 269–274. [[CrossRef](#)]
40. Katsui, N.; Matsue, H.; Hirata, T.; Masamune, T. Phytosterols and triterpenes in roots of the “kidney bean” (*Phaseolus vulgaris* L.). *Bull. Chem. Soc. Jpn.* **1972**, *45*, 223–226. [[CrossRef](#)]
41. Zhang, X.; Geoffroy, P.; Miesch, M.; Julien-David, D.; Raul, F.; Aoudé-Werner, D.; Marchioni, E. Gram-scale chromatographic purification of  $\beta$ -sitosterol synthesis and characterization of  $\beta$ -sitosterol oxides. *Steroids* **2005**, *70*, 886–895. [[CrossRef](#)]
42. Foley, D.A.; O’Callaghan, Y.; O’Brien, N.M.; McCarthy, F.O.; Maguire, A.R. Synthesis and characterization of stigmaterol oxidation products. *J. Agric. Food Chem.* **2010**, *58*, 1165–1173. [[CrossRef](#)] [[PubMed](#)]
43. Grishko, V.V.; Nogovitsina, E.M.; Ivshina, I.B. Optimization of conditions for biocatalytic production of stigmast-4-en-3-one. *Chem. Nat. Compd.* **2012**, *48*, 432–435. [[CrossRef](#)]
44. Ambrus, G.; Ilkőy, É.; Jekkel, A.; Horváth, G.; Böcskei, Z. Microbial transformation of  $\beta$ -sitosterol and stigmaterol into 26-oxygenated derivatives. *Steroids* **1995**, *60*, 621–625. [[CrossRef](#)]
45. Chang, Y.C.; Chang, F.R.; Wu, Y.C. The constituents of *Lindera glauca*. *J. Chin. Chem. Soc.* **2000**, *47*, 373–380. [[CrossRef](#)]
46. Yue, J.M.; Chen, S.N.; Lin, Z.W.; Sun, H.D. Sterols from the fungus *Lactarium volumus*. *Phytochemistry* **2001**, *56*, 801–806. [[CrossRef](#)]
47. Fujimoto, H.; Nakamura, E.; Okuyama, E.; Ishibashi, M. Six immunosuppressive features from an ascomycete, *Zopfiella longicaudata*, found in a screening study monitored by immunomodulatory activity. *Chem. Pharm. Bull.* **2004**, *52*, 1005–1008. [[CrossRef](#)]
48. Chen, Y.K.; Kuo, Y.H.; Chiang, B.H.; Lo, J.M.; Sheen, L.Y. Cytotoxic activities of 9,11-dehydroergosterol peroxide and ergosterol peroxide from the fermentation mycelia of *Ganoderma lucidum* cultivated in the medium containing leguminous plants on Hep 3B cells. *J. Agric. Food Chem.* **2009**, *57*, 5713–5719. [[CrossRef](#)]
49. Buděšínský, M.; Vokáč, K.; Harmatha, J.; Cvačka, J. Additional minor ecdysteroid components of *Leuzea carthamoides*. *Steroids* **2008**, *73*, 502–514. [[CrossRef](#)]
50. Zhou, W.; Guo, S. Components of the sclerotia of *Polyporus umbellatus*. *Chem. Nat. Compd.* **2009**, *45*, 124–125. [[CrossRef](#)]
51. Kuo, Y.H.; Yeh, M.H. Chemical constituents of heartwood of *Bauhinia purpurea*. *J. Chin. Chem. Soc.* **1997**, *44*, 379–383. [[CrossRef](#)]
52. Wu, Z.H.; Liu, T.; Gu, C.X.; Shao, C.L.; Zhou, J.; Wang, C.Y. Steroids and triterpenoids from the brown alga *Kjellmaniella crassifolia*. *Chem. Nat. Compd.* **2012**, *48*, 158–160. [[CrossRef](#)]
53. Khan, A.Q.; Ahmed, Z.; Kazmi, S.N.H.; Malik, A.; Afza, N. The structure and absolute configuration of cyclotirucananol, a new triterpene from *Euphorbia tirucalli* Linn. *Z. Naturforsch. B* **1988**, *43B*, 1059–1062. [[CrossRef](#)]
54. Ayatollahi, A.M.; Ghanadian, M.; Afsharypuor, S.; Mesaik, M.A.; Abdalla, O.M.; Shahlaei, M.; Farzandi, G.; Mostafavi, H. Cycloartanes from *Euphorbia aellenii* Rech. f. and their antiproliferative activity. *Iran. J. Pharm. Res.* **2011**, *10*, 105–112. [[PubMed](#)]
55. Lee, C.K.; Chang, M.H. The chemical constituents from the heartwood of *Eucalyptus citriodora*. *J. Chin. Chem. Soc.* **2000**, *47*, 555–560. [[CrossRef](#)]
56. Yang, N.Y.; Tao, W.W.; Duan, J.A. Antithrombotic flavonoids from the faeces of *Trogopterus xanthipes*. *Nat. Prod. Res.* **2010**, *24*, 1843–1849. [[CrossRef](#)]
57. Kwon, D.J.; Bae, Y.S. Chemical constituents from the stem bark of *Acer barbinerve*. *Chem. Nat. Compd.* **2011**, *47*, 636–638. [[CrossRef](#)]
58. Luyen, B.T.L.; Tai, B.H.; Thao, N.P.; Eun, K.J.; Cha, J.Y.; Xin, M.J.; Lee, Y.M.; Kim, Y.H. Anti-inflammatory components of *Euphorbia humifusa* Willd. *Bioorg. Med. Chem. Lett.* **2014**, *24*, 1895–1900. [[CrossRef](#)]

59. Chang, Y.; Zhang, P.; Zhang, X.; Chen, J.; Rausch, W.D.; Gula, A.; Bao, B. Cytotoxic activities of flavonoids from a traditional Mongolian medicinal herb *Clematis aethusifolia* Turcz. *Nat. Prod. Res.* **2017**, *31*, 1223–1227. [CrossRef]
60. Madikizela, B.; Aderogba, M.A.; Van Staden, J. Isolation and characterization of antimicrobial constituents of *Searsia chirindensis* L. (Anacardiaceae) leaf extracts. *J. Ethnopharmacol.* **2013**, *150*, 609–613. [CrossRef]
61. Rastrelli, L.; Saturnino, P.; Schettino, O.; Dini, A. Studies on the constituents of *Chenopodium pallidicaule* (Cañihua) seeds. Isolation and characterization of two new flavonol glycosides. *J. Agric. Food Chem.* **1995**, *43*, 2020–2024. [CrossRef]
62. Seshadri, T.R.; Vydeeswaran, S. Chrysoeriol glycosides and other flavonoids of *Rungia repens* flowers. *Phytochemistry* **1972**, *11*, 803–806. [CrossRef]
63. Olennikov, D.N.; Kashchenko, N.I. Calendosides I–IV, new quercetin and isorhamnetin rhamnoglucosides from *Calendula officinalis*. *Chem. Nat. Compd.* **2014**, *50*, 633–637. [CrossRef]
64. Phechrmeekha, T.; Sritularak, B.; Likhitwitayawuid, K. New phenolic compounds from *Dendrobium capillipes* and *Dendrobium secundum*. *J. Asian Nat. Prod. Res.* **2012**, *14*, 748–754. [CrossRef]
65. Yildiz, I.; Sen, O.; Erenler, R.; Demirtas, I.; Behcet, L. Bioactivity-guided isolation of flavonoids from *Cynanchum acutum* L. subsp. *sibiricum* (willd.) Rech. f. and investigation of their antiproliferative activity. *Nat. Prod. Res.* **2017**, *31*, 2629–2633.
66. Leite, J.P.V.; Rastrelli, L.; Romussi, G.; Oliveira, A.B.; Vilegas, J.H.Y.; Vilegas, W.; Pizza, C. Isolation and HPLC quantitative analysis of flavonoid glycosides from Brazilian beverages (*Maytenus ilicifolia* and *M. aquifolium*). *J. Agric. Food Chem.* **2001**, *49*, 3796–3801. [CrossRef]
67. Yu, H.P.; Hsieh, P.W.; Chang, Y.J.; Chung, P.J.; Kuo, L.M.; Hwang, T.L. 2-(2-Fluoro-benzamido)benzoate ethyl ester (EFB-1) inhibits superoxide production by human neutrophils and attenuates hemorrhagic shock-induced organ dysfunction in rats. *Free Radic. Biol. Med.* **2011**, *50*, 1737–1748. [CrossRef]
68. Chen, C.Y.; Liaw, C.C.; Chen, Y.H.; Chang, W.Y.; Chung, P.J.; Hwang, T.L. A novel immunomodulatory effect of ugonin U in human neutrophils via stimulation of phospholipase C. *Free Radic. Biol. Med.* **2014**, *72*, 222–231. [CrossRef]
69. Pham, C.T.N. Neutrophil serine proteases: Specific regulators of inflammation. *Nat. Rev. Immunol.* **2006**, *6*, 541–550. [CrossRef]

**Sample Availability:** Samples of all the isolated compounds are available from the authors.



© 2019 by the authors. Licensee MDPI, Basel, Switzerland. This article is an open access article distributed under the terms and conditions of the Creative Commons Attribution (CC BY) license (<http://creativecommons.org/licenses/by/4.0/>).

RESEARCH

Open Access



# Combining hydrophilic chemotherapy and hydrophobic phytotherapy via tumor-targeted albumin–QDs nano-hybrids: covalent coupling and phospholipid complexation approaches

Dina G. Zayed<sup>1,2</sup>, Shaker M. Ebrahim<sup>3</sup>, Maged W. Helmy<sup>4</sup>, Sherine N. Khattab<sup>1,5</sup>, Mohammed Bahey-El-Din<sup>6</sup>, Jia-You Fang<sup>7,8,9\*</sup>, Kadria A. Elkhodairy<sup>1,2</sup> and Ahmed O. Elzoghby<sup>1,2,10,11\*</sup>

## Abstract

**Background:** The rationale of this study is to combine the merits of both albumin nanoparticles and quantum dots (QDs) in improved drug tumor accumulation and strong fluorescence imaging capability into one carrier. However, premature drug release from protein nanoparticles and high toxicity of QDs due to heavy metal leakage are among challenging hurdles. Following this platform, we developed cancer nano-theranostics by coupling biocompatible albumin backbone to CdTe QDs and mannose moieties to enhance tumor targeting and reduce QDs toxicity. The chemotherapeutic water soluble drug pemetrexed (PMT) was conjugated via tumor-cleavable bond to the albumin backbone for tumor site-specific release. In combination, the herbal hydrophobic drug resveratrol (RSV) was preformulated as phospholipid complex which enabled its physical encapsulation into albumin nanoparticles.

**Results:** Albumin–QDs theranostics showed enhanced cytotoxicity and internalization into breast cancer cells that could be traced by virtue of their high fluorescence quantum yield and excellent imaging capacity. In vivo, the nanocarriers demonstrated superior anti-tumor effects including reduced tumor volume, increased apoptosis, and inhibited angiogenesis in addition to non-immunogenic response. Moreover, in vivo bioimaging test demonstrated excellent tumor-specific accumulation of targeted nanocarriers via QDs-mediated fluorescence.

**Conclusion:** Mannose-grafted strategy and QD-fluorescence capability were beneficial to deliver albumin nanocarriers to tumor tissues and then to release the anticancer drugs for killing cancer cells as well as enabling tumor imaging facility. Overall, we believe albumin–QDs nanopatform could be a potential nano-theranostic for bioimaging and targeted breast cancer therapy.

**Keywords:** Albumin nanoparticles, QDs, Resveratrol, Pemetrexed, Mannose targeting, Breast cancer, Theranostics

\*Correspondence: fajy@mail.cgu.edu.tw; aelzoghby@bwh.harvard.edu; ahmed\_elzoghby@alexu.edu.eg

<sup>7</sup> Pharmaceuticals Laboratory, Graduate Institute of Natural Products, Chang Gung University, Taoyuan 333, Taiwan

<sup>10</sup> Present Address: Division of Engineering in Medicine, Department of Medicine, Brigham and Women's Hospital, Harvard Medical School, Boston, MA 02115, USA

Full list of author information is available at the end of the article





## Background

Nano-theranostics can provide both therapeutic and diagnostic capabilities via a singular drug nanocarrier [1]. Limitations of current imaging techniques lead to design of sensitive and biospecific new imaging probes. Quantum dots (QDs) as new imaging probes, 2–10 nm in diameter. They possess strong photoluminescence (PL) with a high molar extinction coefficient values compared with organic dyes in addition to broad absorption with narrow symmetric emission spectra. Some concerns were raised regarding QDs toxicity, in particular for cadmium-containing QDs due to the release of Cd ions and reactive oxygen species (ROS) generation [2]. Other studies confirmed that ROS generated by QDs help induce more apoptosis and thus converted the QDs toxicity into a therapeutic modality [3]. Recently, great interest has been raised towards the fabrication of cadmium-free QDs to be used for biological applications such as ZnS and ZnO QDs; unfortunately, they exhibited weaker PL emission than Cd-containing QDs. Therefore, researchers are now paying more effort to decreasing toxicity of the highly fluorescent Cd-containing QDs.

Among the most outstanding strategies to reduce their toxicity, QDs were conjugated via tumor-cleavable bond to actively-targeted delivery systems to maximize their accumulation in tumor cells and inhibit their release into circulation [4]. Similar literature reported the tumor-specific release of QDs coupled to NPs by amide bond. Methotrexate (MTX) was covalently conjugated to L-cysteine capped CdSe QDs through a strong amide bond forming MTX-QD nano-conjugates, this conjugate can't be cleaved in PBS. However, once taken up by the cells, the amide bond is enzymatically cleaved by the action of the endosomal/lysosomal machineries of the target cells and thus releasing MTX molecules and the QDs into the cytoplasmic milieu of the cells. Cellular uptake study revealed that 71% of MTX-QD nanoconjugate accumulated in KB cancer cells [5]. Receptor-targeted nano-sized carriers can facilitate tumor targeting via the enhanced tumor permeability and retention (EPR) effect, followed by binding to receptors over-expressed by cancer cells leading to enhanced internalization via endocytosis [6, 7]. Cancer cells were found to overexpress C-type lectin receptors (CLRs) essentially required for binding with carbohydrates such as mannose. It is widely known that mannose bind strongly to mannose receptor (MR) overexpressed on the surface of human breast cancerous cells [8]. However, the interaction between a single mannose and MR is weak thus nanoparticles can provide a platform for the multivalent presentation of mannose, which increases the binding intensity and specificity between mannose-functionalized nanocarriers and overexpressed MRs on cancer cells [9].

Pemetrexed (PMT) is an antifolate cytotoxic drug delivered into cells via folate transport systems where it is transformed to polyglutamate derivatives by folyl-polyglutamate synthase [10]. Unlike methotrexate which targets a single enzyme critical in purine and pyrimidine synthesis, PMT and its polyglutamate derivatives inhibit three enzymes; dihydrofolate reductase, thymidylates synthase, and glycinamide ribonucleotide formyltransferase. The multiple enzyme inhibitory effect of PMT helps overcoming intrinsic resistance accompanied by mutation of one of these enzymes. However, the relative lack of PMT specificity resulted in toxic dose-related adverse effects that may limit its therapeutic effect such as myelosuppression, hepatic enzyme elevations, maculopapular rash, emesis and diarrhea. To reduce its toxicity, PMT was encapsulated into nanocarriers including PEG-peptide-PCL NPs [11] and lipid-polymer hybrid NPs [12]. The small size (below 100 nm) of NPs containing both PMT and miR-21 antisense oligonucleotide, enabled their passive tumor targeting and enhanced uptake into U87MG human glioblastoma cells [12]. On the other hand, Resveratrol (RSV), a natural polyphenol and phytoalexin, demonstrated a strong anti-cancer activity. However, its low aqueous solubility and poor bioavailability hinder its clinical utility. To overcome this challenge, RSV was incorporated into different nano-formulations to enhance its solubility and bioavailability [13].

Different from cancer monotherapy, combination therapy has the advantage of harmonizing different signaling pathways as well as amplifying the therapeutic effect by overcoming resistance to cancer monotherapy [14]. In our laboratory, co-loading of celecoxib and letrozole into protamine-coated oily-core nanocapsules enhanced their anti-cancer efficacy against breast cancer cells in vitro and in vivo compared to single free drugs [15]. The combined treatment with RSV and PMT was previously reported to demonstrate a synergistic growth inhibition of human NSCLC H520 and H1975 cells compared to either treatment alone [16]. On another avenue, co-treatment of MSTO-211 and A549 cells with RSV and PMT was found to reduce ROS generation in both cells more efficiently than in cells treated with PMT alone. Therefore, in addition to synergism, it was postulated that RSV may confer protection against apoptosis induced by PMT so help decrease PMT toxicity [17].

In this study, we propose for the first time up to our knowledge, mannosylated BSA-QDs nano-theranostics for targeted co-delivery of PMT and RSV to breast cancer. First, the hydrophilic cytotoxic drug, PMT, was covalently-bonded to the surface of BSA via amide bond stable at systemic circulation but can be cleaved at tumor cells thus enabling its specific release at tumor sites and reducing its systemic toxicity. Second, to overcome its

high lipophilicity, RSV was pre-formulated as phosphatidylcholine complex (RSV-PC) prior to incorporation into the hydrophilic matrix of BSA NPs. Third, to achieve active tumor-targeting, the surface of BSA NPs was decorated with D-mannose for binding to MRs overexpressed by human breast cancer cells. Finally, for theranostic applications, water-soluble thiol capped CdTe QDs were conjugated to the surface of BSA NPs via tumor cleavable bond to inhibit release of Cd ions into circulation thus reducing QDs toxicity. The developed delivery system was thoroughly investigated in vitro and in vivo to prove the anti-tumor superiority of the combined drug nano-carriers compared with free drugs and their combination.

## Materials and methods

### Materials

Resveratrol (RSV) and pemetrexed-disodium (PMT) were purchased from Xi'an natural field bio-technique Co., Ltd. (Shaanxi, China). Bovine serum albumin (BSA), sodium borohydride ( $\text{NaBH}_4$ ), cadmium chloride ( $\text{CdCl}_2 \cdot 2.5\text{H}_2\text{O}$ ), sodium hydroxide, disodium hydrogen phosphate ( $\text{Na}_2\text{HPO}_4$ ), thioglycolic acid (TGA), tellurium powder (99.999%), fetal bovine serum (FBS), 3-(4,5-dimethylthiazolyl-2)-2,5-diphenyltetrazolium bromide (MTT), mannitol, D-mannose, dimethyl sulfoxide (DMSO), *N*-(3-dimethylaminopropyl), *N'*-ethylcarbodiimide hydrochloride (EDC-HCl) (purity > 98%), *N*-hydroxysuccinimide (NHS), Triton X100, haematoxylin solution, eosin solution and Canada balsam were purchased from Sigma-Aldrich (St. Louis, USA). 2-(4-ethoxyphenyl)-6-[6-(4-methylpiperazin-1-yl)-1*H*-benzimidazol-2-yl]-1*H*-benzimidazole (Hoechst) was purchased from Thermo-Fisher (Waltham, MA, USA). DPX mounting medium was obtained from Loba Chemie Pvt. Ltd. (Mumbai, India). Fat-free soybean phospholipids with 70% phosphatidylcholine (Lipoid S75) were kindly provided by Lipoid (Ludwigshafen, Germany). Absolute ethanol, methanol, tertiary butyl alcohol (TBA) and orthophosphoric acid were from ADWIC, El-Nasr Pharmaceutical Chemicals Co., (Cairo, Egypt). Acetonitrile HPLC grade was obtained from JT Baker (Phillipsburg, NJ, USA). Peroxidase-conjugated anti-mouse IgG and 3,3',5,5'-tetramethylbenzidine (TMB) were purchased from KPL Inc., (Gaithersburg, USA). Mouse anti-Ki-67 monoclonal antibody was obtained from Santa Cruz Biotechnology (Cat no. sc-23900). Human MCF-7 and MDA-MB-231 breast adenocarcinoma cells were supplied by the American Type Culture Collection (ATCC).

### Synthesis of CdTe QDs

Water soluble TGA-capped CdTe QDs were synthesized in accordance with the modified coordinating solvent method [18]. Briefly, 0.158 g  $\text{CdCl}_2 \cdot 2.5\text{H}_2\text{O}$  and 150  $\mu\text{l}$  TGA were dissolved in 100 ml deionized water.

The solution pH was adjusted to 10.0 using 1.0 M NaOH solution. This Cd source solution was then deoxygenated in a three-neck flask by bubbling nitrogen gas for at least 30 min and refluxed at 100 °C. Meanwhile, 0.06 g Te powder and 0.07 g  $\text{NaBH}_4$  were mixed into 10 ml deionized water forming a black mixture. The mixture was then continuously stirred under nitrogen gas at 60 °C until the black color disappeared and the purple colored NaHTe was obtained. The recently prepared NaHTe solution was then injected into the three-neck flask under nitrogen atmosphere. CdTe QDs start to form and grow upon refluxing at 100 °C under nitrogen atmosphere for 2 h with a condenser attached. Samples of the reaction mixture solution were taken at specified time intervals (5:120 min) and the absorption spectrum was taken to monitor the growth of the clusters.

### Characterization of CdTe QDs

The absorption spectra of CdTe QDs were recorded via T80 UV-visible spectrophotometer (PG Instruments, UK). The diameter of synthesized QDs was determined based on the following equation [18]:

$$D = 9.8127 \times 10^{-7} \lambda^3 - 1.7147 \times 10^{-3} \lambda^2 + 1.0064 \lambda - 194.84 \quad (1)$$

where *D* (nm) is the diameter of QDs, and  $\lambda$  (nm) is the wavelength of the first excitonic absorption peak.

The fluorescence intensity and emission spectra were recorded at excitation wavelength of 450 nm by LS 55 fluorescence spectrophotometer (PerkinElmer, USA). TEM analysis as well as the zeta potential of QDs were estimated following the experimental method detailed in Additional file 1.

### Preparation of RSV/PMT-BSA NPs (F1)

PMT-BSA conjugate was prepared by carbodiimide coupling [19] while RSV-PC complex was prepared via freeze-drying technique [20] (Methodology is detailed in Additional file 1). BSA NPs were fabricated by an established desolvation process. Briefly, 100 mg of PMT-BSA conjugate was dissolved in 4.0 ml NaCl solution (10 mM) and adjusted to pH 7.4. RSV-PC complex (eq. to 10 mg RSV) was pre-dissolved in the aqueous BSA-PMT solution and left to incubate under magnetic stirring for 1 h before desolvation step. The NPs were formed by continuous dropwise addition of 8.0 ml ethanol (1 ml/min) under magnetic stirring. 55  $\mu\text{l}$  of 8% v/v glutaraldehyde was then added for crosslinking of the desolvated particles. The formed NPs were left overnight under magnetic stirring and then centrifuged twice at 16,000 rpm for 30 min at 4 °C for purification (3–30 KS Sigma, Germany).

### Preparation of RSV/PMT-BSA-QDs NPs (F2)

For activation of carboxylate groups of TGA-capped QDs, EDC-HCl (0.024 g, 0.12 mmol) and NHS (0.015 g, 0.12 mmol) were added to 2 ml of CdTe QDs dispersion in water (adjusted to pH 7.4 using 0.1 M HCl) under stirring for 30 min. The previously prepared RSV/PMT-BSA NPs solution was added to the reaction solution and left for 24 h under stirring. Finally, the NPs were centrifuged at 16,000 rpm for 30 min at 4 °C to separate the excess un-reacted reagents and redispersed in water to be used for further characterization.

### Preparation of mannose-targeted RSV/PMT-BSA-QDs NPs (F3)

For preparation of mannosylated-BSA NPs, the prepared RSV/PMT-BSA-QDs NPs solution was mixed with 15 mg D-mannose pre-dissolved in 4.0 ml water. The solution pH was adjusted to 4.0 using 0.1 M acetic acid and left in a type 3047 Kottermann shaking water bath (Hanigsen, Germany) at 45 °C for 4 h. Mannosylated BSA NPs solution was then purified by dialysis against deionized water for 24 h, with water being replaced every 3–5 h to remove un-reacted mannose.

### Solid state characterization

The FTIR spectra and DSC thermograms of free drugs and drug-loaded nanocarriers were recorded with the procedures mentioned in Additional file 1 [21, 22]. Moreover, nuclear magnetic resonance (NMR) spectra (<sup>1</sup>H-NMR) were recorded using JEOL 500 MHz spectrometer (Tokyo, Japan) at ambient temperature for BSA, mannose and mannose-BSA NPs. Chemical shifts are recorded in ppm and referenced relative to residual solvent.

### Physicochemical characterization of dual drug-loaded BSA NPs

The methodologies for assessing drug loading, nanoparticle size and zeta potential [23], drug release [24], morphology, stability [25], redispersibility, hemolytic and serum stability [26] were performed as described and detailed in Additional file 1.

### In vitro cytotoxicity and uptake study

The in vitro cytotoxicity of free RSV, free PMT, free RSV/PMT solution and different dual drug loaded BSA-QDs NPs against human breast cancer MCF-7 and MDA-MB-231 cells were evaluated by MTT assay performed as described and detailed in Additional file 1. Combination Index (CI) and Dose Reduction Index (DRI) were calculated using CompuSyn software (version 1) to ensure the superiority of different nanocarriers compared to the free

combination [6]. Cellular uptake of targeted and non-targeted BSA-QDs NPs and free QDs into MCF-7 breast cancer cells was evaluated using confocal microscopy as described previously [27] and detailed in Additional file 1.

### In vivo studies

#### Animals

The anti-tumor efficacy of drug loaded NPs (F2, F3 and F4) was evaluated compared to free RSV, free PMT and RSV/PMT solution on female mice housed in stainless steel mesh cages following standard protocol mentioned in Additional file 1.

#### Development of tumor model

7–8 weeks aged female BALB/C mice were housed in a pathogen-free environment at 7 mice/cage. They were provided with autoclaved non-fluorescented mouse chow and water. Ehrlich ascites tumor (EAT) cells, given from the National Institute of Cancer, Egypt, were collected from the ascitic fluid of BALB/C mice harboring 8–10 days old ascitic tumor. Almost, 10<sup>7</sup> of EAT cells suspended in PBS were injected into the left side of the mammary fat pad of BALB/C female mice. Tumor growth was estimated daily until its volume reached 100 mm<sup>3</sup>. Tumor volume was determined by measuring both perpendicular diameters of the tumor using a micrometer based on the following equation [28]:

$$\text{Tumor volume} = L \times W^2 \times 0.5 \quad (2)$$

where W is tumor width, L is tumor length.

#### In vivo anti-tumor efficacy

Animal groups (7 mice each) included untreated positive control, negative control, free RSV, free PMT, free combined RSV/PMT solution, F2 (RSV/PMT-BSA-QDs NPs), F3 (Mann-targeted RSV/PMT BSA-QDs NPs) and F4 (Mann-targeted RSV/PMT BSA NPs) treated group; in addition to blank BSA NPs. Free drugs or NPs equivalent to 4 mg/kg PMT and 2.3 mg/kg RSV were injected i.v. through the tail vein into EAT-bearing mice three times per week for 3 weeks. The mice body weight was recorded simultaneously during the treatment. Animals were sacrificed at the end of treatment period. Tumors were isolated and the weights were determined. Each excised tumor was divided into 2 parts for histopathological examination and measurement of tumor growth biomarkers.



## a. Tumor volume

During the treatment course, tumor growth was assessed once per week and the % increase of tumor volume was determined.

## b. Tumor growth biomarkers

The tumor growth biomarkers were determined quantitatively using ELISA. The experimental method is detailed in Additional file 1.

## c. Histopathological and immunohistochemical analysis

The tumor samples were examined for histopathological changes as well as proliferation extent. The experimental method is detailed in Additional file 1.

## d. Tumor localization of NPs

The distribution of BSA-QDs NPs was analyzed using the confocal laser scanning microscopy as described and mentioned in Additional file 1.

**Immunogenicity of the nano-delivery system**

Enzyme-linked immunosorbent assay (ELISA) was used as previously described [29] to check if the BSA

nano-delivery system elicits antibodies against BSA during the experimental treatment protocol (Experimental details are described in Additional file 1).

**Statistical analysis**

Data analysis is detailed in Additional file 1.

**Results and discussion**

Nanocarriers fabricated from natural polymers including proteins and polysaccharides offer various opportunities for tumor-targeted drug delivery applications [30–32]. Albumin can be used as a drug carrier either by incorporation of the drug within its matrix or by conjugation to the functional groups available on the NPs surface. In this study, BSA-QDs NPs for dual delivery of RSV and PMT were developed for breast cancer therapy and imaging (Fig. 1).

**Characterization of the synthesized CdTe QDs**

CdTe QDs are characterized by their strong fluorescence enabling their use in cancer imaging. In our study, highly fluorescent QDs have been prepared using 4:1 Cd:Te molar ratio at pH 10.0 utilizing 150  $\mu$ l TGA as a capping

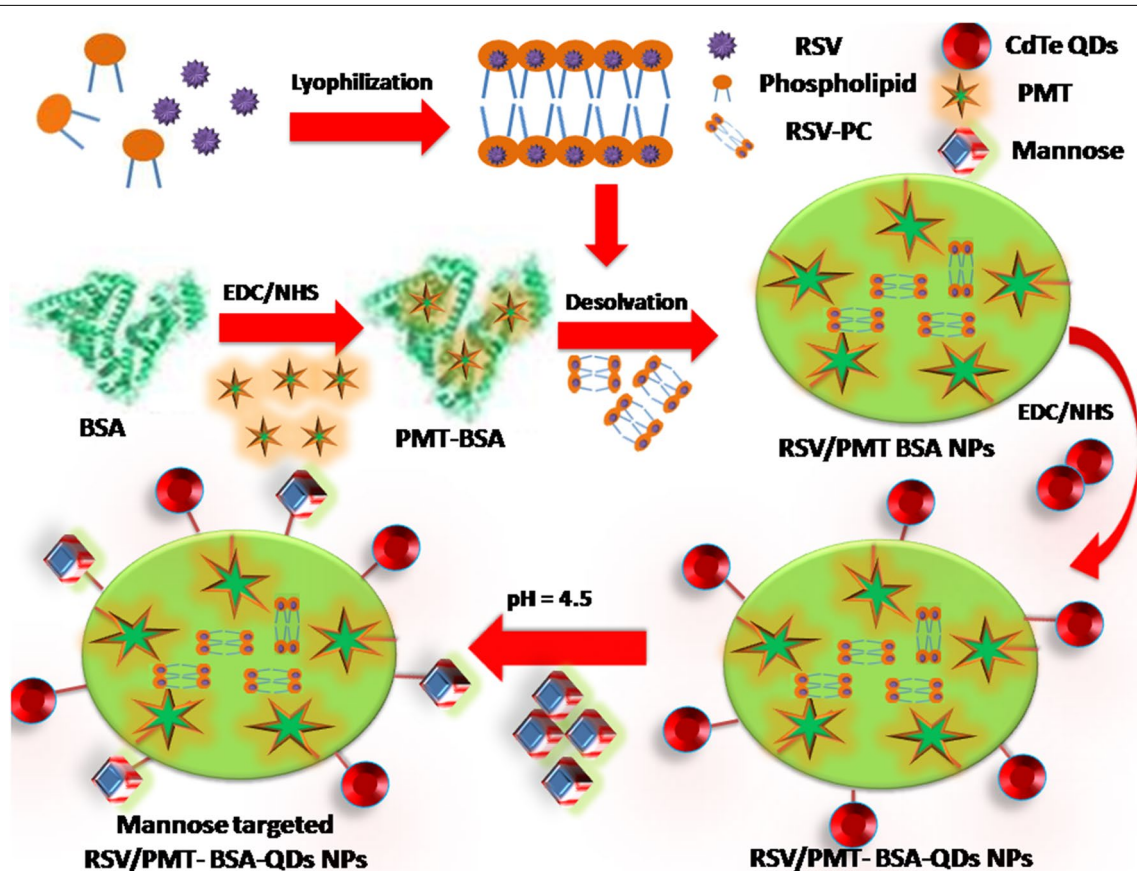


**Fig. 1** Schematic diagram illustrating the preparation steps of Mann-targeted RSV/PMT BSA-QDs NPs (F3)



agent. The fluorescence intensity of CdTe QDs was previously reported to increase with increasing Te concentration till reaching maxima at Cd:Te molar ratio of 4:1 [33]. Finally, the solution pH was adjusted to 10.0 as an optimal value. Sun et al. found that the highest fluorescence intensity of QDs was obtained at pH of 10.5 [34].

During the formation of CdTe QDs, the solution color was changed from colorless to transparent yellow to light brown and finally red brown. This revealed the formation of QDs with different sizes upon increasing the reaction time. From UV–visible spectra of the TGA-capped QDs, it has been observed that QDs started growth at a wavelength of 460 nm (Fig. 2a). As the reaction time passes, the spectra were shifted towards the red region due to the quantum confinement effect indicating the size growth of QDs [18]. From equation one, the size of QDs was calculated to be 3.2 nm at wavelength of 550 nm. At excitation wavelength of 450 nm, the TGA-capped QDs and Mann-targeted RSV/PMT-BSA-QDs NPs (F3) exhibited a characteristic symmetric emission peak at 560 nm (Fig. 2b). The QDs exhibited high adequate emission spectrum

along with high resolution that can be utilized for cancer cell imaging [35]. A slight blue shift in the emission peak of CdTe QDs to 520 nm was observed after conjugation with Mann-targeted RSV/PMT-BSA-QDs NPs (F3) (Fig. 2b). During preparation of CdTe QDs, the thiol groups of TGA stabilizer were conjugated to the QDs surface by SH–Cd coordination. Thus, the free carboxylic group of TGA could be easily coupled to the amino groups of BSA resulting in shift of emission peak towards shorter wavelength. This shift confirmed that the size of the QDs was reduced due to etching of nanocrystals by photo-oxidations or acids as a result of decreasing pH. In our study, pure CdTe QDs were prepared at pH 10.0 while during preparation of F3 nanoparticles [Mann-targeted RSV/PMT BSA-QDs NPs], the pH was decreased to 7.0. Similarly, phospholipid micelles encapsulated DHLA QDs showed a spectral blue shift of 5 nm upon decreasing the pH to 5.0 [36]. As illustrated in HRTEM images, TGA-capped CdTe QDs were well dispersed with an average size of 4–5 nm (Fig. 2c). The good dispersion of QDs was also indicated by the high value of their

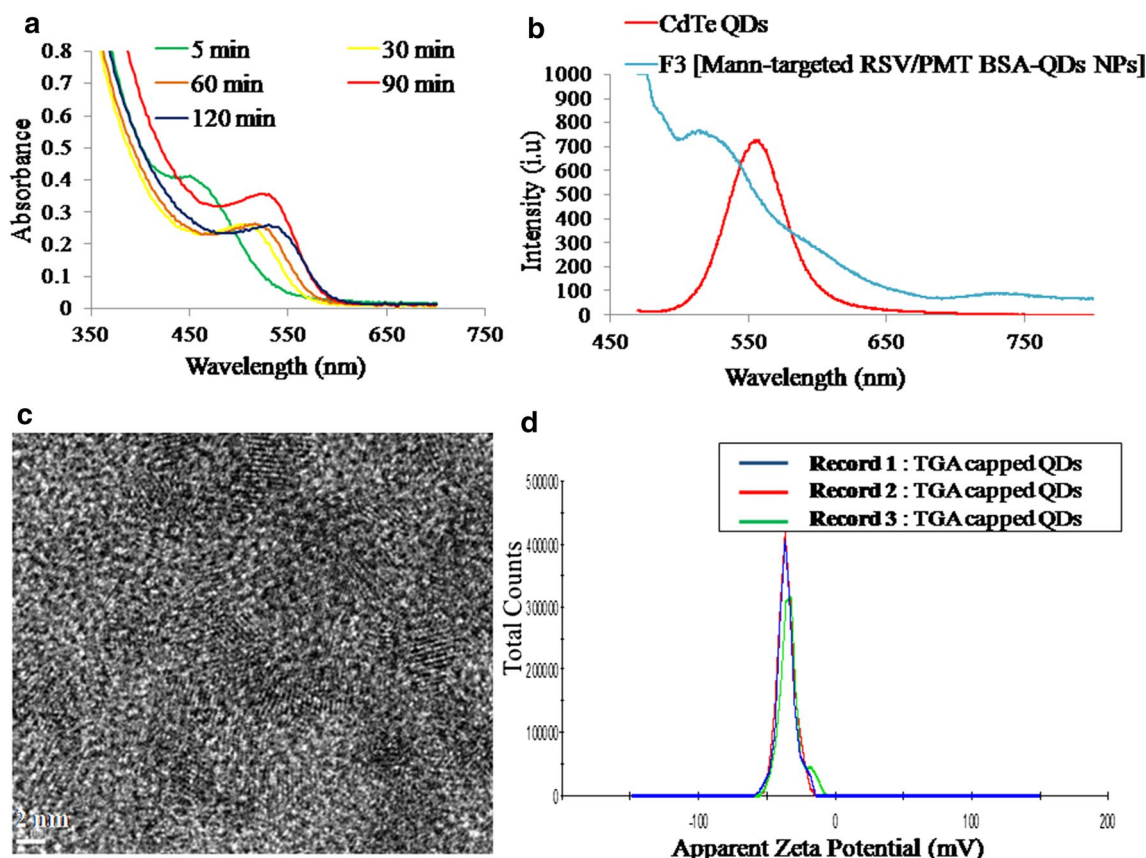


**Fig. 2** UV absorbance measured during the preparation of TGA capped CdTe QDs (a), emission spectra of CdTe QDs and Mann-targeted RSV/PMT BSA-QDs NPs (F3) upon excitation with  $\lambda = 450$  nm (b), TEM images of TGA capped CdTe QDs (c) and their corresponding zeta potential distribution diagram (d)

zeta potential ( $-35.8$  mV) which could be attributed to the free carboxylic groups of TGA (Fig. 2d). The size obtained by HRTEM was similar or slightly higher than that calculated from absorption measurements at wavelength of 550 nm (3.2 nm). TEM measures the diameter of the particle with its surface attached ligands and strongly associated solvent molecules while the size calculated from absorption spectrum is only based on QDs distribution [18].

#### Physicochemical characterization of drug-loaded BSA NPs

In our study, to develop dual drug-loaded BSA NPs, the chemotherapeutic water soluble drug, PMT, was firstly conjugated to BSA via carbodiimide coupling reaction. PMT carboxylate groups were activated and reacted with the free amino groups of BSA to form an amide bond. BSA-PMT NPs were prepared by desolvation where addition of ethanol to aqueous BSA-PMT solution diminished its water solubility leading to its precipitation followed by condensation with glutaraldehyde for hardening of the formed coacervates [30]. By virtue of the abundant binding sites of albumin for hydrophobic drugs, we have incorporated the water insoluble herbal drug, RSV, into the hydrophilic albumin matrix [30]. To facilitate its dispersion in aqueous solution, RSV-phospholipid complex (RSV-PC) was formed to enhance the drug water solubility and hence RSV could be incorporated in the albumin matrix. The RSV-PC complex was formed via van der Waals forces and hydrogen bonds between the phospholipid polar head and the polar functionalities of RSV (details of the physicochemical characteristics of RSV-PC complex are in Additional file 1) [22]. Similarly, phospholipid was used for complexation with the water insoluble drug, teniposide to improve its solubility and thus facilitated its incorporation into albumin NPs with encapsulation efficiency of 82.27% [37]. The prepared RSV/PMT-BSA NPs (F1) showed an average size of  $142.8 \pm 5.72$  nm and zeta potential of  $-31.7 \pm 1.5$  mV providing highly electrostatic repulsive stabilization of the particles (Table 1). The encapsulation efficiency of RSV was  $65.33 \pm 5.8\%$  while the conjugation efficiency of PMT was  $63.3 \pm 2.1\%$ .

In a consequent step, for development of theranostic NPs, the carboxylate groups of TGA-CdTe QDs were coupled to the surface amino groups of dual drug-loaded BSA NPs to elaborate albumin-inorganic nano-hybrids. RSV/PMT-BSA-QDs NPs (F2) demonstrated a size of  $154.8 \pm 6.6$  nm with a surface charge of  $-27 \pm 1.1$  mV (Additional file 1: Figure S1). Finally, to develop actively-targeted NPs, RSV/PMT-BSA-QDs NPs (F2) were reacted with D-mannose via Maillard reaction to form Schiff's base [38]. The successfulness of the mannosylation reaction was indicated by sugar detection according to the phenol-sulfuric acid test. In this method, hexoses are dehydrated by sulfuric acid to hydroxymethyl furfural which then reacts with phenol to produce a yellow-gold color (Additional file 1: Figure S2) [39]. Further confirmation of the mannosylation reaction was revealed by the increase in the net negative charge of BSA upon coupling with mannose from  $-7.0$  to  $-12.0$  mV revealing a reduction in the number of free amino groups. In the study of Bejaars et al., the surface charge of albumin became more negative with more mannose groups conjugated to its structure [40]. Moreover,  $^1\text{H-NMR}$  spectra of mannose-BSA NPs revealed the characteristic peaks of mannose protons (Additional file 1: Figure S3). Mann-targeted RSV/PMT BSA-QDs NPs (F3) showed an average size of  $193.9 \pm 4.8$  and zeta potential of  $-33.1 \pm 1.2$  with a narrow size distribution ( $\text{PDI} = 0.184$ ) (Fig. 3a). When observed by TEM, Mann-targeted RSV/PMT BSA-QDs NPs (F3) were in the size range of 95–100 nm with a spherical shape and smooth surface without any aggregation confirming high colloidal stability (Fig. 3b). The apparent size measured by TEM was slightly less than that measured by dynamic light scattering due to dehydration-induced shrinkage of particles during preparation for TEM analysis [41, 42].

#### In vitro drug release

A biphasic release profile of entrapped RSV from the BSA-PMT NPs was observed. After the first 2 h, about 20.6% of RSV was released from Mann-targeted RSV/PMT BSA-QDs NPs (F3) corresponding to the surface-adsorbed drug fraction. This relatively fast release phase was followed by a sustained RSV release of about 63.4%

**Table 1** Composition and physicochemical characteristics of blank and drug-loaded BSA NPs

	Formula	Particle size (nm)	Zeta potential (mV)	PDI	%RSV EE	%PMT CE
F1*	RSV/PMT-BSA NPs	$142.8 \pm 5.7$	$-31.7 \pm 1.5$	0.158	$65.33 \pm 5.8$	$63.3 \pm 2.1$
F2	RSV/PMT-BSA-QDs NPs	$154.8 \pm 6.6$	$-27.2 \pm 1.1$	0.202	$67.34 \pm 6.1$	$64.2 \pm 2.3$
F3	Mann-targeted RSV/PMT-BSA-QDs NPs	$193.9 \pm 4.8$	$-33.1 \pm 1.2$	0.184	$68.1 \pm 5.1$	$50.9 \pm 1.9$
F4	Mann-targeted RSV/PMT-BSA NPs	$155.5 \pm 3.9$	$-32.7 \pm 1.4$	0.117	$65.2 \pm 4.9$	$57.8 \pm 3.6$

\* All NPs were prepared using 100 mg PMT-BSA, RSV/PC complex eq. to 10 mg RSV, and 55  $\mu\text{l}$  (8%v/v) glutaraldehyde as a cross-linking reagent

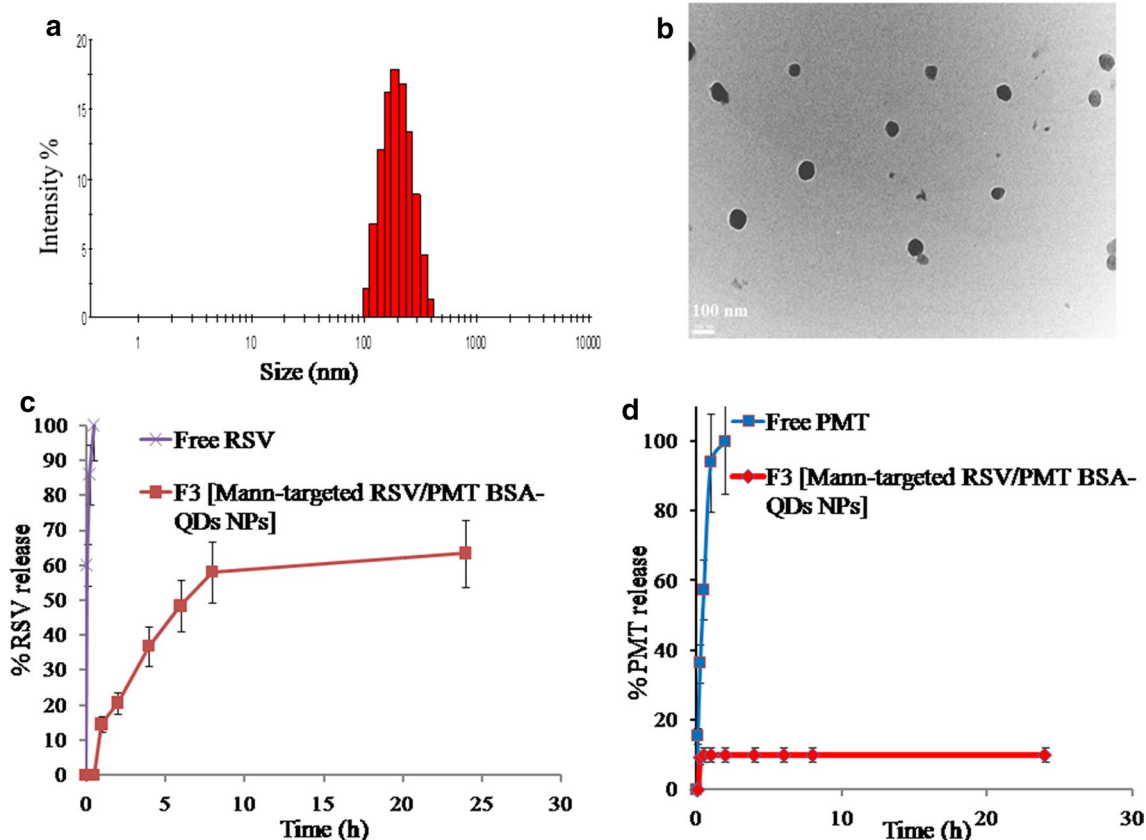


**Fig. 3** Size distribution diagram of Mann-targeted RSV/PMT BSA-QDs NPs (F3) (a), TEM images showing morphology of Mann-targeted RSV/PMT BSA-QDs NPs (F3) (b) and in-vitro release study of RSV (c) and PMT (d) from (F3) in PBS (pH 7.4) at 100 rpm and 37 °C using dialysis bag method

after 24 h corresponding to the drug fraction entrapped inside the nanomatrix [43]. In comparison, free RSV was completely released after only 2 h (Fig. 3c).

In contrast, the release rate of PMT was very much slower with only 5% released from Mann-targeted RSV/PMT BSA-QDs NPs (F3) after 30 min in comparison to the rapid complete release of free PMT after 2 h (Fig. 3d). This small drug fraction released may be explained by the loss of physically bound drug associated within the hydrophobic binding sites of albumin. After 24 h, 90% of the drug was still linked to the protein. This high stability of the PMT-BSA conjugate can be ascribed to the strong amide bond between the conjugated drug and BSA. Similarly, about 95 and 91% of paclitaxel [44] and methotrexate [45], respectively remained linked to HSA after 72 h of incubation in pH 7.4 PBS indicating the stability of their conjugates. Based on these findings, it can be hypothesized that direct conjugation of PMT to the protein backbone will hinder its release in the circulation after i.v. administration of our NPs resulting in very low drug concentration; hence less side effects are expected whereas released at tumor sites after bond cleavage via

lysosomal enzymes. On the contrary, when PMT was physically encapsulated into PEG-peptide-PCL NPs, an initial burst of more than 30% of the drug in the first 3 h was observed [11].

#### Solid state characterization

RSV in its natural state exists as crystals, which are characterized by the melting endothermic peak around 265 °C in its thermogram (Additional file 1: Figure S4A). The thermogram of RSV-PC complex demonstrated a broad peak at 281.567 °C, indicating a successful complexation between RSV and phosphatidylcholine [46, 47]. On the other hand, PMT thermogram demonstrated three characteristic peaks at 91.784, 153.818 and 243.8 °C [48]. The endothermic peak of RSV has been disappeared in the thermograms of the non-targeted (F2) and targeted (F3) BSA NPs, suggesting that RSV was molecularly dispersed as amorphous state into the protein matrix. On the other hand, PMT endothermic peaks at 91.784 and 243.8 °C have disappeared, while its endothermic peak at 153.818 °C has been shifted to 150.1 °C with sharper intensity in the thermogram of both NPs which indicates

successful conjugation between PMT and BSA, rather than existing in a free state. In the FTIR spectra of non-targeted (F2) and targeted (F3) BSA NPs, the characteristic peak of RSV at  $3450\text{--}3100\text{ cm}^{-1}$  corresponding to its three hydroxyl groups stretching, was overlapped with the O–H stretching vibration of BSA at  $3430\text{ cm}^{-1}$  confirming the encapsulation of RSV within BSA NPs (Additional file 1: Figure S4B). Furthermore, the carbonyl stretching peak of PMT COOH group at  $1703\text{ cm}^{-1}$  disappeared due to the conjugation between the drug and BSA (more details in Additional file 1).

#### Physical stability and redispersibility

There were no remarkable changes observed for PS and PDI of Mann-targeted RSV/PMT BSA-QDs NPs (F3) after storage at  $4\text{ }^{\circ}\text{C}$  for 3 months (Fig. 4a). The NPs showed size of  $187\pm 2.3\text{ nm}$  and zeta potential

of  $-23\pm 1.2\text{ mV}$  after 3 months of storage, compared to the initially stored NPs ( $162.4\pm 3.5\text{ nm}$  and  $-26.4\pm 0.87\text{ mV}$ ). The results were in agreement with the high stability of paclitaxel/sorafenib co-loaded BSA NPs with no significant change in PS and zeta potential upon storage for 2 months [49].

To further enhance the storage stability of our developed NPs, they were solidified via lyophilization technique [50]. Using mannitol (5% w/v) as a cryoprotectant to facilitate the drying of NPs and prevent their aggregation, the reconstituted lyophilized Mann-targeted RSV/PMT BSA-QDs NPs (F3) demonstrated PS of  $189.7\pm 6.7\text{ nm}$ , with acceptable redispersibility index value of 0.97 (Table 2) [51]. Similarly, doxorubicin-loaded HSA NPs were freeze-dried using mannitol as a cryoprotectant and showed insignificant size change after reconstitution [52].

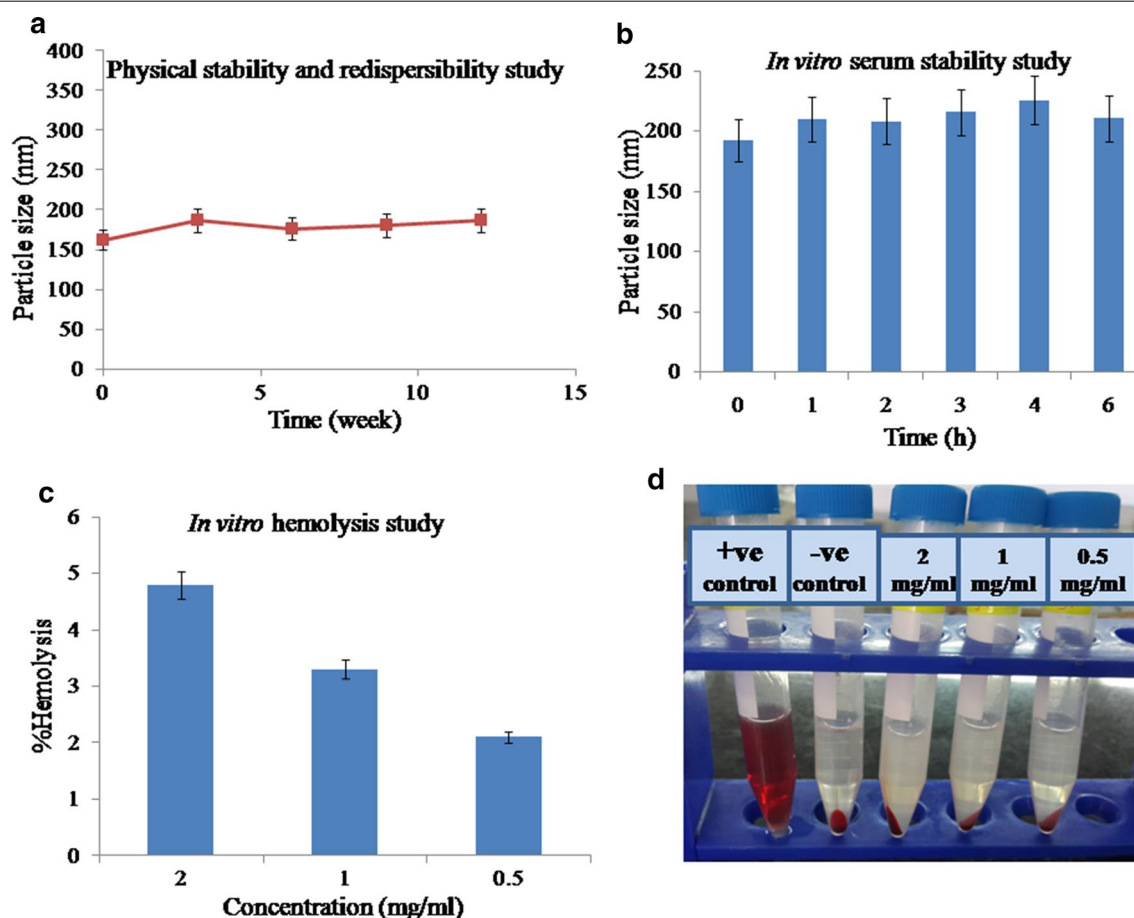


**Fig. 4** Physical stability of Mann-targeted RSV/PMT BSA-QDs NPs (F3) showing the change in particle size with time (a), particle size of F3 after incubation in 10% fetal bovine serum (FBS) for 6 h at  $37\text{ }^{\circ}\text{C}$  (b). Hemolytic potential of dual drug loaded targeted BSA-QDs NPs (F3) showing % hemolysis (c) and hemocompatibility images (d) of F3 after 1 h of incubation at  $37\text{ }^{\circ}\text{C}$



**Table 2** Effect of freeze-drying on the physicochemical characteristics of Mann-targeted RSV/PMT-BSA-QDs NPs (F3)

Formula	Yield (%w/w)	Particle size (nm)		RI*	Zeta potential (mV)	
		Before	After		Before	After
Mann-targeted RSV/PMT-BSA-QDs NPs (F3)	92.30	193.9 ± 4.8	189.7 ± 6.7	0.97	− 33.1 ± 1.2	− 24.3 ± 2.1

\* RI/ redispersibility index (final particle size/initial particle size)

### In vitro hemolysis and serum stability

To further predict the feasibility of i.v. administration, the NPs stability in serum was evaluated. With addition of aqueous serum solution, Mann-targeted RSV/PMT BSA-QDs NPs (F3) showed insignificant change in the size distribution compared with the initially prepared NPs (from  $192.2 \pm 0.802$  to  $210.6 \pm 0.8$  nm). After 4 h of incubation with FBS, the PS of NPs (F3) reached  $225 \pm 3.3$  nm which was decreased to  $210.6 \pm 1.3$  nm after 6 h. This behavior could be ascribed to the association and dissociation of

protein molecules on the surface of NPs during incubation period [53, 54]. The repulsive forces between the negatively charged serum proteins and BSA NPs may explain their high serum stability (Fig. 4b).

Moreover, the hemato-compatibility of Mann-targeted RSV/PMT BSA-QDs NPs (F3) in different concentration ranges (0.5–2 mg/ml) was determined and the leakage of hemoglobin from RBCs was used to quantitatively determine the membrane-damaging properties of NPs (Fig. 4c, d). At a concentration of 2 mg/ml, the NPs demonstrated

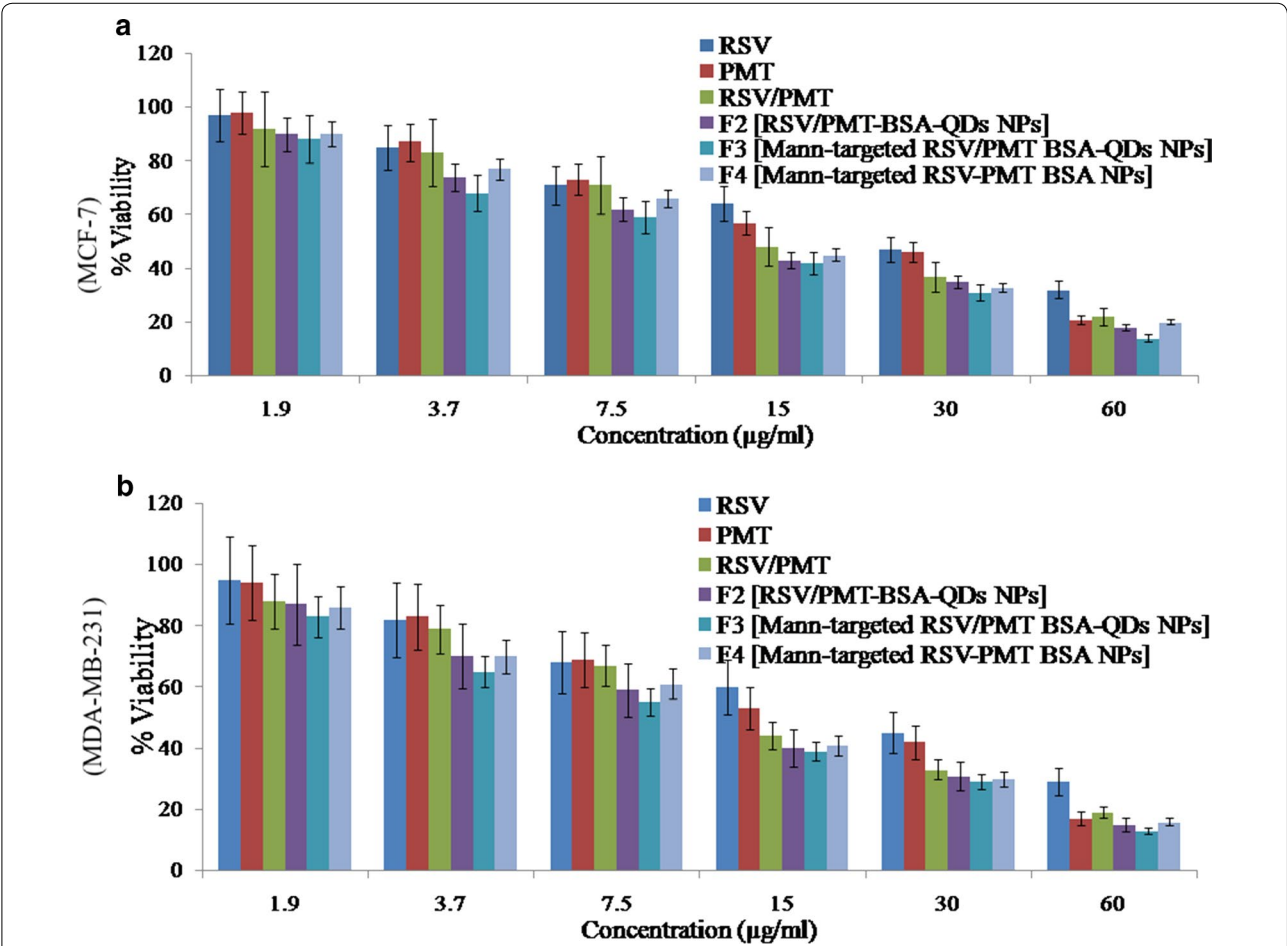


**Fig. 5** Cytotoxicity analysis showing % cell viability of free RSV, free PMT and free RSV/PMT co-solvent compared to the prepared nano-formulations F2 (RSV/PMT-BSA-QDs NPs), F3 (Mann-targeted RSV/PMT BSA-QDs NPs), and F4 (Mann-targeted RSV-PMT BSA NPs) on MCF-7 (a) and MDA-MB-231 (b) breast cancer cell line at the concentration of 0–60 µg/ml after 24 h

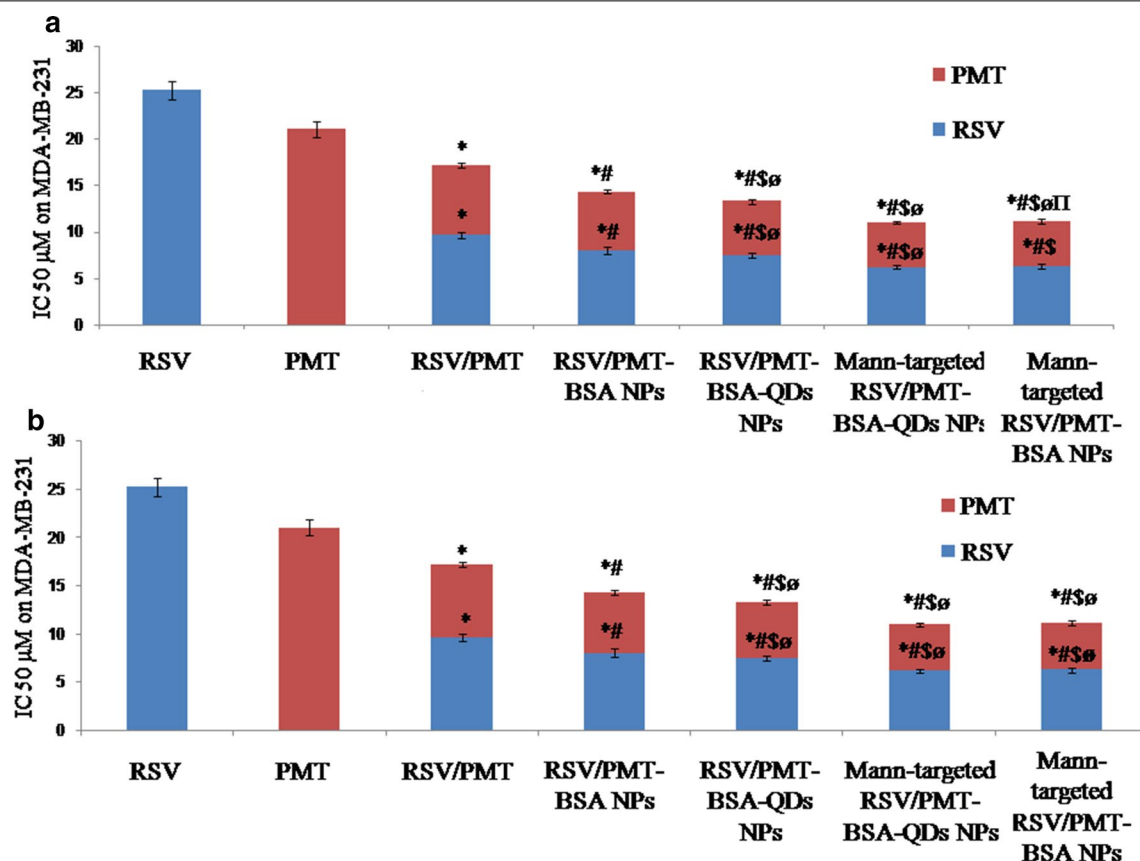


**Fig. 6** IC<sub>50</sub> of free RSV, free PMT and free RSV/PMT co-solvent compared to the prepared nano-formulations F2 (RSV/PMT-BSA-QDs NPs), F3 (Mann-targeted RSV/PMT BSA-QDs NPs), and F4 (Mann-targeted RSV-PMT BSA NPs) on MCF-7 (**a**) and MDA-MB-231 (**b**) breast cancer cell line at the concentration of 0–60 μg/ml after 24 h. \**p* < 0.05 vs. Free drug, #*p* < 0.05 vs. Free RSV/PMT solution, \$*p* < 0.05 vs. the drug in F1, °*p* < 0.05 vs. the drug in F2, "p < 0.05 vs. the drug in F3

**Table 3** IC<sub>50</sub>, Combination Index (CI) and Dose Reduction index (DRI) values of free RSV, free PMT and free RSV/PMT co-solvent compared to the prepared nano-formulations on MCF-7 breast cancer cell line at the concentration of 0–60 μg/ml after 24 h

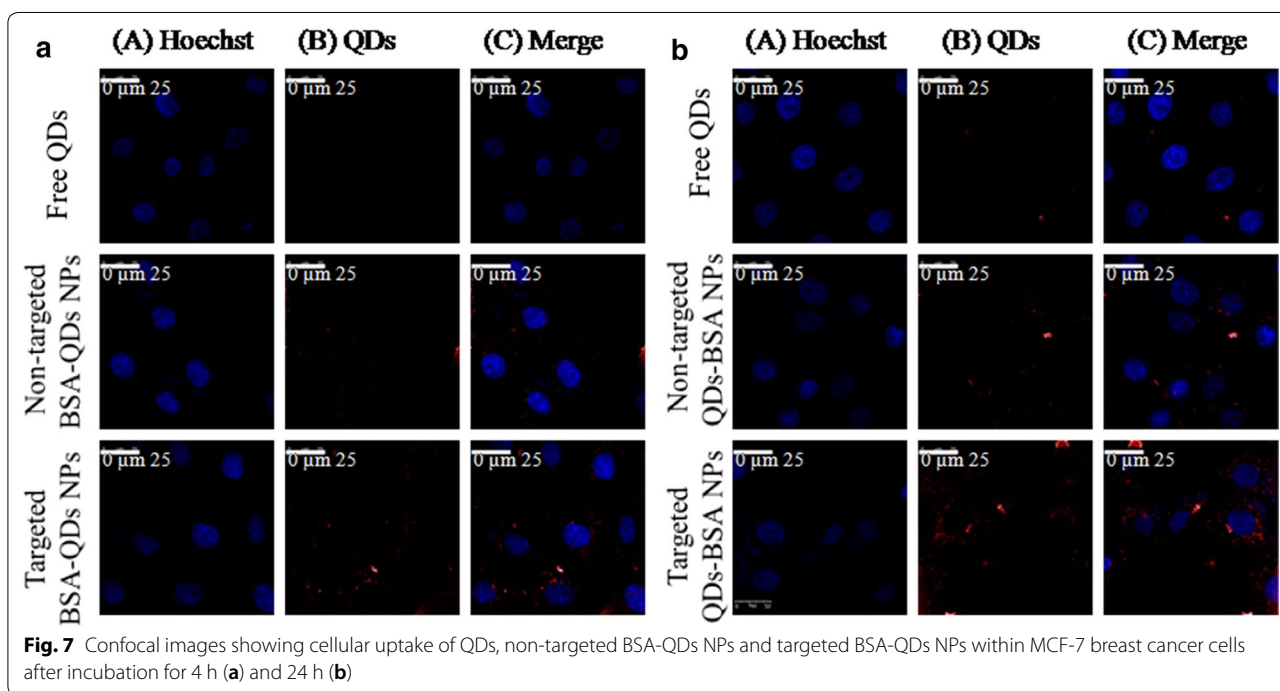
Drug/combo	CI value	Total IC <sub>50</sub> of combination	Dose RSV	Dose PMT	DRI of RSV	DRI of PMT
Free RSV	–	–	22.24	–	–	–
Free PMT	–	–	–	17.21	–	–
Blank NPs	–	–	–	–	–	10,739
RSV/PMT	0.981	13.95	7.86	6.15	2.82	2.79
F1 [RSV/PMT-BSA NPs]	0.926	11.1	6.26	4.89	3.55	3.51
F2 [RSV/PMT-BSA-QDs NPs]	0.909	10.96	6.18	4.83	3.59	3.56
F3 [Mann-targeted RSV/PMT-BSA-QDs NPs]	0.813	9.17	5.17	4.04	4.30	4.25
F4 [Mann-targeted RSV/PMT-BSA NPs]	0.901	10.1	5.69	4.45	3.90	3.86

4.8% hemolysis while lower hemolysis (3.3%) was obtained at a lower NPs concentration of 1 mg/ml. This acceptable hemolytic activity of the prepared NPs could be ascribed to using biodegradable and biocompatible

nanovehicles as albumin, being the major plasma protein. Moreover, albumin was reported to have a preventive effect against erythrocyte hemolysis [55].

**Table 4**  $IC_{50}$ , Combination Index (CI) and Dose Reduction index (DRI) values of free RSV, free PMT and free RSV/PMT co-solvent compared to the prepared nano-formulations on MDA-MB-231 breast cancer cell line at the concentration of 0–60  $\mu\text{g/ml}$  after 24 h

Drug/combo	CI value	Total $IC_{50}$ of combination	Dose RSV	Dose PMT	DRI of RSV	DRI of PMT
RSV	–	–	25.28	–	–	–
PMT	–	–	–	21.06	–	–
Blank NPs	–	–	–	–	–	28,128
RSV/PMT	1.04	17.11	9.65	7.54	2.61	2.79
F1 [RSV/PMT-BSA NPs]	0.975	14.25	8.03	6.28	3.14	3.35
F2 [RSV/PMT-BSA-QDs NPs]	0.931	13.24	7.46	5.83	3.38	3.60
F3 [Mann-targeted RSV/PMT-BSA-QDs NPs]	0.873	10.96	6.18	4.83	4.08	4.35
F4 [Mann-targeted RSV/PMT-BSA NPs]	0.910	11.13	6.27	4.90	4.02	4.29

**Fig. 7** Confocal images showing cellular uptake of QDs, non-targeted BSA-QDs NPs and targeted BSA-QDs NPs within MCF-7 breast cancer cells after incubation for 4 h (a) and 24 h (b)

### Cytotoxicity study

RSV is a phytoestrogen with a greater effect on hormone-responsive MCF-7 breast cancer cells [56]. On the other hand, the cytotoxic drug, PMT inhibits purine and pyrimidine synthesis thus it would have a great impact on MDA-MB-231 triple negative breast cancer cells (TNBC) which are very prone to cytotoxic agents due to the lack of the DNA repairing capability [57]. Blank NPs demonstrated very little toxicity to MCF-7 and MDA-MB-231 cells (viability was >95% after 24 h). The  $IC_{50}$  of free drugs in the mixed RSV/PMT solution at 24 h was 0.5- and 0.7-fold that of RSV on MCF-7 and MDA-MB-231 cells, respectively and was 0.8-fold that of PMT on both

cells. The reduction of  $IC_{50}$  values of the drugs in this combination proved synergistic cytotoxicity which is consistent with the reported synergistic cytotoxicity of RSV/PMT mixture on NSCLC cells [16]. Mann-targeted RSV/PMT BSA-QDs NPs (F3) enhanced the combination potency as demonstrated by the reduced  $IC_{50}$  on both cells compared to the free combined drug solution and the non-targeted RSV/PMT-BSA-QDs NPs (F2) (Fig. 5).

Further statistical analysis was done using CompuSyn software (version 1) described by Chou and Talalay where we used Combination Index (CI) and Dose Reduction Index (DRI) in comparing the different NPs with free drug combination (Fig. 6) [58]. The obtained results

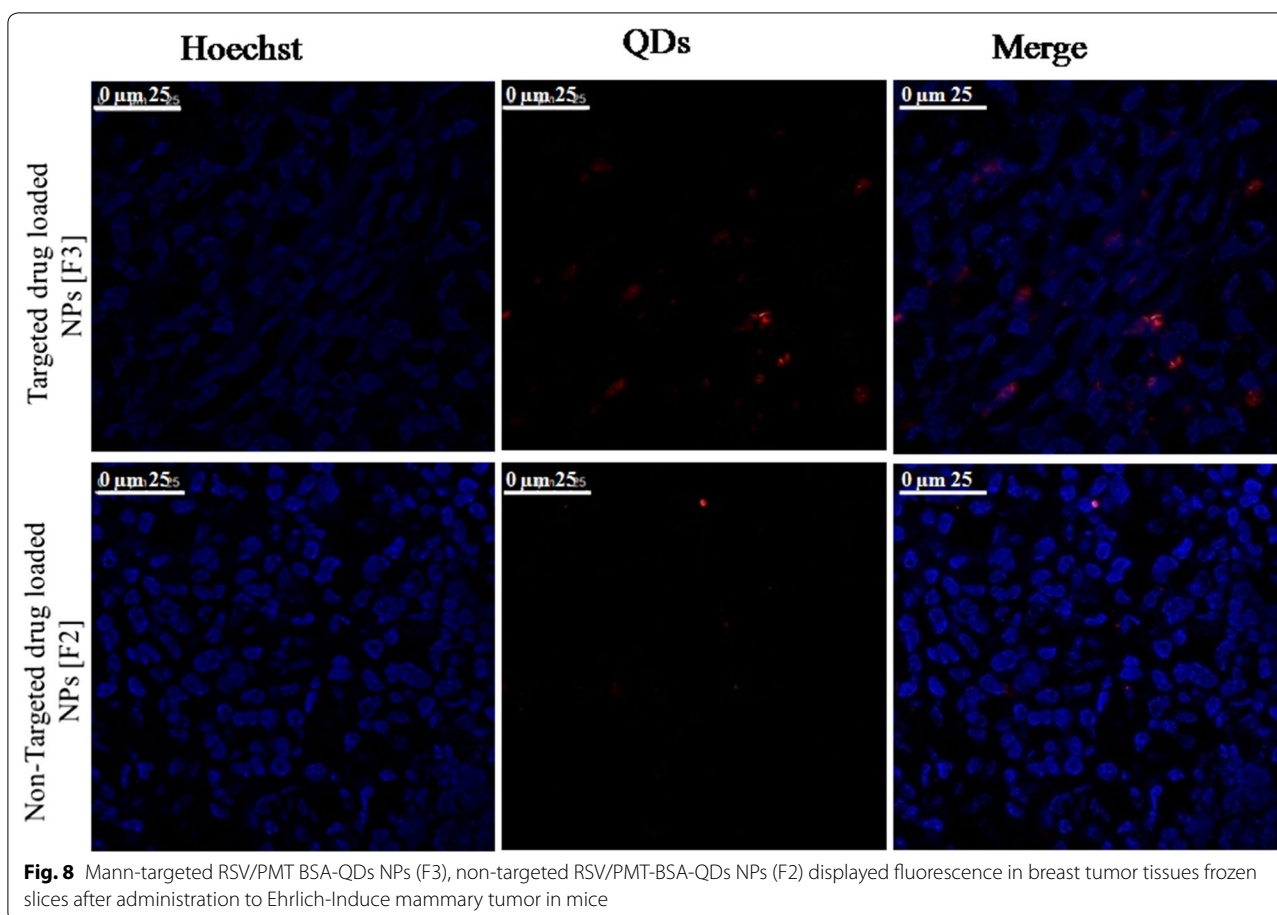


**Fig. 8** Mann-targeted RSV/PMT BSA-QDs NPs (F3), non-targeted RSV/PMT-BSA-QDs NPs (F2) displayed fluorescence in breast tumor tissues frozen slices after administration to Ehrlich-Induce mammary tumor in mice

ensure the superiority of different drug loaded NPs compared to the free combination, especially Mann-targeted RSV/PMT BSA-QDs NPs (F3) where its CI was 0.813 and 0.873 in MCF-7 and MDA-MB-231 cells, respectively, revealing that these NPs succeeded in achieving synergy between RSV and PMT. Moreover, the DRIs of RSV were 4.3 and 4.08 for MCF-7 and MDA-MB-231 cells, respectively in Mann-targeted RSV/PMT BSA-QDs NPs (F3). While the DRIs of PMT were 4.25 and 4.35 for MCF-7 and MDA-MB-231 cells, respectively in Mann-targeted RSV/PMT BSA-QDs NPs (F3). The superior anti-cancer efficacy of mannose-targeted NPs (F3) could be attributed to their higher internalization into breast cancer cells via mannose-receptor mediated endocytosis (Tables 3, 4) [59]. The lower  $IC_{50}$  of BSA-QDs NPs (F2 and F3) than QDs-free BSA NPs F4) may be attributed to ROS generated by QDs which may cause cell apoptosis. A greater cell growth inhibition capability of QDs was also reported by Zhao et al. against HepG2 hepatocellular carcinoma and HeLa cells with 11-fold lower cytotoxicity compared to QSG-7701 human hepatocytes. This preferential killing of cancer cells by QDs can be improved by using more selective targeting ligands which

was achieved in our approach using mannose-targeted BSA-QDs NPs [3]. Thus, the nanotoxicity of QDs can be potentially converted to a new therapeutic option.

#### Intracellular-uptake of NPs

The cellular internalization capacity of Mannose-targeted BSA-QDs NPs, non-targeted BSA-QDs NP and free QDs by MCF-7 breast cancer cells (over-expressing mannose receptors on their surface) was visualized via fluorescent images obtained by confocal laser scanning microscopy and the images were analyzed using Image J software (Fig. 7). The targeted NPs demonstrated higher internalization into the cancer cells in comparison with non-targeted ones as indicated by the strong red fluorescence intensity observed in cells treated with mannose-targeted NPs. On the other hand, weak red fluorescence intensity was demonstrated in the cells incubated with free QDs. After 24 h incubation, the fluorescence intensity for both non-targeted and targeted NPs increased, while free QDs showed the lowest fluorescence intensity. Mannose-functionalized BSA NPs can interact with mannose receptors resulting in enhanced internalization into cancer cells over-expressing those receptors via



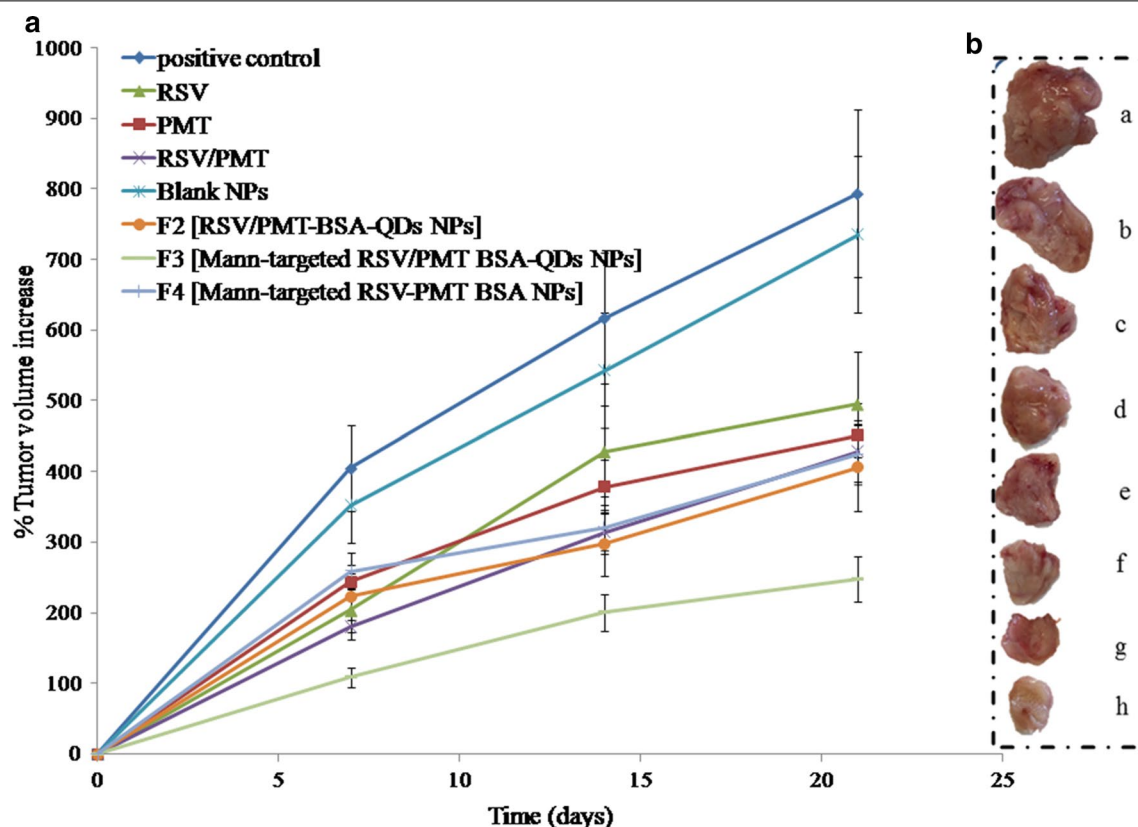


**Fig. 9** In-vivo anti-tumor efficacy showing percentage increase in volume of Ehrlich-induce mammary tumor of mice at indicated time-points along the experiment duration (a) and representative photo of the excised tumor from each group at the end of the study period (b)

endocytosis. Moreover, the uptake of mannose-capped silicon NPs within MCF-7 breast cancer cells was found to be faster than non-functionalized ones. In addition to the role of mannose, albumin-based NPs have been reported to improve accumulation of drugs into tumor cells through interaction with the albumin binding receptors SPARC (secreted protein acidic and rich in cysteine) and albondin (glycoprotein 60) overexpressed on tumor and vascular cells [30].

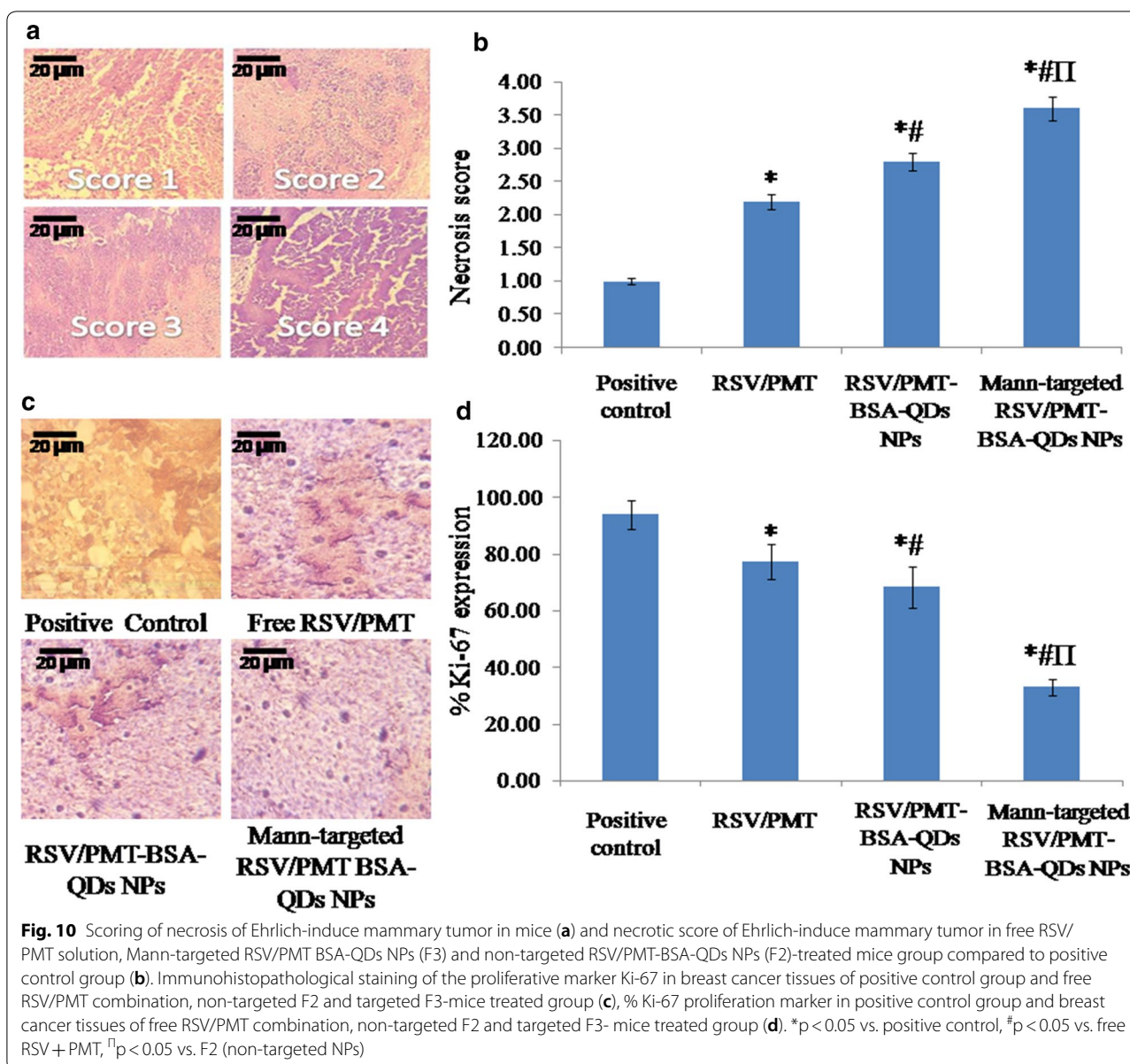
#### Tumor localization of NPs

To trace the NPs accumulation within tumor tissue, the fluorescence of the harvested tumor was visualized via confocal microscope imaging. Higher fluorescence intensity was detected in the tumor tissues of mice groups treated with Mann-targeted RSV/PMT BSA-QDs NPs (F3) compared to non-targeted RSV/PMT-BSA-QDs NPs (F2) which ensures their effective localization in the tumor tissues (Fig. 8). Thus, active targeting with mannose has enhanced the tumor accumulation of NPs in comparison with non-targeted ones. The strong fluorescence of QDs enabled imaging of the NPs accumulated

in tumor tissue thus confirming the suitability of our NPs for theranostic applications.

#### In vivo anti-tumor efficacy

The in vivo antitumor activity of the dual-drug loaded BSA NPs was further investigated on Ehrlich ascites mammary tumor bearing mice. At the end of study, the un-treated positive control group had demonstrated the highest and uncontrollable % increase of tumor volume corresponding to 793.98%. Co-administration of free RSV/PMT co-solvent system succeeded in limiting the % increase of tumor volume to 429% which is higher than each drug alone. On the other direction, the developed NPs demonstrated a significant ( $p < 0.05$ ) remarkable reduction of tumor growth in comparison with the positive control and free drug-treated groups. The most powerful suppression of tumor growth was demonstrated by Mann-targeted RSV/PMT BSA-QDs NPs (F3) showing 247% increase in tumor volume, respectively compared to 405% for non-targeted RSV/PMT-BSA-QDs NPs (F2). Moreover, it is worthy to note that coupling of QDs to BSA NPs was found to exert an additional suppressive effect on tumor growth besides their imaging



capability. Mann-targeted RSV/PMT BSA-QDs NPs (F3) displayed 247% increase in tumor volume which was significantly ( $p < 0.05$ ) lower than its counterpart NPs without QDs (Mann-targeted RSV-PMT BSA NPs, F4) with 425% increase in tumor volume (Fig. 9a, b). The *in vivo* therapeutic action of QDs was previously proved using hepatocellular carcinoma animal model where Zhao et al. prepared polyamine-coated CdSe/ZnS QDs and tested its therapeutic effect on hepatocellular carcinoma Hep G2, and hepatocyte QSG-7701 cells. It was found that the  $IC_{50}$  values of QDs at 48 h are 2.51 and 26.65  $\mu$ M for HepG2 and QSG-7701 cells, respectively. This approximately 11-fold difference reflected the preferential cell

killing capabilities of QDs between the two cell lines, a desired property that can be further improved by using more selective targeting ligands. Several lines of evidence suggest that the antitumor effect of QDs rises from ROS-induced cell apoptosis. *In vivo*, the mean survival time of tumor-bearing mice could be extended by 2.5 times when treated with QDs. These results demonstrated the possibility of converting nano-toxicity of QDs to antitumor activity [3].

Moreover, animals' body weight changes (as an important pointer for animal health) were recorded during the study period. It was observed that mice treated with free drugs appeared weak and demonstrated a reduction in

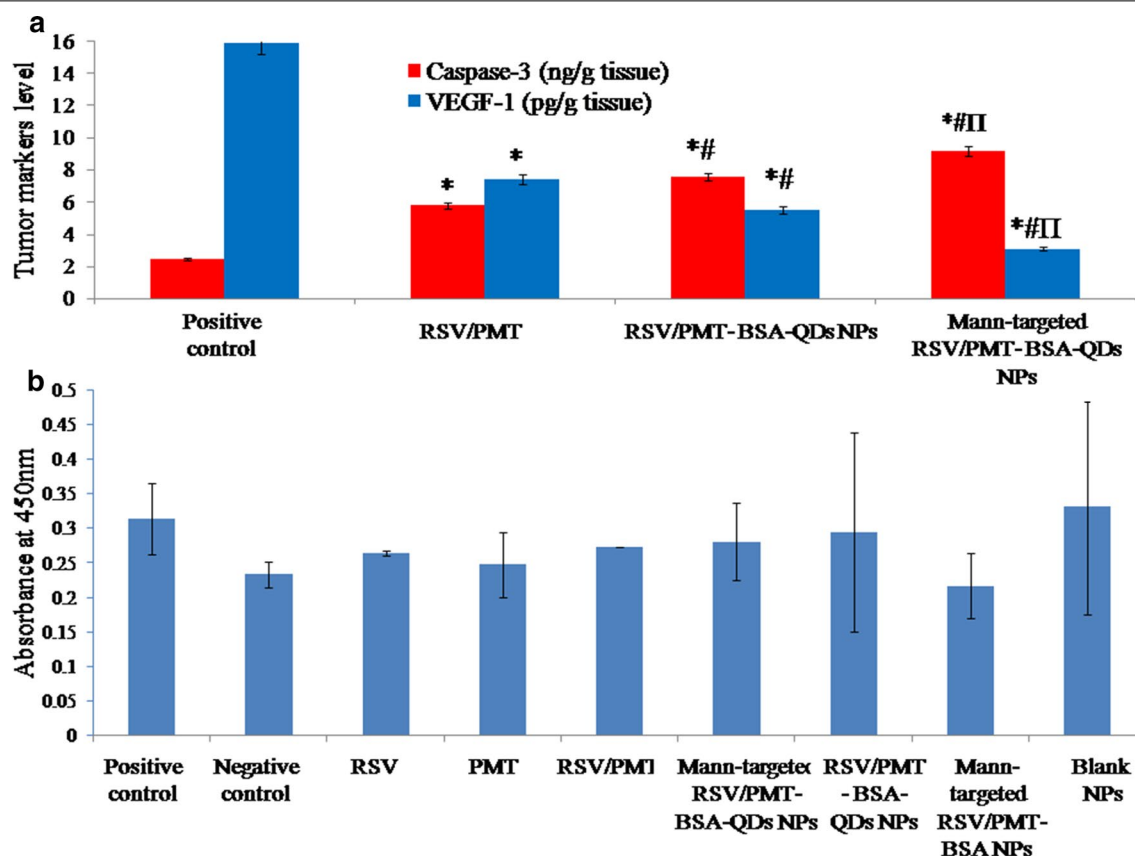


**Fig. 11** Comparison between the studied groups [free RSV/PMT co-solvent Mann-targeted RSV/PMT BSA-QDs NPs (F3) and non-targeted RSV/PMT-BSA-QDs NPs (F2)-mice treated groups] in addition to the positive control group according to active caspase-3 and VEGF-1 levels (a). \* $p < 0.05$  vs. positive control, # $p < 0.05$  vs. free RSV + PMT,  $\Pi p < 0.05$  vs. F2 (non-targeted NPs). Assessment of immunogenicity of the BSA nano-delivery systems (b). No significant difference was found in immunogenic response between the treated groups and the control group ( $p > 0.05$  by ANOVA test and Tukey–Kramer post hoc multiple comparison test)

their body weight after treatment while no observable bodyweight loss was noticed in mice groups treated with drug-loaded NPs (F2 and F3). Thus, the prepared NPs succeeded to reduce the toxicity of free drugs throughout experimental period (Details of the body weight measurements are in Additional file 1: Table S1, Figure S5).

Figure 10a, b showed scoring of necrosis of Ehrlich-induced mammary tumor in mice. The targeted and non-targeted drug-loaded NPs (F3 and F2, respectively) showed significantly ( $p < 0.05$ ) higher necrosis compared to the positive control group thus confirming their efficacy. Furthermore, immunohistochemical analysis revealed a significantly ( $p < 0.05$ ) reduced staining density of the proliferation protein Ki-67 in the tumor samples of mice treated with targeted and non-targeted NPs (F3 and F2, respectively) (32.9 and 68.31% Ki-67 expression, respectively) compared to positive control groups (93.92% Ki-67 expression) (Fig. 10c, d). This reflected the particularly high suppressive power of NPs on

proliferation of tumor cells thereby inhibiting the tumor growth [60].

Relative to the positive control group, the targeted and non-targeted dual drug-loaded NPs (F3 and F2, respectively) exhibited a significantly higher ( $p < 0.05$ ) apoptotic effect with 3.724- and 3.07-folds increase in Caspase-3 level, respectively versus only 2.35-folds elevation for free RSV/PMT combination (Fig. 11a) [14]. Moreover, the targeted and non-targeted NPs (F3 and F2, respectively) also succeeded to significantly ( $p < 0.05$ ) reduce the level of angiogenic factor VEGF-1 by 5.125- and 2.883-folds, respectively versus 2.127-folds reduction for free RSV/PMT combination as compared to the positive control (Fig. 11a) [28].

#### Immunogenicity of the BSA nano-delivery system

One of the concerns with the use of protein-based NPs is the risk of immunogenicity when administered in vivo. Many studies have used albumin-based NPs by i.v. injections and no immunogenic or antigenic response to

albumin NPs was reported [30]. In our study, no significant difference in the level of anti-BSA IgG antibodies was observed between any of the treated groups and the non-treated group. This demonstrates that under the experimental conditions of the animal trial, the BSA delivery system was not immunogenic (Fig. 11b).

From all the above mentioned results, it is clear that the anti-tumor efficacy of PMT has been enhanced in a multi-step approach including: (a) co-administration of RSV with PMT, may maximize the therapeutic effect of both drugs via modulating different signaling pathways thus leading to higher anti-tumor efficacy, reduced toxicity and may also overcome the multi-drug resistance, (b) incorporation of the drug combination into BSA NPs, to benefit from albumin-mediated accumulation of drugs into tumor tissue via binding to albumin and SPARC, the small NP size-mediated EPR effect as well as the sustained drug release profile. Specifically, covalent attachment of PMT to albumin structure hindered its release into circulation and enabled tumor-specific drug release, (c) active targeting of the dual drug-loaded NPs via mannose coupling imparted the ability to interact with mannose receptors overexpressed on the surface of breast cancer cells allowing more internalization of NPs and hence better drug accumulation in tumor cells, (d) incorporation of QDs by conjugation to NPs surface not only enabled imaging of the tumor for theranostic applications and revealing NPs tissue distribution but also contributed to enhance the anti-tumor efficacy may be via ROS generation mechanism. Moreover, covalent coupling rather than physical encapsulation enables tumor-specific release of QDs thus reducing their systemic toxicity.

## Conclusion

In summary, we designed a multifunctional nanoplatform of mannose-coupled BSA-QD NPs for targeted synergistic co-delivery of PMT and RSV as well as to enable a fluorescence-based imaging of breast cancer cells. The formulated dual drug-loaded nanocarriers demonstrated optimal physicochemical properties of small size, high drug loading, retarded drug release, low hemolytic activity, good colloidal and serum stability as well as non-immunogenicity. This nanoplatform could be successfully internalized by breast cancer cells resulting in enhanced cytotoxicity. In addition, systemic delivery of this nanoplatform remarkably reduced the tumor volume in vivo. Finally, this work provides a new theranostic platform of mannosylated albumin-QD nanohybrids for targeted co-delivery of PMT and RSV to breast cancer cells.

## Additional file

**Additional file 1.** The additional information file include Characterization of the synthesized CdTe QDs, Preparation of PMT-conjugated BSA (PMT-BSA), Preparation of RSV-PC complex, Solid state characterization including FTIR Spectroscopy and DSC Thermograms, methodology of physicochemical characterization of dual drug-loaded BSA NPs including Drug loading and encapsulation efficiency, Particle size and zeta potential analysis, In vitro drug release, Physical stability study, Freeze drying and redispersibility, Morphological analysis, In vitro hemolysis and serum stability, In vitro cytotoxicity, Cellular-uptake study, the methodology of In vivo studies including Tumor growth biomarkers, Histopathological analysis, Immunohistochemical analysis, Quantification of the proliferative marker Ki-67 by image analysis technique and tissue localization of NPs, Immunogenicity of the nano-delivery system, Statistical analysis, the analysis of the FTIR study and body weight measurement study and the table of body weight average of mice groups. It also includes five figures which are: **Figure S1.** Physicochemical properties of the prepared RSV/PMT-BSA-QDs NPs (F2); size distribution diagram of non-targeted drug loaded BSA-QDs NPs (F2) (A) and their corresponding zeta potential distribution (B). **Figure S2.** A photograph illustrating the phenol sulfuric acid test of BSA (A) and Mannose-BSA NPs conjugate (B). **Figure S3.** <sup>1</sup>H-NMR spectra of mannose-BSA, BSA and mannose revealing the presence of mannose protons in the spectra of mannose-BSA conjugate. **Figure S4.** DSC thermogram of RSV, RSV-PC complex, PMT, RSV/PMT-BSA-QDs NPs (F2) and Mann-targeted RSV/PMT BSA-QDs NPs (F3) (A) and Fourier Transform Infrared (FTIR) spectra of RSV, RSV-PC complex, PMT, F2 and F3 (B). **Figure S5.** In-vivo anti-tumor efficacy showing change in body weights measurements of mice at indicated time-points along the experiment duration (C).

## Abbreviations

BSA NPs: bovine serum albumin nanoparticles; CLRs: C-type lectin receptors; CI: Combination Index; DSC: differential scanning calorimetry; DRI: Dose Reduction Index; DLS: dynamic light scattering microscope; EAT: Ehrlich ascites tumor; ELISA: enzyme linked immunosorbent assay; EPR: enhanced permeability and retention; FBS: fetal bovine serum; HPLC: high performance liquid chromatography; IC<sub>50</sub>: inhibitory concentration; MR: mannose receptor; MDR: multi-drug resistance; NMR: nuclear magnetic resonance; PMT: pemetrexed; PBS: phosphate buffer saline; PC: phosphatidylcholine; PL: photoluminescence; PDI: polydispersity index; QDs: quantum dots; ROS: reactive oxygen species; RSV: resveratrol; RES: reticuloendothelial system; SPARC: secreted protein acidic and rich cysteine; TEM: transmission electron microscope; TNBC: triple negative breast cancer; VEGF-1: vascular endothelial growth factor.

## Authors' contributions

DGZ and AOE designed the study and prepared the original manuscript. SME supervised the preparation and characterization of CdTe QDs. MWH conducted the in vitro cytotoxicity studies as well as in vivo animal study and analyzed the data. MB performed the immunogenicity of BSA test. SNK analyzed the results of the FTIR and NMR studies. KAE, AOE and JYF revised the whole manuscript. All authors were engaged in commenting on the manuscript. All authors read and approved the final manuscript.

## Author details

<sup>1</sup> Cancer Nanotechnology Research Laboratory (CNRL), Faculty of Pharmacy, Alexandria University, Alexandria 21521, Egypt. <sup>2</sup> Department of Industrial Pharmacy, Faculty of Pharmacy, Alexandria University, Alexandria 21521, Egypt. <sup>3</sup> Department of Materials Science, Institute of Graduate Studies and Research, Alexandria University, Alexandria 21526, Egypt. <sup>4</sup> Department of Pharmacology and Toxicology, Faculty of Pharmacy, Damanhour University, Damanhur, Egypt. <sup>5</sup> Department of Chemistry, Faculty of Science, Alexandria University, Alexandria 21321, Egypt. <sup>6</sup> Department of Microbiology and Immunology, Faculty of Pharmacy, Alexandria University, Alexandria 21521, Egypt. <sup>7</sup> Pharmaceuticals Laboratory, Graduate Institute of Natural Products, Chang Gung University,



Taoyuan 333, Taiwan. <sup>8</sup> Research Center for Industry of Human Ecology and Research Center for Chinese Herbal Medicine, Chang Gung University of Science and Technology, Kweishan, Taoyuan 333, Taiwan. <sup>9</sup> Department of Anesthesiology, Chang Gung Memorial Hospital, Kweishan, Taoyuan 333, Taiwan. <sup>10</sup> Present Address: Division of Engineering in Medicine, Department of Medicine, Brigham and Women's Hospital, Harvard Medical School, Boston, MA 02115, USA. <sup>11</sup> Harvard-MIT Division of Health Sciences and Technology, Cambridge, MA 02139, USA.

#### Acknowledgements

The authors would like to thank Science and Technology Development Fund (STDF), Ministry of Scientific Research, Egypt for their financial support.

#### Competing interests

The authors declare that they have no competing interests.

#### Availability of data and materials

The dataset used or analyzed during the study are available from the corresponding author on reasonable request.

#### Consent for publication

Not applicable.

#### Ethics approval and consent to participate

The study was approved by the local ethics committee.

#### Funding

This work was supported by the research Grant (No. 15053) of Science and Technology Development Fund (STDF), Ministry of Scientific Research, Egypt.

#### Publisher's Note

Springer Nature remains neutral with regard to jurisdictional claims in published maps and institutional affiliations.

Received: 15 October 2018 Accepted: 7 January 2019

Published online: 19 January 2019

#### References

- Elzoghby AO, Hemasa AL, Freag MS. Hybrid protein-inorganic nanoparticles: from tumor-targeted drug delivery to cancer imaging. *J Control Release*. 2016;243:303–22.
- Derfus AM, Chan WC, Bhatia SN. Probing the cytotoxicity of semiconductor quantum dots. *Nano Lett*. 2004;4(1):11–8.
- Zhao M-X, et al. Therapeutic effect of quantum dots for cancer treatment. *RSC Adv*. 2016;6(114):113791–5.
- Freag M, Elzoghby A. Protein-inorganic nanohybrids: a potential symbiosis in tissue engineering. *Curr Drug Targets*. 2018;19(16):1897–904.
- Johari-Ahar M, et al. Methotrexate-conjugated quantum dots: synthesis, characterisation and cytotoxicity in drug resistant cancer cells. *J Drug Target*. 2016;24(2):120–33.
- Abdelaziz HM, et al. Inhalable particulate drug delivery systems for lung cancer therapy: nanoparticles, microparticles, nanocomposites and nanoaggregates. *J Control Release*. 2018;269:374–92.
- Freag MS. Hyaluronate-lipid nanohybrids: fruitful harmony in cancer targeting. *Curr Pharm Des*. 2017;23:5283–91.
- Ye Z, et al. Tumour-targeted drug delivery with mannose-functionalized nanoparticles self-assembled from amphiphilic  $\beta$ -cyclodextrins. *Chem Eur J*. 2016;22(43):15216–21.
- Qi Z, et al. Multivalency at interfaces: supramolecular carbohydrate-functionalized graphene derivatives for bacterial capture, release, and disinfection. *Nano Lett*. 2015;15(9):6051–7.
- Adjei AA. Pemetrexed (Alimta<sup>®</sup>): a novel multitargeted antifolate agent. *Expert Rev Anticancer Ther*. 2003;3(2):145–56.
- Lu N, et al. Superior antimetastatic effect of pemetrexed-loaded gelatinase-responsive nanoparticles in a mouse metastasis model. *Anticancer Drugs*. 2012;23(10):1078–88.
- Küçüktürkmen B, et al. Co-delivery of pemetrexed and miR-21 antisense oligonucleotide by lipid-polymer hybrid nanoparticles and effects on glioblastoma cells. *Drug Dev Ind Pharm*. 2017;43(1):12–21.
- Neves AR, et al. Novel resveratrol nanodelivery systems based on lipid nanoparticles to enhance its oral bioavailability. *Int J Nanomed*. 2013;8:177.
- Elzoghby AO, et al. Superiority of aromatase inhibitor and cyclooxygenase-2 inhibitor combined delivery: hyaluronate-targeted versus PEGylated protamine nanocapsules for breast cancer therapy. *Int J Pharm*. 2017;529(1–2):178–92.
- Elzoghby AO, et al. Multi-reservoir phospholipid shell encapsulating protamine nanocapsules for co-delivery of letrozole and celecoxib in breast cancer therapy. *Pharm Res*. 2017;34(9):1956–69.
- Chen R-S, et al. Pemetrexed downregulates ERCC1 expression and enhances cytotoxicity effected by resveratrol in human nonsmall cell lung cancer cells. *Naunyn Schmiedeberg's Arch Pharmacol*. 2013;386(12):1047–59.
- Hwang K-E, et al. Pemetrexed induces apoptosis in malignant mesothelioma and lung cancer cells through activation of reactive oxygen species and inhibition of sirtuin 1. *Oncol Rep*. 2015;33(5):2411–9.
- Ebrahim S, et al. CdTe quantum dots as a novel biosensor for *Serratia marcescens* and lipopolysaccharide. *Spectrochim Acta Part A Mol Biomol Spectrosc*. 2015;150:212–9.
- Nakajima N, Ikada Y. Mechanism of amide formation by carbodiimide for bioconjugation in aqueous media. *Bioconjug Chem*. 1995;6(1):123–30.
- El-Far SW, et al. Phytosomal bilayer-enveloped casein micelles for code-livery of monascus yellow pigments and resveratrol to breast cancer. *Nanomedicine*. 2018;13(5):481–99.
- Elzoghby AO, et al. Swellable floating tablet based on spray-dried casein nanoparticles: near-infrared spectral characterization and floating matrix evaluation. *Int J Pharm*. 2015;491(1–2):13–22.
- Freag MS, Saleh WM, Abdallah OY. Exploiting polymer blending approach for fabrication of buccal chitosan-based composite sponges with augmented mucoadhesive characteristics. *Eur J Pharm Sci*. 2018;120:10–9.
- Elzoghby AO, et al. Shell-crosslinked zein nanocapsules for oral codelivery of exemestane and resveratrol in breast cancer therapy. *Nanomedicine*. 2017;12(24):2785–805.
- Khattab SN, et al. Design and synthesis of new s-triazine polymers and their application as nanoparticulate drug delivery systems. *New J Chem*. 2016;40(11):9565–78.
- El-Far SW, et al. Phytosomal bilayer-enveloped casein micelles for code-livery of monascus yellow pigments and resveratrol to breast cancer. *Nanomedicine*. 2018;13(5):481–99.
- Elgindy N, et al. Biopolymeric nanoparticles for oral protein delivery: design and in vitro evaluation. *J Nanomed Nanotechnol*. 2011;2(3):110.
- Zhen X, et al. Cellular uptake, antitumor response and tumor penetration of cisplatin-loaded milk protein nanoparticles. *Biomaterials*. 2013;34(4):1372–82.
- Freag MS, et al. Layer-by-layer-coated lyotropic liquid crystalline nanoparticles for active tumor targeting of rapamycin. *Nanomedicine*. 2016;11(22):2975–96.
- Podaralla S, et al. Synthesis of novel biodegradable methoxy poly (ethylene glycol)-zein micelles for effective delivery of curcumin. *Mol Pharm*. 2012;9(9):2778–86.
- Elzoghby AO, Elgohary MM, Kamel NM. Chapter six-implications of protein- and peptide-based nanoparticles as potential vehicles for anti-cancer drugs. *Adv Protein chem Struct Biol*. 2015;98:169–221.
- Elzoghby A. Editorial (thematic issue: nanocarriers based on natural polymers as platforms for drug and gene delivery applications). *Curr Pharm Des*. 2016;22(22):3303–4.
- Sabra S, et al. Self-assembled nanocarriers based on amphiphilic natural polymers for anti-cancer drug delivery applications. *Curr Pharm Des*. 2017;23:5213–29.
- Feteha M, et al. Effects of mercaptopropionic acid as a stabilizing agent and Cd: Te ion ratio on CdTe and CdHgTe quantum dots properties. *J Mater Sci Mater Electron*. 2012;23(11):1938–43.
- Mandal A, Tamai N. Influence of acid on luminescence properties of thioglycolic acid-capped CdTe quantum dots. *J Phys Chem C*. 2008;112(22):8244–50.

35. Zorman B, Ramakrishna MV, Friesner R. Quantum confinement effects in CdSe quantum dots. *J Phys Chem*. 1995;99(19):7649–53.
36. Debruyne D, et al. The pH-dependent photoluminescence of colloidal CdSe/ZnS quantum dots with different organic coatings. *Nanotechnology*. 2015;26(25):255703.
37. He X, et al. Encapsulation of teniposide into albumin nanoparticles with greatly lowered toxicity and enhanced antitumor activity. *Int J Pharm*. 2015;487(1):250–9.
38. Zhang Q, et al. A perspective on the Maillard reaction and the analysis of protein glycation by mass spectrometry: probing the pathogenesis of chronic disease. *J Proteome Res*. 2008;8(2):754–69.
39. Dubois M, et al. Colorimetric method for determination of sugars and related substances. *Anal Chem*. 1956;28(3):350–6.
40. Beljaars L, et al. Albumin modified with mannose 6-phosphate: a potential carrier for selective delivery of antifibrotic drugs to rat and human hepatic stellate cells. *Hepatology*. 1999;29(5):1486–93.
41. Das S, Banerjee R, Bellare J. Aspirin loaded albumin nanoparticles by coacervation: implications in drug delivery. *Trends Biomater Artif Organs*. 2005;18(2):203–12.
42. Freag MS, Saleh WM, Abdallah OY. Self-assembled phospholipid-based phytosomal nanocarriers as promising platforms for improving oral bio-availability of the anticancer celestrol. *Int J Pharm*. 2018;535(1–2):18–26.
43. Jithan A, et al. Preparation and characterization of albumin nanoparticles encapsulating curcumin intended for the treatment of breast cancer. *Int J Pharm Invest*. 2011;1(2):119.
44. Sepehri N, et al. Human serum albumin conjugates of 7-ethyl-10-hydroxycamptothecin (SN38) for cancer treatment. *BioMed Res Int*. 2014;2014:963507.
45. Dosio F, et al. Folate-mediated targeting of albumin conjugates of paclitaxel obtained through a heterogeneous phase system. *Int J Pharm*. 2009;382(1):117–23.
46. Freag MS, Elnaggar Y, Abdallah OY. Lyophilized phytosomal nanocarriers as platforms for enhanced diosmin delivery: optimization and ex vivo permeation. *Int J Nanomedicine*. 2013;8:2385–97.
47. Torky AS, et al. Novel skin penetrating berberine oleate complex capitalizing on hydrophobic ion pairing approach. *Int J Pharm*. 2018;549(1–2):76–86.
48. Soni K, Mujtaba A, Kohli K. Lipid drug conjugate nanoparticle as a potential nanocarrier for the oral delivery of pemetrexed diacid: formulation design, characterization, ex vivo, and in vivo assessment. *Int J Biol Macromol*. 2017;103:139–51.
49. Zhang J-Y, et al. Preparation of the albumin nanoparticle system loaded with both paclitaxel and sorafenib and its evaluation in vitro and in vivo. *J Microencapsul*. 2011;28(6):528–36.
50. Kabary DM, et al. Hyaluronate/lactoferrin layer-by-layer-coated lipid nanocarriers for targeted co-delivery of rapamycin and berberine to lung carcinoma. *Colloids Surf B*. 2018;169:183–94.
51. Elgindy N, et al. Lyophilization monophase solution technique for preparation of amorphous flutamide dispersions. *Drug Dev Ind Pharm*. 2011;37(7):754–64.
52. Anhorn MG, Mahler H-C, Langer K. Freeze drying of human serum albumin (HSA) nanoparticles with different excipients. *Int J Pharm*. 2008;363(1):162–9.
53. Göppert T, Müller R. Adsorption kinetics of plasma proteins on solid lipid nanoparticles for drug targeting. *Int J Pharm*. 2005;302(1):172–86.
54. Sabra SA, et al. Self-assembled amphiphilic zein-lactoferrin micelles for tumor targeted co-delivery of rapamycin and wogonin to breast cancer. *Eur J Pharm Biopharm*. 2018;128:156–69.
55. Elblbesy MA. Hemocompatibility of albumin nanoparticles as a drug delivery system—an in vitro study. *J Biomater Nanobiotechnol*. 2016;7(02):64.
56. Sakamoto T, et al. Effects of diverse dietary phytoestrogens on cell growth, cell cycle and apoptosis in estrogen-receptor-positive breast cancer cells. *J Nutr Biochem*. 2010;21(9):856–64.
57. Jia T, et al. The differential susceptibilities of MCF-7 and MDA-MB-231 cells to the cytotoxic effects of curcumin are associated with the PI3 K/Akt-SKP2-Cip/Kips pathway. *Cancer Cell Int*. 2014;14(1):126.
58. Chou T, Talalay P. Applications of the median-effect principle for the assessment of low-dose risk of carcinogens and for the quantitation of synergism and antagonism of chemotherapeutic agents. *New Avenues Dev Cancer Chemother*. 1987;8:37–64.
59. Byeon HJ, et al. Doxorubicin-loaded nanoparticles consisted of cationic- and mannose-modified-albumins for dual-targeting in brain tumors. *J Control Release*. 2016;225:301–13.
60. Kaczmarek E, Gorna A, Majewski P. Techniques of image analysis for quantitative immunohistochemistry. *Rocz Akad Med Białymst*. 2004;49(Suppl 1):155–8.

**Ready to submit your research? Choose BMC and benefit from:**

- fast, convenient online submission
- thorough peer review by experienced researchers in your field
- rapid publication on acceptance
- support for research data, including large and complex data types
- gold Open Access which fosters wider collaboration and increased citations
- maximum visibility for your research: over 100M website views per year

**At BMC, research is always in progress.**

Learn more [biomedcentral.com/submissions](https://biomedcentral.com/submissions)



## ORIGINAL ARTICLE

# Gut commensal *Parabacteroides goldsteinii* plays a predominant role in the anti-obesity effects of polysaccharides isolated from *Hirsutella sinensis*

Tsung-Ru Wu,<sup>1,2</sup> Chuan-Sheng Lin,<sup>1,3,4,5,6</sup> Chih-Jung Chang,<sup>1,3,4,5,6</sup> Tzu-Lung Lin,<sup>1</sup> Jan Martel,<sup>3,5</sup> Yun-Fei Ko,<sup>5,7,8</sup> David M Ojcius,<sup>3,5,9</sup> Chia-Chen Lu,<sup>10</sup> John D Young,<sup>3,5,7,8,11</sup> Hsin-Chih Lai<sup>1,3,4,5,6,12,13,14</sup>

► Additional material is published online only. To view, please visit the journal online (<http://dx.doi.org/10.1136/gutjnl-2017-315458>).

For numbered affiliations see end of article.

## Correspondence to

Dr John D Young, Center for Molecular and Clinical Immunology, Chang Gung University, Gueishan, Taoyuan 33302, Taiwan; [jdyoung@mail.cgu.edu.tw](mailto:jdyoung@mail.cgu.edu.tw) and Dr Hsin-Chih Lai, Department of Medical Biotechnology and Laboratory Science, College of Medicine, Chang Gung University, Gueishan, Taoyuan 33302, Taiwan; [hclai@mail.cgu.edu.tw](mailto:hclai@mail.cgu.edu.tw)

T-RW, C-SL and C-JC contributed equally.

Received 13 October 2017

Revised 22 June 2018

Accepted 22 June 2018



© Author(s) (or their employer(s)) 2018. No commercial re-use. See rights and permissions. Published by BMJ.

**To cite:** Wu T-R, Lin C-S, Chang C-J, et al. Gut Epub ahead of print: [please include Day Month Year]. doi:10.1136/gutjnl-2017-315458

## ABSTRACT

**Objective** The medicinal fungus *Ophiocordyceps sinensis* and its anamorph *Hirsutella sinensis* have a long history of use in traditional Chinese medicine for their immunomodulatory properties. Alterations of the gut microbiota have been described in obesity and type 2 diabetes. We examined the possibility that *H. sinensis* mycelium (HSM) and isolated fractions containing polysaccharides may prevent diet-induced obesity and type 2 diabetes by modulating the composition of the gut microbiota.

**Design** High-fat diet (HFD)-fed mice were treated with HSM or fractions containing polysaccharides of different molecular weights. The effects of HSM and polysaccharides on the gut microbiota were assessed by horizontal faecal microbiota transplantation (FMT), antibiotic treatment and 16S rDNA-based microbiota analysis.

**Results** Fraction H1 containing high-molecular weight polysaccharides (>300 kDa) considerably reduced body weight gain (~50% reduction) and metabolic disorders in HFD-fed mice. These effects were associated with increased expression of thermogenesis protein markers in adipose tissues, enhanced gut integrity, reduced intestinal and systemic inflammation and improved insulin sensitivity and lipid metabolism. Gut microbiota analysis revealed that H1 polysaccharides selectively promoted the growth of *Parabacteroides goldsteinii*, a commensal bacterium whose level was reduced in HFD-fed mice. FMT combined with antibiotic treatment showed that neomycin-sensitive gut bacteria negatively correlated with obesity traits and were required for H1's anti-obesogenic effects. Notably, oral treatment of HFD-fed mice with live *P. goldsteinii* reduced obesity and was associated with increased adipose tissue thermogenesis, enhanced intestinal integrity and reduced levels of inflammation and insulin resistance.

**Conclusions** HSM polysaccharides and the gut bacterium *P. goldsteinii* represent novel prebiotics and probiotics that may be used to treat obesity and type 2 diabetes.

## INTRODUCTION

Obesity is a metabolic disorder associated with increased risk of developing type 2 diabetes mellitus, cardiovascular disease and cancer.<sup>1–4</sup> Obesity is characterised by body weight gain, accumulation

## Significance of this study

### What is already known on this subject?

- Diet-induced dysbiosis and leaky gut contribute to the development of obesity and type 2 diabetes.
- Polysaccharides derived from medicinal fungi such as *Ganoderma lucidum* reduce weight gain in obese mice.
- *Hirsutella sinensis* mycelium (HSM) produces anti-inflammatory, hypoglycaemic and lipid-lowering effects in animals.

### What are the new findings?

- High-molecular weight polysaccharides (>300 kDa) derived from HSM produce anti-obesogenic and antidiabetic effects in obese mice.
- HSM polysaccharides reverse obesity-induced gut dysbiosis and leaky gut, and reduce metabolic endotoxemia, inflammation, insulin resistance and dyslipidemia.
- HSM polysaccharides modulate the composition of the gut microbiota, notably by enriching the gut bacterium *Parabacteroides goldsteinii*.
- Oral treatment of obese mice with live *P. goldsteinii* bacteria prevents body weight gain, improves intestinal integrity and reduces inflammation and insulin resistance.

### How might it impact on clinical practice in the foreseeable future?

- High-molecular weight polysaccharides derived from HSM represent novel prebiotics to treat obesity and type 2 diabetes.
- *P. goldsteinii* is a novel probiotic bacterium that may be used to treat obesity and associated metabolic disorders.

of fat tissues, gut microbiota dysbiosis,<sup>5</sup> leaky gut,<sup>6</sup> metabolic endotoxemia,<sup>6,7</sup> chronic inflammation,<sup>6,8</sup> insulin resistance<sup>6,9,10</sup> and adipocyte hypertrophy.<sup>11</sup> Excess body weight also contributes to the development of non-alcoholic fatty liver disease (NAFLD) and non-alcoholic steatohepatitis (NASH).<sup>9</sup>

Recent studies indicate that gut microbiota dysbiosis is associated with disrupted gut barrier

function and metabolic endotoxemia.<sup>12–15</sup> Strategies that restore the gut microbiota have thus been proposed to prevent and treat obesity.<sup>16–19</sup> Diet represents a critical factor that affects host metabolism by modulating the gut microbiota.<sup>20</sup> Several studies have shown that modulation of the gut microbiota using prebiotics and probiotics may improve intestinal integrity and host metabolism and reduce obesity and chronic inflammation.<sup>17–21–24</sup> Polysaccharides and dietary fibre can reduce body weight and exert anti-inflammatory effects by enhancing the growth of specific anti-obesogenic gut bacteria and the production of microbiota-derived metabolites.<sup>25–27</sup> However, further studies are needed to better understand the complex interactions between diet, prebiotics and the gut microbiota.

Many herbal remedies used in traditional Chinese medicine (TCM) exert anti-obesogenic and antidiabetic effects.<sup>28</sup> One class of traditional remedies consists of medicinal fungi, such as *Ophiocordyceps sinensis* and *Ganoderma lucidum*, which contain a wide range of immunomodulatory and bioactive compounds.<sup>29–32</sup> We previously observed that *G. lucidum* reduces obesity in high-fat diet (HFD)-fed mice by modulating the composition of the gut microbiota.<sup>33</sup> The caterpillar fungus, *O. sinensis* (also called cordyceps), and its anamorph, *Hirsutella sinensis*, also produce immunomodulatory, anti-inflammatory, hypoglycaemic and lipid-lowering effects,<sup>34–35</sup> but the possibility that this fungus may induce anti-obesogenic effects has not been examined.

In the present study, we show that a water extract of *H. sinensis* mycelium (HSM) and polysaccharide-containing fractions isolated from the extract reduce body weight and accumulation of fat tissues in a murine model of diet-induced obesity. Further experiments showed that neomycin-sensitive bacteria including *Parabacteroides goldsteinii* are required for the anti-obesogenic effects of HSM polysaccharides. Thus, our results reveal the existence of a new commensal bacterial species responsible for the anti-obesogenic effects of fungal polysaccharides.

## METHODS

### Animal experiments

Four-week-old C57BL/6J male mice were purchased from the NARLab facility (Taiwan). Animals were housed four to five individuals per cage with free access to food and sterile drinking water (DW) (reverse osmosis grade) in a temperature-controlled room (21°C±2°C) under a 12 hours dark-light cycle. After an accommodation period of 1 week, mice were fed for 12 weeks with standard chow diet (chow, 13.5% of energy from fat; LabDiet 5001; LabDiet, USA) or HFD (60% of energy from fat; TestDiet 58Y1; TestDiet, USA). Mice were supplemented daily with 100 µL of sterile saline (vehicle), HSM (20 mg/kg) or polysaccharide fractions H1–H4 (20 mg/kg) by intragastric gavage. At the time indicated, non-fasting animals were anaesthetised and whole blood was withdrawn by cardiac puncture. Visceral adipose tissues (ie, epididymal white adipose tissues) and the liver were removed and weighed. Organs and tissues were immersed in liquid nitrogen and stored at –80°C for further analysis.

### Preparation of HSM water extract and polysaccharides

*H. sinensis* strain CGB 999335 was isolated and cultured as described previously.<sup>36</sup> HSM consisted of <10% crude fibre; >3% polysaccharides; crude proteins at 42.8 g/100 g; crude fat at 8.2 g/100 g; carbohydrates at 31.9 g/100 g; amino acids at 7.8 g/100 g and sodium at 242.7 mg/100 g. Calories were measured at 373 kcal per 100 g. HSM water extract and

polysaccharide fractions were prepared as described earlier for *G. lucidum*.<sup>33</sup>

### Measurement of serum cytokines

Whole blood was withdrawn by cardiac puncture in tubes containing no anticoagulant (BD, USA). Blood was allowed to clot for 30 min. Solutions were centrifuged at 15 000g for 1 min and supernatants (serum) were collected. ELISA kits were used to measure interleukin (IL)-1β and tumour necrosis factor-α (TNF-α) from serum according to the manufacturer's instructions (R&D Systems, USA).

### Serum endotoxin detection

Serum endotoxin was quantified using a *Limulus amaebocyte* lysate (LAL) kit (Cambrex Bio Science, USA) according to the manufacturer's instructions.

Briefly, serum samples were diluted 1:10 to 1:1000 in endotoxin-free water (Lonza, USA), heated at 70°C for 10–15 min and processed according to the manufacturer's protocol. Recovery rate was determined based on the net lipopolysaccharide (LPS) concentration of spiked samples supplemented with LPS (0.1 EU/mL, Sigma, USA). Samples with a recovery rate of at least 50% were considered.

### Measurement of homeostatic model assessment-insulin resistance index

Fasting blood glucose was measured using glucometer strips (Johnson & Johnson Medical Devices, Hong Kong) as done before.<sup>37</sup> Fasting insulin was measured using a commercial ELISA kit (Mercodia, Sweden). Homeostatic model assessment-insulin resistance (HOMA-IR) was calculated using the following equation: fasting glucose (mg/dL) × fasting insulin (µU/mL)/405.

### In vivo intestinal permeability assay

Intestinal permeability was assessed in vivo following oral administration of fluorescein-isothiocyanate (FITC)-dextran (4 kDa; Sigma), a high molecular weight glucose polymer which, based on the information provided by the manufacturer, is neither digested nor absorbed by healthy mice. Animals were orally gavaged with FITC-dextran (44 mg/100 g), 4 hours before sacrifice. Whole blood was obtained by cardiac puncture before killing. Serum was diluted with phosphate-buffered saline (PBS) and fluorescence was monitored using a spectrophotofluorometer (Synergy HT, BioTek, USA) using excitation at 485 nm and emission at 528 nm. A standard curve was prepared based on a series of twofold dilution of FITC-dextran in PBS. Serum from mice that had not received FITC-dextran was used as background control.

### In vitro Caco-2 cell monolayer permeability assay

Human Caco-2 cells were purchased from European Collection of Authenticated Cell Cultures (UK). Caco-2 cells were cultured in Dulbecco's modified Eagle's medium supplemented with 10% fetal bovine serum, 50 U/mL penicillin and streptomycin at 37°C under 5% CO<sub>2</sub>. Caco-2 cells (1 × 10<sup>5</sup>) were grown on polyethylene terephthalate membrane-based transwell plates (0.4 µm pores; Millipore, USA) for 21 days to reach confluence (trans-epithelial electrical resistance (TEER) >1000 Ωcm<sup>2</sup>). Caco-2 monolayer grown on the apical side of transwells were treated with LPS (100 µg/mL; O111:B4, Sigma) and 1 mg/mL of H1 or 50 multiplicity of infection of *P. goldsteinii*. LPS diluted in serum-free medium served as a positive control, and serum-free



medium as vehicle control. TEER values were monitored for 12 hours using a Millicell-ERS-2 volt-ohm metre (Millipore).

### Antibiotic treatment

For in vivo antibiotic treatment, HFD-fed mice were treated with either H1 or saline, combined with 50 µg/mL clindamycin (C) (Goldbio, USA), 50 µg/mL metronidazole (M) (Sigma), 50 µg/mL penicillin (P) (Sigma), 25 µg/mL vancomycin (V) (Sigma) and/or 50 µg/mL neomycin (N) (Sigma) in sterile DW for 12 weeks. For ex vivo faecal microbiota transplantation (FMT), HFD-fed mice (aged 5 weeks, male) were treated daily with H1 or saline by oral gavage for 6 weeks. During week 4 to week 6 (total of 14 days), faecal microbiota from each donor mouse was collected daily, treated with antibiotics, pooled, mixed and stored at -80°C. To prepare faecal microbiota, faeces pellets (150–180 mg) were collected daily in sterile tubes, prior to suspension and homogenisation in 1 mL of PBS. After centrifugation at 2000g at 4°C for 1 min, bacteria-enriched supernatants were collected and centrifuged 5 min at 15 000g. Bacterial pellets were resuspended in 1 mL of sterile saline containing the antibiotics CMPV, neomycin or CMPVN, followed by stationary incubation under aerobic conditions at 37°C for 2 hours. After antibiotic treatment, faecal microbiota specimens were collected, washed twice with saline, resuspended in 700 µL of saline with 20% (v/v) glycerol and stored at -80°C. HFD-fed mice (aged 5 weeks, male) were treated daily with faecal microbiota transplants from each donor group via oral gavage for 12 weeks.

### Caecal microbiota analysis

Caecal microbiota DNA was extracted using the QIAamp DNA Stool Mini Kit (Qiagen, USA) and applied to amplification of V3-V4 regions of 16S rDNA. Caecal microbiota composition was assessed using Illumina HiSeq sequencing of 16S rDNA amplicon and QIIME-based microbiota analysis. The detailed procedure of caecal microbiota DNA extraction, sequencing and library construction and microbiota analysis pipeline is described in the supplementary methods.

### *P. goldsteinii* cultivation, preparation and treatment

*P. goldsteinii* (ATCC BAA-1180, also called JCM 13446) was purchased from the American Type Culture Collection (ATCC, USA). Bacteria were grown at 37°C in a Whitley DG250 anaerobic chamber (Don Whitley, UK) with mixed anaerobic gas (5% carbon dioxide, 5% hydrogen, 90% nitrogen). Anaerobicity was confirmed using an anaerobic indicator (Oxoid, UK). *P. goldsteinii* was cultivated on anaerobic blood agar (Creative, Taiwan) and liquid thioglycollate medium (BD). *P. goldsteinii* was collected by centrifugation and resuspended in sterile saline. Mice were treated daily with  $4 \times 10^7$  colony-forming units of *P. goldsteinii* by oral gavage. Heat-killed or pasteurised *P. goldsteinii* were prepared by heating bacteria at 100°C for 15 min or 70°C for 30 min, respectively. Mice were treated daily with either heat-killed or pasteurised *P. goldsteinii* by oral gavage.

### Statistical analysis

Statistical analysis was performed using GraphPad Prism V.7.0a (GraphPad Software, USA). Data are shown as means±SD and medians±IQR for parametric and non-parametric analysis, respectively. Differences between two groups were assessed using unpaired two-tailed Student's t-test. Data sets involving more than two groups were assessed by one-way analysis of variance (ANOVA) followed by Bonferroni's post hoc test or by the non-parametric Kruskal-Wallis test with Dunn's multiple

comparisons test. Bacterial species with statistically significant difference were assessed using Metastats.<sup>38</sup> Levels of bacterial species showing statistically significant differences in Metastats data were also evaluated using the non-parametric Kruskal-Wallis test with false discovery rate (FDR) correction for multiple testing (<5%).<sup>39</sup> Correlation coefficients between bacterial species and obesity traits were determined using Spearman's correlation analysis. P values <0.05 were considered to be statistically significant. Where indicated in the figure legends, the method described by Benjamini *et al*<sup>39</sup> was also used to evaluate FDR (<5%) for estimated p values.

## RESULTS

### HSM and polysaccharide fractions reduce body weight in HFD-fed mice

To test the effects of HSM on body weight, we fed mice with an HFD for 12 weeks and supplemented the animals' diet with daily administration of HSM water extract or saline as negative control (see online supplementary figure S1A). Compared with the chow diet, mice fed an HFD showed increased body weight, visceral fat mass, liver weight, serum triglycerides and HOMA-IR index values (see online supplementary figure S1B-H). Notably, HSM significantly reduced these obesity traits in a dose-dependent manner (see online supplementary figure S1B-H).

To identify the compounds responsible for HSM's anti-obesogenic effects, we fractionated the HSM water extract into four fractions based on molecular weight (figure 1A and supplementary table S1). Administration of fraction H1, which contained polysaccharides with a molecular weight above 300 kDa (see online supplementary table S1), reduced body weight by ~50% after 12 weeks compared with HFD (figure 1B-D). Fraction H1 also reduced visceral fat and HOMA-IR index in HFD-fed mice, producing effects similar to those observed for the HSM water extract (figure 1E,F). While fraction H4 containing oligosaccharides and carbohydrates of low molecular weight did not affect body weight or obesity traits, fractions H2 (10–300 kDa) and H3 (<10 kDa) reduced visceral fat pad mass, but produced no effect on body weight or HOMA-IR index (figure 1B-F).

### HSM-derived polysaccharides reduce metabolic disorders in HFD-fed mice

HSM and H1 did not affect energy intake (see online supplementary figure S2A) or fat absorption (see online supplementary figure S2B), indicating that these treatments did not modulate appetite or lipid absorption. In addition, HSM and H1 did not affect caecal or colonic production of short-chain fatty acids (SCFAs), such as acetate, propionate or butyrate (see online supplementary figure S3). On the other hand, HSM and H1 reduced serum triglycerides (see online supplementary figure S4A) and gene expression involved in lipolysis, lipid transport and uptake and lipogenesis in adipose and hepatic tissues (see online supplementary figure S4B,C). HSM and H1 enhanced gene expression associated with hepatic β-oxidation, compared with the HFD group (see online supplementary figure S4C, Acsl3). In comparison, fractions H2–H4 affected some but not all lipid metabolism parameters (see online supplementary figure S4).

HSM and H1–H3 treatment reduced fasting glucose compared with HFD, while only HSM and H1 reduced fasting insulin (see online supplementary figure S5A,B). HSM and fractions H1–H3 improved glucose tolerance in the oral glucose tolerance test (see online supplementary figure S5C,D), but

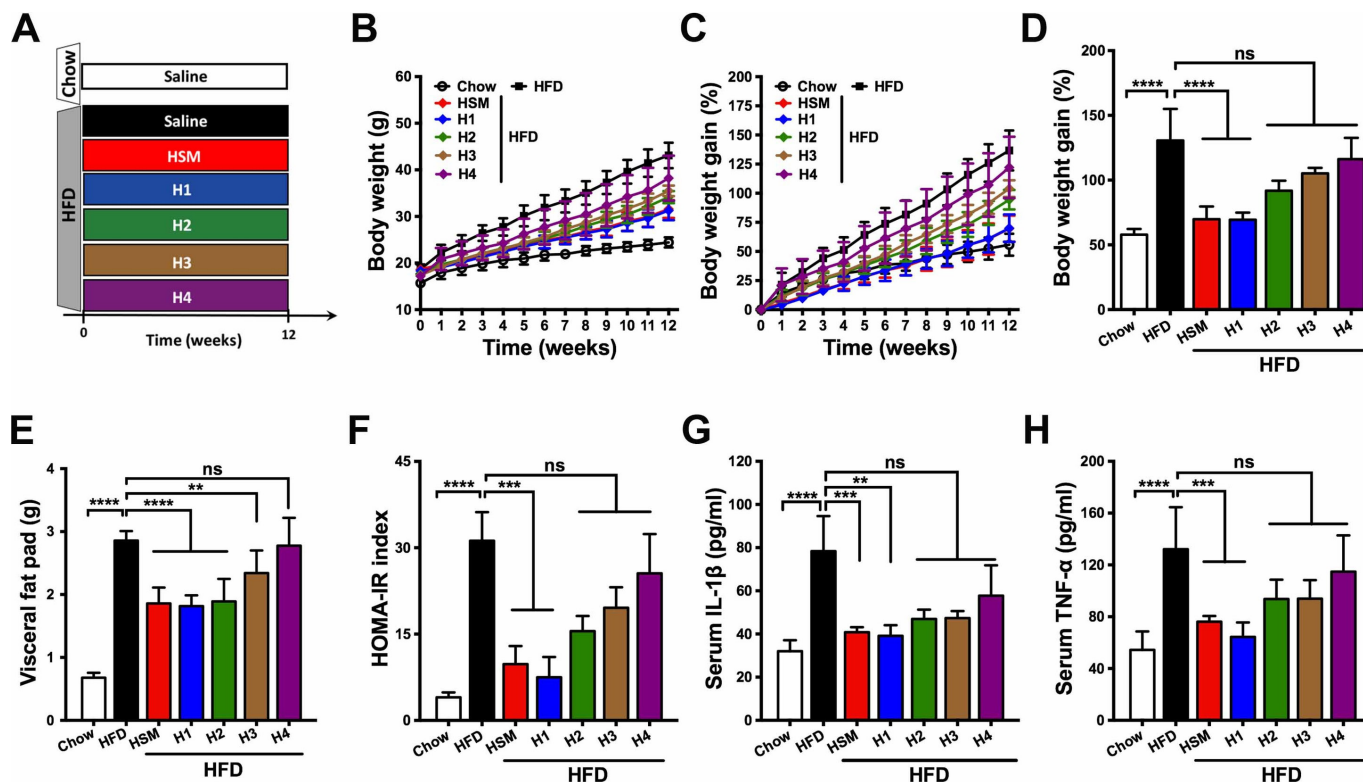


**Figure 1** *Hirsutella sinensis* mycelium (HSM) and H1 reduce diet-induced obesity and metabolic disorders. (A) Chow-fed mice and high-fat diet (HFD)-fed mice were treated daily with control saline, HSM water extract (HSM) (20 mg/kg) or HSM-derived fractions (H1–H4) (20 mg/kg) for 12 weeks by oral gavage. (B) Body weight and (C) relative body weight were measured throughout the 12-week period. Obesity traits including (D) body weight gain, (E) visceral fat pad weight (epididymal white adipose tissue), (F) homeostatic model assessment–insulin resistance (HOMA-IR) index, (G) serum interleukin (IL)-1 $\beta$  and (H) serum tumour necrosis factor- $\alpha$  (TNF- $\alpha$ ) were measured after 12 weeks of treatment as described in the 'Methods' section. Data are presented as means $\pm$ SD from three independent experiments (n=10–15 mice per group). Statistical analysis was performed using one-way analysis of variance followed by Bonferroni's post hoc test and false discovery rate (FDR) correction for multiple testing. \*\*p<0.01; \*\*\*p<0.001; \*\*\*\*p<0.0001; ns, not statistically significant.

only HSM and H1 improved insulin sensitivity in the insulin tolerance test (see online supplementary figure S5E, F).

HSM and H1 reduced serum levels of the pro-inflammatory cytokines IL-1 $\beta$  and TNF- $\alpha$ , compared with HFD (figure 1G,H). Consistent with the effects described above on lipid metabolism (see online supplementary figure S4), HSM and H1 reduced adipocyte hypertrophy and the number of crown-like structures (CLS)—tissue lesions in which macrophages surround dead adipocytes (see online supplementary figure S6). We monitored expression of mitochondrial uncoupling protein 1 (UCP1), which was identified earlier as a major regulator of thermogenesis in adipose tissues.<sup>40</sup> HSM and H1 increased UCP1 mRNA and protein expression in brown adipose tissues (BATs) and inguinal white adipose tissues (iWATs) compared with the HFD group (see online supplementary figure S7), suggesting that HSM and H1 may increase thermogenesis. Furthermore, HSM and H1 reduced signs of NAFLD and NASH, including liver cell hypertrophy and accumulation of lipid droplets, in the liver of HFD-fed mice (see online supplementary figure S8 and supplementary dataset S1). While HSM and H1 produced a modest but statistically significant reduction of body weight in chow-fed mice, the treatments did not affect visceral fat weight, HOMA-IR index or pro-inflammatory cytokine levels in this group (see online supplementary figure S9). These results indicate

that HSM and H1 produce anti-obesogenic, antidiabetic and anti-inflammatory effects in HFD-fed mice.

### HSM and H1 prevent leaky gut and metabolic endotoxemia

Previous studies have shown that an HFD reduces expression of intestinal tight junction proteins (eg, zonula occludens-1 (ZO-1)) and disrupts gut barrier integrity, leading to translocation of bacterial LPS into the blood (ie, metabolic endotoxemia) and producing inflammation and insulin resistance.<sup>5–7 15 41</sup> Notably, HSM and H1 significantly reduced serum endotoxin levels (figure 2A) and intestinal permeability (figure 2B) in HFD-fed mice. These observations were accompanied by increased expression of ZO-1 (figure 2C) and reduced mRNA expression of pro-inflammatory cytokines (figure 2D,E) in the colon of mice treated with HSM or H1. In contrast, fractions H2–H4 failed to reverse serum endotoxemia (figure 2A), intestinal permeability (figure 2B) or expression of colonic pro-inflammatory cytokines or ZO-1 (figure 2C–E). HSM and H1 significantly increased levels of regulatory T cells expressing the anti-inflammatory cytokine IL-10 in colonic lamina propria of HFD-fed mice (figure 2F), while reducing levels of M1 macrophages expressing pro-inflammatory IL-1 $\beta$  (figure 2G). In addition, H1 reduced LPS-induced disruption of cell monolayers (figure 2H, measured using the TEER assay) and increased ZO-1 mRNA expression (figure 2I) in colonic Caco-2 cells.

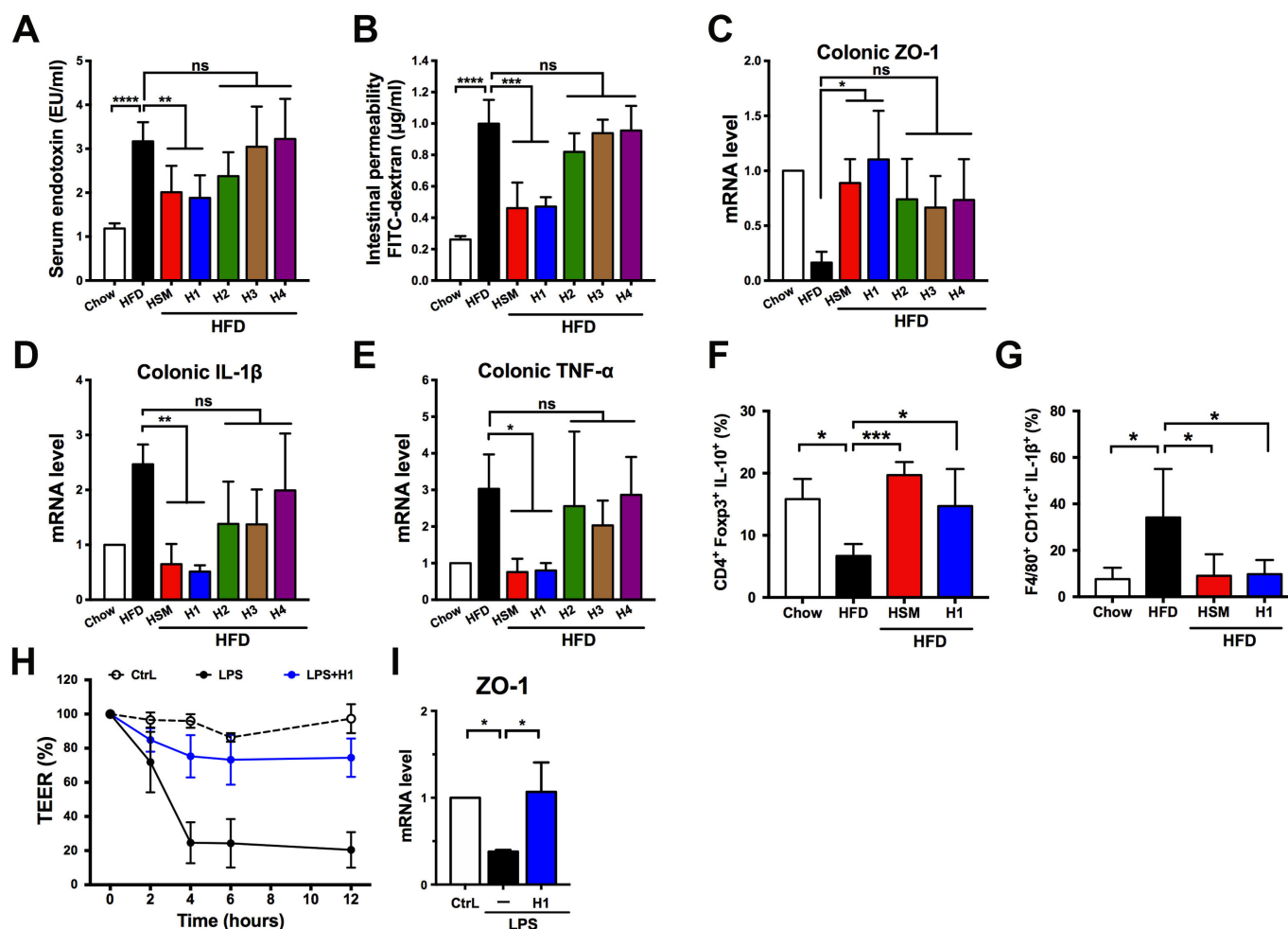


**Figure 2** *Hirsutella sinensis* mycelium (HSM) and H1 improve intestinal integrity and produce immunomodulatory effects. Experiments were performed as in figure 1. (A) Serum endotoxin and (B) intestinal permeability were measured as described in the 'Methods' section. (C) Zonula occludens-1 (ZO-1), (D) interleukin (IL)-1β and (E) tumour necrosis factor-α (TNF-α) expression in proximal colon was examined using quantitative real-time PCR (qRT-PCR). Expression levels were normalised to glyceraldehyde 3-phosphate dehydrogenase and expressed as relative fold changes compared with the chow group. Levels of (F) IL-10-expressing regulatory T cells and (G) IL-1β-expressing M1 macrophages were analysed using flow cytometry. (H) In vitro Caco-2 cell permeability was monitored using the transepithelial electrical resistance (TEER) assay. (I) ZO-1 expression in Caco-2 cells was examined using qRT-PCR. Caco-2 cells were treated with control (Ctrl) serum-free medium, lipopolysaccharide (LPS) or LPS plus H1 for 12 hours. Expression levels were normalised to 18S rRNA and expressed as relative fold changes compared with the vehicle control. Data are presented as means±SD from three independent experiments (A, B, n=10–15 mice/group; H, I, duplicate/group) or two independent experiments (C–G; n=5–10 mice per group). Statistical analysis was performed using one-way analysis of variance followed by Bonferroni's post hoc test and false discovery rate correction for multiple testing. \*P<0.05; \*\*p<0.01; \*\*\*p<0.001; \*\*\*\*p<0.0001; ns, not significant. FITC, fluorescein-isothiocyanate.

### The anti-obesogenic effects of HSM and H1 are transferable by faecal transplantation

The gut microbiota contributes to the development of diet-induced obesity and associated metabolic disorders.<sup>12–15</sup> Given that HSM and H1 reduced serum endotoxemia and intestinal permeability (figure 2A,B), we examined whether the beneficial effects of HSM and H1 may be mediated by the gut microbiota. Faecal microbiota from HFD-fed or chow-fed mice treated with saline, HSM, fraction H1 or fraction H4 were transplanted into HFD-fed recipients (see online supplementary figure S10A). FMT from HSM-treated, H1-treated or chow-treated mice reduced body weight gain and obesity traits in HFD recipients (see online supplementary figure S10B–G,I). FMT from HSM, H1 or chow groups increased colonic ZO-1 mRNA expression compared with the controls (see online supplementary figure S10H). Furthermore, FMT from HSM, H1 or

chow groups reduced adipocyte hypertrophy and CLS lesions (see online supplementary figure S11), as well as signs of NAFLD and NASH in the liver of HFD recipients (see online supplementary figure S12). In contrast, FMT derived from saline-treated or H4-treated, HFD-fed mice failed to reverse obesity traits in HFD-fed recipients (see online supplementary figures S10–12). These results suggest that the gut microbiota mediates the anti-obesogenic effects produced by HSM and H1.

### Neomycin abolishes H1's anti-obesogenic effects

To determine whether the anti-obesogenic effects of H1 are dependent on the presence of specific gut bacteria, we treated H1-fed HFD mice with a cocktail of antibiotics, which included clindamycin (C), metronidazole (M), penicillin (P), vancomycin (V) and neomycin (N) in DW (figure 3A). Compared with the

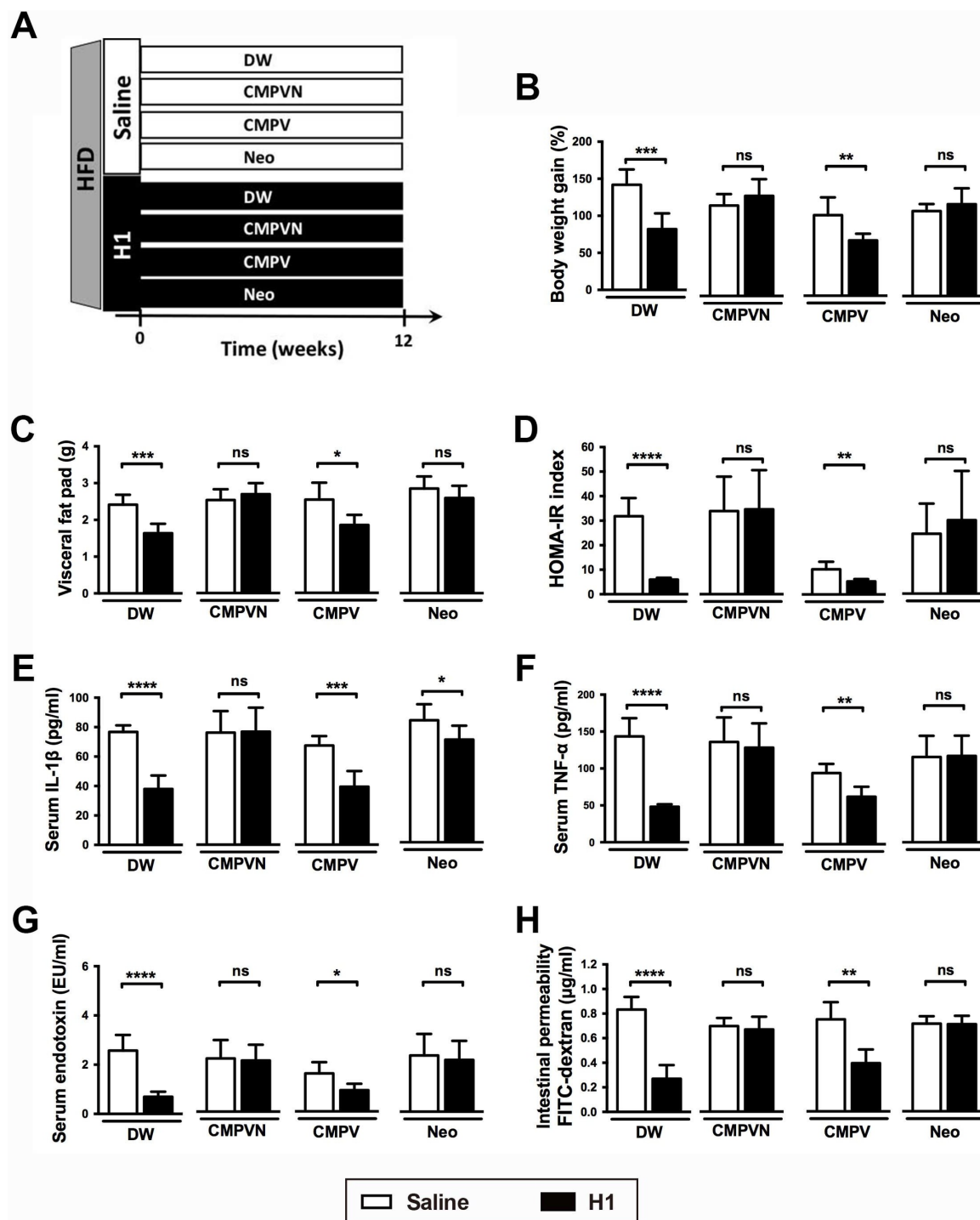


**Figure 3** H1 produces anti-obesogenic effects via neomycin-sensitive gut bacteria. (A) Saline-treated or H1-treated high-fat diet (HFD)-fed mice were treated orally with antibiotics in sterile drinking water (DW) for 12 weeks as described in the 'Methods' section. Obesity traits including (B) body weight gain, (C) visceral fat pad weight, (D) homeostatic model assessment-insulin resistance (HOMA-IR) index, (E) serum interleukin (IL)-1 $\beta$ , (F) serum tumour necrosis factor- $\alpha$  (TNF- $\alpha$ ), (G) serum endotoxin (lipopolysaccharide (LPS)) and (H) intestinal permeability were measured after 12 weeks of treatment. Data are presented as means $\pm$ SD (n=6 mice/group). Statistical analysis was performed using unpaired Student's t-test between saline and H1 groups, followed by false discovery rate correction for multiple testing. \*P<0.05; \*\*p<0.01; \*\*\*p<0.001; \*\*\*\*p<0.0001; C, clindamycin; FITC, fluorescein-isothiocyanate; M, metronidazole; P, penicillin; V, vancomycin; N or Neo, neomycin; ns, not significant.

antibiotic-free DW control group in which H1 reduced body weight gain and obesity traits (figure 3B–H and supplementary figures S13–15, DW control group), treatment with the CMPVN antibiotic cocktail abolished H1's anti-obesogenic effects (figure 3B–H and supplementary figures S14 and 15, CMPVN treatment).

To determine whether a single antibiotic from the cocktail may be responsible for these effects, we treated mice with individual antibiotics (see online supplementary figure S13A). Of note, with the exception of serum IL-1 $\beta$  (figure 3E), neomycin consistently abrogated H1's anti-obesogenic effects (figure 3B–H, supplementary figure S13B–G and supplementary figures S14 and 15,



Neo treatment), whereas, with few exceptions, the other single antibiotic treatments failed to block H1's effects (see online supplementary figure S13B–G). Furthermore, H1's anti-obesogenic effects were not affected by an antibiotic cocktail lacking neomycin (figure 3B–H and supplementary figures S14 and 15, CMPV treatment). Neomycin-sensitive gut bacteria may therefore be required for H1's anti-obesogenic effects.

### Identification of neomycin-sensitive gut bacteria enriched by H1

We used next-generation 16S rDNA sequencing to analyse the changes produced by H1 in the gut microbiota. Sequencing analysis of caecal samples (figure 4A) produced an average of  $117\,633 \pm 13\,834$  effective reads per sample that covered rare new phylotypes and broad bacterial diversity (see online supplementary dataset S2). Weighted UniFrac-based principal coordinate analysis revealed distinct clustering of microbiota for each group (see online supplementary figure S16A). Pairwise comparisons using the permutational multivariate analysis of variance (PERMANOVA) test indicated a statistically significant separation between groups ( $p < 0.05$ ), except for the comparison between CMPVN and CMPV ( $p = 0.41$ ). Analysis of distance matrix revealed that the gut microbiota of neomycin-treated mice clustered with that of HFD-fed mice (see online supplementary figure S16B), revealing similarities between the microbiota of these samples.

We used Metastats analysis to identify the bacteria altered by H1 and neomycin in HFD-fed mice. Operational taxonomic units showing a significant difference between H1 and the other HFD groups were searched against the GenBank sequence database. Overall, 40 bacterial species were significantly altered by H1 in HFD or antibiotics-treated mice (figure 4B,C and supplementary dataset S3). When compared with HFD, H1 altered 16 bacterial species (figure 4B,C; H1 vs HFD, 11 increased species highlighted in red and five reduced species highlighted in green in figure 4C; see also supplementary dataset S3). In H1-treated HFD groups, supplementation with CMPV, neomycin or CMPVN, respectively altered 19, 25 or 27 bacterial species (figure 4B,C; species highlighted in red or green in figure 4C). The chow treatment only affected the levels of nine bacterial species compared with HFD (figure 4B,C; chow vs HFD), indicating that H1 modulates the gut microbiota in a specific manner.

We sought to identify the bacterial species in the H1 group whose abundance was altered by both neomycin and CMPVN. Detailed analysis showed that, among the 40 bacterial species identified, 9 species were modulated in the same direction by both neomycin and CMPVN (figure 4B,C and supplementary dataset S3), including 6 species whose levels were enriched by H1 (*P. goldsteinii*, *Flintibacter butyricus*, *Intestinimonas butyriciproducens*, *Clostridium cocleatum*, *Clostridium viride* and *Anaerotruncus colihominis*) and 3 species whose levels were reduced by H1 (*Pseudomonas aeruginosa*, *Escherichia coli* and *Shewanella algae*). In contrast, three enriched species (*Ruminococcus flavefaciens*, *Butyrivibrio hungatei* and *Ruminococcus bromii*) and three depleted species (*Mucispirillum schaedleri*, *Dorea longicatena* and *Romboutsia timonensis*) were significantly modulated by H1 but reversed by neomycin treatment. Species whose levels were enriched by H1 but reduced by CMPVN included *Ruminococcus gnavus*, *Ochrobactrum anthropic* and *Delftia acidovorans*.

Among the altered species identified, *M. schaedleri*, *D. longicatena*, *R. timonensis*, *E. coli* and *S. algae* represent endotoxin-producing bacteria whose levels increased in obese

animals.<sup>33 42 43</sup> Notably, several altered species, including *P. goldsteinii*, *C. cocleatum*, *A. colihominis* and *R. flavefaciens*, were reduced in obese animals and humans.<sup>33 44 45</sup> Our results showed that several bacterial species were altered in the same direction in the HFD group by CMPV, neomycin and CMPVN (figure 4C). Of note, the levels of four species, including *P. goldsteinii*, *I. butyriciproducens*, *C. cocleatum* and *S. algae*, were significantly altered by H1 but reversed by neomycin and CMPVN (figure 4C).

We examined whether obesity-related traits correlated with the levels of neomycin-sensitive gut bacteria enriched by H1. Spearman's correlation analysis showed that the levels of these bacteria negatively correlated with obesity traits (figure 4D). Notably, among these bacteria, *P. goldsteinii* was highly enriched by H1 treatment (figure 4B,C and supplementary dataset S3) and this species negatively correlated with all obesity traits (figure 4D and supplementary dataset S4). The levels of other H1-modulated neomycin-sensitive bacteria were also associated with *P. goldsteinii* levels (see online supplementary figure S17). These results suggest that *P. goldsteinii* and the neomycin-sensitive gut microbiota might mediate the anti-obesogenic effects of H1.

### Ex vivo neomycin treatment abolishes the anti-obesogenic effects of H1

To eliminate potential side effects produced by antibiotics on the host, we treated faecal microbiota with antibiotics ex vivo prior to FMT (ex-FMT; figure 5A). Faecal microbiota specimens collected daily from H1-treated HFD-fed mice were incubated with antibiotics or saline, followed by washing steps and oral administration into HFD-fed recipients (figure 5A). As expected, the HFD-induced obesity traits of HFD recipients were significantly reduced by ex-FMT from H1-treated mice (figure 5B–H, H1 vs HFD), and these effects were abolished by ex-FMT from neomycin-treated or CMPVN-treated animals (figure 5B–H). In contrast, ex-FMT from CMPV-treated H1-faecal microbiota prevented obesity traits in HFD animals (figure 5B–H, CMPV).

### *P. goldsteinii* levels negatively correlate with obesity traits in ex vivo FMT

We analysed the microbiota of ex-FMT mice to identify bacteria that were enriched by H1 but reduced by neomycin or CMPVN in donor and recipient mice. In the donor group, when compared with HFD, levels of eight bacterial species were significantly altered by H1 but reversed by neomycin and CMPVN (figure 6A,B and supplementary dataset S5). These bacteria included six species whose levels were enriched by H1 (*P. goldsteinii*, *Clostridium perfringens*, *C. viride*, *Adlercreutzia equolifaciens*, *Paenibacillus glucanolyticus* and *Bradyrhizobium japonicum*) and two species whose levels were reduced by H1 (*Lactobacillus johnsonii* and *Lactobacillus reuteri*; figure 6A,B and supplementary dataset S5). Among these bacteria, *P. goldsteinii* was significantly enriched in H1 donor mice but considerably reduced by neomycin or CMPVN (figure 6A,B). Accordingly, *P. goldsteinii* was also enriched in H1-recipient mice but reduced in CMPVN-recipient mice (figure 6C,D and supplementary dataset S6). Based on quantitative PCR, we observed that the absolute *P. goldsteinii* count increased following H1 treatment but the bacterial count was considerably reduced by neomycin or CMPVN in both donor and recipient mice (figure 6E). Notably, both the absolute count (copy number) and relative level of *P. goldsteinii* were negatively associated with obesity traits (figure 6F).

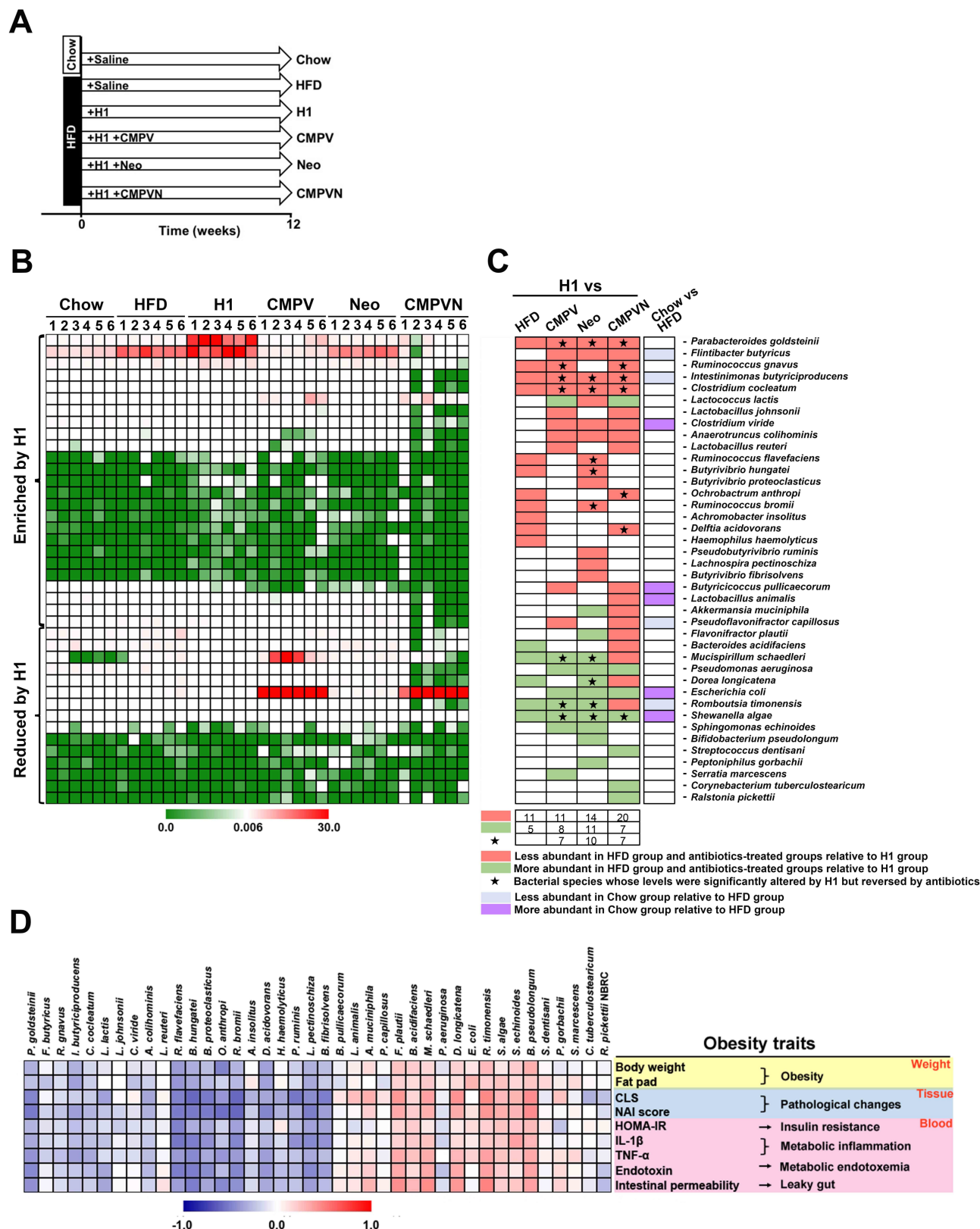


**Figure 4** H1 enriches a population of neomycin-sensitive gut bacteria that negatively correlates with obesity traits. (A) Mice were treated for 12 weeks as indicated. (B) Heatmap showing the levels of 40 bacterial species significantly altered by high-fat diet (HFD) or antibiotics in comparison with the H1 group based on Metastats analysis. (C) Bacterial species from panel B and changes induced by the treatments indicated. Green and red entries indicate species that were respectively more and less abundant in the HFD group and antibiotics-treated groups relative to H1. Purple and blue entries indicate species that were respectively more and less abundant in the chow group relative to the HFD group. Black stars indicate bacterial species whose levels were significantly altered by H1 but reversed by antibiotics. (D) Spearman's correlation analysis between the 40 identified bacterial species and obesity traits. False discovery rate correction for multiple testing was used. CLS, crown-like structure; HOMA-IR, homeostatic model assessment-insulin resistance; IL, interleukin; NAI, non-alcoholic steatohepatitis activity index; TNF- $\alpha$ , tumour necrosis factor-alpha.

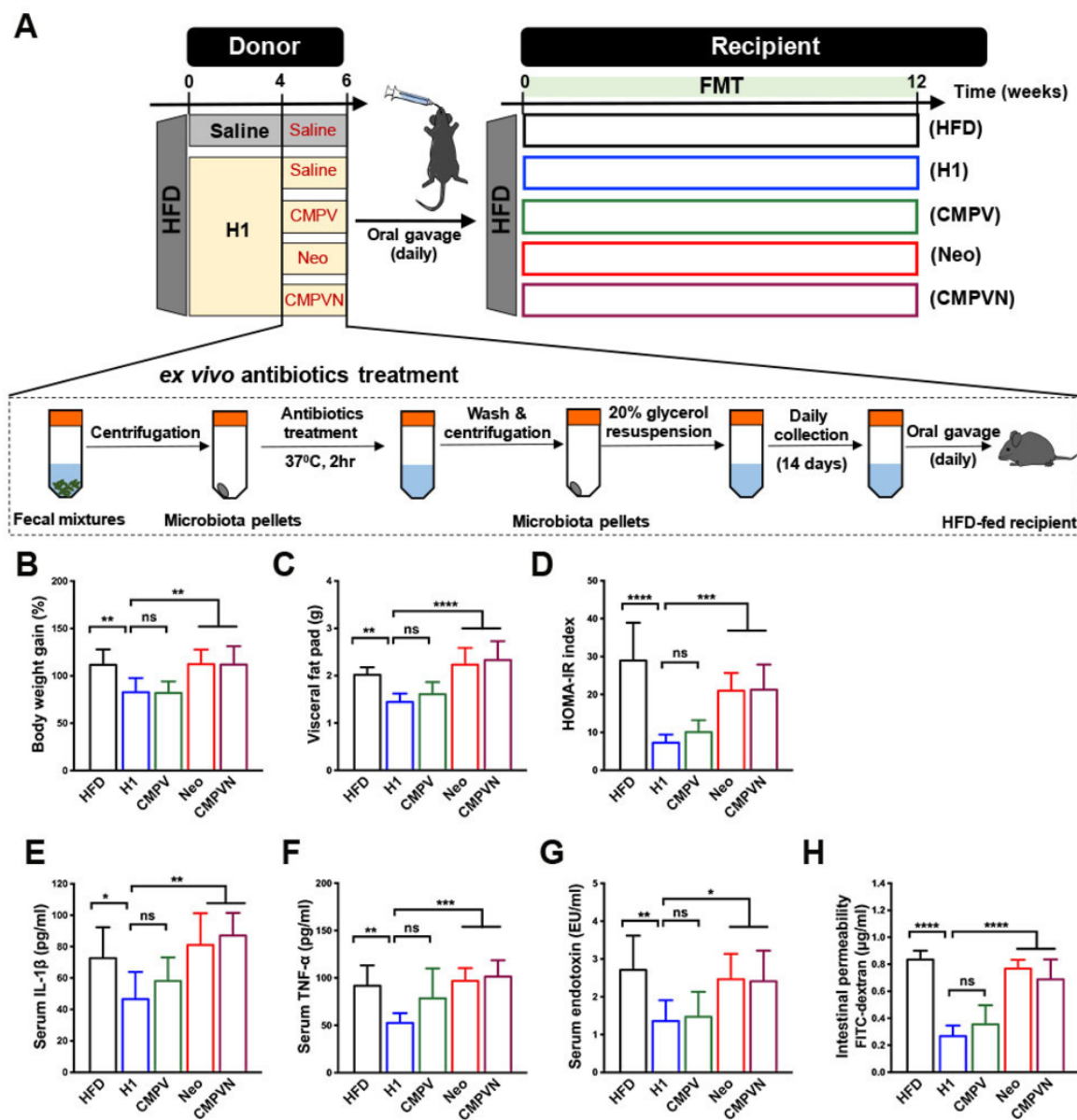


**Figure 5** Ex vivo neomycin treatment abolishes the anti-obesogenic effects of faecal microbiota transplantation (FMT) from H1-treated mice. (A) Diagram of ex vivo antibiotics treatment of faecal bacteria before FMT (ex-FMT). High-fat diet (HFD)-fed donor mice were treated daily with saline or H1 by oral gavage for 6 weeks. H1-treated faeces samples were collected daily from week 4 to 6, followed by a series of steps for ex vivo antibiotics treatment (CMPV, Neo, CMPVN or saline; see the enlarged rectangle). Faecal microbiota from saline-treated HFD-fed mice was used as a negative control. Faecal microbiota samples collected for 2 weeks from each donor mice were pooled and an equal volume was transferred to HFD-fed mice by oral gavage for 12 weeks. Obesity traits measured in recipients after 12 weeks included (B) body weight gain, (C) visceral fat pad weight, (D) homeostatic model assessment-insulin resistance (HOMA-IR) index, (E) serum interleukin (IL)-1 $\beta$ , (F) serum tumour necrosis factor- $\alpha$  (TNF- $\alpha$ ), (G) serum endotoxin and (H) intestinal permeability. Data are presented as means $\pm$ SD from two independent experiments (n=9). Data were analysed using one-way analysis of variance followed by Bonferroni's post hoc test and false discovery rate correction for multiple testing. \* $P$ <0.05; \*\* $P$ <0.01; \*\*\* $P$ <0.001; \*\*\*\* $P$ <0.0001; ns, not significant; FITC, fluorescein-isothiocyanate.

### *P. goldsteinii* prevents diet-induced obesity and metabolic disorders

In order to confirm that *P. goldsteinii* had colonised mice in FMT experiments, we examined the levels of *P. goldsteinii* in caecal microbiota of HFD-fed mice treated with saline, HSM or H1 as well as in their recipients. Levels of *P. goldsteinii* between paired donors and recipients were similar (see online supplementary figure S18A,B), indicating an efficient transfer of *P. goldsteinii* during FMT. Moreover, colonisation was observed in HFD-fed mice treated with neomycin for 8 weeks and which received a

single oral gavage of *P. goldsteinii* (see online supplementary figure S18C).

These results prompted us to examine whether *P. goldsteinii* produces anti-obesogenic effects in HFD-fed mice. We treated HFD-fed mice daily with a commercial strain of *P. goldsteinii* or saline for 8 weeks (figure 7A). *P. goldsteinii* treatment significantly reduced body weight gain (20%–35% reduction), visceral fat, HOMA-IR index, serum levels of IL-1 $\beta$  and endotoxin and intestinal permeability (figure 7B–G), and these results were accompanied by reduced IL-1 $\beta$  mRNA expression and



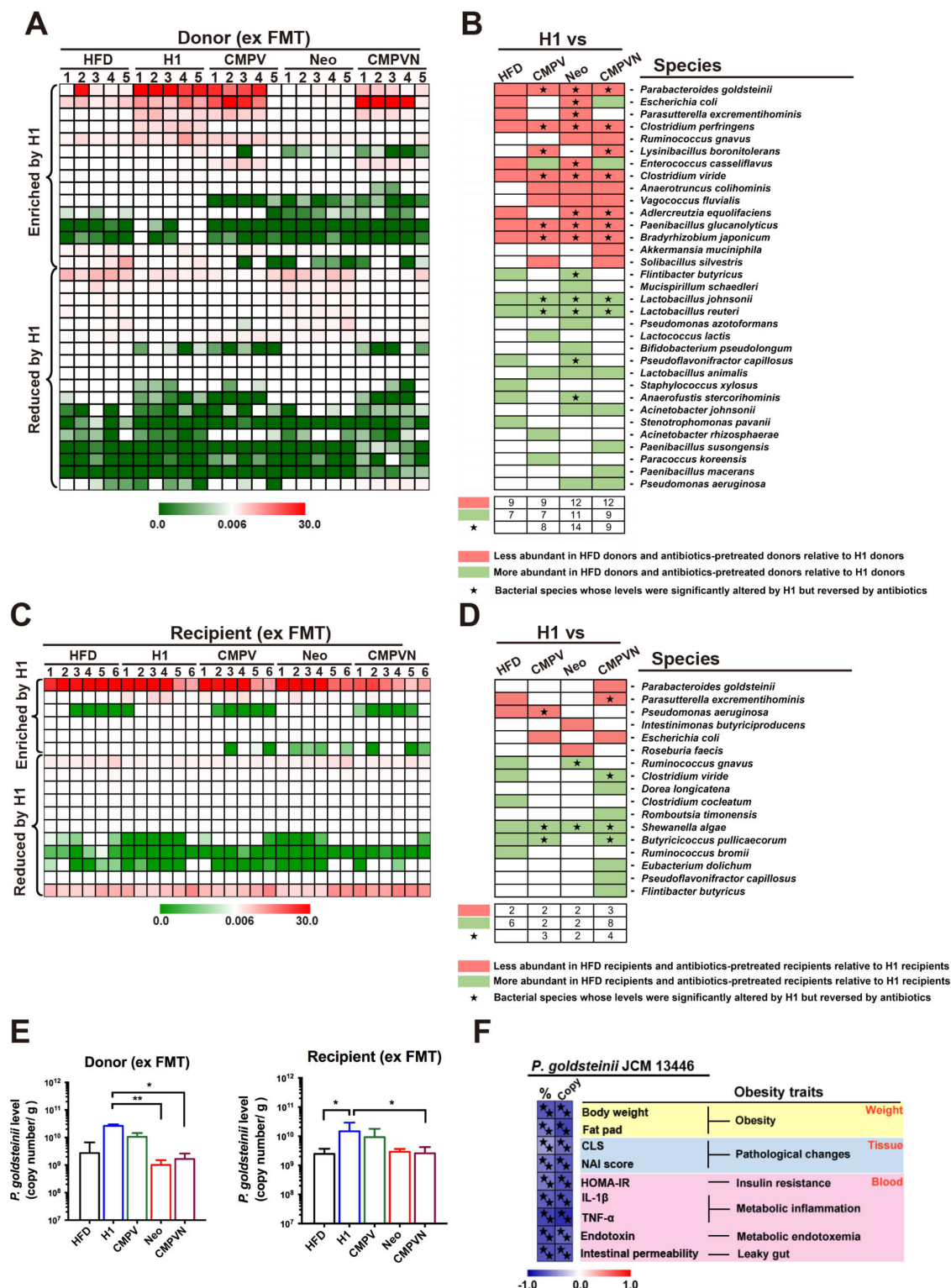


**Figure 6** *Parabacteroides goldsteinii* is enriched in ex vivo faecal microbiota transplantation (ex FMT) H1 donor and recipient mice and negatively correlates with obesity traits. The ex-FMT experiments are depicted in figure 5A. (A) Heatmap abundance and (B) bacterial species information showing 33 bacterial species significantly altered by H1 in donor groups based on Metastats analysis. (C) Heatmap abundance and (D) bacterial species information showing 17 bacterial species significantly altered by H1 in recipient groups based on Metastats analysis. In panels (B) and (D), green and red entries indicate species that were respectively more and less abundant in the high-fat diet (HFD) group and ex vivo antibiotics-treated groups relative to H1. Black stars indicate bacterial species whose levels were significantly altered by H1 but reversed by antibiotics. (E) Absolute quantification (copy number) of *P. goldsteinii* in ex-FMT donor groups (left panel) and recipient groups (right panel). Data are presented as medians±IQR (n=5 and n=6 for donor and recipient groups, respectively). (F) Spearman's correlation analysis of relative abundance (%) and absolute count (copy) of *P. goldsteinii* and obesity traits. In this panel, black stars indicate statistically significant difference based on Spearman's correlation analysis and false discovery rate correction (<5%). \*P<0.05; \*\*p<0.01; CLS, crown-like structures; HOMA-IR, homeostatic model assessment-insulin resistance; IL, interleukin; NAI, non-alcoholic steatohepatitis activity index; TNF-α, tumour necrosis factor-alpha.



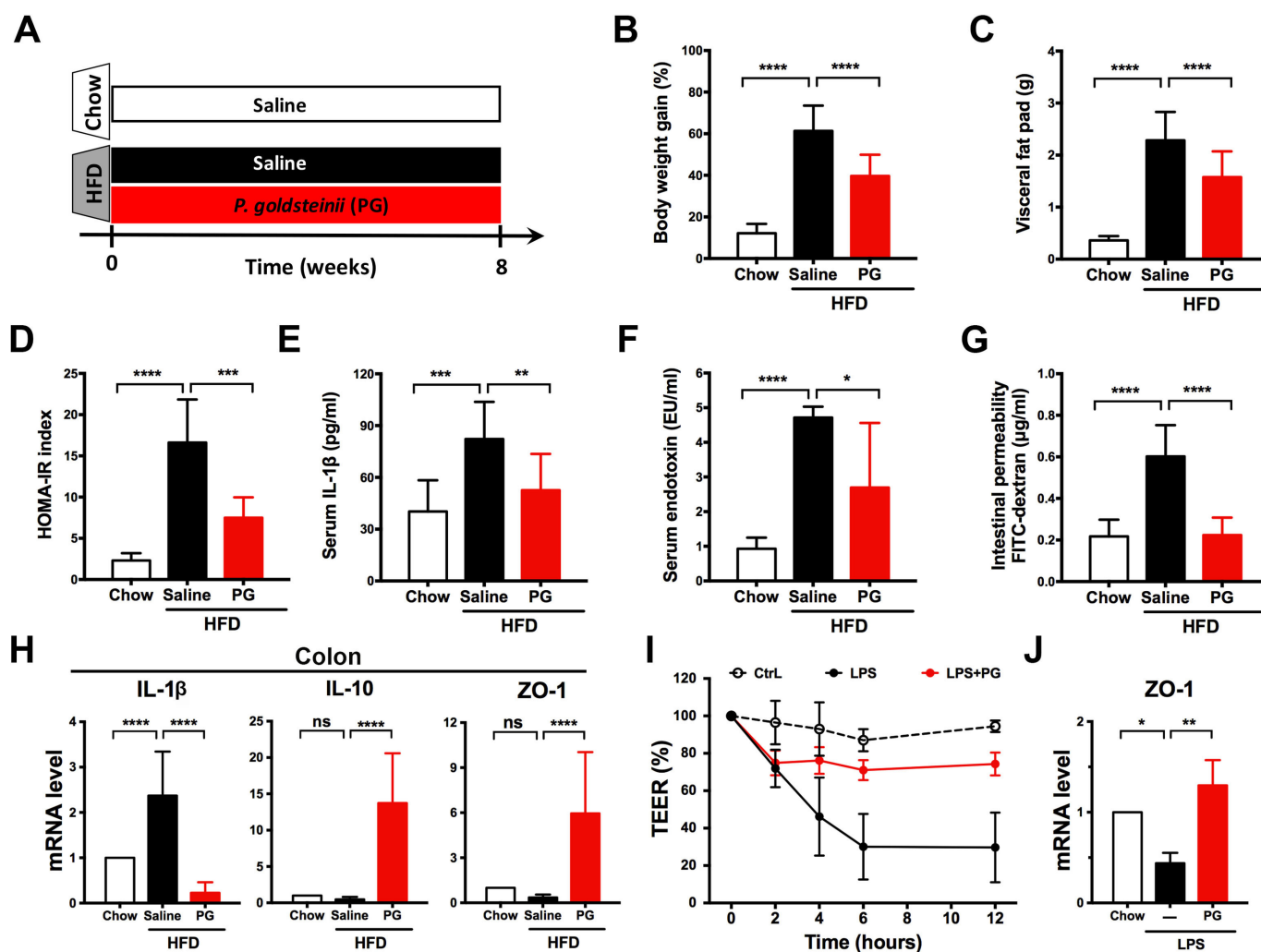


**Figure 7** *Parabacteroides goldsteinii* (PG) reduces diet-induced obesity and metabolic disorders. (A) Chow-fed mice and high-fat diet (HFD)-fed mice were treated daily with saline or PG ( $4 \times 10^7$  colony-forming units) by oral gavage for 8 weeks. Obesity traits including (B) body weight gain, (C) visceral fat pad, (D) homeostatic model assessment-insulin resistance (HOMA-IR) index, (E) serum interleukin (IL)-1 $\beta$ , (F) serum endotoxin and (G) intestinal permeability were measured after 8 weeks of treatment. (H) IL-1 $\beta$ , IL-10 and ZO-1 expression in proximal colon was examined using quantitative real-time PCR (qRT-PCR). Expression was normalised to glyceraldehyde 3-phosphate dehydrogenase and expressed as relative fold changes compared with the chow group. (I) Caco-2 cell permeability was monitored in vitro using the transepithelial electrical resistance (TEER) assay. (J) Zonula occludens-1 (ZO-1) expression in Caco-2 cell monolayers was examined using qRT-PCR. Expression was normalised to 18S rRNA and expressed as relative fold changes compared with the vehicle control (Ctrl). Data are presented as means  $\pm$  SD of three independent experiments.  $n=16-19$  mice for panels B, C;  $n=6$  for panels D, F, G;  $n=11$  for panels E, H;  $n=3$  for panels I, J. Data were analysed using one-way analysis of variance followed by Bonferroni's post hoc test and false discovery rate correction for multiple testing. \* $P < 0.05$ ; \*\* $p < 0.01$ ; \*\*\* $p < 0.001$ ; \*\*\*\* $p < 0.0001$ ; ns, not significant.

increased IL-10 and ZO-1 mRNA expression in colon tissues (figure 7H). *P. goldsteinii* treatment also effectively reduced cell monolayer disruption and restored tight junction ZO-1 expression in LPS-treated Caco-2 cell monolayers (figure 7I,J). In chow-fed mice, *P. goldsteinii* treatment reduced body weight, but did not affect other obesity-related traits (see online supplementary figure S19). *P. goldsteinii* treatment reduced adipocyte hypertrophy and CLS lesions in adipose tissues of HFD-fed mice (see online supplementary figure S20). *P. goldsteinii* significantly increased UCP1 mRNA and protein expression in BATs and iWATs (see online supplementary figure S21), suggesting that the bacterium may induce thermogenesis. Furthermore, *P. goldsteinii* reduced signs of NAFLD and NASH in HFD-fed mice (see online supplementary figure S22), and normalised gene expression involved in lipid transport, lipogenesis and  $\beta$ -oxidation in the liver (see online supplementary figure S23,

no statistically significant effect was noted for SREBP1c). Notably, administration of either heat-killed or pasteurised *P. goldsteinii* failed to reduce body weight or visceral fat accumulation (see online supplementary figure S24), indicating that live bacteria are required to induce anti-obesogenic effects. Finally, *P. goldsteinii* treatment did not affect liver or kidney functions in chow-fed or HFD-fed mice (see online supplementary table S2). *P. goldsteinii* therefore induces anti-obesogenic, anti-inflammatory and antidiabetic effects in obese animals.

## DISCUSSION

Although previous studies have shown that the medicinal fungus *O. sinensis* may lower blood glucose and lipid levels in type 2 diabetes in mice,<sup>46-49</sup> the possibility that this fungus may modulate the gut microbiota and reduce body weight in

animals had not been examined. Our study shows that a water extract of the *H. sinensis* fungus (ie, HSM) and a fraction containing high-molecular weight polysaccharides (ie, fraction H1) reduce diet-induced obesity and metabolic disorders by modulating gut microbiota composition, improving intestinal integrity and inducing thermogenesis. H1 treatment reverses HFD-induced gut dysbiosis and increases the level of *P. goldsteinii* and other neomycin-sensitive bacteria. Such changes in the composition of the gut microbiota in turn improve HFD-induced intestinal integrity and insulin sensitivity, and

reduce metabolic endotoxemia, inflammation, fat deposition, adipose tissue pathology and the development of fatty liver disease (figure 8). We also observed that H1 reduced LPS-induced cellular permeability in human intestinal Caco-2 cells (figure 2H,I), indicating that H1 may improve intestinal integrity independently of the gut microbiota.

Our results show that *P. goldsteinii* treatment reduces obesity and metabolic disorders in HFD-fed mice, in addition to maintaining intestinal integrity, inducing thermogenesis and reducing endotoxemia and inflammation (figure 7A–H and

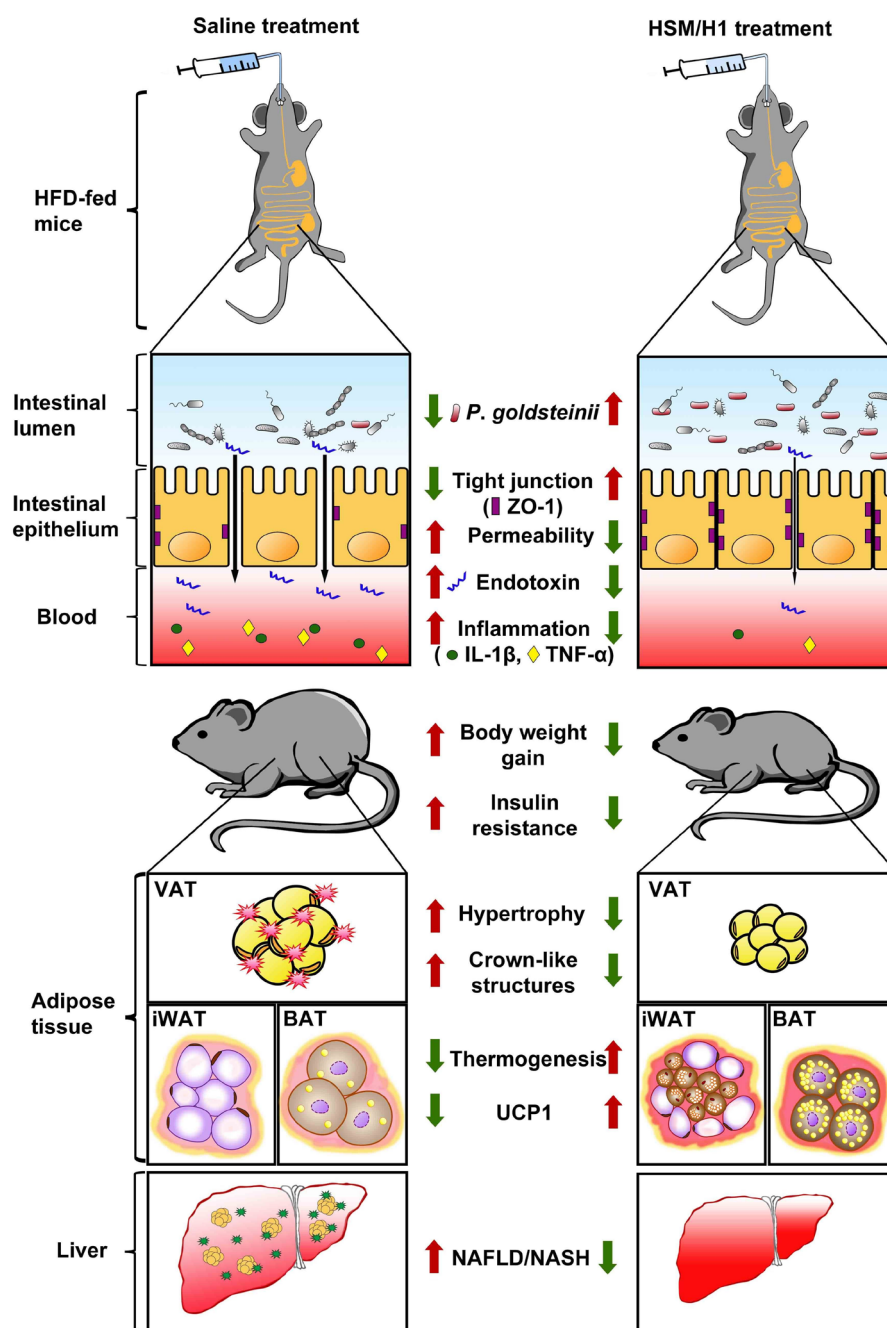


**Figure 8** Proposed model for the anti-obesogenic effects of *Hirsutella sinensis* mycelium (HSM) and H1 in high-fat diet (HFD)-fed mice. Treatment with HSM or H1 produces many beneficial changes on HFD-fed mice, including increasing *Parabacteroides goldsteinii* levels, tight junction expression and thermogenesis, while reducing gut permeability, blood endotoxin levels, inflammation and body weight. HSM and H1 also reduce insulin resistance, adipocyte hypertrophy, crown-like structures and signs of fatty liver disease (non-alcoholic fatty liver disease (NAFLD)/non-alcoholic steatohepatitis (NASH)). BAT, brown adipose tissue; IL, interleukin; iWAT, inguinal white adipose tissue; TNF- $\alpha$ , tumour necrosis factor-alpha; UCP1, uncoupling protein 1; VAT, visceral adipose tissue; ZO-1, zonula occludens-1.

supplementary figure S21). Intriguingly, a recent study showed that zwitterionic capsular polysaccharides derived from various commensal gut bacteria produce anti-inflammatory effects by inducing regulatory T cells.<sup>50</sup> Our observations that *P. goldsteinii* treatment induces expression of IL-10 (figure 7H) and helps maintain intestinal integrity (figure 7G,I,J) support the possibility that the bacterium may preserve intestinal homeostasis and improve gut barrier functions in vivo.

Our previous study showed that polysaccharides isolated from a water extract of the medicinal fungus *G. lucidum* also produce anti-obesogenic effects in HFD-fed mice.<sup>33</sup> Compared with the *G. lucidum* polysaccharides identified earlier, the monosaccharide composition of H1 identified here shows a higher content of mannose, galactose, N-galactosamine, N-glucosamine, rhamnose and fucose (see online supplementary table S3). Cordyceps polysaccharides have been found to contain  $\beta$ -glucans, heteroglycans and cordyglucans,<sup>29</sup> but the molecular structure and functional motifs of H1's high-molecular weight polysaccharides remain to be determined. While polysaccharides are predominantly enriched during water-based extraction procedures such as the one used to prepare the H1 fraction, we could not exclude the possibility that other bioactive molecules present in the extract may also contribute to the anti-obesogenic effects of this fraction. Moreover, we previously observed that *P. goldsteinii* levels in the gut microbiota of HFD-fed mice increased following treatment with *G. lucidum* polysaccharides,<sup>33</sup> suggesting that this commensal bacterial species may mediate the anti-obesogenic effects of polysaccharides isolated from various medicinal fungi.

The breakdown of polysaccharides and dietary fibre in mammals is mainly performed by intestinal bacteria, such as *Bacteroides thetaiotaomicron* and *Bacteroides fragilis*,<sup>51–54</sup> resulting in modulation of nutrient absorption and energy levels. HSM and H1 treatment did not alter energy intake, stool fat content or intestinal SCFA production (see online supplementary figures S2 and S3), indicating that the anti-obesity effects of H1 are not due to reduction of appetite, modulation of nutrient absorption or enhanced production of SCFAs. The reduction of *P. goldsteinii* levels by HFD and enrichment of this bacterial species by fungal polysaccharides indicate that the gut microbiota of polysaccharide-treated mice may contain higher levels of bacteria that preferentially metabolise polysaccharides. Enrichment of *P. goldsteinii* by H1 is also associated with reduced levels of bacterial species that are positively associated with obesity, such as *M. schaedleri* and *S. algae* (figure 4C).<sup>33 42 43 55</sup>

We observed that the anti-obesogenic effects of H1 are dependent on neomycin-sensitive gut bacteria (figures 3–6). The presence of a population of neomycin-sensitive gut bacteria and its association with obesity-related traits (figure 4D) suggests a potential beneficial interplay between these bacteria and energy regulation and metabolism. In the present study, H1 treatment did not affect the level of known commensal bacteria that possess anti-obesogenic properties, such as *A. muciniphila*,<sup>23 56</sup> *L. reuteri*<sup>57</sup> or *L. johnsonii*<sup>58</sup> (figure 4C). Further study of the functional gut microbiota and examination of their mechanism of action will be required to identify new strategies to prevent and treat obesity and related metabolic disorders.<sup>59</sup>

Several medicinal fungi and plants produce beneficial effects on obesity and diabetes by modulating a variety of physiological pathways in the body.<sup>28</sup> In comparison to fractions H2 to H4, which produced small effects on a limited number of obesity traits (see for instance figure 1E and supplementary

figure S4), HSM and fraction H1 produced consistent anti-obesogenic, antidiabetic and anti-inflammatory effects on all major obesity traits examined in HFD-fed mice, including HOMA-IR index (figure 1F), inflammation (figure 1G,H), metabolic endotoxemia (figure 2A) and intestinal permeability (figure 2B). Furthermore, besides reducing gene expression involved in lipogenic pathways in adipose and hepatic tissues (see online supplementary figure S4B,C), treatment with HSM and H1 significantly induced  $\beta$ -oxidation in the liver (see online supplementary figure S4C, Acl3). These results suggest that HSM and H1 may target specific metabolic and immunological pathways to normalise inflammatory markers and the metabolic profile of obese mice.

In conclusion, our results indicate that a water extract of a medicinal fungus and its high-molecular weight polysaccharide fraction reduce obesity, inflammation and diabetes-related symptoms by modulating the composition of the gut microbiota. Our findings show that both HSM and its high-molecular weight polysaccharides may be used as prebiotics—while the intestinal bacterium *P. goldsteinii* may be used as a probiotic—to prevent and treat obesity and the associated metabolic disorders.

#### Author affiliations

<sup>1</sup>Department of Medical Biotechnology and Laboratory Science, College of Medicine, Chang Gung University, Gueishan, Taiwan

<sup>2</sup>Graduate Institute of Biomedical Sciences, College of Medicine, Chang Gung University, Gueishan, Taiwan

<sup>3</sup>Center for Molecular and Clinical Immunology, Chang Gung University, Gueishan, Taiwan

<sup>4</sup>Microbiota Research Center, Chang Gung University, Gueishan, Taiwan

<sup>5</sup>Chang Gung Immunology Consortium, Linkou Chang Gung Memorial Hospital, Gueishan, Taiwan

<sup>6</sup>Research Center for Emerging Viral Infections, Chang Gung University, Gueishan, Taiwan

<sup>7</sup>Chang Gung Biotechnology Corporation, Taipei, Taiwan

<sup>8</sup>Biochemical Engineering Research Center, Ming Chi University of Technology, Taishan, Taiwan

<sup>9</sup>Department of Biomedical Sciences, University of the Pacific, Arthur Dugoni School of Dentistry, San Francisco, California, USA

<sup>10</sup>Department of Respiratory Therapy, Fu Jen Catholic University, Xinzhuang, Taiwan

<sup>11</sup>Laboratory of Cellular Physiology and Immunology, Rockefeller University, New York, USA

<sup>12</sup>Department of Laboratory Medicine, Linkou Chang Gung Memorial Hospital, Gueishan, Taiwan

<sup>13</sup>Research Center for Chinese Herbal Medicine, College of Human Ecology, Chang Gung University of Science and Technology, Gueishan, Taiwan

<sup>14</sup>Research Center for Food and Cosmetic Safety, College of Human Ecology, Chang Gung University of Science and Technology, Gueishan, Taiwan

**Acknowledgements** The authors would like to thank Dr Yu-Lun Kuo (Biotools) for the kind assistance with microbiota sequencing and analysis as well as Dr Yueh-Hsia Chiu (Chang Gung University) regarding the statistical analysis. The authors would also like to thank Drs Yu-Huan Tsai (Chang Gung University) and Julieta Schachter (Universidade Federal de Rio de Janeiro, Brazil) for their comments on the manuscript.

**Contributors** T-RW, C-SL and C-JC conceived the project, contributed to experimental design, performed experiments, interpreted the results, prepared the figures and wrote the manuscript; T-LL performed experiments and interpreted the results; JDY and H-CL conceived and supervised the project, interpreted the results and wrote the manuscript; JM, DMO and C-CL interpreted the results and wrote the manuscript; Y-FK provided the HSM extract and polysaccharides fractions; all authors discussed the results and approved the manuscript.

**Funding** The authors' work is supported by the Primordia Institute of New Sciences and Medicine; the Research Center for Emerging Viral Infections (Chang Gung University); the Featured Areas Research Center Program, which is part of the Higher Education Sprout Project of the Ministry of Education of Taiwan; by grants MOST105-2320-B-182-032-MY3, MOST105-2320-B-030-004, MOST103-2321-B-182-014-MY3 and MOST107-3017-F-182-001 from the Ministry of Science and Technology of Taiwan; and by grants BMRPA04, CMRPD1E0073, CMRPD1F0123, CORPD1F0011-3, QZRPD142 and QZRPD146 from Chang Gung Memorial Hospital.



**Competing interests** Y-FK is President of Chang Gung Biotechnology Corporation. JDY is Chairman of the Board of Chang Gung Biotechnology Corporation. The authors own patents related to the preparation and use of medicinal fungi and probiotics.

**Patient consent** Not required.

**Ethics approval** This study was approved by Chang Gung University's Institutional Animal Care and Use Committee (Document No. CGU11-117). Experiments were performed in accordance with the guidelines.

**Provenance and peer review** Not commissioned; externally peer reviewed.

## REFERENCES

- Caballero B. The global epidemic of obesity: an overview. *Epidemiol Rev* 2007;29:1–5.
- Haslam DW, James WP. Obesity. *Lancet* 2005;366:1197–209.
- World Health Organization. Obesity and overweight. 2018 <http://www.who.int/mediacentre/factsheets/fs311/en/>.
- Visscher TL, Seidell JC. The public health impact of obesity. *Annu Rev Public Health* 2001;22:355–75.
- Turnbaugh PJ, Ley RE, Mahowald MA, et al. An obesity-associated gut microbiome with increased capacity for energy harvest. *Nature* 2006;444:1027–131.
- Cani PD, Bibiloni R, Knauf C, et al. Changes in gut microbiota control metabolic endotoxemia-induced inflammation in high-fat diet-induced obesity and diabetes in mice. *Diabetes* 2008;57:1470–81.
- Cani PD, Possemiers S, Van de Wiele T, et al. Changes in gut microbiota control inflammation in obese mice through a mechanism involving GLP-2-driven improvement of gut permeability. *Gut* 2009;58:1091–103.
- Cani PD, Amar J, Iglesias MA, et al. Metabolic endotoxemia initiates obesity and insulin resistance. *Diabetes* 2007;56:1761–72.
- Hotamisligil GS. Inflammation and metabolic disorders. *Nature* 2006;444:860–7.
- Kennedy A, Martinez K, Chuang CC, et al. Saturated fatty acid-mediated inflammation and insulin resistance in adipose tissue: mechanisms of action and implications. *J Nutr* 2009;139:1–4.
- Morris DL, Cho KW, Delproposto JL, et al. Adipose tissue macrophages function as antigen-presenting cells and regulate adipose tissue CD4+ T cells in mice. *Diabetes* 2013;62:2762–72.
- Ridaura VK, Faith JJ, Rey FE, et al. Gut microbiota from twins discordant for obesity modulate metabolism in mice. *Science* 2013;341:1241214.
- Dethlefsen L, McFall-Ngai M, Relman DA. An ecological and evolutionary perspective on human-microbe mutualism and disease. *Nature* 2007;449:811–8.
- Yoshimoto S, Loo TM, Atarashi K, et al. Obesity-induced gut microbial metabolite promotes liver cancer through senescence secretome. *Nature* 2013;499:97–101.
- Hersoug LG, Möller P, Loft S. Gut microbiota-derived lipopolysaccharide uptake and trafficking to adipose tissue: implications for inflammation and obesity. *Obes Rev* 2016;17:297–312.
- Aguirre M, Venema K. The art of targeting gut microbiota for tackling human obesity. *Genes Nutr* 2015;10:472.
- Anand G, Zarrinpar A, Loomis R. Targeting Dysbiosis for the Treatment of Liver Disease. *Semin Liver Dis* 2016;36:037–47.
- Delzenne NM, Cani PD, Everard A, et al. Gut microorganisms as promising targets for the management of type 2 diabetes. *Diabetologia* 2015;58:2206–17.
- Scott KP, Antoine JM, Midtvedt T, et al. Manipulating the gut microbiota to maintain health and treat disease. *Microb Ecol Health Dis* 2015;26:25877.
- Sonnenburg JL, Bäckhed F. Diet-microbiota interactions as moderators of human metabolism. *Nature* 2016;535:56–64.
- Delzenne NM, Neyrinck AM, Bäckhed F, et al. Targeting gut microbiota in obesity: effects of prebiotics and probiotics. *Nat Rev Endocrinol* 2011;7:639–46.
- Everard A, Lazarevic V, Derrien M, et al. Responses of gut microbiota and glucose and lipid metabolism to prebiotics in genetic obese and diet-induced leptin-resistant mice. *Diabetes* 2011;60:2775–86.
- Everard A, Belzer C, Geurts L, et al. Cross-talk between *Akkermansia muciniphila* and intestinal epithelium controls diet-induced obesity. *Proc Natl Acad Sci U S A* 2013;110:9066–71.
- Wang J, Tang H, Zhang C, et al. Modulation of gut microbiota during probiotic-mediated attenuation of metabolic syndrome in high fat diet-fed mice. *Isme J* 2015;9:1–15.
- De Vadder F, Kovatcheva-Datchary P, Goncalves D, et al. Microbiota-generated metabolites promote metabolic benefits via gut-brain neural circuits. *Cell* 2014;156:84–96.
- Nakamura YK, Omaye ST. Metabolic diseases and pro- and prebiotics: Mechanistic insights. *Nutr Metab* 2012;9:60.
- Parnell JA, Reimer RA. Prebiotic fiber modulation of the gut microbiota improves risk factors for obesity and the metabolic syndrome. *Gut Microbes* 2012;3:29–34.
- Martel J, Ojcius DM, Chang CJ, et al. Anti-obesogenic and antidiabetic effects of plants and mushrooms. *Nat Rev Endocrinol* 2017;13:149–60.
- El Enshasy HA, Hatti-Kaul R. Mushroom immunomodulators: unique molecules with unlimited applications. *Trends Biotechnol* 2013;31:668–77.
- Wasser SP. Medicinal mushroom science: Current perspectives, advances, evidences, and challenges. *Biomed J* 2014;37:345–56.
- Martel J, Ko YF, Ojcius DM, et al. Immunomodulatory Properties of Plants and Mushrooms. *Trends Pharmacol Sci* 2017;38:967–81.
- Martel J, Ko YF, Liao JC, et al. Myths and Realities Surrounding the Mysterious Caterpillar Fungus. *Trends Biotechnol* 2017;35:1017–21.
- Chang CJ, Lin CS, Lu CC, Cc L, et al. *Ganoderma lucidum* reduces obesity in mice by modulating the composition of the gut microbiota. *Nat Commun* 2015;6:7489.
- Lo HC, Hsieh C, Lin FY, et al. A Systematic Review of the Mysterious Caterpillar Fungus *Ophiocordyceps sinensis* in Dong-ChongXiaCao (Dong Chong Xia Cao) and Related Bioactive Ingredients. *J Tradit Complement Med* 2013;3:16–32.
- Zhu ZY, Liu XC, Fang XN, et al. Structural characterization and anti-tumor activity of polysaccharide produced by *Hirsutella sinensis*. *Int J Biol Macromol* 2016;82:959–66.
- Ko YF, Liao JC, Lee CS, et al. Isolation, Culture and Characterization of *Hirsutella sinensis* Mycelium from Caterpillar Fungus Fruiting Body. *PLoS One* 2017;12:e0168734.
- Wang CY, Liao JK. A mouse model of diet-induced obesity and insulin resistance. *Methods Mol Biol* 2012;821:421–33.
- White JR, Nagarajan N, Pop M. Statistical methods for detecting differentially abundant features in clinical metagenomic samples. *PLoS Comput Biol* 2009;5:e1000352.
- Benjamini Y, Krieger AM, Yekutieli D. Adaptive linear step-up procedures that control the false discovery rate. *Biometrika* 2006;93:491–507.
- Shabalina IG, Petrovic N, de Jong JM, et al. UCP1 in brite/beige adipose tissue mitochondria is functionally thermogenic. *Cell Rep* 2013;5:1196–203.
- Kim KA, Gu W, Lee IA, et al. High fat diet-induced gut microbiota exacerbates inflammation and obesity in mice via the TLR4 signaling pathway. *PLoS One* 2012;7:e47713.
- Johnson-Henry KC, Donato KA, Shen-Tu G, et al. *Lactobacillus rhamnosus* strain GG prevents enterohemorrhagic *Escherichia coli* O157:H7-induced changes in epithelial barrier function. *Infect Immun* 2008;76:1340–8.
- Chiu CM, Huang WC, Weng SL, et al. Systematic analysis of the association between gut flora and obesity through high-throughput sequencing and bioinformatics approaches. *Biomed Res Int* 2014;2014:1–10.
- Lee H, Ko G. Effect of metformin on metabolic improvement and gut microbiota. *Appl Environ Microbiol* 2014;80:5935–43.
- Clarke SF, Murphy EF, Nilaweera K, et al. The gut microbiota and its relationship to diet and obesity: new insights. *Gut Microbes* 2012;3:186–202.
- Kan WC, Wang HY, Chien CC, et al. Effects of Extract from Solid-State Fermented *Cordyceps sinensis* on Type 2 Diabetes Mellitus. *Evid Based Complement Alternat Med* 2012;2012:1–10.
- Koh JH, Kim JM, Chang UJ, et al. Hypocholesterolemic effect of hot-water extract from mycelia of *Cordyceps sinensis*. *Biol Pharm Bull* 2003;26:84–7.
- Li SP, Zhang GH, Zeng Q, et al. Hypoglycemic activity of polysaccharide, with antioxidation, isolated from cultured *Cordyceps* mycelia. *Phytomedicine* 2006;13:428–33.
- Shi B, Wang Z, Jin H, et al. Immunoregulatory *Cordyceps sinensis* increases regulatory T cells to Th17 cell ratio and delays diabetes in NOD mice. *Int Immunopharmacol* 2009;9:582–6.
- Neff CP, Rhodes ME, Arnolds KL, et al. Diverse Intestinal Bacteria Contain Putative Zwitterionic Capsular Polysaccharides with Anti-inflammatory Properties. *Cell Host Microbe* 2016;20:535–47.
- Krajmalnik-Brown R, Ilhan ZE, Kang DW, et al. Effects of gut microbes on nutrient absorption and energy regulation. *Nutr Clin Pract* 2012;27:201–14.
- Ravcheev DA, Godzik A, Osterman AL, et al. Polysaccharides utilization in human gut bacterium *Bacteroides thetaiotaomicron*: comparative genomics reconstruction of metabolic and regulatory networks. *BMC Genomics* 2013;14:873.
- Schwalm ND, Townsend GE, Groisman EA. Multiple Signals Govern Utilization of a Polysaccharide in the Gut Bacterium *Bacteroides thetaiotaomicron*. *MBio* 2016;7:e01342-16.
- Wexler HM. Bacteroides: the good, the bad, and the nitty-gritty. *Clin Microbiol Rev* 2007;20:593–621.
- Ravussin Y, Koren O, Spor A, et al. Responses of gut microbiota to diet composition and weight loss in lean and obese mice. *Obesity* 2012;20:738–47.
- Schneeberger M, Everard A, Gómez-Valadés AG, et al. *Akkermansia muciniphila* inversely correlates with the onset of inflammation, altered adipose tissue metabolism and metabolic disorders during obesity in mice. *Sci Rep* 2015;5:16643.
- Qiao Y, Sun J, Xia S, et al. Effects of different *Lactobacillus reuteri* on inflammatory and fat storage in high-fat diet-induced obesity mice model. *J Funct Foods* 2015;14:424–34.
- Xin J, Zeng D, Wang H, et al. Preventing non-alcoholic fatty liver disease through *Lactobacillus johnsonii* B515 by attenuating inflammation and mitochondrial injury and improving gut environment in obese mice. *Appl Microbiol Biotechnol* 2014;98:6817–29.
- Pedersen HK, Gudmundsdottir V, Nielsen HB, et al. Human gut microbes impact host serum metabolome and insulin sensitivity. *Nature* 2016;535:376–81.





# Predicting Intraserotypic Recombination in Enterovirus 71

Andrew Woodman,<sup>a</sup> Kuo-Ming Lee,<sup>b</sup> Richard Janissen,<sup>c</sup> Yu-Nong Gong,<sup>b</sup> Nynke H. Dekker,<sup>c</sup> Shin-Ru Shih,<sup>b,d,e,f</sup> Craig E. Cameron<sup>a</sup>

<sup>a</sup>Department of Biochemistry and Molecular Biology, The Pennsylvania State University, University Park, Pennsylvania, USA

<sup>b</sup>Research Center for Emerging Viral Infections, Chang Gung University, Taoyuan, Taiwan

<sup>c</sup>Department of Bionanoscience, Kavli Institute of Nanoscience, Delft University of Technology, Delft, The Netherlands

<sup>d</sup>Department of Medical Biotechnology and Laboratory Science, College of Medicine, Chang Gung University, Taoyuan, Taiwan

<sup>e</sup>Department of Laboratory Medicine, Linkou Chang Gung Memorial Hospital, Taoyuan, Taiwan

<sup>f</sup>Research Center for Chinese Herbal Medicine, Research Center for Food and Cosmetic Safety, and Graduate Institute of Health Industry Technology, College of Human Ecology, Chang Gung University of Science and Technology, Taoyuan, Taiwan

**ABSTRACT** Enteroviruses are well known for their ability to cause neurological damage and paralysis. The model enterovirus is poliovirus (PV), the causative agent of poliomyelitis, a condition characterized by acute flaccid paralysis. A related virus, enterovirus 71 (EV-A71), causes similar clinical outcomes in recurrent outbreaks throughout Asia. Retrospective phylogenetic analysis has shown that recombination between circulating strains of EV-A71 produces the outbreak-associated strains which exhibit increased virulence and/or transmissibility. While studies on the mechanism(s) of recombination in PV are ongoing in several laboratories, little is known about factors that influence recombination in EV-A71. We have developed a cell-based assay to study recombination of EV-A71 based upon previously reported assays for poliovirus recombination. Our results show that (i) EV-A71 strain type and RNA sequence diversity impacts recombination frequency in a predictable manner that mimics the observations found in nature; (ii) recombination is primarily a replicative process mediated by the RNA-dependent RNA polymerase; (iii) a mutation shown to reduce recombination in PV (L420A) similarly reduces EV-A71 recombination, suggesting conservation in mechanism(s); and (iv) sequencing of intraserotypic recombinant genomes indicates that template switching occurs by a mechanism that may require some sequence homology at the recombination junction and that the triggers for template switching may be sequence independent. The development of this recombination assay will permit further investigation on the interplay between replication, recombination and disease.

**IMPORTANCE** Recombination is a mechanism that contributes to genetic diversity. We describe the first assay to study EV-A71 recombination. Results from this assay mimic what is observed in nature and can be used by others to predict future recombination events within the enterovirus species A group. In addition, our results highlight the central role played by the viral RNA-dependent RNA polymerase (RdRp) in the recombination process. Further, our results show that changes to a conserved residue in the RdRp from different species groups have a similar impact on viable recombinant virus yields, which is indicative of conservation in mechanism.

**KEYWORDS** conservation, EV-A71, predictive, replicative recombination

The *Enterovirus* genus in the family *Picornaviridae* currently consists of 15 species. Outside rhinoviruses, the enteroviruses responsible for human mortality and morbidity fall specifically into groups A, B, C, and D (1, 2). This group of viruses, typified by poliovirus (PV), has a 7.5-kb positive-sense RNA genome that encodes a single polyprotein that is flanked by noncoding regions. The polyprotein is co- and posttransla-

**Citation** Woodman A, Lee K-M, Janissen R, Gong Y-N, Dekker NH, Shih S-R, Cameron CE. 2019. Predicting intraserotypic recombination in enterovirus 71. *J Virol* 93:e02057-18. <https://doi.org/10.1128/JVI.02057-18>.

**Editor** Julie K. Pfeiffer, University of Texas Southwestern Medical Center

**Copyright** © 2019 American Society for Microbiology. All Rights Reserved.

Address correspondence to Andrew Woodman, [auw23@psu.edu](mailto:auw23@psu.edu), or Craig E. Cameron, [cec9@psu.edu](mailto:cec9@psu.edu).

**Received** 19 November 2018

**Accepted** 19 November 2018

**Accepted manuscript posted online** 28 November 2018

**Published** 5 February 2019

tionally processed by virus-encoded proteases to generate the structural proteins (VP4, VP2, VP3, and VP1), which assemble to form the icosahedral capsid and the nonstructural proteins (2A<sup>Pro</sup>, 2B, 2C, 3A, 3B<sup>VPg</sup>, 3C<sup>Pro</sup>, and 3D<sup>Pol</sup>) that mediate replication of the virus genome (3).

RNA viruses, like those found in the *Enterovirus* genus, exist as a viral quasispecies as a consequence of misincorporations by their error-prone RNA-dependent RNA polymerases (RdRps) during genome replication (4, 5). In addition, recombination enables the exchange of genetic material through a proposed “copy choice” mechanism in which the viral RdRp, along with the nascent RNA, switches templates during replication, creating hybrids between two viruses replicating in the same cell (6–8). As well as being a driver of genetic variation, it is believed that recombination may have evolved in order to “rescue” genomes from deleterious mutations that accumulate during error-prone replication (9).

Enterovirus 71 (EV-A71), a member of the species A group, is an important neurotropic enterovirus for which there is currently no effective therapy or vaccine and manifests most frequently as a childhood illness known as hand, foot, and mouth disease (HFMD) (10). However, acute EV-A71 infection can also be associated with flaccid paralysis, myocarditis, or even fatal encephalitis (10, 11). EV-A71 variants have been classified into three groups (GgA, GgB, and GgC), and recombination has been linked to the founding of each subgroup lineage (12). More importantly, cocirculation of the species A EV-A71 and coxsackievirus A16 (CV-A16) viruses has been associated with large-scale outbreaks of HFMD (13, 14). Sequence analysis of clinical isolates obtained since 2008 from patients with fatal neurological symptoms has demonstrated that these cases are mainly due to subgenogroup C4 of EV-A71, which was previously identified as an EV-A71/CV-A16 recombinant virus (15, 16). In related enteroviruses, recombinant forms defined by serotype according to their capsid proteins, have been shown to emerge, prevail, and then disappear in temporal epidemiological surveys of globally distributed serotypes (12, 17, 18). In many of these examples, the recombinants are pathogenic.

It is evident that recombination is a critical driver of virus evolution with medically important consequences. While the triggers and mechanisms of recombination in PV are starting to be understood (19–21), the ability to predict the likelihood of a recombination event between circulating viruses of public health relevance has not been available. We wanted to use the cell-based approaches that have been developed to study recombination in PV as a tool to test whether recombination events for EV-A71 in cell culture mimic what is observed in nature (22). In order to study recombination in EV-A71, we have developed a robust, reproducible cell-based assay. The established *in vitro* assay based upon the previously reported assays for PV (19–21) consists of two genomes, each containing a different deleterious (and nonreverting) modification that prevents the production of viable progeny. Only a recombination event between the two genomes can produce viable virus. Current investigations of PV recombination have shown that targeted mutations to the RdRp of the donor and acceptor templates can significantly alter the yield of recombinant virus (19, 21). We introduced a similar RdRp mutation (L420A in PV and L421A in EV-A71) into our cell-based recombination assay and demonstrate a significant reduction in recombinant yield. The same mutation had no impact on replication but led to an EV-A71 virus population that was ultrasensitive to the antiviral ribavirin. We expanded our assay to consider the role of cell-mediated nonreplicative recombination since this pathway is known to occur for PV (23, 24). Our results indicate that only a minor amount of EV-A71 recombinant virus is produced via this mechanism, further supporting the interpretation that recombination is primarily RdRp mediated. Crucially, we tested the biological relevance of our assay by expanding it to include two additional circulating strains of EV-A71: a strain known to recombine (C4) and a strain that is not recombinogenic (B5). Our results show important significant differences in viable recombinant virus yield that mimic observations found in nature. Limited sequencing of recombinant genomes suggested that no sequence motif acted as a trigger for recombination, but it did show

that RNA sequence complementarity at the recombination site may be important, adding support to the widely accepted “copy choice” mechanism of template switching. We believe that this assay can be used as a tool to predict the likelihood of recombination between current circulating EV-A71 strains.

(This article was submitted to an online preprint archive [25].)

## RESULTS

**Development of an EV-A71 cell-based recombination assay.** In order to predict recombination events in EV-A71 an experimental system is required. The study of viral factors that modulate enterovirus recombination have benefited from the recent development of recombination specific cell-based assays in PV that use parental templates that are only able to produce viable virus via recombination (19–21). A suitable “donor” template for the assay was the already-established subgenogroup C2 EV-A71 (TW/2231/98) subgenomic replicon, where a firefly luciferase reporter replaces the entire P1 region (26) (Fig. 1A). We modified the replicon by engineering a hammerhead ribozyme immediately 5′ of the internal ribosomal entry sequence (IRES), a change that would ensure an authentic genomic sequence following *in vitro* RNA transcription (27). The modification led to a significant improvement in replication in human embryonic rhabdomyosarcoma (RD) cells with a 3- $\log_{10}$  increase in reporter signal (a surrogate marker for genome replication) compared to the unmodified replicon (data not shown). One recently used assay for the study of PV recombination, known as CRE-REP (20), uses an acceptor template that has characterized mutations within the 2C Oril stem-loop that inhibits positive-sense RNA synthesis (28, 29). The EV-A71 Oril has not been fully characterized so similar mutations to the predicted stem-loop in 2C were not considered. In addition, mutations to the Oril of the related coxsackievirus B3 have been shown to revert, or produce virus with 5′ RNA truncations (30, 31). The “acceptor” template in our assay was the EV-A71 C2-MP4 strain (32) that had a region removed within the 3D coding region of the genome that encompasses the active site of the RdRp (EV-A71 $\Delta$ 3D), similar to an acceptor template used in a PV model for recombination (21). After cotransfection of donor and acceptor RNA templates into permissive cells, a viral-RdRp-mediated template switch from donor to acceptor may produce a fully functional recombinant genome (Fig. 1A). Cell-based studies on the dynamics of EV-A71 replication are primarily carried out in RD or African green monkey (Vero) cells, which are susceptible to EV-A71 infection due to the expression of the receptor SCARB2 (33). Since enterovirus recombination has been shown to be a replicative process (19–21), we wanted to select a cell type for any EV-A71 recombination assay that would be optimal for replication of the donor replicon template. We initially quantified the luciferase signal, a marker for RNA replication, at 8 h after the transfection of RD and Vero cells with the EV-A71 C2 replicon RNA. The results indicated that Vero cells were suboptimal for any future recombination assays as the luciferase signal was significantly lower (nearly 2  $\log_{10}$ ) than that produced in the RD cell line (data not shown). A subsequent cotransfection of RD cells with donor and acceptor RNA templates in equimolar ratios yielded viable recombinant virus ( $8.8 \times 10^3$  PFU/ml  $\pm 2 \times 10^3$ ) (Fig. 1B), an amount in line with previous studies that used PV as a model (19–21). Transfection of the donor and acceptor RNA templates alone produced no viable virus (Fig. 1B). To ensure that the observed virus was recombinant and to gain insight into the location of template switching, individual viruses were plaque purified and subjected to reverse transcription-PCR (RT-PCR) sequence analysis. Both donor and acceptor templates are derived from the EV-A71 subgenogroup C2 parental strains and share high sequence similarity (99.3% at the RNA level). Precise identification of the site of recombination would therefore be difficult. In two examples (Fig. 1C), the location of recombination was shown to fall within the 2A region. The first recombinant has a junction that falls within a 34-nucleotide window of shared homology between donor and acceptor templates. Similarly, the second recombinant has a junction that falls within a larger, 248-nucleotide window. Importantly, all isolated sequences were recombinant, validating the experimental approach.

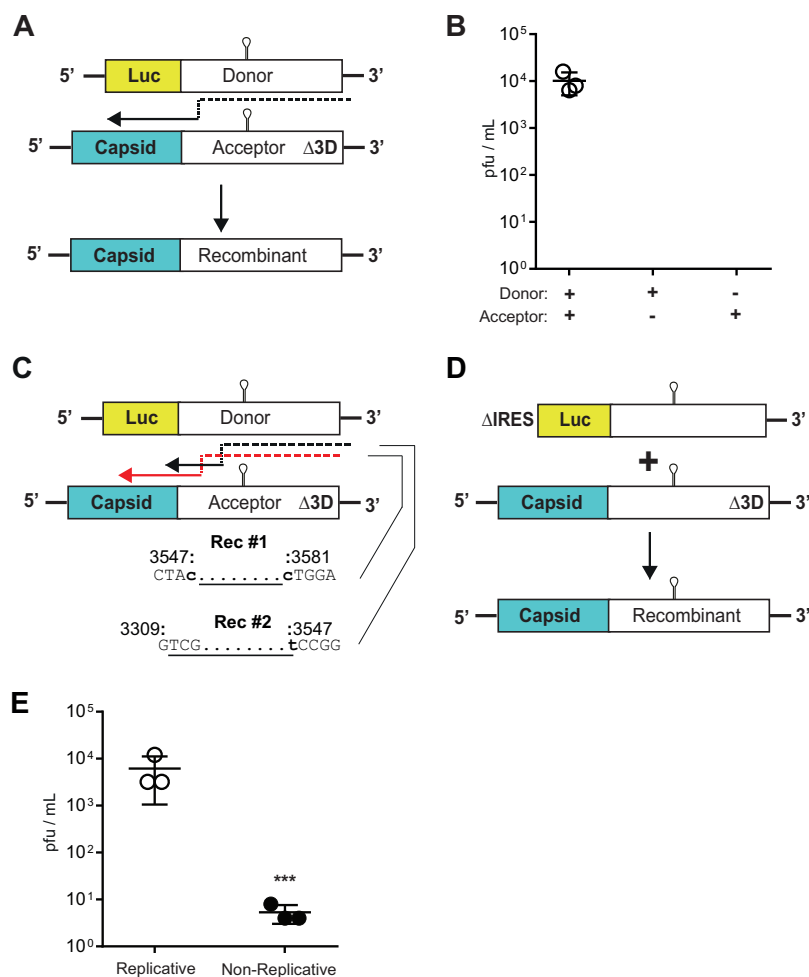


**FIG 1** Enterovirus 71 (EV-A71) recombination in RD cells is primarily replicative. (A) Cell-based EV-A71 recombination assay. C2 strain firefly luciferase-encoding subgenomic replicon (donor) and full-length EV-A71 C2-MP4 strain genome (acceptor) carrying a lethal deletion of the 3D<sup>pol</sup> region were cotransfected in an equimolar ratio into RD cells. A fully functional virus genome can be produced via an RdRp template switch from donor to acceptor (indicated by dashed black arrow). (B) Only upon cotransfection can replication-competent virus be generated (PFU/ml  $\pm$  standard deviations [SD];  $n = 3$ ). (C) Example sequences of plaque-purified recombinant virus from C2/C2 (left panel). Dashed arrows indicate predicted paths of viral RdRp upon template switching. Numbering refers to the position upon the acceptor templates. Lowercase, boldface nucleotides indicate the 5' and 3' boundaries of recombination. The underlined sequences indicate region of homology. (D) Nonreplicative recombination assay. IRES deletion of the C2 donor template inhibits translation. The acceptor template remains the same as in panel A. Viable virus will only be produced via a cell-mediated event. (E) Yield of recombinant virus (PFU/ml  $\pm$  SD;  $n = 3$ ) originating from transfection in equimolar ratio of replicative and nonreplicative partners. Statistical analyses were performed using an unpaired, two-tailed  $t$  test (\*\*\*,  $P = 0.0001$ ).

**EV-A71 recombination is primarily a replicative process.** We generated an additional parental genome that would be unable to replicate in order to confirm whether the recombination we were observing was from a replicative process and therefore different from nonreplicative recombination (23, 34–36). We removed the entire IRES from the EV-A71 C2 subgenomic replicon producing the C2- $\Delta$ IRES replicon template. This inhibits the translation of the viral RNA, ensuring that no active RdRp is produced (Fig. 1D). The second RNA partner in this “nonreplicative” assay was the same acceptor template shown in Fig. 1A (EV-A71 $\Delta$ 3D). Importantly, both templates carried the relevant coding sequences that would produce a viable virus if a nonreplicative mechanism of recombination occurred (Fig. 1D). In a side-by-side experiment with the replicative recombination assay (Fig. 1A), equimolar ratios of replicative partners and the newly developed nonreplicative partners were transfected into RD cells. Quantifi-



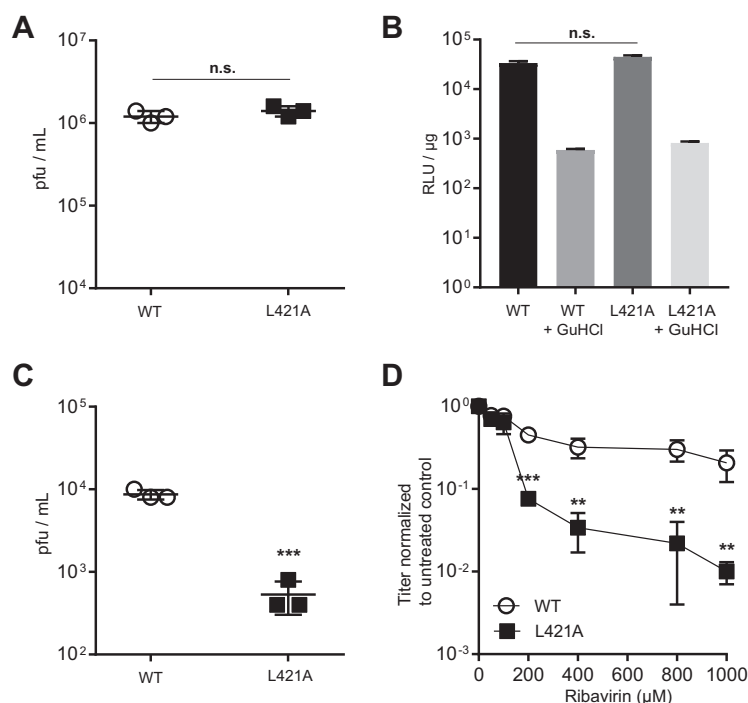


**FIG 2** Mutation to the donor RdRp inhibits recombination and increases susceptibility to ribavirin. (A) L421A mutation does not impact virus yield. Yields of virus are shown for wild-type EV-A71 C2-MP4 and the L421A variant after transfection of RNA (PFU/ml  $\pm$  SD;  $n = 3$ ). (B) L421A mutation does not impact donor template replication. Cells were transfected with 250 ng of wild-type EV-A71 replicon and the L421A variant with or without 4 mM guanidine hydrochloride. The luciferase activity is reported in relative light units (RLU) per microgram of total protein in the extract at 8 h posttransfection. (C) L421A inhibits EV-A71 replicative recombination. Yields of recombinant virus following transfection of either wild-type or L421A variant donor template with acceptor RNA in RD cells were determined (PFU/ml  $\pm$  SD;  $n = 3$ ). Statistical analyses were performed using an unpaired, two-tailed  $t$  test (\*\*\*,  $P = 0.0003$ ). (D) EV-A71 L421A population is highly susceptible to ribavirin. RD cells were infected at an MOI 0.1 with wild-type or L421A variant EV-A71 C2-MP4 virus in the presence of various concentrations of ribavirin. After achieving a CPE, virus supernatant was clarified and used for a plaque assay. Results show titer of virus normalized to an untreated control (PFU/ml  $\pm$  SD;  $n = 3$ ). Statistical analyses were performed using an unpaired, two-tailed  $t$  test (\*\*\*,  $P = 0.0004$ ; \*\*,  $P < 0.005$ ).

cation of virus at 60 h posttransfection showed that the replicative partners were able to produce significantly more viable recombinant virus ( $5.4 \times 10^3$  PFU/ml  $\pm 2 \times 10^3$ ) compared to the nonreplicative assay ( $\sim 10$  PFU/ml) (Fig. 1E). This result is highly suggestive that recombination in EV-A71 is primarily a replicative process that is RdRp mediated, similar to that observed for PV (19–21).

**An RdRp mutation impairs recombination but not replication.** Current investigations of PV recombination have shown that targeted mutations to the RNA-dependent RNA polymerase (RdRp) can have a significant impact upon the yield of recombinant virus (19–21). An L420A change within the RdRp coding region has been shown to significantly inhibit recombination in a PV model (21). The leucine residue is conserved in the prototype strains of EV-A, -B, -C, and -D (position 421 of the RdRp coding region in EV-A71). We therefore reasoned that if the underlying mechanism(s) of recombination were conserved between enterovirus species, a similar modification to the RdRp of the donor template might inhibit recombination in the newly developed EV-A71 recombination assay. We first introduced the L421A modification into the EV-A71 C2-MP4 full-length clone and quantified virus production after transfection of RNA into RD cells. No significant difference in virus yield was observed compared to the wild type (Fig. 2A). In addition, the luciferase signal with or without guanidine hydrochloride of the L421A C2 replicon template was similar to the wild-type replicon at 8 h posttransfection (Fig. 2B). Taken together, the two experiments demonstrated that the L421A variant has no negative impact upon replication, an important prerequisite for

interpretation of any recombination assay. We then carried out a recombination assay to investigate the impact of the L421A mutation on virus yield. After transfection of wild-type parental RNA, an average recombinant yield of  $8.6 \times 10^3$  PFU/ml ( $\pm 1 \times 10^3$  PFU/ml) was observed. In contrast, when the L421A mutation was present in the RdRp donor template the yield of recombinant was significantly reduced by >10-fold, measuring an average of  $5.3 \times 10^2$  PFU/ml ( $\pm 2 \times 10^2$  PFU/ml) (Fig. 2C). Recombination has been proposed as an adaptive mechanism that generates combinations of beneficial mutations and/or removal of deleterious mutations that may appear in a population of viruses after replication (37, 38). If this hypothesis is correct, then a virus population that is unable to “purge” deleterious mutations via recombination should be highly susceptible to mutagenic compounds such as nucleoside analogues. Indeed, a population of PV carrying the L420A mutation has been shown to be highly susceptible to the mutagen ribavirin (21). Kempf et al. proposed that this is not related to RdRp fidelity but rather a direct result of inhibiting recombination. We tested an EV-A71 population carrying the similar L421A mutation. RD cells were infected at a multiplicity of infection (MOI) of 0.1 in the presence of increasing concentrations of ribavirin. Viable virus was then quantified by PFU and normalized to an untreated control. The results showed that concentrations of ribavirin of  $>200 \mu\text{M}$  led to a significant decrease in the viability of the L421A EV-A71 population compared to wild-type (Fig. 2D). Importantly, the results with the L421A variant further support the interpretation that recombination in EV-A71 is a replicative process and potentially indicate that the mechanism(s) of recombination and the consequences thereof in enteroviruses may indeed be conserved across species groups.

**Use of alternate donor templates significantly impacts recombinant virus yield in a predictive manner.** The main goal of developing the EV-A71 recombination assay was to test its predictive power in reproducing what is observed in nature. In order to do this, two additional subgenomic replicons (donor templates) were engineered and introduced into the assay. Importantly, both donor templates were developed from the current circulating clinical isolates TW-00073-2012 and TW-50144-2013, with phylogenetic analysis placing them within the C4 and B5 subgenogroups, respectively (Fig. 3). At the RNA level, the donor replicon C4 and B5 strains both share ~80% RNA sequence homology with the acceptor template C2 strain within the region of recombination (Table 1). The majority of nucleotide differences are, however, at the wobble-base position since the amino acid homology to the acceptor template is ~95% for both replicon strains (Table 1). Importantly, current phylogenetic data show the C4 group has evolved by genetic shift through intra- and intertypic recombination events. Indeed, the C4 subgenotype is characterized by a higher similarity to the prototype CV-A16 virus (G-10) at the P2 and P3 region (Fig. 3, marked in green). In contrast, analysis of B5 members clusters them in an independent clade within the genotype B group and suggests that evolution has been limited to genetic drift only (Fig. 3, orange arrow). Since the B5 subgenogroup is not associated with current circulating recombinant viruses, we hypothesized that the B5 donor template in our recombination assay may produce significantly lower recombinant yield compared to the C2 and C4 donor templates. A single-step growth curve for the EV-A71 C4 and B5 clinical isolates indicated no significant difference in replication (Fig. 4A). In addition, we tested the replication kinetics of the new subgenomic replicons using a luciferase time course assay (Fig. 4B). The results show a similar luciferase signal as a function of time for all three donor templates, with the B5 replicon producing a marginally higher reporter signal at each time point compared to the C2 and C4 strains. Because there was no significant difference in replication between the three donor templates, a subsequent recombination assay was carried out for each pairing. Quantification of recombinant virus showed that alternate donor templates did indeed significantly impact viable recombinant yield (Fig. 4C). All of the combinations tested produced detectable virus ( $\text{C2/C2} = 6.9 \times 10^3$  PFU/ml  $\pm 2.4 \times 10^3$ ,  $\text{C4/C2} = 4.2 \times 10^2$  PFU/ml  $\pm 10^2$ , and  $\text{B5/C2} = 5.6 \times 10^1$  PFU/ml  $\pm 10$ ), and all of the viruses produced were recombinant (see representative sequences in Fig. 4D and E). If RNA sequence homology is the driving

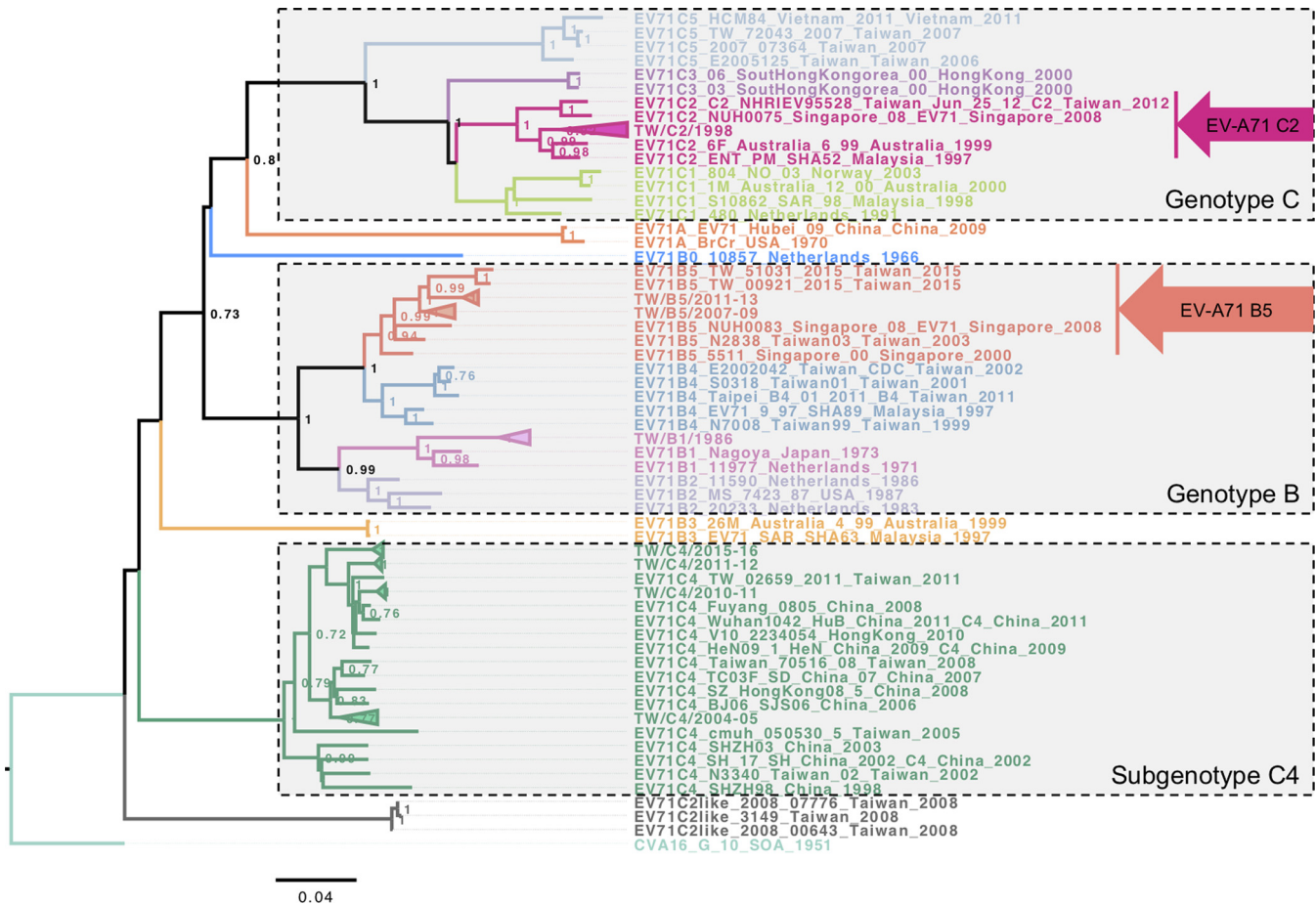


**FIG 3** Phylogenetic analysis of EV-A71 genotypes B and C. Neighbor-joining phylogenetic analysis of EV-A71 genotypes B and C was based on their P2-P3 genome region, rooted by the coxsackievirus (CV) A16 prototype strain G10 (isolated in 1951). The subtrees show mixed clusters of evolutionary intra- and intertypic recombination events of analyzed EV-A71 sequences (*n* = 182). EV-A71 subgenotypes and genotypes are depicted in different colors. The subgenotype B5 (orange arrow) is located within the genotype B cluster, showing a ladder-like evolutionary scale. In contrast to other subgenotypes of genotype C, the subgenotype C4 (labeled in green) forms an outgroup of genotype C, close to other recombinogenic EV-A71 strains (e.g., B3 and C2-like) and the prototype CV-A16 sequence. The probabilities of replicate trees in which associated taxa clustered together in the bootstrapped data (1,000 replicates) are shown next to the branches. The phylogenetic tree is drawn to scale, with branch lengths representing the numbers of base substitutions per site.

force for RdRp mediated “copy choice” recombination, then the significantly higher yield for the C2/C2 partners compared to the other two conditions is not surprising, given the RNA sequence homology between donor and acceptor templates is >99%. However, the C4 and B5 replicons shared similar divergence in RNA sequence to the acceptor, but the yield of recombinant virus was significantly different. This result indeed followed what is observed in nature and suggests that the *in vitro* cell-based assay has some power for predicting the efficiency of EV-A71 intraserotypic recomb-

**TABLE 1** Nucleotide and amino acid identity between donor template (C4 and B5 strains) and acceptor template (C2 strain)<sup>a</sup>

EV-A71 strain	Sequence type	Identity (%)											
		Overall	VP4	VP2	VP3	VP1	2A	2B	2C	3A	3B	3C	3D
C4	Nucleotide	83.3	88.9	91.3	91.9	90.5	<b>84.9</b>	<b>74.7</b>	<b>79.0</b>	<b>76.4</b>	<b>75.8</b>	<b>75.8</b>	<b>77.9</b>
	Amino acid	96.7	100.0	100.0	99.6	98.7	97.3	92.9	96.7	94.2	90.9	94.0	93.9
B5	Nucleotide	80.1	80.7	81.2	82.0	83.1	<b>81.2</b>	<b>75.8</b>	<b>79.7</b>	<b>78.1</b>	<b>80.3</b>	<b>77.3</b>	<b>79.1</b>
	Amino acid	95.5	100.0	97.6	97.1	97.3	96.7	91.9	95.7	93.0	95.5	91.8	93.7

<sup>a</sup>Consensus sequences of the C4 and B5 subgenotypes were used to perform the pairwise sequence alignments with the C2 acceptor template strain. The EV-A71 full-genome sequences used to calculate the consensus are described by Lee et al. (22). The sequence identities at the RNA and amino acid levels are denoted as percentages. Boldfacing indicates sequence identities at the RNA level to the C2 acceptor template in the region where recombination can occur.

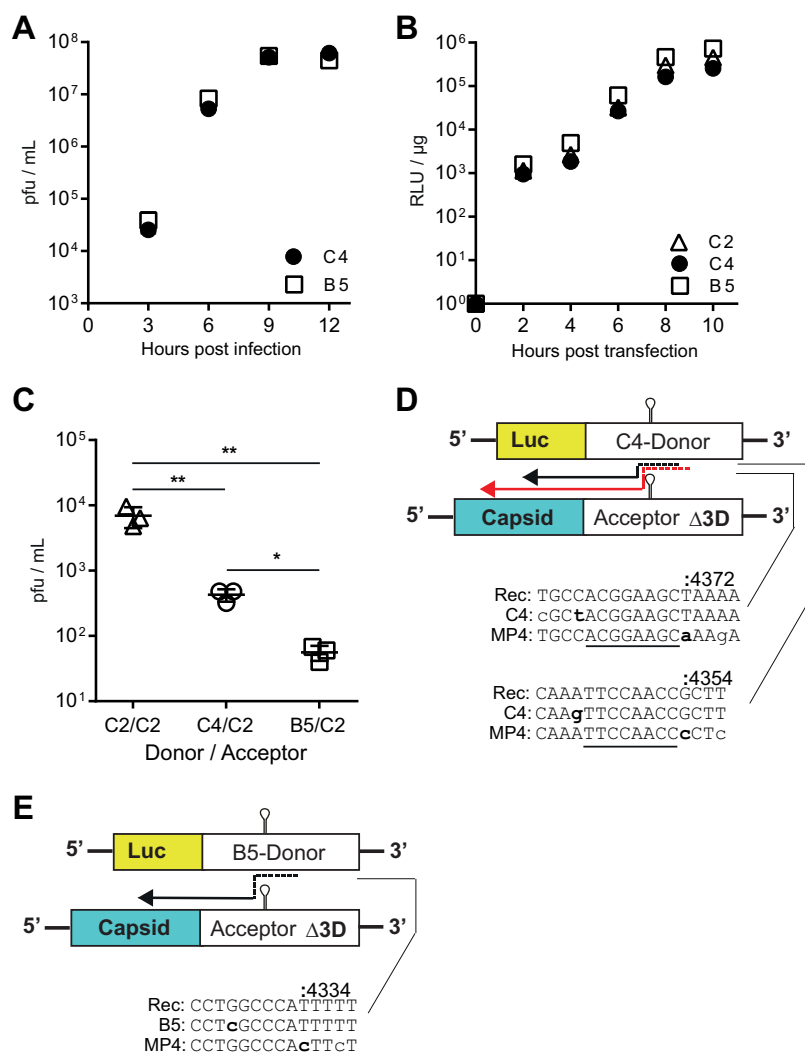


**FIG 4** Alternate donor templates significantly impact viable recombinant frequency in a predictable manner. (A) Single-step growth curve at an MOI 10 of EV-A71 C4 and B5 strains shows no significant difference in replication. (B) C2, C4, and B5 subgenomic replicon firefly luciferase time courses. Cells were transfected with 250 ng of each respective EV-A71 replicon, and the luciferase activity is reported in RLU per microgram of total protein in the extract. (C) EV-A71 recombination assay. RD cells were transfected with the various EV-A71 subgenomic replicon donors and EV71 $\Delta$ 3D RNA. The results show the yield of recombinant virus (PFU/ml  $\pm$  SD;  $n = 3$ ). Statistical analyses were performed using an unpaired, two-tailed  $t$  test (\*\*,  $P < 0.01$ ; \*,  $P < 0.05$ ). (D and E) Representative recombinant sequences of plaque-purified recombinant virus from C4/C2 (D) and B5/C2 (E). Dashed arrows indicate predicted paths of viral RdRp upon template switching. Numbering refers to the position on the acceptor templates. Lowercase, boldface nucleotides indicate the 5' and 3' boundaries of recombination. Underlined sequences indicate regions of homology.

nation. We concluded that subtle underlying differences at either the RNA or proteome level inhibit recombination with B5 subgenogroup members. Experiments to characterize these differences are ongoing.

**Isolated recombinant viruses show homology at the recombination junction(s) and that the trigger for recombination is sequence independent.** The exact location of recombination from the primary C2/C2 recombinant viruses isolated in this study was impossible to identify due to the high sequence similarity of the two parental templates (Fig. 1C). Since the C4 and B5 templates had  $\sim 20\%$  divergence at the RNA level within the P2 and P3 regions, where template switching would occur (Table 1), identification of recombinant junction would in principle be easier. Of note, only one independent B5/C2 recombinant sequence was identified (Fig. 4E). Because the yield of



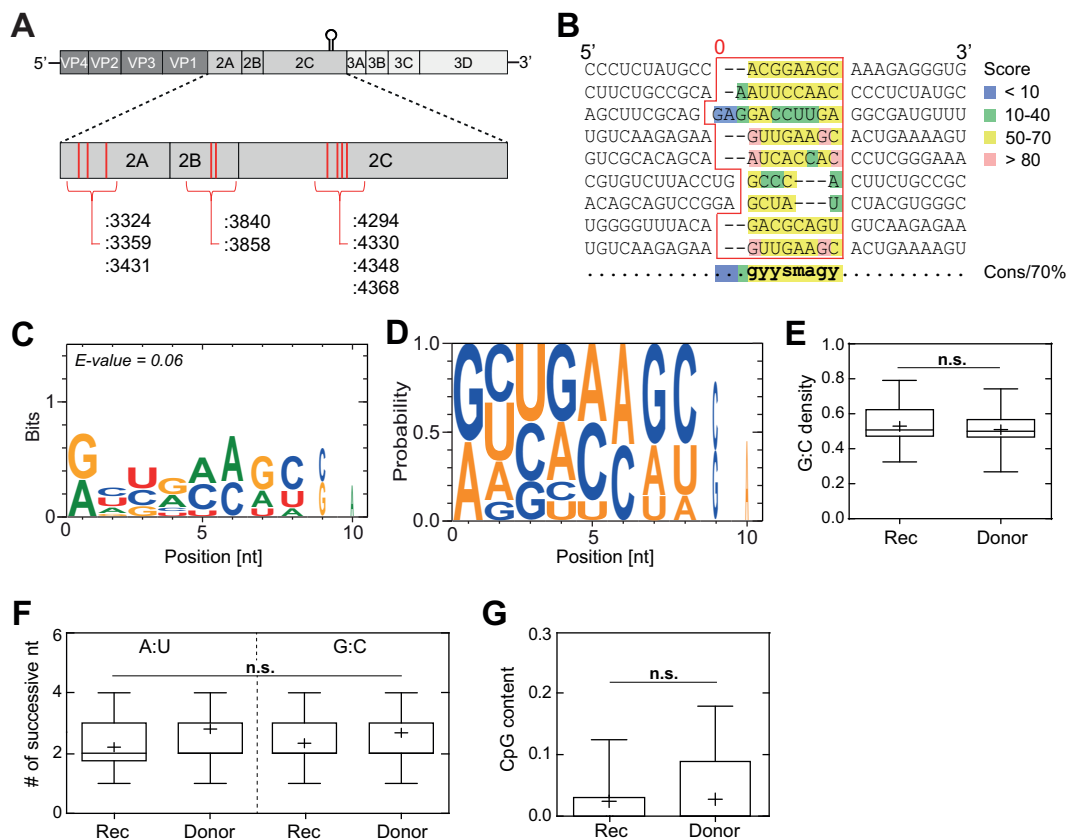


**FIG 5** Intraserotypic recombination between EV-A71 C2 and C4 subgenotypes requires homology at the recombination junction, but the triggers for template-switching are sequence independent. (A) Positions of template-switching events observed during intratypic recombination between the EV-A71 C2 and C4 subgenotypes. The individual positions of observed strand switching across the P2 genome region are marked in red, including their corresponding nucleotide sequence numbers with respect to the C2 acceptor strand. (B) Sequences of bona fide C2/C4 recombinant viruses. The red border highlights the matching homologous sequences at the recombination sites with lengths between 5 and 11 nucleotides ( $\bar{x} = 7 \pm 2$  nucleotides). The sequences were subject to M-COFFEE, a multiple sequence alignment algorithm, to identify possible gapped sequence motifs. Scores of  $< 50$  are considered to exhibit poor sequence consistency (scores range from 0 to 100). The sequence homology for the matching homologous sequences was found to be  $58\% \pm 2\%$ . A consensus sequence with 70% probability is shown below using IUPAC nomenclature. (C) Logo of ungapped *de novo* sequence motif search using the MEME algorithm that represents a sequence-aligned, position-dependent nucleotide probability matrix. The resulting motif sequence with an E value of 0.06 and a bit value of  $< 1$  show no statistical significance and thus failed to find a sequence motif as a recombination trigger. (D) Probability of position-dependent nucleotides at the homologous recombination sequences without sequence alignment. (E to G) The G-C nucleotide density (E), numbers of successive G-C/A-U bases (F), and CpG contents (G) of the homologous recombination sequences and the entire C2 genome (10-nucleotide sequence window) exhibit no significant differences. Statistical analysis was performed using a one-way, two-tailed analysis of variance with comparative Tukey *post hoc* test (n.s., not significant).

recombinant virus from this combination was very low (mean,  $5.6 \times 10^1$  PFU/ml), this finding may be unsurprising and may represent the sole recombinant in the population. The C4/C2 intraserotypic pairing provided more viable recombinants which were subsequently used for sequence analysis. Plaque purified viruses were characterized by RT-PCR analysis in a window between the end of P1 and P2 (Fig. 5A). All recombinant viruses identified were derived from the parental genomes, as expected. In all examples, a region of between 5 and 11 nucleotides of shared homology between donor and acceptor templates was identified at the recombination junction with no insertions or deletions (Fig. 5A). The identified homologous sequences shared a sequence homology of only  $58\% \pm 2\%$  and were subject to *de novo* sequence motif search to identify possible conserved sequences that may trigger the observed recombination events. Potentially, the cell-based recombination assay only provides information of secondary recombination products that do not necessarily represent the primary recombinant product, so we hypothesized that these may still share similar sequence motifs, if any

exist. We first analyzed the identified sequences with M-COFFEE (39), a multiple sequence alignment algorithm that allows gaps between sequence regions (Fig. 5B) to allow best alignment. The computation was set to combine the following alignment algorithms: MAFFT, ClustalW, DIALIGN-TX, POA, MUSCLE, T-COFFEE, PCMA, and PROBCONS. The algorithm was not able to identify a highly conserved sequence motif, and the proposed consensus sequence with a probability of 70% only exhibited a few guanines as conserved nucleotides within the sequences. Further analysis with MEME (Fig. 5C) (40), which searches for ungapped sequence motifs, also failed to identify a sequence-dependent recombination trigger (E value = 0.06). The position-dependent nucleotide probabilities (Fig. 5D) exhibit, similar to the M-COFFEE results, that guanines are most abundant in the homologue sequences. This result gave rise to the assumption that G-C-rich sequence regions or CpG/ApU dinucleotide bias may trigger RdRp template switching, as previous studies suggest (9, 41). To evaluate this hypothesis, we compared the homologous and donor template sequences in regard to the A-U and G-C nucleotide density (Fig. 5E), the number of successive G-C and A-U base pairs (Fig. 5F), and CpG density (Fig. 5G). The analyses showed no significant differences between the donor template nucleotide composition and the sequences identified at the recombination junctions. Taken together, the limited sequence analysis results yielded no indication of any sequence-dependent recombination trigger.

## DISCUSSION

Though EV-A71 infection generally causes mild diseases like HFMD in children, it can lead to severe cardiorespiratory and neurological complications (42). Intratypic recombination between circulating strains of EV-A71 and intertypic recombination with species coxsackievirus A produces the outbreak-associated strains of EV-A71, which exhibit increased virulence and/or transmissibility (15, 43). The subsequent human mortality and morbidity associated with such events can be substantial (44). All of our current understanding of recombination in the generation of new strains of enteroviruses are based upon retrospective phylogenetic analysis which shows us that recent intra- and intertypic EV-A71 recombination events are limited to members of the same species group (13, 14, 16, 42). In addition, the production of chimeric enterovirus genomes in other studies indicates a high level of plasticity (45–47). This plasticity, however, seems to be limited to intraspecies members, since no recent evidence for interspecies enterovirus recombination has been documented. Is this just due to cocirculation? Or is it due to genomic/proteomic compatibilities that are only available with other group members?

Ongoing studies using the prototypical species C enterovirus, PV, have provided unique insights into the potential triggers and mechanisms of recombination (19, 21). In general, all recent publications support the notion of replicative RdRp-mediated recombination as the primary source of new virus hybrid genome (19–21). Our major aim was to use this knowledge to develop an assay that would allow prediction of recombination between current circulating EV-A71 strains. This study reports the development of the first non-polio enterovirus recombination assay that will allow for the continued study of recombination in this medically important group of viruses. Since recombination frequencies in the closely related PV have been shown to occur at between  $10^{-4}$  to  $10^{-5}$  (6, 48), any impact on overall replication of the virus would impact any recombination event. Our data suggest that a minimal amount of EV-A71 recombination can occur in a process that is independent of replication and mediated by the host cell environment, potentially in a similar manner to that observed for PV by Gmyl et al. (23, 24) and other RNA viruses such as hepatitis C (35). However, we believe that our cell-based recombination assays (Fig. 1) show that recombination in EV-A71 is primarily RdRp mediated and therefore mechanistically similar to the replicative recombination observed for PV (19–21). This interpretation is supported by the results shown in Fig. 2. The L420 residue in the RdRp of PV is in a region of the polymerase that directly interacts with the viral RNA (21). This residue is conserved in EV-A71 and is located at position L421. Studies in PV have shown that a L420A mutation can inhibit

replicative recombination by  $\sim 100$ -fold, while having no impact upon replication (21). The same mutation in EV-A71 also produced a similar phenotype. Recombination was significantly reduced while having no impact upon replication of the full-length virus or replicon donor template (Fig. 2). The structures of the RdRp from PV and EV-A71 are very similar, and many key residues are conserved. The observation of reduced recombination from the same mutation to a similar region upon the RdRp is strongly suggestive of conservation in mechanism. In support of this, a similar mutation of the Gly-64 residue that has been shown to be important for fidelity in PV has also been engineered into EV-A71, with a similar outcome (49, 50). Current opinion proposes that enteroviruses have evolved to recombine in order to overcome the deleterious impacts of high mutation rates in order to maintain population fitness (37, 38). Or, alternatively, it may be as a consequence/by-product of replication speed (51). In either circumstance, a reduction in recombination rate should negatively impact the fitness of the viral population. The L421A mutation led to the EV-A71 population being significantly more susceptible to the nucleoside analogue mutagen ribavirin than the wild type (Fig. 2D). Again, this phenotype is conserved in PV.

We introduced additional circulating EV-A71 partners (subspecies C4 and B5) (Fig. 4). Both shared similar RNA sequence similarity to the acceptor template in the P2 and P3 regions at  $\sim 80$  and  $\sim 95\%$  at the amino acid level (Table 1). However, the phylogenetic tree (Fig. 3) of the C4 strain strongly suggests that it has evolved by genetic drift and shift (recombination). In contrast, the B5 phylogeny (Fig. 3) currently shows no evidence of shift, with evolution being limited to genetic drift only. The yield of C4/C2 recombinant was significantly lower than the C2/C2 pairing. This was not surprising since similar observations have been seen with the intertypic PV1/PV3 CRE-REP partners (20) and are presumably a reflection of the RNA sequence divergence. What cannot be explained by RNA sequence divergence is the significantly lower B5/C2 recombinant yield. Could the reduced yield with this pairing be due to lack of opportunity, i.e., distinct sites of RNA replication within the cell which decrease the likelihood of mixed replication complexes where RdRp-mediated template-switching can occur (52)? Or, could it occur as a result of a nonfunctional proteome following recombination? Potentially, recombinant RNA is being formed but may be noninfectious following packaging, i.e., the genome may be unable to replicate due to incorrect polyprotein processing or may lack suitable protein-protein interactions required for packaging (53). The latter hypothesis is somewhat supported by phylogenetic analysis of isolated circulating EV-A71 recombinant virus, which suggest functionality of the encoded polyprotein is the key determinant of viability, since recombination "hot spots" primarily localize to gene boundaries within the nonstructural region (11, 22, 42). Experimentation is under way to identify the limitations to B5/C2 recombination. However, and most importantly, these observations represent what is currently being observed in nature; the B5 strain is circulating as a pure lineage and is not associated with current recombination events.

Historical studies of circulating PV recombinant virus identified an ApU dinucleotide bias immediately prior to the recombination junction (41). Alternatively, cell-based studies have suggested that RNA structure and GC-rich regions are triggers for RdRp template switching (9). Our analyses of possible conserved sequence motifs and nucleotide composition at the identified recombination junctions yielded no indication of sequence-dependent triggers of template switching. The viable recombinant viruses that were isolated from the C4/C2 and B5/C2 recombination assays had regions of homology that were between 5 and 11 nucleotides in length (Fig. 5), which suggests that RNA sequence homology between parental partners may be important. This observation is suggestive of a "copy choice" mechanism of recombination between parental templates (6), although all historical analysis of circulating recombinant viruses are based upon evolved genomes that may not necessarily represent the primary product of recombination. Indeed, recent studies in PV suggest that recombination may be biphasic, where promiscuous sequence-independent template switching occurs that is followed by secondary selection of the most "replication-competent" viruses that show homology at the recombination junctions (20). Conceivably, the sequences we

identified from our C4/C2 intraserotypic pairing may not necessarily represent the primary product of recombination, but those that have been selected via secondary recombination events or viability. Our observations of homology at the recombination junctions are therefore consistent with the recombinant isolates observed from similar assays that have used PV as a model (20).

We believe that our described EV-A71-specific recombination assay and the results within will provide the basis for the further dissection of this key evolutionary process that may be conserved across species groups. Further, we propose that this cell-based recombination assay has some power in predicting the efficiency of recombination between the current circulating EV-A71 strains that are of public health relevance.

## MATERIALS AND METHODS

**Cell culture.** Adherent monolayers of African green monkey (Vero) and human embryonic rhabdomyosarcoma (RD) were grown in Dulbecco modified Eagle medium. Media were supplemented with 100 U/ml penicillin, 100  $\mu$ g/ml streptomycin, and 10% heat-inactivated fetal bovine serum. All cells were passaged in the presence of trypsin-EDTA. Where stated, guanidine hydrochloride (Sigma) was added to the growth medium at 4 mM. Wild-type and recombinant EV-A71 viruses were recovered after transfection of RNA generated *in vitro* (see below) from full-length cDNA or from recombination assay parental partners. Virus was quantified by PFU/ml.

**Plasmids, *in vitro* transcription, cell transfection, and recombinant virus quantification.** The mouse adapted EV-A71 C2-MP4 infectious clone (32) was kindly provided by Jen-Reng Wang (Cheng Kung University, Taiwan) and modified by insertion of a ribozyme sequence between the T7 promoter and viral genome sequence in a pBR-derived plasmid. The EV-A71 C2 replicon was modified from a previously described EV-A71 C2-2231 replicon (26) by the addition of a T7-ribozyme and a poly(A) sequence inserted at the 5' and 3' ends of the replicon sequence in a pBR-derived plasmid (Table 2). The EV-A71 C4 replicon was constructed from the infectious clone, which was derived from the clinical strain TW-00073-2012. Full-length genome with 5' T7/ribozyme and 3' poly(A) were amplified using PCR and cloned into the pCRII-TOPO vector (Thermo Fisher). In order to construct the replicon, a cassette consisting of the SacII restriction enzyme site and the 2Apro cleavage site was inserted into the 5'UTR/VP1 and VP4/2A boundaries, respectively. The P1 fragment of the cassette-containing plasmid was later replaced by the luciferase coding sequence by SacII restriction enzyme digestion. A similar strategy was utilized to construct the B5 infectious clone and subgenomic replicon based on the sequence of clinical strain TW-50144-2013 (22). The EV-A71 $\Delta$ 3D template was constructed from the full-length EV-A71 C2-MP4 infectious clone by the removal of ~800 nucleotides between the blunt-cutting restriction sites (ScaI and NruI) within the 3D<sup>pol</sup> coding region. The C2- $\Delta$ IRES replicon was constructed by removal of the majority of the IRES region between two ApaI restriction sites located at positions 37 and 767 of the EV-A71 C2 replicon template. The C2-L421A mutant replicon and infectious clone were constructed by site-directed mutagenesis. All primers used for plasmid construction are listed in Table 2. The EV-A71 C2 replicon and C2- $\Delta$ IRES replicon were linearized with Sall. The EV-A71-MP4 and EV-A71 $\Delta$ 3D cDNAs were linearized with EagI. The EV-A71 C4 and B5 replicons were linearized with NotI. All linearized cDNA was transcribed *in vitro* using T7 RNA polymerase treated with 2 U of DNase Turbo (Thermo Fisher) to remove residual DNA template. The RNA transcripts were purified by using an RNeasy minikit (Qiagen) before spectrophotometric quantification. Purified RNA in RNase-free H<sub>2</sub>O was transfected into cell lines by using TransMessenger (Qiagen). The mixture was incubated according to the manufacturer's instructions and added to RD cell monolayers in 12-well tissue culture plates (typically 250 ng of replicon [donor] and 190 ng of  $\Delta$ 3D [acceptor] templates). Virus yield was quantified by plaque assay. Briefly, media, supernatant, and cells were harvested at time points posttransfection (specified in main text), subjected to three freeze-thaw cycles, and clarified. Supernatant was then used on fresh RD cells in 12-well plates, and virus infection continued for 30 min. The medium was then removed, and the cells were subjected to 2 $\times$  phosphate-buffered saline (PBS; pH 7.4) washes before a 1% (wt/vol) agarose medium overlay was added. The cells were incubated for 3 to 4 days and then fixed and stained with crystal violet for virus quantification. All recombination assays were carried out in triplicate.

**Ribavirin sensitivity assay.** RD cells were treated with ribavirin for 3 h before infection (the doses are specified in Fig. 2). Ribavirin-treated cells were then infected at an MOI of 0.1 with either wild type or an L421A variant of EV-A71-C2-MP4 in triplicate. After infection, the cells were washed with three times with PBS, and the medium was replaced with ribavirin. Infection proceeded until a cytopathic effect (CPE) was observed. Cells and supernatant were freeze-thawed three times, the medium was clarified, and the virus was quantified by a plaque assay. Yields of virus were then normalized to a carrier-treated (dimethyl sulfoxide) control.

**Single-step growth curve of the EV-A71 C4 and B5 full-length viruses.** RD cells in 6-well plates were infected by each virus at an MOI of 10 in triplicate in serum-free media. One hour later, the cells were extensively washed by PBS and refreshed in 2% serum-containing medium. Virus was harvested at different time points postinfection, and the virus yield was quantified by a plaque assay.

**Luciferase assays.** Supernatant was removed from transfected cell monolayers, and cells were briefly washed with PBS and lysed using 100  $\mu$ l of 1 $\times$  Glo lysis buffer (Promega) per well in a 12-well plate. The oxidation reaction was catalyzed by the addition of 10  $\mu$ l of cell lysate to 10  $\mu$ l at room temperature using Bright-Glo luciferase assay system (Promega) substrate. The luciferase activity was measured using



**TABLE 2** Oligonucleotides used in the study

Oligonucleotide	Sequence (5'–3') <sup>a</sup>
L421A-F	CTCCCTCTGCTTAGCAGCATGGCACAACG
L421A-R	CGTTGTGCCATGCTGCTAAGCAGAGGGAG
MP4 3156-F	ACGTTCTCAGTGCGGACTGTAG
C2/4 5057-R	CCTTGAAAAAGAGCTTC
C4-5'UTR-SacII-2A-F	CATGCCGCGGATCACCACCTTGTTTCGCAAGTGCCAC
C4-5'UTR-SacII-2A-R	GAACCAAGAGTGGTGATCCGCGGCATGTTAGCTGTATTAAG
C4-P1/P2-SacII-2A-F	TGGGCCGCGGATCACCACCTTGGAATTTGGACAACAGTCTG
C4-P1/P2-SacII-2A-R	AATTTCCCAAGAGTGGTGATCCGCGGCCCAAGAGTGGTGATCGCTG
SacII-Luc-F	ACCCCGCGGATGGAAGACGCCAAAAAC
SacII-Luc-R	TAACCGCGGCACGCGCATCTTCCGCC
ΔP1C4-MluI-2A-F	CTTAATACAGCTAAACATGACGCGTATCACCACCTTTGG
ΔP1C4-MluI-2A-R	CCAAGAGTGGTGATACGCGTCATGTTAGCTGTATTAAG
B5 5'UTR-MluI-R	AATACGCGTCATGTTAATTGTATTAAGGGTC
MluI-B5-2A-F	ATGACGCGTATTACTACCTCGGAAAGTTC
MluI-Luc-F	ACCACGCGTATGGAAGACGCCAAAAAC
MluI-Luc-R	TAAACGCGTCACGCGCATCTTCCGCC

<sup>a</sup>Underscored sequences represent restriction enzyme sites used for plasmid construction.

a luminometer with values normalized to the protein content of the extract according to a protocol described previously (54).

**Recombinant virus sequencing.** Recombinant viruses were isolated from individual plaques by incubating the medium/agar plug overnight in 1× PBS. Viral RNA was isolated using a Qiagen viral RNA isolation kit according to the manufacturer's protocol. RNA was reverse transcribed with oligo(T) primer using Superscript II (Invitrogen) according to the manufacturer's protocol. PCR was carried from the P1 region of the acceptor template to the end of the P2 region of the donor by using Phusion high-fidelity DNA polymerase (NEB) according to the manufacturer's protocol. PCR products were gel purified, A-tailed, and subcloned into a pCRII-TOPO vector (Thermo Fisher) for sequencing. Clustal Omega was used for sequence alignment to identify recombinant junctions.

**Phylogenetic analysis of the P2-P3 region of the EV-A71.** The evolutionary history of EV-A71 and its relationship with CV-A16 was inferred using the neighbor-joining method and constructed in MEGA7 (55). Sequences, including 182 EV-A71 sequences and the prototype sequence of CV-A16, were analyzed and rooted with the CV-A16 prototype strain G10 isolated in 1951 (22). To specifically discriminate the recombinogenic property of different genotype/subgenotype of EV-A71, P2-P3 rather than the VP1 region was analyzed. The probability of replicate trees in which the associated taxa clustered together was determined from bootstrapped data (1,000 replicates) (56). The evolutionary distances were computed via MEGA7 using the Jukes-Cantor method and are expressed as the numbers of base substitutions per site. All positions with <95% site coverage were eliminated.

## ACKNOWLEDGMENTS

C.E.C., N.H.D., and S.R.S. were funded by grant RGP0011/2015 from the Human Frontier Science Program. This research was further funded by National Institutes of Health grant R01AI45818 to C.E.C. In addition, S.R.S. was also supported by grants from the Ministry of Science and Technology (MOST), Taiwan (MOST 107-3017-F-182-001), and the Research Center for Emerging Viral Infections from The Featured Areas Research Center Program within the framework of the Higher Education Sprout Project by the Ministry of Education in Taiwan.

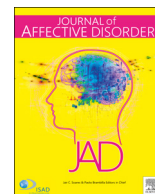
We thank Calvin Yeager for critical readings of the manuscript.

## REFERENCES

- Hyypia T, Hovi T, Knowles NJ, Stanway G. 1997. Classification of enteroviruses based on molecular and biological properties. *J Gen Virol* 78: 1–11. <https://doi.org/10.1099/0022-1317-78-1-1>.
- Adams MJ, Lefkowitz EJ, King AMQ, Bamford DH, Breitbart M, Davison AJ, Ghabrial SA, Gorbalenya AE, Knowles NJ, Krell P, Lavigne R, Prangishvili D, Sanfacon H, Siddell SG, Simmonds P, Carstens EB. 2015. Ratification vote on taxonomic proposals to the International Committee on Taxonomy of Viruses. *Arch Virol* 160:1837–1850. <https://doi.org/10.1007/s00705-015-2425-z>.
- Cameron CE, Oh HS, Moustafa IM. 2010. Expanding knowledge of P3 proteins in the poliovirus lifecycle. *Future Microbiol* 5:867–881. <https://doi.org/10.2217/fmb.10.40>.
- Domingo E, Baranowski E, Escarmis C, Sobrino F, Holland JJ. 2002. Error frequencies of picornavirus RNA polymerases: evolutionary implications for virus populations, p 285–298. In Semler B, Wimmer E (ed), *Molecular Biology of Picornavirus*. ASM Press, Washington, DC. <https://doi.org/10.1128/9781555817916.ch23>.
- Vignuzzi M, Stone JK, Arnold JJ, Cameron CE, Andino R. 2006. Quasispecies diversity determines pathogenesis through cooperative interactions in a viral population. *Nature* 439:344–348. <https://doi.org/10.1038/nature04388>.
- Kirkegaard K, Baltimore D. 1986. The mechanism of RNA recombination in poliovirus. *Cell* 47:433–443. [https://doi.org/10.1016/0092-8674\(86\)90600-8](https://doi.org/10.1016/0092-8674(86)90600-8).
- Lai MMC. 1992. Genetic recombination in RNA viruses. *Curr Top Microbiol Immunol* 176:21–32.

8. Cooper PD, Steiner-Pryor A, Scotti PD, Delong D. 1974. Nature of poliovirus genetic recombinants. *J Gen Virol* 23:41–49. <https://doi.org/10.1099/0022-1317-23-1-41>.
9. Runckel C, Westesson O, Andino R, DeRisi JL. 2013. Identification and manipulation of the molecular determinants influencing poliovirus recombination. *PLoS Pathog* 9(2):e1003164. <https://doi.org/10.1371/journal.ppat.1003164>.
10. Shih SR, Stollar V, Li ML. 2011. Host factors in enterovirus 71 replication. *J Virol* 85:9658–9666. <https://doi.org/10.1128/JVI.05063-11>.
11. Zhang C, Zhu R, Yang Y, Chi Y, Yin J, Tang X, Yu L, Zhang C, Huang Z, Zhou D. 2015. Phylogenetic analysis of the major causative agents of hand, foot, and mouth disease in Suzhou City, Jiangsu province, China, in 2012–2013. *Emerg Microbes Infect* 4:e12. <https://doi.org/10.1038/emi.2015.12>.
12. McWilliam Leitch EC, Cabrerizo M, Cardoso J, Harvala H, Ivanova OE, Koike S, Kroes AC, Lukashev A, Perera D, Roivainen M, Susi P, Trallero G, Evans DJ, Simmonds P. 2012. The association of recombination events in the founding and emergence of subgenogroup evolutionary lineages of human enterovirus 71. *J Virol* 86:2676–2685. <https://doi.org/10.1128/JVI.06065-11>.
13. Li L, He Y, Yang H, Zhu J, Xu X, Dong J, Zhu Y, Jin Q. 2005. Genetic characteristics of human enterovirus 71 and coxsackievirus A16 circulating from 1999 to 2004 in Shenzhen, People's Republic of China. *J Clin Microbiol* 43:3835–3839. <https://doi.org/10.1128/JCM.43.8.3835-3839.2005>.
14. Ang LW, Koh BK, Chan KP, Chua LT, James L, Goh KT. 2009. Epidemiology and control of hand, foot and mouth disease in Singapore, 2001–2007. *Ann Acad Med Singapore* 38:106–112.
15. Liu W, Wu S, Xiong Y, Li T, Wen Z, Yan M, Qin K, Liu Y, Wu J. 2014. Co-circulation and genomic recombination of coxsackievirus A16 and enterovirus 71 during a large outbreak of hand, foot, and mouth disease in Central China. *PLoS One* 9:e96051. <https://doi.org/10.1371/journal.pone.0096051>.
16. Zhang Y, Zhu Z, Yang W, Ren J, Tan X, Wang Y, Mao N, Xu S, Zhu S, Cui A, Zhang Y, Yan D, Li Q, Dong X, Zhang J, Zhao Y, Wan J, Feng Z, Sun J, Wang S, Li D, Xu W. 2010. An emerging recombinant human enterovirus 71 responsible for the 2008 outbreak of hand foot and mouth disease in Fuyang City of China. *Virol J* 7:94. <https://doi.org/10.1186/1743-422X-7-94>.
17. Leitch ECM, Bendig J, Cabrerizo M, Cardoso J, Hyypia T, Ivanova OE, Kelly A, Kroes ACM, Lukashev A, MacAdam A, McMinn P, Roivainen M, Trallero G, Evans DJ, Simmonds P. 2009. Transmission networks and population turnover of echovirus 30. *J Virol* 83:2109–2118. <https://doi.org/10.1128/JVI.02109-08>.
18. McWilliam Leitch EC, Cabrerizo M, Cardoso J, Harvala H, Ivanova OE, Kroes ACM, Lukashev A, Muir P, Odoom J, Roivainen M, Susi P, Trallero G, Evans DJ, Simmonds P. 2010. Evolutionary dynamics and temporal/geographical correlates of recombination in the human enterovirus echovirus types 9, 11, and 30. *J Virol* 84:9292–9300. <https://doi.org/10.1128/JVI.00783-10>.
19. Woodman A, Arnold JJ, Cameron CE, Evans DJ. 2016. Biochemical and genetic analysis of the role of the viral polymerase in enterovirus recombination. *Nucleic Acids Res* 44:6883–6895. <https://doi.org/10.1093/nar/gkw567>.
20. Lowry K, Woodman A, Cook J, Evans DJ. 2014. Recombination in enteroviruses is a biphasic replicative process involving the generation of greater-than genome length 'imprecise' intermediates. *PLoS Pathog* 10(6):e1004191. <https://doi.org/10.1371/journal.ppat.1004191>.
21. Kempf BJ, Peersen OB, Barton DJ. 2016. Poliovirus polymerase Leu420 facilitates RNA recombination and ribavirin resistance. *J Virol* 90:8410–8421. <https://doi.org/10.1128/JVI.00078-16>.
22. Lee KM, Gong YN, Hsieh TH, Woodman A, Dekker NH, Cameron CE, Shih SR. 2018. Discovery of enterovirus A71-like nonstructural genomes in recent circulating viruses of the enterovirus A species. *Emerg Microbes Infect* 7:111. <https://doi.org/10.1038/s41426-018-0107-0>.
23. Gmyl AP, Belousov EV, Maslova SV, Khitrina EV, Chetverin AB, Agol VI. 1999. Nonreplicative RNA recombination in poliovirus. *J Virol* 73:8958–8965.
24. Gmyl AP, Korshenko SA, Belousov EV, Khitrina EV, Agol VI. 2003. Non-replicative homologous RNA recombination: promiscuous joining of RNA pieces? *RNA* 9:1221–1231. <https://doi.org/10.1261/rna.5111803>.
25. Woodman A, Lee K-M, Janissen R, Gong Y-N, Shih S-R, Dekker NH, Cameron CE. 2018. Predicting intra- and intertypic recombination in enterovirus 71. *bioRxiv* <https://doi.org/10.1101/445783>.
26. Tang WF, Huang RT, Chien KY, Huang JY, Lau KS, Jheng JR, Chiu CH, Wu TY, Chen CY, Horng JT. 2016. Host microRNA miR-197 plays a negative regulatory role in the enterovirus 71 infectious cycle by targeting the RAN protein. *J Virol* 90:1424–1438. <https://doi.org/10.1128/JVI.02143-15>.
27. Herold J, Andino R. 2000. Poliovirus requires a precise 5' end for efficient positive-strand RNA synthesis. *J Virol* 74:6394–6400. <https://doi.org/10.1128/JVI.74.14.6394-6400.2000>.
28. Goodfellow IG, Kerrigan D, Evans DJ. 2003. Structure and function analysis of the poliovirus cis-acting replication element (CRE). *RNA* 9:124–137. <https://doi.org/10.1261/rna.2950603>.
29. Goodfellow IG, Polacek C, Andino R, Evans DJ. 2003. The poliovirus 2C cis-acting replication element-mediated uridylation of VPg is not required for synthesis of negative-sense genomes. *J Gen Virol* 84:2359–2363. <https://doi.org/10.1099/vir.0.19132-0>.
30. Smithee S, Tracy S, Chapman NM. 2015. Mutational disruption of cis-acting replication element 2C in coxsackievirus B3 leads to 5'-terminal genomic deletions. *J Virol* 89:11761–11772. <https://doi.org/10.1128/JVI.01308-15>.
31. Smithee S, Tracy S, Chapman NM. 2016. Reversion to wild type of a mutated and nonfunctional coxsackievirus B3CRE(2C). *Virus Res* 220:136–149. <https://doi.org/10.1016/j.virusres.2016.04.016>.
32. Wang YF, Chou CT, Lei HY, Liu CC, Wang SM, Yan JJ, Su IJ, Wang JR, Yeh TM, Chen SH, Yu CK. 2004. A mouse-adapted enterovirus 71 strain causes neurological disease in mice after oral infection. *J Virol* 78:7916–7924. <https://doi.org/10.1128/JVI.78.15.7916-7924.2004>.
33. Yamayoshi S, Fujii K, Koike S. 2014. Receptors for enterovirus 71. *Emerg Microbes Infect* 3:e53. <https://doi.org/10.1038/emi.2014.49>.
34. Gmyl AP, Korshenko SA, Belousov EV, Khitrina EV, Agol VI. 2003. Non-replicative homologous RNA recombination: promiscuous joining of RNA pieces? *RNA* 9:1221–1231. <https://doi.org/10.1261/rna.5111803>.
35. Scheel TKH, Galli A, Li Y-P, Mikkelsen LS, Gottwein JM, Bukh J. 2013. Productive homologous and non-homologous recombination of hepatitis C virus in cell culture. *PLoS Pathog* 9(3):e1003228. <https://doi.org/10.1371/journal.ppat.1003228>.
36. Gallei A, Pankraz A, Thiel HJ, Becher P. 2004. RNA recombination *in vivo* in the absence of viral replication. *J Virol* 78:6271–6281. <https://doi.org/10.1128/JVI.78.12.6271-6281.2004>.
37. Muller HJ. 1964. The relation of recombination to mutational advance. *Mutat Res* 1:2–9. [https://doi.org/10.1016/0027-5107\(64\)90047-8](https://doi.org/10.1016/0027-5107(64)90047-8).
38. Simon-Loriol E, Holmes EC. 2011. Why do RNA viruses recombine? *Nat Rev Microbiol* 9:617–626. <https://doi.org/10.1038/nrmicro2614>.
39. Moretti S, Armougom F, Wallace IM, Higgins DG, Jongeneel CV, Notredame C. 2007. The M-Coffee web server: a meta-method for computing multiple sequence alignments by combining alternative alignment methods. *Nucleic Acids Res* 35:W645–W648. <https://doi.org/10.1093/nar/gkm333>.
40. Bailey TL, Boden M, Buske FA, Frith M, Grant CE, Clementi L, Ren JY, Li WW, Noble WS. 2009. MEME SUITE: tools for motif discovery and searching. *Nucleic Acids Res* 37:W202–W208. <https://doi.org/10.1093/nar/gkp335>.
41. Kew O, Morris-Glasgow V, Landaverde M, Burns C, Shaw J, Garib Z, Andre J, Blackman E, Freeman CJ, Jorba J, Sutter R, Tambini G, Venczel L, Pedreira C, Laender F, Shimizu H, Yoneyama T, Miyamura T, van der Avoort H, Oberste MS, Kilpatrick D, Cochi S, Pallansch M, de Quadros C. 2002. Outbreak of poliomyelitis in Hispaniola associated with circulating type 1 vaccine-derived poliovirus. *Science* 296:356–359. <https://doi.org/10.1126/science.1068284>.
42. Yip CC, Lau SK, Lo JY, Chan KH, Woo PC, Yuen KY. 2013. Genetic characterization of EV71 isolates from 2004 to 2010 reveals predominance and persistent circulation of the newly proposed genotype D and recent emergence of a distinct lineage of subgenotype C2 in Hong Kong. *Virol J* 10:222. <https://doi.org/10.1186/1743-422X-10-222>.
43. Huang SC, Hsu YW, Wang HC, Huang SW, Kiang D, Tsai HP, Wang SM, Liu CC, Lin KH, Su IJ, Wang JR. 2008. Appearance of intratypic recombination of enterovirus 71 in Taiwan from 2002 to 2005. *Virus Res* 131:250–259. <https://doi.org/10.1016/j.virusres.2007.10.002>.
44. Gan ZK, Jin H, Li JX, Yao XJ, Zhou Y, Zhang XF, Zhu FC. 2015. Disease burden of enterovirus 71 in rural central China: a community-based survey. *Hum Vaccin Immunother* 11:2400–2405. <https://doi.org/10.1080/21645515.2015.1059980>.
45. Combélas N, Holmblat B, Joffret M-L, Colbere-Garapin F, Delpeyroux F. 2011. Recombination between poliovirus and coxsackie A viruses of species C: a model of viral genetic plasticity and emergence. *Viruses* 3:1460–1484. <https://doi.org/10.3390/v3081460>.

46. Bessaud M, Joffret ML, Blondel B, Delpeyroux F. 2016. Exchanges of genomic domains between poliovirus and other cocirculating species C enteroviruses reveal a high degree of plasticity. *Sci Rep* 6:38831. <https://doi.org/10.1038/srep38831>.
47. Jiang P, Faase JA, Toyoda H, Paul A, Wimmer E, Gorbalenya AE. 2007. Evidence for emergence of diverse polioviruses from C-cluster coxsackie A viruses and implications for global poliovirus eradication. *Proc Natl Acad Sci U S A* 104:9457–9462. <https://doi.org/10.1073/pnas.0700451104>.
48. Kirkegaard K, Baltimore D. 1986. RNA recombination in poliovirus. *J Cell Biochem* 1986:289–289.
49. Meng T, Kwang J. 2014. Attenuation of human enterovirus 71 high-replication-fidelity variants in AG129 mice. *J Virol* 88:5803–5815. <https://doi.org/10.1128/JVI.00289-14>.
50. Sadeghipour S, Bek EJ, McMinn PC. 2013. Ribavirin-resistant mutants of human enterovirus 71 express a high replication fidelity phenotype during growth in cell culture. *J Virol* 87:1759–1769. <https://doi.org/10.1128/JVI.02139-12>.
51. Fitzsimmons WJ, Woods RJ, McCrone JT, Woodman A, Arnold JJ, Yen-nawar M, Evans R, Cameron CE, Lauring AS. 2018. A speed-fidelity trade-off determines the mutation rate and virulence of an RNA virus. *PLoS Biol* 16(6):e2006459. <https://doi.org/10.1371/journal.pbio.2006459>.
52. Egger D, Bienz K. 2002. Recombination of poliovirus RNA proceeds in mixed replication complexes originating from distinct replication start sites. *J Virol* 76:10960–10971. <https://doi.org/10.1128/JVI.76.21.10960-10971.2002>.
53. Liu Y, Wang C, Mueller S, Paul AV, Wimmer E, Jiang P. 2010. Direct interaction between two viral proteins, the nonstructural protein 2C(ATPase) and the capsid protein VP3, is required for enterovirus morphogenesis. *PLoS Pathog* 6(8):e1001066. <https://doi.org/10.1371/journal.ppat.1001066>.
54. Weeks SA, Lee CA, Zhao Y, Smidansky ED, August A, Arnold JJ, Cameron CE. 2012. A polymerase mechanism-based strategy for viral attenuation and vaccine development. *J Biol Chem* 287:31618–31622. <https://doi.org/10.1074/jbc.C112.401471>.
55. Kumar S, Stecher G, Tamura K. 2016. MEGA7: molecular evolutionary genetics analysis version 7.0 for bigger datasets. *Mol Biol Evol* 33: 1870–1874. <https://doi.org/10.1093/molbev/msw054>.
56. Felsenstein J. 1985. Confidence limits on phylogenies: an approach using the bootstrap. *Evolution* 39:783–791. <https://doi.org/10.2307/2408678>.



## Research paper

# Risks of bipolar disorder, depressive disorder, and traumatic brain injury among siblings of patients with attention-deficit hyperactivity disorder



Wei Han-Ting<sup>a,f,g,1</sup>, Pan Tai-Long<sup>i,j,k,1</sup>, Hsu Ju-Wei<sup>a,b,\*</sup>, Huang Kai-Lin<sup>a,b</sup>, Bai Ya-Mei<sup>a,b</sup>,  
Ko Nai-Ying<sup>h</sup>, Su Tung-Ping<sup>a,b,e</sup>, Li Cheng-Ta<sup>a,b</sup>, Tsai Shih-Jen<sup>a,b</sup>, Lin Wei-Chen<sup>a,b</sup>,  
Chen Tzeng-Ji<sup>c,d</sup>, Chen Mu-Hong<sup>a,b,\*</sup>

<sup>a</sup> Department of Psychiatry, Taipei Veterans General Hospital, Taipei, Taiwan

<sup>b</sup> Department of Psychiatry, College of Medicine, National Yang-Ming University, Taipei, Taiwan

<sup>c</sup> Department of Family Medicine, Taipei Veterans General Hospital, Taipei, Taiwan

<sup>d</sup> Institute of Hospital and Health Care Administration, National Yang-Ming University, Taipei, Taiwan

<sup>e</sup> Department of Psychiatry, Cheng Hsin General Hospital, Taipei, Taiwan

<sup>f</sup> Division of Psychiatry, Kunming Branch, Taipei City Hospital, Taipei, Taiwan

<sup>g</sup> Branch of Linsen, Chinese Medicine and Kunming, Taipei City Hospital, Taipei, Taiwan

<sup>h</sup> Department of Nursing, College of Medicine, National Cheng Kung University and Hospital, Tainan, Taiwan

<sup>i</sup> School of Traditional Chinese Medicine, Chang Gung University, Taoyuan, Taiwan

<sup>j</sup> Liver Research Center, Chang Gung Memorial Hospital, Taoyuan, Taiwan

<sup>k</sup> Research Center for Food and Cosmetic Safety, Research Center for Chinese Herbal Medicine, College of Human Ecology, Chang Gung University of Science and Technology, Taoyuan, Taiwan

## ARTICLE INFO

## Keywords:

Unaffected siblings

ADHD

Unipolar depression

Bipolar disorder

Traumatic brain injury

## ABSTRACT

**Background:** Previous studies have suggested that the unaffected siblings of patients with attention-deficit hyperactivity disorder (ADHD) experience deficits in attention, impulsivity control, and behavior inhibition, which are associated with health-risk behaviors. However, risks to mental and physical health among the unaffected siblings of ADHD probands have rarely been investigated.

**Methods:** Using the Taiwan National Health Insurance Research Database, 5128 unaffected siblings of ADHD probands born between 1980 and 2000 were included in our study along with 20,512 age- and sex-matched controls, and they were followed from 1996 or birth until the end of 2011. Mental and physical health risks, including affective disorders, traumatic brain injury (TBI), and sexually transmitted infection were identified during the follow-up period.

**Results:** Logistic regression analyses with adjustments for demographic data showed that the unaffected siblings were more likely to develop unipolar depression (odds ratio [OR]: 1.76, 95% confidence interval [CI]: 1.39–2.22), bipolar disorder (OR: 2.10, 95% CI: 1.09–4.05), and TBI (OR: 1.24, 95% CI: 1.14–1.36) than were the control group.

**Discussion:** The unaffected siblings of patients with ADHD were prone to developing unipolar depression, bipolar disorder, and TBI later in life.

## 1. Introduction

Attention-deficit hyperactivity disorder (ADHD) begins in childhood and manifests as inability to marshal and sustain attention as well as modulate activity levels and impulsive actions (Biederman, 2005; Biederman and Faraone, 2005; Rappley, 2005). ADHD is one of the most common neurodevelopmental disorders and is highly prevalent in

children, adolescents, and young adults worldwide. It affects approximately 5–7% of children and adolescents and 2% of young adults, with a male to female ratio in the range of 3:1–4:1 (Biederman and Faraone, 2005; Vitola et al., 2017; Asherson et al., 2016). Previous studies have stated that multiple genetic and environmental factors induce a spectrum of neurobiological vulnerabilities to ADHD (Biederman, 2005; Biederman and Faraone, 2005; Rappley, 2005).

\* Corresponding authors at: Department of Psychiatry, No. 201, Shih-Pai Road, Sec. 2, Taipei 11217, Taiwan.

E-mail addresses: [jwhtsu@vghtpe.gov.tw](mailto:jwhtsu@vghtpe.gov.tw) (J.-W. Hsu), [kremer7119@gmail.com](mailto:kremer7119@gmail.com) (M.-H. Chen).

<sup>1</sup> Equally contributed.

<https://doi.org/10.1016/j.jad.2018.11.057>

Received 21 June 2018; Received in revised form 6 September 2018; Accepted 3 November 2018

Available online 05 November 2018

0165-0327/ © 2018 Published by Elsevier B.V.



Increasing evidence has indicated that unaffected siblings of ADHD patients may share a common endophenotype with their ADHD siblings and exhibit some deficits in attention, behavior inhibition, and emotional regulation (van Dongen et al., 2015; Oerlemans et al., 2015; Yang et al., 2011; Rommelse et al., 2007). By using Conners' Parent Rating Scale, van Dongen et al. compared the ADHD symptoms of children with ADHD, their unaffected siblings, and healthy controls. They found that the unaffected siblings had higher ADHD-symptom levels than the controls but lower levels than their siblings with ADHD (van Dongen et al., 2015). By comparing cognitive function (i.e., attention, working memory, and executive function) between unaffected siblings and controls, Oerlemans et al. demonstrated that unaffected siblings had poorer performance in attention, working memory, behavior inhibition, and executive function tasks than did the control group (Oerlemans et al., 2015). The core ADHD symptoms (inattention, hyperactivity, and impulsivity) shared by ADHD patients and their siblings have been linked to various adverse impacts on subsequent mental and physical health (Biederman, 2005; Biederman and Faraone, 2005; Rappley, 2005; Chen et al., 2018).

Previous studies have reported association between ADHD and subsequent affective disorders, substance or alcohol use disorders, and physical illnesses related to health-risk behaviors, such as traumatic brain injury (TBI) and sexually transmitted infection (STI) (Biederman, 2005; Biederman and Faraone, 2005; Rappley, 2005; Chen et al., 2018; Merrill et al., 2009). However, the mental and physical health risks have been investigated less frequently among the unaffected siblings of ADHD probands. A cross-sectional study composed of 136 adolescents with ADHD, 136 siblings, and 136 age- and sex-matched healthy controls suggested that the siblings of ADHD patients were more likely than the controls to receive diagnoses of unipolar depression or anxiety disorders (Yang et al., 2011). A four-year follow-up study of the siblings of patients with ADHD and control families revealed that the high-risk siblings showed evidence of neuropsychological and psychosocial dysfunction and experienced significant increases in behavioral and affective disorders (Faraone et al., 1996). The major limitations of these studies were the small sample sizes, cross-sectional study designs, and limited follow-up durations. In addition, although increasing evidence supports a significant relationship between ADHD symptoms and the risks of TBI and STI occurrence (Chen et al., 2018; Merrill et al., 2009), no studies have investigated such physical health risks among the unaffected siblings of patients with ADHD.

In this study, the Taiwan National Health Insurance Research Database (NHIRD) was used to investigate mental and physical health risks among the unaffected siblings of patients with ADHD by employing a large sample size and a longitudinal follow-up study design. We hypothesized that the unaffected siblings would be more likely than the control group to develop mental and physical health risks, such as affective disorders, TBI, and STI, during the follow-up.

## 2. Methods

### 2.1. Data source

Taiwan National Health Insurance Research Database (NHIRD) which consists of healthcare data from >99% of the entire Taiwan population is audited and released by National Health Research Institute for scientific and study purposes. Comprehensive information on insured individuals is included in the database, including demographic data, dates of clinical visits, disease diagnoses, and medical interventions. Individual medical records included in the NHIRD are anonymous to protect patient privacy. In this study, 5253 patients (4269 males, 984 females) with ADHD were identified, with an average age of  $15.60 \pm 4.50$  years and an average ADHD diagnosis age of  $10.06 \pm 4.20$  years. Using each resident's unique personal identification number, all of the information was linked. Subsequently, following the method of Kuo et al., family kinships in the NHIRD were used for

genealogy reconstruction (Kuo et al., 2015). The diagnostic codes used were based on the International Classification of Diseases, 9th Revision, Clinical Modification (ICD-9-CM). The NHIRD has been used extensively in many epidemiologic studies in Taiwan (Chen et al., 2015, 2016, 2018; Cheng et al., 2018).

### 2.2. Inclusion criteria for the unaffected siblings of patients with ADHD and the control group

Individuals who were born between 1980 and 2000 and had no diagnosis of ADHD (ICD-9-CM code: 314) at any time but had any sibling with ADHD were enrolled as the ADHD sibling cohort. The age-, sex-, and birth time-matched (1:4) control cohort was randomly identified after eliminating the study cases, those who were diagnosed with ADHD at any time, and those with any sibling with ADHD. Diagnosis of ADHD was given by board certified psychiatrists or child and adolescent psychiatrist based on comprehensive diagnostic interview and their clinical judgment. ADHD sibling cohort and control cohort were followed from 1996 or the birth time to the end of 2011 for the investigation of occurrence of mental and physical health risk in our study. Mental health risks included unipolar depressive disorder, bipolar disorder, substance use disorders, and alcohol use disorders. Physical health risks included traumatic brain injury (ICD-9-CM codes: 800–804, 850–854, 959.01) and sexually transmitted infection (HIV, syphilis, genital warts, gonorrhea, chlamydial infection, and trichomoniasis). All mental disorders were given by board-certificated psychiatrists or child and adolescent psychiatrists and all physical diseases were given by board-certificated physicians. Level of urbanization (level 1 to level 5; level 1: most urbanized region; level 5: least urbanized region) was also assessed for our study (Liu et al., 2006). This study was approved by the Institutional Review Board of Taipei Veterans General Hospital.

### 2.3. Statistical analysis

For between-group comparisons, the *F* test was used for continuous variables and Pearson's  $\chi^2$  test for nominal variables, where appropriate. Logistic regression models with the adjustment of demographic data (age, sex, income, and level of urbanization) were performed to calculate the odds ratio of developing any mental and physical health risk between ADHD sibling cohort and control cohort. Additional logistic regression analyses stratified by sex were also examined to investigate the role of sex in the risks of subsequent mental and physical diseases. A 2-tailed *P*-value of less than 0.05 was considered statistically significant. All data processing and statistical analyses were performed with statistical package for social science (SPSS) version 17 software (SPSS Inc.) and statistical analysis software (SAS) version 9.1 (SAS Institute, Cary, NC).

## 3. Results

In all, 5128 unaffected individuals who had the siblings with ADHD and 20,512 age-/sex-matched controls were included in our study. During the follow-period, the ADHD sibling cohort had a higher prevalence of developing unipolar depression (2.0% vs. 1.0%,  $p < 0.001$ ), bipolar disorder (0.3% vs. 0.1%,  $p < 0.001$ ), and TBI (15.4% vs. 12.9%,  $p < 0.001$ ) than the controls did (Table 1). The prevalence of intelligence disability, substance/alcohol use disorders and STIs did not differ between cohorts (Table 1). The ADHD sibling cohort resided more in urbanized region ( $p < 0.001$ ).

Logistic regression analyses with the adjustment of age, sex, income, and level urbanization showed that individuals who had the siblings with ADHD were more likely to develop unipolar depression (OR: 1.76, 95% CI: 1.39–2.22), bipolar disorder (OR: 2.10, 95% CI: 1.09–4.05), and TBI (OR: 1.24, 95% CI: 1.14–1.36) compared with the control group (Table 2). Stratified by sex, logistic regression analyses found

**Table 1**

Demographic data and incidence of the mental and physical health risks among siblings of ADHD patients and controls.

	Siblings of ADHD patients (n = 5128)	Controls (n = 20,512)	p-value
Age in the end of study (years, SD)	17.99 (4.97)	17.99 (5.01)	>0.999
Sex (n, %)			1.000
Male	2146 (41.8)	8584 (41.8)	
Female	2982 (58.2)	11,928 (58.2)	
Incidence of physical health risks			
STI (n, %)	93 (1.8)	326 (1.6)	0.267
Age at first STI (years, SD)	17.09 (7.38)	15.84 (7.12)	0.139
TBI (n, %)	788 (15.4)	2640 (12.9)	<0.001
Age at first TBI (years, SD)	10.41 (6.65)	10.72 (6.88)	0.260
Incidence of mental health risks			
Intelligence disability	46 (0.9)	137 (0.7)	0.091
Age at intelligence disability (years, SD)	10.96 (6.05)	9.63 (5.37)	0.162
Depressive disorders (n, %)	104 (2.0)	239 (1.0)	<0.001
Age at depressive disorders (years, SD)	18.25 (4.56)	18.60 (4.42)	0.504
Bipolar disorders (n, %)	14 (0.3)	26 (0.1)	0.027
Age at bipolar disorders (years, SD)	19.23 (3.97)	19.54 (3.79)	0.809
Alcohol use disorders (n, %)	23 (0.4)	70 (0.3)	0.244
Age at alcohol use disorders (years, SD)	18.07 (6.94)	18.47 (6.20)	0.797
Substance use disorders (n, %)	23 (0.4)	96 (0.5)	0.900
Age at substance use disorders (years, SD)	19.83 (5.69)	20.90 (4.88)	0.364
Level of urbanization (n, %)			<0.001
1 (most urbanized)	1727 (33.7)	5924 (28.9)	
2	1734 (33.8)	6397 (31.2)	
3	770 (15.0)	3654 (17.8)	
4	571 (11.1)	2793 (13.6)	
5 (most rural)	326 (6.4)	1744 (8.5)	

STI: sexually transmitted infection; TBI: traumatic brain injury; ADHD: attention-deficit hyperactivity disorder; SD: standard deviation.

that brothers of ADHD patients had an increased risk of developing unipolar depression (OR: 1.86, 95% CI: 1.25–2.77), bipolar disorder (OR: 3.74, 95% CI: 1.34–10.41), and TBI (OR: 1.30, 95% CI: 1.15–1.47) compared with the controls; sisters of ADHD patients were prone to developing unipolar depression (OR: 1.71, 95% CI: 1.27–2.29), TBI (OR: 1.20, 95% CI: 1.06–1.35), and STIs (OR: 1.43, 95% CI: 1.10–1.86) compared with the controls (Table 3).

#### 4. Discussion

The results of the study supported our hypothesis that unaffected siblings—both brothers and sisters—of ADHD patients were more likely than controls to have mental and physical health risks (including unipolar depression, bipolar disorder, and TBI). The study further revealed that only sisters of patients with ADHD had an increased risk of developing an STI later in life compared with the controls.

As mentioned in the introduction, ADHD symptoms adversely impacted the mental health of the siblings of ADHD probands (Yang et al., 2011; Listug-Lunde et al., 2008; King et al., 2016; Larsson et al., 2013). Listug-Lunde et al. assessed the psychological symptoms of 41 unaffected siblings of ADHD probands and 30 controls and found that unaffected siblings had higher scores for inattention, hyperactivity, and depression and anxiety symptoms than did the controls (Listug-Lunde et al., 2008). King et al. evaluated the impacts of ADHD probands' behavioral and emotional problems on their unaffected siblings and family, and they reported greater levels of feeling rejected and neglected by parents among unaffected siblings as well as more conflictual intrafamilial relationships (King et al., 2016). Conflictual relationships and chaotic dynamics within a family may increase risks of mental health problems, including depression and anxiety, among family members (King et al., 2016). By comparing the presence of psychiatric disorders in the siblings of ADHD patients with that in age- and sex-matched control, Yang et al. demonstrated that the siblings were more likely than controls to be diagnosed with depression and anxiety disorders (Yang et al., 2011). Larsson et al. assessed the risk of bipolar disorder among the siblings of ADHD patients and showed that they had an increased likelihood of developing bipolar disorder (OR: 2.22, 95%

CI: 1.98–2.50) compared with the control group (Larsson et al., 2013). Similarly to previous studies, we found that unaffected siblings of ADHD probands were more likely than the controls to develop unipolar depression or bipolar disorder. The results may further support the familial coaggregation of ADHD and affective disorders (unipolar depression and bipolar disorder) and suggest that having siblings with ADHD is a risk factor of subsequent unipolar depression and bipolar disorder.

In addition to the risk of mental health problems, the risks to physical health are crucial public health and psychiatric issues for the unaffected siblings of ADHD probands. Increasing evidence suggests a significant association between the diagnosis and symptoms of ADHD and health-risk behaviors (e.g., risky sexual behavior and risky driving) as well as related physical diseases (e.g., TBI and STI) (Hosain et al., 2012; Ramos Olazagasti et al., 2013; Graziano et al., 2015; Nada-Raja et al., 1997). Graziano et al. evaluated ADHD symptoms and health-risk behaviors in 555 college students and found a significant relationship between ADHD symptoms and health-risk behaviors such as risky driving (Graziano et al., 2015). By assessing the relationship between ADHD symptoms and driving offenses in adolescents, Nada-Raja et al. revealed that ADHD symptomatology is strongly associated with driving offenses. Moreover, they revealed that ADHD symptomatology in female adolescents was significantly associated with driving offenses and traffic accidents (Nada-Raja et al., 1997). Hosain et al. assessed ADHD symptoms and the lifetime risk of STI by administering the Adult ADHD Self-Report Scale to a sample of 462 young women (aged 18–30 years). They demonstrated that those with a lifetime history of STI exhibited more inattentiveness and hyperactivity and impulsivity symptoms than those without a lifetime history of STI (Hosain et al., 2012). As mentioned, the siblings of ADHD probands exhibited higher ADHD-symptom levels than did the controls, perhaps due to the greater chance of diseases related to health-risk behaviors. However, no previous studies have investigated the risks of TBI and STI among the unaffected siblings of ADHD probands. In this study, which included more than 5000 unaffected siblings and more than 20,000 age- and sex-matched controls, we found that the unaffected siblings of ADHD probands had an increased risk of developing TBI later in life compared

**Table 2**  
Logistic regression analyses of the mental and physical health risks among siblings of ADHD patients and controls \*.

	Mental health risks			Physical health risks		
	Depressive disorders (OR, 95% CI)	Bipolar disorders (OR, 95% CI)	Alcohol use disorders (OR, 95% CI)	Substance use disorders (OR, 95% CI)	STI (OR, 95% CI)	TBI (OR, 95% CI)
Siblings of ADHD patients	<b>1.76 (1.39–2.22)</b>	<b>2.10 (1.09–4.05)</b>	1.30 (0.81–2.10)	0.99 (0.63–1.58)	1.18 (0.93–1.49)	<b>1.24 (1.14–1.36)</b>
Controls	1 (ref.)	1 (ref.)	1 (ref.)	1 (ref.)	1 (ref.)	1 (ref.)

STI: sexually transmitted infection; TBI: traumatic brain injury; ADHD: attention-deficit hyperactivity disorder; OR: odds ratio; CI: confidence interval.  
\*: adjusted for demographic data.  
**Bold** type means the statistical significance.

with the control group. In addition, the unaffected sisters of ADHD probands were more than controls likely to develop an STI during the study period.

Based on the above evidence, we proposed a biopsychosocial model to explain the risk of subsequent mood disorders and TBI among the unaffected siblings of patients with ADHD. Patients with ADHD and their unaffected siblings may have common biological characteristics of inattention, hyperactivity, impulsivity, and executive dysfunction (van Dongen et al., 2015; Oerlemans et al., 2015). They would be more likely to grow up in a chaotic and unfavorable environment (e.g. low social class, marital discord, parental criminality and mental disorders) compared with non-ADHD controls (Biederman et al., 1995). The additive and interactive impacts of the biological trait and adverse environment increased the likelihood of developing mood disorders and health-risk behaviors among the unaffected siblings of patients with ADHD.

Finally, sex also affected the risks to mental and physical health among the unaffected siblings of ADHD probands. In our study, we found that only brothers of ADHD probands were more likely than controls to develop bipolar disorder and that only sisters had a higher risk than controls of developing an STI during follow-up. A longitudinal follow-up study suggested that ADHD symptoms, including affective disorders and behavioral problems, increased the long-term risks to mental health more strongly in males than in females (Smith et al., 2017). However, Cortese et al. reported that, despite having lower rates of hyperactive symptoms than men with ADHD, women with ADHD had similar ADHD subtype profiles and rates of risky behaviors as well as significantly more internalized symptoms and perceived mental health impairment (Cortese et al., 2016). Further studies are necessary to clarify the effect of sex on risks to mental and physical health among siblings of ADHD probands.

Several study limitations should be addressed. First, the prevalence of mental disorders and physical diseases may have been underestimated because only those who received a medical consultation were included in the NHIRD. However, the diagnoses of mental and physical illnesses were provided by board-certificated psychiatrists and physicians, improving the diagnostic validity. Second, the NHIRD does not provide information on the subthreshold ADHD symptoms of unaffected siblings of ADHD probands; therefore, we could not investigate the association between subthreshold ADHD symptoms and the risk of subsequent risks to mental and physical health. Additional clinical studies are required to clarify this association. Third, the NHIRD does not provide information on factors such as psychosocial stress, personal lifestyle, and environment; therefore, we were unable to investigate their potential influence.

In conclusion, the unaffected siblings of ADHD probands were more likely than controls to develop unipolar depression, bipolar disorder, TBI, and STI later in life. The increased likelihood of subsequent unipolar depression and bipolar disorders in the unaffected siblings may indicate a familial coaggregation of ADHD and affective disorders. In addition, our study was the first study to report the risk of subsequent TBI and STI in the unaffected siblings of patients with ADHD. The elevated risk of TBI and STI in the unaffected siblings may suggest a shared endophenotype of ADHD between patients with ADHD and their siblings. We recommend that clinical psychiatrists and physicians focus on the risks to mental and physical health among the unaffected siblings of ADHD probands, and we suggest that early identification and assessment may be necessary for this high-risk population.

**5. Contributions**

Dr. M.H.C., Prof T.L.P., Dr. H.T.W., and Dr. J.W.H. designed the study, wrote the protocol and manuscripts.

Dr. Y.M.B., Dr. T.P.S., Prof N.Y.K., Dr. K.L.H., Dr. C.T.L., Dr. S.J.T., and Dr. W.C.L. assisted with the preparation and proof-reading of the manuscript.

**Table 3**Logistic regression analyses of the mental and physical health risks among siblings of ADHD patients and controls, stratified by sex <sup>a</sup>.

Mental health risks				Physical health risks	
Depressive disorders (OR, 95% CI)	Bipolar disorders (OR, 95% CI)	Alcohol use disorders (OR, 95% CI)	Substance use disorders (OR, 95% CI)	STI (OR, 95% CI)	TBI (OR, 95% CI)
Brothers of ADHD patients vs. controls <b>1.86 (1.25–2.77)</b>	<b>3.74 (1.34–10.41)</b>	1.17 (0.58–2.40)	0.63 (0.31–1.28)	0.63 (0.37–1.09)	<b>1.30 (1.15–1.47)</b>
Sisters of ADHD patients vs. controls <b>1.71 (1.27–2.29)</b>	1.42 (0.58–3.44)	1.42 (0.75–2.70)	1.59 (0.85–2.97)	<b>1.43 (1.10–1.86)</b>	<b>1.20 (1.06–1.35)</b>

STI: sexually transmitted infection; TBI: traumatic brain injury; ADHD: attention-deficit hyperactivity disorder; OR: odds ratio; CI: confidence interval.

**Bold** type means the statistical significance.<sup>a</sup> adjusted for demographic data.

Dr. Y.M.B., Dr. T.J.C., and Dr. M.H.C. provided the advices on statistical analysis.

## 6. Conflict of interest

No conflict of interest.

## Funding source

The study was supported by grant from Taipei Veterans General Hospital (V103E10-001, V104E10-002, V105E10-001-MY2-1, V105A-049, V106B-020, V107B-010, V107C-181) and Ministry of Science and Technology, Taiwan (107-2314-B-075-063-MY3). The funding source had no role in any process of our study.

## Financial disclosure

All authors have no financial relationships relevant to this article to disclose.

## Acknowledgment

We thank Mr I-Fan Hu for his friendship and support.

We thank Dr. M.H.C., Dr. H.T.W., Dr. J.W.H. and Prof T.L.P., who designed the study, wrote the protocol and manuscripts, Dr. T.P.S., Prof N.Y.K., Dr. Y.M.B., Dr. C.T.L., Dr. S.J.T., Dr. K.L.H., Dr. T.L.P., and Dr. W.C.L., who assisted with the preparation and proof-reading of the manuscript, and Dr. Y.M.B., Dr. T.J.C., and Ms W.H.C., who provided the advices on statistical analysis.

## References

- Asherson, P., Buitelaar, J., Faraone, S.V., Rohde, L.A., 2016. Adult attention-deficit hyperactivity disorder: key conceptual issues. *Lancet Psychiatry* 3 (6), 568–578.
- Biederman, J., 2005. Attention-deficit/hyperactivity disorder: a selective overview. *Biol. Psychiatry* 57 (11), 1215–1220.
- Biederman, J., Faraone, S.V., 2005. Attention-deficit hyperactivity disorder. *Lancet* 366 (9481), 237–248.
- Biederman, J., Milberger, S., Faraone, S.V., Kiely, K., Guite, J., Mick, E., et al., 1995. Family-environment risk factors for attention-deficit hyperactivity disorder. A test of Rutter's indicators of adversity. *Arch. Gen. Psychiatry* 52 (6), 464–470.
- Chen, M.H., Hsu, J.W., Huang, K.L., Bai, Y.M., Ko, N.Y., Su, T.P., et al., 2018. Sexually transmitted infection among adolescents and young adults with attention-deficit/hyperactivity disorder: a nationwide longitudinal study. *J. Am. Acad. Child Adolesc. Psychiatry* 57 (1), 48–53.
- Chen, M.H., Lan, W.H., Hsu, J.W., Huang, K.L., Su, T.P., Li, C.T., et al., 2016. Risk of developing type 2 diabetes in adolescents and young adults with autism spectrum disorder: a nationwide longitudinal study. *Diabetes Care* 39 (5), 788–793.
- Chen, M.H., Pan, T.L., Li, C.T., Lin, W.C., Chen, Y.S., Lee, Y.C., et al., 2015. Risk of stroke among patients with post-traumatic stress disorder: nationwide longitudinal study. *Br. J. Psychiatry* 206 (4), 302–307.
- Cheng, C.M., Chang, W.H., Chen, M.H., Tsai, C.F., Su, T.P., Li, C.T., et al., 2018. Co-aggregation of major psychiatric disorders in individuals with first-degree relatives with schizophrenia: a nationwide population-based study. *Mol. Psychiatry* 23 (8), 1756–1763.
- Cortese, S., Faraone, S.V., Bernardi, S., Wang, S., Blanco, C., 2016. Gender differences in adult attention-deficit/hyperactivity disorder: results from the National Epidemiologic Survey on alcohol and related conditions (NESARC). *J. Clin. Psychiatry* 77 (4), e421–e428.
- Faraone, S.V., Biederman, J., Mennin, D., Gershon, J., Tsuang, M.T., 1996. A prospective four-year follow-up study of children at risk for ADHD: psychiatric, neuropsychological, and psychosocial outcome. *J. Am. Acad. Child Adolesc. Psychiatry* 35 (11), 1449–1459.
- Graziano, P.A., Reid, A., Slavec, J., Paneto, A., McNamara, J.P., Geffken, G.R., 2015. ADHD symptomatology and risky health, driving, and financial behaviors in college: the mediating role of sensation seeking and effortful control. *J. Atten. Disord.* 19 (3), 179–190.
- Hosain, G.M., Berenson, A.B., Tennen, H., Bauer, L.O., Wu, Z.H., 2012. Attention deficit hyperactivity symptoms and risky sexual behavior in young adult women. *J. Womens Health* 21 (4), 463–468.
- King, K., Alexander, D., Seabi, J., 2016. Siblings' Perceptions of their ADHD-diagnosed sibling's impact on the family system. *Int. J. Environ. Res. Public Health* 13 (9).
- Kuo, C.F., Grainge, M.J., Valdes, A.M., See, L.C., Luo, S.F., Yu, K.H., et al., 2015. Familial aggregation of systemic lupus erythematosus and coaggregation of autoimmune diseases in affected families. *JAMA Intern. Med.* 175 (9), 1518–1526.
- Larsson, H., Ryden, E., Boman, M., Langstrom, N., Lichtenstein, P., Landen, M., 2013. Risk of bipolar disorder and schizophrenia in relatives of people with attention-deficit hyperactivity disorder. *Br. J. Psychiatry* 203 (2), 103–106.
- Listug-Lunde, L., Zevenbergen, A.A., Petros, T.V., 2008. Psychological symptomatology in siblings of children with ADHD. *J. Atten. Disord.* 12 (3), 239–247.
- Liu, C.Y., Hung, Y.T., Chuang, Y.L., Chen, Y.J., Weng, W.S., Liu, J.S., 2006. Incorporating development stratification of Taiwan townships into sampling design of large scale health interview survey. *J. Health Manag.* 4, 1–22.
- Merrill, R.M., Lyon, J.L., Baker, R.K., Gren, L.H., 2009. Attention deficit hyperactivity disorder and increased risk of injury. *Adv. Med. Sci.* 54 (1), 20–26.
- Nada-Raja, S., Langley, J.D., McGee, R., Williams, S.M., Begg, D.J., Reeder, A.I., 1997. Inattentive and hyperactive behaviors and driving offenses in adolescence. *J. Am. Acad. Child Adolesc. Psychiatry* 36 (4), 515–522.
- Oerlemans, A.M., Hartman, C.A., de Bruijn, Y.G., Franke, B., Buitelaar, J.K., Rommelse, N.N., 2015. Cognitive impairments are different in single-incidence and multi-incidence ADHD families. *J. Child Psychol. Psychiatry Allied Disciplines* 56 (7), 782–791.
- Ramos Olazagasti, M.A., Klein, R.G., Mannuzza, S., Belsky, E.R., Hutchison, J.A., Lashua-Shriftman, E.C., et al., 2013. Does childhood attention-deficit/hyperactivity disorder predict risk-taking and medical illnesses in adulthood? *J. Am. Acad. Child Adolesc. Psychiatry* 52(2):153–162 e4.
- Rappley, M.D., 2005. Clinical practice. Attention deficit-hyperactivity disorder. *N. Engl. J. Med.* 352 (2), 165–173.
- Rommelse, N.N., Oosterlaan, J., Buitelaar, J., Faraone, S.V., Sergeant, J.A., 2007. Time reproduction in children with ADHD and their nonaffected siblings. *J. Am. Acad. Child Adolesc. Psychiatry* 46 (5), 582–590.
- Smith, E., Meyer, B.J., Koerting, J., Laver-Bradbury, C., Lee, L., Jefferson, H., et al., 2017. Preschool hyperactivity specifically elevates long-term mental health risks more strongly in males than females: a prospective longitudinal study through to young adulthood. *Eur. Child Adolesc. Psychiatry* 26 (1), 123–136.
- Vitola, E.S., Bau, C.H., Salum, G.A., Horta, B.L., Quevedo, L., Barros, F.C., et al., 2017. Exploring DSM-5 ADHD criteria beyond young adulthood: phenomenology, psychometric properties and prevalence in a large three-decade birth cohort. *Psychol. Med.* 47 (4), 744–754.
- van Dongen, E.V., von Rhein, D., O'Dwyer, L., Franke, B., Hartman, C.A., Heslenfeld, D.J., et al., 2015. Distinct effects of ASD and ADHD symptoms on reward anticipation in participants with ADHD, their unaffected siblings and healthy controls: a cross-sectional study. *Mol. Autism* 6, 48.
- Yang, L.K., Shang, C.Y., Gau, S.S., 2011. Psychiatric comorbidities in adolescents with attention-deficit hyperactivity disorder and their siblings. *Can. J. Psychiatry* 56 (5), 281–292.





# BRAF protein immunoprecipitation, elution, and digestion from cell extract using a microfluidic mixer for mutant BRAF protein quantification by mass spectrometry

Yen-Heng Lin<sup>1,2,3</sup> · Heng-Yun Chang<sup>2</sup> · Chia-Chun Wu<sup>4</sup> · Chia-Wei Wu<sup>2</sup> · Kai-Ping Chang<sup>3,5</sup> · Jau-Song Yu<sup>4,5,6,7</sup>

Received: 3 September 2018 / Revised: 23 October 2018 / Accepted: 3 December 2018  
© Springer-Verlag GmbH Germany, part of Springer Nature 2019

## Abstract

This study utilized a microfluidic mixer for the sample pretreatment of cell extracts for target protein quantification by mass spectrometers, including protein immunoprecipitation and protein enzymatic digestion. The time of sample pretreatment was reduced and thus the throughput of quantitative mutant proteins was increased by using the proposed method. Whole cell lysates of the cancer cell line HT-29 with gene mutations were used as the sample. The target protein BRAF was immunoprecipitated using magnetic beads in a pneumatic micromixer. Purified protein was then eluted and digested by trypsin in another two micromixers to yield peptide fragments in the solution. Using stable isotope-labeled standard as the internal control, wild-type and mutant BRAF proteins were quantified using mass spectrometry, which could be used for cancer screening. Compared with conventional methods in which protein immunoprecipitation lasts overnight, the micromixer procedure takes only 1 h, likely improving the throughput of mutant BRAF protein quantification by mass spectrometry.

**Keywords** Micromixer · Immunoprecipitation · Enzymatic digestion · Mutant BRAF · Mass spectrometry · Protein quantification

## Introduction

According to the World Health Organization, cancer has become the leading cause of death worldwide [1, 2]. Although significant progress has been made in cancer therapy during the past two decades, the survival rate of cancer patients has not significantly improved. The main reason is that most cancer patients have progressed into advanced stages by the time of diagnosis, which explains the low cure rate. The stage of

cancer has a strong correlation with the survival rate of cancer patients. Therefore, early detection and treatment can effectively improve the survival rate and reduce the financial burden on patients. Finding biomarkers that are highly expressed even at the early stage of cancer is very important and can also be used for the assessment of patient prognosis [3, 4].

v-raf murine sarcoma viral oncogene homolog B1 (BRAF) is a member of the RAF kinase family, and proteins encoded by the BRAF gene mainly function in cell growth regulation.

**Electronic supplementary material** The online version of this article (<https://doi.org/10.1007/s00216-018-1536-2>) contains supplementary material, which is available to authorized users.

✉ Yen-Heng Lin  
yenheng@mail.cgu.edu.tw

✉ Jau-Song Yu  
yusong@mail.cgu.edu.tw

<sup>1</sup> Department of Electronic Engineering, Chang Gung University, 259 Wen-Hua 1st Road, Kwei-Shan, Taoyuan 333, Taiwan

<sup>2</sup> Graduate Institute of Biomedical Engineering, Chang Gung University, Kwei-Shan, Taoyuan 333, Taiwan

<sup>3</sup> Department of Otolaryngology-Head & Neck Surgery, Chang Gung Memorial Hospital, Linkou 333, Taiwan

<sup>4</sup> Graduate Institute of Biomedical Sciences, Chang Gung University, 259 Wen-Hua 1st Road, Kwei-Shan, Taoyuan 333, Taiwan

<sup>5</sup> Molecular Medicine Research Center, Chang Gung University, Taoyuan, Taiwan

<sup>6</sup> Liver Research Center, Chang Gung Memorial Hospital, Linkou 333, Taiwan

<sup>7</sup> Research Center for Food and Cosmetic Safety, Research Center for Chinese Herbal Medicine, College of Human Ecology, Chang Gung University of Science and Technology, Taoyuan 333, Taiwan

Among the human cancers described so far, BRAF V600E is the most common oncogenic BRAF mutation [5]. Currently, the highest mutation rate has been found in melanoma [6], which is 40–60%. For other cancers such as the papillary thyroid cancer, colorectal cancer, and serous ovarian cancer, the mutation rates are 45%, 5–15%, and 35%, respectively [7, 8]. The current methods for the detection of BRAF mutation start with extracting DNA from patient's biopsy specimen and then analyzing it using restriction fragment length polymorphism (RFLP) analysis, single-strand conformational polymorphism (SSCP) analysis, pyrosequencing, shifted termination assay (STA), or allele-specific PCR. The above methods all use DNA as the target for detection. However, not all genes are translated into protein. Proteins are important macromolecules responsible for cell functions; therefore, directly targeting mutant BRAF (mtBRAF) protein translated from mutated DNA has become a very interesting research area in cancer screening [9–11].

Generally, protein assays are based on antibodies, such as Western blot and ELISA. Regarding the analysis of mtBRAF protein, a BRAF V600E-specific antibody (VE1) had been produced to detect this mutated protein in formalin-fixed, paraffin-embedded (FFPE) tissue samples by immunohistochemistry, which is considered to be a qualitative, rather than precisely quantitative method [12]. Moreover, there is no ELISA available currently for accurate quantification of mtBRAF protein in complex biological samples. Recently, our group developed a mass spectrometry-based method to facilitate the quantification of mtBRAF protein and its wild-type cognate (wtBRAF) in complex biological samples [13], in which total BRAF proteins were first immunoprecipitated (IP) from the sample, digested by trypsin, and then quantified by mass spectrometry with spike-in stable isotope-labeled peptide standards as reference.

In recent years, the use of mass spectrometry has greatly advanced proteome research. For example, mass spectrometry can quantify the expression of all proteins in cells, interaction between proteins, and posttranslational modifications in a short duration. Multiple reaction monitoring mass spectrometry (MRM-MS) technology can rapidly quantify the proteins in large quantities of specific body fluid samples [14–16], making it ideal for searching new cancer-associated protein biomarkers. MRM-MS technology can quantify proteins at extremely low levels of fmol to amol, which is sufficient to detect small amounts of protein in complex samples [17]. In addition, the use of stable isotope-labeled (SIS) standards as the control for absolute quantity ensures the accuracy of protein quantification [18–20]. However, at present, one of the major constraints in the quantitative detection of proteins by targeted mass spectrometry is the time for protein sample preparation. Generally, during quantitative mass spectrometry of specific intracellular proteins, the sample preparation duration is much longer than that required for mass spectrometric

analysis itself. For example, it takes approximately 20 h for sample preparation from specific protein immunoprecipitation in whole cell lysates of cancer cells to the elution and digestion of target proteins [13], whereas the time for liquid chromatography-mass spectrometry is approximately 60 min [21]. The long sample preparation time make it impossible to improve the analysis throughput. Moreover, these sample preparation steps must be handled by well-trained biochemical analysts.

Microfluidic technology has been widely used in biochemical analysis. Because of its small size and automatic control, it is suitable for reducing the pretreatment time of protein samples. For example, adding columnar structures in microchannels to increase surface area to bind antibodies or adding magnetic beads with modified antibodies allows rapid immunoprecipitation of the target protein in microchannels [22–24]. Furthermore, the modified high-surface-area magnetic bead was also demonstrated for its use in the fast separation of target biomolecules [25, 26]. Digital microfluidics has been used for the immunoprecipitation of proteins. Working with magnetic beads, the system can complete the immunoprecipitation of human serum albumin in 30 min [27]. In addition, microfluidic chips can also be used to assist protein digestion. Trypsin was attached on the surface of the microchannels with nanostructures [28, 29], fibers [30, 31], or magnetic beads [32–34], which were then implanted into the microchannels. Protein samples flowing through such channels would be digested into peptides. The abovementioned findings suggest that the use of microfluidic chips for protein sample pretreatment has the advantages of fast speed and the ability to integrate other functional microfluidic components. Therefore, this study used microfluidic technology to shorten the time required for protein sample pretreatment to increase the throughput of the quantitative detection of proteins using mass spectrometry. In addition, we hope that with the proper integration of the micromixer, the entire process of sample preparation can be integrated in a single chip with automated operation.

## Materials and methods

### Design and fabrication of micromixer

The micromixer is driven by a pneumatic force, as shown in Fig. 1a. It consists of three layers of polydimethylsiloxane (PDMS) structure—the top layer has a sample reaction well, the middle layer is an elastic PDMS film that is used to drive and mix the fluid, and the bottom layer has four separate air chambers. The mechanism of the micromixer is shown in Fig. 1b. The air chambers are divided into four separate areas according to the size of the wells above, and the air in these four areas can be sequentially pumped out, clockwise or

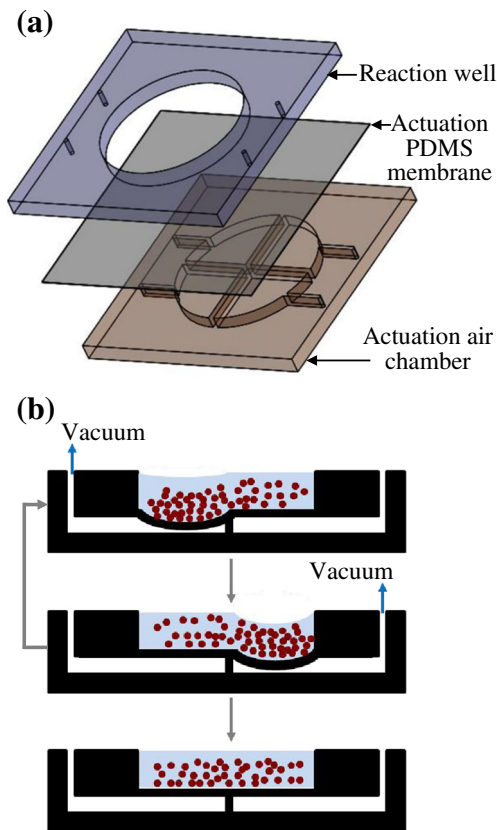


**Fig. 1** **a** The design of the pneumatic micromixer. The micromixer consists of three layers of PDMS structure: a sample reaction well in the top layer, a PDMS film in the middle layer, and four separate air chambers in the bottom layer. **b** The schematic illustration of the operation of the micromixer. The gas in the air chambers is pumped out by negative pressure in clockwise or anticlockwise direction sequentially so that the film above the air chamber is depressed downward, causing the fluid above the film to swirl and promote sample mixing

counterclockwise, making the PDMS film above the air chamber to sequentially depress, which causes the fluid above the film to stir in a vortex. The well for protein immunoprecipitation should hold a volume of 500  $\mu\text{L}$ , with a diameter of 18 mm and a depth of 2 mm, whereas that for protein elution and digestion should hold a volume of 200  $\mu\text{L}$ , with a diameter of 12 mm and a depth of 2 mm. The height of the air chambers at the bottom layer is 1 mm.

The fabrication of the micromixer is described as follows: first, the polymethylmethacrylate (PMMA) master mold was prepared using a CNC Engraving Machine (EGX-400, Roland Inc., Japan). The PDMS A and the B reagents (SYLGARD 184B, DOW CORNING, USA) were mixed at a weight ratio of 10:1 and thoroughly stirred. The PDMS mixture was degassed by vacuum for approximately 30 min before pouring it into the master mold. Then, the PDMS and mold were heated at 80  $^{\circ}\text{C}$  in an oven (DO60, DENG YNG, Taiwan) for approximately 1 h until the PDMS completely solidified. After demold, the entry and exit holes for fluid and air were

punched into the PDMS solid using a biopsy punch (0.5 mm, ProSciTech, Australia). To make the middle layer film, 5 g of PDMS was poured at the center of a 10  $\times$  10 cm PMMA substrate that was placed on a spin coater (MS-A100, MIKASA, Japan) and rotated at 500 rpm for 10 s followed by 1000 rpm for 10 s to produce a PDMS film of approximately 110  $\mu\text{m}$  thickness. Finally, the three PDMS layers were bonded together by oxygen plasma (HARRICK PLASMA, Ithaca, NY, USA).

## Procedures of sample pretreatment for wtBRAf and mtBRAf protein quantification

Before using mass spectrometry to quantify a specific protein in cell lysates, the target protein can be rapidly immunoprecipitated from the cell lysates, eluted into solution, and digested to small peptides. The wtBRAf and mtBRAf surrogate peptides were selected using software to compare the BRAf DNA mutation sites and included peptides IGDPGLATVK (wild type) and IGFGFLATEK (mutant) [13]. Three micromixers were used to shorten the time for protein immunoprecipitation, elution, and digestion, respectively. The procedure is shown in Fig. 2. Before the sample was loaded into the micromixer, the cell extracts with a total protein content of 500  $\mu\text{g}$  were prepared and the total volume was brought up to 500  $\mu\text{L}$  by adding homogenization buffer. To prepare magnetic beads bound with anti-BRAf antibodies, the protocol provided by the magnetic bead manufacturer was followed. The 500  $\mu\text{L}$  cell lysates was loaded into the first micromixer with 5  $\mu\text{L}$  magnetic beads ( $2 \times 10^9$  beads/mL) and incubated at room temperature for 60 min. The magnetic beads were then immobilized by an external magnet while the other proteins in the cell extracts were removed by washing thrice. The magnetic beads, which had captured BRAf protein, were transferred to a second micromixer for BRAf protein elution. The volume of the micromixer for elution was 200  $\mu\text{L}$ . The immunoprecipitated magnetic beads were mixed with 200  $\mu\text{L}$  5% acetic acid (AA) for 1 min and then the eluted BRAf protein was dissolved in the AA solution. The supernatant was then transferred into a microtube, and the solvent was evaporated using a high-speed vacuum centrifuge (Labconco, USA) and replaced with 190  $\mu\text{L}$  of 100 mM ammonium bicarbonate (ABC) solution (pH = 7.93). The resulting solution was loaded into a third micromixer with a volume of 200  $\mu\text{L}$ , and 10  $\mu\text{L}$  of trypsin (20 ng/mL dissolved in ABC buffer) was added for BRAf protein digestion. The reaction was ended by adding 0.1% trifluoroacetic acid/0.1% formic acid at the same volume as the sample to the solution. Finally, the mtBRAf and wtBRAf were quantified using mass spectrometry.

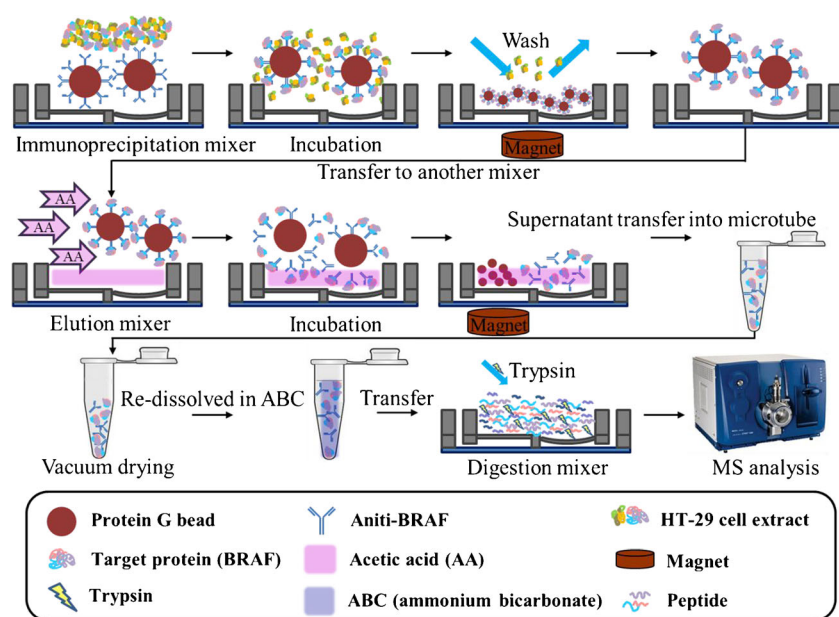


**Fig. 2** Operation procedures of the pretreatment of protein samples with micromixers. Immunoprecipitation is performed in a micromixer, and the target protein BRAF in the lysates of HT-29 cells was purified. Next is protein elution. To prevent the non-specific protein adhering to the micromixer from immunoprecipitation, magnetic beads are first transferred to another micromixer, and then the BRAF protein is eluted in a 5% AA solution. Finally, BRAF is digested into peptides for

quantitative measurement using mass spectrometry. Because trypsin works in an alkaline environment, the acid elution solution needs to be replaced with alkaline ABC by microtube and vacuum drying method. The sample is then transferred into the third micromixer for trypsin digestion, and the digested sample can be quantitatively analyzed by mass spectrometry

## Experimental setup and reagent preparation

The experimental setup is shown in Fig. 3. The pneumatic micromixer is controlled by the LabVIEW software (Version 11.0, National Instruments, USA) through a digital analog converter (Data Acquisition, DAQ, USB-6281, National Instruments), which sends signal to the solenoid valve (S070M-SBG-32, SMC, Japan) to control the frequency at which the air pressure is applied. The solenoid valve is connected to a negative pressure source of  $-80$  kPa. When the

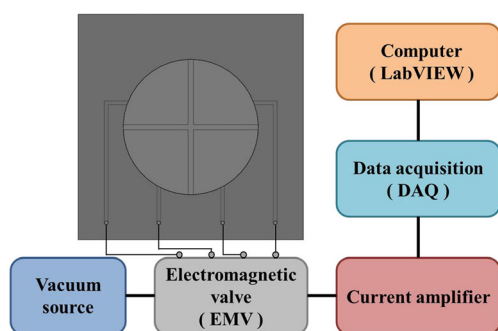


**Fig. 3** Experimental setup of the pneumatic micromixer. Each separate air chamber is connected to a solenoid valve that is connected to a vacuum pressure source. The LabVIEW software was used to switch the EMV on and off through a digital analog converter, so that the four chambers can be sequentially vacuumed. The applied frequency of the micromixer can also be controlled

solenoid valve opens, the negative pressure causes the PDMS film in the chip to depress. The reagents used in the experiment included magnetic beads (Dynabeads Protein G, Thermo Fisher Scientific Inc.), PBS buffer (0.14 M NaCl, 2.7 mM KCl, 8.1 mM  $\text{Na}_2\text{HPO}_4 \cdot 2\text{H}_2\text{O}$ , 1.8 mM  $\text{KH}_2\text{PO}_4$ , pH 7.4, Thermo Fisher Scientific Inc.), monoclonal mouse Raf-B antibody (F-7 anti-BRAF, Santa Cruz Biotechnology, USA), protein homogenization buffer (10 mM Tris-HCl, 1 mM EDTA, 1 mM EGTA, 50 mM NaCl, 50 mM NaF, 20 mM  $\text{Na}_4\text{P}_2\text{O}_7$ , 1 mM  $\text{Na}_3\text{VO}_4$ , 1 mM PMSF, 1 mM benzamidine, 0.5 g/mL leupeptin, and 1% Triton-X100, pH 7.4), ammonium bicarbonate buffer (Sigma-Aldrich), and sequencing grade trypsin (Promega, USA). The BRAF protein sample was extracted from human colorectal adenocarcinoma cell strain (HT-29), which contains both wtBRAF and mtBRAF proteins. The HT-29 cell was purchased from the Food Industry Research and Development Institute (FIRDI, Taiwan) and cultured in RPMI 1640 medium with 10% FBS and 100 units/mL of penicillin/streptomycin (Thermo Fisher Scientific Inc., USA) at 5%  $\text{CO}_2$  and 37 °C. The procedure to obtain cell extracts was as follows: the cells were washed twice with PBS buffer and lysed using lysis buffer (10 mM Tris-HCl pH 7.4, 2 mM EDTA, 1 mM EGTA, 50 mM NaCl, 1% Triton X-100, 1 mM benzamidine, 1 mM phenylmethylsulfonyl fluoride, 0.5 mg/mL aprotinin, 50 mM NaF, 20 mM sodium pyrophosphate, and 0.2 mM sodium orthovanadate) for 30 min in ice bath. The resulting cell



lysates were centrifuged at 12,000g rpm for 30 min at 4 °C. The supernatant was collected and used as the cell extracts. Total protein in the cell extracts was quantified using a BCA assay kit (Pierce, Thermo Scientific, USA).

## Analysis of protein samples

Protein quantification was performed by quantitative LC-SIM-AIMS analysis using tandem Fourier transform electric field orbit trap mass spectrometer (LTQ Orbitrap, Thermo Fisher Scientific, CA, USA) [13] and by semi-quantitative Western blot. The mass spectrometry method is described as follows: two SIS peptides (heavy peptides) with the same sequence as the wtBRAF and mtBRAF peptides and known concentration were added in the sample as internal standards. The sequence of the synthesized wtBRAF heavy SIS peptide is [IGDFGLATVK ( $^{13}\text{C}/^{15}\text{N}$ )] and that of the mtBRAF heavy SIS peptide is [IGDFGLATEK ( $^{13}\text{C}/^{15}\text{N}$ )] (New England Peptide Inc., USA). The  $^{12}\text{C}$  and  $^{14}\text{N}$  of the terminal amino acid of the peptide were replaced by  $^{13}\text{C}$  and  $^{15}\text{N}$ , respectively. The liquid chromatographic retention times of the SIS and endogenous peptides (light peptides) were the same (due to the same sequence), but their masses ( $m$ ) were different, so their mass-to-charge ratios ( $m/z$ ) could be differentiated and simultaneously detected by LTQ Orbitrap using single ion monitoring (SIM) mode. The following MS/MS analyses were acquired according to the accurate inclusion mass screening (AIMS) of  $m/z$  for light and heavy version of wtBRAF and mtBRAF peptides, respectively. Using the ratio of signal intensity between the SIS and endogenous peptides on the mass spectrum, the quantity of the endogenous peptide can be calculated. In Western blot, the eluted protein sample was heated in a sample buffer (10% SDS, 0.5 M Tris-HCL, 87% glycerol, 0.05% bromophenol blue, 10%  $\beta$ -mercaptoethanol) to break the disulfide bond and denature the protein into primary structure. The sample was ready for Western blot once it cooled down to room temperature. Protein molecules were separated by their different migration rates in the electric field, and the separated proteins in the gel were transferred to the PVDF membrane. The membrane was immunostained to emit chemical luminescence for photography. The band area of BRAF proteins in the gel image was semi-quantitatively analyzed using the ImageJ software.

## Results and discussion

### Micromixer operating frequency optimization

Two types of micromixer with different volumes were designed, namely 500  $\mu\text{L}$  type for protein immunoprecipitation and 200  $\mu\text{L}$  type for protein elution and digestion. The PDMS film in the mixer was driven in a clockwise direction by a

negative pressure of 80 kPa to mix the fluid and magnetic beads above the film. The optimal operating frequency was determined for each micromixer type. For this, the micromixer was loaded with the same amount of magnetic beads required for the experiment in PBS buffer and driven at the frequency of 2.5, 5, 10, and 25 Hz. A photograph was taken every second for observation in 0–4 s. For the 500- $\mu\text{L}$  mixer (Fig. 4a), the magnetic beads were the most rapidly dispersed at 5 Hz, whereas for the 200- $\mu\text{L}$  micromixer (Fig. 4b), the beads were the most rapidly dispersed at 10 Hz. Higher driving frequency did not increase the mixing efficiency, which may be because the vibration frequency of the PDMS film could not keep up with the driving frequency when the latter was set too high, thereby the film failed to effectively and completely vibrate [35]. The optimal driving frequencies for the two mixer types were different presumably because the 500- $\mu\text{L}$  mixer had a

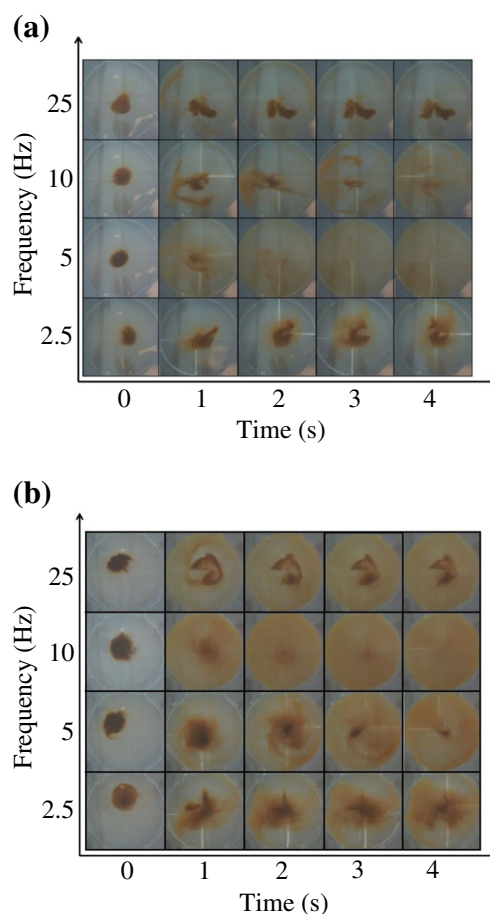


**Fig. 4** Optimal driving frequency of the two micromixers with different volumes. The driving pressure is – 80 kPa for both. Solenoid valves were set at different driving frequencies while the mixing of the beads in the solution was observed. **a** The image shows that the magnetic beads were evenly dispersed in approximately 4 s when the mixing frequency was 5 Hz for the micromixer with a diameter of 18 mm (volume, 500  $\mu\text{L}$ ). **b** The continuously captured images show that magnetic beads were evenly dispersed at the driving frequency of 10 Hz for the micromixer with a diameter of 12 mm (volume, 200  $\mu\text{L}$ )

larger air chamber and the time constant of inflation was larger, so when the driving frequency was  $> 5$  Hz, the vibration frequency of the PDMS film already could not keep up with the driving frequency of the air pressure, whereas the PDMS film of the 200- $\mu$ L mixer could still keep up with the driving air pressure at 10 Hz.

### Optimization of immunoprecipitation time

The correlation between the operation time of the micromixer and the immunoprecipitation efficiency of BRAF protein was determined. The sample used is described in “[Procedures of sample pretreatment for wtBRAF and mtBRAF protein quantification](#).” The cell extracts with a total protein content of 500  $\mu$ g and the magnetic beads immobilized with the anti-BRAF antibody were loaded into the 500- $\mu$ L micromixer and mixed at 5 Hz at room temperature for 10, 30, and 60 min, respectively. To compare the immunoprecipitation efficiency with that of the microtube method at the same temperature for the same time period, the same reagents were mixed in a microtube and stirred using a shaking mixer (Intelli-Mixer RM-2, ELMI, Latvia). Besides, the traditional method of immunoprecipitation conducted in microtube at 4 °C for 16–18 h [13] was considered as the 100% efficiency control. After immunoprecipitation, the BRAF on the beads and in the supernatant was semi-quantitatively analyzed by Western blot and ImageJ software. The BRAF on the beads was eluted in heated sample buffer at 100 °C for 10 min. The results of the semi-quantitative analysis are shown in Fig. 5. Each experiment was repeated thrice with micromixers, and the results were compared against the corresponding control. The quantity of the purified BRAF protein increased with the mixing time, and the yield of purified protein obtained from micromixer in 60 min reached 91.5% of that from the

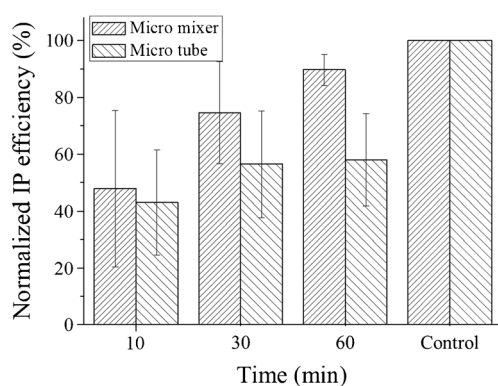


**Fig. 5** Comparison of BRAF protein immunoprecipitation using microtube and micromixer; the reaction time was 10, 30, and 60 min ( $n = 3$ ), respectively. The results show that mixing for 60 min in the micromixer achieved 91.5% of the purified product compared with mixing with the conventional method which typically reacts for overnight. The immunoprecipitation efficiency of the micromixer gradually exceeded that of the microtube over time

conventional method (control). In addition, the micromixer vs. microtube immunoprecipitation test at the same condition showed that over time, the immunoprecipitation efficiency of the micromixer gradually exceeded that of the microtube, probably because the active air pressure driving of the micromixer increased the probability of collision between BRAF proteins and magnetic beads while preventing the beads from precipitating, thereby improving the immunoprecipitation efficiency. The Western blot result of three immunoprecipitations performed with micromixers is shown in Electronic Supplementary Material (ESM) Fig. S1. The amount of BRAF protein in the supernatant was also analyzed to confirm the immunoprecipitation results. The efficiency of BRAF protein immunoprecipitation can be semi-quantitatively estimated to be approximately 26.78% ( $100\% - (\text{supernatant} / \text{cell extract}) \times 100\%$ ) for a 60-min reaction.

### Optimization of conditions for protein elution and digestion

To evaluate the protein elution time in the micromixer, the BRAF protein was first immunoprecipitated by using magnetic beads in the microtube. Then, the immunoprecipitated BRAF protein on the beads was eluted into the solution by the micromixer. The elution was achieved by creating an acidic environment to break the bonds between the protein and the antibody. The beads from immunoprecipitation reaction were transferred in 200  $\mu$ L of 5% AA, loaded into a 200- $\mu$ L micromixer, and stirred under room temperature at 10 Hz for 1, 2, 4, and 8 min, respectively. The results were compared with those of microtube elution for 8 min and were semi-quantitatively analyzed using Western blot (as shown in Fig. 6). The amount of BRAF protein eluted by micromixer for 1–8 min was similar to each other and to that eluted by microtube under the same conditions. The bonds between the antibodies, magnetic beads, and proteins were mainly reversible non-covalent bonds and, thus, were easily broken to allow quick elution once the solution turned acidic after adding AA.

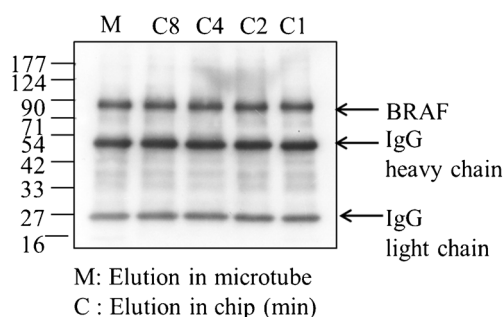


**Fig. 6** Results of BRAF protein elution using a micromixer for 1, 2, 4, and 8 min. Western blot analysis shows that elution efficiencies of the micromixer for 1–8 min were all similar to those of the microtube for 8 min

Therefore, the elution time for the chip was set at 1 min. The efficiency of protein elution was estimated to be approximately 50%, which is close to our previous study using microtube-based approach [13]. Although the digestion of antibodies would increase the complexity of the samples for downstream mass spectrometry analysis, however, the increase in sample complexity can be overcome by the subsequent liquid chromatography separation before mass spectrometry analysis. The peptide sample was first separated on an analytic C18 column with a 70-min linear gradient to reduce the sample complexity and the resolved fractions were further analyzed by LTQ-Orbitrap. The MS/MS analysis was acquired according to the accurate inclusion mass screening (AIMS) of  $m/z$  510.789, 514.797, 525.777, and 529.784 for the light and heavy versions of wtBRAF and mtBRAF peptides, respectively.

To determine the optimal tryptic digestion time for micromixer, the following steps were performed. The overnight microtube immunoprecipitation reaction was eluted for 8 min, and the solvent of the elute was evaporated using high-speed centrifuge and replaced with 190  $\mu$ L of 100 mM ABC solution. The ABC solution provides an alkaline environment, which is a favorable pH value for the trypsin. The sample was mixed with 10  $\mu$ L of trypsin (in ABC, 20 ng/mL) and loaded into the micromixer for BRAF protein digestion. The mixture was stirred at 10 Hz for 10, 30, 60, 90, or 120 min, respectively, at room temperature. The enzyme reaction was ended by adding acid. After digestion, the amount of surrogate peptides of the mtBRAF and wtBRAF released over different mixing times was quantified by LC-SIM-AIMS to assess the efficiency of the protein digestion. The results are shown in Fig. 7 ( $n=3$ ). The longer the reaction time, the more mtBRAF and wtBRAF surrogate peptides were released from the sample. The result of the

10-min digestion was close to the detection limit, and one of the three repeat experiments did not contain enough peptides to be detected by mass spectrometry. In addition, the reliability of the protein digestion experiment was also evaluated using the ratio of mtBRAF and wtBRAF. Theoretically, the mtBRAF/wtBRAF value is fixed; except for the 10-min reaction, the ratios calculated from the 30-, 60-, 90-, and 120-min digestions were 0.85, 0.52, 0.42, and 0.35, respectively. Compared with others, the ratio of the 30-min reaction was particularly high, which may be due to insufficient digestion time. Because trypsin has to cut out the surrogate peptide from the BRAF protein, if the digestion time is insufficient, the number of digested BRAF molecules, especially digested in surrogate peptide sites, was not enough, so that the mtBRAF/wtBRAF may not reach a stable value. The mtBRAF/wtBRAF value obtained by this digestion micromixer ranged from 0.35 to 0.52. The present data suggest that the results from reactions of 60 min were relatively accurate. Note that compared to our previous study using overnight microtube-based approach for digestion, the reduction in digestion time was mainly due to the digestion protocol change. In our previous study, the goal was to prove the concept of the methodology for the quantitative detection of mutant BRAF protein. Therefore, the overnight digestion was to ensure complete digestion of the protein. In contrast, this study was focused on rapid detection. Therefore, the ratio of mtBRAF/wtBRAF was the most important indicator for evaluation. As a result, 1 h of protein digestion in the micromixer can provide sufficient peptides for detection. Furthermore, it is known that fast digestion of protein can be achieved by immobilizing trypsin on the microbead, which provides more surface area of trypsin for reaction [36, 37]. In this study, pneumatic micromixer was used to facilitate the mixing of BRAF protein and trypsin enzyme in solution. However, we believe that this may not improve the digestion efficiency as much as the aforementioned one.

Finally, the micromixers with optimal operation conditions were used to perform the sample pretreatment for BRAF protein in HT-29 cell extracts. The experimental procedure is shown in “[Procedures of sample pretreatment for wtBRAF and mtBRAF protein quantification](#).” The BRAF protein in cell extracts was immunoprecipitated, eluted, and digested using micromixers. Afterward, mass spectrometry was conducted using heavy SIS peptide as the internal standard (mtBRAF and wtBRAF were both 1 fmol), and the results are shown in Fig. 8. The total amount of the wtBRAF peptide fragments was 0.68 fmol (Fig. 8a), whereas that of the mtBRAF peptide fragments was 0.33 fmol (Fig. 8b), and the ratio of mtBRAF/wtBRAF was 0.49. The time required for protein immunoprecipitation and digestion was shortened

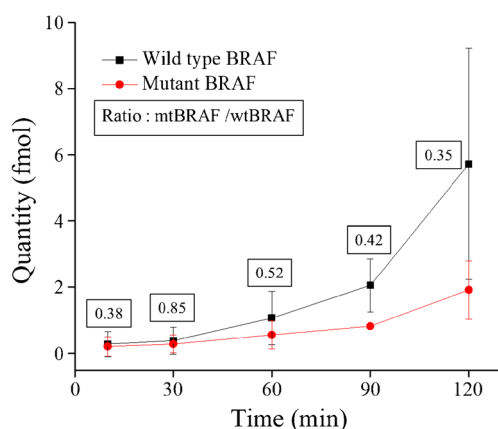


**Fig. 7** The use of a micromixer for BRAF protein digestion for 10, 30, 60, 90, and 120 min, and the quantification of the digestion result using mass spectrometry. The figure shows that the longer the mixing time, the more wtBRAF and mtBRAF endogenous peptides were released

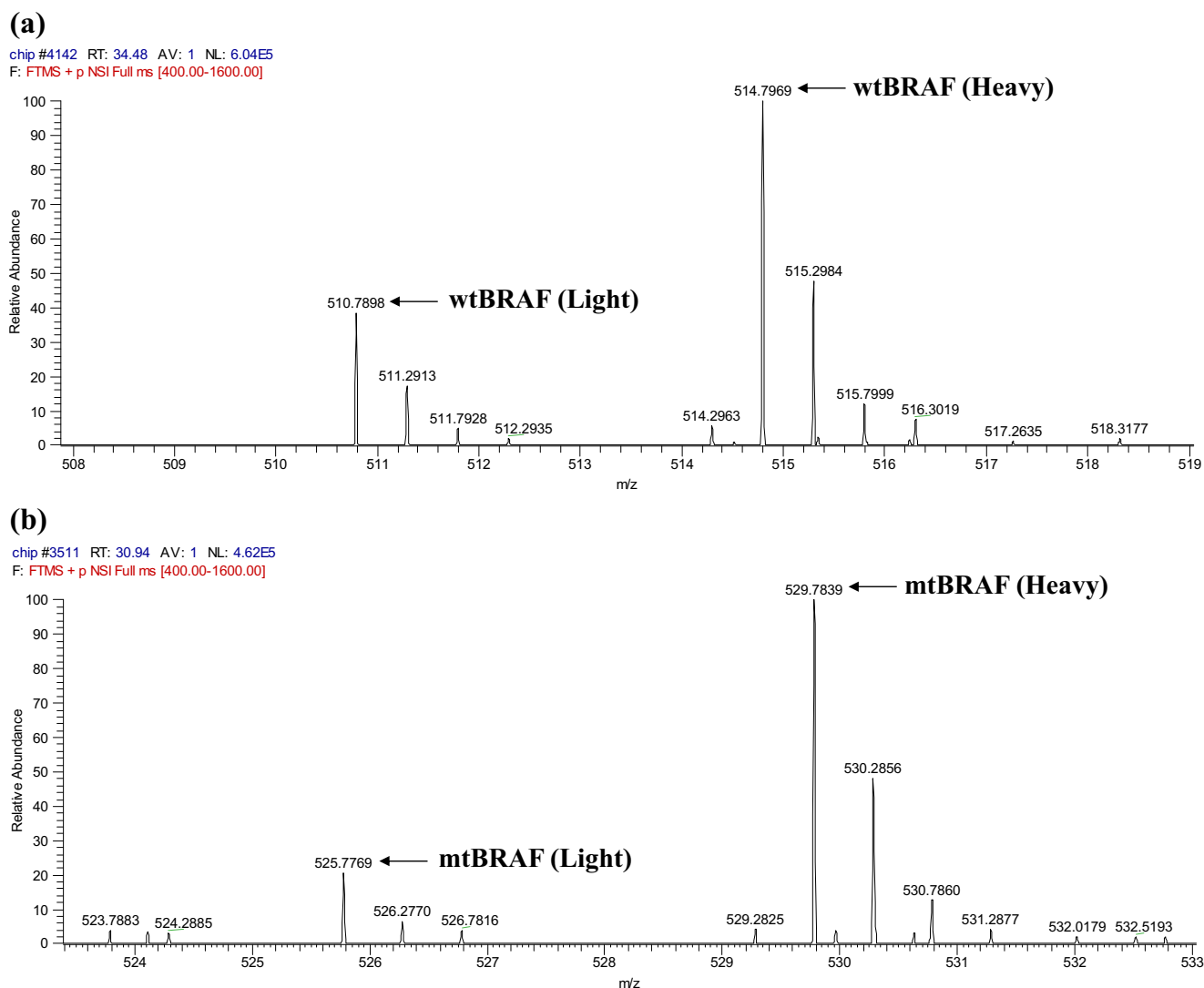


**Fig. 8** Micromixers were used for pretreatment of cell lysate sample, including protein immunoprecipitation, elution, and digestion, and the processed sample was mixed with heavy SIS peptide to quantify the protein content using mass spectrometry. **a** The 510.7898 and 514.7969

peaks are the light and heavy wtBRAF peptides, respectively, and **b** the 525.7769 and 529.7839 peaks are the light and heavy mtBRAF peptides, respectively. The amounts of SIS peptide added were both 1 fmol

from overnight each to 1 h each, thereby greatly reducing the pretreatment time of protein samples for mutant BRAF protein detection.

## Conclusion

The micromixer can greatly shorten the sample pretreatment time of protein immunoprecipitation, elution, and digestion. Using the immunoprecipitation mixer (500  $\mu$ L) for 60 min can achieve 91.5% efficiency of the conventional immunoprecipitation method which typically reacts for overnight. In addition, we found that using the digestion micromixer (200  $\mu$ L) for 60 min can obtain sufficient surrogate peptides for mass spectrometry detection. Increasing the reaction time leads to

more target peptide fragments being released. We found that one limitation should be overcome for the integration of protein immunoprecipitation, elution, and digestion processes in a single microfluidic chip. The protein elution is performed in an acidic solution, whereas the following trypsin digestion requires an alkaline environment. The solvent replacement in between still has to be manually performed, making the entire sample pretreating process difficult to automate. We have tested neutralizing the acidity of AA with Tris buffer before trypsin digestion. Western blot analysis indicated that the BRAF protein can be digested in neutralized buffer. However, although BRAF protein was digested, the neutralization reaction generated too much salt in the sample, which interfered with the mass spectrometric analysis in detecting the surrogate peptide of BRAF. In addition, it is known that



magnetic beads are compatible for protein digestion [36, 37]. We also try to evaluate the digestion efficiency of BRAF protein attached on the magnetic bead without elution process. We expect that the immunoprecipitation, elution, and digestion processes can be automated in one integrated chip so that the protein sample pretreatment for mutant BRAF protein detection can be shortened and automated.

**Funding information** The authors would like to thank the Ministry of Science and Technology of Taiwan and the Chang Gung Memorial Hospital for their funding support (105-2221-E-182-036-MY3, CMRPD2F0241, BMRPC01, CLRPD190018). This study was also supported by the “Molecular Medicine Research Center, Chang Gung University” from The Featured Areas Research Center Program within the framework of the Higher Education Sprout Project by the Ministry of Education (MOE) in Taiwan.

## Compliance with ethical standards

**Conflict of interest** The authors declare that they have no conflicts of interest.

**Publisher's note** Springer Nature remains neutral with regard to jurisdictional claims in published maps and institutional affiliations.

## References

- Siegel R, Ma J, Zou Z, Jemal A. Cancer statistics, 2014. *CA-Cancer J Clin*. 2014;64(1):9–29. <https://doi.org/10.3322/caac.21208>.
- Bray F, Jemal A, Grey N, Ferlay J, Forman D. Global cancer transitions according to the human development index (2008–2030): a population-based study. *Lancet Oncol*. 2012;13(8):790–801. [https://doi.org/10.1016/S1470-2045\(12\)70211-5](https://doi.org/10.1016/S1470-2045(12)70211-5).
- Hu S, Arellano M, Boontheung P, Wang J, Zhou H, Jiang J, et al. Salivary proteomics for oral cancer biomarker discovery. *Clin Cancer Res*. 2008;14(19):6246–52. <https://doi.org/10.1158/1078-0432.Ccr-07-5037>.
- Ye B, Cramer DW, Skates SJ, Gygi SP, Pratomo V, Fu L, et al. Haptoglobin- $\alpha$  subunit as potential serum biomarker in ovarian cancer: identification and characterization using proteomic profiling and mass spectrometry. *Clin Cancer Res*. 2003;9(8):2904–11.
- Davies H, Bignell GR, Cox C, Stephens P, Edkins S, Clegg S, et al. Mutations of the BRAF gene in human cancer. *Nature*. 2002;417:949. <https://doi.org/10.1038/nature00766>.
- Johnson AS, Crandall H, Dahlman K, Kelley MC. Preliminary results from a prospective trial of preoperative combined BRAF and MEK-targeted therapy in advanced BRAF mutation-positive melanoma. *J Am Coll Surg*. 2015;220(4):581–93.e1. <https://doi.org/10.1016/j.jamcollsurg.2014.12.057>.
- Xing M. BRAF mutation in thyroid cancer. *Endocr Relat Cancer*. 2005;12(2):245–62. <https://doi.org/10.1677/erc.1.0978>.
- Kim HO, Kim BG, Cha SJ, Park YG, Lee TJ. Clinicopathologic significance of BRAF mutation and extracellular signal regulated kinase 1/2 expression in patients with a colorectal adenocarcinoma. *Ann Coloproctol*. 2015;31(1):9–15. <https://doi.org/10.3393/ac.2015.31.1.9>.
- Wang Q, Chaerkady R, Wu J, Hwang HJ, Papadopoulos N, Kopelovich L, et al. Mutant proteins as cancer-specific biomarkers. *Proc Natl Acad Sci U S A*. 2011;108(6):2444–9. <https://doi.org/10.1073/pnas.1019203108>.
- Carey KD, Garton AJ, Romero MS, Kahler J, Thomson S, Ross S, et al. Kinetic analysis of epidermal growth factor receptor somatic mutant proteins shows increased sensitivity to the epidermal growth factor receptor tyrosine kinase inhibitor, erlotinib. *Cancer Res*. 2006;66(16):8163–71. <https://doi.org/10.1158/0008-5472.Can-06-0453>.
- Koperek O, Kornauth C, Capper D, Berghoff AS, Asari R, Niederle B, et al. Immunohistochemical detection of the BRAF V600E-mutated protein in papillary thyroid carcinoma. *Am J Surg Pathol*. 2012;36(6):844–50. <https://doi.org/10.1097/PAS.0b013e318246b527>.
- Capper D, Preusser M, Habel A, Sahm F, Ackermann U, Schindler G, et al. Assessment of BRAF V600E mutation status by immunohistochemistry with a mutation-specific monoclonal antibody. *Acta Neuropathol*. 2011;122(1):11–9. <https://doi.org/10.1007/s00401-011-0841-z>.
- Chen H, Hsiao Y-C, Chiang S-F, Wu C-C, Lin Y-T, Liu H, et al. Quantitative analysis of wild-type and V600E mutant BRAF proteins in colorectal carcinoma using immunoenrichment and targeted mass spectrometry. *Anal Chim Acta*. 2016;933:144–55. <https://doi.org/10.1016/j.aca.2016.05.037>.
- Chen Y-T, Chen H-W, Domanski D, Smith DS, Liang K-H, Wu C-C, et al. Multiplexed quantification of 63 proteins in human urine by multiple reaction monitoring-based mass spectrometry for discovery of potential bladder cancer biomarkers. *J Proteome*. 2012;75(12):3529–45. <https://doi.org/10.1016/j.jprot.2011.12.031>.
- Addona TA, Abbatiello SE, Schilling B, Skates SJ, Mani DR, Bunk DM, et al. Multi-site assessment of the precision and reproducibility of multiple reaction monitoring-based measurements of proteins in plasma. *Nat Biotechnol*. 2009;27:633. <https://doi.org/10.1038/nbt.1546>.
- Kuzyk MA, Smith D, Yang J, Cross TJ, Jackson AM, Hardie DB, et al. Multiple reaction monitoring-based, multiplexed, absolute quantitation of 45 proteins in human plasma. *Mol Cell Proteomics*. 2009;8(8):1860–77. <https://doi.org/10.1074/mcp.M800540-MCP200>.
- Wolf-Yadlin A, Hautaniemi S, Lauffenburger DA, White FM. Multiple reaction monitoring for robust quantitative proteomic analysis of cellular signaling networks. *Proc Natl Acad Sci U S A*. 2007;104(14):5860–5. <https://doi.org/10.1073/pnas.0608638104>.
- Keshishian H, Addona T, Burgess M, Kuhn E, Carr SA. Quantitative, multiplexed assays for low abundance proteins in plasma by targeted mass spectrometry and stable isotope dilution. *Mol Cell Proteomics*. 2007;6(12):2212–29. <https://doi.org/10.1074/mcp.M700354-MCP200>.
- Geiger T, Wisniewski JR, Cox J, Zanivan S, Kruger M, Ishihama Y, et al. Use of stable isotope labeling by amino acids in cell culture as a spike-in standard in quantitative proteomics. *Nat Protoc*. 2011;6:147. <https://doi.org/10.1038/nprot.2010.192>.
- Anderson NL, Anderson NG, Haines LR, Hardie DB, Olafson RW, Pearson TW. Mass spectrometric quantitation of peptides and proteins using stable isotope standards and capture by anti-peptide antibodies (SISCAPA). *J Proteome Res*. 2004;3(2):235–44. <https://doi.org/10.1021/pr034086h>.
- Gillette MA, Carr SA. Quantitative analysis of peptides and proteins in biomedicine by targeted mass spectrometry. *Nat Methods*. 2012;10:28. <https://doi.org/10.1038/nmeth.2309>.
- Sandison ME, Cumming SA, Kolch W, Pitt AR. On-chip immunoprecipitation for protein purification. *Lab Chip*. 2010;10(20):2805–13. <https://doi.org/10.1039/C005295G>.
- He M, Crow J, Roth M, Zeng Y, Godwin AK. Integrated immunoisolation and protein analysis of circulating exosomes using microfluidic technology. *Lab Chip*. 2014;14(19):3773–80. <https://doi.org/10.1039/C4LC00662C>.

24. McKenzie KG, Lafleur LK, Lutz BR, Yager P. Rapid protein depletion from complex samples using a bead-based microfluidic device for the point of care. *Lab Chip*. 2009;9(24):3543–8. <https://doi.org/10.1039/B913806D>.
25. Cheng G, Liu Y-L, Zhang J-L, Sun D-H, Ni J-Z. Lanthanum silicate coated magnetic microspheres as a promising affinity material for phosphopeptide enrichment and identification. *Anal Bioanal Chem*. 2012;404(3):763–70. <https://doi.org/10.1007/s00216-012-6150-0>.
26. Cheng G, Wang Z-G, Liu Y-L, Zhang J-L, Sun D-H, Ni J-Z. Magnetic affinity microspheres with meso-/macroporous shells for selective enrichment and fast separation of phosphorylated biomolecules. *ACS Appl Mater Interfaces*. 2013;5(8):3182–90. <https://doi.org/10.1021/am400191u>.
27. Seale B, Lam C, Rackus DG, Chamberlain MD, Liu C, Wheeler AR. Digital microfluidics for immunoprecipitation. *Anal Chem*. 2016;88(20):10223–30. <https://doi.org/10.1021/acs.analchem.6b02915>.
28. Cheng G, Hao S-J, Yu X, Zheng S-Y. Nanostructured microfluidic digestion system for rapid high-performance proteolysis. *Lab Chip*. 2015;15(3):650–4. <https://doi.org/10.1039/C4LC01165A>.
29. Liu Y, Lu H, Zhong W, Song P, Kong J, Yang P, et al. Multilayer-assembled microchip for enzyme immobilization as reactor toward low-level protein identification. *Anal Chem*. 2006;78(3):801–8. <https://doi.org/10.1021/ac051463w>.
30. Bao H, Chen Q, Zhang L, Chen G. Immobilization of trypsin in the layer-by-layer coating of graphene oxide and chitosan on in-channel glass fiber for microfluidic proteolysis. *Analyst*. 2011;136(24):5190–6. <https://doi.org/10.1039/C1AN15690J>.
31. Fan H, Chen G. Fiber-packed channel bioreactor for microfluidic protein digestion. *Proteomics*. 2007;7(19):3445–9. <https://doi.org/10.1002/pmic.200700505>.
32. Liu J, Lin S, Qi D, Deng C, Yang P, Zhang X. On-chip enzymatic microreactor using trypsin-immobilized superparamagnetic nanoparticles for highly efficient proteolysis. *J Chromatogr A*. 2007;1176(1):169–77. <https://doi.org/10.1016/j.chroma.2007.10.094>.
33. Li Y, Xu X, Yan B, Deng C, Yu W, Yang P, et al. Microchip reactor packed with metal-ion chelated magnetic silica microspheres for highly efficient proteolysis. *J Proteome Res*. 2007;6(6):2367–75. <https://doi.org/10.1021/pr060558r>.
34. Slovakova M, Minc N, Bilkova Z, Smadja C, Faigle W, Fütterer C, et al. Use of self assembled magnetic beads for on-chip protein digestion. *Lab Chip*. 2005;5(9):935–42. <https://doi.org/10.1039/B504861C>.
35. Sung-Yi Y, Jr-Lung L, Gwo-Bin L. A vortex-type micromixer utilizing pneumatically driven membranes. *J Micromech Microeng*. 2009;19(3):035020.
36. Cheng G, Zheng S-Y. Construction of a high-performance magnetic enzyme nanosystem for rapid tryptic digestion. *Sci Rep*. 2014;4:6947. <https://doi.org/10.1038/srep06947>.
37. Cheng G, Chen P, Wang Z-G, Sui X-J, Zhang J-L, Ni J-Z. Immobilization of trypsin onto multifunctional meso-/macroporous core-shell microspheres: a new platform for rapid enzymatic digestion. *Anal Chim Acta*. 2014;812:65–73. <https://doi.org/10.1016/j.aca.2013.12.035>.

Review

# In Vivo Rodent Models of Type 2 Diabetes and Their Usefulness for Evaluating Flavonoid Bioactivity

Jia-You Fang <sup>1,2,3,4,†</sup> , Chih-Hung Lin <sup>5,†</sup>, Tse-Hung Huang <sup>6,7,8,9</sup> and Shih-Yi Chuang <sup>1,\*</sup>

<sup>1</sup> Pharmaceutics Laboratory, Graduate Institute of Natural Products, Chang Gung University, Kweishan, Taoyuan 33302, Taiwan; fajy@mail.cgu.edu.tw

<sup>2</sup> Chinese Herbal Medicine Research Team, Healthy Aging Research Center, Chang Gung University, Kweishan, Taoyuan 33302, Taiwan

<sup>3</sup> Research Center for Food and Cosmetic Safety and Research Center for Chinese Herbal Medicine, Chang Gung University of Science and Technology, Kweishan, Taoyuan 33302, Taiwan

<sup>4</sup> Department of Anesthesiology, Chang Gung Memorial Hospital, Kweishan, Taoyuan 33302, Taiwan

<sup>5</sup> Center for General Education, Chang Gung University of Science and Technology, Kweishan, Taoyuan 33302, Taiwan; chlin@mail.cgu.edu.tw

<sup>6</sup> Department of Traditional Chinese Medicine, Chang Gung Memorial Hospital, Keelung 20401, Taiwan; huangtsehung@gmail.com

<sup>7</sup> School of Traditional Chinese Medicine, Chang Gung University, Kweishan, Taoyuan 33302, Taiwan

<sup>8</sup> Graduate Institute of Health Industry Technology, Chang Gung University of Science and Technology, Kweishan, Taoyuan 33303, Taiwan

<sup>9</sup> School of Nursing, National Taipei University of Nursing and Health Sciences, Taipei 112, Taiwan

\* Correspondence: clemencechuang@gmail.com; Tel.: +886-3-2118800; Fax: +886-3-2118236

† Equal contribution.

Received: 21 December 2018; Accepted: 22 February 2019; Published: 28 February 2019



**Abstract:** About 40% of the world's population is overweight or obese and exist at risk of developing type 2 diabetes mellitus (T2D). Obesity is a leading pathogenic factor for developing insulin resistance (IR). It is well established that IR and a progressive decline in functional  $\beta$ -cell mass are hallmarks of developing T2D. In order to mitigate the global prevalence of T2D, we must carefully select the appropriate animal models to explore the cellular and molecular mechanisms of T2D, and to optimize novel therapeutics for their safe use in humans. Flavonoids, a group of polyphenols, have drawn great interest for their various health benefits, and have been identified in naturally occurring anti-diabetic compounds. Results from many clinical and animal studies demonstrate that dietary intake of flavonoids might prove helpful in preventing T2D. In this review, we discuss the currently available rodent animal models of T2D and analyze the advantages, the limitations of each T2D model, and highlight the potential anti-diabetic effects of flavonoids as well as the mechanisms of their actions.

**Keywords:** flavonoid; antioxidant; type 2 diabetes; animal model

## 1. Type 2 Diabetes

Diabetes mellitus is a chronic metabolic disease that is characterized by a relative lack of insulin, resulting in hyperglycemia. Chronic hyperglycemia can lead to a variety of complications such as neuropathy, nephropathy, and retinopathy, as well as increased risk of cardiovascular disease [1]. The prevalence of diabetes mellitus is rapidly rising. The International Diabetes Federation (IDF) estimated that 425 million adults (aged 20–79 years) had diabetes mellitus globally in 2017, and further estimated that a US \$727 billion (12% of global health expenditure) was spent on treating diabetes mellitus and its related complications [2]. About 1 in 11 adults have diabetes mellitus, with 90% of these adults having type 2 diabetes mellitus (T2D); Asia is the center of this global T2D epidemic [3].

It is now well-recognized that T1D is an autoimmune disorder characterized by the destruction of insulin-producing pancreatic  $\beta$ -cells [4]. However, T2D is characterized by insulin resistance (IR) and the pancreatic  $\beta$ -cell failure to sufficiently compensate (Figure 1). T2D is an acquired syndrome characterized by several defects in the regulation of glucose homeostasis, including elevated blood glucoside levels, increased hepatic glucose production, deficient insulin secretion, IR, and/or pancreas  $\beta$ -cell dysfunction [1,2]. As reported by the World Health Organization [3], T2D comprises approximately 90% of all cases of diabetes, and an estimated 15 million people globally have T2D, a figure that could double by 2025. While the genetic architecture might partially determine an individual's response to environmental changes, the main drivers of the global epidemic of T2D are the rise in obesity, a sedentary lifestyle, energy-dense diets, and population ageing. Therefore, animal models of T2D tend to include models of IR and/or models of  $\beta$ -cell failure. Many animal models of T2D are obese, reflecting the human condition where obesity is closely linked to T2D development. Preclinical animal models have provided considerable valuable information about obesity and T2D. Despite constant improvements and refinements in cell-based applications, careful metabolic assessment of compound effects in in vivo models is vital before drugs can be considered for clinical evaluation and commercialization.

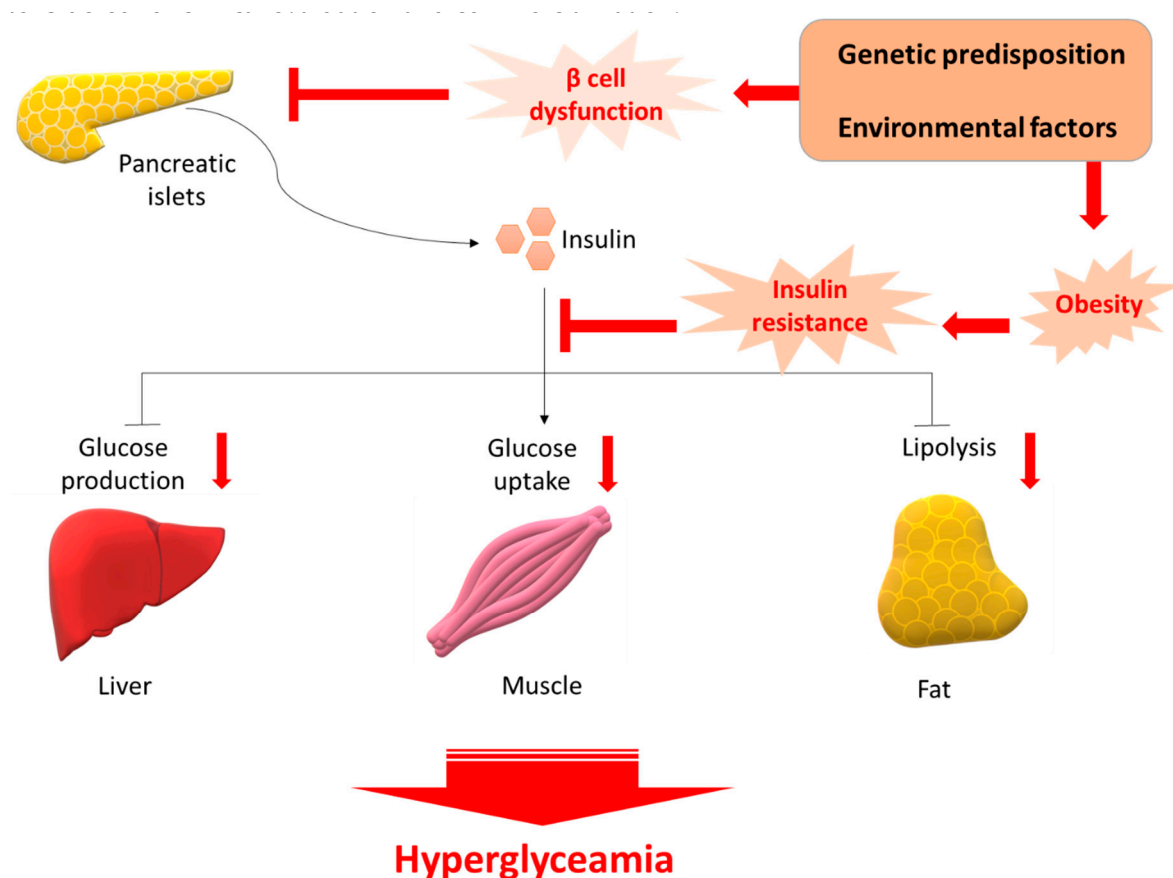


**Figure 1.** Pathology of T2D.  $\beta$  cell dysfunction and insulin resistance occurs following insult from several genetic predisposition and environmental factors. Initially the  $\beta$ -cell compensates by increasing the release of insulin; however, over time this compensatory mechanism fails and reduction in  $\beta$ -cell mass is evident. The reduced plasma insulin results in an increase in glucose levels. Glucose-sensitive tissues, including liver, muscle, and adipocytes, are unable to accommodate the increased glucose concentration. Persistent glucose release preserves the hyperglycemic environment, leading ultimately to T2D.



## 2. Animal Models of T2D

Animal models remain indispensable for discovering, validating, and optimizing novel therapeutics for their safe use in humans. Different T2D animal models, ranging from non-mammalian models to nonhuman primates, each have distinct advantages and limitations. Here, we have summarized the key information on currently available animal models of T2D, offering guidance as to the usefulness, advantages and limitations of these models depending on the species (Figure 2), altered pathway, environmental conditions, and genetic background.

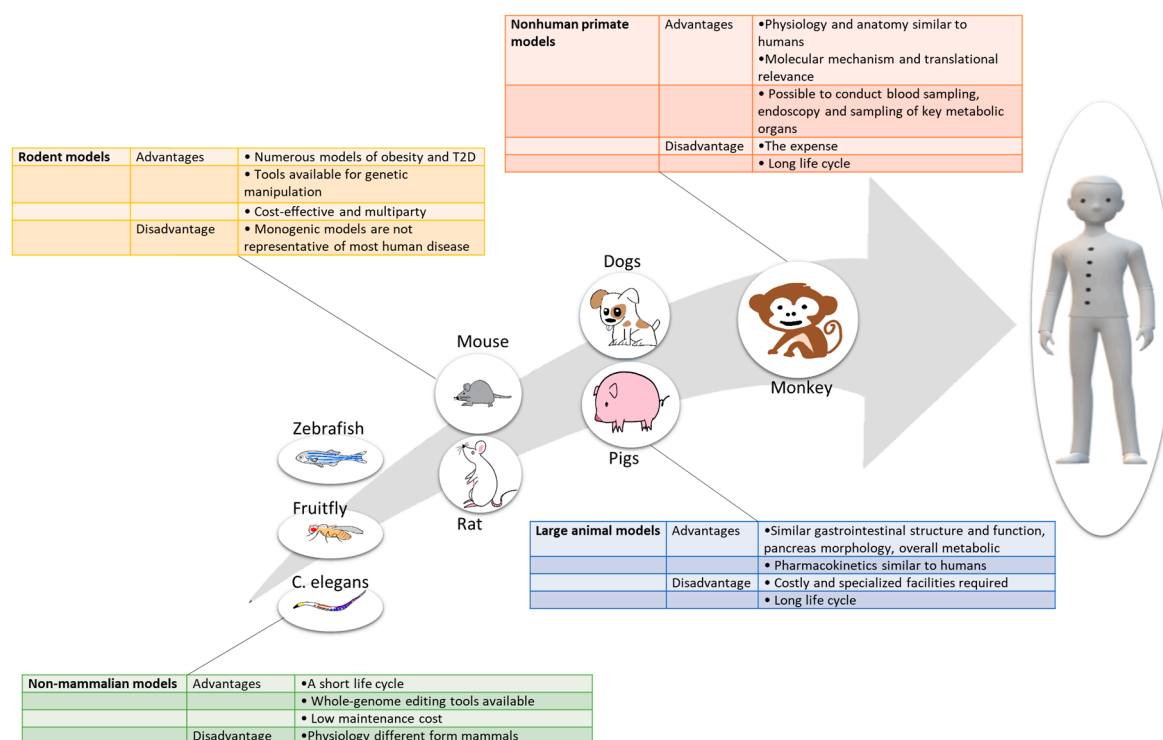


**Figure 2.** Major advantages and disadvantages of different classes of animal models used in T2D research.

### 2.1. Non-Mammalian Models

As a general rule of the laboratory T2D study, roundworm *C. elegans* [5], fruit fly *Drosophila melanogaster* [6], and zebrafish *Danio rerio* [7] are the non-mammalian models usually established in laboratory settings. Schlotterer et al. [8] established *C. elegans* as a model for diabetes research through the responses of *C. elegans* to being fed high glucose concentrations; it was shown that their lifespan is reduced by increased reactive oxygen species (ROS) generation and advanced glycation end products (AGEs)-modification of proteins. Moreover, the inhibition of the activities of the DAF-16 and the heat shock factor (HSF-1), which are also both inhibited by insulin signaling, were also suggested to underlie glucose-induced lifespan reductions [9]. *Drosophila melanogaster* could emerge as a powerful system for dissecting the genetics of IR and secretion because the mechanisms of glucose homeostasis are conserved between flies and humans, and the fruit fly allows for substantial ease of experimental and genetic manipulation in comparison to rodent models [10]. Park et al. [11] generated a double-tagged insulin-like peptide 2 (ilp2HF) to monitor its secretion. They found a marked increase in ilp2HF-circulating levels upon re-feeding after a 24 h fast; it is likely a result of glucose sensing by glucose transporter type (GLUT) 1 in the insulin-producing cells (IPCs), as IPC-specific knockdown of *Glut1* decreased circulating ilp2HF. Insulin-resistant *Drosophila* have also been generated by rearing flies on high-sugar diet (HSD). HSD causes IR with decreasing insulin-like peptides expression; these flies develop hyperglycemia through the production of a robust suppression of Lst, a negative regulator

of insulin-like peptides production and secretion [12,13]. Both nutritional and genetic approaches have also been used to generate T2D models in zebrafish. Several studies suggest that the immersion of zebrafish in glucose solution is a widely used model to induce diabetic phenotypes, including elevated blood glucose levels and impaired response to exogenous insulin [14,15]. Chen et al. developed two transgenic zebrafish models of IR in skeletal muscle and liver, a result achieved through ablation of the insulin receptors [16,17]. Another type of diabetes, MODY (maturity-onset diabetes of the young), is a rare, autosomal dominant, noninsulin-dependent, and monogenic form of diabetes resulting from pancreatic  $\beta$ -cell dysfunction [18]. A zebrafish mutant line, with mutations in hepatocyte nuclear factor 1 $\beta$ , exhibits pancreas hypoplasia and reduced  $\beta$ -cell numbers [19,20]; it closely mimics established human diseases, such as the MODY form of diabetes. Curado et al. [21] were able to study  $\beta$ -cell regenerative capacity by the addition of a prodrug metronidazole that induces cell death of the  $\beta$ -cells in zebrafish transgenic lines. Non-mammalian models have the advantage of low maintenance cost, short life cycle, and availability of long-term gene-editing tools quantification. However, their translational value is limited given their physiology difference to mammals.

## 2.2. Large Animal Models

Dogs and pigs are the large animal models used for translational studies in research on obesity and diabetes mellitus [22,23]. The canine model is especially powerful in allowing quantification of liver glucose uptake; researchers can induce diabetes mellitus in dogs with pancreatectomy or with the use of alloxan and/or streptozotocin (STZ) [24,25]. In these models, metabolic defects are evident in all of them, including increased visceral, subcutaneous, and total adipose tissue mass, increased IR and a  $\beta$ -cell defect. The dog model also provides invasive measures and assessments impossible in humans or rodent models, particularly for studies involving oral administration of compounds because canine gastrointestinal anatomy and physiology are highly similar to those of human beings. The pig is another large animal model used for diabetes mellitus; it shares the structure and function of the gastrointestinal tract, the development and morphology of the pancreas, and overall metabolic status with humans [26]. Genetic engineering of pigs represents an approach for diabetes mellitus research, including transgenic pigs expressing a dominant-negative glucose-dependent insulinotropic polypeptide receptor (GIPR) [27] and ubiquitous expression of a dominant-negative human hepatocyte nuclear factor 1 $\alpha$  (HNF1A) [28]. High fat and cholesterol (HFC) diets with or without STZ have been adapted for the establishment of pig models for T2D [29,30]. While pigs are increasingly used as models for obesity and diabetes mellitus research, dogs remain an important model in this field.

## 2.3. Nonhuman Primate Models

While other animal models provide insights into the mechanisms underlying T2D, they are limited in their translatability to humans. The nonhuman primate shares more metabolic similarities with the human, making it an ideal model for the investigation of T2D and use in preclinical trials [31]. A long history of studying nonhuman primates for translational research in T2D, and the most commonly used species include rhesus macaques (*Macaca mulatta*), cynomolgus monkeys (*Macaca fascicularis*), baboons (*Papio species*), African Green Monkeys (*Chlorocebus species*), and common marmosets (*Callithrix jacchus*) [32]. A number of models are in use for the study of T2D in nonhuman primates, including high fructose-fed nonhuman primate models [33], diet-induced nonhuman primate models [34], and aged-spontaneous T2D nonhuman primate models [35]. The presence of islet amyloidosis, IR to  $\beta$ -cell failure, and overt diabetes mellitus characteristic of T2D in humans is also observed in diabetic monkeys, implicating a similar etiology of islet lesions in monkeys and humans [36,37]. Given the substantial cost of conducting clinical trials with humans, studies in non-human primate models represent a cost-effective avenue for studying T2D strategy. However, the use of nonhuman primate models is an expense in biomedical research, and relatively few laboratories are equipped to accommodate such studies.

## 2.4. Rodent Models

### 2.4.1. Monogenic Models

The rodent has proven to be a reliable model for discovering and validating new treatments for T2D (Table 1). Compared to non-mammalian species, as mammals, the physiology of mice and rats is closer to that of humans. We here review commonly used rodent models to study glucose metabolism which show good translatability to the diagnostic of T2D in humans. While obesity in humans is rarely caused by a monogenic mutation, monogenic models of obesity are commonly used in T2D research. The most widely used monogenic models of obesity are defective in leptin signaling. Leptin induces satiety, and thus, a lack of functional leptin in these animals causes hyperphagia and subsequent obesity. These models include the Lep<sup>ob/ob</sup> mouse [38–40], which is deficient in leptin, and the Lepr<sup>db/db</sup> mouse and Zucker Diabetic Fatty (ZDF) rat, which are deficient in the leptin receptor [41,42]. These models are also used to test new therapies for T2D.

The Lep<sup>ob/ob</sup> mouse is a model of severe obesity derived from a spontaneous mutation on chromosome 6 discovered in an outbred colony at Jackson Laboratory in 1949 [43]. The phenotype was bred into C57BL/6J mouse, but it was not until 1994 that the mutated protein was identified as leptin [44]. The obesity was observed at 2 weeks of age, and the mice develop hyperinsulinemia. By 7–12 weeks, hyperglycemia is apparent; at this point, pancreatic  $\beta$ -cell compensation occurs, and increased insulin levels bring glucose homeostasis under control, after which they fall as the mouse ages. In addition, other metabolic aberrations include hyperlipidemia; hepatic fatty acid synthesis was increased 6-fold per total liver and 2.2-fold per total small intestine [45]. The severity of the diabetes in Lep<sup>ob/ob</sup> mouse is strongly dependent upon the strain's genetic background. With the C57BL/KsJ background, Lep<sup>ob/ob</sup> mouse develops more severe hyperglycemia and diabetes, accompanied by increasing insulin levels, followed by  $\beta$ -cell failure, and often dies by 6 months of age [46]. Other different background strains have been studied, including the BALB/cJ background [47] at 27 weeks of age have a 35–40% reduction in weight gain with elevations in fed insulin and plasma triglycerides levels. The Lepr<sup>db/db</sup> mouse originated from the Jackson Laboratory, and are deficient in the leptin receptor [48]. The Lepr<sup>db/db</sup> resembles Lep<sup>ob/ob</sup> mouse in terms of a rapid development of obesity, but the diabetes syndrome is more severe. Depending upon their genetic background, the Lepr<sup>db/db</sup> mouse in the C57BL/6J inbred strain is a rapid development of obesity at 3–4 weeks, blood glucose level at 7 weeks of age and hyperglycemia developing at 4–8 weeks. The Lepr<sup>db/db</sup> mouse with the C57BL/KsJ background develops more severe diabetes and has a relatively short lifespan [49].

The Zucker Fatty (ZF) rats were discovered in 1961 after a cross of Merck M-strain and Sherman rats. They harbor a missense mutation (fatty, fa) in the leptin receptor gene (Lepr) and become obese at around 4 weeks of age [50]. These rats are also hyperinsulinemic, hyperlipidemic, and hypertensive. ZDF rats derived from a mutation in the ZF rat strains exhibit less obesity than the ZF rats but have more severe IR, which they are unable to compensate for due to increased apoptosis levels in  $\beta$ -cells; they are widely used for research on T2D [51]. They are characterized by initial hyperinsulinemia at 8 weeks of age followed by decreased insulin levels and signs of diabetic complications usually develop at 10 weeks [49,52].

Those findings underline the fact that although the monogenetic models are indeed a valuable and useful animal model of T2D and do have a role in terms of teasing out the mechanism and mode of action of these diseases, but the human obesity phenotype is caused by the interplay between a long list of genes and the environment. Notably, few cases of human obesity can be accounted for mutations in leptin or the leptin receptor. Thus, it does not reflect the complete background of T2D in humans based on its monogenic cause of obesity or T2D and will therefore not always be predictive of the effects of pharmaceutical treatments in humans.

#### 2.4.2. Polygenic Models

Polygenic models of obesity may provide a more accurate model of the human condition. A variety of different polygenic mouse models of obesity, glucose intolerance and diabetes exist, allowing a variety of genotypes and susceptibilities to be studied. However, unlike the monogenic models, there are no wild-type controls. Since the obesity is induced by environmental manipulation rather than genes, it is thought to model the human situation more accurately than monogenic models. The diet-induced obesity (DIO) model has considerable direct validity with human obesity, and is a widely used paradigm to study the interaction of diet and genes in manifest obesity and IR [53]. The inbred C57BL/6J mouse strain, first described in 1988, is a polygenic obesity-prone mouse strain widely used as a model for DIO [54] because it is prone to develop obesity and glucose intolerance and moderate IR, making them especially intriguing models to study human obesity resistance. However, a report [55] on the effects of a drug on overt diabetes end points, suggests that the C57BL/6J model for DIO is not the ideal choice because this strain rarely develops frank hyperglycemia and/or islet atrophy when fed an obesogenic diet. In contrast, the rather closely related but distinct C57BL/6N strain develops hepatosteatosis, hyperglycaemia and hyperinsulinaemia following 3 weeks on an HFD [56,57]. It means that they have considerable genetic variation, which investigators should take into account when determining sample size. The DIO rat and mouse offer more human-like models, where the obesity is based on several factors, including an excess intake of calories.

The New Zealand Obese (NZO) mouse is another inbred polygenic strain created by selective breeding that develops obesity and T2D. Adiposity in the NZO mouse is driven by a moderate hyperphagia, which may be a consequence of leptin resistance as these mice are hyperleptinemic at 9–12 weeks of age, and causes disturbances related to both pancreatic and hepatic defects [58]. When fed a carbohydrate-containing diet, there is a dramatic effect on the pancreatic islets including a loss of serine/threonine-protein kinase (AKT) activation, decreased expression of GLUT2 essential for insulin synthesis and  $\beta$ -cell integrity [59]. Similar to what occurs in humans, the onset of T2D in NZO mice decidedly depends on the degree of hepatosteatosis early in life [60]. TALLYHO/Jng mice are another emerging, polygenic model for moderate obesity and diabetes [61]. TALLYHO/Jng mice were inbred from two Theiler Original outbred mice that showed polyuria and glucosuria [62], selecting for mice at each generation that demonstrated  $\beta$ -cell hypertrophy, hyperplasia with hyperinsulinemia, severe dyslipidemia, and hyperglycemia. IR in white adipose tissue is associated with reduced GLUT4 cycling and increased insulin receptor substrate 1 (IRS-1) degradation [63]. Both male and female TALLYHO/Jng mice become moderately obese; hyperglycaemia is limited to male mice, and develops as early as at 10–14 weeks of age [64]. In 1952, Kondo et al. [65] established many mouse strains, and then Nakamura et al. found that the KK mouse among these inbred strains spontaneously develops diabetic characteristics, including obesity, hyperinsulinemia, and IR in both muscle and adipose tissue [66]. This mouse strain also shows signs of diabetic nephropathy [67]. Due to the relatively mild diabetes and obesity in KK mouse, a derivative of this strain is the KK-A<sup>y</sup> mouse, which was created by transferring the yellow obese gene (A<sup>y</sup>) into KK mouse by crossing yellow obese mice with KK mice [68].

#### 2.5. Chemical-Induced Model of T2D

T2D is increasing in prevalence worldwide, and is strongly associated with obesity and IR, as well as defects in pancreatic  $\beta$ -cell function and mass, thus precipitating a disease characterized by impeding the critical regulatory influence of insulin on glucose, lipid and protein metabolism [69]. Characterized and clinically relevant T2D animal models are required to create and achieve the aim of testing new therapeutics. An example of a chemical-induced animal model of diabetes is the high-fat diet/streptozotocin-treated (HFD/STZ) animal model. This model involves a combination of an HFD to bring about hyperinsulinemia, IR, and/or glucose intolerance followed by subsequent injection of a low dose (~30–40 mg/kg intraperitoneally) STZ, which results in severe reduction in functional  $\beta$ -cell mass [70]. Together, these two stressors are designed to mimic the pathology of T2D, though on a shorter timescale than found in the human condition. The key advantage of this non genetic model is



that researchers can customize it to resemble the slow pathogenesis of T2D that occurs in most humans, encompassing the slow development from adult-onset DIO to glucose intolerance, IR, the resulting compensatory insulin release, and finally STZ-induced partial  $\beta$ -cell death. Despite its limitations and the wide variety of both the high-fat fed regimen [71] and the STZ treatment [72], the HFD/STZ is a reasonable animal model of T2D mainly representing the later stage of the disease, depending on the amount of residual  $\beta$ -cell mass.

**Table 1.** List of selected rodent models potentially useful in type 2 diabetes research.

Strain or Method	Species	Obesity	Hyperpagia	Hyperglycaemia	Insulin Resistance	Hyperinsulinaemia	T2D
<b>Monogenic</b>							
Lep <sup>ob/ob</sup>	Mouse	++	+	+	++	++	-
Lepr <sup>db/db</sup>	Mouse	++	+	+	++	++	+
ZDF	Rat	-	-	+	++	+	+
<b>Polygenic</b>							
C57BL/6J	Mouse	+	+	-	+	-	-
C57BL/6N	Mouse	-	-	+	++	-	-
KK-A <sup>y</sup>	Mouse	+	+	+	++	+	+
NZO	Mouse	++	++	+	++	+	+
TALLYO/Jng	Mouse	+	+	+	++	+	+
KK-A <sup>y</sup>	Mouse	-	-	+	++	+	+
<b>Chemical-induced</b>							
HFD/STZ	Mouse, Rat	+	+	+	+	+	+

-, absent; +, mild; ++, severe; DIO, diet-induced obesity; HFD, high-fat diet. SD, standard diet; T2DM, type 2 diabetes mellitus; VMH, ventromedial hypothalamus.

### 3. Flavonoids and Their Effects on T2D

Flavonoids belong to a large group of polyphenols; they mainly accumulate in the edible parts of plants, particularly in fruits, vegetables, herbs, chocolate, tea, seeds, flowers, and red wine [73]. More than 9000 flavonoids have been identified from plant sources [74], and their daily intake varies between 20 mg and 500 mg, mainly from dietary supplements including tea, red wine, apples, onions, and tomatoes [75]. The basic chemical structural of flavonoids consists two benzene rings (A and B) linked by a three-carbon chains, forming an oxygenated heterocycle (ring C); they provide attractive color pigments such as yellow, red, blue, and purple in plants. Flavonoids are classified according to their chemical structure. These medicinal herbs have been traditionally used for the treatment of T2D; among the phytochemical compounds, flavonoids, and their derivatives are more under attention due to their hypoglycemic activity [76]. Flavonoids are classified subclasses based on chemical structures, six of which are: Anthocyanidins, flavan-3-ols, flavonols, flavones, flavanones, and isoflavones (Table 2). Flavonoids have antioxidative properties that protect the body against the deleterious effects of hyperglycemia in T2D, by acting on biological targets such as  $\alpha$ -glucosidase, glucose co-transporter, or aldose reductase. These antioxidants have been proposed as potential anti-diabetic drugs by acting as biological targets involved in T2D development. In current years, various approaches have been made to utilize the flavonoids in vivo rodent models by incorporating a few novel methods to improve its antidiabetic activity. They are categorized in Table 3.

**Table 2.** Major subclasses of flavonoids with examples and some of the major dietary sources.

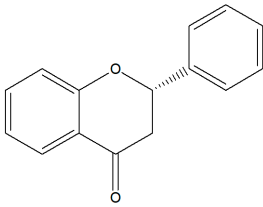
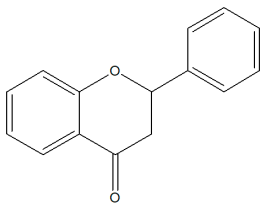
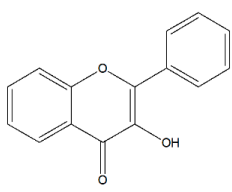
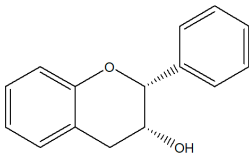
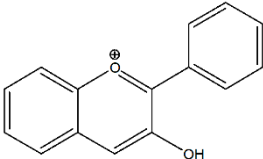
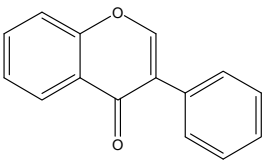
Flavonoid Subclasses	Color	Compounds	Dietary Sources
Flavanones 	Colorless, Pale Yellow	Hesperetin, Naringenin, Eriodictyol, Naringin	Grapefruit, lemon, orange, grapefruit juice, lemon juice, orange juice.
Flavones 	Pale Yellow	Luteolin, Apigenin, Vitexin, Orientin	Celery seed, dried parsley, thyme), celery, parsley, peppers.
Flavonols 	Pale Yellow	Quercetin, Kaempferol, Myricetin, Isorhamnetin, Rutin, Tiliroside, Aromadendrin, Silymarin, Silybin	Capers, apples, cranberries, arugula, asparagus, broccoli, cabbage, chives, coriander, endive, fennel, ginger, mustard greens, okra, onions, peppers, beans,
Flavan-3-ols (Flavanols) 	Colorless	Catechin, Gallocatechin, Epicatechin, Epigallocatechin, Epicatechin 3-gallate, Theaflavin, Theaflavin 3-gallate,	Apples, broad beans, pecans, pistachio, wine, cocoa, tea, soybeans.

Table 2. Cont.

Flavonoid Subclasses	Color	Compounds	Dietary Sources
Anthocyanidins 	Blue, Red, Violet	Cyanidin, Delphinidin, Malvidin, Pelargonidin, Peonidin, Petunidin	Berries, blackberries, blueberry, cranberry, currants, grapes, plum, red cabbage, eggplant, pecans, pistachio, wine, black beans.
Isoflavones 	Colorless	Daidzein, Genistein, Glycitein	Red clover, soybeans and soybean products (milk, flour, yogurt and others).

### 3.1. Flavonol

Flavonols are the most abundant flavonoids in the plant kingdom. The main dietetic flavonols include quercetin, rutin, kaempferol, isorhamnetin, and myricetin [77,78], while the most ubiquitous compounds are glycosylated derivatives of quercetin and kaempferol; in nature, these two molecules have respectively about 280~350 different glycosidic combinations. Quercetin is ubiquitously present in fruits and vegetables and considered a strong antioxidant, anti-inflammation against proinflammatory cytokines production [79,80], platelet aggregation prevention, and anti-diabetes effects [81,82]. Recently, quercetin has been shown to enhance insulin secretion via  $\text{Ca}^{2+}$  and ERK1/2 signaling pathway [83], acts as partial agonists of PPAR $\gamma$  [84], and potentiates ERK1/2 phosphorylation [85] in vitro. Studies have been conducted on the effects of quercetin in animals with T2D, quercetin ameliorates hyperglycemia (lower glucose plasma levels) and dyslipidemia (an increase in plasma adiponectin and HDL-cholesterol, decreases in plasma total cholesterol and plasma triacylglycerols) and improves the antioxidant status in type 2 diabetic *Lepr<sup>db/db</sup>* mouse [86]. A study showed that transforming the growth factor- $\beta$ 1 (TGF- $\beta$ 1) and connective tissue growth factor (CTGF) has an essential impact on diabetic nephropathy. A report showed that HFD/STZ-induced rats treated with quercetin saw a reduction in their weight ratio of kidney and body, and attenuated expressions of CTGF and TGF- $\beta$ 1 in the renal tissues [87,88]. A recent report indicates that diets rich in flavonoids are associated with a lower incidence of T2D [89]. Among the flavonol subclass, quercetin, and myricetin intake was associated with a lower incidence of T2D in European populations [90]. Another report suggests that daily intakes of quercetin from apple and orange is inversely related to the prevalence of T2D: 8.35% in men and 4.68% in women in a Chinese population [76]. Rutin can be broadly extracted from natural plant sources such as buckwheat, citrus fruits, grapes, lemons, and berries, and was also reported to have anti-obesity and anti-diabetic functions [91]. Rutin potentiates insulin receptor kinase to enhance insulin-dependent GLUT4 translocation through the enhancement of insulin receptor kinase activity, thereby activating the insulin signaling pathway, causing increased GLUT4 translocation and increased glucose uptake [92]. Rutin was also found to activate liver enzymes linked with the gluconeogenic and lipid metabolic processes. It reduced the alanine aminotransferase, aspartate aminotransferase activities and advanced glycation end products level in serum. It also potentiated the phosphorylation of phosphatidylinositol-4,5-bisphosphate 3-kinase (PI3K), Akt, glycogen synthase kinase-3 beta protein in the liver tissue of *Lepr<sup>db/db</sup>* mouse [93], and was shown to influence glucose uptake in the rat soleus muscle [94]. Rutin was also reported to reduce the levels of plasma glucose, glycosylated hemoglobin (HbA1c), a glycated (beta-N-1-deoxy fructosyl) hemoglobin, and proinflammatory cytokines, and improved antioxidant and plasma lipid profiles in HFD/STZ-induced diabetic rats fed with 100 mg/kg rutin in their diet [95,96]. Particularly, rutin can meliorate metabolic abnormalities, oxidative stress, inflammation, and cellular apoptosis pathways in an STZ-induced diabetic rat model [97]. Kaempferol is an important flavonoid in herbal foods, and is reported to effectively inhibit inflammation and ameliorate insulin resistance by the beneficial regulation of the IRS-1 function [98]. Kaempferol exhibits anti-diabetic effect in multiple mechanisms, including anti-oxidative, anti-inflammatory, antihyperlipidemic, and pancreatic  $\beta$ -cell protection [99–101]. Recent studies show that HFD/STZ-induced diabetic rats ameliorate blood lipids and insulin with the treatment of kaempferol orally ingested for 10 weeks, and effectively restored IR induced alteration of glucose disposal through the inhibition of the phosphorylation of IRS-1, IKK/NF- $\kappa$ B signal and further proinflammatory cytokines tumor necrosis factor- $\alpha$  (TNF- $\alpha$ ) and interleukin-6 (IL-6) levels [102,103]. Troxerutin is a flavonol, a type of flavonoid, derived from rutin, which can be used to treat thrombosis, cerebrovascular diseases, and edemas. However, troxerutin administration significantly reduced heart rate, blood pressure, blood glucose, and plasma triglyceride levels, as well as significantly reduced reactive oxygen species, NF- $\kappa$ B levels, and suppressed the phosphorylated forms of AKT, c-Jun N-terminal kinase (JNK) and IRS-1 in a rat model of T2D [104].



### 3.2. Isoflavone

Isoflavones are reported to have beneficial antioxidant and estrogenic effects in the treatment of cardiovascular diseases and may lower the risk of several cancers [105,106]. Isoflavones are predominantly found in soy beans and other leguminous plants, and are known to be the richest sources of the active isoflavones, including genistein and daidzein [107]. Genistein has the ability to increase insulin secretion in the pancreatic islets of adult mice through a reduced intracellular calcium concentration effect [108]. Genistein also induces cAMP, stimulates protein kinase A in pancreatic islet's cell linings (PC12) [109], and regulates the insulin-induced glucose passage because of the conformational changes of the GLUT4, without affecting the translocation of GLUT4 in adipocytes [110]. Further studies showed that genistein acts as a direct inhibitor of the insulin-induced glucose passage in 3T3-L1 adipocytes [111]. In vivo experiments showed that dietary intake of genistein (250 mg·kg<sup>-1</sup> diet) improved hyperglycemia, glucose tolerance, and blood insulin level, and increased the number of insulin-positive  $\beta$ -cell in islets, promoted islet  $\beta$ -cell survival, and preserved islet mass in HFD/STZ-induced diabetic mice [112]. In the ZDF rat model, genistein showed an increased GLUT4 expression level and larger soleus muscle fiber areas as well as regulation of estrogen receptor signaling pathways [113]. In the ovariectomized diabetic rat model, genistein has shown anti-diabetic and anti-inflammatory effects to markedly increase SIRT1 protein, and decreased IL-1 $\beta$  and NF- $\kappa$ B proteins levels compared to control groups [114]. SIRT1, a deacetylase, is expressed in the endocrine cells of the Langerhans islets and has been reported to inhibit NF- $\kappa$ B by deacetylating p65 and protect  $\beta$ -cells from cytokines [115]. In Lep<sup>ob/ob</sup> mouse model, the genistein-fed group increases plasma levels of triiodothyronine (T3) and decreases in the protein expression of renal 11 $\beta$ -hydroxysteroid dehydrogenase type 2 (11 $\beta$ -HSD2), suggesting a thermogenic effect on energy expenditure, T3 production, and corticosterone status [116]. Daidzein belongs to the isoflavone subclass of flavonoids, and is present predominantly in the form of glucosides in various plants, including red clover, alfalfa, soybean, and some legumes [117]. Previous studies suggest that daidzein exerts anti-diabetic effects by improving glucose and lipid metabolism, and downregulating blood glucose, total cholesterol levels, and improving glucose uptake via GLUT4 translocation, as well as AMP-activated protein kinase (AMPK) activation [118–121]. In in vivo studies, Cheong et al. [122] demonstrated that 0.1% daidzein in the diet for 4 weeks suppressed the rise in fasting glucose, lipid levels, and IR and AMPK activation in gastrocnemius muscle compared to the diabetic (Lepr<sup>db/db</sup> mouse) control group. In addition, daidzein also reduced blood glucose and urinary glucose excretion in KK-A<sup>y</sup> mice [122]. Using Lepr<sup>db/db</sup> mouse, another study by Park et al. [118] also demonstrated that daidzein (0.2 g/kg diet, 6 weeks) supplementation improved glucose and lipid metabolism and regulated hepatic glucose (GK, G6Pase, and PEPCK) and lipid- (FAS, CPT, and  $\beta$ -oxidation) regulating enzyme activities compared to those seen in diabetic control group.

### 3.3. Flavanones

Naringenin and hesperidin, the two major flavanones that are abundant in citrus fruits (such as grapefruit, orange and tomato) have been reported to possess antioxidant, anti-diabetic, lipid-lowering, anti-atherogenic, and anti-inflammatory activities [123,124]. Oral treatment of naringenin (25 mg/kg) exerts significant inhibition of intestinal  $\alpha$ -glucosidase activity in vivo [125], thereby delaying the absorption of carbohydrates in HFD/STZ-induced diabetic rats, thus resulting in significant lowering of postprandial blood glucose levels. In the livers of Lepr<sup>db/db</sup> mouse, naringin improves hyperlipidemia and hyperglycemia by partly regulating the fatty acid and cholesterol metabolism, and affecting the gene expression of glucose-regulating enzymes. Furthermore, naringin may upregulate hepatic and adipocyte PPAR $\gamma$  and GLUT4 to regulate the expression of hepatic enzymes involved in glycolysis and gluconeogenesis, thereby improving hyperglycemia [126]. Oral treatment of naringenin in the HFD/STZ-induced diabetic rat model involves enhancement of reverse cholesterol transport and paraoxonase activity [127], and decreases levels of glucose, HbA1c, MDA, NO, TNF- $\alpha$ , and IL-6 in HFD/STZ-induced diabetic rats [128]. Neohesperidin, a flavanone glycoside found in citrus fruits, is the

7-O-neohesperidose derivative of hesperetin. Neohesperidin significantly decreases serum triglycerides, total cholesterol and liver index, inhibits lipid accumulation in the liver, and decreases the size of epididymal adipocyte in the KK-A<sup>y</sup> mice. Gene expression of stearoyl-CoA desaturase 1 (SCD-1) and fatty acid synthase (FAS) are significantly inhibited, and elevated level of phosphorylation of hepatic AMPK is observed in neohesperidin-treated mice. Therefore, the activation of the AMPK pathway and regulation of its target genes, including SCD-1, FAS, and ACOX, may play important roles in the hypoglycemic and hypolipidemic effects [129]. Hesperidin and naringenin, were reported to be beneficial for lowering blood glucose levels by upregulating hepatic glucokinase, PPAR $\gamma$ , and adipocyte GLUT4 in the Lepr<sup>db/db</sup> mouse model [126].

### 3.4. Flavan-3-ols (Flavanols)

Drinking green tea has long been found to have an anti-diabetes effect [130]. Kim et al. [131] found that green tea catechins can protect the pancreas from oxidative damage, and green tea extract can enhance GLUT4 expression, increase glucose tolerance, promote glucose uptake, and decrease oxidative stress in diabetic rats [132]. Jingqi et al. [133] found that catechins exact anti-IR effect, significantly decrease glucose levels and increase glucose tolerance in KK-A<sup>y</sup> animals by reducing ROS content and JNK phosphorylation and promoting GLUT4 translocation.

### 3.5. Flavones

Flavones differ from other flavonoids in that they have a double bond between C2 and C3 in the flavonoid skeleton, there is no substitution at the C3 position, and they are oxidized at the C4 position. Flavones from plants are typically conjugated as 7-O-glycosides; they contain apigenin, such as passionflower and chamomile, and have been used as traditional medicines for hundreds of years to treat a variety of diseases. In T2D studies, apigenin was intragastrically administered at 50 or 100 mg/kg once a day for 6 weeks in the HFD/STZ-induced diabetic rat model to investigate the effect of diabetes mellitus. Compared with the diabetic control group, apigenin significantly decreased the levels of blood glucose, serum lipid, malonaldehyde, ICAM-1 and IR index, and improved impaired glucose tolerance [134]. Another report investigated the role of apigenin in controlling damaged vital tissues in HFD/STZ-induced diabetic rats. Enhanced GLUT4 translocation and downregulated CD38 expression by apigenin were observed. Apigenin was also found to control blood glucose level, along with the protection of vital organs eventually damaged during diabetes. Baicalein is a flavonoid originally isolated from the traditional herbal remedy known as Chinese skullcap, which exhibits strong free radical scavenging [135]. Using the HFD/STZ-induced diabetic mouse model, and the administered 250 or 500 mg baicalein/kg diet, Fu et al. [136] found that baicalein treatment significantly improved hyperglycemia, glucose tolerance, insulin levels, and preserved islet mass by inhibiting apoptosis.

### 3.6. Anthocyanidins

Anthocyanidins are another class of flavonoids widely distributed in the human diet in apples, berries, red grapes, eggplant, red cabbage and radishes. Dietary consumption of anthocyanins is high compared to other flavonoids, owing to their wide distribution in plant materials. Considerable attention has been given to anthocyanins because of their potential health benefits, including anti-inflammatory, antioxidant, anti-obesity, and anti-diabetic effects. Cyanidin and its glycosides belong to anthocyanins and have been demonstrated to inhibit intestinal  $\alpha$ -glucosidase and pancreatic  $\alpha$ -amylase in vitro [137]. Cyanidin-3-glucoside, one of the most prevalent anthocyanins existing in our diet, ameliorates hyperglycemia and insulin sensitivity via the activation of AMPK in KK-A<sup>y</sup> mouse [138], and this activation is accompanied by the up-regulation of GLUT4 in skeletal muscle and the downregulation of gluconeogenesis in the liver. Guo et al. [139] also showed that dietary cyanidin-3-glucoside significantly lowers fasting glucose levels and markedly improves the insulin sensitivity, macrophage infiltration, and the mRNA levels of MCP-1, TNF- $\alpha$  and IL-6 in adipose tissue, and modulates the JNK/forkhead box O1 signaling pathway in liver and adipose tissues of the HFD and Lepr<sup>db/db</sup> mouse model.

**Table 3.** Important anti-diabetic potential and the underlying mechanism of dietary flavonoids in selected rodent T2D models.

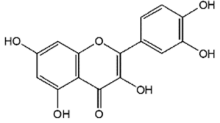
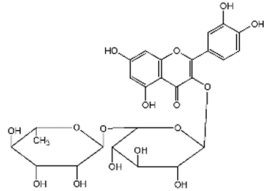
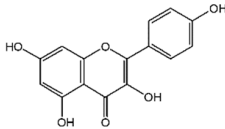
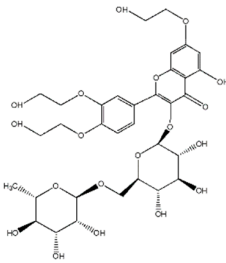
Flavonoids	Structural Formula	Sources	Pathways/Target Molecules	Experimental Model	References
<b>Flavonols</b>					
Quercetin		<i>Edgeworthia gardneri</i>	↑Intracellular $\text{Ca}^{2+}$ , ↑the ratio of Bcl-2/BAX, ↑mitochondria membrane potential.	Lepr <sup>db/db</sup> mouse	[83,86]
			↑Serum insulin levels, ↓MIP-1 $\alpha$ , Bax/Bcl2 ratio, protein disulfide isomerase activity	HFD/STZ-induced diabetic rat	[88]
Rutin		Buckwheat, oranges, grapes, lemons, limes, peaches and berries	↑Body weight, ↓plasma glucose and HbA1c, proinflammatory cytokines, ↑the depleted liver antioxidant status and serum lipid profile, ↑oxidative stress.	HFD/STZ-induced diabetic rats	[96,97]
			↑Insulin IRS-2/PI3K/Akt/GSK-3 $\beta$ signal pathway, ↑hepatocyte proliferation, ↓blood glucose level and generation of AGEs	Lepr <sup>db/db</sup> mouse	[93]
Kaempferol		Tea, cruciferous vegetables, grapefruit, Ginkgo biloba L., and some edible berries	↑Antioxidant status, ↓of lipid peroxidation markers, ↑membrane-bound ATPases.	HFD/STZ-induced diabetic rat	[101,103]
Troxeutin		Sophora japonica	↓Heart rate, blood pressure, blood glucose and plasma triglyceride levels	HFD/STZ induced diabetic rat	[104]

Table 3. Cont.

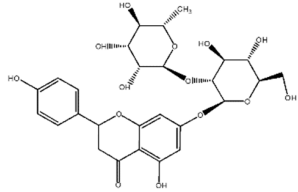
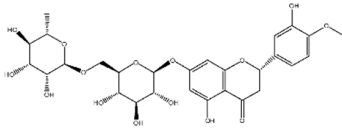
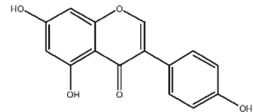
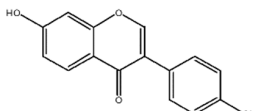
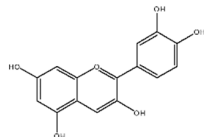
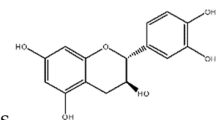
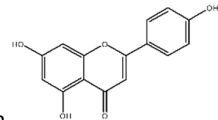
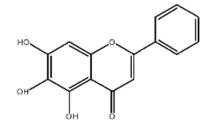
Flavonoids	Structural Formula	Sources	Pathways/Target Molecules	Experimental Model	References
<b>Flavanones</b>					
Naringin		Citrus fruits and Grapefruit	↓ $\alpha$ -glucosidase activity	Lepr <sup>db/db</sup> mouse	[123,125]
			↑Cholesterol transport and paraoxonase activity, ↓ levels of glucose, HbA1c, MDA, NO, TNF- $\alpha$ and IL-6	HFD/STZ-induced diabetic rats	[127,128]
Hesperidin		Citrus fruits	↓Hyperglycemia, ↑plasma insulin, ↓PEPCK and G6Pase expression, ↑ $\beta$ -cell function	Lepr <sup>db/db</sup> mouse	[126]
<b>Isoflavones</b>					
Genistein		Soybeans and soy food	↓Plasma levels of corticosterone, ↓expression of 11 $\beta$ -HSD1	Lep <sup>ob/ob</sup> mouse	[116]
			↓hyperglycemia, ↓glucose tolerance, and blood insulin level, ↑ $\beta$ -cell mass	HFD/STZ-induced diabetic rat	[112]
Daidzein		Soybeans and legumes	↑GLUT4 expression level and larger soleus muscle fiber areas, ↑estrogen receptor signaling	ZDF rat	[113]
			↓Fasting glucose, lipid levels and insulin resistance, ↑AMPK activation	KK-A <sup>y</sup> and Lep <sup>ob/ob</sup> mouse	[122]
			↑insulin/glucagon ratio, ↓hepatic glucokinase activity and hepatic fatty acid synthase, ↓plasma total cholesterol, triglyceride	Lepr <sup>db/db</sup> mouse	[118]



Table 3. Cont.

Flavonoids	Structural Formula	Sources	Pathways/Target Molecules	Experimental Model	References
Anthocyanidins					
Cyanidin 3-glucoside		Fruits, vegetables, berries, and red wine	↓ Blood glucose levels, ↑ insulinsensitivity, ↑AMPK activation, ↑GLUT-4,	KK-A <sup>y</sup> mouse	[138]
			↓Macrophage infiltration and the mRNA levels of MCP-1, TNF-α and IL-6	HFD fed and Lepr <sup>db/db</sup> mouse	[139]
Flavan-3-ols (Flavanols)					
Catechins		Green tea	↓Glucose levels, ↑glucose tolerance, ↓ROS decreased JNK phosphorylation, ↑GLUT-4 translocation	KK-A <sup>y</sup> mouse, HFD-induced obese rat	[133]
Flavones					
Apigenin		Celery, parsley	↓Glucose, serum lipid, ICAM-1 and insulin resistance index, ↑glucose tolerance	HFD/STZ-induced diabetic rat	[134]
Baicalein			↓Blood glucose, serum lipid, ↑SOD activity, ↑glucose tolerance,	HFD/STZ-induced diabetic rat	[134]
			↓hyperglycemia, ↑insulin secretion	HFD/STZ-induced diabetic mouse	[136]

↑: increase; ↓: decrease.

#### 4. Conclusions

Diabetes mellitus is now a major global public health problem. The existing animal therapeutic approaches and models to treat diabetes mellitus and obesity cannot replace clinical human disease studies. However, animal models of targeted T2D diseases offer useful complementary models for selected scientific questions, such as the study food intake, nutrient portioning, body fat distribution, systemic glucose metabolism, and many other key aspects of metabolic health and disease. Flavonoids are a potential alternative treatment strategy for the development of effective and safe anti-obesity and anti-diabetes drugs. Currently, there are no recommendations regarding the optimal content of flavonoids and their subclasses in a diet. However, the results of the presented studies prove a potential beneficial role of flavonoids in the prevention and treatment of T2D. This review suggests the important role of flavonoids in enhancing insulin secretion, reducing apoptosis and promoting the proliferation of pancreatic  $\beta$ -cells, reducing IR, inflammation, and oxidative stress in muscle and promoting translocation of GLUT4 via PI3K/AKT and AMPK pathways. Choosing the right models and using appropriate animal models provide successful discovery and development of safer and more potent therapeutics with the potential to stop the obesity and T2D pandemics.

**Author Contributions:** Conceptualization, J.-Y.F. and S.-Y.C.; Methodology, C.-H.L.; Data Collection, C.-H.L. and T.-H.H.; Writing-Original Draft Preparation, C.-H.L. and S.-Y.C.; Writing-Review & Editing, T.-H.H. and J.-Y.F.

**Funding:** The authors are grateful for financial support from Ministry of Science and Technology of Taiwan (MOST-105-2320-B-182-010-MY3) and Chang Gung Memorial Hospital (CMRPG2F0291-2).

**Conflicts of Interest:** The authors declare no conflict of interest. The funders had no role in the design of the study; in the collection, analyses, or interpretation of data; in the writing of the manuscript, and in the decision to publish the results.

#### References

1. American Diabetes Association. Diagnosis and classification of diabetes mellitus. *Diabetes Care* **2010**, *33*, S62–S69. [[CrossRef](#)] [[PubMed](#)]
2. Bloomgarden, Z. Questioning glucose measurements used in the International Diabetes Federation (IDF) Atlas. *J. Diabetes* **2016**, *8*, 746–747. [[CrossRef](#)] [[PubMed](#)]
3. Zheng, Y.; Ley, S.H.; Hu, F.B. Global aetiology and epidemiology of type 2 diabetes mellitus and its complications. *Nat. Rev. Endocrinol.* **2018**, *14*, 88–98. [[CrossRef](#)] [[PubMed](#)]
4. Atkinson, M.A.; Eisenbarth, G.S.; Michels, A.W. Type 1 diabetes. *Lancet* **2014**, *383*, 69–82. [[CrossRef](#)]
5. Schulz, T.J.; Zarse, K.; Voigt, A.; Urban, N.; Birringer, M.; Ristow, M. Glucose restriction extends *Caenorhabditis elegans* life span by inducing mitochondrial respiration and increasing oxidative stress. *Cell Metab.* **2007**, *6*, 280–293. [[CrossRef](#)] [[PubMed](#)]
6. Leopold, P.; Perrimon, N. *Drosophila* and the genetics of the internal milieu. *Nature* **2007**, *450*, 186–188. [[CrossRef](#)] [[PubMed](#)]
7. Oka, T.; Nishimura, Y.; Zang, L.; Hirano, M.; Shimada, Y.; Wang, Z.; Umemoto, N.; Kuroyanagi, J.; Nishimura, N.; Tanaka, T. Diet-induced obesity in zebrafish shares common pathophysiological pathways with mammalian obesity. *BMC Physiol.* **2010**, *10*, 21. [[CrossRef](#)] [[PubMed](#)]
8. Schlotterer, A.; Kukudov, G.; Bozorgmehr, F.; Hutter, H.; Du, X.; Oikonomou, D.; Ibrahim, Y.; Pfisterer, F.; Rabbani, N.; Thornalley, P.; et al. *C. elegans* as model for the study of high glucose-mediated life span reduction. *Diabetes* **2009**, *58*, 2450–2456. [[CrossRef](#)] [[PubMed](#)]
9. Lee, S.J.; Murphy, C.T.; Kenyon, C. Glucose shortens the life span of *C. elegans* by downregulating DAF-16/FOXO activity and aquaporin gene expression. *Cell Metab.* **2009**, *10*, 379–391. [[CrossRef](#)] [[PubMed](#)]
10. Graham, P.; Pick, L. *Drosophila* as a Model for Diabetes and Diseases of Insulin Resistance. *Curr. Top. Dev. Biol.* **2017**, *121*, 397–419. [[CrossRef](#)] [[PubMed](#)]
11. Park, S.; Alfa, R.W.; Topper, S.M.; Kim, G.E.; Kockel, L.; Kim, S.K. A genetic strategy to measure circulating *Drosophila* insulin reveals genes regulating insulin production and secretion. *PLoS Genet.* **2014**, *10*, e1004555. [[CrossRef](#)] [[PubMed](#)]

12. Musselman, L.P.; Fink, J.L.; Narzinski, K.; Ramachandran, P.V.; Hathiramani, S.S.; Cagan, R.L.; Baranski, T.J. A high-sugar diet produces obesity and insulin resistance in wild-type *Drosophila*. *Dis. Models Mech.* **2011**, *4*, 842–849. [[CrossRef](#)] [[PubMed](#)]
13. Alfa, R.W.; Park, S.; Skelly, K.R.; Poffenberger, G.; Jain, N.; Gu, X.; Kockel, L.; Wang, J.; Liu, Y.; Powers, A.C.; et al. Suppression of insulin production and secretion by a incretin hormone. *Cell Metab.* **2015**, *21*, 323–334. [[CrossRef](#)] [[PubMed](#)]
14. Capiotti, K.M.; Antonioli, R., Jr.; Kist, L.W.; Bogo, M.R.; Bonan, C.D.; Da Silva, R.S. Persistent impaired glucose metabolism in a zebrafish hyperglycemia model. *Comp. Biochem. Physiol. B Biochem. Mol. Biol.* **2014**, *171*, 58–65. [[CrossRef](#)] [[PubMed](#)]
15. Gleeson, M.; Connaughton, V.; Arneson, L.S. Induction of hyperglycaemia in zebrafish (*Danio rerio*) leads to morphological changes in the retina. *Acta Diabetol.* **2007**, *44*, 157–163. [[CrossRef](#)] [[PubMed](#)]
16. Maddison, L.A.; Joest, K.E.; Kammeyer, R.M.; Chen, W. Skeletal muscle insulin resistance in zebrafish induces alterations in beta-cell number and glucose tolerance in an age- and diet-dependent manner. *Am. J. Physiol. Endocrinol. Metab.* **2015**, *308*, E662–E669. [[CrossRef](#)] [[PubMed](#)]
17. Yin, L.; Maddison, L.A.; Li, M.; Kara, N.; LaFave, M.C.; Varshney, G.K.; Burgess, S.M.; Patton, J.G.; Chen, W. Multiplex Conditional Mutagenesis Using Transgenic Expression of Cas9 and sgRNAs. *Genetics* **2015**, *200*, 431–441. [[CrossRef](#)] [[PubMed](#)]
18. Fajans, S.S.; Bell, G.I.; Polonsky, K.S. Molecular mechanisms and clinical pathophysiology of maturity-onset diabetes of the young. *N. Engl. J. Med.* **2001**, *345*, 971–980. [[CrossRef](#)] [[PubMed](#)]
19. Sun, Z.; Hopkins, N. *hnf1b*, the MODY5 and familial GCKD-associated gene, regulates regional specification of the zebrafish gut, pronephros, and hindbrain. *Genes Dev.* **2001**, *15*, 3217–3229. [[CrossRef](#)] [[PubMed](#)]
20. Lancman, J.J.; Zvenigorodsky, N.; Gates, K.P.; Zhang, D.; Solomon, K.; Humphrey, R.K.; Kuo, T.; Setiawan, L.; Verkade, H.; Chi, Y.I.; et al. Specification of hepatopancreas progenitors in zebrafish by *hnf1ba* and *wnt2bb*. *Development* **2013**, *140*, 2669–2679. [[CrossRef](#)] [[PubMed](#)]
21. Curado, S.; Anderson, R.M.; Jungblut, B.; Mumm, J.; Schroeter, E.; Stainier, D.Y. Conditional targeted cell ablation in zebrafish: a new tool for regeneration studies. *Dev Dyn.* **2007**, *236*, 1025–1035. [[CrossRef](#)] [[PubMed](#)]
22. Ionut, V.; Liu, H.; Mooradian, V.; Castro, A.V.; Kabir, M.; Stefanovski, D.; Zheng, D.; Kirkman, E.L.; Bergman, R.N. Novel canine models of obese prediabetes and mild type 2 diabetes. *Am. J. Physiol. Endocrinol. Metab.* **2010**, *298*, E38–E48. [[CrossRef](#)] [[PubMed](#)]
23. Grussner, R.; Nakhleh, R.; Grussner, A.; Tomadze, G.; Diem, P.; Sutherland, D. Streptozotocin-induced diabetes mellitus in pigs. *Horm. Metab. Res.* **1993**, *25*, 199–203. [[PubMed](#)]
24. Pagliassotti, M.J.; Moore, M.C.; Neal, D.W.; Cherrington, A.D. Insulin is required for the liver to respond to intraportal glucose delivery in the conscious dog. *Diabetes* **1992**, *41*, 1247–1256. [[CrossRef](#)] [[PubMed](#)]
25. Ionut, V.; Woolcott, O.O.; Mkrtchyan, H.J.; Stefanovski, D.; Kabir, M.; Iyer, M.S.; Liu, H.; Castro, A.V.; Wu, Q.; Broussard, J.L.; et al. Exenatide Treatment Alone Improves beta-Cell Function in a Canine Model of Pre-Diabetes. *PLoS ONE* **2016**, *11*, e0158703. [[CrossRef](#)] [[PubMed](#)]
26. Koopmans, S.J.; Schuurman, T. Considerations on pig models for appetite, metabolic syndrome and obese type 2 diabetes: From food intake to metabolic disease. *Eur. J. Pharmacol.* **2015**, *759*, 231–239. [[CrossRef](#)] [[PubMed](#)]
27. Renner, S.; Fehlings, C.; Herbach, N.; Hofmann, A.; von Waldthausen, D.C.; Kessler, B.; Ulrichs, K.; Chodnevskaja, I.; Moskalenko, V.; Amselgruber, W.; et al. Glucose intolerance and reduced proliferation of pancreatic beta-cells in transgenic pigs with impaired glucose-dependent insulinotropic polypeptide function. *Diabetes* **2010**, *59*, 1228–1238. [[CrossRef](#)] [[PubMed](#)]
28. Umeyama, K.; Watanabe, M.; Saito, H.; Kurome, M.; Tohi, S.; Matsunari, H.; Miki, K.; Nagashima, H. Dominant-negative mutant hepatocyte nuclear factor 1alpha induces diabetes in transgenic-cloned pigs. *Transgen. Res* **2009**, *18*, 697–706. [[CrossRef](#)] [[PubMed](#)]
29. Podell, B.K.; Ackart, D.F.; Richardson, M.A.; DiLisio, J.E.; Pulford, B.; Basaraba, R.J. A model of type 2 diabetes in the guinea pig using sequential diet-induced glucose intolerance and streptozotocin treatment. *Dis. Models Mech.* **2017**, *10*, 151–162. [[CrossRef](#)] [[PubMed](#)]
30. Schlosser, M.J.; Kapeghian, J.C.; Verlangieri, A.J. Effects of streptozotocin in the male guinea pig: a potential animal model for studying diabetes. *Life Sci.* **1984**, *35*, 649–655. [[CrossRef](#)]

31. Pound, L.D.; Kievit, P.; Grove, K.L. The nonhuman primate as a model for type 2 diabetes. *Curr. Opin. Endocrinol. Diabetes Obes.* **2014**, *21*, 89–94. [[CrossRef](#)] [[PubMed](#)]
32. Kleinert, M.; Clemmensen, C.; Hofmann, S.M.; Moore, M.C.; Renner, S.; Woods, S.C.; Huypens, P.; Beckers, J.; de Angelis, M.H.; Schurmann, A.; et al. Animal models of obesity and diabetes mellitus. *Nat. Rev. Endocrinol.* **2018**, *14*, 140–162. [[CrossRef](#)] [[PubMed](#)]
33. Kavanagh, K.; Wylie, A.T.; Tucker, K.L.; Hamp, T.J.; Gharaibeh, R.Z.; Fodor, A.A.; Cullen, J.M. Dietary fructose induces endotoxemia and hepatic injury in calorically controlled primates. *Am. J. Clin. Nutr.* **2013**, *98*, 349–357. [[CrossRef](#)] [[PubMed](#)]
34. Higgins, P.B.; Bastarrachea, R.A.; Lopez-Alvarenga, J.C.; Garcia-Forey, M.; Proffitt, J.M.; Voruganti, V.S.; Tejero, M.E.; Mattern, V.; Haack, K.; Shade, R.E.; et al. Eight week exposure to a high sugar high fat diet results in adiposity gain and alterations in metabolic biomarkers in baboons (*Papio hamadryas* sp.). *Cardiovasc. Diabetol.* **2010**, *9*, 71. [[CrossRef](#)] [[PubMed](#)]
35. Hansen, B.C.; Newcomb, J.D.; Chen, R.; Linden, E.H. Longitudinal dynamics of body weight change in the development of type 2 diabetes. *Obesity* **2013**, *21*, 1643–1649. [[CrossRef](#)] [[PubMed](#)]
36. Hansen, B.C. Pathophysiology of obesity-associated type II diabetes (NIDDM): Implications from longitudinal studies of non-human primates. *Nutrition* **1989**, *5*, 48–50. [[PubMed](#)]
37. de Koning, E.J.; Bodkin, N.L.; Hansen, B.C.; Clark, A. Diabetes mellitus in *Macaca mulatta* monkeys is characterised by islet amyloidosis and reduction in beta-cell population. *Diabetologia* **1993**, *36*, 378–384. [[CrossRef](#)] [[PubMed](#)]
38. Trayhurn, P.; Thurlby, P.L.; James, W.P. Thermogenic defect in pre-obese ob/ob mice. *Nature* **1977**, *266*, 60–62. [[CrossRef](#)] [[PubMed](#)]
39. Himms-Hagen, J.; Desautels, M. A mitochondrial defect in brown adipose tissue of the obese (ob/ob) mouse: Reduced binding of purine nucleotides and a failure to respond to cold by an increase in binding. *Biochem. Biophys. Res. Commun.* **1978**, *83*, 628–634. [[CrossRef](#)]
40. Thurlby, P.L.; Trayhurn, P. Regional blood flow in genetically obese (ob/ob) mice. The importance of brown adipose tissue to the reduced energy expenditure on non-shivering thermogenesis. *Pflugers Arch.* **1980**, *385*, 193–201. [[CrossRef](#)] [[PubMed](#)]
41. D'Souza, A.M.; Johnson, J.D.; Clee, S.M.; Kieffer, T.J. Suppressing hyperinsulinemia prevents obesity but causes rapid onset of diabetes in leptin-deficient Lep(ob/ob) mice. *Mol. Metab.* **2016**, *5*, 1103–1112. [[CrossRef](#)] [[PubMed](#)]
42. Leifheit-Nestler, M.; Wagner, N.M.; Gogiraju, R.; Didie, M.; Konstantinides, S.; Hasenfuss, G.; Schafer, K. Importance of leptin signaling and signal transducer and activator of transcription-3 activation in mediating the cardiac hypertrophy associated with obesity. *J. Transl. Med.* **2013**, *11*, 170. [[CrossRef](#)] [[PubMed](#)]
43. Ingalls, A.M.; Dickie, M.M.; Snell, G.D. Obese, a new mutation in the house mouse. *J. Hered.* **1950**, *41*, 317–318. [[CrossRef](#)] [[PubMed](#)]
44. Zhang, Y.; Proenca, R.; Maffei, M.; Barone, M.; Leopold, L.; Friedman, J.M. Positional cloning of the mouse obese gene and its human homologue. *Nature* **1994**, *372*, 425–432. [[CrossRef](#)] [[PubMed](#)]
45. Memon, R.A.; Grunfeld, C.; Moser, A.H.; Feingold, K.R. Fatty acid synthesis in obese insulin resistant diabetic mice. *Horm. Metab. Res.* **1994**, *26*, 85–87. [[CrossRef](#)] [[PubMed](#)]
46. Coleman, D.L.; Hummel, K.P. The influence of genetic background on the expression of the obese (Ob) gene in the mouse. *Diabetologia* **1973**, *9*, 287–293. [[CrossRef](#)] [[PubMed](#)]
47. Qiu, J.; Ogus, S.; Mounzih, K.; Ewart-Toland, A.; Chehab, F.F. Leptin-deficient mice backcrossed to the BALB/cJ genetic background have reduced adiposity, enhanced fertility, normal body temperature, and severe diabetes. *Endocrinology* **2001**, *142*, 3421–3425. [[CrossRef](#)] [[PubMed](#)]
48. Hummel, K.P.; Dickie, M.M.; Coleman, D.L. Diabetes, a new mutation in the mouse. *Science* **1966**, *153*, 1127–1128. [[CrossRef](#)] [[PubMed](#)]
49. Srinivasan, K.; Ramarao, P. Animal models in type 2 diabetes research: An overview. *Indian J. Med. Res.* **2007**, *125*, 451–472. [[PubMed](#)]
50. Phillips, M.S.; Liu, Q.; Hammond, H.A.; Dugan, V.; Hey, P.J.; Caskey, C.J.; Hess, J.F. Leptin receptor missense mutation in the fatty Zucker rat. *Nat. Genet.* **1996**, *13*, 18–19. [[CrossRef](#)] [[PubMed](#)]
51. Pick, A.; Clark, J.; Kubstrup, C.; Levisetti, M.; Pugh, W.; Bonner-Weir, S.; Polonsky, K.S. Role of apoptosis in failure of beta-cell mass compensation for insulin resistance and beta-cell defects in the male Zucker diabetic fatty rat. *Diabetes* **1998**, *47*, 358–364. [[CrossRef](#)] [[PubMed](#)]



52. Shibata, T.; Takeuchi, S.; Yokota, S.; Kakimoto, K.; Yonemori, F.; Wakitani, K. Effects of peroxisome proliferator-activated receptor- $\alpha$  and - $\gamma$  agonist, JTT-501, on diabetic complications in Zucker diabetic fatty rats. *Br. J. Pharmacol.* **2000**, *130*, 495–504. [[CrossRef](#)] [[PubMed](#)]
53. Nilsson, C.; Raun, K.; Yan, F.F.; Larsen, M.O.; Tang-Christensen, M. Laboratory animals as surrogate models of human obesity. *Acta Pharmacol. Sin.* **2012**, *33*, 173–181. [[CrossRef](#)] [[PubMed](#)]
54. Surwit, R.S.; Kuhn, C.M.; Cochrane, C.; McCubbin, J.A.; Feinglos, M.N. Diet-induced type II diabetes in C57BL/6J mice. *Diabetes* **1988**, *37*, 1163–1167. [[CrossRef](#)] [[PubMed](#)]
55. Leiter, E.H. Mice with targeted gene disruptions or gene insertions for diabetes research: Problems, pitfalls, and potential solutions. *Diabetologia* **2002**, *45*, 296–308. [[CrossRef](#)] [[PubMed](#)]
56. Mekada, K.; Abe, K.; Murakami, A.; Nakamura, S.; Nakata, H.; Moriwaki, K.; Obata, Y.; Yoshiki, A. Genetic differences among C57BL/6 substrains. *Exp. Anim.* **2009**, *58*, 141–149. [[CrossRef](#)] [[PubMed](#)]
57. Kahle, M.; Horsch, M.; Fridrich, B.; Seelig, A.; Schultheiss, J.; Leonhardt, J.; Irmeler, M.; Beckers, J.; Rathkolb, B.; Wolf, E.; et al. Phenotypic comparison of common mouse strains developing high-fat diet-induced hepatosteatosis. *Mol. Metab.* **2013**, *2*, 435–446. [[CrossRef](#)] [[PubMed](#)]
58. Jurgens, H.S.; Neschen, S.; Ortmann, S.; Scherneck, S.; Schmolz, K.; Schuler, G.; Schmidt, S.; Bluher, M.; Klaus, S.; Perez-Tilve, D.; et al. Development of diabetes in obese, insulin-resistant mice: Essential role of dietary carbohydrate in beta cell destruction. *Diabetologia* **2007**, *50*, 1481–1489. [[CrossRef](#)] [[PubMed](#)]
59. Kluth, O.; Mirhashemi, F.; Scherneck, S.; Kaiser, D.; Kluge, R.; Neschen, S.; Joost, H.G.; Schurmann, A. Dissociation of lipotoxicity and glucotoxicity in a mouse model of obesity associated diabetes: Role of forkhead box O1 (FOXO1) in glucose-induced beta cell failure. *Diabetologia* **2011**, *54*, 605–616. [[CrossRef](#)] [[PubMed](#)]
60. Lange, C.; Jeruschke, K.; Herberg, L.; Leiter, E.H.; Junger, E. The diabetes-prone NZO/Hl strain. Proliferation capacity of beta cells in hyperinsulinemia and hyperglycemia. *Arch. Physiol. Biochem.* **2006**, *112*, 49–58. [[CrossRef](#)] [[PubMed](#)]
61. Leiter, E.H.; Strobel, M.; O'Neill, A.; Schultz, D.; Schile, A.; Reifsnyder, P.C. Comparison of Two New Mouse Models of Polygenic Type 2 Diabetes at the Jackson Laboratory, NONcNZO10Lt/J and TALLYHO/JngJ. *J. Diabetes Res.* **2013**, *2013*, 165327. [[CrossRef](#)] [[PubMed](#)]
62. Kim, J.H.; Saxton, A.M. The TALLYHO mouse as a model of human type 2 diabetes. *Methods Mol. Biol.* **2012**, *933*, 75–87. [[CrossRef](#)] [[PubMed](#)]
63. Wang, Y.; Nishina, P.M.; Naggert, J.K. Degradation of IRS1 leads to impaired glucose uptake in adipose tissue of the type 2 diabetes mouse model TALLYHO/Jng. *J. Endocrinol.* **2009**, *203*, 65–74. [[CrossRef](#)] [[PubMed](#)]
64. Nakamura, N. Reduced aldehyde dehydrogenase activity and arginine vasopressin receptor 2 expression in the kidneys of male TALLYHO/JngJ mice of prediabetic age. *Endocrine* **2011**, *40*, 379–385. [[CrossRef](#)] [[PubMed](#)]
65. Clee, S.M.; Attie, A.D. The genetic landscape of type 2 diabetes in mice. *Endocr. Rev.* **2007**, *28*, 48–83. [[CrossRef](#)] [[PubMed](#)]
66. Nakamura, M.; Yamada, K. Studies on a diabetic (KK) strain of the mouse. *Diabetologia* **1967**, *3*, 212–221. [[CrossRef](#)] [[PubMed](#)]
67. Ikeda, H. KK mouse. *Diabetes Res. Clin. Pract.* **1994**, *24*, S313–S316. [[CrossRef](#)]
68. Nishimura, M. KK and KK-Ay strains of mice. *Nihon Rinsho* **1998**, *56*, 708–713. [[PubMed](#)]
69. Bell, G.I.; Polonsky, K.S. Diabetes mellitus and genetically programmed defects in beta-cell function. *Nature* **2001**, *414*, 788–791. [[CrossRef](#)] [[PubMed](#)]
70. Skovso, S. Modeling type 2 diabetes in rats using high fat diet and streptozotocin. *J. Diabetes Investig.* **2014**, *5*, 349–358. [[CrossRef](#)] [[PubMed](#)]
71. Reed, M.J.; Meszaros, K.; Entes, L.J.; Claypool, M.D.; Pinkett, J.G.; Gadbois, T.M.; Reaven, G.M. A new rat model of type 2 diabetes: The fat-fed, streptozotocin-treated rat. *Metabolism* **2000**, *49*, 1390–1394. [[CrossRef](#)] [[PubMed](#)]
72. Srinivasan, K.; Viswanad, B.; Asrat, L.; Kaul, C.L.; Ramarao, P. Combination of high-fat diet-fed and low-dose streptozotocin-treated rat: A model for type 2 diabetes and pharmacological screening. *Pharmacol. Res.* **2005**, *52*, 313–320. [[CrossRef](#)] [[PubMed](#)]
73. Manach, C.; Scalbert, A.; Morand, C.; Remesy, C.; Jimenez, L. Polyphenols: Food sources and bioavailability. *Am. J. Clin. Nutr.* **2004**, *79*, 727–747. [[CrossRef](#)] [[PubMed](#)]

74. Wang, Y.; Chen, S.; Yu, O. Metabolic engineering of flavonoids in plants and microorganisms. *Appl. Microbiol. Biotechnol.* **2011**, *91*, 949–956. [[CrossRef](#)] [[PubMed](#)]
75. Kozłowska, A.; Szostak-Wegierek, D. Flavonoids—Food sources and health benefits. *Rocz. Panstw. Zakł. Hig.* **2014**, *65*, 79–85. [[PubMed](#)]
76. Yao, Z.; Gu, Y.; Zhang, Q.; Liu, L.; Meng, G.; Wu, H.; Xia, Y.; Bao, X.; Shi, H.; Sun, S.; et al. Estimated daily quercetin intake and association with the prevalence of type 2 diabetes mellitus in Chinese adults. *Eur. J. Nutr.* **2018**. [[CrossRef](#)] [[PubMed](#)]
77. Crozier, A.; Jaganath, I.B.; Clifford, M.N. Dietary phenolics: Chemistry, bioavailability and effects on health. *Nat. Prod. Rep.* **2009**, *26*, 1001–1043. [[CrossRef](#)] [[PubMed](#)]
78. Williamson, G. The role of polyphenols in modern nutrition. *Nutr. Bull.* **2017**, *42*, 226–235. [[CrossRef](#)] [[PubMed](#)]
79. Lee, K.M.; Hwang, M.K.; Lee, D.E.; Lee, K.W.; Lee, H.J. Protective effect of quercetin against arsenite-induced COX-2 expression by targeting PI3K in rat liver epithelial cells. *J. Agric. Food Chem.* **2010**, *58*, 5815–5820. [[CrossRef](#)] [[PubMed](#)]
80. Ramyaa, P.; Krishnaswamy, R.; Padma, V.V. Quercetin modulates OTA-induced oxidative stress and redox signalling in HepG2 cells—Up regulation of Nrf2 expression and down regulation of NF-kappaB and COX-2. *Biochim. Biophys. Acta* **2014**, *1840*, 681–692. [[CrossRef](#)] [[PubMed](#)]
81. Iskender, H.; Dokumacioglu, E.; Sen, T.M.; Ince, I.; Kanbay, Y.; Saral, S. The effect of hesperidin and quercetin on oxidative stress, NF-kappaB and SIRT1 levels in a STZ-induced experimental diabetes model. *Biomed. Pharmacother.* **2017**, *90*, 500–508. [[CrossRef](#)] [[PubMed](#)]
82. Roslan, J.; Giribabu, N.; Karim, K.; Salleh, N. Quercetin ameliorates oxidative stress, inflammation and apoptosis in the heart of streptozotocin-nicotinamide-induced adult male diabetic rats. *Biomed. Pharmacother.* **2017**, *86*, 570–582. [[CrossRef](#)] [[PubMed](#)]
83. Zhuang, M.; Qiu, H.; Li, P.; Hu, L.; Wang, Y.; Rao, L. Islet protection and amelioration of type 2 diabetes mellitus by treatment with quercetin from the flowers of *Edgeworthia gardneri*. *Drug Des. Dev. Ther.* **2018**, *12*, 955–966. [[CrossRef](#)] [[PubMed](#)]
84. Fang, X.K.; Gao, J.; Zhu, D.N. Kaempferol and quercetin isolated from *Euonymus alatus* improve glucose uptake of 3T3-L1 cells without adipogenesis activity. *Life Sci.* **2008**, *82*, 615–622. [[CrossRef](#)] [[PubMed](#)]
85. Youl, E.; Bardy, G.; Magous, R.; Cros, G.; Sejalón, F.; Virsolvy, A.; Richard, S.; Quignard, J.F.; Gross, R.; Petit, P.; et al. Quercetin potentiates insulin secretion and protects INS-1 pancreatic beta-cells against oxidative damage via the ERK1/2 pathway. *Br. J. Pharmacol.* **2010**, *161*, 799–814. [[CrossRef](#)] [[PubMed](#)]
86. Jeong, S.M.; Kang, M.J.; Choi, H.N.; Kim, J.H.; Kim, J.I. Quercetin ameliorates hyperglycemia and dyslipidemia and improves antioxidant status in type 2 diabetic db/db mice. *Nutr. Res. Pract.* **2012**, *6*, 201–207. [[CrossRef](#)] [[PubMed](#)]
87. Lai, P.B.; Zhang, L.; Yang, L.Y. Quercetin ameliorates diabetic nephropathy by reducing the expressions of transforming growth factor-beta1 and connective tissue growth factor in streptozotocin-induced diabetic rats. *Ren. Fail.* **2012**, *34*, 83–87. [[CrossRef](#)] [[PubMed](#)]
88. Gaballah, H.H.; Zakaria, S.S.; Mwafy, S.E.; Tahooun, N.M.; Ebeid, A.M. Mechanistic insights into the effects of quercetin and/or GLP-1 analogue liraglutide on high-fat diet/streptozotocin-induced type 2 diabetes in rats. *Biomed. Pharmacother.* **2017**, *92*, 331–339. [[CrossRef](#)] [[PubMed](#)]
89. Ryden, L.; Grant, P.J.; Anker, S.D.; Berne, C.; Cosentino, F.; Danchin, N.; Deaton, C.; Escaned, J.; Hammes, H.-P.; Huikuri, H.; et al. ESC guidelines on diabetes, pre-diabetes, and cardiovascular diseases developed in collaboration with the EASD—Summary. *Diab. Vasc. Dis. Res.* **2014**, *11*, 133–173. [[CrossRef](#)] [[PubMed](#)]
90. Zamora-Ros, R.; Forouhi, N.G.; Sharp, S.J.; Gonzalez, C.A.; Buijsse, B.; Guevara, M.; van der Schouw, Y.T.; Amiano, P.; Boeing, H.; Bredsdorff, L.; et al. Dietary intakes of individual flavanols and flavonols are inversely associated with incident type 2 diabetes in European populations. *J. Nutr.* **2014**, *144*, 335–343. [[CrossRef](#)] [[PubMed](#)]
91. Huang, W.Y.; Zhang, H.C.; Liu, W.X.; Li, C.Y. Survey of antioxidant capacity and phenolic composition of blueberry, blackberry, and strawberry in Nanjing. *J. Zhejiang Univ. Sci. B* **2012**, *13*, 94–102. [[CrossRef](#)] [[PubMed](#)]

92. Hsu, C.Y.; Shih, H.Y.; Chia, Y.C.; Lee, C.H.; Ashida, H.; Lai, Y.K.; Weng, C.F. Rutin potentiates insulin receptor kinase to enhance insulin-dependent glucose transporter 4 translocation. *Mol. Nutr. Food Res.* **2014**, *58*, 1168–1176. [[CrossRef](#)] [[PubMed](#)]
93. Liang, W.; Zhang, D.; Kang, J.; Meng, X.; Yang, J.; Yang, L.; Xue, N.; Gao, Q.; Han, S.; Gou, X. Protective effects of rutin on liver injury in type 2 diabetic db/db mice. *Biomed. Pharmacother.* **2018**, *107*, 721–728. [[CrossRef](#)] [[PubMed](#)]
94. Kappel, V.D.; Cazarolli, L.H.; Pereira, D.F.; Postal, B.G.; Zamoner, A.; Reginatto, F.H.; Silva, F.R. Involvement of GLUT-4 in the stimulatory effect of rutin on glucose uptake in rat soleus muscle. *J. Pharm. Pharmacol.* **2013**, *65*, 1179–1186. [[CrossRef](#)] [[PubMed](#)]
95. Stanley Mainzen Prince, P.; Kamalakkannan, N. Rutin improves glucose homeostasis in streptozotocin diabetic tissues by altering glycolytic and gluconeogenic enzymes. *J. Biochem. Mol. Toxicol.* **2006**, *20*, 96–102. [[CrossRef](#)] [[PubMed](#)]
96. Niture, N.T.; Ansari, A.A.; Naik, S.R. Anti-hyperglycemic activity of rutin in streptozotocin-induced diabetic rats: An effect mediated through cytokines, antioxidants and lipid biomarkers. *Indian J. Exp. Biol.* **2014**, *52*, 720–727. [[PubMed](#)]
97. Kamalakkannan, N.; Prince, P.S. Antihyperglycaemic and antioxidant effect of rutin, a polyphenolic flavonoid, in streptozotocin-induced diabetic wistar rats. *Basic Clin. Pharmacol. Toxicol.* **2006**, *98*, 97–103. [[CrossRef](#)] [[PubMed](#)]
98. Kim, O.K.; Jun, W.; Lee, J. Effect of Cudrania tricuspidata and Kaempferol in Endoplasmic Reticulum Stress-Induced Inflammation and Hepatic Insulin Resistance in HepG2 Cells. *Nutrients* **2016**, *8*, 60. [[CrossRef](#)] [[PubMed](#)]
99. Zhang, Y.; Liu, D. Flavonol kaempferol improves chronic hyperglycemia-impaired pancreatic beta-cell viability and insulin secretory function. *Eur. J. Pharmacol.* **2011**, *670*, 325–332. [[CrossRef](#)] [[PubMed](#)]
100. Chang, C.J.; Tzeng, T.F.; Liou, S.S.; Chang, Y.S.; Liu, I.M. Kaempferol regulates the lipid-profile in high-fat diet-fed rats through an increase in hepatic PPAR $\alpha$  levels. *Planta Med.* **2011**, *77*, 1876–1882. [[CrossRef](#)] [[PubMed](#)]
101. Al-Numair, K.S.; Chandramohan, G.; Veeramani, C.; Alsaif, M.A. Ameliorative effect of kaempferol, a flavonoid, on oxidative stress in streptozotocin-induced diabetic rats. *Redox Rep.* **2015**, *20*, 198–209. [[CrossRef](#)] [[PubMed](#)]
102. Luo, C.; Yang, H.; Tang, C.; Yao, G.; Kong, L.; He, H.; Zhou, Y. Kaempferol alleviates insulin resistance via hepatic IKK/NF-kappaB signal in type 2 diabetic rats. *Int. Immunopharmacol.* **2015**, *28*, 744–750. [[CrossRef](#)] [[PubMed](#)]
103. Al-Numair, K.S.; Veeramani, C.; Alsaif, M.A.; Chandramohan, G. Influence of kaempferol, a flavonoid compound, on membrane-bound ATPases in streptozotocin-induced diabetic rats. *Pharm. Biol.* **2015**, *53*, 1372–1378. [[CrossRef](#)] [[PubMed](#)]
104. Yu, Y.; Zheng, G. Troxerutin protects against diabetic cardiomyopathy through NFkappaB/AKT/IRS1 in a rat model of type 2 diabetes. *Mol. Med. Rep.* **2017**, *15*, 3473–3478. [[CrossRef](#)] [[PubMed](#)]
105. Mu, H.; Bai, Y.H.; Wang, S.T.; Zhu, Z.M.; Zhang, Y.W. Research on antioxidant effects and estrogenic effect of formononetin from Trifolium pratense (red clover). *Phytomedicine* **2009**, *16*, 314–319. [[CrossRef](#)] [[PubMed](#)]
106. Adlercreutz, H. Phytoestrogens: Epidemiology and a possible role in cancer protection. *Environ. Health Perspect.* **1995**, *103*, 103–112. [[CrossRef](#)] [[PubMed](#)]
107. Zaheer, K.; Humayoun Akhtar, M. An updated review of dietary isoflavones: Nutrition, processing, bioavailability and impacts on human health. *Crit. Rev. Food Sci. Nutr.* **2017**, *57*, 1280–1293. [[CrossRef](#)] [[PubMed](#)]
108. Jonas, J.C.; Plant, T.D.; Gilon, P.; Detimary, P.; Nenquin, M.; Henquin, J.C. Multiple effects and stimulation of insulin secretion by the tyrosine kinase inhibitor genistein in normal mouse islets. *Br. J. Pharmacol.* **1995**, *114*, 872–880. [[CrossRef](#)] [[PubMed](#)]
109. Liu, J.; Zheng, X.; Yin, F.; Hu, Y.; Guo, L.; Deng, X.; Chen, G.; Jiajia, J.; Zhang, H. Neurotrophic property of geniposide for inducing the neuronal differentiation of PC12 cells. *Int. J. Dev. Neurosci.* **2006**, *24*, 419–424. [[CrossRef](#)] [[PubMed](#)]

110. Smith, R.M.; Tiesinga, J.J.; Shah, N.; Smith, J.A.; Jarett, L. Genistein inhibits insulin-stimulated glucose transport and decreases immunocytochemical labeling of GLUT4 carboxyl-terminus without affecting translocation of GLUT4 in isolated rat adipocytes: Additional evidence of GLUT4 activation by insulin. *Arch. Biochem. Biophys.* **1993**, *300*, 238–246. [[CrossRef](#)] [[PubMed](#)]
111. Bazuine, M.; van den Broek, P.J.; Maassen, J.A. Genistein directly inhibits GLUT4-mediated glucose uptake in 3T3-L1 adipocytes. *Biochem. Biophys. Res. Commun.* **2005**, *326*, 511–514. [[CrossRef](#)] [[PubMed](#)]
112. Fu, Z.; Gilbert, E.R.; Pfeiffer, L.; Zhang, Y.; Fu, Y.; Liu, D. Genistein ameliorates hyperglycemia in a mouse model of nongenetic type 2 diabetes. *Appl. Physiol. Nutr. Metab.* **2012**, *37*, 480–488. [[CrossRef](#)] [[PubMed](#)]
113. Weigt, C.; Hertrampf, T.; Flenker, U.; Hulsemann, F.; Kurnaz, P.; Fritzemeier, K.H.; Diel, P. Effects of estradiol, estrogen receptor subtype-selective agonists and genistein on glucose metabolism in leptin resistant female Zucker diabetic fatty (ZDF) rats. *J. Steroid Biochem. Mol. Biol.* **2015**, *154*, 12–22. [[CrossRef](#)] [[PubMed](#)]
114. Yousefi, H.; Alihemmati, A.; Karimi, P.; Alipour, M.R.; Habibi, P.; Ahmadiasl, N. Effect of genistein on expression of pancreatic SIRT1, inflammatory cytokines and histological changes in ovariectomized diabetic rat. *Iran J. Basic Med. Sci.* **2017**, *20*, 423–429. [[CrossRef](#)] [[PubMed](#)]
115. Lee, J.H.; Song, M.Y.; Song, E.K.; Kim, E.K.; Moon, W.S.; Han, M.K.; Park, J.W.; Kwon, K.B.; Park, B.H. Overexpression of SIRT1 protects pancreatic beta-cells against cytokine toxicity by suppressing the nuclear factor-kappaB signaling pathway. *Diabetes* **2009**, *58*, 344–351. [[CrossRef](#)] [[PubMed](#)]
116. Rockwood, S.; Broderick, T.L.; Al-Nakkash, L. Feeding Obese Diabetic Mice a Genistein Diet Induces Thermogenic and Metabolic Change. *J. Med. Food* **2018**, *21*, 332–339. [[CrossRef](#)] [[PubMed](#)]
117. Ahmed, T.; Javed, S.; Tariq, A.; Budzynska, B.; D’Onofrio, G.; Daglia, M.; Nabavi, S.F.; Nabavi, S.M. Daidzein and its Effects on Brain. *Curr. Med. Chem.* **2017**, *24*, 365–375. [[CrossRef](#)] [[PubMed](#)]
118. Ae Park, S.; Choi, M.S.; Cho, S.Y.; Seo, J.S.; Jung, U.J.; Kim, M.J.; Sung, M.K.; Park, Y.B.; Lee, M.K. Genistein and daidzein modulate hepatic glucose and lipid regulating enzyme activities in C57BL/KsJ-db/db mice. *Life Sci.* **2006**, *79*, 1207–1213. [[CrossRef](#)] [[PubMed](#)]
119. Cederroth, C.R.; Vinciguerra, M.; Gjinovci, A.; Kuhne, F.; Klein, M.; Cederroth, M.; Caille, D.; Suter, M.; Neumann, D.; James, R.W.; et al. Dietary phytoestrogens activate AMP-activated protein kinase with improvement in lipid and glucose metabolism. *Diabetes* **2008**, *57*, 1176–1185. [[CrossRef](#)] [[PubMed](#)]
120. As, D.; Sarkar, S.; Bordoloi, J.; Wann, S.B.; Kalita, J.; Manna, P. Daidzein, its effects on impaired glucose and lipid metabolism and vascular inflammation associated with type 2 diabetes. *Biofactors* **2018**, *44*, 407–417. [[CrossRef](#)]
121. Cheong, S.H.; Furuhashi, K.; Ito, K.; Nagaoka, M.; Yonezawa, T.; Miura, Y.; Yagasaki, K. Antihyperglycemic effect of equol, a daidzein derivative, in cultured L6 myocytes and ob/ob mice. *Mol. Nutr. Food Res.* **2014**, *58*, 267–277. [[CrossRef](#)] [[PubMed](#)]
122. Cheong, S.H.; Furuhashi, K.; Ito, K.; Nagaoka, M.; Yonezawa, T.; Miura, Y.; Yagasaki, K. Daidzein promotes glucose uptake through glucose transporter 4 translocation to plasma membrane in L6 myocytes and improves glucose homeostasis in Type 2 diabetic model mice. *J. Nutr. Biochem.* **2014**, *25*, 136–143. [[CrossRef](#)] [[PubMed](#)]
123. Jung, U.J.; Lee, M.K.; Jeong, K.S.; Choi, M.S. The hypoglycemic effects of hesperidin and naringin are partly mediated by hepatic glucose-regulating enzymes in C57BL/KsJ-db/db mice. *J. Nutr.* **2004**, *134*, 2499–2503. [[CrossRef](#)] [[PubMed](#)]
124. Rani, N.; Bharti, S.; Krishnamurthy, B.; Bhatia, J.; Sharma, C.; Kamal, M.A.; Ojha, S.; Arya, D.S. Pharmacological Properties and Therapeutic Potential of Naringenin: A Citrus Flavonoid of Pharmaceutical Promise. *Curr. Pharm. Des.* **2016**, *22*, 4341–4359. [[CrossRef](#)] [[PubMed](#)]
125. Priscilla, D.H.; Roy, D.; Suresh, A.; Kumar, V.; Thirumurugan, K. Naringenin inhibits alpha-glucosidase activity: A promising strategy for the regulation of postprandial hyperglycemia in high fat diet fed streptozotocin induced diabetic rats. *Chem. Biol. Interact.* **2014**, *210*, 77–85. [[CrossRef](#)] [[PubMed](#)]
126. Jung, U.J.; Lee, M.K.; Park, Y.B.; Kang, M.A.; Choi, M.S. Effect of citrus flavonoids on lipid metabolism and glucose-regulating enzyme mRNA levels in type-2 diabetic mice. *Int. J. Biochem. Cell Biol.* **2006**, *38*, 1134–1145. [[CrossRef](#)] [[PubMed](#)]
127. Rotimi, S.O.; Adelani, I.B.; Bankole, G.E.; Rotimi, O.A. Naringin enhances reverse cholesterol transport in high fat/low streptozocin induced diabetic rats. *Biomed. Pharmacother.* **2018**, *101*, 430–437. [[CrossRef](#)] [[PubMed](#)]



128. Mahmoud, A.M.; Ashour, M.B.; Abdel-Moneim, A.; Ahmed, O.M. Hesperidin and naringin attenuate hyperglycemia-mediated oxidative stress and proinflammatory cytokine production in high fat fed/streptozotocin-induced type 2 diabetic rats. *J. Diabetes Complicat.* **2012**, *26*, 483–490. [[CrossRef](#)] [[PubMed](#)]
129. Jia, S.; Hu, Y.; Zhang, W.; Zhao, X.; Chen, Y.; Sun, C.; Li, X.; Chen, K. Hypoglycemic and hypolipidemic effects of neohesperidin derived from *Citrus aurantium* L. in diabetic KK-A(y) mice. *Food Funct.* **2015**, *6*, 878–886. [[CrossRef](#)] [[PubMed](#)]
130. Mackenzie, T.; Leary, L.; Brooks, W.B. The effect of an extract of green and black tea on glucose control in adults with type 2 diabetes mellitus: Double-blind randomized study. *Metabolism* **2007**, *56*, 1340–1344. [[CrossRef](#)] [[PubMed](#)]
131. Kim, M.J.; Ryu, G.R.; Chung, J.S.; Sim, S.S.; Min, D.S.; Rhie, D.J.; Yoon, S.H.; Hahn, S.J.; Kim, M.S.; Jo, Y.H. Protective effects of epicatechin against the toxic effects of streptozotocin on rat pancreatic islets: In vivo and in vitro. *Pancreas* **2003**, *26*, 292–299. [[CrossRef](#)] [[PubMed](#)]
132. Janle, E.M.; Portocarrero, C.; Zhu, Y.; Zhou, Q. Effect of long-term oral administration of green tea extract on weight gain and glucose tolerance in Zucker diabetic (ZDF) rats. *J. Herb. Pharmacother.* **2005**, *5*, 55–65. [[CrossRef](#)] [[PubMed](#)]
133. Yan, J.; Zhao, Y.; Suo, S.; Liu, Y.; Zhao, B. Green tea catechins ameliorate adipose insulin resistance by improving oxidative stress. *Free Radic. Biol. Med.* **2012**, *52*, 1648–1657. [[CrossRef](#)] [[PubMed](#)]
134. Ren, B.; Qin, W.; Wu, F.; Wang, S.; Pan, C.; Wang, L.; Zeng, B.; Ma, S.; Liang, J. Apigenin and naringenin regulate glucose and lipid metabolism, and ameliorate vascular dysfunction in type 2 diabetic rats. *Eur. J. Pharmacol.* **2016**, *773*, 13–23. [[CrossRef](#)] [[PubMed](#)]
135. Kang, K.A.; Zhang, R.; Piao, M.J.; Chae, S.; Kim, H.S.; Park, J.H.; Jung, K.S.; Hyun, J.W. Baicalein inhibits oxidative stress-induced cellular damage via antioxidant effects. *Toxicol. Ind. Health* **2012**, *28*, 412–421. [[CrossRef](#)] [[PubMed](#)]
136. Fu, Y.; Luo, J.; Jia, Z.; Zhen, W.; Zhou, K.; Gilbert, E.; Liu, D. Baicalein Protects against Type 2 Diabetes via Promoting Islet beta-Cell Function in Obese Diabetic Mice. *Int. J. Endocrinol.* **2014**, *2014*, 846742. [[CrossRef](#)] [[PubMed](#)]
137. Akkarachiyasit, S.; Charoenlertkul, P.; Yibchok-Anun, S.; Adisakwattana, S. Inhibitory activities of cyanidin and its glycosides and synergistic effect with acarbose against intestinal alpha-glucosidase and pancreatic alpha-amylase. *Int. J. Mol. Sci.* **2010**, *11*, 3387–3396. [[CrossRef](#)] [[PubMed](#)]
138. Kurimoto, Y.; Shibayama, Y.; Inoue, S.; Soga, M.; Takikawa, M.; Ito, C.; Nanba, F.; Yoshida, T.; Yamashita, Y.; Ashida, H.; et al. Black soybean seed coat extract ameliorates hyperglycemia and insulin sensitivity via the activation of AMP-activated protein kinase in diabetic mice. *J. Agric. Food Chem.* **2013**, *61*, 5558–5564. [[CrossRef](#)] [[PubMed](#)]
139. Guo, H.; Xia, M.; Zou, T.; Ling, W.; Zhong, R.; Zhang, W. Cyanidin 3-glucoside attenuates obesity-associated insulin resistance and hepatic steatosis in high-fat diet-fed and db/db mice via the transcription factor FoxO1. *J. Nutr. Biochem.* **2012**, *23*, 349–360. [[CrossRef](#)] [[PubMed](#)]



© 2019 by the authors. Licensee MDPI, Basel, Switzerland. This article is an open access article distributed under the terms and conditions of the Creative Commons Attribution (CC BY) license (<http://creativecommons.org/licenses/by/4.0/>).



## Research articles

## Dual targeted magnetic photosensitive liposomes for photothermal/photodynamic tumor therapy

Anilkumar T.S.<sup>a</sup>, Yu-Jen Lu<sup>b</sup>, Huai-An Chen<sup>a</sup>, Hao-Lung Hsu<sup>a</sup>, Gils Jose<sup>a</sup>, Jyh-Ping Chen<sup>a,c,d,e,\*</sup><sup>a</sup> Department of Chemical and Materials Engineering, Chang Gung University, Kwei-San, Taoyuan 33302, Taiwan, ROC<sup>b</sup> Department of Neurosurgery, Chang Gung Memorial Hospital, Linkou, Kwei-San, Taoyuan 33305, Taiwan, ROC<sup>c</sup> Department of Plastic and Reconstructive Surgery and Craniofacial Research Center, Chang Gung Memorial Hospital, Kwei-San, Taoyuan 33305, Taiwan, ROC<sup>d</sup> Research Center for Chinese Herbal Medicine and Research Center for Food and Cosmetic Safety, College of Human Ecology, Chang Gung University of Science and Technology, Kei-San, Taoyuan 33302, Taiwan, ROC<sup>e</sup> Department of Materials Engineering, Ming Chi University of Technology, New Taipei City 24301, Taiwan, ROC

## ARTICLE INFO

## Keywords:

Magnetic liposomes  
Magnetic nanoparticles  
Indocyanine green  
Photothermal therapy

## ABSTRACT

In this work, we prepared a nano-vehicle for dual targeted (magnetic and ligand) and dual mode (photothermal/photodynamic) cancer therapy. For this purpose, magnetic photosensitive liposomes (MPLs) from 1,2-distearoyl-sn-glycero-3-phosphocholine, dimethyldioctadecyl ammonium bromide (DDAB) and cholesterol were prepared using solvent evaporation/hydration technique to encapsulate the photosensitizer indocyanine green (ICG) and citric acid-coated MNPs (CMNPs). Hyaluronic acid-polyethylene glycol (HA-PEG) was coated to the MPLs by self-assembly of HA-PEG on liposome surface through ionic interactions between negatively charged HA and positively charged lipid DDAB to fabricate HA-PEG-MPLs with ~220 nm particle size. The HA-PEG-MPLs aqueous solution showed highly efficient photothermal effects as the solution temperature reaches 45 °C in 3 min after exposure to near infrared (NIR) 808 nm laser at 2 W/cm<sup>2</sup>. The in vitro cell culture experiments after treating human glioblastoma cells (U-87MG) with HA-PEG-MPLs confirmed enhanced cytotoxicity after 4 min exposure to NIR laser. A xenograft tumor model from subcutaneously implanted U87MG cells in nude mice demonstrated accumulation of HA-PEG-MPLs at tumor sites. By combination with successive NIR laser treatment, tumor growth could be prevented and the tumor volume at the end of treatment was 12.7% that of the control. Excellent and consistent anti-tumor efficacy with laser + HA-PEG-MPLs treatment was also demonstrated from the survival rates of animals, in vivo bioluminescence imaging and histology of tumor sections.

## 1. Introduction

As one of the biggest diseases in the world challenging the lives of all age groups, cancer is uncontrolled growth of cells, which may occur in any kind of tissue in the human body. Surgery, chemotherapy and radiation therapy are the main anti-tumor therapeutic approaches. Nonetheless, chemotherapy is associated with the downside effect of non-specific targeting of cancer cells and destroying normal/healthy cells apart from cancer cells during the course of the treatment [1]. To overcome this undesirable effect, targeted delivery of chemotherapeutic drugs with nano-carriers was introduced to transport drugs precisely to the tumor site for killing cancer cells [2,3]. Liposomes have been widely studied as effective nano-carriers for drugs because they are biocompatible and biodegradable and can be loaded with large quantities of drugs [4]. Liposomes surface could be also modified with ligand molecules that would be recognized by receptor molecules on the

surface of cancer cells, such as antibodies, folic acid and hyaluronic acid (HA) to increase the intracellular cellular uptake of liposomes into tumor cells [5]. In addition, liposomes with a “stealth” property could be prepared by modification with polyethylene glycol (PEG) on liposome surface to prevent its rapid clearance by the mononuclear phagocyte system during circulation and increase liposome half-life in vivo [6]. In the past decade, liposomal formulations have been broadly used to enhance the effectiveness of drug delivery via several paths. The favourable outcome of liposomes as drug carriers have been echoed in a number of liposome-based formulations, which are commercially available or currently undergoing clinical trials [7–9].

Photothermal therapy (PTT) and photodynamic therapy (PDT) are alternative therapies to treat cancer. In PDT, a specific photosensitizer (PS) was irradiated with a specific wavelength of light, which leads to energy transfer to oxygen molecules by generating cytotoxic reactive oxygen species (ROS) [10]. The ROS can rapidly cause significant

\* Corresponding author at: 259 Wen-Hwa 1st Road, Kwei-San, Taoyuan 33302, Taiwan, ROC.

E-mail address: [jpchen@mail.cgu.edu.tw](mailto:jpchen@mail.cgu.edu.tw) (J.-P. Chen).<https://doi.org/10.1016/j.jmmm.2018.10.020>

Received 24 June 2018; Received in revised form 2 October 2018; Accepted 4 October 2018

Available online 09 October 2018

0304-8853/ © 2018 Elsevier B.V. All rights reserved.

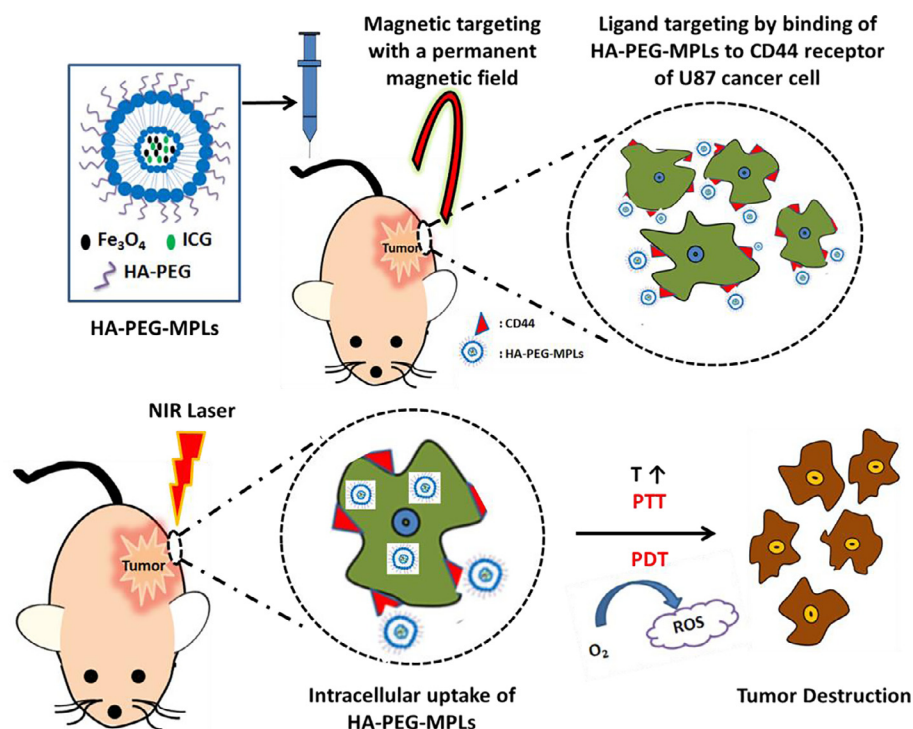


Fig. 1. Schematic illustration of HA-PEG-MPLs for dual targeted photothermal/photodynamic cancer therapy.

toxicity, leading to cell death via apoptosis or necrosis. On the other hand, the PS should be with minimally cytotoxicity in the absence of external photo-activating light. The PDT antitumor effects are driven based on three interrelated mechanisms, including direct cytotoxic effects on tumor cells, damage to the tumor vasculature and induction of a robust inflammatory reaction that can lead to development of systemic immunity [11,12]. Among several PS that acquire excitation energy in the near-infrared (NIR) region, ICG is the only approved clinical imaging and diagnosis agent by the U.S. Food and Drug Administration (FDA). ICG is also been widely applied to assess hepatic function, ophthalmic angiography, and surgical navigation [13,14]. The PTT is based on heat production when a photo-absorbing agent is irradiated with NIR laser light, as this heat can result in burning the cancer cells [14]. During the treatment, NIR laser light penetrates safely through the tissue to reach the tumor site. This penetrating NIR radiation can be transduced into local heat by a PTT agent accumulated in the cancer cells and thus cause effective damage of the targeted tumor regions. Different materials have been reported as a PTT agent, including organic compounds (e.g., ICG and polyaniline) inorganic nanomaterials (e.g., magnetic nanoparticles, metal chalcogenide, and carbon-based materials) [14–16].

Magnetic nanoparticles (MNPs) are effective guiding tool that could be driven to a precise targeted site with an external magnetic field. This advantageous factor of MNPs are widely exploited in many biomedical applications such as in targeted drug delivery systems and disease diagnosis [17]. By incorporating MNPs in liposomes, magnetic liposomes for site-specific accumulation of anticancer drugs in cancer cells by magnetic targeting were also reported [18]. Although the photothermal effect of MNPs after exposing to NIR laser is useful for PTT [19], supplementary of MNPs-based hyperthermia with other forms of cancer therapy such as chemotherapy, radiotherapy and combinatory PTT/PDT are deemed advantageous to enhance the therapeutic outcomes [20,21].

In this work, we developed dual targeted magnetic photosensitive liposomes (MPLs) for dual mode cancer therapy. Magnetic targeting was achieved by incorporating MNPs in liposomes while ligand targeting was accomplished by self-assembly of HA-PEG onto cationic

MPLs to form HA-PEG-MPLs. In the latter approach, HA could bind with the over-expressed CD44 receptor on the cell surface of human primary glioblastoma cell line U87MG for receptor-mediated ligand targeting [22,23] while PEG helps to prolong the blood circulation of HA-liposomes in the body. With encapsulated ICG and MNPs within the aqueous core of liposomes, HA-PEG-MPLs were used as a PTT/PDT dual modal nano-sized therapeutic agent for efficient cancer therapy in vivo (Fig. 1).

## 2. Materials and methods

### 2.1. Materials

Fe (II) chloride tetrahydrate (99%) and Fe (III) chloride hexahydrate (97%) were purchased from Acros. Copper (II) sulfate pentahydrate ( $\text{CuSO}_4 \cdot 5\text{H}_2\text{O}$ ) was purchased from Merck (Darmstadt, Germany). Sodium hyaluronate (HA) was purchased from Shandong Freda Biochem. Co. (China). 1,2-Distearoyl-sn-glycero-3-phosphocholine (DSPC) was purchased from Avanti Polar Lipids, Inc. (USA). Methoxypolyethylene glycol amine (MPEG-NH<sub>2</sub>) (M.W. = 5000), 1-ethyl-3-(3-dimethylaminopropyl)carbodiimide (EDC), potassium thiocyanate (KSCN), 4-morpholineethanesulfonic acid monohydrate (MES monohydrate), dimethyldioctadecyl ammonium bromide (DDAB), cholesterol (CH), ICG and Triton X-100 were purchased from Sigma-Aldrich Co. (USA). All other chemicals were of reagent grade and used without further purification.

### 2.2. Synthesis of citric acid coated iron oxide magnetic nanoparticles (CMNPs)

The CMNPs were prepared by the chemical precipitation method as described before with slight modification [24]. Briefly, MNPs were first prepared by dissolving 0.875 g  $\text{FeCl}_2$  and 2.375 g  $\text{FeCl}_3$  ( $\text{Fe}^{2+}:\text{Fe}^{3+} = 1:2$ ) in 40 mL of double-distilled water (DDI water) in a three-neck flask and continuously stirred at 100 rpm in the presence of nitrogen gas for 15 min at 70 °C–80 °C. After increasing the stirring rate to 1100 rpm, 5 mL  $\text{NH}_4\text{OH}$  (28%) was added to the flask and stirred for

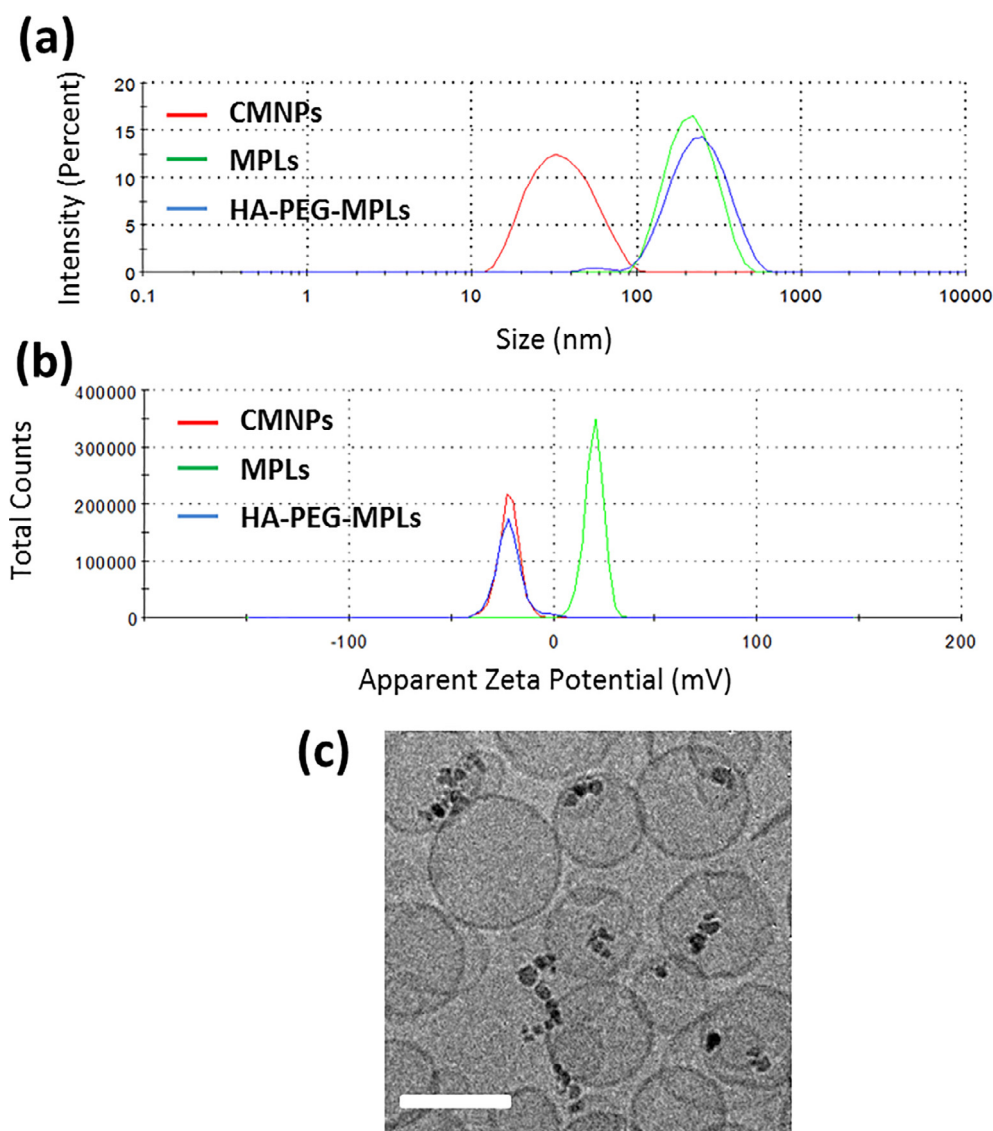


**Fig. 2.** (a) Particle size distribution from dynamic light scattering and (b) apparent zeta potential distribution of CMNPs, MPLs and HA-PEG-MPLs. (c) cryo-TEM image of HA-PEG-MPLs with CMNP agglomerates (black dots) entrapped inside the liposomes (bar = 200 nm).

**Table 1**

Particle size and zeta potential of CMNPs, MPLs and HA-PEG-MPLs. The data are expressed as means  $\pm$  standard deviations ( $n = 6$ ).

Sample	Particle Size (nm)	Polydispersity index	Zeta Potential (mV)
CMNPs	$31.4 \pm 3.3$	$0.22 \pm 0.02$	$-21.7 \pm 3.4$
MPLs	$195.0 \pm 20.6^*$	$0.26 \pm 0.04^*$	$19.4 \pm 4.7^*$
HA-PEG-MPLs	$221.9 \pm 16.9^*$	$0.29 \pm 0.03^*$	$-20.0 \pm 4.2^{*,\#}$

\*  $p < 0.05$  compared with CMNPs.

#  $p < 0.05$  compared with MPLs.

additional 30 min. To coat citric acid on MNPs, the temperature of the solution was increased to 95 °C and citric acid (1 mg/mL) was added drop by drop. The reaction was allowed to proceed further for 90 min. After cooled down to room temperature, the solution was diluted to twice its volume with DDI water and subject to magnetic separation with a permanent magnet for 10 min. The supernatant containing CMNPs was continuous washed with 0.5 L of DDI water in a 30 kDa molecular weight cut-off (MWCO) hollow fiber module (Spectrum Laboratories) to remove excess citric acid and  $\text{NH}_4\text{OH}$ .

### 2.3. Synthesis of HA-PEG

HA-PEG was synthesised according to the method described before [25] with some modification. 1.2 g (1  $\mu\text{mol}$ ) of HA and 5 mg MPEG-NH<sub>2</sub> (1  $\mu\text{mol}$ ) were mixed in 100 mL of 50 mM MES monohydrate buffer (pH 6.5). To this solution, 0.192 g (1 mmol) of EDC was added and allowed to react for 12 h at room temperature. The solution was dialyzed against DDI water for 48 h at room temperature to remove excess MPEG-NH<sub>2</sub> with 10 kDa MWCO dialysis tubing.

### 2.4. Preparation of liposomes

Magnetic photosensitive liposomes (MPLs) were prepared by using solvent evaporation, hydration, sonication and extrusion [26,27]. Lipid mixtures of DSPC, CH and DDAB (molar ratio 5:3:1) were taken in a round-bottom flask. This mixture was dissolved in chloroform/methanol solution (2:1, v/v). The organic solvent was removed using a rotary evaporator (EYELA N-1200AVF, Japan) at 100 psi and 54 °C with a water bath for 20 min. The solvent was then completely removed in a vacuum oven overnight to form a thin phospholipid film on the wall of the round-bottom flask. The resulting dry thin film was re-hydrated with a phosphate buffer (10 mM, pH 7.4) solution containing CMNPs



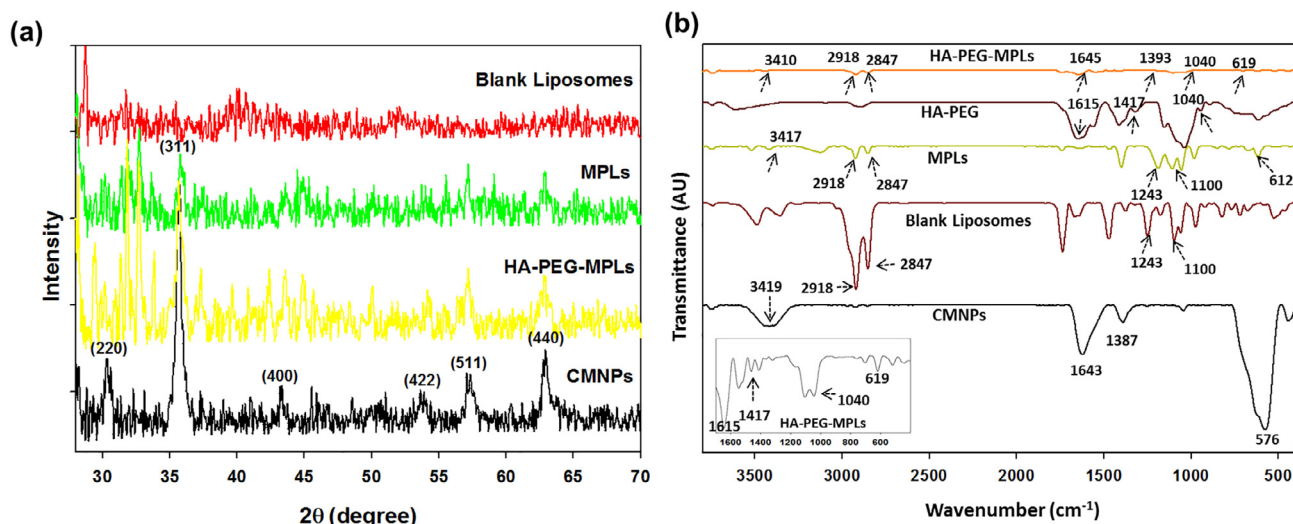


Fig. 3. Characterization of different samples by X-ray diffraction (XRD) (a) and Fourier transform infrared (FTIR) (b).

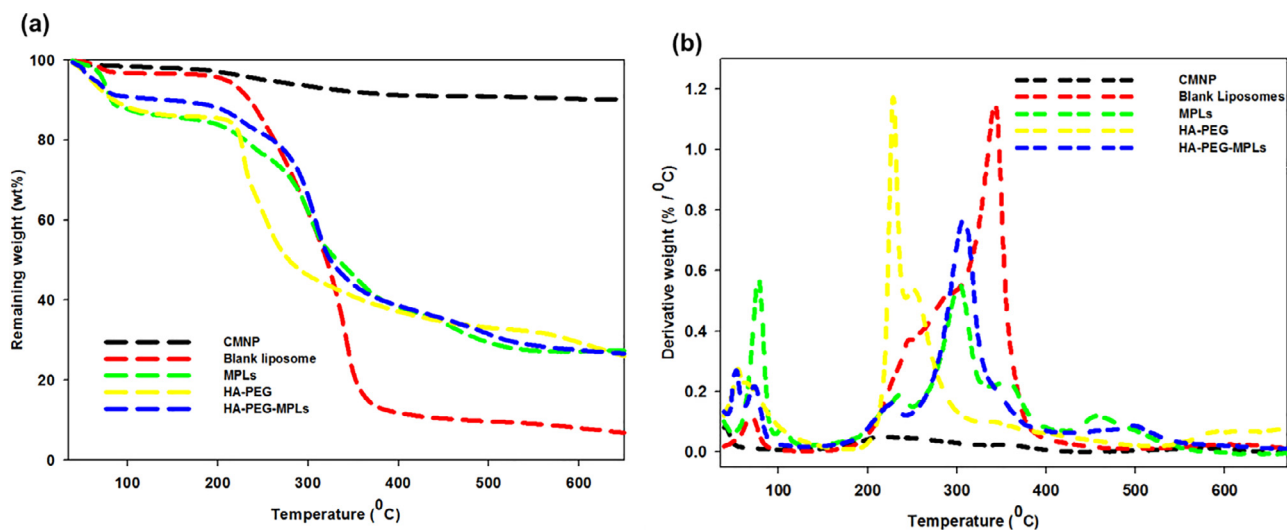


Fig. 4. Characterization of different samples by thermogravimetric analysis (TGA) (a) and differential thermal analysis (DTA) (b).

(0.3 mg/mL), ICG (50 µg/mL), and CuSO<sub>4</sub>·5H<sub>2</sub>O (300 mM) for 20 min at 54 °C. The hydrated solution was then sonicated for 15 min. After sonication, the MPLs were extruded for 20 cycles using double-stacked polycarbonate membranes with 0.2 µm pore size (Whatman, NJ, USA) in a commercial temperature-controlled barrel extruder (Lipex® Extruder, TRANSFERRA Nanosciences Inc., Canada). The un-encapsulated CMNPs were removed by centrifugation for 10 min at 1000g. The resulted solution was ultra-centrifuged for 30 min at 60,000g. For preparation of HA-PEG-MPLs, MPLs solution in distilled water (1 mg/mL) were sonicated for 10 min before adding HA-PEG (0.5 mg/mL) drop-wise and gently shaken at 4 °C overnight. The HA-PEG-MPLs solution was centrifuged to remove excess HA-PEG at 45,000g for 20 min at 20 °C and re-suspended in distilled water by sonicating for 5 min. Blank liposomes without MNPs and ICG were similarly prepared for comparison.

## 2.5. Determination of encapsulation efficiency of CMNPs and ICG

The amount of CMNPs in MPLs was determined by a spectrophotometric method [27]. Briefly, to 40 µL of MPLs solution, 10 µL of Triton X-100 (1% v/v) was added and incubated for 10 min at 43 °C. Then, 450 µL HCl (37%) and 500 µL of 40 mM KSCN were added to the samples and incubated for 5 min. The absorbance of the solution was

measured at 480 nm in a UV-VIS Spectrophotometer. The CMNPs concentration was then determined from a standard curve prepared beforehand. The ICG concentration was determined from the absorbance of MPLs in 80% methanol at 785 nm with a standard curve [28]. The encapsulation efficiency (EE) and loading efficiency (LE) of CMNPs and ICG was calculated using the following equations.

$$EE (\%) = \frac{\text{Weight of encapsulated CMNPs or ICG}}{\text{Weight of CMNP or ICG initially added}} \times 100 \quad (1)$$

$$LE (\%) = \frac{\text{Weight of encapsulated CMNPs or ICG}}{\text{Weight of liposomes}} \times 100 \quad (2)$$

## 2.6. Characterization of HA-PEG-MPLs

The particles size and zeta potential of CMNPs, MPLs and HA-PEG-MPLs were determined by dynamic light scattering (DLS) using a Zetasizer Nano ZS (Malvern Instruments Ltd., Worcestershire, UK). The DLS analysis was performed at a scattering angle of 173° at 25 °C in the auto-measuring mode. Particles dispersions were diluted with DDI water for measurements. The structure of CMNPs in HA-PEG-MPLs was observed by cryogenic transmission electron microscopy (cryoTEM). The cryo-fixed specimens were mounted into a Gatan cryo-holder

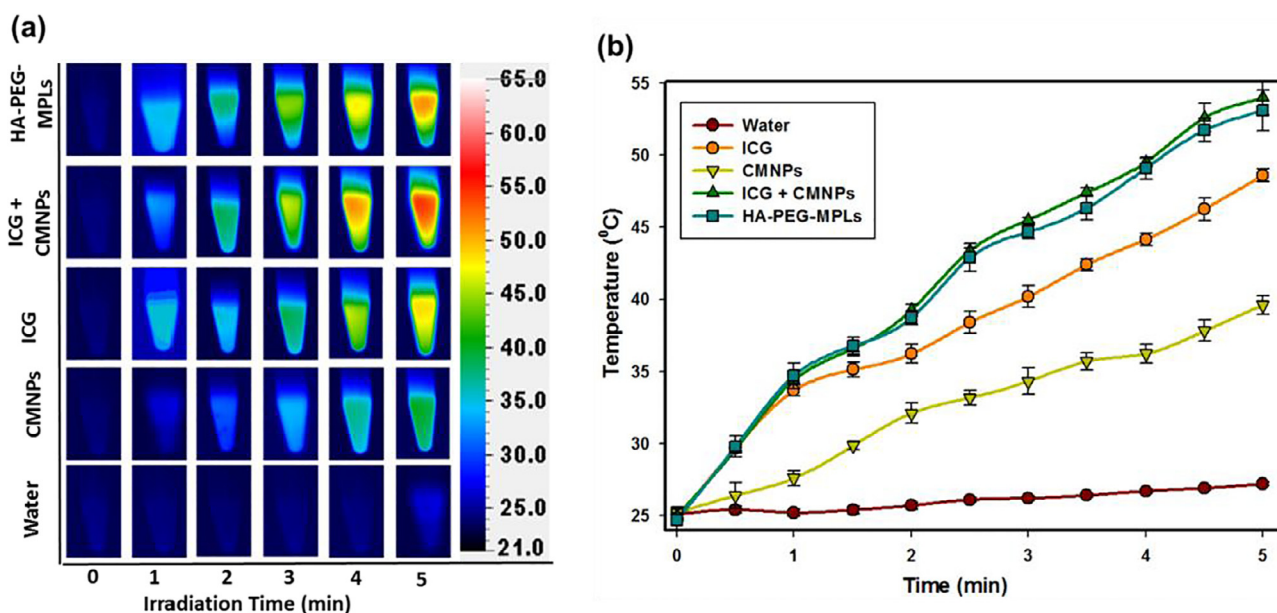


Fig. 5. The ex vivo photothermal effects from infrared thermal camera images (a) and peak temperature profiles (b) for HA-PEG-MPLs, ICG + CMNPs, CMNPs, ICG and water with continuous NIR laser irradiation (808 nm, 2.0 W/cm<sup>2</sup> for 5 min).

(Model 914, Gatan Inc.) for direct observation at  $-170^{\circ}\text{C}$  at 120 kV using a JEOL JEM-1400 TEM (Tokyo, Japan). Thermogravimetric analysis (TGA) was conducted with 8–10 mg of powder sample in nitrogen atmosphere from 25 to  $750^{\circ}\text{C}$ , with a heating rate of  $10^{\circ}\text{C}/\text{min}$  using a Q50 TGA from TA Instruments (New Castle, DE, USA). For Fourier transform infrared spectroscopy (FTIR) spectrum, the sample was blended with KBr, compressed to form a pellet and analyzed with a TENSOR II FTIR spectrometer (Bruker Optics Inc., Billerica, MA, USA). The transmission spectra were obtained from 400 to  $4000\text{ cm}^{-1}$  at  $2.5\text{ mm/s}$  with a resolution of  $4\text{ cm}^{-1}$ . For X-ray diffraction (XRD) analysis of the crystallographic characteristic of samples, a D2 Phaser X-ray powder diffractometer (Bruker, WI, USA) was used by scanning in the  $2\theta$  range of  $20\text{--}70^{\circ}$  with  $\text{CuK}\alpha$  radiation. The crystalline grain size was determined from the strongest plane (3 1 1) reflection peak using the Debye-Scherrer equation.

$$D = \frac{\kappa\lambda}{\beta\cos\theta} \quad (3)$$

where  $\kappa$  is dimensionless shape factor, close to unity, normally taken as 0.9,  $\lambda$  is the wavelength of X-ray,  $\beta$  is full width at half max (FWHM) of the diffraction peak,  $\theta$  is the Bragg angle and  $D$  is the average size of the crystalline domains.

## 2.7. Temperature elevation induced by NIR laser irradiation

The temperature profile of different samples after exposure to laser irradiation was determined from thermal images captured with a thermal camera (InfReC Thermo GEAR G100EX, Nippon Avionics Co., Tokyo, Japan). Aqueous suspension of HA-PEG-MPLs, mixture of ICG and CMNPs, ICG, CMNPs and distilled water in Eppendorf tube (0.5 mL) were irradiated by NIR 808 nm laser at  $2\text{ W/cm}^2$  for 5 min. The amount of ICG in the solution was kept constant for ICG, mixture of ICG and CMNPs and HA-PEG-MPLs samples ( $6.53\text{ }\mu\text{g/mL}$ ) while the amount of CMNPs was fixed at  $282\text{ }\mu\text{g/mL}$  for CMNPs and HA-PEG-MPLs samples [14,29]. The temperatures of the solutions were monitored at 30 s intervals.

## 2.8. In vitro cell culture experiments

For in vitro cytotoxicity tests,  $2.5 \times 10^3$  U87MG cells were seeded

to each well of a 96-well cell culture plate and cultured in Dulbecco's Modified Eagle Medium (DMEM) supplemented with 10% fetal bovine serum overnight in a humidified  $\text{CO}_2$  incubator at  $37^{\circ}\text{C}$  under 5%  $\text{CO}_2$  atmosphere. The cell culture medium was replaced with HA-PEG-MPLs of various concentrations in DMEM and incubated at  $37^{\circ}\text{C}$  for 10 h in a humidified  $\text{CO}_2$  incubator for intracellular uptake of HA-PEG-MPLs. The medium in each well was then completely removed and replaced with fresh medium. Each well was exposed to 808 nm NIR laser light at  $2\text{ W/cm}^2$  for 4 min [30]. After irradiation, the plate was incubated again for 30 min before determining cell viability by MTT assays with 3-(4,5-dimethylthiazol-2-yl)-2,5-diphenyltetrazolium bromide using a microplate reader at 540 nm. Live/Dead cell assays were performed with U87MG cells to verify the photothermal effects by using  $1 \times 10^4$  U87MG cells in 24-well cell culture plates. After treatment with HA-PEG-MPLs at  $2\text{ mg/mL}$  in DMEM at  $37^{\circ}\text{C}$  for 10 h, the existing medium in the well was replaced with fresh medium and each well was irradiated with 808 nm NIR laser at  $2\text{ W/cm}^2$  for 4 min. After irradiation, the plate was incubated again for 30 min before staining with calcein AM/ethidium homodimer in the LIVE/DEAD™ Viability/Cytotoxicity Kit for mammalian cells (Thermo Fisher Scientific) and observed under an inverted fluorescence microscope (Olympus IX-71, Tokyo, Japan). The temperature profiles in the cell culture plate after exposure to laser irradiation was also monitored from thermal images captured with a thermal camera (InfReC Thermo GEAR G100EX, Nippon Avionics Co., Tokyo, Japan).

## 2.9. In vivo antitumor efficacy

Female BALB/c nude mice weighing approximately 15–20 g (4–6 weeks old) were purchased from the National Laboratory Animal Center (Taipei, Taiwan). All animal experiments were conducted according to protocols approved by the Institutional Animal Care and Use Committee of Chang Gung University. To establish the xenograft tumor model,  $1 \times 10^6$  U87MG cells were administered by subcutaneous injection into the right flank of the nude mice at day 0. When the tumor volumes had grown to approximately  $50\text{--}80\text{ mm}^3$  (day 10), mice were randomly divided into three groups (4 mice in each group) for treatment. Group 1: intravenous injection with  $200\text{ }\mu\text{L}$  of saline (control) at day 10, 14, 17 and 20; group 2: intravenous injection with  $200\text{ }\mu\text{L}$  of saline at day 10, 14, 17 and 20 and irradiation with 808 nm laser at

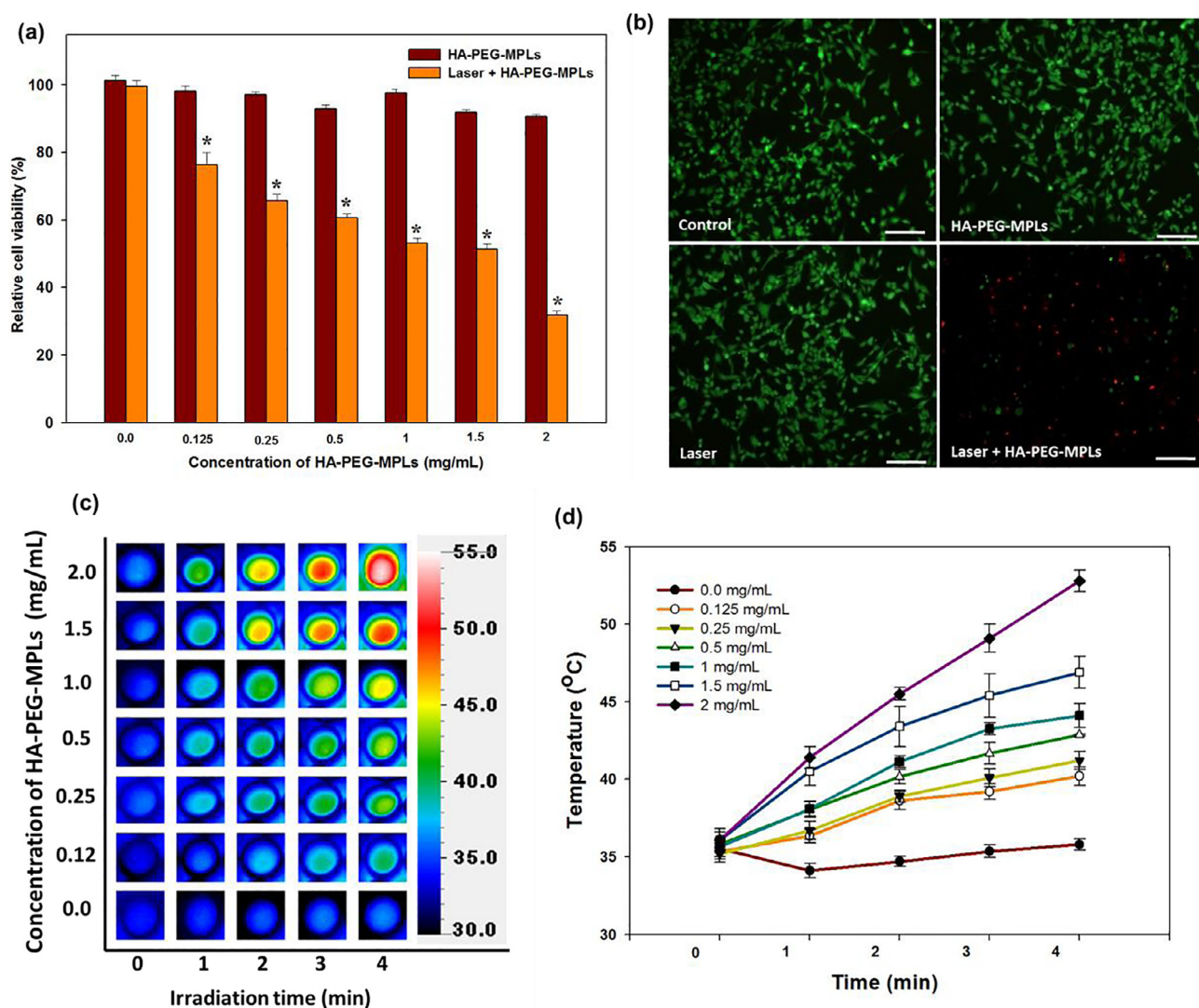


**Fig. 6.** The in vitro cell cytotoxicity and live/dead cell assays. (a) Relative viability of U87MG cells incubated 10 h with different concentrations of HA-PEG-MPLs with or without 808 nm laser irradiation ( $2 \text{ W/cm}^2$  for 4 min) ( $n = 5$ ). \*  $p < 0.05$  compared HA-PEG-MPLs. (b) Fluorescence microscopy images of U87MG cells incubated 10 h with HAPEG-MPLs (2 mg/mL) and exposed to the 808 nm laser irradiation ( $2 \text{ W/cm}^2$  for 4 min). Live and dead cells were stained with calcein AM (green color) and ethidium homodimer-1 (red color), respectively. Bar = 100  $\mu\text{m}$ . The temperature profile images captured with an infrared thermal camera (c) and peak temperature profiles (d) are shown for different liposome concentrations used for cell culture. (For interpretation of the references to colour in this figure legend, the reader is referred to the web version of this article.)

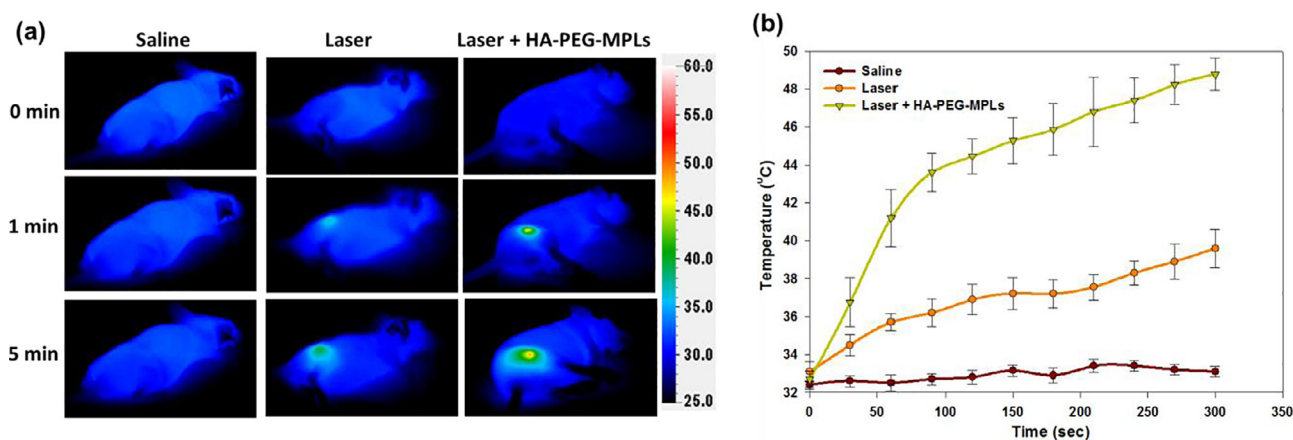


**Fig. 7.** In vivo photothermal effects of tumor-bearing mice after injection with saline, injection with saline followed by NIR laser irradiation (808 nm at  $2.0 \text{ W/cm}^2$ ) and injection with HA-PEG-MPLs followed by NIR laser irradiation (808 nm at  $2.0 \text{ W/cm}^2$ ). (a) IR thermal images showing the temperature changes in tumor areas of mice after different treatments. (b) Peak temperature profiles in tumors after different treatments.



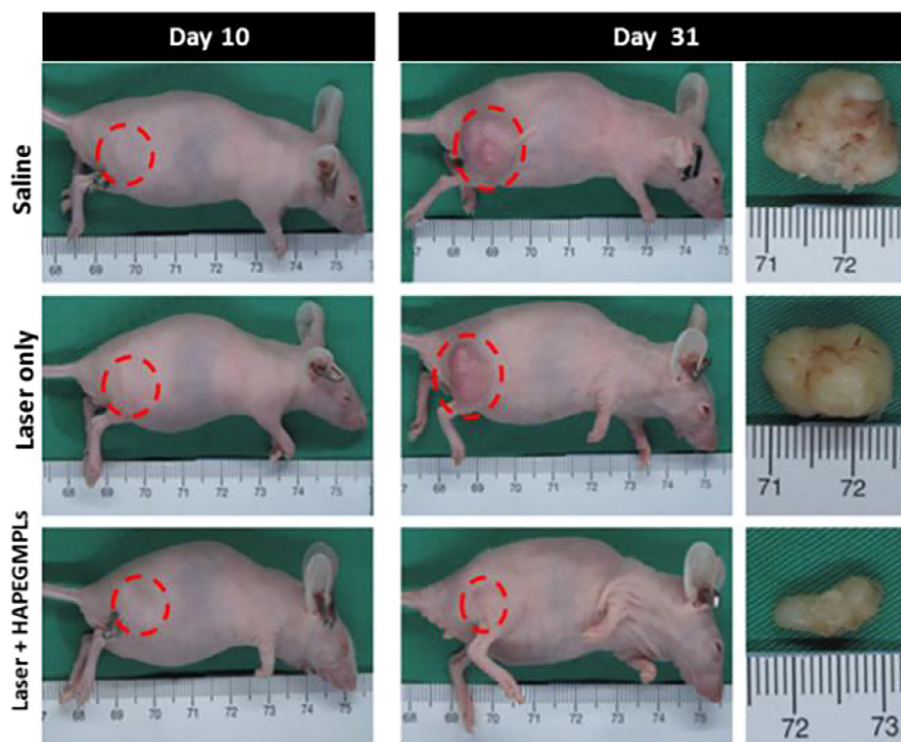


**Fig. 8.** Representative photographs of the tumor-bearing 10 days and 31 days post-implantation of U87MG tumor cells. Treatment started on day 10. The retrieved tumors on day 31 were also shown for each group.

2.0 W/cm<sup>2</sup> for 5 min after each injection (laser); group 3, intravenous injection with 200  $\mu$ L of HA-PEG-MPLs (3 mg/mL) at day 10, 14, 17 and 20, followed by placing a permanent magnet (1400 Gauss) at the vicinity of the tumor site for 90 min and irradiation with 808 nm NIR laser at 2.0 W/cm<sup>2</sup> for 5 min after each injection (laser + HA-PEG-MPLs). The temperature distribution around the tumor area was determined from thermal images captured with an infrared thermal camera (Thermo GEAR G100EX, Tokyo, Japan). The body weight and tumor size was continuously monitored twice a week. The tumor size was measured using a calliper, from which the tumor volume was calculated according to the length and width of the tumor as  $\text{length} \times (\text{width})^2/2$  [14,31]. For ethical reasons, animals were euthanized when the volume of the implanted tumor reached 1 cm<sup>3</sup> and the survival curve was determined from the remaining mice.

For histological analysis, one mouse from each group was sacrificed at day 34. The tumor was harvested immediately from the animal and preserved in formaldehyde. The tumor tissue was treated with 10% phosphate buffered formalin, followed by paraffin-embedment and sectioned into  $\sim 5 \mu\text{m}$  thickness for hematoxylin and eosin (H&E) staining. For immunohistochemical (IHC) staining, the paraffin-embedded tumor tissue was stained for the cell proliferation marker Ki-67 with the UltraVision™ Quanto Detection System HRP DAB (Thermal Fisher Scientific) and counterstained with hematoxylin. The primary antibody used was rabbit anti-Ki-67 monoclonal antibody from Thermal Fisher Scientific (MA5-14520).

#### 2.10. In vivo IVIS imaging

Since the U87MG glioblastoma cell line was genetically engineered to express the firefly luciferase gene [32], we used bioluminescence imaging to evaluate the anti-tumor efficacy based on the bioluminescence intensity (BLI) from each mouse. At day 14, 18, 24 and 27 post-implantation, 0.1 mL of luciferase (15 mg/mL) was injected intraperitoneally into the mouse and bioluminescence imaging was performed using non-invasive in vivo imaging system (IVIS) (Xenogen

IVIS-200, Caliper Life Sciences, Hopkinton, MA, USA). The BLI was determined at baseline at day 10 (i.e. before treatment) and at each time point after treatment by measuring the total peak BLI through standardized regions of interest (ROIs) in tumor by using the Living Image® 4.0 software. The normalized BLI was calculated from the total bioluminescent signal intensity at each time point after normalizing by the total signal intensity at baseline. To study the tumor-targeting ability of HA-PEG-MPLs, tumor-bearing mice were injected intravenously with 200  $\mu$ L of HA-PEG-MPLs (3 mg/mL) or 200  $\mu$ L saline intravenously. Magnetic guidance was achieved by an external magnetic field (1400 Gauss) for 2 h and fluorescence imaging was carried out with IVIS at 745 nm/850 nm excitation/emission wavelength for detection of ICG.

#### 2.11. Statistical analyses

All data were subjected to analysis one-way analysis of variance (ANOVA) and reported as mean  $\pm$  standard deviation (SD). Turkey's post-hoc test was used to determine the difference between any two groups with  $p$  value < 0.05 considered to be statistically significant.

### 3. Results and discussion

#### 3.1. Characterization of HA-PEG-MPLs

We first coated HA-PEG to MPLs, which entrap ICG and MNPs, to fabricate HA-PEG-MPLs similar to the layer-by-layer technology where multilayer films of oppositely charged polyelectrolytes were coated alternatively to liposomes [33]. The distribution of hydrodynamic diameters and zeta potentials of CMNPs, MPLs and HA-PEG-MPLs are shown in Fig. 2a and b while their average values are compared in Table 1. As MPLs are formed from DDAB, they are cationic liposomes and have a positive zeta potential. As HA is an anionic glycosaminoglycan while PEG does not contained any charged groups, the zeta potential of liposomes shifted from 19.4 mV for MPLs to  $-20.0$  mV for



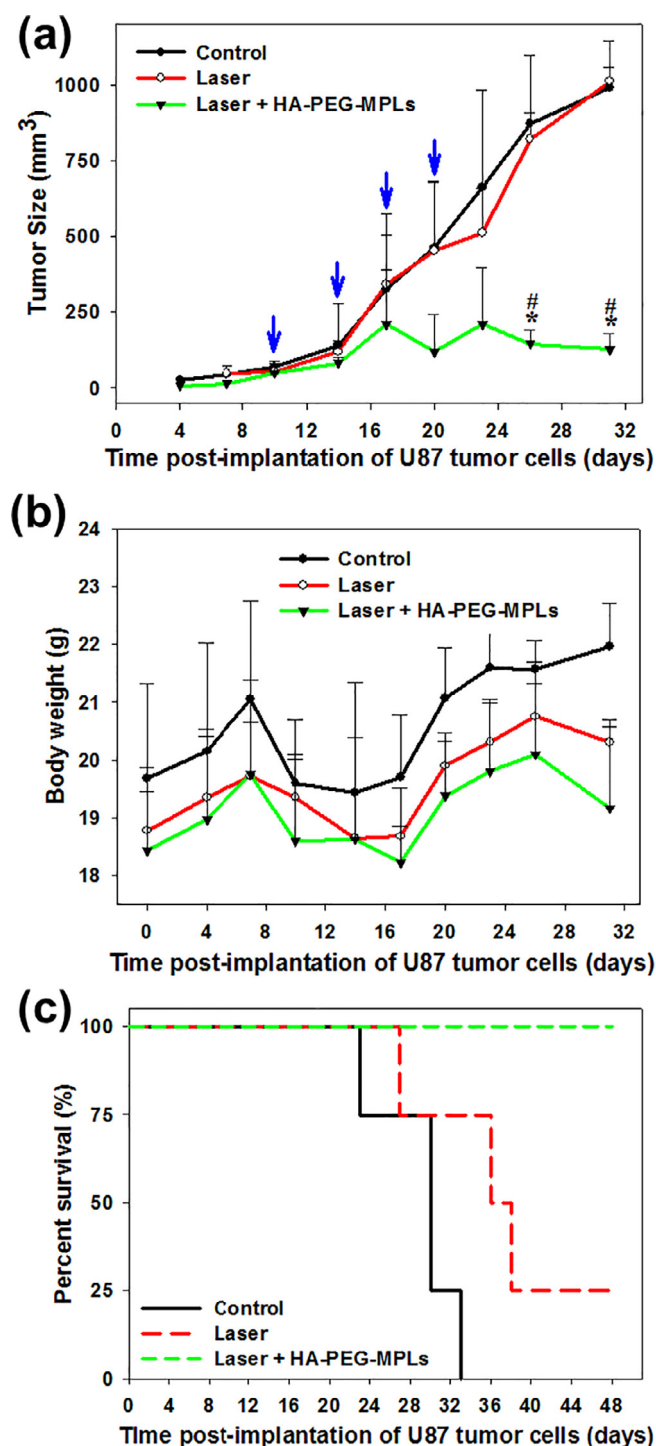


Fig. 9. The tumor volume (a), body weight (b) and survival curve (c) after different treatments. The blue arrows in (a) indicated the times for laser irradiation in the laser and laser + HA-PEG-MPLs groups (2.0 W/cm<sup>2</sup> for 5 min). The mice were sacrificed when the tumor volume reached 1000 mm<sup>3</sup>, from which survival curves were calculated (c).

HA-PEG-MPLs, which confirms that HA-PEG is successfully coated onto the surface of MPLs through ionic interactions. There is no statistical difference in average particle size between MPLs and HA-PEG-MPLs, indicating the self-assembly of HA-PEG on MPLs provide a simple yet efficient method to introduce HA as a targeting ligand. In addition, PEG could be introduced together with HA to extend blood-circulation time of HA-PEG-MPLs while minimizes the clearance by the reticuloendothelial system (RES) when macrophages in the RES located in

the liver and the spleen vividly take up particles bound with serum proteins, which could be reduced by surface modification by PEG [34]. The restriction of the particle size of HA-PEG-MPLs to ~220 nm will also improve the enhanced permeability and retention (EPR) effect as the nano-sized vehicle with long circulation times could leak preferentially into tumor tissue through a leaky tumor vasculature and be retained in the tumor bed due to reduced lymphatic drainage [35]. The structures of HA-PEG-MPLs characterized by cryo-TEM showed agglomerate of discrete CMNPs of ~15 nm size in the aqueous core surrounded by a lipid bilayer and with a particle size consistent with that from DLS measurements (Fig. 2c). For encapsulation efficacy, the EE value was  $91.7 \pm 2.1\%$  for CMNPs and  $12.1 \pm 3.8\%$  for ICG while the LE value was  $13.5 \pm 2.3\%$  for CMNPs and  $0.38 \pm 0.10\%$  for ICG.

Fig. 3a shows X-ray diffraction (XRD) patterns of CMNPs, MPLs and HA-PEG-MPLs in comparison with that of blank liposomes (liposomes prepared similarly but without CMNPs and ICG). For CMNPs, MPLs and HA-PEG-MPLs, six diffraction peaks at  $2\theta = 30.2^\circ, 35.4^\circ, 43.2^\circ, 53.4^\circ, 57.2^\circ$  and  $62.7^\circ$  could be indexed to the (2 2 0), (3 1 1), (4 0 0), (4 2 2), (5 1 1), and (4 4 0) planes of a cubic cell. The crystalline structure of the particle can be confirmed to correspond to that of a magnetite structure (JCPDS card number 19-0629), confirming that all resultant nanoparticles were pure Fe<sub>3</sub>O<sub>4</sub> with a cubic spinel structure of the magnetite [24,31,36]. This could be further confirmed from the XRD patterns observed for blank liposomes, where no diffraction peaks corresponding to CMNPs could be observed. It is also evident that co-encapsulation of CMNPs with ICG in liposomes did not lead to change in the crystalline phase of CMNPs. The average crystal grain size calculated from the Scherrer equation is from 13.3 to 15.1 nm from the strongest (3 1 1) diffraction peak for all CMNPs-containing samples.

In Fig. 3b, the FTIR analysis of CMNPs showed the strongest peak at  $3419 \text{ cm}^{-1}$ , indicating the presence of -OH vibrations. The peak at  $576 \text{ cm}^{-1}$  indicated the existence of Fe-O stretching bond in the nanoparticles [37]. The characteristic peaks of citric acid at  $1394$  and  $1735 \text{ cm}^{-1}$ , due to the symmetric vibration and asymmetric stretching of C-O from -COOH group and C=O from -COOH, were shifted to  $1387$  and  $1643 \text{ cm}^{-1}$  in CMNPs, respectively. This observation is a direct evidence to support that citric acid was coated onto the surface of MNPs via chemisorption of carboxylate groups. In blank liposomes, the characteristic peaks of DSPC showed the CH<sub>2</sub> symmetric and asymmetric stretch modes at  $2847 \text{ cm}^{-1}$  and  $2918 \text{ cm}^{-1}$ , while the phosphate group (P=O) of symmetric and asymmetric stretch modes showed characteristic peaks at  $1100 \text{ cm}^{-1}$  and  $1243 \text{ cm}^{-1}$  [38,39]. For MPLs the strongest bands at  $2918 \text{ cm}^{-1}$  and  $2847 \text{ cm}^{-1}$  represented the CH<sub>2</sub> symmetric and asymmetric stretch modes. Also, the characteristic peaks at  $612 \text{ cm}^{-1}$  and  $3417 \text{ cm}^{-1}$  corresponding to the Fe-O stretching and -OH vibrations of CMNPs confirmed the existence of CMNPs inside the liposomes. In the spectrum of HA-PEG, the absorption peaks at  $1615 \text{ cm}^{-1}$  and  $1417 \text{ cm}^{-1}$  represented the symmetric and asymmetric stretching vibration bands of the carboxyl group while the peak at  $1040 \text{ cm}^{-1}$  could be attributed to the C-O-C stretching [23,40]. In the FTIR spectrum of HA-PEG-MPLs, all expected and existing peaks existed, with specific reference to the peaks assigned to HA-PEG (shown in the enlarged spectrum in the insert of Fig. 3b), suggesting that HA-PEG is successfully coated on MPLs to form HA-PEG-MPLs as driven by ionic interactions.

The thermogravimetric analysis (TGA) and differential thermal analysis (DTA) curves of CMNPs, blank liposomes, MPLs, HA-PEG and HA-PEG-MPLs were shown in Fig. 4. A ~10% weight loss was observed at  $700^\circ\text{C}$  in CMNPs due to thermal decomposition of -OH functional groups [31,41]. For blank liposomes, after an initial weight loss due to water, substantial weight loss (~85%) from  $240^\circ\text{C}$  to  $380^\circ\text{C}$  was observed with a decomposition peak temperature at  $\sim 340^\circ\text{C}$  to result in ~8% residual weight at  $700^\circ\text{C}$ . In contrast, MPLs showed higher thermal stability and less weight loss (74%) due to CMNPs in the liposomes and the peak decomposition temperature shifted to  $300^\circ\text{C}$ . For HA-PEG, the early weight loss from  $60^\circ\text{C}$  to  $100^\circ\text{C}$  represents the

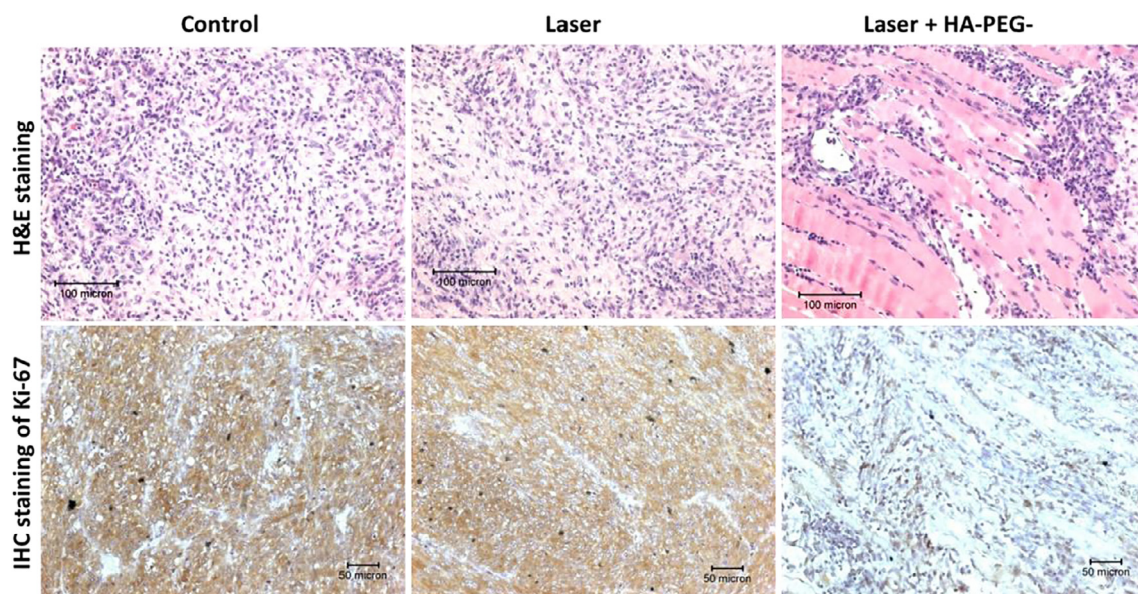


**Fig. 10.** H&E (bar = 100 µm) and immunohistochemical (IHC) staining of Ki-67 (bar = 50 µm) of tumor sections after different treatments 34 days post-implantation of U87MG tumor cells.

vanishing of residually bound water mostly to HA. A thermal decomposition started from 200 °C to 280 °C with the maximum weight loss peak at 251 °C and weight loss of ~72% after reaching 700 °C [23]. Considering HA-PEG-MPLs, the DTA curve showed all decomposition peaks due to MPLs (300 °C) and HA-PEG (251 °C) and showed similar weight loss (~73%) to MPLs, confirming the encapsulation CMNPs in HA-PEG-MPLs and HA-PEG coating on HA-PEG-MPLs.

### 3.2. Ex vivo photothermal effects of HA-PEG-MPLs

The photothermal effect of HA-PEG-MPLs was first studied when solutions of HA-PEG-MPLs, ICG, CMNPs and ICG + CMNPs at the same concentrations of ICG and CMNPs (6.53 µg/mL ICG and 282 µg/mL CMNPs) were exposed to 808 nm laser light irradiation at 2.0 W/cm<sup>2</sup> up to 5 min. The temperature rise as a function of light exposure time was monitored using an infrared thermal camera (Fig. 5). There was no obvious temperature change observed when distilled water was exposed to NIR laser. In comparison, under the same laser irradiation conditions, the solution temperature reached 55.2 °C, 54 °C, 49 °C and 38 °C for HA-PEG-MPLs, ICG + CMNP, ICG and CMNPs, respectively. The combinations of ICG and CMNPs could enhance the photothermal effect from ICG or CMNP alone. In addition, HA-PEG-MPLs and ICG + CMNPs showed comparable temperature profiles, indicating their encapsulation in HA-PEG-MPLs does not lead to diminished photothermal efficacy. Considering the thermal effects of CMNPs, magnetic hyperthermia of Fe<sub>3</sub>O<sub>4</sub> MNPs produced via dipole relaxation is usually achieved under an alternating magnetic field [42]. Nonetheless, the technique requires high current and voltage due to large air volume within the applied field in which energy cannot be easily focused. Only very recently, NIR light induced photothermal effect for Fe<sub>3</sub>O<sub>4</sub> MNPs has been reported for its good photothermal converting efficiency for photothermal ablation of tumors [43]. Taken together, ICGs and CMNPs showed photothermal effects, endorsing HA-PEG-MPLs to be an effective photothermal nano-agent for PTT.

### 3.3. In vitro cytotoxicity of HA-PEG-MPLs

To examine the cytotoxicity of HA-PEG-MPLs against tumor cells, U87MG cells were contacted with HA-PEG-MPLs of different concentrations for 10 h before irradiation with 808 nm NIR laser at 2 W/cm<sup>2</sup> for 4 min. The cell viability was determined through MTT assays.

As shown from Fig. 6a, U87MG cells exposed to the laser light showed significant difference in cell viability compared with those without laser irradiation at every HA-PEG-MPLs concentration. The enhanced cytotoxicity toward U87MG is also dose-dependent on HA-PEG-MPLs concentrations. In contrast, no obvious decrease in cell viability was observed upon exposure to HA-PEG-MPLs at all concentrations but without laser irradiation. This photothermal effect of HA-PEG-MPLs was further confirmed from the live/dead cell assays where live and dead U87MG cell could be identified by staining with calcein AM and ethidium homodimer-1, respectively. As shown in Fig. 6b, treatment with HA-PEG-MPLs or laser irradiation alone did not influence the cell viability from the control judging from the abundance of live cells (green fluorescence) with no observable dead cells (red fluorescence). In contrast, laser + HA-PEG-MPLs treatment led to a drastic change in fluorescence signals where minimum live cells together with abundant dead cells were observed. The empty space observed for this group may be occupied by dead cells that were detached from the surface of the cell culture plate during the washing step. Indeed, those results underlines that either laser or HA-PEG-MPLs alone did not lead to killing of cancer cells but only HA-PEG-MPLs plus laser irradiation could effectively lead to PTT/PDT dual mode killing of cancer cells. Fig. 6c and d show the temperature increase in the cell culture plate after laser irradiation is correlated with the increase of liposome concentration for cell culture, which results in lower cell viability as shown in Fig. 6a due to increased intracellular liposome concentration.

### 3.4. In vivo effects of HA-PEG-MPLs

To study the efficiency of HA-PEG-MPLs for in vivo cancer therapy, xenograft tumor model in nude mice was established by subcutaneously implanted U87MG cells. Ten days post-implantation, when the tumor size reached 50–80 mm<sup>3</sup>, different treatments were started. The photothermal effect of the tumor-bearing mice in vivo was first monitored with an infrared thermal camera as shown Fig. 7a. There was no temperature increase found after 5 min for the control group injected with saline. In the group injected with saline and treated with laser, in contrast with the ex vivo photothermal effect observed in Fig. 5, there was a slight increase in temperature from 33.1 °C to 39.6 °C in 5 min (Fig. 7b). However, this slight increase in temperature would not lead to tumor destruction as magnetic hyperthermia for cancer treatment involved temperatures from 41 °C to 46 °C [44]. In the group injected



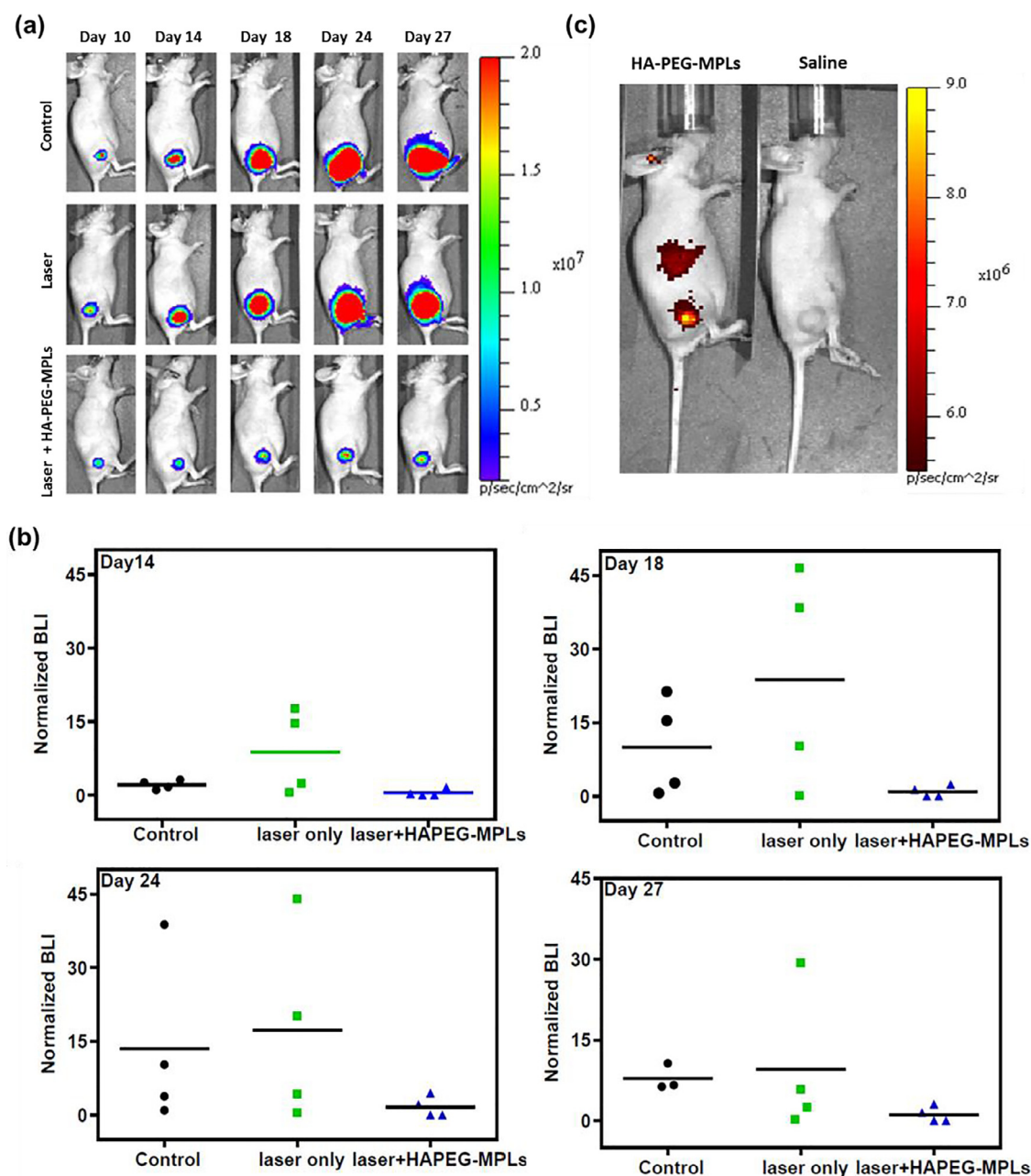


**Fig. 11.** The in vivo bioluminescence and fluorescence imaging by IVIS. The anti-tumor efficacy was shown from the bioluminescence imaging pictures (a) and the normalized bioluminescence intensity (BLI) at different time points after different treatments (b). For targeting effects, the fluorescence imaging pictures 2 h after injection with HA-PEG-MPLs or saline are shown in (c).

with HA-PEG-MPLs combined with laser irradiation, there is a rapid increase in temperature from 32.9 °C to 42.7 °C within 1 min and then reaching 49.3 °C in the next 4 min (Fig. 7b).

Gross images of the tumor-bearing mice on day 10 (treatment started) and day 31 post-implantation of U87MG cells demonstrated the apparent tumor size difference of the laser + HA-PEG-MPLs group from the other two groups with tumors removed from the animals on day 31 supporting the excellent anti-tumor effects (Fig. 8). The tumor volume was recorded every 3 days from day 0 to day 31. The tumor volume increased rapidly with time for the control and laser groups (Fig. 9a). However, the tumor volume in the laser + HA-PEG-MPLs group remained below 150 mm<sup>3</sup> throughout the observation period. Specifically, the tumor volumes of the control and laser groups were 7.7–7.9 times that of the laser + HA-PEG-MPLs group at the end of the observation period (day 31).

The mice did not exhibit any significant difference in body weights between groups (Fig. 9b). However, mice in the control group without laser treatment showed a trend of better weight gain compared to other groups with laser treatment, which is consistent with the general perception that laser exposure leads to weight loss. The mouse was sacrificed when the tumor volume reached 1000 mm<sup>3</sup> and survival curve was constructed from the percentage of remaining mice in each group (Fig. 9c). The mean survival times for the control and laser groups were 30 and 36 days, respectively. In contrast, all mice in the laser + HA-PEG-MPLs group survive throughout experiment period up to 48 days post-implantation of tumor cells. Taken together, the remarkable cancer treatment efficacy was achieved by PDT/PTT from the laser + HA-PEG-MPLs group.

Based on results of H&E staining of tumor tissue on day 31, no evidence of necrosis was observed for the control and laser groups

(Fig. 10). In contrast, cavitation phenomenon in coagulative necrosis was observed in the laser + HA-PEG-MPLs group. Cancer therapy should also inhibit proliferation of cancer cells from histology of tumor tissue. The Ki-67 protein is used as a proliferation marker in tumor specimens and its IHC expression has prognostic and predictive value in cancer [45]. The IHC staining of tumor sections associated with Ki-67 protein in Fig. 10 clearly indicated that a greater number of actively proliferating tumor cells existed in tumor sections from the control and the laser groups. In contrast, the tissue sections from the tumor treated with laser + HA-PEG-MPLs showed very weak Ki-67 immunoreactivity and minimum Ki-67 protein production. Therefore, we conclude that laser + HA-PEG-MPLs can provide effective anticancer activity to effectively inhibit proliferation of cancer cells.

### 3.5. *In vivo* antitumor and tumor targeting effects from IVIS imaging

Taking advantage of the luciferase activity in implanted U87MG cells, antitumor efficacy was also monitored by *in vivo* bioluminescence imaging after intraperitoneal injection of luciferin and imaging with IVIS. Fig. 11a shows the representative lateral IVIS images of individual mouse from different groups at different time points. In control and laser groups, the BLI increased rapidly with time while in the laser + HA-PEG-MPLs group the BLI apparently remained constant. To further elucidate the treatment efficacy quantitatively, the normalized BLI values (normalized to start of treatment on day 10) of all mice were plotted in Fig. 11b. As evident from the figure, the laser + HA-PEG-MPLs group showed the lowest and the least scattered normalized BLI values among all groups at all time points, endorsing the efficacy and consistency of using HA-PEG-MPLs for combined PTT/PDT.

The tumor-targeting ability of the HA-PEG-MPLs could be also assessed by IVIS with fluorescence imaging from the fluorescent characteristics of encapsulated ICG in HA-PEG-MPLs. As shown in the Fig. 11c, after injection of HA-PEG-MPLs and magnetic guidance for 2 h with a magnet at the tumor site, enhanced accumulation of HA-PEG-MPLs was found at the tumor site, which could be identified in the image with high fluorescence signal [46]. Meanwhile a lower signal showed only in the liver/spleen of mouse could be identified among all organs, which was consistent with a previous report indicating PEG-containing liposomes were mainly accumulated to elevated levels in spleen and liver of mice from the biodistribution study [47]. Therefore, we could confirm that magnetic targeting plus the EPR effects, delivery of HA-PEG-MPLs to solid tumors within a short time (< 2 h) is possible, which upon short-term laser exposure will lead to effective cancer therapy based on combined PTT/PDT as revealed from the xenograft tumor model.

## 4. Conclusion

Dual targeted HA-PEG-MPLs could be prepared for entrapping CMNPs and ICG and coated with HA-PEG by self-assembly. Photothermal effects after short-term exposure to NIR laser light endorsed HA-PEG-MPLs to be a suitable nano-agent for PTT/PDT as justified from enhanced cytotoxicity toward U87MG cancer cells *in vitro*. With xenograft mice tumor model, we successfully demonstrated that, due to the targeting effects, HA-PEG-MPLs injected intravenously could be preferentially accumulated at the tumor site *in vivo* to prevent tumor growth after combination with successive short-term NIR laser irradiation. Taken together, this study successfully provided a simple yet effective alternative modality for cancer nanotherapy based on magnetic carriers.

## Acknowledgements

The financial assistance was provided by grants from the Ministry of Science and Technology, Taiwan (MOST106-2221-E-182-056-MY3) and Chang Gung Memorial Hospital (BMRP249, CMRPD2G0081 and

CMRPD2G0082). The Center for Advanced Molecular Imaging and Translation at Chang Gung Memorial Hospital, Linkou, and technical assistance provided by Yu-Tin Lai are acknowledged for IVIS experiments.

## References

- [1] C.P. Leamon, J.A. Reddy, Folate-targeted chemotherapy, *Adv. Drug Deliv. Rev.* 56 (2004) 1127–1141.
- [2] D. Peer, J.M. Karp, S. Hong, O.C. Farokhzad, R. Margalit, R. Langer, Nanocarriers as an emerging platform for cancer therapy, *Nat. Nanotechnol.* 2 (2007) 751–760.
- [3] B. Bahrami, M. Hojjat-Farsangi, H. Mohammadi, E. Anvari, G. Ghalamfarsa, M. Yousefi, Nanoparticles and targeted drug delivery in cancer therapy, *Immunol. Lett.* 190 (2017) 64–83.
- [4] J.H. Fendler, A. Romero, Liposomes as drug carriers, *Life Sci.* 20 (1977) 1109–1120.
- [5] P. Sapra, T.M. Allen, Ligand-targeted liposomal anticancer drugs, *Prog. Lipid Res.* 42 (2003) 439–462.
- [6] M.L. Immordino, F. Dosio, L. Cattel, Stealth liposomes: review of the basic science, rationale, and clinical applications, existing and potential, *Int. J. Nanomed.* 1 (2006) 297–315.
- [7] R. Sen, S. Sahoo, S. Satpathy, Liposomes as drug delivery system: a brief review, *Int. J. Drug Deliv. Res.* 5 (2014) 62–75.
- [8] R. Kaur, H. Kaur, G. Joshi, T. Matta, Liposomes: a review in cancer therapy, *Res. J. Pharm. Biol. Chem. Sci.* 7 (2016) 2273–2290.
- [9] M.K. Riaz, M.A. Riaz, X. Zhang, C. Lin, K.H. Wong, X. Chen, Surface functionalization and targeting strategies of liposomes in solid tumor therapy: a review, *Int. J. Mol. Sci.* 19 (2018).
- [10] U. Chitgupi, Y. Qin, J.F. Lovell, Targeted nanomaterials for phototherapy, *Nanotheranostics* 1 (2017) 38–58.
- [11] E.J. Hong, D.G. Choi, M.S. Shim, Targeted and effective photodynamic therapy for cancer using functionalized nanomaterials, *Acta Pharm. Sin. B* 6 (2016) 297–307.
- [12] P. Agostinis, K. Berg, K.A. Cengel, T.H. Foster, A.W. Girotti, S.O. Gollnick, Photodynamic therapy of cancer: an update, *CA Cancer J. Clin.* 61 (2011) 250–281.
- [13] C. Zeng, W. Shang, X. Liang, X. Liang, Q. Chen, C. Chi, Cancer diagnosis and imaging-guided photothermal therapy using a dual-modality nanoparticle, *ACS Appl. Mater. Interfaces* 8 (2016) 29232–29241.
- [14] C. Niu, Y. Xu, S. An, M. Zhang, Y. Hu, L. Wang, Near-infrared induced phase-shifted ICG/Fe<sub>3</sub>O<sub>4</sub> loaded PLGA nanoparticles for photothermal tumor ablation, *Sci. Rep.* 7 (2017) 5490.
- [15] V. Shanmugam, S. Selvakumar, C.S. Yeh, Near-infrared light-responsive nanomaterials in cancer therapeutics, *Chem. Soc. Rev.* 43 (2014) 6254–6287.
- [16] R. Mendes, P. Pedrosa, J.C. Lima, A.R. Fernandes, P.V. Baptista, Photothermal enhancement of chemotherapy in breast cancer by visible irradiation of gold nanoparticles, *Sci. Rep.* 7 (2017) 10872.
- [17] X. Mou, Z. Ali, S. Li, N. He, Applications of magnetic nanoparticles in targeted drug delivery system, *J. Nanosci. Nanotechnol.* 15 (2015) 54–62.
- [18] P. Pradhan, R. Banerjee, D. Bahadur, C. Koch, O. Mykhaylyk, C. Plank, Targeted magnetic liposomes loaded with doxorubicin, *Methods Mol. Biol.* 605 (2010) 279–293.
- [19] M. Chu, Y. Shao, J. Peng, X. Dai, H. Li, Q. Wu, Near-infrared laser light mediated cancer therapy by photothermal effect of Fe<sub>3</sub>O<sub>4</sub> magnetic nanoparticles, *Biomaterials* 34 (2013) 4078–4088.
- [20] X. Guo, W. Li, L. Luo, Z. Wang, Q. Li, F. Kong, External magnetic field-enhanced chemo-photothermal combination tumor therapy via iron oxide nanoparticles, *ACS Appl. Mater. Interfaces* 9 (2017) 16581–16593.
- [21] S. Klein, A. Sommer, L.V.R. Distel, J.-L. Hazemann, W. Kröner, W. Neuhuber, Superparamagnetic iron oxide nanoparticles as novel x-ray enhancer for low-dose radiation therapy, *J. Phys. Chem. B* 118 (2014) 6159–6166.
- [22] X. Yang, A. Iyer, A. Singh, L. Milane, E. Choy, F.J. Hornicek, X. Yang, A.K. Iyer, A. Singh, L. Milane, E. Choy, F.J. Hornicek, Cluster of differentiation 44 targeted hyaluronic acid based nanoparticles for mdr1 siRNA delivery to overcome drug resistance in ovarian cancer, *Pharm. Res.* 32 (2015) 2097–2109.
- [23] B.-P. Jiang, L. Zhang, Y. Zhu, X.-C. Shen, S.-C. Ji, X.-Y. Tan, Water-soluble hyaluronic acid-hybridized polyaniline nanoparticles for effectively targeted photothermal therapy, *J. Mater. Chem. B* 3 (2015) 3767–3776.
- [24] H.-L. Hsu, J.-P. Chen, Preparation of thermosensitive magnetic liposome encapsulated recombinant tissue plasminogen activator for targeted thrombolysis, *J. Magn. Magn. Mater.* 427 (2017) 188–194.
- [25] K. Moriyama, T. Ooya, N. Yui, Hyaluronic acid grafted with poly(ethylene glycol) as a novel peptide formulation, *J. Control. Release* 59 (1999) 77–86.
- [26] S. Khadke, P. Stone, A. Rozhin, J. Kroonen, Y. Perrie, Point of use production of liposomal solubilised products, *Int. J. Pharm.* 537 (2018) 1–8.
- [27] D. Frascione, C. Diwoky, G. Almer, P. Opriessnig, C. Vonach, K. Gradauer, Ultrasmall superparamagnetic iron oxide (USPIO)-based liposomes as magnetic resonance imaging probes, *Int. J. Nanomed.* 7 (2012) 2349–2359.
- [28] H.-J. Yoon, H.-S. Lee, J.-Y. Lim, J.-H. Park, Liposomal indocyanine green for enhanced photothermal therapy, *ACS Appl. Mater. Interfaces* 9 (2017) 5683–5691.
- [29] Y. Ma, S. Tong, G. Bao, C. Gao, Z. Dai, Indocyanine green loaded SPIO nanoparticles with phospholipid-PEG coating for dual-modal imaging and photothermal therapy, *Biomaterials* 34 (2013) 7706–7714.
- [30] S. Uthaman, A.P. Mathew, H.J. Park, B.-I. Lee, H.-S. Kim, K.M. Huh, IR 780-loaded hyaluronic acid micelles for enhanced tumor-targeted photothermal therapy, *Carbohydr. Polym.* 181 (2018) 1–9.
- [31] Y.J. Lu, P.Y. Lin, P.H. Huang, C.Y. Kuo, K.T. Shalunon, M.Y. Chen, J.P. Chen,



- Magnetic graphene oxide for dual targeted delivery of doxorubicin and photo-thermal therapy, *Nanomaterials* 8 (2018) 193.
- [32] O. Szentirmai, C.H. Baker, N. Lin, S. Szucs, M. Takahashi, S. Kiryu, Noninvasive bioluminescence imaging of luciferase expressing intracranial U87 xenografts: correlation with magnetic resonance imaging determined tumor volume and longitudinal use in assessing tumor growth and antiangiogenic treatment effect, *Neurosurgery* 58 (2006) 365–372.
- [33] S. Jeon, C.Y. Yoo, S.N. Park, Improved stability and skin permeability of sodium hyaluronate-chitosan multilayered liposomes by layer-by-layer electrostatic deposition for quercetin delivery, *Colloids Surf. B* 129 (2015) 7–14.
- [34] A.L. Klibanov, K. Maruyama, V.P. Torchilin, L. Huang, Amphipathic poly-ethyleneglycols effectively prolong the circulation time of liposomes, *FEBS Lett.* 268 (1990) 235–237.
- [35] H. Maeda, Tumor-selective delivery of macromolecular drugs via the EPR effect: background and future prospects, *Bioconjug. Chem.* 21 (2010) 797–802.
- [36] D. Singh, R.K. Gautam, R. Kumar, B.K. Shukla, V. Shankar, V. Krishna, Citric acid coated magnetic nanoparticles: synthesis, characterization and application in removal of Cd(II) ions from aqueous solution, *J. Water Process Eng.* 4 (2014) 233–241.
- [37] N.S. Baharin, N. Muhamad Sarih, S. Mohamad, Novel functionalized polythiophene-coated Fe<sub>3</sub>O<sub>4</sub> nanoparticles for magnetic solid-phase extraction of phthalates, *Polymers* 8 (2016) 117.
- [38] R. Perrotta, M. Prieto, S. Alonso, N. Chiramon, DSPC liposomes improve transport of L-cysteine and reduce metabolic activity, *Brit. Biotechnol. J.* 12 (2016) 1–11.
- [39] M.L. Briuglia, C. Rotella, A. McFarlane, D.A. Lamprou, Influence of cholesterol on liposome stability and on in vitro drug release, *Drug Deliv. Transl. Res.* 5 (2015) 231–242.
- [40] K.-H. Chang, H.-T. Liao, J.-P. Chen, Preparation and characterization of gelatin/hyaluronic acid cryogels for adipose tissue engineering: in vitro and in vivo studies, *Acta Biomater.* 9 (2013) 9012–9026.
- [41] S. Ghosh, A.Z. Badruddoza, K. Hidajat, Uddin M. Shahab, Adsorptive removal of emerging contaminants from water using superparamagnetic Fe<sub>3</sub>O<sub>4</sub> nanoparticles bearing aminated  $\beta$ -cyclodextrin, *J. Environ. Chem. Eng.* 1 (2013) 122–130.
- [42] I.S. Smolkova, N.E. Kazantseva, V. Babayan, P. Smolka, H. Parmar, J. Vilcakova, Alternating magnetic field energy absorption in the dispersion of iron oxide nanoparticles in a viscous medium, *J. Magn. Magn. Mater.* 374 (2015) 508–515.
- [43] S. Shen, S. Wang, R. Zheng, X. Zhu, X. Jiang, D. Fu, Magnetic nanoparticle clusters for photothermal therapy with near-infrared irradiation, *Biomaterials* 39 (2015) 67–74.
- [44] A. Jordan, R. Scholz, P. Wust, H. Föhling, F. Roland, Magnetic fluid hyperthermia (MFH): cancer treatment with AC magnetic field induced excitation of biocompatible superparamagnetic nanoparticles, *J. Magn. Magn. Mater.* 201 (1999) 413–419.
- [45] L.P. Feeley, A.M. Mulligan, D. Pinnaduwa, S.B. Bull, I.L. Andrusis, Distinguishing luminal breast cancer subtypes by Ki67, progesterone receptor or TP53 status provides prognostic information, *Mod. Pathol.* 27 (2014) 554–561.
- [46] Z. Belhadj, C. Zhan, M. Ying, X. Wei, C. Xie, Z. Yan, W. Lu, Multifunctional targeted liposomal drug delivery for efficient glioblastoma treatment, *Oncotarget* 8 (2017) 66889–66900.
- [47] P. Crosasso, M. Ceruti, P. Brusa, S. Arpicco, F. Dosio, L. Cattel, Preparation, characterization and properties of sterically stabilized paclitaxel-containing liposomes, *J. Control. Release* 63 (2000) 19–30.

## Article

# Heterogeneous Nuclear Ribonucleoproteins A1 and A2 Function in Telomerase-Dependent Maintenance of Telomeres

Tong-Hong Wang <sup>1,2,†</sup> , Chin-Chuan Chen <sup>2,3,†</sup>, Yuan-Chao Hsiao <sup>4</sup>, Yu-Han Lin <sup>1</sup>, Wen-Chieh Pi <sup>4</sup>, Pei-Rong Huang <sup>4</sup>, Tzu-Chien V. Wang <sup>4</sup> and Chi-Yuan Chen <sup>1,2,\*</sup>

<sup>1</sup> Graduate Institute of Health Industry Technology and Research Center for Food and Cosmetic Safety, Research Center for Chinese Herbal Medicine, College of Human Ecology, Chang Gung University of Science and Technology, Tao-Yuan 333, Taiwan; cellww@gmail.com (T.-H.W.); evalin012880@gmail.com (Y.-H.L.)

<sup>2</sup> Tissue Bank, Chang Gung Memorial Hospital, Linkou, Tao-Yuan 333, Taiwan; chinchuan@mail.cgu.edu.tw

<sup>3</sup> Graduate Institute of Natural Products, Chang Gung University, Tao-Yuan 333, Taiwan

<sup>4</sup> Department of Molecular and Cellular Biology, College of Medicine, Chang Gung University, Tao-Yuan 333, Taiwan; c11kkh@gmail.com (Y.-C.H.); gratuit777@gmail.com (W.-C.P.); telomerase0701@gmail.com (P.-R.H.); tcvwg@mail.cgu.edu.tw (T.-C.V.W.)

\* Correspondence: d49417002@gmail.com; Tel.: +886-3-321-8999 (ext. 5113)

† These authors contributed equally to this work.

Received: 26 January 2019; Accepted: 4 March 2019; Published: 8 March 2019



**Abstract:** The A/B subfamily of heterogeneous nuclear ribonucleoproteins (hnRNPs A/B), which includes hnRNP A1, A2/B1, and A3, plays an important role in cell proliferation. The simultaneous suppression of hnRNP A1/A2, but not the suppression of hnRNP A1 or A2 alone, has been shown to inhibit cell proliferation and induce apoptosis in cancer cells, but not in mortal normal cells. However, the molecular basis for such a differential inhibition of cell proliferation remains unknown. Here, we show that the simultaneous suppression of hnRNP A1 and hnRNP A2 resulted in dysfunctional telomeres and induced DNA damage responses in cancer cells. The inhibition of apoptosis did not alleviate the inhibition of cell proliferation nor the formation of dysfunctional telomeres in cancer cells depleted of hnRNP A1/A2. Moreover, while proliferation of mortal normal fibroblasts was not sensitive to the depletion of hnRNP A1/A2, the ectopic expression of hTERT in normal fibroblasts rendered these cells sensitive to proliferation inhibition, which was associated with the production of dysfunctional telomeres. Our study demonstrates that hnRNP A1 and A2 function to maintain telomeres in telomerase-expressing cells only, suggesting that the maintenance of functional telomeres in telomerase-expressing cancer cells employs factors that differ from those used in the telomerase-negative normal cells.

**Keywords:** telomeres; telomerase; hnRNP A1/A2; DNA damage responses; apoptosis

## 1. Introduction

Telomeres are specialized structures found at the ends of chromosomes in eukaryotic cells. Human telomeres contain repeats of the sequence CCCTAA/TTAGGG, varying in length from 2 to 50 kilobase pairs, and a short single-stranded G-rich 3' overhang. DNA is tightly associated with a complex of 6 telomere-specific proteins (POT1, TRF1, TRF2, TPP1, RAP1, and TIN2) known as the shelterin complex, and with surrounding chromatin regulatory factors [1–3]. Functional telomeres also play an important role in genome stability [3–5], while dysfunctional telomeres activate damage responses mediated by ATM (ataxia telangiectasia, mutated) and ATR (ATM and Rad3-related)

kinases, triggering growth arrest, senescence, and apoptosis, as well as increasing end-to-end fusions and anaphase bridges [3]. Dysfunctional telomeres are produced through various mechanisms. For example, telomere attrition represents a normal mechanism that limits the replicative potential of human somatic cells and can serve as a tumor-suppressor pathway in potential cancer cells. Telomere attrition occurs when the ends of linear chromosomes are not completely replicated by normal DNA polymerase. The gradual loss of telomeric DNA with each round of DNA replication subsequently depletes the telomere reserves, resulting in growth arrest accompanied by senescence or apoptosis, a process known as replicative senescence [4,5]. Telomere dysfunction can also arise due to loss or malfunction of telomere-regulating factors. Meanwhile, inhibition or deletion of individual shelterin complex components has been shown to lead to chromosomal abnormalities, cell cycle arrest, and activation of the DNA damage response (DDR) pathway [6–9].

Heterogeneous nuclear ribonucleoproteins (hnRNPs) constitute a large family of proteins associated with nascent pre-mRNAs, which are packaged into hnRNP particles [10–12]. Members of the A/B subfamily of hnRNPs (hnRNP A/Bs), which include hnRNP A1, A2/B1, and A3, are the most abundant hnRNPs in the nucleus of proliferating cells. The major nuclear function of hnRNP A/Bs is thought to involve interactions with RNA, which modulates mRNA packaging, splicing, trafficking, and stability [13,14]. In addition, a role for hnRNP A/Bs in telomere maintenance has also been suggested, since these proteins are able to bind to the single-stranded telomeric repeat sequence of DNA *in vitro* and have been reported to associate with telomeres *in vivo* [15–17]. It has been demonstrated that hnRNP A1 functions as a positive regulator of telomere length *in vivo* [15,18], although conflicting results have also been reported [19]. In contrast, hnRNP A3 has been reported as a negative regulator of telomere length maintenance [20]. However, despite these findings, little is known about the functional overlap or antagonism among members of the hnRNP A/B family in telomere maintenance.

Evidence suggests that hnRNPs A/B play an important role in cell proliferation. For example, the proliferation-dependent expression of hnRNP A1 and A2 has been reported in various cell types [21,22], and while transient RNAi-induced suppression of hnRNP A1, A2, and A3 alone does not appear to affect proliferation, simultaneous suppression of hnRNP A1/A2, A1/A3, or A2/A3 has been shown to significantly reduce the rate of proliferation in a number of different cancer cells [23,24]. Interestingly, the simultaneous suppression of hnRNP A1/A2 has also been shown to induce apoptosis in cancer cells, but not in normal mortal cells [24]. However, the molecular basis of this differential induction of apoptosis in cancer cells remains unknown.

hnRNP A1 and A2 are known to bind to single-stranded telomeric repeat sequences of DNA and to telomeric repeat-containing RNA (TERRA) [16,18,25–27]. Such binding activity also affects the binding of other proteins to telomeric G-rich single strands present in the displaced strand of the t-loop structure or in the 3' overhang [28,29], thereby affecting telomere maintenance. hnRNP A1 has also been shown to act in association with TERRA and POT1 (protection of telomeres 1) to displace RPA (replication protein A) from telomeric single-stranded DNA, suggesting that hnRNP A1 promotes telomere-capping to preserve genomic integrity [30]. Moreover, cells lacking hnRNP A1 exhibit impaired RPA-to-POT1 switching, resulting in DDR at telomeres during mitosis as well as telomere fragility [31]. Although hnRNP A2 is thought to possess activity similar to that of hnRNP A1 in displacing RPA from telomeric single-stranded DNA [30], it is unknown whether they share functional redundancy in telomere maintenance *in vivo*. In view of the fact that simultaneous suppression of hnRNP A1/A2 is required to inhibit cell proliferation and induce apoptosis in cancer cells, but not in normal mortal cells [24], and the fact that telomerase is expressed in cancer cells but not normal mortal cells, we hypothesized that the hnRNP A1/A2 are involved in telomere maintenance in telomerase-expressing cells. In this study, we employed transient RNA interference (RNAi)-mediated suppression of hnRNP A1 or A2 to determine the role of these two proteins in telomere maintenance and to whether telomere maintenance activity requires the expression of telomerase.

## 2. Results

### 2.1. Induction of DDR by Depletion of both hnRNP A1 and A2 in Cancer Cells

Evidence suggests that hnRNP A1 and A2 share redundant functions in cell proliferation. For example, although transient RNAi-mediated suppression of hnRNP A1 or A2 alone does not appear to inhibit cell proliferation, simultaneous suppression has been shown to reduce the proliferation rate and induce apoptosis in a number of different types of cancer cells [23,24,32]. Moreover, in view of recent findings establishing an important role for hnRNP A1 and A2 in telomere maintenance [30,31], it is likely that the functional redundancy of hnRNP A1 and A2 in cell proliferation may be related to their role in maintaining functional telomeres. To address this, we examined whether DDR is induced by the depletion of hnRNP A1 or A2, since it is known to be triggered by dysfunctional telomeres. Cancer cell lines A549, CL1-5, and SAS were transfected with siRNAs targeting hnRNP A1 and A2, and the expression levels of hnRNP A1, A2, and  $\gamma$ H2AX (a DDR marker), were assessed by western blotting. As shown in Figure 1A, treatment of cells with siRNAs targeting hnRNP A1 and hnRNP A2 effectively reduced levels of the targeted proteins. Meanwhile, depletion of hnRNP A1 or A2 alone did not induce  $\gamma$ H2AX, unlike the simultaneous suppression of hnRNP A1 and A2 (hnRNP A1/A2), which did so in all 3 cancer cell lines. Under the same experimental conditions, we also confirmed earlier observations that the simultaneous depletion of hnRNP A1 and A2, but not the depletion of hnRNP A1 or A2 alone, is required for the inhibition of cell proliferation and induction of apoptosis in cancer cells [32]. We also revealed that telomere lengths in the hnRNP A1/A2-depleted cells were unaltered (Figure 1B).

To further understand the induction of DDR in hnRNP A1/A2-depleted cells, we chose to conduct detailed studies on one cancer cell line, A549. First, we performed immunofluorescence staining to examine the distribution of  $\gamma$ H2AX in A549 cells. Representative results are shown in Figure 1C.  $\gamma$ H2AX foci were detected in less than 2% of nuclei of A549 cells transfected with siNT, siA1, or siA2, but were present in about 40% of cells transfected with siA1/A2 (Figure 1D).

### 2.2. Co-Localization of $\gamma$ H2AX with MDC1 and Telomeres

Because  $\gamma$ H2AX foci are known to associate with DNA double-strand breaks (DSBs) and DNA DSB repair proteins, we examined whether the  $\gamma$ H2AX foci induced in cells depleted of hnRNP A1/A2 also co-localized with MDC1 (mediator of DNA damage checkpoint 1), a DNA DSB repair protein. As shown in Figure 2A, while a weak staining of MDC1 was detected in the nuclei of A549 cells transfected with siNT, siA1, or siA2, strong staining was observed in cells transfected with siA1/A2 and in those treated with etoposide, used as a positive control. More than 60% of  $\gamma$ H2AX foci were co-localized with MDC1 foci in cells depleted of hnRNP A1/A2 and in etoposide-treated cells, suggesting that  $\gamma$ H2AX foci are associated with DNA DSBs (Figure 2A).

To test the possibility that dysfunctional telomeres are produced in cells depleted of hnRNP A1/A2, we also examined whether the induced  $\gamma$ H2AX foci were co-localized with telomeres. Representative results of the co-localization of  $\gamma$ H2AX foci with telomeric DNA are presented in Figure 2B. In A549 cells depleted of both hnRNP A1 and A2, 1–5  $\gamma$ H2AX foci co-localized with telomere DNA in about 40% of  $\gamma$ H2AX-positive nuclei.



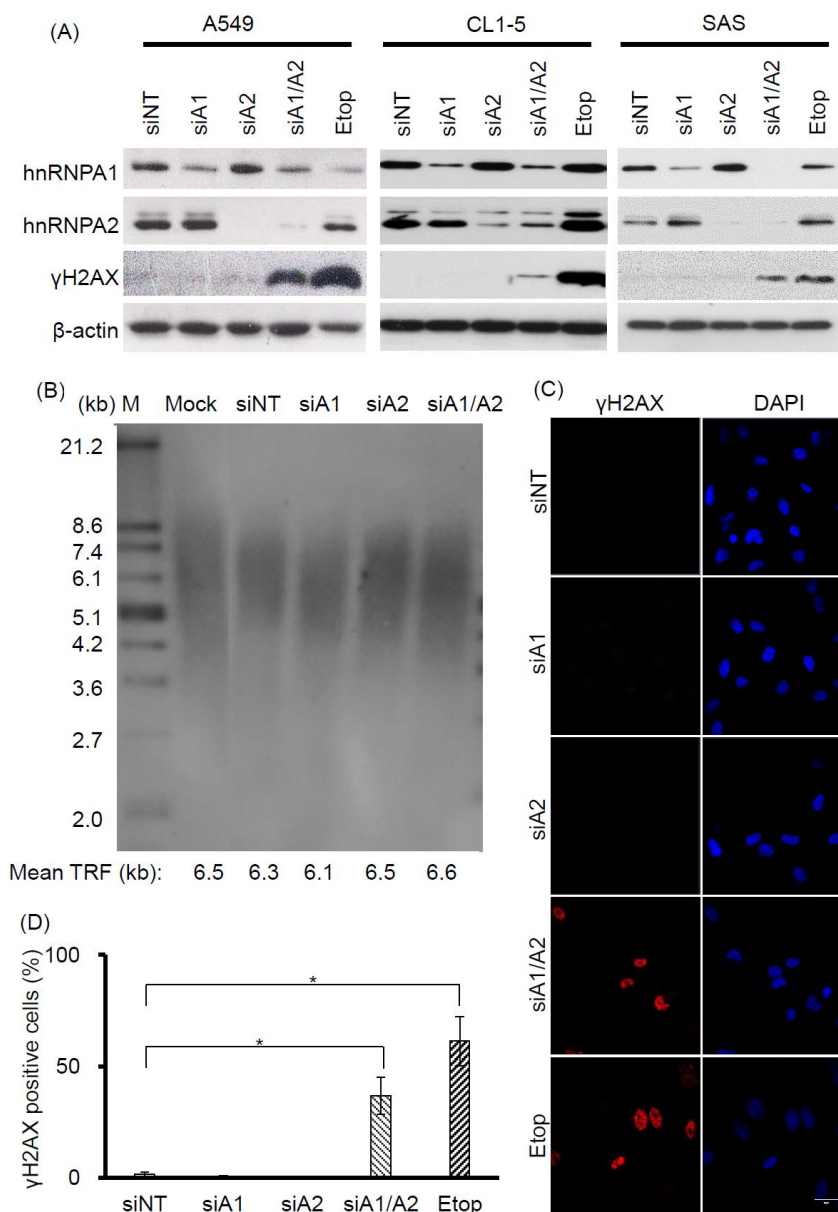


**Figure 1.** Effects of depleting hnRNP A1 and/or hnRNP A2 on induction of DNA damage response (DDR). **(A)** Induction of  $\gamma$ H2AX. A549, CL1-5, and SAS cells were transfected with siRNA targeting hnRNP A1 (siA1), hnRNP A2 (siA2), both hnRNP A1 and A2 (siA1/A2), or with a non-targeting sequence (siNT) for 72 h. Cell lysates were analyzed for expression levels of hnRNP A1, hnRNP A2, and  $\gamma$ H2AX by western blotting.  $\beta$ -Actin served as a loading control, and cells treated with 50  $\mu$ M etoposide (Etop) for 12 h served as a positive control; **(B)** Effect of depleting hnRNP A1 and hnRNP A2 on telomere length in A549 cells. A549 cells were transfected with siRNA targeting hnRNP A1 (siA1), hnRNP A2 (siA2), both hnRNP A1 and A2 (siA1/A2), or with a non-targeting sequence (siNT) for 96 h. The genomic DNA was purified and subjected to telomeric restriction fragment (TRF) length assay, as described in the materials and methods section. Mean TRF length is indicated at the bottom of each lane. Lane M: molecular weight markers. Mock was treated with transfection reagent only; **(C)** A549 cells were fixed and immunostained for  $\gamma$ H2AX (red), and nuclei were counterstained with 4',6-diamidino-2-phenylindole (DAPI, blue). Cells treated with 50  $\mu$ M etoposide (Etop) for 12 h served as a positive control. The scale bar equals 20  $\mu$ m. **(D)** The percentage of nuclei showing positive staining for  $\gamma$ H2AX was determined from an analysis of ~100 nuclei from each experiment. Positive  $\gamma$ H2AX staining is operationally defined here as the detection of 3 or more  $\gamma$ H2AX foci in a nucleus. Data shown are mean  $\pm$  SD from 3 independent experiments. \*  $p < 0.05$  versus siNT control.

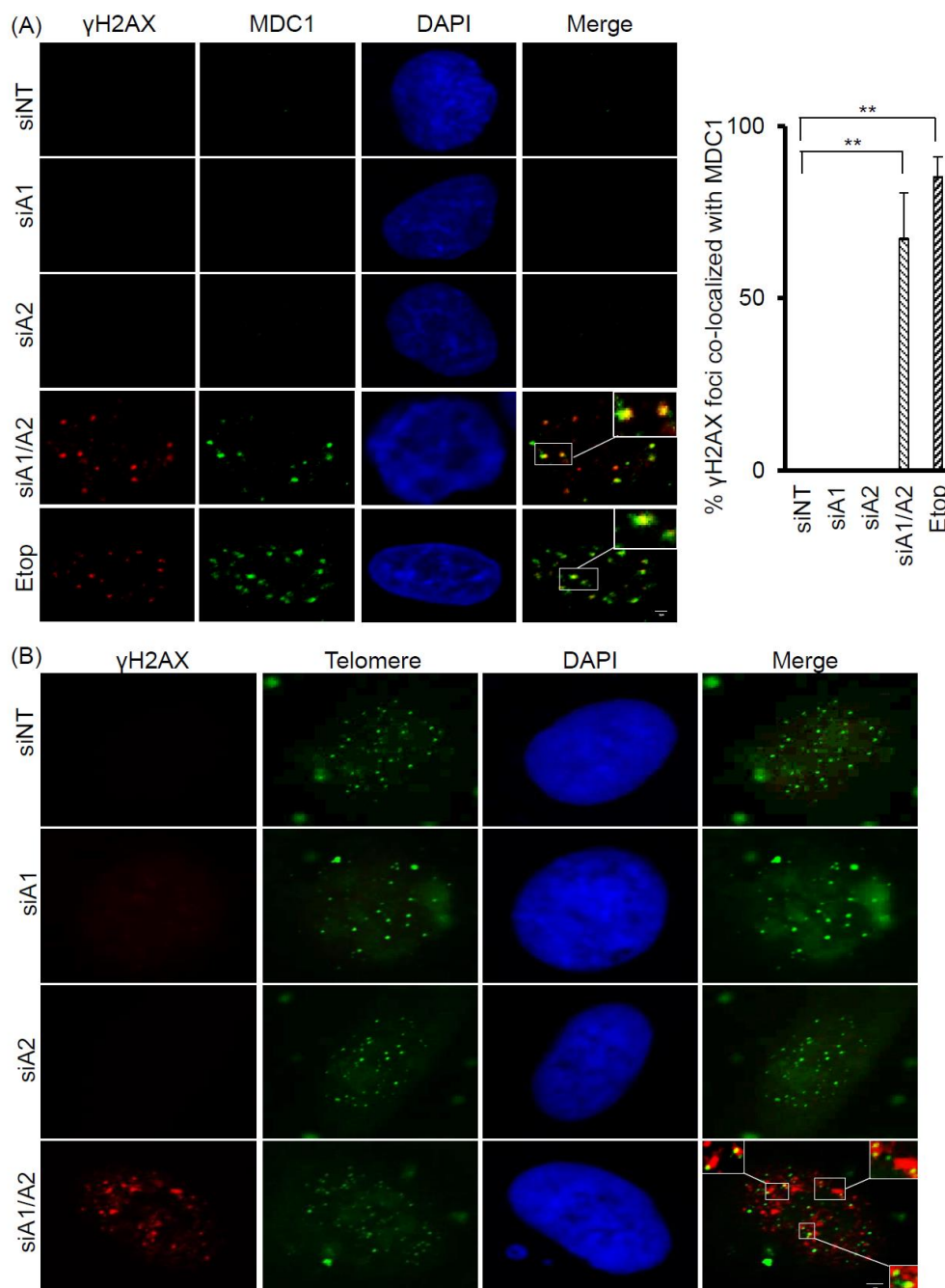


**Figure 2.** Co-localization of  $\gamma$ H2AX with MDC1 and telomere DNA in A549 cells depleted of hnRNP A1/A2. **(A)** A549 cells were transfected with siRNA targeting hnRNP A1 (siA1), hnRNP A2 (siA2), both hnRNP A1 and A2 (siA1/A2), or with a non-targeting sequence (siNT) for 72 h. Cells were fixed and immunostained for  $\gamma$ H2AX (red) and MDC1 (green), and nuclei were counterstained with DAPI (blue). A549 cells treated with 50  $\mu$ M etoposide (Etop) for 12 h served as a positive control. The percentage of  $\gamma$ H2AX foci that co-localized with MDC1 (see marked squares for examples) was determined from 50  $\gamma$ H2AX-positive nuclei; data from 3 experiments are summarized in the right panel. \*\*  $p < 0.01$  versus siNT control; The bar equals 2  $\mu$ m. **(B)** Cells were stained for  $\gamma$ H2AX (red) and then for telomeric DNA using FISH with fluorescein isothiocyanate (FITC)-conjugated oligonucleotides (green).  $\gamma$ H2AX foci that colocalized with telomere DNA are illustrated in the boxed regions. The scale bar equals 2  $\mu$ m.

### 2.3. Failure of Apoptosis Inhibition to Prevent Formation of Dysfunctional Telomeres in Cells Depleted of hnRNP A1/A2

Our observation that  $\gamma$ H2AX foci were co-localized with telomeres suggests that cells depleted of hnRNP A1/A2 produce dysfunctional telomeres. Because dysfunctional telomeres are known to induce apoptosis [29,33], and because apoptotic DNA fragmentation is known to result in  $\gamma$ H2AX phosphorylation [34], this finding suggests that the induction of apoptosis and inhibition of cell proliferation following simultaneous depletion of hnRNP A1/A2 [23,24,32] is caused primarily by dysfunctional telomeres. Alternatively, the formation of dysfunctional telomeres and the induction of apoptosis may also be independent of each other. To address this, we examined the effects of apoptosis inhibition on cell proliferation and the induction of the DDR indicator  $\gamma$ H2AX. A549 cells were transfected with siRNAs targeting hnRNP A1 and/or A2 for 48 h then cultured in the presence or absence of the pan-caspase inhibitor Z-VAD-FMK (carbobenzoxy-valyl-alanyl-aspartyl-[O-methyl]-fluoromethylketone) for the indicated times. The transfected cells were then analyzed for activation of apoptosis, expression of  $\gamma$ H2AX, and cell proliferation. As shown in Figure 3A, no apoptosis was detected in cells transfected with siNT, siA1 or siA2. In contrast, the activation of caspase-7 and -8, cleavage of poly-(ADP-ribose) polymerase (PARP), and increased levels of  $\gamma$ H2AX were detected in cells depleted of hnRNP A1/A2. Moreover, in the presence of Z-VAD-FMK,  $\gamma$ H2AX levels were greatly reduced in association with an inhibition of caspase-7 and -8 activation and PARP cleavage, suggesting that  $\gamma$ H2AX formation is strongly associated with the induction of apoptosis. However, the inhibition of apoptosis by Z-VAD-FMK did not restore the proliferative capacity of cells depleted of hnRNP A1/A2 (Figure 3B), suggesting that the inhibition of cell proliferation caused by depletion of hnRNP A1/A2 is not primarily attributable to apoptosis. Importantly, although the number of  $\gamma$ H2AX foci in hnRNP A1/A2-depleted cells was greatly reduced by an inhibition of apoptosis, the formation of dysfunctional telomeres, as detected by the co-localization of  $\gamma$ H2AX with TRF2 (telomeric repeat binding factor 2) in  $\gamma$ H2AX-positive nuclei, was unaffected (Figure 3C). To rule out the possibility that the observed failure to restore cell proliferation capacity was attributable to late inhibition of apoptosis, we examined the effects of inhibiting apoptosis at the beginning of siRNA transfection. Similar to the results shown in Figure 3, an early inhibition of apoptosis also failed to alleviate the production of dysfunctional telomeres and inhibit cell proliferation (Figure 4) in hnRNP A1/A2-depleted A549 cells. These results are consistent with the hypothesis that the formation of dysfunctional telomeres is the primary cause of the inhibition of cell proliferation induced by depletion of hnRNP A1/A2.

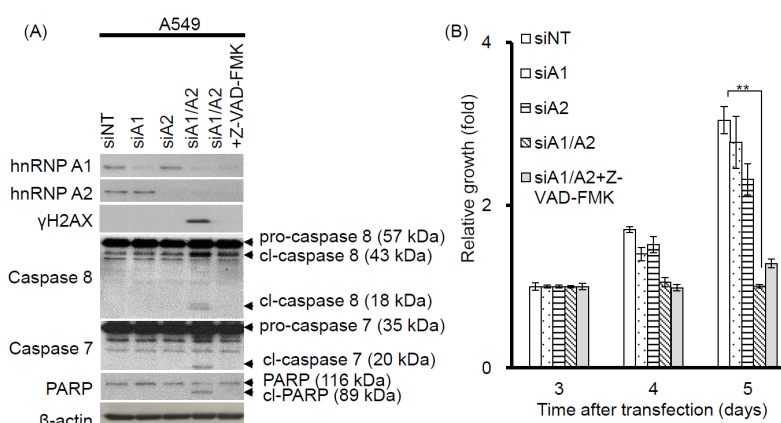
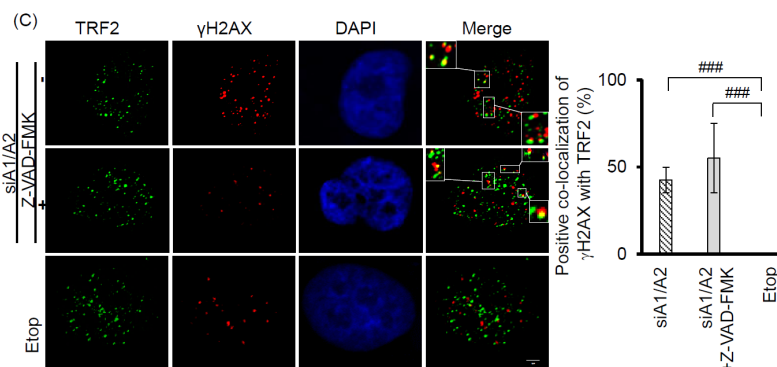
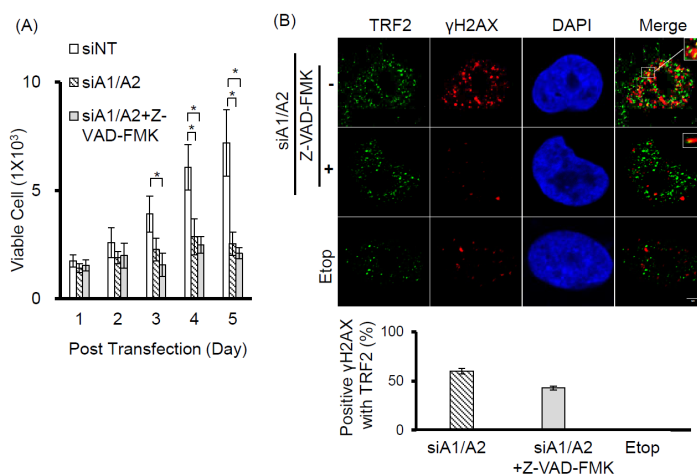


Figure 3. Cont.



**Figure 3.** Effects of the apoptosis inhibitor Z-VAD-FMK on the induction of apoptosis, cell proliferation, and DDR. (A) A549 cells were transfected with siRNAs targeting hnRNP A1 (siA1), hnRNP A2 (siA2), both hnRNP A1 and A2 (siA1/A2), or with a non-targeting sequence (siNT) for 48 h. Cells transfected with siA1/A2 were cultured in the presence or absence of 20 mM Z-VAD-FMK for 24 h, while other transfected cells were cultured in the absence of Z-VAD-FMK for 24 h. Cell lysates were then analyzed for expression of hnRNP A1, A2, and γH2AX, as well as for the cleavage products of caspase-7 (cl-caspase-7), caspase-8 (cl-caspase-8), and PARP (cl-PARP) by western blotting. β-Actin served as a loading control; (B) Treated cells were cultured in regular medium and monitored for cell proliferation using trypan blue staining. The results shown are pooled from 2 independent experiments. \*\*  $p < 0.01$ , significant difference from siNT control; (C) Cells were fixed and immunostained for γH2AX (red) and TRF2 (Telomeric repeat-binding factor 2, green), and nuclei were counterstained with DAPI (blue). γH2AX foci that co-localized with TRF2 are indicated in the boxed regions. A549 cells treated with 50 μM etoposide (Etop) for 12 h served as a positive control. The percentage of nuclei showing co-localization of γH2AX with TRF2 was determined from analysis of 50 γH2AX-positive nuclei from each experiment. The results shown in the right panel are mean ± SD from 3 independent experiments. ###  $p < 0.001$ , significant difference from etoposide control. The scale bar equals 2 μm.



**Figure 4.** Effects of early apoptosis inhibition on DDR and cell proliferation. (A) A549 cells were transfected with siRNA targeting sequences for both hnRNP A1 and A2 (siA1/A2) in the presence or absence of 20 mM of Z-VAD-FMK. Cells transfected with a non-target sequence (siNT) in the absence of Z-VAD-FMK served as a control. The transfected cells were cultured and monitored for cell proliferation using trypan blue staining. The data shown are pooled from 2 independent experiments; (B) After 72 h of transfection, the cells were fixed and immunostained for γH2AX (red) and TRF 2 (green), and the nuclei were counterstained with DAPI (blue). The foci of γH2AX that co-localized with TRF2 are indicated by marked squares. Cells treated with 50 μM of etoposide (Etop) for 12 h served as a negative control. The percentage of positive co-localization of γH2AX with TRF2 was determined from analysis of 30 γH2AX-positive nuclei from each experiment. The data shown in the bottom panel are from 2 independent experiments. \*  $p < 0.05$  versus siNT control. The scale bar equals 2 μm.



#### 2.4. Telomerase Dependence of the Induction of DDR and Dysfunctional Telomeres in Cells Depleted of hnRNP A1/A2

Although the depletion of hnRNP A1/A2 has been shown to inhibit cell proliferation in most cancer cells, it does not inhibit cell proliferation in normal mortal human cells [24]. One reason for this is thought to be the major differences between normal mortal cells and cancer cells in telomerase activity, which is expressed in most cancer cells, but not in normal somatic cells [35,36]. To test the hypothesis that the expression of telomerase is required for the inhibition of cell proliferation by the depletion of hnRNP A1/A2, we examined the effects of telomerase expression on the sensitivity of normal mortal fibroblasts to the depletion of hnRNP A1 and/or A2. As shown in Figure 5A, while normal fibroblasts HFF3, MRC5, and HFB cells expressed little or no telomerase activity, ectopic expression of hTERT resulted in high expression of telomerase activity comparable to that of cancer cells (A549). Moreover, treatment of these cells with siRNAs targeting hnRNP A1 and/or hnRNP A2 effectively reduced levels of the targeted proteins (Figure 6A). Meanwhile, the depletion of hnRNP A1 or A2 (siA1 or siA2) alone did not inhibit cell proliferation of mortal or hTERT-immortalized normal fibroblasts HFF3, MRC5, or HFB (Figure 5B–D), unlike simultaneous suppression (siA1/A2), which resulted in significant inhibition of cell proliferation in hTERT-immortalized normal fibroblasts, but not mortal fibroblasts (Figure 5B–D). These results confirm earlier findings [24] that simultaneous suppression of hnRNP A1/A2 does not inhibit cell proliferation in mortal normal cells.

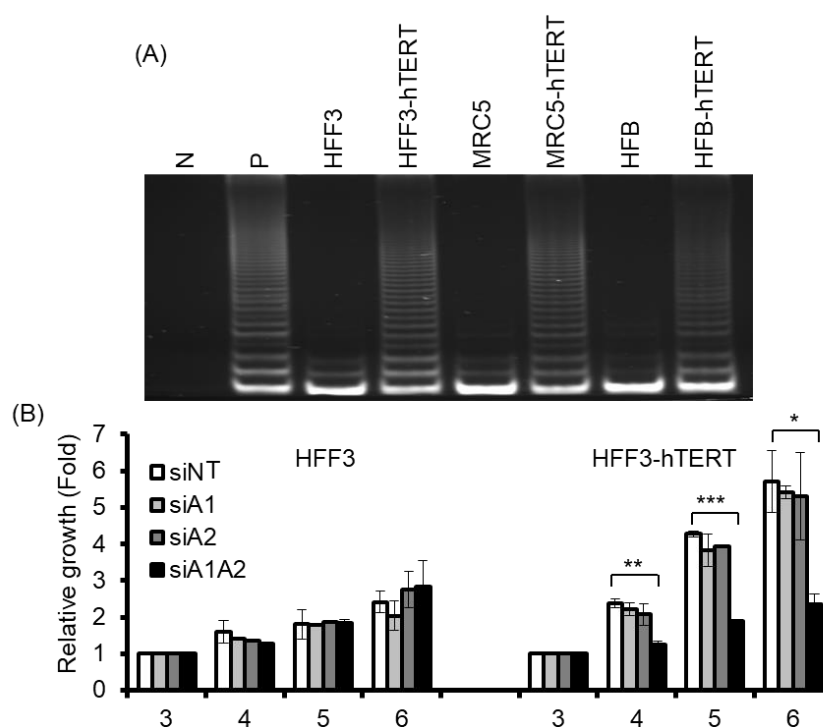
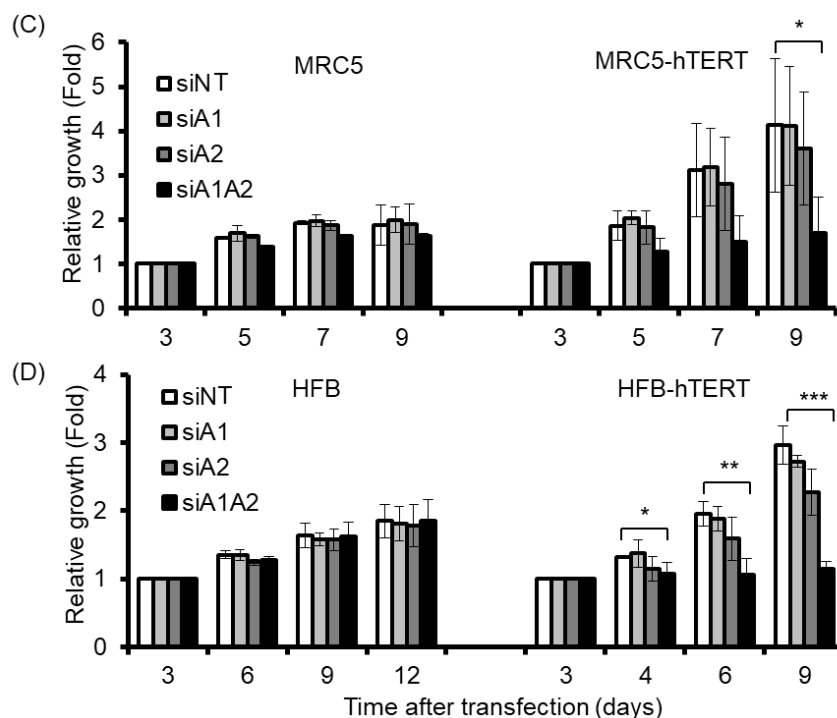
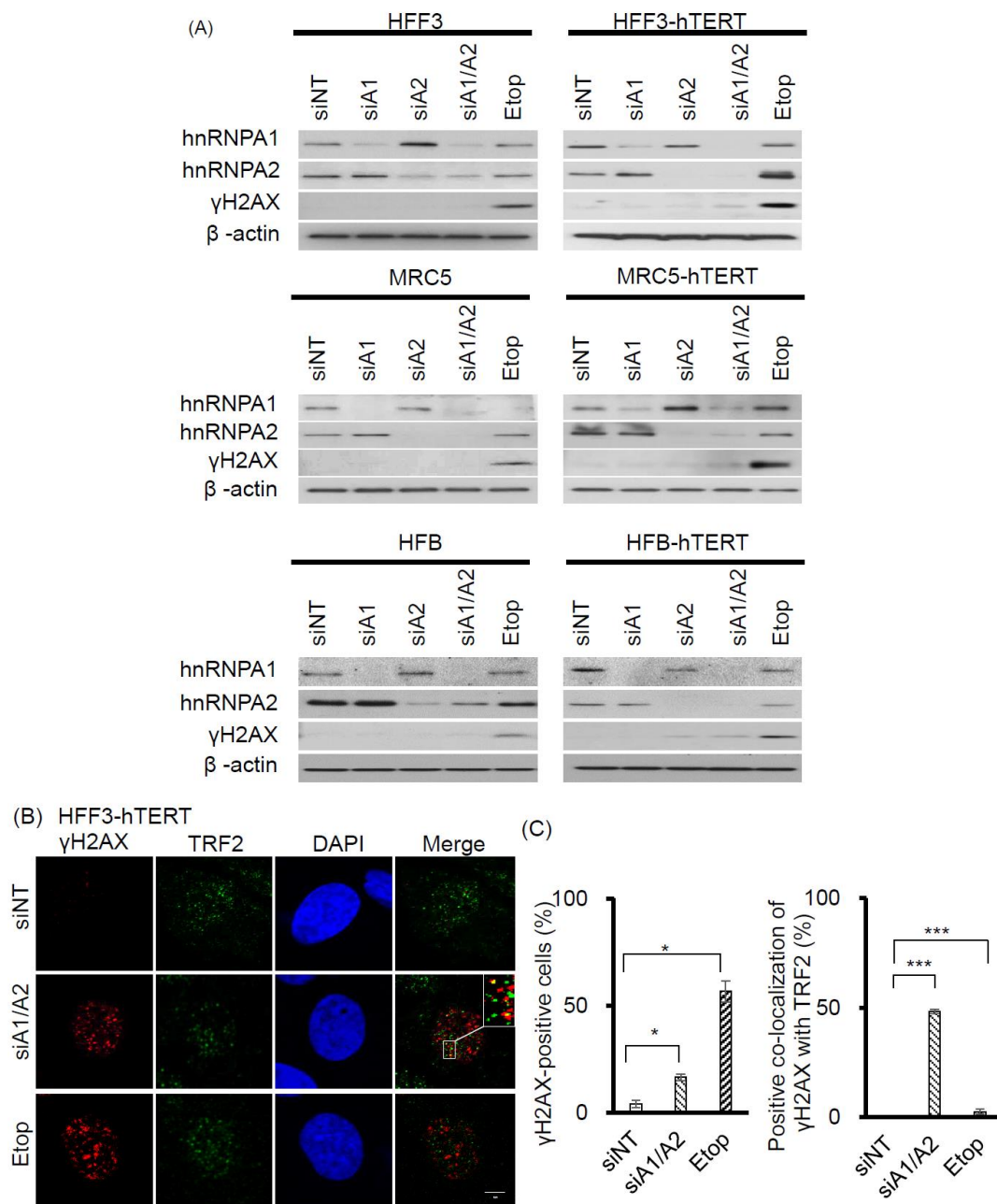


Figure 5. Cont.



**Figure 5.** Effects of suppressing hnRNP A1 and/or A2 on cell proliferation of normal fibroblasts and hTERT-immortalized normal fibroblasts. (A) Cell lysates from normal fibroblasts (HFF3, MRC5, and HFB) and hTERT-immortalized normal fibroblasts (hFF3-hTERT, MRC5-hTERT, and HFB-hTERT) were assayed for telomerase activity, as described in the materials and methods section. N represents a negative control with no cell extract, while P is a positive control with cell extract from telomerase-positive A549 cells; (B–D) Normal fibroblasts and hTERT-immortalized normal fibroblasts were transfected with siRNA targeting hnRNPA1 (siA1), hnRNPA2 (siA2), both hnRNP A1 and A2 (siA1/A2), or with a non-targeting sequence (siNT) for 72 h. Transfected cells were cultured in regular medium and monitored for cell proliferation using trypan blue staining. The results shown are pooled from 2 independent experiments. \*  $p < 0.05$ , \*\*  $p < 0.01$  and \*\*\*  $p < 0.001$  versus siNT control.

Interestingly, the expression of telomerase activity in normal fibroblasts also rendered these cells sensitive to the inhibition of proliferation following the simultaneous suppression of hnRNP A1/A2 (Figure 5). To determine whether this inhibition of cell proliferation in hTERT-immortalized normal fibroblasts was attributable to the formation of dysfunctional telomeres, we examined the induction and localization of  $\gamma$ H2AX in hnRNP A1/A2-depleted cells. As shown in Figure 6A, the depletion of hnRNP A1 or A2 (siA1 or siA2) alone did not induce the formation of  $\gamma$ H2AX in normal mortal or hTERT-immortalized fibroblasts HFF3, MRC5, or HFB (Figure 6A), the only exception being very weak induction of  $\gamma$ H2AX in the siA2-treated HFB-hTERT cells. Meanwhile, the simultaneous suppression of hnRNP A1 and A2 (siA1/A2) resulted in the induction of low levels of  $\gamma$ H2AX in normal hTERT-immortalized fibroblasts, but not in normal mortal fibroblasts. To determine whether this induction of  $\gamma$ H2AX was associated with dysfunctional telomeres, we examined the localization of  $\gamma$ H2AX in hnRNP A1/A2-depleted HFF3-hTERT cells by immunofluorescence staining. Representative results of  $\gamma$ H2AX foci and TRF2 protein co-localization experiments are shown in Figure 6B, with a summary shown in Figure 6C. Although the percentage of  $\gamma$ H2AX-positive nuclei in hnRNP A1/A2-depleted hTERT-HFF3 cells (Figure 6C, left panel) was less than that observed in A549 cells (Figure 1C), a similar degree of  $\gamma$ H2AX-TRF2 co-localization was observed in  $\gamma$ H2AX-positive nuclei from both hnRNP A1/A2-depleted hTERT-HFF3 (Figure 6C, right panel) and A549 cells (Figure 3C). These findings suggest that dysfunctional telomeres are produced in hTERT-HFF3 cells depleted of hnRNP A1/A2.



**Figure 6.** Effects of suppressing hnRNP A1 and/or A2 on DDR in normal fibroblasts and hTERT-immortalized normal fibroblasts. (A) Normal fibroblasts (HFF3, MRC5, and HFB) and hTERT-immortalized normal fibroblasts (HFF3-hTERT, MRC5-hTERT, and HFB-hTERT) were transfected with siRNA targeting hnRNPA1 (siA1), hnRNPA2 (siA2), both hnRNP A1 and A2 (siA1/A2), or with a non-targeting sequence (siNT). After 72 h, cell lysates were analyzed for expression levels of hnRNP A1, hnRNP A2, and  $\gamma$ H2AX by Western blotting.  $\beta$ -Actin served as a loading control, and cells treated with 50  $\mu$ M etoposide (Etop) for 12 h served as a positive control; (B) Transfected HFF3-hTERT cells were fixed and immunostained for  $\gamma$ H2AX (red) and TRF2 (green), and nuclei were counterstained with DAPI (blue). HFF3-hTERT cells treated with 50  $\mu$ M etoposide (Etop) for 12 h were included as a control; the scale bar equals 5  $\mu$ m. (C) The percentage of nuclei positive for  $\gamma$ H2AX staining was determined from analysis of ~100 nuclei from each experiment; the data shown in the left panel are from 2 independent experiments. The percentage of  $\gamma$ H2AX co-localized with TRF2 was determined from analysis of 50  $\gamma$ H2AX-positive nuclei from each experiment; the results shown in the right panel are from 2 independent experiments. \*  $p < 0.05$  and \*\*\*  $p < 0.001$  versus siNT control.

### 3. Discussion

In this study, we showed that the simultaneous depletion of hnRNP A1 and A2, but not the depletion of hnRNP A1 or A2 alone, induces dysfunctional telomeres and DDR in cancer cells (Figures 1 and 2). The dysfunctional telomeres produced in hnRNP A1/A2 depleted cancer cells were not attributed to short telomeres (Figure 1B), suggesting that there was no dysregulated erosion of telomeres. Because dysfunctional telomeres are known to trigger apoptosis and cell senescence, it is likely that the inhibition of proliferation and induction of apoptosis in cancer cells [23,24,32] following a simultaneous depletion of hnRNP A1/A2 is caused primarily by the formation of dysfunctional telomeres. Consistent with this, we found that the inhibition of apoptosis did not alleviate the production of dysfunctional telomeres (Figures 3C and 4B) or the inhibition of cell proliferation (Figures 3B and 4A).

Our finding that dysfunctional telomeres are produced only in cells depleted of both hnRNP A1 and A2 is consistent with the hypothesis that these 2 proteins perform complementary functions in telomere maintenance. However, the depletion of hnRNP A1/A2 did not inhibit cell proliferation in normal mortal human cells [24]. One reason for this is may be the major difference between normal mortal cells and cancer cells in telomerase activity, which is expressed in most cancer cells, but not in normal mortal cells. We therefore postulate that, in the presence of telomerase activity, the single-strand G-rich 3' overhang is extended by telomerase, replicated by lagging-strand DNA synthesis, and assembled into functional telomeres (Figure 7). It is likely that hnRNP A1/A2 and TERRA function to displace RPA [30], facilitating a lagging-strand DNA synthesis and/or the assembly of functional telomeres. Consistent with this, we revealed that, while a simultaneous depletion of hnRNP A1/A2 did not induce DDR or inhibit cell proliferation in mortal HFF3, MRC5, or HFB cells, an immortalization of these cells by ectopic expression of hTERT rendered these telomerase-expressing normal cells sensitive to the inhibitory effects of simultaneous depletion (Figure 5). In this context, it is worthy to note that although dysfunctional telomeres are produced in the hTERT-immortalized HFF3 by simultaneous depletion of hnRNP A1/A2 (Figure 6), no apoptosis induction was observed in these depleted cells (unpublished results). It is likely that the dysfunctional telomeres produced in hTERT-immortalized normal cells only induce cell senescence. Lastly, it should be noted that some cancer cells employ alternative lengthening of telomeres (ALT) during telomere length maintenance. ALT is a homology-directed recombination-dependent replication pathway that utilizes telomeric templates for synthesis [37]; however, its precise protein requirements remain unknown. Whether or not hnRNP A1/A2 are essential components of the ALT therefore requires further analysis.

This study has substantiated for a role of hnRNP A/Bs in telomere maintenance. While the ability of hnRNP A/Bs to bind to the single-stranded telomeric repeat sequence of DNA and TERRA may account for the major function of these proteins in telomere maintenance, little is known if these proteins may also be involved in the regulation of hTERT expression or the recruitment of telomerase to telomeres. The hnRNP A1 has been reported to interact with the human telomerase holoenzyme and stimulate telomerase activity [15,18]. A splice variant of hnRNP A2, hnRNP A2\*, has been shown to bind telomeric DNA and telomerase in vitro and to unfold telomeric G-quadruplex DNA to exposes 5 nt of the 3' telomere tail [38]. Therefore, both hnRNP A1 and hnRNP A2 appear to participate at multiple steps of telomere maintenance.

The specific expression of telomerase in most cancers suggests the potential application of telomerase targeting in cancer therapy. Various telomerase-based therapeutic strategies have been explored in the past, such as immunotherapy, hTERT-promoter-based gene therapy, and the inhibition of telomerase activity [39–41]. Our demonstration of a role for hnRNP A1/A2 in telomerase-dependent telomere maintenance therefore suggests a novel approach for telomerase-based cancer therapy. The inhibition of telomerase-dependent telomere maintenance (Figure 7) is anticipated to result from the formation of dysfunctional telomeres, which can rapidly inhibit cell proliferation and induce apoptosis only in telomerase-positive cancer cells. A detailed molecular understanding of telomerase-dependent telomere maintenance as well as an analysis of the agents that specifically interfere with this process should therefore be examined in the future.



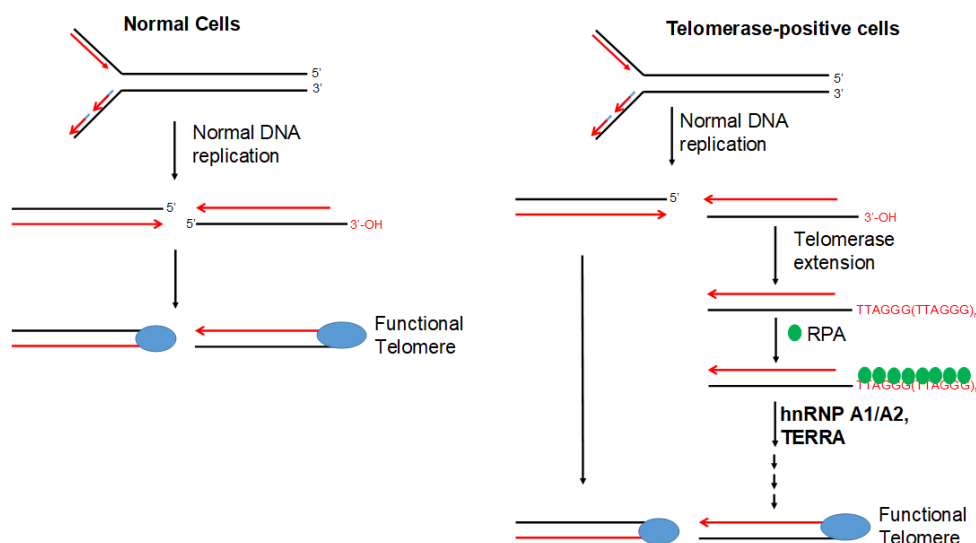


**Figure 7.** Model of telomerase-dependent maintenance of telomeres. Normal cells do not express telomerase, and the ends of their chromosomes are replicated by regular DNA replication enzymes before being assembled into functional telomeres. In telomerase-positive cells (e.g., cancer cells), the 3' G-rich single-strand tail can be extended by synthesis of TTAGG repeats, which are thought to be initially bound by RPA. The extended long G-rich strand subsequently serves as a template for lagging-strand DNA synthesis before being assembled into a functional telomere. In this model, hnRNP A1/A2 is thought to facilitate lagging-strand synthesis and/or assembly of a functional telomere structure, possibly by acting together with TERRA to displace RPA.

## 4. Materials and Methods

### 4.1. Culture Media, Antibodies, and Oligonucleotides

The culture media and fetal bovine serum were purchased from Life Technologies (Grand Island, NY, USA). The antibodies against the following proteins were obtained from the indicated vendors: cleaved PARP (Asp214) and  $\gamma$ H2AX (9718), (Cell Signaling Technology, Temecula, CA, USA); hnRNP A1 (F-8) and hnRNP A2 (EF-67) (Santa Cruz Biotechnology, Inc., Santa Cruz, CA, USA); TRF2 (Millipore, Billerica, MA, USA);  $\beta$ -actin (Sigma-Aldrich, St. Louis, MO, USA); MDC-1 (M2444) (Sigma-Aldrich); caspase-7 (9492), -8 (9746), and PARP (9542) (Cell Signaling Technology). The FITC 488-OO-(CCCTAA)<sub>3</sub> PNA probe (F1009) was obtained from Panagene (Daejeon, Korea), and etoposide (E1383) was purchased from Sigma-Aldrich. Superscript III reverse transcriptase, TRIzol reagent, and antibiotics were obtained from Gibco-BRL (San Francisco, CA, USA). The broad-spectrum caspase inhibitor Z-VAD-FMK was purchased from Promega (Fitchburg, WI, USA). Gel electrophoresis reagents were obtained from Bio-Rad (Berkeley, CA, USA).

### 4.2. Cell Lines and Culture

The NSCLC cell line, A549, was obtained from the American Type Culture Collection (Manassas, VA, USA). The CL1-5 cell line was derived from NSCLC CL1-0 cells by the selection of increased invasion ability using a Transwell plates [42]. CL1-5 and A549 cells express wild-type EGFR [43]. Normal human lung fibroblasts (MRC5) were purchased from The Food Industry Research and Development Institute in Taiwan. Human skin fibroblasts (HFB) were kindly provided by Dr. P. C. Yang of Taiwan University. The immortalization of MRC5 and HFB cells by ectopic expression of hTERT (human telomerase reverse transcriptase) was carried out as described previously for normal human foreskin fibroblasts (HFF3) [44]. Normal human fibroblasts (HFF3, MRC5, HFB) and hTERT-immortalized normal fibroblasts (HFF3-hTERT, MRC5-hTERT, and HFB-hTERT) were cultured in Dulbecco's modified Eagle's medium supplemented with 10% fetal bovine serum, 100 units/mL

penicillin, 100 units/mL streptomycin, and 0.25 mg/mL amphotericin. Culture of the human lung cancer cell lines A549 and CL1-5, and human tongue squamous carcinoma cell line SAS was carried out as described previously [32,45]. Cells were grown at 37 °C in a humidified 5% CO<sub>2</sub> incubator.

#### 4.3. RNA Interference

Target genes were downregulated by RNAi-mediated inhibition of mRNA expression using a mixture of 4 small interfering RNAs (siRNAs) for each target gene (ON-TARGETplus SMARTpool; Dharmacon, Lafayette, CO, USA) [32]. The siGENOME nontargeting siRNA pool (Dharmacon) was used as a control. The siRNA sequences were run through BLAST searches to ensure that each siRNA targeted only 1 human gene. The 4 siRNAs targeting human hnRNP A1 mRNA (GenBank accession No. NM\_002136) covered the following sequences: A1-1, CGGAAACCUUGGUGUAGUU (nucleotides 1545–1563); A1-2, GGGAAUGAAGCUUGUGUAU (nucleotides 1709–1727); A1-3, CAACUUCGUCGUGGAGGA (nucleotides 746–764); and A1-4, UAGAAUCCUUCAGGGUGA (nucleotides 1468–1486). The 4 siRNAs targeting hnRNP A2 mRNA (GenBank accession no. NM\_002137) covered the following sequences: A2-1, CGGUGGAAAUUUCGGACCA (nucleotides 825–843); A2-2, GCUGUUUGUUGGCGGAAUU (nucleotides 519–537); A2-3, GGAGAGUAGUUGAGCCAAA (nucleotides 443–461); and A2-4, GAGGAGGAUCUGAUGGAUA (nucleotides 863–881). Transfection was performed using Dharmafect 1 transfection reagent (Dharmacon) according to the manufacturer's instructions. Briefly, exponentially growing cells were seeded in regular growth medium without antibiotics at 40–50% confluence. After 24 h, cells were transfected with siRNAs and incubated for indicated times.

#### 4.4. Cell Proliferation Assays

Cell proliferation was assayed using an MTT assay kit (Sigma-Aldrich) and by staining with trypan blue (to determine the number of viable cells) as described previously [32].

#### Western Blotting

Western blotting was performed as described previously [32].

#### 4.5. Telomerase Assay

A PCR-based telomeric amplification protocol [35] was used to assay telomerase activity. The preparation of cell extracts, PCR amplification conditions, and analysis of PCR products by electrophoresis on polyacrylamide gel were performed as described previously [46].

#### 4.6. Determination of Telomere Length

Measurements of telomeric restriction fragment (TRF) length were performed using a TeloTAGGG Telomere Length Assay Kit (Roche, Basel, Switzerland) as described previously [20]. Quantification of telomere length was performed using ImageQuant software (GE Healthcare Life Sciences, Molecular Dynamics GmbH, Krefeld, Germany) and TELORUN.

#### 4.7. Immunofluorescence Confocal Microscopy

Immunofluorescence staining of target proteins was performed as described previously [17] with some modifications. Briefly, cells on slides were fixed in 4% paraformaldehyde, permeabilized, and stained with anti-γH2AX, anti-TRF2, or anti-MDC1 antibodies. After washing three times with phosphate buffer saline (PBS) containing 0.1% Triton X-100, cells were incubated with Texas red- or fluorescein isothiocyanate (FITC)-conjugated secondary antibodies (Molecular Probes, Eugene, OR, USA) for 45 min at room temperature. Staining of interphase nuclei of telomeres by fluorescence in situ hybridization (FISH) was performed as described previously [47] with some modifications. Briefly, dehydrated slides were overlaid with 0.8 µg/mL of FITC 488-OO-(CCCTAA)<sub>3</sub> PNA probe (Panagene) in the PNA hybridization solution (10 mM NaHPO<sub>4</sub>, 10 mM NaCl, 20 mM Tris, pH 7.5,

70% [*v/v*] formamide), incubated at 80 °C for 5 min, and hybridized at room temperature for 16 h. Slides were washed with PNA wash I (PBS/0.1% Tween-20), followed by PNA wash II (2X SSC/0.1% Tween-20), and mounted with Fluoroshield containing 4',6-diamidino-2-phenylindole (DAPI; F6057, Sigma-Aldrich). Immunofluorescence analyses were carried out under a confocal microscope (LSM 700; Carl Zeiss, Jena, Germany) and the results were processed using Zen 2009 software (Carl Zeiss).

#### 4.8. Statistics

All data are presented as mean  $\pm$  SD. Statistical comparison of multiple-groups results was performed by One-Way ANOVA (Analysis of Variance), followed by *post hoc* Mann–Whitney *U* test. A *p*-value of  $< 0.05$  was considered statistically significant.

### 5. Conclusions

This study reported for the first time that hnRNP A1 and A2 function in the maintenance of telomeres in telomerase-expressing cells, explaining earlier findings that simultaneous suppression of hnRNA1 and A2 inhibits cell proliferation and induces apoptosis in cancer cells, but not in normal mortal cells. Because the formation of dysfunctional telomeres rapidly inhibits cell proliferation and induces apoptosis, and because telomerase is expressed in most cancer cells but not in normal cells, inhibition of telomerase-dependent maintenance of telomeres could provide an attractive novel approach for telomerase-based cancer therapy.

**Author Contributions:** C.-Y.C. and T.-C.V.W. conceived the original idea. T.-H.W., C.-C.C., T.-C.V.W. and C.-Y.C. designed the experiments. Y.-C.H., Y.-H.L., W.-C.P., P.-R.H., C.-C.C. and T.-H.W. conducted the experiments and analyzed results. P.-R.H., Y.-C.H. and Y.-H.L. performed the bioinformatics analysis. C.-Y.C. and T.-C.V.W. wrote the manuscript, and T.-H.W. and C.-C.C. edited the manuscript.

**Funding:** This work was supported by grants from Chang Gung Memorial Hospital (CMRPD1F0452 to Chin-Chuan Chen, and CMRPF1G0121 to Chi-Yuan Chen), and the Ministry of Science and Technology, Taiwan (MOST 106-2320-B-255-006- to Chi-Yuan Chen). The funders had no role in the study design, data collection or analysis, the decision to publish, or manuscript preparation.

**Acknowledgments:** We would like to thank the Genomic Medicine Core Laboratory at Chang Gung Memorial Hospital at Lin-Kou, Taiwan, for assistance of data analysis. We thank Jang-Hau Lian for his excellent technical assistance.

**Conflicts of Interest:** The authors declare that they have no conflicts of interest.

### References

1. Blasco, M.A. The epigenetic regulation of mammalian telomeres. *Nat. Rev. Genet.* **2007**, *8*, 299–309. [[CrossRef](#)] [[PubMed](#)]
2. Liu, D.; O'Connor, M.S.; Qin, J.; Songyang, Z. Telosome, a mammalian telomere-associated complex formed by multiple telomeric proteins. *J. Biol. Chem.* **2004**, *279*, 51338–51342. [[CrossRef](#)] [[PubMed](#)]
3. Palm, W.; de Lange, T. How shelterin protects mammalian telomeres. *Ann. Rev. Genet.* **2008**, *42*, 301–334. [[CrossRef](#)] [[PubMed](#)]
4. Blackburn, E.H. Structure and function of telomeres. *Nature* **1991**, *350*, 569–573. [[CrossRef](#)] [[PubMed](#)]
5. Campisi, J.; Kim, S.H.; Lim, C.S.; Rubio, M. Cellular senescence, cancer and aging: The telomere connection. *Exp. Gerontol.* **2001**, *36*, 1619–1637. [[CrossRef](#)]
6. Hockemeyer, D.; Palm, W.; Else, T.; Daniels, J.P.; Takai, K.K.; Ye, J.Z.; Keegan, C.E.; de Lange, T.; Hammer, G.D. Telomere protection by mammalian POT1 requires interaction with TPP1. *Nat. Struct. Mol. Biol.* **2007**, *14*, 754–761. [[CrossRef](#)] [[PubMed](#)]
7. Kim, S.H.; Beausejour, C.; Davalos, A.R.; Kaminker, P.; Heo, S.J.; Campisi, J. TIN2 mediates functions of TRF2 at human telomeres. *J. Biol. Chem.* **2004**, *279*, 43799–43804. [[CrossRef](#)]
8. Sarthy, J.; Bae, N.S.; Scraftford, J.; Baumann, P. Human RAP1 inhibits non-homologous end joining at telomeres. *EMBO J.* **2009**, *28*, 3390–3399. [[CrossRef](#)]
9. Xin, H.; Liu, D.; Wan, M.; Safari, A.; Kim, H.; Sun, W.; O'Connor, M.S.; Songyang, Z. TPP1 is a homologue of ciliate TEBP-beta and interacts with POT1 to recruit telomerase. *Nature* **2007**, *445*, 559–562. [[CrossRef](#)]

10. Dreyfuss, G.; Matunis, M.J.; Pinol-Roma, S.; Burd, C.G. hnRNP proteins and the biogenesis of mRNA. *Ann. Rev. Biochem.* **1993**, *62*, 289–321. [[CrossRef](#)]
11. Pinol-Roma, S.; Choi, Y.D.; Matunis, M.J.; Dreyfuss, G. Immunopurification of heterogeneous nuclear ribonucleoprotein particles reveals an assortment of rna-binding proteins. *Genes Dev.* **1988**, *2*, 215–227. [[CrossRef](#)] [[PubMed](#)]
12. Han, S.P.; Tang, Y.H.; Smith, R. Functional diversity of the hnRNPs: Past, present and perspectives. *Biochem. J.* **2010**, *430*, 379–392. [[CrossRef](#)] [[PubMed](#)]
13. He, Y.; Smith, R. Nuclear functions of heterogeneous nuclear ribonucleoproteins A/B. *Cell. Mol. Life Sci.* **2009**, *66*, 1239–1256. [[CrossRef](#)] [[PubMed](#)]
14. Krecic, A.M.; Swanson, M.S. HnRNP complexes: Composition, structure, and function. *Curr. Opin. Cell Biol.* **1999**, *11*, 363–371. [[CrossRef](#)]
15. LaBranche, H.; Dupuis, S.; Ben-David, Y.; Bani, M.R.; Wellinger, R.J.; Chabot, B. Telomere elongation by hnRNP A1 and a derivative that interacts with telomeric repeats and telomerase. *Nat. Genet.* **1998**, *19*, 199–202. [[CrossRef](#)]
16. Moran-Jones, K.; Wayman, L.; Kennedy, D.D.; Reddel, R.R.; Sara, S.; Snee, M.J.; Smith, R. HnRNP A2, a potential ssDNA/RNA molecular adapter at the telomere. *Nucleic Acids Res.* **2005**, *33*, 486–496. [[CrossRef](#)]
17. Huang, P.R.; Hung, S.C.; Wang, T.C. Telomeric DNA-binding activities of heterogeneous nuclear ribonucleoprotein A3 in vitro and in vivo. *Biochim. Biophys. Acta* **2010**, *1803*, 1164–1174. [[CrossRef](#)]
18. Zhang, Q.S.; Manche, L.; Xu, R.M.; Krainer, A.R. HnRNP A1 associates with telomere ends and stimulates telomerase activity. *RNA* **2006**, *12*, 1116–1128. [[CrossRef](#)]
19. Dallaire, F.; Dupuis, S.; Fiset, S.; Chabot, B. Heterogeneous nuclear ribonucleoprotein A1 and UP1 protect mammalian telomeric repeats and modulate telomere replication in vitro. *J. Biol. Chem.* **2000**, *275*, 14509–14516. [[CrossRef](#)]
20. Huang, P.R.; Tsai, S.T.; Hsieh, K.H.; Wang, T.C. Heterogeneous nuclear ribonucleoprotein A3 binds single-stranded telomeric DNA and inhibits telomerase extension in vitro. *Biochim. Biophys. Acta* **2008**, *1783*, 193–202. [[CrossRef](#)]
21. Celis, J.E.; Bravo, R.; Arenstorf, H.P.; LeSturgeon, W.M. Identification of proliferation-sensitive human proteins amongst components of the 40 S hnRNP particles. Identity of hnRNP core proteins in the hela protein catalogue. *FEBS Lett.* **1986**, *194*, 101–109. [[CrossRef](#)]
22. LeSturgeon, W.M.; Beyer, A.L.; Christensen, M.E.; Walker, B.W.; Poupore, S.M.; Daniels, L.P. The packaging proteins of core hnRNP particles and the maintenance of proliferative cell states. *Cold Spring Harb. Symp. Quant. Biol.* **1978**, *42*, 885–898. [[CrossRef](#)] [[PubMed](#)]
23. He, Y.; Brown, M.A.; Rothnagel, J.A.; Saunders, N.A.; Smith, R. Roles of heterogeneous nuclear ribonucleoproteins a and b in cell proliferation. *J. Cell Sci.* **2005**, *118*, 3173–3183. [[CrossRef](#)] [[PubMed](#)]
24. Patry, C.; Bouchard, L.; Labrecque, P.; Gendron, D.; Lemieux, B.; Toutant, J.; Lapointe, E.; Wellinger, R.; Chabot, B. Small interfering RNA-mediated reduction in heterogeneous nuclear ribonucleoparticle A1/A2 proteins induces apoptosis in human cancer cells but not in normal mortal cell lines. *Cancer Res.* **2003**, *63*, 7679–7688. [[PubMed](#)]
25. Deng, Z.; Norseen, J.; Wiedmer, A.; Riethman, H.; Lieberman, P.M. TERRA RNA binding to TRF2 facilitates heterochromatin formation and ORC recruitment at telomeres. *Mol. Cell* **2009**, *35*, 403–413. [[CrossRef](#)]
26. Rippe, K.; Luke, B. TERRA and the state of the telomere. *Nat. Struct. Mol. Biol.* **2015**, *22*, 853–858. [[CrossRef](#)]
27. Redon, S.; Zemp, I.; Lingner, J. A three-state model for the regulation of telomerase by TERRA and hnRNPA1. *Nucleic Acids Res.* **2013**, *41*, 9117–9128. [[CrossRef](#)]
28. Blackburn, E.H. Switching and signaling at the telomere. *Cell* **2001**, *106*, 661–673. [[CrossRef](#)]
29. Griffith, J.D.; Comeau, L.; Rosenfield, S.; Stansel, R.M.; Bianchi, A.; Moss, H.; de Lange, T. Mammalian telomeres end in a large duplex loop. *Cell* **1999**, *97*, 503–514. [[CrossRef](#)]
30. Flynn, R.L.; Centore, R.C.; O’Sullivan, R.J.; Rai, R.; Tse, A.; Songyang, Z.; Chang, S.; Karlseder, J.; Zou, L. TERRA and hnRNPA1 orchestrate an RPA-to-POT1 switch on telomeric single-stranded DNA. *Nature* **2011**, *471*, 532–536. [[CrossRef](#)]
31. Sui, J.; Lin, Y.F.; Xu, K.; Lee, K.J.; Wang, D.; Chen, B.P. DNA-PKcs phosphorylates hnRNP-A1 to facilitate the RPA-to-POT1 switch and telomere capping after replication. *Nucleic Acids Res.* **2015**, *43*, 5971–5983. [[CrossRef](#)] [[PubMed](#)]



32. Chen, C.Y.; Jan, C.I.; Pi, W.C.; Wang, W.L.; Yang, P.C.; Wang, T.H.; Karni, R.; Wang, T.C. Heterogeneous nuclear ribonucleoproteins A1 and A2 modulate expression of TID1 isoforms and EGFR signaling in non-small cell lung cancer. *Oncotarget* **2016**, *7*, 16760–16772. [[CrossRef](#)] [[PubMed](#)]
33. de Lange, T. Protection of mammalian telomeres. *Oncogene* **2002**, *21*, 532–540. [[CrossRef](#)] [[PubMed](#)]
34. Rogakou, E.P.; Nieves-Neira, W.; Boon, C.; Pommier, Y.; Bonner, W.M. Initiation of DNA fragmentation during apoptosis induces phosphorylation of H2AX histone at serine 139. *J. Biol. Chem.* **2000**, *275*, 9390–9395. [[CrossRef](#)] [[PubMed](#)]
35. Kim, N.W.; Piatyszek, M.A.; Prowse, K.R.; Harley, C.B.; West, M.D.; Ho, P.L.; Coviello, G.M.; Wright, W.E.; Weinrich, S.L.; Shay, J.W. Specific association of human telomerase activity with immortal cells and cancer. *Science* **1994**, *266*, 2011–2015. [[CrossRef](#)] [[PubMed](#)]
36. Shay, J.W.; Bacchetti, S. A survey of telomerase activity in human cancer. *Eur. J. Cancer* **1997**, *33*, 787–791. [[CrossRef](#)]
37. Sobinoff, A.P.; Pickett, H.A. Alternative lengthening of telomeres: DNA repair pathways converge. *Trends Genet.* **2017**, *33*, 921–932. [[CrossRef](#)]
38. Wang, F.; Tang, M.L.; Zeng, Z.X.; Wu, R.Y.; Xue, Y.; Hao, Y.H.; Pang, D.W.; Zhao, Y.; Tan, Z. Telomere- and telomerase-interacting protein that unfolds telomere g-quadruplex and promotes telomere extension in mammalian cells. *Proc. Natl. Acad. Sci. USA* **2012**, *109*, 20413–20418. [[CrossRef](#)]
39. Jafri, M.A.; Ansari, S.A.; Alqahtani, M.H.; Shay, J.W. Roles of telomeres and telomerase in cancer, and advances in telomerase-targeted therapies. *Genome Med.* **2016**, *8*, 69. [[CrossRef](#)]
40. Zanetti, M. A second chance for telomerase reverse transcriptase in anticancer immunotherapy. *Nat. Rev. Clin. Oncol.* **2017**, *14*, 115–128. [[CrossRef](#)]
41. Jager, K.; Walter, M. Therapeutic targeting of telomerase. *Genes* **2016**, *7*, 39. [[CrossRef](#)] [[PubMed](#)]
42. Chu, Y.W.; Yang, P.C.; Yang, S.C.; Shyu, Y.C.; Hendrix, M.J.; Wu, R.; Wu, C.W. Selection of invasive and metastatic subpopulations from a human lung adenocarcinoma cell line. *Am. J. Respir. Cell Mol. Biol.* **1997**, *17*, 353–360. [[CrossRef](#)] [[PubMed](#)]
43. Chen, C.Y.; Yu, Z.Y.; Chuang, Y.S.; Huang, R.M.; Wang, T.C. Sulforaphane attenuates EGFR signaling in NSCLC cells. *J. Biomed. Sci.* **2015**, *22*, 38. [[CrossRef](#)] [[PubMed](#)]
44. Wu, Y.H.; Cheng, M.L.; Ho, H.Y.; Chiu, D.T.; Wang, T.C. Telomerase prevents accelerated senescence in glucose-6-phosphate dehydrogenase (G6PD)-deficient human fibroblasts. *J. Biomed. Sci.* **2009**, *16*, 18. [[CrossRef](#)] [[PubMed](#)]
45. Chen, C.Y.; Chiou, S.H.; Huang, C.Y.; Jan, C.I.; Lin, S.C.; Hu, W.Y.; Chou, S.H.; Liu, C.J.; Lo, J.F. TID1 functions as a tumour suppressor in head and neck squamous cell carcinoma. *J. Pathol.* **2009**, *219*, 347–355. [[CrossRef](#)] [[PubMed](#)]
46. Sheng, W.Y.; Chien, Y.L.; Wang, T.C. The dual role of protein kinase C in the regulation of telomerase activity in human lymphocytes. *FEBS Lett.* **2003**, *540*, 91–95. [[CrossRef](#)]
47. Cesare, A.J.; Kaul, Z.; Cohen, S.B.; Napier, C.E.; Pickett, H.A.; Neumann, A.A.; Reddel, R.R. Spontaneous occurrence of telomeric DNA damage response in the absence of chromosome fusions. *Nat. Struct. Mol. Biol.* **2009**, *16*, 1244–1251. [[CrossRef](#)]



© 2019 by the authors. Licensee MDPI, Basel, Switzerland. This article is an open access article distributed under the terms and conditions of the Creative Commons Attribution (CC BY) license (<http://creativecommons.org/licenses/by/4.0/>).

## RESEARCH ARTICLE

# Neurosteroid allopregnanolone inhibits glutamate release from rat cerebrocortical nerve terminals

Yi Chang<sup>1,2</sup> | Hsi Lung Hsieh<sup>4</sup> | Shu Kuei Huang<sup>5</sup> | Su Jane Wang<sup>2,3</sup> 

<sup>1</sup>Department of Anesthesiology, Shin Kong Wu Ho-Su Memorial Hospital, Taipei, Taiwan

<sup>2</sup>School of Medicine, Fu Jen Catholic University, New Taipei City, Taiwan

<sup>3</sup>Research Center for Chinese Herbal Medicine, College of Human Ecology, Chang Gung University of Science and Technology, Taoyuan, Taiwan

<sup>4</sup>Department of Nursing, Division of Basic Medical Sciences, Research Center for Chinese Herbal Medicine, and Graduate Institute of Health Industry Technology, Chang Gung University of Science and Technology, Tao-Yuan, Taiwan

<sup>5</sup>Department of Anesthesiology, Far-Eastern Memorial Hospital, New Taipei City, Taiwan

## Correspondence

Su Jane Wang, School of Medicine, Fu Jen Catholic University, 510, Chung-Cheng Rd., Hsin-Chuang, New Taipei 24205, Taiwan.  
Email: med0003@mail.fju.edu.tw

## Funding information

Shin Kong Wu Ho-Su Memorial Hospital, Grant/Award Number: 106-SKH-FJH-03

## Abstract

Allopregnanolone, an active metabolite of progesterone, has been reported to exhibit neuroprotective activity in several preclinical models. Considering that the excitotoxicity caused by excessive glutamate is implicated in many brain disorders, the effect of allopregnanolone on glutamate release in rat cerebrocortical nerve terminals and possible underlying mechanism were investigated. We observed that allopregnanolone inhibited 4-aminopyridine (4-AP)-evoked glutamate release, and this inhibition was prevented by chelating the extracellular  $\text{Ca}^{2+}$  ions and the vesicular transporter inhibitor. Allopregnanolone reduced the elevation of 4-AP-evoked intrasynaptosomal  $\text{Ca}^{2+}$  levels, but did not affect the synaptosomal membrane potential. In the presence of N-, P/Q-, and R-type channel blockers, allopregnanolone-mediated inhibition of 4-AP-evoked glutamate release was markedly reduced; however, the intracellular  $\text{Ca}^{2+}$ -release inhibitors did not affect the allopregnanolone effect. Furthermore, allopregnanolone-mediated inhibition of 4-AP-evoked glutamate release was completely abolished in the synaptosomes pretreated with inhibitors of  $\text{Ca}^{2+}$ /calmodulin, adenylate cyclase, and protein kinase A (PKA), namely calmidazolium, MDL12330A, and H89, respectively. Additionally, the allopregnanolone effect on evoked glutamate release was antagonized by the GABA<sub>A</sub> receptor antagonist SR95531. Our data are the first to suggest that allopregnanolone reduce the  $\text{Ca}^{2+}$  influx through N-, P/Q-, and R-type  $\text{Ca}^{2+}$  channels, through the activation of GABA<sub>A</sub> receptors present on cerebrocortical nerve terminals, subsequently suppressing the  $\text{Ca}^{2+}$ -calmodulin/PKA cascade and decreasing 4-AP-evoked glutamate release.

## KEYWORDS

allopregnanolone,  $\text{Ca}^{2+}$ -calmodulin/AC/PKA, GABA<sub>A</sub> receptor, glutamate release, synaptosomes, VDCCs

## 1 | INTRODUCTION

Allopregnanolone (3 $\alpha$ -hydroxy-5 $\alpha$ -pregnan-20-one) is an active metabolite of progesterone and is widely distributed in the brain including the hippocampus and cortex (Baulieu, Robel, & Schumacher, 2001; Saalman, Kirkcaldie, Waldron, & Calford, 2007). Allopregnanolone has analgesic, anesthetic, antidepressant, and anxiolytic properties (Patte-Mensah, Meyer, Taleb, & Mensah-Nyagan, 2014; Schüle, Nothdurfter, & Rupprecht, 2014), and its neuroprotective activity has been demonstrated in various experimental models (Guennoun et al., 2015). In vitro it was shown to decrease oxygen-glucose deprivation- or  $\text{H}_2\text{O}_2$ -induced neuronal death in cultured hippocampal neurons, cerebellar Purkinje cells, and human neuroblastoma SH-SY5Y cells (Kelley et al., 2008; Lejri et al., 2017; Radley, Akram, Grubb, & Gibson, 2012). In vivo

it attenuates brain damage and cognitive deficits induced by ischemia, amyloid  $\beta$  protein, and traumatic brain injury in rats (Chen et al., 2011; He, Hoffman et al., 2004; Sayeed, Guo, Hoffman, & Stein, 2006; Wang et al., 2010). Further, brain allopregnanolone levels are decreased in patients with Alzheimer's disease (Marx et al., 2006; Naylor et al., 2010). However, the precise mechanisms contributing to the neuroprotective effects of allopregnanolone in the brain are not completely understood.

One hypothesis suggests that the neuroprotective effect of allopregnanolone is associated with a reduction in the release of glutamate, a major excitatory neurotransmitter in mammalian central nervous system (CNS) (Headley & Grillner, 1990). Previous studies have shown that allopregnanolone can decrease glutamate release in mechanically dissociated hippocampal CA3 neurons and rat striatal slices (Iwata, Wakita, Shin, Fukuda, & Akaike, 2013; Yunes, Estrella, García, Lara, & Cabrera, 2015); however, this effect has not been examined directly in nerve terminal preparations. The mechanism through which allopregnanolone acts at the presynaptic level to inhibit glutamate release is particularly pertinent to brain disease because the excitotoxicity caused by excessive glutamate is critical in the pathogenesis of various brain disorders, including cerebral ischemia, stroke, brain trauma, and even neurodegenerative diseases such as Alzheimer's and Parkinson's disease (Hynd, Scott, & Dodd, 2004; Lau & Tymianski, 2010; Mehta, Prabhakar, Kumar, Deshmukh, & Sharma, 2013).

The objective of the present study was to investigate the effect of allopregnanolone on glutamate release and to characterize its underlying molecular mechanisms in rat cerebrocortical nerve terminals (synaptosomes), a system particularly suited to study presynaptic phenomena (Raiteri & Raiteri, 2000). This investigation is crucial for understanding the role of allopregnanolone in the brain and for exploiting its potential for therapeutic interventions.

## 2 | MATERIALS AND METHODS

### 2.1 | Chemicals

4-aminopyridine (4-AP), bafilomycin A1, DL-threo- $\beta$ -benzyloxyaspartate (DL-TBOA),  $\omega$ -conotoxin GVIA ( $\omega$ -CgTX GVIA),  $\omega$ -agatoxin IVA ( $\omega$ -Aga IVA),  $\omega$ -conotoxin MVIIC ( $\omega$ -CgTX MVIIC), dantrolene, 7-chloro-5-(2-chlorophenyl)-1,5-dihydro-4,1-benzothiazepin-2(3H)-one (CGP37157), isoguvacine, SR95531 and calmidazolium were purchased from Tocris Cookson (Bristol, UK). Fura-2-acetoxymethyl ester (Fura-2-AM) and 3', 3', 3'-dipropylthiadicarbocyanine iodide [DiSC<sub>3</sub>(5)] were purchased from Invitrogen (Carlsbad, CA, USA). Allopregnanolone and all other reagents were purchased from Sigma-Aldrich (St. Louis, MO, USA).

### 2.2 | Experimental animals

Male Sprague Dawley rats (150–200 g) were purchased from BioLASCO (Taiwan Co., Ltd, Taipei, Taiwan) and were housed under controlled conditions with food and water available ad libitum. The experimental procedures were accordance with the National Institutes of Health Guide for the Care and Use of Laboratory (NAC, 2011), and they were approved by the Institutional Animal Care and Use Committee at the Fu Jen Catholic University.

### 2.3 | Preparation of synaptosomes

Rats were sacrificed by decapitation, and the cerebral cortex was rapidly removed at 4°C. Percoll-purified synaptosomes were prepared according to previous studies (Lin, Lu, Huang, & Wang, 2012; Nicholls & Sihra, 1986; Rodríguez-Moreno & Sihra, 2004). The final synaptosomal fraction was resuspended in approximately 2–3 ml HEPES buffer medium (HBM, mM: NaCl, 140; KCl, 5; NaHCO<sub>3</sub>, 5; MgCl<sub>2</sub>·6H<sub>2</sub>O, 1; Na<sub>2</sub>HPO<sub>4</sub>, 1.2; glucose, 10; HEPES, 10; pH 7.4) and protein concentration (0.5 mg protein/ml) determined using the Bradford assay. The synaptosomes were stored on ice as drained pellets and used within 4 h.

### 2.4 | Glutamate release

The release of endogenous glutamate was measured using a continuous fluorimetric assay, based on the reduction of nicotinamide adenine dinucleotide phosphate (NADP<sup>+</sup>) to NADPH catalyzed by glutamate dehydrogenase (GDH) in the presence of glutamate. NADPH gives rise to a strong fluorimetric signal at 460 nm when excited at 340 nm (Lin et al., 2013; Nicholls & Sihra, 1986). In brief, pelleted synaptosomes were resuspended in HBM containing 16  $\mu$ M bovine serum albumin (BSA) and transferred to a 1-cm<sup>2</sup> quartz cuvette in a Perkin-Elmer LS-55 spectrofluorimeter equipped with a magnetic stirrer (PerkinElmer Life and Analytical Sciences, Waltham, MA, USA). NADP<sup>+</sup> (2 mM) and GDH (50 units/ml) were added in the presence of CaCl<sub>2</sub> (1.2 mM). After 10 min, the background fluorescence of NADPH was measured for 5 min. At that point, glutamate release was evoked by adding 4-AP (1 mM) to the preparation, and the fluorescence of NADPH was measured for 10 min. A standard of exogenous glutamate (5 nmol) was added at the end of each experiment. The value of the fluorescence change produced by the standard addition was used to calculate the released glutamate as nmol glutamate/mg synaptosomal protein. Data were accumulated at 2-s

intervals. Release values quoted in the text and depicted in bar graphs are levels attained at steady-state after 5 min of depolarization (nmol/mg/5 min). Cumulative data were analyzed using Lotus 1–2–3.

## 2.5 | Synaptosomal membrane potential

The synaptosomal membrane potential can be monitored by positively charged membrane potential-sensitive carbocyanine dyes such as DiSC<sub>3</sub>(5) (Akerman, Scott, Heikkilä, & Heinonen, 1987). Synaptosomes were resuspended in HBM containing BSA and the synaptosomal suspension stirred in a thermostatted cuvette in a Perkin-Elmer LS-55 spectrofluorimeter. After 3 min of incubation, 5  $\mu$ M DiSC<sub>3</sub>(5) was added and allowed to equilibrate before the addition of CaCl<sub>2</sub> (1.2 mM) after 4 min of incubation. 4-AP was added to depolarize the synaptosomes at 10 min, and DiSC<sub>3</sub>(5) fluorescence was monitored at excitation and emission wavelengths of 646 and 674 nm, respectively, and data accumulated at 2-s intervals. Cumulative data were analyzed in Lotus 1–2–3, and results are expressed in fluorescence units.

## 2.6 | Synaptosomal cytosolic Ca<sup>2+</sup> concentration ([Ca<sup>2+</sup>]<sub>C</sub>)

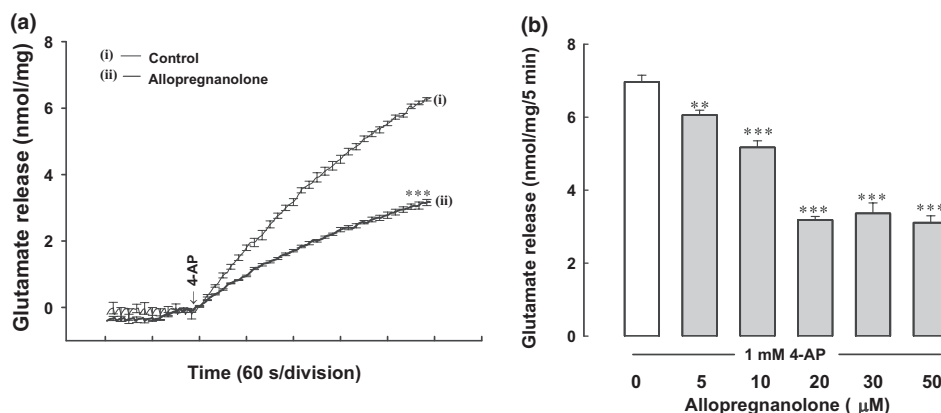
Synaptosomes were preincubated in HBM containing 5  $\mu$ M fura-2 and 0.1 mM CaCl<sub>2</sub> for 30 min at 37°C in a stirred test tube. After fura-2 loading, synaptosomes were centrifuged in a microfuge for 30 s, the pellet resuspended in HBM containing BSA and the synaptosomal suspension stirred in a thermostatted cuvette in a Perkin-Elmer LS-55 spectrofluorimeter. CaCl<sub>2</sub> (1.2 mM) was added after 5 min and further additions were made after a further 5 min. Fluorescence data were accumulated at excitation wavelengths of 340 and 380 nm (emission wavelength 505 nm) at 2-s intervals. [Ca<sup>2+</sup>]<sub>C</sub> (nM) was calculated using the equations described previously (Grynkiewicz, Poenie, & Tsien, 1985).

## 2.7 | Data and statistical analysis

Data are presented as mean  $\pm$  SEM. Student's unpaired *t* test or one-way ANOVA was used for the statistical analysis by employing SPSS software (Version 17.0; SPSS Inc., Chicago, IL, USA). Differences at the *p* < 0.05 level were considered statistically significant.

## 3 | RESULTS

Synaptosomes were purified from the cerebral cortex of rats, and exposed to the K<sup>+</sup> channel blocker 4-aminopyridine (4-AP), an agent whose action most closely mimics physiological stimulation (Nicholls, 1998), to assess glutamate release. Under control conditions, 4-AP (1 mM) evoked a glutamate release of  $6.9 \pm 0.2$  nmol/mg/5 min from synaptosomes incubated with 1.2 mM CaCl<sub>2</sub> (Figure 1a). Preincubation with allopregnanolone (20  $\mu$ M) for 10 min before 4-AP addition caused an inhibition of the 4-AP-evoked glutamate release by approximately 55% [ $3.1 \pm 0.1$  nmol/mg/5 min; *t*(11) = 14.2, *p* < 0.001; Figure 1a]. Allopregnanolone did not affect the basal, preddepolarization glutamate level. The effect of allopregnanolone was concentration-dependent; the maximal inhibition was observed when the compound was applied at 20  $\mu$ M, and the IC<sub>50</sub> value was 10  $\mu$ M (Figure 1b).



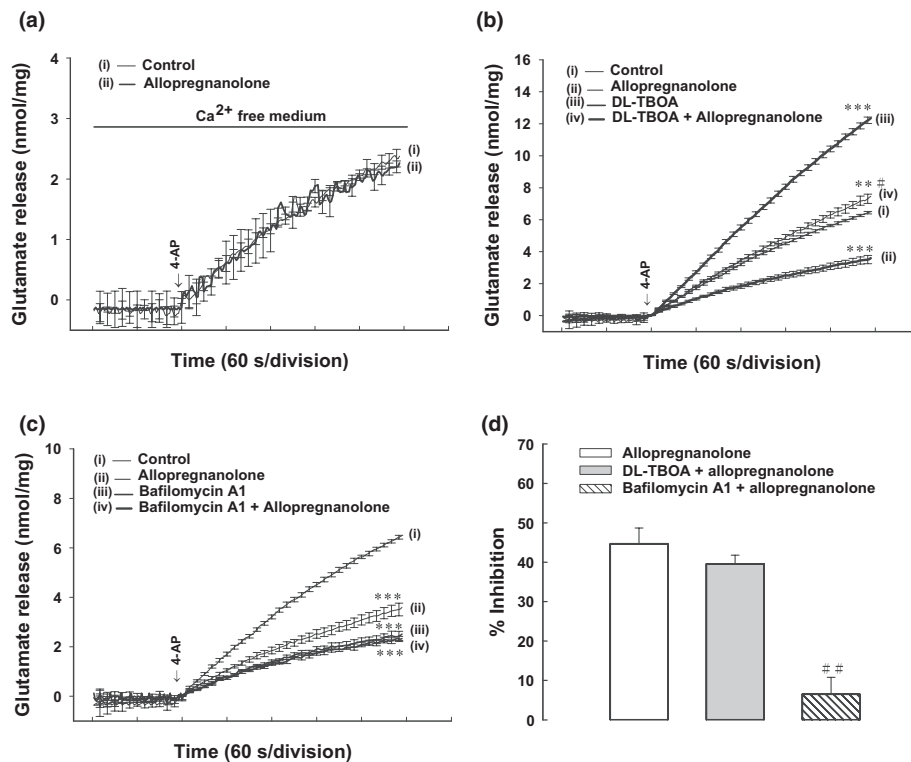
**FIGURE 1** Allopregnanolone inhibits the 4-AP-evoked release of glutamate in cerebrocortical nerve terminals of rats. (a) Glutamate release was evoked by the addition of 1 mM 4-AP in the absence (control) or in the presence of 20  $\mu$ M allopregnanolone, added 10 min before depolarization. (b) Concentration-dependent inhibition of the 1 mM 4-AP-evoked glutamate release by allopregnanolone. The data represent the mean  $\pm$  SEM. (*n* = 5–8). \*\**p* < 0.01, \*\*\**p* < 0.001 versus control group (two-tailed Student's *t* test)



Figure 2a shows that calcium-free medium containing 300  $\mu\text{M}$  EGTA reduced the 4-AP-evoked glutamate release [ $F(2,14) = 695.6$ ;  $p < 0.001$ ]. This  $\text{Ca}^{2+}$ -independent component of the 4-AP-evoked glutamate release was unaffected by 20  $\mu\text{M}$  of allopregnanolone ( $p = 0.6$ ). DL-TBOA (10  $\mu\text{M}$ ), a nonselective inhibitor of all excitatory amino acid transporter subtypes, increased the 4-AP-evoked glutamate release ( $p < 0.001$ ). In the presence of DL-TBOA, allopregnanolone (20  $\mu\text{M}$ ) was able to produce a  $39.6\% \pm 2.2\%$  inhibition on 4-AP-evoked glutamate release [ $F(2,14) = 102.6$ ;  $p < 0.001$ ; Figure 2b], which was similar to that observed for the  $44.7\% \pm 4.0\%$  inhibition produced by allopregnanolone alone ( $p > 0.05$ ; Figure 2d). By contrast, bafilomycin A1 (0.1  $\mu\text{M}$ ), a vesicular transporter inhibitor, inhibited the 4-AP-evoked glutamate release and prevented the inhibitory effect of allopregnanolone (20  $\mu\text{M}$ ) on 4-AP-evoked glutamate release [ $F(2,12) = 394.7$ ;  $p < 0.001$ ]. In the five tested synaptosomal preparations, no statistical difference was observed between the release after bafilomycin A1 alone and after the bafilomycin A1 and allopregnanolone treatment ( $p = 0.5$ ; Figure 2c). On average, allopregnanolone resulted in a  $6.5\% \pm 4.3\%$  inhibition on 4-AP-evoked glutamate release after treatment with bafilomycin A1, which was significantly different the inhibition of allopregnanolone alone ( $44.7\% \pm 4.0\%$ ;  $p < 0.05$ ; Figure 2d). These results indicate that allopregnanolone influences the release of glutamate induced by a decrease in vesicular exocytosis.

Table 1 shows the effect of allopregnanolone on the synaptosomal plasma membrane potential. The synaptosomal membrane potential can be monitored by positively charged membrane potential-sensitive cationic cyanide dye DiSC<sub>3</sub>(5). 4-AP (1 mM) application caused an increase in DiSC<sub>3</sub>(5) fluorescence. Preincubation with allopregnanolone (20  $\mu\text{M}$ ) for 10 min before 4-AP addition did not alter the resting membrane potential, and had no significant effect on the 4-AP-mediated increase in DiSC<sub>3</sub>(5) fluorescence [ $t(8) = 0.34$ ,  $p = 0.71$ ; Table 1]. Table 1 also shows the  $[\text{Ca}^{2+}]_c$  levels determined in synaptosomes pretreated with fura-2. The stimulation of synaptosomes with 1 mM 4-AP caused an increase in  $[\text{Ca}^{2+}]_c$  levels to a plateau level ( $p < 0.001$ ). Preincubation with allopregnanolone (20  $\mu\text{M}$ ) for 10 min before 4-AP addition did not significantly affect basal Ca levels but reduced the 4-AP-evoked  $[\text{Ca}^{2+}]_c$  increase by 55% [ $t(8) = 8.9$ ,  $p < 0.001$ ]. Table 2 shows that 15 mM KCl effected a controlled glutamate release of  $6.3 \pm 0.1$  nmol/mg/5 min, which was also decreased to  $2.9 \pm 0.3$  nmol/mg/5 min by allopregnanolone (20  $\mu\text{M}$ ) [ $t(8) = 11.4$ ,  $p < 0.001$ ].

Figure 3a,b show that application of 2  $\mu\text{M}$   $\omega$ -conotoxin GVIA ( $\omega$ -CgTX GVIA; N-type  $\text{Ca}^{2+}$  channel blocker) or 500 nM  $\omega$ -agatoxin IVA ( $\omega$ -Aga IVA; P/Q-type  $\text{Ca}^{2+}$  channel blocker) reduced 4AP-evoked glutamate release to  $4.2 \pm 0.2$  ( $p < 0.001$ ) or  $3.9 \pm 0.2$  nmol/mg/5 min ( $p < 0.001$ ), respectively. In the presence of  $\omega$ -CgTX GVIA or  $\omega$ -Aga IVA alone, allopregnanolone (20  $\mu\text{M}$ ) could still effectively reduced release



**FIGURE 2** Effect of external calcium omission, the glutamate transporter blocker DL-TBOA, and the vesicular transporter inhibitor bafilomycin A1 on the allopregnanolone-mediated inhibition of 4-AP-evoked glutamate release. (a–c) The effect of 20  $\mu\text{M}$  allopregnanolone on glutamate release induced by 1 mM 4-AP in the absence (control) and presence of 300  $\mu\text{M}$  EGTA (calcium-free medium), 10  $\mu\text{M}$  DL-TBOA or 0.1  $\mu\text{M}$  bafilomycin A1. (d) Comparison of the inhibition of glutamate release with allopregnanolone alone and in the presence of DL-TBOA or bafilomycin A1. The data represent the mean  $\pm$  SEM. ( $n = 5–6$ ). \*\*\* $p < 0.001$  versus the control group (two-tailed Student's  $t$  test). # $p < 0.05$  versus the DL-TBOA-treated group (one-way ANOVA). ## $p < 0.05$  versus the allopregnanolone alone group (one-way ANOVA)

**TABLE 1** Effect of allopregnanolone on synaptosomal membrane potential and cytosolic  $\text{Ca}^{2+}$  concentration ( $[\text{Ca}^{2+}]_c$ ) in rat cerebrocortical synaptosomes

	Membrane potential (fluorescence units)				$[\text{Ca}^{2+}]_c$ (nM)		
	Basal	4-AP (1 mM)	n		Basal	4-AP (1 mM)	n
Control	0.3 ± 0.1	30.3 ± 2.6***	5		161.8 ± 3.4	196.5 ± 5.4***	5
20 $\mu\text{M}$ allopregnanolone	0.5 ± 0.2	31.7 ± 2.7	5		159.5 ± 2.9	168.5 ± 3.2 <sup>#</sup>	5

\*\*\* $p < 0.001$  versus the control group, <sup>#</sup> $p < 0.001$  versus the 4-AP group.

**TABLE 2** Effect of allopregnanolone on KCl-evoked glutamate release in rat cerebrocortical synaptosomes

	KCl (15 mM)-evoked glutamate release (nmol/mg/5 min)	n
Control	6.3 ± 0.1	5
20 $\mu\text{M}$ allopregnanolone	3.0 ± 0.3***	5

\*\*\* $p < 0.001$  versus the control group.

by  $59.7\% \pm 2.4\%$  or  $57.9\% \pm 3.3\%$ , respectively, which was similar with the inhibition produced by allopregnanolone alone ( $54.9\% \pm 2.6\%$ ;  $p > 0.05$ ; Figure 4). After the combined application of  $\omega$ -Aga IVA and  $\omega$ -CgTX GVIA, when glutamate release was reduced to  $1.9 \pm 0.1$  nmol/mg/5 min ( $p < 0.001$ ), allopregnanolone (20  $\mu\text{M}$ ) caused a marginal further decrease to  $1.8 \pm 0.1$  nmol/mg/5 min, which represented a statistically insignificant change in 4AP-evoked glutamate release resulting from allopregnanolone in the presence of P/Q- and N-type VDCC block ( $p > 0.05$ ; Figure 3c). On average, allopregnanolone resulted in a  $6.6\% \pm 5.5\%$  inhibition on 4-AP-evoked glutamate release after treatment with  $\omega$ -Aga IVA and  $\omega$ -CgTX GVIA, which was significantly different from the inhibition of allopregnanolone alone ( $54.9\% \pm 2.6\%$ ;  $p < 0.05$ ; Figure 4). Thus, the decrease in  $\text{Ca}^{2+}$  influx mediated by N- and P/Q-type  $\text{Ca}^{2+}$  channels appears to be associated with the observed allopregnanolone-mediated inhibition of glutamate release.

In addition, 1  $\mu\text{M}$  nifedipine, a L-type  $\text{Ca}^{2+}$  channel blocker, did not significantly affect the 4-AP-evoked glutamate release ( $p > 0.05$ ; Figure 3d). In the presence of nifedipine, allopregnanolone (20  $\mu\text{M}$ ) inhibited the 4-AP-induced release of glutamate by  $59.3\% \pm 3.5\%$ , which was not significantly different from the inhibition achieved using allopregnanolone alone ( $59.4\% \pm 4.2\%$ ;  $p > 0.05$ ; Figures 3 and 4). Similar results were observed with  $\text{NiCl}_2$  at the 50  $\mu\text{M}$  concentration that selectively blocks T-type  $\text{Ca}^{2+}$  channels (Long et al., 2009). Figure 3e shows that 4-AP-evoked glutamate release under control conditions was unaffected by  $\text{NiCl}_2$ . In the presence of  $\text{NiCl}_2$ , allopregnanolone (20  $\mu\text{M}$ ) still produced  $56.4\% \pm 2.8\%$  decreases in 4-AP-evoked glutamate release ( $p > 0.05$ ; Figures 3 and 4). These results indicate that L- and T-type  $\text{Ca}^{2+}$  channels are not involved in the observed inhibition of glutamate release by allopregnanolone. By contrast, 1  $\mu\text{M}$  SNX-482, a R-type  $\text{Ca}^{2+}$  blocker, did not significantly reduce the release of glutamate evoked by 4-AP ( $p > 0.05$ ; Figure 3f). In the presence of SNX-482, allopregnanolone resulted in an  $40.4\% \pm 1.6\%$  inhibition on 4-AP-evoked glutamate release, which was less than that of the inhibition produced by allopregnanolone alone ( $54.9\% \pm 2.6\%$ ;  $p < 0.05$ ; Figures 3 and 4). This indicates that R-type  $\text{Ca}^{2+}$  channels are partially involved in the action of allopregnanolone.

Dantrolene (100  $\mu\text{M}$ ), a blocker of  $\text{Ca}^{2+}$  release from endoplasmic reticulum ryanodine receptors, reduced the 4-AP (1 mM)-evoked glutamate release, from  $6.5 \pm 0.2$  to  $4.9 \pm 0.2$  nmol/mg/5 min ( $p < 0.001$ ). In the presence of dantrolene (100  $\mu\text{M}$ ), allopregnanolone (20  $\mu\text{M}$ ) was still able to reduce the 4-AP-evoked glutamate release by  $60.8\% \pm 2.8\%$  [ $F(2,13) = 37.5$ ;  $p < 0.001$ ], which was not significantly different from the inhibition of allopregnanolone alone ( $54.9\% \pm 2.6\%$ ;  $p < 0.05$ ; Figure 4). Similarly, CGP37157 (100  $\mu\text{M}$ ), a membrane-permeant blocker of the mitochondrial  $\text{Na}^+/\text{Ca}^{2+}$  exchanger, reduced the release of glutamate evoked by 4-AP ( $p < 0.001$ ). In the presence of CGP37157 (100  $\mu\text{M}$ ), allopregnanolone resulted in a  $55.8\% \pm 5.4\%$  inhibition on 4-AP-evoked glutamate release after treatment with CGP37157, which was similar with the inhibition produced by allopregnanolone alone ( $54.9\% \pm 2.6\%$ ;  $p < 0.05$ ; Figure 4). These results suggested that a reduction of intracellular  $\text{Ca}^{2+}$  release appears not to mediate the inhibitory effect of allopregnanolone on 4-AP-evoked glutamate release.

In synaptic terminals, an increase in cytosolic  $\text{Ca}^{2+}$  has been shown to activate the  $\text{Ca}^{2+}$ -calmodulin/adenylate cyclase (AC)/cyclic adenosine monophosphate (cAMP)/protein kinase A (PKA) cascade, thereby facilitating glutamate release (Andrade-Talavera, Duque-Feria, Sihra, & Rodríguez-Moreno, 2013; Rodríguez-Moreno & Sihra, 2013). Therefore, we hypothesize that the allopregnanolone-mediated inhibition of glutamate release is related to the decrease in  $\text{Ca}^{2+}$  activating calmodulin cascade. To test this possibility, we examined the effect of inhibiting  $\text{Ca}^{2+}$ /calmodulin using the calmodulin antagonist calmidazolium. Figure 5a shows that calmidazolium (25  $\mu\text{M}$ ) reduced the 4-AP (1 mM)-evoked glutamate release ( $p < 0.001$ ) and largely prevented the inhibition of glutamate release by allopregnanolone (20  $\mu\text{M}$ ) [ $F(2,12) = 179.8$ ;  $p < 0.001$ ]. In five synaptosomes tested, allopregnanolone produced a  $0.2\% \pm 0.4\%$  decrease in the 4-AP-evoked glutamate release after the application of calmidazolium, which was significantly different from the inhibition produced by allopregnanolone alone ( $48.0\% \pm 1.1\%$ ;  $p < 0.05$ ; Figure 5d). As with calmidazolium, the AC inhibitor MDL12330A (10  $\mu\text{M}$ ; Figure 5b) or the PKA inhibitor H89 (100  $\mu\text{M}$ ; Figure 5c) reduced the

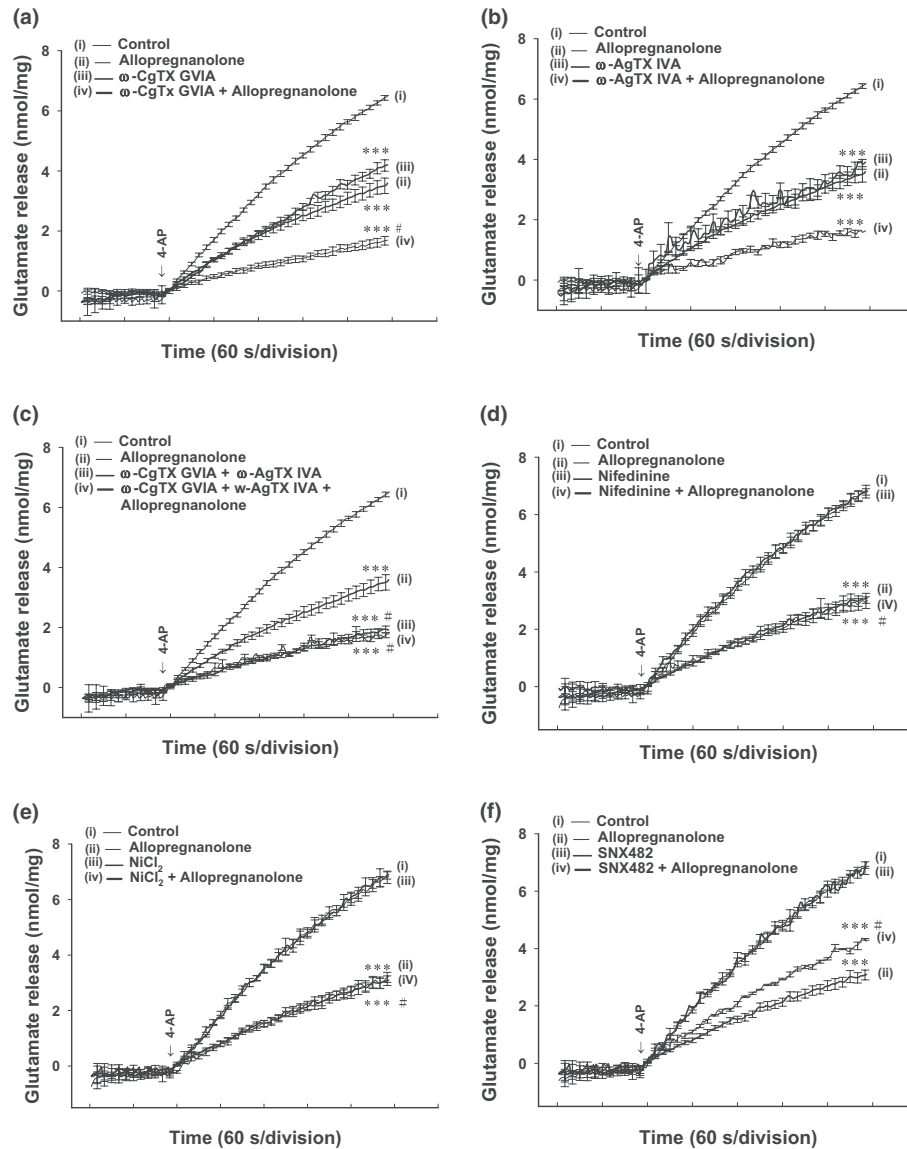


**FIGURE 3** Effects of N-type  $\text{Ca}^{2+}$  channel blocker  $\omega$ -CgTX GVIA, P/Q-type  $\text{Ca}^{2+}$  channel blocker  $\omega$ -Aga IVA, L-type  $\text{Ca}^{2+}$  channel blocker nifedipine, T-type  $\text{Ca}^{2+}$  channel blocker  $\text{NiCl}_2$ , or R-type  $\text{Ca}^{2+}$  channel blocker SNX-482 on the allopregnanolone-mediated inhibition of 4-AP-evoked glutamate release. (a–f) The effect of 20  $\mu\text{M}$  allopregnanolone on glutamate release induced by 1 mM 4-AP in the absence (control) and presence of 2  $\mu\text{M}$   $\omega$ -CgTX GVIA, 500 nM  $\omega$ -Aga IVA, 1  $\mu\text{M}$  nifedipine, 50  $\mu\text{M}$   $\text{NiCl}_2$  or 1  $\mu\text{M}$  SNX482. The data represent the mean  $\pm$  SEM. ( $n = 3$ –8). \*\*\* $p < 0.001$  versus the control group (two-tailed Student's  $t$  test); # $p < 0.05$  versus the  $\omega$ -CgTX GVIA-,  $\omega$ -Aga IVA-, nifedipine-,  $\text{NiCl}_2$ - or SNX482-treated group (one-way ANOVA)

4-AP (1 mM)-evoked glutamate release ( $p < 0.001$ ). In the presence of MDL12330A (10  $\mu\text{M}$ ) or H89 (100  $\mu\text{M}$ ), allopregnanolone-mediated inhibition of 4-AP-evoked glutamate release was abolished. [MDL12330A,  $F(2,12) = 749.9$ ;  $p < 0.001$ ; H89,  $F(2,12) = 39.7$ ;  $p < 0.001$ ]. On average, allopregnanolone resulted in a  $10.1\% \pm 0.4\%$  or  $1.2\% \pm 0.4\%$  inhibition on 4-AP-evoked glutamate release after treatment with MDL12330A or H89, respectively, which were significantly different the inhibition of allopregnanolone alone ( $48.0\% \pm 1.1\%$ ;  $p < 0.05$ ; Figure 5d). These results indicated that the suppression of the  $\text{Ca}^{2+}$ -calmodulin/AC/cAMP/PKA signaling cascade is involved in the allopregnanolone-mediated inhibition of glutamate release from synaptosomes.

Because allopregnanolone-mediated effects have been reported to be associated with the modulation of  $\text{GABA}_A$  receptors (Ishihara, Kawami, Ishida, & Yamazaki, 2013; Knight, Davidson, Young, & Gibson, 2012), the effect of the  $\text{GABA}_A$  receptor agonist isoguvacine was examined. Figure 6a shows that isoguvacine (300  $\mu\text{M}$ ) inhibited 4-AP-evoked glutamate release [ $F(2,12) = 122.8$ ;  $p < 0.001$ ]. In the presence of isoguvacine, allopregnanolone only reduced glutamate release by a further  $0.1 \pm 3.0\%$ , indicating significant reduction compared with that obtained when allopregnanolone was applied alone ( $51.1 \pm 1.1\%$ ;  $p < 0.05$ ; Figure 6a,c). Similar results were also observed using 100  $\mu\text{M}$

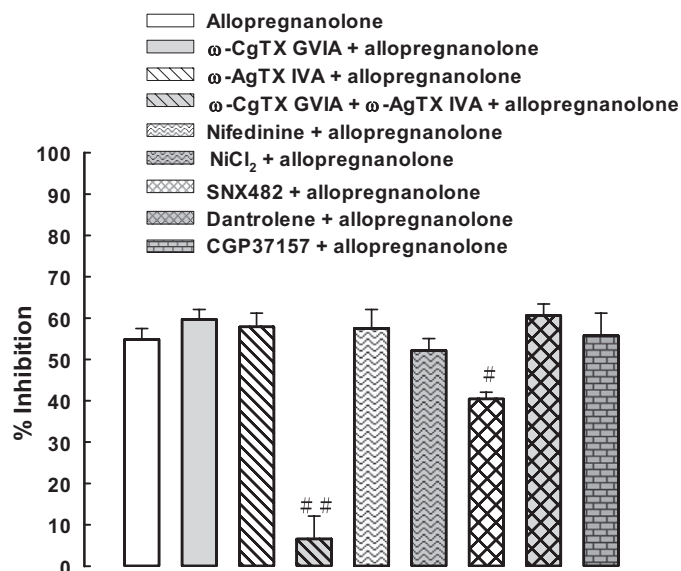


**FIGURE 4** Comparison of the inhibition of glutamate release with allopregnanolone alone and in the presence of  $\omega$ -CgTX GVIA,  $\omega$ -Aga IVA,  $\omega$ -CgTX GVIA and  $\omega$ -Aga IVA, nifedipine, NiCl<sub>2</sub>, SNX482, dantrolene or CGP37157. The data represent the mean  $\pm$  SEM. ( $n = 3-8$ ). #, ## $p < 0.05$  versus the allopregnanolone alone group (one-way ANOVA)

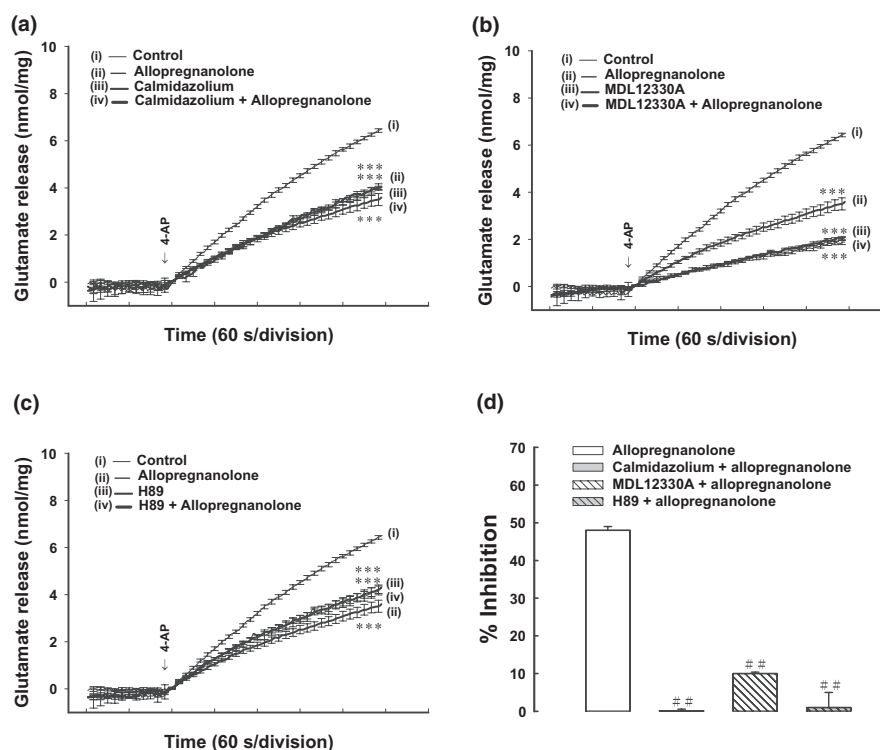


**FIGURE 5** Effects of the calmodulin antagonist calmidazolium, AC inhibitor MDL12330A, and PKA inhibitor H89 on the allopregnanolone-mediated inhibition of 4-AP-evoked glutamate release. (a-c) The effect of 20  $\mu$ M allopregnanolone on glutamate release induced by 1 mM 4-AP in the absence (control) and presence of 25  $\mu$ M calmidazolium, 10  $\mu$ M MDL12330A or 100  $\mu$ M H89. (d) Comparison of the inhibition of glutamate release with allopregnanolone alone and in the presence of calmidazolium, MDL12330A or H89. The data represent the mean  $\pm$  SEM. ( $n = 5$ ). \*\*\* $p < 0.001$  versus the control group (two-tailed Student's  $t$  test). ## $p < 0.05$  versus the allopregnanolone alone group (one-way ANOVA)



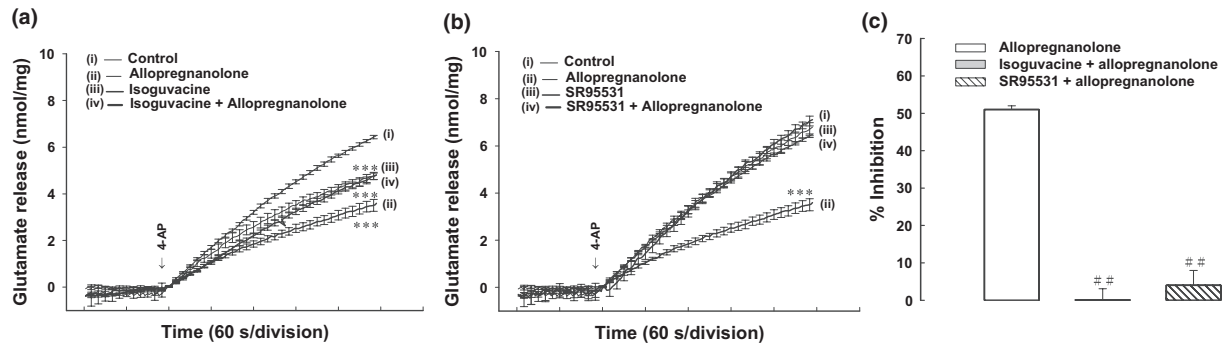


**FIGURE 6** Effects of the GABA<sub>A</sub> receptor agonist isoguvacine and antagonist SR95531 on the allopregnanolone-mediated inhibition of 4-AP-evoked glutamate release. (a, b) The effect of 20  $\mu$ M allopregnanolone on glutamate release induced by 1 mM 4-AP in the absence (control) and presence of 300  $\mu$ M isoguvacine or 100  $\mu$ M SR95531. (c) Comparison of the inhibition of glutamate release with allopregnanolone alone and in the presence of isoguvacine or SR95531. The data represent the mean  $\pm$  SEM. ( $n = 5$ ). \*\*\* $p < 0.001$  versus the control group (two-tailed Student's  $t$  test). ## $p < 0.05$  versus the allopregnanolone alone group (one-way ANOVA)

SR95531, an antagonist of the GABA<sub>A</sub> receptor. In the presence of SR95531 (to block GABA<sub>A</sub> receptors), allopregnanolone failed to effectively inhibit 4-AP-evoked glutamate release [ $F(2,12) = 1.7$ ;  $p > 0.05$ ; Figure 6b]. 100  $\mu$ M SR95531 had no significant effect on 4-AP-evoked glutamate release ( $p = 0.74$ ). On average, allopregnanolone produced a  $4.0\% \pm 4.0\%$  inhibition on 4-AP-evoked glutamate release in the presence of SR95531, which was significantly different the inhibition of allopregnanolone alone ( $51.1 \pm 1.1\%$ ;  $p < 0.05$ ; Figure 6c). Thus, the data favor the activation of GABA<sub>A</sub> receptors in the allopregnanolone-mediated inhibition of glutamate release.

## 4 | DISCUSSION

Previous electrophysiological study by Iwata, et al. (2013) had shown that allopregnanolone at 100 nM inhibits glutamate release in the mechanically dissociated hippocampal CA3 neurons. In their study, the effects of allopregnanolone on glutamate release are monitored indirectly by observing changes in postsynaptic potentials. The use of isolated nerve terminals (synaptosomes) enables a relatively direct evaluation of presynaptic modulation of glutamate release. Here, we have used the synaptosomal model to explore the characteristics and mechanisms of action of allopregnanolone involved in regulating glutamate release in the cerebral cortex. We found that allopregnanolone inhibited the depolarization-evoked Ca<sup>2+</sup>-dependent exocytotic release of glutamate, and this phenomenon was observed to be dose-dependent and was maximal at 20  $\mu$ M, with an IC<sub>50</sub> of 10  $\mu$ M. The concentration of allopregnanolone we used is similar to previous studies, which have shown that 10 to 50  $\mu$ M allopregnanolone inhibits glutamate-induced increases in intracellular Ca<sup>2+</sup> and neuronal death in cultured hippocampal neurons and human NT2 neurons (Frank & Sagratella, 2000; Lockhart et al., 2002). The mechanism(s) contributing to the allopregnanolone-mediated inhibition of glutamate release from cerebrocortical synaptosomes are discussed as follows.

In principle, glutamate release can be modulated at several putative sites in the nerve terminals, including the Na<sup>+</sup> channels, K<sup>+</sup> channels, Ca<sup>2+</sup> channels, as well as release process itself. Na<sup>+</sup> channel inhibition or K<sup>+</sup> channel activation is known to stabilize membrane excitability, which causes a decrease in Ca<sup>2+</sup> entry through N- and P/Q-type Ca<sup>2+</sup> channels and a consequent decrease in glutamate release (Nicholls, 1998; Wu & Saggau, 1997). Our observations suggest that the inhibition of evoked release by allopregnanolone is correlated with a reduction in the activity of N- and P/Q-type Ca<sup>2+</sup> channels without any detectable change in membrane potential. First, 4-AP- versus KCl-evoked glutamate release were significantly inhibited by allopregnanolone. Although 4-AP-evoked glutamate release involves the activation of Na<sup>+</sup> and Ca<sup>2+</sup> channels, 15 mM external KCl-evoked glutamate release involves only Ca<sup>2+</sup> channels (Nicholls, 1998), and this indicates that Na<sup>+</sup> channels are not involved in the inhibitory effect of allopregnanolone on glutamate release. Second, allopregnanolone significantly reduced the evoked increase in intrasynaptosomal Ca<sup>2+</sup> levels. This finding is consistent with a report by Frank and Sagratella (2000), which demonstrated that allopregnanolone decreases glutamate-induced increases in intracellular Ca<sup>2+</sup> in rat hippocampal slices. Third, allopregnanolone did not affect the synaptosomal plasma membrane potential either in the resting state or after depolarization with 4-AP. This suggests that the effect of allopregnanolone in rat cortical synaptosomes is not caused by the attenuation of membrane depolarization, leading to reducing Ca<sup>2+</sup> influx and glutamate release. Finally, the allopregnanolone-mediated inhibition of 4-AP-evoked glutamate release was decreased after the combined application of  $\omega$ -CgTX GVIA (to block N-type VDCCs) and  $\omega$ -Aga IVA (to block P/Q-type VDCCs) or SNX482 (to block R-type Ca<sup>2+</sup> channels), but it was insensitive to nifedipine (a L-type Ca<sup>2+</sup> channel blocker), NiCl<sub>2</sub> (a T-type Ca<sup>2+</sup> channel blocker), dantrolene and CGP37157 (intracellular Ca<sup>2+</sup> release blockers). However, under conditions in which N-, P/Q-, and R-type Ca<sup>2+</sup> channels had been blocked, blockage was not total, probably due to the involvement of other presynaptic pathways. Thus, we conclude the allopregnanolone-mediated inhibition of glutamate release

from rat cerebrocortical nerve terminals due to N-, P/Q-, and R-type  $\text{Ca}^{2+}$  channel suppression. How allopregnanolone affects the activity of these presynaptic  $\text{Ca}^{2+}$  channel activity remains unclear.

An increase in cytosolic  $\text{Ca}^{2+}$  in the nerve terminals is known to affect a  $\text{Ca}^{2+}$ /calmodulin-dependent activation of AC, including AC1 and AC8 (Cooper, 2003; Wang & Storm, 2003). The activation of these ACs increases cAMP levels and activates PKA, which enhances glutamate release (Andrade-Talavera et al., 2013; Rodríguez-Moreno & Sihra, 2013). Whether the observed inhibitory effect of allopregnanolone on the intrasynaptosomal  $\text{Ca}^{2+}$  levels causes a suppression of the  $\text{Ca}^{2+}$ -calmodulin/AC/cAMP/PKA cascade, thereby reducing glutamate release. In elucidating this question, we found that the inhibitory effect of allopregnanolone on 4-AP-evoked glutamate release was prevented by the calmodulin antagonist calmidazolium, the AC inhibitor MDL12330A, and the PKA inhibitor H89, suggesting that the suppression of an  $\text{Ca}^{2+}$ -calmodulin/AC/cAMP/PKA pathway is linked to the action of allopregnanolone. In synaptic terminals, PKA has been shown to phosphorylate numerous synaptic proteins and thereby increases glutamate release (Fykse, Li, & Südhof, 1995; Risinger & Bennett, 1999). Whether modulation of synaptic proteins by PKA or other presynaptic process is involved in the allopregnanolone-mediated inhibition of glutamate release remains to be elucidated.

Interestingly, we also demonstrated that GABA<sub>A</sub> receptor activation is involved in the action of allopregnanolone as the inhibition of glutamate release mediated by allopregnanolone was prevented in synaptosomes treated with GABA<sub>A</sub> receptor agonist and antagonist. Consistent with this action, previous studies have reported that allopregnanolone can modulate the function of GABA<sub>A</sub> receptors (Belelli & Lambert, 2005; Wohlfarth, Bianchi, & Macdonald, 2002). However, the mechanisms that underlie the inhibitory effect of allopregnanolone on glutamate release from the cerebrocortical nerve terminals through presynaptic GABA<sub>A</sub> receptors remain to be elucidated. GABA<sub>A</sub> receptors present at the presynaptic level, and their activation has been shown to reduce VDCCs and glutamate release in rat cerebrocortical nerve terminals (Kullmann et al., 2005; Long et al., 2009; Sieghart, 2006). This inhibition of  $\text{Ca}^{2+}$  influx through GABA<sub>A</sub> receptor activation is thought to occur either through a hyperpolarization of GABA<sub>A</sub> receptor-induced opening of chloride channel (Belelli & Lambert, 2005) or through a depolarized blockade (Long et al., 2009; Yamamoto et al., 2011). Each of these mechanisms may be crucial in the allopregnanolone-mediated inhibition of glutamate release observed in this study. In addition, presynaptic GABA<sub>A</sub> receptor-mediated chloride influx has been shown to reduce the amount of vesicle endocytosis, which subsequently decreases the number of available synaptic vesicles and the release probability (Hull & von Gersdorff, 2004). Thus, the decreased number of synaptic vesicles available for glutamate release may contribute to the observed allopregnanolone-mediated inhibition of glutamate release. This possibility should also be considered.

Allopregnanolone is produced in the brain and has received much attention as neuroprotective agents against different injuries affecting the CNS (Compagnone & Mellon, 2000). For example, allopregnanolone reduces cerebellar purkinje cell or striatal neuronal damage in several in vitro models of ischaemia (Kelley et al., 2008; Knight et al., 2012), as well as attenuate brain damage and cognitive deficits induced by ischemia, amyloid  $\beta$  protein, and traumatic brain injury in rats (Chen et al., 2011; He, Evans et al., 2004; Sayeed et al., 2006; Wang et al., 2010). Several mechanisms have been postulated to underlie the neuroprotective effects of allopregnanolone including neurogenesis (Wang, Johnston, Ball, & Brinton, 2005) and potentiation of GABA<sub>A</sub> receptor activity (Kelley et al., 2008; Knight et al., 2012). In the brain, the ability of allopregnanolone to increase GABA<sub>A</sub> receptor activity can reduce neuronal excitability and hence attenuate excitotoxicity (Lockhart et al., 2002; Sayeed et al., 2006). Excitotoxicity is caused by excessive glutamate release and overstimulation of glutamate receptors, and this glutamate excitotoxicity has been proposed to be involved in the pathogenesis of many brain diseases (Hynd et al., 2004; Lau & Tymianski, 2010; Mehta et al., 2013). Besides its well-known effect on GABA<sub>A</sub> receptors, in this work we have observed that allopregnanolone inhibited evoked glutamate release in synaptosomes isolated from rat cerebral cortex, which may explain, at least in part, for its neuroprotective effect.

In conclusion, the present study is the first to demonstrate that allopregnanolone reduces VDCC activity and  $\text{Ca}^{2+}$ -calmodulin/AC/cAMP/PKA cascade, through the activation of GABA<sub>A</sub> receptors present on cerebrocortical nerve terminals, subsequently reducing glutamate release. Based on our results, we suggest that allopregnanolone might play a physiological role in preventing excessive accumulation of extracellular glutamate, which may result from repetitive activity, thereby exerting a potential neuroprotective effect.

## ACKNOWLEDGMENTS

This work was supported by the research grants from the Shin Kong Wu Ho-Su Memorial Hospital (106-SKH-FJH-03).

## CONFLICT OF INTEREST

The authors declare no competing financial interest.

## ORCID

Su Jane Wang  <http://orcid.org/0000-0002-4675-0259>

## REFERENCES

- Akerman, K. E., Scott, I. G., Heikkilä, J. E., & Heinonen, E. (1987). Ionic dependence of membrane potential and glutamate receptor-linked responses in synaptoneurosome as measured with a cyanine dye, DiS-C2-(5). *Journal of Neurochemistry*, 48, 552–559.
- Andrade-Talavera, Y., Duque-Feria, P., Sihra, T. S., & Rodríguez-Moreno, A. (2013). Pre-synaptic kainate receptor-mediated facilitation of glutamate release involves PKA and Ca(2+) -calmodulin at thalamocortical synapses. *Journal of Neurochemistry*, 126, 565–578.
- Baulieu, E. E., Robel, P., & Schumacher, M. (2001). Neurosteroids: Beginning of the story. *International Review of Neurobiology*, 46, 1–32.
- Belelli, D., & Lambert, J. J. (2005). Neurosteroids: Endogenous regulators of the GABA(A) receptor. *Nature Reviews Neuroscience*, 6, 565–575.
- Chen, S., Wang, J. M., Irwin, R. W., Yao, J., Liu, L., & Brinton, R. D. (2011). Allopregnanolone promotes regeneration and reduces  $\beta$ -amyloid burden in a preclinical model of Alzheimer's disease. *PLoS ONE*, 6, e24293.
- Compagnone, N. A., & Mellon, S. H. (2000). Neurosteroids: Biosynthesis and function of these novel neuromodulators. *Frontiers in Neuroendocrinology*, 21, 1–56.
- Cooper, D. M. (2003). Molecular and cellular requirements for the regulation of adenylate cyclases by calcium. *Biochemical Society Transactions*, 31, 912–915.
- Frank, C., & Sagratella, S. (2000). Neuroprotective effects of allopregnenolone on hippocampal irreversible neurotoxicity in vitro. *Progress in Neuro-Psychopharmacology & Biological Psychiatry*, 24, 1117–1126.
- Fykse, E. M., Li, C., & Südhof, T. C. (1995). Phosphorylation of rabphilin-3A by  $\text{Ca}^{2+}$ /calmodulin- and cAMP-dependent protein kinases in vitro. *Journal of Neuroscience*, 15, 2385–2395.
- Gryniewicz, G., Poenie, M., & Tsien, R. Y. (1985). A new generation of  $\text{Ca}^{2+}$  indicators with greatly improved fluorescence properties. *The Journal of Biological Chemistry*, 260, 3440–3450.
- Guennoun, R., Labombarda, F., Gonzalez Deniselle, M. C., Liere, P., De Nicola, A. F., & Schumacher, M. (2015). Progesterone and allopregnanolone in the central nervous system: Response to injury and implication for neuroprotection. *The Journal of Steroid Biochemistry and Molecular Biology*, 146, 48–61.
- He, J., Evans, C. O., Hoffman, S. W., Oyesiku, N. M., & Stein, D. G. (2004). Progesterone and allopregnanolone reduce inflammatory cytokines after traumatic brain injury. *Experimental Neurology*, 189, 404–412.
- He, J., +, S. W., & Stein, D. G. (2004). Allopregnanolone, a progesterone metabolite, enhances behavioral recovery and decreases neuronal loss after traumatic brain injury. *Restorative Neurology and Neuroscience*, 22, 19–31.
- Headley, P. M., & Grillner, S. (1990). Excitatory amino acids and synaptic transmission: The evidence for a physiological function. *Trends in Pharmacological Sciences*, 11, 205–211.
- Hull, C., & von Gersdorff, H. (2004). Fast endocytosis is inhibited by GABA-mediated chloride influx at a presynaptic terminal. *Neuron*, 44, 469–482.
- Hynd, M. R., Scott, H. L., & Dodd, P. R. (2004). Glutamate-mediated excitotoxicity and neurodegeneration in Alzheimer's disease. *Neurochemistry International*, 45, 583–595.
- Ishihara, Y., Kawami, T., Ishida, A., & Yamazaki, T. (2013). Allopregnanolone-mediated protective effects of progesterone on tributyltin-induced neuronal injury in rat hippocampal slices. *The Journal of Steroid Biochemistry and Molecular Biology*, 135, 1–6.
- Iwata, S., Wakita, M., Shin, M. C., Fukuda, A., & Akaiki, N. (2013). Modulation of allopregnanolone on excitatory transmitters release from single glutamatergic terminal. *Brain Research Bulletin*, 93, 39–46.
- Kelley, M. H., Taguchi, N., Ardeschiri, A., Kuroiwa, M., Hurn, P. D., Traystman, R. J., & Hersen, P. S. (2008). Ischemic insult to cerebellar Purkinje cells causes diminished GABAA receptor function and allopregnanolone neuroprotection is associated with GABAA receptor stabilization. *Journal of Neurochemistry*, 107, 668–678.
- Knight, S. R., Davidson, C., Young, A. M., & Gibson, C. L. (2012). Allopregnanolone protects against dopamine-induced striatal damage after in vitro ischaemia via interaction at GABA A receptors. *Journal of Neuroendocrinology*, 24, 1135–1143.
- Kullmann, D. M., Ruiz, A., Rusakov, D. M., Scott, R., Semyanov, A., & Walker, M. C. (2005). Presynaptic, extrasynaptic and axonal GABAA receptors in the CNS: Where and why? *Progress in Biophysics & Molecular Biology*, 87, 33–46.
- Lau, A., & Tymianski, M. (2010). Glutamate receptors, neurotoxicity and neurodegeneration. *Pflügers Archiv*, 460, 525–542.
- Lejri, I., Grimm, A., Miesch, M., Geoffroy, P., Eckert, A., & Mensah-Nyagan, A. G. (2017). Allopregnanolone and its analog BR 297 rescue neuronal cells from oxidative stress-induced death through bioenergetic improvement. *Biochimica et Biophysica Acta*, 1863, 631–642.
- Lin, T. Y., Chung, C. Y., Lu, C. W., Huang, S. K., Shieh, J. S., & Wang, S. J. (2013). Local anesthetics inhibit glutamate release from rat cerebral cortex synaptosomes. *Synapse (New York, N. Y.)*, 67, 568–579.
- Lin, T. Y., Lu, C. W., Huang, W. J., & Wang, S. J. (2012). Involvement of the cGMP pathway in the osthole-facilitated glutamate release in rat hippocampal nerve endings. *Synapse (New York, N. Y.)*, 66, 232–239.
- Lockhart, E. M., Warner, D. S., Pearlstein, R. D., Penning, D. H., Mehrabani, S., & Boustany, R. M. (2002). Allopregnanolone attenuates N-methyl-D-aspartate-induced excitotoxicity and apoptosis in the human NT2 cell line in culture. *Neuroscience Letters*, 328, 33–36.
- Long, P., Mercer, A., Begum, R., Stephens, G. J., Sihra, T. S., & Jovanovic, J. N. (2009). Nerve terminal GABAA receptors activate  $\text{Ca}^{2+}$ /calmodulin-dependent signaling to inhibit voltage-gated  $\text{Ca}^{2+}$  influx and glutamate release. *The Journal of Biological Chemistry*, 284, 8726–8737.
- Marx, C. E., Trost, W. T., Shampine, L. J., Stevens, R. D., Hulette, C. M., Steffens, D. C., & ... Lieberman, J. A., (2006). The neurosteroid allopregnanolone is reduced in prefrontal cortex in Alzheimer's disease. *Biological Psychiatry*, 60, 1287–1294.
- Mehta, A., Prabhakar, M., Kumar, P., Deshmukh, R., & Sharma, P. L. (2013). Excitotoxicity: Bridge to various triggers in neurodegenerative disorders. *European Journal of Pharmacology*, 698, 6–18.
- National Research Council (US) Committee for the Update of the Guide for the Care and Use of Laboratory Animals. (2011). *Guide for the Care and Use of Laboratory Animals* (8th ed.). Washington (DC): National Academies Press (US).
- Naylor, J. C., Kilts, J. D., Hulette, C. M., Steffens, D. C., Blazer, D. G., Ervin, J. F., ... Marx, C. E. (2010). Allopregnanolone levels are reduced in temporal cortex in patients with Alzheimer's disease compared to cognitively intact control subjects. *Biochimica et Biophysica Acta*, 1801, 951–959.
- Nicholls, D. G. (1998). Presynaptic modulation of glutamate release. *Progress in Brain Research*, 116, 15–22.
- Nicholls, D. G., & Sihra, T. S. (1986). Synaptosomes possess an exocytotic pool of glutamate. *Nature*, 321, 772–773.

- Patte-Mensah, C., Meyer, L., Taleb, O., & Mensah-Nyagan, A. G. (2014). Potential role of allopregnanolone for a safe and effective therapy of neuro-pathic pain. *Progress in Neurobiology*, 113, 70–78.
- Radley, E., Akram, A., Grubb, B. D., & Gibson, C. L. (2012). Investigation of the mechanisms of progesterone protection following oxygen-glucose deprivation in organotypic hippocampal slice cultures. *Neuroscience Letters*, 506, 131–135.
- Raiteri, L., & Raiteri, M. (2000). Synaptosomes still viable after 25 years of superfusion. *Neurochemical Research*, 25, 1265–1274.
- Risinger, C., & Bennett, M. K. (1999). Differential phosphorylation of syntaxin and synaptosome-associated protein of 25 kDa (SNAP-25) isoforms. *Journal of Neurochemistry*, 72, 614–624.
- Rodríguez-Moreno, A., & Sihra, T. S. (2004). Presynaptic kainate receptor facilitation of glutamate release involves protein kinase A in the rat hippocampus. *The Journal of Physiology*, 557, 733–745.
- Rodríguez-Moreno, A., & Sihra, T. S. (2013). Presynaptic kainate receptor-mediated facilitation of glutamate release involves  $\text{Ca}^{2+}$ -calmodulin and PKA in cerebrocortical synaptosomes. *FEBS Letter*, 587, 788–792.
- Saalmann, Y. B., Kirkcaldie, M. T., Waldron, S., & Calford, M. B. (2007). Cellular distribution of the GABAA receptor-modulating 3alpha-hydroxy, 5alpha-reduced pregnane steroids in the adult rat brain. *Journal of Neuroendocrinology*, 19, 272–284.
- Sayeed, I., Guo, Q., Hoffman, S. W., & Stein, D. G. (2006). Allopregnanolone, a progesterone metabolite, is more effective than progesterone in reducing cortical infarct volume after transient middle cerebral artery occlusion. *Annals of Emergency Medicine*, 47, 381–389.
- Schüle, C., Nothdurfter, C., & Rupprecht, R. (2014). The role of allopregnanolone in depression and anxiety. *Progress in Neurobiology*, 113, 79–87.
- Sieghart, W. (2006). Structure, pharmacology, and function of GABAA receptor subtypes. *Advances in Pharmacology*, 54, 231–263.
- Wang, J. M., Johnston, P. B., Ball, B. G., & Brinton, R. D. (2005). The neurosteroid allopregnanolone promotes proliferation of rodent and human neural progenitor cells and regulates cell-cycle gene and protein expression. *Journal of Neuroscience*, 25, 4706–4718.
- Wang, J. M., Singh, C., Liu, L., Irwin, R. W., Chen, S., Chung, E. J., & Brinton, R. D. (2010). Allopregnanolone reverses neurogenic and cognitive deficits in mouse model of Alzheimer's disease. *Proceedings of the National Academy of Sciences of the United States of America*, 107, 6498–6503.
- Wang, H., & Storm, D. R. (2003). Calmodulin-regulated adenylyl cyclases: Cross-talk and plasticity in the central nervous system. *Molecular Pharmacology*, 63, 463–468.
- Wohlfarth, K. M., Bianchi, M. T., & Macdonald, R. L. (2002). Enhanced neurosteroid potentiation of ternary GABA<sub>A</sub> receptors containing the delta subunit. *Journal of Neuroscience*, 22, 1541–1549.
- Wu, L. G., & Saggau, P. (1997). Presynaptic inhibition of elicited neurotransmitter release. *Trends in Neurosciences*, 20, 204–212.
- Yamamoto, S., Yoshimura, M., Shin, M. C., Wakita, M., Nonaka, K., & Akaike, N. (2011). GABAA receptor-mediated presynaptic inhibition on glutamatergic transmission. *Brain Research Bulletin*, 84, 22–30.
- Yunes, R., Estrella, C. R., García, S., Lara, H. E., & Cabrera, R. (2015). Postnatal administration of allopregnanolone modifies glutamate release but not BDNF content in striatum samples of rats prenatally exposed to ethanol. *BioMed Research International*, 2015, 734367.

**How to cite this article:** Chang Y, Hsieh HL, Huang SK, Wang SJ. Neurosteroid allopregnanolone inhibits glutamate release from rat cerebrocortical nerve terminals. *Synapse*. 2019;73:e22076. <https://doi.org/10.1002/syn.22076>





Article

# MicroRNA-29a Disrupts DNMT3b to Ameliorate Diet-Induced Non-Alcoholic Steatohepatitis in Mice

Ya-Ling Yang <sup>1,†</sup>, Hsing-Chun Kuo <sup>2,3,4,5,†</sup>, Feng-Sheng Wang <sup>6</sup> and Ying-Hsien Huang <sup>7,\*</sup> 

<sup>1</sup> Department of Anesthesiology, Kaohsiung Chang Gung Memorial Hospital and Chang Gung University College of Medicine, Kaohsiung 833, Taiwan; yaling453@yahoo.com.tw

<sup>2</sup> Department of Nursing, Chang Gung University of Science and Technology, Chiayi 600, Taiwan; guscsi@gmail.com

<sup>3</sup> Research Fellow, Chiayi Chang Gung Memorial Hospital, Chiayi 600, Taiwan

<sup>4</sup> Research Center for the Industry of Human Ecology and Research Center for Chinese Herbal Medicine, College of Human Ecology, Chang Gung University of Science and Technology, Taoyuan 330, Taiwan

<sup>5</sup> Chronic Diseases and Health Promotion Research Center, CGUST, Chiayi 600, Taiwan

<sup>6</sup> Core Laboratory for Phenomics & Diagnostics, Department of Medical Research, Kaohsiung Chang Gung Memorial Hospital and Chang Gung University College of Medicine, Kaohsiung 833, Taiwan; wangfs@ms33.hinet.net

<sup>7</sup> Department of Pediatrics, Kaohsiung Chang Gung Memorial Hospital and Chang Gung University College of Medicine, Kaohsiung 833, Taiwan

\* Correspondence: yhhuang123@yahoo.com.tw

† These authors contributed equally to this work.

Received: 26 February 2019; Accepted: 24 March 2019; Published: 26 March 2019



**Abstract:** MicroRNA-29 (miR-29) has been found to reduce liver inflammation and fibrosis following a liver injury. Meanwhile, DNA methyltransferase has been reported to participate in the development of non-alcoholic steatohepatitis (NASH). The aim of this study is to investigate the miR-29a regulation of methyltransferase signaling and epigenetic program in NASH progression. **Methods:** miR-29a transgenic mice (miR-29aTg mice) and wild-type littermates were subjected to the methionine-choline-deficient (MCD) diet-induced animal model of NASH. Primary hepatic stellate cells were transfected with a miR-29a mimic and antisense inhibitor. We then analyzed gene expressions with qRT-PCR, immunohistochemical stain, Western blot, and luciferase reporter assay. The results demonstrated that increased miR-29a alleviated the MCD diet-induced body weight loss and steatosis and decreased aspartate aminotransferase (AST) levels in mice. Furthermore, hepatic tissue in miR-29aTg mice displayed a weak fibrotic matrix, as shown with Sirius Red staining concomitant with low fibrotic  $\alpha$ -SMA expression within affected tissues compared to the wild-type mice fed the MCD diet. Forced miR-29a expression reduced the MCD diet exaggeration of reactive oxygen species (ROS) production by immunohistochemically staining 8-OHdG. Increased miR-29a signaling also resulted in the downregulation of DNMT3b, TGF- $\beta$ , IL-6, heme oxygenase-1 (HO-1), p-SMAD3, PI3K, and L3BII expression within the liver tissue. An in vitro luciferase reporter assay further confirmed that miR-29a mimic transfection reduced DNMT3b expression in primary HSCs. Our data provide new insights that miR-29a improves MCD diet-induced liver inflammation, steatosis and fibrosis, and highlight the potential of miR-29a targeted therapy for treating NASH.

**Keywords:** miR-29a; methionine-choline-deficient (MCD) diet; DNMT3b; non-alcoholic steatohepatitis; fibrosis

## 1. Introduction

Non-alcoholic fatty liver disease (NAFLD) occurs when fat is deposited (steatosis) in the liver due to causes besides excessive alcohol use [1] and is one of the most important causes of chronic liver disease. With most studies estimating a prevalence ranging from 25% to 45%, NAFLD increases with the rate of both obesity and diabetes [1,2]. Growing evidence has shown that NAFLD is a major factor in the pathogenesis of insulin resistance, type 2 diabetes, and metabolic syndrome [1], and suggests that diabetes can accelerate NAFLD and liver fibrosis [3]. Non-alcoholic steatohepatitis (NASH), the most extreme form of NAFLD, is considered a key predisposing factor for cirrhosis and has been implicated in the risk of non-viral hepatitis related hepatocellular carcinoma (HCC). Furthermore, it is the most rapidly increasing indication for liver transplantation [1,4]. However, the role of hepatic steatosis in the pathogenesis of NASH and liver fibrosis remains unknown, and few therapeutic agents have yet to improve the liver histology or hepatic protein synthetic function in NASH animal models.

Mice fed methionine-choline-deficient diets (MCD) not only develop fatty liver, but also quickly develop liver fibrosis and hepatocarcinoma [5]. The mechanism of MCD diets responsible for developing fatty liver is associated with the increased synthesis of very-low-density lipoprotein (VLDL) [6] and the subsequently increased cholesterol deposited in the liver. Choline and methionine are dietary methyl donors responsible for maintaining liver function. Previous evidence has demonstrated that rodents given MCD diets have undermethylated DNA methyltransferase genes and thus overexpress these methyltransferases, which explains why these genes are over-methylated despite the methyl-donor deficiency [7]. Controlling epigenetic activity with a DNA methylation inhibitor moderates hepatic wound healing and fibrogenesis [8,9]. In summary, the fibrosis process in the MCD diet animal model is initiated by activating HSC via proinflammatory cytokines and TGF- $\beta$  signaling, as well as a new set of epigenetic marks that transform HSC.

MicroRNAs (miRNAs) are ~22-nucleotide single-stranded non-coding RNAs (guide strands) that reduce endogenous mRNA transcripts [10]. Interestingly, recent studies have demonstrated that miRNAs have important functions in the pathogenesis of steatosis [11] and their epigenetic regulation, which has been shown to coordinate many aspects of fibrogenesis in the liver [12]. In our previous studies [13–19], we have already demonstrated that miR-29a overexpression in cholestatic mice significantly inhibited hepatocellular damage and liver fibrosis. Increased miR-29a function inhibits DNA methyltransferases signaling, thus hindering HSC activation [17]. In addition, elevated miR-29a in SMMC-7721 cells, a steatosis hepatic cell model, has been shown to significantly decrease the free cholesterol accumulation in the cells [20]. Furthermore, Jampoka et al. have found that the serum miR-29a levels were significantly lower in NAFLD patients than in the controls [21]. Therefore, in this study, we used miR-29a transgenic mice (miR-29aTg mice) to test whether miR-29a altered the methyltransferase signaling in diet-induced non-alcoholic steatohepatitis in mice.

## 2. Results

### 2.1. Overexpression of miR-29a Significantly Reduced Hepatocellular Steatosis, Fibrosis, and Damage in MCD Diet Mice

To gain insight into the possible involvement of miR-29a in the development of NASH, we used the MCD diet animal model, which has been shown to induce steatosis, hepatic inflammation, and perisinusoidal fibrosis in the liver [22]. As shown in Figure 1A,B, hematoxylin and eosin stain showed an abundance of fat droplets accumulated in the liver after feeding WT mice the MCD diet for 4 weeks ( $p < 0.001$ ). Compared to the WT littermates, miR-29a overexpression reduced the abundance of fat droplets accumulated in the liver of the miR-29aTg mice (Figure 1A,B,  $p < 0.001$ ). Furthermore, Sirius red stain and western blot also showed a greater accumulation of extracellular matrix (Figure 1C,D) and  $\alpha$ -SMA expression (Figure 1E) in the livers of WT-MCD mice compared to WT-Chou (both  $p < 0.001$ ). However, the miR-29a-MCD mice also had a weaker induction of collagenous matrices and  $\alpha$ -SMA compared to WT-MCD mice ( $p < 0.001$  and  $p = 0.024$ , respectively). Our results indicated that

mice given the MCD diet also had significantly increased aspartate transaminase (AST) and alanine transaminase (ALT) levels in the miR-29aTg mice and WT littermates (all  $p < 0.001$ , Table 1). The overexpression of miR-29a significantly reduced AST levels in the miR-29aTg mice compared with the WT littermates in the MCD diet group. However, we observed no statistically significant difference in ALT levels between miR-29aTg mice and WT littermates in the MCD diet ( $p = 0.983$ ). Collectively, it suggests that the gain of function of miR-29a has a protective effect against MCD diet-induced NASH.

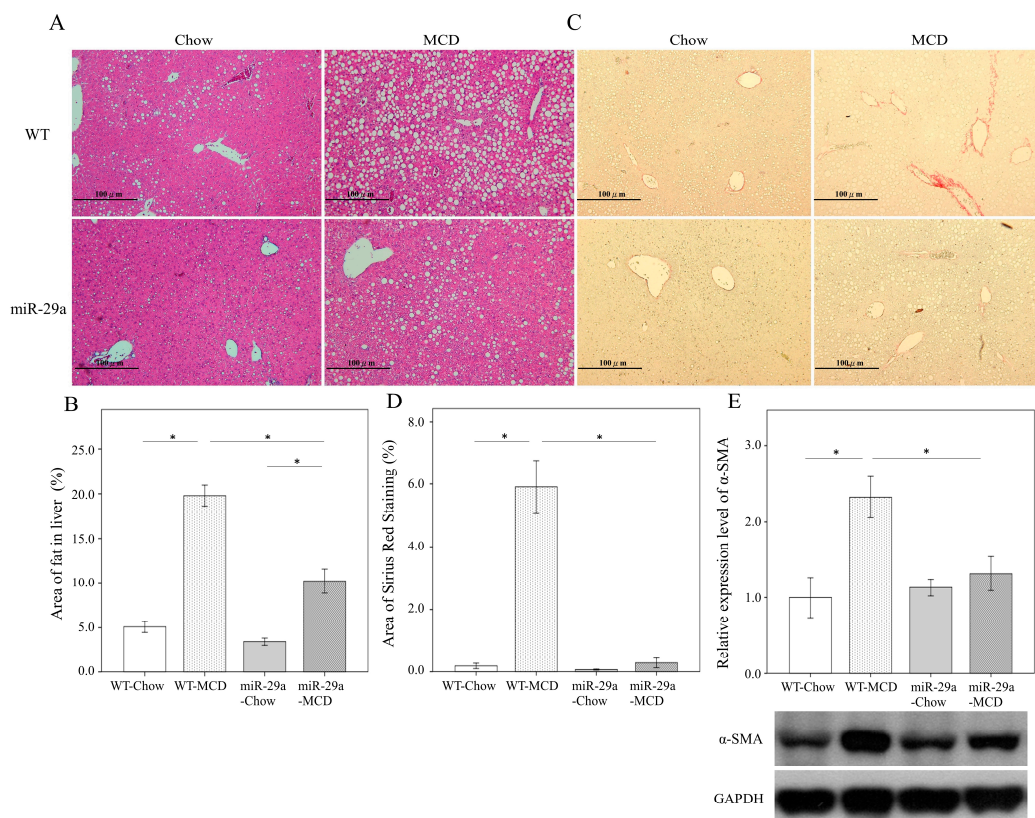


**Figure 1.** Overexpression of miR-29a significantly reduced hepatocellular steatosis and fibrosis in methionine-choline-deficient (MCD) diet mice. The hematoxylin and eosin stain showed an abundance of fat droplets accumulated in the liver after feeding WT mice the MCD diet for 4 weeks (**A,B**,  $p < 0.001$ ). Compared to the WT littermates, miR-29a overexpression reduced the abundance of fat droplets accumulated in the livers of miR-29aTg mice (**A,B**,  $p < 0.001$ ). Furthermore, Sirius red stain and western blot demonstrated a greater accumulation of extracellular matrix (**C,D**) and  $\alpha$ -SMA expression (**E**) in the livers of WT-MCD mice compared to WT-Chow (both  $p < 0.001$ ). However, miR-29a-MCD mice showed a weaker induction of collagenous matrices and  $\alpha$ -SMA compared to WT-MCD mice ( $p < 0.001$  and  $p = 0.024$ , respectively). Data are expressed as the mean  $\pm$  SD of six to eight samples per group. \* indicates a  $p < 0.05$  between the groups.

**Table 1.** Comparison of the changes in the four groups.

	WT-Chow	WT-MCD	miR-29a-Chow	miR-29a-MCD
Body weight (g)	27.79 $\pm$ 4.10	14.69 $\pm$ 1.72 <sup>a</sup>	24.40 $\pm$ 1.81 <sup>a</sup>	14.36 $\pm$ 0.7 <sup>b</sup>
Body weight gain (%)	22.63 $\pm$ 6.20	−46.40 $\pm$ 13.79 <sup>a</sup>	21.06 $\pm$ 4.88	−36.3 $\pm$ 6.68 <sup>b,c</sup>
Liver (g)	1.08 $\pm$ 0.21	0.56 $\pm$ 0.09 <sup>a</sup>	0.97 $\pm$ 0.21	0.49 $\pm$ 0.04 <sup>b</sup>
Liver/body weight (%)	3.88 $\pm$ 0.34	3.79 $\pm$ 0.32	4.02 $\pm$ 1.02	3.41 $\pm$ 0.31
AST (U/L)	73.00 $\pm$ 31.00	192.6 $\pm$ 59.00 <sup>a</sup>	65.25 $\pm$ 21.41	148.09 $\pm$ 36.75 <sup>b,c</sup>
ALT (U/L)	20.00 $\pm$ 10.82	102.6 $\pm$ 92.58 <sup>a</sup>	15.75 $\pm$ 5.59	103.09 $\pm$ 54.05 <sup>b</sup>

WT, wild type; MCS, methionine-choline-deficient; Data expressed as mean  $\pm$  standard deviation; <sup>a</sup>  $p < 0.05$  versus WT-MCS; <sup>b</sup>  $p < 0.05$  versus miR-29a-MCS; <sup>c</sup>  $p < 0.05$  versus WT-MCD.



## 2.2. Increased miR-29a Reduced Oxidative Stress in MCD Diet Mice

To detect oxidative stress in the liver, we immunohistochemically stained 8-OHdG. As demonstrated in Figure 2A,B, the WT-MCD group exhibited an increased expression of 8-OHdG (arrowhead) compared to the WT-Chow group ( $p < 0.001$ ). In the miR-29a-MCD group, the abundance of 8-OHdG were significantly lower than the WT-MCD group ( $p < 0.001$ ), which suggested that oxidative stress was inhibited to miR-29a signaling in the MCD diet-induced NASH.

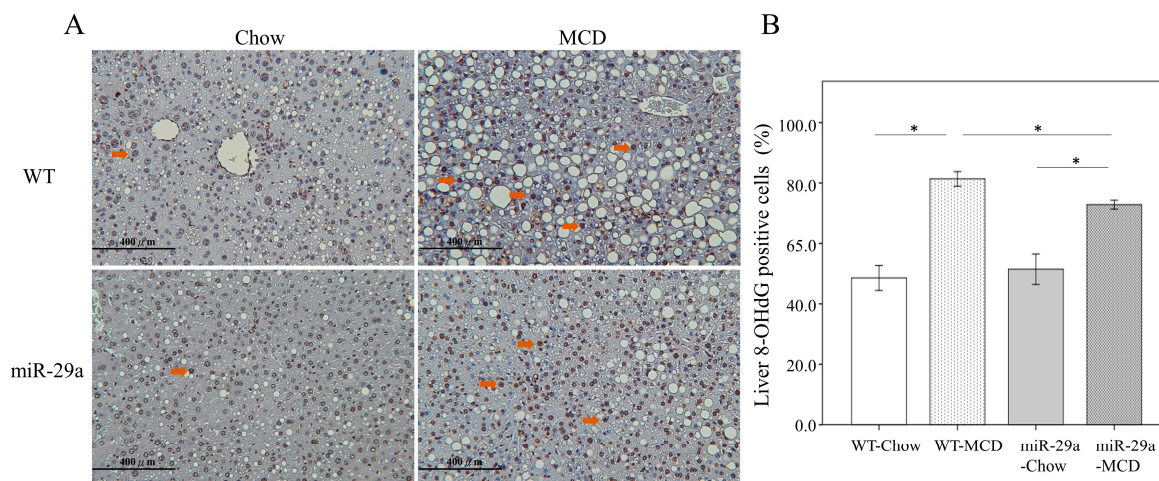


**Figure 2.** Overexpression miR-29a reduced oxidative stress in MCD diet mice. (A) To detect oxidative stress in livers, we used immunohistochemical staining of 8-OHdG. The WT-MCD group exhibited an increased expression of 8-OHdG (arrowhead) compared to the WT-Chow group (B,  $p < 0.001$ ). In the miR-29a-MCD group, the abundance of 8-OHdG was significantly lower than in the WT-MCD group (B,  $p < 0.001$ ), which indicates the inhibition of oxidative stress to miR-29a signaling in MCD diet-induced NASH. Data are expressed as the mean  $\pm$  SD of six to eight samples per group. \* indicates a  $p < 0.05$  between the groups.

## 2.3. Overexpression of miR-29a Reduced DNA Methyltransferases in MCD Diet Mice

We further examined whether the MCD diet altered the concentrations of DNA methyltransferase protein in the hepatic tissue. As shown in Figure 3, the WT-MCD group exhibited increased DNMT3b protein levels when compared to the WT-Chow group ( $p < 0.001$ , respectively). In the miR-29a-MCD group, the abundance of DNMT3b was significantly lower than in the WT-MCD group ( $p = 0.003$ , respectively), which indicates an active response of DNMT 3b to miR-29a signaling in MCD diet-induced NASH.

## 2.4. miR-29a Overexpression Reduces Cytokines and Autophagy in MCD-Diet Liver

We tested whether miR-29a could attenuate proinflammatory cytokine expressions in MCD-diet livers. TGF- $\beta$  and IL-6 are vital for liver fibrogenesis and inflammation [23,24], and HO-1 is a stress-inducible hepatic antioxidant gene in the MCD-induced NASH animal model [25]. qRT-PCR analyses revealed that the MCD-miR29Tg group exhibited a significant decrease in *tgfb1*, *il6*, and *ho-1* transcripts ( $p < 0.001$ , Figure 4A;  $p < 0.001$ , Figure 4B;  $p = 0.002$ , Figure 4C, respectively). Both pSMAD3, a transcriptional activator of TGF- $\beta$ , and p-PI3K have crucial functions in the early activation of HSC [26,27]. Meanwhile, elevated LC3B II expression is an important autophagosomal marker [28]. Using western blot analyses, our study revealed that the miR29-MCD group exhibited a significant decrease in p-SMAD3, p-PI3K, and LC3B II protein levels compared with the WT-MCD group ( $p < 0.001$ , Figure 4D;  $p < 0.001$ , Figure 4E;  $p = 0.005$ , Figure 4F, respectively). These data suggest that the hepatoprotective action of miR-29a in MCD-fed mice is the result of the decrease in ROS generation, profibrotic gene expressions, and autophagy.



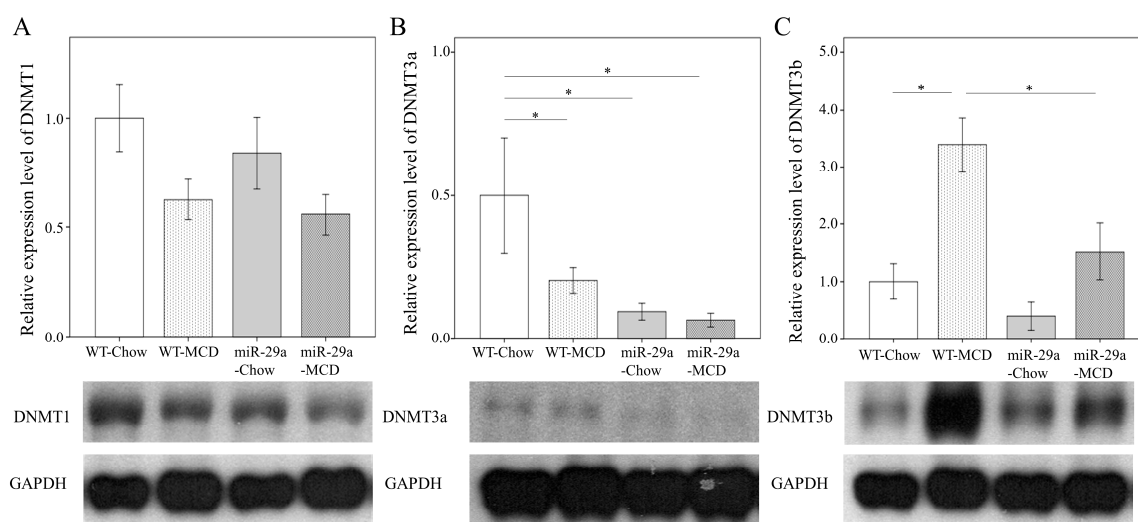


**Figure 3.** Overexpression of miR-29a reduced DNA methyltransferases in MCD diet mice. Comparison of the activation of DNA methyltransferase 1 (A), 3a (B), and 3b (C) in WT and miR-29Tg mice livers. Data from the six to eight samples per group are expressed as mean  $\pm$  SD. \* indicates a  $p < 0.05$  between the groups.

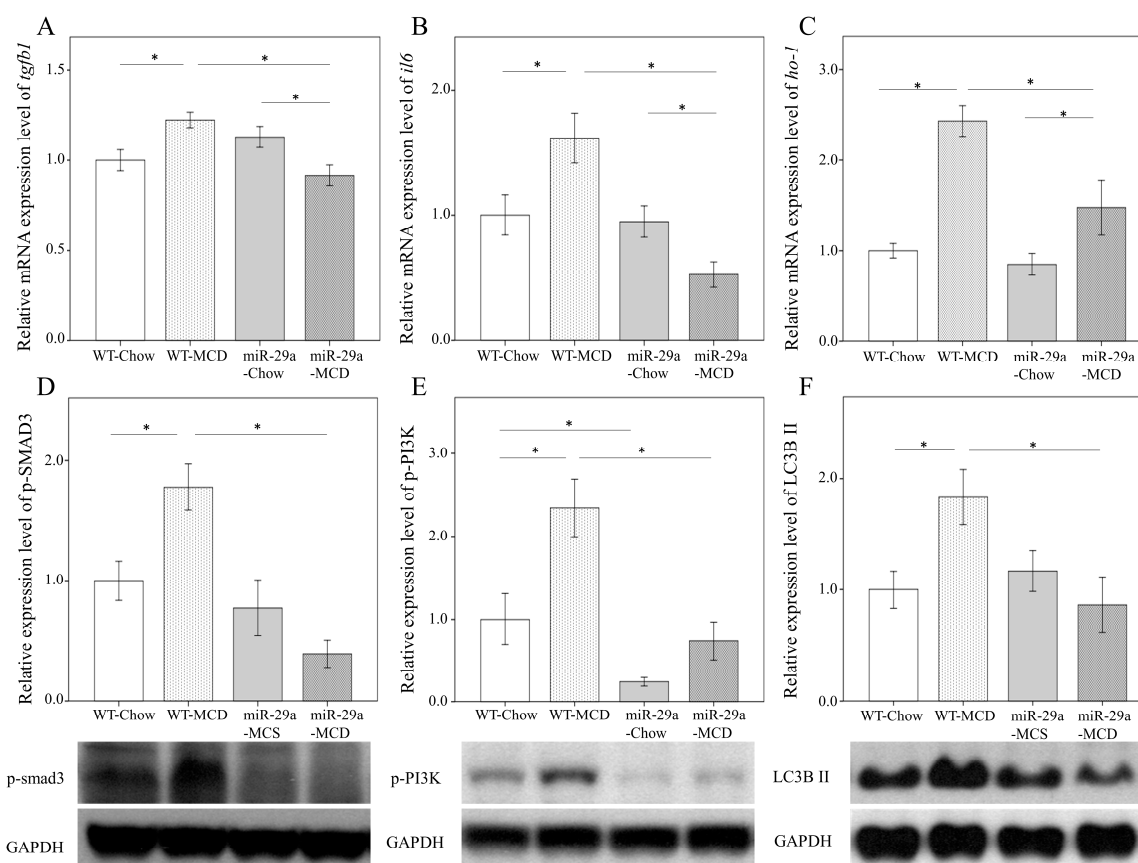


**Figure 4.** Overexpression of miR-29a reduces cytokines and autophagy in MCD-diet mice. Comparison of the mRNA expression of TGF- $\beta$ 1 (A), IL-6 (B), and HO-1 (C), as well as the protein expression of p-SMAD3 (D), p-PI3K (E), and LC3BII (F) in WT and miR-29Tg mice livers. Data from six to eight samples per group are expressed as mean  $\pm$  SD. \* indicates a  $p < 0.05$  between the groups.

### 2.5. miR-29a Targeted the 3'-UTR of DNMT3b

With bioinformatics ([www.mirbase.org](http://www.mirbase.org)) predicting that miR-29a will target DNMT3b expression, we hypothesized that miR-29a may directly affect DNMT3b mRNA expression in HSCs (Figure 5A). As shown in Figure 5B, increasing miR-29a expression significantly reduced the 3'-UTR luciferase reporter activity of DNMT3b, while decreasing it reversed this effect (all  $p < 0.001$ ).

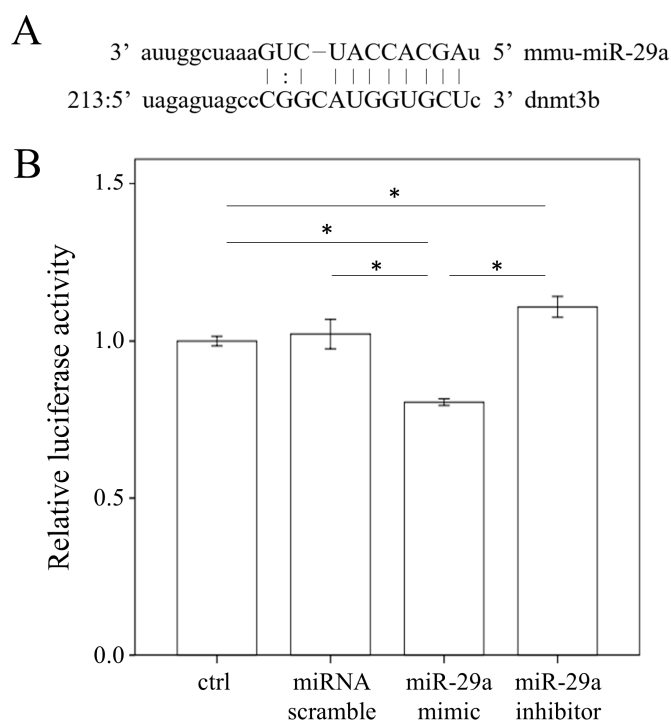


**Figure 5.** DNMT3b is a direct target of miR-29a. **(A)** Bioinformatic prediction indicates that the seed sequence of miR-29a has a high level of complement to DNMT3b 3'UTR. **(B)** miR-29a mimic transfection into primary hepatic stellate cells inhibited the activity of a luciferase reporter gene linked to the 3'UTR of DNMT3b. Data from six to eight samples per group are expressed as mean  $\pm$  SD. \* indicates a  $p < 0.05$  between the groups.

### 3. Discussion

The histological spectrum of non-alcoholic steatohepatitis (NASH) is one of the most commonly occurring chronic liver disease. It ranges from hepatic steatosis to steatohepatitis and fibrosis in the digestive tract and is a risk factor for various metabolic diseases, including obesity, type 2 diabetes, and dyslipidaemia [29–31]. The primary treatment for NASH involves not only reversing the accumulation of Triglycerides (TG) or alanine transaminase (ALT) or aspartate transaminase (AST) in hepatocytes but also effectively curbing hepatitis, thus preventing steatosis from developing into NASH and fibrosis [31]. However, examining how pharmacological compounds prevent NASH syndrome and understanding the mechanisms underlying NASH pathogenesis is critical. Growing evidence in recent years has shown that increased miR-29 significantly restrains human and murine liver fibrosis and the activation of hepatic stellate cells, while its downregulation affects HSC activation [13–18]. In this study, we found that the novel functions of miR-29 on MCD diet include reducing liver steatohepatitis, inflammation, and fibrosis in the livers of miR-29aTg mice. Furthermore, our 8-OHdG study suggested that increased miR-29a results in the inhibition of oxidative stress NASH syndrome in MCD diet. Moreover, the present in vivo study demonstrated that miR-29a-MCD diet livers significantly reduced the expression of TGF- $\beta$ , IL-6, and HO-1 transcripts, as well as p-SMAD3, p-PI3K, and LC3BII, which represented the inhibition of liver inflammation, fibrosis, and autophagy.

The animal model of MCD diet better mimicked the pathological findings of human NASH than did other dietary models [32]. Inflammation, fibrosis and hepatocellular apoptosis developed much more severely and quickly than in mice fed high fat or Western diets [32]. Thus, the MCD diet also better models for study the mechanisms implicated in the pathogenesis of human NASH or therapy testing. However, the MCD model is limited, because it has known disparities with the metabolic profile of human NASH. Instead of being obese, mice fed an MCD diet show significant body weight loss, cachexia and low triglyceride level [33]. Previous studies have shown that long-term administration of a methionine-choline-deficient diets (MCD) lacking methyl donors caused global DNA hypermethylation, which results in fatty liver and fibrosis [7,34]. MCD diet is also an important risk factor since methyl-deficient diets that alter DNMT3b expression may contribute to hypermethylation in specific areas [35,36]. In our study, we have shown significantly decreased DNMT3b levels in the miR-29a-MCD diet group. Our current in vitro study has consistently demonstrated that miR-29a mimic can act as a novel epigenetic regulator by targeting DNMT3b transcript expression in HSCs cells using pMIR-DNMT3b-29a Luciferase reporter activity. We already know that de novo methylation is carried out through DNMT 3a and 3b [37]. Interestingly, Yang et al. have uncovered that DNMT3b regulates macrophage polarization and inflammation in adipose tissue macrophages [38]. Through epigenetic mechanisms, the elevated saturated fatty acids resulted in increased DNMT3b bound to the promoter region of PPAR $\gamma$ 1, which may contribute to deregulated adipose tissue macrophage polarization and ultimately cause inflammation and insulin resistance [38]. Therefore, determining the mechanism of active responses of DNMT3b to miR-29a signaling in MCD diet-inhibited NASH syndrome is critical.

Mounting evidence has indicated that mitochondrial dysfunction resulting from an excess of ROS can alter calcium homeostasis and protein, while the disruption of endoplasmic reticulum (ER) oxidative stress, which is often known as ER stress or UPR, was found in the livers of patients suffering from NASH and obesity [39]. Meanwhile, recent studies have indicated that autophagy is a vital regulatory pathway in liver fibrosis [40] and has been correlated with a direct contribution to HSC activation [41]. Many studies have proposed oxidative stress as one of the most important factors in NASH progression, including hepatocyte apoptosis and the activation of nonparenchymal Kupffer cell and HSCs [42,43]. The obvious effects of miR-29a-MCD diet livers on reducing hepatic p-SMAD3, p-PI3K, and LC3BII, as well as the expression of the oxidative stress-related abundance of 8-OHdG, seem to be in the attenuation of oxidative stress, hepatocyte inflammation, autophagy, and fibrosis. Recent studies have shown that levels of mTOR significantly restrains human and murine adipogenesis and activation of energy metabolism, as previously determined in human NAFLD, using different adipose tissues, while their downregulation obesity and lipotoxicity [44]. Consistently, it was demonstrated that oleuropein, a plentiful phenolic compound, could alleviate high fat diet-induced hepatosteatosis by targeting autophagy signaling pathway [45]. Here, it found that the novel functions of miR-29 on the phosphorylation of AKT/mTOR indicating control hepatocellular carcinoma cell proliferation via the overexpression of miR-29a [46]. Future studies are required that should focus on the link of miR-29a with mTOR pathway can therefore reflect the changes in gain of miR-29a reversed MCD diet hepatic steatosis.

#### 4. Materials and Methods

##### 4.1. Ethics Statement

Our animal protocol has been reviewed and approved by the Institutional Animal Care and Use Committee (IACUC) of Chang Gung Memorial Hospital (#20161214009). We purchased C57BL/6 mice weighing 25–35 g from BioLASCO Taiwan Co., Ltd. (Taipei, Taiwan) All animals were housed in an animal facility at 22 °C, with a relative humidity of 55%, in a 12 h light/12 h dark cycle, with food and sterile tap water available ad libitum.

#### 4.2. Construction and Breeding of the miR-29a Transgenic Mouse Colony

Transgenic mice with overexpressed miR-29a driven by the phosphoglycerate kinase 1 promoter were bred and housed in a specific pathogen-free rodent barrier, as previously described in another study [1]. The genotype of the transgenic mice was probed with PCR and primers (forward: 5'-GAG GATCCCCTCAAGGAT ACCAAGGGATGAAT-3' and reverse 5'-CTTCTAGAAGGAGTGTTCCTAG GTATCCGTCA-3'). We obtained the wild-type mice from littermates that did not carry the construct.

#### 4.3. Animal Model and Experimental Protocol

Six to eight mice were used for all experiments. The mice were categorized into either the “Chou diet” group or the “MCD diet” group. In the NASH mice model, eight-week-old male C57BL/6J mice (CLEA Japan, Tokyo, Japan) were fed an MCS diet (control diet, A02082003B, OPENSOURCE) and MCD diet (A02082002B, OPENSOURCE) for 4 weeks, respectively. The mice's body weight was recorded daily. Liver tissues were dissected, snap-frozen, and processed to isolate the total RNA and proteins. All specimens were stored at  $-80^{\circ}\text{C}$  until biochemical analysis.

#### 4.4. Histological Analysis

For morphometric studies, liver tissues were preserved in 10% formaldehyde, embedded in paraffin, and cut into 3- $\mu\text{m}$  thick sections stained with hematoxylin-eosin or Sirius red. The size of the fat droplets was assessed through hematoxylin and eosin stain, while liver fibrosis was histologically assessed by quantifying the Sirius red-positive area on 10 low-power (magnification,  $\times 40$ ) fields per slide as described in a previous study [47].

#### 4.5. 8-OHdG (8-Hydroxy-2'-deoxyguanosine)

To detect oxidative stress in the liver, we adopted the immunohistochemical staining of 8-OHdG. The 10% paraffin-embedded tissues were cut into 3- $\mu\text{m}$  thick sections. After deparaffinization and rehydration, the sections were heated in a citrate buffer (10 mM, pH 6, Thermo Fisher Scientific, Waltham, MA, USA) in a microwave for 30 min to retrieve the antigens. After washing with PBS, all sections were stained using the UltraVision Quanto Detection System HRP DAB kit (Thermo Fisher Scientific, Chino, CA, USA) and hybridized with the anti-8-OHdG antibody (JaICA, FSZ, Tokyo, Japan). Then the sections were counterstained with Mayer's hematoxylin (ScyTek Laboratories, UT, USA), dehydrated, and mounted using a mounting medium according to the manufacturer's instructions. The quantification data used image J to count the number of cells and calculate the percentage of dying brown cells.

#### 4.6. Real-Time RT-PCR

We used the total RNA (2  $\mu\text{g}$ ) extracted from the HSC cells ( $1 \times 10^6$ ) or liver tissue to generate cDNA with an oligodeoxynucleotide primer (oligo dT15) pursuant to the transcription protocol (Promega, Madison, WI, USA). We followed the manufacturer's instructions to isolate total microRNA using MicroRNA Isolation Kits (BioChain Institute, Inc., Hayward, Newark, CA, USA). Quantitative RT-PCR between both groups were carried out for *tgfb1*, *il6*, and heme oxygenase-1 (*ho-1*) in the liver.  $\beta$ -actin and sno-202 gene expressions were used to regulate gene and microRNA expression, respectively. qPCR was performed in 10  $\mu\text{L}$  SYBR Green PCR Master Mix (Roche, Basel, Switzerland) containing 10 mM forward primers and reverse primers and approximately 30 ng cDNA. The relative quantification of gene expression was based on the comparative CT method, in which the number of targets was given by  $2^{-(\Delta\text{CT target}-\Delta\text{CT calibrator})}$  or  $2^{-\Delta\Delta\text{CT}}$ . The primer sequences for some of the representative signaling molecules were as follows: *tgfb1*: Forward sequence 5'-ATCCTGTCCAAAC TAAGGCTCG-3, Reverse sequence 5'-GACCTCTTTAGCATAGTAGTCCGC-3'; *il6*: Forward sequence 5'-TTTCCTCTGGTCTTCTGGAGTA-3', Reverse sequence 5'-CTCTGAAGGACTCTGGCTTTG-3';



heme oxygenase-1(ho-1): Forward sequence 5'-GCCGAGAATGCTGAGTTCAT-3', Reverse sequence 5'-CTGCTTGTTCGCTCTATCT-3'.

#### 4.7. Western Blotting

The 30- $\mu$ g protein extracts were mixed with a sample buffer, boiled for 10 min, and followed by electrophoresis using 8–15% sodium dodecyl sulfate-polyacrylamide gels. We transferred the proteins in the gels to a polyvinylidene difluoride membrane and incubated the blots with primary antibodies against,  $\alpha$ -SMA (abcam, JHY, Cambridge, UK), DNMT1 (Santa Cruz, CA, USA), DNMT3a (Santa Cruz, CA, USA), DNMT3b (Santa Cruz, CA, USA), p-PI3K (PROTEINTECH, Rosemont, IL, USA), p-SMAD3 (abcam, JHY, Cambridge, UK), LC3B II (Cell signaling, Danvers, MA, USA), and GAPDH (PROTEINTECH, IL, USA) for protein control. After washing the blots with tris-buffered saline and incubating them with horseradish peroxidase-coupled anti-rabbit immunoglobulin-G antibodies (dilution, 1:5000), HRP anti-mouse immunoglobulin-G antibodies (dilution, 1:10,000), and HRP anti-goat immunoglobulin-G antibodies (dilution, 1:10,000) at room temperature for 1 h, we developed them with enhanced chemiluminescence detection (GE Healthcare Biosciences AB, Uppsala, Sweden), exposed them to film, and quantified the signals using densitometry.

#### 4.8. Primary HSC Isolation and Culture

Primary HSCs were isolated from the C57BL/6 livers with sequential digestion of the liver with pronase and collagenase, followed by density gradient centrifugation in 8.5% Nycodenz (Sigma-Aldrich, St. Louis, MO, USA) as previously described in another one of our studies [14]. In short, cells were maintained in Dulbecco's Modified Eagle's medium (DMEM; Gibco, Thermo Fisher Scientific, Inc., Waltham, MA, USA) with 10% fetal bovine serum. The HSCs had a quiescent phenotype after spending 1 day in culture and developed an activated phenotype after 7–14 days. We carried out the passage of the cultured cells after they reached confluence and performed our experiments using cells between passages 8 and 10.

#### 4.9. RNAi Transfection

We used the primary HSC isolation and culture methods that were previously described [47]. Primary HSCs were seeded into 6-cm dishes ( $9 \times 10^5$  cells/dish) overnight and then transfected with a miR-29a precursor (a miR-29a mimic, GE Healthcare Dharmacon, Inc., Lafayette, CO, USA), miR-29a antisense oligonucleotide (GE Healthcare Dharmacon, Inc., Lafayette, CO, USA), or miR control (GE Healthcare Dharmacon, Inc., Lafayette, CO, USA) for 24 h using the Lipofectamine<sup>TM</sup> RNAiMAX Transfection Reagent (Invitrogen, Carlsbad, CA, USA) in accordance with the manufacturer's instructions [27].

#### 4.10. Luciferase Reporter Assay

With bioinformatics ([www.mirbase.org](http://www.mirbase.org)) predicting that miR-29a would target DNMT3b expression, we hypothesized that miR-29a may also directly affect DNMT3b mRNA expression in HSCs. The sequences were annealed and cloned into the pMIR-Report<sup>TM</sup> Luciferase plasmid (Applied Biosystems, Foster City, CA, USA) to generate the pMIR-DNMT3b-29a vector in accordance with the manufacturer's instructions. DNMT3b-3'UTR for miR-29a (position 228–234): forward, 5'-CACCTGTCCCCTTCCTTAGC-3'; reverse, 5'-ACATTCGCAAAA GCGTGCTC-3'. The plasmids were purified using EasyPrep EndoFree Maxi Plasmid Extraction Kit (BIOTOOLS, Ltd., New Taipei, Taiwan). We used empty-vector pMIR without the inserts as a negative control and pMIR-Report  $\beta$ -gal control plasmid for transfection normalization. Primary HSCs were cultured in 24-well plates and transfected with 800 ng of pMIR-29a or pMIR together with 100 ng of pMIR- $\beta$ -gal and 20 pmol of miR-29a precursor or miRNC (GenePharma, Suzhou, China). Lipofectamine 2000 was used for transfection. Forty-eight hours after transfection, luciferase and  $\beta$ -gal activity were measured using the Dual-Light System (Applied Biosystems).

#### 4.11. Statistical Analysis

All values in the figures and tables are expressed as mean  $\pm$  standard deviation (SD). Quantitative data were analyzed using one-way analysis of variance when appropriate. We adopted the least significant difference (LSD) test for post-hoc testing when appropriate. Two-sided *p*-values less than 0.05 were considered statistically significant.

### 5. Conclusions

Our results demonstrated that the epigenetic mechanism of miR-29a in the mitigation of liver fibrosis and hepatic inflammation targets DNMT3b and thus hinders ROS production with a decreased expression of proinflammatory cytokines and autophagy in the MCD diet-induced NASH animal model. Analysis of the results presented here highlights the benefit that controlling miR-29a signaling can serve as an innovative strategy for treating NASH.

**Author Contributions:** Conceive and designed the experiments: Y.-L.Y., H.-C.K., and Y.-H.H. Performed the experiments: Y.-L.Y., H.-C.K., and F.-S.W. Analyzed the data: Y.-L.Y., H.-C.K., and Y.-H.H. Interpretation of the results: Y.-L.Y., F.-S.W. and Y.-H.H. Contributed reagents/materials/analysis tools: F.-S.W., and Y.-L.Y. Preparation of the manuscript: Y.-L.Y., H.-C.K., and Y.-H.H.

**Funding:** This study was supported by grants from the National Health Research Institute (NHRI-EX107-10736SI), Ministry of Science and Technology, Taiwan (106-2314-B-182A-141 -MY3) and Chang Gung Memorial Hospital, Taiwan (CMRPG810941 and 8G1342). However, these organizations had no part in the study design, data collection and analysis, publication decisions, or preparation of the manuscript.

**Acknowledgments:** The authors would like to thank Yuan-Ting Chuang and Chia-Ling Wu for assisting with this article.

**Conflicts of Interest:** The authors hereby declare no conflict of interest.

### References

1. Rinella, M.E. Nonalcoholic fatty liver disease: A systematic review. *JAMA* **2015**, *313*, 2263–2273. [\[CrossRef\]](#)
2. Williams, C.D.; Stengel, J.; Asike, M.I.; Torres, D.M.; Shaw, J.; Contreras, M.; Landt, C.L.; Harrison, S.A. Prevalence of nonalcoholic fatty liver disease and nonalcoholic steatohepatitis among a largely middle-aged population utilizing ultrasound and liver biopsy: A prospective study. *Gastroenterology* **2011**, *140*, 124–131. [\[CrossRef\]](#)
3. Loomba, R.; Abraham, M.; Unalp, A.; Wilson, L.; Lavine, J.; Doo, E.; Bass, N.M. The Nonalcoholic Steatohepatitis Clinical Research Network. Association between diabetes, family history of diabetes, and risk of nonalcoholic steatohepatitis and fibrosis. *Hepatology* **2012**, *56*, 943–951. [\[CrossRef\]](#)
4. Singal, A.K.; Hasanin, M.; Kaif, M.; Wiesner, R.; Kuo, Y.F. Nonalcoholic steatohepatitis is the most rapidly growing indication for simultaneous liver kidney transplantation in the United States. *Transplantation* **2015**, *100*, 607–612. [\[CrossRef\]](#)
5. Mehedint, M.G.; Zeisel, S.H. Choline's role in maintaining liver function: New evidence for epigenetic mechanisms. *Curr. Opin. Clin. Nutr. Metab. Care* **2013**, *16*, 339–345. [\[CrossRef\]](#)
6. Cole, L.K.; Vance, J.E.; Vance, D.E. Phosphatidylcholine biosynthesis and lipoprotein metabolism. *Biochim. Biophys. Acta* **2012**, *1821*, 754–761. [\[CrossRef\]](#)
7. Kovacheva, V.P.; Mellott, T.J.; Davison, J.M.; Wagner, N.; Lopez-Coviella, I.; Schnitzler, A.C.; Blusztajn, J.K. Gestational choline deficiency causes global and Igf2 gene DNA hypermethylation by up-regulation of Dnmt1 expression. *J. Biol. Chem.* **2007**, *282*, 31777–31788. [\[CrossRef\]](#)
8. Sheen-Chen, S.M.; Lin, C.R.; Chen, K.H.; Yang, C.H.; Lee, C.T.; Huang, H.W.; Huang, C.Y. Epigenetic histone methylation regulates transforming growth factor beta-1 expression following bile duct ligation in rats. *J. Gastroenterol.* **2014**, *49*, 1285–1297. [\[CrossRef\]](#)
9. Perugorria, M.J.; Wilson, C.L.; Zeybel, M.; Walsh, M.; Amin, S.; Robinson, S.; White, S.A.; Burt, A.D.; Oakley, F.; Tsukamoto, H.; et al. Histone methyltransferase ASH1 orchestrates fibrogenic gene transcription during myofibroblast transdifferentiation. *Hepatology* **2012**, *56*, 1129–1139. [\[CrossRef\]](#)

10. Roderburg, C.; Urban, G.W.; Bettermann, K.; Vucur, M.; Zimmermann, H.; Schmidt, S.; Janssen, J.; Koppe, C.; Knolle, P.; Castoldi, M.; et al. Micro-RNA profiling reveals a role for miR-29 in human and murine liver fibrosis. *Hepatology* **2011**, *53*, 209–218. [[CrossRef](#)]
11. Su, Q.; Kumar, V.; Sud, N.; Mahato, R.I. MicroRNAs in the pathogenesis and treatment of progressive liver injury in NAFLD and liver fibrosis. *Adv. Drug. Deliv. Rev.* **2018**, *129*, 54–63. [[CrossRef](#)]
12. Moran-Salvador, E.; Mann, J. Epigenetics and Liver Fibrosis. *Cell Mol. Gastroenterol. Hepatol.* **2017**, *4*, 125–134. [[CrossRef](#)]
13. Tiao, M.M.; Wang, F.S.; Huang, L.T.; Chuang, J.H.; Kuo, H.C.; Yang, Y.L.; Huang, Y.H. MicroRNA-29a protects against acute liver injury in a mouse model of obstructive jaundice via inhibition of the extrinsic apoptosis pathway. *Apoptosis* **2014**, *19*, 30–41. [[CrossRef](#)]
14. Huang, Y.H.; Tiao, M.M.; Huang, L.T.; Chuang, J.H.; Kuo, K.C.; Yang, Y.L.; Wang, F.S. Activation of mir-29a in activated hepatic stellate cells modulates its profibrogenic phenotype through inhibition of histone deacetylases 4. *PLoS ONE* **2015**, *10*, e0136453. [[CrossRef](#)] [[PubMed](#)]
15. Huang, Y.H.; Yang, Y.L.; Huang, F.C.; Tiao, M.M.; Lin, Y.C.; Tsai, M.H.; Wang, F.S. MicroRNA-29a mitigation of endoplasmic reticulum and autophagy aberrance counteracts in obstructive jaundice-induced fibrosis in mice. *Exp. Biol. Med. (Maywood)* **2018**, *243*, 13–21. [[CrossRef](#)]
16. Lin, Y.C.; Wang, F.S.; Yang, Y.L.; Chuang, Y.T.; Huang, Y.H. MicroRNA-29a mitigation of toll-like receptor 2 and 4 signaling and alleviation of obstructive jaundice-induced fibrosis in mice. *Biochem. Biophys. Res. Commun.* **2018**, *496*, 880–886. [[CrossRef](#)] [[PubMed](#)]
17. Huang, Y.H.; Yang, Y.L.; Wang, F.S. The Role of miR-29a in the regulation, function, and signaling of liver fibrosis. *Int. J. Mol. Sci.* **2018**, *19*, 1889. [[CrossRef](#)]
18. Li, S.C.; Wang, F.S.; Yang, Y.L.; Tiao, M.M.; Chuang, J.H.; Huang, Y.H. Microarray study of pathway analysis expression profile associated with MicroRNA-29a with regard to murine cholestatic liver injuries. *Int. J. Mol. Sci.* **2016**, *17*, 324. [[CrossRef](#)]
19. Huang, Y.H.; Kuo, H.C.; Yang, Y.L.; Wang, F.S. MicroRNA-29a is a key regulon that regulates BRD4 and mitigates liver fibrosis in mice by inhibiting hepatic stellate cell activation. *Int. J. Med. Sci.* **2019**, *16*, 212–220. [[CrossRef](#)]
20. Liu, M.X.; Gao, M.; Li, C.Z.; Yu, C.Z.; Yan, H.; Peng, C.; Li, Y.; Li, C.G.; Ma, Z.L.; Zhao, Y.; et al. Dicer1/miR-29/HMGCR axis contributes to hepatic free cholesterol accumulation in mouse non-alcoholic steatohepatitis. *Acta Pharm. Sin.* **2017**, *38*, 660–671. [[CrossRef](#)]
21. Jampoka, K.; Muangpaisarn, P.; Khongnomnan, K.; Treeprasertsuk, S.; Tangkijvanich, P.; Payungporn, S. Serum miR-29a and miR-122 as potential biomarkers for Non-Alcoholic Fatty Liver Disease (NAFLD). *Microna* **2018**, *7*, 215–222. [[CrossRef](#)] [[PubMed](#)]
22. Mridha, A.R.; Wree, A.; Robertson, A.A.B.; Yeh, M.M.; Johnson, C.D.; Van Rooyen, D.M.; Haczeyni, F.; Teoh, N.C.; Savard, C.; Ioannou, G.N.; et al. NLRP3 inflammasome blockade reduces liver inflammation and fibrosis in experimental NASH in mice. *J. Hepatol.* **2017**, *66*, 1037–1046. [[CrossRef](#)] [[PubMed](#)]
23. Gressner, A.M.; Weiskirchen, R.; Breitkopf, K.; Dooley, S. Roles of TGF-beta in hepatic fibrosis. *Front. Biosci.* **2002**, *7*, 793–807. [[CrossRef](#)]
24. Nguyen, G.; Park, S.Y.; Le, C.T.; Park, W.S.; Choi, D.H.; Cho, E.H. Metformin ameliorates activation of hepatic stellate cells and hepatic fibrosis by succinate and GPR91 inhibition. *Biochem. Biophys. Res. Commun.* **2018**, *495*, 2649–2656. [[CrossRef](#)]
25. Li, W.; Ma, F.; Zhang, L.; Huang, Y.; Li, X.; Zhang, A.; Hou, C.; Zhu, Y.; Zhu, Y. S-propargyl-cysteine exerts a novel protective effect on methionine and choline deficient diet-induced fatty liver via Akt/Nrf2/HO-1 pathway. *Oxid. Med. Cell. Longev.* **2016**, *2016*, 1–17. [[CrossRef](#)] [[PubMed](#)]
26. Yoshida, K.; Murata, M.; Yamaguchi, T.; Matsuzaki, K. TGF-beta/Smad signaling during hepatic fibro-carcinogenesis (review). *Int. J. Oncol.* **2014**, *45*, 1363–1371. [[CrossRef](#)] [[PubMed](#)]
27. Cai, C.X.; Buddha, H.; Castellino-Prabhu, S.; Zhang, Z.; Britton, R.S.; Bacon, B.R.; Neuschwander-Tetri, B.A. Activation of insulin-PI3K/Akt-p70S6K pathway in hepatic stellate cells contributes to fibrosis in nonalcoholic steatohepatitis. *Dig. Dis. Sci.* **2017**, *62*, 968–978. [[CrossRef](#)] [[PubMed](#)]
28. Meng, D.; Li, Z.; Wang, G.; Ling, L.; Wu, Y.; Zhang, C. Carvedilol attenuates liver fibrosis by suppressing autophagy and promoting apoptosis in hepatic stellate cells. *Biomed. Pharm.* **2018**, *108*, 1617–1627. [[CrossRef](#)]
29. Anderson, N.; Borlak, J. Molecular mechanisms and therapeutic targets in steatosis and steatohepatitis. *Pharm. Rev.* **2008**, *60*, 311–357. [[CrossRef](#)] [[PubMed](#)]

30. Tiniakos, D.G.; Vos, M.B.; Brunt, E.M. Nonalcoholic fatty liver disease: Pathology and pathogenesis. *Annu. Rev. Pathol.* **2010**, *5*, 145–171. [[CrossRef](#)]
31. Dowman, J.K.; Armstrong, M.J.; Tomlinson, J.W.; Newsome, P.N. Current therapeutic strategies in non-alcoholic fatty liver disease. *Diabetes Obes. Metab.* **2011**, *13*, 692–702. [[CrossRef](#)] [[PubMed](#)]
32. Lau, J.K.; Zhang, X.; Yu, J. Animal models of non-alcoholic fatty liver disease: Current perspectives and recent advances. *J. Pathol.* **2017**, *241*, 36–44. [[CrossRef](#)] [[PubMed](#)]
33. Rinella, M.E.; Green, R.M. The methionine-choline deficient dietary model of steatohepatitis does not exhibit insulin resistance. *J. Hepatol.* **2004**, *40*, 47–51. [[CrossRef](#)] [[PubMed](#)]
34. Tryndyak, V.P.; Latendresse, J.R.; Montgomery, B.; Ross, S.A.; Beland, F.A.; Rusyn, I.; Pogribny, I.P. Plasma microRNAs are sensitive indicators of inter-strain differences in the severity of liver injury induced in mice by a choline- and folate-deficient diet. *Toxicol. Appl. Pharmacol.* **2012**, *262*, 52–59. [[CrossRef](#)]
35. Elsharkawy, A.M.; Oakley, F.; Mann, D.A. The role and regulation of hepatic stellate cell apoptosis in reversal of liver fibrosis. *Apoptosis* **2005**, *10*, 927–939. [[CrossRef](#)] [[PubMed](#)]
36. Kadayifci, F.Z.; Zheng, S.; Pan, Y.X. Molecular mechanisms underlying the link between diet and DNA methylation. *Int. J. Mol. Sci.* **2018**, *19*, 4055. [[CrossRef](#)]
37. Mantovani, A.; Sica, A.; Sozzani, S.; Allavena, P.; Vecchi, A.; Locati, M. The chemokine system in diverse forms of macrophage activation and polarization. *Trends Immunol.* **2004**, *25*, 677–686. [[CrossRef](#)] [[PubMed](#)]
38. Yang, X.; Wang, X.; Liu, D.; Yu, L.; Xue, B.; Shi, H. Epigenetic regulation of macrophage polarization by DNA methyltransferase 3b. *Mol. Endocrinol.* **2014**, *28*, 565–574. [[CrossRef](#)]
39. Sharma, N.K.; Das, S.K.; Mondal, A.K.; Hackney, O.G.; Chu, W.S.; Kern, P.A.; Rasouli, N.; Spencer, H.J.; Yao-Borengasser, A.; Elbein, S.C. Endoplasmic reticulum stress markers are associated with obesity in nondiabetic subjects. *J. Clin. Endocrinol. Metab.* **2008**, *93*, 4532–4541. [[CrossRef](#)]
40. Yi, D.Q.; Yang, X.F.; Liao, D.F.; Wu, Q.; Fu, N.; Hu, Y.; Cao, T. Effect of autophagy over liver diseases. *Chin. Med. Sci. J. (Chung-kuo i hsueh k'o hsueh tsa chih)* **2016**, *31*, 65–68. [[CrossRef](#)]
41. Kim, R.S.; Hasegawa, D.; Goossens, N.; Tsuchida, T.; Athwal, V.; Sun, X.; Robinson, C.L.; Bhattacharya, D.; Chou, H.I.; Zhang, D.Y.; et al. The XBP1 arm of the unfolded protein response induces fibrogenic activity in hepatic stellate cells through autophagy. *Sci. Rep.* **2016**, *6*, 39342. [[CrossRef](#)]
42. Takaki, A.; Kawai, D.; Yamamoto, K. Multiple hits, including oxidative stress, as pathogenesis and treatment target in non-alcoholic steatohepatitis (NASH). *Int. J. Mol. Sci.* **2013**, *14*, 20704–20728. [[CrossRef](#)] [[PubMed](#)]
43. Hernandez-Gea, V.; Hilscher, M.; Rozenfeld, R.; Lim, M.P.; Nieto, N.; Werner, S.; Devi, L.A.; Friedman, S.L. Endoplasmic reticulum stress induces fibrogenic activity in hepatic stellate cells through autophagy. *J. Hepatol.* **2013**, *59*, 98–104. [[CrossRef](#)] [[PubMed](#)]
44. Estep, J.M.; Goodman, Z.; Sharma, H.; Younossi, E.; Elarainy, H.; Baranova, A.; Younossi, Z. Adipocytokine expression associated with miRNA regulation and diagnosis of NASH in obese patients with NAFLD. *Liver Int. Off. J. Int. Assoc. Study Liver* **2015**, *35*, 1367–1372. [[CrossRef](#)] [[PubMed](#)]
45. Porcu, C.; Sideri, S.; Martini, M.; Cocomazzi, A.; Galli, A.; Tarantino, G.; Balsano, C. Oleuropein induces AMPK-Dependent autophagy in NAFLD mice, regardless of the gender. *Int. J. Mol. Sci.* **2018**, *19*, 3948. [[CrossRef](#)]
46. Zhu, X.C.; Dong, Q.Z.; Zhang, X.F.; Deng, B.; Jia, H.L.; Ye, Q.H.; Qin, L.X.; Wu, X.Z. MicroRNA-29a suppresses cell proliferation by targeting SPARC in hepatocellular carcinoma. *Int. J. Mol. Med.* **2012**, *30*, 1321–1326. [[CrossRef](#)]
47. Yang, Y.L.; Wang, F.S.; Li, S.C.; Tiao, M.M.; Huang, Y.H. MicroRNA-29a alleviates bile duct ligation exacerbation of hepatic fibrosis in mice through epigenetic control of methyltransferases. *Int. J. Mol. Sci.* **2017**, *18*, 192. [[CrossRef](#)] [[PubMed](#)]



© 2019 by the authors. Licensee MDPI, Basel, Switzerland. This article is an open access article distributed under the terms and conditions of the Creative Commons Attribution (CC BY) license (<http://creativecommons.org/licenses/by/4.0/>).